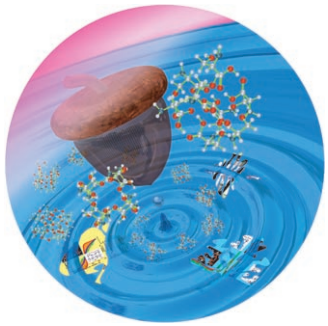
Cover Picture

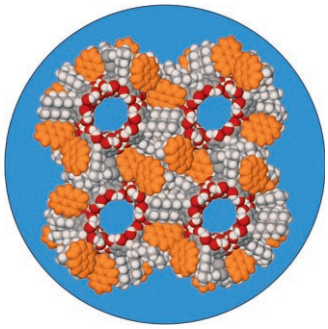


Justin O. Ehresmann, Philip W. Kletnieks, Ann Liang, Vinesh A. Bhirud, Olesya P. Bagatchenko, Eric J. Lee, Meghan Klaric, Bruce C. Gates,* and James F. Haw*

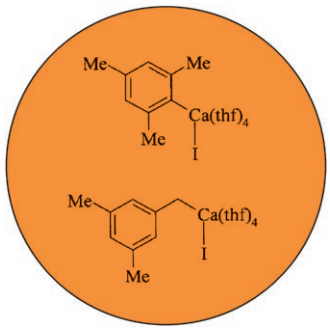
Zeolite-supported transition-metal catalysts are of importance in the petrochemical industry. However, the fabrication and characterization of well-defined systems remains a challenge. In their Communication on page 574 ff., B. C. Gates, J. F. Haw, and co-workers present computational and experimental evidence that the rhodium complex $\{Rh(C_2H_4)_2\}$ supported on zeolite Y is a single-site catalyst with a uniform structure. The cover picture shows the rotation of the ethylene ligands about the Rh^+ center (green sphere).



Serine Octamers
In their Review on page 554 ff., R. G. Cooks and S. C. Nanita examine the generation of homochirality in reactions of serine octamers with the help of powerful mass-spectrometric methods.



Organic Nanotubes
In their Communication on page 570 ff., J. L. Atwood and co-workers describe the synthesis of a new class of organic nanotubes from pyrogallo[4]arenes and the possibility of including multiple guests within such tubular arrays.



Grignard reagents
Mesitylcalcium iodide, a heavy Grignard reagent, and its rearrangement into 3,5-dimethylbenzylcalcium iodide are described by M. Westerhausen et al. in their Communication on page 609 ff.

Contents

VIP ***The following Communications have been judged by at least two referees to be "very important papers" and will be published online at www.angewandte.org soon:***

*J. Deschamp, O. Chuzel, J. Hannedouche, O. Riant**
Highly Diastereo- and Enantioselective Copper-Catalyzed Tandem Conjugated Reduction/Aldol Reaction to Ketones

J. W. Bode, R. M. Fox, K. D. Baucom*
Chemoselective Amide Ligations by Decarboxylative Condensations of *N*-Alkylhydroxylamines and α-Keto Acids

A. Oleksi, A. G. Blanco, R. Boer, I. Usón, J. Aymamí, A. Rodger, M. J. Hannon, M. Coll**
Molecular Recognition of a Three-Way DNA Junction by a Metallosupramolecular Helicate

J. E. Banham, C. R. Timmel, R. J. M. Abbott, S. M. Lea, G. Jeschke**
A New Tool for Characterization of Weak Protein–Protein Interactions: Evidence from DEER for the Trimerization of a von Willebrand Factor A Domain in Solution

B. H. Lipshutz, B. A. Frieman, A. E. Tomaso, Jr.*
Copper-in-Charcoal (Cu/C): Heterogeneous, Copper-Catalyzed Asymmetric Hydrosilylations

J. T. Shaw, J. M. Mitchell*
A Structurally Diverse Library of Polycyclic Lactams Resulting from the Systematic Placement of Proximal Functional Groups

Meeting Reviews

Antibiotics and Much More — *K. Krohn* — **536**

Books

Quaternary Stereocenters — Jens Christoffers, Angelika Baro — *reviewed by M. Oestreich* — **540**

Elegant Solutions — Philip Ball — *reviewed by P. Cintas* — **541**

Highlights

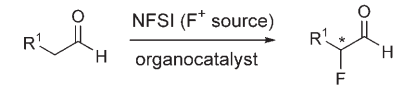
Organocatalysis

P. M. Pihko* — **544 – 547**

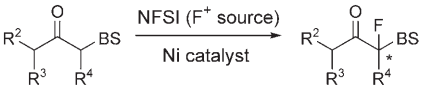
Enantioselective α-Fluorination of Carbonyl Compounds: Organocatalysis or Metal Catalysis?

Five ground-breaking studies in enantioselective α-fluorination of carbonyl compounds have been disclosed. Four describe the use of amine organocatalysts to promote the asymmetric fluorination of aldehydes, whereas the fifth describes a highly enantioselective fluorination of carbonyl compounds capable of two-point binding (e.g. β-ketoesters). NFSI = *N*-fluorobenzenesulfonimide.

Enders, Jorgensen, Barbas, MacMillan:



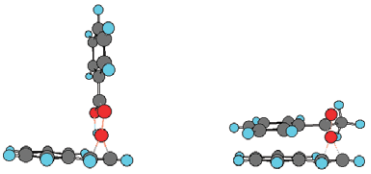
Shibata/Toru:



Synthetic Methods

U. M. Lindström,*
F. Andersson — **548 – 551**

Hydrophobically Directed Organic Synthesis

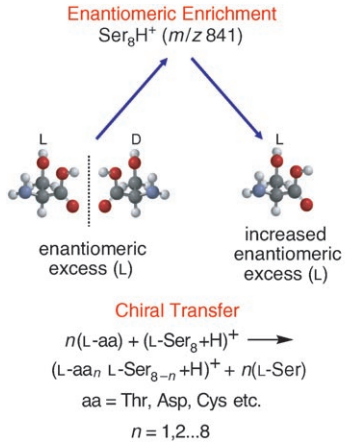


Going with the flow: Nature has perfected the use of hydrophobic interactions in biochemical processes. Some recent work on synthesis has shown that reactions in water may be predisposed to favor transition states that optimize hydrophobic interactions (see picture). Thus, it should in principle be possible to use hydrophobic interactions as a nonbonding element of control for synthetic reactions in water.

InterScience

© 2006 Wiley-VCH Verlag GmbH & Co. KGaA, Weinheim

Reviews



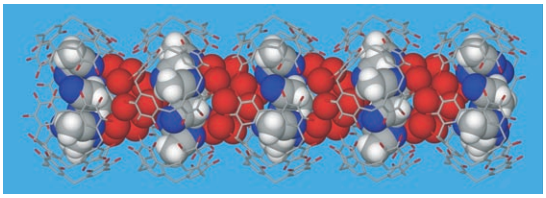
A remarkable example of magic-number clustering and chiral recognition in molecular aggregates is shown by serine octamers, which partly explains two essential steps in the origin of homochirality: enantiomeric enrichment and chiral transfer (see picture). Extensive investigations over the past five years have revealed many facts about the structure(s), chemistry, and mechanism of formation of serine octamers.

Mass Spectrometry

S. C. Nanita, R. G. Cooks* ___ **554 – 569**

Serine Octamers: Cluster Formation, Reactions, and Implications for Biomolecule Homochirality

Communications

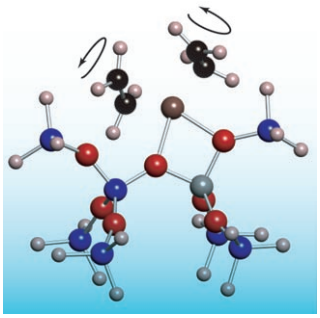


The last straw: Sonication of *C*-hexylpyrogallol[4]arene with pyrene, acetonitrile, and water results in the formation of crystalline organic nanotubes. Alternating pockets of acetonitrile and water are contained within the large internal diameter of the tube formed by the calixarenes (see picture; the tube and solvent molecules are shown as stick and space-filling representations, respectively).

Nanostructures

S. J. Dalgarno, G. W. V. Cave, J. L. Atwood* ___ **570 – 574**

Toward the Isolation of Functional Organic Nanotubes



The proof of the pudding is in the analysis! The mononuclearity of the metal in a zeolite-supported Rh^+ catalyst with two exchangeable ethylene ligands (see picture; Rh brown, C black, Al gray, O red, Si blue) was confirmed through EXAFS studies, and its dynamic uniformity was demonstrated through variable-temperature NMR spectroscopic studies.

Supported Catalysts

J. O. Ehresmann, P. W. Kletnieks, A. Liang, V. A. Bhirud, O. P. Bagatchenko, E. J. Lee, M. Klaric, B. C. Gates,* J. F. Haw* ___ **574 – 576**

Evidence from NMR and EXAFS Studies of a Dynamically Uniform Mononuclear Single-Site Zeolite-Supported Rhodium Catalyst

For the USA and Canada:
ANGEWANDTE CHEMIE International Edition (ISSN 1433-7851) is published weekly by Wiley-VCH PO Box 191161, D 69451 Weinheim, Germany. Air freight and mailing in the USA by Publications Expediting Inc. 200 Meacham Ave., Elmont, NY 11003. Periodicals postage paid at Jamaica NY 11431. US POSTMASTER: send address changes to *Angewandte Chemie*, Wiley-VCH, 111 River Street, Hoboken, NJ 07030. Annual subscription price for institutions: US$ 5685/5168 (valid for print and electronic / print or electronic delivery); for individuals who are personal members of a national chemical society prices are available on request. Postage and handling charges included. All prices are subject to local VAT/sales tax.

© 2006 Wiley-VCH Verlag GmbH & Co. KGaA, Weinheim

The best in chemistry –

for more than a hundred years



A Journal of the Gesellschaft Deutscher Chemiker

Angewandte
International Edition **Chemie**

www.angewandte.org

1888: ***The beginning of a success story***

Constant Innovations

1962: *First issue of the International Edition*
1976: *Graphical abstracts*
1979: *Cover pictures*
1988: *Centenary of Angewandte*
1989: *Routine use of color*
1991: *New section: Highlights*
1992: *Computerized editorial tracking system*
1995: *Internet service for readers*
1998: *Regular press service; full-text online*
2000: *New section: Essays; EarlyView: Communications available online ahead of the printed version*
2001: *New section: Minireviews*
2002: *Online submission of manuscripts*
2003: *Weekly publication; new section: News; new layout*
2004: *Backfiles (1962-1997); ManuscriptXpress: Online system for authors and referees*



Angewandte's advisors...

Wolfgang A. Herrmann
Technische Universität München

»***Angewandte Chemie*** *is at home in Germany and successful in the world. This journal has developed as the international community of chemists has grown together. Today,* ***Angewandte*** *is of central importance for modern chemists. It is the only journal I afford not to hurry through in the office – it's my "home is my castle journal"!«*

Angewandte Chemie International Edition *is a journal of the German Chemical Society (GDCh)*

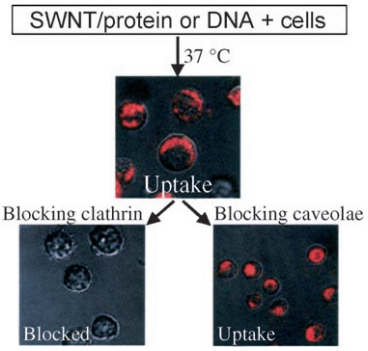
GDCh

WILEY InterScience® DISCOVER SOMETHING GREAT

WILEY-VCH

19981506_gu

Endocytosis or not endocytosis: The pathway of the internalization of single-walled carbon nanotube (SWNT) conjugates into mammalian cells was determined to be energy-dependent endocytosis through clathrin-coated pits.

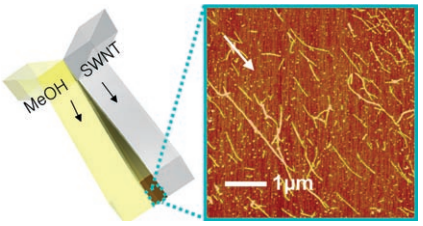


Nanotechnology

N. W. S. Kam, Z. Liu, H. Dai* **577 – 581**

Carbon Nanotubes as Intracellular Transporters for Proteins and DNA: An Investigation of the Uptake Mechanism and Pathway

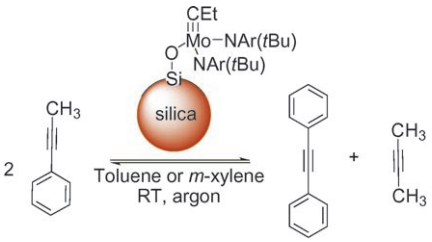
Well-defined patterns of single-walled carbon nanotubes (SWNTs) with controlled density and alignment were produced by using controlled flocculation in multistream laminar microfluidic networks (see picture). Complex, well-defined SWNT patterns could be generated by control of flow and substrate conditions.



Electronic Devices

J.-U. Park, M. A. Meitl, S.-H. Hur, M. L. Usrey, M. S. Strano, P. J. A. Kenis, J. A. Rogers* **581 – 585**

In Situ Deposition and Patterning of Single-Walled Carbon Nanotubes by Laminar Flow and Controlled Flocculation in Microfluidic Channels



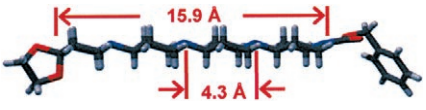
An alkylidyne molybdenum amide complex is attached to nontoxic, amorphous silica to form a highly active, recyclable heterogeneous catalyst for alkyne metathesis. The catalyst does not undergo alkyne polymerization, can be utilized at a loading of <1 mol% at room temperature, and has shown unprecedented metathesis activity for the homodimerization of 2-propynylthiophene, a substrate that was previously problematic for alkyne metathesis.

Synthetic Methods

H. Weissman, K. N. Plunkett, J. S. Moore* **585 – 588**

A Highly Active, Heterogeneous Catalyst for Alkyne Metathesis

An oligomeric backbone of piperidine rings can be synthesized by solution or solid-phase synthesis. These oligomers adopt well-defined, rodlike structures with all the piperidine residues in chair conformations (see picture) both in solution (D_2O, CD_3OD) and the solid state.



Molecular Rods

V. Semetey, D. Moustakas, G. M. Whitesides* **588 – 591**

Synthesis and Conformational Study of Water-Soluble, Rigid, Rodlike Oligopiperidines

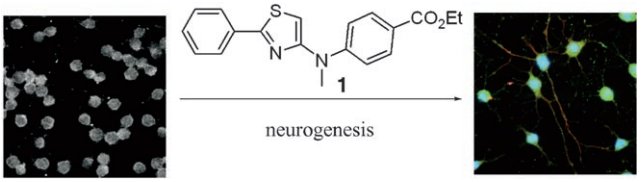
© 2006 Wiley-VCH Verlag GmbH & Co. KGaA, Weinheim

Contents

Neurochemistry

M. Warashina, K. H. Min, T. Kuwabara, A. Huynh, F. H. Gage, P. G. Schultz,* S. Ding* _____ **591 – 593**

A Synthetic Small Molecule That Induces Neuronal Differentiation of Adult Hippocampal Neural Progenitor Cells

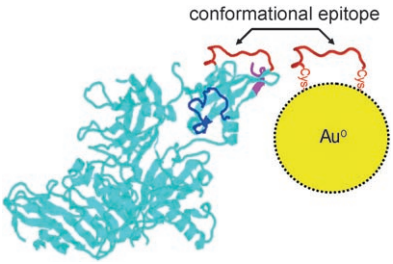


Brain power: An image-based screen of a chemical library was carried out to identify molecules that regulate the differentiation of adult rat hippocampal neural stem cells. Neuropathiazol (**1**) induces selective neuronal differentiation and competitively suppresses astrocyte differentiation. This compound should be a useful tool to study the processes that control stem-cell fate both in vitro and in vivo.

Antibodies

A. E. Gerdon, D. W. Wright,* D. E. Cliffel* _____ **594 – 598**

Epitope Mapping of the Protective Antigen of *B. anthracis* by Using Nanoclusters Presenting Conformational Peptide Epitopes



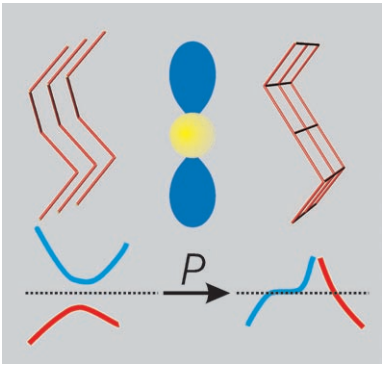
Secondary choice: Conformational and linear peptide epitopes from the protective antigen of *B. anthracis* were presented on the surface of monolayer-protected clusters to produce immunoreactive nanostructures. Quartz crystal microbalance studies of these antigen mimics with antibodies suggested a significant difference between two epitopes with identical primary structure but different secondary structure.

Lone Pairs of Electrons

S. Deng, J. Köhler, A. Simon* **599 – 602**

Unusual Lone Pairs in Tellurium and Their Relevance for Superconductivity

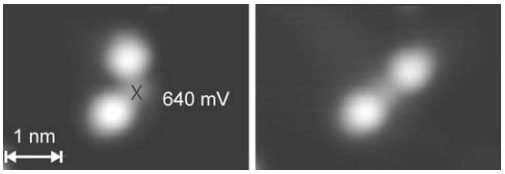
When pairs break up: Ab initio calculations are used to quantitatively characterize the stability and shape of an unusual type of lone pair in tellurium. By comparing the calculated band structures for tellurium under ambient and high pressure, it is shown that the flat/steep-band condition necessary for superconductivity is created for the high-pressure modification Te-II through the delocalization and breakdown of the lone pairs (see scheme).



Single-Molecule Studies

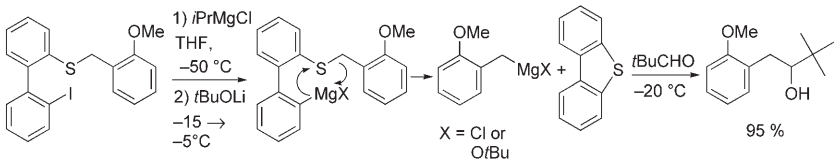
J. Henzl, M. Mehlhorn, H. Gawronski, K.-H. Rieder, K. Morgenstern* **603 – 606**

Reversible *cis–trans* Isomerization of a Single Azobenzene Molecule



Single working molecule: The controlled *cis–trans* isomerization (see picture; left *cis*, right *trans* isomer) of a single molecule of the azobenzene derivative Disperse Orange 3 on a Au(111) metal surface is acccomplished by injection of tunneling electrons at a certain position (cross in left picture) into the molecule.

© 2006 Wiley-VCH Verlag GmbH & Co. KGaA, Weinheim

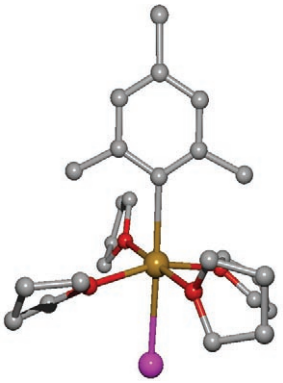


Switch it: Iodobiphenyl thioethers readily undergo an iodine–magnesium exchange followed by, after the addition of *t*BuOLi, an intramolecular sulfur–magnesium exchange, which provides benzylic magnesium reagents in excellent yield through a fragmentation reaction.

Exchange Reactions

A. H. Stoll, A. Krasovskiy, P. Knochel* ——— **606 – 609**

Functionalized Benzylic Magnesium Reagents through a Sulfur–Magnesium Exchange

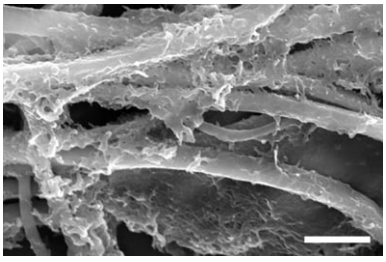


Heavy Grignard reagent: Despite the low reactivity of the calcium metal and the high reactivity of the resulting Ca–C bonds, the synthesis of mesitylcalcium iodide (see structure: purple I, orange Ca, red O, gray C) succeeded at very low temperatures. This compound decomposes by ether cleavage and rearrangement to the 3,5-dimethylbenzylcalcium iodide, even at low temperatures.

Grignard Reagents VIP

R. Fischer, M. Gärtner, H. Görls, M. Westerhausen* ——— **609 – 612**

Synthesis of 2,4,6-Trimethylphenylcalcium Iodide and Degradation in THF Solution



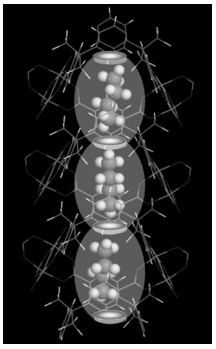
Enzymatic polymer synthesis is of considerable interest because of the synthetic advantages afforded by biological catalysts. Silicatein enzymes have shown broad synthetic utility for inorganic materials, and recombinant and native silicateins have been applied in the preparation of poly(L-lactide) (PLA). The picture shows native silicatein filaments coated with PLA (scale bar = 4 μm).

Enzyme Catalysis

P. Curnow, D. Kisailus, D. E. Morse* ——— **613 – 616**

Biocatalytic Synthesis of Poly(L-lactide) by Native and Recombinant Forms of the Silicatein Enzymes

Separating the wheat from the chaff: The microporous metal–organic framework (MMOF) of $[Cu(hfipbb)(H_2hfipbb)_{0.5}]$ is based on a bimetallic paddle-wheel building block and comprises 1D tubular microchannels formed by the interpenetration of two identical 4^4 nets. The channels are hydrophobic and have the ideal size and shape to selectively adsorb C_2, C_3, and *n*-C_4 olefins and alkanes (see picture).



Microporous Materials

L. Pan, D. H. Olson, L. R. Ciemnolonski, R. Heddy, J. Li* ——— **616 – 619**

Separation of Hydrocarbons with a Microporous Metal–Organic Framework

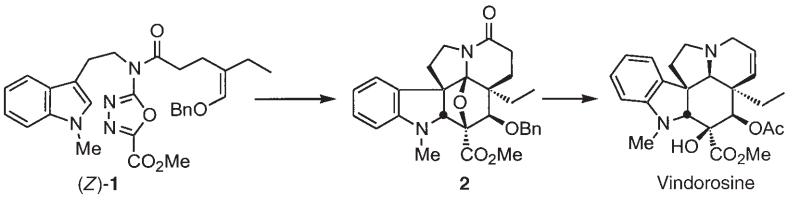
© 2006 Wiley-VCH Verlag GmbH & Co. KGaA, Weinheim

Contents

Total Synthesis

G. I. Elliott, J. Velcicky, H. Ishikawa, Y. Li, D. L. Boger* ——— 620 – 622

Total Synthesis of (−)- and *ent*-(+)-Vindorosine: Tandem Intramolecular Diels–Alder/1,3-Dipolar Cycloaddition of 1,3,4-Oxadiazoles

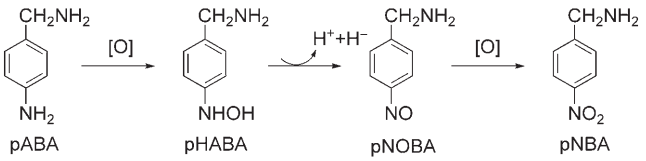


From tandem to pentacycle: The intramolecular tandem [4+2]/[3+2] cycloaddicycloaddition cascade of 1,3,4-oxadiazole (*Z*)-**1** to give the pentacyclic skeleton **2** of (−)- and *ent*-(+)-vindorosine introduces all the requisite substituents and functionality in a single step by which three new rings and four C–C bonds form and all six key stereocenters are installed.

Enzyme Catalysis

J. Lee, H. Zhao* ——— 622 – 625

Mechanistic Studies on the Conversion of Arylamines into Arylnitro Compounds by Aminopyrrolnitrin Oxygenase: Identification of Intermediates and Kinetic Studies

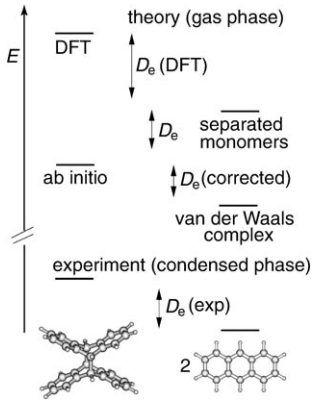


Rieske business! The Rieske *N*-oxygenase, aminopyrrolnitrin oxygenase (PrnD), catalyzes the unusual oxidation of arylamines to arylnitro compounds. Kinetic analysis has confirmed that PrnD catalyzes the conversion of the substrate pABA (4-aminobenzylamine) through at least three consecutive reactions: two monooxygenation steps and one dehydrogenation step (see scheme).

Noncovalent Interactions

S. Grimme,* C. Diedrich, M. Korth ——— 625 – 629

The Importance of Inter- and Intramolecular van der Waals Interactions in Organic Reactions: the Dimerization of Anthracene Revisited

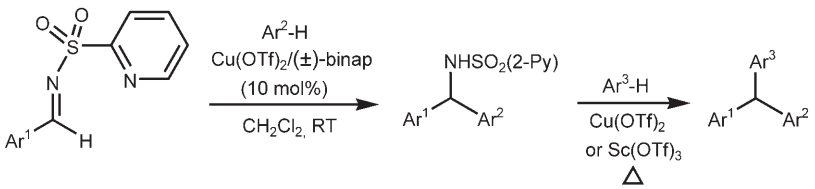


A delicate balance between inter- and intramolecular van der Waals effects can significantly influence the thermodynamics of organic reactions. These "weak interactions" are often underestimated but sum up even for the simple example of the dimerization of anthracene to relative effects of about 10–15 kcal mol^{-1}. It is furthermore shown why common density functional theory yields a seemingly right answer for the wrong reason.

Homogeneous Catalysis

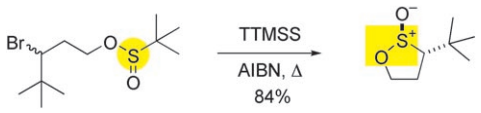
J. Esquivias, R. Gómez Arrayás,* J. C. Carretero* ——— 629 – 633

A Copper(II)-Catalyzed Aza-Friedel–Crafts Reaction of *N*-(2-Pyridyl)sulfonyl Aldimines: Synthesis of Unsymmetrical Diaryl Amines and Triaryl Methanes



The choice of the (2-pyridyl)sulfonyl moiety as an N-protecting group and Cu(OTf)$_2$/(±)-binap as catalyst system lead to a highly efficient aza-Friedel–Crafts reaction of electron-rich arenes (Ar^2-H) and heteroarenes with *N*-sulfonyl imines. This protocol is also amenable to the synthesis of unsymmetrical triaryl methanes through a second electrophilic aromatic substitution with a different electron-rich arene (Ar^3-H; see scheme).

© 2006 Wiley-VCH Verlag GmbH & Co. KGaA, Weinheim

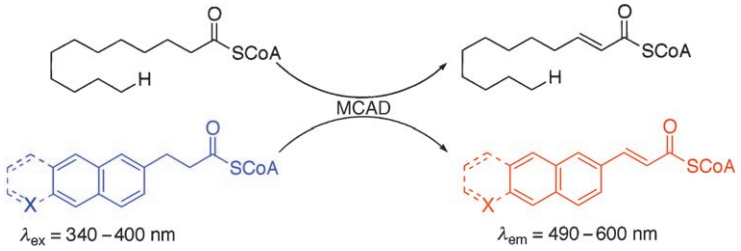


Ring road: Cyclic sulfinates and sulfinamides can be synthesized by homolytic substitution to give alkyl and benzofused families of compounds. The presence of an additional heteroatom in the ring allows the preparation of sulfur-based heterocycles that are useful synthetic intermediates (see scheme). The stereogenic sulfur atom transfers its chirality to prochiral radicals. TTMSS = tris(trimethylsilyl)silane, AIBN = azobisisobutyronitrile.

Sulfur Heterocycles

J. Coulomb, V. Certal, L. Fensterbank,* E. Lacôte,* M. Malacria* ____ **633 – 637**

Formation of Cyclic Sulfinates and Sulfinamides through Homolytic Substitution at the Sulfur Atom



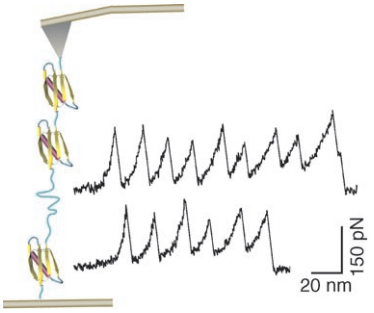
Not fussy: A systematic study revealed considerable substrate tolerance of medium-chain acyl-CoA dehydrogenase (MCAD), a member of the β-oxidation pathway for the degradation of fatty acids. Three fluorogenic reporter substrates were developed, which in turn allowed for selective, sensitive, and continuous monitoring of MCAD activity in tissue homogenates.

Enzyme Promiscuity

M. K. Froemming, D. Sames* **637 – 642**

Fluoromorphic Substrates for Fatty Acid Metabolism: Highly Sensitive Probes for Mammalian Medium-Chain Acyl-CoA Dehydrogenase

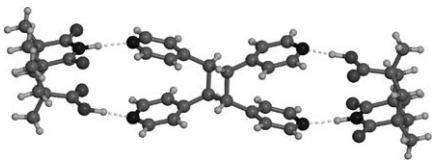
The unique topology of the B1 immunoglobulin G (IgG) binding domain of streptococcal protein G (GB1) leads to its remarkable mechanical stability. This nonmechanical protein is shown to be mechanically stable and to unfold at about 180 pN (the force-extension curves (right) shown demonstrate the mechanical unraveling of each GB1 domain in the polyprotein which is made of direct tandem repeats of GB1 (left)).



Protein Engineering

Y. Cao, C. Lam, M. Wang, H. Li* ____ **642 – 645**

Nonmechanical Protein Can Have Significant Mechanical Stability



A rare single crystal to single crystal transformation leads to a [2+2] photodimerization of homoditopic olefins (*trans*-1,2-bis(4-pyridyl)ethylene) assembled and preorganized within hydrogen-bonded quaternary complexes by using Rebek's imide. In this way a *rctt*-tetrakis(4-pyridyl)cyclobutane (see picture) was obtained stereospecifically in up to 100% yield.

Supramolecular Chemistry

D. B. Varshney, X. Gao, T. Friščić, L. R. MacGillivray* ____ **646 – 650**

Heteroditopic Rebek's Imide Directs the Reactivity of Homoditopic Olefins within Desolvated Quaternary Assemblies in the Solid State

© 2006 Wiley-VCH Verlag GmbH & Co. KGaA, Weinheim

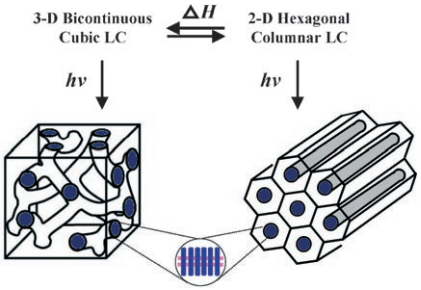
Contents

Liquid Crystals

L. Y. Jin, J. Bae, J.-H. Ryu, M. Lee* ——— **650 – 653**

Ordered Nanostructures from the Self-Assembly of Reactive Coil–Rod–Coil Molecules

Keeping in shape: Polymerizable coil–rod–coil molecules self-organize into 2D columnar and 3D bicontinuous liquid crystals whose supramolecular architectures and lattice dimensions are preserved upon photopolymerization (see picture). Nanofibers resulting from the photopolymerization of the 2D structures are utilized as nanoreactors for Suzuki coupling reactions.

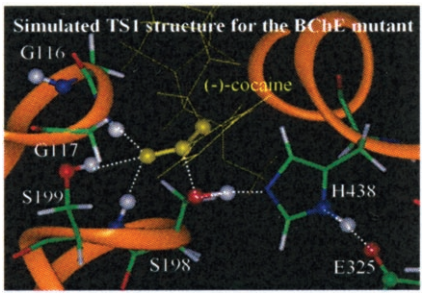


Enzyme Engineering

D. Gao, H. Cho, W. Yang, Y. Pan, G. Yang, H.-H. Tai, C.-G. Zhan* ——— **653 – 657**

Computational Design of a Human Butyrylcholinesterase Mutant for Accelerating Cocaine Hydrolysis Based on the Transition-State Simulation

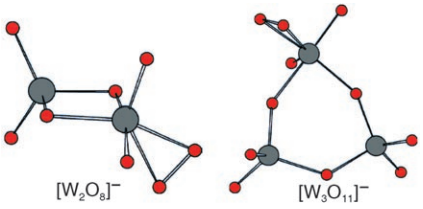
Breaking down cocaine: The transition-state simulation predicts a significantly more stable transition-state structure (see model; C: green, O: red, H: gray, N: blue, cocaine atoms: yellow) for the rate-determining first reaction step (TS1) of the (−)-cocaine hydrolysis catalyzed by a mutant of human butyrylcholinesterase (BChE).



Cluster Compounds

X. Huang, H.-J. Zhai, T. Waters, J. Li,* L.-S. Wang* ——— **657 – 660**

Experimental and Theoretical Characterization of Superoxide Complexes $[W_2O_6(O_2^-)]$ and $[W_3O_9(O_2^-)]$: Models for the Interaction of O_2 with Reduced W Sites on Tungsten Oxide Surfaces



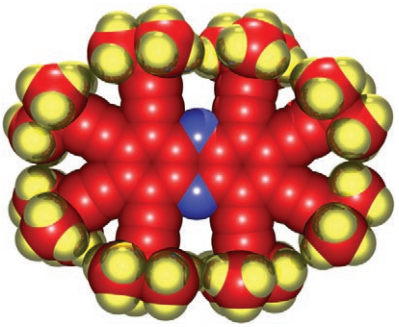
Photoelectron spectroscopic analysis and DFT calculations of two O-rich tungsten oxide clusters $[W_2O_8]^-$ and $[W_3O_{11}]^-$ showed these anions are superoxide complexes $[W_2O_6(O_2^-)]$ and $[W_3O_9(O_2^-)]$. The data suggest that the clusters $[W_2O_6]^-$ and $[W_3O_9]^-$ can activate O_2 through a one-electron transfer to form superoxide, which makes them simple molecular models for the chemisorption of O_2 at reduced defect sites on tungsten oxide surfaces.

Heteroacenes

S. Miao, C. G. Bangcuyo, M. D. Smith, U. H. F. Bunz* ——— **661 – 665**

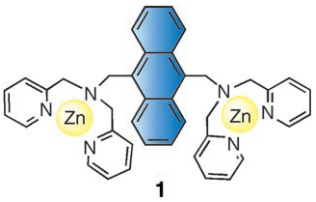
Derivatives of Octaethynylphenazine and Hexaethynylquinoxaline

Pocketing metals with alkynes: The spectral responses of the peralkynylated heteroacenes hexaethynylquinoxaline and octaethynylphenazine (see structure; N blue, C red, H yellow) on the presence of metal cations are more-pronounced for the phenazine derivative, demonstrating that the presence of the lateral alkyne substituents improves the metal-ion-binding capability of the pyrazine motif.



© 2006 Wiley-VCH Verlag GmbH & Co. KGaA, Weinheim

Reality check: The fluorescent probe **1** is applied to a real-time glycosyltransferase assay. The fluorescence of **1** increases with the progress of the glycosyl transfer reaction. The high sensitivity and reliable output of the method under multisubstrate enzymatic conditions make it suitable for the high-throughput screening of glycosyltransferase inhibitors.



1

Fluorescent Probes

J. Wongkongkatep, Y. Miyahara, A. Ojida, I. Hamachi* ——— **665 – 668**

Label-Free, Real-Time Glycosyltransferase Assay Based on a Fluorescent Artificial Chemosensor

WILEY InterScience®
DISCOVER SOMETHING GREAT

"**Hot Papers**" are chosen by the Editors for their importance in a rapidly evolving field of high current interest. A preview with the graphical abstracts of these articles can be found on the *Angewandte Chemie* homepage in Wiley InterScience at www.angewandte.org.

All articles in *Angewandte Chemie* are published online several weeks ahead of print. They are found under the "**EarlyView**" link on the journal's homepage in Wiley InterScience.

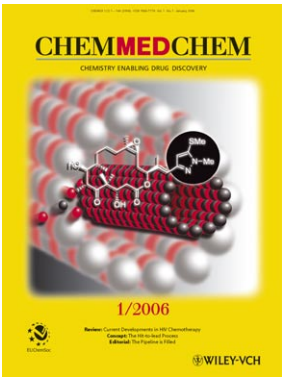
Service

Keywords ——— ***670***

Authors ——— ***671***

Angewandte's Sister Journals ——— ***672***

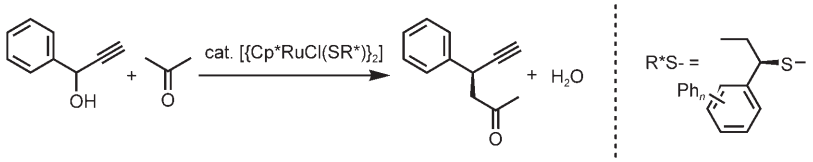
Preview ——— ***675***



For more information on ChemMedChem see www.chemmedchem.org

Corrigendum

The table of contents entry for this paper contained an incorrect figure. The corrected entry is shown below.



Enantioselective propargylic substitution reactions of propargylic alcohols with acetone catalyzed by a diruthenium complex give the propargylic alkylated products in good yields with up to 82% *ee* (see scheme). A π–π interaction of phenyl rings between the ligand and allenylidene moieties is considered to play a crucial role in achieving such a high selectivity. Cp* = pentamethylcyclopentadiene.

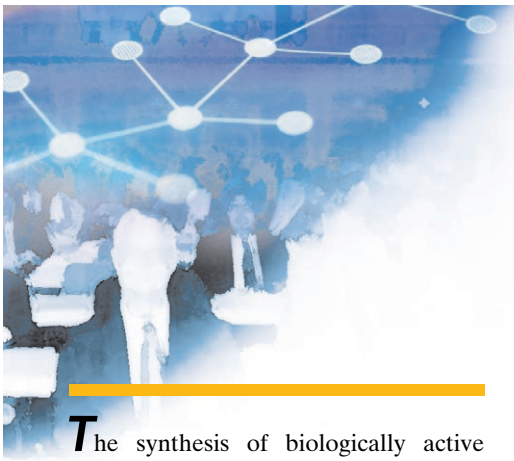
Ruthenium-Catalyzed Asymmetric Propargylic Substitution Reactions of Propargylic Alcohols with Acetone

Y. Inada, Y. Nishibayashi,* S. Uemura ——— **7715–7717**

Angew. Chem. Int. Ed. **2005**, *44*

DOI 10.1002/anie.200502981

 © 2006 Wiley-VCH Verlag GmbH & Co. KGaA, Weinheim



Antibiotics and Much More**

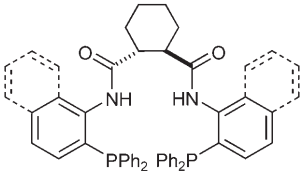
*Karsten Krohn**

The synthesis of biologically active natural and synthetic compounds is without doubt a topical field of activity. A forum for the exchange of the most recent results in this area was provided by the 9th International Conference on the Chemistry of Antibiotics and Other Bioactive Compounds (ICCA-9), organized by Stéphane Quideau (University of Bordeaux), which took place in Arcachon (France) during September 25–29, 2005. A feature of this series of conferences is the participation of researchers from both academia and industry: This year, industrial chemists represented about a third of the 140 participants.

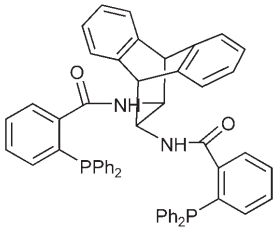
The focus of the conference was bioactive compounds—not just antibiotics, which were discussed in only about a third of the lectures. Nevertheless, the increasingly observed resistance of bacteria to antibiotics has lent an urgency to research into antibiotics. Who better to introduce this topic than C. Walsh (Harvard Medical School),[1] who recently appeared as the editor of a whole volume of *Chemical Reviews*[2] on this theme? Indeed, the theme of the development of resistance stood at the center of his plenary lecture "*Antibiotics: Past, Present, Future*". On the basis of the most recent results on the mechanisms of action of antibiotics, Walsh stated that the development of resistance is unavoidable and a further rapid proliferation of multidrug resistance has to be expected. Even today, about 30% of enterococci are resistant towards vancomycin, leading to a mortality rate of around 25% in infected, immune-deficient patients. Added to this, the large gap in the development of new antibiotics that after almost 40 years was interrupted with the oxazolidinones (2000) and daptomycin (2003) appears critical. The upshot of his lecture was the requirement for increased research efforts in this area to find new targets, new molecules, and a greater level of success in the discovery of antibiotics that are active against resistant pathogens.

Closely associated with the synthesis of natural products is the continued development of synthetic methods. A prime example of this was given at the beginning by J. Mulzer (University of Vienna, Austria), who presented the most recent results on two difficult problems: control of the *E*/*Z* geometry of the double bond (e.g. in epothilones) and stereocontrol of radical processes in conjunction with isoprostane syntheses. As an example, the metathesis reaction in the Danishefsky epothilone synthesis gives only a 1:1 ratio of the *E*/*Z* isomers;[3] however, the selectivity is improved by a new concept that involves the fragmentation of β-hydroxy esters (simultaneous elimination of CO_2 and HOR) starting from cyclic precursors (Scheme 1).

The control of stereochemistry and the development of new synthetic strategies was discussed in the plenary lecture by B. M. Trost (Stanford University). The "taming" of radical cyclizations for a stereoselective outcome was introduced with the example of the synthesis of siccanin. The efficiency and the diversity of substrates controlled by palladium- or ruthenium-catalyzed allylations with the assistance of C_2-symmetric amidophosphines **1a**, **1b**, and **2** was demonstrated impressively with many examples of natural product syntheses.



1a, **1b**

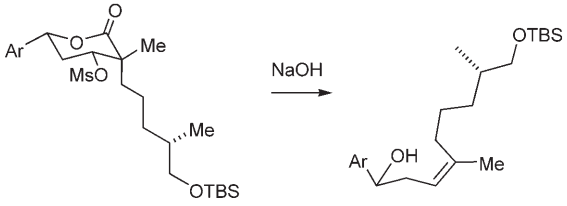


2

The synthesis of active antitumor polyketides (mostly macrolides) remains a challenge in synthetic chemistry owing to their low natural abundance. These polyketides also include modulators of apoptosis such as (−)-rasfonin or (−)-apoptolidin (**3**), the synthetic approaches of which were described by R. K. Boeckman, Jr (University of Rochester, USA). From the point of view of methodology, oxazaborilidines or aluminum-ate complexes have been

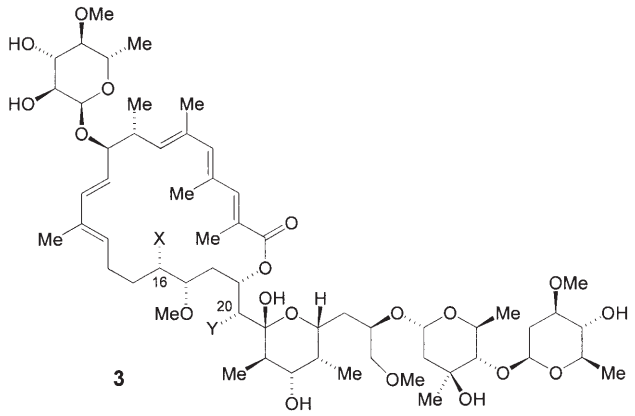
[*] Prof. Dr. K. Krohn
Department of Chemistry
University of Paderborn
Warburgerstrasse 100
33098 Paderborn (Germany)
Fax: (+49) 525-1603-245
E-mail: karsten.krohn@uni-paderborn.de

[**] 9th International Conference on the Chemistry of Antibiotics and Other Bioactive Compounds, Arcachon, France, September 25–29, 2005.



Scheme 1. *anti*-Elimination of CO_2H and MsOH to *Z*-dienes. Ms = methanesulfonyl; TBS = *tert*-butyldimethylsilyl.

InterScience
© 2006 Wiley-VCH Verlag GmbH & Co. KGaA, Weinheim

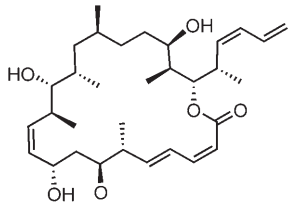


3

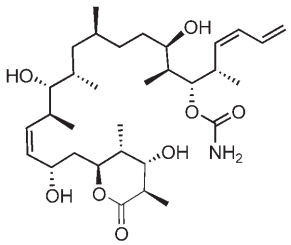
developed as enantioselective catalysts for Mukaiyama-type reactions. Chiral auxiliaries such as Oppolzer lactams or chiral starting materials such as the chiral bisepoxide of butadiene also offer further opportunities for innovation in the bidirectional construction of unsymmetric 1,2-diols.

G. A. Sulikowski (Vanderbilt University, USA) presented a new total synthesis of the complex apoptolidinone, which was previously synthesized by the groups of Nicolaou,[4] Koert,[5] and Crimmins[6]. The synthesis comprised only 14 steps in the longest linear sequence and covered many aspects of modern stereoselective synthetic chemistry. Once again, the metathesis reaction played a key role and was applied several times both intermolecularly and intramolecularly. The principles of ring-rearrangement metathesis (RRM) and diastereoselective double RRM was subsequently demonstrated by S. Blechert (Technical University of Berlin, Germany), with new examples of the efficient synthesis of nitrogen-containing heterocycles.

The synthesis of antitumor macrolides from marine sponges has been developed to perfection by I. Paterson (Cambridge University, UK) and coworkers. The importance of synthesis for both structural elucidation and to supply material for biological testing was highlighted with the example of dictyostatin, which was isolated by Petitt et al. in 1994 (only 1.35 mg from over 400 kg sponge).[7] In the nanomolecular range, dictyostatin inhibits the proliferation of taxol-resistant mammary, ovarian, and colon cancer cells. At the same time, the revised structure of dictyostatin (**4**) demonstrates its analogy to discodermolide (**5**), whose synthesis has recently become interesting from an industrial point of view.[8] The newly assigned stereochemistry of dictyostatin was confirmed completely by synthesis and moreover also agreed with the results obtained in parallel by Curran and co-workers.[9] The stereochemical structure of spirastrellolid A was also revised by Paterson and co-workers with the aid of spectroscopic techniques and synthesis.



revised structure of Dictyostatin (**4**)

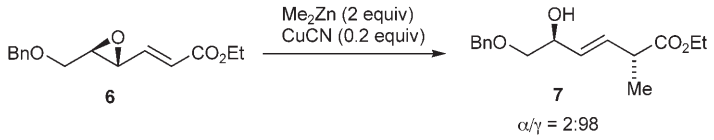


Discodermolide (**5**)

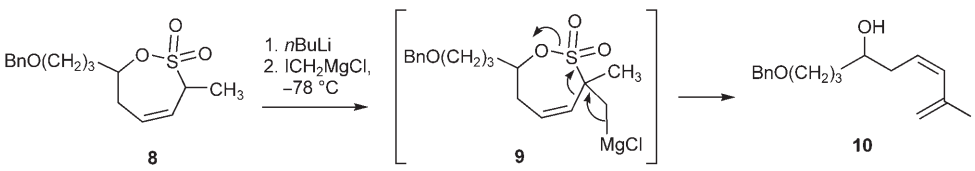
The synthesis of natural products of polyketide origin was described by M. Miyashita (Hokkaido University, Japan). During the course of the synthesis of zincophorin, new reagents were developed that display remarkable regio- and stereoselectivity on open-chain systems. One example is illustrated by the opening of the unsaturated epoxide **6**, which is transformed into the allyl alcohol **7** with high regio- and stereoselectivity (Scheme 2). Miyashita also described the synthesis of zoanthamine and norzoanthamine, both highly complex biologically active compounds with anti-osteoporotic and analgesic activity, which was carried out in 41 steps with a remarkable overall yield of 3.5 %.[10]

A general solution for the construction of conjugated *Z*-dienols, which occur in many biologically active natural products such as dictyostatin, discodermolide, or mycothiazole, was described by J. Cossy (ESPCI, Paris, France). The efficiency of the method was demonstrated with a series of total syntheses including that of mycothiazole. After deprotonation, the sultone **8,** which was prepared by metathesis, was converted with ICH_2MgCl into **9**, which in turn fragmented to the conjugated *Z*-dienol **10** by expulsion of SO_2 (Scheme 3).

Somewhat smaller molecules also represent a challenge, as discussed by L. Chabaud (Y. Landais' group; University of Bordeaux, France). The synthesis of the hydroxylated pyrrolizidine alkaloid 3-*epi*-hyacinthacine A_1 was achieved by carboazidation of chiral allylsilanes in only 13 steps in 8 % overall yield.[11] The trend towards simplified



Scheme 2. Opening of the unsaturated epoxide **6**, which is transformed into the allyl alcohol **7**. Bn = benzyl.



Scheme 3. Synthesis of the conjugated *Z*-dienol **10** from intermediate **9** with expulsion of SO_2.

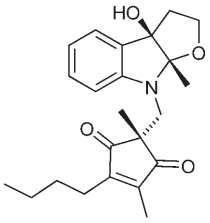
© 2006 Wiley-VCH Verlag GmbH & Co. KGaA, Weinheim

structures and the determination of the structural features essential for biological activity were discussed by M. E. Maier (University of Tübingen, Germany) in his talk "*Synthetic Strategies Towards Benzolactone Collections*". The most well-known example of these benzolactones of high biological activity is perhaps the salicylihalamide family. He showed that indeed such benzolactones can be constructed with relative ease from epichlorohydrin by a sequence of standard reactions such as the Mitsunobu reaction, the ring-closing metathesis reactions, or transition-metal-catalyzed couplings. A similar concept in the search for structural features essential for biological activity also resounded in the lecture by M. Braun (University of Düsseldorf, Germany), who described the systematic synthesis of arylindanyl ketones as new peptidyl-prolyl *cis*/*trans*-isomerase inhibitors that catalyze the *cis* and *trans* isomerization of peptidyl-prolyl bonds.

Besides polypropionates, aromatic or quinoid polyketides are often characterized by interesting biological activity. Particularly interesting currently are the angularly constructed ring systems of the angucyclins, gilvocarcins, and kinamycins, to which six lectures of the symposium were devoted. A particular highlight was the lecture by K. Suzuki (Tokyo Institute of Technology, Japan), who described the total syntheses of benanomicin B (**11**),[12] TAN-1065, and ravidomycin (**12**). The enantioselective construction of the diol in benanomicin B was achieved by chirality transfer of axial to central chirality. The key step in the construction of *C*-glycosides, such as in ravidomycin (**12**), was the rearrangement of *O*- to *C*-glycosides catalyzed by the hard Lewis acids of the early transition metals such as $[(Cp)_2Hf]Cl(ClO_4)$. This reaction is of fundamental importance for the synthesis of many bioactive *C*-glycosides. Kinamycin (**13**), derived biosynthetically from angucyclinen, is active at 50 nM concentrations against Gram-positive bacteria such as *Staphylococcus aureus*. Detailed mechanistic investigations into the role and reactivity of the diazo group, which is rarely found in natural products, was discussed by K. Feldmann (Pennsylvania State University, USA).

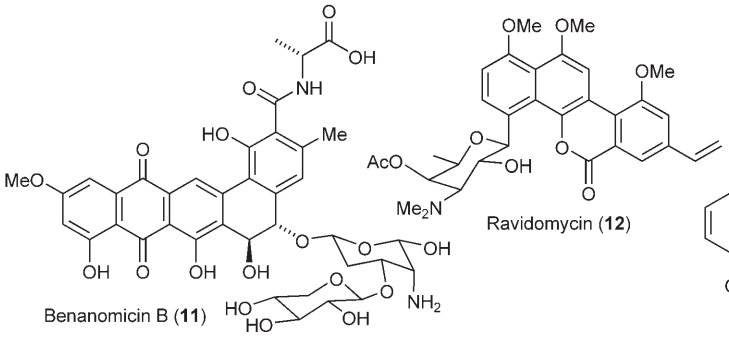
The naphthopyran antibiotics nanaomycin, kalafungin, and medermycin, also fall within the group of aromatic polyketides, and their comprehensive syntheses were described by K. Tatsuta (Waseda University, Japan). Rhamnose was used as a chiral template by Tatsuta in the synthesis of the chiral part of the naphthopyran antibiotics. That this "ex chiral pool" approach remains topical in asymmetric synthesis was illustrated by the discussions of M. Chmielewski (Polish Academy of Science, Poland), J. Thiem (University of Hamburg, Germany), and K. Krohn (University of Paderborn, Germany). This approach is useful not only in preparing unusual structures such as oxo analogues of the penicillins and cephalosporins or seven- and eight-membered cyclitol mimetics, but it also has potential in the preparation of building blocks for the synthesis of macrolides.

Another part of the conference was devoted specifically to different aspects of special antitumor activity. F. Roussi (ICSN, Gif-sur-Yvette, France) demonstrated that a number of steroid-like choline derivatives could imitate the action of taxols with respect to the organization of microtubuli. J. Dubois (also ICSN, France) reported on the synthesis of protein farnesyl transferase inhibitors. Although ene-diynes have found no entry into therapy owing to their high toxicity, they remain of interest as substrates for the investigation of the Bergman cyclization, as discussed by A. Basak (Indian Institute of Technology, India). T. Sunazuka (Kitasato University, Japan) reported the first total synthesis of madindolines, which have attracted interest as selective interleukin 6 inhibitors.



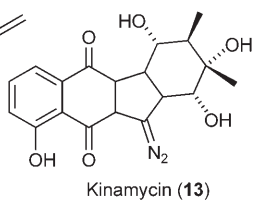
Madindoline A (**14**)

A considerable problem in chemotherapy of tumors is systemic toxicity, and the development of selective preparations is urgently needed. In his lecture "*New Prodrugs of Cytotoxic Antibiotics for a Selective Treatment of Cancer*", L. F. Tietze (University of Göttingen, Germany) described a concept based on the selective transformation of a precursor ("prodrug") into the active cytotoxic compound by a conjugated enzyme that releases the cyctotoxic compound and a monoclonic antibody that binds to the tumor-associated antigens.[13] The success of the concept is associated with a series of conditions such as, in particular, a large difference between the toxicity of the "prodrug" and the active principle (ratio of ED_{50} values greater than 1000). Through an extensive program of synthesis, many highly promising new products such as **15** that are derived from the natural product duocarmycin were isolated.

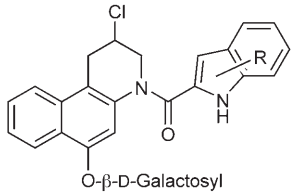


Benanomicin B (**11**)

Ravidomycin (**12**)



Kinamycin (**13**)



O-β-D-Galactosyl

15

© 2006 Wiley-VCH Verlag GmbH & Co. KGaA, Weinheim

The ICCA series of conferences has established itself at the highest level as a forum for the presentation of the most recent syntheses in the area of active natural and synthetic products (not just antibiotics). The next symposium in the USA (Nashville, TN) is already awaited with anticipation.

[1] C. Walsh, *Antibiotics: Actions, Origins, Resistance*, ASM, Washington, DC, **2003**.

[2] C. Walsh, G. D. Wright (Guest Editors), *Chem. Rev.* **2005**, *105*, 391 – 774.

[3] D. Meng, P. Bertinato, A. Balog, D.-S. Su, T. Kamanecka, E. J. Sorensen, S. J. Danishefsky, *J. Am. Chem. Soc.* **1997**, *119*, 10073 – 10092.

[4] K. C. Nicolaou, Y. Li, K. Sugita, H. Monenschein, P. Guntupalli, H. J. Mitchell, K. C. Fylaktakidou, D. Vourloumis, P. Giannakakou, A. O'Brate, *J. Am. Chem. Soc.* **2003**, *125*, 15443—15454.

[5] H. Wehlan, M. Dauber, M.-T. Mujica Fernaud, J. Schuppan, R. Mahrwald, B. Ziemer, M.-E. Juarez Garcia, U. Koert, *Angew. Chem.* **2004**, *116*, 4698 – 4702; *Angew. Chem. Int. Ed.* **2004**, *43*, 4597 – 4601.

[6] M. T. Crimmins, H. S. Christie, K. Chaudhary, A. Long, *J. Am. Chem. Soc.* **2005**, *127*, 13810 – 13812.

[7] G. R. Pettit, Z. A. Cichacz, F. Gao, M. R. Boyd, J. M. Schmidt, *J. Chem. Soc. Chem. Commun.* **1994**, 1111 – 1112.

[8] S. J. Mickel, G. H. Sedelmeier, D. Niederer, R. Daeffler, A. Osmani, K. Schreiner, M. Seeger-Weibel, B. Bérod, K. Schaer, R. Gamboni, *Org. Process Res. Dev.* **2004**, *8*, 92 – 100, and four subsequent reports in the same issue.

[9] Y. Shin, J.-H. Fournier, Y. Fukui, A. M. Brückner, D. P. Curran, *Angew. Chem.* **2004**, *116*, 4734 – 4737; *Angew. Chem. Int. Ed.* **2004**, *43*, 4634 – 4637.

[10] M. Miyashita, M. Sakai, I. Hattori, M. Sasaki, K. Tanino, *Science* **2004**, *305*, 495 – 499.

[11] L. Chabaud, Y. Landais, P. Renaud, *Org. Lett.* **2005**, *7*, 2587 – 2590.

[12] K. Ohmori, M. Tamiya, M. Kitamura, H. Kato, M. Oorui, K. Suzuki, *Angew. Chem.* **2005**, *117*, 3939-3942; *Angew. Chem. Int. Ed.* **2005**, *44*, 3871 – 3874.

[13] Review: L. F. Tietze, T. Feuerstein, *Curr. Pharm. Des.* **2003**, *9*, 2155 – 2175.

DOI: 10.1002/anie.200504256

© 2006 Wiley-VCH Verlag GmbH & Co. KGaA, Weinheim

Organocatalysis

DOI: 10.1002/anie.200502425

Enantioselective α-Fluorination of Carbonyl Compounds: Organocatalysis or Metal Catalysis?

*Petri M. Pihko**

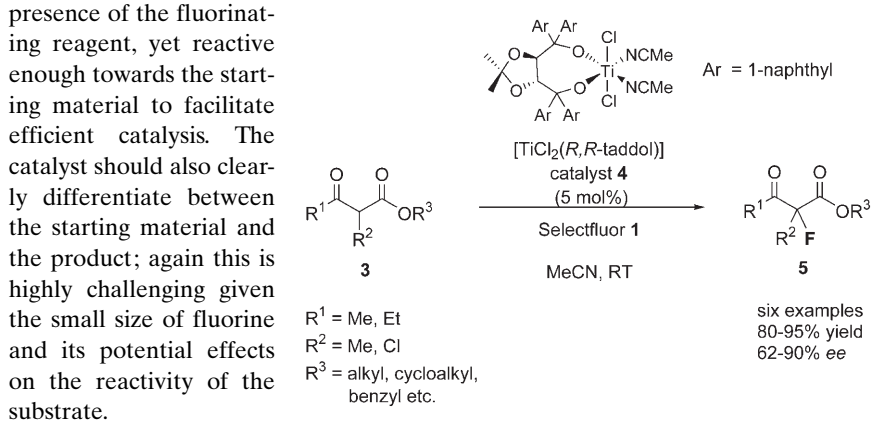
Keywords:
aldehydes · asymmetric catalysis · electrophilic substitution · fluorination · organocatalysis

Fluorine occupies a very special position in the periodic table. As the most electronegative element, incorporation of fluorine into organic molecules perturbs the electron density of the compound over several sigma bonds, affecting the pK_a values of X–H bonds over a long range. In contrast to other carbon–halogen bonds, the carbon–fluorine bond is very strong and aliphatic fluorinated compounds are attacked by nucleophiles only with difficulty.[1] In medicinal chemistry applications, fluorinated compounds impart substantial metabolic stability to drug candidates.[2] These highly advantageous effects associated with fluorine substitution have motivated a truly intense effort into the synthesis and characterization of novel fluorine-containing compounds.

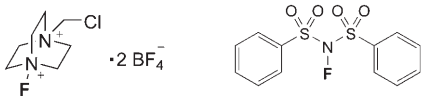
The level of synthetic control that is required for the effective utilization of fluorinated compounds presents serious challenges. Successful fluorination reactions must be chemoselective and regioselective—not at all a trivial task given the extremely high reactivity of elemental fluorine, and the fact that monofluorinated compounds are much more easily deprotonated than the nonfluorinated starting materials! Furthermore, introduction of fluorine in a diastereo- and enantiocontrolled manner presents enormous challenges, especially under catalytic conditions. The catalyst must be compatible with and stable in the presence of the fluorinating reagent, yet reactive enough towards the starting material to facilitate efficient catalysis. The catalyst should also clearly differentiate between the starting material and the product; again this is highly challenging given the small size of fluorine and its potential effects on the reactivity of the substrate.

In spite of these challenges, several highly successful strategies for catalytic enantioselective fluorination have been developed. The development of stable sources of electrophilic fluorine, selectfluor[3] and *N*-fluorobenzenesulfonimide (NFSI),[4] have had a tremendous impact on the development of fluorine chemistry (Scheme 1),[5] and they have facilitated the first truly catalytic asymmetric fluorination reactions. The first example of an enantioselective catalytic α-fluorination was disclosed by Togni and Hintermann in 2000 (Scheme 2).[6] The taddol–titanium complex **4** effectively catalyzes the α-fluorination of β-ketoesters with 33–90% *ee* in the presence of selectfluor as the source of electrophilic fluorine. In 2002, Sodeoka and co-workers disclosed a highly practical method for enantioselective fluorination of β-ketoesters with NFSI.[7] Later, the groups of Togni, Cahard, and Shibata also extended the range of useful metal–ligand combinations to Cu^{II}– and Ni^{II}–bisoxazoline complexes as well as Ru^{II}–complexes.[8] These pioneering developments have been elegantly summarized in the recent review on asymmetric fluorination by Ma and Cahard.[8d]

As an alternative to metal-based catalysis, organocatalytic methods in which the catalyst is devoid of metals have enjoyed an explosive growth in recent years. The first example of an organocatalytic fluorination process was the phase-transfer-catalyzed fluorination reported by Kim and Park in 2002 (Scheme 3).[9] This is, of course, not an entirely organo-mediated process since a stoichiometric amount of metal carbonate or hydroxide is used as the base. Independent work from the laboratories of Cahard and Shibata also identified



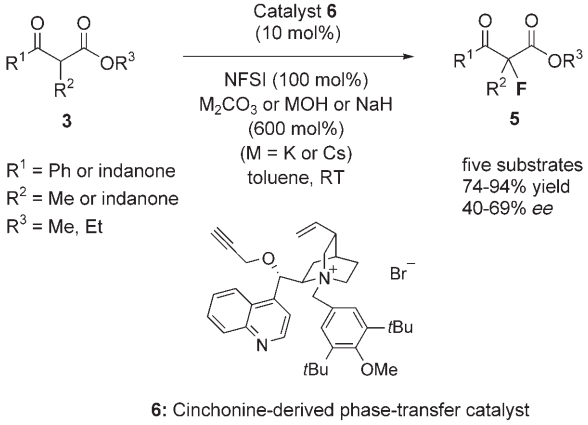
Scheme 2. Seminal example of enantioselective fluorination by Togni and Hintermann.[6]



Scheme 1. Sources of electrophilic fluorine.

[*] Dr. P. M. Pihko
Laboratory of Organic Chemistry
Department of Chemical Technology
Helsinki University of Technology
02015 TKK (Finland)
Fax: (+358) 9-451-2538
E-mail: petri.pihko@tkk.fi

InterScience
© 2006 Wiley-VCH Verlag GmbH & Co. KGaA, Weinheim



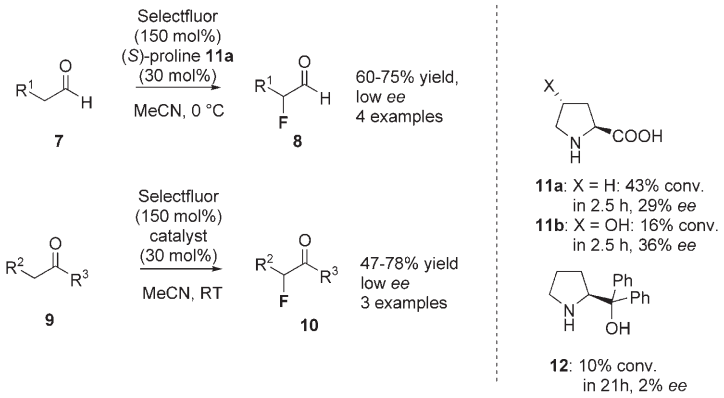
6: Cinchonine-derived phase-transfer catalyst

Scheme 3. Enantioselective fluorination with a phase-transfer catalyst.[9]

cinchona alkaloids and their derivatives as viable reagents for enantioselective fluorinations with selectfluor.[10] However, in these cases, an excess of the alkaloid must be employed, and the *N*-fluoro species derived from the alkaloids have been identified as the true fluorinating reagents.[11]

In March 2005, Enders and Hüttl published the first example of a purely organocatalytic fluorination process.[12] In this study, proline and its derivatives emerged as successful catalysts for the α-fluorination of aldehydes and ketones with selectfluor (Scheme 4). With aldehydes, the reaction times were as short as 2.5 h; however, prolonged reaction times were still required for ketones. Unfortunately, the observed enantioselectivities were still very low, ranging from 0 to 36 % *ee* with cyclohexanone as the test substrate.

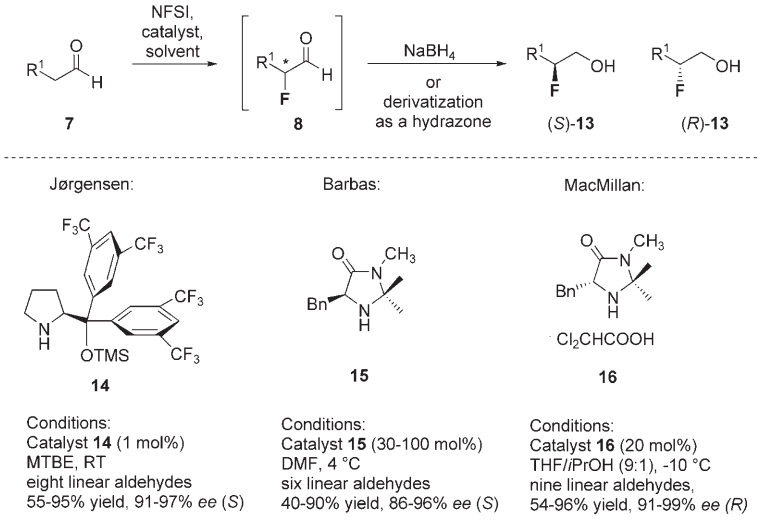
By the time the work of Enders and Hüttl was published, three more organocatalytic enantioselective α-fluorination reactions had been submitted for publication and were released within a few weeks of each other. In these papers, the Jørgensen,[13] Barbas,[14] and MacMillan[15] groups each describe highly enantioselective variants of organocatalytic α-fluorinations of aldehydes by using a variety secondary amines or amine salts as catalysts (Scheme 5).



Scheme 4. Organocatalytic fluorination study by Enders and Hüttl and examples of typical catalysts used.[12]

In contrast to Enders and Hüttl, the three groups reported success with NFSI as the fluorine source. Barbas and coworkers point out that in the fluorination of 2-phenylpropionaldehyde, NFSI gave significantly higher enantioselectivities than selectfluor, although both were equally reactive. The success of NFSI with aldehydes but not with ketones might, in part, be attributed to the considerably higher reactivity of aldehydes under enamine catalysis.[16] Interestingly, Beeson and MacMillan document that acetone could even be used as a *solvent* in the α-fluorination reaction without detectable loss in efficiency.

Although all three studies recommend the use of NFSI, the optimized conditions described by each of these groups are quite different.[17] In agreement with Enders, both Jørgensen and Barbas report that proline is an active catalyst but affords the product with low *ee* values only. The Jørgensen group has developed a number of proline-based organocatalysts for enamine and iminium catalysis.[18] Of these, the bulky silylated prolinol derivative **14** emerged as a highly active and enantioselective catalyst (Scheme 5), with methyl *tert*-butyl ether (MTBE) as the solvent of choice. In contrast, the Barbas group finally converged on the use of the free-base form of the imidazolidinone **15** as the catalyst. *N*,*N*-dimethylformamide turned out to be the solvent of choice since it greatly inhibited the formation of the α,α-difluorinated product.

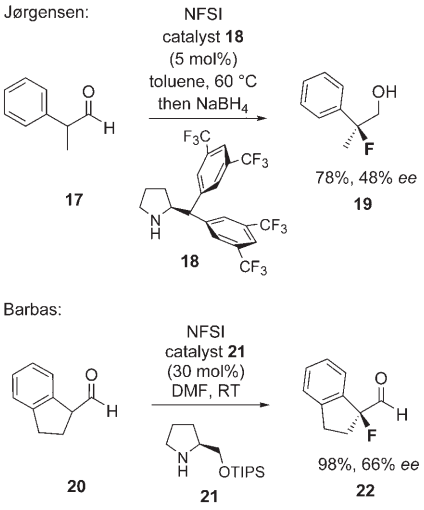


Scheme 5. Highly enantioselective organocatalytic α-fluorination of aldehydes from the groups of Jørgensen,[13] Barbas,[14] and MacMillan.[15] Bn = benzyl; TMS = trimethylsilyl.

© 2006 Wiley-VCH Verlag GmbH & Co. KGaA, Weinheim

By employing the dichloroacetic acid salt **16** of the imidazolidinone, MacMillan and co-workers were able to develop a highly enantioselective α-fluorination protocol in which a mixture of THF and 2-propanol was employed as the reaction medium.[15] Notably, catalyst loadings as low as 2.5 mol% were also feasible when the reaction was performed at room temperature.

These organocatalytic α-fluorination reactions were not limited to linear aldehydes. Both Jørgensen and Barbas also report the direct α-fluorination of α-branched aldehydes, resulting in the generation of fluorine-substituted quaternary stereogenic centers (Scheme 6).

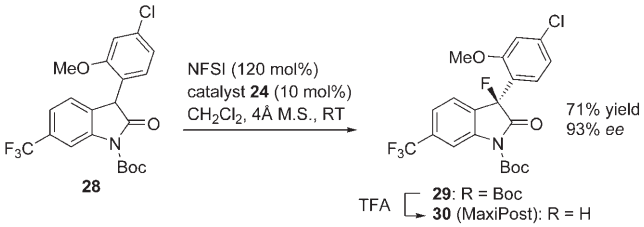


Scheme 6. Examples of organocatalytic enantioselective α-fluorinations of α-branched aldehydes from the Jørgensen and Barbas groups.[13,14] DMF = *N*,*N*-dimethylformamide; TIPS = triisopropylsilyl.

Given the difficulties experience by Enders and Hüttl with the enantioselective α-fluorination of ketones,[12] the development of a highly enantioselective organocatalytic α-fluorination of other carbonyl compounds still presents a formidable challenge. In the case of readily enolizable substrates, a suitable metal catalyst might, however, be able to assist in enolization and promote a highly enantioselective reaction provided that the appropriate ligand is chosen.

In June 2005, another success story in enantioselective fluorination was published: the Shibata and Toru groups, working in collaboration with Kanemasa, disclosed a highly enantioselective catalytic fluorination and chlorination reaction protocol with the Ni^{II}–dfbox catalyst system (Scheme 7).[19] Compared with previous results obtained with simple bisoxazoline ligands, the dbfox-Ph ligands turned out to be exceptionally enantioselective in the catalytic α-fluorination of β-ketoesters such as **23** and **26**. The catalyst loading could be decreased to 2 mol% without loss of yield or enantioselectivity.

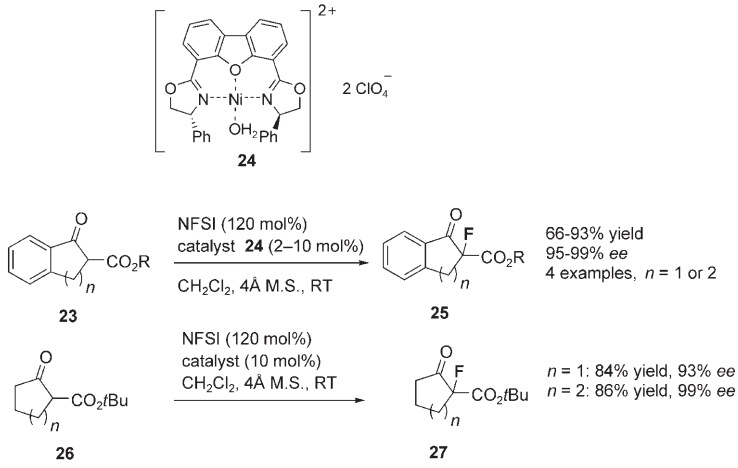
What makes this catalyst system highly remarkable is that it also provides direct access to α-fluorinated oxindoles such as **29** (Scheme 8). The fluorooxindole product was readily converted into BMS-204352 (**30**), also known as MaxiPost, a potent opener of maxi-K channels.[20] The Shibata/Toru study represents the first catalytic enantioselective route to this highly interesting drug candidate.



Scheme 8. Catalytic enantioselective synthesis of MaxiPost (**30**; BMS-204352) by using the Shibata/Toru fluorination protocol.[19] Boc = *tert*-butoxycarbonyl.

In summary, in a matter of three months, five ground-breaking, highly successful examples of catalytic enantioselective fluorination reactions appeared in the chemical literature. Of course, there are still important gaps to be filled by future studies, such as the direct, highly enantioselective fluorination of ketones. Nevertheless, together these studies illustrate very nicely both the power of organocatalysis to promote highly chemo- and enantioselective reactions with reactive aldehydes and the ability of metal catalysts to promote highly enantioselective reactions under highly demanding circumstances.[21] The story of catalytic enantioselective fluorinations, as it unfolded in mid-2005, shows clearly how organocatalytic and the metallocatalytic approaches are now truly complementary.

Published online: December 21, 2005



Scheme 7. Examples of Ni^{II}–dbfox-catalyzed highly enantioselective α-fluorination reactions of carbonyl compounds from the Shibata and Toru groups.[19] M.S. = molecular sieves.

[1] For general overviews of fluorine chemistry, see: a) M. Shimizu, T. Hiyama, *Angew. Chem.* **2005**, *117*, 218; *Angew. Chem. Int. Ed.* **2005**, *44*, 214, and references therein; b) P. Kirsch, *Modern Fluoroorganic Chemistry*, Wi-

 © 2006 Wiley-VCH Verlag GmbH & Co. KGaA, Weinheim

ley-VCH, Weinheim, **2004**; c) B. E. Smart, *J. Fluorine Chem.* **2001**, *109*, 3.
[2] a) For an important early review on the subject, see: J. T. Welch, *Tetrahedron* **1987**, *43*, 3123; b) Special Issue on "Fluorine in the Life Sciences", *ChemBioChem* **2004**, *5*, 557 – 726.
[3] For a recent Review on selectfluor, see: P. T. Nyffeler, S. G. Durón, M. D. Burkart, S. P. Vincent, C.-H. Wong, *Angew. Chem.* **2005**, *117*, 196; *Angew. Chem. Int. Ed.* **2005**, *44*, 192.
[4] E. Differding, H. Ofner, *Synlett* **1991**, 187.
[5] For reviews of electrophilic fluorinating agents, see: a) reference [1a]; b) K. Mikami, Y. Itoh, M. Yamanaka, *Chem. Rev.* **2004**, *104*, 1; c) G. S. Lal, G. P. Pez, R. G. Syvret, *Chem. Rev.* **1996**, *96*, 1737; d) J. A. Wilkinson, *Chem. Rev.* **1992**, *92*, 505.
[6] L. Hintermann, A. Togni, *Angew. Chem.* **2000**, *112*, 4530; *Angew. Chem. Int. Ed.* **2000**, *39*, 4359.
[7] Y. Hamashima, K. Yagi, H. Takano, L. Tamas, M. Sodeoka, *J. Am. Chem. Soc.* **2002**, *124*, 14530.
[8] a) Cu: J.-A. Ma, D. Cahard, *Tetrahedron: Asymmetry* **2004**, *15*, 1007; b) Cu and Ni: N. Shibata, T. Ishimaru, T. Nagai, J. Kohno, T. Toru, *Synlett* **2004**, 1703; c) The work of Togni, Mezzetti, and co-workers on Ru^{II} complexes in enantioselective fluorination has been described in a recent review: H. Ibrahim, A. Togni, *Chem. Commun.* **2004**, 1147; d) for an informative and up-to-date review on the development of enantioselective fluorination reactions, see: J.-A. Ma, D. Cahard, *Chem. Rev.* **2004**, *104*, 6119; e) for previous highlights on α-halogenation reactions, see: S. France, A. Weatherwax, T. Lectka, *Eur. J. Org. Chem.* **2005**, 475; f) M. Oestreich, *Angew. Chem.* **2005**, *117*, 2376; *Angew. Chem. Int. Ed.* **2005**, *44*, 2324.
[9] D. Y. Kim, E. J. Park, *Org. Lett.* **2002**, *4*, 545.
[10] a) D. Cahard, C. Audouard, J.-C. Plaquevent, N. Roques, *Org. Lett.* **2000**, *2*, 3699; b) N. Shibata, E. Suzuki, Y. Takeuchi, *J. Am. Chem. Soc.* **2000**, *122*, 10728; c) N. Shibata, E. Suzuki, T. Asahi, M. Shiro, *J. Am. Chem. Soc.* **2001**, *123*, 7001.
[11] The cinchona alkaloid mediated enantioselective fluorination can be equally well performed with *N*-fluoro cinchona alkaloid (Shibata et al.) or with the isolated *N*-fluoroammonium salts (Cahard et al.) generated in situ. For highly informative discussions, see reference [8d].
[12] D. Enders, M. R. M. Hüttl, *Synlett* **2005**, 991.
[13] M. Marigo, D. Fielenbach, A. Braunton, A. Kjærsgaard, K. A. Jørgensen, *Angew. Chem.* **2005**, *117*, 3769; *Angew. Chem. Int. Ed.* **2005**, *44*, 3703.
[14] D. D. Steiner, N. Mase, C. F. Barbas III, *Angew. Chem.* **2005**, *117*, 3772; *Angew. Chem. Int. Ed.* **2005**, *44*, 3706.
[15] T. D. Beeson, D. W. C. MacMillan, *J. Am. Chem. Soc.* **2005**, *127*, 8826.
[16] The higher reactivity of aldehydes over ketones in enamine catalysis has been documented in aldol, α-amination, and α-oxygenation processes: P. I. Dalko, L. Moisan, *Angew. Chem.* **2004**, *116*, 5248; *Angew. Chem. Int. Ed.* **2004**, *43*, 5138.
[17] With the exception of the study by Barbas and co-workers, all α-fluoroaldehydes were immediately reduced to the corresponding α-fluoroalcohols **13** owing to the instability and volatility of the aldehyde products; see: F. A. Davis, P. V. N. Kasu, G. Sundarababu, H. Qi, *J. Org. Chem.* **1997**, *62*, 7546.
[18] For examples, see: M. Marigo, T. C. Wabnitz, D. Fielenbach, K. A. Jørgensen, *Angew. Chem.* **2005**, *117*, 804; *Angew. Chem. Int. Ed.* **2005**, *44*, 794.
[19] N. Shibata, J. Kohno, K. Takai, T. Ishimaru, S. Nakamura, T. Toru, S. Kanemasa, *Angew. Chem.* **2005**, *117*, 4276; *Angew. Chem. Int. Ed.* **2005**, *44*, 4204.
[20] Development of MaxiPost: V. K. Gribkoff, D. J. Post-Munson, S. W. Yeola, C. G. Boissard, P. Hewawasam, WO0230868, **2002** [*Chem. Abstr.* **2002**, *136*, 319398].
[21] A direct comparison of metal catalysts and organocatalysts is provided by the recently published studies on the α-amination of β-ketoesters. The α-amination products can be obtained in up to 90% *ee* by using cinchona alkaloids as catalysts: a) S. Saaby, M. Bella, K. A. Jørgensen, *J. Am. Chem. Soc.* **2004**, *126*, 8120; b) P. M. Pihko, A. Pohjakallio, *Synlett* **2004**, 2115; in contrast, the Cu^{II}–bisoxazoline complexes afford the α-amination products in outstanding enantioselectivity (up to 99% *ee* in many cases): c) M. Marigo, K. Juhl, K. A. Jørgensen, *Angew. Chem.* **2003**, *115*, 1405; *Angew. Chem. Int. Ed.* **2003**, *42*, 1367; clearly, other factors such as chemoselectivity, reaction rate, ease of operation, and cost of the catalyst are also issues that need to be taken into account in selecting the asymmetric catalyst.

 © 2006 Wiley-VCH Verlag GmbH & Co. KGaA, Weinheim

Synthetic Methods

DOI: 10.1002/anie.200502882

Hydrophobically Directed Organic Synthesis

Ulf M. Lindström and Fredrik Andersson*

Keywords:
hydrophobic effect · solvent effects · synthetic methods · water chemistry

The recent surge of interest, as well as progress, in the use of water as a solvent for synthetic chemistry holds great promise for the future in terms of the cheaper and less-hazardous production of chemicals. Researchers in this area are also discovering that water may offer new possibilities in organic synthesis because of its unique physical and chemical properties that so clearly distinguishes it from other solvents.[1] Recently, significant advances have been made towards directing the selectivity of synthetic organic reactions in water through the interaction of nonpolar, or hydrophobic, regions of the reactants. These forces are normally too weak to compete with any steric and electronic effects in organic solvents. In water, on the other hand, hydrophobic surfaces associate strongly as a result of the tendency of water to exclude nonpolar species and thus minimize the Gibbs energy of solvation, a phenomenon known as the hydrophobic effect. In other words, reactions in water may be predisposed to favor transition states that optimize hydrophobic interactions. Thus, it should in principle be possible to use hydrophobic interactions as a nonbonding element of control for synthetic reactions in water.

It has been known for some time that hydrophobic interactions can have a significant influence on organic reactions.[2] It was discovered in pioneering studies on Diels–Alder reactions in water by the research groups of Breslow and Grieco in the early 1980s that such reactions often proceed with much higher rates than in organic solvents. The accelerating effect of water has been ascribed to a number of factors, including the hydrophobic effect as well as hydrogen bonding between water molecules and reactants. In addition, the *endo*/*exo* selectivities for many of the Diels–Alder reactions studied were significantly higher in water than in organic solvents, and favored the more compact *endo* transition state. In view of the fact that 25 years have passed since the first ground-breaking observations, surprisingly little effort has gone into exploring the potential of hydrophobic interactions in organic synthesis. This situation has largely arisen because of the fact that most chemists have not considered water as being a useful solvent for synthesis. Concerns about poor solubility and adverse reactivity of the solvent with catalysts and functional groups have hampered the wider implementation of water as a reaction medium. However, as recent research in the area has shown, these concerns may have been overstated, and the many benefits of using water call for it to be explored to its fullest potential and scope.[3] Herein we highlight attempts to design reactions in water that make use of hydrophobic interactions to achieve selectivity.

Wang, Li, and co-workers described aqueous Rh^{I}-catalyzed additions of aryl bismuth and aryl lead reagents to alkyl glyoxylates.[4] The addition of tris(2-naphthyl)bismuth to (−)-menthyl glyoxylate in water led to only 13% *de*, while the reaction with (−)-8-phenylmenthyl glyoxylate gave 85% *de* (Table 1; cod = cycloocta-1,5-diene). The higher *de* value was attributed to a π-stacking interaction leading to selective blocking of one diastereotopic face of the aldehyde (Figure 1). Previous studies suggest that the hydrophobic effect may enforce existing attractive interactions, and thus it is not unlikely that water could add additional stability to the π interaction

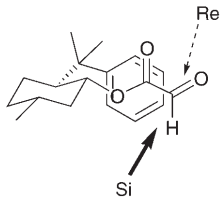
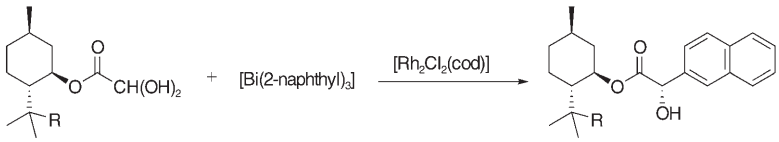


Figure 1. Diastereoselectivity promoted by a π-stacking interaction, which is enforced in water through the hydrophobic effect. Copyright Elsevier Science.

Table 1: Rh^{I}-catalyzed reactions of chiral glyoxylate hydrates with tris(2-naphthyl)bismuth in water and THF.[4]



Solvent	R	*T* [°C]	Yield [%]	*de* [%]
water	Me	50	68	13
water	Ph	50	81	85
water/THF 4:1	Ph	40	73	46
THF	Ph	40	71	36

[*] Dr. U. M. Lindström, F. Andersson
Department of Organic Chemistry
Lund University
P.O. Box 124, 221 00 Lund (Sweden)
Fax: (+46) 46-222-8209
E-mail: ulf.lindstrom@organic.lu.se

WILEY InterScience DISCOVER SOMETHING GREAT

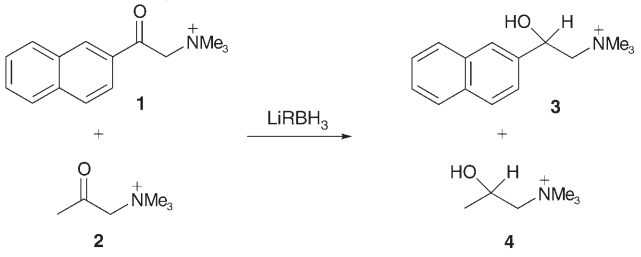
© 2006 Wiley-VCH Verlag GmbH & Co. KGaA, Weinheim

between the carbonyl group and the phenyl ring.[5] In fact, diastereoselectivities were significantly lower for reactions in THF or dichloromethane than in water, despite the aqueous reactions being heterogeneous and run at higher temperature (Table 1). This work gives a hint to the untapped potential of designing reactions in which nonpolar, chiral auxiliaries containing large hydrophobic surfaces are used to achieve discrimination of diastereotopic faces.

Perhaps the most elaborate and ambitious studies so far on hydrophobically directed synthetic reactions are currently underway by Breslow and coworkers. For example, in 2002 they showed that hydrophobic interactions may determine the ratio of O versus C alkylation in alkylations of phenoxide ions in water.[6] Recognizing the potential of hydrophobically induced selectivity, Biscoe and Breslow explored the use of hydrophobic reducing agents in reductions of ketones in water. They performed competition reactions of the quaternized β-ketoamines **1** and **2** with differently substituted borohydrides to give either **3** or **4** (Table 2).[7] As expected, the nonhydrophobic reducing agent $LiBH_4$ showed almost no selectivity between the two ketones (53:47). On the other hand, a significant preference (67:33) for reduction of the more hydrophobic ketone **1** was observed when $LiPhBH_3$ was employed. No such change was observed in methanol, thus reflecting the absence of the hydrophobic effect in methanol. The selectivity observed in water could be enhanced (72:28) by salting out the solution with LiCl. Finally, performing the reduction with lithium pentafluorophenyl borohydride ($LiC_6F_5BH_3$) provided further improvement in selectivity (91:9), presumably as a result of an elevated hydrophobicity resulting from the fluorination. Again, addition of LiCl resulted in better selectivity (95:5). An important lesson from this study was that increased hydrophobicity seems to be directly related to increased reactivity for reductions in water. In another study, Breslow and co-workers used hydrophobic borohydrides to control the regioselective reduction of the sulfated naturally occurring steroid **5** (Table 3).[8] Reduction proceeded with significant selectivity (87:13) for the intrinsically more-reactive 17-keto group to give **7** when the reaction was performed in water using $LiBH_4$. A remarkable reversal of selectivity was observed when the reduction was performed instead with $LiC_6F_5BH_3$ in 4 M $LiCl/D_2O$. Under these conditions optimized for "hydrophobic control", the reduction of the 6-keto group was strongly favored (85:15) over the reduction of the 17-keto group to give **6**. The difference in selectivity between the nonhydrophobic and hydrophobic conditions corresponds to a nearly 40-fold increase in the relative rate. Both keto groups in **5** are in hydrophobic environments and the large dependence of the selectivity on the hydrophobicity of the reducing agent is somewhat surprising. Further experiments indicated that the saturated framework surrounding the 17-keto group is less conducive to efficient hydrophobic packing than the unsaturated, flat environment of the 6-keto group.

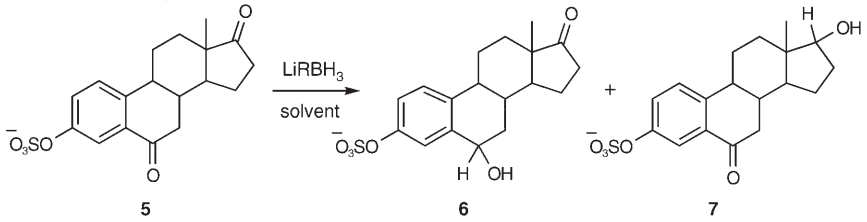
Another important contribution was the recent disclosure that epoxidations of olefins can be selectively accelerated by the use of a hydrophobic oxidizing agent.[9] In this study, Biscoe and Breslow emphasized the importance of having an accurate understanding of the transition-state geometry when developing hydrophobic reagents. For example, the lack of acceleration of the hydrophobic rate when various peracids were screened was explained by invoking recently published computational transition-state models of perbenzoic acid epoxidation in which the hydrophobic phenyl ring is required to assume a position highly unfavorable for hydrophobic interaction with the olefin (Figure 2a). On the other hand, calculations of transition states for dioxirane or oxaziridinium cation epoxidations suggest a geometry that would be conducive to hydrophobic interaction (Figure 2b). Indeed, by employing the hydrophobic oxaziridinium salts **8** and **9** in competition experiments of cinnamic acid derivatives (**10**) and crotonic acid (**11**) it was possible to effect relative rate increases that were up to an order of magnitude higher than the largest in-

Table 2: Ratios of products (**3**:**4**) formed in the competition reactions of quaternized β-keto amines **1** and **2** with substituted borohydrides under different reaction conditions.[7]



R	D_2O	$LiCl/D_2O$	CD_3OD
H	53:47	58:42	35:65
Ph	67:33	72:28	38:62
C_6F_5	91:9	95:5	54:46

Table 3: Ratios of products **6**:**7** formed in the reduction of **5** under different reaction conditions.[8]



R	D_2O	4 M $LiCl/D_2O$	1:1 CD_3OD/D_2O
H	13:87	14:86	10:90
Ph	60:40	69:31	32:68
C_6F_5	78:22	85:15	46:54

© 2006 Wiley-VCH Verlag GmbH & Co. KGaA, Weinheim

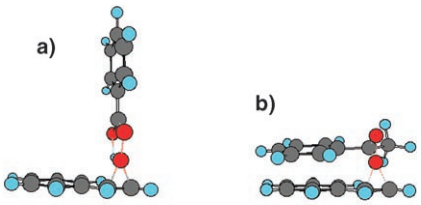
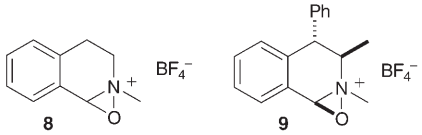


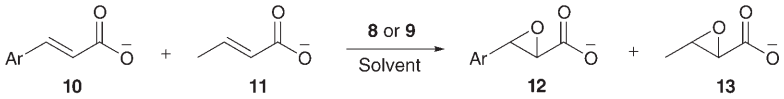
Figure 2. Transition-state models of the epoxidation of styrene with a) perbenzoic acid and b) the dioxirane derived from acetophenone. Copyright American Chemical Society.

creases observed in hydride reductions. Some of the results from this study are shown in Table 4. Dimethyl dioxirane (DMDO) was used as a nonhydrophobic control. The epoxidations show a very large increase in selectivity for the hydrophobic cinnamic acid derivatives **10** when using either **8** or **9** instead of DMDO. A striking example is the competition reaction of the 2-naphthyl olefin and crotonic acid, where changing from DMDO to **9** leads to an increase in selectivity for the more hydrophobic olefin from 68:32 to 99.8:0.2, which corresponds to a 240-fold increase in the relative rate. However, the differences in selectivity on going from nonhydrophobic conditions (water/isopropyl alcohol 1:1) to pure water, while significant enough to indicate a positive influence of hydrophobic interactions, are still modest and one should keep in mind that other binding forces not so affected by the nature of the solvent are likely to be involved. A nice extension of this study was the development of a catalytic version using substoichiometric amounts of the iminium precursor of the oxaziridinium salt **8** and oxone as the co-oxidant (Scheme 1).

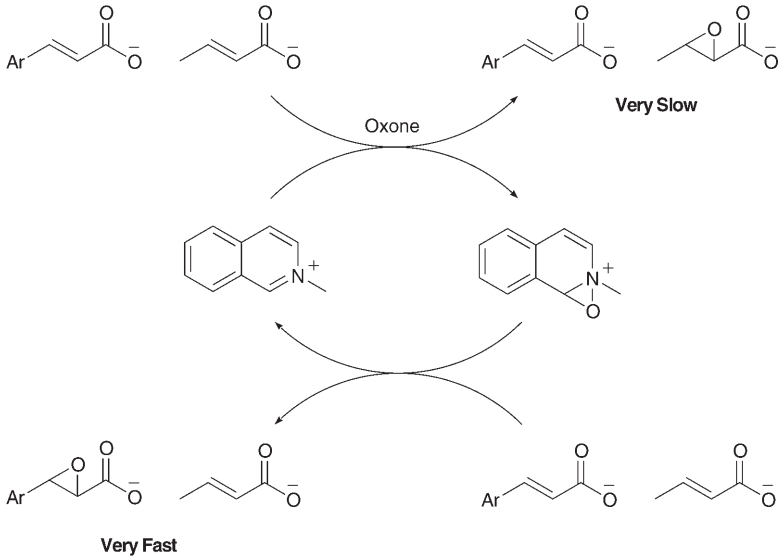
In conclusion, organic synthesis in water is a rapidly growing area of research with an exciting future. Recent findings presented herein suggest that selective hydrophobic acceleration will play an interesting and important part of this development. However, the wider applicability of this approach still remains to be established. The design of stereoselective reactions based on hydrophobic interactions is an area of great potential that is still largely unexplored. Early studies indicate that the use of hydrophobic chiral auxiliaries is a useful strategy worth pursuing. For all intents and purposes, improved theoretical and experimental models are required to more effectively distinguish hydrophobic interactions from other nonbonding interactions and to reliably and accurately quantify its contribution to various synthetic reactions in water.

Table 4: Ratio of epoxide products (**12**/**13**) formed in the competition reactions of cinnamic acid derivatives (**10**) and crotonic acid (**11**) with dioxirane and oxaziridinium epoxidizing reagents **8** and **9**.[9]





Ar	Solvent	DMDO	**8**	**9**
Ph	D_2O	61:39	96.5:3.5	98.1:1.9
Ph	*i*PrOD/D_2O 1:1	59:41	88:12	91.8:8.2
p-$CF_3C_6H_4$	D_2O	22:78	84:16	92.7:7.3
p-$CF_3C_6H_4$	*i*PrOD/D_2O 1:1	22:78	54:46	69:31
2-naphthyl	D_2O	68:32	98.7:1.3	99.8:0.2
2-naphthyl	*i*PrOD/D_2O 1:1	66:32	95.9:4.1	98.1:1.9



Scheme 1. Catalytic cycle using hydrophobic iminium salts. Copyright American Chemical Society.

Published online: December 12, 2005

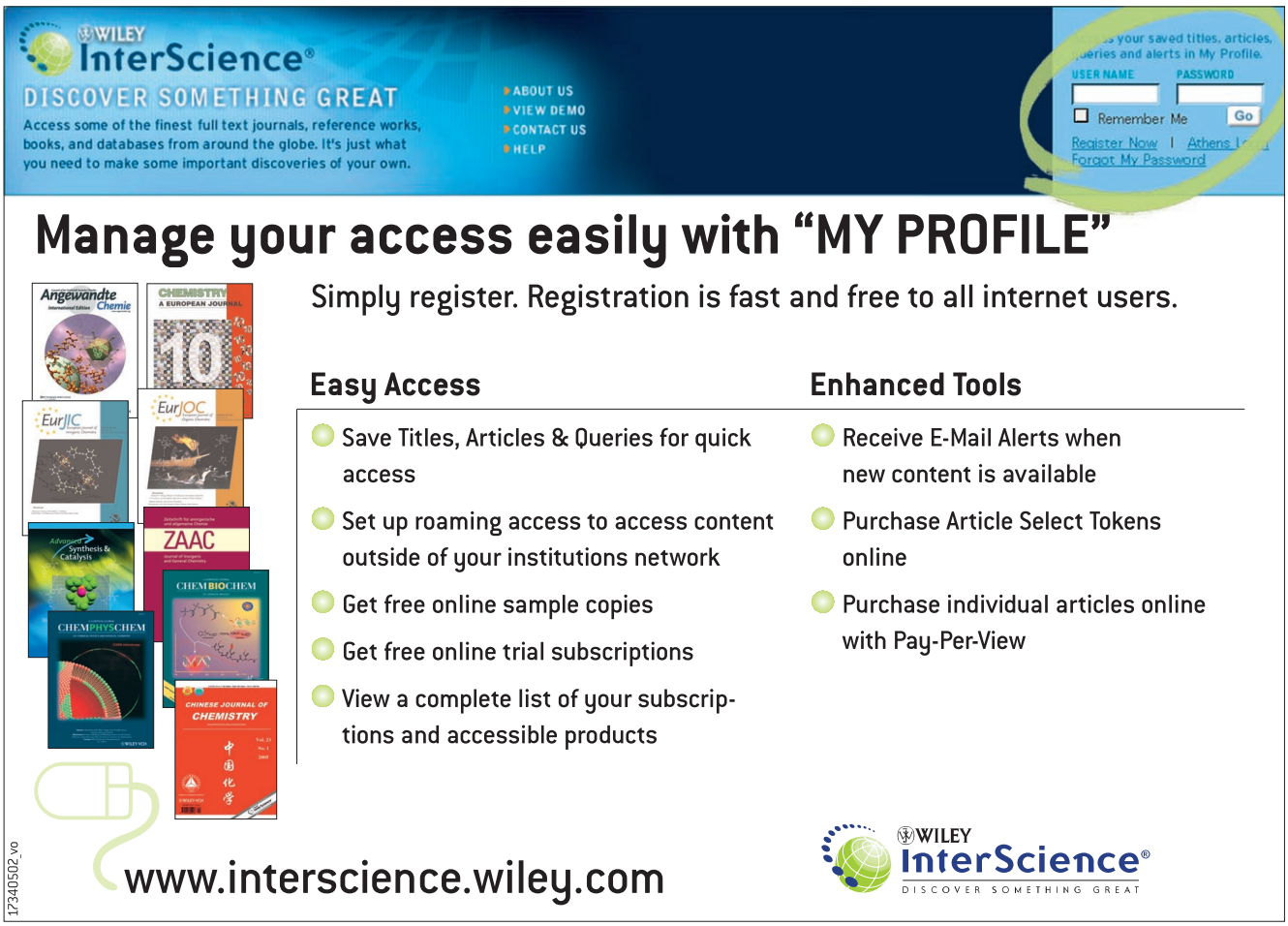
[1] For recent reviews on organic synthesis in water, see: a) C. J. Li, *Chem. Rev.* **2005**, *105*, 3095–3166; b) U. M. Lindström, *Chem. Rev.* **2002**, *102*, 2751; c) *Organic Synthesis in Water* (Ed.: P. Grieco), Blackie, London, **1998**; d) C. J. Li, T. H. Chan, *Organic Reactions in Aqueous Media*, Wiley, New York, **1997**; see also thematic issue: "Organic Reactions in Water", *Adv. Synth. Catal.* **2002**, *344*(3–4).

[2] For reviews on hydrophobic interactions and chemical reactivity, see: a) O. Sijbren, J. B. F. N. Engberts, *Org. Biomol. Chem.* **2003**, *1*, 2809; b) R. Breslow, *Acc. Chem. Res.* **2004**, *37*, 471; c) R. Breslow, *Acc. Chem. Res.* **1991**, *24*, 159.

[3] For a recent study on the reactivity of hydrophobic compounds in water, see: S. Narayan, J. Muldoon, M. G. Finn, V. V. Fokin, H. C. Kolb, K. B. Sharpless, *Angew. Chem.* **2005**, *117*, 3275; *Angew. Chem. Int. Ed.* **2005**, *44*, 3339.

 © 2006 Wiley-VCH Verlag GmbH & Co. KGaA, Weinheim

[4] R. Ding, C. S. Ge, Y. J. Chen, D. Wang, C. J. Li, *Tetrahedron Lett.* **2002**, *43*, 7789.
[5] O. Sijbren, J. B. F. N. Engberts, *J. Am. Chem. Soc.* **1999**, *121*, 6798, and references therein.
[6] R. Breslow, K. Groves, M. U. Mayer, *J. Am. Chem. Soc.* **2002**, *124*, 3622.
[7] M. Biscoe, R. Breslow, *J. Am. Chem. Soc.* **2003**, *125*, 12718.
[8] M. R. Biscoe, C. Uyeda, R. Breslow, *Org. Lett.* **2004**, *6*, 4331.
[9] M. R. Biscoe, R. Breslow, *J. Am. Chem. Soc.* **2005**, *127*, 10812.



 © 2006 Wiley-VCH Verlag GmbH & Co. KGaA, Weinheim

DOI: 10.1002/anie.200501328

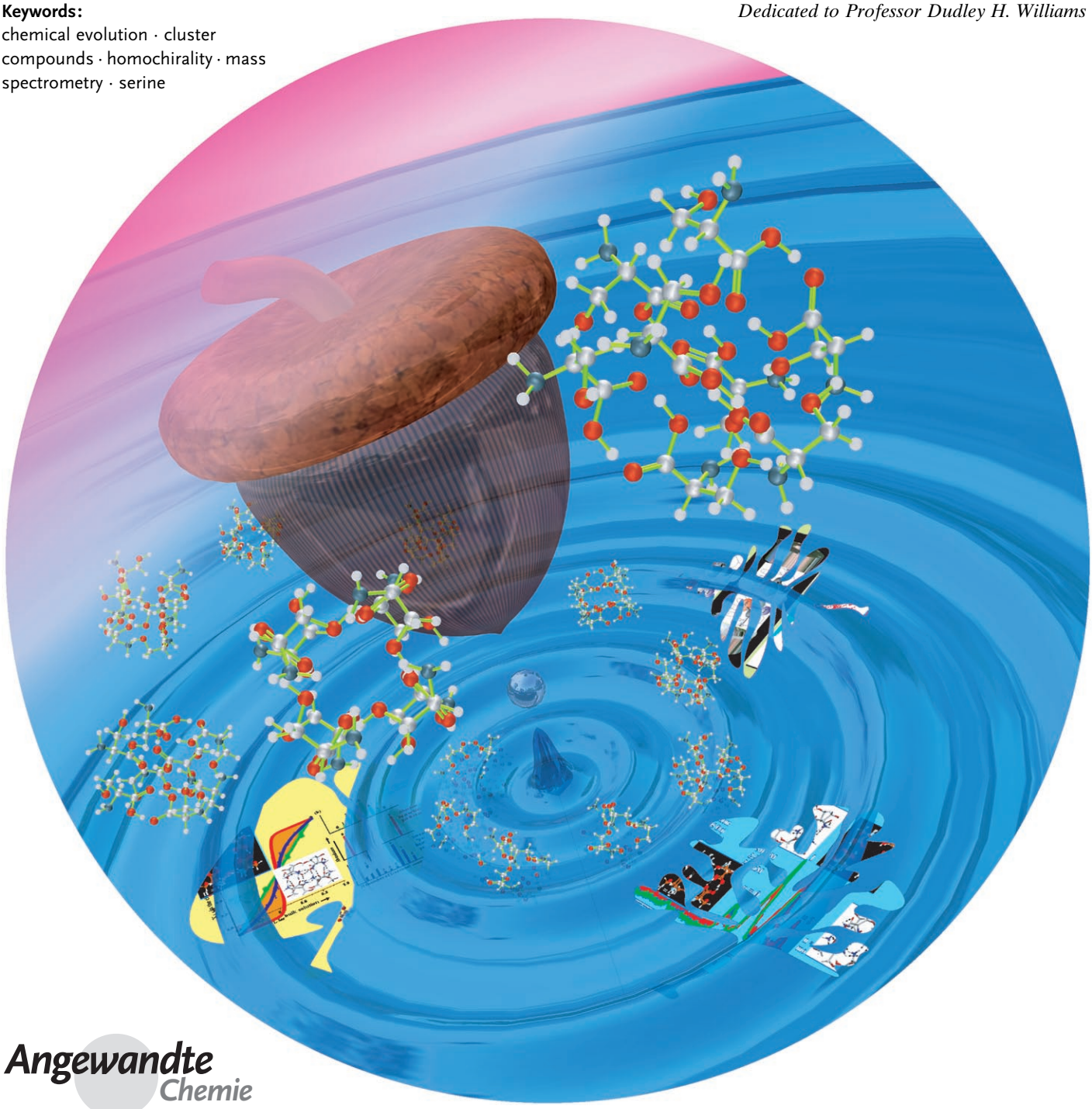
Mass Spectrometry

Serine Octamers: Cluster Formation, Reactions, and Implications for Biomolecule Homochirality**

*Sergio C. Nanita and R. Graham Cooks**

Keywords:
chemical evolution · cluster compounds · homochirality · mass spectrometry · serine

Dedicated to Professor Dudley H. Williams



© 2006 Wiley-VCH Verlag GmbH & Co. KGaA, Weinheim

The emergence of homochirality continues to be one of the most challenging topics associated with the origin of life. One possible scenario is that aggregates of amino acids might have been involved in a sequence of chemical events that led to chiral biomolecules in self-replicating systems, that is, to homochirogenesis. Serine is the amino acid of principal interest, since it forms "magic-number" ionic clusters composed of eight amino acid units, and the clusters have a remarkable preference for homochirality. These serine octamer clusters (Ser_8) can be generated under simulated prebiotic conditions and react selectively with other biomolecules. These observations led to the hypothesis that serine reactions were responsible for the first chiral selection in nature which was then passed through chemical reactions to other amino acids, saccharides, and peptides. This Review evaluates the chemistry of Ser_8 clusters and the experimental evidence that supports their possible role in homochirogenesis.

From the Contents

1. Introduction 555

2. Formation of the Serine Octamer 557

3. Chemistry of Serine and its Octamer 559

4. Proposed Role of the Serine Octamer in Homochirogenesis 565

5. Summary and Outlook 566

1. Introduction

1.1. The Origin of Life

Oparin[1] and Haldane[2] were amongst the first modern scientists to propose hypotheses regarding the origin of life. Their work included proposals about the prebiotic composition of the Earth and the evolution of living organisms, and it contributed to the creation of a fascinating and controversial area of science in which there remain many unanswered questions. Early in the 20th century, Löb[3] was able to synthesize simple amino acids such as glycine in experiments that involved the use of ultraviolet radiation and electric discharges, with formaldehyde being used as the carbon source. In the 1950s Miller and Urey[4] performed their renowned experiments on the conversion of simple compounds into amino acids. Working both independently[5–8] and jointly,[4] they demonstrated that amino acids, in the presence of other biologically relevant molecules, can be generated by applying electrical discharges to gaseous mixtures of simple compounds presumed to have been present on the prebiotic Earth.[4,6] These[4,6–8] and more-refined experiments[9] in which the synthesized products were identified by means of relatively modern analytical techniques such as ion-exchange chromatography/mass spectrometry, demonstrate routes to the abiotic synthesis of amino acids that are relevant to the origin of biopolymers.(For a short review of the experiments relevant to the origin of life, from the 19th century to Miller's experiment, see reference [10].)

A competitive theory suggests that small biomolecules were synthesized in the interstellar medium and delivered to Earth over an extended period. Scientists have evaluated this possibility by studying the formation of amino acids under simulated extraterrestrial conditions[11,12] and by searching for chiral amino acids and organic compounds in meteorites.[13–15] The fact that the Earth is a planet contaminated with amino acids creates an analytical challenge: extraterrestrial samples are easily contaminated, and the provenance of the amino acids reportedly found in some meteorites has been the subject of debate.[16]

There is also laboratory experimental evidence for oligomerization reactions[17–20] which may replicate the synthesis of the first biologically relevant polymers. It has been proposed that, early in the course of biochemical evolution, RNA molecules may have acted as primitive enzymes ("RNA world"). Orgel has demonstrated that RNA can self-replicate and, like protein-based enzymes, it can catalyze reactions.[21–23]

The organization of living systems at the molecular level is remarkable; amongst many noteworthy features is the fact that the residues that make up biological macromolecules exist in just one enantiomeric form (L-amino acids and D-saccharides). In fact, as Clemmer and co-workers have recently argued,[24] the high selectivity of biochemical reactions that drive life requires homochiral biopolymers:[24,25] a protein synthesized with a random composition of amino acid enantiomers could not have the specificity needed to function. Homochirality provides the specific three-dimensional

[*] Dr. S. C. Nanita,[+] Prof. Dr. R. G. Cooks
Purdue University
Department of Chemistry
560 Oval Drive, West Lafayette, IN 47907 (USA)
Fax: (+1) 765-494-9421
E-mail: cooks@purdue.edu

[+] Current address:
DuPont Crop Protection
Stine-Haskell Research Center
1090 Elkton Road, Newark, DE 19714 (USA)

[**] The two enantiomers of the amino acid serine represent the starting point in a series of chemical events that may have led, via the serine octamer, to chiral accumulation and ultimately to the birth of homochiral life. In the Frontispiece, the blue water represents the primordial matrix, serine stirs the terrestrial pot, and by still puzzling processes, life—represented by the acorn—swirls out from the prebiotic system. The picture was created by Zheng Ouyang.

© 2006 Wiley-VCH Verlag GmbH & Co. KGaA, Weinheim

arrangement of amino acid residues in enzymes, which over time has been crafted for optimum function.[26] The important questions that remain unanswered regarding this enantiomeric specificity are: 1) Was there a single chiral progenitor molecule, and if so what was it? 2) Why are L-amino acids and D-saccharides the enantiomers that exist in biopolymers in most living organisms? This subject is currently being investigated widely.[27–31] This Review deals with the most chemical of the challenging problems associated with the emergence of life: the origin of homochirality.

1.2. Homochirality

Pasteur was among the first scientists to recognize chirality, a result of his experiments on the two enantiomeric forms of tartaric acid which he separated by hand.[32] Since then, chirality has become important in many areas of science, and in particular chiral signatures are significant tools in ongoing searches for past or contemporaneous occurrence of life in the solar system.[33] The chirality of the common α-amino acids has often been the focus of interest in considerations of homochirogenesis and in the analysis of meteorites and other experiments relevant to searches for life.[34,35] Chiral composition has also been employed in methods of dating fossils[36] and organic marine sediments.[37,38] This is possible because the racemization rates of most amino acids are very low. For example, the half-life for the racemization reaction of isoleucine is 4.4×10^6 years at pH 7.6 and 0 °C.[37]

It has been proposed that homochirality may have initially originated in one particular chiral compound[28] or molecular assembly,[39] and then transferred to other biomolecules. Such a process may have taken place through a sequence of events which can be encapsulated in three (not necessarily sequential) steps: 1) mirror-symmetry breaking, 2) enantiomeric enrichment (also known as chiral enrichment), and 3) chiral transmission.[40] Mirror-symmetry breaking[41] is the process through which a minute enantiomeric imbalance is postulated to have been first created, and it is a key step in homochirogenesis.[28,42,43] It must have involved discrimination against one of the enantiomeric forms by physical, chemical, and/or statistical processes. Mirror-symmetry breaking might be an intrinsic property of matter and originate in the avoidance of parity violation in the weak nuclear force, thus giving rise to an intrinsic energy difference between enantiomers.[44–48] Alternatively, naturally occurring nonbiological phenomena acting over a racemic primitive Earth may have led to mirror-symmetry breaking. Such phenomena include circularly polarized ultraviolet light (UV-CPL),[28,49–53] magnetic fields ("the magnetochiral effect"),[54,55] and even vortex motion.[56]

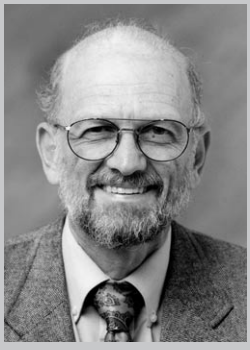
Enantiomeric enrichment involves the build-up of a much larger enantiomeric excess of a particular primitive molecule and culminates in the selection of the pure isomer. Examples of this process are known to take place on surfaces of both mineral crystals[57,58] and water (at the air/solution interface).[59,60] Hazen et al. have demonstrated that the enantiomorphous faces of calcite can induce enantioselective adsorption of organic molecules.[58] However, it must be noted that in this case the problem of mirror-symmetry breaking is simply shifted from a preexisting organic material to an inorganic one, since an excess of a mineral surface that favors the adsorption of L-amino acids is required. Enantiomeric enrichment has also been demonstrated by Green et al. in polymerization reactions, where the polymers are preferentially formed from homochiral units in a process known as "majority rules".[61–64] Other examples of enantiomeric enrichment are asymmetric syntheses[65,66] and self-replication of biomolecules such as peptides.[67] This last example of course cannot explain the earlier occurrence of prebiological enantiomeric enrichment.

Chiral transmission, the third and final step in the triad mentioned above, is the transfer of chirality from one molecule or molecular assembly to another. Such a process has been shown to occur in clusters of serine molecules,[40] where the homochiral preference of a molecular assembly (serine octamer[39,68–72]) is transferred to other amino acids (or sugars) through entantioselective substitution reactions.[40,73] The process of enantiomeric enrichment of organic molecules on calcite could also be classified as chiral transmission. In this case, the symmetry-breaking step would consist of producing an imbalance that favored the existence of particular faces of calcite where adsorption of L-amino acids occurs preferentially, thus allowing a chiral transmission process in which the chirality of the inorganic substrate is transferred to the organic amino acid.

Serine, to an extent not approached by any of the other coding amino acids, forms particularly stable "magic-number" clusters which have a remarkable preference for homochirality.[39,68–72] Experimental evidence which links serine clusters to the enantiomeric enrichment[74,75] and



Sergio C. Nanita began his studies at the University of Puerto Rico (Río Piedras) with Prof. Osvaldo Rosario where he worked on Environmental and Analytical Chemistry, and in 2001 he obtained a B.S. in Chemistry. In 2005 he obtained a PhD in Analytical Chemistry from Purdue University. During his PhD with Prof. R. Graham Cooks, he studied analytical applications of mass spectrometry, noncovalently bound clusters of small biomolecules, and chiral recognition, focusing on the serine octamer and the origin of homochirality. He is currently a Section Research Chemist at DuPont Co.



R. Graham Cooks has been the Henry Bohn Hass Distinguished Professor of Chemistry at Purdue University since 1990. He is interested in fundamental phenomena associated with collisions of ions and molecules, tandem mass spectrometry, and desorption ionization. His work on the kinetic method of measuring thermochemical quantities has provided a new method of chiral analysis. Several mass spectrometers have been constructed in his laboratory, most recently miniature instruments for in situ analysis. He has authored 750 publications and served as PhD thesis advisor to 95 students.

 © 2006 Wiley-VCH Verlag GmbH & Co. KGaA, Weinheim

chiral transmission[40,73,76] steps of homochirogenesis has been reported, and is thus suggestive of a role for serine and its homochiral clusters in homochirogenesis. This Review explores the evidence for this hypothesis as well as other aspects of the chemistry of these interesting clusters.

2. Formation of the Serine Octamer

2.1. Aerosols

The serine octamer, a stable magic-number cluster, was first discovered[39,68,69] through experiments that involved electrospray ionization (ESI)[77,78] using relatively concentrated (0.01 M) aqueous solutions of serine. Ions are generated by ESI as a consequence of solvent evaporation from a spray of charged microdroplets of the solution.[77,78] This particular ionization method is known to provide gentle conditions and serine clusters were observed in the course of systematic studies on the clustering of each of the natural amino acids.[68,79] Electrospray ionization has also been employed extensively in attempts to characterize solution-phase molecular assemblies,[80–85] including specific noncovalent enzyme complexes which might be transferred from solution to the gas phase.[82] However, the connection between species observed in ESI mass spectra and solution-phase aggregates is not fully established, and the ions observed in ESI mass spectra may not be directly related to preexisting solution-phase species. Rather, the serine octamers observed through ESI might be formed during the droplet evaporation process. What is known is that the protonated serine octamer is very stable in the gas phase (Figure 1).[39] The near-absence of the

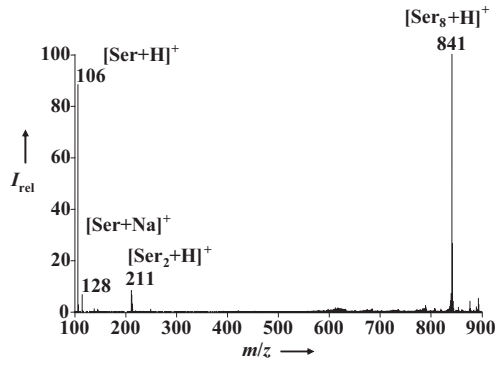


Figure 1. Typical electrospray mass spectrum of a 0.01 M solution of serine in methanol:water 50:50 v/v. Reproduced with permission from reference [39]. Copyright 2001, American Chemical Society.

neighboring clusters $[Ser_7+H]^+$ and $[Ser_9+H]^+$ makes the serine octamer a remarkable example of magic-number clustering,[86] comparable to the highly preferred clusters of carbon, Buckminsterfullerene ($C_{60}^{+\bullet}$).[87] Equally remarkable is the enantioselectivity exhibited in Ser_8 cluster formation (see Section 2.4).

Other spray ionization techniques derived from ESI have also been employed to study serine clusters.[76,86,88] They include cold spray ionization (CSI),[89,90] sonic spray ionization (SSI),[91,92] and electrosonic spray ionization (ESSI).[93,94] All are believed to provide gentler ("softer") ionization conditions than the original electrospray method, and ESSI in particular has the quality of softly generating fully desolvated ions.[93,94] The "softness" of the ionization methods used to study clusters by mass spectrometry has proven to be crucial—it affects the distribution of cluster ions observed in the spectra. One of the first examples of magic-number clusters was presented by Searcy and Fenn in the 1970s.[95] These authors studied the distribution of protonated water clusters formed in a supersonic free-jet expansion and found that the formation of particular magic-number clusters is dependent on the energetic conditions of the experiment.[95] In an analogous way, the relative abundance of the protonated serine octamer with respect to other cluster sizes also varies as a function of the conditions of the experiment. The gentler ionization provided by methods such as SSI explains why, in some experiments,[76] magic-number serine octamers are generated in even higher amounts than by ESI spectra. All reported mass spectra of serine obtained using ESI and related ionization methods show the protonated octamer $[Ser_8+H]^+$ as a magic-number cluster.[76,86,88] In addition, other cationic and anionic forms of Ser_8 also show this behavior under suitable conditions, thus suggesting the magic-number clustering to be a characteristic of the neutral molecular cluster, and not merely of its ionic form.[96]

The above ionization methods based on aerosol sprays may be models for naturally occurring aqueous aerosols (for example, hot springs, water falls, etc.) which might therefore also produce clustering of the solute. Prebiotic aerosols have previously been considered as favorable environments for processes relevant to the origin of life.[97–100] Most notably, micrometer-size vesicles with organic walls and an aqueous core, as formed in aerosols,[97,98] have been proposed as favorable media for prebiotic reactions such as oligomerization.[98,99] In each droplet of an aerosol, reagents (solutes) experience an increase in concentration through water evaporation, which favors reactions by Le Chatelier's principle. Among the ionization methods employed so far to study the serine octamer, sonic spray (SSI), which forms ions simply through solution nebulization assisted by a sheath gas of high velocity,[91,92] seems to best simulate prebiotic aerosols, since, unlike ESI, it does not require application of a high voltage. As shown later in Section 3.1, SSI is very effective at generating Ser_8 ions with high chiral specificity. Serine octamer ions have also been generated and studied in experiments intended to simulate other prebiotic conditions, as discussed in the next two sections.

2.2. Evaporation

Magic-number serine octamer ions can be generated through vigorous evaporation of aqueous solutions of serine.[101] This is achieved by rapidly heating small amounts of the solution on a hot metal surface kept at an appropriate temperature between 200–250 °C.[101] Figure 2 illustrates the experimental arrangement and shows a typical mass spectrum.[101] The octamers are generated in the ambient environ-

© 2006 Wiley-VCH Verlag GmbH & Co. KGaA, Weinheim

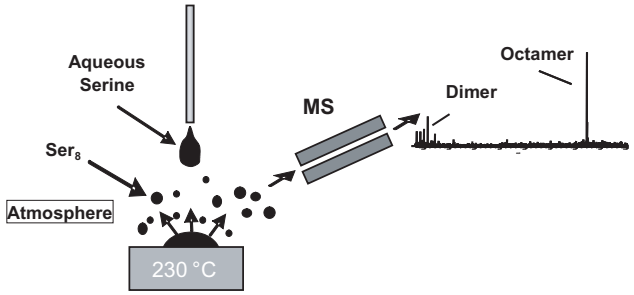


Figure 2. Experimental arrangement that allows the formation of serine octamers upon vigorous evaporation of aqueous solutions of serine. Reproduced from reference [101]. Copyright 2004, Royal Society of Chemistry.

ment, then sampled and identified using a mass spectrometer. The temperature of the surface was kept around the Leidenfrost point of water.[102,103] At this temperature, water vapor creates a cushion between the liquid droplet and the hot surface, therefore decreasing the efficiency of heat transfer. That is why serine octamer ions were suggested to be formed in these experiments through evaporation of the solution from the surface of small droplets that "levitate" over the metal surface.[101] These experiments mimic conditions believed to have been common on the prebiotic Earth: hot surfaces in contact with aqueous solutions of organic materials were likely a common scenario.[104]

2.3. Sublimation

A third method[101] that can be employed to form serine octamers in the open atmosphere involves heating crystalline serine on a metal surface. The sublimate is then sampled by a mass spectrometer fitted with an atmospheric pressure ionization (API) source, for example, a corona discharge. Figure 3a illustrates the experimental arrangement used to generate serine clusters through thermal desorption from the crystal.[101] As in the case of solution evaporation (Section 2.2), protonated serine octamers are readily formed from solid serine. Figure 3b shows representative temperature-dependent mass spectra recorded upon heating crystalline L-serine.[105] At relatively low temperatures, for example, 150 °C, solid serine mainly sublimes in the form of monomers, but as the temperature of the surface is increased, serine dimers and octamers appear. Since the melting point of serine is about 220–230 °C and octameric clusters appear below this temperature, it seems that neutral serine octamers are either the product of sublimation directly from the crystalline state of serine, or—less likely—are formed by nucleation of serine monomers in the gas phase immediately after the monomeric units have sublimed.

The results described in Sections 2.1, 2.2, and 2.3 refer to experiments where $[Ser_8+H]^+$ ions are formed from homochiral L-serine. The chiral effects associated with the generation of serine octamers have also been characterized in detail through experiments that compare the formation of the clusters of interest from homochiral and heterochiral systems (see Section 2.4).

2.4. Chirality in Cluster Formation

It has long been known that serine octamers are formed in greater abundance from homochiral than racemic solutions.[39,68–71] Figure 4 shows a comparison of octamer formation from solutions containing serine of various enantiomeric purity. A minimum signal intensity for $[Ser_8+H]^+$ ions (m/z 841) is obtained in the case of mass spectra recorded for racemic solutions.[39] This finding is consistent with the serine octamer having a preference for homochirality. However, when the experimental data are compared to the predicted result for absolute homochiral preference (from the binomial theorem), it is evident that the homochiral preference in the serine octamer is strong but not absolute under the conditions of the particular experiment (see Figures 4 and 5). Qualitatively the same result has been seen in experiments performed in different types of mass spectrometers.[69–72,106,107]

Isotopic labeling of the serine enantiomers allows one to reliably distinguish the enantiomeric composition of serine octamers by mass spectrometry. Figure 5 shows a mass spectrum from an isotope-labeling experiment where the deuterated L isomer (2,3,3-L-[D_3]serine) is present in a racemic mixture.[106,107] A method has been developed[69,71] which corrects for statistical contributions in the evaluation of the enantioselectivity involved in cluster formation,[69,71] thus allowing a direct comparison of the relative chiral preference or stability of clusters containing different numbers of L or D enantiomers. This methodology has been applied successfully to the case of the serine octamers, thereby confirming that these clusters have a strong preference for homochirality (the clusters L-Ser_8 and D-Ser_8 are preferred over all other possible combinations).[69,71] The

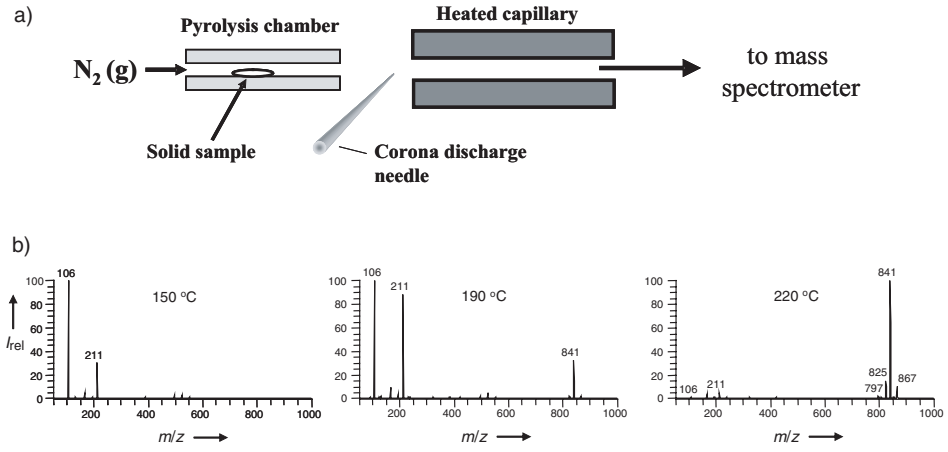


Figure 3. a) Experimental arrangement employed for the sublimation of serine crystals. Corona discharge ionization yields protonated serine octamers which are subsequently detected by mass spectrometry.[101] b) Mass spectra of the sublimate of serine recorded as a function of temperature.

 © 2006 Wiley-VCH Verlag GmbH & Co. KGaA, Weinheim

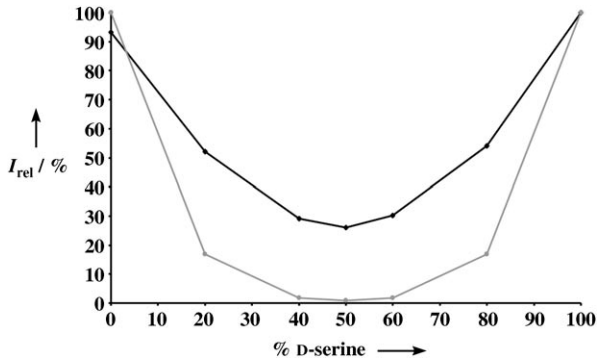


Figure 4. Chiral effects associated with the formation of serine octamers: The signal intensity of m/z 841 is plotted as a function of the enantiomeric composition of the serine solution. The maximum signal is obtain for homochiral solutions, while a minimum is obtained for the racemate. ◆ MS data; ● prediction based on a binomial distribution. Adapted with permission from reference [39]. Copyright 2001, American Chemical Society.

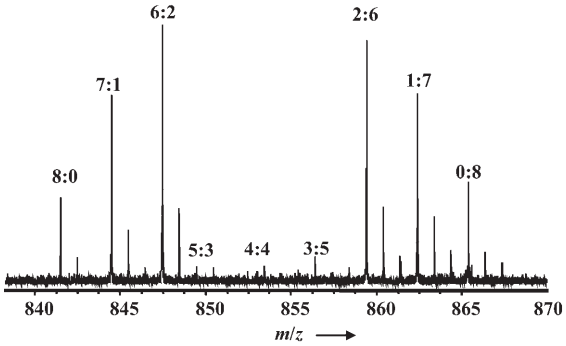


Figure 5. Typical isotope-labeling pattern in the electrospray mass spectrum of Ser_8 formed from a solution containing 0.01 M D-Ser (105 Da) and 0.01 M 2,3,3-L-[D_3]Ser (108 Da) in methanol/water/acetic acid (49:49:2 v/v).[107] Statistical weighting hs to be used to obtain relative probabilities as given in Figure 4.

high chiral selectivity of the serine octamer has been observed not only in the spray ionization experiments, but also in octamers generated by solution evaporation and by sublimation of serine crystals.[101]

The clustering tendencies of all 20 naturally occurring amino acids (together with the chiral preferences associated with their formation) have been studied by spray ionization methods.[68,79,105] A few amino acids other than serine form clusters enantioselectively, but only under especially mild conditions.[86,108] For example, threonine[108] and proline[24] form homochiral octamers and dodecamers, respectively. However, these systems are nowhere near as stable as the serine octamer and the preference for homochiral clusters is much lower. A systematic study[105] of the clustering preferences of amino acids through sublimation from the crystal (as discussed for serine in Section 2.3) has also proven that the octamer represents the most stable (magic[109]) cluster of serine and confirmed its uniqueness among the other amino acids (Figure 6).

In summary, serine forms homochiral octameric clusters in several processes which simulate prebiotic conditions to a

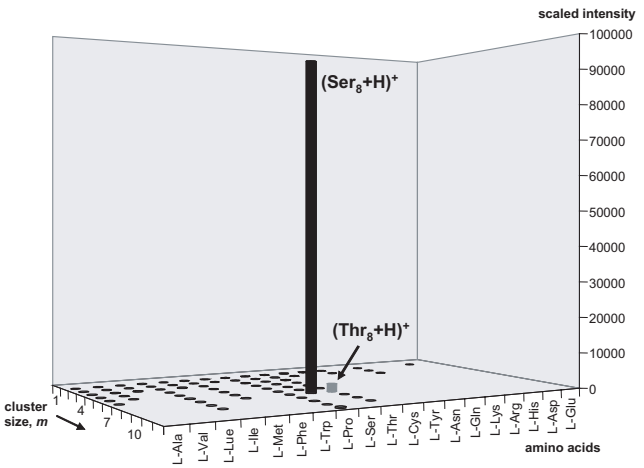


Figure 6. Magic-number character of clusters of amino acids formed through sublimation from the crystal. Scaled intensities correspond to $I_m^2/(I_{m-1} \times I_{m+1})$, where I is the intensity of the cluster signal and m is the cluster size.

greater or smaller degree.[39,68–71,76,86,88,101] The processes described in this section start with serine in the solid, solution, and gaseous phases. Even though the cluster can be formed from initial material which may be in different physical states, it remains unclear whether serine octamers exist in the solid phase (as subunits of the crystal) or as preexisting clusters in solution. What is certain, from all the mass spectrometry experiments, is that Ser_8 ions: 1) exhibit a strong preference for homochirality, 2) appear as magic-number clusters in the mass spectra of serine, and 3) are very stable in the gas phase. These data provide an intriguing basis for non-mass-spectrometric studies of serine aimed at searching for the existence of stable neutral and charged octamers in media other than the gas phase.

3. Chemistry of Serine and its Octamer

3.1. Substitution of Amino Acids and Sugars

If the serine octamer indeed played a key role in the origin of homochirality then appropriate reactions, specifically enantioselective reactions with compounds known or suspected to be present on the early Earth, should reveal or suggest this. One such reaction illustrates how the chiral signature of serine can be transferred to other amino acids. Other reactions provide connections with simple sugars, such as glyceraldehyde, as well as hexoses.

Electrospray ionization of solutions containing serine and another biomolecule (for example, another amino acid or a sugar such as glucose) results in substitution reactions[40,73,76,108,110] taking place, with replacement of one or more serine molecules in the octamer by the corresponding number of molecules of the other biomolecule. A general equation for the serine/amino acid substitution reaction is shown in Scheme 1. Mixed serine/amino acid octamers have been generated from binary mixtures containing serine and another amino acid.[76] Strong chiral effects accompany the

 © 2006 Wiley-VCH Verlag GmbH & Co. KGaA, Weinheim

$$n(\text{L-aa}) + (\text{L-Ser}_8\text{+H})^+ \longrightarrow (\text{L-aa}_n\ \text{L-Ser}_{8-n}\text{+H})^+ + n(\text{L-Ser})$$

aa = Thr, Asp, Cys, etc.

n = 1,2...8

Scheme 1. General representation of amino acid substitution reactions in the serine octamer. The reaction has been observed in the protonated octamer, but is postulated to also occur in the corresponding neutral cluster.

formation of these clusters. A mixture of threonine and serine of the same chirality under sonic spray conditions (SSI, no electric field) yields a series of octamer ions (serine/threonine 8:0, 7:1, 6:2, 5:3, … 0:8), thus revealing a continuous transition from the protonated serine to the protonated threonine octamer. In the corresponding heterochiral mixture, the preference for the homochiral product limits the extent of the substitution reaction.[108] Experiments involving cysteine, the sulfur analogue of serine, yielded similar results (Table 1). In the case of amino acids with larger side chains

Table 1: Relative abundance of substituted L-serine octamer ions.[a]

	Number of incorporations							
Amino acid	1	2	3	4	5	6	7	8
glycine	100	81	–	–	–	–	–	–
L-alanine	100	74	–	–	–	–	–	–
L-leucine	89	100	–	–	–	–	–	–
L-threonine	2	14	55	95	100	88	37	1
L-cysteine	68	100	61	43	18	10	2	1
L-phenylalanine	74	100	22	8	–	–	–	–
L-tyrosine	100	84	12	–	–	–	–	–
L-tryptophane	94	100	7	2	–	–	–	–
L-asparagine	76	100	8	–	–	–	–	–
L-histidine	100	96	–	–	–	–	–	–
D-alanine	100	66	–	–	–	–	–	–
D-leucine	82	100	–	–	–	–	–	–
D-threonine	64	100	5	–	–	–	–	–
D-cysteine	78	100	4	–	–	–	–	–
D-phenylalanine	97	100	–	–	–	–	–	–
D-tyrosine	100	68	–	–	–	–	–	–
D-tryptophane	100	57	–	–	–	–	–	–
D-asparagine	100	48	–	–	–	–	–	–
D-histidine	100	86	–	–	–	–	–	–

[a] 0.01 M solutions (MeOH/water 1:1) of L-serine and another amino acid were mixed in a 1:1 ratio. These spectra are strongly dependent on the spray conditions. Reproduced with permission from reference [76]. Copyright 2003, American Chemical Society.

(for example, phenylalanine and tryptophan) a preference for the incorporation of amino acids of like configuration was again observed, although substitution reactions occur to a more limited extent as a result of steric effects. The results of sonic spray experiments on binary mixtures containing serine and various other amino acids are summarized in Table 1.[76] Prominent signals corresponding to products with two substituted serine molecules were observed in most experiments. Product clusters from multiple amino acid substitutions are also evident, especially when the amino acid chosen has the same configuration as serine.[40,76] The main finding of these experiments is that amino acid substitution reactions in the serine octamer occur readily and they operate enantioselectively.[40,76,108]

Substitution reactions in clusters have been observed, not only with amino acids as reagent monomers, but also with saccharides[73,108] such as glyceraldehyde, glucose, and inositol. Glucose (Glc) can substitute for serine molecules in the octamer to form the magic-number cluster $[Ser_6\,Glc_3 + Na]^+$ at m/z 1193. The serine/glucose substitution reaction is accompanied by strong chiral effects which have been studied using isotope labeling (with both 2,3,3-L-[D_3]serine[108] and [$^{13}C_6$]-labeled D-glucose[73]), and by tandem mass spectrometry. The cluster containing the nonbiological enantiomer L-glucose is formed in much lower amounts than that containing the natural D-glucose. For example, the signal intensities of the clusters $[\text{L-Ser}_6\text{L-Glc}_3 + Na]^+$ and $[\text{L-Ser}_6\text{D-Glc}_3 + Na]^+$ were approximately 1×10^5 and 3×10^5 counts, respectively, in tandem mass spectra recorded under identical conditions (Figure 7). The breakdown plots (fragmentation signatures) also reveal that activated $[\text{L-Ser}_6\text{L-Glc}_3 + Na]^+$ dissociates more readily and produces an additional fragment not seen in the MS/MS of $[\text{L-Ser}_6\text{D-Glc}_3 + Na]^+$. This result suggests that the L-serine/L-glucose cluster is less stable. The isotope-labeling experiments[73,108] also demonstrate that the substitution reaction described here is favored for L-serine/D-glucose over the L-serine/L-glucose case.

3.2. Prebiotic Chemistry of Serine

One of the most intriguing and prebiotically relevant chemical properties of serine is the relative ease with which it can be converted into other amino acids and to other suspected primordial molecules. It is known that thermal degradation of serine can produce glycine, ethanolamine (EtAm), acetaldehyde, and pyruvic acid.[111] Scheme 2 shows a possible mechanism for the formation of these products by thermolysis.

Although the primary reaction products do not retain the chiral center, they are biologically significant; for example, pyruvic acid is known to participate in anaerobic respiration. Secondary reaction products of the thermal decomposition of serine (not shown in Scheme 2) include the amino acids alanine[111] and leucine, which are chiral. It has been proposed that the conversion of serine into other biologically relevant compounds through thermal decomposition may involve dehydroserine as an intermediate.[73,111] This product is the result of dehydration with loss of the hydrogen atom at the α-carbon position (Scheme 2).[73]

Of great interest is the fact that while serine is converted into other compounds during its thermal decomposition, the reaction products can immediately undergo the same substitution reactions with the serine octamer as mentioned in Section 3.1. This process is particularly relevant in the case of chiral products (for example, the amino acids). A simple experiment demonstrated both the formation of glycine, alanine, leucine, and ethanolamine (primary and secondary reaction products of the thermal decomposition of serine), together with the occurrence of substitution reactions of the

 © 2006 Wiley-VCH Verlag GmbH & Co. KGaA, Weinheim

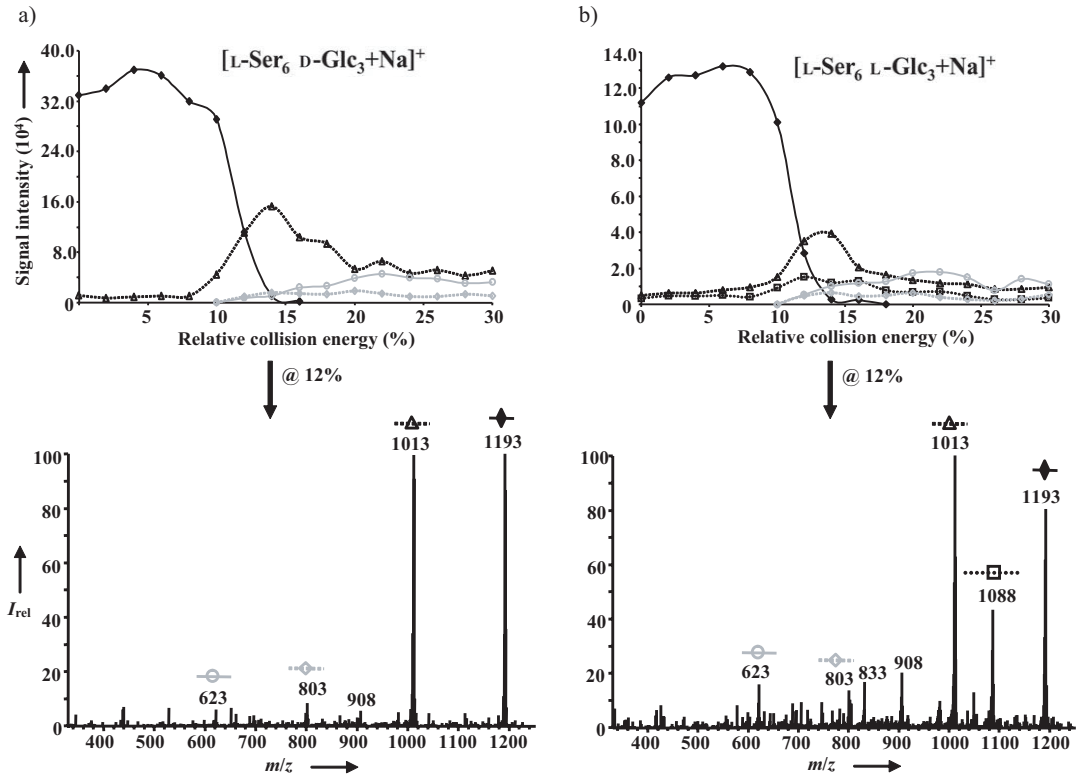
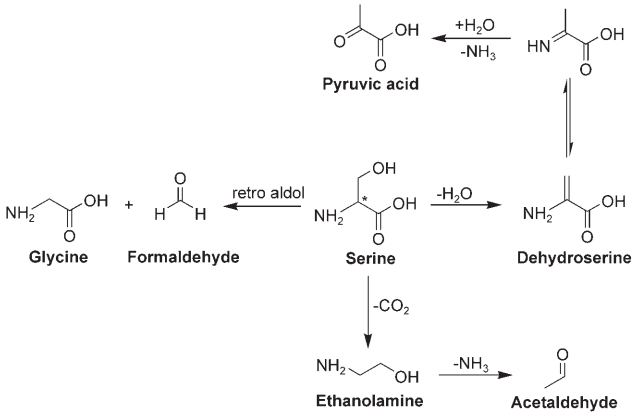


Figure 7. Tandem mass spectral data of the cluster ions: a) $[\text{L-Ser}_6\,\text{D-Glc}_3+\text{Na}]^+$ (m/z 1193) formed from a mixture of 0.01 M L-serine and 0.01 M D-glucose (1:1), and b) $[\text{L-Ser}_6\,\text{L-Glc}_3+\text{Na}]^+$ (m/z 1193) formed from a mixture of 0.01 M L-serine and 0.01 M L-glucose (1:1). The difference in stability between the isomeric clusters can be seen by comparing their respective breakdown plots. The additional fragment ion at m/z 1088 in the L-serine/L-glucose case correspond to the loss of one neutral serine.



Scheme 2. Primary products of the thermal decomposition reaction of serine. Glycine and other suspected prebiotic compounds are formed. The asterisk marks the chiral center of serine. Modified with permission from reference [111]. Copyright 2000, American Chemical Society.

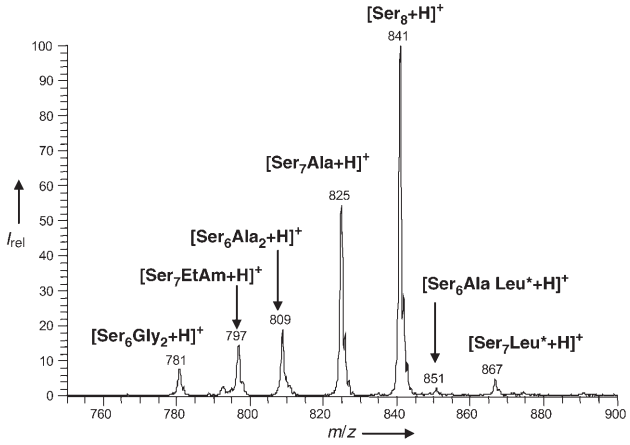


Figure 8. Mass spectrum of the sublimate of serine (surface temperature was 230 °C): The data shows $[\text{Ser}_8+\text{H}]^+$ ions as well as the products of reactions involving serine.

octamer. The formation of the serine octamer, as well as the products of substitution reactions, occurs on heating serine in air at atmospheric pressure; the clusters and reaction products are simply sampled from the ambient environment into a mass spectrometer for analysis. Figure 8 shows a mass spectrum which includes thermal decomposition products of serine incorporated into the octamer through substitution reactions.[112]

Serine has also been detected as a product in experiments that simulate synthesis of amino acids under prebiotic conditions.[9] Serine can also be formed from putative primitive molecules such as formaldehyde and glycine by means of an aldol condensation reaction (see Scheme 2).[111] Taken together, all the experimental evidence points towards serine as a likely prebiotic molecule.

 © 2006 Wiley-VCH Verlag GmbH & Co. KGaA, Weinheim

Serine is distinctive in one further aspect: it is one of two amino acids[113] with low energy barriers for epimerization (L-serine⇄D-serine).[73] This is true for both the free amino acid[73,114] and serine residues in proteins.[115,116] The results of an experiment demonstrating that serine can undergo epimerization at a neutral pH value are shown in Figure 9. The

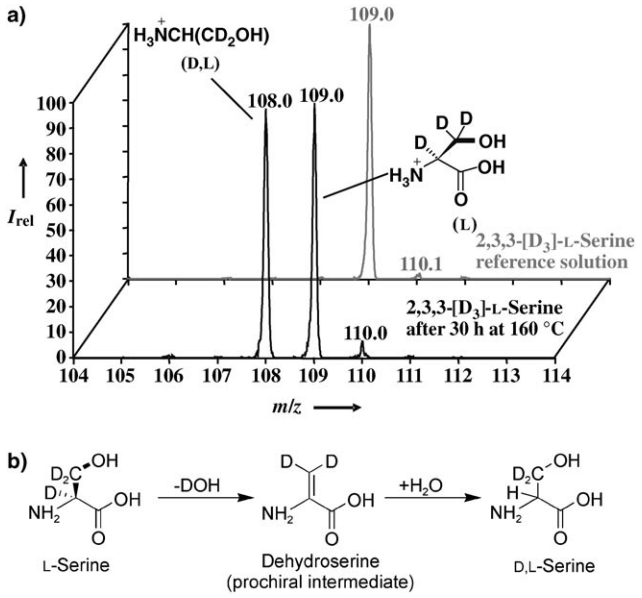


Figure 9. a) Electrospray mass spectra showing the epimerization reaction product of deuterated L-serine. The experiment was performed by heating a serine solution in a sealed ampoule at 160 °C for 30 h. Spectra for the epimerized sample and a control, blank sample are shown.[73] b) Proposed mechanism for the facile epimerization of serine.

facile configuration interconversion in serine represents a process that could be particularly susceptible to external chiral agents (UV-CPL, magnetic fields, etc.), which may affect the equilibrium of the epimerization reaction and thus favor the formation of one enantiomer over the other.

3.3. Metaclusters and Other Serine Aggregates

Protonated serine octamers are known to occur as aggregates in the form of multiply charged 16-mers, 24-mers, and 32-mers.[39,70,71,117] The metaclusters $[Ser_{16}+2H]^{2+}$, $[Ser_{24}+3H]^{3+}$, and $[Ser_{32}+4H]^{4+}$ have been examined in experiments in which ion mobility spectrometry (IMS)[70,71] and high-resolution mass spectrometry[106,107] have been used to distinguish them from the singly protonated serine octamer, since all have exactly the same mass-to-charge ratio (m/z 841) for the main isotopic form. Ion mobility[118] can resolve isobaric ions based on differences in their mobility through a flight tube which contains a buffer gas at relatively high pressure (usually between 1 and 760 Torr). Figure 10 shows the ion mobility spectrum of protonated serine clusters (m/z 841); the individual signals correspond to $[Ser_8+H]^+$, $[Ser_{16}+2H]^{2+}$, and $[Ser_{24}+3H]^{3+}$.[71] Since the mobility of

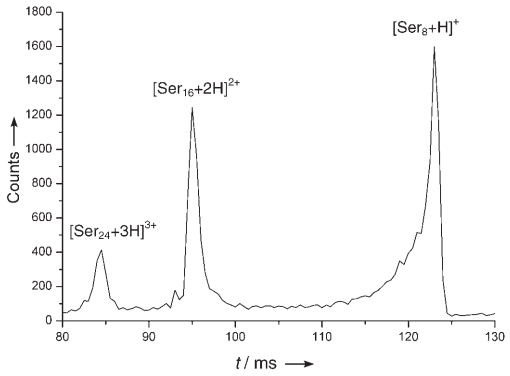


Figure 10. Ion mobility spectrum for m/z 841. The three isobaric ions $[Ser_8+H]^+$, $[Ser_{16}+2H]^{2+}$, and $[Ser_{24}+3H]^{3+}$ are separated on the basis of their respective ion mobilities. Reproduced with permission from reference [71]. Copyright 2002, American Chemical Society.

ions through the drift tube depends on their shape and size, the IMS technique allows calculation of the cross-sections of ions directly from mobility data.[118,119] The methodology has been tested extensively with many systems[118–121] and is accepted as an accurate way (within 1–2%) of measuring the average cross-sections of ions. A summary of experimental cross-section measurements for serine clusters is shown in Table 2.[70,71] There is a consensus that the experimental cross-

Table 2: Experimentally determined cross-section of the serine octamer and its metaclusters.[70,71]

Cluster size	Charge state	Ω_{exp} [Å^2]	
		Ref. [71]	Ref. [70]
8	+1	187	191.4
16	+2	285	294.0
24	+3	380	392.4

section of the singly protonated serine octamer is around 190 Å^2. However, evidence shows (section 3.4.2) that there are two isomeric forms of protonated serine octamers, only one of which apparently is generated in or survives the IMS experiments.

High-resolution measurements made using an Orbitrap mass spectrometer[122,123] have also been used to distinguish the metaclusters of the protonated serine octamers.[106] The high mass resolving power of this instrument allows identification of contributions from the multiply charged aggregates $[Ser_{16}+2H]^{2+}$ and $[Ser_{24}+3H]^{3+}$, not on the basis of the signal at m/z 841, but rather on the basis of their respective heavy isotopes containing a single ^{13}C atom at m/z 841.5 and 841.33, respectively. In addition, these experiments demonstrated that the relative abundances of $[Ser_8+H]^+$, $[Ser_{16}+2H]^{2+}$, and $[Ser_{24}+3H]^{3+}$ are dependent on pressure and the conditions of the experiments: under more energetic conditions $[Ser_{16}+2H]^{2+}$ and $[Ser_{24}+3H]^{3+}$ dissociate and only serine octamers are present.[106]

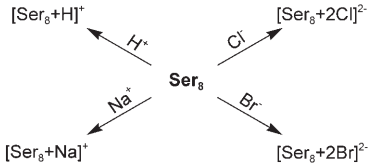
Under very mild conditions,[86] such as those achieved in experiments done using SSI in an ion mobility/time of flight mass spectrometer (IMS-TOF),[124] very large serine clusters

© 2006 Wiley-VCH Verlag GmbH & Co. KGaA, Weinheim

can be observed.[86] Some of the serine aggregates formed contain over 600 serine molecules.[86] Figure 11 shows the isotopically labeled SSI-IMS-TOF mass spectra of racemic serine. The data confirm the remarkable preference for the homochiral octamer. In addition, a cluster containing 17 serine molecules $[Ser_{17}+H]^+$ also has a preference for homochirality, although to a smaller extent.[86] Crystal-like gas-phase growth is suggested to be responsible for the formation of these higher serine cluster ions, particularly the very large aggregates of nanometer size.[86]

The serine octamer has been observed not only as the protonated adduct but also as adducts with sodium[90,117] and other metal ions such as Cu^{2+}, namely, as $[Ser_8+Na]^+$ and $[Ser_8+Cu-H]^+$, respectively.[73] Amongst the transition metals, copper in particular is suspected of playing a role in the origin of life,[18,125] since it catalyzes biologically relevant reactions, for example, the important salt-induced formation of peptides.[18] Cluster ions in general represent a fundamental and favorable site for chemical reactions to occur, especially when a metal is present in the cluster.[126] What is remarkable is that the various adducts of serine octamers possess the same chemical characteristics, such as homochiral preference, cluster stability, and magic-number character. This observation suggests the observed chemical properties are intrinsic to a neutral serine octamer. Negatively charged dihalide adducts of serine octamers also undergo the same enantioselective chemistry of positively charged adducts (Scheme 3), thus providing further support for the hypothesis about the existence of a neutral homochiral octamer.[96]

Corona discharge ionization of serine vapor containing octamers has been achieved in experiments described in Section 2.3 (Figure 3). This data is interpreted as suggesting that neutral octamers are generated under ambient conditions from the sublimation of serine. Even though these studies have revealed similarities between the chemical properties of anionic and cationic adducts, there is only indirect evidence regarding the characteristics of the as-yet-unknown neutral octamer; there is a need for further investigations aimed at the direct observation of the neutral cluster.



Scheme 3. Dihalide adducts of the serine octamer show similar chemical behavior to the well-known positively charged octamers. It has been proposed that the enantioselective formation and substitution reactions observed for all these ions simply reflects the behavior of the as-yet-unknown neutral serine octamer. Reproduced with permission from reference [96]. Copyright 2005, American Chemical Society.

3.4. Structure of the Octamer

3.4.1. Dissociation

Tandem mass spectrometry (MS/MS) has been employed in an attempt to characterize the structural features of the serine octamer.[39,71,127] Collision-induced dissociation mass spectra of serine suggest that homochiral octamers are

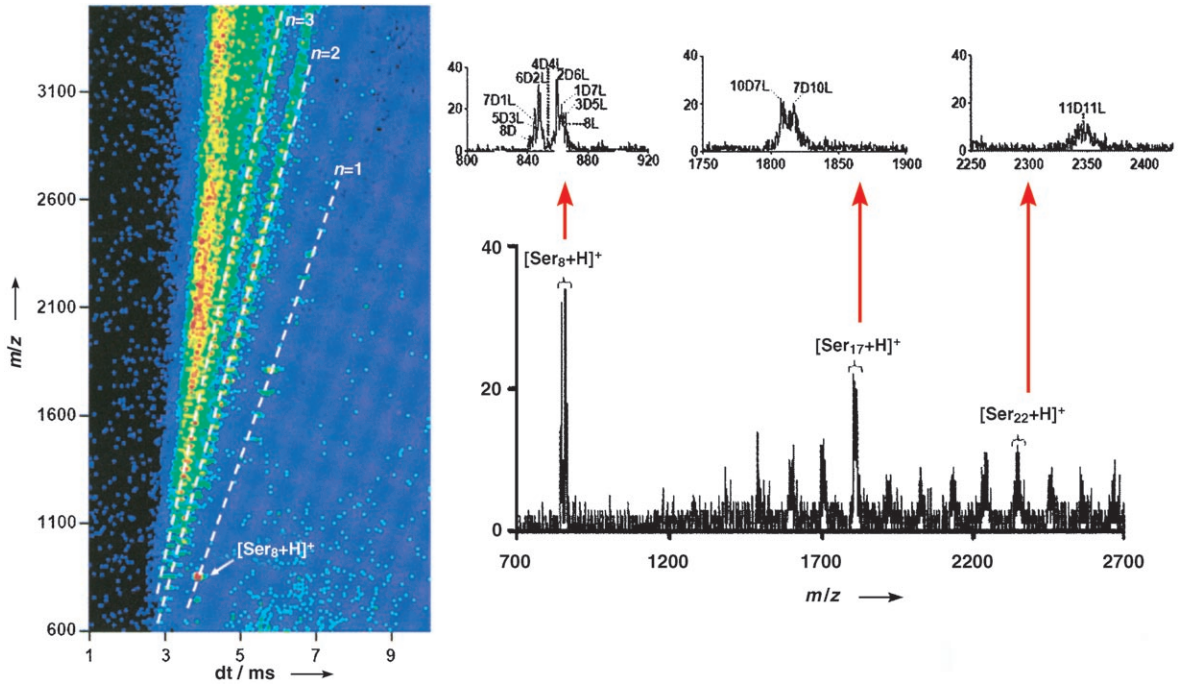


Figure 11. Sonic spray ion mobility mass spectra of a 0.01 M solution of a racemic mixture of 2,3,3-L-$[D_3]$Ser (108 Da) and D-Ser (105 Da).[86] There are two intriguing features of the data: 1) very large aggregates can be observed and 2) the "split" signals for the serine octamer and serine 17-mer demonstrate a preference for homochirality. dt = drift time. Reproduced with permission from reference [86]. Copyright 2004, American Chemical Society.

© 2006 Wiley-VCH Verlag GmbH & Co. KGaA, Weinheim

composed of dimeric subunits of serine since neutral dimers are lost readily.[39] Figure 12 shows that octamers, upon excitation, mainly dissociate by the loss of neutral serine dimers.

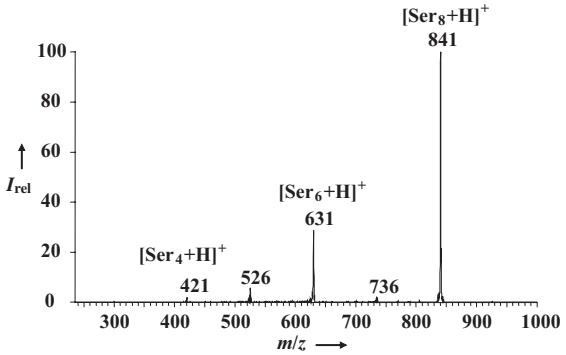


Figure 12. Tandem mass spectra of $[Ser_8+H]^+$ ions. Note that loss of a neutral serine dimer represents the favored fragmentation channel. Reproduced with permission from reference [39]. Copyright 2001, American Chemical Society.

Other experiments have been used to examine the energetic requirements for the dissociation of octamers ionized in other ways (for example, by addition of H^+, Cl^-, and Br^-).[75,96] These data allow a qualitative comparison of the stability of different adducts of the homochiral octamer. The extent of fragmentation as a function of collision energy revealed that the protonated serine octamer is more stable than the dihalide adducts (that is, a higher energy input is require to induce fragmentation).[96] It has been suggested that chloride and bromide ions weaken Ser-Ser interactions in the cluster through their steric demands.[96]

3.4.2. *Hydrogen/Deuterium Exchange*

Hydrogen/deuterium (H/D) exchange reactions[128–130] are known to be a useful—but difficult-to-interpret—source of structural information about gas-phase ions.[131] Conformers can often be distinguished based on different H/D exchange reaction rates. H/D exchange reactions have been employed to characterize serine and its clusters.[110,132–138] The first experiments of this kind revealed that at least two isomers of the protonated serine octamer exist.[134] Later studies confirmed this result.[136,137]

Hydrogen/deuterium exchange reactions of serine octamers have also been carried out in a high-resolution prototype Orbitrap mass spectrometer. The design of the Orbitrap[122] allows H/D exchange reactions to be carried out on trapped ions in the linear quadrupole trap of the ion guide; hence unlike other methods employed,[132–134] the reaction time can be controlled precisely. The degree of H/D exchange depends on the number of collisions between serine octamers and the deuterating agent (in this case CH_3OD). Therefore, the extent of the exchange reaction can be controlled experimentally by varying the partial pressure of the deuterating agent and/or by varying the reaction time. Figure 13 shows electrospray mass spectra of hydrogen/deuterium exchange reactions of serine

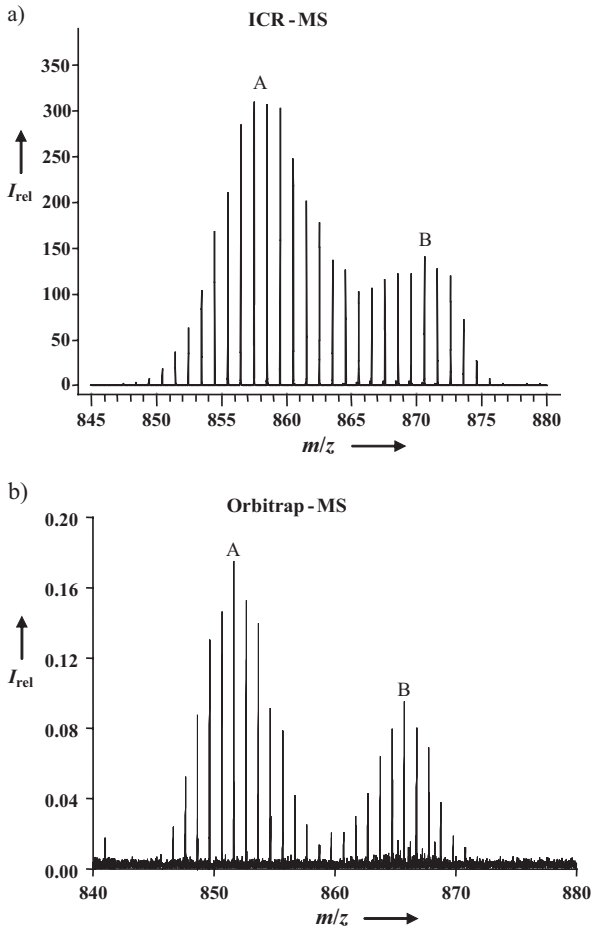


Figure 13. Hydrogen/deuterium exchange mass spectra of serine octamers performed using: a) an FT-ICR mass spectrometer (reproduced with permission from reference [135]. Copyright 2004, IM Publications; www.impub.com.uk), and b) an FT-Orbitrap mass spectrometer (reproduced with permission from reference [134]. Copyright 2003, American Chemical Society). Signals arise from different isotopomers of serine octamers, where *m/z* 841 corresponds to the octamer with 33 protons, while *m/z* 874 is the fully deuterated octamer. The use of different experimental conditions (namely, pressure and reaction time) and deuterating reagents (ND_3 in (a) and CH_3OD in (b)) gives rise to the small difference in separation between ion populations A and B.

octamers performed in both the FT-ICR[135–137] and in the Orbitrap[106,107,134] mass spectrometers. The data show two distinct distributions of serine octamers which have been identified as two conformations of the cluster and are designated A and B for convenience. Closer examination of the data shows that a distribution of metaclusters ($[Ser_{16}+2H]^{2+}$ and $[Ser_{24}+3H]^{3+}$) with exchange patterns corresponding to population B can also be observed as a minor feature in Figure 13b.

These H/D exchange reactions show that while serine octamers exist in at least two isomeric forms, A and B,[134–137] only conformer A displays chiral effects (see reference [134] for details) and this form is therefore believed to be responsible for the stereoselective chemistry. On the basis of the H/D exchange data, it is suggested that conformer B is

 © 2006 Wiley-VCH Verlag GmbH & Co. KGaA, Weinheim

more capable of forming metaclusters than A.[134] It has also been suggested, on the basis of the H/D exchange reaction rates,[137] that isomer A is composed of zwitterionic serine molecules; isomer B could correspond to an octamer made of non-zwitterionic (neutral) serine molecules.[134,137]

It is still unclear why ion mobility experiments[70,71,86] do not show two isomers of the protonated serine octamer. One possibility is that, under the conditions of the IMS experiments, only the homochiral structure A is formed (that is, isomer B is collisionally activated and therefore dissociates, as suggested recently by Mazurek et al.[137]).

3.4.3. Calculations

As discussed previously in Sections 3.4.1 and 3.4.2, structural information about serine octamers has been obtained by means of tandem mass spectrometry (MS/MS),[39,71,127] ion mobility experiments,[70,71,86] and hydrogen/deuterium exchange reactions.[110,132–138] Insights into the structure of serine octamers also come from infrared multiphoton dissociation (IRMPD),[139,140] as well as quantum mechanical calculations.[39,71,72] It is known that at least two isomers of the octameric cluster exist (based on H/D exchange experiments);[134–137] however, only one, isomer A, is of interest in connection with homochirogenesis, since it is the one responsible for the stereospecific chemistry.

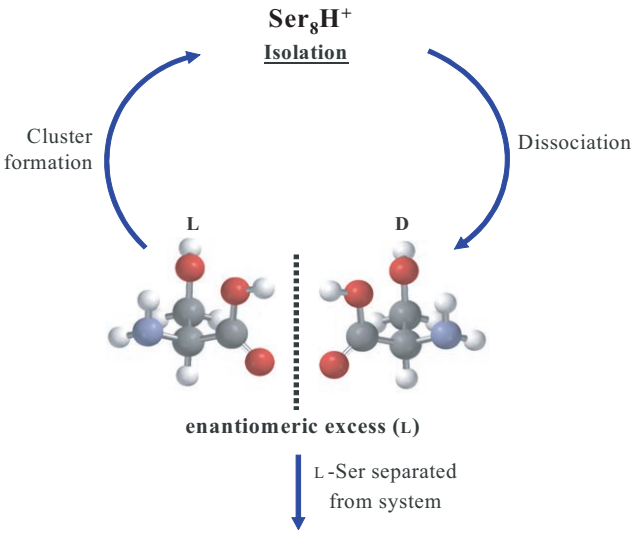
Two classes of structures for the homochiral serine octamer have been proposed on the basis of quantum mechanical calculations.[39,71,72] These structures represent octamers which are composed by zwitterionic[71,72] or non-zwitterionic ("neutral")[39] serine monomers. In 2002, Schalley and Weis[72] critically reviewed the experimental facts about the serine octamer structure together with the calculated geometries proposed in the literature. Even though there are still no established structures for these homochiral octamers, there appears to be agreement on the following conclusions: 1) octamers are likely to be composed of dimeric subunits of serine; 2) the homochiral (8L or 8D) serine octamer must be more stable than heterochiral (for example, 4L:4D) serine octamers corresponding to isomer A, while the homochiral and heterochiral B-type octamers may be almost equally stable; 3) the structure of the homochiral octamer must support/allow, under the energetic conditions at which experimental data are recorded, the observed substitution reactions; 4) the structure of the isomer A serine octamer must be compact, such that its dimensions are consistent with a cross-section of approximately 190 Å^2, as measured in ion mobility experiments.

Clearly there is still work to be done to solve the problem of the structures of the serine octamers. A likely possibility is that conformer A is zwitterionic while B is composed of non-zwitterionic ("neutral") units.[134,137] Non-mass-spectrometric studies employing techniques such as Raman spectroscopy should allow the direct detection of serine octamers under ambient conditions (for example, atmospheric pressure) and may provide structural details about these species.

4. Proposed Role of the Serine Octamer in Homochirogenesis

4.1. Enantiomeric Enrichment

The enantiomeric enrichment step in the sequence of three steps proposed (Section 1.2) to be involved in homochirogenesis consists of the accumulation of a large enantiomeric excess of the key molecule. It has been demonstrated experimentally for serine. This was done by processes which involve cycles of formation and dissociation of the homochiral octamers.[74,75] When octamers are formed from nonracemic heterochiral solutions of serine, they are generated enantiomerically enriched with respect to the enantiomeric composition of the original solution (this is expected on a simple statistical basis). The process described in Scheme 4 allows enantiomeric enrichment to be achieved for serine monomers.



Scheme 4. Nonracemic serine solutions yield octameric ions which show enantiomeric enrichment relative to the original solution. Dissociation of these octamers yields enantiomerically enriched monomeric serine, which in theory can be separated from the system or cycled back to the original L/D mixture.[74,75]

Two independent experiments[74,75] which employed tandem mass spectrometry and ion soft-landing,[141,142] respectively, have been performed to demonstrate the feasibility of enantiomeric enrichment in serine. In the first experiment, octamers were generated from solutions containing 2,3,3-L-[D_3]serine and D-serine in different proportions, isolated by mass analysis, and then fragmented in the mass spectrometer.[74,75] The experiment showed that enantiomerically enriched monomers are obtained by this route.

Enantiomeric enrichment in serine has also been achieved through ion soft landing, a preparative form of mass spectrometry which allows enantiomerically enriched serine to be recovered from the process and subjected to further analysis. Figure 14 shows the experimental setup employed, in which enantiomerically enriched serine is recovered after soft-landing of octameric cluster ions onto a gold surface. The

© 2006 Wiley-VCH Verlag GmbH & Co. KGaA, Weinheim

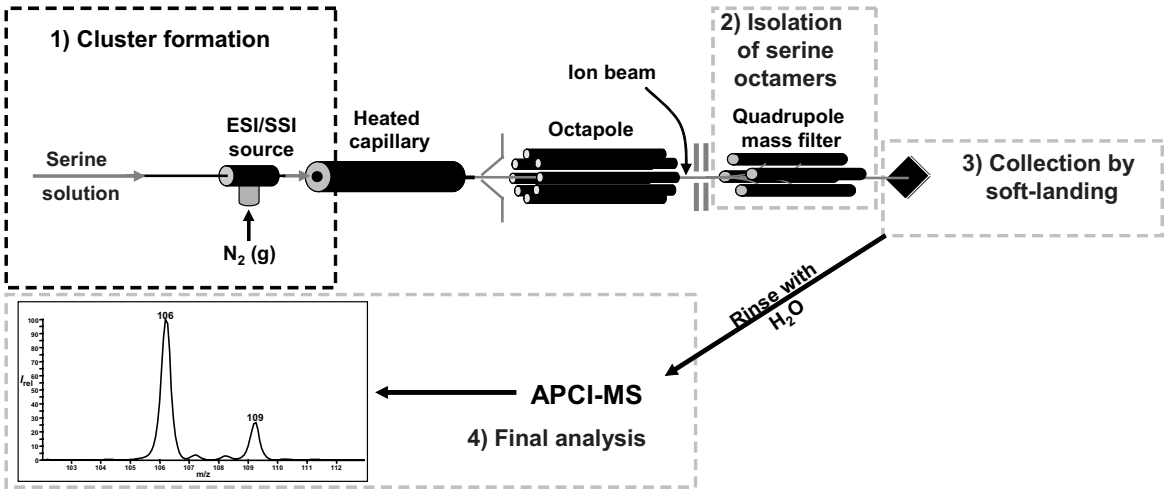


Figure 14. Schematic representation of the process followed to recover enantiomerically enriched serine through a combination of cluster formation/dissociation and ion soft-landing steps.[74,75]

sequence involves serine octamers being generated by means of ESI and/or SSI, isolated in the mass spectrometer, and then collected by soft-landing. Solutions of the isolated and intact serine molecules are then analyzed by APCI-MS. The experiments were performed with initial serine mixtures which contained an enantiomeric excess of the L isomer of 20%; after octamer formation, isolation, and collection through soft-landing, the enantiomeric excess was increased to about 50%. Statistical analysis has been used to derive an expression[74] to explain the enantiomeric enrichment observed in cycles of formation/dissociation of serine octamers. The theory and experimental results show good agreement (Figure 15).[74]

4.2. Chiral Transmission

Chiral transmission, the step in homochirogenesis that involves the transfer of stereochemical configuration from one molecule or molecular assembly to another, can be explained by means of the enantioselective substitution reactions of the octamer (see Section 3.1 for details).[40,73,110] Examples of these reactions are shown in Table 1. These data demonstrate that, even though other biomolecules may not form enantioselective clusters, serine can impose its configuration on them, thus enforcing a restriction on the configuration of other amino acids and sugars through substitution reactions.[40,73] The fact that these reactions are favored for the enantiomeric combinations that exist in life, especially L-serine/L-amino acids and L-serine/D-sugars, is noteworthy.

5. Summary and Outlook

Serine forms octameric clusters through various processes which occur under conditions that may be similar to prebiotic conditions on Earth.[39,68–71,76,86,88,101] These octamers represent a remarkable example of magic-number clusters, which are very stable and exhibit a strong preference for homochirality. The fact that serine has been detected as a product in experiments that aim to simulate syntheses of amino acids under prebiotic conditions,[9] and that it is also the product of reactions that involve primitive molecules such as formaldehyde and glycine,[111] makes us conclude that serine was likely a prebiotic molecule and that it may have played the key role in the chemistry of homochirogenesis. The facile chiral interconversion reaction in serine makes this system particularly susceptible to external chiral agents and may have facilitated mirror-symmetry breaking. This possibility, combined with the intrinsic prebiotically relevant chemistry of serine (for example, decomposition to other amino acids and primordial compounds) and the enantioselective substitution reactions of the serine octamer with other amino acids and sugars which are favored for the enantiomers present in life, strengthens the hypothesis that serine and its octamer may have been involved in homochirogenesis. As a minimum, the experimental facts recounted here reveal that enantiomeric enrichment and chiral transmission reactions can occur by means of the serine octamer.

The presence of homochiral serine octamers in the solution and solid phases remains to be demonstrated directly, as does the existence of stable neutral octamers. Non-mass-spectrometric studies (for example, Raman and NMR spectroscopy) of serine may provide the necessary evidence to solve these problems. The elucidation of the structure(s) of these octameric clusters continues to prove challenging; conclusive evidence for mirror-symmetry breaking does not yet exist for any system, and serine is no exception.

Support from the National Science Foundation (CHE-04-12782) and the U.S. Department of Energy (DE-FG02-94ER14470) is acknowledged. We are indebted to Mark M. Green (Polytechnic University, Brooklyn NY) for providing helpful suggestions prior to publication of this Review. We also thank Radu Popa (University of Southern California, Los Angeles), Ulf Mazurek (Hebrew University of Jerusalem), and Helmut Schwarz (Technical University of Berlin) for fruitful discussions, as well as David Clemmer (Indiana University),

 © 2006 Wiley-VCH Verlag GmbH & Co. KGaA, Weinheim

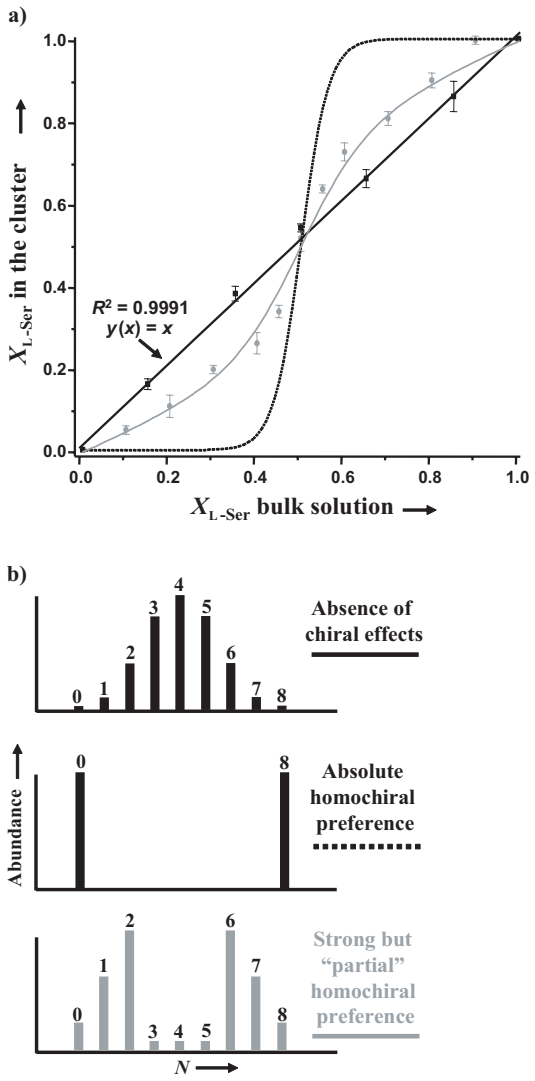


Figure 15. a) Experimental and predicted values for the chiral composition of serine after dissociation of its octamers. Circles correspond to the molar fraction of L-Ser (X_L) calculated from experimental data recorded for the dissociation of serine octamers formed from mixtures of 2,3,3-L-[D_3]Ser/D-Ser. The gray line corresponds to the predicted X_L value for serine octamers (partial enantioselectivity), while the black dotted line is the maximum enantiomeric enrichment curve for serine octamers, that is, for the ideal case of absolute homochiral preference (where only formation of D-Ser_8 and L-Ser_8 is allowed). Results from a reference experiment, 2,3,3-L-[D_3]Ser/L-Ser mixture, are shown as a black line. b) An illustrative distribution of octamers that give rise to the experimental results and theory shown in (a). N = number of L-serine molecules. Reprinted with permission from reference [74]. Copyright 2004, American Society for Mass Spectrometry.

Zoltan Takats (Academy of Science, Budapest, Hungary), and Pengxiang Yang (Purdue University) for extensive discussions and collaborations.

Received: April 16, 2005

[1] A. I. Oparin, *The Origin of Life*, Macmillan, New York, **1938**.
[2] J. B. S. Haldane, *Possible Worlds, and Other Papers*, Harper & Brothers, New York, **1928**.
[3] W. Löb, *Ber. Dtsch. Chem. Ges.* **1913**, *46*, 684.
[4] S. L. Miller, H. C. Urey, *Science* **1959**, *130*, 245 – 251.
[5] H. C. Urey, *Proc. Natl. Acad. Sci. USA* **1952**, *38*, 351 – 363.
[6] S. L. Miller, *Science* **1953**, *117*, 528 – 529.
[7] S. L. Miller, *Biochim. Biophys. Acta* **1957**, *23*, 480 – 489.
[8] S. L. Miller, *J. Am. Chem. Soc.* **1955**, *77*, 2351 – 2360.
[9] D. Ring, Y. Wolman, N. Friedmann, S. L. Miller, *Proc. Natl. Acad. Sci. USA* **1972**, *69*, 765 – 768.
[10] J. L. Bada, A. Lazcano, *Science* **2003**, *300*, 745 – 746.
[11] M. P. Bernstein, J. P. Dworkin, S. A. Sandford, G. W. Cooper, L. J. Allamandola, *Nature* **2002**, *416*, 401 – 403.
[12] G. M. Muñoz Caro, U. J. Meierhenrich, W. A. Schutte, B. Barbier, A. A. Segovia, H. Rosenbauer, W. H.-P. Thiemann, A. Brack, J. M. Greenberg, *Nature* **2002**, *416*, 403 – 406.
[13] J. R. Cronin, S. Pizzarello, *Science* **1997**, *275*, 95.
[14] M. H. Engel, S. A. Macko, *Nature* **1997**, *389*, 265 – 268.
[15] J. R. Cronin, S. Pizzarello, *Adv. Space Res.* **1999**, *23*, 293 – 299.
[16] J. L. Bada, D. P. Glavin, G. D. McDonald, L. Becker, *Science* **1998**, *279*, 362 – 365.
[17] S. Chang, J. Flores, C. Ponnamperuma, *Proc. Natl. Acad. Sci. USA* **1969**, *64*, 1011 – 1015.
[18] M. G. Schwendinger, R. Tauler, S. Saetia, K. R. Liedl, A. H. Eder, T. R. Kroemer, B. M. Rode, *Inorg. Chim. Acta* **1995**, *228*, 207 – 214.
[19] J. G. Nery, G. Bolbach, I. Weissbuch, M. Lahav, *Angew. Chem.* **2003**, *115*, 2207 – 2211; *Angew. Chem. Int. Ed.* **2003**, *42*, 2157 – 2161.
[20] L. Leman, L. Orgel, R. Ghadiri, *Science* **2004**, *306*, 283 – 286.
[21] L. E. Orgel, R. Lohrmann, *Acc. Chem. Res.* **1974**, *7*, 368 – 377.
[22] L. E. Orgel, *Trends Biochem. Sci.* **1998**, *23*, 491 – 495.
[23] L. E. Orgel, *Science* **2000**, *290*, 1306 – 1307.
[24] R. R. Julian, S. Myung, D. E. Clemmer, *J. Phys. Chem. B* **2005**, *109*, 440 – 444.
[25] M. Bolli, R. Micura, A. Eschenmoser, *Chem. Biol.* **1997**, *4*, 309 – 320.
[26] J. R. Knowles, W. J. Albery, *Acc. Chem. Res.* **1977**, *10*, 105 – 111.
[27] W. A. Bonner, *Origins Life Evol. Biosphere* **1991**, *21*, 59 – 111.
[28] R. Popa, *J. Mol. Evol.* **1997**, *44*, 121 – 127.
[29] M. Avalos, R. Babiano, P. Cintas, J. L. Jiménez, J. C. Palacios, *Chem. Commun.* **2000**, 887 – 892.
[30] A. Jorissen, C. Cerf, *Origins Life Evol. Biosphere* **2002**, *32*, 129 – 142.
[31] P. Cintas, *Angew. Chem.* **2002**, *114*, 1187 – 1193; *Angew. Chem. Int. Ed.* **2002**, *41*, 1139 – 1145.
[32] M. L. Pasteur, *Ann. Chim. Phys.* **1848**, *24*, 442 – 459.
[33] J. I. Lunine, *Proc. Natl. Acad. Sci. USA* **2001**, *98*, 809 – 814.
[34] L. D. Hutt, D. P. Glavin, J. L. Bada, R. A. Mathies, *Anal. Chem.* **1999**, *71*, 4000 – 4006.
[35] M. Crisma, A. Moretto, F. Formaggio, B. Kaptein, Q. B. Broxterman, C. Toniolo, *Angew. Chem.* **2004**, *116*, 6863 – 6867; *Angew. Chem. Int. Ed.* **2004**, *43*, 6695 – 6699.
[36] J. L. Bada, R. Protsch, *Proc. Natl. Acad. Sci. USA* **1973**, *70*, 1331 – 1334.
[37] J. L. Bada, B. P. Luyendyk, J. B. Maynard, *Science* **1970**, *170*, 730 – 732.
[38] J. Wehmiller, P. E. Hare, *Science* **1971**, *173*, 907 – 911.
[39] R. G. Cooks, D. Zhang, K. J. Koch, F. C. Gozzo, M. N. Eberlin, *Anal. Chem.* **2001**, *73*, 3646 – 3655.
[40] K. J. Koch, F. C. Gozzo, S. C. Nanita, Z. Takats, M. N. Eberlin, R. G. Cooks, *Angew. Chem.* **2002**, *114*, 1797 – 1800; *Angew. Chem. Int. Ed.* **2002**, *41*, 1721 – 1724.
[41] M. Avalos, R. Babiano, P. Cintas, J. L. Jimenez, J. C. Palacios, *Tetrahedron: Asymmetry* **2004**, *15*, 3171 – 3175.
[42] A. J. Macdermott, *Origins Life Evol. Biosphere* **1995**, *25*, 191 – 199.
[43] M. Avalos, R. Babiano, P. Cintas, J. L. Jimenez, J. C. Palacios, *Origins Life Evol. Biosphere* **2004**, *34*, 391 – 405.

© 2006 Wiley-VCH Verlag GmbH & Co. KGaA, Weinheim

[44] A. Bakasov, T. K. Ha, M. Quack, *J. Chem. Phys.* **1998**, *109*, 7263 – 7285.
[45] R. Berger, M. Quack, G. S. Tschumper, *Helv. Chim. Acta* **2000**, *83*, 1919 – 1950.
[46] M. Shinitzky, F. Nudelman, Y. Barda, R. Haimovitz, E. Chen, D. W. Deamer, *Origins Life Evol. Biosphere* **2002**, *32*, 285 – 297.
[47] P. Schwerdtfeger, J. Gierlich, T. Bollwein, *Angew. Chem.* **2003**, *115*, 1331 – 1334; *Angew. Chem. Int. Ed.* **2003**, *42*, 1293 – 1296.
[48] R. Wesendrup, J. K. Laerdahl, R. N. Compton, P. Schwerdtfeger, *J. Phys. Chem. A* **2003**, *107*, 6668 – 6673.
[49] K. S. Burnham, G. B. Schuster, *J. Am. Chem. Soc.* **1999**, *121*, 10245 – 10246.
[50] J. Bailey, *Origins Life Evol. Biosphere* **2001**, *31*, 167 – 183.
[51] J. H. Hough, J. A. Bailey, A. Chrysostomou, T. M. Gledhill, P. W. Lucas, M. Tamura, S. Clark, J. Yates, F. Menard, *Adv. Space Res.* **2001**, *27*, 313 – 322.
[52] G. Balavoine, A. Moradpour, H. B. Kagan, *J. Am. Chem. Soc.* **1974**, *96*, 5152 – 5158.
[53] J. Li, G. B. Schuster, K.-S. Cheon, M. M. Green, J. V. Selinger, *J. Am. Chem. Soc.* **2000**, *122*, 2603 – 2612.
[54] G. L. J. A. Rikken, E. Raupach, *Nature* **2000**, *405*, 932 – 935.
[55] L. Van Wullen, *ChemPhysChem* **2001**, *2*, 107 – 108.
[56] B. L. Feringa, *Science* **2001**, *292*, 2021 – 2022.
[57] K. Soai, S. Osanai, K. Kadowaki, S. Yonekubo, T. Shibata, I. Sato, *J. Am. Chem. Soc.* **1999**, *121*, 11235 – 11236.
[58] R. M. Hazen, T. R. Filley, G. A. Goodfriend, *Proc. Natl. Acad. Sci. USA* **2001**, *98*, 5487 – 5490.
[59] C. Alonso, R. Eliash, T. R. Jensen, K. Kjaer, M. Lahav, L. Leiserowitz, *J. Am. Chem. Soc.* **2001**, *123*, 10105 – 10106.
[60] H. Zepik, E. Shavit, M. Tang, T. R. Jensen, K. Kjaer, G. Bolbach, L. Leiserowitz, I. Weissbuch, M. Lahav, *Science* **2002**, *295*, 1266 – 1269.
[61] M. M. Green, K.-S. Cheon, S.-Y. Yang, J.-W. Park, S. Swansburg, W. Liu, *Acc. Chem. Res.* **2001**, *34*, 672 – 680.
[62] M. M. Green, B. A. Garetz, B. Munoz, H. Chang, S. Hoke, R. G. Cooks, *J. Am. Chem. Soc.* **1995**, *117*, 4181 – 4182.
[63] M. M. Green, J. V. Selinger, *Science* **1998**, *282*, 880.
[64] M. M. Green, J.-W. Park, T. Sato, A. Teramoto, S. Lifson, R. L. B. Selinger, J. V. Selinger, *Angew. Chem.* **1999**, *111*, 3328 – 3345; *Angew. Chem. Int. Ed.* **1999**, *38*, 3138 – 3154.
[65] B. L. Feringa, R. A. Van Delden, *Angew. Chem.* **1999**, *111*, 3624 – 3645; *Angew. Chem. Int. Ed.* **1999**, *38*, 3419 – 3438.
[66] S. Pizzarello, A. L. Weber, *Science* **2004**, *303*, 1151.
[67] A. Saghatelian, Y. Yokobayashi, K. Soltani, M. R. Ghadiri, *Nature* **2001**, *409*, 797 – 801.
[68] D. Zhang, K. J. Koch, W. A. Tao, R. G. Cooks, *Proceedings of the 48th ASMS Conference on Mass Spectrometry and Allied Topics*, Long Beach, CA, USA, **2000**.
[69] R. Hodyss, R. R. Julian, J. L. Beauchamp, *Chirality* **2001**, *13*, 703 – 706.
[70] A. E. Counterman, D. E. Clemmer, *J. Phys. Chem. B* **2001**, *105*, 8092 – 8096.
[71] R. R. Julian, R. Hodyss, B. Kinnear, M. Jarrold, J. L. Beauchamp, *J. Phys. Chem. B* **2002**, *106*, 1219 – 1228.
[72] C. A. Schalley, P. Weis, *Int. J. Mass Spectrom.* **2002**, *221*, 9 – 19.
[73] Z. Takats, S. C. Nanita, R. G. Cooks, *Angew. Chem.* **2003**, *115*, 3645 – 3647; *Angew. Chem. Int. Ed.* **2003**, *42*, 3521 – 3523.
[74] S. C. Nanita, Z. Takats, S. Myung, D. E. Clemmer, R. G. Cooks, *J. Am. Soc. Mass Spectrom.* **2004**, *15*, 1360 – 1365.
[75] S. C. Nanita, Z. Takats, R. G. Cooks, *Proceedings of the 52nd ASMS Conference on Mass Spectrometry and Allied Topics*, Nashville, TN, USA, **2004**.
[76] Z. Takats, S. C. Nanita, R. G. Cooks, G. Schlosser, K. Vekey, *Anal. Chem.* **2003**, *75*, 1514 – 1523.
[77] J. B. Fenn, M. Mann, C. K. Meng, S. F. Wong, C. M. Whitehouse, *Science* **1989**, *246*, 64 – 71.
[78] J. B. Fenn, *Angew. Chem.* **2003**, *115*, 3999 – 4024; *Angew. Chem. Int. Ed.* **2003**, *42*, 3871 – 3894.
[79] P. Nemes, G. Schlosser, K. Vékey, *J. Mass Spectrom.* **2005**, *40*, 43 – 49.
[80] R. D. Smith, K. J. Light-Wahl, B. E. Winger, J. A. Loo, *Org. Mass Spectrom.* **1992**, *27*, 811 – 821.
[81] D. Zhang, L. Wu, K. J. Koch, R. G. Cooks, *Eur. Mass Spectrom.* **1999**, *5*, 353 – 361.
[82] J. A. Loo, *Int. J. Mass Spectrom.* **2000**, *200*, 175 – 186.
[83] R. R. Julian, R. Hodyss, J. L. Beauchamp, *J. Am. Chem. Soc.* **2001**, *123*, 3577 – 3583.
[84] K. J. Koch, T. Aggerholm, S. C. Nanita, R. G. Cooks, *J. Mass Spectrom.* **2002**, *37*, 676 – 686.
[85] T. Aggerholm, S. C. Nanita, K. Koch, R. G. Cooks, *J. Mass Spectrom.* **2003**, *38*, 87 – 97.
[86] S. Myung, R. R. Julian, S. C. Nanita, R. G. Cooks, D. E. Clemmer, *J. Phys. Chem. B* **2004**, *108*, 6105 – 6111.
[87] H. W. Kroto, J. R. Heath, S. C. O'Brien, R. F. Curl, R. E. Smalley, *Nature* **1985**, *318*, 162 – 163.
[88] M. Kunimura, S. Sakamoto, K. Yamaguchi, *Org. Lett.* **2002**, *4*, 347 – 350.
[89] S. Sakamoto, M. Fujita, K. Kim, K. Yamaguchi, *Tetrahedron* **2000**, *56*, 955 – 964.
[90] K. Yamaguchi, *J. Mass Spectrom.* **2003**, *38*, 473 – 490.
[91] A. Hirabayashi, M. Sakairi, H. Koizumi, *Anal. Chem.* **1994**, *66*, 4557 – 4559.
[92] A. Hirabayashi, M. Sakairi, H. Koizumi, *Anal. Chem.* **1995**, *67*, 2878 – 2882.
[93] Z. Takats, J. M. Wiseman, B. Gologan, R. G. Cooks, *Anal. Chem.* **2004**, *76*, 4050 – 4058.
[94] J. M. Wiseman, Z. Takáts, B. Gologan, V. J. Davisson, R. G. Cooks, *Angew. Chem.* **2005**, *117*, 935 – 938; *Angew. Chem. Int. Ed.* **2005**, *44*, 913 – 916.
[95] J. C. Searcy, J. B. Fenn, *J. Chem. Phys.* **1974**, *61*, 5282 – 5288.
[96] S. C. Nanita, R. G. Cooks, *J. Phys. Chem. B* **2005**, *109*, 4748 – 4753.
[97] D. J. Donaldson, D. Anderson, *J. Phys. Chem. A* **1999**, *103*, 871 – 876.
[98] C. M. Dobson, G. B. Ellison, A. F. Tuck, V. Vaida, *Proc. Natl. Acad. Sci. USA* **2000**, *97*, 11864 – 11868.
[99] D. J. Donaldson, A. F. Tuck, V. Vaida, *Origins Life Evol. Biosphere* **2002**, *32*, 237 – 245.
[100] D. J. Donaldson, H. Tervahattu, A. F. Tuck, V. Vaida, *Origins Life Evol. Biosphere* **2004**, *34*, 57 – 67.
[101] Z. Takats, R. G. Cooks, *Chem. Commun.* **2004**, 444 – 445.
[102] K. J. Baumeister, F. F. Simon, *J. Heat Transfer* **1973**, *95*, 166 – 173.
[103] P. Tartarini, G. Lorenzini, M. R. Randi, *Heat Mass Transfer* **1999**, *34*, 437 – 447.
[104] Experiments on mixtures of serine with other amino acids and other prebiotically relevant compounds are underway.
[105] P. Yang, R. G. Cooks, unpublished results.
[106] H. Li, A. A. Makarov, R. Noll, J. M. Hardman, G. Wu, W. Plass, R. G. Cooks, *Proceedings of the 51th ASMS Conference on Mass Spectrometry and Allied Topics*, Montréal, QC, Canada, **2003**.
[107] H. Li, PhD thesis, Purdue University (West Lafayette, Indiana, USA), **2003**.
[108] S. C. Nanita, Z. Takats, R. G. Cooks, *Proceedings of the 51th ASMS Conference on Mass Spectrometry and Allied Topics*, Montréal, QC, Canada, **2003**.
[109] For a mathematical definition of a magic-number cluster, see D. Zhang, R. G. Cooks, *Int. J. Mass Spectrom.* **2000**, *195*/196, 667 – 684.
[110] S. Gronert, R. A. J. O'Hair, A. E. Fagin, *Chem. Commun.* **2004**, 1944 – 1945.

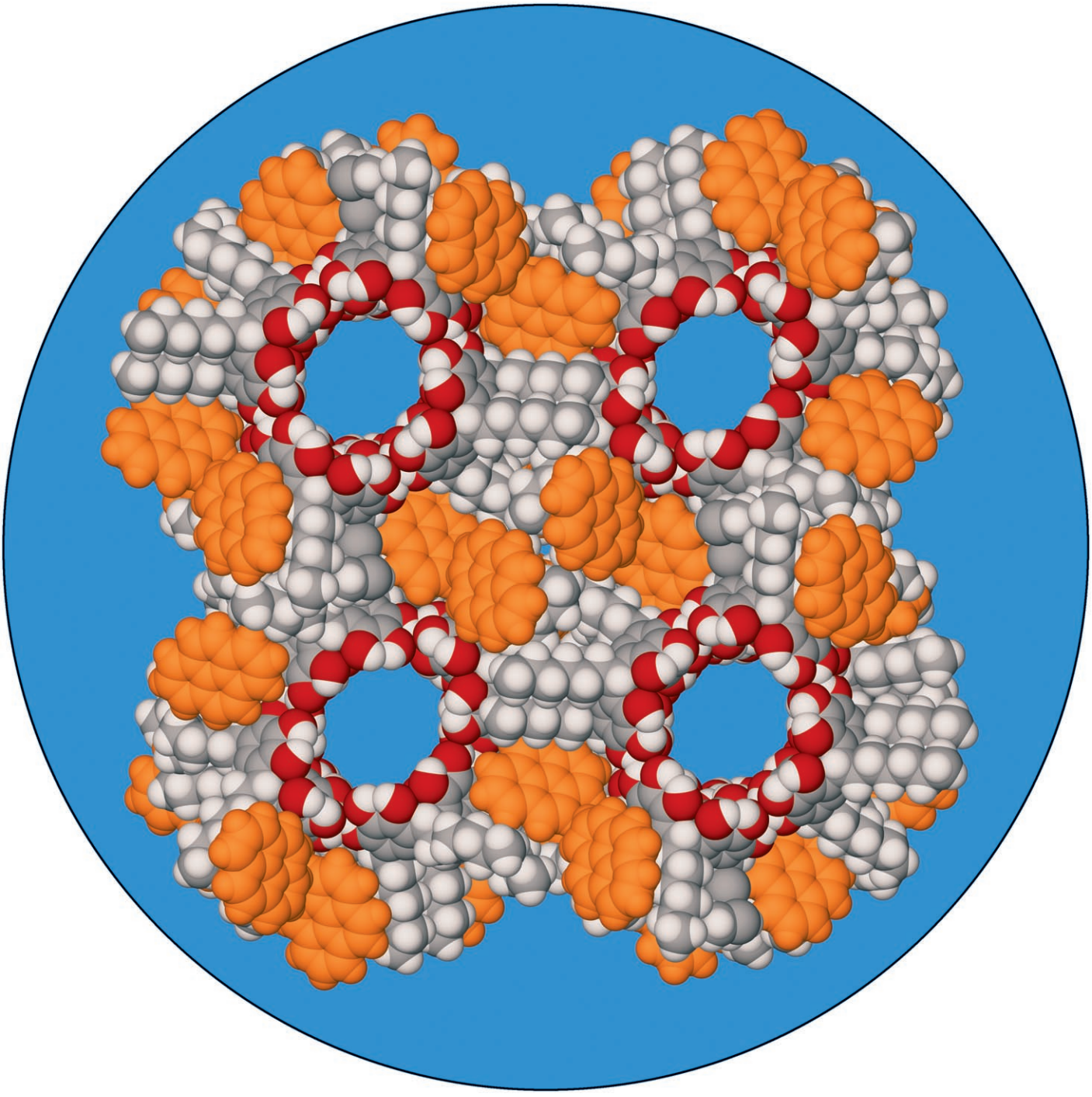
 © 2006 Wiley-VCH Verlag GmbH & Co. KGaA, Weinheim

[111] V. A. Yaylayan, A. Keyhani, A. Wnorowski, *J. Agric. Food Chem.* **2000**, *48*, 636 – 641.
[112] In these experiments, serine octamers were generated by means of sublimation (as discussed in Section 2.3). Thermal decomposition reactions of serine also take place at elevated temperatures, thereby yielding the products.
[113] Aspartic acid is also known to epimerize easily.
[114] G. Nouadje, M. Nertz, F. Courderc, *J. Chromatogr. A* **1995**, *716*, 331 – 334.
[115] J. L. Bada, *Methods Enzymol.* **1984**, *106*, 98 – 115.
[116] D. E. Schwass, J. W. Finley, *J. Agric. Food Chem.* **1984**, *32*, 1377 – 1382.
[117] K. J. Koch, F. C. Gozzo, D. Zhang, M. N. Eberlin, R. G. Cooks, *Chem. Commun.* **2001**, 1854 – 1855.
[118] D. E. Clemmer, M. F. Jarrold, *J. Mass Spectrom.* **1997**, *32*, 577 – 592.
[119] P. Dugourd, R. R. Hudgins, M. F. Jarrold, *Chem. Phys. Lett.* **1997**, *267*, 186 – 192.
[120] S. L. Bernstein, T. Wyttenbach, A. Baumketner, J.-E. Shea, G. Bitan, D. B. Teplow, M. T. Bowers, *J. Am. Chem. Soc.* **2005**, *127*, 2075 – 2084.
[121] E. S. Baker, M. J. Manard, J. Gidden, M. T. Bowers, *J. Phys. Chem. B* **2005**, *109*, 4808 – 4810.
[122] A. A. Makarov, *Anal. Chem.* **2000**, *72*, 1156 – 1162.
[123] M. Hardman, A. A. Makarov, *Anal. Chem.* **2003**, *75*, 1699 – 1705.
[124] S. Myung, Y. J. Lee, M. H. Moon, J. Taraszka, R. Sowell, S. Koeniger, A. E. Hilderbrand, S. J. Valentine, L. Cherbas, P. Cherbas, T. C. Kaufman, D. F. Miller, Y. Mechref, M. V. Novotny, M. A. Ewing, C. R. Sporleder, D. E. Clemmer, *Anal. Chem.* **2003**, *75*, 5137 – 5145.
[125] B. M. Rode, Y. Suwannachot, *Coord. Chem. Rev.* **1999**, *190–192*, 1085 – 1099.
[126] D. K. Böhme, H. Schwarz, *Angew. Chem.* **2005**, *117*, 2388 – 2406; *Angew. Chem. Int. Ed.* **2005**, *44*, 2336 – 2354.
[127] P. Hvelplund, J. Rangama, B. Liu, A. B. Nielsen, S. B. Nielsen, S. Tomita, *Proceedings of the 52nd ASMS Conference on Mass Spectrometry and Allied Topics*, Nashville, TN, USA, **2004**.
[128] S. Campbell, M. T. Rodgers, E. M. Marzluff, J. L. Beauchamp, *J. Am. Chem. Soc.* **1994**, *116*, 9765 – 9766.
[129] S. Campbell, M. T. Rodgers, E. M. Marzluff, J. L. Beauchamp, *J. Am. Chem. Soc.* **1995**, *117*, 12840 – 12854.
[130] Z. Takats, G. Schlosser, K. Vekey, *Int. J. Mass Spectrom.* **2003**, *228*, 729 – 741.
[131] S. J. Valentine, D. E. Clemmer, *J. Am. Chem. Soc.* **1997**, *119*, 3558 – 3566.
[132] O. Geller, C. Lifshitz, *Int. J. Mass Spectrom.* **2003**, *227*, 77 – 85.
[133] P. Ustyuzhanin, J. Ustyuzhanin, C. Lifshitz, *Int. J. Mass Spectrom.* **2003**, *223–224*, 491 – 498.
[134] Z. Takats, S. C. Nanita, G. Schlosser, K. Vekey, R. G. Cooks, *Anal. Chem.* **2003**, *75*, 6147 – 6154.
[135] U. Mazurek, M. A. McFarland, A. G. Marshall, C. Lifshitz, *Eur. J. Mass Spectrom.* **2004**, *10*, 755 – 758.
[136] U. Mazurek, B. G. Reuben, M. A. McFarland, A. G. Marshall, C. Lifshitz, *Proceedings of the 52nd ASMS Conference on Mass Spectrometry and Allied Topics*, Nashville, TN, USA, **2004**.
[137] U. Mazurek, O. Geller, C. Lifshitz, M. A. McFarland, A. G. Marshall, B. G. Reuben, *J. Phys. Chem. A* **2005**, *109*, 2107 – 2112.
[138] R. A. J. O'Hair, S. Gronert, A. Fagin, *Proceedings of the 52nd ASMS Conference on Mass Spectrometry and Allied Topics*, Nashville, TN, USA, **2004**.
[139] H. Y. Hwang, C. Lin, H. Oh, K. Breuker, B. K. Carpenter, F. W. McLafferty, *Proceedings of the 52nd ASMS Conference on Mass Spectrometry and Allied Topics*, Nashville, TN, USA, **2004**.
[140] H.-B. Oh, C. Lin, H. Y. Hwang, H. Zhai, K. Breuker, V. Zabrouskov, B. K. Carpenter, F. W. McLafferty, *J. Am. Chem. Soc.* **2005**, *127*, 4076 – 4083.
[141] S. A. Miller, H. Luo, S. J. Pachuta, R. G. Cooks, *Science* **1997**, *275*, 1447 – 1450.
[142] Z. Ouyang, Z. Takats, T. A. Blake, B. Gologan, A. J. Guymon, J. M. Wiseman, J. C. Oliver, V. J. Davisson, R. G. Cooks, *Science* **2003**, *301*, 1351 – 1354.

© 2006 Wiley-VCH Verlag GmbH & Co. KGaA, Weinheim

Communications

DOI: 10.1002/anie.200503035



The spheroidal arrangement of *C*-hexylpyrogallo[4]arene can be converted into organic nanotubes of a similar "footprint" by means of sonication and co-crystallization with pyrene (or 1-bromopyrene) in aqueous acetonitrile solution. For more details, see the Communication by J. L. Atwood and co-workers on the following pages.

WILEY InterScience DISCOVER SOMETHING GREAT
© 2006 Wiley-VCH Verlag GmbH & Co. KGaA, Weinheim

Nanostructures

DOI: 10.1002/anie.200503035

Toward the Isolation of Functional Organic Nanotubes**

*Scott J. Dalgarno, Gareth W. V. Cave, and Jerry L. Atwood**

The discoveries of buckminsterfullerene (C_{60}) and single-walled carbon nanotubes (SWNTs) represent two very significant advances in the last two decades.[1,2] Both types of material have found utility in important areas such as superconductivity and molecular electronics.[3] Whilst the synthesis and functionalization of carbon nanotubes is now developing rapidly, the materials produced are often costly, irregular in shape, and are typically found to aggregate in large bundles, thus making manipulation somewhat less than straightforward.

Given the intense focus on buckyballs and SWNTs, it is surprising that significantly less efforts have been directed to developing the synthesis of alternative multicomponent organic nanospheres and tubules. Such molecular arrangements present the opportunity for the encapsulation or hosting of suitable guest species within the large resultant internal cavities or channels and also show vast potential for use in the nanotechnology industry. A major problem associated with this goal is that of achieving control over the many intermolecular interactions that stabilize such supramolecular assemblies. Such control has been achieved to some extent with *p*-sulfonatocalix[4]arene, 12 molecules of which can be controlled to assemble around the vertices of nanometer-scaled icosahedra or cuboctahedra.[4,5] The resultant supramolecular geometries are dependent upon both the guest molecules and the metal counterions employed, but both have substantial internal cavity volumes in the 1000–1500 Å^3 range. Additionally, variation of the reaction conditions can result in the formation of related nanotubules, the diameters of which are similar to those of the nanospheroids.

To the best of our knowledge—and without considering, for example, the channels found in zeolites or engineered porous crystals—only a limited number of purely organic nanotubes that have large internal channel volumes have been reported to date.[6,7] The majority of these nanotubes were formed through the self-assembly of cyclic oligomers composed of peptides,[6a] ureas,[6b] or carbohydrates.[6c] Artzner and co-workers documented the remarkable self-assembly of an octapeptide into nanotubes with dimensions that approach those of viral capsids in both solution and the solid state.[7] However, in the context of the present study, an important example of a multicomponent organic nanotube was that formed by the back-to-back solid-state assembly of calix[4]hydroquinone.[8] The crystalline assembly was stabilized by π-stacking interactions between adjacent calixarene moieties. Although these channels could be used to form ultrathin silver nanowires it is difficult to envisage a point at which the assembly could maintain both structure and function in the solution phase.

Six molecules of *C*-methylresorcin[4]arene (**1**) and eight molecules of water self-assemble into a purely organic spheroid of nanometer dimensions that is stabilized by a large number of hydrogen-bonding interactions between the hydroxy groups on the upper rim of the calixarene units and water molecules at the seams of the nanospheroid.[9] Mattay and co-workers described the self-assembly of *C*-isobutylpyrogallol[4]arene into a hexameric capsule arrangement which is reminiscent of that formed with **1**.[10] Some of our recent work has focused on the organization of guest molecules with nanospheroids composed of *C*-alkylpyrogallol[4]arenes **2** whilst also establishing quantitative and reproducible recrystallization procedures from a particular solvent (ethyl acetate).[11,12] Also, solution-phase studies for nanospheroids of **1** and **2** have been developed and scrutinized through a number of spectroscopic techniques to demonstrate the stability of these assemblies in a variety of solvents.[9,13–19] Given that the "footprint" of an SWNT is approximately equal to the diameter of a buckyball[1,2] and that a similar phenomenon is observed with the above-mentioned *p*-sulfonatocalix[4]arene nanospheroids and nanotubules,[4,5] we reasoned that it should be possible to form a purely organic nanotube (from either **1** or **2**) that would be of similar diameter to the corresponding nanospheroids. This is indeed the case for **2**, at least, and we show herein that sonication can be used to construct organic nanotubes that show the possibility for existence and function in the solution phase.

Sonication of a hot solution of *C*-*n*-hexylpyrogallol[4]-arene (PgC6, **3**) and pyrene (**4a**) (or 1-bromopyrene (**4b**)) in acetonitrile/water, followed by cooling of the solution and slow solvent evaporation overnight resulted in the growth of large single crystals of **5** that were suitable for diffraction studies (Figure 1).[20–22] The resolved structure shows the asymmetric unit of **5** to comprise two molecules of PgC6 (**3**) and two molecules of pyrene, as well as a total of 4.5 molecules of acetonitrile and 5.5 molecules of water.

Symmetry expansion of the asymmetric unit shows that the calixarene units form cyclic or disclike tetramers through eight crystallographically unique hydrogen bonds (O···O distances range from 2.702–2.916 Å). These tetramers link together in a tubular fashion through six crystallographically unique interdisc hydrogen-bonding interactions (O···O distances range from 2.742–3.010 Å; Figure 1), with each tetramer being rotated by approximately 45° relative to an axis

[*] Dr. S. J. Dalgarno, Dr. G. W. V. Cave,[+] Prof. J. L. Atwood
Department of Chemistry
University of Missouri-Columbia
601 South College Avenue, Columbia, MO 65211 (USA)
Fax: (+1) 573-882-2754
E-mail: atwoodj@missouri.edu

[+] Current address:
School of Biomedical and Natural Sciences
Nottingham Trent University
Clifton Lane, Nottingham, NG11 8NS (UK)

[**] We thank the NSF for financial support.

Supporting information for this article is available on the WWW under http://www.angewandte.org or from the author.

 © 2006 Wiley-VCH Verlag GmbH & Co. KGaA, Weinheim

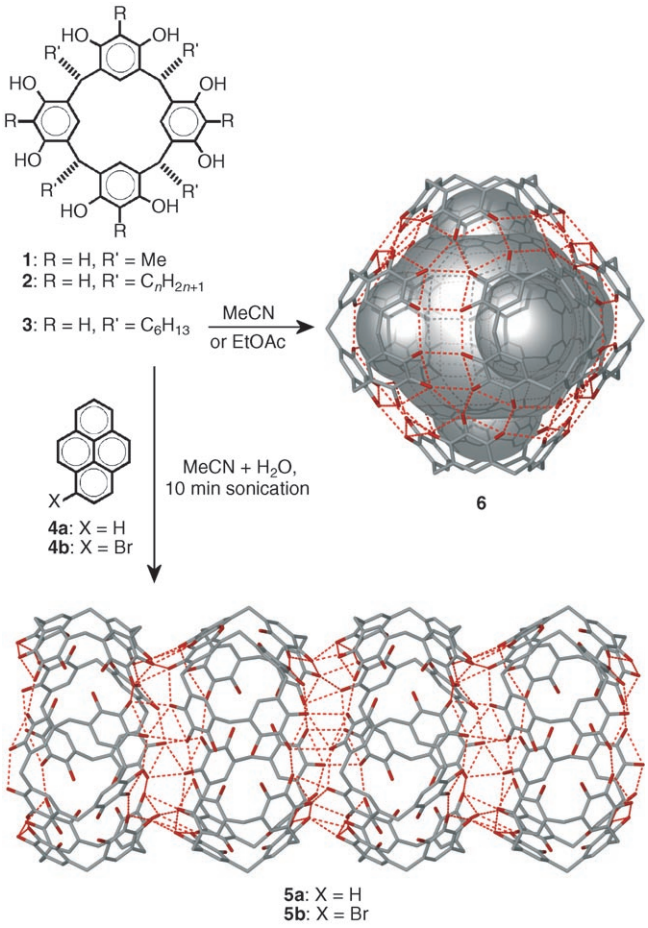


Figure 1. Conditions for the assembly of PgC6 (**3**) into organic nanospheroids (**6**) and nanotubes (**5a** or **5b**) through hydrogen-bonding interactions. For clarity, the *n*-hexyl side chains on the calixarene moieties are omitted.

running down the nanotube array. Examination of the footprint of the tube shows the dimensions between opposite calixarene centroids within each disc to be approximately 13.7 × 15.5 Å^2 (Figure 2). These dimensions are indicative of each disc adopting a slightly elliptical shape in the solid state. Opposing pairs of calixarenes within the corresponding PgC6 nanospheroid **6** grown from a solution of **3** in anhydrous acetonitrile have roughly equal cross-sphere separations and hence adopt a more spherical shape (see Figures 1 and 2).[23] Although there are slight differences in shape between the cross-sectional regions of each assembly, this is notably the third such example where spheres have been converted into nanotubes, hence suggesting not only that a general trend is developing but that any multicomponent spheroidal arrangement which contains large building blocks may exhibit similar behavior.[1–2,4–5]

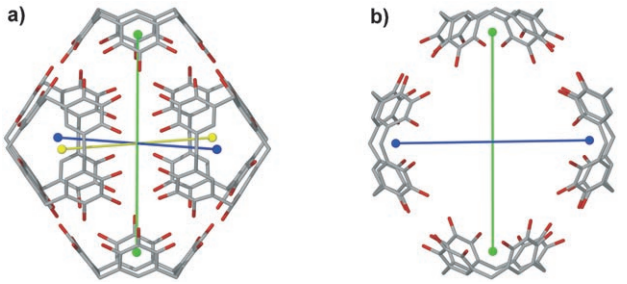


Figure 2. Distances between opposite calixarene pairs in spheroidal (a) and nanotubular (b) assemblies of PgC6. a) The three cross-sphere distances in **6** are roughly equal (green axis = 14.573; blue axis = 14.789; yellow axis = 14.884 Å), hence indicating a near-spheroidal shape. b) The dimensions of the cross-section of the nanotube **5** differ markedly (green axis = 15.486; blue axis = 13.679 Å) and show the calixarene tetramers adopt a slightly elliptical conformation. For clarity, the orientation of the sphere is skewed and the *n*-hexyl side chains on the calixarenes are omitted.

Upon examination, the calixarene discs that form the tube **5** through hydrogen-bonding interactions are found to shroud alternating solvent microenvironments of acetonitrile and water (Figure 3). These unprecedented organic nanotube solvent microenvironments are not only stabilized by a large number of intra- and interenvironment hydrogen-bonding interactions but they are also shielded from the exterior of the assembly (Figure 3b) and thus show the potential for simultaneous inclusion of different guest molecules within the walls of such nanotubular arrays. Unfortunately the presence of the PgC6 nanotubes **5** in the solution phase was ambiguous from FTIR studies.

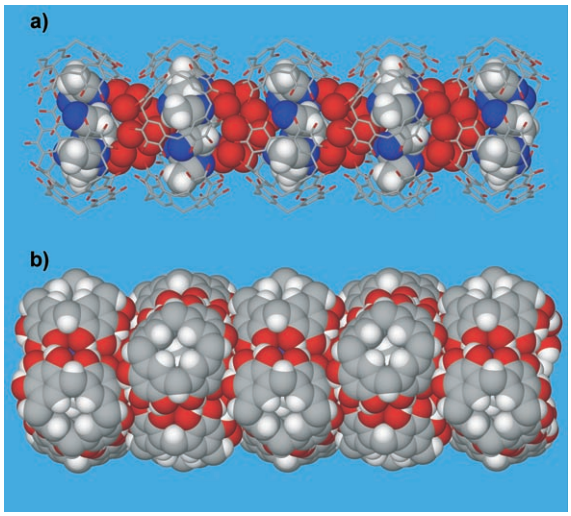


Figure 3. Partial (a) and full (b) space-filling views of the nanotubes **5** constructed from PgC6. a) The calixarene moities are shown in stick representation to emphasize the alternating acetonitrile and water microenvironments found in the tubular assembly. b) Full space-filling representation shows the calixarenes to shield the solvent microenvironments from the exterior of the nanotube through hydrogen-bonding interactions with the upper rim of the calixarene. For clarity, the *n*-hexyl side chains on the calixarene units are omitted. O red, N blue, C gray, H white.

When the alkyl chains on the lower rim of PgC6 are considered in the extended structure (Figure 4), it is immediately obvious that the exterior of the organic nanotubes interact through a large number of Van der Waals interactions between neighboring hydrophobic chains and intercalated pyrene molecules. The intercalation of hydrophobic pyrene

 © 2006 Wiley-VCH Verlag GmbH & Co. KGaA, Weinheim

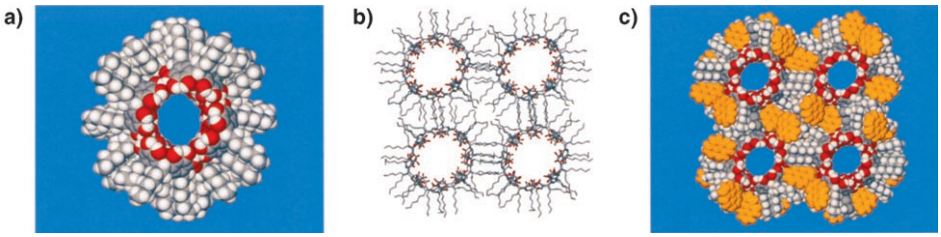


Figure 4. Different views of the extended structure of the organic nanotubes formed with PgC6 (**3**), pyrene (**4a**), acetonitrile, and water. a) View down the center of a single space-filled nanotube. b) Four neighboring nanotubes are shown in stick representation. c) View down four space-filling nanotubes showing the intercalated *exo*-tube pyrene molecules (orange). For clarity, solvent molecules are omitted in all parts and pyrene molecules are omitted in (a) and (b).

molecules within the outer layer of the tubes suggests that the presence of a suitable surfactant molecule, perhaps one that bears pyrene-functionalized tails, could lead to the isolation of such organic nanotubular arrays in the solution phase—a prospect we are currently exploring. Nanotubular arrays such as these could prove immensely useful for both industrial and academic communities alike if they were to be freestanding in the solution phase, be able to host or transport guest molecules, or act, for example, as regioselective catalysts or perhaps as microfilters in the solid state.

To conclude, we have demonstrated the formation of *C*-*n*-hexylpyrogallol[4]arene-based organic nanotubes **5** in the solid state that show some potential to maintain their structure in the solution phase. The nanotube cores are of similar dimensions to the nanospheroids **6** generated under different solvent conditions and are separated from typical calixarene-to-calixarene π-stacking interactions by the presence of hydrophobic tails that intercalate with one another and additional polyaromatic molecules (pyrene or bromopyrene). These organic nanotubes display alternating solvent microenvironments, thus demonstrating the hosting of disparate molecular material. In addition, we have noted the third such example where a sphere can be engineered into a related tube, thus indicating that any multicomponent spheroidal arrangement should be examined for similar behavior. Studies on the construction of alternative supramolecular arrangements with pyrogallol[4]arenes and the isolation of single and functional organic nanotubes in both the solid and solution states are in progress.

Received: August 25, 2005
Revised: September 13, 2005
Published online: December 27, 2005

Keywords: calixarenes · hydrogen bonds · nanostructures · self-assembly · supramolecular chemistry

[1] H. W. Kroto, J. R. Heath, S. C. O'Brien, R. F. Curl, R. E. Smalley, *Nature* **1985**, *318*, 162–163.
[2] A. P. Ramirez, R. C. Haddon, O. Zhou, R. M. Fleming, J. Zhang, S. M. McClure, R. E. Smalley, *Science* **1994**, *265*, 84–86.
[3] M. S. Dresselhaus, G. Dresselhaus, P. C. Eklund, *Science of Fullerenes and Carbon Nanotubes: Their Properties and Applications*, Academic Press, San Diego, **1995**.
[4] G. W. Orr, L. J. Barbour, J. L. Atwood, *Science* **1999**, *285*, 1049–1052.
[5] J. L. Atwood, L. J. Barbour, S. J. Dalgarno, M. J. Hardie, C. L. Raston, H. R. Webb, *J. Am. Chem. Soc.* **2004**, *126*, 13170–13171.
[6] a) M. R. Ghadiri, J. R. Granja, R. A. Milligan, D. E. McRee, N. Khazanovich, *Nature* **1993**, *366*, 324–327; J. D. Hartgerink, J. R. Granja, R. A. Milligan, M. R. Ghadiri, *J. Am. Chem. Soc.* **1996**, *118*, 43–50; b) V. Semetey, C. Didierjean, J.-P. Briand, A. Aubry, G. Guichard, *Angew. Chem.* **2002**, *114*, 1975–1978; *Angew. Chem. Int. Ed.* **2002**, *41*, 1895–1898; c) G. Gattuso, S. Menzer, S. A. Nepogodiev, J. F. Stoddart, D. J. Williams, *Angew. Chem.* **1997**, *109*, 1615–1617; *Angew. Chem. Int. Ed. Engl.* **1997**, *36*, 1451–1454.
[7] C. Valéry, M. Paternostre, B. Robert, T. Gulik-Krzywicki, T. Narayanan, J.-C. Dedieu, M.-L. Torres, R. Cherif-Cheikh, P. Calvo, F. Artzner, *Proc. Natl. Acad. Sci. USA* **2003**, *100*, 10258–10262.
[8] B. H. Hong, S. C. Bae, C.-W. Lee, S. Jeong, K. S. Kim, *Science* **2001**, *294*, 348–351.
[9] L. R. MacGillivray, J. L. Atwood, *Nature* **1997**, *389*, 469–472.
[10] T. Gerkensmeier, W. Iwanek, C. Agena, R. Frölich, S. Kotila, C. Näther, J. Mattay, *Eur. J. Org. Chem.* **1999**, *9*, 2257–2262.
[11] J. L. Atwood, L. J. Barbour, A. Jerga, *Proc. Natl. Acad. Sci. USA* **2002**, *99*, 4837–4841.
[12] G. W. V. Cave, J. Antesberger, L. J. Barbour, R. M. McKinlay, J. L. Atwood, *Angew. Chem.* **2004**, *116*, 5879–5882; *Angew. Chem. Int. Ed.* **2004**, *43*, 5263–5266.
[13] A. Shivanyuk, J. Rebek, Jr., *Proc. Natl. Acad. Sci. USA* **2002**, *99*, 4775–4777.
[14] A. Shivanyuk, J. Rebek, Jr., *J. Am. Chem. Soc.* **2003**, *125*, 3432–3433.
[15] L. C. Palmer, J. Rebek, Jr., *Org. Biomol. Chem.* **2004**, *2*, 3051–3059.
[16] J. Rebek, Jr., *Angew. Chem.* **2005**, *117*, 2104–2115; *Angew. Chem. Int. Ed.* **2005**, *44*, 2068–2078.
[17] J. L. Atwood, L. J. Barbour, A. Jerga, *Chem. Commun.* **2001**, *22*, 2376–2377.
[18] L. Avram, Y. Cohen, *J. Am. Chem. Soc.* **2002**, *124*, 15148–15149.
[19] L. Avram, Y. Cohen, *J. Am. Chem. Soc.* **2004**, *126*, 11556–11563.
[20] In a typical experiment, a 1:1 mixture of PgC6 (**3**) and pyrene (**4a**) or 1-bromopyrene (**4b**) was dissolved in hot acetonitrile/water (≈5:2 by volume). The solution was sonicated for around 10 min and then left to stand overnight. Slow evaporation of the solvent resulted in the formation of large single crystals of **5a** or **5b**, respectively, that were suitable for X-ray diffraction studies. Data for both crystal structures were collected on a Bruker SMART 1000 CCD diffractometer. CCDC 282089 and 282090 contain the supplementary crystallographic data for this paper. These data can be obtained free of charge from The Cambridge Crystallographic Data Centre via www.ccdc.cam.ac.uk/data_request/cif.
[21] Crystallographic data for pyrene-containing nanotube **5a** (CCDC 282089): $C_{145}H_{188.50}N_{4.50}O_{29.50}$, $M_r = 2444.33$, $0.35 \times 0.26 \times 0.22$ mm^3, orthorhombic, $a = 35.446(7)$, $b = 36.868(7)$, $c = 22.124(4)$ Å, $V = 28913(10)$ Å^3, space group *Pccn*, $Z = 8$, $\rho_{calcd} = 1.123$, $\lambda(Mo_{K\alpha}) = 0.70930$ Å, $T = 173(2)$ K, 203224 reflections, 31906 unique (13021 observed, $R_{int} = 0.140$), $R_1 = 0.0941$, $\omega R_2 = 0.2913$ for 1507 parameters and two restraints.

 © 2006 Wiley-VCH Verlag GmbH & Co. KGaA, Weinheim

[22] Crystallographic data for 1-bromopyrene-containing nanotube **5b** (CCDC 282090): $C_{145}H_{188.50}Br_2N_{4.50}O_{30.50}$, $M_r = 2642.32$, $0.40 \times 0.32 \times 0.26\ mm^3$, orthorhombic, $a = 35.588(7)$, $b = 36.995(7)$, $c = 22.211(4)$ Å, $V = 29242(10)$ Å^3, space group *Pccn*, $Z = 8$, $\rho_{calcd} = 1.200$, $\lambda(Mo_{K\alpha}) = 0.70930$ Å, $T = 173(2)$ K, 139038 reflections, 32127 unique (15395 observed, $R_{int} = 0.0657$), $R_1 = 0.1176$, $\omega R_2 = 0.3222$ for 1627 parameters and one restraint. The structure showed significant disorder around the 1-bromopyrene molecules and this was modeled as satisfactorily as possible. The structure of the 1-bromopyrene derivative differs from that of the pyrene derivative by one water of crystallization. See Supporting Information for details of the asymmetric unit and figures of the extended structure.

[23] S. J. Dalgarno, J. Antesberger, R. M. McKinlay, J. L. Atwood, unpublished results.

 © 2006 Wiley-VCH Verlag GmbH & Co. KGaA, Weinheim

Supported Catalysts

DOI: 10.1002/anie.200502864

Evidence from NMR and EXAFS Studies of a Dynamically Uniform Mononuclear Single-Site Zeolite-Supported Rhodium Catalyst**

Justin O. Ehresmann, Philip W. Kletnieks, Ann Liang, Vinesh A. Bhirud, Olesya P. Bagatchenko, Eric J. Lee, Meghan Klaric, Bruce C. Gates, and James F. Haw**

The best transition-metal complex catalysts are characterized by both high activities and high selectivities, with the latter typically associated with the uniqueness of the catalytic species. Optimal use in technology also demands ease of separation of catalysts from products, and the goal of efficient separation has been a primary motivation for research with supported metal complexes, which offer the added benefit of being resistant to corrosion. General challenges in the synthesis of practical single-site catalysts on supports include the following: a) low catalytic activity associated with non-optimal ligands, which include the support and ligands remaining from the precursor metal complex that is adsorbed on the support; b) non-uniform distribution of metal sites as a consequence of the intrinsic heterogeneity of the surfaces of the inorganic support; and c) loss of structural integrity of the catalysts during operation, sometimes associated with reduction and sintering of the metal to form species of non-uniform (and often poorly characterized) metal nuclearity and often undesired oxidation states of the metal.

Several research groups have pursued the synthesis and testing of organometallic precursors suitable for the preparation of supported catalysts and meet the criteria stated above.[1,2] In particular, Basset and co-workers[1] have developed precursors that, when bonded to silica, closely mimic structures that may exist in catalytic cycles, with the expectation that these surface species will readily enter catalytic cycles once presented with suitable reagents (point (a), above).[1]

We have been drawn to zeolites as potential supports because their well-defined, highly uniform adsorption sites seem to address point (b) above.[3,4] As shown below and elsewhere, EXAFS (extended X-ray absorption fine structure) spectroscopy, used in concert with IR and NMR spectroscopic techniques, provides the means to test directly the efficacy of synthetic procedures intended to provide specific mononuclear (or polynuclear) metal sites.[5]

Herein, we report the synthesis of the first supported mononuclear Rh^+ species with exchangeable ethylene ligands; the support is dealuminated zeolite Y. The isotopically unmodified ethylene ligands (natural abundance) introduced in the synthesis of the catalyst are easily and completely exchanged by either ^2H- or ^{13}C-labeled ethylene, as verified by IR and NMR spectroscopy, respectively. Furthermore, the as-synthesized or ^{13}C-exchanged ethylene ligands readily undergo reduction with autogenous hydrogen (i.e., reverse spillover), as expected for an active catalyst.

Central to this report, by using variable-temperature ^{13}C CP-MAS (cross-polarization magic-angle spinning) NMR spectroscopy we observed that all of the [$^{13}C_2$]ethylene ligands on the zeolite-supported catalyst undergo anisotropic rotation at the same frequency at a given temperature which is characteristic of the precursor compound either in solution or as a crystalline compound.[6] Given the extreme sensitivity of dynamical barriers to electronic and steric effects, we consider this observation to be a convincing demonstration of the structural uniformity or our supported metal sites.[7]

The active site of the zeolite-supported rhodium catalyst (Figure 1) is represented as a structure optimized at the B3LYP level using appropriate basis sets and a cluster model of a zeolite anion site. Table 1 provides a summary of the structural parameters that were optimized on the basis of EXAFS data which characterize the supported metal complex. These data compare favorably with the coordination numbers and distances indicated in Figure 1 and, where appropriate, with the crystal structure of the precursor complex, acetylacetonatobis(ethylene)rhodium ([Rh(acac)-$(C_2H_4)_2$]).[8] We emphasize the lack of a Rh–Rh contribution in the EXAFS data, consistent with the presence of exclusively mononuclear rhodium within the catalyst. The experimental Rh–O coordination number is 2.2 ± 0.4, representing the coordination of Rh to the zeolite framework. The Rh–O

[*] J. O. Ehresmann,[+] P. W. Kletnieks,[+] O. P. Bagatchenko, E. J. Lee, M. Klaric, Prof. Dr. J. F. Haw
Department of Chemistry
University of Southern California
Los Angeles, CA 90089-1661 (USA)
Fax: (+1) 213-740-0930
E-mail: jhaw@usc.edu
A. Liang, V. A. Bhirud, Prof. Dr. B. C. Gates
Department of Chemical Engineering and Materials Science
University of California at Davis, CA 95616 (USA)
[+] These authors contributed equally to this work.

[**] This work was supported by the Department of Energy (DE-FG02-04ER15598, DE-FG02-04ER15600). We are grateful to the USC Center for High Performance Computing for granting computer time.

InterScience
© 2006 Wiley-VCH Verlag GmbH & Co. KGaA, Weinheim

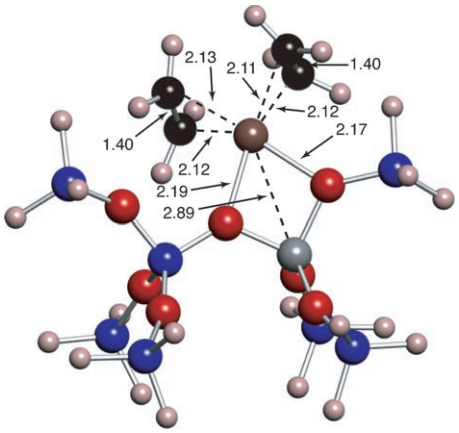


Figure 1. Geometry of $\{Rh(C_2H_4)_2\}$ bonded to a zeolite anion cluster, optimized at the B3LYP level. Rh brown, C black, Al gray, O red, Si blue, H beige.

Table 1: Fit parameters for EXAFS data and bond lengths/distances from density functional calculations (B3LYP level) for the DAY-zeolite-supported rhodium complex.[a]

Shell	Distance [Å][b]	*R* [Å]	*N*	$\Delta\sigma^2$ [Å^2]	ΔE_0 [eV]
Rh–Rh	–	–	–	–	–
Rh–O_s[c]	2.18	2.19	2.2	0.00673	−3.05
Rh–C	2.12	2.09	3.9	0.00345	3.24
Rh–O_l[d]	3.58	3.41	0.7	−0.00371	6.55
Rh–Al	2.89	2.92	0.4	0.00221	0.68

[a] Scanned at 77 K and $<10^{-5}$ Torr. Notation: N = coordination number; R = absorber–backscatter distance; $\Delta\sigma^2$ = Debye–Waller factor; ΔE_0 = inner potential correction. The approximate experimental uncertainties of the contributions other than for Rh–Al are as follows: N ±20%; R ±1%; the errors representative of the Rh–Al contribution are greater than these and are not well characterized. [b] Average bond lengths/distances determined at the B3LYP level. [c] s = short. [d] l = long.

bond distance is 2.19 Å, consistent with previously reported distances for rhodium complexes bonded to oxide supports.[9]

The Rh–C coordination number was determined to be approximately 3.9, as would be expected for ethylene that is π-bonded to Rh. The structure is also in line with the expectation of two ethylene units ligated to each Rh atom, although the data do not definitively confirm this. The Rh–C bond length, determined from the EXAFS data to be 2.09 Å, is close to the value determined by X-ray crystallography for the precursor $[Rh(acac)(C_2H_4)_2]$ (2.13, 2.14 Å).[10] The Rh–Al coordination number was determined to be 0.4, but this contribution could be determined only tentatively, as the error bound is high. The Rh–Al distance determined by EXAFS spectroscopy was 2.92 Å (compare with the calculated value of 2.89 Å, Figure 1).

The ^{13}C CP-MAS NMR spectra in Figure 2a decisively demonstrate that the supported rhodium complex has intact π-bonded ethylene ligands and that no other carbonaceous species were introduced during the $[^{13}C_2]$ethylene-exchange procedure. The single resonance at $\delta = 60$ ppm is in excellent agreement with the values reported for the precursor complex

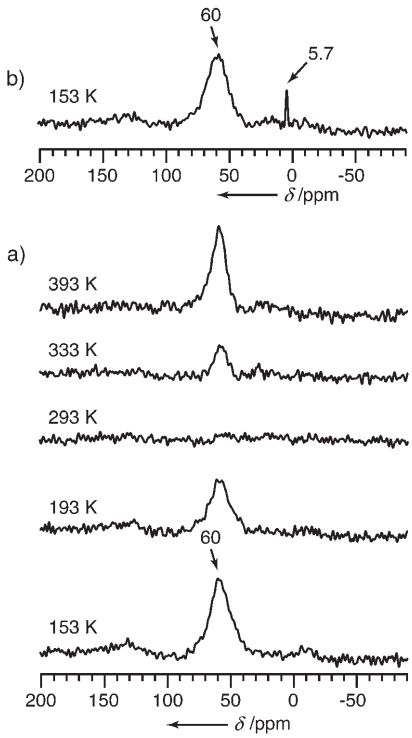


Figure 2. ^{13}C CP-MAS spectra (75.4 MHz) of the sample formed from $[Rh(acac)(C_2H_4)_2]$ and dealuminated zeolite Y and then exchanged with ^{13}C-labeled ethylene. a) Variable-temperature spectra showing the temperature dependence of the signal intensity. b) Spectrum obtained at low temperature after heating and subsequent cooling of the sample which demonstrates the results of a reverse-spillover reaction. The signal at $\delta = 5.7$ ppm corresponds to ethane.

in solution ($\delta = 59.54$ ppm) and for the crystalline solid ($\delta =$ 59.4 and 60.3 ppm).[6]

Most important, by acquiring ^{13}C CP-MAS NMR spectra of the supported complex over a range of temperatures (Figure 2a) we observed a temperature dependence of the line width, similar to that reported by others for a crystalline sample of the precursor complex.[6] As was determined in earlier work, the ^{13}C resonance of the π-bonded ethylene ligands is broadened as a result of a conflict of ^1H–^{13}C dipolar decoupling and random anisotropic reorientation of the ^1H–^{13}C bond vector. When these two dynamical processes occur on the same timescale for *all* spin-pairs in the sample, the carbon resonance is broadened in its entirety and, correspondingly, no signal was observed for our sample at temperatures near room temperature with a 27-kHz proton dipolar decoupling field. If the metal sites of our zeolite-supported rhodium catalyst were structurally diverse, this diversity would map into a distribution of rotational barriers for the ethylene ligands and some of the sites would yield sharp ^{13}C components at each temperature investigated, as we have verified by using other less-uniform support materials (data not shown).[11] The rotational barrier for ethylene ligands in our supported complex will be sensitive to both electronic and steric interactions. The result that all ethylene ligands in our catalyst have a common rotational barrier is powerful evidence that we have synthesized a supported rhodium complex that has a degree of structural—and hence

 © 2006 Wiley-VCH Verlag GmbH & Co. KGaA, Weinheim

dynamical—uniformity, characteristic of crystalline complexes and solution species. Thus, we propose that this sample is a true supported molecular catalyst.

Our justification for referring to the sample as a catalyst includes the result shown in Figure 2b: upon first heating the NMR probe in the rotor and then by acquiring the ^{13}C NMR spectrum at lower temperatures, we observed a sharp resonance at $\delta = 5.7$ ppm, assigned to gas-phase and/or physisorbed [$^{13}C_2$]ethane. Autogenous reduction reactions of this sort are known to be the result of reverse-spillover, in which hydrogen associated with the support material, for example, as OH groups, migrates to the metal site to provide H_2 equivalents.[12]

The absence of a Rh–Rh contribution (and thus mononuclear rhodium), as indicated by the EXAFS data (Table 1), combined with the Rh–O coordination number of approximately 2 (representing the coordination of Rh to two oxygen atoms of the zeolite framework, with a Rh–O distance of 2.19 Å) are consistent with bonding of Rh to the support[9] after dissociation from the acac ligands of the precursor.

Experimental Section

Highly dealuminated HY zeolite (DAY zeolite; Zeolyst International; atomic ratio of Si/Al ≈ 30) was calcined in O_2 at 773 K for 4 h and evacuated for 16 h at 773 K, isolated, and stored in a glovebox until used in the preparation of the supported rhodium complex. *n*-Pentane solvent (Fisher, 99%) was dried and purified by refluxing over sodium benzophenone ketyl and deoxygenated by purging with N_2. The precursor metal complex [$Rh(C_2H_4)_2(C_5H_7O_2)$] (Strem, 99%) was brought into contact with the treated zeolite in a slurry in dried, deoxygenated *n*-pentane at 200 K. The Rh content of the resultant powders was 1 wt%.

EXAFS spectra of the supported catalyst were measured at Beamline X-18B at the National Synchrotron Light Source at Brookhaven National Laboratory at a temperature near 77 K, with cells and methods as previously reported.[13] EXAFS data were analyzed using standard software. IR spectra were measured as reported previously and showed loss of the acac ligand.[14]

The ethylene ligands of the as-synthesized catalyst were exchanged with [$^{13}C_2$]ethylene using multiple contacts with pressures of [$^{13}C_2$]ethylene of less than 1.5 Torr and exposure times of less than 1 min. GC-MS analysis of gas fractions drawn from the vacuum line was used to validate the exchange procedure. Variable-temperature in situ ^{13}C CP-MAS NMR measurements were performed with a sealed rotor and standard methods, as described elsewhere.[15,16] The ^1H decoupling power level was 27 kHz.

Computational modeling of the structure was carried out at the B3LYP level by using the Stuttgart rsc basis functions with relativistic effective core potentials on Rh and Ahlrich's triple-zeta polarization basis sets on all other atoms.[17]

Received: August 11, 2005
Published online: December 27, 2005

Keywords: density functional calculations · EXAFS spectroscopy · NMR spectroscopy · rhodium · supported catalysts

[1] C. Coperet, M. Chabanas, R. P. Saint-Arroman, J.-M. Basset, *Angew. Chem.* **2003**, *115*, 164–191; *Angew. Chem. Int. Ed.* **2003**, *42*, 156–181.
[2] J. Guzman, B. C. Gates, *Dalton Trans.* **2003**, *17*, 3303–3318.
[3] W. M. H. Sachtler, *Acc. Chem. Res.* **1993**, *26*, 383–387.
[4] J. F. Goellner, B. C. Gates, G. N. Vayssilov, N. Rösch, *J. Am. Chem. Soc.* **2000**, *122*, 8056–8066.
[5] B.-K. Teo in *EXAFS Spectroscopy: Techniques and Applications* (Eds.: B.-K. Teo, D. C. Joy), Plenum, New York, **1981**, pp. 13–58.
[6] S. A. Vierkötter, C. E. Barnes, G. L. Garner, L. G. Butler, *J. Am. Chem. Soc.* **1994**, *116*, 7445–7446.
[7] T. A. Albright, R. Hoffmann, J. C. Thibeault, D. L. Thorn, *J. Am. Chem. Soc.* **1979**, *101*, 3801–3812.
[8] D. W. Price, M. G. B. Drew, K. K. Hii, J. M. Brown, *Chem. Eur. J.* **2000**, *6*, 4587–4596.
[9] O. Alexeev, B. C. Gates, *Top. Catal.* **2000**, *10*, 273–293.
[10] J. A. Evans, D. R. Russell, *Chem. Commun.* **1971**, *4*, 197–198.
[11] V. A. Bhirud, J. O. Ehresmann, P. W. Kletnieks, J. F. Haw, B. C. Gates, *Langmuir*, **2005**, DOI: 10.1021/la052268f, in press.
[12] W. C. Conner, J. L. Falconer, *Chem. Rev.* **1995**, *95*, 759–788.
[13] J. Guzman, B. C. Gates, *J. Am. Chem. Soc.* **2004**, *126*, 2672–2673.
[14] J. Guzman, B. C. Gates, *Angew. Chem.* **2003**, *115*, 714–717; *Angew. Chem. Int. Ed.* **2003**, *42*, 690–693.
[15] J. F. Haw, G. C. Campbell, R. C. Crosby, *Anal. Chem.* **1986**, *58*, 3172–3177.
[16] J. F. Haw, J. B. Nicholas, T. Xu, L. W. Beck, D. B. Ferguson, *Acc. Chem. Res.* **1996**, *29*, 259–267.
[17] Gaussian 03 (Revision A.1), M. J. Frisch, G. W. Trucks, H. B. Schlegel, G. E. Scuseria, M. A. Robb, J. R. Cheeseman, J. A. Montgomery, Jr., T. Vreven, K. N. Kudin, J. C. Burant, J. M. Millam, S. S. Iyengar, J. Tomasi, V. Barone, B. Mennucci, M. Cossi, G. Scalmani, N. Rega, G. A. Petersson, H. Nakatsuji, M. Hada, M. Ehara, K. Toyota, R. Fukuda, J. Hasegawa, M. Ishida, T. Nakajima, Y. Honda, O. Kitao, H. Nakai, M. Klene, X. Li, J. E. Knox, H. P. Hratchian, J. B. Cross, C. Adamo, J. Jaramillo, R. Gomperts, R. E. Stratmann, O. Yazyev, A. J. Austin, R. Cammi, C. Pomelli, J. W. Ochterski, P. Y. Ayala, K. Morokuma, G. A. Voth, P. Salvador, J. J. Dannenberg, V. G. Zakrzewski, S. Dapprich, A. D. Daniels, M. C. Strain, O. Farkas, D. K. Malick, A. D. Rabuck, K. Raghavachari, J. B. Foresman, J. V. Ortiz, Q. Cui, A. G. Baboul, S. Clifford, J. Cioslowski, B. B. Stefanov, G. Liu, A. Liashenko, P. Piskorz, I. Komaromi, R. L. Martin, D. J. Fox, T. Keith, M. A. Al-Laham, C. Y. Peng, A. Nanayakkara, M. Challacombe, P. M. W. Gill, B. Johnson, W. Chen, M. W. Wong, C. Gonzalez, J. A. Pople, Gaussian, Inc., Pittsburgh, PA, **2003**.

 © 2006 Wiley-VCH Verlag GmbH & Co. KGaA, Weinheim

Nanotechnology

DOI: 10.1002/anie.200503389

Carbon Nanotubes as Intracellular Transporters for Proteins and DNA: An Investigation of the Uptake Mechanism and Pathway**

*Nadine Wong Shi Kam, Zhuang Liu, and Hongjie Dai**

New materials for the intracellular transport of biological cargos such as DNA, proteins, and drug molecules have been actively sought to effectively breach the cell-membrane barriers for delivery and enabling functionality of extracellular agents. Single-walled carbon nanotubes (SWNT) have been recently shown to shuttle various molecular cargos inside living cells including proteins, short peptides, and nucleic acids.[1–8] The internalized nanotubes were found to be biocompatible and nontoxic at the cellular level. Furthermore, a very recent study has established targeted internalization of SWNTs into cancer cells that express specific cell-surface receptors and subsequent use as high near-infrared (NIR) absorbing agents for cancer-cell destruction without harming normal cells.[7] Release of oligodeoxynucleotides from SWNT transporters in vitro has also been demonstrated by NIR excitation of nanotubes that are located inside living cells. The utilization of the intrinsic physical properties of SWNTs allows the realization of a new class of biotransporters and opens up new possibilities in drug delivery and NIR radiation therapy.

At the present time, several fundamental issues remain to be addressed for the use of carbon nanotubes as potential biological transporters. One such issue is the entry mechanism that regulates the cellular internalization of SWNTs and their cargos. We[1,2] have suggested that SWNTs traverse the cellular membrane through endocytosis, whereas Pantarotto et al.[5] have suggested an energy independent nonendocytotic mechanism that involves insertion and diffusion of nanotubes through the lipid bilayer of the cell membrane. Detailed work to establish the cellular uptake mechanism and pathway for SWNTs is currently lacking.

Herein, we present the first systematic investigation of the cellular uptake mechanism and pathway for carbon nanotubes. We first show that intracellular transportation of proteins and DNA by SWNTs is indeed general, thus further confirming the transporter ability of these materials. We then present evidence that shows clathrin-dependent endocytosis as the pathway for the uptake of various SWNT conjugates with proteins and DNA. We also discuss the differences between the nanotube materials and the experimental procedures used in our work and by Pantarotto et al. who suggested an energy-independent nonendocytotic uptake of nanotubes. In our current work, we aim to clearly establish the intracellular uptake mechanism of SWNTs in the form of individual and small bundles with lengths of <1 micron and to avoid any confusion and controversy over the cellular-uptake mechanism for these materials.

To investigate the generality of carbon nanotubes for the transportation of proteins and DNA inside mammalian cells, we used, in our current work, two different mammalian cells lines, adherent HeLa cells and non-adherent HL60 cells. Control experiments were carried out through the incubation of cells in protein and DNA solutions in the absence of nanotubes. In parallel experiments, HeLa and HL60 cells were incubated with various noncovalent protein–SWNT and DNA–SWNT conjugates (Figure 1a, b) and analyzed by both

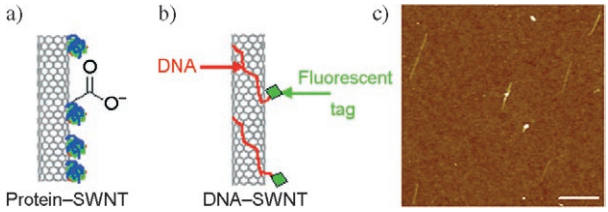


Figure 1. Schematic representation of a) protein–SWNT and b) DNA–SWNT. c) AFM image of DNA–SWNT deposited on a SiO_2 substrate (scale bar = 200 nm).

flow cell cytometry and confocal fluorescence microscopy. Unless otherwise stated, the SWNTs that were used were short ($\approx$50–200 nm, afforded by sonication), individual, and small bundles of nanotubes as characterized by atomic force microscopy (AFM; Figure 1c). Acid oxidized SWNTs were used for noncovalent conjugation with proteins and non-oxidized, as-grown SWNTs were used to complex with DNA molecules (see Experimental Section).

With these nanotubes of different functionalization, molecular cargos, and fluorescent tagging, we consistently observed, by confocal fluorescence microscopy imaging, cellular uptake of the protein–SWNT and DNA–SWNT conjugates by both HeLa and HL60 cells (representative image of uptake shown in Figure 2a) after incubation at 37 °C. The successful uptake of both SWNT conjugates was further confirmed by flow cell cytometry measurements (Figure 2d, see fluorescence signal under 'protein–SWNT' and 'DNA–SWNT' labels, respectively) from a population of $\approx$10000 cells. The noncovalent conjugations between proteins and DNA and SWNTs are sufficiently strong for entry as carrier–cargo complexes into living cells. This was shown by the little intracellular uptake of fluorescently tagged proteins and DNA molecules without nanotube transporters (Figure 2d low fluorescence levels under 'protein' and 'DNA' respectively). The existence of SWNTs inside cells was also evidenced by a recent finding that SWNTs inside living cells can be excited optically by NIR laser light. Continuous NIR radiation of SWNTs inside cells was also shown to lead to cell death owing to the high NIR absorbance of SWNTs and the

[*] N. W. S. Kam, Z. Liu, Prof. H. Dai
Department of Chemistry
Stanford University
Stanford, CA 94305 (USA)
Fax: (+1) 650-725-0259
E-mail: hdai@stanford.edu

[**] This work was supported by a Stanford Interdisciplinary Translational Research Grant.

© 2006 Wiley-VCH Verlag GmbH & Co. KGaA, Weinheim

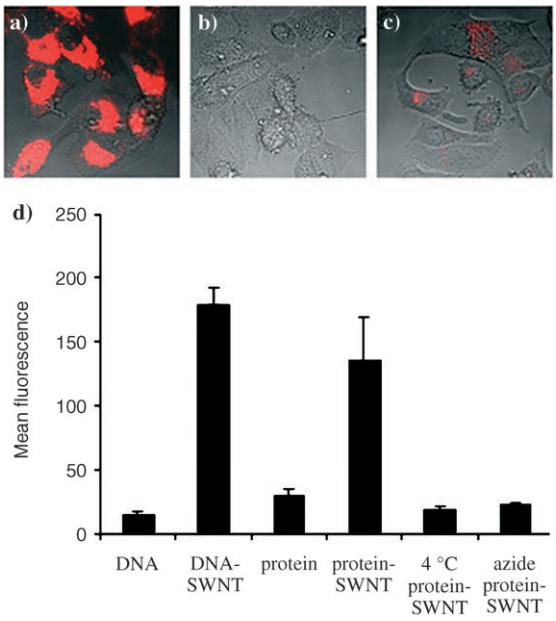


Figure 2. Confocal microscopy images of HeLa cells after incubation in fluorescently labeled DNA–SWNT at a) 37 °C, b) 4 °C, and c) after pretreatment with NaN_3. d) Flow cell cytometry data for HL60 cells that were incubated in fluorescently labeled pure DNA or protein solutions without nanotubes (labeled 'DNA' and 'protein', respectively), DNA–SWNT and SA–SWNT at 37 °C, and for protein–SWNT at 37 °C in cells incubated at 4 °C or pretreated with sodium azide.

resultant heating in vitro.[7] In the case of DNA–SWNT conjugates, DNA cargos can be detached from the SWNT carriers, after cellular internalization, by short NIR pulsing to transiently excite the nanotubes. The detached DNA molecules can subsequently undergo nuclear translocation and enter the cell nucleus.[7]

Next, we carried out a systematic investigation of the cellular internalization mechanism and pathway for SWNT conjugates. Endocytosis is known as a general entry mechanism for various extracellular materials and is an energy-dependent uptake[9–11] that is hindered when incubations are carried out at low temperature (4 °C instead of 37 °C) or in ATP (adenosine triphosphate) depleted environments.[10–12] Cellular incubations with our SWNT conjugates were carried out at 4 °C and with cells pretreated with NaN_3 in parallel with our regular incubation conditions. Treatment with NaN_3 is known to disturb the production of ATP in cells, thus hindering the endocytotic pathway. Indeed, the fluorescence levels observed with confocal microscopy from cells (after incubation in SWNT conjugates at 4 °C (Figure 2b) and ATP depletion by NaN_3 (Figure 2c)) were low. This therefore indicates endocytosis as the internalization mechanism for the uptake of SWNT conjugates at 37 °C. This was further confirmed by flow cytometry measurements, which indicated a significant reduction in cellular uptake at 4 °C and under the azide ATP depletion conditions (Figure 2d).

The endocytosis pathway encompasses several subcategories, including phagocytosis, pinocytosis, and clathrin-dependent receptor-mediated and clathrin-independent endocytosis.[10] Internalization through clathrin-dependent endocytosis occurs when the clathrin coat on the plasma membrane forms invaginations in the membrane leading to the budding of clathrin-coated vesicles.[10] The extracellular species located on the cell membrane are trapped within the vesicles and brought inside the cells. On the other hand, clathrin-independent endocytosis can occur through the caveolae or lipid-raft pathway. Caveolae are flask-shaped membrane invaginations on cell surfaces that are rich in cholesterol and sphingomyelin.[13]

Receptor-mediated endocytosis through clathrin-coated pits is the most common pathway of endocytosis. To assess the role of clathrin in the internalization of SWNTs, we carried out incubations under conditions that are known to disrupt the formation of clathrin-coated vesicles on the cell membrane. Such a treatment consisted of pretreating the cells with either sucrose (hypertonic treatment) or a K^+-depleted medium prior to exposure to the SWNT conjugates.[14–17] These pretreatments drastically reduced the level of cellular uptake of SWNTs as deduced from the cell cytometry data (Figure 3a), therefore suggesting the clathrin pathway for endocytotic cellular uptake of SWNTs.

As transferrin is well established to be internalized through the clathrin-mediated endocytosis pathway, we carried out control experiments in which the cells were

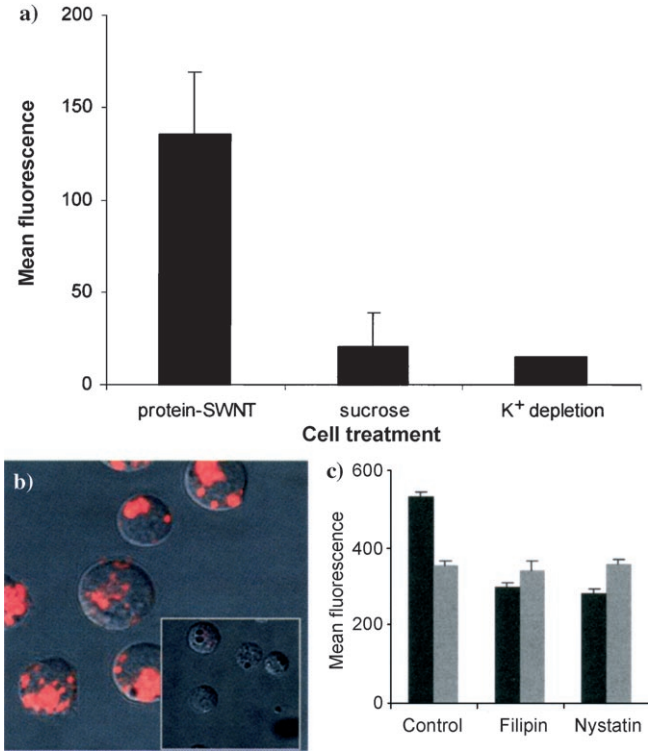


Figure 3. a) Flow cell cytometry data obtained after incubation in protein–SWNT solutions for untreated cells, cells pretreated with 0.45 M sucrose, and K^+-depleted medium, respectively. b) A confocal image that shows cellular uptake of a rhodamine-labeled transferrin protein in HL-60 cells at 37 °C. The inset shows the lack of uptake of the transferrin protein after pretreatment of cells in sucrose. c) Flow cytometry data of cells after incubation in cholera-toxin B (black bars) and BSA–SWNT (gray bars) for HeLa cells without any pretreatment (control) and cells pretreated with filipin and nystatin, respectively.

 © 2006 Wiley-VCH Verlag GmbH & Co. KGaA, Weinheim

incubated in solutions of fluorescently (rhodamine) labeled transferrin under similar experimental conditions as those used for the nanotubes. Indeed, we observed that transferrin uptake was blocked (similar to our SWNTs) after the cells were incubatated in transferrin solutions at low temperature and after pretreatment with a sucrose solution or K^+ depleted buffer. As an example, Figure 3b shows a confocal image of cells with normal transferrin uptake and a lack of uptake after sucrose pretreatment (inset).

To further elucidate SWNT cellular uptake, we investigated the possibility of cellular entry by SWNT conjugates through the caveolae or lipid-rafts pathway. As caveolae-dependent cell entry relies on the presence of cholesterol domains, we pretreated cells with the drugs filipin and nystatin, which are known to disrupt the cholesterol distribution within the cell membrane. Figure 3c shows the flow cytometry data that were obtained after incubations in protein–SWNT conjugates for cells with and without filipin and nystatin pretreatment, respectively. In stark contrast to the clathrin-blocking experiments, we observed that pretreatment of cells with these drugs had no blocking effect on the cellular uptake of SWNTs (Figure 3c gray bars), which suggests little or no involvement of the caveolae-dependent cell-entry pathway for nanotubes. As a control experiment, we carried out cellular-uptake experiments of fluorescently labeled cholera-toxin B (CTX-B), which is a protein with multivalent ligand whose receptor GMl resides in the caveolae and is known to be internalized through a caveolae-mediated endocytosis pathway. Indeed, we observed that the uptake of CTX-B by our cell lines was substantially blocked (by $\approx 50\,\%$) by pretreatment with filipin and nystatin (Figure 3c black bars) under the same experimental conditions as those used for our nanotubes. Taken together, our experimental data suggest that cellular internalization of SWNT conjugates with proteins and DNA is through the clathrin-dependent endocytosis pathway.

Our results above clearly differ from the suggestion by Pantorotto et al.[5] that nanotube uptake by living cells through an energy-independent nonendocytotic pathway involves insertion and diffusion of nanotubes across cell membranes. We note, however, that there are several differences in both the nanotube material and experimental procedures that were used between the two studies. Pantorotto et al. employed materials that contained positively charged peptide-functionalized bundles and aggregates of SWNTs (which were microns in length and submicron in bundle size) as characterized by microscopy (see supplementary information of Reference [5]). The coexistence of nanotubes and cells was observed after incubation at 4 °C followed by rinsing and fixing of the cells. This led to the suggested nonblocking of nanotube uptake at 4 °C and thus nonendocytotic uptake.[5]

In an effort to investigate the effect of size on SWNT uptake, we obtained DNA–SWNT conjugates that contained longer (200 nm–2 μm, mean ≈ 750 nm) and larger (up to 15 nm measured by AFM, Figure 4a) SWNT bundles through a reduction in sonication time for the raw hipco material and by using only mild centrifugation to remove the large aggregates. Confocal imaging revealed cellular uptake of

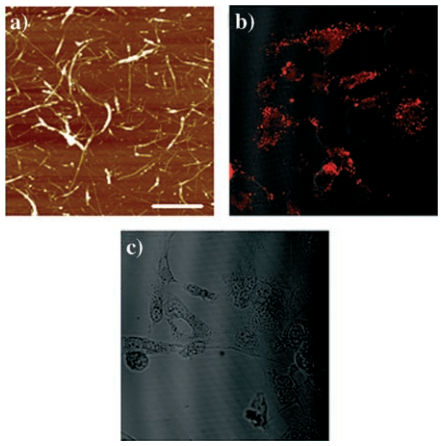


Figure 4. a) Atomic force microscopy image of relatively long bundles of nanotubes (scale bar = 500 nm). b) and c) Confocal image of HeLa cells after incubation in solutions of long nanotubes at b) 37 °C and c) 4 °C, respectively.

these ≈ 750-nm SWNT conjugates upon incubation with HeLa cells at 37 °C (Figure 4b) and the lack of uptake at 4 °C (Figure 4c). These results were similar to those obtained with our regular, short (≈ 200 nm) SWNTs. Nevertheless, a quantitative comparison of uptake for the two materials is difficult owing to inhomogeneous SWNT length distributions between the two samples and the tendency of lower aqueous stability for the longer SWNTs. Our attempt to obtain even larger SWNT aggregates for cellular-uptake experiments, as in Reference [5], failed owing to the poor stability of large SWNT aggregates.

It remains unclear what the precise uptake pathway is for micron-scale SWNT aggregates, as was observed by Pantorotto et al., both at 37 °C and 4 °C. The proposed insertion, diffusion, and penetration mechanism should not operate for such large micron-sized structures. It has been shown previously that materials >1 μm in size generally have difficulty undergoing endocytotic cellular uptake, even at 37 °C.[18] One possibility is that large positively charged peptide-functionalized SWNT aggregates exhibit a high tendency to associate with negative cell-surface species, which gives rise to a false uptake result. This has been shown to be the cause of artifactual cellular uptake of HIV-tat peptides at 4 °C.[19] Regardless of the cause, we believe that large SWNT aggregates are clearly not desired for biological transporter applications owing to the lower aqueous stability, higher tendency for nonspecific association with cell surfaces, and lower ability to traverse various biological membrane barriers.

In summary, we have shown that short SWNTs with various functionalizations are capable of the transportation of proteins and oligonucleotides into living cells and that the cellular-uptake mechanism is energy-dependent endocytosis. The detailed endocytosis pathway for short, well-dispersed SWNT conjugates is mainly through clathrin-coated pits rather than caveolae or lipid rafts. Establishment of the entry mechanism is of fundamental importance and will facilitate future developments of carbon-nanotube transporters for biological-delivery applications.[20]

 © 2006 Wiley-VCH Verlag GmbH & Co. KGaA, Weinheim

Experimental Section

Materials: Bovine serum albumin (BSA) and streptavidin (SA) labeled with an alexa fluor 488 dye were obtained from Molecular Probes Inc. DNA oligonucleotides were obtained from the PAN Facility at Stanford University. All tissue culture materials were obtained from Invitrogen and all chemicals used for the endocytosis-mechanism experiments were obtained from Sigma-Aldrich.

SWNT conjugate preparation.

Protein–SWNT: Single-walled carbon nanotubes (SWNT) made through the Hipco process were treated by sonication and acid reflux as described previously to afford short, ($\approx$200 nm) water-soluble nanotubes that contain acidic surface groups.[1,2] Fluorescently labeled BSA or SA in a concentration range of 100 nM–1 μM was then mixed with the oxidized nanotubes for 1–2 h. The proteins were found to bind nonspecifically to the nanotubes to form protein–SWNT conjugates.[2]

DNA–SWNT: SWNTs made through the Hipco process was sonicated in a solution of a fluorescently labeled 15-mer oligonucleotide (CATTCCGAGTGTCCA-X in which X = Cy3 or fluorescein isothiocyanate (FITC)) for $\approx$30 min to 1 h (DNA concentration $\approx$2–10 μM). The resultant suspension was centrifuged at 24000 g for $\approx$6 h to remove large impurities in the sample. The sonication/centrifugation process was repeated twice. The final decanted solution contained mostly SWNTs that are 50–200 nm in length (the apparent height or diameter of the tubes is in the range of $\approx$1–5 nm as determined by AFM topography measurements that correspond to individual and small bundles of SWNTs) wrapped by DNA oligonucleotides.[21]

Long SWNT conjugate preparation: DNA–SWNT conjugates were prepared as described above, with the sonication time reduced to $\approx$10–20 min. The resultant suspension was centrifuged at 10000 g for $\approx$15 min to remove large impurities in the sample. The final supernatant was analyzed by AFM and found to contain bundles of nanotubes that ranged from 200 nm–2 μm in length and had an apparent height or diameter between 3 and 15 nm.

Cellular incubation in nanotube conjugates: Two cell lines, human promyelomonocytic HL60 cells and cervical cancer HeLa cells were used in the current work. HL60 were cultured in RPMI (Roswell Park Memorial Institute) 1640 medium supplemented with 10% fetal bovine serum (FBS), whereas HeLa cells were cultured in DMEM medium supplemented with 10% FBS and 1% penicillin–streptomycin. The cells were suspended in phosphate-buffered saline (PBS) solution, mixed with a SWNT conjugate, rhodamine-labeled transferring, or FITC-labeled cholera-toxin B, and incubated for 1–3 h at 37°C (except for the low-temperature 4°C incubations). The concentration of SWNTs in the incubation solution was typically $\approx$2.5 mg L^{-1} as measured by the UV/Vis–NIR absorption spectrum, and the cell density was $\approx 2–3 \times 10^5$ cells/well. Adherent HeLa cells were either trypsinized to detach from the petri dishes to form a suspension, or were seeded overnight in chambered cover slides.

Endocytosis mechanism investigation.

Low temperature incubation at 4°C: Cellular incubations were carried out as described above with the solution kept at 4°C, instead of the regular 37°C condition.

Incubation of cells in SWNT conjugates under ATP depletion: For the ATP-depletion studies, the cells were preincubated in PBS buffer solution and supplemented with 10 mM NaN_3 and 50 mM 2-deoxy-D-glucose for 30 min at 37°C followed by incubation in a solution of either DNA–SWNT or protein–SWNT conjugates.

Hypertonic incubation: For the hypertonic treatment, the cells were preincubated for 30 min in PBS buffer solution and supplemented with 0.45 M sucrose before exposure to the SWNT conjugate 37°C.

Potassium-depletion incubation. The K^+ depletion was achieved by preincubation of the cells in a potassium-free buffer that consists of HEPES *N*-(2-hydroxyethyl)piperazine-*N*-[2-ethanesulfonic acid], NaCl, $MgCl_2$, and D-glucose for 30 min at 37°C prior to incubation in a nanotube solution.

Filipin and nystatin treatment. For these incubations, the cells are pretreated in PBS buffer solution and supplemented with filipin (5 μg mL^{-1}) and nystatin (10 μg mL^{-1}) for 30 min followed by exposure to a SWNT conjugate at 37°C.

Confocal microscopy. After incubation, the non-adherent cells were washed by centrifugation twice and resuspended in ice-cold PBS buffer solution. For adherent cells, the cell medium was removed from the chambered cover slides, washed, and replaced with ice-cold PBS buffer solution. For analysis, about 20 μL of non-adherent cell suspension was dropped onto a cover glass slide and then imaged immediately with a Zeiss LSM510 confocal microscope. Adherent HeLa cells were imaged directly on the chambered cover glass.

Flow Cell Cytometry. For cell cytometry, adherent cells were detached from the surface by treatment with trypsin–EDTA and received similar subsequent treatment as the non-adherent cells. After incubation, the cells were washed, resuspended in ice-cold PBS buffer solution, and supplemented with 2% propidium iodide (PI). The mean fluorescence was measured from $\approx$10000 cells by using flow cytometry (Becton Dickinson FACScan). Cells that were stained with propidium iodide (corresponding to naturally occurring dead cells) were excluded from the data analysis.

Received: September 25, 2005
Revised: October 10, 2005
Published online: December 13, 2005

Keywords: cellular uptake · DNA · drug delivery · endocytosis · nanotubes

[1] N. W. S. Kam, H. Dai, *J. Am. Chem. Soc.* **2005**, *127*, 6021.
[2] N. W. S. Kam, T. C. Jessop, P. A. Wender, H. Dai, *J. Am. Chem. Soc.* **2004**, *126*, 6850.
[3] Q. Lu, J. M. Moore, G. Huang, A. S. Mount, A. M. Rao, L. L. Larcom, P. C. Ke, *Nano Lett.* **2004**, *4*, 2473.
[4] A. Bianco, J. Hoebeke, S. Godefroy, O. Chaloin, D. Pantarotto, J.-P. Briand, S. Muller, M. Prato, C. D. Partidos, *J. Am. Chem. Soc.* **2005**, *127*, 58.
[5] D. Pantarotto, J. Briand, M. Prato, A. Bianco, *Chem. Commun.* **2004**, *1*, 16.
[6] D. Pantarotto, R. Singh, D. McCarthy, M. Erhardt, J. P. Briand, M. Prato, K. Kostarelos, A. Bianco, *Angew. Chem.* **2004**, *116*, 5354; *Angew. Chem. Int. Ed.* **2004**, *43*, 5242.
[7] N. W. S. Kam, M. O'Connell, J. A. Wisdom, H. Dai, *Proc. Natl. Acad. Sci. USA* **2005**, *102*, 11600.
[8] N. W. S. Kam, Z. Liu, H. Dai, *J. Am. Chem. Soc.* **2005**, *127*, 12492.
[9] M. Marsh, H. T. McMahon, *Science* **1999**, *285*, 215.
[10] S. Murkherjee, R. N. Ghosh, F. R. Maxfield, *Phys. Rev.* **1997**, *77*, 759.
[11] S. C. Silverstein, R. M. Steinman, Z. A. Cohn, *Annu. Rev. Biochem.* **1977**, *46*, 669.
[12] S. L. Schmid, L. L. Carter, *J. Cell Biol.* **1990**, *111*, 2307.
[13] R. D. Singh, V. Puri, J. T. Valiyaveettil, D. L. Marks, R. Bittman, R. E. Pagano, *Mol. Biol. Cell* **2003**, *14*, 3254.
[14] J. Heuser, R. G. W. Anderson, *J. Cell Biol.* **1989**, *108*, 389.
[15] J. M. Larkin, M. S. Brown, J. L. Goldstein, R. G. W. Anderson, *Cell* **1983**, *33*, 273.
[16] I. H. Madshus, K. Sandvig, S. Olsnes, B. van Deurs, *J. Cell. Physiol.* **1987**, *131*, 14.
[17] M. G. Qaddoumi, H. J. Gukasyan, J. Davda, V. Labhasetwar, K. J. Kim, V. H. Lee, *Mol. Vision* **2003**, *9*, 559.
[18] J. Rejman, V. Oberle, I. S. Zuhorn, D. Hoesktra, *Biochem. J.* **2004**, *377*, 159.

 © 2006 Wiley-VCH Verlag GmbH & Co. KGaA, Weinheim

[19] T. B. Potocky, A. K. Menon, S. H. Gellman, *The J. Biol. Chem.* **2003**, *278*, 50188.
[20] During the writing of this paper, a publication appeared on the uptake of multiple-walled carbon nanotubes and DNA cargos that revealed inhibition of uptake at 4°C and suggested the endocytosis pathway.Y. Liu, D.-C. Wu, W.-D. Zhang, X. Jiang, C.-B. He, T. S. Chung, S. H. Goh, K. W. Leong, *Angew. Chem.* **2005**, *44*, 4860; *Angew. Chem. Int. Ed.* **2005**, *44*, 4782.
[21] M. Zheng, A. Jagota, E. D. Semke, B. A. Diner, R. S. Mclean, S. R. Lustig, R. E. Richardson, N. G. Tassi, *Nat. Mater.* **2003**, *2*, 338.

 © 2006 Wiley-VCH Verlag GmbH & Co. KGaA, Weinheim

Electronic Devices

DOI: 10.1002/anie.200501799

In Situ Deposition and Patterning of Single-Walled Carbon Nanotubes by Laminar Flow and Controlled Flocculation in Microfluidic Channels**

*Jang-Ung Park, Matthew. A. Meitl, Seung-Hyun Hur, Monica L. Usrey, Michael S. Strano, Paul J. A. Kenis, and John A. Rogers**

The remarkable electrical, mechanical, and chemical properties of single-walled carbon nanotubes (SWNTs) create interest in their potential use as semiconducting or conducting elements in sensors, nanoscale transistors, and in large-area electronic systems. As a result, considerable research focuses on developing techniques for depositing and patterning SWNTs from solution, as individuals or aggregates, with well-controlled coverage and alignment. Langmuir–Blodgett techniques[1–4] and various schemes of deposition from solution[5–15] have been studied extensively. Although these methods exhibit attractive features, they each have some combination of disadvantages, such as low deposition rate, inability to control tube alignment and/or to deposit over large areas, required chemical modification of the SWNTs or substrates, or the need for organic solvents that are incompatible with plastic device components (organic electrodes, semiconductors, or substrates). A recently described alternative technique uses a controlled flocculation process to drive individual tubes out of an aqueous suspension and onto a substrate.[16] The deposition speed of this approach can be high, the tube coverage (i.e. the number of tubes per unit area) can be controlled over a wide range, and the form of the tubes (isolated individual tubes or bundles) can be defined by the processing conditions. The approach is also compatible with a wide range of substrates and it does not require chemical modification of the tubes or the substrates. However, this method does not allow the local orientation of the deposited nanotubes to be defined in a spatially dependent manner. Depositing and patterning SWNTs in a single step are also difficult, and secondary procedures must be used to transfer the nanotubes onto substrates incompatible with spin coating (e.g., curved surfaces).

Herein we introduce a technique for patterning and depositing SWNTs through the use of controlled flocculation in laminar microfluidic networks. This method generates well-defined patterns of aligned SWNT films with controlled density and alignment on a variety of flat and curved surfaces. We present the essential chemical and physical aspects of this approach, demonstrate the important capabilities, and present examples for use in the fabrication of organic electronic devices.

In the controlled flocculation approach, an aqueous suspension of surfactant-stabilized SWNTs is combined with a solvent, such as methanol, that is miscible with water and exhibits a strong affinity for the surfactant. When the methanol lowers the concentration of surfactant available to interact with the SWNTs to values below the critical micellar concentration, the tubes are no longer well suspended. In this situation, interactions between tubes can lead to the formation of bundles, and interactions with adjacent solid surfaces can cause the tubes to coat these surfaces. The introduction of streams of methanol and aqueous suspensions of SWNTs into a microfluidic channel in which fluid flow is laminar leads to diffusive mixing only near the liquid–liquid interface between the two streams flowing in parallel.[17,18] The interaction between the methanol and the SWNT suspension at this interface leads to the deposition of SWNTs on the solid surfaces near this interface. The velocity profiles of the local flow fields determine the orientation of the tubes. The duration of the flows and their velocities as well as the concentration of the SWNT suspension determine the coverage. Figure 1a shows this process as implemented with microfluidic streams joined by a Y-junction. For the work described herein, we form the fluidic channels by placing a stamp of the elastomer poly(dimethylsiloxane) (PDMS) against the surface of a substrate to be patterned (Figure 1b). Syringe pumps introduce the SWNT solution and methanol

[*] J.-U. Park, M. A. Meitl, S.-H. Hur, Prof. Dr. J. A. Rogers
Department of Materials Science and Engineering
Department of Electrical and Computer Engineering
Department of Chemistry
Beckman Institute, and Frederick Seitz Materials Research Laboratory
University of Illinois at Urbana-Champaign
Urbana, IL (USA)
Fax: (+1) 271-244-1190
E-mail: jrogers@uiuc.edu
M. L. Usrey, Prof. Dr. M. S. Strano, Prof. Dr. P. J. A. Kenis
Department of Chemical & Biomolecular Engineering, and Beckman Institute
University of Illinois at Urbana-Champaign
Urbana, IL (USA)

[**] The authors thank the Center for Nanoscale Chemical Electrical Mechanical Manufacturing Systems at the University of Illinois (funded by the National Science Foundation under grant DMI-0328162) and the Center for Microanalysis of Materials at the University of Illinois (partially supported by the U.S. Department of Energy under grant DEFG02-91-ER45439). M.S.S. acknowledges funding from the U.S. National Science Foundation Career award CTS-0449147.

 © 2006 Wiley-VCH Verlag GmbH & Co. KGaA, Weinheim

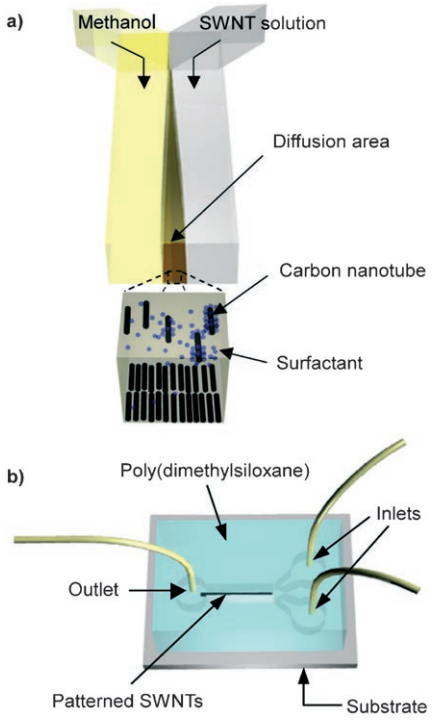


Figure 1. a) A microfluidic Y-junction for patterning single-walled carbon nanotubes (SWNTs) by multiphase laminar flow and controlled flocculation, and b) a microfluidic patterning device built with poly(dimethylsiloxane).

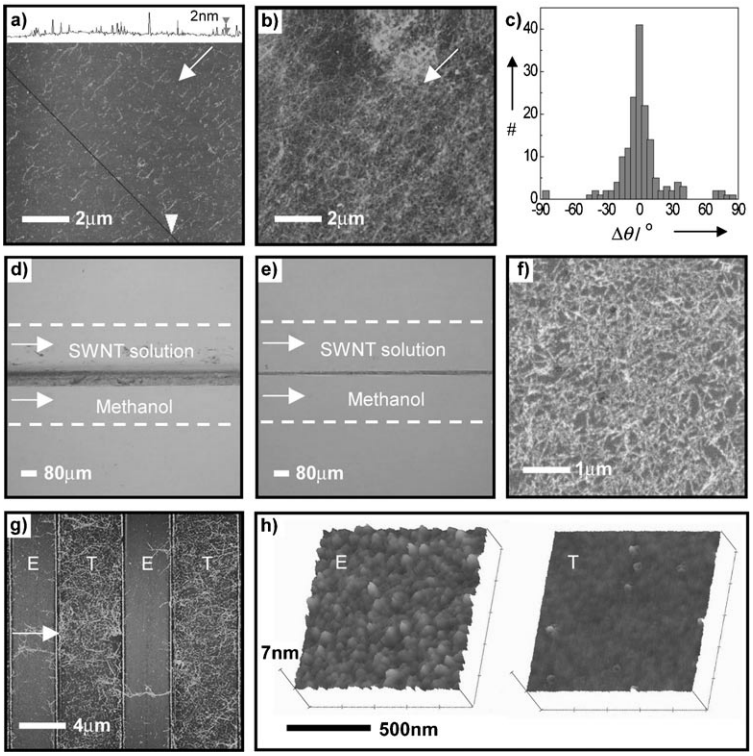


Figure 2. AFM and optical micrograph images of SWNT films fabricated by laminar flow under different flow conditions and substrates. Arrows indicate the flow direction. a) Parallel array of SWNTs deposited onto a Si wafer at an average flow velocity (V_a) of 17 mm s^{-1} for 5 min; tube alignment is in the flow direction. b) SWNTs deposited on a Si wafer at the same velocity ($V_a = 17$ mm s^{-1}) for 15 min showing that coverage of deposited SWNTs increases with flow duration. c) Angular distribution of SWNTs with respect to flow direction in Figure 2a. In this case, # is nanotube count and $\Delta\theta$ is orientation. d) Stripe of SWNTs deposited at an average velocity of 17 mm s^{-1} with methanol (1 mL) and SWNT solution (1 mL). e) Stripe of SWNTs deposited at an average velocity of 170 mm s^{-1} and the same volumes of methanol and SWNT. The width of the stripe decreases with increasing flow velocity. f) SEM image of high-coverage SWNT films patterned in (d). g) AFM image of SWNTs coated onto a surface with patterned lines of electron-beam evaporated (E) and thermally grown (T) SiO_2. The coverage of SWNTs is higher on T-SiO_2 than on E-SiO_2. h) Comparison of the morphology of E-SiO_2 (RMS roughness: 0.535 nm) and T-SiO_2 (RMS roughness: 0.162 nm) surfaces, as measured by AFM.

into the microfluidic networks and accurately control the flow velocities. Peeling the stamp away from the substrate after flowing the liquids for the desired time and washing with methanol and acetone to remove residual surfactant complete the patterning and deposition process.

Figure 2 presents results that illustrate some important aspects of this process. The duration of the flow determines the coverage of the deposited SWNTs. The total volume of methanol and SWNT suspension that flow through a fluidic channel increases linearly with flow duration for constant flow velocity. As a result, the number of deposited SWNTs increases with flow duration. Figures 2a and b show low and high coverage SWNTs formed by short (5 min) and long (15 min) flow durations, respectively. For low coverage, AFM analysis indicates that the SWNTs are present as individual tubes or small bundles. In this case, the SWNTs align parallel to the flow direction (Figure 2c). The full width at half maximum (FWHM) of the angular distribution of SWNT orientation, as measured by analysis of AFM images, is $\approx 10°$ at a flow velocity $V_a = 17$ mm s^{-1}. Carbon nanotubes flowing in a microfluidic channel are affected by shear flow, and hence tubes are aligned in the flow direction.[19,20] As higher flow velocity generates larger shear forces, the degree of alignment increases with V_a.[14,20] For high coverages, the SWNTs have a smaller degree of alignment (Figures 2b, f, and g; part T) than in the case of low-coverage films, for identical flow velocities and substrate surfaces in Figure 2a and c. The relatively thick and nonuniform layers of surfactant that deposit with the SWNTs can frustrate the alignment of SWNTs deposited at the later stages of the process. In all cases, this surfactant was washed away prior to the collection of the AFM images. The flow velocities determine the widths of the patterned stripes of SWNTs (Figures 2d, e, and f). In this case, the SWNTs were deposited with sufficient flow durations that they formed thick films that were visible to the naked eye. Diffusion between the SWNT solution and methanol at the fluidic interface controls the deposition and hence an increase in the flow velocities decreases the diffusion time and, therefore, the widths of the deposited lines of SWNTs. These widths do not depend on the depths of the microfluidic channels significantly. This result suggests that most of the deposited nanotubes originate from locations in the suspension close to the substrate.

We were able to pattern the tubes with this technique onto a wide range of substrates, including plastics,[16,21] without the

 © 2006 Wiley-VCH Verlag GmbH & Co. KGaA, Weinheim

need to functionalize the substrates or the tubes with chemistries designed to create strong interactions. (We even observed nanotubes deposited on the low-surface-energy PDMS surfaces of the microfluidic channels, near the interface between the methanol/SWNT suspension.) The details concerning, for example, the degree of alignment or the coverage for a given flow velocity and duration do, however, depend on interactions between the SWNTs and the substrates. As an example, we deposited SWNTs on a substrate with stripes of SiO_2 deposited by electron beam evaporation (E) and thermal oxidation (T) on silicon wafers. The coverage was higher on T-SiO_2 than E-SiO_2 (Figure 2g). We speculate the rough surface of the E-SiO_2 (RMS = 0.53 nm, as measured by AFM) decreased the contact area and, therefore, the interaction strength with SWNTs compared to the relatively smooth surface of the T-SiO_2 (RMS = 0.16 nm; (Figure 2h).[16]

Figure 3 shows other important features of this procedure. The PDMS elements defining the microfluidic channels are mechanically flexible; they can be draped over or bent around curved or uneven surfaces of the type that are difficult to process by spin coating. In this manner, it is possible to deposit and pattern SWNTs with geometries similar to that illustrated in Figure 2 on the curved surfaces of spherical lenses, for example, as shown in Figure 3a. In addition, curvilinear lines, in which the orientation of the SWNTs follows the local tangent, can be patterned by use of microfluidic channels with suitable geometries (Figure 3b). By controlling the relative flow rates of the methanol and the SWNT suspension, the positions of the deposited SWNT stripes can be adjusted relative to the sidewalls of the fluidic channels. Changing the flow rates dynamically during the deposition sweeps the fluidic interface across the channel to generate wide SWNT stripes or multiple, parallel narrow stripes. Figure 3c shows an example of this capability, and a plot of the relative position of the SWNT stripe patterned through the liquid–liquid interface as a function of relative flow rates. Once deposited, the SWNTs adhere sufficiently strongly to most substrates so that they can be further processed by liftoff, etching, etc. by using standard spin cast photoresists as masking layers. Figure 3d shows a narrow gap (10 μm) etched through the center of a deposited SWNT stripe by patterning photoresist, performing reactive ion etching, and then removing the resist. This structure can be used as a pair of electrodes for various applications.

As an example of the ability to build high-quality devices with SWNTs deposited by laminar flow and controlled flocculation, we fabricated organic thin film transistors (OTFTs) in which high-density SWNT networks serve as source/drain electrodes (Figure 4). By controlling the flow duration, SWNT stripes with electrical behavior ranging from insulating (low coverage) to semiconducting (moderate coverage; above percolation threshold for the semiconducting tubes)[16,22–24] to metallic (high coverage; above percolation threshold for the metallic tubes) could be produced. Figure 4a shows the resistivity (ρ) of the deposited SWNT networks (with values as low as $\approx 0.04\ \Omega$ cm) as a function of SWNT solution volume. As coverage of SWNT network increases, more conducting paths are formed and hence the

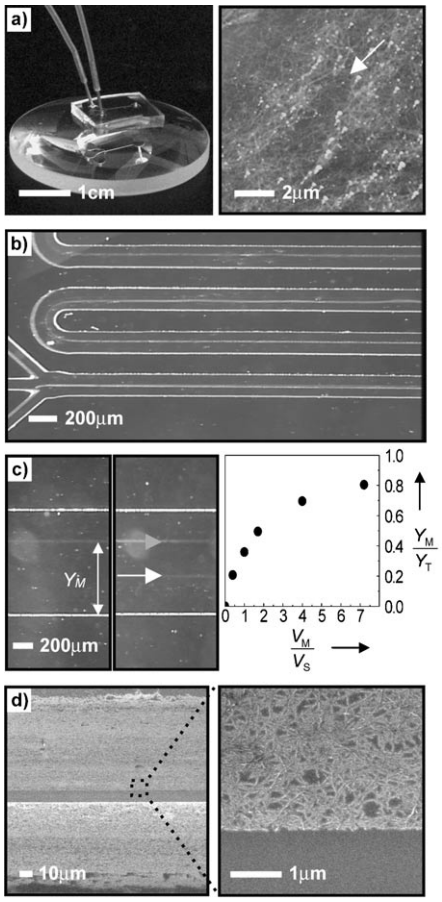


Figure 3. Various patterns of SWNT networks. a) Optical image of a microfluidic patterning system conformably contacted to the curved surface of a lens, and AFM image of SWNTs deposited on this lens (diameter: 4 cm, effective focal length: 10 cm). b) Optical micrograph of an SWNT line deposited in the middle of a serpentine microfluidic channel. c) Optical micrograph of multiple SWNT stripes fabricated in a single channel (channel width: 1 mm, height: 50 μm). Gray and white arrows indicate SWNT stripes patterned first and second, respectively. The position of the SWNT stripe (Y_M/Y_T) is defined by the position of the liquid–liquid interface position, which can be controlled by the flow rate ratio (V_M/V_S) of the two streams (Y_M and Y_T; width of the methanol stream and fluidic channel, and V_S and V_M; flow rate of SWNT solution and methanol, respectively). d) SEM image of SWNT networks deposited over a wide area and then patterned by conventional photolithographic procedures. To form this film, three streams (center stream: SWNT solution, and outside two streams: methanol) flowed in a microfluidic channel (width: 500 μm, height: 50 μm) and the flow rate ratio (V_M/V_S) was changed from 1 to 50 continuously by modulating V_S at constant $V_M = 50\ \mu L\,min^{-1}$. An open gap in the SWNT film was formed by O_2 plasma etching through a photodefined layer of photoresist.

resistivity decreases. This dependence of resistivity on the network coverage can be described by standard percolation theory [Eq. (1)].

$$\log\rho = -\alpha \log (N - N_C) + \text{const} \qquad (1)$$

N is the coverage of the conducting sticks, and N_C is the critical coverage where the first percolative path across a sample is formed. The inset of Figure 4a shows a fit of this

 © 2006 Wiley-VCH Verlag GmbH & Co. KGaA, Weinheim

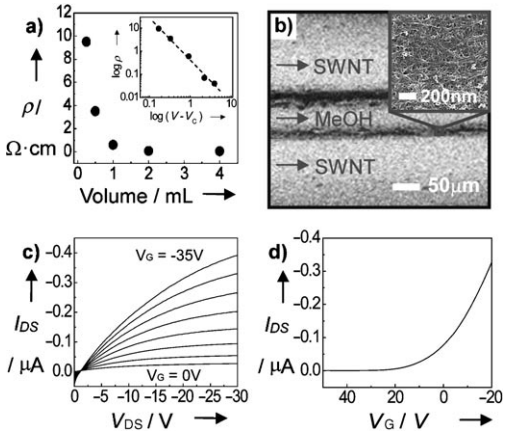


Figure 4. Fabrication of a transistor in which high-coverage SWNT networks patterned by multiphase laminar flow serve as electrodes (source and drain). a) Resistivity of the networks (ρ) as a function of the SWNT solution volume. The inset shows the power fit in the percolation region. b) SEM image of two SWNT network lines patterned in a microfluidic channel using three-phase laminar flows. The inset shows the high coverage SWNT networks that can be produced. These two stripes served as source/drain electrodes of a transistor. The channel length was controlled only by flow velocities of the three fluidic streams. c) Current (I_{DS})–voltage (V_{DS}) characteristics of the SWNT-based OTFT. A thermally evaporated layer (20-nm thick) of pentacene provided the semiconducting layer. d) Gate modulation of I_{DS} in the saturation regime.

equation to our data, using the SWNT solution volume (V) and critical volume (V_C) instead of ($N-N_C$). In this case the experimentally measured value of V_C was 80 μL. This fit yields a value of $\alpha = 1.7$, which is similar to the known values ($1.3 < \alpha < 1.9$) for SWNT networks in two dimensions.[25] For the fabrication of the SWNT-electrode transistor, two lines of high-density SWNT networks with low resistivity ($\approx 0.04\ \Omega$cm) were patterned onto a a highly doped Si wafer with a SiO_2 top layer (gate dielectric, thickness: 300 nm) by three-phase (SWNT solution/methanol/SWNT solution) laminar flow inside a microfluidic channel (height: 50 μm, width: 500 μm; Figure 4b). These two SWNT lines serve as source/drain electrodes; the relative flow velocities of the solutions control the channel length of the transistor (distance between the two SWNT lines: 50 μm). After defining the channel width (250 μm) by O_2 plasma etching, a thin layer of pentacene (thickness: 20 nm) was thermally evaporated onto the electrodes and in the gap at a deposition rate of ≈ 1 Å s^{-1}. Figure 4c and d show the current–voltage (I–V) and transfer characteristics of the resulting SWNT-electrode OTFT. The effective mobility (μ_{eff}), evaluated in the saturation regime (ignoring contacts), and on/off ratio were 0.011 ± 0.001 cm^2 V^{-1} s^{-1} and ≈ 1000:1, respectively. From Figure 4c, the device resistance in the on state (R_{ON}) was 52 ± 7 MΩ at voltage $V_G - V_T \approx -30$ V. The resistance of SWNT source/drain electrodes (R_{SWNT}) was about 2000 times smaller than the R_{ON}. For comparison, we fabricated OTFTs that used pentacene and gold source/drain with the same dimensions as the SWNT device. In this case, μ_{eff} values and on/off ratios of this gold OTFT were similar to those of the SWNT OTFT. The R_{ON} value of the gold-electrode device obtained at the same $V_G - V_T$ voltage was 48 ± 9 MΩ. The parasitic resistance (R_P) of the gold-electrode device was found to be 80 ~ 110 kΩ by using a scaling analysis approach described elsewhere.[26] This value of R_P is smaller than R_{ON}. For these devices, then, the electrical properties of the source/drain electrodes and their contact resistance with the semiconductor do not strongly influence the transistor performance. The SWNT electrodes have advantages, however, for certain applications as they can exhibit good optical transparency. Also, there is evidence that SWNT–pentacene contacts are more efficient than those formed by Au–pentacene.[27] These differences might become important at channel lengths shorter than those investigated herein.

In conclusion, the combined use of multistream laminar flow in microfluidic channels and controlled flocculation yields a simple but powerful method for depositing and patterning SWNTs in forms ranging from aligned collections of individual tubes to thick network mats. Flow velocities, deposition times, channel geometries, multiphase flows, and dynamic control of flow histories can all be exploited to generate complex patterns of SWNTs that are difficult to construct with other techniques. Working OTFTs that use conducting SWNT lines as source/drain electrodes illustrate one of the possible electronic and sensing devices that can be fabricated.

Experimental Section

SWNT solution: Single-walled carbon nanotubes produced by the laser ablation method were suspended in aqueous sodium dodecyl benzensulfonate (SDBS; 1 wt %).[28] The concentration was typically 10 mg mL^{-1} and no further purification step was carried out after the suspension.

Microfluidic system: A negative photoresist (SU8, Micro Chemical Corp.) of 50-μm thickness was spin-coated onto Si wafers and patterned with high-resolution transparency photomasks by photolithography. PDMS prepolymer and curing agent (Sylgard184, Dow Corning Corp.) (10:1 *w*/*w*) were mixed thoroughly and degassed in vacuum. This solution was poured on the masters (photoresist patterns) and cured at 65 °C for 4 h. After peeling the PDMS molds from the masters, the PDMS molds were either 1) conformably contacted to the substrate by nonspecific surface adhesion forces, or 2) chemically bonded through -OH groups generated by exposing O_2 plasma (O_2 plasma cleaner, Harrick Scientific Corp) on the surface of the PDMS and the SiO_2 surface of the substrate. Chemical bonding was required because the conformal contact was not sufficient to prevent the delamination of the PDMS molds when a curved substrate was used as shown in Figure 3a or when three streams were used as shown in Figure 4b.

Deposition of SWNTs: After 10-nm thick E-SiO_2 was patterned onto T-SiO_2 by the liftoff process, SWNTs were deposited in a microfluidic channel. In this case, the height of the fluidic channel (50 μm) was much higher than the thickness relief (10 nm) of the surface stripe.

Received: May 24, 2005
Revised: September 29, 2005
Published online: December 8, 2005

Keywords: carbon · microfluidics · nanotubes · patterning · transistors

 © 2006 Wiley-VCH Verlag GmbH & Co. KGaA, Weinheim

[1] V. Kristic, G. S. Duesberg, J. Muster, M. Burghard, S. Roth, *Chem. Mater.* **1998**, *10*, 2338 – 2340.
[2] Y. Guo, J. Wu, Y. Zhang, *Chem. Phys. Lett.* **2002**, *362*, 314 – 318.
[3] N. P. Armitage, J. C. P. Gabriel, G. Grüner, *J. Appl. Phys.* **2004**, *95*, 3228 – 3230.
[4] Y. Kim, N. Minami, W. Zhu, S. Kazaoui, R. Azumi, M. Matsumoto, *Jpn. J. Appl. Phys.* **2003**, *42*, 7629 – 7634.
[5] M. R. Diehl, S. N. Yaliraki, R. A. Beckman, M. Barahona, J. R. Heath, *Angew. Chem.* **2002**, *114*, 363 – 366; *Angew. Chem. Int. Ed.* **2002**, *41*, 353 – 356.
[6] H. Shimoda, S. J. Oh, H. Z. Geng, R. J. Walker, X. B. Zhang, L. E. McNeil, O. Zhou, *Adv. Mater.* **2002**, *14*, 899 – 901.
[7] M. Burghard, G. Duesberg, G. Philipp, J. Muster, S. Roth, *Adv. Mater.* **1998**, *10*, 584 – 588.
[8] S. G. Rao, L. Huang, W. Setyawan, S. Hong, *Nature* **2003**, *425*, 36 – 37.
[9] M. D. Lay, J. P. Novak, E. S. Snow, *Nano Lett.* **2004**, *4*, 603 – 606.
[10] S. Gerdes, T. Ondarçuhu, S. Cholet, C. Joachim, *Europhys. Lett.* **1999**, *48*, 292 – 298.
[11] S. J. Oh, Y. Cheng, J. Zhang, H. Shimoda, O. Zhou, *Appl. Phys. Lett.* **2003**, *82*, 2521 – 2523.
[12] K. H. Choi, J. P. Bourgoin, S. Auvray, D. Esteve, G. S. Duesberg, S. Roth, M. Burghard, *Surf. Sci.* **2000**, *462*, 195 – 202.
[13] J. Liu, M. J. Casavant, M. Cox, D. A. Walters, P. Boul, W. Lu, A. J. Rimberg, K. A. Smith, D. T. Colbert, R. E. Smalley, *Chem. Phys. Lett.* **1999**, *303*, 125 – 129.
[14] a) H. Ko, S. Peleshanko, V. V. Tsukruk, *J. Phys. Chem. B* **2004**, *108*, 4385 – 4393; b) V. V. Tsukruk, H. Ko, S. Peleshanko, *Phys. Rev. Lett.* **2004**, *92*, 065502.
[15] J. C. Lewenstein, T. P. Burgin, A. Ribayrol, L. A. Nagahara, R. K. Tsui, *Nano Lett.* **2002**, *2*, 443 – 446.
[16] M. A. Meitl, Y. Zhou, A. Gaur, S. Jeon, M. L. Usrey, M. S. Strano, J. A. Rogers, *Nano Lett.* **2004**, *4*, 1643 – 1647.
[17] a) P. J. A. Kenis, R. F. Ismagilov, G. M. Whitesides, *Science* **1999**, *285*, 83 – 85; b) B. Zhao, J. S. Moore, D. J. Beebe, *Science* **2001**, *291*, 1023 – 1026.
[18] R. F. Ismagilov, A. D. Stroock, P. J. A. Kenis, G. M. Whitesides, *Appl. Phys. Lett.* **2000**, *76*, 2376 – 2378.
[19] Z. Fan, S. G. Advani, *Polymer* **2005**, *46*, 5232 – 5240.
[20] Y. Huang, X. Duan, Q. Wei, C. M. Lieber, *Science* **2001**, *291*, 630 – 633.
[21] N. Saran, K. Parikh, D. Suh, E. Muñoz, H. Kolla, S. K. Manohar, *J. Am. Chem. Soc.* **2004**, *126*, 4462 – 4463.
[22] E. S. Snow, J. P. Novak, P. M. Campbell, D. Park, *Appl. Phys. Lett.* **2003**, *82*, 2145 – 2147.
[23] Y. Zhou, A. Gaur, S. H. Hur, C. Kocabas, M. A. Meitl, M. Shim, J. A. Rogers, *Nano Lett.* **2004**, *4*, 2031 – 2035.
[24] C. Kocabas, M. A. Meitl, A. Gaur, M. Shim, J. A. Rogers, *Nano Lett.* **2004**, *4*, 2421 – 2426.
[25] L. Hu, D. S. Hecht, G. Grüner, *Nano Lett.* **2004**, *4*, 2513 – 2517.
[26] J. Zaumseil, K. W. Baldwin, J. A. Rogers, *J. Appl. Phys.* **2003**, *93*, 6117 – 6124.
[27] M. Lefenfeld, G. Blanchet, J. A. Rogers, *Adv. Mater.* **2003**, *15*, 1188 – 1191.
[28] V. C. Moore, M. S. Strano, E. H. Haroz, R. H. Hauge, R. E. Smalley, *Nano Lett.* **2003**, *3*, 1379 – 1382.

 © 2006 Wiley-VCH Verlag GmbH & Co. KGaA, Weinheim

Synthetic Methods

DOI: 10.1002/anie.200502840

A Highly Active, Heterogeneous Catalyst for Alkyne Metathesis**

*Haim Weissman, Kyle N. Plunkett, and Jeffrey S. Moore**

Highly active alkyne-metathesis catalysts have been realized by exchanging the amide ligands on molybdenum(VI) alkylidyne trisamide complexes **1** with simple phenols,[1,2] such as 4-nitrophenol, or by use of chlorotrisamide Mo(IV) complexes.[3] In spite of this practical utility, these catalysts can become deactivated over time, apparently through a bimolecular dimerization pathway.[4] The polymerization of 2-butyne, the metathesis by-product obtained from propynyl substrates,[1a,b] is another interfering reaction which occurs when the catalytic reaction is preformed at room temperature. Herein, we describe a heterogeneous, alkyne-metathesis catalyst that avoids the use of phenolic ligands. The supported catalyst exhibits very high activity at room temperature while showing exceptional selectivity for catalyzing alkyne metathesis rather than alkyne polymerization, even on a preparative scale.

We investigated the coordination of the molybdenum center to amorphous silica to avoid bimolecular decomposition with minimal changes to the electronic structure of the catalyst. The similarity of the pK_a values of the phenolic hydroxy and silanol groups was the basis for this choice.[5,6] Mortreux et al. have pioneered similar, although less well-defined, approaches by impregnating [Mo(CO)$_6$] on silica.[2e,7a] Alumina- and titania-supported molybdenum species have also been reported.[7] However, none of these previous systems were particularly efficient; all required high temperatures (160–350 °C) to obtain turn-over frequencies (TOFs) of several turnovers per hour.[7,8] Utilization of organic silanols as cocatalysts with molybdenum hexacarbonyl for alkyne metathesis were somewhat successful, yet high catalyst

[*] Dr. H. Weissman, Dr. K. N. Plunkett, Prof. J. S. Moore
Department of Chemistry
University of Illinois
470B Roger Adams Lab
600 South Mathews Avenue, Urbana, IL 61801 (USA)
Fax: (+1) 217-244-8024
E-mail: jsmoore@uiuc.edu

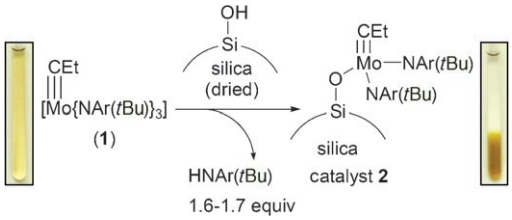
[**] This work is supported by the National Science Foundation (Grant No. 0345254) and the US Department of Energy, Division of Materials Sciences (Award No. DEFG02-91ER45439), through the Frederick Seitz Materials Research Laboratory at the University of Illinois at Urbana. We thank Wei Zhang for fruitful discussions and Dr. Paul Molitor for his help recording the ^{13}C-MAS NMR spectra. We would also like to thank Richard Haasch for help with the X-ray photoelectron spectroscopy (XPS) measurements, which were performed in the Center for Microanalysis and Materials, University of Illinois, which is partially supported by the US Department of Energy Award No. DEFG02-91ER45439.

Supporting information for this article is available on the WWW under http://www.angewandte.org or from the author.

 © 2006 Wiley-VCH Verlag GmbH & Co. KGaA, Weinheim InterScience

loading and temperatures above 150 °C were again required.[8a,9] Basset and co-workers reported the impregnation of silica surfaces with well-defined molybdenum, tungsten, and rhenium alkylidyne complexes for olefin metathesis.[10] It was suggested that α-hydrogen elimination was responsible for metal-carbene formation and thus, possibly, for deactivation of possible alkyne metathesis.[9e] Only the silica-supported rhenium catalyst [(SiO)Re(C–*t*Bu)(=CH–*t*Bu)(CH_2Bu)] has been mentioned briefly as a well-defined precursor for heterogeneous alkyne metathesis.[10d]

In a typical procedure, a solution of precursor **1** in toluene is added to a suspension of silica[11] with an approximately equimolar ratio of silanols and molybdenum. After stirring for one minute at room temperature, the honey-brown color of the solution transfers onto the silica (Scheme 1). The



Scheme 1. Reaction of Mo precursor **1** with a silica surface. The images show the capture of **1** from solution onto silica to produce an active catalyst.

amount of residual molybdenum in the washings was determined to be 0.7 % of the starting material, thus indicating >99 % of **1** reacted with the silica. Based on the characterization data described below, the resulting structure is consistent with catalyst **2** shown in Scheme 1.

Elemental analysis of the impregnated silica indicated that the surface contained 1.56 ± 0.04 wt. % molybdenum and 4.2 ± 0.6 wt. % carbon, thus suggesting that the average Mo/aniline ratio on the surface was approximately 1:1.35 (Scheme 1). This ratio was independently verified by measuring the quantity of aniline released and collected in the washings. Further evidence for the formation of **2** was obtained from IR spectroscopy. The SiO–H stretching band at 3747 cm^{-1} observed in unmodified silica was absent in the spectrum of **2**, thus indicating consumption of the surface silanols groups. Bands at 3020, 1592, and 1460 cm^{-1} in the spectrum of **2** indicate the presence of a substituted aromatic moiety, and the bands at 2971–2871 and 1390–1361 cm^{-1} indicate the existence of an aliphatic moiety (see the Supporting Information).

To further confirm the immobilization of the complex onto the silica surface, X-ray photoelectron spectra of catalyst **2** were obtained and compared to the X-ray photoelectron spectra of the crystalline precursor **1**. A 1.4-eV shift in the peak that corresponds to the Mo 3d electrons is evident for **2** (Figure 1), which is consistent with a significant change in the coordination sphere of the molybdenum center (Figure 1). Similar trends have been observed for other high-oxidation state Mo species when ligands are changed by the introduction of more electron-withdrawing groups.[12] This shift suggests the reduction of electron density around the Mo

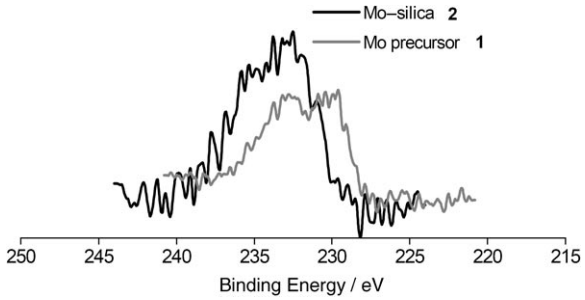


Figure 1. X-ray photoelectron spectroscopy data for the peak that corresponds to the Mo 3d electrons of crystalline precursor **1** and the supported catalyst **2**.

center, a likely result of an exchange between an amide and an oxide ligand. A similar increase of 1.2 eV in the N 1s binding energy is also evident (see the Supporting Information). This energy change is consistent with amido ligands bound to a more Lewis acidic Mo center (e.g., a Mo center bound to an oxide ligand).

To prove the existence of the carbyne[12] on the silica surface of **2**, we measured the ^{13}C-MAS NMR spectrum at natural abundance (Figure 2). A peak at $\delta = 330$ ppm corresponding to a typical chemical shift for Mo≡C in the liquid phase[14] and other silica-impregnated molybdenum alkylidyne complexes is evident.[15] Resonances at 100–145 ppm and 0–40 ppm are consistent with aromatic and aliphatic carbon atoms on the surface, respectively.

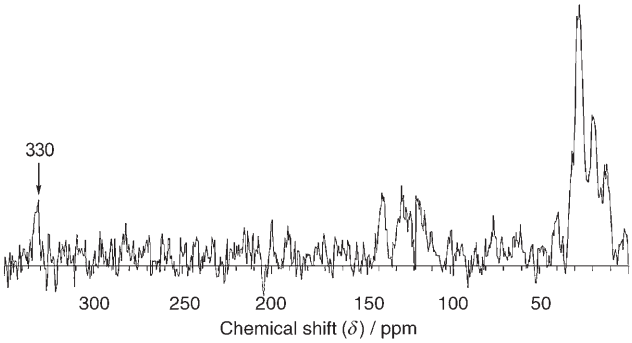
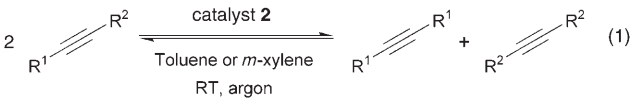


Figure 2. ^{13}C-MAS NMR spectrum of **2**.

Alkyne-metathesis reactions [Eq. (1)] were performed differently to test the metathesis activity of **2**. In a typical



(1)

experiment, **2** was preweighed into an NMR tube and the substrate was introduced in a solution of [D_8]toluene. In experiments testing the recycling capability of the silica support, a suspension of **2** was centrifuged, the solvent decanted, and the silica was rinsed once with [D_8]toluene before the addition of the next batch of substrate.

 © 2006 Wiley-VCH Verlag GmbH & Co. KGaA, Weinheim

Alkyne-metathesis experiments with catalyst **2** are summarized in Table 1. The scope of metathesis activity was probed with 2-propynylthiophene (**3**), 1-phenyl-1-butyne (**4**), 1-phenyl-1-propyne (**5**), 3-butynyl methyl benzoate (**6**), 3-propynyl methyl benzoate (**7**), 3-heptyne (**8**), 3-hexyne (**9**), and 3-octyne (**10**), and four different catalyst loadings were tested. Half-lives at room temperature of less than 1 h were generally observed, even with as little as a catalyst loading of 0.8 mol% (based on Mo). Table 2 shows $k_{2,obs}$ and TOF values from the alkyne homodimerization reactions of **4**–**7**, 4-(1-butynyl)anisole (**11**), and 4-(1-propynyl)anisole (**12**) [Eq. (2)]. The steric and electronic trends seen in Tables 1 and 2 parallel those observed for the analogous **1**/phenol system.[1,2] More significantly, high catalytic activity is achieved for **2**, even though its molybdenum alkylidyne moieties likely contain a mixture of nitrogen- and oxygen-containing ligands.

Table 1: Values of $t_{1/2}$ for metathesis reactions[a] of **3**–**10**.

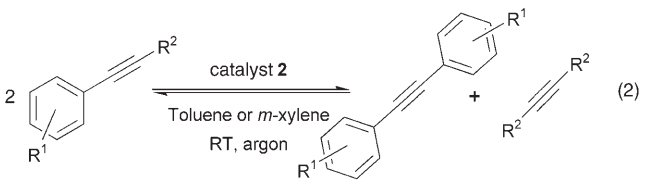
Entry	Substrate	R^1	R^2	Catalyst loading [mol%][b]	$t_{1/2}$ [min][c]
1	**3**	2-thiophenyl	Me	4.0	<10[d]
2	**4**	Ph	Et	0.8	<5[e]
3				0.4	<8[f]
4				0.2	11[g]
5	**5**	Ph	Me	0.2	20[g]
6	**6**	3-methyl benzoate	Et	4.0	<5[d]
7				0.8	<10[e]
8				0.4	40[f]
9	**7**	3-methyl benzoate	Me	0.2	14[g]
10	**8**[h]	Et	*n*Pr	0.8	<5[e]
11	**9** **10**[h]	Et *n*Pr	Et *n*Pr	0.8	<5[e]

[a] Conditions: 24 °C, [D_8]toluene (600 μL). [b] Load of **2** relative to substrate. [c] $t_{1/2}$ = time for the reaction to proceed to half of the final equilibrium concentrations. [d] Substrate amount = 62.5 μmol. [e] Substrate amount = 62.5 μmol. [f] Substrate amount = 125 μmol. [g] Substrate amount = 250 μmol. [h] Carried out in *m*-xylene (600 μL).

Table 2: Values of $k_{2,obs}$ and TOF for the homodimerization of **4**–**7**, **11**, and **12**.[a]

Entry	Substrate	R^1	R^2	$k_{2,obs}$ [$M^{-1}\,min^{-1}$]	TOF [$mol_p\,mol_c^{-1}\,s^{-1}$]
1	**11**	MeO	Et	0.24	0.31
2	**12**	MeO	Me	0.058	0.087
3	**4**	H	Et	0.19	0.33
4	**5**	H	Me	0.031	0.051
5	**6**	*m*-MeO_2C	Et	0.068	0.13
6	**7**	*m*-MeO_2C	Me	0.023	0.046

[a] The alkyne substrate (167 μmol) was added to a NMR tube containing **2** (0.30 mol%) in [D_8]toluene (600 μL).



No oligomerization of the alkyne substrates or the products was observed by ^1H NMR spectroscopic analysis for all the reactions, even after several days. A mass balance higher than 93% was established with an internal standard. The fact that **2** was able to metathesize propynyl derivatives, including the unprecedented homodimerization of 2-propynyl thiophene,[3c,d] demonstrates the success of the heterogeneous approach in constricting the coordination sphere around the molybdenum center. Good metathesis activity with **2** is observed under conditions that were impossible in the past because of problems with polymerization. Recyclability was tested with **3** as the substrate and an initial catalyst loading of 4.0 mol% of **2**. Cycles 1–3 produced conversions of 45, 52, and 32%, respectively, thus suggesting the recyclability of the catalyst. The activity with **4** as the substrate at a catalyst loading of 0.2 mol% was measured to monitor the stability of solid **2**. The catalytic activity of **2** stored at room temperature in an argon-filled dry box remained relatively unchanged for at least two weeks.

We tested the homodimerization of 1-phenyl-1-propyne at room temperature under vacuum-driven conditions to demonstrate the applicability of this system for preparative synthesis. The yield of the isolated and purified homodimer on a 7.5-mmol scale was 88%.

A series of experiments was preformed to confirm catalysis takes place on the support rather than in solution. First, we confirmed that a solution of precursor **1** is catalytically inactive at room temperature. Second, filtrates obtained from suspensions of catalyst **2** exhibit no residual metathesis activity. Similarly, when a substrate suspended with **2** is removed before reaching equilibrium, metathesis activity ceases. Finally, activity resumes as soon as the filtrate is combined with recovered **2**.

We have developed a readily accessible heterogeneous system that exhibits high catalytic activity and good stability, probably because bimolecular deactivation is prevented.[1a,b] The catalyst can be utilized with a loading of less than 1% at room temperature. Several other benefits of the catalytic system have also been found. The system is resistant to alkyne polymerization, which is problematic for similar homogeneous catalysts.[1a,b] Catalyst **2** is recyclable, shows activity over at least three cycles, and has unprecedented metathesis activity for the homodimerization of 2-propynylthiophene, a substrate unable to undergo metathesis with any other known catalyst system.[16] The study of ring-closing alkyne-metathesis[2a,17] activity and other types of metal oxides in this catalyst system are under way. Our results for these studies will be reported elsewhere.

Received: August 10, 2005
Published online: December 15, 2005

Keywords: alkynes · heterogeneous catalysis · metathesis · molybdenum · silica

 © 2006 Wiley-VCH Verlag GmbH & Co. KGaA, Weinheim

[1] a) W. Zhang, S. Kraft, J. S. Moore, *Chem. Commun.* **2003**, 832; b) W. Zhang, S. Kraft, J. S. Moore, *J. Am. Chem. Soc.* **2004**, *126*, 329; c) W. Zhang, J. S. Moore, *J. Am. Chem. Soc.* **2004**, *126*, 12796; d) W. Zhang, J. S. Moore, *Macromolecules* **2004**, *37*, 3973; e) J. M. Blackwell, J. S. Figueroa, F. H. Stephens, C. C. Cummins, *Organometallics* **2003**, *22*, 3351.

[2] a) A. Fürstner, P. W. Davies, *Chem. Commun.* **2005**, 2307; b) V. Sashuk, J. Ignatowska, K. Grela, *J. Org. Chem.* **2004**, *69*, 7748; c) L. Kloppenburg, D. Jones, U. H. F. Bunz, *Macromolecules* **1999**, *32*, 4194; d) L. Kloppenburg, D. Song, U. H. F. Bunz, *J. Am. Chem. Soc.* **1998**, *120*, 7973; e) A. Mortreux, J. C. Delgrange, M. Blanchard, B. Lubochinsky, *J. Mol. Catal.* **1977**, *2*, 73; f) A. Mortreux, M. Blanchard, *Chem. Commun.* **1974**, 786; g) N. G. Pschirer, W. Fu, R. D. Adams, U. H. F. Bunz, *Chem. Commun.* **2000**, 87; h) A. Fürstner, G. Seidel, *J. Organomet. Chem.* **2000**, *606*, 75; i) D. Villemin, P. Cadiot, *Tetrahedron Lett.* **1982**, *23*, 5139; j) N. Kaneta, K. Hikichi, S.-i. Asaka, M. Uemura, M. Mori, *Chem. Lett.* **1995**, 1055; k) N. Kaneta, T. Hirai, M. Mori, *Chem. Lett.* **1995**, 627.

[3] a) A. Fürstner, L. Turet, *Angew. Chem.* **2005**, *117*, 3528; *Angew. Chem. Int. Ed.* **2005**, *44*, 3462; b) A. Fürstner, D. De Souza, L. Parra-Rapado, J. T. Jensen, *Angew. Chem.* **2003**, *115*, 5516; *Angew. Chem. Int. Ed.* **2003**, *42*, 5358; c) A. Fürstner, C. Mathes, *Org. Lett.* **2001**, *3*, 221; d) A. Fürstner, C. Mathes, C. W. Lehmann, *Chem. Eur. J.* **2001**, *7*, 5299; e) A. Fürstner, K. Radkowski, J. Grabowski, C. Wirtz, R. Mynott, *J. Org. Chem.* **2000**, *65*, 8758; f) A. Fürstner, K. Grela, C. Mathes, C. W. Lehmann, *J. Am. Chem. Soc.* **2000**, *122*, 11799; g) A. Fürstner, C. Mathes, C. W. Lehmann, *J. Am. Chem. Soc.* **1999**, *121*, 9453.

[4] R. R. Schrock, *Polyhedron* **1995**, *14*, 3177.

[5] M. D. Liptak, K. C. Gross, P. G. Seybold, S. Feldgus, G. C. Shields, *J. Am. Chem. Soc.* **2002**, *124*, 6421.

[6] a) S. Grasser, C. Haessner, K. Kohler, F. Lefebvre, J.-M. Basset, *Phys. Chem. Chem. Phys.* **2003**, *5*, 1906; b) T. W. Dijkstra, R. Duchateau, R. A. van Santen, A. Meetsma, G. P. A. Yap, *J. Am. Chem. Soc.* **2002**, *124*, 9856.

[7] a) A. Mortreux, F. Petit, M. Blanchard, *J. Mol. Catal.* **1980**, *8*, 97; b) "Metathesis process and catalyst": S. G. Kukes, R. L. Banks, U.S. patent 4,465,890, **1984**.

[8] "Catalyst Composition to Effect Metathesis of Acetylenes": R. R. Schrock, US patent 4,427,595, **1984**.

[9] D. Villemin, M. Heroux, V. Blot, *Tetrahedron Lett.* **2001**, *42*, 3701.

[10] a) C. Coperet, M. Chabanas, R. P. Saint-Arroman, J.-M. Basset, *Angew. Chem.* **2003**, *115*, 164; *Angew. Chem. Int. Ed.* **2003**, *42*, 156; b) M. Chabanas, A. Baudouin, C. Coperet, J.-M. Basset, W. Lukens, A. Lesage, S. Hediger, L. Emsley, *J. Am. Chem. Soc.* **2003**, *125*, 492; c) M. Chabanas, A. Baudouin, C. Coperet, J.-M. Basset, *Chem. Eur. J.* **2003**, *9*, 971; d) M. Chabanas, A. Baudouin, C. Coperet, J.-M. Basset, *J. Am. Chem. Soc.* **2001**, *123*, 2062; e) E. L. Roux, M. Taoufik, M. Chabanas, D. Alcor, A. Baudouin, C. Coperet, J. Thivolle-Cazat, J.-M. Basset, A. Lesage, S. Hediger, L. Emsley, *Organometallics* **2005**, *24*, 4274.

[11] Silica M5 was pretreated at 400 °C for 4 h with a gradient of 2.5 °C min^{-1} under dry O_2. A solution of **1** (50.0 mg, 7.51 mM) in toluene (10 mL) was added to silica (350 mg) and vortexed for 1 min. The modified silica was used directly or precipitated by centrifugation, rinsed several times, and lyophilized from benzene.

[12] S. J. N. Burgmayer, H. L. Kaufmann, G. Fortunato, P. Hug, B. Fischer, *Inorg. Chem.* **1999**, *38*, 2607.

[13] The stretch for a metal alkylidyne moiety falls in the region of 1270–1420 cm^{-1};[14] in our system, this region is masked by absorptions for silica and aliphatic chains.

[14] W. A. Nungent, J. M. Mayer, *Metal–Ligand Multiple Bonds*, Wiley Interscience, New York, USA, **1988**, pp. 123–144.

[15] R. P. Saint-Arroman, M. Chabanas, A. Baudouin, C. Coperet, J.-M. Basset, A. Lesage, L. Emsley, *J. Am. Chem. Soc.* **2001**, *123*, 3820.

[16] U. H. F. Bunz, *Acc. Chem. Res.* **2001**, *34*, 998.

[17] a) K. C. Nicolaou, P. G. Bulger, D. Sarlah, *Angew. Chem.* **2005**, *117*, 5005; *Angew. Chem. Int. Ed.* **2005**, *44*, 4490; b) A. Fürstner, *Angew. Chem.* **2000**, *112*, 3140; *Angew. Chem. Int. Ed.* **2000**, *39*, 3012.

 © 2006 Wiley-VCH Verlag GmbH & Co. KGaA, Weinheim

Molecular Rods

DOI: 10.1002/anie.200502991

Synthesis and Conformational Study of Water-Soluble, Rigid, Rodlike Oligopiperidines**

*Vincent Semetey, Demetri Moustakas, and George M. Whitesides**

Herein, we describe the preparation of oligopiperidines as a new family of water-soluble, rigid oligomers. The design of molecules with nanometer dimensions, defined shapes, and physical properties (solubility, conductivity, etc.) is a matter of considerable interest in macromolecular chemistry.[1,2] "Molecular rods" are rigid, linear macromolecules that constitute promising materials for applications in nanotechnology, such as spacers, wires, and construction elements.[3] The poor water solubility of many current examples of molecular rods[1,4] limit their applications, particularly in biology. Only a few bio-oligomers exhibit a rigid-rod structure,[2c] of which oligoprolines, which have been considered the most rigid,[5] have been used as spacers in biochemistry.[6] The structure of these compounds is, however, still a subject of discussion. Levins and Schafmeister reported the synthesis of a water-soluble molecular rod based on fused diketopiperazine oligomers starting from a complex building block.[7]

We hypothesized that an oligomeric backbone of piperidine rings would be a rigid rod, with the piperidine moieties adopting chair conformations in aqueous solution.[8] We have developed a synthesis of representative members of this class of molecules and investigated their conformations in polar solvents, including deuterated water. We are particularly interested in the possibility that they might serve as extended,

[*] Dr. V. Semetey, Dr. D. Moustakas, Prof. G. M. Whitesides
Department of Chemistry and Chemical Biology
Harvard University
12 Oxford Street, Cambridge, MA 02138 (USA)
Fax: (+1) 617-495-9857
E-mail: gwhitesides@gmwgroup.harvard.edu

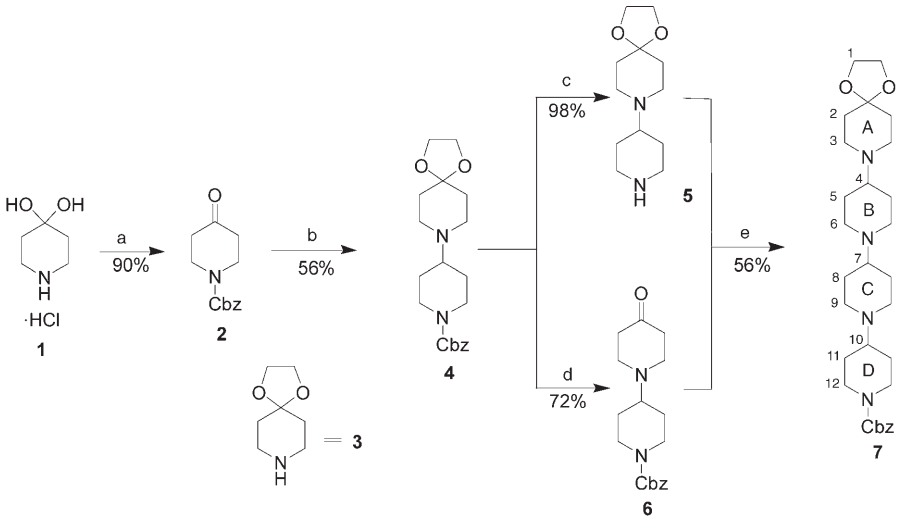
[**] This work was supported by the NIH (Grant GM30367). V.S. acknowledges La Ligue contre le Cancer for a postdoctoral fellowship. Initial design of this project was carried out by Dr. Val Martichonok.

Supporting information for this article is available on the WWW under http://www.angewandte.org or from the author.

WILEY InterScience DISCOVER SOMETHING GREAT
© 2006 Wiley-VCH Verlag GmbH & Co. KGaA, Weinheim

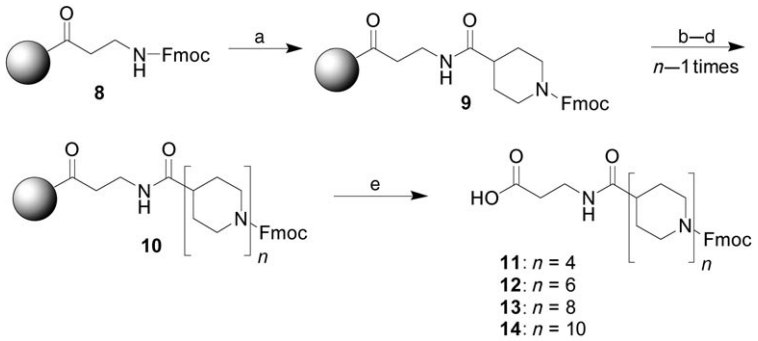
water-soluble linkers or scaffolds for the oligovalent display of ligands.

Scheme 1 outlines the strategy used to synthesize the oligopiperidines in solution. In this strategy, elongation is based on iterative reductive amination. We protected the commercially available 4,4-piperidinediol hydrochloride (**1**) with a benzyloxycarbonyl (Cbz) group to obtain **2**. This compound was allowed to react with 1,4-dioxa-8-aza-spiro-[4.5]decane (**3**) in the presence of triacetoxyborohydride to afford piperidinopiperidin-4-one **4** diprotected with a cyclic ketal and a Cbz group.[9] Compound **4** led to two further intermediates. Its catalytic hydrogenation yielded compound **5**, and treatment of which with a concentrated aqueous HCl solution afforded compound **6**. Reductive amination of **5** and **6** yielded the tetramer derivative **7**.



Scheme 1. Solution-phase synthesis of tetrapiperidine **7**. a) Na_2CO_3, CbzCl; b) 1,4-dioxa-8-aza-spiro-[4.5]decane (**3**), $NaBH(OAc)_3$, 1,2-dichloroethane; c) Pd/C, H_2, EtOH; d) concentrated HCl, 0 °C to room temperature, 20 min; e) $NaBH(OAc)_3$, 1,2-dichloroethane.

We used solid-phase techniques to synthesize oligopiperidines up to ten units in length (Scheme 2). Solid-phase synthesis of oligopiperidine was performed on preloaded Fmoc-β-Ala Wang resin **8** (Fmoc = 9-fluorenylmethoxycarbonyl) on a 50-μmol scale. After deprotection with 20% piperidine in dimethylformamide (DMF), the resin was allowed to react with the *N*-Fmoc-protected isonipecotic acid in the presence of benzotriazolyl-*N*-oxy-tris(dimethylamino)phosphonium (BOP reagent) and the Hunig base to afford **9**. We assembled building blocks to form the molecular rod by using a sequential procedure: deprotection, reductive amination with Fmoc-4-piperidone, and capping with acetic anhydride. The resin was then washed and dried prior to treatment with trifluoroacetic acid (TFA)/H_2O (95:5) for 2 h. HPLC purification on a C_{18} column and lyophilization afforded pure oligopiperidines **10** and **11**.



Scheme 2. General procedure for the solid-phase synthesis of oligopiperidine. a) Fmoc-isonipecotic acid, BOP, $NEt(iPr)_2$ in DMF; b) 20% piperidine in DMF, 20 min; c) Fmoc-4-piperidone, $NaBH(OAc)_3$ in 1,2-dichloroethane, 2×60 min; d) acetic anhydride, $NEt(iPr)_2$, CH_2Cl_2; e) TFA/H_2O (95:5).

The structure of **7** was investigated by 1D and 2D NMR spectroscopy in CD_3OD. This solvent was used because it produced a larger dispersion of chemical shifts than solvents such as $CDCl_3$ or D_2O. The spin systems of all four piperidine residues were unambiguously identified from COSY experiments. The sequence was assigned on the basis of NOESY experiments (mixing time = 400 ms) and was deduced from the strong NOE interaction connectivities between piperidine rings. Analysis of 1D spectra recorded between 273 and 323 K at 10 K increments revealed that the coupling values are only weakly affected by temperature changes; we infer that a single conformation dominates over this range of temperature. In the ^1H NMR spectrum recorded at room temperature, in CD_3OD, and at 500 MHz (Figure 1), the axial and equatorial protons of the piperidine rings B, C, and D (H5, H6, H8, H9, H11, and H12) are discernible. The eight ring protons (H2 and H3) of the piperidine ring A appear as two triplets at $\delta = 2.66$ and 1.71 ppm; this observation indicates that the axial and equatorial positions in this ring exchange rapidly on the NMR time scale through combined nitrogen inversion and chair–chair inversion. Rings B–D all display approximately the same series of signals with 1) a triplet of triplets for H4, H7, and H10, all in axial positions and 2) significant chemical-shift differences ($0.4 < \Delta\delta_{ae} < 1.4$ ppm) between the axial and the equatorial sites of each methylene group with the axial proton at higher field. These characteristics provide strong evidence that all of these rings have the same chair conformation.[10] The chemical-shift difference between H12a and H12e in ring D is accentuated by the location of H12e in the shielding zone of the Cbz group.

NOESY experiments at 298 K with a mixing time of 400 ms yielded additional information about the three-dimensional structure of the tetrapiperidine **7**. Several inter- and intraresidue

 © 2006 Wiley-VCH Verlag GmbH & Co. KGaA, Weinheim

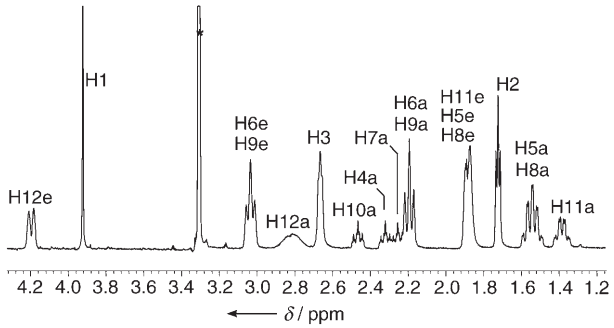


Figure 1. ^{1}H NMR spectrum (500 MHz) of tetrapiperidine derivative **7** in CD_3OD.

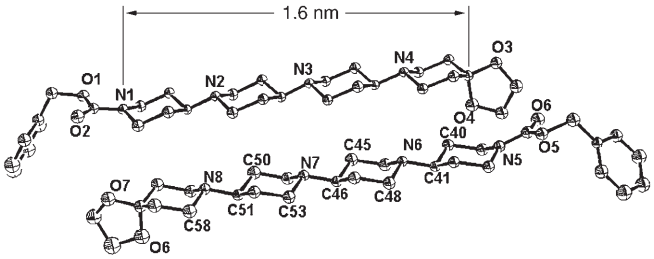


Figure 3. ORTEP diagram of the crystal structure of **7** (50% thermal ellipsoids; protons are omitted for clarity). Selected distances [Å] and torsion angles [°]: N5-N6 4.273, N6-N7 4.339, N7-N8 4.357; C48-N6-C41-C40 178.6(5), C53-N7-C46-C45 179.9(5), C58-N8-C51-C50 179.9(5).

NOE interactions were extracted and are consistent with the presence of a rodlike conformation (Figure 2). Intraresidue NOE interactions confirmed the existence of a chair geometry in piperidine rings. Interresidue NOE interactions

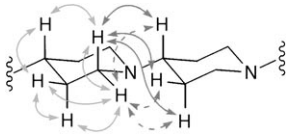


Figure 2. Intra- and interresidue NOE interactions found between two piperidine units.

revealed: 1) a linear structure with each piperidine unit in an equatorial position and 2) the existence of several conformations of the N–C bond between each piperidine unit that are probably the three minimum-energy staggered conformations of this bond.[11] The same characteristic NOE interactions were found with a small model molecule, methylpiperidinopiperidine (see the Supporting Information). The ^{1}H NMR spectra of **7** and methylpiperidinopiperidine (see the Supporting Information) in deuterated water exhibit approximately the same characteristic pattern of signals as that in CD_3OD, with significant chemical-shift differences between axial and equatorial protons from the same methylene group; these characteristics indicate the presence of a unique structure in methanol and water. IR analysis of the oligopiperidine **7** in $CDCl_3$ and the Bohlmann band at 2814 cm^{-1} (see the Supporting Information) provide further evidence in favor of an extended structure in which the piperidine rings are in equatorial positions.[10a] Collectively, these data strongly suggest that **7** adopts a well-defined rodlike structure in solution.

The slow evaporation of a solution of **7** in deuterated methanol yielded crystals of the unprotected base suitable for X-ray structural determination.[12] The unit cell contains two tetrapiperidine **7** molecules. The conformations of these two molecules differ in the arrangement of their Cbz groups. Their ORTEP representations clearly reveal linear rodlike structures (Figure 3). The molecules each consist of four piperidine rings in chair conformations. All piperidine segments occupy the equatorial position on each connected ring and are separated by approximately 4.3 Å.

Molecular dynamics (MD) simulations on the oligomer **7** were performed at 300, 350, and 400 K to characterize the conformational ensemble of the oligopiperidine as a function of increasing temperature. For each temperature, the system was equilibrated for 10 ps using a 2-fs time step, during which time the temperature was ramped from 0 K to the final system temperature (300, 350, or 400 K). Production simulations were run for 1 ns using a 2-fs time step. Snapshots of the system were written out every ten steps to insure that fine details of the system were observed. To determine how linear the geometry of the molecule remained during each simulation, two metrics were used. The first is the length of the major axis, defined as the distance between two carbon atoms at the opposite ends of the molecule (Table 1), which was

Table 1: Statistics of the major-axis length (measured from the carbon atoms labeled A and B) distributions of **7** observed in three MD simulations.



Temperature [K]	Mean length [Å]	Standard deviation
300	15.0	0.4
350	14.9	0.7
400	14.9	0.9

measured for each snapshot in each MD trajectory. The second is the major axis angle, formed by the previously defined major-axis carbon atoms and a central nitrogen atom in the molecule (see the Supporting Information). These two values characterize the overall geometry of the molecule during the simulations, thus describing its tolerance for stretching, compressing, and bending. The distributions of the oligopiperidine lengths remain fairly invariant across all three temperatures simulated (Table 1), thus indicating that the linear geometry of this molecule, and its corresponding ability to resist stretching and compressing, is stable across a large range of temperatures.

Furthermore, the values of the major-axis angles indicate that the molecule remains very extended through simulations

 © 2006 Wiley-VCH Verlag GmbH & Co. KGaA, Weinheim

at all three temperatures. At higher temperature simulations, the distribution of the major axis angle values has an increased mean and a decreased variance. This implies that as the temperature increases, the oligopiperidine structure tends to bend less and remain slightly more fully extended. Altogether, these data demonstrate that these oligopiperidine molecules adopt a stable linear conformation. Visual inspection of the simulation trajectories confirms that the molecule retains an extended structure throughout the entire simulation. Although rotations about the C–N bonds occur, these rotations result in only small deviations around the linear geometry of the molecule.

This report describes a simple, inexpensive, and widely accessible method for the preparation of rigid, rodlike oligopiperidines with a defined length of up to ten units (4.3 nm length). This oligomeric system does not require control of the stereochemistry at the Cγ position of the piperidine ring, but rather allows the molecule to equilibrate into the proper conformations. Because of their structure, we expect these molecules to be more resistant to proteolysis than polyprolines. These well-defined, water-soluble molecules may provide access to materials with well-defined structures (e.g., rigid linkers, construction elements, etc.).

Received: August 22, 2005
Published online: December 12, 2005

Keywords: molecular dynamics · molecular rods · NMR spectroscopy · oligomers · structure elucidation

[1] a) P. F. H. Schwab, M. D. Levin, J. Michl, *Chem. Rev.* **1999**, *99*, 1863 – 1933; b) J. S. Moore, *Acc. Chem. Res.* **1997**, *30*, 402 – 413; c) J. M. Tour, *Acc. Chem. Res.* **2000**, *33*, 791 – 804.
[2] a) S. H. Gellman, *Acc. Chem. Res.* **1998**, *31*, 173 – 180; b) R. P. Cheng, S. H. Gellmann, W. F. DeGrado, *Chem. Rev.* **2001**, *101*, 3219 – 3232; c) D. J. Hill, J. M. Matthiew, R. B. Prince, T. S. Hughes, J. S. Moore, *Chem. Rev.* **2001**, *101*, 3893 – 4011.
[3] N. Sakai, J. Mareda, S. Matile, *Acc. Chem. Res.* **2005**, *38*, 79 – 87.
[4] a) N. Aratani, H. S. Cho, T. K. Ahn, S. Cho, D. Kim, H. Sumi, A. Osuka *J. Am. Chem. Soc.*, **2003**, *125*, 9668 – 9681; b) C. Xu, A. Wakamiya, S. Yamaguchi, *J. Am. Chem. Soc.* **2005**, *127*, 1638 – 1639.
[5] a) L. Stryer, R. P. Haugland, *Proc. Natl. Acad. Sci. USA* **1967**, *58*, 719 – 726; b) B. Schuler, E. A. Lipman, P. J. Steinbach, M. Kumke, W. A. Eaton, *Proc. Natl. Acad. Sci. USA* **2005**, *102*, 2754 – 2759.
[6] a) P. S. Arora, A. Z. Ansari, T. P. Best, M. Ptashne, P. Dervan, *J. Am. Chem. Soc.* **2002**, *124*, 13067 – 13071; b) H. Ungar-Waron, D. Gurari, E. Hurwitz, M. Sela, *Eur. J. Immunol.* **1973**, *4*, 201 – 205.
[7] C. G. Levins, C. E. Schafmeister, *J. Am. Chem. Soc.* **2003**, *125*, 4702 – 4703.
[8] R. J. Willemse, J. J. Piet, J. M. Warman, F. Hartl, J. W. Verhoeven, A. M. Brouwer, *J. Am. Chem. Soc.* **2000**, *122*, 3721 – 3730.
[9] A. F. Abdel-Magid, K. G. Carson, B. D. Harris, C. A. Maryanoff, R. D. Shah, *J. Org. Chem.* **1996**, *61*, 3849 – 3862.
[10] a) F. W. Vierhapper, E. L. Eliel, *J. Org. Chem.* **1979**, *44*, 1081 – 1087; b) E. L. Eliel, F. W. Vierhapper, *J. Am. Chem. Soc.* **1975**, *97*, 2424 – 2430; c) E. L. Eliel, F. W. Vierhapper, *J. Am. Chem. Soc.* **1974**, *96*, 2257 – 2259.
[11] C. Jaime; E. J. Ōsawa, *J. Chem. Soc. Chem. Commun.* **1983**, *12*, 708 – 709.
[12] Crystal data: $C_{30}H_{46}N_4O_4$, $M_r = 526.71\ g\,mol^{-1}$, colorless needle, crystal size: $0.10 \times 0.08 \times 0.04\ mm^3$, $a = 9.1261(14)$, $b = 11.4111(17)$, $c = 105.305(16)$ Å, $\alpha = 90$, $\beta = 90$, $\gamma = 90°$, $V = 10966(3)$ Å^3, $T = 193(2)$ K, orthorhombic, space group *Pbca*, $Z = 16$, $\rho_{calcd} = 1.276\ Mg\,m^{-3}$. Crystallographic data were collected using a Bruker SMART CCD (charge-coupled device) based diffractometer equipped with an Oxford Cryostream low-temperature apparatus operating at 193 K, $\lambda = 0.71073$ Å. 32596 measured reflections, 5102 unique ($R_{int} = 0.0505$), the structure was solved by direct methods and refined by full matrix least squares on F^2 for all data to $R_1 = 0.0850$ ($I > 2\sigma(I)$) and $wR_2 = 0.1729$ ($I > 2\sigma(I)$). CCDC 263974 contains the supplementary crystallographic data for this paper. These data can be obtained free of charge from The Cambridge Crystallographic Data Centre via www.ccdc.cam.ac.uk/data_request/cif.

 © 2006 Wiley-VCH Verlag GmbH & Co. KGaA, Weinheim

Neurochemistry

DOI: 10.1002/anie.200503089

A Synthetic Small Molecule That Induces Neuronal Differentiation of Adult Hippocampal Neural Progenitor Cells**

Masaki Warashina, Kyung Hoon Min, Tomoko Kuwabara, Alexis Huynh, Fred H. Gage, Peter G. Schultz, and Sheng Ding**

Neural stem/progenitor cells have been identified in several regions of the adult brain, including the subventricular zone and the dentate gyrus of the hippocampus. They are multipotent in vitro (i.e., they can give arise to neurons, astrocytes, and oligodendrocytes) and have been shown to contribute to neurogenesis in adulthood.[1,2] The discovery of neural stem/progenitor cells (NPCs) in the adult central nervous system has created considerable interest in the development of stem-cell-based therapies for neurodegenerative disease.[2–4] How-

[*] Dr. M. Warashina,[+] Dr. K. H. Min,[+] Dr. P. G. Schultz, Dr. S. Ding
Department of Chemistry and
The Skaggs Institute for Chemical Biology
The Scripps Research Institute
10550 North Torrey Pines Road, SR202, La Jolla, CA 92037 (USA)
Fax: (+1) 858-784-9440
E-mail: schultz@scripps.edu
sding@scripps.edu
Dr. T. Kuwabara, A. Huynh, Dr. F. H. Gage
The Salk Institute for Biological Studies
La Jolla, CA 92186 (USA)
[+] These authors contributed equally to this paper.

[**] This work was supported by the Novartis Research Foundation and the Skaggs Institute for Chemical Biology (P.G.S.), and partially by the Postdoctoral Fellowship Program of the Korea Science and Engineering Foundation (K.H.M). This is manuscript 17710-CH of the Scripps Research Institute.

Supporting information for this article is available on the WWW under http://www.angewandte.org or from the author.

© 2006 Wiley-VCH Verlag GmbH & Co. KGaA, Weinheim
InterScience

ever, the molecular mechanisms that underlie stem-cell-fate specification are still poorly understood, and we lack robust and selective methods to control the differentiation programs of NPCs. Although several agents, including retinoic acid (RA),[1] leukemia inhibitory factor (LIF),[5] and insulin-like growth factor-1 (IGF-1),[6] have been found to direct neuronal, astroglial, and oligodendrocytic differentiation, they either are pleiotropic or have poor in vivo activities. Moreover, relatively little is known about the endogenous molecules that control stem-cell fate. Consequently, the generation of small molecules that can direct differentiation of adult NPCs could provide useful chemical tools to probe signaling pathways that control neuronal specification and could ultimately facilitate therapeutic application of NPCs. Herein, we report the identification and preliminary characterization of a novel small molecule, neuropathiazol, that selectively induces neuronal differentiation of multipotent hippocampal neural progenitor cells.

To screen for small-molecule inducers of neuronal differentiation, a primary neural progenitor (HCN) cells isolated from adult rat hippocampus were used. Although it has been shown that HCN cells can differentiate into neurons, astrocytes, and oligodendrocytes in vitro and can functionally integrate into existing neuronal networks in vivo, HCN cells very rarely differentiate into neuronal and astroglial lineages without treatment with exogenous factors, for example, with RA or LIF in the absence of basic fibroblast growth factor (bFGF): In contrast, a relatively large percentage of HCN cells are induced to differentiate into oligodendrocytes at high cell density by the insulin present in N2 supplemented medium. The extremely low frequency of 'spontaneous' (cell autonomous) neuronal and astroglial differentiation of HCN cells makes them a good in vitro model system to screen for novel chemical regulators.

HCN cells were expanded and maintained in an undifferentiated state on a polyornithine/laminin-coated dish in a defined serum-free growth medium (DMEM/F12 supplemented with N2 and bFGF (20 ng mL^{-1})) in a homogeneous monolayer. Neuronal and astroglial differentiation were analyzed directly with double immunofluorescence staining of βIII tubulin (TuJ1) as a neuronal marker and of glial fibrillary acidic protein (GFAP) as an astroglial marker. A combinatorial heterocycle library of 50000 compounds was screened by using undifferentiated, early passage HCN cells, which were plated onto polyornithine/laminin-coated 384-well plates at a density of 6000 cells/well in complete growth medium. After overnight incubation, the medium was exchanged with bFGF-free basal medium, and the compounds (final concentration of 5 μM) were added to each well. After treatment with the compounds for four days, the cells were fixed and stained with βIII tubulin/TuJ1 and GFAP antibodies, the morphology of positively stained cells was analyzed, and the number of cells with the desired phenotypes were counted.

A class of 4-aminothiazoles, which induces specific neuronal differentiation in a dose-dependent manner, was identified. To improve the potency and specificity of these compounds further, a sublibrary of 4-aminothiazole compounds was generated by the reaction of α-chloroacetylanilines and thiobenzamides (Scheme 1) and their activity was assayed. This structure–activity relationship (SAR) study revealed that: 1) aminomethylation (i.e., $R^3 = Me$) significantly enhanced activity relative to other substituents at the R^3 position, 2) substitution of R^1 with 4-Cl and 4-CF_3 leads to a decrease in activity, and 3) R^2 substitution at the *meta* position or the presence of a hydrogen-bond donor dramatically decreases activity. Compound **1**, neuropathiazol (Scheme 1), has the highest activity among the analogues tested (representative analogues and their relative activity are provided in the Supporting Information).

Treatment of HCN cells with neuropathiazol significantly slowed cell proliferation (Figure 1) without visible cytotoxic

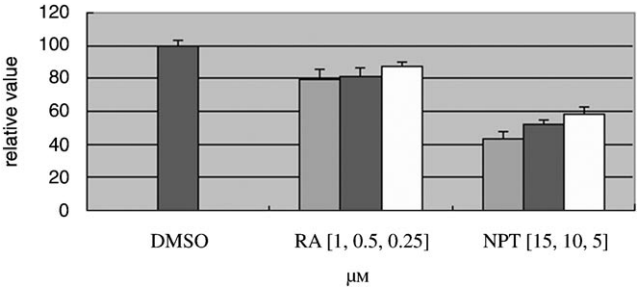
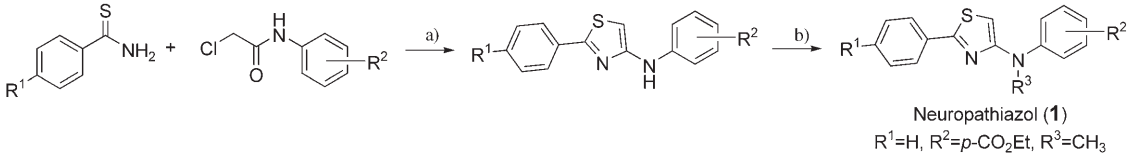


Figure 1. BrdU proliferation assay. Neuropathiazol inhibits proliferation of HCN neural progenitor cells. HCN cells treated with RA (1 μM, 0.5 μM, and 0.25 μM) or neuropathiazol (NPT) (15 μM, 10 μM, and 5 μM) for 5 h in bFGF-free N2 medium were labeled with BrdU for 2 h, and BrdU-positive cells were counted.

effects; more than 90% of the cells differentiated into neuronal cells as determined by immunostaining with TuJ1 and the characteristic neuronal morphology. RA, however, showed weaker antiproliferation activity and significant cytotoxicity over 2 μM in growth factor (bFGF or LIF/BMP2)-free basal medium. GFAP-positive cells were very rarely detected after neuropathiazol treatment, indicating that neuropathiazol specifically induces a neuronal lineage (Figure 2B). In contrast, relatively large numbers of both neuronal and astroglial cells were found with RA-induced differentiation of HCN cells, which indicates that RA is not very specific (Figure 2A). Longer treatment of HCN cells (7 days) with neuropathiazol led to positive staining for later-



Scheme 1. Synthesis of 4-aminothiazole analogues. Reagents: a) DMF (or EtOH), 80°C, overnight; b) NaH, RX, room temperature, 2 h.

 © 2006 Wiley-VCH Verlag GmbH & Co. KGaA, Weinheim

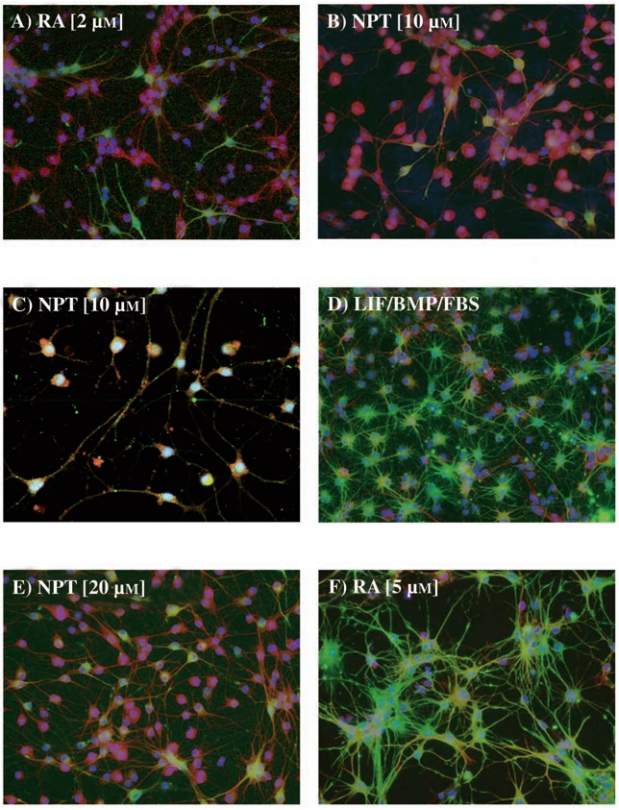


Figure 2. Neuropathiazol specifically induces neuronal differentiation of adult hippocampal neural progenitor (HCN) cells. HCN cells in N2 media were treated with A) retinoic acid (RA; 2 μM) or B) neuropathiazol (10 μM) for four days and immunostained with TuJ1 (red) and GFAP (green). C) Mature neurons were observed with Map2ab (red) and neurofilament-H (green) antibodies after treatment with neuropathiazol (10 μM) for 7 days. D) Astroglial differentiation of HCN cells was strongly induced by LIF/BMP/FBS treatment (LIF (50 ng mL^{-1}), BMP2 (50 ng mL^{-1}), and FBS (0.5%)). E) Astroglial differentiation can be inhibited by neuropathiazol (20 μM), but not by RA (5 μM; F). Cells were stained with markers for neurons (TuJ1, red) and astrocytes (GFAP, green), and also with DAPI (blue) for nuclei.

stage neuronal markers including neurofilament-H and Map2(a+b), which indicates that neuropathiazol-treated HCN cells can differentiate into mature neurons (Figure 2C).

Moreover, RT-PCR of marker genes showed that Sox2 (a neural progenitor marker)[7] was downregulated and NeuroD1 (a neuronal cell marker)[8] was upregulated upon treatment with neuropathiazol (Figure 3). Interestingly, neuropathiazol can also inhibit astroglial differentiation that was induced by LIF and BMP2 (Figure 2E), whereas RA cannot (Figure 2F). This suggests that neuropathiazol functions by a different mechanism and has a more specific neurogenic-inducing activity than RA.

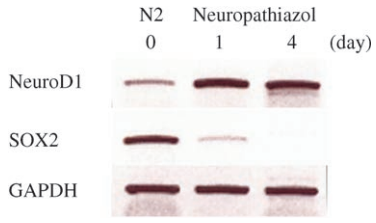


Figure 3. HCN cells were incubated with neuropathiazol (10 μM) or in compound-free N2 medium (N2; supplemented growth media without bFGF) and mRNA levels were determined by semiquantitative RT-PCR analysis.

In conclusion, the small molecule neuropathiazol, which induces neuronal differentiation of multipotent adult hippocampal neural progenitor cells, was identified by a high-throughput image-based screen. Neuropathiazol is a more selective inducer of neuronal differentiation than RA and can competitively suppress astrogliogenesis by LIF/BMP2/FBS in a dose-dependent manner. Further experiments are required, however, to determine the precise molecular target of neuropathiazol. Nonetheless, neuropathiazol will be a useful tool for studying the molecular mechanisms that determine cell fate with the ultimate goal of stem-cell therapy.

Received: August 31, 2005
Published online: December 2, 2005

Keywords: drug design · neurochemistry · neuronal differentiation · neuropathiazol · stem cells

[1] a) P. S. Eriksson, E. Perfilieva, T. Bjork-Eriksson, A. M. Alborn, C. Nordborg, D. A. Peterson, F. H. Gage, *Nat. Med.* **1998**, *4*, 1313–1317; b) T. D. Palmer, J. Takahashi, F. H. Gage, *Mol. Cell. Neurosci.* **1997**, 8, 389–404.
[2] D. N. Abrous, M. Koehl, M. L. Moal, *Physiol. Rev.* **2005**, *85*, 523–569.
[3] a) N. Picard-Riera, B. Nait-Oumesmar, A. Baron-Van Evercooren, *J. Neurosci. Res.* **2004**, 76, 223–231; b) T. J. Shors, G. Miesegaes, A. Beylin, M. Zhao, T. Rydel, E. Gould, *Nature* **2001**, *410*, 372–376; c) D. C. Lie, H. Song, S. A. Colamarino, G. L. Ming, F. H. Gage, *Annu. Rev. Pharmacol. Toxicol.* **2004**, *44*, 399–421.
[4] K. Jin, A. L. Peel, X. O. Mao, L. Xie, B. A. Cottrell, D. C. Henshall, D. A. Greenberg, *Proc. Natl. Acad. Sci. USA* **2004**, 101, 343–347.
[5] K. Nakashima, M. Yanagisawa, H. Arakawa, N. Kimura, T. Hisatsune, M. Kawabata, K. Miyazono, T. Taga, *Science* **1999**, *284*, 479–482.
[6] J. Hsieh, J. B. Aimone, B. K. Kaspar, T. Kuwabara, K. Nakashima, F. H. Gage, *J. Cell Biol.* **2004**, *164*, 111–122.
[7] a) T. Kuwabara, J. Hsieh, K. Nakashima, K. Taira, F. H. Gage, *Cell* **2004**, *116*, 779–793; b) M. Bylund, E. Andersson, B. G. Novitch, J. Muhr, *Nat. Neurosci.* **2003**, *6*, 1162–1168.
[8] M. Liu, S. J. Pleasure, A. E. Collins, J. L. Noebels, F. J. Naya, M. J. Tsai, D. H. Lowenstein, *Proc. Natl. Acad. Sci. USA* **2000**, *97*, 865–870.

© 2006 Wiley-VCH Verlag GmbH & Co. KGaA, Weinheim

Antibodies

DOI: 10.1002/anie.200503328

Epitope Mapping of the Protective Antigen of *B. Anthracis* by Using Nanoclusters Presenting Conformational Peptide Epitopes**

Aren E. Gerdon, David W. Wright, and David E. Cliffel**

Epitope mapping is the process of determining the major antibody binding sites on an antigen and can provide valuable information to one who is attempting to understand an antigen's mode of action or produce an antiviral vaccine. There are established techniques for the mapping of an antigen, including Western Blot analysis, X-ray crystallography, NMR spectroscopy, antibody competition assays, site-specific mutagenesis, and flow cytometry.[1–4] Each of these techniques have advantages and disadvantages and tend to excel in one particular aspect of epitope mapping. Many of these experiments place emphasis on distinguishing between discontinuous epitopes (contact points are far apart in amino acid sequence but proximal through space) and continuous epitopes (sequential amino acid sequence).[5] Unfortunately, these techniques often ignore conformations intrinsic to sequential epitopes. Consequently, many mapping techniques lack the ability to maintain the secondary structure (local conformation) of antigens or ignore it entirely despite the tremendous impact secondary structure can have on the location of contact points and, ultimately, antigenicity. Peptide epitopes are another tool for mapping sequential epitopes and have traditionally been used in the creation of synthetic peptide libraries and in phage display methods.[1,6] Again, these methods preclude the study of secondary structure, although they offer the best potential to incorporate conformation.

Research herein has established a method for the study of secondary-structure conformational effects on monoclonal-antibody binding to peptide epitopes. According to this method, we have effectively mapped monoclonal antiprotective antigen (anti-PA) antibodies to a protein conformational-loop region through the assembly of a conformational-loop epitope on a nanoparticle. Previously, cyclization of peptides has approximated loop structures with limited success,[7] but the development and presentation of a peptide that reconstitutes a physiological conformation is paramount (Figure 1).

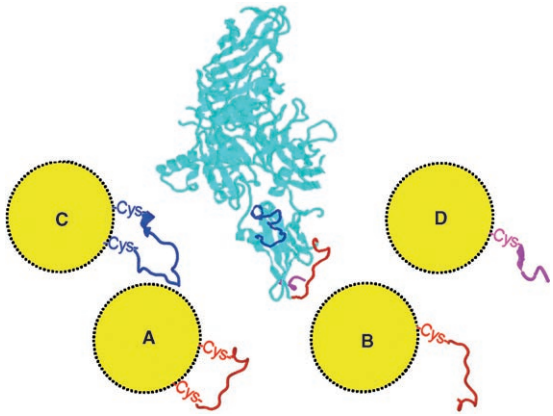


Figure 1. X-ray crystal structure of the protective antigen of *B. anthracis* (middle) and illustrations of PA mimics highlighting the conformational and linear epitopes. Three known epitopes are highlighted in the crystal structure: amino acids 680–692 (red), 703–722 (blue), 730–735 (magenta).[3,4,8–11] Composition of antigen mimics are as follows: A) PA680B–MPC = $Au_{807}Tiop_{290}Pep_4$; B) PA680M–MPC = $Au_{807}Tiop_{294}Pep_4$; C) PA703B–MPC = $Au_{807}Tiop_{282}Pep_8$; D) PA730M–MPC = $Au_{807}Tiop_{288}Pep_{10}$.

We have emphasized loop structures for several reasons: 1) surface accessible loops are abundant in many protein antigens, 2) previous epitope-mapping experiments have revealed loops as common antibody binding sites,[1,5,8,9] 3) loops are more amenable to nanocluster recapitulation when compared with other types of secondary structures. Surface accessible loops also lack steric interference and are highly solvated.

An example of a loop-rich protein is the protective antigen (PA) of *B. anthracis*, which is one of three protein precursors to the anthrax toxin. Edema factor (EF) and lethal factor (LF) depend on PA for membrane transport and activation and as a result, the binding of PA to the cell membrane is crucial for toxicity. PA has been a target for immunological studies that have shown that levels of anti-PA antibodies correlate well with an immunity to anthrax. Further examination has identified two loops and the C terminus as cell-receptor binding sites, and therefore, possible sites for toxin neutralization by immunoglobulin G (Figure 1).[2,4,8–11] Recent studies[3] with denatured and non-denatured PA confirm the necessity of conformation in loop structures and also suggest the presence of a linear epitope, such as the C terminus. The identification of these loops, and the high priority that anthrax has received owing to its potential as a bioterrorism agent make PA an excellent model for the design of complex, conformational nanostructures that mimic an antigen and have the ability to interface with biological systems.

Research at this interface between biology and nanomaterials is of recent interest and has produced a number of

[*] A. E. Gerdon, Dr. D. W. Wright, Dr. D. E. Cliffel
Department of Chemistry
Vanderbilt University
Station B 351822
Nashville, TN 37235 (USA)
Fax: (+1) 615-343-1234
E-mail: david.wright@vanderbilt.edu
d.cliffel@vanderbilt.edu

[**] This research was funded in part by a Vanderbilt Institute of Chemical Biology fellowship (A.E. Gerdon), the Chemical Biology Interface training grant (AE Gerdon, T32 GM065086), and the Vanderbilt Institute of Nanoscale Science and Engineering (A.E. Gerdon). DWW acknowledges support from the SouthEast Regional Center of Excellence for Biodefense (NIH U54 AI57157-03).

Supporting information for this article is available on the WWW under http://www.angewandte.org or from the author.

InterScience
© 2006 Wiley-VCH Verlag GmbH & Co. KGaA, Weinheim

exciting and successful examples of well-defined interfaces.[12,13] Progress towards specifically interfacing immunology with nanoparticles is highlighted by an important approach that made use of a peptide epitope that is known to bind monoclonal antibodies associated with the human malarial parasite, *P. falciparum*. This was the first example of antigen-encapsulated nanoclusters that assemble with antibodies through the antibody/epitope interface.[14] A more-recent example used glutathione-encapsulated nanoclusters and polyclonal antiglutathione antibodies. This approach confirmed the ability to assemble single-component monolayer nanoclusters with antibodies and provided an analytical technique for rigorous evaluation of interface assembly by using the quartz crystal microbalance.[15]

More-complex nanostructures, which specifically present peptide epitopes in a dual-component monolayer, require scaffold properties that are common to monolayer-protected clusters (MPCs). MPCs capped with a tiopronin ligand are water soluble, their average diameter (ranging from approximately 2 to 5 nm) is on the order of small proteins,[15–17] they are easily characterized by conventional techniques and have convenient optical and electronic properties,[18] the ligand (a thiolated derivative of glycine) is relevant to biological systems and provides the cluster with an overall negative charge.[17] Further functionalization of the cluster through ligand coupling or place-exchange reactions is facile and has been well studied.[19]

Presentation of peptide epitopes on the surface of Tiop–MPC can provide functionality and has been carried out through well-characterized place-exchange reactions.[19,20] This provides the ease of functionalization of MPCs, which makes them attractive as protein mimics and as functional nanostructures. An important feature of place-exchange reactions and the presentation of conformational peptide epitopes is the idea that fast-exchange sites are not static. Evidence for this has come from the exchange of several different ligands onto the same MPC[21,22] and from an inability to completely remove ligands that had been previously exchanged onto a cluster.[19,22] A significant implication of these results is the ability of thiolate to migrate across the monolayer of an MPC. This migration might allow for the faithful reconstitution of a peptide epitope if the two ends of a bidentate ligand are able to move and position themselves at a distance similar to that in their physiological conformation.

The peptide epitopes, shown in Table 1, were synthesized for presentation on MPCs. Cystein (cys) residues were added at the N and/or C terminus to promote bidentate or monodentate exchange and alanine (ala) residues were similarly added for a lack of reactivity or presentation. Concurrently, water-soluble, nanometer-sized, monolayer-protected clusters were synthesized with tiopronin, a glycine derivative, as the passivating ligand as was reported previously.[15,17] Careful characterization allowed for the calculation of a diameter of 3.5 ± 1.0 nm and an estimated composition of $Au_{807}Tiop_{298}$ (207 kDa; see the Supporting Information). This size is close to the estimated optimal MPC size for the bidentate attachment of peptide PA680B (see the Supporting Information). The epitope and MPC scaffold were then brought together through place-exchange reactions to produce functional nanostructures.[19,22] Following each exchange, the extent of presentation was determined by ^{1}H NMR spectroscopy (see the Supporting Information). A cartoon schematic and final composition of antigen mimics can be seen in Figure 1.

Table 1: Amino acid sequences for peptides used in antigen mimic design.[a]

Peptide	Sequence	MW [Da]	Reference
PA680B	**C** KYNDK LPLYI SNP **C**	1771	[3, 4, 8–11]
PA680M	KYNDK LPLYI SNP **C**	1668	[3, 4, 8–11]
PA680A	**AA** KYNDK LPLYI SNP **A**	1778	[3, 4, 8–11]
PA703B	**C** KENTI INPSE NGDTS TNGIK **C**	2339	[8–11]
PA730M	**C** KGYEI G	769	[4]

[a] Highlighted cys (**C**) and ala (**A**) were not part of the epitope but added for functionalization and immobilization purposes.

The faithful reconstruction of epitope loops in a physiologically relevant conformation is predicated based on the ability to assemble loop peptides in a bidentate fashion. A linear epitope, such as the C terminus of PA (PA730M), can easily be attached to the MPC in a monodentate fashion that affords the peptide a good chance of maintaining its correct conformation. On the other hand, peptide epitopes from flexible loop regions of proteins cannot undergo monodentate attachment and be expected to adopt the correct conformation. Immobilization of both ends of the peptide in a bidentate, bivalent model restrains the peptide and promotes a conformation comparable with its native form. This is not an attempt to "fold" the peptide, rather an attempt at placing the peptide in an environment similar to that of the intact protein.

One challenge was in the characterization of the mode of attachment. The diversity of particle size can affect loop attachment and create a large combinatorial set of epitope conformations. Techniques such as CD and two-dimensional NMR spectroscopy have been successful in the evaluation of peptide conformation. However, low concentration of peptides on the surface of the MPC, cluster absorbance, and characteristically broad NMR peaks limit the applicability to this study. Instead, the mode of peptide attachment to the nanocluster was probed with a free-thiol labeling molecule, Ellman's Reagent (ER).[23] The reaction of ER with free peptide PA680M produced a characteristic yellow color and, after purification, showed thiol derivatization in ^{1}H NMR and MALDI-MS spectra. Conversely, the reaction of ER with PA680B–nanocluster complex did not show any indication of derivatization (see the Supporting Information). Labeling experiments with ER have supported bidentate attachment through the indication of a lack of free, unattached thiol in an MPC solution (see the Supporting Information) but provide no information on conformation.

A further test of epitope conformation showed a difference in antibody binding between a linear and conformational antigen mimic. As a result, the development of a sensitive, selective, quantitative assay that allowed for 3D-nanocluster substrates, multilayer adsorptions, and nonrigid biological recognition was required. The quartz-crystal microbalance (QCM) has recently been demonstrated to be well suited for this type of assay.[15] It has been used in the study of a variety of biological and nonbiological systems[15,24] and has numer-

 © 2006 Wiley-VCH Verlag GmbH & Co. KGaA, Weinheim

ous benefits over other techniques that compete for the study of nanoscale assembly.[13] A sensitive and selective immunosensor that involves a piezoelectric quartz crystal with a gold electrode and sequential layering of polyelectrolyte,[25,26] MPC, and blocking with bovine serum albumin (BSA), leads to the immobilization of antigen mimics and thus provides a foundation for antibody screening. The results of representative adsorption and average binding of polyelectrolyte (0–30 min), MPC (30–60 min), and BSA (80–100 min) can be seen in Figure 2 and Table 2, respectively (see also the Supporting Information). MPC antigen mimics bound to the sensor to varying degrees as a result of differences in peptide presentation and ionic charge. Although this might affect the density of the peptide available for antibody binding, it will not affect the affinity (K_a) of the antibody/epitope interaction.[20] Binding studies involved seven mouse monoclonal anti-PA antibodies obtained from Biodesign International. These antibodies were known to bind both the full-sized PA (83 kDa) and the furin-cleaved PA (63 kDa) (according to Western Blot) but had not been tested for their ability to neutralize the toxin.[27] To map the antibodies to different conformational and linear regions of the antigen, the antibodies were screened at constant concentration against the four PA mimics. At a relatively low concentration of antibody (124 nM), screening experiments provided qualitative information on the recognition or lack of recognition and as such, guided further studies (Table 2). The results of the screening experiments suggest cross reactivity for several antibodies, and antibody 110 was identified as being potentially selective for the conformational epitope spanning amino acids 680–692.

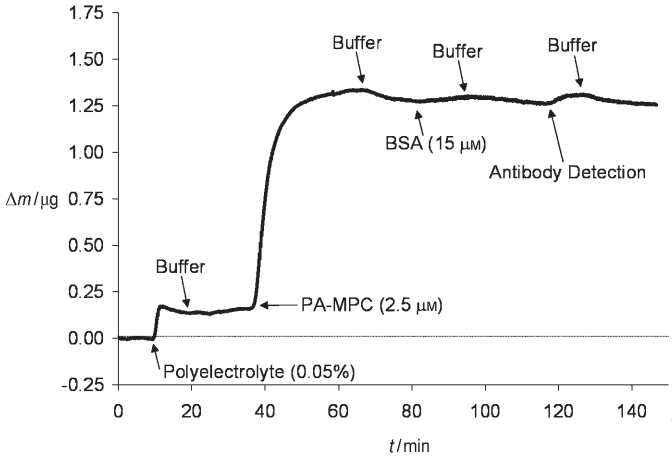


Figure 2. Representative polyelectrolyte, PA680B–MPC, BSA, and antibody 110 binding in phosphate buffer solution.

Table 2: Results of immunosensor assembly (μg) and for screening monoclonal anti-PA antibodies (124 nM) against four antigen mimics (in ng).[a]

	PA680B	PA680M	PA703B	PA730M
Ave PolyE	0.16 ± 0.03	0.16 ± 0.03	0.16 ± 0.03	0.16 ± 0.03
Ave MPC	1.12 ± 0.06	0.80 ± 0.07	0.73 ± 0.06	0.68 ± 0.07
Ave BSA	0.06 ± 0.05	0.13 ± 0.05	0.14 ± 0.02	0.21 ± 0.02
mAb 110	20	10	0	0
mAb 201	15	0	10	14
mAb 301	0	10	0	0
mAb 410	10	0	10	16
mAb 501	10	10	0	11
mAb 601	10	10	0	10
mAb 613	13	0	10	10

[a] Screening was completed by using QCM and all values represent changes in mass. Data suggest antibody 110 as having strong and specific interaction with PA680B–MPC.

This antibody was studied in more detail through variation of the antibody concentration and the ionic strength of buffer solutions. Seven experiments for each of the two antigen mimics (PA680B–MPC and PA680M–MPC), differing only in mode of peptide attachment (bidentate versus monodenate), showed saturation of the immunosensor. The four-highest concentrations for each mimic were fit to a logarithmic curve (Figure 3). Equilibrium association constants (K_a) were determined for each mimic by fitting the four-highest concentrations to a Langmuir adsorption isotherm (Table 3).[13,15,28] PA680B–MPC had a K_a of $(5.9 \pm 0.7) \times 10^6\,M^{-1}$, which falls within a general range for immunoaffinity

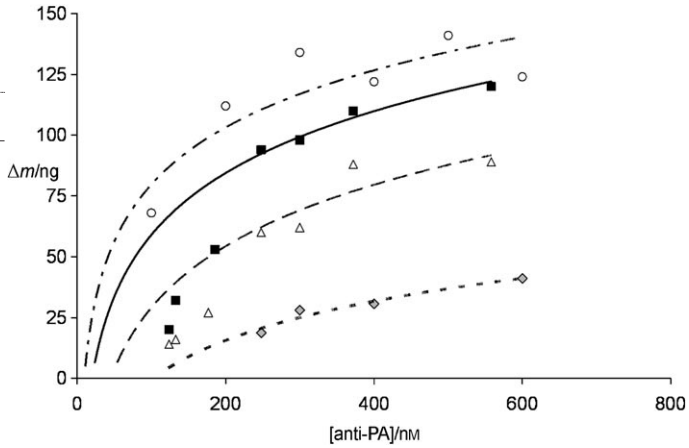


Figure 3. Plot of Δm against [anti-PA] for PA protein antigen (○) with logarithmic fit to six doses (– – –), PA680B–MPC (■) with logarithmic fit to four doses of high concentration (——), MPC–PA680M (△) with logarithmic fit to four doses of high concentration (– – –), and PA680B–MPC (◇) in PBS with logarithmic fit (-----) showing saturation of the immunosensor in all cases.

Table 3: Results from equilibrium calculations for two antigen mimics and the Protective Antigen protein.[a]

Antigen	[NaCl] mM	Equilibrium Constants K_a [$\times 10^6\,M^{-1}$]
MPC-PA680B	0	5.9 ± 0.7
	0	4.0 ± 0.8[b]
	150	2 ± 1
MPC-PA680M	0	2.6 ± 0.9
	150	–[c]
Protective Antigen	0	12 ± 6

[a] Experiments were conducted in phosphate buffer solution (no added NaCl) or in phosphate-buffered saline solution (150 mM NaCl). [b] Equilibrium constant calculated from kinetic constants, where $K_a = k_f/k_r$. [c] Unable to calculate owing to a lack of binding.

 © 2006 Wiley-VCH Verlag GmbH & Co. KGaA, Weinheim

of 10^6–$10^{10}\,\text{M}^{-1}$ [29] and shows an increased affinity over a previously reported glutathione-presenting nanocluster with polyclonal antibody ($K_a = 3.6 \times 10^5\,\text{M}^{-1}$).[15] Antibody 110 had a decreased affinity for the linear epitope-presenting nanocluster (PA680M–MPC, $K_a = (2.6 \pm 0.9) \times 10^6\,\text{M}^{-1}$), which suggests a real difference between peptide epitopes of identical primary structure but different secondary structure.

These results were validated through control experiments by using Tiop–MPC and buffer solutions of increasing ionic strength (Figure 4). Salt gradients are typically used in affinity

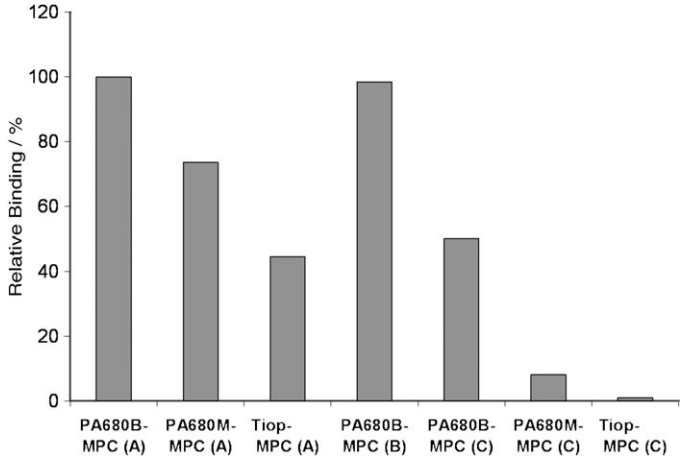


Figure 4. Relative binding percent for antibody 110 (300 nM) to seven different nanocluster systems, normalized to density of nanocluster displayed on immunosensor surface. All samples were run in phosphate buffer solution (50 mM) with varying concentrations of NaCl (A = 0 mM, B = 50 mM, C = 150 mM).

chromatography and are known to decrease weak interactions.[30] In initial studies, the background antibody binding to Tiop–MPC and PA680M–MPC in phosphate buffer solution (50 mM) was relatively high. The addition of NaCl (150 mM) decreased the weak, nonspecific adsorption seen in Tiop–MPC and PA680M–MPC but had a significantly lower effect on PA680B–MPC. Furthermore, a decreased concentration of NaCl (50 mM) had essentially no effect on antibody binding to PA680B–MPC. This allowed for the study of concentration dependence of antibody 110 binding to PA680B–MPC in high-ionic-strength buffer solution. The association constant ($K_a = (2 \pm 1) \times 10^6\,\text{M}^{-1}$) was only slightly less than that calculated in low-ionic-strength buffer solution (Figure 3) and confirmed strong recognition and limited nonspecific adsorption.

Kinetic information calculated for PA680B–MPC ($k_f = (9 \pm 2) \times 10^3\,\text{M}^{-1}\,\text{s}^{-1}$ and $k_r = (2.3 \pm 0.5) \times 10^{-3}\,\text{s}^{-1}$) from the time-dependent binding curves supports the equilibrium data and the immunorecognition of antibodies to conformational mimics. The equilibrium adsorption constant, K_a, is equal to the ratio of k_f/k_r and was calculated to be $(4.0 \pm 0.8) \times 10^6\,\text{M}^{-1}$, which correlates well with the K_a found in the previous method (Figure 3). Kinetic constants relate to the kinetics of polyclonal antibody binding to glutathione–MPC, with $k_f = 5.4 \times 10^1\,\text{M}^{-1}\,\text{s}^{-1}$ and $k_r = 1.5 \times 10^{-4}\,\text{s}^{-1}$.[15] It is reasonable that this forward rate constant is less than that for monoclonal anti-PA antibody owing to the heterogeneity of the polyclonal anti-glutathione sample. The binding kinetics for the snake neurotoxin, α-bungarotoxin, to synthetic peptide mimotopes have been reported[31] with k_f in the range of 10^1–$10^4\,\text{M}^{-1}\,\text{s}^{-1}$ and k_r in the range of 10^{-3}–$10^{-4}\,\text{s}^{-1}$. The kinetic rate constants for antibody 110 binding to PA680B–MPC also fall within these ranges.

Antibody binding to an intact protein antigen was studied for comparison with the antigen mimics. The antibody was shown to specifically bind the protein with a K_a value slightly larger than that calculated for the nanocluster antigen mimic (Figure 3, Table 3). The antibody did display high background adsorption to BSA in phosphate buffer solution (50 mM), but decreased in high-ionic-strength buffer solution, whereas antibody binding to PA was only slightly affected by an increase in ionic strength. Furthermore, anti-hemagglutinin (HA) antibody, which is not specific for PA, showed no binding to PA in low-ionic-strength buffer solution. The similarity between antigen and antigen-mimic K_a values points to the exceptional reconstitution of the conformational peptide epitope on the surface of the nanocluster.

The sum of these results suggests several things about the efficacy of these complex antigen mimics. First, it is apparent that we are able to successfully assemble peptides on nanoclusters to produce functional, immunoreactive nanoscale components. Second, we are able to employ functionalized nanoclusters in the screening of available monoclonal antibodies and effectively map an antibody to a peptide epitope. Finally, we were able to differentiate between conformational and linear epitopes and map a monoclonal antibody accordingly. Antibody 110 has an apparent increased affinity ($> 2\times$) for the conformational antigen mimic over the linear antigen mimic and an even greater affinity difference when in isotonic ionic-strength buffer solutions. Control experiments confirmed the enhanced affinity and placed the antigen mimic in the same affinity range as the intact protein. These antibodies could be used in the selection and isolation of tight binding, conformationally relevant antigen mimics, therefore providing information which could guide future mimic assembly. The placement of artificial conformational epitopes on a nanoparticle framework represents a significant early advance in our ability to control immunomodulation at the nanoscale.

Received: September 19, 2005
Published online: December 15, 2005

Keywords: antibodies · biomimetic synthesis · biosensors · immunoassays · nanostructures

[1] G. E. Morris, in *Epitope Mapping Protocols, Vol. 66*, Humana Press, Totowa, NJ, **1996**, pp. 1–9.
[2] E. Santelli, L. A. Bankston, S. H. Leppla, R. C. Liddington, *Nature* **2004**, *430*, 905–908.
[3] M. A. Wild, H. Xin, T. Maruyama, M. J. Nolan, P. M. Calveley, J. D. Malone, M. R. Wallace, K. S. Bowdish, *Nat. Biotechnol.* **2003**, *21*, 1305–1306.
[4] D. S. Reed, J. Smoll, P. Gibbs, S. Little, *Cytometry* **2002**, *49*, 1–7.

 © 2006 Wiley-VCH Verlag GmbH & Co. KGaA, Weinheim

[5] M. H. V. Van Regenmortel, *Philos. Trans. R. Soc. London Ser. B* **1989**, *323*, 451 – 466.
[6] S. R. Whaley, D. S. English, E. L. Hu, P. F. Barbara, A. M. Belcher, *Nature* **2000**, *405*, 665 – 668.
[7] S. Misumi, M. Endo, R. Mukai, K. Tachibana, M. Umeda, T. Honda, N. Takamune, S. Shoji, *J. Biol. Chem.* **2003**, *278*, 32335 – 32343.
[8] S. Leppla, J. Robbins, R. Schneerson, J. Shiloach, *J. Clin. Invest.* **2002**, *109*, 141 – 144.
[9] C. Petosa, R. J. Collier, K. R. Klimpel, S. H. Leppla, R. C. Liddington, *Nature* **1997**, *385*, 833 – 838.
[10] S. Little, J. P. Novak, J. R. Lowe, S. Leppla, Y. Singh, K. R. Klimpel, B. C. Lidgerding, A. Friedlander, *Microbiology* **1996**, *142*, 707 – 715.
[11] H. C. Flick-Smith, N. J. Walker, P. Gibson, H. Bullifent, S. Hayward, J. Miller, R. W. Titball, E. D. Williamson, *Infect. Immun.* **2002**, *70*, 1653 – 1656.
[12] C. M. Niemeyer, *Angew. Chem.* **2001**, *113*, 4254 – 4287; *Angew. Chem. Int. Ed.* **2001**, *40*, 4128 – 4158.
[13] A. E. Gerdon, D. W. Wright, D. E. Cliffel in *Characterization Tools for Nanosystems in Life Sciences* (Ed.: C. Kumar), Wiley-VCH, New York, **2005**, pp. 109 – 144.
[14] J. M. Slocik, J. T. Moore, D. W. Wright, *Nano Lett.* **2002**, *2*, 169 – 173.
[15] A. E. Gerdon, D. W. Wright, D. E. Cliffel, *Anal. Chem.* **2005**, *77*, 304 – 310.
[16] A. C. Templeton, S. Chen, S. M. Gross, R. W. Murray, *Langmuir* **1999**, *15*, 66 – 76.
[17] A. C. Templeton, D. E. Cliffel, R. W. Murray, *J. Am. Chem. Soc.* **1999**, *121*, 4845 – 4849.
[18] M. J. Hostetler, J. E. Wingate, C.-J. Zhong, J. E. Harris, R. W. Vachet, M. R. Clark, J. D. Londono, S. T. Green, J. J. Stokes, G. D. Wignall, G. L. Glish, M. D. Porter, N. D. Evans, R. W. Murray, *Langmuir* **1998**, *14*, 17 – 30.
[19] M. J. Hostetler, A. C. Templeton, R. W. Murray, *Langmuir* **1999**, *15*, 3782 – 3789.
[20] A. E. Gerdon, D. W. Wright, D. E. Cliffel, *Biomacromolecules* **2005**, *6*, 3419 – 3424.
[21] R. S. Ingram, M. J. Hostetler, R. W. Murray, *J. Am. Chem. Soc.* **1997**, *119*, 9175 – 9178.
[22] A. C. Templeton, M. J. Hostetler, E. K. Warmoth, S. Chen, C. M. Hartshorn, V. M. Krishnamurthy, M. D. E. Forbes, R. W. Murray, *J. Am. Chem. Soc.* **1998**, *120*, 4845 – 4849.
[23] Ellman's Reagent, http://www.piercenet.com/files/0311h4.pdf, **2004**.
[24] A. Janshoff, H. J. Galla, C. Steinem, *Angew. Chem.* **2000**, *112*, 4164 – 4195; *Angew. Chem. Int. Ed.* **2000**, *39*, 4004 – 4032.
[25] G. Decher, *Science* **1997**, *277*, 1232 – 1237.
[26] A. A. Mamedov, A. Belov, M. Giersig, N. N. Mamedova, N. A. Kotov, *J. Am. Chem. Soc.* **2001**, *123*, 7738 – 7739.
[27] Biodesign International, http://www.biodesign.com, **2004**.
[28] The rate of antibody adsorption is directly proportional to the bulk concentration of antibody (rate = k_f[antibody]). In the time frame of this experiment (10 min flow at 30 μL/min) high concentrations of antibody reached equilibrium, but low concentrations did not. For this reason, low concentrations did not give changes in mass that are consistent with equilibrium adsorption and were not used in calculations.
[29] D. L. Nelson, M. M. Cox, *Lehninger Principles of Biochemistry*, 3rd ed., Worth Publishers, New York, **2000**.
[30] M. A. J. Godfrey in *Affinity Separations* (Ed.: P. Matejtschuk), IRL, Oxford, **1997**, pp. 141 – 193.
[31] L. Bracci, L. Lozzi, B. Lelli, A. Pini, P. Neri, *Biochemistry* **2001**, *40*, 6611 – 6619.

 © 2006 Wiley-VCH Verlag GmbH & Co. KGaA, Weinheim

Lone Pairs of Electrons

DOI: 10.1002/anie.200502673

Unusual Lone Pairs in Tellurium and Their Relevance for Superconductivity**

*Shuiquan Deng, Jürgen Köhler, and Arndt Simon**

"Lone-pair" configurations of nonbonding electron pairs have always been used by chemists and physicists as a basis for rationalizing the structures of elements, molecules, and solid-state compounds.[1,2] Prominent examples are molecular structures described with the valence-shell electron-pair repulsion (VSEPR) model,[3] hypervalent compounds,[4] as well as the structural properties of "lone-pair ions" with the ns^2 configuration, for example, In^+, Sn^{2+}, and Sb^{3+}. The stereochemical activity of a lone pair depends on the types of ligands coordinated to the atom, on the temperature and pressure,[2,5] and, in particular, on the atomic number. Relativistic effects cause a larger decrease in energy for s than for p states with the same principal quantum number, resulting in an inert pair effect.[1c,d,6] This effect is also relevant for s^2p^n configurations, for example, the s^2p^4 configuration of the chalcogen elements.[7] These elements exhibit a rich structural chemistry,[8] with phases ranging from insulating to superconducting.[9]

Chemical bonding in the chalcogens has been analyzed with the vector charge density wave (VCDW) model,[7b,c] by treating the ns^2 pair as a core state because of the large s–p separation.[10] Interestingly, the resulting np^4 valence electron configuration is threefold degenerate (($p_{x^2}p_yp_z$), ($p_xp_{y^2}p_z$), and ($p_xp_yp_{z^2}$)), which means that the lone pair can have three different orientations. In spite of their crucial importance within the VCDW model, the existence and ordering of p^2-type lone pairs in the structures of the chalcogens have not been demonstrated quantitatively to date.

Herein, we present results from ab initio calculations, which allow a quantitative description of these types of lone pairs in a localized state, of their breakdown and delocalization under pressure, and of their relevance for superconductivity. We chose the element tellurium, because the first members, Te-I and Te-II, in a series of high-pressure phases up to Te-V, are structurally well characterized and exhibit semiconducting, metallic, and superconducting properties.

The ambient-pressure phase Te-I is composed of helical chains with 283.5 pm intra- and 349.1 pm interchain distances.[11] In the structure of Te-II, which is formed above approximately 4 GPa, these discrete chains are condensed into puckered layers with intralayer Te–Te distances ranging from 284.8 to 309.8 pm and shortest interlayer Te–Te distances of 333.3 pm.[12] Both structures are compared in Figure 1.

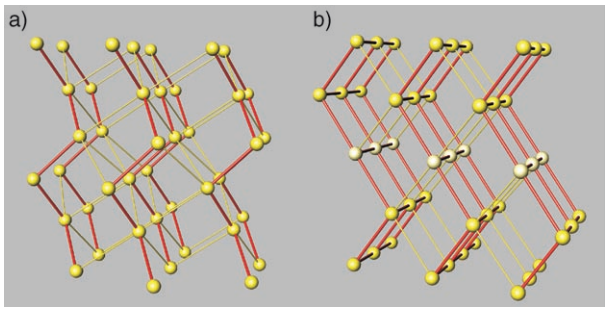


Figure 1. Perspective drawings of the crystal structures of a) Te-I and b) Te-II (Te1: light yellow spheres, Te2: yellow spheres). The red sticks correspond to the short Te–Te distances (283.5 pm in Te-I, and 284.8–309.8 pm in Te-II), and the thinner yellow sticks to longer Te–Te distances (349.1 pm in Te-I, and 333.3–340 pm in Te-II).

The electron localization function (ELF)[13] is a measure of the localization of an electron, which is based on the Pauli exclusion principle.[13a] It is defined to take maximum values in the "bosonic" regime of the electronic states.[13c] Since a lone pair is composed of a pair of electrons with opposite spin, it can be viewed as a localized boson. Thus, the ELF is often used as a tool to visualize a lone pair.[13] In Figure 2a, the lone pairs as described by the VCDW model for Te-I are shown. For comparison, the result of an ab initio tight-binding linear muffin tin orbital (TB-LMTO) calculation,[14,15] visualized through the ELF is shown in Figure 2b. With respect to a primitive cubic arrangement of the atoms, the lone pairs lengthen four of the nearest-neighbor distances around each site, while the two single-electron components are involved in bonds, which are indicated by thick lines in Figure 2a. In the VCDW model, the degeneracy of the lone pairs is removed by lowering the symmetry from cubic to trigonal.

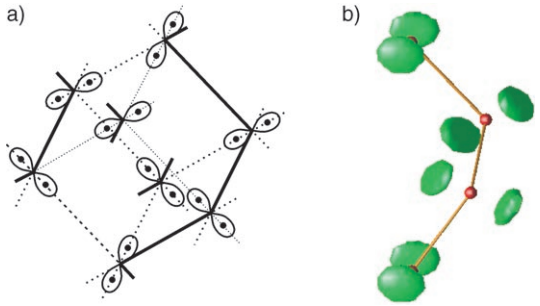


Figure 2. a) VCDW model of a cubic primitive lattice of tellurium. For clarity, only lone pairs and covalent bonds (thick lines) are shown; the two one-electron components of the vector field on each lattice site have been omitted. b) ELF visualization of the TB-LMTO model. The calculated isosurface corresponding to a value 0.8 is shown for a single helical chain of Te-I.

The chemical and structural significance of electron–electron repulsion is incorporated within the VSEPR model; however, this is only done qualitatively in terms of repulsion

[*] Dr. S. Deng, Priv.-Doz. Dr. J. Köhler, Prof. Dr. A. Simon
Max-Planck-Institut für Festkörperforschung
Heisenbergstrasse 1, 70569 Stuttgart (Germany)
Fax: (+49) 711-689-1642
E-mail: a.simon@fkf.mpg.de

[**] The authors thank Dr. O. Gunnarsson for helpful discussions.

© 2006 Wiley-VCH Verlag GmbH & Co. KGaA, Weinheim

between lone pairs, as well as between lone and bonding pairs. As first suggested by Fukutome,[7b,c] the unusual lone pair in the np^4 configuration results from the Coulomb interaction (U) among the p electrons, as the four valence electrons should otherwise be evenly distributed over the p_x, p_y, and p_z orbitals with an occupancy of $^4/_3$. Herein, we calculate U_p for the tellurium atom,[16] and for Te-I,[17] using the ab initio constrained occupation number approach.[18] For the tellurium atom, $U_p^0 = 8.31$ eV is calculated, which agrees well with the value of 8.59 eV determined semiempirically from the experimental atomic spectra.[19] The repulsion is significantly reduced by Coulomb screening, which leads to calculated values of $U_p = 1.16$ eV for the atom and $U_p^{solid} = 1.09$ eV for Te-I.[20] The small difference between both values clearly indicates that the screening is mainly due to interaction of the electrons on a single atom, and that the low value of U_p is the origin of the lone pair. The value of U_p^{solid} provides a rough estimate for the stability of the lone pairs in Te-I. Hence, energy changes on the order of 1 eV that, for example, occur through a closer mutual approach of the tellurium atoms under high pressure, can break the lone pair.

Band-structure calculations for Te-I[21] and Te-II[22] reveal the differences in the chemical bonding of the two modifications. In the energy window between −14 and 4 eV, the band structure of Te-I is composed of four groups of bands (Figure 3a). Each group comprises three bands which arise from the helical modulation of a straight chain of tellurium atoms. The group centered at −12 eV is of mainly s character, while those at −3, −1, and 1 eV correspond to p-type bonding states, or to p-type lone-pair states with antibonding character.[23] The band gap determined from our TB-LMTO calculations is 0.336 eV,[24] in very good agreement with the experimental value of 0.334 eV.[25] Note that both our TB-LMTO and our full-potential (FP) LMTO calculations clearly show that the frontier orbitals have a significant s component.

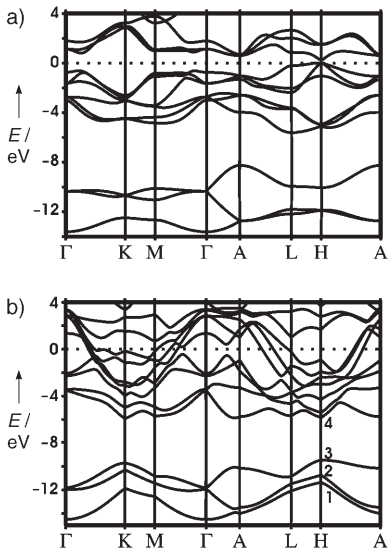


Figure 3. Band structures along selected symmetry directions from FP-LMTO calculations for a) Te-I and b) Te-II. In (b), the band states at point H are numbered consecutively from bottom to top (for clarity, only 1 to 4 are indicated).

Without sp hybridization, the band structure is dramatically changed, and Te-I develops metallic character. This result is consistent with the structure shown in Figure 2b, in which the Te-Te-Te angle is, however, 103.14° instead of 90°, and the relative orientation of the lone pairs shown in the ELF plot deviates from the 90° angle predicted by the VCDW model. However, qualitatively, the VCDW model agrees quite well with the ELF description.

Clearly, the treatment of the $5s^2$ level as a corelike state in the VCDW model is over-simplified. The sp hybridization stabilizes the lone pair and changes the relative orientation of the lone pairs, as compared to the VCDW model. The importance of sp mixing in understanding many puzzling structural phenomena in hypervalent compounds has also been emphasized by other authors.[4]

The localized lone pairs are lost under pressure in Te-II, which is metallic. This change is clearly seen in the band structure calculated for Te-II, which is presented in Figure 3b. For better comparison, the first Brillouin zone was chosen to be identical to that for Te-I,[26] because both crystal structures are very similar. The results of earlier band-structure calculations have to be revised,[27] as they were based on monoclinic, instead of the recently discovered triclinic, symmetry of Te-II.[12]

The separation of s and p bands remains for Te-II, and the low-lying s bands do not change much, apart from the removal of degeneracy at the zone boundaries as a result of the triclinic distortion. In particular, the band dispersions along Γ–A are almost identical in Te-I and Te-II, reflecting similar interactions in the chain directions for both modifications. However, pronounced changes occur to the p-type bands, because of the formation of interchain bonds in Te-II. Figure 4 shows a comparison of the chemical bonding in Te-I

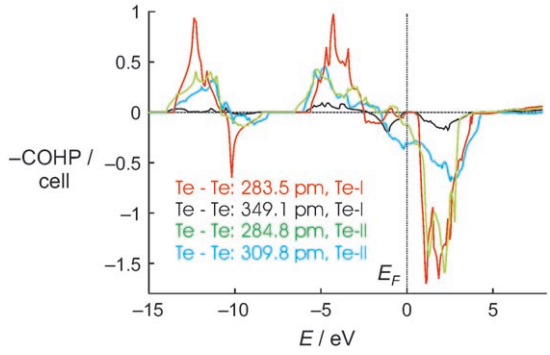


Figure 4. Selected COHP curves for intra- and interchain Te–Te bonds in Te-I and Te-II.

and Te-II, as measured with the crystal orbital Hamilton population (COHP).[28] In Te-I, the intrachain interaction is much stronger than the interchain one. The top of the lone-pair bands has antibonding character, in agreement with an earlier analysis.[29] It is clear from Figure 4 that for Te-II the intra- and interchain interactions are comparable below the Fermi level. However, both display a more pronounced antibonding character near the Fermi level. This observation is easily rationalized in terms of an increased Coulomb

 © 2006 Wiley-VCH Verlag GmbH & Co. KGaA, Weinheim

repulsion between the lone pairs owing to reduced interchain distances. The rather small absolute values of COHP around the Fermi level in Te-I, as well as the band gap in this modification, along with the changes in these features with the transition from Te-I to Te-II give further evidence for the existence of lone pairs in Te-I and their breakdown in Te-II. The calculated orbital compositions of these bands confirms their p character.[23]

The strong antibonding interaction near the Fermi level in Te-II transforms lone-pair bands into highly dispersive ("steep") bands along several directions, for example, H–A or A–L (Figure 3b). In addition, parts of the p-type antibonding conduction band are pushed down in energy, for example, at the H, K, L, and M points. This process results in a band with little dispersion along the Γ–K direction, and in a tiny flat feature near the Fermi level in the M–Γ direction. Such characteristic sections of bands satisfy the conditions of a "flat" band in the flat/steep-band scenario for superconductivity.[30] The localized lone pairs of Te-I are broken into itinerant electrons in Te-II. Indeed, the ELF isosurface of Te-II, calculated at the value of 0.8 used for Te-I in Figure 1b, reveals only insignificant lone-pair characteristics for both kinds of tellurium atoms.

Whereas Te-I is semiconducting, Te-II is a superconductor,[31] and its band structure satisfies the condition for superconductivity in our flat/steep-band scenario. We have shown earlier that this condition is necessary, but not sufficient.[32] The required conditions are closely related to the presence of a lone pair in Te-I and its "virtual" presence through electron–phonon coupling in Te-II. The flat/steep-band scenario for Te-II originates from the lone pair, that is, a pair of electrons with opposite spin, which can be viewed as a hard-core boson or Anderson bipolaron.[33] Under ambient conditions in Te-I, the electron pair forms a boson lattice with negligible hopping probability. In Te-II, these bosons exist virtually in a "gaseous" state, which "condenses" to a "liquid" in the superconducting state.

In summary, we have quantitatively characterized an unusual type of lone pair formed by Coulomb interactions. Its transition from a localized to an itinerant state has been studied with first-principle methods. Our work documents the origin of the flat/steep-band features in the electronic structure of the high-pressure Te-II modification, which are prerequisites for superconductivity. These arguments can also be applied to other elements, for example, bismuth and its transition from semimetal, to metal, to superconductor under pressure[34] and in the amorphous state.[35] A quite general perspective emerges, in that holes can be introduced into lone-pair bands (for example, through chemical doping) to make compounds with lone pairs metallic and even superconducting.

Received: July 29, 2005
Revised: September 8, 2005
Published online: December 19, 2005

Keywords: ab initio calculations · ELF (Electron Localization Function) · high-pressure chemistry · superconductivity · tellurium

[1] a) H. G. Grimm, A. Sommerfeld, *Z. Phys.* **1926**, *36*, 36; b) N. V. Sidgwick, H. M. Powell, *Proc. R. Soc. London Ser. A* **1940**, *176*, 153; c) M. L. Cohen, V. Heine, *Solid State Phys.* **1970**, *24*, 37; d) V. Heine, D. Weaire, *Solid State Phys.* **1970**, *24*, 250.

[2] a) U. Häussermann, P. Berastegui, S. Carlson, J. Haines, J.-M. Léger, *Angew. Chem.* **2001**, *113*, 4760; *Angew. Chem. Int. Ed.* **2001**, *40*, 4624; b) I. Lefebvre, M. A. Szymanski, J. Olivier-Fourcade, J. C. Jumas, *Phys. Rev. B* **1998**, *58*, 1896.

[3] R. J. Gillespie, R. S. Nyholm, *Q. Rev. Chem. Soc.* **1957**, *11*, 339.

[4] a) G. A. Papoian, R. Hoffmann, *Angew. Chem.* **2000**, *112*, 2500; *Angew. Chem. Int. Ed.* **2000**, *39*, 2408; b) A. Ienco, R. Hoffmann, G. Papoian, *J. Am. Chem. Soc.* **2001**, *123*, 2317.

[5] U. Schwarz, H. Hillebrecht, M. Kaupp, K. Syassen, H. G. von Schnering, G. Thiele, *J. Solid State Chem.* **1995**, *118*, 20.

[6] P. Pyykkö, *Chem. Rev.* **1988**, *88*, 563.

[7] a) J. D. Joannopulos, M. Schlüter, M. L. Cohen, *Phys. Rev. B* **1975**, *11*, 2186; b) H. Fukutome, *Prog. Theor. Phys.* **1984**, *71*, 1; c) T. Oka, H. Fukutome, *Prog. Theor. Phys.* **1988**, *79*, 608.

[8] a) Y. Akahama, M. Kobayashi, H. Kawamura, *Phys. Rev. B* **1993**, *47*, 20; b) Y. Akahama, M. Kobayashi, H. Kawamura, *Phys. Rev. B* **1993**, *48*, 6862; c) H. Fujihisa, Y. Akahama, H. Kawamura, H. Yawamaki, M. Sakashita, T. Yamada, K. Honda, T. Le Bihan, *Phys. Rev. B* **2004**, *70*, 134106.

[9] E. Gregoryanz, V. Struzhkin, R. J. Hemley, M. I. Eremets, H.-K. Mao, Y. A. Timofeev, *Phys. Rev. B* **2002**, *65*, 064504.

[10] The energy gaps between the $ns^{1/2}$ and $np^{1/2}$ levels for the respective atoms were obtained from full relativistic calculations based on the local-density approximation (LDA).[10a,b] The values are 10.00, 10.46, and 8.57 eV for sulfur ($n=3$), selenium ($n=4$), and tellurium ($n=5$), respectively. a) J. F. Janak, V. L. Moruzzi, A. R. Williams, *Phys. Rev. B* **1975**, *12*, 1257; b) D. A. Liberman, D. T. Cromer, J. T. Waber, *Comput. Phys. Commun.* **1971**, *2*, 107.

[11] C. Adenis, V. Langer, O. Lindqvist, *Acta Crystallogr. Sect. C* **1989**, *45*, 941.

[12] C. Hejny, M. I. McMahon, *Phys. Rev. B* **2004**, *70*, 184109.

[13] a) A. D. Becke, K. E. Edgecombe, *J. Chem. Phys.* **1990**, *92*, 5397; b) A. Savin, O. Jepsen, O. K. Andersen, H. Preuss, H. G. von Schnering, *Angew. Chem.* **1992**, *104*, 186; *Angew. Chem.* **1992**, *31*, 187; c) B. Silvi, A. Savin, *Nature* **1994**, *371*, 683; d) J. K. Burdett, T. A. McCormick, *J. Phys. Chem. A* **1998**, *102*, 6366.

[14] R. Tank, O. Jepsen, A. Burkhardt, O. K. Andersen, *TB-LMTO-ASA (version 4.7)*, MPI für Festkörperforschung, Stuttgart, Germany, **1998**.

[15] The experimental crystallographic data for Te-I reported in reference [11] were used throughout this work. The "combined correction"[15a] to the atomic-sphere approximation (ASA) was used to obtain more accurate Hamiltonian operators and overlap matrices. The exchange-correlation potential of the density functional theory was calculated according to von Barth and Hedin.[15b] Unless otherwise stated, the relativistic effect was always treated at the level of Darwin and with a mass–velocity correction. All $\boldsymbol{k}$-space integrations were performed with the tetrahedron method, using 3050 irreducible $\boldsymbol{k}$ points.[15c] The tellurium 5s, 5p, 5d, and 5f orbitals were included in the calculations with the 5d and 5f orbitals down-folded, so that they were not included in the basis set. These two orbitals can carry charges without any contribution to the Hamiltonian operators and overlap matrices. To avoid overly large atomic sphere overlap, the interstitial region was filled with empty spheres, for which only the s orbital was included in the basis set. a) O. K. Andersen, *Phys. Rev. B* **1975**, *12*, 3060; b) U. von Barth, L. Hedin, *J. Phys. C* **1971**, *4*, 2064; c) P. Blöchl, O. Jepsen, O. K. Andersen, *Phys. Rev. B* **1986**, *34*, 2439.

[16] The definitions of the respective parameters are the same as those for O in reference [18c]. U_p^0: $E(p^4s^0)+E(p^2s^0)-2E(p^3s^0)$,

 © 2006 Wiley-VCH Verlag GmbH & Co. KGaA, Weinheim

U_p: $E(p^4s^0)+E(p^2s^2)-2E(p^3s^1)$, where the superscript 0 of U denotes the pure parameter.

[17] In an ideal situation, an "impurity" atom imbedded in an infinite crystal needs to be considered. In practice, a supercell of suitable size can often satisfy this requirement. For Te, a supercell which doubles the original unit cell along the c axis was chosen, because the nearest-neighbor distances along the a and b axes are already quite large. This supercell includes the second- and third-nearest neighbors with respect to the impurity tellurium atom, while in many cases it has been found that a supercell which includes only the nearest neighbors is sufficient.[18b,c] U can be calculated as the difference between the total energies of two crystals with different occupancies for the orbital of interest, or calculated by the change in the eigenvalue of the respective orbital [Eq. (1)], where i denotes the orbital of interest of the impurity atom, and ε_F is the Fermi energy introduced to correct the finite supercell effect.[18b] The numbers in parentheses denote the occupancies for the up and down spin states. In our calculations, all tellurium atoms have the same initial electronic configuration ($5s^25p^4$) except for the impurity tellurium atom, for which the occupancy of the 5p orbital is assigned according to Equation (1). The total number of electrons was kept unchanged. The FP-LMTO method (NMTASA code)[17a] with an LDA formula from reference [17b] was used for the calculations. The 5p orbital of the impurity tellurium atom is isolated with respect to the system to avoid double counting and the change of its occupancy. a) S. Y. Savrasov, *Phys. Rev. B* **1996**, *54*, 16470; b) J. F. Janak, V. L. Moruzzi, A. R. Williams, *Phys. Rev. B* **1975**, *12*, 1257.

$$U = \varepsilon_{i\uparrow}(n/2+1/2,n/2)-\varepsilon_{i\uparrow}(n/2+1/2,n/2-1) \\ -\varepsilon_F(n/2+1/2,n/2)+\varepsilon_F(n/2+1/2,n/2-1) \quad (1)$$

[18] a) O. Gunnarsson, O. K. Andersen, O. Jepsen, J. Zaanen, *Phys. Rev. B* **1989**, *39*, 1708; b) V. I. Anisimov, O. Gunnarsson, *Phys. Rev. B* **1991**, *43*, 7570; c) A. K. McMahan, R. M. Martin, S. Satpathy, *Phys. Rev. B* **1988**, *38*, 6650.

[19] S. Fraga, J. Karwowski, K. M. S. Saxena, *Atomic energy levels, Vol. 4*, Elsevier, New York, **1979**.

[20] For solid Te-I, the 6s and 5d orbitals are treated as bands. Thus, the change in the number of conduction electrons owing to the variation of the occupancy of the "impurity" Te-5p orbital can be accommodated by the whole crystal. The occupancies of all orbitals in the atom are fixed. Therefore, the dynamic effects of the screening are fully neglected in the calculations.

[21] For the TB-LMTO-ASA calculations on Te-I, we used the same parameters as in reference [15]. However, the code was changed to let the crystallographic c axis coincide with the z axis of the Cartesian system and to let the a axis be in the xz plane. This change was made to allow a better comparison with the electronic structure of tellurium under pressure. For the FP-LMTO (NMTPLW code) calculations on Te-I,[17a] a 2κ–5s, 5p, 5d basis set was used for the valence states of Te, while the 4d state was treated as a semicore state. In the interstitial region, the pseudo-LMTOs were expanded in plane waves up to 10.2, 15.4, and 22.0 Ryd (388, 708, and 1204 plane waves) for the 5s, 5p, and 5d orbitals, respectively. An $18\times18\times18$ $\boldsymbol{k}$ mesh was used in the self-consistent calculations for the energy states. The general-gradient approximation (GGA)[21a] was used to correct the LDA of reference [17b]. a) J. P. Perdew, Y. Wang, *Phys. Rev. B* **1992**, *45*, 13244.

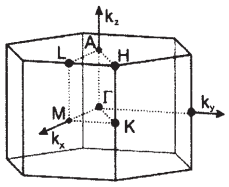
[22] The crystallographic data for Te-II were taken from reference [12]. However, since the original unit cell setting was nonstandard, we transformed it into a standard one. The final unit cell parameters are $a=776.07$, $b=780.29$, $c=735.77$ pm, $\alpha=156.66$, $\beta=148.42$, $\gamma=45.75°$. The atomic coordinates were also transformed accordingly. In this setting, the helical chain of tellurium atoms runs along the c axis, as it does in Te-I. For the TB-LMTO calculations on Te-II, an $18\times18\times18$ $\mathbf{k}$ mesh was chosen. The other parameters were chosen as for Te-I (see reference [15]). For the FP-LMTO calculations on Te-II, the pseudo-LMTOs were expanded in plane waves up to 8.54, 12.4, and 18.1 Ryd. (240, 412, and 722 plane waves) for the 5s, 5p, and 5d orbitals of Te1, respectively, while for Te2, the pseudo-LMTOs were expanded in plane waves up to 10.0, 14.6, and 21.4 Ryd. (286, 536, and 946 plane waves) for the 5s, 5p, and 5d orbitals, respectively.

[23] The calculated compositions for some band states are $\psi(H1)=$ 95.5 % Te(5s) + 4.14 % Te(5p) + 0.36 % Te(5d); $\psi(H5)=$ 1.12 % Te(5s) + 96.88 % Te(5p) + 1.99 % Te(5d); $\psi(H9)=$ 4.31 % Te(5s) + 93.16 % Te(5p) + 2.53 % Te(5d); $\psi(H10)=$ 3.42 % Te(5s) + 88.17 % Te(5p) + 8.41 % Te(5d).

[24] The very good agreement between the TB-LMTO band gap and the experimental value seems accidental, because LDA often underestimates the band gap. Moreover, our FP-LMTO method gives a band gap of only 0.247 eV.

[25] C. B. à la Guillaume, J. M. Debever, *Solid State Commun.* **1965**, *3*, 19.

[26] Brillouin zone for Te-I and Te-II:



[27] a) G. Doerre, J. D. Joannopoulos, *Phys. Rev. Lett.* **1979**, *43*, 1040; b) Y. Shimoi, H. Fukutome, *Prog. Theor. Phys.* **1992**, *87*, 307.

[28] R. Dronskowski, P. E. Blöchl, *J. Phys. Chem.* **1993**, *97*, 8617.

[29] A. Decker, G. A. Landrum, R. Dronskowski, *Z. Anorg. Allg. Chem.* **2002**, *628*, 295.

[30] a) A. Simon, *Angew. Chem.* **1997**, *109*, 1872; *Angew. Chem. Int. Ed. Engl.* **1997**, *36*, 1788; b) S. Deng, A. Simon, J. Köhler, *Angew. Chem.* **1998**, *110*, 664; *Angew. Chem. Int. Ed.* **1998**, *37*, 640; c) S. Deng, A. Simon, J. Köhler, *Struct. Bonding (Berlin)* **2005**, *114*, 103.

[31] a) F. P. Bundy, K. J. Dunn, *Phys. Rev. Lett.* **1980**, *44*, 1623; b) Y. Akahama, M. Kobayashi, H. Kawamura, *Solid State Commun.* **1992**, *84*, 803.

[32] S. Deng, A. Simon, J. Köhler, *Solid State Sci.* **2000**, *2*, 31.

[33] R. Micnas, J. Ranninger, S. Robaszkiewwicz, *Rev. Mod. Phys.* **1990**, *62*, 113.

[34] M. A. Il'ina, E. S. Itskevich, E. M. Dizhur, *Sov. Phys.-JETP* **1972**, *34*, 1263.

[35] a) J. S. Moodera, R. Meservey, *Phys. Rev. B* **1990**, *42*, 179; b) T. T. Chen, J. T. Chen, J. D. Leslie, H. J. T. Smith, *Phys. Rev. Lett.* **1969**, *22*, 526.

 © 2006 Wiley-VCH Verlag GmbH & Co. KGaA, Weinheim

Single-Molecule Studies

DOI: 10.1002/anie.200502229

Reversible *cis–trans* Isomerization of a Single Azobenzene Molecule**

*Jörg Henzl, Michael Mehlhorn, Heiko Gawronski, Karl-Heinz Rieder, and Karina Morgenstern**

Since isomers may differ substantially in physical and chemical properties, isomerization offers the possibility of converting less desirable compounds into isomers with desirable properties. The isomerization of dye molecules, such as derivatives of azobenzene ($C_6H_5N{=}NC_6H_5$), has attracted much attention owing to the high potential of these compounds for applications in optoelectronic devices, for example, optical memory, photooptical switches, and displays.[1] Azobenzene has been used as a photoregulator to form or dissociate a duplex that regulates the geometry and function of biomolecules.[2] Azobenzene undergoes a reversible light-induced conformational transition of the N–N double bond between an extended (*trans*) and a compact (*cis*) conformation in the gas phase and in solution.[1] In nature, specific functions are frequently realized with the aid of such *cis–trans* isomerization reactions of molecules. Here we describe the *cis–trans* isomerization of individual molecules of the azobenzene derivative Disperse Orange 3 on Au(111) triggered by tunneling electrons. Inducing chemical reactions of specific single molecules is one intriguing aspect. In a more general context, the understanding and control of molecular functions on a single-molecule level is essential in nanoscale science.[3]

The photoswitching of fluorescence properties of single molecules observed with single-molecule spectroscopy has developed rapidly in recent years.[4] The controlled displacement of parts of a molecule might be of further interest for future molecule-based electronic devices.[5] It has been proposed based on calculations that an azobenzene molecule between two gold electrodes can serve as a switch operable at room temperature.[6] This integration of molecules into larger circuits is hardly imaginable without their arrangement on surfaces. However, it is not immediately obvious whether steric hindrance, surface bonding, or alternative mechanisms of relaxation prevent the *cis–trans* isomerization of molecules in direct contact with metal surfaces.

Disperse Orange 3 (NH_2-C_6H_4-N=N-C_6H_4-NO_2; structure shown in the inset in Figure 1a) is an azobenzene derivative with two substituents, NO_2 and NH_2. From adsorption experiments of substituted benzenes in connection with tight-binding calculations[7] we expect the substituents to dominate the scanning tunneling microscopy (STM) image of the molecule. Thus we could identify dimers (four protrusions, D) and monomers (two protrusions, M) in the STM image (Figure 1a). This assignment is corroborated by electron-induced dissociation of a dimer into two monomers (at 2.1 V; Figure 1b). While the monomers in Figure 1a are straight, those in Figure 1b are bent. This immediately suggests that the former are in the *trans* form, while the latter are in the *cis* form.

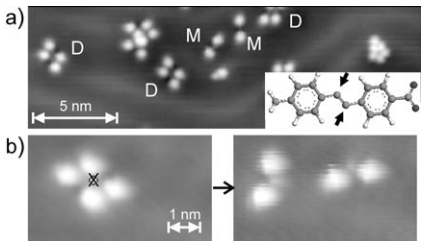


Figure 1. Disperse Orange 3 on Au(111): a) Large-scale image after deposition of 0.05 molecules nm^{-2} on Au(111) at 230 K; dimers are marked with D, monomers with M; tunneling parameters: $U = 228$ mV, $I = 11$ pA. Inset: Ball-and-stick model of the molecule; arrows point to lone-pair orbitals. b) Dissociation of a dimer into two monomers by application of 2.1 V for 200 ms; the position of the tip is indicated with a cross; left: before manipulation; right: after manipulation. $U = 337$ mV, $I = 9.4$ pA.

By placing the STM tip above a molecule, we could transfer energy into the molecule by means of inelastically tunneling electrons. The resulting excitation of specific chemical bonds may lead to rotation or translation of small molecules,[8] to desorption,[9] to selective bond breaking,[10] to dissociation within an assembly,[11] to polymerization (both tip-induced and photoinduced),[13] or to the separation of hydrogen-bonded molecules, as demonstrated in Figure 1b. Here, we use the same method to show for the first time that the reversible electron-induced *cis–trans* isomerization of a single molecule is feasible.

In Figure 2a–c some images are shown of a monomer that was switched successfully more than 70 times between three configurations—two bent forms and one elongated form. A steep change in the tunneling current (Figure 2d) indicates the success of the manipulation, and the manipulation yield per electron can be calculated for different electron energies (Figure 2e). The threshold is 650 meV for changes from the elongated (*trans*) and ≤ 640 meV from the bent (*cis*) configuration. The different threshold voltages are indicative of changes to the electronic structure of the molecule upon isomerization. These voltages lie far below the photoisomerization voltages of azobenzene in the gas phase, which correspond to irradiation with ultraviolet ($\lambda \approx 350$ nm;

[*] Prof. K. Morgenstern
Institut für Festkörperphysik Abteilung Oberflächen
Universität Hannover
Appelstrasse 2, 30167 Hannover (Germany)
Fax: (+49) 511-762-4877
E-mail: morgenstern@fkp.uni-hannover.de
J. Henzl, M. Mehlhorn, H. Gawronski, Prof. K.-H. Rieder
Institut für Experimentalphysik, FB Physik
Freie Universität Berlin
Arnimallee 14, 14195 Berlin (Germany)

[**] We acknowledge financial support from the VolkswagenStiftung within the program "Physik, Chemie und Biologie mit Einzelmolekülen".

 © 2006 Wiley-VCH Verlag GmbH & Co. KGaA, Weinheim

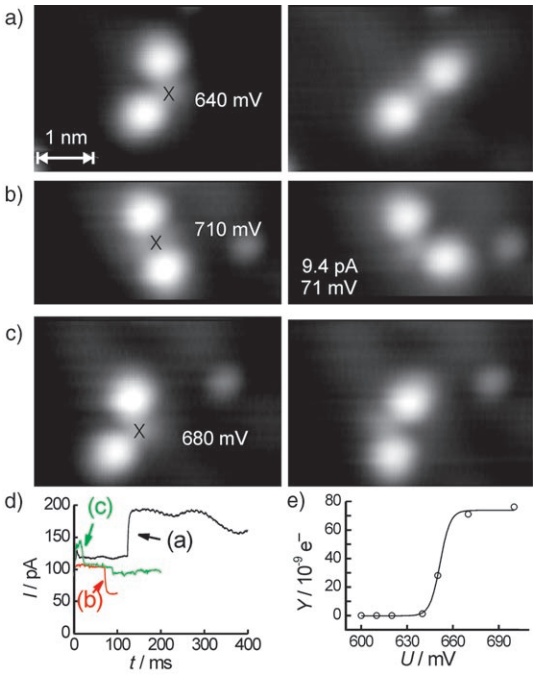


Figure 2. Isomerization of an azobenzene derivative: a–c) Images recorded of a molecule that was switched with indicated electron energy; left column: before manipulation, electrons are injected with indicated bias voltage at the position marked with a cross; right column: after manipulation. $U = 71$ mV, $I = 9.4$ pA. d) Plot of the current during the manipulations (a)–(c); sharp changes are indicative of the conductance change during isomerization. e) Plot of the isomerization yield Y vs. bias voltage V for *trans–cis* isomerization or for diffusion which is also induced.

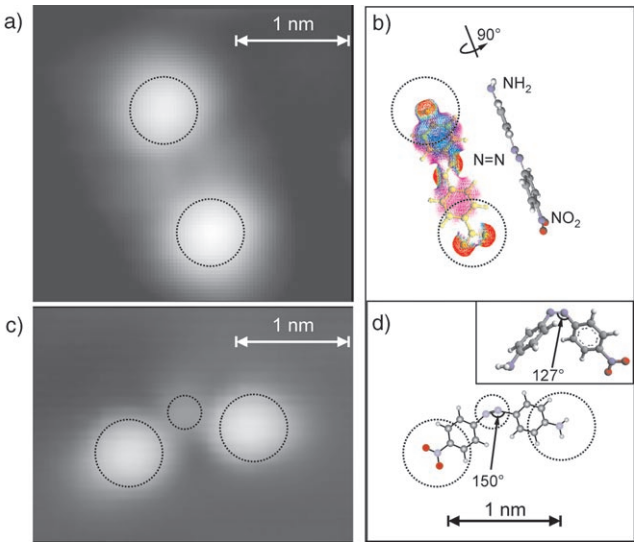


Figure 3. High-resolution images and structural formula of the monomer. a) STM image of the *trans* isomer; $U = 71$ mV, $I = 9.4$ pA. b) Ball-and-stick model of the *trans* isomer as optimized in the gas phase with ArgusLab 4.0;[19] the ESP density is indicated in color: red indicates areas of high electron density. c) STM image of the *cis* isomer; $U = 337$ mV, $I = 9.4$ pA. d) Ball-and-stick model of the *cis* isomer on the surface as deduced from the STM image; correspondence of functional groups to circles is extracted from (b); inset: *cis* isomer in the gas phase as optimized with ArgusLab 4.0;[19] dashed circles are identical in (a) and (b), and in (c) and (d).

3.55 eV) and blue ($\lambda \approx 440$ nm; 2.82 eV) light for the isomerization from the stable *trans* configuration and metastable *cis* configuration, respectively.[1] This suggests that the isomerization is not due to excitation into the S_1 state of the molecule as in photoisomerization but is induced in the ground state. In the ground electronic state, the energy of the *trans*-azobenzene is 0.6 eV lower than the energy of the *cis* structure,[12] and they are separated by an energy barrier of approximately 1.6 eV (measured from *trans* to *cis*).[14] This value is still far more than the excitation energy in our experiment.

To understand the isomerization in more detail, we need to identify the different parts of the molecules, which is possible with the high resolution of our STM. Figure 3 shows the two types of monomers in submolecular resolution along with ball-and-stick models. In STM images of the *trans* molecule (Figure 3a) we observe a weak increase in intensity between the two dominant protrusions, which are 1.15 nm apart. In the gas phase the equilibrium structure of the molecule is almost planar (Figure 3b). This geometry is favorable for adsorption on metal surfaces, because the adsorption of aromatic π systems parallel to the surface is energetically preferred. Comparison to the molecular structure calculated in the gas phase (see Figure 3b) shows that the maxima of the larger protrusions are centered above the nitrogen atoms of the NH_2 and NO_2 substituents (cf. Ref.[9]); the increase in intensity between these protrusions is indicative of the N–N double bond. The high negative density in the electrostatic potential (ESP) corresponds to protrusions in our STM image.

A planar molecular structure in the *cis* configuration is complicated by the steric repulsion of the phenyl groups. In the gas phase, the molecule circumvents this problem by rotating the phenyl groups around the N–C bond (see inset in Figure 3d). The STM images of the *cis* isomers do not correspond to this nonplanar molecule (Figure 3c). Alternative to rotational relaxation, an increase in the bond angle could minimize steric hindrance while allowing the phenyl groups to assume the energetically preferred planar adsorption geometry. Based on the relationship of the protrusions to the molecular structure as identified in the *trans* configuration (Figure 3a,b), we deduce that the STM image of the molecule in Figure 3c corresponds to the modified geometry shown in Figure 3d. Thus, we find that the bond angle is increased from 127° in the gas phase to ≈150° on the surface. This allows both phenyl groups to lie in parallel to the surface. The increased bond angle indicates a partial charge transfer from the molecule to the metal. Either the partial charge is transferred from the lone pair or the double bond is weakened. This in turn suggests that the azo group is adsorbed on a on-top place. Thus it has surface contact.

Based on the structural model, the isomerization shown in Figure 2 can be interpreted as an conversion from a planar *cis* to the *trans* configuration (Figure 2a) and vice versa (Figure 2b). Azobenzene bears lone-pair orbitals at the nitrogen atoms of the N–N double bond. Therefore, isomerization might be result from rotation around the N–N double bond or the inversion of one of the N–C bonds with the lone pair of

 © 2006 Wiley-VCH Verlag GmbH & Co. KGaA, Weinheim

the nitrogen. Rotation seems unlikely for a molecule adsorbed on a surface. Furthermore, calculations have shown that inversion is the preferred pathway for the ground-state isomerization in the gas phase.[15] We also exclude the so-called hula–twist pathway, which has been suggested for the *cis–trans* isomerization of the retinal chromophore within its limited volume[16] and observed recently for stilbene,[17] because this necessitates an energetically unfavorable vertical displacement of a phenyl group. We thus interpret the observed isomerization as an inversion of one of the N–C bonds with the lone pair of the nitrogen. In addition, inversion of both N–C bonds simultaneously leads to a switching from one *cis* to another mirror-symmetric *cis* configuration (Figure 2c). The increased bond angle of the molecule in connection with chemisorption to the surface lowers the activation barrier to 650 meV, as compared to 1.6 eV in the gas phase value. Vibrational modes that are likely to be involved in the inversion are NNC bending modes, both in-plane and out-of-plane. These lie below 65 meV in energy[18] and are thus in the range of typical external vibrational modes of aromatic molecules which are responsible for induced diffusion. Thus, modes with similar energy for one vibrational quantum are responsible for both the observed isomerization and diffusion. The high activation energy suggests an excitation to a highly excited state of $\nu \approx 10$. As we are able to induce the isomerization with these energies only when the tip is in close proximity to the N=N group, it is possible that the primary excited mode is a N=N stretching mode at $\approx$180–190 meV.[18]

The images in Figure 4 supports the interpretation given in the previous paragraph. In this experiment electron-induced manipulation was used to fix a molecule of Disperse Orange 3 (upper two protrusions) to two other (NO_2- or NH_2-) substituted benzene molecules. By using electrons with energies above the gas-phase barrier, the molecule isomerizes from a bent (Figure 4a) to an elongated form (Figure 4b) and then to a differently bent form (Figure 4c). This form shows a much smaller angle, and the left part of the molecule is unstable under imaging conditions, indicating a three-dimensional relaxation. Again, this isomerization is reversible (Figure 4c,d).

To complete the picture we return to the dimers in Figure 1a. A high-resolution image shows that the dimer consists of two planar *cis* molecules and that the the two N=N groups are in close proximity (Figure 5a). The structural

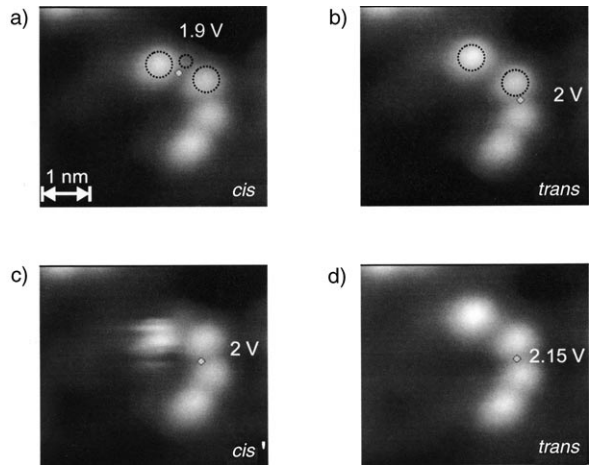


Figure 4. Isomerization of an azobenzene derivative covalently connected to other (NO_2- or NH_2-)substituted benzene units: a)–d) sequence of four manipulations (indicated voltage was applied for 200 ms). At this resolution only the end groups are clearly visible and the position of the molecule is indicated clearly in (a) and (b). In (c) the position of the *cis* isomer is less clear since the unbound group (left protrusion) moves during scanning.

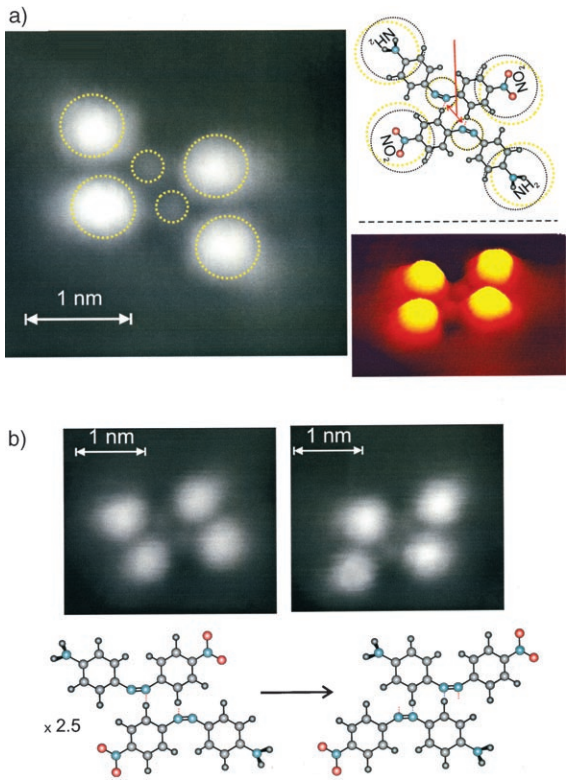


Figure 5. High-resolution STM images and ball-and-stick model for the dimer and conformational change due to hydrogen rearrangement: a) STM image of the dimer ($U = 10$ mV, $I = 20$ pA), corresponding ball-and-stick model, and a 3D view of a different, mirror-symmetric dimer ($U = 10$ mV, $I = 200$ pA); yellow circles in the model are taken from the STM image; monomers including black circles are taken directly from Figure 3d; red arrow points to the two hydrogen bonds; dashed line indicates the mirror plane. b) Conformational change of the dimer demonstrating the change in the relative position of the N=N groups ($U = 6$ mV, $I = 8.5$ pA); ball-and-stick model showing the change in the relative orientation of the molecule and the corresponding change in the hydrogen bonds.

model superimposed over the maxima in the STM image reveals that these dimers are stabilized by two hydrogen bonds to the lone pairs of the nitrogen atoms with a hydrogen-bond length of 230 pm. Two mirror-symmetric dimmers exist (compare 2D to 3D image in Figure 5a). Isomerization of molecules within the dimer is sterically obstructed and indeed was not possible at any voltage below the dissociation voltage of the dimer (see Figure 1b). Electron injection leads to a change in relative positions of the two molecules. The high-

 © 2006 Wiley-VCH Verlag GmbH & Co. KGaA, Weinheim

resolution images of the two conformations (Figure 5b) show that before the manipulation the N=N group of the upper molecule lies to the left of the N=N group of the lower molecule, and after the manipulation, vice versa. Thus, the relative orientation of the two molecules through a rearrangement of the hydrogen bonds between two molecules was achieved (see ball-and-stick model). This conformational change is also reversible and it is bistable.

In summary, we have shown that controlled *cis–trans* isomerization of a single molecule on a metal surface is feasible by tunneling electrons. However, even on weakly interacting surfaces such as Au(111) the potential energy surface of this isomerization is not the same as in the gas phase. For the azobenzene derivative Disperse Orange 3, isomerization is based on inversion and occurs in the ground state.

Experimental Section

Au(111) was cleaned by repeated cycles of Ne^+ sputtering and annealing to 800 K. Disperse Orange 3 was dosed from a Knudsen cell onto the surface held at 230 K. The sample was then transferred to a custom-built low-temperature STM, which was operated at 5 K for this measurement. All preparations, transfers, and measurements took place in a home-built ultra-high-vacuum system with a base pressure below 5×10^{-10} mbar.

Received: June 24, 2005
Revised: October 14, 2005
Published online: December 13, 2005

Keywords: isomerization · scanning probe microscopy · single-molecule studies · surface chemistry

[1] a) T. Ikeda, O. Tsutsumi, *Science* **1995**, *268*, 1873 – 1875; b) N. Tamai, H. Miyasaka, *Chem. Rev.* **2000**, *100*, 1875 – 1890.
[2] a) H. Asanuma, T. Takarada, T. Yoshida, D. Tamaru, X. Liang, M. Komiyama, *Angew. Chem.* **2001**, *113*, 2743 – 2745; *Angew. Chem. Int. Ed.* **2001**, *40*, 2671 – 2673, ; b) H. Asanuma, T. Itoa, T. Yoshida, D. Tamaru, X. Liang, M. Komiyama, *Angew. Chem.* **1999**, *111*, 2547 – 2549; *Angew. Chem. Int. Ed.* **1999**, *38*, 2393 – 2395.
[3] a) J. K. Gimzewski, C. Joachim, *Science* **1999**, *283*, 1683 – 1688; b) Z. J. Donhauser, B. A. Mantooth, K. F. Kelly, L. A. Bumm, J. D. Monnell, J. J. Stapleton, D. W. Price, Jr., A. M. Rawlett, D. L. Allara, J. M. Tour, P. S. Weiss, *Science* **2001**, *292*, 2303 – 2307; c) A. J. Heinrich, C. P. Lutz, J. A. Gupta, D. M. Eigler, *Science* **2002**, *298*, 1381 – 1387.
[4] a) R. M. Dickson, A. B. Cubitt, R. Y. Tsien, W. E. Moerner, *Nature* **1997**, *388*, 355 – 358; b) M. Irie, T. Fukaminato, T. Sasaki, N. Tamai, T. Kawai, *Nature* **2002**, *420*, 759 – 760; c) T. Fukaminato, T. Sasaki, T. Kawai, N. Tamai, M. Irie, *J. Am. Chem. Soc.* **2004**, *126*, 14843 – 14849; d) S. Habuchi, R. Ando, P. Dedecker, W. Verheijen, H. Mizumo, A. Miyawaki, J. Hofkens, *Proc. Natl. Acad. Sci. USA* **2005**, *102*, 9511 – 9516.
[5] C. Joachim, J. K. Gimzewski, A. Aviram, *Nature* **2000**, *408*, 541 – 548.
[6] C. Zhang, M.-H. Du, H.-P. Cheng, X.-G. Zhang, A. E. Roitberg, J. L. Krause, *Phys. Rev. Lett.* **2004**, *92*, 158301.
[7] J. Nieminen, E. Niemi, V. Simic-Milosevic, K. Morgenstern, *Phys. Rev. B* **2005**, *72*, 195421.
[8] a) W. Ho, *J. Chem. Phys.* **2002**, *117*, 11033 – 11061; b) T. Komeda, Y. Kim, M. Kawai, B. N. J. Persson, H. Ueba, *Science* **2002**, *295*, 2055 – 2058.
[9] J. I. Pascual, N. Lorente, Z. Song, H. Conrad, H.-P. Rust, *Nature* **2003**, *423*, 525 – 528.
[10] S.-W. Hla, L. Bartels, G. Meyer, K. H. Rieder, *Phys. Rev. Lett.* **2000**, *85*, 2777 – 2780.
[11] K. Morgenstern, K. H. Rieder, *Chem. Phys. Lett.* **2002**, *358*, 250 – 256.
[12] F. W. Schulze, H. J. Petrick, H. K. Cammenga, H. Klinge, *Z. Phys. Chem. Neue Fol.* **1977**, *107*, 1 – 4743.
[13] A. Miuara, S. De Feyter, M. M. S. Abdel-Mottaleb, A. Gequiere, P. C. M. Grim, G. Moessner, M. Sieffert, M. Klapper, K. Müllen, F. C. De Schryver, *Langmuir* **2003**, *19*, 6474 – 6482.
[14] E. R. Talaty, J. C. Fargo, *Chem. Commun.* **1967**, *2*, 65 – 66.
[15] P. Cattaneo, M. Persico, *Phys. Chem. Chem. Phys.* **1999**, *1*, 4739 – 4743.
[16] R. S. H. Liu, D. T. Browne, *Acc. Chem. Res.* **1986**, *19*, 42 – 48.
[17] W. Fuß, C. Kosmidis, W. E. Schmid, S. A. Truslin, *Angew. Chem.* **2004**, *116*, 4273 – 4277; *Angew. Chem. Int. Ed.* **2004**, *43*, 4178 – 4182.
[18] a) D. R. Armstrong, J. Clarkson, W. E. Smith, *J. Phys. Chem.* **1995**, *99*, 17825 – 17831; b) N. Biswas, S. Umapathy, *J. Phys. Chem. A* **1997**, *101*, 5555 – 5566.
[19] M. A. Thomson, ArgusLab 4.0, Planaria Software, LCC, Seattle, WA, www.arguslab.com.

 © 2006 Wiley-VCH Verlag GmbH & Co. KGaA, Weinheim

Exchange Reactions

DOI: 10.1002/anie.200501882

Functionalized Benzylic Magnesium Reagents through a Sulfur–Magnesium Exchange**

*Armin H. Stoll, Arkady Krasovskiy, and Paul Knochel**

The preparation of benzylic magnesium compounds has been studied extensively because of the high reactivity and synthetic utility of these reagents.[1] Although the direct insertion of magnesium into benzylic bromides is possible, the formation of Wurtz homocoupling products complicates this approach, especially when electron-rich benzylic halides are used as substrates. Herein, we report the preparation of functionalized benzylic magnesium reagents by using a new sulfur–magnesium exchange reaction.[2,3] We prepared *o*-(*o*-

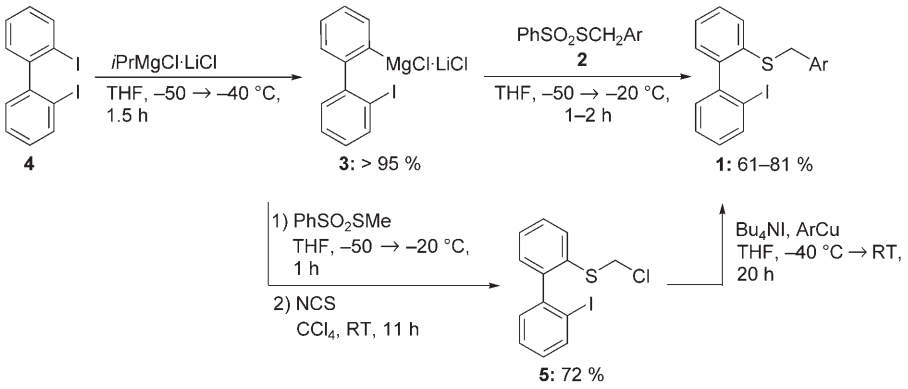
[*] Dipl.-Chem. A. H. Stoll, Dr. A. Krasovskiy, Prof. Dr. P. Knochel
Department Chemie, Ludwig-Maximilians-Universität München
Butenandtstrasse 5–13, Haus F, 81377 München (Germany)
Fax: (+49) 89-2180-77680
E-mail: paul.knochel@cup.uni-muenchen.de

[**] We thank the Fonds der Chemischen Industrie, the Deutsche Forschungsgemeinschaft (DFG), and the Merck Research Laboratories (MSD) for financial support. We also thank Chemetall GmbH (Frankfurt) and BASF AG (Ludwigshafen) for generous gift of chemicals.

Supporting information for this article is available on the WWW under http://www.angewandte.org or from the author.

WILEY InterScience DISCOVER SOMETHING GREAT
© 2006 Wiley-VCH Verlag GmbH & Co. KGaA, Weinheim

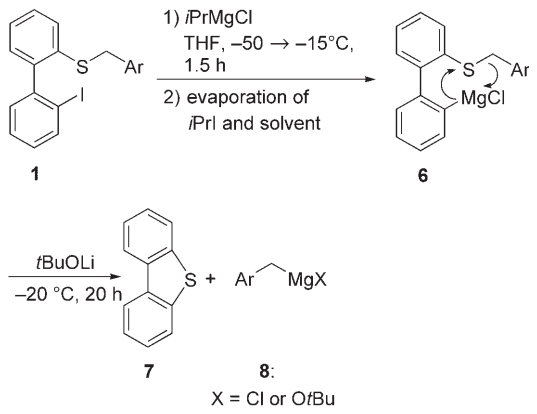
iodophenyl)phenylthio derivatives[4] of type **1** because a range of functionalized benzylic derivatives are readily available through the reaction of thiosulfonates **2** with the monomagnesium derivative **3** of 2,2′-diiodobiphenyl (**4**) (Scheme 1).[5,6]



Scheme 1. Preparation of benzylic *o*-(*o*-iodophenyl)phenylthio derivatives **1** with thiosulfonates **2**, or through chloromethyl thioether **5** and aryl copper derivatives. NCS = *N*-chlorosuccinimide

The required thiosulfonates **2** were prepared either by the reaction of $PhSO_2Na$ with disulfides[7] or by the reaction of $PhSO_2SNa$ with various benzylic halides in *N*,*N*-dimethylformamide[8] (see Supporting Information). Alternatively, the benzylic *o*-(*o*-iodophenyl)phenylthio derivatives **1** can also be synthesized from **4** through the two-step preparation of the chloromethyl thioether **5**, which was obtained in 72% overall yield.[9] Treatment of **5** with various aryl copper derivatives (ArCu, 1.5 equiv; −40 °C→RT, 20 h), in the presence of Bu_4NI (1.0 equiv), directly produces the benzylic thioethers **1** in satisfactory yields.

The reaction of the aryl iodide **1** with *i*PrMgCl (1.1 equiv) at −50→−15 °C affords the expected I/Mg exchange product **6**. Remarkably, the treatment of the aryl magnesium derivative **6** with *t*BuOLi (0.1–1.0 equiv)[10] triggers a new intramolecular sulfur–magnesium exchange reaction that leads to the stable heterocycle **7** and to the benzylic magnesium reagents **8** after approximately 20 h at −20 °C (Scheme 2). Evaporation of the solvent and *i*PrI before the addition of



Scheme 2. Preparation of functionalized benzylic magnesium derivatives by using an intramolecular S/Mg exchange reaction.

*t*BuOLi improves the yields by avoiding alkylation side reactions.

The role of *t*BuOLi may be explained tentatively through the assumption of the formation of a magnesiate intermediate ($ArMg(OtBu)Cl^-Li^+$), which has a more reactive carbon–magnesium bond and initiates the sulfur–magnesium exchange. Thus, the reaction of *o*-(*o*-iodophenyl)phenyl benzyl thioether (**1a**) with *i*PrMgCl (1.1 equiv; −50→−20 °C, 1.5 h) followed by evaporation of the solvent (10^{-1} mmHg, 25 °C, 2 h), redissolution in THF, and addition of *t*BuOLi (1.0 equiv; −20 °C, 20 h) provide the benzylic magnesium derivative **8a**. Subsequent reaction with various electrophiles such as benzaldehyde, pivaldehyde (Table 1, entries 1 and 2), 6-bromo-1-methoxycyclohexene (Table 1, entry 3), benzoyl chloride, and cyclohexanecarbonyl chloride (Table 1, entries 4 and 5) lead to the expected products **9a** (75%), **9b** (85%), **9c** (82%), **9d** (90%), and **9e** (78%), respectively, in excellent yields.

The reaction with acid chlorides requires successive transmetalation of the benzylic magnesium reagent **8a** with $ZnCl_2$ and $CuCN{\cdot}2\,LiCl$[11] to avoid homocoupling of the sensitive benzylic copper intermediate that is obtained by direct transmetalation from **8a**. Interestingly, the sulfur–magnesium exchange reactions of substrates **1** in which the benzylic moiety bears electron-withdrawing substituents such as bromine, chlorine, or trifluoromethyl groups (Table 1, entries 6–13, **8b–f**) do not need the addition of *t*BuOLi and are complete within a few hours. Electron-donating groups, such as the methoxy group, are compatible with the S–Mg exchange reaction and lead to benzylic magnesium species such as **8g** (Table 1, entries 14 and 15). The reaction with electrophiles such as pivaldehyde and benzoyl chloride lead to the expected products **9n** (95%) and **9o** (81%). Interestingly, the benzylic magnesium reagent can also be generated in the presence of an electrophile (Barbier conditions). Thus, treatment of the biphenyl derivative **1h** with *i*PrMgCl (1.05 equiv, -50→10 °C) in the presence of an electrophile (a nitrile such as 4-bromobenzonitrile (0.9 equiv) or an alkyl iodide such as butyl iodide (2.0 equiv)) leads to the desired products **9p** (79%) and **9q** (90%), respectively (Scheme 3).

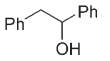
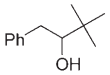
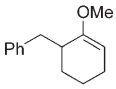
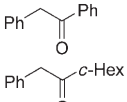
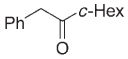
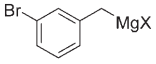
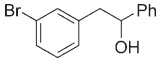
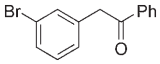
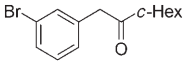
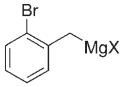
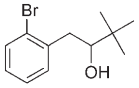
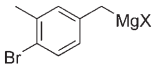
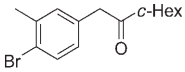
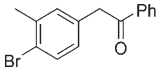
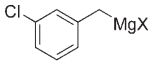
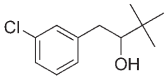
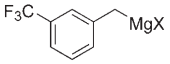
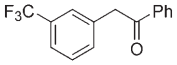
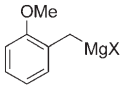
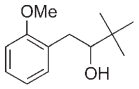
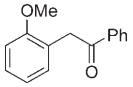
In summary, we have developed a new synthesis of functionalized benzylic magnesium compounds by using a novel sulfur–magnesium exchange reaction. Extensions of this method to the preparation of other magnesium reagents are currently underway in our laboratory.

Experimental Section

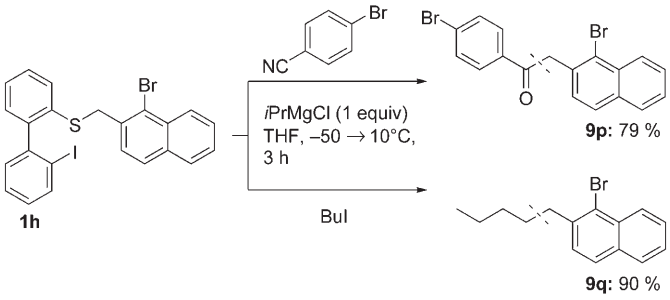
Typical procedure (**9n**): A dry and argon-flushed 50-mL Schlenk flask, equipped with a magnetic stirring bar and a septum, was charged with 2′-iodo-2-(2-methoxybenzylsulfanyl)biphenyl (**1g**) (216 mg, 0.50 mmol) and THF (1 mL). The solution was cooled to

 © 2006 Wiley-VCH Verlag GmbH & Co. KGaA, Weinheim

Table 1: Products of type **9** obtained by the reaction of benzylic magnesium derivatives through a S/Mg exchange.

Entry	Benzylic Mg reagent[a]		Electrophile	Product **9**		Yield [%][b]
1	$PhCH_2MgX$	**8a**	PhCHO		**9a**	75
2		**8a**	*t*BuCHO		**9b**	85
3		**8a**			**9c**	82
4		**8a**	PhCOCl		**9d**	90[c]
5		**8a**	*c*-HexCOCl		**9e**	78[c]
6		**8b**	PhCHO		**9f**	89
7		**8b**	PhCOCl		**9g**	82[c]
8		**8b**	*c*-HexCOCl		**9h**	80[c]
9		**8c**	*t*BuCHO		**9i**	81
10		**8d**	*c*-HexCOCl		**9j**	81[c]
11		**8d**	PhCOCl		**9k**	86[c]
12		**8e**	*t*BuCHO		**9l**	70
13		**8f**	PhCOCl		**9m**	89[c]
14		**8g**	*t*BuCHO		**9n**	95
15		**8g**	PhCOCl		**9o**	81[c]

[a] X = Cl or O*t*Bu. [b] Yield of isolated analytically pure compound. [c] Reaction performed after the successive addition of $ZnCl_2$ (1 equiv) and CuCN·2 LiCl (1 equiv).



Scheme 3. Reaction of benzylic *o*-(*o*-iodophenyl)phenylthio derivative **1h** with *i*PrMgCl under Barbier conditions.

−50 °C, and *i*PrMgCl (0.58 mL, 0.55 mmol, 0.95 M in THF) was added slowly through a syringe. The reaction mixture was then immediately concentrated (10^{-1} mmHg, 25 °C, 1 h). The resultant white precipitate was dissolved in THF (2 mL) and concentrated again as described above. THF (1.5 mL) was used to dissolve the residue a second time, and completion of the I–Mg exchange was checked by GC analysis with tetradecane as an internal standard. A solution of *t*BuOLi (0.50 mL. 0.50 mmol, 1.0 M in THF) was then added at −15 °C, and the mixture was stirred for 18 h at −5 °C to give the benzylic magnesium reagent **8g**. The reaction mixture was cooled to −20 °C and pivaldehyde (35 mg, 0.40 mmol) was added. After additional stirring 40 min at this temperature the reaction mixture was quenched with water (100 mL), extracted with Et_2O (3 × 150 mL), and dried over Na_2SO_4. After filtration, the solvent was evaporated in vacuo. Purification by flash chromatography (pentane/Et_2O = 5:1) yielded **9n** (79 mg, 95 %) as a colorless oil.

Received: May 31, 2005
Revised: August 25, 2005
Published online: December 15, 2005

 © 2006 Wiley-VCH Verlag GmbH & Co. KGaA, Weinheim

Keywords: benzylic organometallic compounds · cross-coupling · fragmentation · Grignard reaction · organocopper compounds

[1] a) T. R. van den Ancker, C. L. Raston, *Organometallics* **1995**, *14*, 584; b) T. Alonso, S. Harvey, P. C. Junk, C. L. Raston, B. Skelton, A. H. White, *Organometallics* **1987**, *6*, 2110; c) H. Appler, L. W. Gross, B. Mayer, W. P. Neumann, *J. Organomet. Chem.* **1985**, *291*, 9; d) J. Scholz, K.-H. Thiele, *J. Organomet. Chem.* **1986**, *314*, 7; e) R. D. Rieke, *Acc. Chem. Res.* **1977**, *10*, 301; f) S. Harvey, C. L. Raston, *J. Chem. Soc. Chem. Commun.* **1988**, 652; g) L. M. Engelhardt, S. Harvey, C. L. Raston, A. H. White, *J. Organomet. Chem.* **1988**, *341*, 39; h) T. M. Nicoletti, C. L. Raston, M. V. Sargent, *J. Chem. Soc. Chem. Commun.* **1990**, 133; i) H. J. R. de Boer, O. S. Akkerman, F. Bickelhaupt, *J. Organomet. Chem.* **1987**, *321*, 291; j) T. R. van den Ancker, S. Harvey, C. L. Raston, *J. Organomet. Chem.* **1995**, *502*, 35; k) S. Harvey, P. C. Junk, C. L. Raston, G. Salem, *J. Org. Chem.* **1988**, *53*, 3134.

[2] The sulfoxide–magnesium exchange reaction is well known and especially useful for the preparation of new magnesium carbenoids; see: a) T. Satoh, K. Horiguchi, *Tetrahedron Lett.* **1995**, *36*, 8235; b) T. Satoh, T. Oohara, Y. Ueda, K. Yamakawa, *J. Org. Chem.* **1989**, *54*, 3130; c) T. Satoh, K. Takano, H. Ota, H. Someya, K. Matsuda, M. Koyama, *Tetrahedron* **1998**, *54*, 5557; d) R. W. Hoffmann, P. G. Nell, *Angew. Chem.* **1999**, *111*, 354; *Angew. Chem. Int. Ed.* **1999**, *38*, 338; e) R. W. Hoffmann, B. Hölzer, O. Knopff, K. Harms, *Angew. Chem.* **2000**, *112*, 3206; *Angew. Chem. Int. Ed.* **2000**, *39*, 3072; f) R. W. Hoffmann, B. Hölzer, O. Knopff, *Org. Lett.* **2001**, *3*, 1945; g) R. W. Hoffmann, *Chem. Soc. Rev.* **2003**, *32*, 225; h) V. Schulze, P. G. Nell, A. Burton, R. W. Hoffmann, *J. Org. Chem.* **2003**, *68*, 4546; i) B. Hölzer, R. W. Hoffmann, *Chem. Commun.* **2003**, 732.

[3] For a related reductive sulfur–magnesium exchange reaction that generates allylic magnesium reagents, see: D. Cheng, S. Zhu, Z. Yu, T. Cohen, *J. Am. Chem. Soc.* **2001**, *123*, 30.

[4] Related compounds of this class were used for the rapid and mild generation of various carbon radicals: a) T. Ooi, M. Furuya, D. Sakai, J. Hokke, K. Maruoka, *Synlett* **2001**, 541; b) T. Ooi, D. Sakai, M. Takada, N. Komatsu, K. Maruoka, *Synlett* **2001**, 791; c) T. Ooi, M. Furuya, D. Sakai, K. Maruoka, *Adv. Synth. Catal.* **2001**, *343*, 166.

[5] W. Neugebauer, A. J. Kos, P. v. R. Schleyer, *J. Organomet. Chem.* **1982**, *228*, 107.

[6] The use of 2,2′-dibromobiphenyl instead of **4** is unfortunately not possible, although the corresponding bromo derivatives **1** can be prepared (see Supporting Information). The Br/Mg exchange does not occur to a significant extent under the typical reaction conditions.

[7] K. Fujiki, N. Tanifuji, Y. Sasaki, T. Yokoyama, *Synthesis* **2002**, 343.

[8] D. Scholz, *Liebigs Ann. Chem.* **1984**, 259.

[9] P. G. Theobald, W. H. Okamura, *J. Org. Chem.* **1990**, *55*, 741.

[10] Lithium chloride also promotes the sulfur–magnesium exchange reaction. For the activation of magnesium derivatives with LiCl, see: A. Krasovskiy, P. Knochel, *Angew. Chem.* **2004**, *116*, 3396; *Angew. Chem. Int. Ed.* **2004**, *43*, 3333.

[11] P. Knochel, M. C. P. Yeh, S. C. Berk, J. Talbert, *J. Org. Chem.* **1988**, *53*, 2390.

 © 2006 Wiley-VCH Verlag GmbH & Co. KGaA, Weinheim

DOI: 10.1002/anie.200503452

Synthesis of 2,4,6-Trimethylphenylcalcium Iodide and Degradation in THF Solution**

*Reinald Fischer, Martin Gärtner, Helmar Görls, and Matthias Westerhausen**

In contrast to the alkyl- and arylmagnesium halides prepared by Grignard by direct synthesis more than a hundred years ago, the organometallic chemistry of the heavier alkaline-earth metals has received little attention.[1] The main reasons for this are the difficult preparation and the high reactivity of the resulting organometallic compounds. On the one hand, calcium, strontium, and barium metals are not very reactive and must be activated prior to use. On the other hand, the organometallic derivatives tend to cleave ether. Furthermore, owing to the highly ionic metal–carbon bonds these compounds often are insoluble in common organic solvents. In order to overcome these problems several preparative procedures have been developed.[1,2] The main access routes to organocalcium compounds are:

1) the reaction of halogenated hydrocarbons with calcium vapor (cocondensation reaction),[3,4]
2) the insertion of calcium into a carbon–halogen bond in solution (direct synthesis),[5]
3) the substitution of a less electropositive metal by calcium (transmetalation),[6,7]
4) the deprotonation of H-acidic hydrocarbons by calcium or calcium compounds (metalation),[8]
5) the reaction of a organopotassium compound with anhydrous CaI_2 (metathesis reaction).[9,10]

Beckmann described the synthesis of phenylcalcium iodide in 1905; he applied the direct synthesis in diethyl ether and activated the alkaline-earth metal with a trace of iodine.[11] More than 80 years later the synthesis of diphenylcalcium in THF at −20 °C was reported by Bickelhaupt and co-workers.[12] However, neither yields nor physical data were presented. These phenylcalcium compounds were characterized and identified by derivatization, for example, by hydrolysis or reactions with aldehydes, ketones, esters, vinylalkynes, or chlorostannanes followed by hydrolytic workup procedures.

Neither reliable spectroscopic data nor structural parameters of the heavy Grignard reagents have been published.

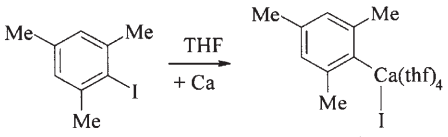
[*] Dr. R. Fischer, Dipl.-Chem. M. Gärtner, Dr. H. Görls, Prof. M. Westerhausen
Institute of Inorganic and Analytical Chemistry
Friedrich-Schiller-Universität Jena
August-Bebel-Strasse 2, 07743 Jena (Germany)
Fax: (+49) 3641-948-102
E-mail: m.we@uni-jena.de

[**] We thank the Deutsche Forschungsgemeinschaft (DFG, Bonn-Bad Godesberg) for financial support.

 © 2006 Wiley-VCH Verlag GmbH & Co. KGaA, Weinheim InterScience

Even less is known about substituted phenylcalcium halides, although several alkyl[4,9,10] and alkynyl derivatives[8] have been structurally investigated. However, a very recent success was achieved with the complexes $[F_5C_6M(Ar'\text{-}NNN\text{-}Ar'')]$ by pentafluoro substitution of the phenyl group and by shielding of the reactive M–C bond with the bulky aryl substituents Ar′ and Ar″. As a result of the small coordination number of 3 for calcium, a short Ca–C bond of 250(1) pm was observed.[13] Here we present the first structural proof of a simple heavy Grignard reagent and investigations concerning its high reactivity.

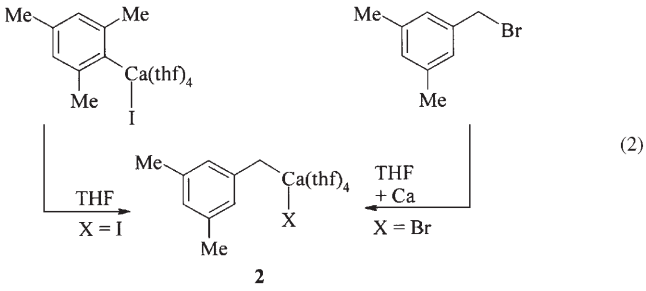
The reaction of iodo-2,4,6-trimethylbenzene (mesityl iodide) with activated calcium metal at low temperatures in THF quantitatively yielded colorless 2,4,6-trimethylphenylcalcium iodide (**1**) [Eq. (1)]. When the solution was warmed



(1)

1

above 0 °C it turned yellow, and even at −20 °C a slow color change occurred. After addition of D_2O to the yellow solution, mesitylene with the deuterium atom in a methyl group was observed, which suggests the formation of 3,5-dimethylbenzylcalcium iodide according to Equation (2). In



(2)

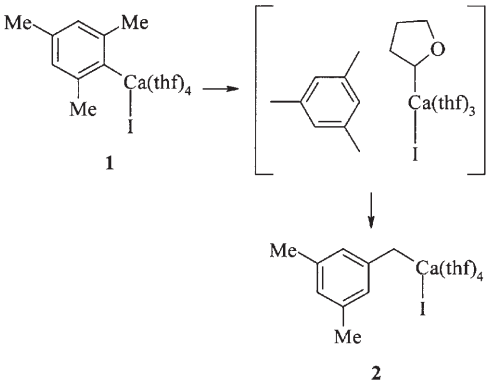
2

order to verify the rearrangement reaction we examined the reaction at 0 °C by NMR spectroscopy. The intensity of the signals of **1** decreased and finally disappeared, and at the same time signals of 1,3,5-trimethylbenzene (mesitylene) and 3,5-dimethylbenzyl groups appeared and increased in intensity. Mesitylene originated from the ether cleavage reactions already reported for the bis(trimethylsilyl)amides of barium.[14]

To verify the formation of **2** we performed the direct synthesis with 3,5-dimethylbenzyl bromide and calcium. Compound **2** was obtained in a poor yield of approximately 15 %, and bis(3,5-dimethylphenyl)ethane originating from the Wurtz-type coupling reaction was the major product. The NMR data of this benzyl derivative and of **2** were identical.

The high stability of benzylcalcium compounds as a result of the delocalization of the anionic charge was demonstrated earlier.[10] Mesityllithium,[15] dimesitylberyllium,[16] and dimesitylmagnesium[17] are known. However, only mesityllithium undergoes a similar rearrangement, which was observed above −10 °C in a THF solution with formation of 3,5-dimethylbenzyllithium.[18] In pentane in the absence of THF such rearrangement reactions were not observed.[19]

To clarify the mechanism of this rearrangement, we isolated compound **1** was isolated and dried it under vacuum; the resulting colorless powder was then redissolved in $[D_8]$THF. In a 2.0 M solution the decomposition was much slower by a factor of approximately 5 to 8, which indicates the involvement of the THF ligands in the rearrangement process. Accordingly the first reaction step is the deprotonation of THF[20] by the mesityl group (formation of C_6H_3-1,3,5-Me_3). The intermediate α-deprotonated THF can either undergo intramolecular ether cleavage or, in a less favored reaction, remetalate the mesitylene at a methyl group (formation of the 3,5-dimethylbenzyl anion) [Eq. (3)]. The ratio of the 3,5-



(3)

1 **2**

dimethylbenzyl to the ether-cleavage products is approximately 1:5. The large effect of the deuterium on the reaction rate suggests that the deprotonation of THF is much slower than the protonation of mesitylene or the ether-cleavage reaction. These investigations indicate that a simple 1,3-H shift within the mesityl group is unlikely.

The molecular structure of **1** is represented in Figure 1. The phenyl group and the iodide are in a *trans* arrangement (C1-Ca-I 177.4(1)°). The mesityl substituent is slightly dis-

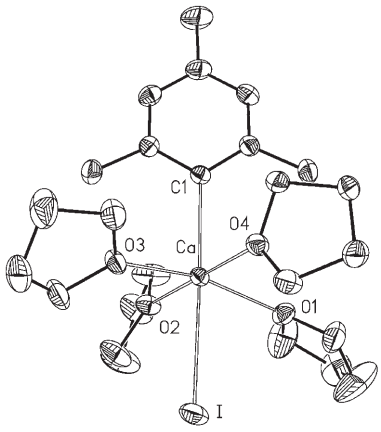


Figure 1. Molecular structure of **1** in the crystal (ellipsoids at a probability level of 40 %, hydrogen atoms omitted for clarity). Selected bond lengths (pm): Ca–I 320.84(9), Ca–C1 257.4(4), Ca–O1 240.2(3), Ca–O2 240.9(3), Ca–O3 239.3(3), Ca–O4 241.9(3).

 © 2006 Wiley-VCH Verlag GmbH & Co. KGaA, Weinheim

torted: The *ipso* carbon atom C1 is pulled out of the plane of the phenyl group, thus leading to an elongation of the C1–C2 (140.2(7) pm) and C1–C6 bonds (143.2(6) pm) as well as a narrow C2-C1-C6 angle of only 114.2(4)°. This fact can be explained by the high ionicity of the Ca–C bond and by the enhanced spatial demand of the {CaI(thf)$_4$ moiety compared to that of the bonding electron pairs of the *ortho* methyl groups. Similar distortions are a common feature in highly ionic aryl compounds and have also been observed for [(thf)$_2$Li-C$_6$H$_2$-2,4,6-Me$_3$]$_2$.[15] The Ca–C bond length compares well with those of other organocalcium compounds, taking the importance of the coordination number of Ca and the bulk of the substituents into account (Table 1). In [Ca$_4$(μ_4-O)(C$_6$H$_3$-2,6-(OMe)$_2$)$_6$], in which the aryl groups bridge the

Table 1: Comparison of Ca–C bond lengths of selected organocalcium compounds.

	CN (Ca)[a]	Ca–C [pm]	Ref.
[Ca{C(SiMe$_3$)$_3$}$_2$]	2	246	[9]
[F$_5$C$_6$-Ca(Ar′-NNN-Ar″)][b]	3	250	[13]
[(diox)$_2$Ca(CH(SiMe$_3$)$_2$)$_2$][b]	4	248	[4]
[(thf)$_4$Ca(CH$_2$Ph)$_2$]	4	258	[10c]
[(thf)$_2$Ca(C(SiMe$_3$)$_2$Ph)$_2$]	4	265	[10a]
[Mes-CaI(thf)$_4$] (**1**)[b]	6	257	
[{(thf)Ca-O-C$_6$H$_4$-CH-PPh′$_2$)}$_4$][b]	6	259	[21]
[(thf)$_4$Ca(CH(SiMe$_3$)(C$_6$H$_4$-NMe$_2$)$_2$]	6	263	[10b]
[([18]crown-6)Ca(C≡C-SiPh$_3$)$_2$]	8	254	[8b]
[(thf)$_2$Ca(Me$_3$Si-(CH)$_3$-SiMe$_3$)$_2$][c]	8	265	[22]

[a] Coordination number of calcium. [b] Ar′: C$_6$H$_3$-2,6-Mes$_2$; Ar″: C$_6$H$_4$-2-(C$_6$H$_2$-2,4,6-*i*Pr$_3$); Mes: 2,4,6-trimethylphenyl, mesityl; diox: 1,4-dioxane; Ph′: *p*-tolyl. [c] Bis[1,3-bis(trimethylsilyl)allyl]calcium complex.

edges of an oxygen-centered Ca$_4$ tetrahedron, longer Ca–C bonds between 271.6(4) and 278.5(4) pm were observed.[23]

In the molecular structure the two THF ligands containing O1 and O3 are bent towards the iodine atom as a result of the steric repulsion between these fragments and the *ortho* methyl groups of the mesityl substituent. In addition, these ligands are turned toward the CaO$_4$ plane, whereas the other THF molecules are oriented propellerlike to this plane.

The THF complex of 2,4,6-mesitylcalcium iodide is the first example of an isolated and structurally characterized heavy Grignard reagent. The easy access of this highly reactive compound, which can be handled at very low temperatures, could give new impetus to the yet unknown organometallic chemistry of the heavy alkaline-earth metals. In addition we could elucidate the steps of the degradation reaction and show that rather than an intramolecular 1,3-H shift a sequence of deprotonation of THF and subsequent deprotonation of mesitylene leads to the benzyl anion.

Experimental Section

All manipulations were carried out under an anhydrous argon atmosphere. The solvents were thoroughly dried and distilled under an argon atmosphere.

Synthesis of [MesCaI(thf)$_4$] (**1**): A 500-mL Schlenk flask containing glass balls (diameter 5 mm), activated calcium (1.84 g, 45.9 mmol), and 90 mL of THF was cooled to −78 °C. Iodo-2,4,6-trimethylbenzene (7.5 g, 30.9 mmol) was added, and the flask was shaken for 5 h. During this time the temperature was kept below −50 °C. The glass balls and the excess calcium metal were removed at temperatures below −30 °C, and the filtrate (90% yield of organocalcium compound calculated by acid consumption of an aliquot) was stored overnight at −78 °C. The colorless precipitate of **1** (3.46 g, 6.0 mmol, 19.4%) was collected on a cooled frit and dried in vacuo.

Crystalline **1** decomposes above −10 °C, whereas in solution decomposition was observed already above −30 °C. Compound **1** shows excellent solubility in aromatic hydrocarbons and ethers. In the ^{1}H NMR spectra at 250 K there are two sets of signals for the mesityl group in a molecular ratio of 3:2 most probably due to a Schlenk equilibrium which gives MesCaI and CaMes$_2$. Above 310 K only one set of resonances is detected. ^{1}H NMR (200.1 MHz, [D$_8$]THF, 250 K): δ = 2.02 (3H, s, *p*-CH$_3$), 2.24 (6H, s, *o*-CH$_3$), 6.36 ppm (2H, s, *m*-CH) and the second set: δ = 2.04 (3H, s, *p*-CH$_3$), 2.31 (6H, s, *o*-CH$_3$), 6.38 ppm (2H, s, *m*-CH); ^{13}C{^{1}H} NMR (50.3 MHz, [D$_8$]THF, 250 K): δ = 21.6 (*p*-CH$_3$), 27.7 (*o*-CH$_3$), 124.2 (*m*-CH), 131.0 (*p*-C), 147.1 (*o*-C), 182.5 ppm (*i*-C) and the second set: δ = 21.7 (*p*-CH$_3$), 28.2 (*o*-CH$_3$), 123.7 (*m*-CH), 131.1 (*p*-C), 146.6 (*o*-C), 183.0 ppm (*i*-C).

Rearrangement of **1**: An NMR tube containing a solution of **1** in [D$_8$]THF and THF (molar ratio 10:1) and benzene as a internal standard was kept in a NMR spectrometer at 273 K. The reaction course was followed by NMR spectroscopy. The colorless solution turned more and more yellow as **2** formed. ^{1}H NMR (200.1 MHz, [D$_8$]THF, 250 K): δ = 1.40 (2H, s, Ca-CH$_2$), 1.90 (6H, s, *m*-CH$_3$), 5.48 (1H, s, *p*-CH), 5.99 ppm (2H, s, *o*-CH); ^{13}C{^{1}H} NMR (50.3 MHz, [D$_8$]THF, 250 K): δ = 22.9 (*m*-CH$_3$), 41.2 (CH$_2$-Ca), 112.1 (*p*-CH), 118.0 (*o*-CH), 136.2 (*m*-C), 160.2 ppm (*i*-C).

Deuterolysis of **2** with D$_2$O: One-tenth of the filtrate of compound **1** was stirred overnight in an ice bath. The solution turned yellow. The volatile components of the reaction mixture were removed in vacuo, and the residue was treated with 1.0 mL of D$_2$O and 1.5 mL of CDCl$_3$ were added. The organic layer was separated and examined by ^{13}C NMR spectroscopy. ^{13}C{^{1}H} NMR (50.3 MHz, CDCl$_3$): δ = 20.7 (t, ^1J(^{13}C,D) = 19.5 Hz, CH$_2$D), 21.0 (CH$_3$), 126.8 (CH), 137.5 ppm (C).

X-ray structure determination of **1**: The intensity data was collected on a Nonius Kappa CCD diffractometer using graphite-monochromated Mo$_{K\alpha}$ radiation. Data was corrected for Lorentz polarization and for absorption effects.[24–26] The structure was solved by direct methods (SHELXS[27]) and refined by full-matrix least squares techniques against F_o^2 (SHELXL-97[28]). The hydrogen atoms were included at calculated positions with fixed thermal parameters. All non-hydrogen atoms except for the solvent molecules were refined anisotropically.[28] XP (SIEMENS Analytical X-ray Instruments, Inc.) and POVRAY were used for structure representations.

Crystal data for **1**:[29] C$_{25}$H$_{43}$CaIO$_4$·0.75 C$_4$H$_8$O, M = 628.65 g mol^{-1}, colorless prism, dimensions 0.05 × 0.05 × 0.05 mm^3, monoclinic, space group $P2_1/c$, a = 17.4431(6), b = 13.1064(5), c = 16.9127(7) Å, β = 116.183(2)°, V = 3469.8(2) Å^3, T = −90 °C, Z = 4, $\rho_{calcd.}$ = 1.203 g cm^{-3}, μ(Mo$_{K\alpha}$) = 10.98 cm^{-1}, multiscan, transmission min.: 0.9426, transmission max.: 0.9778, F(000) = 1312, 24085 reflections in h(−22/22), k(−17/15), l(−21/20), measured in the range 2.68° ≤ θ ≤ 27.48°, completeness θ_{max} = 99.7%, 7917 independent reflections, R_{int} = 0.044, 5342 reflections with $F_o > 4\sigma(F_o)$, 312 parameters, 0 restraints, $R1_{obs}$ = 0.060, wR^2_{all} = 0.196, GOOF = 1.036, largest difference peak and hole: 1.328/−1.148 e Å^{-3}.

Received: September 29, 2005
Published online: December 19, 2005

Keywords: arylcalcium iodides · calcium · Grignard reaction · synthetic methods

 © 2006 Wiley-VCH Verlag GmbH & Co. KGaA, Weinheim

[1] T. P. Hanusa, *Polyhedron* **1990**, *9*, 1345 – 1362; T. P. Hanusa, *Chem. Rev.* **1993**, *93*, 1023 – 1036; T. P. Hanusa, *Coord. Chem. Rev.* **2000**, *210*, 329 – 367; M. Westerhausen, *Angew. Chem.* **2001**, *113*, 3063 – 3065; *Angew. Chem. Int. Ed.* **2001**, *40*, 2975 – 2977; J. S. Alexander, K. Ruhlandt-Senge, *Eur. J. Inorg. Chem.* **2002**, 2761 – 2774.

[2] K. Mochida, *Sci. Synth.* **2004**, *7*, 677 – 684.

[3] K. Mochida, H. Ogawa, *J. Organomet. Chem.* **1983**, *243*, 131 – 135; K. Mochida, T. Yamanishi, *J. Organomet. Chem.* **1987**, *332*, 247 – 252.

[4] F. G. N. Cloke, P. B. Hitchcock, M. F. Lappert, G. A. Lawless, B. Royo, *J. Chem. Soc. Chem. Commun.* **1991**, 724 – 726.

[5] M. A. Zemlyanichenko, N. I. Sheverdina, I. M. Viktorova, V. A. Chernoplekova, N. P. Barminova, K. A. Kocheshkov, *Dokl. Akad. Nauk SSSR* **1970**, *194*, 95 – 97; A. V. Bogatskii, T. K. Chumachenko, A. E. Kozhukhova, M. V. Grenaderova, *Zh. Obshch. Khim.* **1972**, *42*, 403 – 409; N. Nariyoshi, A. Matsumura, S. Yamashita, *J. Org. Chem.* **1973**, *38*, 4268 – 4270; N. Kawabata, A. Matsumura, S. Yamashita, *Tetrahedron* **1973**, *29*, 1069 – 1071; A. V. Bogatskii, T. K. Chumachenko, A. E. Derkach-Kozhukhova, L. N. Lyamtseva, E. S. Suprinovich, *Zh. Obshch. Khim.* **1977**, *47*, 2297 – 2305.

[6] T. Kanda, T. Sugino, N. Kambe, N. Sonoda, *Phosphorus Sulfur Silicon Relat. Elem.* **1992**, *67*, 103 – 106.

[7] I. E. Paleeva, N. I. Sheverdina, M. A. Zemlyanichenko, K. A. Kocheshkov, *Dokl. Akad. Nauk SSSR* **1973**, *210*, 1134 – 1135; I. E. Paleeva, N. I. Sheverdina, K. A. Kocheshkov, *Zh. Obshch. Khim.* **1974**, *44*, 1135 – 1137.

[8] a) D. J. Burkey, T. P. Hanusa, *Organometallics* **1996**, *15*, 4971 – 4976; b) D. C. Green, U. Englich, K. Ruhlandt-Senge, *Angew. Chem.* **1999**, *111*, 365 – 367; *Angew. Chem. Int. Ed.* **1999**, *38*, 354 – 357.

[9] C. Eaborn, S. A. Hawkes, P. B. Hitchcock, J. D. Smith, *Chem. Commun.* **1997**, 1961 – 1962.

[10] a) F. Feil, S. Harder, *Organometallics* **2000**, *19*, 5010 – 5015; b) S. Harder, F. Feil, A. Weeber, *Organometallics* **2001**, *20*, 1044 – 1046; c) S. Harder, S. Müller, E. Hübner, *Organometallics* **2004**, *23*, 178 – 183.

[11] E. Beckmann, *Ber. Dtsch. Chem. Ges.* **1905**, *38*, 904 – 906.

[12] P. R. Markies, T. Nomoto, G. Schat, O. S. Akkerman, F. Bickelhaupt, *Organometallics* **1991**, *10*, 3826 – 3837.

[13] S.-O. Hauber, F. Lissner, G. B. Deacon, M. Niemeyer, *Angew. Chem.* **2005**, *117*, 6021 – 6025; *Angew. Chem. Int. Ed.* **2005**, *44*, 5871 – 5875.

[14] a) D. C. Bradley, M. B. Hursthouse, A. A. Ibrahim, K. M. A. Malik, M. Motevalli, R. Möseler, H. Powell, J. D. Runnacles, A. C. Sullivan, *Polyhedron* **1990**, *9*, 2959 – 2964; b) J. S. Alexander, K. Ruhlandt-Senge, *Angew. Chem.* **2001**, *113*, 2732 – 2734; *Angew. Chem. Int. Ed.* **2001**, *40*, 2658 – 2660; c) J. S. Alexander, K. Ruhlandt-Senge, H. Hope, *Organometallics* **2003**, *22*, 4933 – 4937.

[15] M. A. Beno, H. Hope, M. M. Olmstead, P. P. Power, *Organometallics* **1985**, *4*, 2117 – 2121; For this kind of distortions see also: C. Elschenbroich, A. Salzer; *Organometallics: A Concise Introduction*, 2. ed., VCH, Weinheim, **2001**.

[16] K. Ruhlandt-Senge, R. A. Bartlett, M. M. Olmstead, P. P. Power, *Inorg. Chem.* **1993**, *32*, 1724 – 1728.

[17] K. M. Waggoner, P. P. Power, *Organometallics* **1992**, *11*, 3209 – 3214.

[18] W. Bauer, W. R. Winchester, P. von R. Schleyer, *Organometallics* **1987**, *6*, 2371 – 2379.

[19] G. Fraenkel, S. Subramanian, A. Chow, *J. Am. Chem. Soc.* **1995**, *117*, 6300 – 6307.

[20] For a review on ether-cleavage reactions see: A. Maercker, *Angew. Chem.* **1987**, *99*, 1002 – 1019; *Angew. Chem. Int. Ed. Engl.* **1987**, *26*, 972 – 989.

[21] V. Knapp, G. Müller, *Angew. Chem.* **2001**, *113*, 187 – 190; *Angew. Chem. Int. Ed.* **2001**, *40*, 183 – 186.

[22] M. J. Harvey, T. P. Hanusa, V. G. Young, *Angew. Chem.* **1999**, *111*, 241 – 242; *Angew. Chem. Int. Ed.* **1999**, *38*, 217 – 219.

[23] C. Ruspic, S. Harder, *Organometallics* **2005**, *24*, 5506 – 5508.

[24] COLLECT, Data Collection Software, Nonius B.V., Netherlands, **1998**.

[25] "Processing of X-Ray Diffraction Data Collected in Oscillation Mode": Z. Otwinowski, W. Minor in *Methods in Enzymology, Vol. 276, Macromolecular Crystallography, Part A* (Eds.: C. W. Carter, R. M. Sweet), Academic Press, New York, **1997**, pp. 307 – 326.

[26] SORTAV, R. H. Blessing, *Acta Crystallogr. Sect. A* **1995**, *51*, 33 – 38.

[27] G. M. Sheldrick, *Acta Crystallogr. Sect. A* **1990**, *46*, 467 – 473.

[28] G. M. Sheldrick, SHELXL-97 (Release 97-2), University of Göttingen, Germany, **1997**.

[29] CCDC-285199 (**1**) contains the supplementary crystallographic data for this paper. These data can be obtained free of charge from The Cambridge Crystallographic Data Centre via www.ccdc.cam.ac.uk/data_request/cif.

 © 2006 Wiley-VCH Verlag GmbH & Co. KGaA, Weinheim

Enzyme Catalysis

DOI: 10.1002/anie.200502738

Biocatalytic Synthesis of Poly(L-Lactide) by Native and Recombinant Forms of the Silicatein Enzymes**

*Paul Curnow, David Kisailus, and Daniel E. Morse**

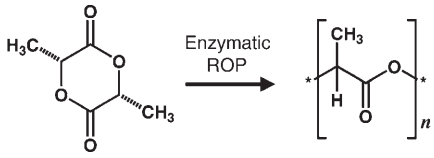
The synthesis and application of biocompatible and biodegradable polymers have recently emerged as areas of great interest. These materials are rapidly becoming viable alternatives to biologically intractable polymers for industrial uses such as packaging.[1] They are uniquely suited to specialist biomedical applications, such as the encapsulation and controlled release of bioactive molecules[2–5] and as scaffolds for tissue engineering.[6,7] Herein, we describe a novel enzymatic method for the low-temperature synthesis and surface deposition of one such polymer, poly(L-lactide) (PLA).

We have previously described the unusual utility of silicatein enzymes in the synthesis of inorganic materials. These proteins were first identified as filamentous aggregates occluded within the silica spicules of the Pacific demosponge *Tethya aurantia*. These filaments were subsequently found to consist of three individual protein species, which we have termed silicateins (silica protein) α, β, and γ according to their differential migration on an SDS-PAGE gel.[8] The filaments demonstrated unusual catalytic and templating activities, such that they were capable of biocatalytically directing the in vitro polycondensation of 1) polymeric silica and polysilsesquioxanes,[9] 2) nanocrystalline/amorphous titanium dioxide,[10] and 3) gallium oxohydroxide and spinel gallium oxide[11] from stable, water-soluble precursors under mild temperature and pH conditions.

Silicatein-α, which makes up 70% of the filaments by weight, has a surprisingly similar sequence identity to the family of papainlike cysteine proteases. Crucially, however, in silicatein-α, the active site cysteine is replaced with a serine. The corresponding decrease in the nucleophilicity of the catalytic triad considerably reduces the efficiency of silicatein-α as a protease.[9,12] We have suggested that this low catalytic activity is critical when the enzyme is applied to inorganic systems as the kinetically limited production of reactive-product species results in the slow growth of materials at the filament surface. This generates inorganic products with a nanoscale and/or microscale order that are otherwise unobtainable under ambient conditions.

We have recently also created a silicatein-based whole-cell biocatalyst through the recombinant expression of silicatein-α at the external surface of cells of the bacterium *Escherichia (E) coli*. This was achieved through the insertion of silicatein-α within the first extracellular loop of a recombinant form of the *E. coli* outer membrane protein A (OmpA).[13] We found that the advantages of silicatein-based synthesis are retained in this whole-cell system, and we are able to generate layered titanium phosphates at the outer membrane of silicatein-displaying cells at physiologically relevant temperature and pH.

Herein, we expand the range of products amenable to silicatein-based synthesis through the generation of PLA from the cyclic precursor L-lactide through a biocatalytically controlled ring-opening polymerization (ROP) (Scheme 1).



Scheme 1. Ring-opening polymerization (ROP) of poly(L-lactide).

Silicatein filaments and heat-denatured controls were reacted with L-lactide in an organic solvent and the results were investigated by using scanning electron microscopy (SEM). The filament surface is normally smooth, as is shown in Figure 1a. The heat-denatured filaments showed little change in surface morphology after incubation with L-lactide for 16 h (Figure 1b). In contrast, native filaments are seen to accumulate PLA at the filament surface (Figure 1c). Over longer timescales, coagulated structures were seen in which product formation was sufficient to join individual filaments (Figure 1d).

We also investigated the capacity of silicatein-displaying cells to synthesize PLA. Solubilized L-lactide was introduced to a suspension of silicatein-displaying cells in isotonic phosphate-buffered saline (PBS) solution. After overnight incubation (Figure 2a), polymeric products were apparent at the cell surface and were characterized by an increase in cell

[*] Professor D. E. Morse
Department of Molecular, Cellular and Developmental Biology
University of California at Santa Barbara
Santa Barbara, CA 93106-9610 (USA)
Fax: (+1) 805-893-8062
E-mail: d_morse@lifesci.ucsb.edu
Dr. P. Curnow, Dr. D. Kisailus, Professor D. E. Morse
Institute of Collaborative Biotechnologies
California NanoSystems Institute
Marine Biotechnology Center and
Department of Molecular, Cellular and Developmental Biology
University of California at Santa Barbara
Santa Barbara, CA 93106 (USA)

[**] We thank Dr T. Mates for his expert assistance with the collection and analysis of XPS data. This work was supported in part by grants from the U.S. Dept. of Energy (DE-FG03-02ER46006), the Institute for Collaborative Biotechnologies through grant DAAD19-03-D-0004 from the U.S. Army Research Office, NASA (University Research, Engineering and Technology Institute on Bio Inspired Materials (BIMat) under award No. NCC-1-02037 and NAG1-01-003), the NOAA National Sea Grant College Program, U.S. Department of Commerce (NA36RG0537, Project R/MP-92) through the California Sea Grant College System, and the MRSEC Program of the National Science Foundation under award No. DMR00-80034 to the UCSB Materials Research Laboratory. The U.S. Government is authorized to reproduce and distribute copies for governmental purposes.

Supporting information for this article is available on the WWW under http://www.angewandte.org or from the author.

 © 2006 Wiley-VCH Verlag GmbH & Co. KGaA, Weinheim

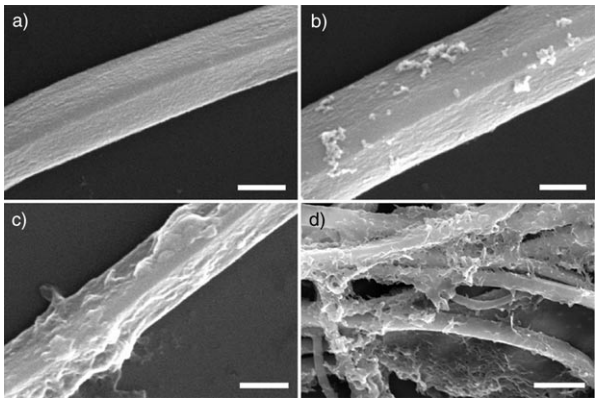


Figure 1. Silicatein filaments catalyze the synthesis of poly(L-lactide). a) Unreacted filament; b) denatured control, 16 h incubation with L-lactide; c) and d) filaments after incubation with L-lactide for 16 h and 90 h respectively. (a–c), Scale bar = 1 μm; d) scale bar = 4 μm.

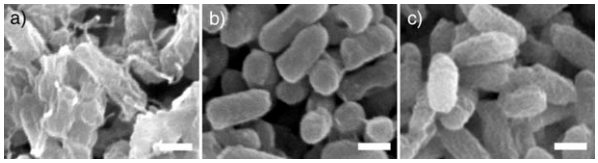


Figure 2. Cell-based synthesis of poly(L-lactide). *E. coli* cells displaying silicatein-α at the cell surface synthesize polymeric products a) apparent as thread-like structures between cells and as increased cell surface roughness. This product was significantly reduced in control cells that were preincubated with b) the protease inhibitor PMSF and c) in cells expressing recombinant OmpA only. Scale bar = 0.5 μm.

surface roughness and as "threads" between cells. These products were significantly reduced when cell suspensions were preincubated with the protease inhibitor phenylmethylsulfonyl fluoride (PMSF) (Figure 2b) and in cell preparations that expressed recombinant OmpA only (Figure 2c). Analysis by TEM further confirms the presence of surface products in filament-based and cell-based syntheses (see the Supporting Information).

As a result of the similarity between these data and our previous experiments with inorganic materials, we became interested to determine whether any crystalline organic-surface products might be observed. PLA has pseudo-orthorhombic[14] and hexagonal[15] phases that are typically formed by annealing from the molten state for several hours at $>130\,^{\circ}C$.[15–17] Crystals can also be grown from solutions in organic solvents at lower temperatures and over long-time periods.[15,18] However, selected-area electron diffraction patterns of both the filament and cell surfaces (see the Supporting Information) definitively show that only an amorphous polymer is formed during silicatein-based synthesis.

X-ray photoelectron spectroscopy (XPS) was used to analyze the PLA product on silicatein filaments. The XPS spectrum of PLA is relatively simple owing to the chemical simplicity of the repeat unit. The C1s orbital consists of approximately equivalent contributions from C–H, C–O, and C=O groups that occur at normalized binding energies of 285.0, 286.9, and 289.0 eV, respectively.[19–22] The O1s orbital is composed of two equivalent component peaks at normalized binding energies of 532.0 eV (C=O) and 533.4 eV (**O**–C=O).[22]

High-resolution scans of regions that correspond to the C1s, O1s, and N1s orbitals (Figure 3a–f) were recorded and

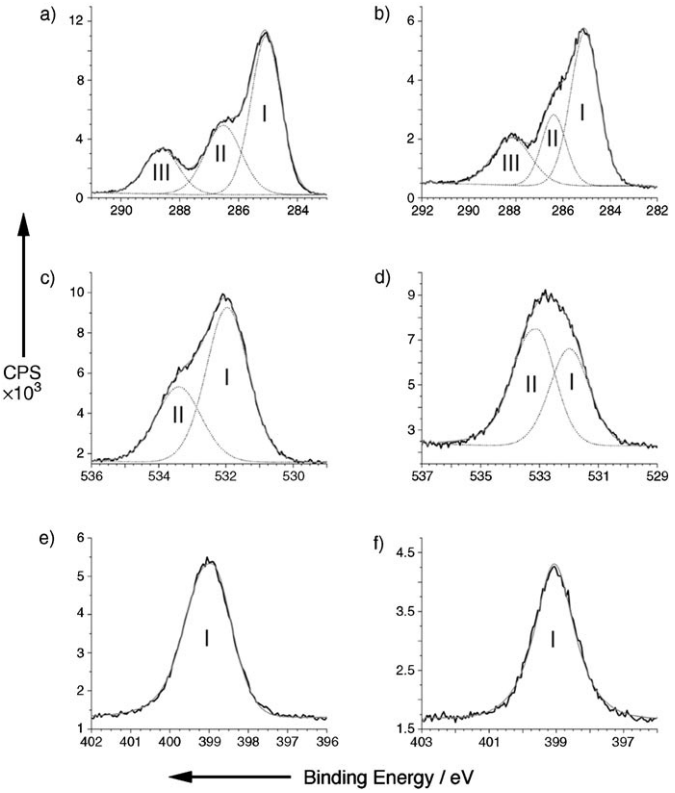


Figure 3. High-resolution XPS spectra of a), c), and e) filament controls and b), d), and f) filaments after reaction with L-lactide for 3 days. The synthetic component peaks of C1s (a and b), O1s (c and d), and N1s (e and f) orbitals are shown (see also Table 1). —— = experimental data; - - - - - = fitted components; —— = envelope of fitted data; CPS = counts per second

analyzed by curve fitting of synthetic component peaks. Native filaments that were reacted with L-lactide, demonstrated a relative increase in the C1s (Figure 3a,b) and O1s (Figure 3c,d) spectra at binding energies that are typically associated with ester groups ($\approx$288.5 eV and $\approx$533.2 eV, respectively). Quantitative values derived from these experiments are shown in Table 1. We concluded that the increase in these signals represents the formation of PLA at the filament surface.

The inherent gross surface roughness of the silicatein samples is nonideal for XPS analysis and results in peak broadening.[23] The individual orbital spectra of samples incubated with L-lactide are 0.5–1 eV broader than those in the control experiments; and full width at half maximum (FWHM) values of component peaks are >1.2. These considerations, combined with the complexities of the filament background signal (Figure 3a,c,e), obliged us to use a simplistic approach to peak fitting. Although this prevents a

 © 2006 Wiley-VCH Verlag GmbH & Co. KGaA, Weinheim

Table 1: Position and quantification of component peaks from Figure 3.

Sample	Orbital	Peak	BE [eV][a]	FWHM [eV]	Composition [%]	Assignment
filament	C1s	I	285.07	1.20	53.73	**C**-C, **C**-H
		II	286.52	1.46	28.8	**C**-O, **C**-N
		III	288.61	1.36	17.47	**C**=O, O=**C**-O
	O1s	I	531.96	1.48	65.66	C=**O**, N-C=**O**
		II	533.41	1.59	34.34	C-**O**, **O**=C-**O**-C
	N1s	I	398.94	1.23	100	**N**-H, **N**-C, **N**-C=O
filament +lactide	C1s	I	285.08	1.42	55.02	**C**-C, **C**-H
		II	286.39	1.23	21.95	**C**-O, **C**-N
		III	288.17	1.93	23.03	**C**=O, O=**C**-O
	O1s	I	531.98	1.58	42.53	C=**O**, N-C=**O**
		II	533.09	1.52	57.47	C-**O**, **O**=C-**O**-C
	N1s	I	399.06	1.37	100	**N**-H, **N**-C, **N**-C=O

[a] BE = binding energy.

more detailed analysis of individual spectral components, it is sufficient for our purposes to confirm the synthesis of PLA.

Current limitations of this silicatein-based synthesis include the small quantities of enzyme available, the potential passivation of the catalytic surface, and competition from water. Furthermore, product isolation is complicated by the intimate contacts formed between the product and the reactive surfaces. As the enzyme is a catalyst rather than a ROP initiator, however, the product is expected to be adsorbed to the surfaces rather than covalently bound. Because of these inherent constraints, we have thus far been unable to generate the high product yields necessary to further characterize the PLA product by standard techniques such as NMR, IR, gel permeation chromatography and MS. We were also unable to determine the molecular-mass average of the product. Nevertheless, the observations reported here provide a first proof-of-principle that silicatein is capable of catalyzing the polymerization of the PLA precursor.

The controlled, surface-templated enzymatic synthesis of organic polymers at low temperature, shown here for the first time, has great promise as a nanotechnological tool. It has already been shown that polymer blends and organic/inorganic composites can be formed thorough enzymatic methods.[24,25] We therefore hope to extend the silicatein technology to the synthesis of a range of oriented PLA composites including materials with characteristics such as electrical conductivity[26] and those that incorporate bioactive glass[27] and hydroxyapatite.[28]

Experimental Section

Silicatein filaments were prepared from the silica spicules of *Tethya aurantia* by hydrofluoric acid demineralization according to standard methods.[8,9] For control experiments, protein denaturation was carried out at 100 °C for 2 h. As previously described, silicatein-α (Sil) is cloned into the first external loop of the *E. coli* OmpA resulting in the surface display of the recombinant fusion protein OmpA-Sil.[13] Briefly, the *E. coli* strain MC1061 was transformed with a derivative of pBAD33,[29] which contains the OmpA-Sil insert,[13,30] and grown in chloramphenicol-supplemented LB broth at 37 °C to a cell density of 0.9 at A_{600}. Protein expression was induced by the addition of L-(+)-arabinose to a final concentration of 0.2 % (w/v). At 6 h post induction, cultures were harvested in 50 mL aliquots by centrifugation at 3500 *g*, snap frozen and stored as pellets at −80 °C. When required, pellets ($\approx 5 \times 10^{10}$ cells) were washed with 50 mL of an isotonic PBS solution (8 M NaCl, 0.2 g L^{-1} KCl, 1.44 g L^{-1} Na_2HPO_4, 0.24 g L^{-1} KH_2PO_4, pH 7.4) and resuspended in PBS (10 mL).

L-Lactide (purchased from Sigma) was stored under argon at 4 °C and dissolved, as required, in chloroform/methanol/water, 1:1:0.08 (50 mM v/v) for filaments or in methanol ($\approx$ 1 M saturated solution) for cells. For the reaction with filaments, filament samples (1 mg) were pelleted at 6000 *g* for 15 min and resuspended in the lactide solution (400 μL) before being reacted at 16 °C and rotated on a mill for 16–90 h. For the cell-based reaction, lactide (0.5 mL of the 1 M solution) was introduced to the cells (10 mL) in PBS solution and reacted with gentle agitation for 16 h at 16 °C. The polymeric product was isolated from the cell solution by allowing it to settle under gravity. In control samples, OmpA-Sil cells were either incubated for 30 min with the protease inhibitor PMSF (0.1 mM) (purchased from Sigma) or cells that only express a recombinant OmpA were used.

For microscopic analysis, filament and cell samples were extracted from the aqueous phase by centrifugation and washed three times with milliQ water (1 mL). For SEM, samples were then dried directly onto glass cover slips (filaments) or lyophilyzed and transferred to cover slips with a plastic pipette tip (cells) prior to analysis with a Vega TS 5130 MM instrument (Tescan, Czech Republic) at an accelerating voltage of 20 kV. An energy dispersive spectrometer (EDS) attachment (IXRF Systems, Houston, TX) was used for elemental mapping of selected regions. For TEM, samples were dried onto holey-carbon copper grids (Ted Pella, Redding, CA) before imaging at 200 kV (FEI T-20, Hilllsboro, Oregon). Selected area electron diffraction patterns (SAEDs) were subsequently recorded from various surface regions. In all cases, representative micrographs were taken at random locations within the samples.

For XPS, filaments (5 mg) were reacted with L-lactide for three days as described above. Control reactions in which L-lactide was omitted were also performed. Samples were thoroughly washed in chloroform/methanol (1:1; v/v) and dried before being transferred to double-adhesive copper tape and analyzed with a Kratos Axis Ultra XPS instrument (Kratos Analytical, Chestnut Ridge, NY) by using a monochromatic $Al_{K\alpha}$ source (1486.6 eV) at 225 W. Spectra were acquired in the fixed analyzer transmission mode with vacuum maintained at 3.5×10^{-8} torr. Survey data were recorded between 0–600 eV at 160 eV pass energy and 0.5 eV/step and high-resolution spectra of the C1s, O1s and N1s regions were recorded at 20 eV pass energy and 0.05 eV/step. Dwell times varied between 150–400 ms.

Data analysis and curve fitting was performed with the CasaXPS software. Regions of interest were fit to the lowest possible number of synthetic component peaks with a mixed Gaussian/Lorentzian line shape by using the background of Tougaard. All residuals (difference between experimental data and fitted envelope) were less than 1.5. Component quantification was performed by using appropriate sensitivity factors provided within the software. FWHM values were slightly larger than anticipated, which is attributed to the relative roughness of the sample surface. Peak assignments were referenced to literature data and to the C1s aliphatic carbon peak at 285 eV.

Received: August 3, 2005
Revised: October 6, 2005
Published online: December 19, 2005

Keywords: biosynthesis · biotechnology · enzyme catalysis · polymers · ring-opening polymerization

 © 2006 Wiley-VCH Verlag GmbH & Co. KGaA, Weinheim

[1] R. Auras, B. Harte, S. Selke, *Macromol. Biosci.* **2004**, *4*, 835.
[2] Y. Lu, S. C. Chen, *Adv. Drug Delivery Rev.* **2004**, *56*, 1621.
[3] N. K. Varde, D. W. Pack, *Expert Opin. Biol. Ther.* **2004**, *4*, 35.
[4] S. Jilek, H. P. Merkle, E. Walter, *Adv. Drug Delivery Rev.* **2005**, *57*, 377.
[5] W. Jiang, R. K. Gupta, M. C. Deshpande, S. P. Schwendeman, *Adv. Drug Delivery Rev.* **2005**, *57*, 391.
[6] A. Moreno-Borchart, *EMBO Rep.* **2004**, *5*, 1025.
[7] X. Liu, P. X. Ma, *Ann. Biomed. Eng.* **2004**, *32*, 477.
[8] K. Shimizu, J. N. Cha, G. D. Stucky, D. E. Morse, *Proc. Natl. Acad. Sci. USA* **1998**, *95*, 6234.
[9] J. N. Cha, K. Shimizu, Y. Zhou, S. C. Christiansen, B. F. Chmelka, G. D. Stucky, D. E. Morse, *Proc. Natl. Acad. Sci. USA* **1999**, *96*, 361.
[10] J. L. Sumerel, W. Yang, D. Kisailus, J. C. Weaver, J. H. Choi, D. E. Morse, *Chem. Mater.* **2003**, *15*, 4804.
[11] D. Kisailus, J. H. Choi, J. C. Weaver, W. Yang, D. E. Morse, *Adv. Mater.* **2004**, *16*, 314.
[12] Y. Zhou, K. Shimizu, J. N. Cha, G. D. Stucky, D. E. Morse, *Angew. Chem.* **1999**, *111*, 826; *Angew. Chem. Int. Ed.* **1999**, *38*, 780.
[13] P. Curnow, P. D. Bessette, D. Kisailus, M. M. Murr, P. S. Daugherty, D. E. Morse, *J. Am. Chem. Soc.* **2005**, *127*, 1579.
[14] P. de Santis, A. J. Kovacs, *Biopolymers* **1968**, *6*, 299.
[15] B. Kalb, A. J. Pennings, *Polymer* **1980**, *21*, 607.
[16] H. Tsuji, K. Nakahara, *J. Appl. Polym. Sci.* **2002**, *86*, 186.
[17] T. Iwata, Y. Doi, *Macromolecules* **1998**, *31*, 2461.
[18] T. Miyata, T. Masuko, *Polymer* **1997**, *38*, 4003.
[19] H. Zhu, J. Ji, Q. Tan, M. A. Barbosa, J. Shen, *Biomacromolecules* **2003**, *4*, 378.
[20] K. M. Shakesheff, C. Evora, I. Soriano, R. Langer, *J. Colloid Interface Sci.* **1997**, *185*, 538.
[21] G. C. M. Steffens, L. Nothdurft, G. Buse, H. Thissen, H. Hocker, D. Klee, *Biomaterials* **2002**, *23*, 3523.
[22] *The XPS of polymers database*, SurfaceSpectra, Manchester, UK.
[23] M. A. Kelley in *Surface analysis by Auger and X-ray photoelectron spectroscopy* (Eds.: D. Briggs, J. T. Grant), SurfaceSpectra, Manchester, UK, **2003**.
[24] Y. Feng, D. Klee, H. Hocker, *Macromol. Biosci.* **2004**, *4*, 587.
[25] E. Helwig, B. Sandner, U. Gopp, F. Vogt, S. Warterwig, S. Henning, *Biomaterials* **2001**, *22*, 2695.
[26] G. Shi, M. Rouabhia, Z. Wang, L. H. Dao, Z. Zhang, *Biomaterials* **2004**, *25*, 2477.
[27] K. Zhang, Y. Wang, M. A. Hillmyer, L. F. Francis, *Biomaterials* **2004**, *25*, 2489.
[28] Y. Shikinami, M. Okuno, *Biomaterials* **2001**, *22*, 3197.
[29] L.-M. Guzman, D. Belin, M. J. Carson, J. Beckwith, *J. Bacteriol.* **1995**, *177*, 4121.
[30] P. H. Bessette, J. J. Rice, P. S. Daugherty, *Protein Eng. Des. Sel.* **2004**, *17*, 731.

 © 2006 Wiley-VCH Verlag GmbH & Co. KGaA, Weinheim

Microporous Materials

DOI: 10.1002/anie.200503503

Separation of Hydrocarbons with a Microporous Metal–Organic Framework**

*Long Pan, David H. Olson, Lauren R. Ciemnolonski, Ryan Heddy, and Jing Li**

The past decade has witnessed a rapid growth of interest in the field of metal–organic frameworks (MOFs). Microporous metal–organic framework (MMOF) materials, a subset of the general family of MOFs, are of particular attraction owing to their potential application in gas separation, storage, molecular magnetism, and heterogeneous catalysis.[1] While many new structures are being discovered each year, the gas-adsorption properties of only a very small number of them have been investigated, which has prompted us to explore the scope of their unique sorption properties.

Unlike those of zeolites, the surfaces and voids of MMOF structures are typically composed of aromatic rings and other organic moieties,[2,3] and their pore structures are often quite complex and different from those of oxide-based materials.[2,3] The pore diameters of MMOFs generally fall in the region of micropores, often ultra-micropores.[2b] Their pore structures can be designed and modified to yield the desired shape, size, and surface characteristics. Among the reported sorption studies, the focus has been primarily on small gases such as Ar, N_2, H_2, O_2, CO_2, and C_2H_2.[2a,b,4] To date, there have been no reports of the separation of hydrocarbons with MOFs except for one simulation study.[5] Herein we report the first case in which the potential to separate hydrocarbons by using metal–organic-based sorbent material is observed.

We have recently designed and synthesized a group of MMOFs with a general formula [M(hfipbb)L_x] (M is Co, Cu, or Zn; L can be pyriding, 3-picoline, or 4-picoline; H_2hfipbb is 4,4′-(hexafluoroisopropylidene) bis(benzoic acid)). These are 3D[2a] or 2D[6] framework structures built upon paddle-wheel metal clusters (nodes) and a V-shaped dicarboxylate ligand, H_2hfipbb. These structures contain irregular-shaped micro-channels, with alternating large cages (or chambers) and small entrances (or necks) that connect these cages.

The crystal structure of 3D [Cu(hfipbb)(H_2hfipbb)$_{0.5}$] (**1**) is shown in Figure 1 a.[7] Each copper center has a square-pyramidal coordination environment. Two copper atoms share four carboxylate groups of the four hfipbb ligands, which are located in the equatorial plane, to form a paddle-

[*] Dr. L. Pan, Prof. D. H. Olson, L. R. Ciemnolonski, R. Heddy, Prof. J. Li
Department of Chemistry and Chemical Biology
Rutgers University
Piscataway, NJ 08854 (USA)
Fax: (+1) 732-445-5312
E-mail: jingli@rutchem.rutgers.edu

[**] Acknowledgment is made to the donors of The Petroleum Research Fund, administrated by the ACS, for support of this research. The authors are grateful to the National Science Foundation for partial support through Grant No. DMR-0422932.

InterScience
© 2006 Wiley-VCH Verlag GmbH & Co. KGaA, Weinheim

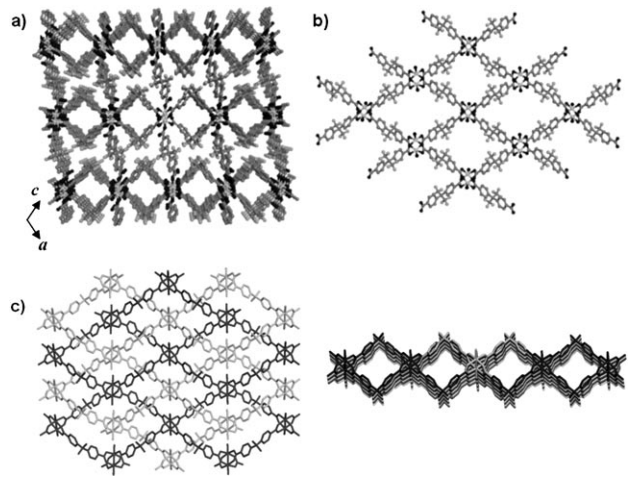


Figure 1. a) View of structure **1**. b) The core motif in **1**, in which each $\{Cu_2\}$ paddle-wheel unit interconnects with four neighboring $\{Cu_2\}$ units through four hfipbb ligands to form an undulating 4^4 2D net. c) Two such 2D nets, identical in structure (shown in dark and light gray), interpenetrate to form a layer composed of 1D tubular microchannels. Left: top view; Right: side view.

wheel with a Cu–Cu interatomic distance of 2.645 Å as shown in Figure 2. Each paddle-wheel unit binds to four adjacent paddle-wheel units through the four remaining carboxylate



Figure 2. Representation of {Cu2} paddle wheel (light gray Cu, dark gray C, black O).

groups of hfipbb to form an undulating 2D network with 4^4 topology (Figure 1 b).[8] Two such identical networks interpenetrate to form a layered structure consisting of microchannels, as shown in Figure 1 c. The adjacent layers are further interconnected by monodentate carboxylate groups of H_2hfipbb ligands that bind to the apical position of the metal centers to generate a 3D network (Figure 1 a).

The microchannels of these frameworks typically have strong interactions with hydrocarbons, which results in large values for the heat of adsorption; they are also hydrophobic, thus allowing the separation of nonpolar molecules from water. We have investigated the sorption properties of **1**, one of the most thermally stable $[M(hfipbb)L_x]$-type structures,[6] by using several organic hydrocarbons of different shapes, sizes, and polarities. Both experimental and simulated adsorption measurements have been conducted. The pore volume of structure **1** is modest, about 0.070 $cm^3 g^{-1}$. However, **1** exhibits unique adsorption properties as it adsorbs propane and butane rapidly (Figure 3) but does not adsorb pentane or higher normal or branched hydrocarbons

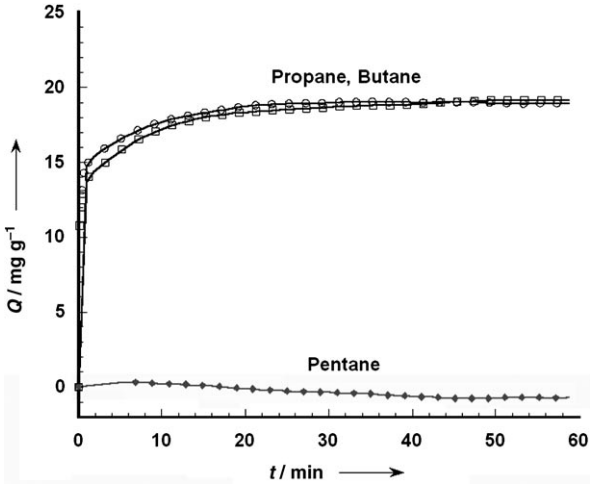


Figure 3. Adsorption of propane (○), butane (□), and pentane (◆) at 90 °C and 650 torr in **1** as a function of time. *Q* is the weight of hydrocarbon molecules adsorbed in the adsorbent.

(Table 1). It is worth noting that all zeolites that adsorb butane also adsorb higher alkanes and do not have a fixed

Table 1: Sorption properties of **1** at 25 °C.

Hydrocarbon	P/P^o [a]	Sorption (wt %)
methanol	0.60	2.0
propane	0.062	2.6
propene	0.019	2.0
n-butane	0.33	4.0
2-methylpropane	≈0.1	0.0
n-pentane	0.100	0.0
3-methylbutane	≈0.1	0.0
n-hexane	0.071	0.0
3-methylpentane	0.078	0.0

[a] *P* is the partial pressure of the adsorbate and P^o is the vapor pressure of the adsorbate at the sorption temperature.

carbon-number cutoff for adsorption. Thus, the microchannels in **1** are unique in being able to separate normal C_2, C_3, and *n*-C_4 olefins and alkanes from all branched alkanes and all normal hydrocarbons above C_4. To the best of our knowledge, there are no existing adsorbents capable of separating normal C_4 from higher normal alkanes and olefins. Compound **1** is the first material found to have such capability. This unusual property is attributed to a narrowing of the channels at intervals of 7.3 Å (the length of the large chamber or cage), which is just greater than the length of *n*-C_4, approximately 6.9 Å, and just less than the length of *n*-C_5, about 8.1 Å. The diameter of the neck is approximately 3.2 Å (2 Å is allowed for the size of the two hydrogen atoms on the surface of the neck). Thus, the neck is too small for this region to be an equilibrium position for alkanes with diameters of around

 © 2006 Wiley-VCH Verlag GmbH & Co. KGaA, Weinheim

3.9 Å but large enough to allow the passage of normal alkanes while excluding branched alkanes.

In addition to the experimental adsorption measurements, the Sorption module of the Cerius2 program was used to perform gas-sorption simulations. These calculations indicate that if pentane were to locate in the large chamber area of the microchannel, the closest H–H interatomic distance between the molecule and the wall would be 1.86 Å, which is too small to be reasonable. The calculations predict that a maximum of one propane or butane molecule is adsorbed per cage, as illustrated in Figure 4. The calculations also indicate that

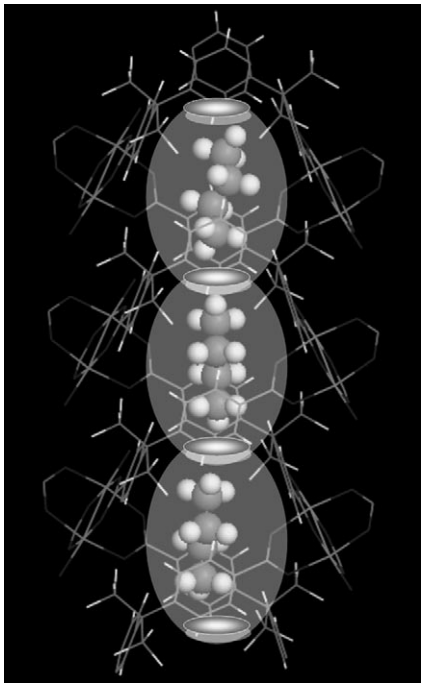


Figure 4. Arrangement of butane molecules in the microchannel of **1**, with one molecule per cage.

essentially no pentane is adsorbed, which is in agreement with the experimental results. Helium-adsorption simulation reveals the pore-filling pattern shown in Figure 5. A view along [100] indicates clearly the formation of a microchannel as a result of the repetition of an oval-shaped cage with a narrow neck region. The substantial amount of 2,2-dimethylpropane accommodated, 0.89 molecules per cage, but no 2,2,3-trimethylbutane is also consistent with the oval-shaped description of the cages (see Table 2). The sorption simulations also indicate that 2,2-dimethylbutane does not adsorb, that is, it does not fit in the chamber area. Thus, the shape of the molecules is critical.

Adsorption isotherms for propane and butane in **1** are shown in Figure 6. Values for zero-loading heat of adsorption, calculated from these data from the Clausius–Clapeyron equation, are 47 kJ mol^{-1} for propane and 50 kJ mol^{-1} for butane. The value of 47 kJ mol^{-1} for propane is higher than the values of 41 and 34 kJ mol^{-1}, which were reported for propene adsorbed by the pure-silica 8-ring zeolites, ITQ-12 and Si-CHA, respectively.[9] The higher value of 41 kJ mol^{-1}

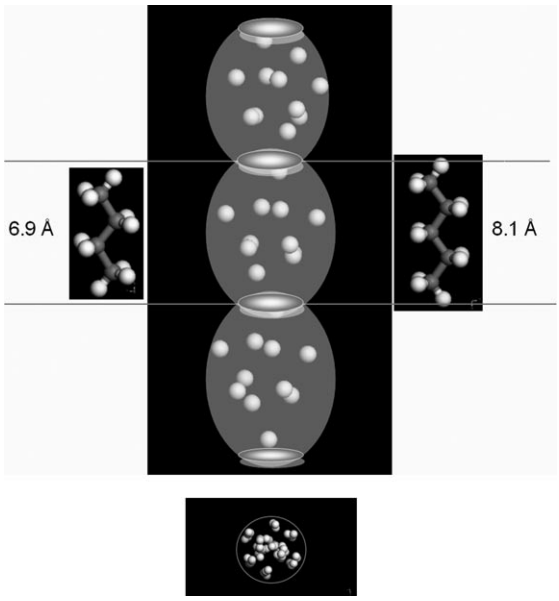


Figure 5. Top: The shape of a microchannel outlined by fitting He sorption at 298 °C and 10 atm by Cerius2 simulation. Butane and pentane are shown in real scale. Clearly, pentane (C_5) is longer than the chamber. Bottom: Top view of the adsorbed He atoms in the microchannel.

Table 2: Sorption capacities simulated by using Cerius2/Sorption.[a]

Hydrocarbon	*T* [K]	*P* [kPa]	*Q* [mol/cage]
propane	303	80	0.98
butane	298	243	0.81
trans-butene	303	80	0.62
cis-butene	303	80	0.87
2-methylbutane	303	80	0.68
2,2-dimethylpropane	303	80	0.89
2,2-dimethylbutane	303	80	0.04
pentane	303	9	0.06
2,2,3-trimethylbutane	303	80	0.00
2,2-dimethylpentane	303	80	0.00

[a] Calculated by using Monte Carlo placement of molecules. Thus, the results reflect cage size and shape but not the ability of the molecules to pass through the narrow neck region.

for ITQ-12 is attributed to its smaller adsorption cavity size and consequently greater adsorbate–adsorbent interaction. Compound **1** also adsorbs 2.0 wt % of methanol at $P/P^\circ = 0.6$ (80 torr) and 25 °C, which shows that it is capable of gas-phase separation of methanol from water (Table 1).

In conclusion, MMOFs built upon bimetallic paddle wheels contain 1D microchannels with hydrophobic internal surfaces. These channels consist of alternating oval-shaped large chambers and narrow windows. The most striking feature of these microchannels is their unique sorption properties, including shape and size selectivity for hydrocarbons. Compound **1** is the first adsorbent capable of separating normal C_4 from higher normal alkanes and olefins. This work reveals the potential of microporous metal–organic framework materials for applications in various hydrocarbon separations.

 © 2006 Wiley-VCH Verlag GmbH & Co. KGaA, Weinheim

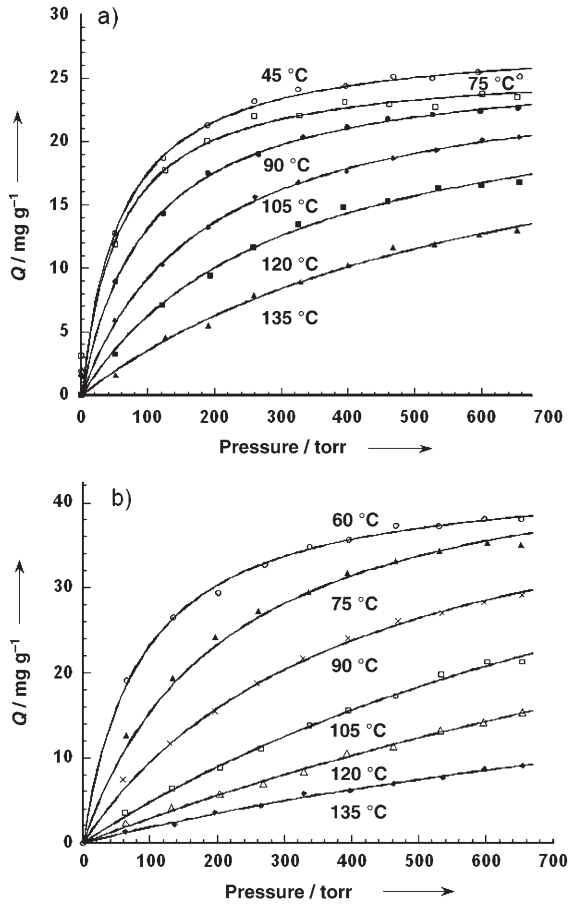


Figure 6. a) Propane adsorption isotherms for **1** at several temperatures (45, 75, 90, 105, 120, and 135 °C). b) Butane adsorption isotherms for **1** at 60, 75, 90, 105, 120, and 135 °C.

Experimental Section

Synthesis of **1**: Hydrothermal reactions of $Cu(NO_3)_2{\cdot}3H_2O$ (0.029 g, 0.12 mmol) with excess H_2hfipbb (0.195 g, 0.5 mmol) in deionized water (5 mL; mole ratio 1.2:5:2278) at 125 °C for 3 days produced blue columnlike crystals of **1** in quantitative yield. The product was washed with *N*,*N*-dimethylformamide (DMF; 10 mL) three times to remove excess H_2hfipbb.[2a]

Adsorption measurements were carried out on a computer-controlled thermogravimetric balance consisting of a TA51 electrobalance with associated TA-2000/PC control system, and a series of mass flow controllers and a Eurotherm temperature controller. This flow-through, one-atmosphere electrobalance system was controlled by the LabView program through Kinetic Systems Interface. In addition to the experimental adsorption measurements, the Sorption function of the Cerius2 program was used to simulate gas-sorption processes.

Received: October 3, 2005
Published online: December 15, 2005

Keywords: adsorption · hydrocarbons · hydrothermal synthesis · microporous materials

[1] a) S. Kitagawa, R. Kitaura, S.-i. Noro, *Angew. Chem.* **2004**, *116*, 2388; *Angew. Chem. Int. Ed.* **2004**, *43*, 2334; b) J. L. C. Rowsell, O. M. Yaghi, *Angew. Chem.* **2005**, *117*, 4748; *Angew. Chem. Int. Ed.* **2005**, *44*, 4670; c) S. R. Batten, *Curr. Opin. Solid State Mater. Sci.* **2001**, *5*, 107; d) D. Maspoch, D. Ruiz-Molina, J. Veciana, *J. Mater. Chem.* **2004**, *14*, 2713; e) D. Moulton, M. J. Zaworotko, *Curr. Opin. Solid State Mater. Sci.* **2002**, *7*, 117; f) J. A. Real, A. B. Gaspar, M. C. Munoz, *Dalton Trans.* **2005**, *12*, 2062; g) M. J. Rosseinsky, *Microporous Mesoporous Mater.* **2004**, *73*, 15.

[2] a) L. Pan, M. B. Sander, X. Huang, J. Li, M. Smith, E. Bittner, B. Bockrath, J. K. Johnson, *J. Am. Chem. Soc.* **2004**, *126*, 1308; b) J.-Y. Lee, L. Pan, S. K. Kelly, T. J. Emge, J. Jagiello, J. Li, *Adv. Mater.* **2005**, *17*, 2730; c) L. Pan, H.-M. Liu, X.-G. Lei, X.-Y. Huang, D. H. Olson, N. J. Turro, J. Li, *Angew. Chem.* **2003**, *115*, 560; *Angew. Chem. Int. Ed.* **2003**, *42*, 542; d) L. Pan, H.-M. Liu, S. P. Kelly, X.-Y. Huang, D. H. Olson, J. Li, *J. Chem. Soc. Chem. Commun.* **2003**, 854.

[3] a) A. Vishnyakov, P. I. Ravikovitch, A. V. Neimark, M. Buelow, Q. M. Wang, *Nano Lett.* **2003**, *3*, 713; b) X. Zhao, B. Xiao, A. J. Fletcher, K. M. Thomas, D. Bradshaw, M. J. Rosseinsky, *Science* **2004**, *306*, 1012.

[4] a) N. L. Rosi, J. Eckert, M. Eddaoudi, D. T. Vodak, J. Kim, M. O'Keeffe, O. M. Yaghi, *Science* **2003**, *300*, 1127; b) G. Férey, M. Latroche, C. Serre, F. Millange, T. Loiseau, A. Percheron-Guégan, *Chem. Commun.* **2003**, 2976; c) L. Pan, K. M. Adams, H. E. Hernandez, X. Wang, C. Zheng, Y. Hattori, K. Kaneko, *J. Am. Chem. Soc.* **2003**, *125*, 3062; d) D. N. Dybtsev, H. Chun, S. H. Yoon, D. Kim, K. Kim, *J. Am. Chem. Soc.* **2004**, *126*, 32; e) J. L. C. Rowsell, A. R. Millward, K. S. Park, O. M. Yaghi, *J. Am. Chem. Soc.* **2004**, *126*, 5666; f) X. Zhao, B. Xiao, A. J. Fletcher, K. M. Thomas, D. Bradshaw, M. J. Rosseinsky, *Science* **2004**, *306*, 1012; g) B. Kesanli, Y. Cui, M. R. Smith, E. W. Bittner, B. C. Bockrath, W. B. Lin, *Angew. Chem.* **2005**, *117*, 74; *Angew. Chem. Int. Ed.* **2005**, *44*, 72; h) J.-Y. Lee, J. Jagiello, J. Li, *J. Solid State Chem.* **2005**, *178*, 2527; i) J. L. C. Rowsell, O. M. Yaghi, *Angew. Chem.* **2005**, *117*, 4748; *Angew. Chem. Int. Ed.* **2005**, *44*, 4670; j) E. Y. Lee, S. Y. Jang, M. P. Suh, *J. Am. Chem. Soc.* **2005**, *127*, 6374; k) Y. Kubota, M. Takata, R. Matsuda, R. Kitaura, S. Kitagawa, K. Kato, M. Sakata, T. C. Kobayashi, *Angew. Chem.* **2005**, *117*, 942; *Angew. Chem. Int. Ed.* **2005**, *44*, 920; l) H. Chun, D. N. Dybtsev, H. Kim, K. Kim, *Chem. Eur. J.* **2005**, *11*, 3521; m) S. S. Kaye, J. R. Long, *J. Am. Chem. Soc.* **2005**, *127*, 6506; n) M. Dincă, J. R. Long, *J. Am. Chem. Soc.* **2005**, *127*, 9376; o) R. Matsuda, R. Kitaura, S. Kitagawa, Y. Kubota, R. V. Belosludov, T. C. Kobayashi, H. Sakamoto, T. Chiba, M. Takata, Y. Kawazoe, Y. Mita, *Nature* **2005**, *436*, 238; p) S. Bourrelly, P. Llewellyn, C. Serre, F. Millange, T. Loiseau, G. Ferey, *J. Am. Chem. Soc.* **2005**, *127*, 139, 13519.

[5] T. Düren, R. Q. Snurr, *J. Phys. Chem. B* **2004**, *108*, 15703.

[6] L. Pan, M. B. Sander, X. Y. Huang, J. Li, unpublished results.

[7] Crystal data for **1**: space group $P2/n$, $a = 18.723(4)$, $b = 7.271(1)$, $c = 20.481(4)$ Å, $\beta = 107.02(3)°$, $V = 2666.1(9)$ Å^3, $Z = 4$, $\rho_{calcd} = 1.619$ Mg m^{-3}.

[8] S. R. Batten, R. Robson, *Angew. Chem.* **1998**, *110*, 1558; *Angew. Chem. Int. Ed.* **1998**, *37*, 1460.

[9] a) D. H. Olson, M. A. Camblor, L. A. Villaescusa, G. H. Kuehl, *Microporous Mesoporous Mater.* **2004**, *67*, 27; b) D. H. Olson, X. Yang, M. A. Camblor, *J. Phys. Chem. B* **2004**, *108*, 11044.

 © 2006 Wiley-VCH Verlag GmbH & Co. KGaA, Weinheim

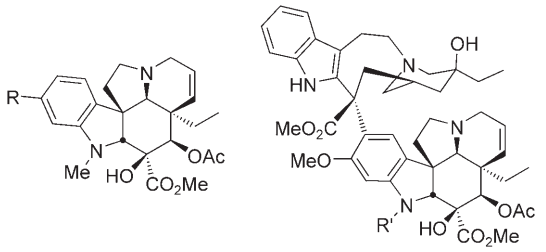
Total Synthesis

DOI: 10.1002/anie.200503024

Total Synthesis of (−)- and *ent*-(+)-Vindorosine: Tandem Intramolecular Diels–Alder/1,3-Dipolar Cycloaddition of 1,3,4-Oxadiazoles**

*Gregory I. Elliott, Juraj Velcicky, Hayato Ishikawa, YongKai Li, and Dale L. Boger**

Vindorosine (**1**) is among the most complex, highly functionalized, and stereochemically rich natural products within a family of more than 90 alkaloids isolated from the Madagascan periwinkle (*Catharanthus roseus* (L.) G. Don).[1] The related C16-methoxy derivative vindoline (**2**) constitutes the

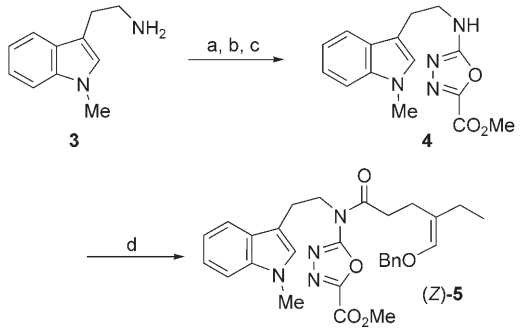


lower portion of vinblastine, which together with vincristine represent an important class of clinically effective anticancer therapeutics.[2]

As a consequence of its structural challenge and its relationship to vindoline, vindorosine has been the subject of a series of beautiful and historically important total syntheses.[3] In conjunction with our interest in developing an effective synthetic approach to vincristine and vinblastine, we report herein an unusually concise total synthesis of vindorosine developed as a prelude to efforts on vindoline[4] enlisting a tandem [4+2]/[3+2] cycloaddition cascade of 1,3,4-oxadiazoles. Limited reports of the cycloaddition reactions of electron-deficient and typically symmetrical 1,3,4-oxadiazoles have been detailed. In these studies, the groups of Vasilíev,[5] Sauer,[6] Seitz,[7] and most recently Warrener[8] have found that 1,3,4-oxadiazoles behave as electron-deficient azadienes and participate in intermolecular inverse-electron-demand Diels–Alder reactions to provide 2:1 cycloadducts with olefinic dienophiles.

The total synthesis of vindorosine (**1**) is based on a much more efficient intramolecular variant of the tandem [4+2]/[3+2] cycloaddition reaction that was inspired by the structures of the natural products.[9] The present reaction cascade is initiated by an intramolecular inverse-electron-demand Diels–Alder reaction of an electron-rich dienophile tethered to the 1,3,4-oxadiazole and is followed by the loss of N_2 and a subsequent intramolecular 1,3-dipolar cycloaddition of a tethered indole that proceeds with exclusive *endo* diastereoselectivity,[10] directed to the face of the 1,3-dipole opposite the fused lactam. This cycloaddition cascade not only produces the pentacyclic skeleton of **1** and introduces all the requisite substituents and functionality, but it also sets each of the six stereocenters found in vindorosine in a single step. As such, the 1,3,4-oxadiazole cycloaddition cascade, which introduces three new rings and four C–C bonds as well as all six key stereocenters, is ideally suited for the preparation of this class of natural products.

The requisite *N*-alkyl-2-amino-1,3,4-oxadiazole **4** was prepared in three steps (Scheme 1) from *N*-methyltryptamine (**3**).[9c] Thus, after treatment of **3** with CDI, the resulting



Scheme 1. Reagents and conditions: a) CDI, THF/CH_2Cl_2, 23 °C, 89%; b) methyl oxalylhydrazide, AcOH, THF, 40 °C, 93%; c) TsCl, Et_3N, CH_2Cl_2, 23 °C, 83%; d) (*Z*)-5-benzyloxy-4-ethylpent-4-enoic acid, EDCI, DMAP, CH_2Cl_2, 0–23 °C, 96%. Bn = benzyl, CDI = 1,1-carbonyldiimidazole, Ts = *p*-toluenesulfonyl, EDCI = 1-ethyl-3-(3-dimethylaminopropyl)-carbodiimide, DMAP = 4-(dimethylamino)pyridine.

imidazole urea (89%) was combined with methyl oxalylhydrazide to give the semicarbazide (93%), which was dehydrated to oxadiazole **4** (83%) by treatment with *p*-toluenesulfonyl chloride and triethylamine in CH_2Cl_2.[9c] Oxadiazole **4** was coupled with (*Z*)-5-benzyloxy-4-ethylpent-4-enoic acid to provide (*Z*)-**5** (96%), the precursor for the cycloaddition.

The cyclization of (*Z*)-**5** occurs in excellent yield when warmed in triisopropylbenzene for 60 h (Figure 1) to afford cycloadduct **6a** (78%) as a single detectable diastereomer. Initial attempts to cyclize (*Z*)-**5** provided **6a** in low yield (< 30% at > 5 mM), which is in contrast to the cyclization of the corresponding *E* isomer, (*E*)-**5**, which provides the C4 diastereomer **6b** in 86%.[9a] However, simple dilution of the reaction mixture led to improved yields (up to 78%). The results of a study of this unusual concentration effect are illustrated in Figure 1 and Table 1. A rather dramatic

[*] Dr. G. I. Elliott, Dr. J. Velcicky, Dr. H. Ishikawa, Dr. Y. Li, Prof. D. L. Boger
Department of Chemistry and
The Skaggs Institute for Chemical Biology
The Scripps Research Institute
10550 North Torrey Pines Road, La Jolla, CA 92037 (USA)
Fax: (+1) 858-784-7550
E-mail: boger@scripps.edu

[**] We gratefully acknowledge the financial support of the National Institutes of Health (CA42056) and the Skaggs Institute for Chemical Biology.

Supporting information for this article is available on the WWW under http://www.angewandte.org or from the author.

InterScience
© 2006 Wiley-VCH Verlag GmbH & Co. KGaA, Weinheim

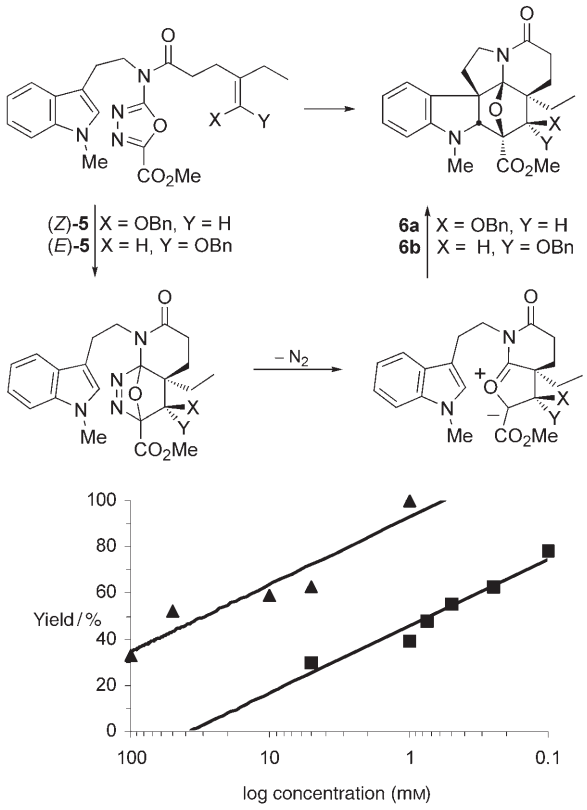


Figure 1. Concentration dependence of the yield of cycloaddition for the (*E*)-**5** (▲) and (*Z*)-**5** (■) in TIPB.

relationship between concentration and yield is observed, and this effect is most pronounced with (*Z*)-**5** which suggests that a competitive bimolecular reaction of **5** may compete with the intramolecular cycloaddition cascade at the higher reaction concentrations.

The enantiomers of cycloadduct **6a** proved readily separable by chiral-phase chromatography (semipreparative ChiralCel OD column, $2 \times 25\,cm^2$, 20% *i*PrOH in hexane, $10\,mL\,min^{-1}$, $t_R = 15.2$ and 21.3 min, $\alpha = 1.40$), which provided access to either enantiomer on a preparatively useful scale (150 mg/injection). α-Hydroxylation of cycloadduct **6a** was achieved by treatment of the lactam enolate with $(TMSO)_2$ and was followed by a direct quench of the reaction with TIPSOTf to provide silyl ether **7** in 60%. The α-hydroxylation reaction proceeded in a diastereoselective manner to provide **7** as a single diastereomer bearing an equatorial alcohol substituent (H7; dd, $J = 12.3$, 6.2 Hz) as a result of the approach of the electrophile from the least-hindered convex face of the enolate. The amide **7** was converted into thioamide **8** (93%) with Lawesson's reagent.[11] Reduction of the thioamide with Raney nickel[10] occurred cleanly in 2 h, but the reaction was allowed to proceed longer (16 h), leading to subsequent cleavage of the benzyl ether to provide the alcohol **9** (80%) directly in a single step (Scheme 2, only the natural enantiomer is shown).

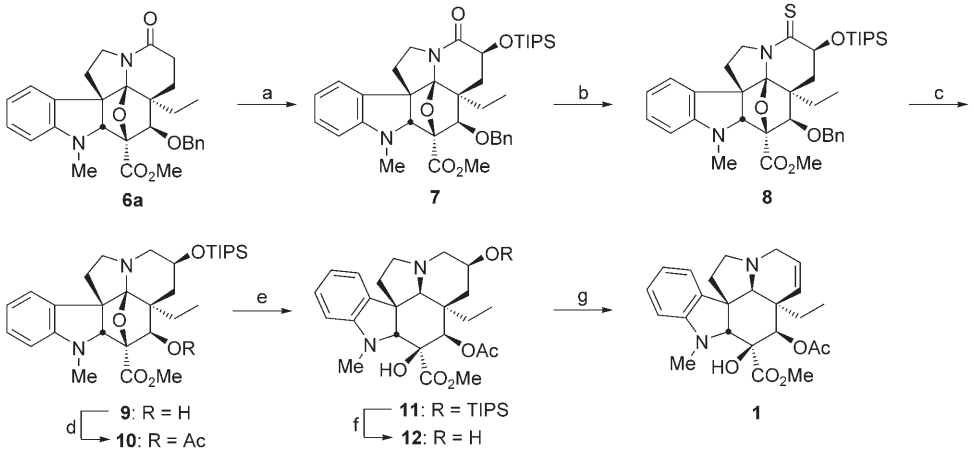
Table 1: Concentration dependence of the yield of cycloaddition.

Compound	Conc [mM]	Yield [%]
(*Z*)-**5**[a]	5	30
(*Z*)-**5**[a]	1	39
(*Z*)-**5**[a]	0.75	48
(*Z*)-**5**[a]	0.50	55
(*Z*)-**5**[a]	0.25	63
(*Z*)-**5**[a]	0.10	78
(*E*)-**5**[b]	50	40
(*E*)-**5**[b]	10	47
(*E*)-**5**[b]	5	56 (50–86)[c]
(*E*)-**5**[b]	1	76
(*E*)-**5**[d]	100	33
(*E*)-**5**[d]	50	52
(*E*)-**5**[d]	10	59
(*E*)-**5**[d]	5	64
(*E*)-**5**[d]	1	> 95

[a] Conditions: 230 °C, TIPB, 60 h. [b] Conditions: 180 °C, *o*-DCB, 24 h. [c] Preparative scale, multiple runs. [d] Conditions: 230 °C, TIPB, 18 h. TIPB = 1,3,5-triisopropylbenzene, *o*-DCB = *o*-dichlorobenzene.

Acetylation of secondary alcohol **9** with acetic anhydride (97%), followed by a diastereoselective reductive opening of the oxido bridge of **10** (93%, H_2/PtO_2),[10] and subsequent deprotection of the TIPS ether **11** with Bu_4NF afforded diol **12** (99%). A final regioselective elimination of the secondary alcohol **12** using Ph_3P/DEAD provided vindorosine (**1**, 74%), which was identical in all comparable respects with properties reported for the natural material.

In conclusion, an unusually concise total synthesis of the vinca alkaloid vindorosine has been developed. The key step in the synthesis is a highly efficient and diastereoselective intramolecular tandem [4+2]/[3+2] cycloaddition reaction of 1,3,4-oxadiazole that allows direct access to the pentacyclic aspidosperma skeleton in a reaction cascade that not only



Scheme 2. Reagents and conditions: a) 1. LDA, $(TMSO)_2$, THF −40 °C; 2. TIPSOTf, iPr_2NEt, 23 °C, 60%; b) Lawesson's reagent, toluene, 100 °C, 93%; c) Raney Ni, H_2, THF, 23 °C, 80%; d) Ac_2O, NaOAc, 23 °C, 97%; e) PtO_2, H_2 (40 psi), MeOH/EtOAc (1:1), 23 °C, 93%; f) Bu_4NF, THF, 0–23 °C, 99%; g) Ph_3P/DEAD, THF, 23 °C, 74%. LDA = lithium diisopropylamide, TMS = trimethylsilyl, TIPS = triisopropylsilyl, OTf = trifluoromethanesulfonate, DEAD = diethyl azodicarboxylate.

© 2006 Wiley-VCH Verlag GmbH & Co. KGaA, Weinheim

results in the formation of four new C–C bonds and three rings but also introduces all of the requisite functionality and all six stereocenters about the central six-membered ring of the natural product in a single reaction. Further development of the oxadiazole cascade cycloaddition reactions and their potential applications will be reported in due course.

Received: August 24, 2005
Published online: December 15, 2005

Keywords: alkaloids · cycloaddition · natural products · total synthesis

[1] B. K. Moza, J. Trojanek, *Collect. Czech. Chem. Commun.* **1963**, *28*, 1427 – 1433.
[2] Review: R. L. Nobel, *Biochem. Cell Biol.* **1990**, *68*, 1344 – 1351; R. L. Nobel, C. T. Beer, J. H. Cutts, *Ann. N. Y. Acad. Sci.* **1958**, *76*, 882 – 894.
[3] a) G. Buchi, K. E. Matsumoto, H. Nishimura, *J. Am. Chem. Soc.* **1971**, *93*, 3299 – 3301; b) R. Z. Andriamialisoa, N. Langlois, Y. Langlois, *J. Org. Chem.* **1985**, *50*, 961 – 967; c) M. E. Kuehne, D. E. Podhorez, T. Mulamba, W. G. Bornmann, *J. Org. Chem.* **1987**, *52*, 347 – 353; d) Formal syntheses: S. Takano, K. Shishido, M. Sato, K. Ogasawara, *Heterocycles* **1977**, *6*, 1699 – 1704; e) S. J. Veenstra, W. N. Speckamp, *J. Am. Chem. Soc.* **1981**, *103*, 4645 – 4646; f) J. D. Winkler, R. D. Scott, P. G. Williard, *J. Am. Chem. Soc.* **1990**, *112*, 8971 – 8975; g) M. Natsume, I. Utsunomiya, *Chem. Pharm. Bull.* **1984**, *32*, 2477 – 2479; h) Partial synthesis: B. Danieli, G. Lesma, G. Palmisano, R. Riva, *J. Chem. Soc. Chem. Commun.* **1984**, 909 – 911.
[4] Y. Choi, H. Ishikawa, J. Velcicky, G. I. Elliott, M. M. Miller, D. L. Boger, *Org. Lett.* **2005**, *7*, 4539 – 4542.
[5] a) N. V. Vasilíev, Y. E. Lyashenko, A. F. Kolomiets, G. A. Sokolskii, *Khim. Geterotsikl. Soedin.* **1987**, 562; b) N. V. Vasilíev, Y. E. Lyashenko, M. V. Galakhov, A. F. Kolomiets, A. F. Gontar, G. A. Sokolskii, *Khim. Geterotsikl. Soedin.* **1990**, 95 – 100; c) N. V. Vasilíev, Y. E. Lyashenko, A. E. Patalakha, G. A. Sokolskii, *J. Fluorine Chem.* **1993**, *65*, 227 – 231.
[6] F. Thalhammer, U. Wallfahrer, J. Sauer, *Tetrahedron Lett.* **1988**, *29*, 3231 – 3234.
[7] a) G. Seitz, C. H. Gerninghaus, *Pharmazie* **1994**, *49*, 102 – 105; b) G. Seitz, H. Wassmuth, *Chem.-Ztg.* **1988**, *112*, 80 – 81.
[8] a) R. N. Warrener, D. Margetic, P. J. Foley, D. N. Butler, A. Winling, K. A. Beales, R. A. Russell, *Tetrahedron* **2001**, *57*, 571 – 582; b) R. N. Warrener, S. Wang, L. Maksimovic, P. M. Tepperman, D. N. Butler, *Tetrahedron Lett.* **1995**, *36*, 6141 – 6144; c) R. N. Warrener, G. M. Elsey, R. A. Russell, E. R. T. Tiekink, *Tetrahedron Lett.* **1995**, *36*, 5275 – 5278; d) R. N. Warrener, L. Maksimovic, D. N. Butler, *J. Chem. Soc. Chem. Commun.* **1994**, 1831 – 1832; e) R. N. Warrener, D. N. Butler, W. Y. Liao, I. G. Pitt, R. A. Russell, *Tetrahedron Lett.* **1991**, *32*, 1889 – 1892; f) R. N. Warrener, P. Groundwater, I. G. Pitt, D. N. Butler, R. A. Russell, *Tetrahedron Lett.* **1991**, *32*, 1885 – 1888; g) Review: R. N. Warrener, *Eur. J. Org. Chem.* **2000**, 3363 – 3380; h) R. N. Warrener, D. Margetic, E. R. T. Tiekink, R. A. Russell, *Synlett* **1997**, 196 – 198.
[9] a) G. D. Wilkie, G. I. Elliott, B. S. J. Blagg, S. E. Wolkenberg, D. R. Soenen, M. M. Miller, S. Pollack, D. L. Boger, *J. Am. Chem. Soc.* **2002**, *124*, 11292 – 11294; b) S. E. Wolkenberg, D. L. Boger, *J. Org. Chem.* **2002**, *67*, 7361 – 7364; c) Z. Yuan, H. Ishikawa, D. L. Boger, *Org. Lett.* **2005**, *7*, 741 – 744.
[10] a) A. Padwa, A. T. Price, *J. Org. Chem.* **1998**, *63*, 556 – 565; b) A. Padwa, A. T. Price, *J. Org. Chem.* **1995**, *60*, 6258 – 6259.
[11] S. O. Lawesson, B. S. Pedersen, *Tetrahedron* **1979**, *35*, 2433 – 2437.

 © 2006 Wiley-VCH Verlag GmbH & Co. KGaA, Weinheim

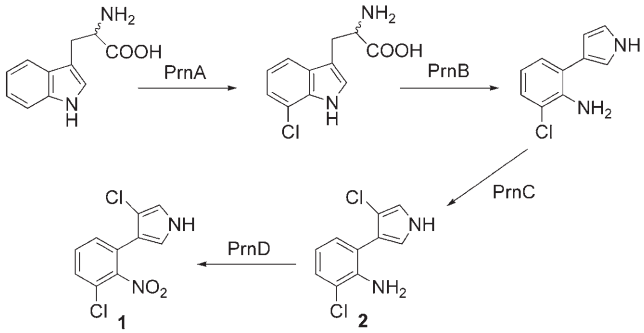
Enzyme Catalysis

DOI: 10.1002/anie.200502903

Mechanistic Studies on the Conversion of Arylamines into Arylnitro Compounds by Aminopyrrolnitrin Oxygenase: Identification of Intermediates and Kinetic Studies**

*Jungkul Lee and Huimin Zhao**

Rieske oxygenases are widespread in nature and catalyze a diverse set of oxidation reactions including *cis*-dihydroxylation, monohydroxylation, desaturation, sulfoxidation, and *O*- and *N*-dealkylation.[1,2] Recently, we reported the characterization of a Rieske *N*-oxygenase, aminopyrrolnitrin oxygenase (PrnD), which catalyzes unusual arylamine oxidation reactions.[3] Although arylamine oxidases seem to be widely distributed and used in a variety of metabolic reactions,[4–9] PrnD represents one of only two known examples of arylamine oxidases or *N*-oxygenases involved in the formation of nitro groups, the other being AurF involved in aureothin biosynthesis.[9] PrnD is involved in the biosynthesis of antibiotic pyrrolnitrin[3-chloro-4-(2′-nitro-3′-chlorophenyl)pyrrole] (**1**), which is produced by many Pseudomonads and displays broad-spectrum antifungal activity.[10] In the proposed biosynthetic pathway of **1** (Scheme 1),[11] PrnD catalyzes the oxidation of the amino group of aminopyrrolnitrin (**2**) to a nitro group to form **1**. Although PrnD has been characterized, no experimental evidence has been available for the mechanism of conversion of the arylamine. Therefore,



Scheme 1. Proposed biosynthetic pathway for pyrrolnitrin **1**.[11]

[*] Dr. J. Lee, Prof. H. Zhao
Department of Chemical and Biomolecular Engineering
University of Illinois at Urbana-Champaign
600 S. Mathews Ave., Urbana, IL 61801 (USA)
Fax: (+1) 217-333-5052
E-mail: zhao5@uiuc.edu

[**] This research was supported by a grant from the Office of Naval Research (N00014–02-1-0725). We thank Ee Lui Ang for his help in homology modeling. J.L. was partially supported by the Korea Research Foundation Grant funded by the Korean Government (Basic Research Promotion Fund, M01-2004-000-10159-0).

Supporting information for this article is available on the WWW under http://www.angewandte.org or from the author.

WILEY InterScience DISCOVER SOMETHING GREAT
© 2006 Wiley-VCH Verlag GmbH & Co. KGaA, Weinheim

we decided to investigate the intermediates formed during the conversion of arylamine into arylnitro compounds, as these might provide valuable mechanistic information.

Rieske oxygenases are typically comprised of two protein components: a terminal oxygenase and a flavin reductase.[12] Thus, a reductase was deemed necessary for the function of PrnD. On the basis of the nonspecificity of the flavin reductase,[21] the unknown reductase for PrnD from the *Pseudomonas* strain was substituted by flavin reductase SsuE from *E. coli*, with optimization of the concentration of SsuE for PrnD activity.[3] As compound **2**, the physiological substrate for PrnD, is not commercially available and is difficult to obtain in large amounts either from natural sources or by chemical synthesis, we used an alternative substrate 4-aminobenzylamine (pABA) to investigate the conversion mechanism of the arylamine. To observe the intermediates, PrnD was rapidly mixed with a 1 mM solution of pABA at 15 °C to slow the reaction, and the reaction mixture was analyzed every 30 min. Rieske [2Fe-2S] cluster-reconstituted PrnD[3] in combination with SsuE reductase showed a significant conversion of the substrate pABA to produce several compounds that migrated in HPLC with retention times of 4.9 min (authentic 4-nitrobenzylamine (pNBA)), 1.9 min (product A), and 4.5 min (product B; Figure 1). These products were absent if heat-denaturated

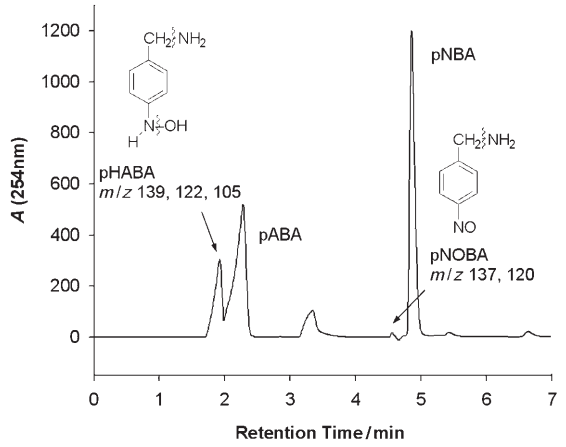


Figure 1. HPLC analysis of the PrnD reaction product. Each product was identified by LC-MS/MS analysis, and the fragmentation patterns are indicated.

PrnD was used or if pABA was omitted from the assay which indicated that the new metabolites were derived enzymatically from pABA. LC-MS/MS analysis of products A and B revealed that these compounds showed the calculated masses ($[M+H]^+$: m/z 139 and 137) of 4-hydroxylaminobenzylamine (pHABA) and 4-nitrosobenzylamine (pNOBA), respectively. Furthermore, it showed the characteristic fragmentation pattern of a hydroxylamine derivative (m/z 122 $[M-16]^+$ and 105 $[M-33]^+$) and a nitroso derivative (m/z 120 $[M-16]^+$), respectively. Thus, pHABA and pNOBA can be considered as intermediates or dead-end products in the dioxygenation of pABA by PrnD. To establish that the hydroxylamine and nitroso compounds are the intermediates in the dioxygenation reaction, it is necessary to show that the partial reaction does occur and that it does so at a rate equal to or greater than the rate of the overall reaction. The intermediacy of the hydroxylamine and nitroso compounds was further assessed through their chemical synthesis and kinetic characterization.

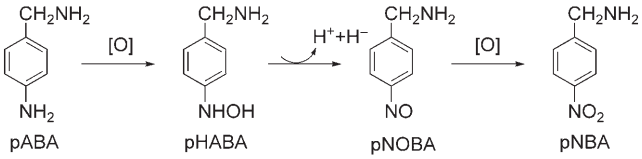
The intermediates pHABA and pNOBA were synthesized from pNBA and pABA, respectively, as described previously[14,15] and were characterized by ^{1}H NMR spectrometry and high-resolution (EI) mass spectrometry.[16] Initial-velocity studies were performed with pHABA and pNOBA as variable substrates in the presence of a fixed concentration of PrnD (≈ 1 μM). The data presented in Table 1 demonstrate

Table 1: Kinetic constants for aminopyrrolnitrin oxygenase.[a]

Substrate	k_{cat} [min^{-1}]	K_m [μM]	k_{cat}/K_m [μM^{-1} min^{-1}]
2	6.8 ± 0.59	191 ± 20	0.036 ± 0.004
pABA	6.5 ± 0.62	379 ± 34	0.017 ± 0.002
pHABA	7.9 ± 0.98	404 ± 56	0.019 ± 0.003
pNOBA	84.5 ± 9.72	580 ± 73	0.146 ± 0.021

[a] K_m = Michaelis constant.

that PrnD catalyzes the oxygenation of pHABA and pNOBA to the common product pNBA, indicating that the rate of oxygenation of the intermediates was high enough for them to be intermediates in the dioxygenation of the arylamine catalyzed by PrnD. As could be predicted from the fact that only small amounts of nitroso intermediate can be detected in the reaction mixture catalyzed by PrnD, the turnover rate of the nitroso compound is approximately 13-fold greater than the overall rate of dioxygenation. Thus, PrnD catalyzes at least three consecutive reactions (Scheme 2), in which the



Scheme 2. Proposed mechanism for bioconversion of arylamines into arylnitro compounds by PrnD.

conversion of arylamine into arylnitro compounds proceeds in two monooxygenation steps and one dehydrogenation step, via hydroxylamine and nitroso compounds as intermediates. The involvement of radical species in the reaction catalyzed by PrnD was excluded in the previous studies.[3]

To investigate the kinetic competence of intermediate pHABA, several PrnD mutants were prepared. The position of site-directed mutagenesis was decided based on homology modeling followed by analysis of the substrate-binding pocket. A homology model of PrnD was built based on the structure of the α-subunit of the naphthalene dioxygenase of *Pseudomonas* sp. strain NCIB 9816-4—the Rieske oxygenase for which a crystal structure was determined.[17] The α-subunit contains a Rieske [2Fe-2S] center and mononuclear non-heme-iron site, which is believed to be the site of activation of molecular oxygen and substrate oxygenation.[18] In consider-

 © 2006 Wiley-VCH Verlag GmbH & Co. KGaA, Weinheim

ation of the hydrophobicity of the residues and the distance between the substrate and the residues in the substrate-binding pocket, three residues (D269, F312, W209) were mutated. The catalytic activities of PrnD mutants of D269A, F312V, and W209A toward pHABA were determined and compared with those of pABA. Wild-type (WT) PrnD exhibited similar activity toward pHABA and pABA, consistent with the notion that formation of intermediate pHABA is a rapid step in WT PrnD. F312V and W209A mutants showed no conversion of either pHABA or pABA. However, D269A mutant PrnD showed much higher activities toward the intermediate pHABA ($k_{cat} = 8.4\ min^{-1}$, $k_{cat}/K_m = 0.020\ \mu M^{-1} s^{-1}$) than pABA ($k_{cat} = 0.3\ min^{-1}$, $k_{cat}/K_m = 0.004\ \mu M^{-1} s^{-1}$). These results indicate that the hydroxylamine intermediate is kinetically competent. In addition, the accumulation of the hydroxylamine intermediate in WT PrnD indicates that its formation is fast relative to its decay. The lack of significant accumulation of the nitroso intermediate suggests that it decays faster than it is formed. Thus, the rate-limiting step is the dehydrogenation of pHABA to give pNOBA. Of note, in the absence of NADPH flavin reductase system, the hydroxylamine intermediate was not oxidized by O_2 to the nitroso intermediate and H_2O_2 was not formed. Artificial electron acceptors such as methylene blue and ferricyanide were less than 10% as effective as O_2 under anoxic conditions. In addition, the D269A mutation significantly slows down the formation of hydroxylamine, suggesting that Asp269 is involved in the early steps of the reaction and likely responsible for the abstraction of a proton from the substrate. A homology model shows that Asp269 is properly positioned in the substrate-binding pocket to perform the proposed function.

To confirm whether one or both oxygen atoms of O_2 were incorporated into the product, we carried out isotope-labeling experiments with $^{18}O_2$. Incorporation of the label was analyzed by ESI/LC-MS. In the first experiment, PrnD was incubated with pABA in an $^{18}O_2$ atmosphere. Unlabeled pNBA showed the molecular ion, $[M+H]^+$, at m/z 153. In contrast, most of the pNBA produced under the $^{18}O_2$ atmosphere revealed the molecular ion at m/z 157, indicating the incorporation of two ^{18}O atoms. In addition, incorporation of one ^{18}O atom into pHABA was demonstrated by the signal for the molecular ion at m/z 141, in comparison to m/z 139 for the unlabeled pHABA. For the second labeling experiment, unlabeled pHABA and pNOBA were incubated in an $^{18}O_2$ atmosphere with PrnD. The incorporation of one ^{18}O atom into pNBA was demonstrated by the molecular ion at m/z 155. In addition, no ^{18}O was incorporated into pNOBA in the reaction of pHABA with PrnD, ruling out the possibility of the involvement of the dihydroxylamine intermediate. Thus two ^{18}O atoms are sequentially incorporated into the product, confirming that the dioxygenation by PrnD proceeds in a consecutive monooxygenase-type reaction. Note that some iron(II)-dependent oxygenases have been reported to be bifunctional or even trifunctional, catalyzing several consecutive oxidative transformations within a single biosynthetic pathway.[19,20]

In this study, we have obtained direct evidence for the involvement of hydroxylamine and nitroso intermediates in the PrnD-catalyzed oxygenation reaction of arylamines, substantiating for the first time the catalytic mechanism for the conversion of arylamines into arylnitro compounds. The intermediates are at least partially released from the active site of the enzyme during catalysis, providing a rare example of three consecutive chemical reactions catalyzed by one active site. This may be the primary mechanism by which arylamines are oxygenated to give arylnitro compounds in biological processes. The characterization of PrnD adds a new and interesting member to the family of Rieske nonheme-iron oxygenases and demonstrates the pathway for the formation of arylnitro compounds in nature.

Experimental Section

Site-directed mutagenesis of pTKXb-PrnD was carried out by using the QuikChange site-directed mutagenesis kit from Stratagene (La Jolla, CA). The pTKXb-prnD plasmid was used as the DNA template.[3] Trp209 and Asp269 residues were mutated to Ala individually. Residue Phe312 was mutated to Val. The plasmids containing the correct mutant genes were cloned into pMAL-c2x and then used to transform *E. coli* BL21(DE3), and colonies selected by ampicillin resistance were used for protein expression. The PrnD mutants were expressed, purified, and reconstituted with Fe^{2+} and S^{2-} according to the same procedure for the wild-type enzyme, as described elsewhere.[3]

Enzyme activity was routinely assayed by HPLC. The assay mixture (0.5 mL final volume) contained 500 μM NADPH, 3 μM FMN, 500 μM substrate, and SsuE and PrnD (SsuE/PrnD molar ratio of 4.0) in 20 mM TrisHCl at pH 7.8 and was stirred at 30 °C. Reactions were initiated by addition of PrnD to the reaction mixture and analyzed by HPLC. One unit of activity was defined as the amount of enzyme forming 1 μmol of product per minute at 30 °C under standard assay conditions, calculated from the rate of substrate depletion. Kinetic parameters determined in atmospheric oxygen were obtained by fitting the data to the Michaelis–Menten equation.

For labeling studies with $^{18}O_2$, two vials, one containing substrate and one containing holo-PrnD reaction mixture, were degassed by application of a vacuum and flushed with argon three times. The anaerobic holo-PrnD solution was transferred to the vial containing the substrate. The argon was removed by application of a vacuum, and finally $^{18}O_2$ was allowed to enter into the vial. After incubation for 1 h at 30 °C, the reaction was analyzed by HPLC coupled to an electrospray ionization (EI) mass spectrometer (TSQ Quantum, ThermoFinnigan, San Jose, CA) in positive-ion mode. A linear gradient of MeOH (0–75%) in aqueous acetic acid (0.1%) was used.

Products of enzyme reactions were analyzed by an Agilent 1100 Series HPLC System. The sample was eluted on a ZORBAX SB-C8 Column (4.6 × 150 mm^2, Agilent). HPLC parameters were as follows: 25 °C; solvent A: 1% acetic acid in water; solvent B: methanol; gradient: 5% B for 2 min; then to 100% B in 18 min, and finally maintain at 100% B for 2 min; flow rate: 1.0 mL min^{-1}; detection by UV absorbance at 254 nm. Hydrogen peroxide was determined by monitoring the oxidation of 2,2′-azino-bis(3-ethylbenzthiazoline-6-sulfonic acid) in the presence of horseradish peroxidase at 725 nm, as described previously.[21]

Received: August 16, 2005
Published online: December 12, 2005

Keywords: amines · enzyme catalysis · oxygenation · reaction mechanisms · reactive intermediates

 © 2006 Wiley-VCH Verlag GmbH & Co. KGaA, Weinheim

[1] M. Costas, M. P. Mehn, M. P. Jensen, L. Que, *Chem. Rev.* **2004**, *104*, 939.
[2] S. M. Resnick, K. Lee, D. T. Gibson, *J. Ind. Microbiol. Biotechnol.* **1996**, *17*, 438.
[3] J. K. Lee, M. Simurdiak, H. Zhao, *J. Biol. Chem.* **2005**, *280*, 36719.
[4] C. Rebstock, H. J. Crooks, J. Controulis, Q. Bartz, *J. Am. Chem. Soc.* **1949**, *71*, 2458.
[5] M. Morris, G. Pagan, H. Warmke, *Science* **1954**, *119*, 322.
[6] G. C. Lancini, D. Kluepfel, E. Lazzari, G. Sartori, *Biochim. Biophys. Acta* **1966**, *130*, 37.
[7] R. R. King, C. H. Lawrence, L. A. Calhoun, *Phytochemistry* **1998**, *49*, 1265.
[8] B. Meunier, S. P. de Visser, S. Shaik, *Chem. Rev.* **2004**, *104*, 3947.
[9] J. He, C. Hertweck, *J. Am. Chem. Soc.* **2004**, *126*, 3694.
[10] P. E. Hammer, D. S. Hill, S. T. Lam, K. H. Van Pée, J. M. Ligon, *Appl. Environ. Microbiol.* **1997**, *63*, 2147.
[11] K. H. Van Pée, O. Salcher, F. Lingens, *Angew. Chem.* **1980**, *92*, 855; *Angew. Chem. Int. Ed. Engl.* **1980**, *19*, 828.
[12] J. R. Mason, R. Cammack, *Annu. Rev. Microbiol.* **1992**, *46*, 277.
[13] S. Keller, T. Wage, K. Hohaus, M. Holzer, E. Eichhorn, K. H. Van Pée, *Angew. Chem.* **2000**, *112*, 2380; *Angew. Chem. Int. Ed.* **2000**, *39*, 2300.
[14] C. Theodore, F. G. William, *J. Org. Chem.* **1972**, *37*, 741.
[15] R. H. Richard, P. B. Raymond, *J. Am. Chem. Soc.* **1960**, *82*, 3454.
[16] pHABA: ^{1}H NMR ([D$_6$]acetone, 500 MHz): $\delta = 2.92$ (br s, NH$_2$), 1.91 (br s, NHOH), 4.38 (d, 2H), 6.63 (d, 2H), 7.02 (d, 1H), 7.28 ppm (d, 1H); HR-EI-MS: *m*/*z* calcd for pHABA [M^+]: 138.07931; found: 138.07914. pNOBA: ^{1}H NMR ([D$_6$]acetone, 500 MHz): $\delta = 3.39$ (br s, NH$_2$), 4.18 (s, 2H), 7.81 (d, 2H), 8.23 ppm (d, 2H); HR-EI-MS: *m*/*z* calcd for pNOBA [M^+]: 136.06367; found: 136.06366.
[17] B. Kauppi, K. Lee, E. Carredano, R. E. Parales, D. T. Gibson, H. Eklund, S. Ramaswamy, *Structure* **1998**, *6*, 571.
[18] C. S. Butler, J. R. Mason, *Adv. Microb. Physiol.* **1997**, *38*, 47.
[19] Z. H. Zhang, J. S. Ren, D. K. Stammers, J. E. Baldwin, K. Harlos, C. J. Schofield, *Nat. Struct. Biol.* **2000**, *7*, 127.
[20] L. D. Thornburg, M. T. Lai, J. S. Wishnok, J. Stubbe, *Biochemistry* **1993**, *32*, 14023.
[21] D. E. Ward, C. J. Donnelly, M. E. Mullendore, J. van der Oost, W. M. de Vos, E. J. Crane III, *Eur. J. Biochem.* **2001**, *268*, 5816.

 © 2006 Wiley-VCH Verlag GmbH & Co. KGaA, Weinheim

DOI: 10.1002/anie.200502440

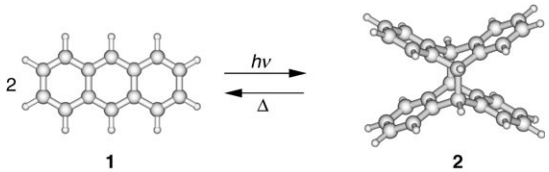
The Importance of Inter- and Intramolecular van der Waals Interactions in Organic Reactions: the Dimerization of Anthracene Revisited**

Stefan Grimme, Christian Diedrich, and Martin Korth*

The van der Waals (also called dispersive) interactions between atoms and molecules play an important role in many chemical systems. They are delicately balanced with electrostatic and exchange/repulsion interactions[1] and together they control, for example, the structures of DNA and proteins, the packing of crystals, the formation of aggregates, host–guest systems, and the orientation of molecules on surfaces or in molecular films.[2] It is generally believed that van der Waals effects are of major importance only for intermolecular situations (for example, weakly bonded complexes), although there are theoretical indications that, for example, protein folding is also significantly influenced by intramolecular van der Waals interactions.[3] It is shown herein for the first time that these effects are also of particular importance for the accurate description of the thermodynamics of "normal" chemical reactions. Furthermore, it will be shown how and why actual implementations of Kohn–Sham density functional theory (DFT)[4] yield a seemingly right answer for the *wrong* reason.

The photodimerization of anthracene (**1**), a clean and reversible reaction that occurs through a [4+4] cycloaddition to yield the covalently bound polycyclic dimer (**2**; Scheme 1), has been known for about 140 years.[5] The dimer is thermally labile at elevated temperatures and reverts back to the monomers, which raised some hopes for its use as a solar energy storage device.

The reaction enthalpy for the dimerization of anthracene has been measured by several methods, under different conditions. 9-Substituted anthracenes have also been investigated (see Ref. [6] and references therein). Experimentally,



1 2

Scheme 1.

[*] Prof. Dr. S. Grimme, Dr. C. Diedrich, M. Korth
Theoretische Organische Chemie
Organisch-Chemisches Institut der Universität Münster
Corrensstrasse 40, 48149 Münster (Germany)
Fax: (+49) 251-83-33412
E-mail: grimmes@uni-muenster.de

[**] This work was supported by the Deutsche Forschungsgemeinschaft in the framework of the SFB 424 ("Molekulare Orientierung als Funktionskriterium in chemischen Systemen"). The authors thank C. Mück-Lichtenfeld for technical assistance.

 © 2006 Wiley-VCH Verlag GmbH & Co. KGaA, Weinheim InterScience

the dissociation was always found to be exothermic, that is, $\Delta H_D < 0$ for $\mathbf{2} \rightarrow 2 \times \mathbf{1}$. The most reliable experimental data are summarized in Table 1, where for convenience theoretical corrections for thermal and zero-point vibrational contributions (and for substituent effects in the last four cases) have been applied to obtain pure electronic dissociation energies D_e for the parent system. These energies can be better compared with theoretical computations that primarily yield energies instead of enthalpies. The corrected values for the substituted compounds should be considered with some care because of the experimentally relevant electrostatic effects in the condensed phase (see below).

Table 1: Summary of experimental (condensed phase) results [kcal mol^{-1}].[a]

Monomer	Method	ΔH_D	D_e
anthracene	heat of combustion, solid[b]	-13 ± 4	-10
anthracene	DSC, solid/melt (479 K)[c]	-6.9 ± 1.5	-4
9-methoxy-anthracene	heat of combustion, solid[d]	-24	-16
9-decyloxy-anthracene	DSC, tetralin solution (370 K)[e]	-7.1 ± 0.7	$+1$
9-cyanoanthracene	DSC, solid/melt[f]	-20 ± 2	-6
9-decylanthracene	DSC, tetralin solution (392 K)[e]	-6.5 ± 0.7	$+1$
anthracene	average		-6 ± 4

[a] ΔH_D is the reaction enthalpy for dimer dissociation and D_e refers to a pure electronic dissociation energy for the parent system. The ZPVE, thermal, and substituent corrections (in the head-to-tail dimers, the decyl(oxy) group has been replaced by ethyl and methoxy groups, respectively) have been obtained at the DFT-D-PBE/TZV(2d,2p) level. The corrections from *E* to *H* are between 2.1 and 2.7 kcal mol^{-1} for the systems considered. [b] Derived from solid-state heats of formation of **1** ($\Delta_f H^0_s = 30$ kcal mol^{-1}[-1]) and **2** ($\Delta_f H^0_s = 73$ kcal mol^{-1}).[8] [c] Differential scanning calorimetry (DSC), Ref. [9]. [d] Ref. [10]. [e] Ref. [6]. [f] Ref. [11].

Although the data show some scatter with relatively large error bars, it is evident that the experimental D_e value for the parent system is negative, probably around -6 kcal mol^{-1} (average) with an estimated uncertainty of ± 4 kcal mol^{-1}.

The reaction was investigated thoroughly by quantum chemical computations in 1999.[6] Quite reasonable agreement with the experimental data was obtained with DFT and Hartree–Fock methods, but even then strikingly different results ($D_e = 20$ kcal mol^{-1}) were obtained from second-order Møller–Plesset (MP2) theory. The better available computer hardware and algorithmic developments in computational quantum chemistry means that it is nowadays possible to push our approximations to the solutions of the electronic Schrödinger equation to a limit, which allows us to resolve this apparent discrepancy. Both **1** and **2** represent quite "normal" organic molecules that lack any apparent complicated electronic structure (for example, biradicalic or extremely unsaturated (metallic) character[12]). Thus, our conclusions have quite important consequences for routine computational modeling studies where similar problems/systems are quite common.

The results of calculated dissociation energies D_e are summarized in Table 2. Systematically improved basis sets up to quadruple-zeta quality (leading to 2140 basis functions for **2**) have been used for the Hartree–Fock (HF) and MP2 methods which allow quite accurate extrapolation to the one-particle basis set limit. One finds from perusing Table 2 that reasonably converged results can be obtained with the cc-pVTZ AO basis. The D_e value at the MP2 basis set limit is estimated to be 20.9 kcal mol^{-1}. Thus, the correlation contribution to the reaction energy is very large (D_e(MP2)$-D_e$(HF) = 42 kcal mol^{-1}), and stabilizing the dimer relative to the two monomers. It is well known, however, that the MP2 method generally overestimates various electron correlation effects,[13] as can be seen from the smaller D_e values at the more reliable QCISD(T) and SCS-MP2 (improved MP2 method, see Ref. [13]) levels. Assuming that MP2 and QCISD(T) have a similar basis set dependence, one can estimate a basis set limit QCISD(T) value of 9.5 kcal mol^{-1} with an estimated uncertainty of about ± 2 kcal mol^{-1}. Strikingly, this value still differs by about 15 kcal mol^{-1} from the experimental value, and even the sign is different (endothermic by theory, exothermic by experiment). This difference prompted us to check the D_e value by an independent, completely different quantum mechanical approach. Diffusion Monte Carlo (DMC) is a stochastic method that allows the electronic Schrödinger equation to be solved directly.[14] Within the fixed-node (FN) approximation, which is necessary to fulfill the Pauli principle, DMC calculations are exact and yield energies including a statistical standard deviation. In our case we get $D_e = 9 \pm 2$ kcal mol^{-1}, which is in perfect agreement with the results from the traditional wave-function methods. We can thus finally state a definite (gas-phase) D_e value that is positive, around 9 kcal mol^{-1}, with a conservative error estimate of ± 3 kcal mol^{-1}.

Table 2: Summary of calculated dissociation energies D_e for the anthracene dimer (**2**).

Method[a]	AO basis	D_e [kcal mol^{-1}]
Hartree–Fock	cc-pVDZ	-15.7
Hartree–Fock	cc-pVTZ	-20.7
Hartree–Fock	cc-pVQZ	-21.1
MP2	cc-pVDZ	24.2
MP2	cc-pVTZ	21.4
MP2	cc-pVQZ	21.0
SCS-MP2	cc-pVTZ	13.4
QCISD	cc-pVDZ	11.9
QCISD(T)	cc-pVDZ	12.7
QCISD(T)	est. cc-pVQZ[b]	9.5
FN-DMC	[c]	9 ± 2
best estimate		9 ± 3
DFT-B3LYP	cc-pVTZ	-25.8
DFT-PBE	TZV(2df,2pd)	-14.5
DFT-D-PBE	TZV(2df,2pd)	-3.7

[a] Single-point calculations using the MP2/TZV(2d,2p) geometry. The effect of full geometry optimization at each theoretical level has been estimated to be ± 1 kcal mol^{-1}. [b] D_e(QCISD(T)/cc-pVDZ) + [D_e(MP2/cc-pVQZ)-D_e(MP2/cc-pVDZ)]. [c] For details see the Methods Section.

We also applied different density functionals to the problem, but found that they all perform in a very similar manner. Representative results with standard functionals (B3LYP[15] and PBE[16]) as well as one with corrections for dispersion interactions (DFT-D[17]), which are notoriously

 © 2006 Wiley-VCH Verlag GmbH & Co. KGaA, Weinheim

poor with current functionals,[18] are also given in Table 2. If one compares these data with our accurate theoretical reference value one can conclude that standard DFT fails completely, and yields negative D_e values similar to the (uncorrelated) HF method. Particularly striking is the poor performace of the commonly used B3LYP functional that leads to a huge and unacceptable error for D_e of about 35 kcal mol^{-1}. At first sight, however, DFT seems to be in good agreement with experiment (which also yields $D_e < 0$), but as will be shown below this results from error compensation between the neglect of inter- and intramolecular van der Waals interactions in the monomers and dimers, respectively.

The first hint to the problem of the discrepancy between ab initio theory and experiment/DFT comes from the large dispersion correction obtained from the DFT-D method. Part of the answer to the problem is related to the large size of the molecules (especially the dimer), with many interatomic distances close to those of typical van der Waals minima. When used together with the PBE density functional, the long-range (R^{-6}) dispersion correction lowers the energy of the dimer relative to two separated anthracene molecules by about 11 kcal mol^{-1}, thus leading finally to a much smaller D_e value of -3.7 kcal mol^{-1} (similar results have also been obtained at the DFT-D level with other functionals). Clearly (and ultimately quite understandably), there are strong intramolecular van der Waals interactions in **2**. One can already see clearly from the structure that the four outer benzene rings are in a stacked arrangement (C···C distances from 270 to 450 pm) which should add roughly 5–10 kcal mol^{-1} internal stabilization compared to $2 \times$ **1**. These effects are entirely a result of long-range electron correlation, and are absent in Hartree–Fock and standard DFT, which calculate that the dimer is too unstable ($D_e < 0$). In contrast, all the correlated ab initio methods (SCS-MP2, QCISD(T), FN-DMC) accurately include long-range electron correlation and yield $D_e > 0$.[19]

However, what about the intermolecular van der Waals interactions mentioned in the title? They are of utmost importance under the experimental conditions, namely, in the condensed phase, for which we consider the following model (Figure 1): the first product of the dissociation of **2** is of course not two infinitely separated anthracene molecules (as hitherto considered in the calculations) but rather a van der Waals complex (**3**) that may later dissociate. Since the complex **3** and **2** have about the same spatial dimensions (surfaces), their solvation enthalpy is roughly the same, and thus need not to be considered further. A simple and computationally straightforward condensed-phase correction to the calculated (separated, gas-phase) D_e value is thus the van der Waals dimer binding energy of the stacked complex (**3**; Figures 1 and 2).

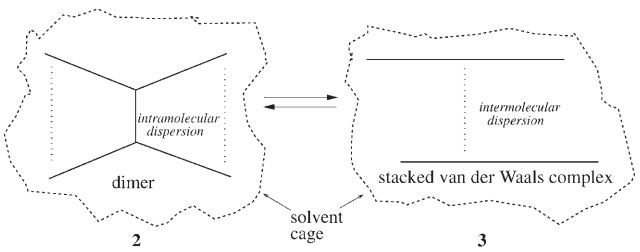


Figure 1. Model for the dimerization of anthracene in the condensed phase.

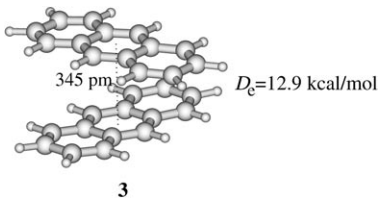


Figure 2. Crossed (D_{2d}) structure (**3**) of the van der Waals complex of two anthracene molecules. The structure has been optimized at the DFT-D-BLYP/TZV(2d,2p) level, while the interaction energy refers to counterpoise-corrected, single-point SCS-MP2/aug-cc-pVTZ computations. Only slightly higher in energy (about 0.2 kcal mol^{-1}) is a displaced, graphite-like structure with C_i symmetry (not shown).

At the very reliable SCS-MP2/aug-cc-pVTZ level (estimated error ± 2 kcal mol^{-1}) we obtain a quite substantial binding energy of 12.9 kcal mol^{-1} for **3**. This result means that when combined with the previous (separated, gas-phase) D_e value of 9 ± 3 kcal mol^{-1} we obtain $2 \times$ **1** as the van der Waals complex that is energetically now *below* **2** (that is, $D_e^{corrected} = -4 \pm 3$ kcal mol^{-1}). This value is (within the error bars) in reasonable agreement with the experimental findings (exergonic dissociation). The model (which is summarized in Figure 3) is supported by the results of calculations performed for the hydrogenation of **1**. This reaction leads to 9,10-dihydroanthracene, which is electronically similar to **2** (that is, has a saturated inner ring and two outer benzene rings) but lacks the intramolecular dispersion interactions. In this case, all applied theoretical methods are in much better agreement with each other and are also close to the experimental value.[20]

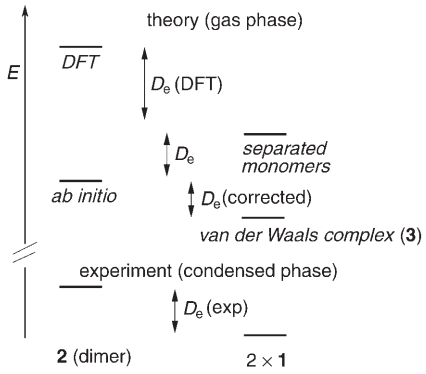


Figure 3. Model to explain the difference between experiment and theory.

It is now clear why the DFT approaches seemingly give the right answer when compared to the experimental results: the neglected intermolecular (monomers) and intramolecular (dimer) van der Waals effects are both of the same magnitude, appear on either side of the reaction equation, and thus their effects fortunately cancel. Note, that our arguments also

 © 2006 Wiley-VCH Verlag GmbH & Co. KGaA, Weinheim

hold for the data derived from, for example, heats of combustion experiments in the solid state (entry 1, Table 1), where one should consider the lattice energies of the reactants as a correction.[21]

In summary, the results of our studies have two major consequences. First, we encourage experimental chemists to conduct gas-phase experiments (or accurate (gas-phase) heat of formation determinations for **2**) to check our theoretical results. We are, however, very sure that our (gas-phase, $R = \infty$) value of $D_e = 9 \pm 3$ kcal mol^{-1} is correct and thus suggest this system as an important benchmark for approximate quantum chemical methods, including dispersion (especially new density functionals). Secondly, we believe that a delicate balance between inter- and intramolecular dispersion effects is a quite general phenomenon for larger molecules that must be considered more carefully in the future. These often so-called "weak interactions" are intuitively underestimated by most chemists,[22] but may sum up to significant effects even in medium-sized molecules. Another good example is the photodimer of C_{60}, where intramolecular dispersion apparently also leads to a change in the sign of D_e.[23]

Methods Section

The (SCS-)MP2 and DFT calculations were performed with the TURBOMOLE suite of programs,[24] and the RICC code developed in our laboratory was used for the QCISD/QCISD(T) treatments. The triple-zeta sets of Ahlrichs and co-workers (TZV[25]) or the correlation consistent sets of Dunning (cc-pVXZ, X = D, T, Q[26]) were employed as the AO basis. In the (SCS-)MP2 and QCISD/QCISD(T) treatments the RI approximation for the two-electron integrals were used.[27] The geometries of **1** and **2** were optimized at the MP2/TZV(2d,2p) level, while the structure of **3** refers to a DFT-D-BLYP/TZV(2d,2p) calculation.[17] Corrections from enthalpies to energies and the substituent effects were obtained from harmonic frequency calculations at the DFT-D-PBE/TZV(2d,2p) level.

FN-DMC calculations were carried out with Amolqc, a QMC program by Lüchow et al.[28] We used guiding functions of the Slater–Jastrow type, with a B3LYP Kohn–Sham determinant and a Schmidt–Moskowitz type correlation function; Kohn–Sham determinants have proven their usefulness for FNDMC in the past.[29,30] Correlation parameters were optimized by variance minimization. To further improve the efficiency of the calculations, we used soft-ECPs developed by Lester and co-workers[31] for carbon atoms. The error introduced by the ECPs (core-valence polarization) was estimated at the Hartree–Fock level to be about 0.4 kcal mol^{-1} for D_e. The orbitals were expanded in GTO triple-ζ valence basis sets. For carbon atoms, they were fully optimized in atomic Hartree–Fock calculations with the ECPs and were augmented by 2d polarization functions from the Dunning cc-pVTZ basis set. For hydrogen atoms we used an optimized triple-ζ basis (contracted from a 611 primitive) set with 2p and 1d polarization functions also taken from the cc-pVTZ basis. The time-step dependence of the results was checked by performing calculations with steps of $0.005\,E_h^{-1}$ and $0.003\,E_h^{-1}$, respectively, which yielded differences
< 1 kcal mol^{-1} for D_e.

Received: July 13, 2005
Published online: December 15, 2005

Keywords: ab initio calculations · anthracene · density functional calculations · noncovalent interactions · solvent effects

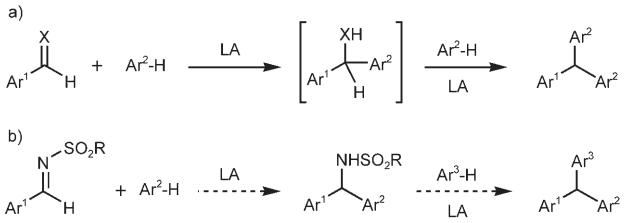
[1] A. J. Stone, *The Theory of Intermolecular Forces*, Oxford University Press, Oxford, **1997**.
[2] J.-M. Lehn, *Supramolecular Chemistry. Concepts and Perspectives*, VCH, Weinheim, **1995**; E. A. Meyer, R. K. Castellano, F. Diederich, *Angew. Chem.* **2003**, *115*, 1244 – 1287; *Angew. Chem. Int. Ed.* **2003**, *42*, 1210 – 1250; N. Kannan, S. Vishveshwara, *Protein Eng.* **2000**, *13*, 753 – 761; P. Hobza, J. Sponer, *Chem. Rev.* **1999**, *99*, 3247 – 3276; I. Dabkowska, H. V. Gonzalez, P. Jurecka, P. Hobza, *J. Phys. Chem. A* **2005**, *109*, 1131 – 1136.
[3] Q. Wu, W. Yang, *J. Chem. Phys.* **2002**, *116*, 515 – 524.
[4] W. Koch, M. C. Holthausen, *A Chemist's Guide to Density Functional Theory*, Wiley-VCH, New York, **2001**.
[5] J. Fritzsche, *J. Prakt. Chem.* **1866**, *101*, 333 – 335.
[6] S. Grimme, S. D. Peyerimhoff, H. Bouas-Laurent, J.-P. Desvergne, H.-D. Becker, S. M. Sarge, H. Dreeskamp, *Phys. Chem. Chem. Phys.* **1999**, *1*, 2457 – 2462.
[7] J. D. Cox, G. Pilcher, *Thermochemistry of Organic and Organometallic Compounds*, Academic Press, New York, **1970**; NIST Standard Reference Database; see http://webbook.nist.gov/chemistry/.
[8] P. Bender, J. Farber, *J. Am. Chem. Soc.* **1952**, *74*, 1450 – 1452.
[9] D. Donati, G. G. T. Guarini, P. Sarti-Fantoni, *Mol. Cryst. Liq. Cryst.* **1981**, *69*, 241 – 243.
[10] J. Bendig, W. Buchwitz, J. Fischer, D. Kreysig, *J. Prakt. Chem.* **1981**, *323*, 485 – 498.
[11] G. G. T. Guarini, P. Sarti-Fantoni, *Mol. Cryst. Liq. Cryst.* **1970**, *6*, 423 – 426.
[12] This qualitative view is supported by the T1 diagnostics of the QCISD calculations, the smallness of the (T) contribution, as well as exploratory MR-MP2 computations.
[13] S. Grimme, *J. Chem. Phys.* **2003**, *118*, 9095 – 9102.
[14] J. B. Anderson, *J. Chem. Phys.* **1975**, *63*, 1499 – 1503; B. L. Hammond, J. W. A. Lester, P. J. Reynolds, *Monte Carlo Methods in Ab Initio Quantum Chemistry*, World Scientific, Singapore, **1994**.
[15] A. D. Becke, *J. Chem. Phys.* **1993**, *98*, 5648 – 5652; P. J. Stephens, F. J. Devlin, C. F. Chablowski, M. J. Frisch, *J. Phys. Chem.* **1994**, *98*, 11623 – 11627.
[16] J. P. Perdew, K. Burke, M. Ernzerhof, *Phys. Rev. Lett.* **1996**, *77*, 3865 – 3868.
[17] S. Grimme, *J. Comput. Chem.* **2004**, *25*, 1463 – 1476.
[18] S. Kristyan, P. Pulay, *Chem. Phys. Lett.* **1994**, *229*, 175 – 180; P. Hobza, J. Sponer, T. Reschel, *J. Comput. Chem.* **1995**, *16*, 1315 – 1325.
[19] There is an additional correlation effect arising from the formal conversion of four π electrons in **1** into two σ bonds in **2** which is also not accounted for accurately by DFT.
[20] The experimental dissociation energy for 9,10-dihydroanthracene $\rightarrow$ **1** + H_2 (derived from experimental heats of formation[7] and vibrational DFT-PBE corrections) is 23 ± 2 kcal mol^{-1}. At MP2/cc-pVTZ, SCS-MP2/cc-pVTZ, QCISD(T)/cc-pVDZ, PBE/cc-pVTZ, and B3LYP/cc-pVTZ theoretical levels (MP2/TZV(2d,2p) geometry) one obtains 21.0, 21.2, 23.5, 17.9, and 16.2 kcal mol^{-1}, respectively.
[21] The lattice enthalpy of **1** (the difference in heats of formation in the gas phase and the solid state) is 25 kcal mol^{-1}.[7] If we assume the same value for **2** we can estimate its gas-phase heat of formation to be 98 kcal mol^{-1}, which leads to an experimental estimate for ΔH_D of about 12 kcal mol^{-1}. The thus obtained endothermicity of the dissociation is in full agreement with our theoretical results.
[22] Data obtained for nonpolar solutes in a nonpolar solvents are usually taken as substitutes for the gas phase.
[23] A. Bihlmeier, C. C. M. Samson, W. Klopper, *Chem. Phys. Chem.*, **2005**, *6*, 2625 – 2632.

 © 2006 Wiley-VCH Verlag GmbH & Co. KGaA, Weinheim

[24] R. Ahlrichs, M. Bär, M. Häser, H. Horn, C. Kölmel, *Chem. Phys. Lett.* **1989**, *162*, 165 – 169; TURBOMOLE (Vers. 5.6): R. Ahlrichs et al, Universität Karlsruhe 2003; see also: http://www.turbomole.com.
[25] A. Schäfer, C. Huber, R. Ahlrichs, *J. Chem. Phys.* **1994**, *100*, 5829 – 5835; the basis sets are available from the TURBOMOLE homepage through the FTP Server Button (in the subdirectories basen, jbasen, and cbasen); see http://www.turbomole.com.
[26] T. H. Dunning, *J. Chem. Phys.* **1989**, *90*, 1007 – 1023.
[27] F. Weigend, M. Häser, *Theor. Chem. Acc.* **1997**, *97*, 331 – 340; F. Weigend, A. Köhn, C. Hättig, *J. Chem. Phys.* **2002**, *116*, 3175 – 3183.
[28] A. Lüchow, J. B. Anderson, *J. Chem. Phys.* **1996**, *105*, 7573 – 7578; S. Sokolova, A. Lüchow, *Chem. Phys. Lett.* **2000**, *320*, 421 – 424; S. Manten, A. Lüchow, *J. Chem. Phys.* **2001**, *115*, 5362 – 5366.
[29] C. Diedrich, A. Lüchow, S. Grimme, *J. Chem. Phys.* **2005**, *122*, 021101.
[30] L. Wagner, L. Mitas, *Chem. Phys. Lett.* **2003**, *370*, 412 – 415.
[31] C. W. Greeff, W. A. Lester, *J. Chem. Phys.* **1998**, *109*, 1607 – 1612; I. Ovcharenko, A. Aspuru-Guzik, W. A. Lester, *J. Chem. Phys.* **2001**, *114*, 7790 – 7794.

 © 2006 Wiley-VCH Verlag GmbH & Co. KGaA, Weinheim

tolerance, either with regard to the arene nucleophile or the electrophilic substrate, still remain for this transformation. For instance, the mono Friedel–Crafts reaction of carbonyl compounds and imines seems to be restricted to highly electrophilic substrates[2] such as glyoxylates,[3] chloral (trichloroacetaldehyde),[4] pyruvates,[5] trifluoromethyl imines,[6] or α-imino esters.[3c,7] In contrast, aromatic aldehydes[8] and their imines,[3c,9] generally evolve according to a double Friedel–Crafts reaction to give symmetrical triaryl methanes due to the intrinsic instability of the intermediate benzylic alcohol (or amine derivative) under the acidic reaction conditions (Scheme 1a). Triaryl methanes display varied



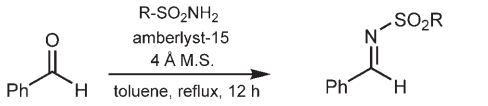
Scheme 1. Synthesis of triaryl methanes from aromatic aldehydes or their imines by a Friedel–Crafts reaction. X = O, NR; LA = Lewis acid; see text for details.

and interesting properties and have received a great deal of attention as leuco dyes,[10] photochromic agents,[11] suitable building blocks for generating dendrimers,[12] and as substrates for theoretical[13] and biological[14] studies. While many methods have been reported for the preparation of symmetrical triaryl methanes,[15] the synthesis of unsymmetrical derivatives is much less developed.[16,17]

As part of an ongoing research program on metal-controlled reactions of appropriately functionalized *N*-sulfonyl imines,[18] we describe here a broad-scope AFCR protocol that allows the selective preparation of structurally diverse unsymmetrical diaryl amines and triaryl methanes by sequential reaction with two different electron-rich aromatic compounds (Scheme 1b).

First, to study the effect of the sulfonyl substitution in AFCR, a set of sulfonyl imines, **1a–e**, of varied electronic and coordination nature were readily prepared in good chemical yields (87–94%) by direct condensation of benzaldehyde with the corresponding sulfonamide (Scheme 2).[19]

We chose the electron-rich *N*-methylindole[20] as model aromatic nucleophile for the AFCR of compounds **1**, and Cu(OTf) or $Cu(OTf)_2$ as catalytic Lewis acids[21] (10 mol%).



1a, R = Tol, 93%
1b, R = 4-$(NO_2)C_6H_4$, 90%
1c, R = 2-thienyl, 90%
1d, R = NMe_2, 94%
1e, R = 2-pyridyl, 87%

Scheme 2. Synthesis of *N*-sulfonyl imines **1a–e**. M.S. = molecular sieves.

Homogeneous Catalysis

DOI: 10.1002/anie.200503305

A Copper(II)-Catalyzed Aza-Friedel–Crafts Reaction of *N*-(2-Pyridyl)sulfonyl Aldimines: Synthesis of Unsymmetrical Diaryl Amines and Triaryl Methanes**

Jorge Esquivias, Ramón Gómez Arrayás, and Juan C. Carretero**

The Lewis acid-catalyzed addition of electron-rich aromatic compounds to aldehydes, ketones and imines, the latter of which is known as the aza-Friedel–Crafts reaction (AFCR), is a synthetically outstanding C–C bond-forming process that leads to functionalized alcohols and amines in a completely atom-economical way.[1] However, despite its significance, a number of unsolved aspects related to functional-group

[*] J. Esquivias, Dr. R. Gómez Arrayás, Prof. Dr. J. C. Carretero
Departamento de Química Orgánica
Facultad de Ciencias
Universidad Autónoma de Madrid
Cantoblanco 28049 Madrid (Spain)
Fax: (+34) 91-497-3966
E-mail: ramon.gomez@uam.es
juancarlos.carretero@uam.es

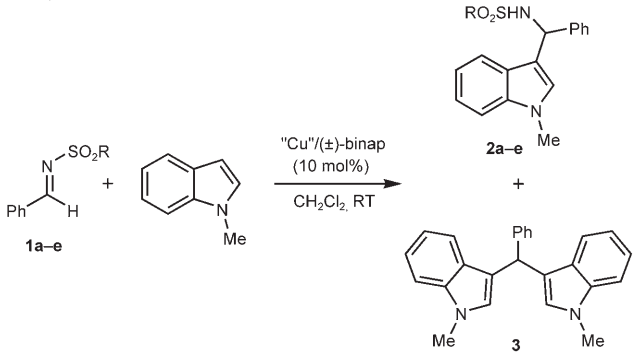
[**] This work was supported by the Ministerio de Educación y Ciencia (MEC, project BQU2003-0508) and the Consejería de Educación de la Comunidad Autónoma de Madrid (Project GR/MAT/0016/2004). J.E. and R.G.A. thank the MEC for a predoctoral fellowship and for a Ramón y Cajal contract, respectively.

Supporting information for this article is available on the WWW under http://www.angewandte.org or from the author.

 © 2006 Wiley-VCH Verlag GmbH & Co. KGaA, Weinheim

The effect of adding phosphane ligands to the reaction media was also examined [(±)-binap, dppf, dppe, and PPh_3], with binap being the most efficient.[22] The results obtained by using the optimal pair $Cu(OTf)_n$/binap (10 mol%) are summarized in Table 1.

Table 1: Cu^I- and Cu^{II}-catalyzed AFCR of sulfonyl imines **1a–e** with *N*-methylindole.



Entry	Imine	R	Copper salt	*t*	Yield [%][a] 2	3
1	**1a**	Tol	Cu(OTf)	72 h	**2a**, 41	–
2	**1a**	Tol	$Cu(OTf)_2$	≤5 min	–	72
3	**1b**	$(p\text{-}NO_2)C_6H_4$	Cu(OTf)	69 h	**2b**, 47	–
4	**1b**	$(p\text{-}NO_2)C_6H_4$	$Cu(OTf)_2$	≤5 min	–	85
5	**1c**	2-thienyl	Cu(OTf)	65 h	**2c**, 50	–
6	**1c**	2-thienyl	$Cu(OTf)_2$	≤5 min	–	80
7	**1d**	NMe_2	Cu(OTf)	70 h	**2d**, 45	–
8	**1d**	NMe_2	$Cu(OTf)_2$	≤5 min	–	82
9	**1e**	2-pyridyl	Cu(OTf)	22 h	**2e**, 72	–
10	**1e**	2-pyridyl	$Cu(OTf)_2$	≤5 min	**2e**, 72	–

[a] Yield of pure product isolated after chromatography.

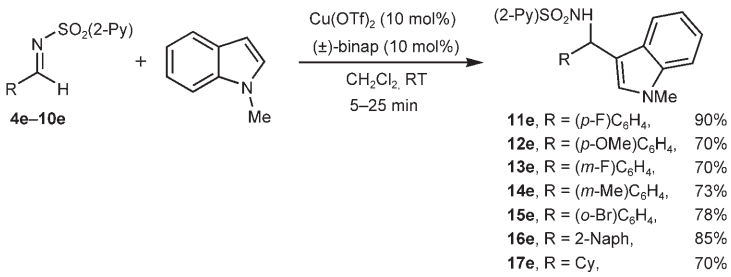
Three important conclusions can be drawn from this study:

a) The more-electrophilic Cu^{II} catalyst is around two orders on magnitude more reactive than the analogous Cu^I catalyst. For instance, the reaction of **1a** catalyzed by Cu(OTf) required 72 h to reach completion[23] (entry 1), whereas in the presence of $Cu(OTf)_2$ the reaction was complete in less than 5 min (entry 2).

b) A different outcome was obtained with substrates **1a–d** in the reactions catalyzed by either Cu(OTf) or $Cu(OTf)_2$. Thus, with the Cu^I-based protocol the mono Friedel–Crafts products **2a–d** were selectively obtained in moderate yield, while the Cu^{II} system provided selectively the bis-indole **3** in good yields (72–85%) with very short reaction times (≤5 min).

c) The 2-pyridylsulfonyl imine **1e** behaves differently to the rest of the sulfonyl imines[24] as the bis-indole product **3** is not detected either in the presence of Cu(OTf) (entry 9) or with $Cu(OTf)_2$ (entry 10).

The role of the 2-pyridylsulfonyl group in controlling the selectivity of the $Cu(OTf)_2$-catalyzed AFCR in favor of the sulfonamide product was confirmed by surveying a variety of substituted 2-pyridylsulfonyl imines. As shown in Scheme 3,



Scheme 3. Study of the substitution at the imine. Cy = cyclohexyl; Naph = naphthyl.

regardless of the electronic and steric nature of the substitution, the $Cu(OTf)_2$/(±)-binap-catalyzed AFCR provided exclusively the pyridylsulfonamide products **11e–17e** in good yields (70–90%). Interestingly, this method can also be applied to aliphatic imine electrophiles (product **17e**), which, to the best of our knowledge, have not been used previously in the AFCR.

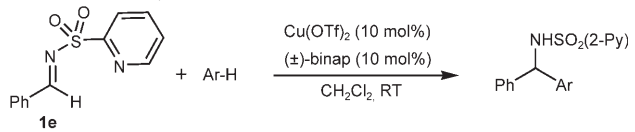
Table 2 shows the scope of the AFCR of imine **1e** with regard to the nucleophilic arene partner. Both heteroaromatic and electron-rich aromatic compounds proved to be very effective, affording the Friedel–Crafts addition product in good yield as a single regioisomer. The reactions with a representative selection of indole derivatives (entries 1–4), *N*-methylpyrrole (entry 5), 2-methoxythiophene (entry 6), and 1,3,5-trimethoxybenzene (entry 10) were particularly fast (≤5 min). Interestingly, substitution at C2 of the indole seems to have no detrimental effect on the reactivity (products **21e** and **22e**). Furan, which is known to be a poorly reactive substrate,[1e,7e] provided the addition product **26e** in 50% yield after 15 h, while the more nucleophilic 2-methoxyfuran furnished the amine **27e** in 69% yield after 90 min. Among nonheteroaromatic nucleophiles, *N*,*N*-dimethyl-3-methoxyaniline, 1-methoxynaphthalene, and 1,3,5-trimethoxybenzene also underwent the AFCR and gave satisfactory product yields (entries 8–10). However, no reaction was observed with less activated aromatic rings, such as *N*,*N*-dimethylaniline or anisole, even after prolonged reaction times.

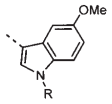
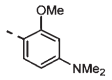
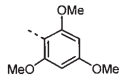
The synthetically relevant deprotection of these pyridylsulfonamide products to give the corresponding diaryl methylamines can be cleanly achieved by treatment with magnesium turnings under neutral reaction conditions (Scheme 4).[25]

To highlight the potential of the pyridylsulfonamide adducts, we set out to develop a sequential, one-pot synthesis of unsymmetrical triaryl methanes by promoting a second electrophilic aromatic substitution with a different electron-rich arene (Ar^3-H). However, once the AFCR between imine **1e** and *N*-methylindole reached completion (monitored by TLC), the addition of 5-methoxy-1-methylindole to the formed **2e** resulted in no reaction at room temperature after 24 h. Gratifyingly, this Cu^{II}-catalyzed sulfonamide displacement proceeded smoothly when the reaction temperature was increased to 40 °C and after 20 min triaryl methane **33** was isolated in 65% yield.[26]

 © 2006 Wiley-VCH Verlag GmbH & Co. KGaA, Weinheim

Table 2: Cu^{II}-catalyzed AFCR of imine **1e** with electron-rich arenes.

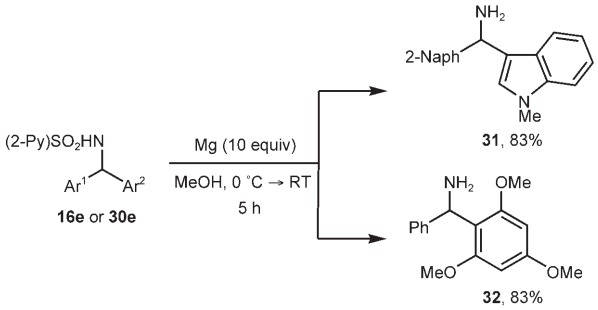


Entry	Ar	Product	*t*	Yield [%][a]
1		**2e**, R = Me **18e**, R = H	≤5 min	72 82
2		**19e**, R = H **20e**, R = Me	≤5 min	89 93
3		**21e**, R = Me **22e**, R = Ph	≤5 min	80 70
4		**23e**	≤5 min	75
5		**24e**	≤5 min	72
6		**25e**	≤5 min	65
7		**26e**, R = H **27e**, R = OMe	15 h 1.5 h	50 69
8		**28e**	8 h	73
9		**29e**	6 h	65
10		**30e**	≤5 min	76

[a] Yield of pure product isolated after chromatography.

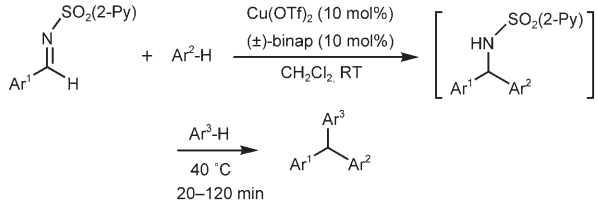
Table 3 shows the wide scope of this one-pot (indolyl)-diaryl methane synthesis with regard to the nature of the aromatic nucleophile Ar^3-H (products **33**–**40**). Even electron-rich indole derivatives (entries 1 and 4), which are known to polymerize easily under acidic conditions,[27] tolerate the mild reaction conditions.

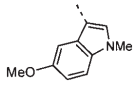
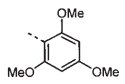
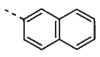
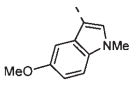
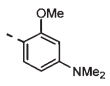
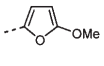
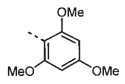
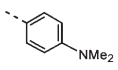
Disappointingly, this one-pot 2-pyridylsulfonamide displacement did not take place with substrates lacking an indolyl group, even under harsher conditions (DCE or CH_3CN, 60 °C). To further extend this methodology to the



Scheme 4. Deprotection of *N*-(2-pyridyl)sulfonyldiaryl amines.

Table 3: One-pot synthesis of unsymmetrical (indolyl)diaryl methanes.



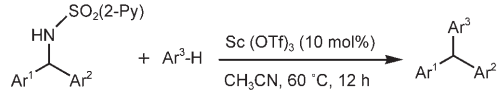
Entry	Ar^1	Ar^2	Ar^3	Product	Yield [%][a]
1				**33**	65
2				**34**	65
3				**35**	57
4				**36**	60
5				**37**	46
6				**38**	63
7				**39**	43
8				**40**	73

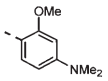
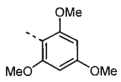
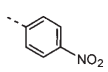
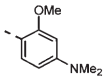
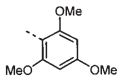
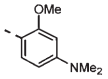
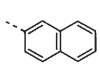
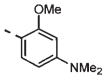
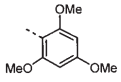
[a] Overall yield of pure product isolated after chromatography.

 © 2006 Wiley-VCH Verlag GmbH & Co. KGaA, Weinheim

case of triaryl methanes that do not necessarily contain an indole moiety, the second electrophilic aromatic substitution was investigated with isolated sulfonamide adducts. After surveying different Lewis acids, we found that this reaction occurs cleanly in the presence of $Sc(OTf)_3$ (10 mol%) in CH_3CN at 60 °C. As shown in Table 4, a variety of unsymmetrical triaryl methanes can be obtained in reasonable yields

Table 4: Synthesis of unsymmetrical triaryl methanes.



Entry	Ar^1	Ar^2	Ar^3	Product	Yield [%][a]
1				**41**	65
2				**42**	65
3				**43**	57
4				**44**	57
5				**45**	57
6				**46**	44

[a] Yield of pure product isolated after chromatography.

(44–65%) by appropriate choice of the Ar^1, Ar^2, and Ar^3 moieties. This methodology provides access to unsymmetrical triaryl methanes containing both electron-rich and electron-poor aromatic rings (e.g., products **42** and **46**), a type of compound that has seldom been studied since their synthesis has not been well established.[28]

In summary, we have developed an efficient $Cu(OTf)_2$-catalyzed AFCR of *N*-sulfonyl imines with electron-rich aromatic and heteroaromatic compounds based on the use of the 2-pyridylsulfonyl moiety as the key controlling unit. This highly reactive protocol displays a wide tolerance both with respect to the imine substrate and the arene nucleophile. In addition, this catalyst system also allows a controlled double electrophilic aromatic substitution, which provides access to unsymmetrical triaryl methanes with wide structural diversity.

Received: September 16, 2005
Published online: December 13, 2005

Keywords: amines · copper · homogeneous catalysis · nitrogen heterocycles · Schiff bases

[1] For reviews on Friedel–Crafts reaction, see: a) *Organic Synthesis* (Ed.: M. B. Smith), McGraw-Hill, New York, **1994**, p. 1313; b) H. Heaney in *Comprehensive Organic Synthesis, Vol. 2* (Eds.: B. M. Trost, I. Fleming), Pergamon, Oxford, **1991**, p. 733; c) *Friedel–Crafts Alkylation Chemistry: A Century of Discovery* (Eds.: R. M. Roberts, A. A. Khalaf), Dekker, New York, **1984**. For recent reviews on asymmetric Friedel–Crafts reactions, see: d) M. Bandini, A. Melloni, A. Umani-Ronchi, *Angew. Chem.* **2004**, *116*, 560; *Angew. Chem. Int. Ed.* **2004**, *43*, 550; e) K. A. Jørgensen, *Synthesis* **2003**, 1117.

[2] To the best of our knowledge, the gold(III)-catalyzed addition of 1,3,5-trimethoxybenzene to the *N*-tosyl imines of benzaldehyde and 4-chlorobenzaldehyde,[7b] and the asymmetric organocatalytic addition of 2-methoxyfuran to aryl aldimines (D. Uraguchi, K. Sorimachi, M. Terada, *J. Am. Chem. Soc.* **2004**, *126*, 11804) are the only examples of the participation of nonactivated imines in the AFCR.

[3] a) Y. Yuan, X. Wang, X. Li, K. Ding, *J. Org. Chem.* **2004**, *69*, 146; b) N. Gatergood, W. Zhuang, K. A. Jørgensen, *J. Am. Chem. Soc.* **2000**, *122*, 12517; c) J. Hao, S. Taktak, K. Aikawa, Y. Yusa, M. Hatano, K. Mikami, *Synlett* **2001**, 1443; d) F. Bigi, G. Bocelli, R. Maggi, G. Sartori, *J. Org. Chem.* **1999**, *64*, 5004.

[4] a) A. Ishii, V. A. Soloshonok, K. Mikami, *J. Org. Chem.* **2000**, *65*, 1597; b) A. Ishii, K. Mikami, *J. Fluorine Chem.* **1999**, *97*, 51; c) F. Bigi, G. Casiraghi, G. Casnati, G. Sartori, G. Gasparri Fava, M. Ferrari Belicchi, *J. Org. Chem.* **1985**, *50*, 5018.

[5] a) M. P. A. Lyle, N. D. Draper, P. D. Wilson, *Org. Lett.* **2005**, *7*, 901; b) A. Corma, H. García, A. Moussaif, M. J. Sabater, R. Zniber, A. Redouane, *Chem. Commun.* **2002**, 1058; c) G. Erker, A. A. H. van der Zeijden, *Angew. Chem.* **1990**, *102*, 543; *Angew. Chem. Int. Ed. Engl.* **1990**, *29*, 517.

[6] a) Y. Gong, K. Kato, H. Kimoto, *Synlett* **2000**, 1058; b) Y. Gong, *Tetrahedron: Asymmetry* **2001**, *12*, 2121.

[7] a) B. Jiang, Z.-G. Huang, *Synthesis* **2005**, 2198; b) Y. Luo, C.-J. Li, *Chem. Commun.* **2004**, 1930; c) Y.-J. Chen, F. Lei, L. Liu, D. Wang, *Tetrahedron* **2003**, *59*, 7609; d) F. Lei, Y.-J. Chen, Y. Siu, L. Liu, D. Wang, *Synlett* **2003**, 1160; e) S. Saaby, P. Bayón, P. S. Aburel, K. A. Jørgensen, *J. Org. Chem.* **2002**, *67*, 4352; f) S. Saaby, X. Fang, N. Gathergood, K. A. Jørgensen, *Angew. Chem.* **2000**, *112*, 4280; *Angew. Chem. Int. Ed.* **2000**, *39*, 4114; g) Y.-J. Chen, C.-S. Ge, D. Wang, *Synlett* **2000**, 1429; h) M. Johannsen, *Chem. Commun.* **1999**, 2233. For the AFCR of the benzoylhydrazone of glyoxalate esters, see: S. Shirakawa, R. Berger, J. L. Leighton, *J. Am. Chem. Soc.* **2005**, *127*, 2858.

[8] a) C. Ramesh, J. Banerjee, R. Pal, B. Das, *Adv. Synth. Catal.* **2003**, *345*, 557; b) J. S. Jadav, B. V. S. Reddy, S. Sunitha, *Adv. Synth. Catal.* **2003**, *345*, 349; c) J. S. Yadav, B. V. S. Reddy, C. V. S. R. Murthy, G. M. Kumar, C. Madan, *Synlett* **2001**, 783; d) M. Alvaro, H. García, A. Sanjuán, M. Esplá, *Appl. Catal. A* **1998**, *175*, 105.

[9] a) B. Temelli, C. Unaleroglu, *Tetrahedron Lett.* **2005**, *46*, 7941; b) B. Ke, Y. Qin, Q. He, Z. Huang, F. Wang, *Tetrahedron Lett.* **2005**, *46*, 1751; c) H. J. Lee, M. R. Seong, H. N. Song, J. N. Kim, *Bull. Korean Chem. Soc.* **1999**, *20*, 267.

[10] R. Muthyala in *Chemistry and Applications of Leuco Dyes* (Eds.: A. R. Katrizky, G. J. Sabongi), Plenum, New York, **1997**.

[11] a) D. F. Duxbury, *Chem. Rev.* **1993**, *93*, 381; b) R. Aldag in *Photochroism: Molecules and Systems* (Eds.: H. Dürr, H. Bouas-Laurent), Elsevier, London, **1990**.

[12] L. A. Baker, L. Sun, R. M. Crooks, *Bull. Korean Chem. Soc.* **2002**, *23*, 647.

[13] a) M. S. Baptista, G. L. Indig, *J. Phys. Chem. B* **1998**, *102*, 4678; b) M. Terrier, T. Boubaker, L. Xiao, P. G. Farrell, *J. Org. Chem.* **1992**, *57*, 3924.

 © 2006 Wiley-VCH Verlag GmbH & Co. KGaA, Weinheim

[14] For the use of photosensitizers in photodynamic therapy against cancer, see: a) M. R. Detty, S. L. Gibson, S. J. Wagner, *J. Med. Chem.* **2004**, *47*, 3897; b) M. Wainwright, D. A. Phoenix, S. M. Burrow, J. Waring, *J. Chemother.* **1999**, *11*, 61. For their use as antiproliferative agents, see: c) R. A. Al-Qawasmeh, Y. Lee, M.-Y. Cao, X. Gu, A. Vassilakos, J. A. Wright, A. Young, *Bioorg. Med. Chem. Lett.* **2004**, *14*, 347.

[15] a) M. Hoffmann, N. Hampel, T. Kanzian, H. Mayr, *Angew. Chem.* **2004**, *116*, 5518; *Angew. Chem. Int. Ed.* **2004**, *43*, 5402; b) P. Shanmuga, L. Varma, *Indian J. Chem. Sect. B* **2001**, *40*, 1258; c) Z.-H. Zhang, F. Yang, T.-S. Li, C.-G. Fu, *Synth. Commun.* **1997**, *27*, 3823; d) U. Pindur, C. Flo, *J. Heterocycl. Chem.* **1989**, *26*, 1563; e) G. Casiraghi, G. Casnati, M. Cornia, G. Sartori, R. Ungaro, *J. Chem. Soc. Perkin Trans. 1* **1974**, 2077; f) H. R. Snyder, M. S. Konecky, *J. Am. Chem. Soc.* **1958**, *80*, 4388; g) H. E. Ungnade, E. W. Crandall, *J. Am. Chem. Soc.* **1949**, *71*, 2209.

[16] For a review on the synthesis of triaryl methanes, see: R. Muthyala, A. R. Katrizky, X. Lan, *Dyes Pigm.* **1994**, *25*, 303.

[17] The only two general methods for the preparation of unsymmetrical triaryl methanes involve the condensation of unsymmetrical diaryl carbinols with electron-rich arenes under strongly acidic conditions or the displacement of the benzotriazole moiety in (benzotriazol-1-yl)diaryl methanes by *p*-(*N*,*N*-dimethylamino)phenylmagnesium bromide or by electron-rich arenes. See: a) S. K. Das, Shagufta, G. Panda, *Tetrahedron Lett.* **2005**, *46*, 3097; b) A. Burmester, H. B. Stegmann, *Synthesis* **1981**, 125; c) E. F. Pratt, L. Q. Green, *J. Am. Chem. Soc.* **1953**, *75*, 275; d) A. R. Katrizky, D. Toader, *J. Org. Chem.* **1997**, *62*, 4137; e) A. R. Katrizky, V. Gupta, C. Garot, C. V. Stevens, M. F. Gordeev, *Heterocycles* **1994**, 38; f) A. R. Katrizky, X. Lan, J. M. Lam, *Chem. Ber.* **1991**, *124*, 1809.

[18] a) J. Esquivias, R. Gómez Arrayás, J. C. Carretero, *J. Org. Chem.* **2005**, *70*, 7451; b) O. García Mancheño, R. Gómez Arrayás, J. C. Carretero, *J. Am. Chem. Soc.* **2004**, *126*, 456.

[19] L. C. Vishwakarma, O. D. Stringer, F. A. Davis, *Org. Synth.* **1987**, *66*, 203.

[20] For the condensation of *N*-tosyl aryl aldimines with a 3-lithioindole derivative, see: J. H. Wynne, W. M. Stalick, *J. Org. Chem.* **2002**, *67*, 5850.

[21] No reaction between **1a** and *N*-methylindole was observed in the absence of the Lewis acid.

[22] In the absence of (±)-binap the reaction between **1a** and *N*-methylindole catalyzed by $Cu(OTf)_2$ becomes much slower (2 h instead of 5 min). Unfortunately, the reaction of **1a** or **1e** in the presence of enantiomerically pure (*R*)-binap, under different reaction conditions, led to virtually racemic products **2a** and **2e**, respectively (< 10% *ee*).

[23] A similar result and reactivity was observed in the presence of other Cu^I salts such as $[Cu(CH_3CN)_4](ClO_4)$.

[24] For other successful applications of the (2-pyridyl)sulfonyl group in transition-metal-catalyzed reactions, see: a) R. Gómez Arrayás, S. Cabrera, J. C. Carretero, *Org. Lett.* **2005**, *7*, 219; b) H. Han, I. Bae, E. J. Yoo, J. Lee, Y. Do, S. Chang, *Org. Lett.* **2004**, *6*, 4109; c) T. Llamas, R. Gómez Arrayás, J. C. Carretero, *Adv. Synth. Catal.* **2004**, *346*, 1641; d) P. Mauleón, J. C. Carretero, *Org. Lett.* **2004**, *6*, 3195.

[25] C. S. Pak, D. S. Lim, *Synth. Commun.* **2001**, *31*, 2209.

[26] No reaction was observed when heating a mixture of isolated **2e** and 5-methoxy-1-methylindole at 60 °C for 5 h in the absence of $Cu(OTf)_2$.

[27] T. Okauchi, M. Itonaga, T. Minami, T. Owa, K. Kitoh, H. Yoshino, *Org. Lett.* **2000**, *2*, 1485.

[28] We have found only two examples of the synthesis of unsymmetrical triaryl methanes that combine both electron-rich and electron-poor aromatic rings, see references [17a, 17d].

 © 2006 Wiley-VCH Verlag GmbH & Co. KGaA, Weinheim

Sulfur Heterocycles

DOI: 10.1002/anie.200503369

Formation of Cyclic Sulfinates and Sulfinamides through Homolytic Substitution at the Sulfur Atom**

Julien Coulomb, Victor Certal, Louis Fensterbank, Emmanuel Lacôte,* and Max Malacria**

Dedicated to the memory of André Rassat

During the last decade, radical reactions have gained wide acceptance as efficient ways to build complex frameworks under mild conditions.[1] This ability is largely a consequence of the broad array of transformations that these reactions can accommodate. Yet, among all the available radical processes, intramolecular homolytic substitutions[2,3] have remained much less exploited than cyclization reactions, despite their strong synthetic potential. One solution to access these reactions is to use heteroatoms such as oxygen,[4] selenium,[5–7] phosphorus,[8,9] or silicon.[10,11] Sulfur is particularly well-suited, and several reactions have been reported that employ homolytic substitution on this particular atom. A variety of different functions have been introduced (sulfides,[12–14] disulfides,[15] thioesters,[16–18] and sulfoxides;[14,19,20] sulfones seem not to be prone to such processes[14,21]), but so far none in which an additional heteroatom was present in the ring next to the sulfur atom, despite the increased potential offered by the heterocyclic adducts.

Sulfinates[22,23] and sulfinamides[24–26] play pivotal roles in modern asymmetric synthesis as key precursors of chiral molecules. As part of our program devoted to new reactions involving sulfur-based moieties,[27–30] we became interested in the synthesis of cyclic sulfinates and sulfinamides because they are versatile synthetic intermediates,[31,32] and have elicited interest in medicinal chemistry.[33,34] They have also been used in materials science as imaging agents.[35] It thus appeared to us that homolytic substitution would be a unique tool to prepare cyclic sulfinates and sulfinamides through an original strategy. Herein, we report the results we gathered along the way.

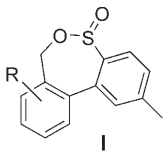
[*] J. Coulomb, Dr. V. Certal, Prof. L. Fensterbank, Dr. E. Lacôte, Prof. M. Malacria
Laboratoire de Chimie Organique (UMR CNRS 7611)
Institut de Chimie Moléculaire (FR 2769)
Université Pierre et Marie Curie
Case 229, 4 place Jussieu, 75252 Paris cedex 05 (France)
Fax: (+33) 1-4427-7360
E-mail: louis.fensterbank@upmc.fr
lacote@ccr.jussieu.fr
malacria@ccr.jussieu.fr

[**] We thank Rhodia for financial support (PhD grant to J.C., postdoctoral grant to V.C.), and Dr. J.-P. Corbet and Dr. G. Mignani (Rhodia) for helpful discussions.

Supporting information for this article is available on the WWW under http://www.angewandte.org or from the author.

© 2006 Wiley-VCH Verlag GmbH & Co. KGaA, Weinheim
InterScience

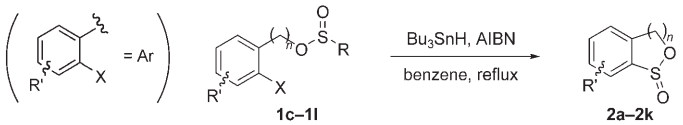
To probe this issue, we initially focused on the readily prepared substrate **1a** (Table 1). Classical tributyltin hydride conditions (Table 1, entry 1) gave an encouraging 62% yield of sultine **2a**, presumably resulting from thiophilic attack by the aryl radical with a concomitant or successive expulsion of the *p*-tolyl radical.[2,36] Besides this homolytic substitution product, the main side product of the reaction was a biarylic adduct (**I**: 11%), which originated from a 7-*endo* cyclization followed by rearomatization. This type of adduct was also obtained in the 5–15% range in other trials (Table 1, entries 2–6).



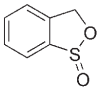
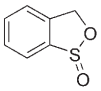
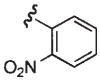
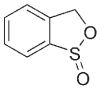
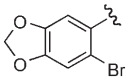
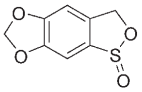
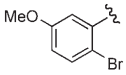
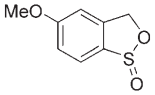
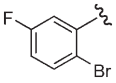
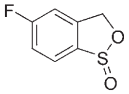
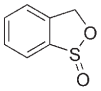
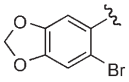
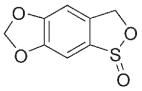
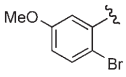
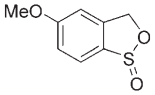
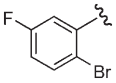
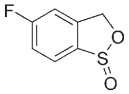
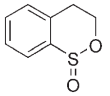
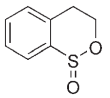
I

We also observed that the homolytic substitution can take place at room temperature, albeit with some erosion of the yield of **2a** (the yields were in the 40% range with the borane/oxygen initiator; the main by-product was the reduced sulfinate isolated in a roughly equimolar amount). Furthermore, TTMSS can replace Bu_3SnH with no significant loss of yield (Table 1, entries 2 and 3). This preliminary synthesis of sultine **2a** drove us to extend the scope of this unprecedented homolytic substitution, and we examined several diversely

Table 1: Synthesis of fused benzosultines.



1c–1l **2a–2k**

Entry	**1**, *n*	Ar	R	Product		Yield [%]
1	**1a**, 1		*p*Tol		**2a**	62
2	**1b**, 1		*p*Tol		**2a**	58[a]
3	**1c**, 1				**2a**	56 (65[a])
4	**1d**, 1		*p*Tol		**2d**	69
5	**1e**, 1		*p*Tol		**2e**	70
6	**1f**, 1		*p*Tol		**2f**	73
7	**1g**, 1		*t*Bu		**2a**	97
8	**1h**, 1		*t*Bu		**2d**	100
9	**1i**, 1		*t*Bu		**2e**	100 (73[b])
10	**1j**, 1		*t*Bu		**2f**	95 (86[b,c])
11	**1k**, 2		*p*Tol		**2k**	45[d]
12	**1l**, 2		*t*Bu		**2k**	89[e] (64[b])

[a] Bu_3SnH was replaced by TTMSS. [b] Conditions: AIBN, Bu_3SnCl (10 mol%), $NaBH_4$ (2 equiv), *t*BuOH, Δ. [c] NMR yield, calculated by using 1,3,5-trimethoxybenzene as an internal standard. [d] Reduced material (48%) was also isolated. [e] Reduced material (5%) was also isolated. TTMSS = tris(trimethylsilyl)silane; AIBN = azobisisobutyronitrile; *p*Tol = *p*-tolyl.

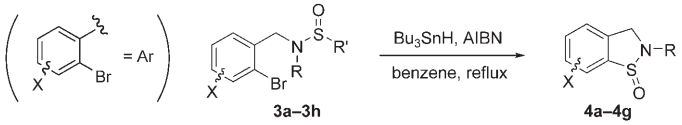
 © 2006 Wiley-VCH Verlag GmbH & Co. KGaA, Weinheim

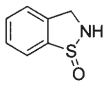
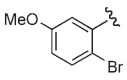
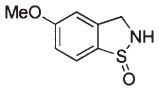
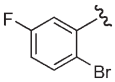
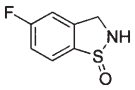
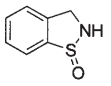
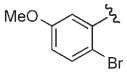
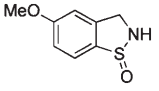
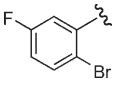
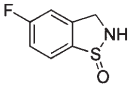
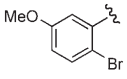
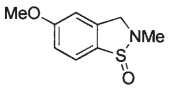
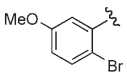
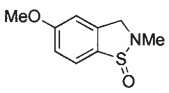
substituted aromatic precursors **1c**–**1l**. Entries 4–6 in Table 1 nicely illustrate the variety of the aromatic substitution pattern compatible with this reaction, including piperonal derivative **1d** and fluorine derivative **1f**. Introduction of a nitro group on the leaving aromatic moiety did not lead to an increase in the yield (Table 1, entry 3). To suppress the biarylic side product, we intended to introduce a new nonaromatic R group with a higher leaving homolytic ability. A *tert*-butyl group appeared to be the logical choice, as *tert*-butyl sulfur species are highly accessible from *tert*-butyldisulfide, and the expulsion of a more stable tertiary radical should be rendered easier. This proved to be the case, as shown with precursors **1g**–**1j**, which yielded essentially quantitative yields of the corresponding sultines **2a** and **2d**–**2f** (Table 1, entries 7–10). Again, use of the borane/oxygen initiator resulted in some formation of reduced material (9%), but the reaction still yielded 90% of **2a** at room temperature. Sultines with a six-membered ring are equally accessible by this method (precursors **1k** and **1l**). In that case, a net-yield increase was observed when using a *tert*-butyl precursor (compare Table 1, entries 11 and 12), and no biarylic by-product was isolated when starting from **1k**. Finally, the fact that catalytic tin hydride (only 10 mol%) conditions could be used is also worthy of note (Table 1, entries 9, 10, and 12).

We then extended this reaction to sulfinamides. It was interesting to verify whether a similar pathway could be followed, because of the different electronic and steric environment. Gratifyingly, cyclic sulfinamides **4** could be obtained. Functionalization on the aromatic moiety was also tolerated (Table 2, entries 1–6). In the case of precursors **3a**–**3c**, the corresponding biaryl products were again detected in a 10–20% yield (based on NMR spectroscopy), but could not be isolated as a result of degradation in the purification process by column chromatography. Logically, this competitive process was eliminated with precursors **3d** and **3e**, and improved yields were observed. However, the introduction of a methyl group on the nitrogen atom proved to be detrimental for both **3g** and **3h**, and lower yields of **4** were obtained. We suspect that the methyl group suffers from 1,5-intramolecular hydrogen abstraction by the highly reactive aryl radical. The resulting stabilized α-amino radical would then undergo fragmentation to give untractable material.

We then examined the case of alkyl radicals (Table 3). The reaction of tolylsulfinates only afforded reduced material, as also reported by Studer et al.[37] Presumably, the expulsion of a high-energy aryl radical would be disfavored and this energetic gap would account for the lack of cyclization. Nonetheless, the *tert*-butyl sulfinates worked well. When Bu_3SnH was used (conditions A), we faced problems during the purification step (Table 3, entries 1, 3, 5, 7, and 9). The sultines were soluble in hexane, and therefore the CH_3CN/hexane separation method could not be used any more. All

Table 2: Synthesis of cyclic sulfinamides.



Entry	Precursor	Ar	R	R′	Product		Yield [%]
1	**3a**		H	*p*Tol		**4a**	58
2	**3b**		H	*p*Tol		**4b**	66
3	**3c**		H	*p*Tol		**4c**	63
4	**3d**		H	*t*Bu		**4a**	85
5	**3e**		H	*t*Bu		**4b**	86
6	**3f**		H	*t*Bu		**4c**	85 (80[a])
7	**3g**		Me	*p*Tol		**4g**	36
8	**3h**		Me	*t*Bu		**4g**	31

[a] Conditions: AIBN, Bu_3SnCl (10 mol%), $NaBH_4$ (2 equiv), *t*BuOH, Δ.

 © 2006 Wiley-VCH Verlag GmbH & Co. KGaA, Weinheim

Table 3: Cyclic sulfinates from an alkyl radical.



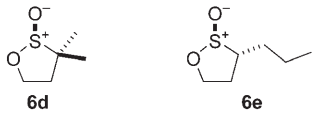
Entry	Precursor	R^1	R^2	Conditions[a]	Product, yield [%]	*trans*/*cis*
1	**5a**	H	H	A	**6a**, 85	–
2	**5a**	H	H	B	**6a**, 65	–
3	**5b**	Me	H	A	**6b**, 60	66:34
4	**5b**	Me	H	B	**6b**, 69	63:37
5	**5c**	*t*Bu	H	A	**6c**, 85	100:0[b]
6	**5c**	*t*Bu	H	B	**6c**, 84	100:0
7	**5d**	Me	Me	A	**6d**, 70	–
8	**5d**	Me	Me	B	**6d**, 63	–
9	**5e**	*n*Pr	H	A	**6e**, 85	69:31
10	**5e**	*n*Pr	H	B[c]	**6e**, 99	63:37

[a] Conditions A: Bu_3SnH, AIBN (10 mol%), benzene, Δ; B: TTMSS, V-501 (25 mol%), benzene, Δ. [b] The product could not be separated from AIBN by-products. The yield was calculated relative to 1,3,5-trimethoxybenzene as internal standard. [c] AIBN was used.

the other methods we tried led to the loss of the products. The yields reported indicate the calculated amount of desired product present in the isolated mixture. Tin by-products (usually 10–30 mol%) were also present. Moreover, some of the products could not be separated from the AIBN residues. We thus changed to TTMSS as mediator and V-501 (azobis-4-cyanovaleric acid) as initiator (conditions B), because we anticipated that separation from the by-products could be achieved readily, either upon aqueous workup or by filtration on silica. This change proved rewarding, as the sultines were obtained in similar yields with no traces of either mediator or initiator residues (Table 3, entries 2, 4, 6, 8, 10).

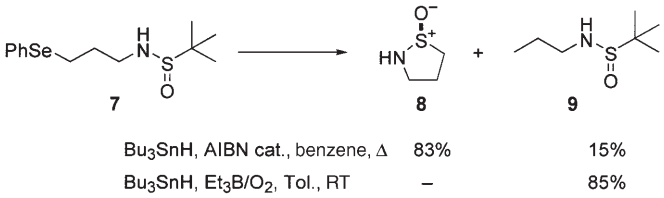
When a prochiral radical was cyclized, the *trans* diastereomers were favored (Table 3, entries 3–6, 9, 10), as evidenced by comparison with known products.[38] The selectivity depends on the size of the substituents. Methyl and propyl groups typically gave a 2:1 selectivity, while the bulky *tert*-butyl group led to the formation of a single diastereomer, which we assumed to be a *trans* isomer by analogy with the methyl case.

Noticeably, the method still worked smoothly with an incoming tertiary radical, that is, with no positive bond-energy balance. Cyclization of **5d** thus delivered sultine **6d**, which is a component of cat's urine (Table 3, entries 7 and 8).[39] Interestingly, sultine-based natural products are not abundant. Yet, both **6d** and **6e** have olfactory or flavor properties,



and small substituent variations seem to lead to strong modifications of the former. For example, cyclization of substrate **5e** quantitatively gave sultine **6e**, which is present in the volatile compounds of yellow passion-fruit extracts.[39] The method we have devised is ideally suited to the preparation of analogues.

We finally examined the cyclization of alkyl sulfinamide **7** (Scheme 1). The reaction still worked and cyclic sulfinamide **8** could be isolated in good yield (83%). However, some reduced material was also obtained. As was expected from



Scheme 1. Cyclization of alkyl sulfinamide **7**.

the previous experiments, lowering the temperature gave only reduced product **9**. This finding represents a noticeable difference compared with the benzofused sultine case, and shows that the formation of cyclic alkyl sulfinamides is a slower process.

In conclusion, we have devised an efficient, general access procedure for cyclic sulfinates and sulfinamides based on homolytic substitution at the sulfur atom. Both purely alkyl and benzofused families of compounds could be accessed. The cyclization of a prochiral radical proceeded with varied stereochemical outcomes, which depended on the size of the incoming radical. Biologically active sultines were quickly prepared by this method, which opens the way to the synthesis of a vast library of analogues. We are currently assessing the process at the stereogenic sulfur atom, with a view to preparing enantiopure sultines and cyclic sulfinamides. Progress along this route will be presented in due course.

Received: September 22, 2005

Keywords: cyclization · radical reactions · sulfinamides · sulfinates · sulfur heterocycles

[1] P. Renaud, M. P. Sibi, *Radicals in Organic Synthesis*, 1st ed., Wiley-VCH, Weinheim, **2001**.
[2] C. H. Schiesser, L. M. Wild, *Tetrahedron* **1996**, *52*, 13265.
[3] J. C. Walton, *Acc. Chem. Res.* **1998**, *31*, 99.
[4] D. Colombani, B. Maillard, *J. Org. Chem.* **1994**, *59*, 4765.
[5] N. Al-Maharik, L. Engman, J. Malmstroem, C. H. Schiesser, *J. Org. Chem.* **2001**, *66*, 6286.
[6] M. W. Carland, R. L. Martin, C. H. Schiesser, *Org. Biomol. Chem.* **2004**, *2*, 2612.
[7] M. C. Fong, C. H. Schiesser, *J. Org. Chem.* **1997**, *62*, 3103.
[8] W. G. Bentrude in *The Chemistry of Organophosphorus Compounds*, *vol. 1* (Ed.: F. R. Hartley), Wiley, Chichester, **1990**, p. 531.
[9] L. Zhang, M. Koreeda, *J. Am. Chem. Soc.* **2004**, *126*, 13190.
[10] A. Studer, H. Steen, *Chem. Eur. J.* **1999**, *5*, 759.
[11] A. Studer, S. Amrein, H. Matsubara, C. H. Schiesser, T. Doi, T. Kawamura, T. Fukuyama, I. Ryu, *Chem. Commun.* **2003**, 1190.
[12] A. L. J. Beckwith, D. R. Boate, *J. Org. Chem.* **1988**, *53*, 4339.
[13] J. A. Kampmeier, T. R. Evans, *J. Am. Chem. Soc.* **1966**, *88*, 4096.
[14] J. A. Kampmeier, R. B. Jordan, M. S. Liu, H. Yamanaka, D. J. Bishop, *ACS Symp. Ser.* **1978**, *69*, 275.
[15] A. L. J. Beckwith, S. A. M. Duggan, *J. Chem. Soc. Perkin Trans. 2* **1994**, 1509.

 © 2006 Wiley-VCH Verlag GmbH & Co. KGaA, Weinheim

[16] L. Benati, R. Leardini, M. Minozzi, D. Nanni, P. Spagnolo, S. Strazzari, G. Zanardi, *Org. Lett.* **2002**, *4*, 3079.
[17] D. Crich, Q. Yao, *J. Org. Chem.* **1996**, *61*, 3566.
[18] D. Crich, Q. Yao, *J. Am. Chem. Soc.* **2004**, *126*, 8232.
[19] A. L. J. Beckwith, D. R. Boate, *J. Chem. Soc. Chem. Commun.* **1986**, 189.
[20] J. E. Lyons, C. H. Schiesser, *J. Chem. Soc. Perkin Trans. 2* **1992**, 1655.
[21] D. Crich, T. K. Hutton, K. Ranganathan, *J. Org. Chem.* **2005**, *70*, 7672.
[22] G. Solladié, J. Hutt, A. Girardin, *Synthesis* **1987**, 173.
[23] J. W. Evans, M. B. Fierman, S. J. Miller, J. A. Ellman, *J. Am. Chem. Soc.* **2004**, *126*, 8134.
[24] F. A. Davis, R. E. Reddy, J. M. Szewczyk, G. V. Reddy, P. S. Portonovo, H. Zhang, D. Fanelli, T. Reddy, P. Zhou, P. J. Carroll, *J. Org. Chem.* **1997**, *62*, 2555.
[25] D. A. Cogan, G. Liu, K. Kim, B. J. Backes, J. A. Ellman, *J. Am. Chem. Soc.* **1998**, *120*, 8011.
[26] P. Zhou, B.-C. Chen, F. A. Davis, *Tetrahedron* **2004**, *60*, 8003.
[27] B. Delouvrié, L. Fensterbank, E. Lacôte, M. Malacria, *J. Am. Chem. Soc.* **1999**, *121*, 11395.
[28] D. Leca, K. Song, M. Albert, M. Grangeio-Gonçalves, L. Fensterbank, E. Lacôte, M. Malacria, *Synthesis* **2005**, 1405.
[29] D. Leca, K. Song, M. Amatore, L. Fensterbank, E. Lacôte, M. Malacria, *Chem. Eur. J.* **2004**, *10*, 906.
[30] D. Leca, A. Toussaint, C. Mareau, L. Fensterbank, E. Lacôte, M. Malacria, *Org. Lett.* **2004**, *6*, 3573.
[31] D. C. Dittmer, M. D. Hoey in *The Chemistry of Sulphinic Acids, Esters, and Their Derivatives* (Ed.: S. Patai), Wiley, Chichester, **1990**, p. 239.
[32] D. Markovic, E. Roversi, R. Scoppelliti, P. Vogel, R. Meana, J. A. Sordo, *Chem. Eur. J.* **2003**, *9*, 4911.
[33] B. Dakova, T. Martens, M. Evers, *Electrochim. Acta* **2000**, *45*, 4525.
[34] J. C. Doré, J. Gilbert, T. Ojasoo, J. P. Raynaud, *J. Med. Chem.* **1986**, *29*, 54.
[35] N. Jubran, A. R. Katritzky, J. V. Ugro, Jr., Patent WO9745273, **1997**.
[36] C. H. Schiesser, L. M. Wild, *J. Org. Chem.* **1999**, *64*, 1131.
[37] M. Bossart, R. Fassler, J. Schoenberger, A. Studer, *Eur. J. Org. Chem.* **2002**, 2742.
[38] See the Supporting Information.
[39] S. Yolka, E. Dunach, M. Loiseau, L. Lizzani-Cuvelier, R. Fellous, S. Rochard, C. Schippa, G. George, *Flavour Fragrance J.* **2002**, *18*, 425.

 © 2006 Wiley-VCH Verlag GmbH & Co. KGaA, Weinheim

Enzyme Promiscuity

DOI: 10.1002/anie.200502675

Fluoromorphic Substrates for Fatty Acid Metabolism: Highly Sensitive Probes for Mammalian Medium-Chain Acyl-CoA Dehydrogenase**

*Mary K. Froemming and Dalibor Sames**

In contrast to the accepted view in biological sciences that enzymes are highly selective for their physiological substrates, substrate promiscuity is a widespread phenomenon.[1] Such functional flexibility may often be observed with enzymes involved in the metabolism of an array of substrates, and examples extend beyond the well-known xenobiotic metabolism.

The exploration of enzyme substrate flexibility for the purpose of the development of metabolic probes and imaging agents represents a guiding concept for a broad program in our laboratories.[2,3] Herein we report the examination of the substrate fidelity of medium-chain acyl-CoA dehydrogenase (MCAD), a key enzyme in the metabolism of fatty acids, which led to the development of fluorogenic and fluoromorphic probes for this enzyme.[4] These indicators allow for selective and sensitive detection of MCAD activity in tissue homogenate.

β-Oxidation of fatty acids represents one of the central metabolic pathways.[5–11] Close examination of this process reveals considerable built-in substrate flexibility. Catabolism of a long-chain fatty acid occurs by repetitive removal of two-carbon units (acetyl-CoA), (Figure 1). Each catalytic turn involves four chemical steps that are catalyzed by enzymes capable of accommodating substrates with a variety of chain lengths. Thus, instead of having a specific enzyme for each intermediate (C_{16}, C_{14}, $C_{12} \rightarrow C_2$), this pathway consists of a few enzymes that show broad and overlapping chain-length specificities.

The overall mechanism for this pathway was proposed on the basis of classical studies conducted by F. Knoop[12] who showed that ω-phenyl fatty acids were metabolized in dogs.

[*] M. K. Froemming, Prof. D. Sames
Department of Chemistry
Columbia University
3000 Broadway, New York, NY 10027 (USA)
Fax: (+1) 212-932-1289
E-mail: sames@chem.columbia.edu

[**] The authors thank Professor Horst Schulz, Wenfeng Yu, and Lina Nie (City University of New York) for assistance with rat homogenates and supplying the rMCAD enzyme; Professor Jung-Ja Kim (Medical College of Wisconsin) for supplying the pSCAD, pMCAD, and hLCAD enzymes; and Dominic Yee for intellectual contributions. This work was generously supported by The G. Harold & Leila Y. Mathers Charitable Foundation. M.K.F. is the recipient of a NSF Predoctoral Fellowship.

Supporting information for this article is available on the WWW under http://www.angewandte.org or from the author.

© 2006 Wiley-VCH Verlag GmbH & Co. KGaA, Weinheim
InterScience

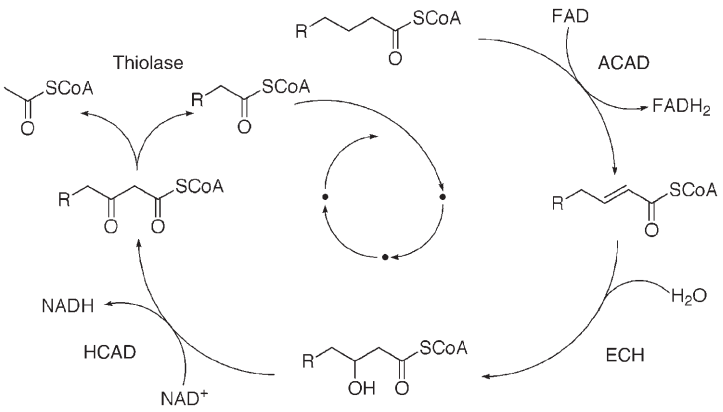


Figure 1. The β-oxidation cycle. The four enzyme families involved in β-oxidation are: acyl-CoA dehydrogenase (ACAD), enoyl-CoA hydratase (ECH), L-3-hydroxyacyl-CoA dehydrogenase (HCAD), and thiolase.

The ingenious use of the phenyl ring as a chemical label suggested a two-carbon degradation pathway but also, from the perspective of this paper, suggested the permissiveness of the entire pathway.[13]

The β-oxidation spiral begins, after the activation (acyl-CoA synthesis) and transport of fatty acids into mitochondria, with the α,β-dehydrogenation of acyl-CoA catalyzed by acyl coenzyme A dehydrogenases (ACADs). This flavin-dependent family consists of nine isozymes, five of which are involved in fatty acid metabolism.[10] Medium-chain acyl-CoA dehydrogenase (MCAD), formerly known as the 'general' ACAD owing to its ability to act on a wide range of chain lengths (C_{16}–C_4, Figure 2), represents an attractive target for the development of reporter substrates.

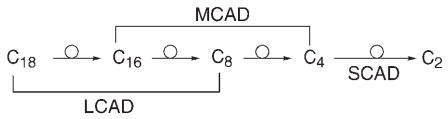


Figure 2. Substrate flexibility of medium-chain acyl-CoA dehydrogenase (MCAD) and long-chain acyl-CoA dehydrogenase (LCAD). These enzymes show broad and overlapping chain-length specificities. Acyl-CoAs with eight (C_8) to 18 (C_{18}) carbon chains are substrates for LCAD, whereas those with four (C_4) to 16 (C_{16}) are substrates for MCAD. SCAD shows low flexibility with butanoyl-CoA (C_4) being the main substrate.

MCAD is also an important target from the medical perspective. MCAD deficiency has recently emerged as a common hereditary disease with severe symptoms.[14–17] Furthermore, growing evidence implicates impaired β-oxidation as an important contributor to the development of a cluster of diseases such as hypertension, insulin resistance, and dyslipidemia, which is referred to as 'metabolic syndrome'.[18–20] Consequently, there is a need for a direct, sensitive, and continuous readout of MCAD enzyme activity in tissue samples and cell lines. Inspired by this challenge, we aimed to develop a fluorometric assay that is based on fluorogenic probes.

To develop fluorogenic MCAD enzyme reporters, two key criteria must be satisfied: 1) dehydrogenation is coupled either to an increase in brightness (fluorogenic) or preferably to a significant shift in emission wavelength (fluoromorphic), and 2) these compounds serve as substrates for MCAD.

Our design was based on a general motif that consists of an organic fluorophore attached to the β-carbon of propionyl-CoA (Figure 3). Dehydrogenation provides the corresponding unsaturated system with an extended π-conjugation that connects the fluorophore and the thioester group. We anticipated that such dramatic expansion of the π-conjugated system would strongly affect the emission profile, most likely shifting the emission to longer wavelengths.

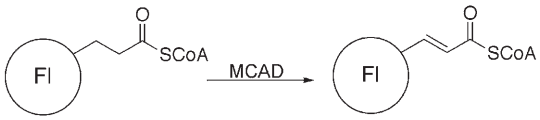


Figure 3. Design of a MCAD fluorescent reporter. Dehydrogenation extends the π-conjugation of the fluorophore, which results in a change in the emission profile. (Fl = organic fluorophore).

It has been shown that Knoop's substrate, 3-phenylpropionyl-CoA, and related compounds are substrates for MCAD; however, neither the substrates nor the products are fluorescent.[21–23] Consequently, we began with naphthalene-based systems, namely compound **1**, the dimethylamino-substituted analogue **2** (Figure 4),[24] and their corresponding products **3** and **4**, respectively. The photophysical measurements revealed that both pairs, **1**/**3** and **2**/**4**, constituted excellent fluoromorphic switches. Between compound **1** and **3**, the emission maximum is red shifted by approximately 50 nm with some overlap between the two curves. A threefold change in the emission intensity could be measured at the emission maximum of each compound, therefore meeting the requirements of a ratiometric probe. A comparison of **2** and **4** revealed a 190-nm shift of the emission and a 100-fold increase in the fluorescence intensity at the emission maximum of compound **4** (Figure 4).[25]

As the emission switch criterion was satisfied, we next addressed the issue of whether compounds **1** and **2** were substrates for MCAD. The activity was tested with purified rat-liver MCAD (rMCAD) by monitoring the reduction of an external electron acceptor (for assay conditions, see Supporting Information). We were gratified to find that compound **1** was a good substrate, however, **2** was completely inert. We hypothesized that the high polarity of the dimethyamino group, not necessarily its size, disfavored the interaction with the hydrophobic pocket of the enzyme. Instructed by these results, we synthesized compounds **5**–**10** to systematically explore two questions: 1) the limits of this enzyme in terms of the size, shape, and polarity of the substrate, and 2) the effect of substituents and other structural variations on emission properties.

Of the series shown in Figure 5, only probes **7** and **9** were substrates for MCAD. The adverse effect of polar substituents was confirmed; compounds **5** and **6** were found to be inert, whereas the conversion of the hydroxy group in **5** into a

 © 2006 Wiley-VCH Verlag GmbH & Co. KGaA, Weinheim

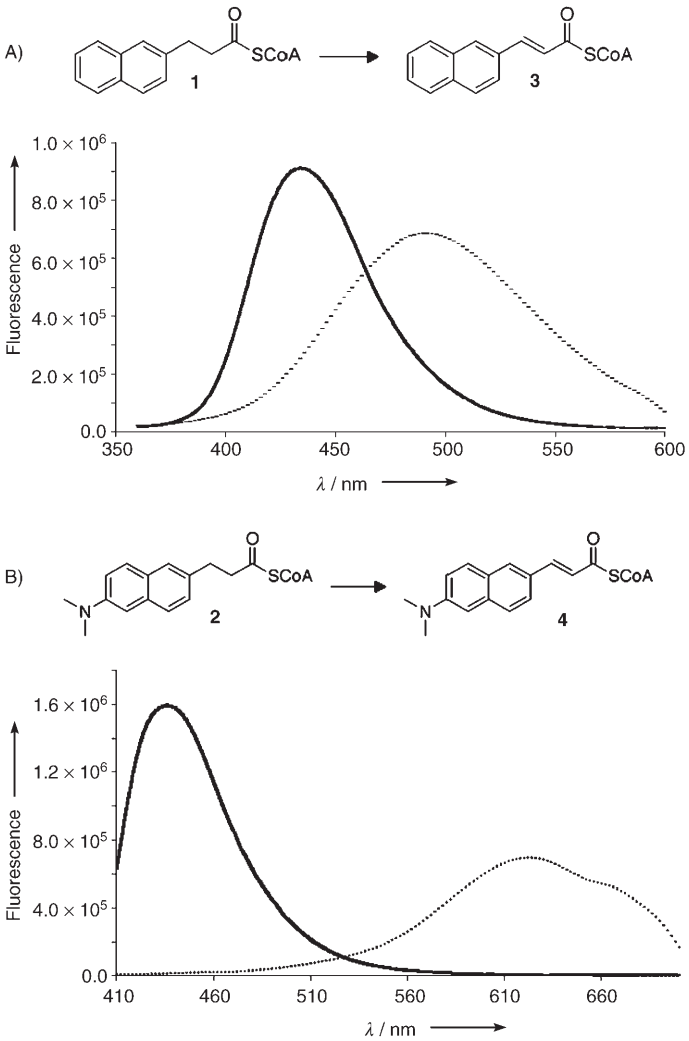


Figure 4. A) Emission spectra of **1** (——) and **3** (-----) ($\lambda_{ex}=340$ nm). B) Emission spectra of **2** (——) and **4** (••••) ($\lambda_{ex}=390$ nm). 50 μM in 100 mM potassium phosphate buffer (pH 8).

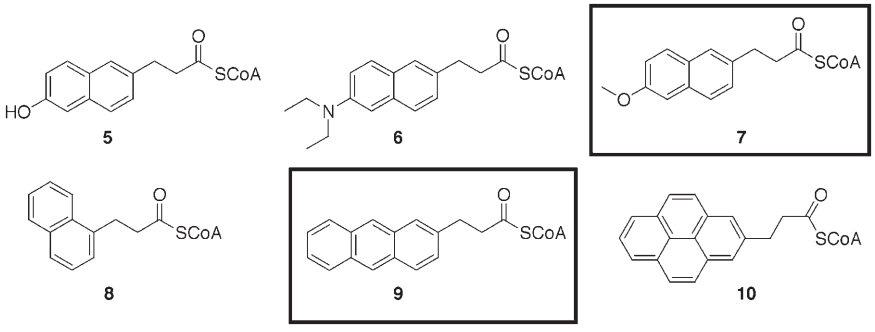


Figure 5. Concurrent exploration of MCAD substrate flexibility and emission properties of fluorophores. Esters **7** and **9** are substrates for MCAD.

methoxy group, as in **7**, furnished a good substrate. The shape of these probes was also of consequence as was demonstrated through the comparison of substrate **1** with its regioisomer **8**. The latter compound, wherein the propionyl chain is attached to C1 instead of C2, was completely inert. This is consistent with structural studies that revealed a narrow active site of MCAD.[10] Interestingly, the attachment of an additional ring to form anthracene was tolerated, demonstrating significant recognition-site flexibility as long as the substrate can assume a narrow shape. The pyrene system **10** was presumably too large and as a result, showed no conversion by the enzyme (Figure 5).

Thus, besides mapping the permissiveness of MCAD, this exercise also identified two new substrates with favorable emission properties (Figure 6). Dehydrogenation of the weakly fluorescent probe **7** led to the highly fluorescent product **11**, which resulted in an 80-fold increase in the emission intensity at 510 nm (fluorogenic probe), whereas conversion of **9** into **12** gave a 150-nm shift in the emission wavelength and afforded an 80-fold increase in emission intensity at 567 nm (fluoromorphic/ratiometric probe). In comparison with probe **1**, better separation of emission curves and a longer emission wavelength was achieved with substrates **7** and **9** (Figure 6).

With three fluorogenic probes in hand, a continuous fluorometric assay was developed and the kinetic parameters were determined for each substrate with rMCAD as well as pig MCAD (pMCAD; Table 1). The fluorometric assay was validated by comparison with the standard spectrophotometric assay (UV/Vis absorption); an excellent agreement was found between these two methods (see Supporting Information). Interestingly, all three probes had K_M^{app} on the same order of magnitude (low micromolar) as the optimum physiological substrate, octanoyl-CoA. Probe **7** had the highest K_M^{app} for both rMCAD and pMCAD, which supports the idea that polar groups disfavor binding to the hydrophobic pocket of the enzyme. In contrast to K_M^{app}, k_{cat} values were significantly lower when compared with octanoyl-CoA (Table 1). Substrate **1** had the largest turnover frequency ($k_{cat}=370\pm10$ and $150\pm4\ min^{-1}$ for rMCAD and pMCAD, respectively); substitution or extension of this motif led to a further decrease in this quantity (Table 1).

We noted that the decrease in enzyme activity ($u\,mg^{-1}$) for each additional phenyl ring in the substrate bears a striking similarity to the chain-length–activity relationship of natural fatty acids (Figure 7). Specifically, 3-phenylpropionyl-CoA had very similar specific activity to the optimal physiological substrate, octanoyl-CoA, whereas probe **1**, which contains the naphthalene system, had a similar activity to dodecanoyl-CoA (C_{12}, lauryl-CoA). Moreover, there was only a fivefold difference in activity between the anthracene probe **9** and palmitoyl-CoA (C_{16}). We propose a simple rationale for these findings based on similarities in the steric demand between the regular fatty acids and synthetic probes. These similarities become apparent when the former substrates are viewed in a folded conformation (Figure 7). X-

 © 2006 Wiley-VCH Verlag GmbH & Co. KGaA, Weinheim

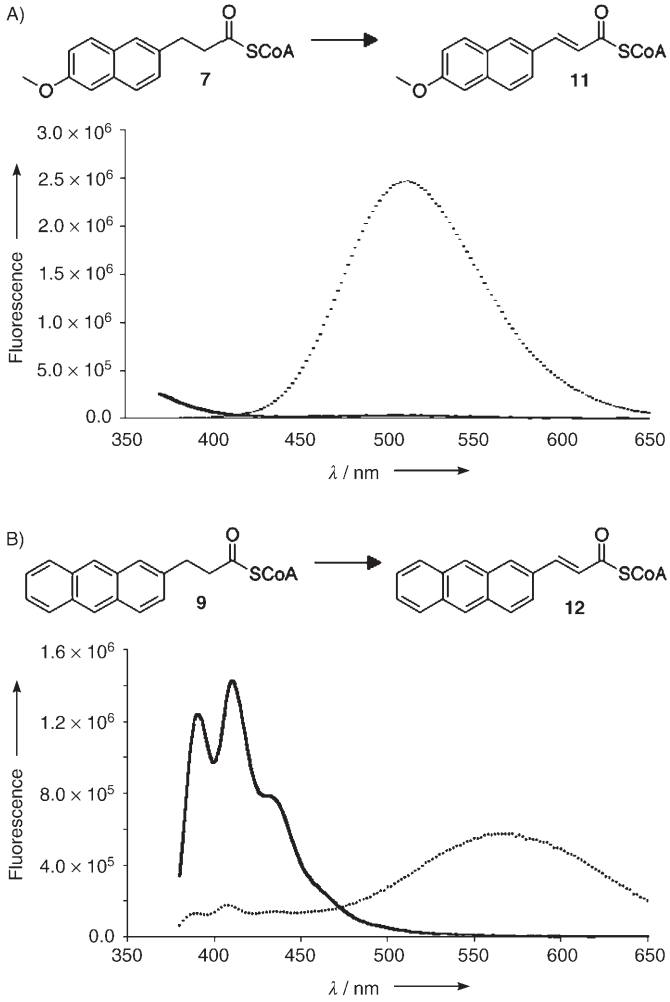
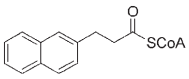
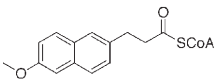
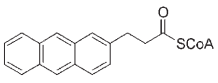


Figure 6. A) Emission spectra of **7** (——) and **11** (-----) (λ_{ex} = 350 nm). B) Emission spectra of **9** (——) and **12** (••••) (λ_{ex} = 356 nm). Compound **7**, **9**, **11**, and **12** (50 μM) in potassium phosphate buffer solution (100 mM, pH 8). The fluorescence is not affected by the assay medium.

Table 1: Kinetic parameters of probes (see Supporting Information).

		K_M^{app} [μM]	k_{cat} [min^{-1}]
octanoyl-CoA	rMCAD[30]	4.0	2142
	pMCAD[31]	2.3 ± 0.1	1176
	rMCAD	2.5 ± 0.2[a]	370 ± 10
	pMCAD	2.3 ± 0.2	150 ± 4
	homogenate	2.2 ± 0.3	–
	rMCAD	6.01 ± 0.7	16.1 ± 0.3
	pMCAD	14.5 ± 1.5	12.3 ± 0.5
	homogenate	3.7 ± 0.4	–
	rMCAD	1.1 ± 0.2	10.4 ± 0.3
	pMCAD	4.5 ± 0.5	13.1 ± 2
	homogenate	1.9 ± 0.4	–

[a] Mean ± S.D. (n = 3).

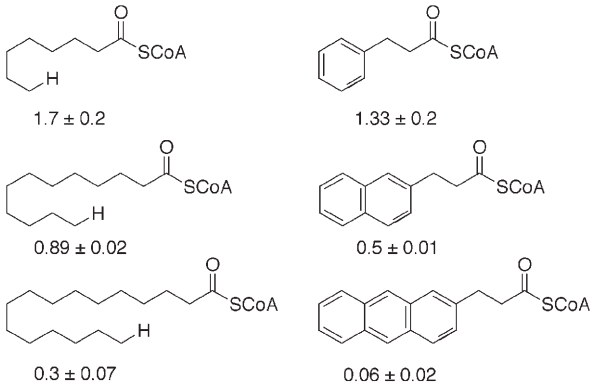


Figure 7. Specific activity (u mg^{-1}) for straight-chain acyl-CoA's and aromatic substrates with rMCAD (see Supporting Information for assay conditions).

Ray crystallographic analysis of the enzyme–substrate complex showed that the active site is not long enough to accommodate long substrates in an extended conformation and, as a result, folding is required (although not to the extent shown in Figure 7).[10,26]

The next major task centered on the evaluation of the possibility of using these substrates as useful probes in tissue samples. This included addressing the issues of selectivity, stability, and the ability to be metabolized by subsequent enzymes of the β-oxidation pathway.

In addition to MCAD, there are two other soluble isozymes of the ACAD family that are involved in the metabolism of straight-chain fatty acids, namely short-chain acyl-CoA dehydrogenase (SCAD) and long-chain acyl-CoA dehydrogenase (LCAD). Purified pig SCAD (pSCAD) and human LCAD (hLCAD) were obtained and tested with probes **1**, **7**, and **9**. Importantly, none of these probes showed any significant activity, which demonstrates a notable selectivity for MCAD within the ACAD family. To address this question in a relevant context, competitive substrate assays were conducted by using rat-liver homogenate (Figure 8). Conversion of the probe by the tissue homogenate was monitored both in the presence and absence of a competitive physiological substrate. Addition of butanoyl-CoA and isovaleryl-CoA, the optimal substrates for SCAD and isovaleryl-CoA dehydrogenase (iVAD), respectively, had no effect, which indicates that probes **1**, **7**, and **9** were not substrates for these enzymes. In contrast, octanoyl-CoA competed with the probes, which led to a significant inhibition of fluorescent product formation. A fivefold excess of octanoyl-CoA completely inhibited dehydrogenation of probe **7** as a result of the weaker binding (higher K_M value) of this reporter substrate. Dehydrogenation of all the probes was inhibited by an excess of palmitoyl-CoA, which was consistent with relatively low K_M as well as low k_{cat} values of this substrate for MCAD (Figure 8). These data, including the experiments with isolated isozymes and tissue homogenates, provided compelling evidence for the high selectivity of the probes **1**, **7**, and **9** for MCAD.

The stability of the fluorescent products **3**, **11**, and **12** was also examined. As these compounds may be metabolized by

 © 2006 Wiley-VCH Verlag GmbH & Co. KGaA, Weinheim

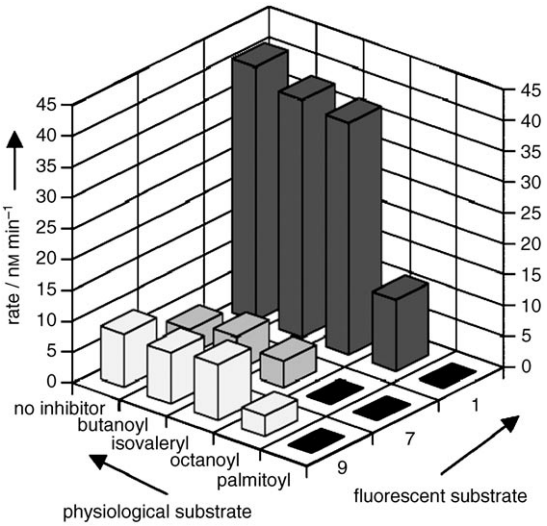


Figure 8. Competitive assays between the fluorogenic substrates (**1**, **7**, and **9**) and the physiological substrates (butanoyl-CoA, isovaleryl-CoA, octanoyl-CoA, and palmitoyl-CoA). Assays were carried out in a 96-well plate with physiological substrate (50 μM), fluorescent substrate (10 μM), and rat-liver homogenate as the enzyme source. The margin of error was $<20\%$ for all assays ($n=3$).

the subsequent enzyme(s) of the β-oxidation pathway, that is, enoyl-CoA hydratase, they were exposed to rat-liver homogenate. Although no hydration occurred, a small decrease in fluorescence was detected with **3** and **11**, which was independent of the homogenate. Rather, products **3** and **11** were subject to photobleaching, whereas compound **12** was stable on the time scale of the experiment. Importantly, photobleaching did not significantly affect the results of the assay.

The relationship between activity and homogenate protein concentration was established for each probe and appears to be linear within narrow ranges of protein concentrations (See Supporting Information). As expected, enzyme activity was dependent on the external electron acceptor, in this case, ferrocenium hexafluorophosphate ($FcPF_6$).[27] When the external oxidant was omitted, probes **1** and **9** were inert, whereas probe **7** gave a detectable residual activity ($\leq 2\%$ of the total activity). As the oxidase activity (direct transfer of electrons to oxygen)[22,23] of the purified MCAD protein was less than 0.03% with probe **7**, the residual activity could be ascribed to either endogenous electron acceptors in the homogenate or peroxisomal acyl-CoA oxidase (ACO).[8] These results indicate that the ACO does not contribute to the observed fluorescent signal in any significant manner, but rather provides further support for high selectivity of these probes for MCAD.

The immediate impact of this study is the ability to monitor MCAD activity in cell and tissue homogenates in a direct and continuous manner, therefore laying the foundation for a new, sensitive, and practical diagnostic test for MCAD deficiency.[28] MCAD deficiency has recently been identified as a common hereditary disease with an estimated occurrence rate of 1:15000 newborns in the US (an incidence rate similar to that of phenylketonuria).[16] This deficiency often results in severe symptoms that resemble those of Reye's syndrome and sudden infant death syndrome. Early diagnosis may prevent the onset of the symptoms through a regulated diet and avoidance of fasting and excessive physical activity.

Generally, fluorometric methods offer superior detection sensitivity (up to two orders of magnitude) in comparison with UV/Vis absorption methods. In this case, the fluorogenic probe **7** allowed for reliable detection of MCAD activity with as little as 0.4 μg of tissue homogenate protein, which is more sensitive than the existing UV/Vis methods.[29] Further to high sensitivity, fluorescence-based measurements may be performed in a high-throughput manner in a routine 96-well-plate format. Based on these results, a new and practical diagnostic test may be developed that offers an attractive alternative to the more involved methods used today (e.g. MS-MS).

In a long-term view, the development of these probes sets the stage for the investigation of the β-oxidation pathway in its intact state. The possibility of measuring and imaging the activity of MCAD, as well as the flux through this pathway, will be examined. This represents an exciting prospect considering the central role of this pathway in a number of metabolic diseases.[17–19]

Received: July 29, 2005
Published online: December 19, 2005

Keywords: enzyme promiscuity · fluorescent probe · medium-chain acyl-CoA dehydrogenase · metabolism · oxidation

[1] P. J. O'Brien, D. Herschlag, *Chem. Biol.* **1999**, *6*, R91 – R105.
[2] D. J. Yee, V. Balsanek, D. Sames, *J. Am. Chem. Soc.* **2004**, *126*, 2282 – 2283.
[3] G. Chen, D. J. Yee, N. G. Gubernator, D. Sames, *J. Am. Chem. Soc.* **2005**, *127*, 4544 – 4545.
[4] By the term 'fluoromorphic probe', we designate a fluorescent compound, which, by the chemical reaction of interest, affords a fluorescent product with a different emission wavelength profile. The term 'ratiometric' is also used for this type of probe.
[5] W. H. Kunau, V. Dommes, H. Schulz, *Prog. Lipid Res.* **1995**, *34*, 267 – 342.
[6] S. Eaton, K. Bartlett, M. Pourfarzam, *Biochem. J.* **1996**, *320*(Pt2), 345 – 357.
[7] S. Ghisla, *Eur. J. Biochem.* **2004**, *271*, 459 – 461.
[8] K. Bartlett, S. Eaton, *Eur. J. Biochem.* **2004**, *271*, 462 – 469.
[9] N. Gregersen, P. Bross, B. S. Andresen, *Eur. J. Biochem.* **2004**, *271*, 470 – 482.
[10] J. J. Kim, R. Miura, *Eur. J. Biochem.* **2004**, *271*, 483 – 493.
[11] S. Ghisla, C. Thorpe, *Eur. J. Biochem.* **2004**, *271*, 494 – 508.
[12] F. Knoop, *Beitr. Chem. Physiol. Pathol.* **1904**, *6*, 150 – 162.
[13] The reverse process, namely fatty acid or polyketide biosynthesis ought to possess similar substrate tolerance. In the latter case, this phenomenon was demonstrated and exploited for the incorporation of non-natural building units to erythronolide antibiotics. J. R. Jacobsen, C. R. Hutchinson, D. E. Cane, C. Khosla, *Science* **1997**, *277*, 367.
[14] S. Kolvraa, N. Gregersen, E. Christensen, N. Hobolth, *Clin. Chim. Acta* **1982**, *126*, 53 – 67.
[15] W. J. Rhead, B. A. Amendt, K. S. Fritchman, S. J. Felts, *Science* **1983**, *221*, 73 – 75.
[16] B. S. Andresen, S. F. Dobrowolski, L. O'Reilly, J. Muenzer, S. E. McCandless, D. M. Frazier, S. Udvari, P. Bross, I. Knudsen, R.

 © 2006 Wiley-VCH Verlag GmbH & Co. KGaA, Weinheim

Banas, D. H. Chace, P. Engel, E. W. Naylor, N. Gregersen, *Am. J. Hum. Genet.* **2001**, *68*, 1408 – 1418.
[17] R. J. Wanders, P. Vreken, M. E. den Boer, F. A. Wijburg, A. H. van Gennip, L. IJLst, *J. Inherited Metab. Dis.* **1999**, *22*, 442 – 487.
[18] G. I. Shulman, *J. Clin. Invest.* **2000**, *106*, 171 – 176.
[19] B. B. Lowell, G. I. Shulman, *Science* **2005**, *307*, 384 – 387.
[20] *J. Am. Med. Assoc.* **2001**, *285*, 2486 – 2497.
[21] K. W. Yao, H. Schulz, *Anal. Biochem.* **1993**, *214*, 528 – 534.
[22] J. T. McFarland, M. Y. Lee, J. Reinsch, W. Raven, *Biochemistry* **1982**, *21*, 1224 – 1229.
[23] J. K. Johnson, Z. X. Wang, D. K. Srivastava, *Biochemistry* **1992**, *31*, 10564 – 10575.
[24] G. Weber, F. J. Farris, *Biochemistry* **1979**, *18*, 3075 – 3078.
[25] The emission intensity is directly proportional to the brightness. See reference [3].
[26] H. J. Lee, M. Wang, R. Paschke, A. Nandy, S. Ghisla, J. J. Kim, *Biochemistry* **1996**, *35*, 12412 – 12420.
[27] T. C. Lehman, D. E. Hale, A. Bhala, C. Thorpe, *Anal. Biochem.* **1990**, *186*, 280 – 284.
[28] It has been shown by others that leukocytes or skin fibroblasts may be used to monitor MCAD activity (see reference [21]).
[29] D. M. Turnbull, K. Bartlett, N. J. Watmough, I. M. Shepherd, H. S. Sherratt, *J. Inherited Metab. Dis.* **1987**, *10*(Suppl 1), 105 – 112.
[30] K. L. Peterson, E. E. Sergienko, Y. Wu, N. R. Kumar, A. W. Strauss, A. E. Oleson, W. W. Muhonen, J. B. Shabb, D. K. Srivastava, *Biochemistry* **1995**, *34*, 14942 – 14953.
[31] Y. Ikeda, K. Okamura-Ikeda, K. Tanaka, *J. Biol. Chem.* **1985**, *260*, 1311 – 1325.

 © 2006 Wiley-VCH Verlag GmbH & Co. KGaA, Weinheim

Protein Engineering

DOI: 10.1002/anie.200502623

Nonmechanical Protein Can Have Significant Mechanical Stability**

*Yi Cao, Canaan Lam, Meijia Wang, and Hongbin Li**

Many proteins function as complex mechanochemical machinery in living cells to constantly sense, generate, and bear mechanical forces.[1] In addition to their biological importance, these mechanical proteins also arouse tremendous interest in nanoscience and technology and have been incorporated into nanomechanical devices for well-defined applications.[2–4] It is clear that these mechanical proteins will find a wide range of applications as building blocks for the bottom-up construction of functional nanomechanical devices.[4,5] Elastomeric proteins are a special class of mechanical proteins.[6] They are placed under mechanical tension under physiological conditions and serve as molecular springs in a variety of biological machines and tissues to establish elastic connections and provide mechanical strength, elasticity, and extensibility.[6–13] Recent developments in single-molecule force spectroscopy have enabled the direct measurement of the mechanical stability and elasticity of elastomeric proteins at the single-molecule level.[7–10,13–16] Combined with molecular dynamics (MD) simulations, single-molecule atomic force microscopy (AFM) studies have revealed rich information about the mechanical architecture and design of elastomeric proteins.[14,17–23] Compared with proteins that commonly do not bear any mechanical functions under physiological conditions, mechanical proteins are just a small fraction of the total proteins inside cells. To construct multifunctional nanomechanical devices, it is desirable to extend single-molecule force-spectroscopic studies to include nonmechanical proteins (such as enzymes), as the abundant nonmechanical proteins may significantly expand the tool box of mechanical proteins, impart novel functionality, and enable applications such as force sensors[24] and switches. A prerequisite for these applications is that these nonmechanical proteins can withstand mechanical tension. It has been proposed that nonmechanical proteins may contain motifs of considerable mechanical stability;[25] however, most of the nonmechanical proteins that have been studied so far, such as barnase and carmodulin, are mechanically labile and only have marginal mechanical stability.[24,26–30] Green fluorescent protein (GFP) is the strongest nonmechanical protein to date and has a mechanical stability of approximately 100 pN.[24] It remains a question whether nonmechanical proteins can have sufficient mechanical stability and be used for mechanical applications. Herein, we use single-molecule AFM and protein engineering to demonstrate that nonmechanical proteins, with desired structure and topology, can have significant mechanical stability.

Extensive studies on the 27th immunoglobulin (I27) domain of the muscle protein titin have provided insight into how the I27 domain achieves high mechanical stability that is critical for the physiological function of titin.[14,17–22] The key structural feature of I27 is that its two terminus β strands are arranged in parallel and bonded by a series of backbone hydrogen bonds (Figure 1 A). Upon stretching from the N and C termini, a shear force is applied to the hydrogen-bonding network between the two terminal β strands, which form the strongest mechanically resistant region.[19,31] This shear topology of the hydrogen-bonding network seems to be a common feature among the stable mechanical proteins studied so far.[7,15,32–35] Based on this topological consideration, we have identified, from the pool of small model proteins that are commonly used in protein-folding studies, nonmechanical protein candidates that might be mechanically stable. The B1 immunoglobulin G (IgG) binding domain of streptococcal protein G is one of the smallest candidates.

[*] Y. Cao, C. Lam, Dr. M. Wang, Prof. Dr. H. Li
Department of Chemistry
The University of British Columbia
2036 Main Mall, Vancouver, BC, V6T1Z1 (Canada)
Fax: (+1) 604-822-2847
E-mail: hongbin@chem.ubc.ca

[**] This work was supported by the Natural Sciences and Engineering Research Council of Canada, Canada Research Chair program, and the start-up fund from the University of British Columbia. Y.C. is partially supported by the Laird Fellowship.

Supporting information for this article is available on the WWW under http://www.angewandte.org or from the author.

InterScience
© 2006 Wiley-VCH Verlag GmbH & Co. KGaA, Weinheim

Protein G of streptococcal is a bacterial cell-wall protein that does not have known mechanical functions. The B1 IgG binding domain of protein G (referred to as GB1 thereafter) is a small α/β protein with only 56 amino acid residues and is composed of a four-strand β sheet packed against a long α helix.[36] The two central strands that comprise the N and C termini are parallel to each other (Figure 1B). An extensive hydrogen-bonding network among the β sheet exists and constitutes a potentially mechanically resistant structural motif. Based on this shear topology, we predict that GB1 will have considerable mechanical stability. This predication was supported by a similar predication made by Li and Makarov[25] based on MD simulation and the topological similarity between the third IgG binding domain of protein G and ubiquitin, which has been shown to be mechanically stable.[32]

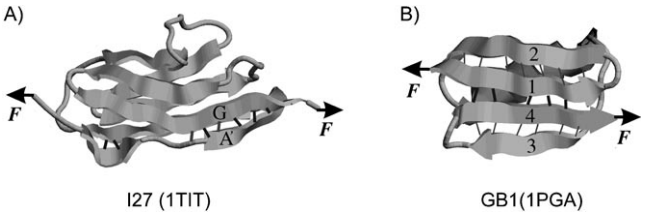


Figure 1. The nonmechanical protein GB1 is predicted to be mechanically stable based on protein topology. A) The topology of the mechanically stable protein I27. The two terminal β strands A′ and G are arranged in parallel and are bonded by a series of backbone hydrogen bonds (indicated by thick, dark lines). Upon stretching (indicated by arrows), the backbone hydrogen bonds between these two strands are subject to a shear force and form the mechanical resistance to stretching. B) The structure of GB1. The two terminal strands (strands 1 and 4) are arranged in a similar fashion to those of I27 and are potentially resistant to mechanical stretching force. GB1 is predicted to have significant mechanical stability. Backbone hydrogen bonds that link β strands 1 and 4 are indicated by thick, dark lines, whereas those linking the remaining part of the β sheet are indicated by thin lines.

We constructed a polyprotein that contains eight direct tandem repeats of the GB1 domain $(GB1)_8$. The polyprotein $(GB1)_8$ was deposited onto a clean glass cover slip, and stretched between the AFM tip and the glass substrate in phosphate buffer solution (PBS). Stretching polyprotein $(GB1)_8$ results in force-extension curves that show characteristic saw-tooth patterns, with as many as eight force peaks (Figure 2A). These force peaks are equally spaced with a peak-to-peak distance of approximately 15 nm, and their amplitudes vary around 180 pN (at a pulling speed of 400 nm s^{-1}). These equally spaced force peaks result from the sequential unfolding of individual GB1 domains in the polyprotein chain,[9,14] whereas the last peak in each force-extension curve corresponds to the extension of the unfolded polyprotein chain and its subsequent detachment from either the AFM tip or substrate. The amplitude of the last peaks varies greatly and can be as high as 1.5 nN, which is clearly different from the mechanical unfolding of the GB1 domains. The force-extension curves can be well described by the wormlike chain (WLC) model of polymer elasticity.[37] Fits of

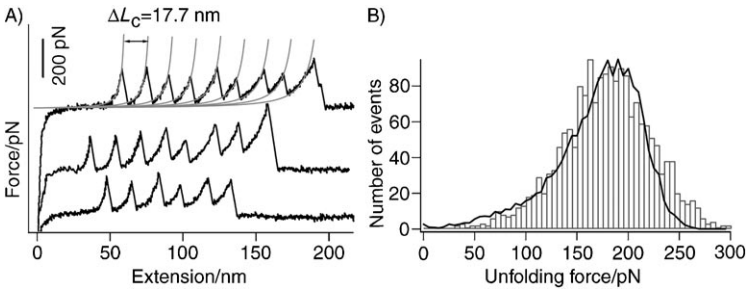


Figure 2. Force-extension measurements reveal that the GB1 protein is mechanically stable. A) Typical force-extension curves measured on $(GB1)_8$ polyproteins that show the characteristic saw-tooth pattern with equally spaced force peaks, which result from the mechanical unraveling of each individual GB1 domain in the polyprotein chain. The last peak in each force-extension curve corresponds to the detachment of the protein from either the AFM tip or substrate. The force-extension curves can be well described by the WLC model of polymer elasticity. The gray lines are WLC model fits to the individual unfolding force peaks with a contour length increment ΔL_c of 17.7 nm. B) Histogram of unfolding forces for the GB1 protein. The gray bars are experimental data measured from approximately 300 force-extension curves (as those shown in A) with a total of 1826 unfolding events at a pulling speed of 400 nm s^{-1}. The unfolding force histogram for GB1 peaks at approximately 178 pN and shows a broad distribution that spans a range of approximately 150 pN. This broad distribution reflects the intrinsic properties that underlie the energy profile of the mechanical unfolding of GB1. The solid, black line is a Monte Carlo simulation of the mechanical unfolding of $(GB1)_8$ polyprotein by using a spontaneous unfolding rate constant α_0 of 0.039 s^{-1}, an unfolding distance Δx_u of 0.17 nm, and a pulling speed of 400 nm s^{-1}.

the WLC model to the consecutive peaks measure a contour length increment of 18.0 ± 0.5 nm (see the Supporting Information), thus indicating that the GB1 protein will extend by approximately 18 nm upon mechanical unraveling.

The contour length increment upon the unfolding of GB1 was calculated to confirm that the saw-tooth patterns observed are due to the mechanical unraveling of an individual GB1 domain. A single GB1 domain is 20.2 nm (56 aa × 0.36 nm aa^{-1}; aa = amino acid residue) long when it is fully stretched, whereas the length of the folded GB1 domain (the distance between its N and C termini) is 2.6 nm.[36] Hence, the mechanical unfolding of a GB1 domain will lengthen the molecule by 17.6 nm, which is in good agreement with the contour length increment between consecutive peaks measured from the force-extension curves. This agreement corroborates that the saw-tooth patterns observed indeed result from the mechanical unfolding of individual GB1 domains in the polyprotein. Therefore, the average unfolding force reflects the average mechanical stability of the GB1 domain, which is approximately 178 ± 40 pN (average ± standard deviation (SD), $n = 1826$) at a pulling speed of 400 nm s^{-1}. This mechanical stability is comparable to that of the I27 domain,[14] a well-studied mechanical protein domain from the muscle protein titin. This result indicates that a nonmechanical protein can have significant mechanical stability, as do mechanical proteins.

The mechanical unfolding of proteins is a stochastic event;[38] therefore, the value of unfolding forces for GB1 vary randomly around the average value of approximately 180 pN. Figure 2B shows the unfolding-force histogram measured from approximately 300 force-extension curves with a total of 1826 unfolding events, such as those shown in Figure 2A. The

 © 2006 Wiley-VCH Verlag GmbH & Co. KGaA, Weinheim

force histogram is centered at 178 pN and shows a broad distribution in unfolding forces, which spans a range of approximately 150 pN. The SD of the unfolding forces for GB1 is 40 pN, which is significantly larger than that of any other protein measured so far.[14,17,18,39] This large variation in unfolding forces is much greater than the experimental uncertainty associated with the force measurements (≈20 pN), thus reflecting the intrinsic properties associated with the underlying energy landscape[38] for the mechanical unfolding of the GB1 domain.

The WLC model fits the force-extension curves of GB1 well and no detectable unfolding intermediate state is observed (see Figure 2A). Hence, the mechanical unfolding of the GB1 domain can be modeled as a two-state process with force-dependent unfolding and folding rate constants.[40] Based on a standard procedure,[14] Monte Carlo simulation was used to reproduce the unfolding-force histogram shown in Figure 2B and extract the information about the unfolding rate constant at zero force α_0 and the unfolding distance Δx_u, which is the distance between the folded state and the transition state along the reaction coordinate. We found that the unfolding-force histogram can be reproduced adequately by using an unfolding rate constant of $0.039\ s^{-1}$ and an unfolding distance of 0.17 nm. The unfolding distance for GB1 is smaller than the typical values (0.25–0.4 nm) of Δx_u for β-sheet proteins,[8,9,14,22] thus suggesting that the transition state for the mechanical unfolding of GB1 is highly nativelike. The unfolding rate constant α_0 is one order of magnitude smaller than the chemical unfolding rate constant at zero denaturant concentration for GB1.[41]

Similar to elastomeric proteins, the unfolding forces of GB1 are found to depend upon the pulling speed at which the protein is stretched and unraveled. The faster the pulling speed is, the higher the unfolding force is required to unravel the GB1 domain. The average unfolding force versus the pulling speed (20–3500 $nm\,s^{-1}$) for GB1 is plotted in Figure 3, and for comparison, the speed dependence of the unfolding force for I27 is also plotted.[14] The data show that the unfolding force for GB1 has a much stronger dependence on the pulling speed than that of the I27 protein.

Monte Carlo simulation was used to fit the speed dependence of the unfolding forces. We found that the speed dependence of the unfolding forces can be well described with $\alpha_0 = 0.039\ s^{-1}$ and $\Delta x_u = 0.17$ nm, which is in good agreement with the estimate from Figure 2.

Compared with the I27 protein,[8,9,14,15,22] the unfolding rate constant α_0 for GB1 is two orders of magnitude bigger than that of I27, yet GB1 is as mechanically stable as I27, which is due to the unusually small unfolding distance Δx_u for GB1. If the distance to the transition state for GB1 were similar to that of I27 (0.25 nm), a mechanical unfolding rate constant of $0.039\ s^{-1}$ would cause the GB1 domain to unfold at an average force of approximately 100 pN at a pulling speed of $400\ nm\,s^{-1}$. A shorter unfolding distance effectively compensates the effect of the faster unfolding rate constant on the mechanical stability, thus illustrating the vital importance of the unfolding distance to the mechanical stability of proteins. It is possible that the small unfolding distance Δx_u directly results from the shear topology and the extensive hydrogen-bonding network of the GB1 protein, thus revealing the physical basis that underlies the hypothesis that the β-sheet proteins of shear topology tend to be mechanically stable.

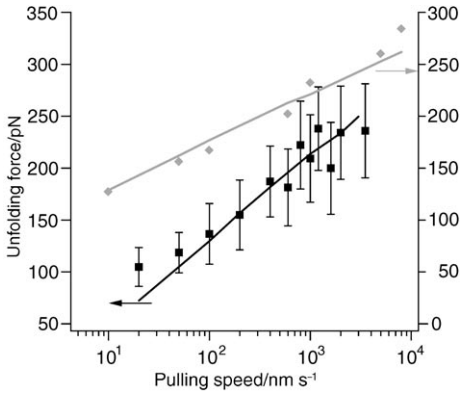


Figure 3. Unfolding kinetics of the GB1 protein. The unfolding forces of GB1 (black squares) strongly depend on the pulling speed at which the polyprotein was stretched and unraveled. The measured unfolding forces at high pulling speed were corrected for the hydrodynamic drag force that acts directly on the AFM cantilever.[44] The unfolding kinetics of GB1 can be reproduced adequately by Monte Carlo simulations with $\alpha_0 = 0.039\ s^{-1}$ and $\Delta x_u = 0.17$ nm (black, solid line). The unfolding distance for GB1 is much smaller than that of other proteins. For comparison, the unfolding kinetics of I27 protein, as well as its Monte Carlo fit, are also plotted (gray diamonds and gray line). The data was taken from ref. [14].

The experimental data reported herein closely matches the prediction made by Li and Makarov for a similar domain from protein G (the third IgG binding domain from streptococcal protein G).[25] Although the structural details differ between these two domains, the mechanical unfolding of both domains involves the separation of the two parallel terminal β strands, which are bonded by a network of hydrogen bonds and constitute the mechanical resistance. A recent study[42] demonstrated that protein L, a structural homologue of GB1, is also mechanically stable and unfolds at approximately 130 pN at a pulling speed of $400\ nm\,s^{-1}$, thus providing additional supporting evidence of the importance of the shear β-sheet topology on the mechanical stability. It is likely that proteins homologous to GB1 share the same feature and constitute a family of proteins that have remarkable mechanical stability. Furthermore, this study can also aid future experimental efforts to search for potential mechanical functions for proteins in vivo.

In summary, we have demonstrated that a nonmechanical protein, such as GB1, can have significant mechanical stability. Our findings corroborate the importance of protein topology for mechanical stability, and we anticipate that by using simple topological considerations more proteins with considerable mechanical stability can be discovered and the tool box of elastomeric proteins will be expanded. This approach will pave the way for the exploitation of nonmechanical proteins with defined functionalities for various nanomechanical applications, such as force sensors and switches.

 © 2006 Wiley-VCH Verlag GmbH & Co. KGaA, Weinheim

Experimental Section

The plasmid that encodes the GB1 protein was generously provided by David Baker of the University of Washington. The GB1 monomer, flanked with a 5′ *BamH*I restriction site and 3′ *Bgl*II, *Kpn*I restriction sites, was amplified by the polymerase chain reaction and subcloned into the pQE80L expression vector. The $(GB1)_8$ polyprotein gene was constructed by using a previously described method[14] based on the identity of the sticky ends generated by the *BamH*I and *Bgl*II restriction enzymes. The $(GB1)_8$ polyproteins were expressed in the DH5α strain and purified by Ni^{2+}-affinity chromatography. The polyprotein was kept at 4 °C in PBS buffer at a concentration of 740 $\mu g\,mL^{-1}$.

Single-molecule AFM experiments were carried out on a custom-built atomic force microscope, which was constructed as described.[43] All the force-extension measurements were carried out in PBS buffer. In a typical experiment, $(GB1)_8$ polyprotein sample (1 μL) was deposited onto a clean glass cover slip covered by PBS buffer (50 μL) and was allowed to adsorb for approximately 5 min. The spring constant of each individual cantilever (Si_3N_4 cantilevers from Vecco, with a typical spring constant of 40 $pN\,nm^{-1}$) was calibrated in solution using the equipartition theorem before and after each experiment.

The mechanical unfolding of the GB1 protein was described as a two-state Markovian process with force-dependent rate constants. Monte Carlo simulations of the stretching of the GB1 polyprotein was carried out according to reported procedures[14] to estimate the unfolding rate constant at zero force α_0 and the distance of the native state to the transition state Δx_u along the reaction coordinate of the mechanical unfolding reaction.

Received: July 26, 2005
Published online: December 13, 2005

Keywords: mechanical properties · protein unfolding · scanning probe microscopy · single-molecule studies

[1] G. Bao, S. Suresh, *Nat. Mater.* **2003**, *2*, 715.
[2] H. Hess, J. Clemmens, C. Brunner, R. Doot, S. Luna, K. H. Ernst, V. Vogel, *Nano Lett.* **2005**, *5*, 629.
[3] R. K. Soong, G. D. Bachand, H. P. Neves, A. G. Olkhovets, H. G. Craighead, C. D. Montemagno, *Science* **2000**, *290*, 1555.
[4] D. S. Goodsell, *Bionanotechnology*, Wiley-Liss, Hoboken, **2004**.
[5] T. Hugel, N. B. Holland, A. Cattani, L. Moroder, M. Seitz, H. E. Gaub, *Science* **2002**, *296*, 1103.
[6] A. S. Tatham, P. R. Shewry, *Trends Biochem. Sci.* **2000**, *25*, 567.
[7] H. Li, W. A. Linke, A. F. Oberhauser, M. Carrion-Vazquez, J. G. Kerkvliet, H. Lu, P. E. Marszalek, J. M. Fernandez, *Nature* **2002**, *418*, 998.
[8] A. F. Oberhauser, P. E. Marszalek, H. P. Erickson, J. M. Fernandez, *Nature* **1998**, *393*, 181.
[9] M. Rief, M. Gautel, F. Oesterhelt, J. M. Fernandez, H. E. Gaub, *Science* **1997**, *276*, 1109.
[10] M. Rief, J. Pascual, M. Saraste, H. E. Gaub, *J. Mol. Biol.* **1999**, *286*, 553.
[11] T. Ohashi, D. P. Kiehart, H. P. Erickson, *Proc. Natl. Acad. Sci. USA* **1999**, *96*, 2153.
[12] M. K. Miller, H. Granzier, E. Ehler, C. C. Gregorio, *Trends Cell Biol.* **2004**, *14*, 119.
[13] P. Carl, C. H. Kwok, G. Manderson, D. W. Speicher, D. E. Discher, *Proc. Natl. Acad. Sci. USA* **2001**, *98*, 1565.
[14] M. Carrion-Vazquez, A. F. Oberhauser, S. B. Fowler, P. E. Marszalek, S. E. Broedel, J. Clarke, J. M. Fernandez, *Proc. Natl. Acad. Sci. USA* **1999**, *96*, 3694.
[15] I. Schwaiger, A. Kardinal, M. Schleicher, A. A. Noegel, M. Rief, *Nat. Struct. Biol.* **2004**, *11*, 81.
[16] I. Schwaiger, C. Sattler, D. R. Hostetter, M. Rief, *Nat. Mater.* **2002**, *1*, 232.
[17] R. B. Best, S. B. Fowler, J. L. Herrera, A. Steward, E. Paci, J. Clarke, *J. Mol. Biol.* **2003**, *330*, 867.
[18] D. J. Brockwell, G. S. Beddard, J. Clarkson, R. C. Zinober, A. W. Blake, J. Trinick, P. D. Olmsted, D. A. Smith, S. E. Radford, *Biophys. J.* **2002**, *83*, 458.
[19] H. Lu, B. Isralewitz, A. Krammer, V. Vogel, K. Schulten, *Biophys. J.* **1998**, *75*, 662.
[20] H. Lu, K. Schulten, *Biophys. J.* **2000**, *79*, 51.
[21] P. E. Marszalek, H. Lu, H. Li, M. Carrion-Vazquez, A. F. Oberhauser, K. Schulten, J. M. Fernandez, *Nature* **1999**, *402*, 100.
[22] P. M. Williams, S. B. Fowler, R. B. Best, J. L. Toca-Herrera, K. A. Scott, A. Steward, J. Clarke, *Nature* **2003**, *422*, 446.
[23] E. Paci, M. Karplus, *Proc. Natl. Acad. Sci. USA* **2000**, *97*, 6521.
[24] H. Dietz, M. Rief, *Proc. Natl. Acad. Sci. USA* **2004**, *101*, 16192.
[25] P. C. Li, D. E. Makarov, *J. Phys. Chem. B* **2004**, *108*, 745.
[26] R. B. Best, B. Li, A. Steward, V. Daggett, J. Clarke, *Biophys. J.* **2001**, *81*, 2344.
[27] G. Yang, C. Cecconi, W. A. Baase, I. R. Vetter, W. A. Breyer, J. A. Haack, B. W. Matthews, F. W. Dahlquist, C. Bustamante, *Proc. Natl. Acad. Sci. USA* **2000**, *97*, 139.
[28] M. Carrion-Vazquez, A. F. Oberhauser, T. E. Fisher, P. E. Marszalek, H. Li, J. M. Fernandez, *Prog. Biophys. Mol. Biol.* **2000**, *74*, 63.
[29] D. J. Brockwell, E. Paci, R. C. Zinober, G. S. Beddard, P. D. Olmsted, D. A. Smith, R. N. Perham, S. E. Radford, *Nat. Struc. Biol.* **2003**, *10*, 872.
[30] Y. Bustanji, B. Samori, *Angew. Chem.* **2002**, *41*, 1616; *Angew. Chem. Int. Ed.* **2002**, *41*, 1546.
[31] H. Li, M. Carrion-Vazquez, A. F. Oberhauser, P. E. Marszalek, J. M. Fernandez, *Nat. Struct. Biol.* **2000**, *7*, 1117.
[32] M. Carrion-Vazquez, H. Li, H. Lu, P. E. Marszalek, A. F. Oberhauser, J. M. Fernandez, *Nat. Struct. Biol.* **2003**, *10*, 738.
[33] A. F. Oberhauser, C. Badilla-Fernandez, M. Carrion-Vazquez, J. M. Fernandez, *J. Mol. Biol.* **2002**, *319*, 433.
[34] J. R. Forman, S. Qamar, E. Paci, R. N. Sandford, J. Clarke, *J. Mol. Biol.* **2005**, *349*, 861.
[35] R. Schoenauer, P. Bertoncini, G. Machaidze, U. Aebi, J. C. Perriard, M. Hegner, I. Agarkova, *J. Mol. Biol.* **2005**, *349*, 367.
[36] A. M. Gronenborn, D. R. Filpula, N. Z. Essig, A. Achari, M. Whitlow, P. T. Wingfield, G. M. Clore, *Science* **1991**, *253*, 657.
[37] J. F. Marko, E. D. Siggia, *Macromolecules* **1995**, *28*, 8759.
[38] E. Evans, K. Ritchie, *Biophys. J.* **1997**, *72*, 1541.
[39] H. Li, A. F. Oberhauser, S. B. Fowler, J. Clarke, J. M. Fernandez, *Proc. Natl. Acad. Sci. USA* **2000**, *97*, 6527.
[40] G. I. Bell, *Science* **1978**, *200*, 618.
[41] E. L. McCallister, E. Alm, D. Baker, *Nat. Struct. Biol.* **2000**, *7*, 669.
[42] D. J. Brockwell, G. S. Beddard, E. Paci, D. K. West, P. D. Olmsted, D. A. Smith, S. E. Radford, *Biophys. J.* **2005**, *89*, 506.
[43] J. M. Fernandez, H. B. Li, *Science* **2004**, *303*, 1674.
[44] I. Schwaiger, M. Schleicher, A. A. Noegel, M. Rief, *EMBO Rep.* **2005**, *6*, 46.

 © 2006 Wiley-VCH Verlag GmbH & Co. KGaA, Weinheim

Supramolecular Chemistry

DOI: 10.1002/anie.200502294

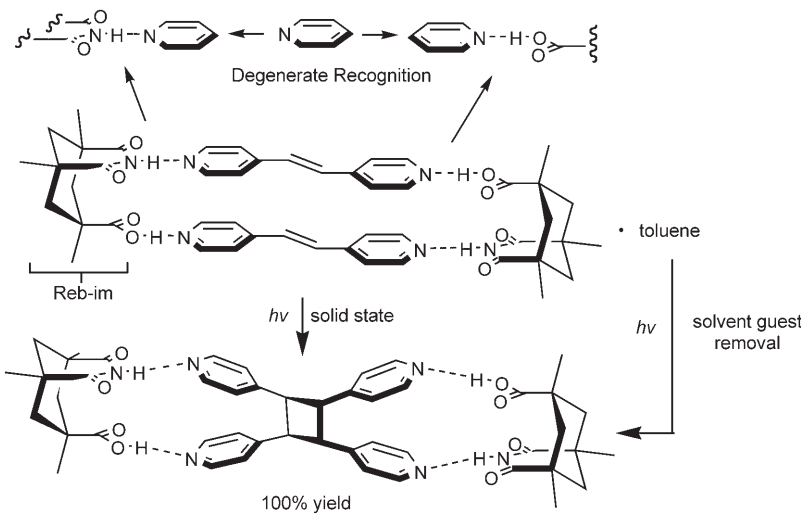
Heteroditopic Rebek's Imide Directs the Reactivity of Homoditopic Olefins within Desolvated Quaternary Assemblies in the Solid State**

*Dushyant B. Varshney, Xiuchun Gao, Tomislav Friščić, and Leonard R. MacGillivray**

Molecules with two different binding sites are important constructs in supramolecular chemistry.[1] Such heteroditopic molecules are designed, a priori, to assemble two different molecules and/or ions within ternary complexes, a process which is exploitable in areas such as separations,[2] nucleobase recognition,[3] and replication.[4] Whereas recent studies involving heteroditopic molecules have focused largely on the binding of ion pairs[2,5] and the programmed assembly of metallosupramolecular architectures,[6] the application of heteroditopic molecules as "artificial enzymes"[7] that direct the formation of covalent bonds[8] remains a worthy goal. Indeed, since the work of Kelly et al. that described a heteroditopic molecule that employed hydrogen bonds to orient two different molecules in solution for an S_N2 reaction,[9] advances have been made in our understanding of self-assembly such that complexes that transcend the ternary level are now viable targets in supramolecular syntheses[8] and may be used to direct the formation of covalent bonds.[8]

With this in mind, we report here the ability of a heteroditopic molecule, in the form of Rebek's imide (Reb-im),[11] to direct a solid-state reaction in which a covalent bond is formed (Scheme 1). Specifically, we reveal that Reb-im assembles two molecules of *trans*-1,2-bis(4-pyridyl)ethylene (4,4′-bpe) within a solvated quaternary complex, in **1**·toluene (where $\mathbf{1} = \{(\text{Reb-im})\cdot(4,4'\text{-bpe})\}_2$), which reacts through an intermolecular [2+2] photodimerization[12] and a rare single crystal to single crystal (SCSC) transformation[13] to give *rctt*-tetrakis(4-pyridyl)cyclobutane (4,4′-tpcb) stereospecifically in up to 100% yield. We demonstrate that Reb-im assembles two identical olefins with two identical recognition sites and, thus, exhibits a novel and unusual form of degeneracy[14] in its recognition abilities. We also provide evidence that supports the structures of such hydrogen-bonded complexes being remarkably robust, being able to operate in the wake of an induced desolvation and phase transition of the solid.[15,16] To our knowledge, Reb-im is the first example of a heteroditopic molecule that directs a chemical reaction in the solid state.[17–19]

Our choice of Reb-im as a heteroditopic molecule that directs a [2+2] photodimerization stems from the nature and positioning of the imide and carboxylic acid functionalities.[11] The two groups lie approximately parallel and separated by 3.5 Å—positions that conform to the geometry criteria of Schmidt for [2+2] photodimerization.[12] Moreover, studies involving the use of Reb-im to serve as a receptor in the solid state,[20] and reports on the ability of derivatives to act as photoreceptors in solution,[21] suggested that the two functionalities could act as hydrogen-bond donor sites that juxtapose two ditopic molecules with complementary acceptor sites in a quaternary complex for reaction in a solid.



Scheme 1.

To test our hypothesis, Reb-im was dissolved in toluene/tetrahydrofuran (60:40 v/v) by heating. A solution of 4,4′-bpe in tetrahydrofuran was added to the resulting solution. Colorless crystals of **1**·toluene suitable for X-ray analysis were obtained in 95% yield by slowly cooling the solution for approximately 6 h. The formulation of **1**·toluene was confirmed by ^{1}H NMR spectroscopy and IR spectroscopy, as well as powder and single-crystal X-ray diffraction data.

A single-crystal X-ray diffraction study of **1**·toluene reveals a quaternary complex, which sits around a crystallographic center of inversion, held together by N–H···N (N···N 2.84(1) Å) and O–H···N (O···N 2.59(1) Å) hydrogen bonds (Figure 1). In this arrangement, Reb-im juxtaposes two molecules of 4,4′-bpe such that the two C=C bonds lie parallel and separated by 3.78 Å (Figure 1a). This position is favorable for a [2+2] photodimerization.[12] The complexes self-

[*] D. B. Varshney, X. Gao, T. Friščić, Prof. L. R. MacGillivray
Department of Chemistry
University of Iowa
Iowa City, IA 52242-1294 (USA)
Fax: (+1) 319-335-1270
E-mail: len-macgillivray@uiowa.edu

[**] We are grateful to the National Science Foundation (CAREER Award, L.R.M., DMR-0133138) for funding. Acknowledgment is also made to the Research Corporation (Research Innovation Award) for financial support.

Supporting information for this article is available on the WWW under http://www.angewandte.org or from the author.

InterScience
© 2006 Wiley-VCH Verlag GmbH & Co. KGaA, Weinheim

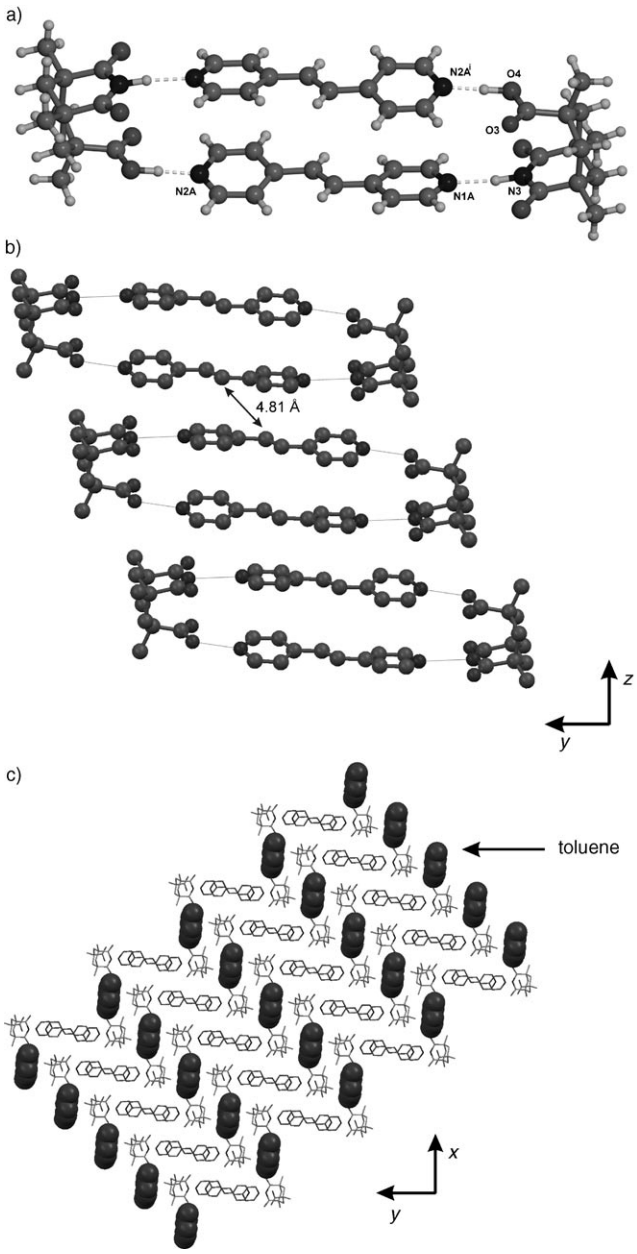


Figure 1. X-ray crystal structure of **1**: ball-and-stick views of a) the quaternary complex **1**, b) nearest-neighbor assemblies, and c) included solvent toluene (space filling model). Selected interatomic distances [Å]: N3···N1A 2.84(1), O4···N2A^{i} 2.59(1). Symmetry operator i: $-x-1$, $-y$, $-z+1$.

assemble along the crystallographic z-axis to form 1D columns with nearest-neighbor assemblies separated by 4.81 Å (Figure 1b). The columns lie offset and parallel to form layers segregated by the included solvent molecules (Figure 1c). This arrangement means that the olefin units of the quaternary complexes are the sole olefins of **1**·toluene organized for photoreaction.

The quaternary complexes of **1**·toluene are photoactive. Specifically, electron density that corresponds to 4,4′-tpcb (yield: 10%), the result of a [2+2] photodimerization between the two olefins of 4,4′-bpe, is observed. The reaction presumably occurred under ambient UV light. Moreover, irradiation of **1**·toluene with UV light (Hg lamp of Rayonet reactor, 350 nm) for approximately one hour produced 4,4′-tpcb in 100% yield, as confirmed by ^{1}H NMR spectroscopic analysis. Thermal gravimetric analysis revealed that the material lost 15% of the toluene solvent during the photoreaction. The loss of the solvent guest was accompanied by a partial loss of crystallinity, as indicated by X-ray powder diffraction analyses (Figure 2a→b).

The observation that **1**·toluene retained its crystallinity upon irradiation with UV light suggested that the reaction could proceed by a rare SCSC transformation.[13] To test this hypothesis, **1**·toluene was irradiated with light of wavelength 419 nm (Rayonet reactor)[13a] for a period of 15 h. Optical microscopy demonstrated that the crystals maintained their transparency. An X-ray diffraction analysis revealed that the photoreaction proceeded by a partial[13b] SCSC transformation (Figure 3). Specifically, 4,4′-tpcb was generated to a maximum of 24% during the transformation and the toluene molecules were retained in the channels. Similar to the reactants, the product interacts with Reb-im through N–H···N (N···N 2.94(1) Å) and O–H···N (O···N 2.75(1) Å) hydrogen bonds. Further irradiation of the solid with UV light for a period of eight days produced 4,4′-tpcb in 100% yield. During this time, the single crystals turned opaque, while 65% of the toluene was lost from the solid. The slow progress of the photoreaction can be attributed to low absorption of the UV light with a wavelength of 419 nm.[13a]

The observation that **1**·toluene maintained its reactivity upon loss of the solvent guest motivated us to determine whether the quaternary assemblies can operate upon removal, and therefore in the complete absence, of the guest.[15,16] Given the fragile nature of organic solids,[16] we anticipated that removal of the guest prior to the photoreaction would likely induce a phase transition or complete collapse of the structure. Such changes to structure, as a result

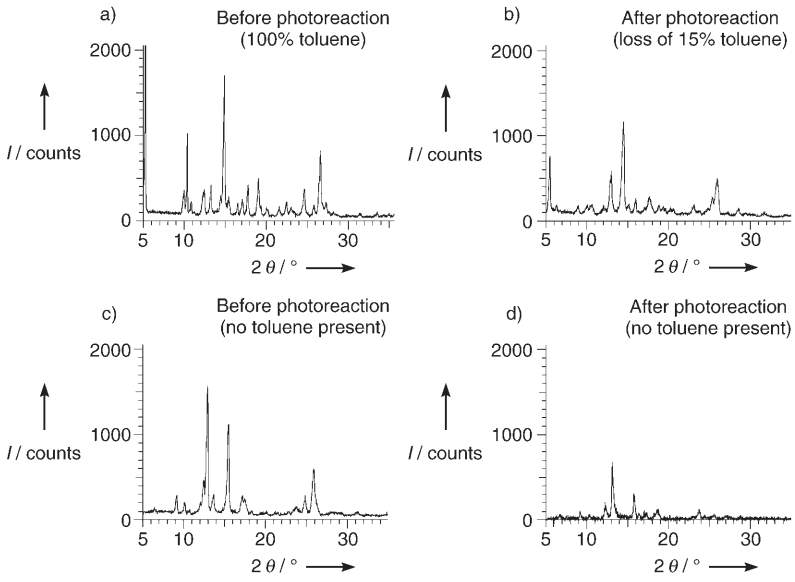


Figure 2. X-ray powder diffraction patterns of **1**·toluene: a) before photoreaction, b) after photoreaction (loss of 15% toluene), c) before photoreaction (no toluene present), and d) after photoreaction (no toluene present).

 © 2006 Wiley-VCH Verlag GmbH & Co. KGaA, Weinheim

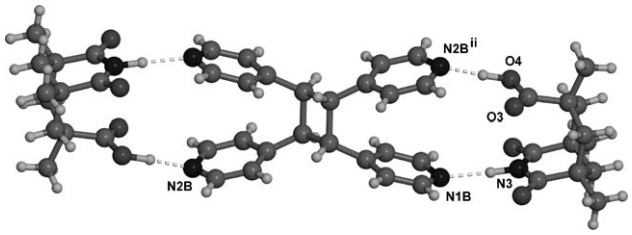


Figure 3. X-ray crystal structure of **1**·toluene (24% 4,4′-tpcb, SCSC): Selected interatomic distances [Å]: N3···N1B 2.90(1), O4···N2B^{ii} 2.65(1). Symmetry operator ii: $-x, -y-1, -z+1$.

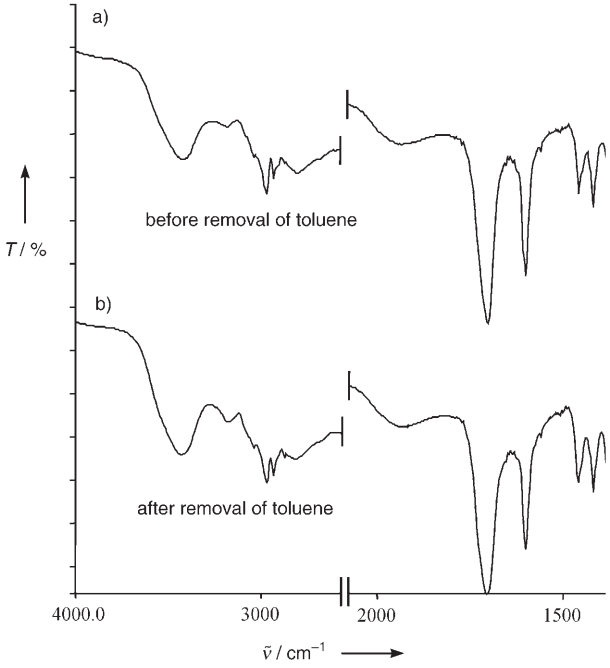
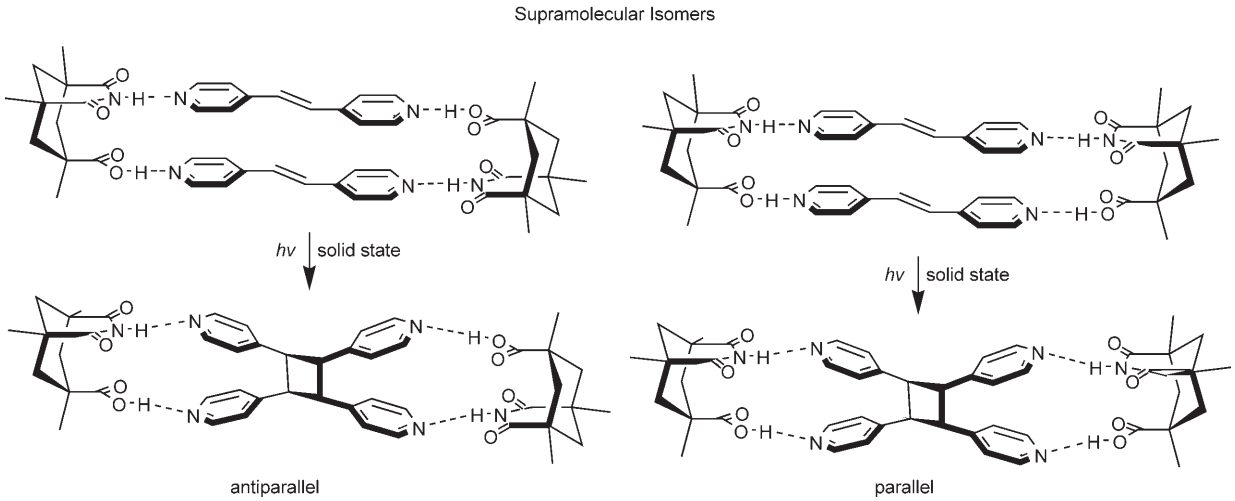


Figure 4. FTIR spectra of the hydrogen-bonding region of **1**·toluene (O–H···N, N–H···N 3100–3600 cm^{-1}; C=O 1600–1750 cm^{-1}): a) in the presence of toluene and b) upon complete removal of toluene.

of the relative weakness of hydrogen bonds, could destroy the self-assembled complexes and thereby render the components of the solid photostable. Thus, **1**·toluene was heated at 90 °C in a vacuum for a period of 10 h.[22] A ^{1}H NMR spectrum indicated that the toluene was completely liberated from the solid. Unsurprisingly, the desolvation induced a phase transition and partial loss of crystallinity (Figure 2a→c).[16] The FTIR spectra of the solid, however, revealed the hydrogen bonding to be the same before and after the phase transition (Figure 4).[23] This observation supports the structures of the quaternary complexes being maintained during removal of the solvent guest and phase transition of the solid. Moreover, irradiation of the desolvated solid with UV light produced 4,4′-tpcb in 100% yield, as confirmed by ^{1}H NMR spectroscopic analysis. An X-ray powder diffraction analysis of the fully reacted solid (Figure 2c→d) demonstrated a further loss of crystallinity, as evidenced by the diffraction pattern exhibiting further line broadening. The fact that 4,4′-tpcb was generated following the phase transition is indicative of the structures of the self-assembled complexes being remarkably robust[16] and suggests that such hydrogen-bonded assemblies may be developed to operate in less organized media (for example, amorphous solids).[24]

The degeneracy[14] of the recognition properties of Reb-im in **1**·toluene is unusual and can be considered counterintuitive.[25] Heteroditopic molecules are designed to bind two different guests, which means the ability of such molecules to bind two identical guests has remained virtually unexplored.[1–6] In the case of **1**·toluene, the quaternary nature of the complex, coupled with the degeneracy of the recognition, presents an opportunity for the self-assembly process to exhibit a unique form of supramolecular isomerism[26] in which Reb-im is oriented either antiparallel or parallel in the complex and solid (Scheme 2). Reb-im is oriented antiparallel in **1**·toluene.[27] The same photoproduct, however, would be expected to form in each solid.

In this study, we identified a role of heteroditopic molecules, in the form of Reb-im, to direct a [2+2] photodimerization within a hydrogen-bonded quaternary complex in the solid state. The reaction proceeded by a SCSC reaction[13] in which the complexes operate upon an induced desolvation and phase transition of the solid. We are now investigating the behavior of Reb-im with other olefins and in



Scheme 2.

 © 2006 Wiley-VCH Verlag GmbH & Co. KGaA, Weinheim

the presence of additional guests. We are also studying such unsymmetrical environments to control the reactivity of two different olefins, where such reactivity may be achieved in amorphous phases,[24] as well as solution.

Experimental Section

Preparation of cocrystals of **1**·toluene: Reb-im was prepared according to the literature.[28] 4,4′-Bpe was commercially available (Aldrich Co.). Reb-im (15 mg) was dissolved in toluene and tetrahydrofuran (3 mL, 60:40 v/v) by heating at 40–50 °C for 2–3 mins. A clear solution of 4,4′-bpe (22 mg) in tetrahydrofuran (0.5 mL) was added to this solution, and stirred for 1 min. Colorless crystals of **1**·toluene suitable for single-crystal X-ray analysis were obtained in 95% yield upon slow cooling of the solution over approximately 6 h.

Solid-state photodimerizations: The UV-irradiation experiments were performed by placing either single crystals or finely ground samples of **1**·toluene between two pyrex plates and turning the sample to ensure uniform irradiation.

^{1}H NMR spectra of **1**·toluene (300 MHz, [D$_6$]DMSO): before UV irradiation: $\delta = 12.17$ (br s, 1H), 10.33 (s, 1H), 8.60 (dd, 4H), 7.60 (dd, 4H), 7.54 (s, 2H), 7.20 (m, 5H), 2.38 (d, 1H), 2.29 (s, 3H), 1.89 (br d, 1H), 1.37 (d, 1H), 1.14 ppm (d, 12H); after UV irradiation (100% yield of 4,4′-tpcb): $\delta = 12.17$ (br s, 1H) 10.33 (s, 1H), 8.34 (dd, 4H), 7.18 (dd, 4H), 7.20 (m, 5H), 4.65 (s, 2H), 2.38 (d,1H), 2.29 (s, 3H), 1.89 (br d, 1H), 1.37 (d, 1H), 1.14 ppm (d, 12H).

X-ray crystallography: Crystal data for **1**·toluene: triclinic, space group $P\bar{1}$, $a = 8.003(1)$, $b = 9.093(1)$, $c = 17.061(2)$ Å, $\alpha = 94.33(1)$, $\beta = 89.93(1)$, $\gamma = 101.95(1)°$, $V = 1210.9(2)$ Å^3, $\rho_{calcd} = 1.28$ g cm^{-1} for $Z = 1$ and $R = 0.059$. Crystal data for **1**·toluene(SCSC): triclinic, space group $P\bar{1}$, $a = 7.974(1)$, $b = 9.115(1)$, $c = 17.088(2)$ Å, $\alpha = 94.39(1)$, $\beta = 89.60(1)$, $\gamma = 101.97(1)°$, $V = 1211.4(1)$ Å^3, $\rho_{calcd} = 1.28$ g cm^{-1} for $Z = 1$ and $R = 0.056$. Mo$_{K\alpha}$ radiation ($\lambda = 0.71070$ Å). All crystal data were measured on a Nonius Kappa CCD single-crystal X-ray diffractometer at liquid-nitrogen temperature. After anisotropic refinement of all non-hydrogen atoms, the aromatic, methylene, and methyl hydrogen atoms were placed in idealized positions and allowed to ride on the atom to which they are attached. All hydroxy and imide hydrogen atoms were located from the final Fourier difference electron density map and refined according to the riding isotropic model. The 4,4′-bpe units of **1**·toluene and **1**·toluene(SCSC) were found disordered with 4,4′-tpcb. The occupational parameters for 4,4′-bpe and 4,4′-tpcb in **1**·toluene and **1**·toluene(SCSC) were determined to be 0.90 and 0.10, and 0.76 and 0.24, respectively. The toluene solvent molecule was found to be disordered over two positions (relative occupancies 0.50/0.50) in each solid. The non-hydrogen atoms of the six-membered ring based on N2B in **1**·toluene(SCSC) was refined with a model based on N1A, with the atoms being forced into planarity (average deviation 0.025 Å). All crystallographic calculations were conducted using SHELXL-97[29] locally implemented on an IBM-compatible pentium-based PC. CCDC-263613 (**1**·toluene) and CCDC-263614 (**1**·toluene-(SCSC)) contain the supplementary crystallographic data for this paper. These data can be obtained free of charge from The Cambridge Crystallographic Data Centre via www.ccdc.cam.ac.uk/data_request/cif.

Received: June 30, 2005
Published online: December 19, 2005

Keywords: cycloaddition · receptors · self-assembly · solid-state reactions · topochemistry

[1] a) J.-M Lehn, *Supramolecular Chemistry*, VCH, Weinheim, **1995**; b) J. W. Steed, J. L. Atwood, *Supramolecular Chemistry*, Wiley, Chichester, **2000**.

[2] a) P. A. Gale, *Coord. Chem. Rev.* **2003**, *240*, 191; b) P. D. Beer, P. A. Gale, *Angew. Chem.* **2001**, *113*, 502; *Angew. Chem. Int. Ed.* **2001**, *40*, 486; c) G. Tumcharern, T. Tuntulani, S. J. Coles, M. B. Hursthouse, J. D. Kilburn, *Org. Lett.* **2003**, *5*, 4971.

[3] a) J. L. Sessler, J. Jayawickramarajah, *Chem. Commun.* **2005**, 1939; b) S. Sivakova, S. J. Rowan, *Chem. Soc. Rev.* **2005**, *34*, 9.

[4] D. H. Lee, J. R. Granja, J. A. Martinez, K. Severin, M. R. Ghadri, *Nature* **1996**, *382*, 525.

[5] a) J. M. Mahoney, J. P. Davis, A. M. Beatty, B. D. Smith, *J. Org. Chem.* **2003**, *68*, 9819; b) J. M. Mahoney, A. M. Beatty, B. D. Smith, *J. Am. Chem. Soc.* **2001**, *123*, 5847.

[6] C. J. Baylies, L. P. Harding, J. C. Jeffrey, T. Riis-Johannessen, C. R. Rice, *Angew. Chem.* **2004**, *116*, 4615; *Angew. Chem. Int. Ed.* **2004**, *43*, 4515.

[7] F. Diederich, P. J. Stang in *Templated Organic Synthesis*, Wiley-VCH, Weinheim, **2000**.

[8] M. C. T. Fyfe, J. F. Stoddart, *Acc. Chem. Res.* **1997**, *30*, 393.

[9] T. R. Kelly, G. J. Bridger, C. Zhao, *J. Am. Chem. Soc.* **1990**, *112*, 8024.

[10] a) D. Philp, J. F. Stoddart, *Angew. Chem.* **1996**, *108*, 1242; *Angew. Chem. Int. Ed. Engl.* **1996**, *35*, 1155; b) S. J. Rowan, S. J. Cantrill, G. R. L. Cousins, J. K. M. Sanders, J. F. Stoddart, *Angew. Chem.* **2002**, *114*, 1528; *Angew. Chem. Int. Ed.* **2002**, *41*, 898–952; c) J. S. Lindsey, *New J. Chem.* **1991**, *15*, 153.

[11] a) J. Rebek, Jr., *Angew. Chem.* **1990**, *102*, 261; *Angew. Chem. Int. Ed. Engl.* **1990**, *29*, 245; b) J. Rebek, Jr., *Acc. Chem. Res.* **1990**, *23*, 399.

[12] G. M. J. Schmidt, *Pure Appl. Chem.* **1971**, *43*, 647.

[13] a) V. Enkelmann, G. Wegner, K. Novak, K. B. Wagener, *J. Am. Chem. Soc.* **1993**, *115*, 10390; b) T. Friščić, L. R. MacGillivray, *Z. Kristallogr.* **2005**, *220*, 351.

[14] S. White, E. E. Baird, P. B. Dervan, *Biochemistry* **1996**, *35*, 12532.

[15] For a discussion on solvent incorporation in solid-state reactions, see: "Photochemical Solid-to-Solid Reactions": A. E. Keating, M. A. Garcia-Garibay in *Molecular and Supramolecular Photochemistry, Vol. 2* (Eds.: V. Ramamurthy, K. Schanze), Marcel Dekker, New York, **1998**.

[16] a) L. R. Nassimbeni, *Acc. Chem. Res.* **2003**, *36*, 631; b) J. L. Atwood, L. J. Barbour, A. Jerga, B. L. Schottel, *Science* **2002**, *298*, 1000.

[17] D. Braga, F. Grepioni, *Angew. Chem.* **2004**, *116*, 4092; *Angew. Chem. Int. Ed.* **2004**, *43*, 4002.

[18] For recent studies to direct the [2+2] photodimerization in the solid state using organic molecules, see: a) A. Natarajan, J. T. Mague, K. Venkatesan, V. Ramamurthy, *Org. Lett.* **2005**, *7*, 1895; b) S. Hirano, S. Toyota, F. Toda, *Chem. Commun.* **2005**, 634; c) T. Caronna, R. Liantonio, T. A. Logothetis, P. Metrangolo, T. Pilati, G. Resnati, *J. Am. Chem. Soc.* **2004**, *126*, 4500; d) X. Gao, T. Friščić, L. R. MacGillivray, *Angew. Chem.* **2003**, *115*, 234; *Angew. Chem. Int. Ed.* **2004**, *43*, 232; e) N. Shan, W. Jones, *Tetrahedron Lett.* **2003**, *44*, 3687; f) D. G. Amirakis, M. A. Garcia-Garibay, S. J. Rowan, J. F. Stoddart, A. J. P. White, D. J. Williams, *Angew. Chem.* **2001**, *113*, 4386; *Angew. Chem. Int. Ed.* **2001**, *40*, 4256; g) L. R. MacGillivray, J. L. Reid, J. A. Ripmeester, *J. Am. Chem. Soc.* **2000**, *122*, 7817; h) Y. Ito, B. Borecka, J. Trotter, J. R. Scheffer, *Tetrahedron Lett.* **1995**, *36*, 6083.

[19] For recent studies to direct the [2+2] photodimerization in the solid state using metal ions, see: a) Q. Chu, D. C. Swenson, L. R. MacGillivray, *Angew. Chem.* **2005**, *117*, 3635; *Angew. Chem. Int. Ed.* **2005**, *44*, 3569; b) N. L. Toh, M. Nagarathinam, J. J. Vittal, *Angew. Chem.* **2005**, *117*, 2277; *Angew. Chem. Int. Ed.* **2005**, *44*, 2237; c) G. S. Papaefstathiou, Z. Zhong, L. Geng, L. R. MacGillivray, *J. Am. Chem. Soc.* **2004**, *126*, 9158.

[20] a) R. Faraoni, R. K. Castellano, V. Gramlich, F. Diederich, *Chem. Commun.* **2004**, 370; b) R. K. Castellano, V. Gramlich, F.

 © 2006 Wiley-VCH Verlag GmbH & Co. KGaA, Weinheim

Diederich, *Chem. Eur. J.* **2002**, *8*, 118; c) R. A. Pascal, Jr., D. M. Ho, *J. Am. Chem. Soc.* **1993**, *115*, 8507.
[21] a) T. Bach, H. Bergmann, K. Harms, *Org. Lett.* **2001**, *3*, 601; b) K. Mori, O. Murai, S. Hashimoto, Y. Nakamura, *Tetrahedron Lett.* **1996**, *37*, 8523.
[22] These conditions can be considered harsh for an organic solid (see Ref. [16a]).
[23] The FTIR spectrum is consistent with the imide and carboxylic acid groups of **1** participating in intermolecular hydrogen bonding. Band assignments: C=O: 1703 cm^{-1} and 1602 cm^{-1}; O-H and N-H (overlap): 3423 cm^{-1} (see: a) R. A. Nyquist, S. L. Fiedler, *Vib. Spectrosc.* **1995**, *8*, 365; b) R. Langner, G. Zundel, *J. Chem. Soc. Faraday Trans.* **1995**, *91*, 3831).
[24] Y. Guo, S. R. Byrn, G. J. Zografi, *Pharm. Pharmacol. Commun.* **2000**, *89*, 128.
[25] For a symmetrical molecule that organizes two different substrates, see: T. R. Kelly, C. Zhao, G. J. Bridger, *J. Am. Chem. Soc.* **1989**, *111*, 3744.
[26] B. Moulton, M. J. Zaworotko, *Chem. Rev.* **2001**, *101*, 1629.
[27] The antiparallel orientation is consistent with the tendency of organic molecules to form centrosymmetric solids, see: G. R. Desiraju in *Crystal Engineering: The Design of Organic Solids*, Elsevier, Amsterdam, **1989**.
[28] J. G. Stack, D. P. Curran, S. V. Geib, J. Rebek, Jr., P. Ballester, *J. Am. Chem. Soc.* **1992**, *114*, 7007.
[29] G. M. Sheldrick, SHELXL-97, Program for Refinement of Crystal Structure, University of Göttingen, Göttingen, Germany, **1997**.

 © 2006 Wiley-VCH Verlag GmbH & Co. KGaA, Weinheim

Liquid Crystals

DOI: 10.1002/anie.200502911

Ordered Nanostructures from the Self-Assembly of Reactive Coil–Rod–Coil Molecules**

*Long Yi Jin, Jinyoung Bae, Ja-Hyoung Ryu, and Myongsoo Lee**

One of the most important challenges in the areas of nanomaterials and biomimetic chemistry is to construct supramolecular structures with well-defined shape and size by the self-assembly of programmed molecules.[1] Control of the supramolecular structure of self-assembling molecules and subsequent cross-linking of specific segments within the organized structure are an efficient way to produce robust organic nanomaterials while maintaining the precise size and shape of the self-assembled nanostructure.[2] Rod-shaped molecules containing flexible chains have been shown to self-assemble into a large variety of supramolecular structures, which include 3D bicontinuous cubic and 2D columnar structures.[3] To enhance the structural robustness of the self-assembled nanoarchitectures, we designed a coil–rod–coil molecule that contains polymerizable vinyl groups in the middle of the rod segment. Herein, we describe the self-assembling behavior of the coil–rod–coil molecule, **1** (Figure 1), which bears reactive divinyl groups in the center of the rod block, and the subsequent polymerization of **1** from an ordered state.

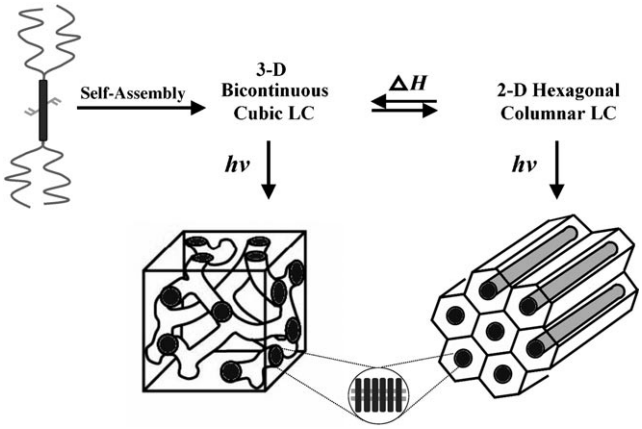


Figure 1. Schematic representation of liquid crystalline phases of **1** and subsequent polymerization to yield ordered nanostructures.

The triblock molecule, **1**, consisting of five biphenyl units linked through benzyl ether linkages and bis(pentaethylene glycol) dendrons as coil segments at both ends of the rod, was synthesized by etherification of penta(ethylene glycol) monomethyl ether and 4,4′-biphenol, and the resulting product was subsequently treated with excess 4,4′-bis(bromomethyl)biphenyl to obtain a white waxy solid, **1c** (Scheme 1). Simple etherification of **1c** with 2,2′-divinyl-4,4′-biphenol in the presence of K_2CO_3 afforded **1**. The final product was characterized by ^{1}H NMR and ^{13}C NMR spectroscopy and by elemental analysis. The results were in full agreement with the structure presented in Scheme 1.

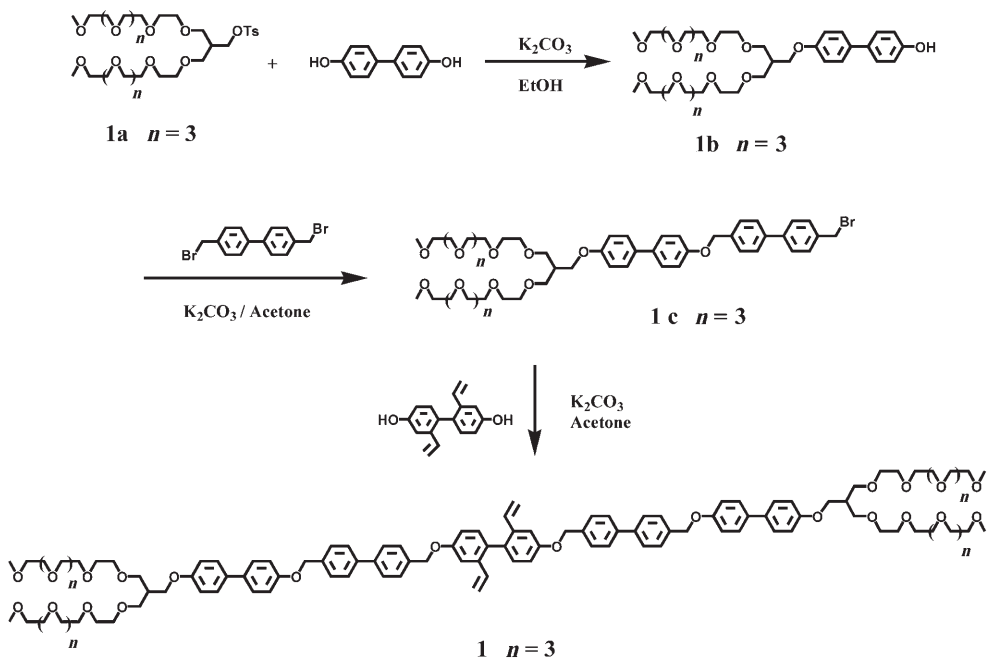
The mesophase structure of **1** was investigated by differential scanning calorimetry (DSC), thermal optical polarized microscopy, and small-angle X-ray scattering (SAXS). On heating, **1** melts into a liquid crystalline phase at 83 °C and then converts into a second liquid crystalline phase which, in turn, undergoes isotropization at 99.5 °C (Figure 2). On slow cooling from the isotropic liquid phase, first a spherulitic texture is observed and finally pseudofocal conic domains develop, which is characteristic of a hexagonal columnar mesophase. On further cooling from the hexagonal columnar

[*] Dr. L. Y. Jin,[+] J. Bae, J.-H. Ryu, Prof. M. Lee
Center for Supramolecular Nano-Assembly and Department of Chemistry
Yonsei University
Shinchon 134, Seoul 120-749 (Korea)
Fax: (+82) 2-393-6096
E-mail: mslee@yonsei.ac.kr
[+] Permanent address: Department of Chemistry
College of Science and Engineering
Yanbian University, Yanji, 133002 (China)

[**] This work was supported by the Creative Research Initiative Program of the Ministry of Science and Technology, Korea, and Pohang Accelerator Laboratory, Korea (for using synchrotron radiation). J.B. thanks the Seoul Science Fellowship Program

Supporting information for this article is available on the WWW under http://www.angewandte.org or from the author.

InterScience
© 2006 Wiley-VCH Verlag GmbH & Co. KGaA, Weinheim



Scheme 1. Synthesis of **1**.

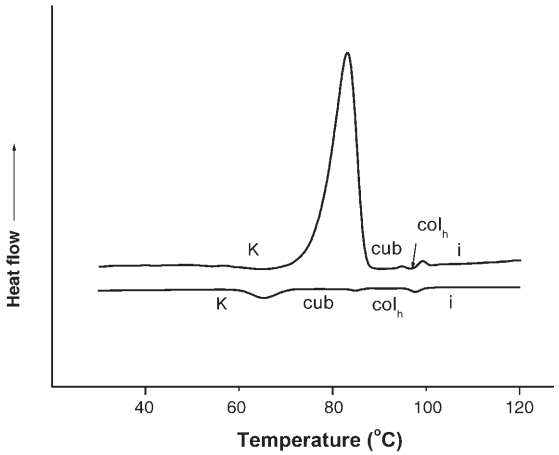


Figure 2. DSC traces of **1** recorded during the heating and cooling scans (K = crystalline, cub = cubic, col$_h$ = hexagonal columnar, i = isotropic phase.

phase, the birefringent texture disappears completely, thus indicating the presence of a cubic mesophase (see Supporting Information).[4] When **1** is in the optically isotropic liquid crystalline phase, the corresponding small-angle X-ray diffraction patterns show a number of sharp reflections (Figure 3a), which can be indexed as a bicontinuous cubic order ($Ia\bar{3}d$ symmetry) with a lattice constant $a = 16.5$ nm.[3b,5] At a wide angle, only a diffuse halo remains as evidence of the lack of any positional long-range order other than the 3D cubic packing of supramolecular units (see Supporting Information). In the birefringent liquid crystalline phase at higher temperature, the SAXS patterns show three sharp reflections that can be assigned as the (10), (11), and (20) reflections of a hexagonal columnar structure with a lattice constant $a =$ 7.4 nm (Figure 3c).[3] These results, together with optical microscopic observations, indicate that **1** exhibits its 3D bicontinuous cubic and hexagonal columnar liquid crystalline phases.

The polymerization of **1** in the liquid crystalline state provides a strategy for constructing well-defined nano-objects if the polymerization proceeds with retention of a liquid crystalline structure. To demonstrate this concept, the photopolymerization of **1** was performed at various liquid crystalline states, with 2,2-dimethoxy-2-phenylacetophenone being used as a photoinitiator. After photopolymerization in each

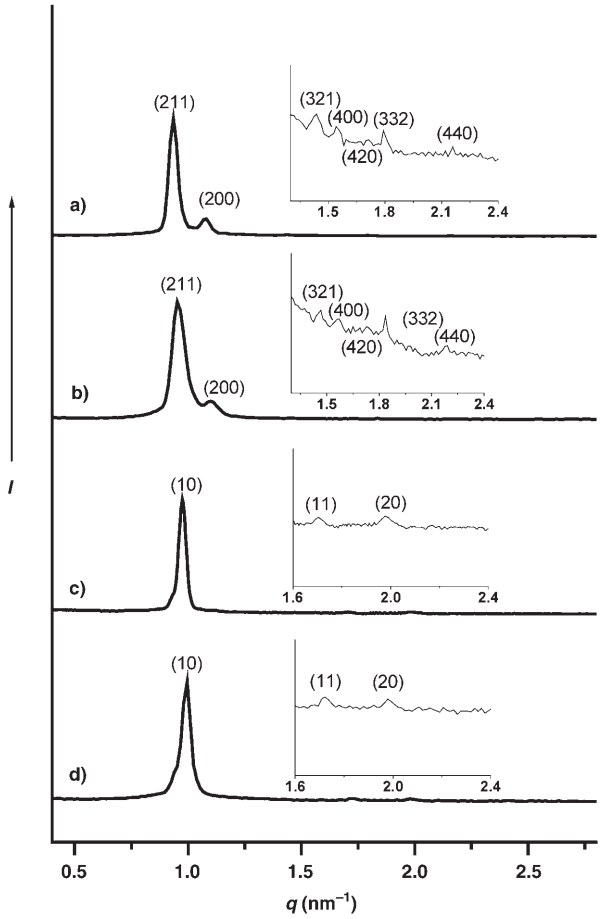


Figure 3. Representative SAXS spectra: a) bicontinuous cubic structure of **1**; b) bicontinuous cubic structure after polymerization at 85 °C; c) hexagonal columnar structure of **1**; d) hexagonal columnar structure after polymerization at 97 °C.

 © 2006 Wiley-VCH Verlag GmbH & Co. KGaA, Weinheim

liquid crystalline phase, FTIR spectroscopy clearly showed that the peaks assigned to the out-of-plane bending band of C–H in the vinyl group at 919 and C=C band at 1640 cm^{-1} were strongly suppressed, which is indicative of extensive polymerization (see Supporting Information).[6] The SAXS pattern of the sample after polymerization at 85 °C shows the same reflections as those of the bicontinuous cubic liquid crystalline structure of **1**. This result is consistent with the preservation of the 3D bicontinuous cubic structure upon polymerization. To corroborate the detailed nanostructures, TEM experiments were performed with the polymerized samples. The TEM images of an ultra-microtomed thin film of the samples (stained with RuO_4) polymerized in the bicontinuous cubic liquid crystalline phase showed tetragonal and hexagonal arrays of dark rod domains in a light coil matrix along the $[01\bar{1}]$ and $[\bar{1}11]$ directions, respectively, which is characteristic of a 3D bicontinuous cubic structure.[7] The lattice constant, calculated to be 16 nm, is in agreement with the value estimated from the SAXS data (Figure 4a, b). Bulk

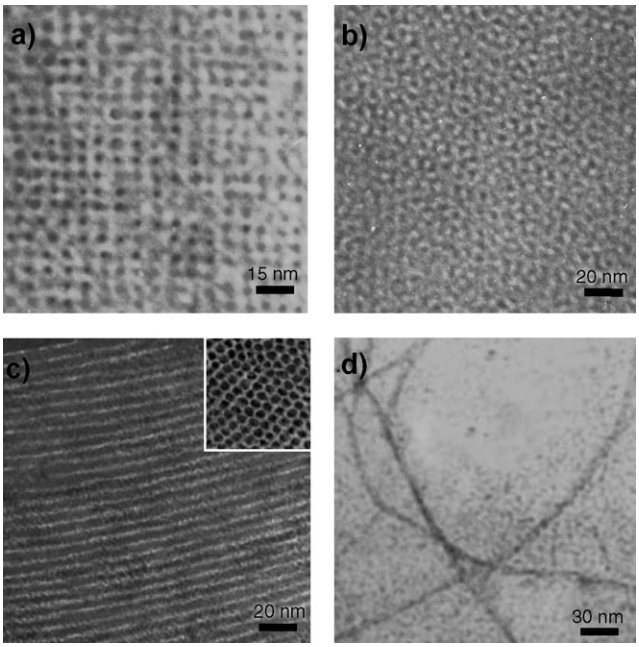


Figure 4. a,b) TEM images of an ultra-microtomed thin film of the sample polymerized in the optically isotropic mesophase stained with RuO_4, which exhibit an ordered array of tetragonal and hexagonal dark rod domains in a light coil matrix along the $[01\bar{1}]$ (a) and $[\bar{1}11]$ directions (b); c) an ultra-microtomed thin film of the sample polymerized in the birefringent mesophase stained with RuO_4, which reveals alternating dark rod layers and light coil layers; the inset shows an in-plane hexagonally ordered array of dark rods in a coil matrix; d) dispersed nanofibers in aqueous solution (stained with RuO_4).

polymerization of **1** at 97 °C also proceeded with retention of the hexagonal columnar liquid crystalline structure, as confirmed by SAXS and TEM (Figure 3b and d). The SAXS pattern showed reflections similar to those of hexagonal columnar mesophase with a small lattice contraction (from 7.4 nm to 7.3 nm) as a consequence of the stitching together of rod segments. This result indicates that polymerization takes place with retention of the 2D liquid crystalline structure. The TEM images stained with RuO_4 showed a hexagonal array of dark aromatic domains in a matrix of light polyethylene oxide chains as well as views in the direction of the column. The interdomain distance appears to be approximately 7 nm, which is consistent with that obtained from the SAXS data (Figure 4c). Interestingly, when the hexagonal columnar structure was sonicated in water for several hours, the solid dispersed into individual nanofibers (Figure 4d). Thus, polymerization takes place only within the cylindrical cores. Bulk polymerization in the hexagonal columnar state gives rise to well-defined nanofibers with a uniform diameter. It should be noted that the wide-angle X-ray scatterings (WAXS) after polymerization in each liquid crystalline state showed that the reflection corresponding to 0.47 nm shifts to a slightly higher angle (0.45 nm), thus indicating that polymerization occurs with only a small degree of shrinkage. This shift is consistent with the results of very small lattice constant reductions in SAXS patterns (see Supporting Information).

Recently, there have been many reports of Suzuki couplings in water,[8a] and we have demonstrated that self-assembled aromatic rod bundles encapsulated by hydrophilic chains can be used as an efficient nanoreactor for Suzuki coupling reactions.[8b] This result motivated us to investigate whether our nanofibers are suitable to use as nanoreactors in aqueous solution because the nanofibers consist of an aromatic core surrounded by hydrophilic chains. To investigate the capability of the nanofibers as a reactor, we have performed the Suzuki coupling reaction with phenyl boronic acid and bromoanisole in the presence of the nanofibers in aqueous solution at room temperature. Remarkably, the reaction conversions were almost quantitative. This reactivity demonstrates that the nanofibers are highly efficient nanoreactors (Table 1). Owing to their covalently fixed characteristics, nanofibers can be easily recycled for use in further reactions by filtering the mixture and washing the nanofibers with ethyl acetate. As shown in Table 1, the nanofibers can be used up to four times and still maintain activity. The aqueous Suzuki coupling reactions in the presence of the nanofibers take place within the aromatic cores of the nanofibers at room temperature as these cores are able to entrap solvophobic aromatic reactants through intermolecular interactions, including hydrophobic interactions and π–π interactions. This entrapment leads to a highly concentrated reaction site that lowers the energy barrier for the coupling reaction. The confinement of the aromatic substrates within the aromatic

Table 1: Suzuki cross-coupling reaction of phenyl boronic acid and bromoanisole in a nanofiber nanoreactor.[a]

Cycle	First	Second	Third	Fourth
yield [%][b]	95	94	93	93

[a] The reaction was carried out in water at room temperature. Reaction conditions: bromoanisole (0.1 mmol), phenyl boronic acid (0.12 mmol), $Pd(OAc)_2$ (0.5 mol%), $P(Ph)_3$ (1.0 mol%), NaOH (0.2 mmol), nanofiber (0.025 mmol), H_2O (10 mL), stirring at room temperature for 12 h. [b] Percent yields are calculated on the basis of GC analysis with xylene used as the internal standard.

 © 2006 Wiley-VCH Verlag GmbH & Co. KGaA, Weinheim

cores of the nanofibers was confirmed by using fluorescence spectroscopy on aryl halides, boronic acids, and triphenylphosphine (see Supporting Information). Upon addition of the aromatic substrates, the fluorescence intensities of the nanofiber solutions were suppressed, thus demonstrating that they are effectively entrapped within the aromatic bundle of the nanofibers.[8]

In summary, we have synthesized a polymerizable coil–rod–coil molecule, which self-organizes into 2D columnar and 3D bicontinuous cubic structures at the liquid crystalline state. Photopolymerizations of **1** in liquid crystalline state proceeds with preservation of the ordered supramolecular architectures and maintenance of the lattice dimensions. Photopolymerization of **1** in the bicontinuous cubic liquid crystalline state gives rise to a 3D ordered nanostructure, while in the hexagonal columnar liquid crystalline state it produces a 2D ordered nanostructure that in aqueous solution can be dispersed into individual nanofibers with a uniform diameter. The remarkable feature of these nanofibers, which have aromatic cores, is their ability to be used as recyclable nanoreactors for room-temperature Suzuki coupling reactions in aqueous solution. The covalent stitching of reactive rod segments within the ordered state by photopolymerization offers a strategy to construct shape-persistent organic nanomaterials with well-defined size and shape, which potentially have applications in macromolecular electronics, nanoreactors, and hybrid nanomaterials.

Received: August 16, 2005
Revised: October 24, 2005
Published online: December 15, 2005

Keywords: liquid crystals · nanotechnology · polymers · supramolecular chemistry · Suzuki coupling

[1] a) T. Shimizu, M. Masuda, H. Minamikawa, *Chem. Rev.* **2005**, *105*, 1401 – 1444; b) F. J. M. Hoeben, P. Jonkheijm, E. W. Meijer, A. P. H. J. Schenning, *Chem. Rev.* **2005**, *105*, 1491 – 1546; c) M. Lee, B.-K. Cho, W.-C. Zin, *Chem. Rev.* **2001**, *101*, 3869 – 3892.

[2] a) E. R. Zubarev, M. U. Pralle, L. Li, S. I. Stupp, *Science* **1999**, *283*, 523 – 526; b) Y.-Y. Won, H. T. Davis, F. S. Bates, *Science* **1999**, *283*, 960 – 963; c) W. Jin, T. Fukushima, A. Kosaka, M. Niki, N. Ishii, T. Aida, *J. Am. Chem. Soc.* **2005**, *127*, 8284 – 8285; d) L. Y. Jin, J.-H. Ahn, M. Lee, *J. Am. Chem. Soc.* **2004**, *126*, 12208 – 12209; e) B. A. Pindzola, J. Jin, D. L. Gin, *J. Am. Chem. Soc.* **2003**, *125*, 2940 – 2949; f) A. Müller, D. F. O'Brien, *Chem. Rev.* **2002**, *102*, 727 – 758.

[3] a) M. Lee, B.-K. Cho, H. Kim, W.-C. Zin, *Angew. Chem.* **1998**, *110*, 661 – 663; *Angew. Chem. Int. Ed.* **1998**, *37*, 638 – 640; b) M. Lee, B.-K. Cho, Y.-G. Jang, W.-C. Zin, *J. Am. Chem. Soc.* **2000**, *122*, 7449 – 7455; c) B.-K. Cho, M. Lee, N.-K. Oh, W.-C. Zin, *J. Am. Chem. Soc.* **2001**, *123*, 9677 – 9678; d) M. Lee, B.-K. Cho, H. Kim, J.-Y. Yoon, W. C. Zin, *J. Am. Chem. Soc.* **1998**, *120*, 9168 – 9179; e) L. Y. Jin, J. Bae, J.-H. Ahn, M. Lee, *Chem. Commun.* **2005**, *9*, 1197 – 1199.

[4] a) D. Demus, L. Richter, *Texture of Liquid Crystals*, Verlag Chemie, Weinheim, **1978**; b) G. W. Gray, J. W. Goodby, *Smectic Liquid Crystals. Textures and Structures*, Leonard Hill, Glasgow, **1984**; c) K. Borisch, S. Diele, P. Göring, H. Kresse, C. Tschierske, *J. Mater. Chem.* **1998**, *8*, 529 – 543.

[5] a) A. K. Khandpur, S. Förster, F. S. Bates, I. W. Hamley, A. J. Ryan, W. Bras, K. Almdal, K. Mortensen, *Macromolecules* **1995**, *28*, 8796 – 8806; b) B.-K. Cho, A. Jain, S. M. Gruner, U. Wiesner, *Science* **2004**, *305*, 1598 – 1601.

[6] Y. Li, Y. Fan, J. Ma, *Polym. Degrad. Stab.* **2001**, *73*, 163 – 167.

[7] a) V. Z.-H. Chan, J. Hoffman, V. Y. Lee, H. Iatrou, A. Avgeropoulos, N. Hadjichristidis, R. D. Miller, E. L. Thomas, *Science* **1999**, *286*, 1716 – 1719; b) C. Yu, Y. Yu, D. Zhao, *Chem. Commun.* **2000**, *7*, 575 – 576; c) R. C. Hayward, P. C. A. Alberius, E. J. Kramer, B. F. Chmelka, *Langmuir* **2004**, *20*, 5998 – 6004.

[8] a) N. E. Leadbeater, M. Marco, *Angew. Chem.* **2003**, *115*, 1445 – 1447; *Angew. Chem. Int. Ed.* **2003**, *42*, 1407 – 1409; b) M. Lee, C.-J. Jang, J.-H. Ryu, *J. Am. Chem. Soc.* **2004**, *126*, 8082 – 8083.

 © 2006 Wiley-VCH Verlag GmbH & Co. KGaA, Weinheim

Enzyme Engineering

DOI: 10.1002/anie.200503025

Computational Design of a Human Butyrylcholinesterase Mutant for Accelerating Cocaine Hydrolysis Based on the Transition-State Simulation**

*Daquan Gao, Hoon Cho, Wenchao Yang, Yongmei Pan, Guangfu Yang, Hsin-Hsiung Tai, and Chang-Guo Zhan**

Cocaine is recognized as the most reinforcing of all drugs of abuse.[1–3] There is no available anticocaine medication. The disastrous medical and social consequences of cocaine addiction have made the development of an effective pharmacological treatment a high priority.[4–6] An ideal anticocaine medication would accelerate cocaine metabolism, thereby producing biologically inactive metabolites by a route similar to the primary cocaine-metabolizing pathway, that is, cocaine hydrolysis catalyzed by plasma enzyme butyrylcholinesterase (BChE).[5,7–11] However, the native BChE has a low catalytic efficiency against naturally occurring (−)-cocaine.[12–15] (−)-Cocaine has a plasma half-life of ≈45–90 min, long enough for manifestation of the central nervous system (CNS) effects, which peak in minutes.[13,16] Here we

[*] D. Gao, H. Cho, W. Yang, Y. Pan, G. Yang, Prof. Dr. H.-H. Tai, Prof. Dr. C.-G. Zhan
Department of Pharmaceutical Sciences
College of Pharmacy
University of Kentucky
725 Rose Street, Lexington, KY 40536 (USA)
Fax: (+1) 859-323-3575
E-mail: zhan@uky.edu

[**] This work was supported by a research grant from the National Institutes of Health/National Institute of Drug Abuse (grant no.: R01 DA013930 to C.-G.Z.). The authors also acknowledge the Center for Computational Sciences (CCS) at University of Kentucky for supercomputing time on Superdome (a shared-memory supercomputer with 256 processors).

Supporting information for this article is available on the WWW under http://www.angewandte.org or from the author.

 © 2006 Wiley-VCH Verlag GmbH & Co. KGaA, Weinheim InterScience

report an unconventional computational design that has led to the discovery of a human BChE mutant with a ≈151-fold improved catalytic efficiency; this mutant can be used as an exogenous enzyme in humans to prevent (−)-cocaine from reaching the CNS. The encouraging outcome not only provides a potential anticocaine medication but also demonstrates that a novel general approach of studying enzymatic mechanisms and computational drug design is promising.

For rational design of a mutant enzyme with a higher catalytic activity for a given substrate, in general, one needs to design a mutation that can accelerate the rate-determining step of the entire catalytic reaction process while the other steps are not slowed down by the mutation. Reported computational modeling and experimental data indicated that the formation of the prereactive BChE–(−)-cocaine complex (ES) is the rate-determining step of (−)-cocaine hydrolysis catalyzed by wild-type BChE,[17–23] whereas the rate-determining step for the faster hydrolysis of the biologically inactive (+)-cocaine enantiomer is the chemical reaction process consisting of four individual reaction steps (Scheme 1).[18] This mechanistic understanding is consistent with the experimental observation[17] that the catalytic rate constant of wild-type BChE against (+)-cocaine is pH-dependent, whereas that of the same enzyme against (−)-cocaine is independent of the pH value. The pH-dependence of the rate constant for (+)-cocaine hydrolysis is clearly associated with the protonation of the H438 residue in the catalytic triad (S198, H438, and E325). For the first and third steps of the reaction process, when H438 is protonated, the catalytic triad cannot function and, therefore, the enzyme becomes inactive. The lower the pH value of the reaction solution, the higher the concentration of protonated H438 and the lower the concentration of the active enzyme. Hence, the rate constant was found to decrease with a decreasing pH value of the reaction solution for the enzymatic hydrolysis of (+)-cocaine.[17] Based on the above mechanistic understanding, the previously reported efforts for rational design of BChE mutants have focused on how to improve the ES formation process.[18,20,24]

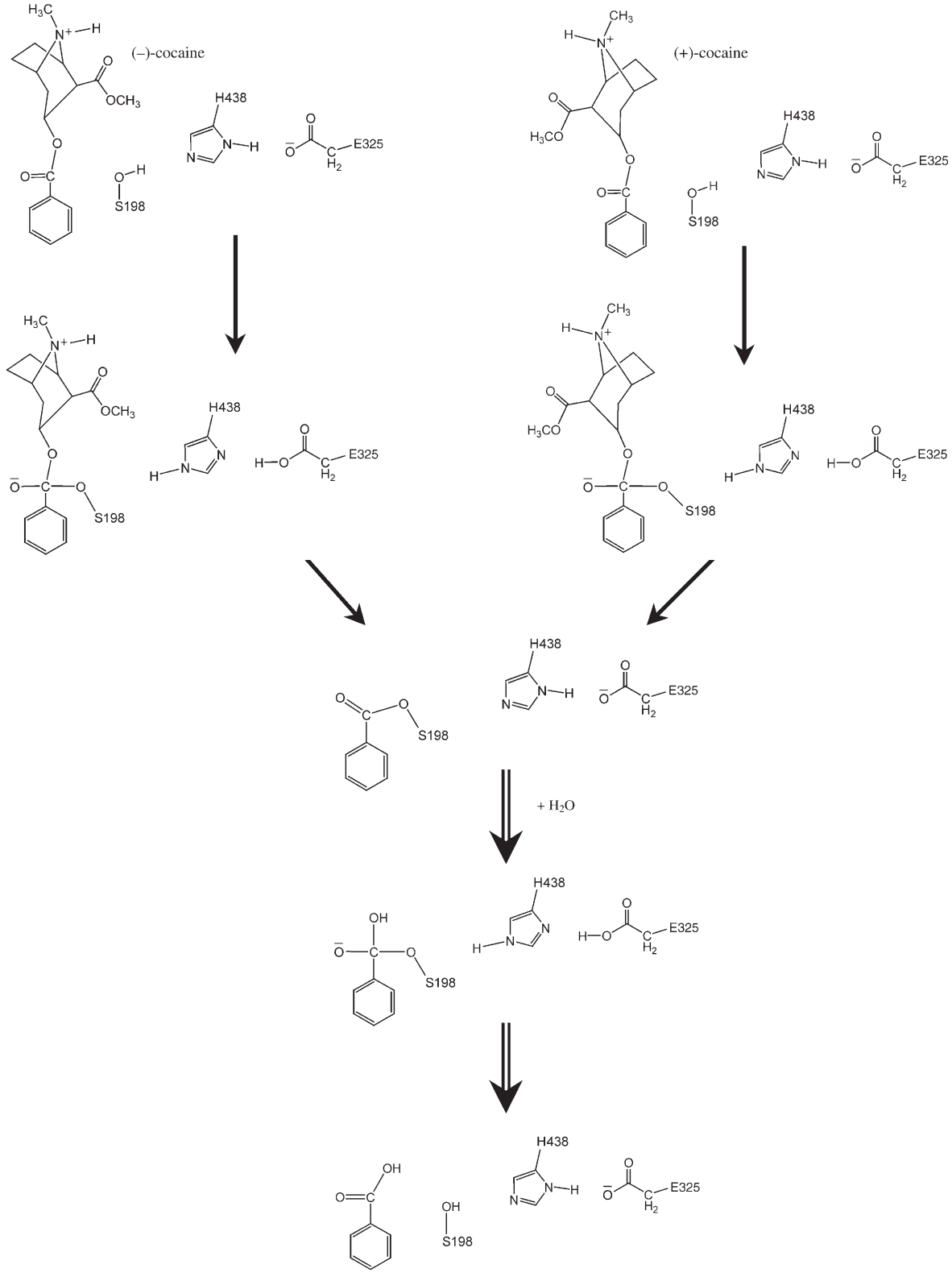
Experimental observation[18] also indicated that the catalytic rate constant of A328W/Y332A BChE is pH-dependent for both (−)- and (+)-cocaine. The pH-dependence reveals that, for both (−)- and (+)-cocaine, the rate-determining step of the hydrolysis catalyzed by A328W/Y332A BChE should be either the first or the third step of the reaction process. Further, if the third step were rate determining, then the catalytic efficiency of the A328W/Y332A mutant against (−)-cocaine should be as high as that of the same mutant against (+)-cocaine because the (−)- and (+)-cocaine hydrolyses share the same third and fourth steps (see Scheme 1). However, it has been observed that the A328W/Y332A mutant only has a ≈9-fold improved catalytic efficiency against (−)-cocaine, whereas the A328W/Y332A mutation does not change the high catalytic activity against (+)-cocaine.[18] This analysis of the experimental and computational data available in the literature clearly shows that the rate-determining step of (−)-cocaine hydrolysis catalyzed by the A328W/Y332A mutant should be the first step of the chemical reaction process. Further, recently reported computational modeling also suggests that the formation of the prereactive BChE–(−)-cocaine complex (ES) is hindered mainly by the bulky side chain of the Y332 residue in wild-type BChE, but the hindering can be removed by the Y332A or Y332G mutation.[20] Therefore, by starting from the A328W/Y332A and A328W/Y332G mutants, our current study for improving the catalytic efficiency of BChE against (−)-cocaine aimed to decrease the energy barrier for the first reaction step without significantly affecting the ES formation and other chemical reaction steps. To achieve this aim, molecular dynamics (MD) simulations[25] were performed to simulate the structures of the first transition state (TS1) for (−)-cocaine hydrolysis catalyzed by wild-type BChE and its various mutants.

We hoped to predict some possible mutations that can lower the energy of the TS1 structure and, therefore, lower the energy barrier for the first reaction step. Apparently, a mutant associated with stronger hydrogen bonding between the carbonyl oxygen atom of (−)-cocaine benzoyl ester and the oxyanion hole of the BChE mutant in the TS1 structure may potentially have a more stable TS1 structure and, therefore, a higher catalytic activity against (−)-cocaine. Hence, hydrogen bonding with the oxyanion hole in the TS1 structure is a crucial factor affecting the transition-state stabilization and the catalytic activity. The possible effects of some mutations on the hydrogen bonding were examined by performing molecular modeling and MD simulations on the TS1 structures for (−)-cocaine hydrolysis catalyzed by wild-type BChE and its various mutants. The initial candidate mutants were chosen by simple geometric consideration of the possible modification of the TS1 structure; only an energy minimization was carried out in the simple geometric consideration of each possible mutant. The MD simulations were then performed only for the candidate mutants whose energy-minimized TS1 structures clearly suggested possibly stronger hydrogen bonding between the carbonyl oxygen atom of (−)-cocaine and the oxyanion hole of the enzyme.

The MD simulation in water was performed for 1 ns or longer to make sure that we obtained a stable MD trajectory for each simulated TS1 structure with the wild-type or mutant BChE. The MD trajectories actually became stable quickly and so did the H···O distances involved in the potential hydrogen bonds between the carbonyl oxygen atom of (−)-cocaine and the oxyanion hole of BChE. The H···O distances in the simulated TS1 structures for wild-type BChE and its four mutants are summarized in Table 1 (see the Supporting Information for the key MD trajectory and MD-simulated TS1 structures).

As seen in Table 1, in the simulated TS1 structures for the wild-type, A328W/Y332A, A328W/Y332G, and F227A/S287G/A328W/Y332M BChEs, the carbonyl oxygen atom of (−)-cocaine can form up to two N−H···O hydrogen bonds with the peptidic NH hydrogen atoms of G117 and A199. The overall strength of the hydrogen bonding between the carbonyl oxygen atom of (−)-cocaine and the oxyanion hole of the enzyme only slightly increases when wild-type BChE is replaced by the A328W/Y332A, A328W/Y332G, or F227A/S287G/A328W/Y332M mutants, as seen from the estimated total hydrogen-binding energy (HBE) values in Table 1. In

 © 2006 Wiley-VCH Verlag GmbH & Co. KGaA, Weinheim



Scheme 1. Schematic representation of BChE-catalyzed hydrolysis of (−)- and (+)-cocaine.

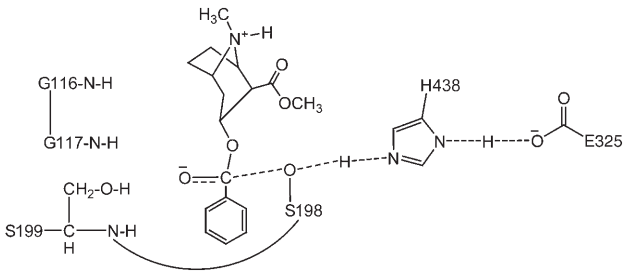
the simulated TS1 structure for A199S/F227A/A328W/Y332G BChE, an O–H···O hydrogen bond is formed between the hydroxy group on the side chain of S199 and the carbonyl oxygen atom of (−)-cocaine, in addition to the two N–H···O hydrogen bonds with the peptidic NH of G117 and S199, as seen in Scheme 2 and Table 1. Due to the additional O–H···O hydrogen bond, the overall strength of the hydrogen bonding with the modified oxyanion hole of A199S/F227A/A328W/

 © 2006 Wiley-VCH Verlag GmbH & Co. KGaA, Weinheim

Table 1: MD-simulated key distances (in Å) and the calculated total hydrogen-bonding energies (HBEs, in kcal mol^{-1}) between the oxyanion hole and the carbonyl oxygen atom of the (−)-cocaine benzoyl ester in the first transition state (TS1) with various BChEs.

Catalyst		Distance[a]				Total HBE value[b]
		D1	D2	D3	D4	
wild-type BChE	average	4.59	2.91	1.92		−5.5 (−4.6)
	maximum	5.73	4.14	2.35		
	minimum	3.35	1.97	1.61		
	fluctuation	0.35	0.35	0.12		
A328W/Y332A mutant	average	3.62	2.35	1.95		−6.2 (−4.9)
	maximum	4.35	3.37	3.02		
	minimum	2.92	1.78	1.61		
	fluctuation	0.23	0.27	0.17		
A328W/Y332G mutant	average	3.60	2.25	1.97		−6.4 (−5.0)
	maximum	4.24	3.17	2.76		
	minimum	2.89	1.77	1.62		
	fluctuation	0.23	0.24	0.17		
F227A/S287G/A328W/Y332M mutant	average	3.80	2.23	1.99		−6.1 (−4.8)
	maximum	4.61	3.08	2.88		
	minimum	3.16	1.75	1.67		
	fluctuation	0.25	0.23	0.18		
A199S/F227A/A328W/Y332G mutant	average	5.18	2.22	1.96	2.11	−9.8 (−7.4)
	maximum	5.94	3.08	2.44	3.30	
	minimum	4.28	1.68	1.65	1.56	
	fluctuation	0.23	0.21	0.13	0.28	

[a] D1, D2, and D3 represent the internuclear distances between the carbonyl oxygen atom of the cocaine benzoyl ester and the NH hydrogen atom of residues 116 (G116), 117 (G117), and 199 (A199 or S199) of BChE, respectively. D4 is the internuclear distance between the carbonyl oxygen atom of the cocaine benzoyl ester and the hydroxy hydrogen atom of the S199 side chain in the A199S/F227A/A328W/Y332G mutant. [b] Calculated by using the empirical HBE equation implemented in the AutoDock 3.0 program suite.[27] The total HBE value is the average of the HBE values calculated by using the instantaneous distances in all of the snapshots. The value in parenthesis is the total HBE value calculated by using the MD-simulated average distances.



Scheme 2. Schematic representation of the transition-state structure TS1 for the first reaction step of (−)-cocaine hydrolysis catalyzed by A199S/F227A/A328W/Y332G BChE.

Y332G BChE becomes significantly stronger than those of the wild-type, A328W/Y332A, A328W/Y332G, and F227A/S287G/A328W/Y332M BChEs, as seen from the estimated total HBE values in Table 1. These computational results suggest that the TS1 structure for (−)-cocaine hydrolysis catalyzed by A199S/F227A/A328W/Y332G BChE should be significantly more stable than that in the reaction catalyzed by the A328W/Y332A, A328W/Y332G, or F227A/S287G/A328W/Y332M mutants, due to the significant increase in the overall strength of hydrogen bonding between the carbonyl oxygen atom of (−)-cocaine and the oxyanion hole of the enzyme.

The aforementioned analysis of the literature[17,18,20] also indicates that the first chemical reaction step associated with TS1 should be the rate-determining step of (−)-cocaine hydrolysis catalyzed by a BChE mutant including a Y332A or Y332G mutation. Thus, the MD simulations predict that A199S/F227A/A328W/Y332G BChE should have a higher catalytic efficiency than the A328W/Y332A, A328W/Y332G, or F227A/S287G/A328W/Y332M BChEs against (−)-cocaine.

The catalytic efficiency (rate of catalysis/Michaelis constant, k_{cat}/K_M) of A328W/Y332A BChE against (−)-cocaine was reported to be $\approx 8.6\times10^6$ M min^{-1},[18] which is ≈9.4 times the k_{cat}/K_M value ($\approx 9.1\times10^5$ M min^{-1}) of wild-type BChE against (−)-cocaine. The catalytic efficiency of A328W/Y332G BChE was found to be slightly higher than that of A328W/Y332A BChE against (−)-cocaine.[20] To examine our theoretical prediction of the higher catalytic activity for A199S/F227A/A328W/Y332G BChE, we produced the A328W/Y332A and A199S/F227A/A328W/Y332G mutants of BChE through site-directed mutagenesis.[26] To minimize the possible systematic experimental errors of the kinetic data, we performed kinetic studies with the two mutants and wild-type BChE under the same conditions and compared the catalytic efficiency of the A328W/Y332A and A199S/F227A/A328W/Y332G BChEs with that of the wild-type for (−)-cocaine hydrolysis at the benzoyl ester group. Based on the kinetic analysis of the measured time-dependent radiometric data and the ELISA data, the ratio of the k_{cat}/K_M value of A328W/Y332A BChE to the k_{cat}/K_M value of wild-type BChE against (−)-cocaine was determined to be ≈8.6. The determined catalytic efficiency ratio of ≈8.6 is in good agreement with the ratio of ≈9.4 determined by Sun et al.[18] Further, by using the same experimental protocol, the ratio of the k_{cat}/K_M value of A199S/F227A/A328W/Y332G BChE to the k_{cat}/K_M value of A328W/Y332A BChE against (−)-cocaine was determined to be ≈16.8. These data indicate that A199S/F227A/A328W/Y332G BChE has a ≈(151 ± 14)-fold improved catalytic efficiency against (−)-cocaine compared to the wild-type; that is, A199S/F227A/A328W/Y332G BChE has a k_{cat}/K_M value of $\approx(1.37\pm0.13)\times10^8$ M min^{-1} against (−)-cocaine.

The catalytic efficiency of A199S/F227A/A328W/Y332G BChE against (−)-cocaine is significantly higher than that of AME-359 (that is, F227A/S287G/A328W/Y332M BChE, $k_{cat}/K_M = 3.1\times10^7$ M min^{-1}, whose catalytic efficiency against (−)-cocaine is the highest within all of the BChE mutants reported so far by other groups),[24] which has a ≈34-fold improved

 © 2006 Wiley-VCH Verlag GmbH & Co. KGaA, Weinheim

catalytic efficiency against (−)-cocaine compared to wild-type BChE. By using our designed A199S/F227A/A328W/Y332G BChE as an exogenous enzyme in human, when the concentration of this mutant is kept the same as that of the wild-type BChE in plasma, the half-life time of (−)-cocaine in plasma should be reduced from the ≈45–90 min to only ≈18–36 s.

In summary, an enzyme mutant is designed in this study based on the transition-state simulation. The designed BChE mutant has a significantly improved catalytic efficiency against (−)-cocaine, thereby demonstrating that transition-state simulation is a promising approach for rational enzyme redesign and drug discovery.

Received: August 24, 2005
Published online: December 15, 2005

Keywords: cocaine · enzymes · molecular dynamics · protein engineering · transition states

[1] J. H. Mendelson, N. K. Mello, *N. Engl. J. Med.* **1996**, *334*, 965.
[2] S. Singh, *Chem. Rev.* **2000**, *100*, 925.
[3] S. Paula, M. R. Tabet, C. D. Farr, A. B. Norman, W. J. Ball, Jr., *J. Med. Chem.* **2004**, *47*, 133.
[4] S. Sparenborg, F. Vocci, S. Zukin, *Drug Alcohol Depend.* **1997**, *48*, 149.
[5] D. A. Gorelick, *Drug Alcohol Depend.* **1997**, *48*, 159.
[6] A. D. Redish, *Science* **2004**, *306*, 1944.
[7] M. M. Meijler, G. F. Kaufmann, L. W. Qi, J. M. Mee, A. R. Coyle, J. A. Moss, P. Wirsching, M. Matsushita, K. D. Janda, *J. Am. Chem. Soc.* **2005**, *127*, 2477.
[8] M. R. A. Carrera, G. F. Kaufmann, J. M. Mee, M. M. Meijler, G. F. Koob, K. D. Janda, *Proc. Natl. Acad. Sci. USA* **2004**, *101*, 10416.
[9] D. W. Landry, K. Zhao, G. X.-Q. Yang, M. Glickman, T. M. Georgiadis, *Science* **1993**, *259*, 1899.
[10] C.-G. Zhan, S.-X. Deng, J. G. Skiba, B. A. Hayes, S. M. Tschampel, G. C. Shields, D. W. Landry, *J. Comput. Chem.* **2005**, *26*, 980.
[11] L. M. Kamendulis, M. R. Brzezinski, E. V. Pindel, W. F. Bosron, R. A. Dean, *J. Pharmacol. Exp. Ther.* **1996**, *279*, 713.
[12] S. J. Gateley, *Biochem. Pharmacol.* **1991**, *41*, 1249.
[13] S. J. Gatley, R. R. MacGregor, J. S. Fowler, A. P. Wolf, S. L. Dewey, D. J. Schlyer, *J. Neurochem.* **1990**, *54*, 720.
[14] S. Darvesh, D. A. Hopkins, C. Geula, *Nat. Rev. Neurosci.* **2003**, *4*, 131.
[15] *Butyrylcholinesterase: Its Function and Inhibitors* (Ed.: E. Giacobini), Dunitz Martin, UK, **2003**.
[16] S. J. Gateley, *Biochem. Pharmacol.* **1991**, *41*, 1249.
[17] H. Sun, J. E. Yazal, O. Lockridge, L. M. Schopfer, S. Brimijoin, Y. P. Pang, *J. Biol. Chem.* **2001**, *276*, 9330.
[18] H. Sun, Y.-P. Pang, O. Lockridge, S. Brimijoin, *Mol. Pharmacol.* **2002**, *62*, 220.
[19] C.-G. Zhan, F. Zheng, D. W. Landry, *J. Am. Chem. Soc.* **2003**, *125*, 2462.
[20] A. Hamza, H. Cho, H.-H. Tai, C.-G. Zhan, *J. Phys. Chem. B* **2005**, *109*, 4776.
[21] D. Gao, C.-G. Zhan, *Proteins* **2005**, in press.
[22] C.-G. Zhan, D. Gao, *Biophys. J.* **2005**, in press.
[23] D. Gao, C.-G. Zhan, *J. Phys. Chem. B* **2005**, in press.
[24] Y. Gao, E. Atanasova, N. Sui, J. D. Pancook, J. D. Watkins, S. Brimijoin, *Mol. Pharmacol.* **2005**, *67*, 204.
[25] See the Supporting Information concerning how classical MD can be employed in a way to simulate the transition state and how the MD simulations were performed.
[26] See the Supporting Information for the experimental materials and methods.
[27] a) G. M. Morris, D. S. Goodsell, R. S. Halliday, R. Huey, W. E. Hart, R. K. Belew, A. J. Olson, *J. Comput. Chem.* **1998**, *19*, 1639; b) based on the general HBE equation, we have $HBE(r) \approx 5\varepsilon r_0^{12}/r^{12} - 6\varepsilon r_0^{10}/r^{10}$, in which r is the H···O distance in the considered hydrogen bond and r_0 is the minimum value of the H···O distance for which the HBE equation can be used. The ε value was determined by using the condition that $HBE(r) = -5.0$ kcal mol^{-1} when $r = 1.90$ Å.

 © 2006 Wiley-VCH Verlag GmbH & Co. KGaA, Weinheim

Cluster Compounds

DOI: 10.1002/anie.200503652

Experimental and Theoretical Characterization of Superoxide Complexes $[W_2O_6(O_2^-)]$ and $[W_3O_9(O_2^-)]$: Models for the Interaction of O_2 with Reduced W Sites on Tungsten Oxide Surfaces**

Xin Huang, Hua-Jin Zhai, Tom Waters, Jun Li, and Lai-Sheng Wang**

High-valent transition-metal oxides (for example, V^V, Mo^{VI}, W^{VI}) are employed in a variety of important oxidation processes, and atmospheric dioxygen is commonly employed as a terminal oxidant.[1] Reoxidation of the metal oxide catalyst proceeds by a complex series of redox reactions, with the initial step generally assumed to be electron transfer from

[*] Dr. J. Li
W. R. Wiley Environmental Molecular Sciences Laboratory
Pacific Northwest National Laboratory, MS K1-96
P.O. Box 999, Richland, WA 99352 (USA)
Fax: (+1) 509-376-0420
E-mail: jun.li@pnl.gov
Dr. X. Huang, Dr. H.-J. Zhai, Dr. T. Waters, Prof. Dr. L.-S. Wang
Department of Physics
Washington State University
2710 University Drive, Richland, WA 99354 (USA)
and
W. R. Wiley Environmental Molecular Sciences Laboratory and Chemical Sciences Division
Pacific Northwest National Laboratory, MS K8-88
P.O. Box 999, Richland, WA 99352 (USA)
Fax: (+1) 509-376-6066
E-mail: ls.wang@pnl.gov

[**] This work was supported by the Chemical Sciences, Geosciences, and Biosciences Division, Office of Basic Energy Sciences, US Department of Energy (DOE) under grant No. DE-FG02-03ER15481 (catalysis center program) and was performed at the W. R. Wiley Environmental Molecular Sciences Laboratory (EMSL), a national scientific user facility sponsored by the DOE Office of Biological and Environmental Research and located at Pacific Northwest National Laboratory, operated for the DOE by Battelle. Calculations were performed at the EMSL Molecular Science Computing Facility.

Supporting information for this article is available on the WWW under http://www.angewandte.org or from the author.

© 2006 Wiley-VCH Verlag GmbH & Co. KGaA, Weinheim

a reduced metal site to dioxygen to form a bound superoxo complex.[2] Metal oxide clusters are being actively studied as model systems to obtain molecular-level information for surface and catalytic processes.[3,4] Herein we present a joint experimental and theoretical study of two O-rich tungsten oxide clusters, $[W_2O_8]^-$ and $[W_3O_{11}]^-$. Their electronic and geometric structures and chemical bonding were investigated by using photoelectron spectroscopy (PES) and density functional theory (DFT) calculations. The two anionic clusters are characterized as $[W_2O_6(O_2^-)]$ and $[W_3O_9(O_2^-)]$, respectively, that is, a superoxide species interacting with the neutral clusters $[W_2O_6]$ and $[W_3O_9]$ (chemisorption). In contrast, the neutral $[W_2O_8]$ and $[W_3O_{11}]$ clusters are found to contain an O_2 molecule weakly interacting with the $[W_2O_6]$ and $[W_3O_9]$ clusters (physisorption). The $[W_2O_8]^-$ and $[W_3O_{11}]^-$ clusters can be considered to be formed by non-dissociative electron transfer of the single W 5d electron in $[W_2O_6]^-$ and $[W_3O_9]^-$ to dioxygen (W 5d→O_2 π*) and are thus ideal molecular models for understanding the importance of reduced metal sites for the activation of O_2 on metal oxide nanostructures and surfaces.

The tungsten oxide clusters were produced by laser vaporization of a tungsten target in the presence of a helium carrier gas seeded with 0.5% O_2 and analyzed by using time-of-flight mass spectrometry.[5] Under the O_2-rich source conditions, clusters of the general formula $[W_nO_m]^-$ were formed, which appeared to terminate at the stoichiometry $[W_nO_{(3n+2)}]^-$ ($n=1$–3) as shown in Figure 1. The mono-

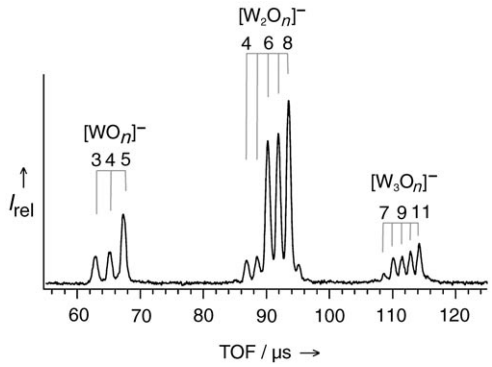


Figure 1. Time-of-flight (TOF) mass spectrum of $[W_mO_n]^-$ clusters produced from laser vaporization of a pure tungsten target in a helium carrier gas containing 0.5% O_2.

tungsten species $[WO_n]^-$ ($n=2$–5) and the ditungsten series $[W_2O_n]^-$ ($n=1$–6) have been reported previously.[6,7] The present communication focuses on two O-rich clusters, $[W_2O_8]^-$ and $[W_3O_{11}]^-$. The photoelectron spectra of these two species recorded at 157 nm are compared with those of the two 1:3-stoichiometric clusters $[W_2O_6]^-$ and $[W_3O_9]^-$ in Figure 2. The spectra of the 1:3-stoichiometric species each exhibit a single, broad, low-binding-energy feature followed by a large energy gap. The low-binding-energy feature is due to detachment of the single W 5d electron in $[W_2O_6]^-$ and $[W_3O_9]^-$,[7,8] and its absence in the spectra of both $[W_2O_8]^-$ and $[W_3O_{11}]^-$ suggests that these clusters are formally W^{VI} d^0 species. The spectra of the two O-rich clusters display

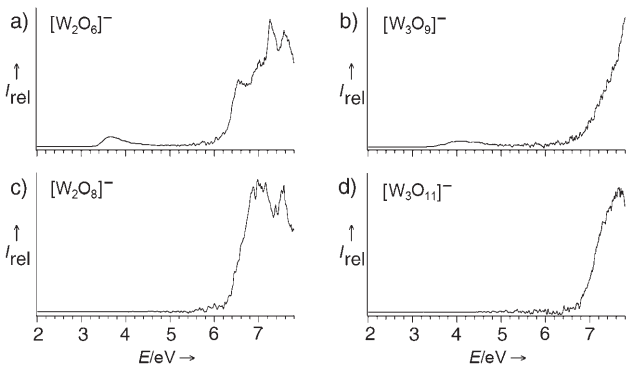


Figure 2. Photoelectron spectra of a) $[W_2O_6]^-$, b) $[W_3O_9]^-$, c) $[W_2O_8]^-$, and d) $[W_3O_{11}]^-$ recorded at 157 nm (7.866 eV).

broad detachment features with very high electron binding energies that are due to electron detachment from oxygen 2p orbitals. The detachment thresholds of $[W_2O_8]^-$ and $[W_3O_{11}]^-$ were estimated from the spectral onset of the first feature as about 6.4 and 6.9 eV, respectively. As shown below, there are large changes in the geometry between the anion and neutral ground states and these detachment thresholds do not represent the adiabatic detachment energies of $[W_2O_8]^-$ and $[W_3O_{11}]^-$.

The structure and bonding of the two clusters $[W_2O_6]^-$ and $[W_3O_9]^-$ have been described previously.[7,8] To obtain insight into the structure and bonding of $[W_2O_8]^-$ and $[W_3O_{11}]^-$ we carried out DFT calculations at the B3LYP level (see Methods Section). A variety of geometries for both the anions and their corresponding neutral species were tested and optimized to search for the global-minimum structures. The lowest-energy structures of the anions are shown in Figure 3 along with those of $[W_2O_6]^-$ and $[W_3O_9]^-$. A subset of the tested structures and their neutral species are given in

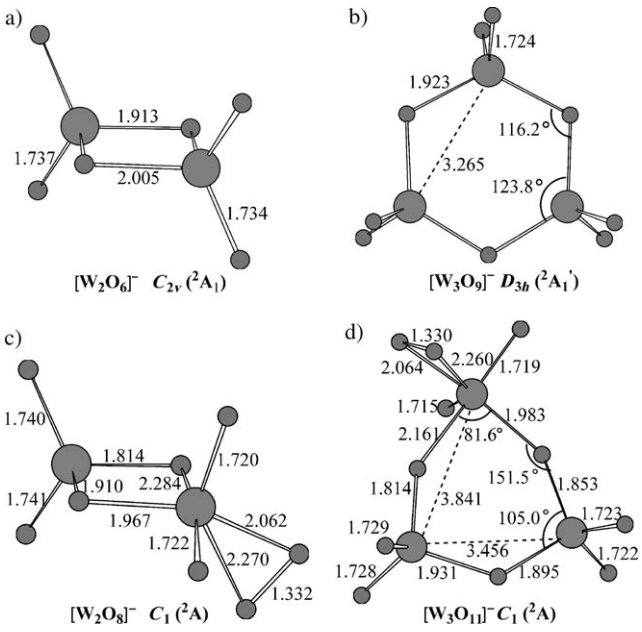


Figure 3. Calculated ground-state structures for a) $[W_2O_6]^-$, b) $[W_3O_9]^-$, c) $[W_2O_8]^-$, and d) $[W_3O_{11}]^-$. Distances in Å.

 © 2006 Wiley-VCH Verlag GmbH & Co. KGaA, Weinheim

the Supporting Information. The optimized structures for $[W_2O_8]^-$ and $[W_3O_{11}]^-$ with C_1 (^{2}A) symmetry bear some resemblance to those of $[W_2O_6]^-$ and $[W_3O_9]^-$, respectively, and can be viewed as the addition of an O_2 unit to one of the tungsten sites in the 1:3-stoichiometric clusters. The calculated O–O bond lengths of the O_2 units (1.33 Å) are very similar to that of the free superoxide (O_2^-) anion (1.34 Å at the B3LYP level), which suggests that these systems can be regarded as an O_2^- ion bound to neutral $[W_2O_6]$ and $[W_3O_9]$ clusters, respectively. The superoxide fragment is bound in an asymmetric, side-on fashion, with W–O bond lengths of 2.06 and 2.27 Å in $[W_2O_8]^-$ and 2.06 and 2.26 Å in $[W_3O_{11}]^-$ (Figure 3).

To gain further insight into the nature of the chemical bonding in the O-rich systems, we analyzed their valence molecular orbitals (MOs). The frontier orbitals of $[W_3O_{11}]^-$ are illustrated in Figure 4. The singly occupied MO is one of

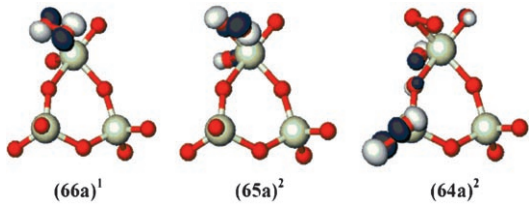


Figure 4. Molecular orbital contour surfaces for the three highest-energy occupied orbitals of $[W_3O_{11}]^-$.

the two π^* orbitals of the bound O_2 unit, and the highest-energy doubly occupied MO is the second π^* orbital of O_2 that is singly occupied in free O_2. This orbital occupation is consistent with the O–O bond length described above and supports the description of $[W_3O_{11}]^-$ as an O_2^- unit bound to the neutral $[W_3O_9]$. The remaining valence MOs are all derived from oxygen 2p orbitals on the terminal and bridging oxo ligands (see, for example, 64a in Figure 4). The valence MOs of $[W_2O_8]^-$ and its chemical bonding are qualitatively similar to those of $[W_3O_{11}]^-$.

The optimized structures of the $[W_2O_8]$ and $[W_3O_{11}]$ neutral clusters (see Supporting Information) are dramatically different. In particular, the calculations predict a large increase in the separation between the O_2 fragment and the tungsten site; the calculated W–O distances increase from 2.06 and 2.27 Å in $[W_2O_8]^-$ to 2.67 and 3.49 Å in neutral $[W_2O_8]$, and from 2.06 and 2.26 Å in $[W_3O_{11}]^-$ to 3.83 and 4.57 Å in $[W_3O_{11}]$. Furthermore, the O–O length in the O_2 unit is reduced from 1.33 Å in the anions to 1.20 Å in the neutral species, which is very close to that of free O_2 (1.21 Å at the B3LYP level). These results suggest that removal of an electron from the doubly occupied π^* orbital of the O_2^- moiety significantly weakens the interaction of O_2 with $[W_2O_6]$ and $[W_3O_9]$, and that $[W_2O_8]$ and $[W_3O_{11}]$ are best described as O_2 physisorption onto $[W_2O_6]$ and $[W_3O_9]$, respectively. It should be pointed out that the weak interaction between O_2 and $[W_2O_6]$ or $[W_3O_9]$ means that the W–O_2 distances in these species calculated by using B3LYP should only be considered qualitatively, as such weak interactions are known to be poorly described by DFT methods.[9] However, the effect of slight changes in these bond lengths on the exact geometry of O_2 in the neutral clusters should not alter the interpretation of the results, and the qualitative conclusions from these calculations are expected to be reliable.

The calculated vertical detachment energies (VDEs) for $[W_2O_8]^-$ and $[W_3O_{11}]^-$ are 6.40 and 6.88 eV, respectively, which are in reasonable agreement with the experimental data (Figure 2). However, the theoretical adiabatic detachment energies of 4.68 and 4.44 eV for $[W_2O_8]^-$ and $[W_3O_{11}]^-$, respectively, are significantly smaller than the corresponding VDEs because of the large structural changes between the ground states of the anions and the neutral species. These results are consistent with the broad photoelectron spectral features shown in Figure 2, which indicates that the experimental threshold values do not represent the adiabatic detachment energies of $[W_2O_8]^-$ and $[W_3O_{11}]^-$ and only represent their upper limits. As shown below, electron detachments involving the O_2^- orbitals from $[W_2O_8]^-$ and $[W_3O_{11}]^-$ are essentially dissociative detachments ($[W_2O_8]^- \rightarrow [W_2O_6] + O_2 + e^-$; $[W_3O_8]^- \rightarrow [W_3O_9] + O_2 + e^-$) because of the weak interaction between the neutral W_2O_6 and W_3O_9 clusters and O_2. VDEs for higher-binding-energy detachment channels were also computed and are shown in the Supporting Information; each VDE was fitted with a Gaussian function of 0.04-eV width to approximately simulate the photoelectron spectra.

To further understand the nature of interactions in $[W_2O_8]^-$ and $[W_3O_{11}]^-$, we computed the dissociation energies for the removal of the O_2 molecule [Eqs. (1) and (2)].[10]

$$[W_2O_8]^- \rightarrow [W_2O_6]^- + O_2 \quad 1.24\,\text{eV} \tag{1}$$

$$[W_3O_{11}]^- \rightarrow [W_3O_9]^- + O_2 \quad 1.42\,\text{eV} \tag{2}$$

The reverse of Equations (1) and (2) can be viewed as the reactions of O_2 with the anionic clusters. The presence of the extra 5d electrons in the $[W_2O_6]^-$ and $[W_3O_9]^-$ ions makes them susceptible to reaction with O_2 through transfer of one electron to O_2 to form the $[W_2O_6(O_2^-)]$ and $[W_3O_9(O_2^-)]$ superoxide complexes, respectively. This result is consistent with the nature of the frontier orbitals in $[W_2O_8]^-$ and $[W_2O_{11}]^-$ (Figure 4), which suggests that the interactions between $[W_2O_6]$ or $[W_3O_9]$ and O_2^- are mainly electrostatic. Conversely, the neutral clusters have extremely weak interactions with O_2 (calculated as < 0.1 eV in both cases) and essentially only form physisorbed $[W_2O_6(O_2)]$ and $[W_3O_9(O_2)]$ van der Waals complexes.[9] This behavior illustrates the importance of electrostatic interactions in the anionic species. In contrast, the O_2 interaction with the smallest 1:3-stoichiometric, neutral $[WO_3]$ cluster is quite different. We showed previously that O_2 and $[WO_3]$ form a charge-transfer complex $[(WO_3^+)(O_2^-)]$ as a result of the low coordination number of W in the C_{3v}-symmetric $[WO_3]$ monomer.[6]

The anionic clusters $[W_2O_6(O_2^-)]$ and $[W_3O_9(O_2^-)]$ can be considered as molecular models for the activation of O_2 through electron transfer between a reduced metal site and dioxygen at a metal oxide surface to form a coordinated

 © 2006 Wiley-VCH Verlag GmbH & Co. KGaA, Weinheim

superoxide species.[2] The present work demonstrates this phenomenon at the molecular level in two model systems. In contrast, the absence of the W 5d electron in the neutral $[W_2O_6]$ and $[W_3O_9]$ clusters leads to physisorbed O_2 in $[W_2O_8]$ and $[W_3O_{11}]$, which can be compared to O_2 interacting with perfect $[WO_3]$ surfaces.

Methods Section

Photoelectron spectroscopy: The photodetachment experiments were carried out by using a magnetic-bottle PES apparatus equipped with a laser-vaporization supersonic-cluster source.[5] Briefly, the $[W_mO_n]^-$ cluster anions were produced by laser vaporization of a pure tungsten target in the presence of helium carrier gas seeded with 0.5% O_2 and were analyzed by using a time-of-flight mass spectrometer. The $[W_2O_8]^-$ and $[W_3O_{11}]^-$ species of current interest were mass-selected and decelerated before being photodetached by a laser beam of wavelength 157 nm (7.866 eV) from an F_2 excimer laser. Photoelectrons were collected at nearly 100% efficiency by the magnetic bottle and analyzed in a 3.5-m long electron flight tube. Photoelectron spectra were calibrated by using the known spectrum of Rh^-, and the energy resolution of the apparatus was $\Delta E_k/E_k \approx 2.5\%$, that is, ca. 25 meV for 1-eV electrons.

Theoretical calculations: The theoretical calculations were performed by using the hybrid DFT method B3LYP.[11] Geometries were optimized by using analytical energy gradients, and vibrational frequency calculations were performed to verify the nature of the stationary points. The Stuttgart 14-valence-electron relativistic pseudopotentials and the (8s7p6d)/(6s5p3d) valence basis sets augmented with two f- and one g-type polarization functions ($\zeta(f) = 0.256, 0.825$; $\zeta(g) = 0.627$) were used for tungsten,[12] and the aug-cc-pVTZ basis set was used for oxygen.[13] Vertical detachment energies (VDEs) were calculated by using a combined ΔSCF-TDDFT approach.[14] In this approach, the ground-state energies of the anions and the neutral species were calculated from the ΔSCF energy difference at the B3LYP level, whereas the excited states of the electron-detached species were obtained from TDDFT calculations of the neutral species. The dissociation energies were calculated as the total energy differences of the relevant species at their ground-state structures. Calculations were carried out by using the NWChem 4.6 program at the Molecular Science Computing Facility located at the Environmental Molecular Sciences Laboratory.[15] Three-dimensional contours of the calculated Kohn–Sham orbitals were generated with the Extensible Computational Chemistry Environment (Ecce) software package.[16]

Received: October 14, 2005
Published online: December 13, 2005

Keywords: density functional calculations · O—O activation · oxygen · photoelectron spectroscopy · tungsten

[1] *Handbook of Heterogeneous Catalysis* (Eds.: G. Ertl, H. Knözinger, J. Weitkamp), Wiley, Weinheim, **1997**, pp. 2541.
[2] a) M. Che, A. J. Tench, *Adv. Catal.* **1983**, *32*, 1; b) K. Dyrek, M. Che, *Chem. Rev.* **1997**, *97*, 305; c) E. Giamello, *Catal. Today* **1998**, *41*, 239; d) M. Anpo, M. Che, B. Fubini, E. Garrone, E. Giamello, M. C. Paganini, *Top. Catal.* **1999**, *8*, 189; e) M. Labanowska, *ChemPhysChem* **2001**, *2*, 712; f) O. Diwald, E. Knözinger, *J. Phys. Chem. B* **2002**, *106*, 3495; g) T. Berger, M. Sterrer, O. Diwald, E. Knözinger, D. Panayotov, T. L. Thompson, J. T. Yates, Jr., *J. Phys. Chem. B* **2005**, *109*, 6061.
[3] For recent reviews see: a) D. K. Böhme, H. Schwarz, *Angew. Chem.* **2005**, *117*, 2388; *Angew. Chem. Int. Ed.* **2005**, *44*, 2336; b) T. M. Bernhardt, *Int. J. Mass Spectrom.* **2005**, *243*, 1; c) K. A. Zemski, D. R. Justes, A. W. Castleman, Jr., *J. Phys. Chem. B* **2002**, *106*, 6136.
[4] For selected examples see: a) J. Döbler, M. Pritzsche, J. Sauer, *J. Am. Chem. Soc.* **2005**, *127*, 10861; b) G. Fu, X. Xu, X. Lu, H. L. Wan, *J. Am. Chem. Soc.* **2005**, *127*, 3989; c) M. L. Kimble, A. W. Castleman, Jr., R. Mitrić, C. Bürgel, V. Bonačić-Koutecký, *J. Am. Chem. Soc.* **2004**, *126*, 2526; d) T. Waters, R. A. J. O'Hair, A. G. Wedd, *J. Am. Chem. Soc.* **2003**, *125*, 3384; e) X. Xu, F. Faglioni, W. A. Goddard III, *J. Phys. Chem. A* **2002**, *106*, 7171; f) A. Muller, R. Maiti, M. Schmidtmann, H. Bogge, S. K. Das, W. J. Zhang, *Chem. Commun.* **2001**, 2126; g) Q. Sun, B. K. Rao, P. Jena, D. Stolcic, Y. D. Kim, G. Gantefor, A. W. Castleman, Jr., *J. Chem. Phys.* **2004**, *121*, 9417; h) B. L. Yoder, J. T. Maze, K. Raghavachari, C. C. Jarrold, *J. Chem. Phys.* **2005**, *122*, 094313.
[5] a) L. S. Wang, H. S. Cheng, J. Fan, *J. Chem. Phys.* **1995**, *102*, 9480; b) L. S. Wang, H. Wu in *Advances in Metal and Semiconductor Clusters. IV. Cluster Materials* (Ed.: M. A. Duncan), JAI, Greenwich, CT, **1998**, pp. 299–343.
[6] H. J. Zhai, B. Kiran, L. F. Cui, X. Li, D. A. Dixon, L. S. Wang, *J. Am. Chem. Soc.* **2004**, *126*, 16134.
[7] H. J. Zhai, X. Huang, L. F. Cui, X. Li, J. Li, L. S. Wang, *J. Phys. Chem. A* **2005**, *109*, 6019.
[8] X. Huang, H. J. Zhai, B. Kiran, L. S. Wang, *Angew. Chem.* **2005**, *117*, 7417; *Angew. Chem. Int. Ed.* **2005**, *44*, 7251.
[9] a) K. Müller-Dethlefs, P. Hobza, *Chem. Rev.* **2000**, *100*, 143; b) R. van Leeuwen, E. J. Baerends, *Phys. Rev. A* **1994**, *49*, 2421.
[10] The $[W_2O_8]^-$ and $[W_3O_{11}]^-$ ions also have another dissociation pathway to release O_2^- with much higher dissociation energies of 4.20 and 3.92 eV, respectively. The difference between this pathway and the O_2 pathway lies in the difference between the electron affinities of O_2 and the $[W_2O_6]$ and $[W_3O_9]$ clusters.
[11] a) A. D. Becke, *J. Chem. Phys.* **1993**, *98*, 1372; b) C. Lee, W. Yang, R. G. Parr, *Phys. Rev. B* **1988**, *37*, 785; c) P. J. Stephens, F. J. Devlin, C. F. Chabalowski, M. J. Frisch, *J. Phys. Chem.* **1994**, *98*, 11623.
[12] a) D. Andrae, U. Haeussermann, M. Dolg, H. Stoll, H. Preuss, *Theor. Chim. Acta* **1990**, 77, 123; b) W. Küchle, M. Dolg, H. Stoll, H. Preuss, *Pseudopotentials of the Stuttgart/Dresden Group 1998* Revision Aug 11, 1998 (http://www.theochem.uni-stuttgart.de/pseudopotentiale); c) J. M. L. Martin, A. Sundermann, *J. Chem. Phys.* **2001**, *114*, 3408.
[13] a) T. H. Dunning, Jr., *J. Chem. Phys.* **1989**, *90*, 1007; b) R. A. Kendall, T. H. Dunning, Jr., R. J. Harrison, *J. Chem. Phys.* **1992**, *96*, 6796.
[14] a) J. Li, X. Li, H. J. Zhai, L. S. Wang, *Science* **2003**, *299*, 864; b) X. Li, B. Kiran, J. Li, H. J. Zhai, L. S. Wang, *Angew. Chem.* **2002**, *114*, 4980; *Angew. Chem. Int. Ed.* **2002**, *41*, 4786.
[15] "NWChem, A Computational Chemistry Package for Parallel Computers, Version 4.6" (2004), Pacific Northwest National Laboratory, Richland, Washington 99352-0999, USA. See Supporting Information.
[16] Extensible Computational Chemistry Environment (Ecce). http://ecce.emsl.pnl.gov/.

 © 2006 Wiley-VCH Verlag GmbH & Co. KGaA, Weinheim

Heteroacenes

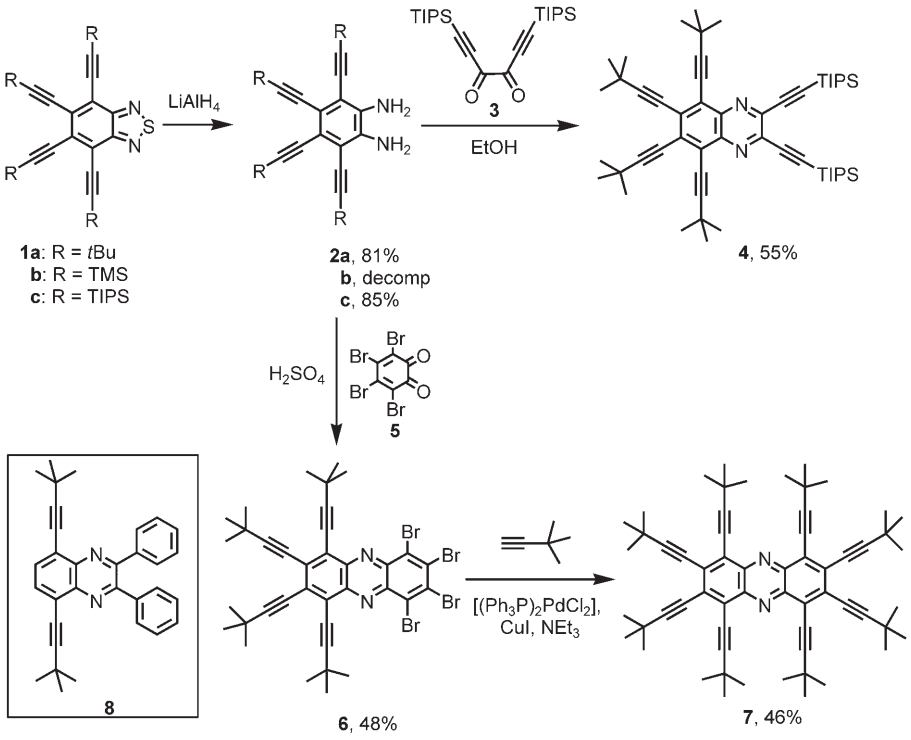
DOI: 10.1002/anie.200502067

Derivatives of Octaethynylphenazine and Hexaethynylquinoxaline**

*Shaobin Miao, Carlito G. Bangcuyo, Mark D. Smith, and Uwe H. F. Bunz**

In 1986, hexaethynylbenzene, the first peralkynylated π perimeter, was obtained by Vollhardt and co-workers.[1] Since then, peralkynylated cyclobutadiene complexes, cymantrenes, ferrocenes, cylcopentadienyl radicals, thiophenes, and extended systems derived from tetraethynylethylenes and hexaethynylbenzenes have been reported.[2–7] Peralkynylated N-heterocycles are scarce, and only recently peralkynylpyrazinophorphyrazine and triethynyltriazine were reported.[8,9] Dialkynylated pentacenes, hexacenes, and heptacenes play a significant role in materials science and are fairly easily accessible.[10] Peralkynylated acenes as a class, however, are entirely unknown; the peri interactions in acenes would result in steric crowding of the alkynes and their all-too-close spacing would lead to Bergman-type reactions. If the peri interactions could be removed in naphthalene, anthracene, or the larger acenes, peralkynylation should be possible: Hexaethynylquinoxaline and octaethynylphenazine are attractive synthetic targets that might show promise as n-type semiconductors and as unusual sensory platforms for metal cations.[11] Herein, we report the synthesis of the first representatives of the heteroacenes, namely, hexaethynylquinoxaline and octaethynylphenazine.

Tetraethynylbenzothiadiazoles **1a–c** are easily available by Pd-catalyzed alkynylation of tetrabromobenzothiadiazole.[12] The attempted reduction of **1b** with $LiAlH_4$ led to decomposition of the starting material without the formation of an isolable product, probably through desilylation and concomitant polymerization (Scheme 1). Desulfurization of the sterically more shielded derivatives **1a** and **1c** with $LiAlH_4$ furnished spectroscopically pure **2a** and **2c** after aqueous workup. Both products are stable under ambient conditions for a day or so, after which they decompose (observed as darkening), presumably by oxidation of the amine groups. To secure the structure of **2a**, we attempted to crystallize it from dichloromethane; microcrystalline powders formed. Upon crystallization from hexafluorobenzene, a suitable single-crystalline specimen was obtained.[13]



Scheme 1. Synthesis of hexaethynylquinoxaline (**4**), octaethynylphenazine (**7**), and the quinoxaline **8**. TMS = trimethylsilyl; TIPS = triisopropylsilyl.

Figure 1 shows a ball-and-stick representation of **2a**. A weak F···H hydrogen bond (2.36 Å) is apparent between an amine group of **2a** and a fluorine substituent of the hexafluorobenzene. The electron-poor hexafluorobenzene and the electron-rich diamine **2a** lie on top of each other, as would be expected from the electrostatic potentials of these

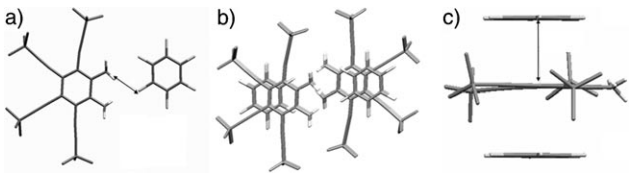


Figure 1. Stick representation of the complex **2a**·C_6F_6. a) NH···F hydrogen bond indicated by arrow (2.36(3) Å, 152°). b) Stacking of the molecules, viewed along the crystallographic *a* axis. c) The distance between C_6F_6 and **2a** in the stacks, as indicated by the arrow, is 3.29 Å (view shown along the crystallographic *b* axis).[13]

[*] Dr. S. Miao, Dr. C. G. Bangcuyo, Prof. Dr. U. H. F. Bunz
School of Chemistry and Biochemistry
Georgia Institute of Technology
770 State Street, Atlanta, GA 30332 (USA)
Fax: (+1) 404-385-1795
E-mail: uwe.bunz@chemistry.gatech.edu
Dr. M. D. Smith
Department of Chemistry and Biochemistry
University of South Carolina
Columbia, SC 29208 (USA)

[**] We thank the Petroleum Research Funds for support and Prof. Christoph Fahrni (School of Chemistry and Biochemistry, Georgia Institute of Technology) for the analysis of the binding constants of **4**, **7**, and **8** with metal ions.

 © 2006 Wiley-VCH Verlag GmbH & Co. KGaA, Weinheim

molecules.[14] A tightly packed, π–π-stacked structure results; compound **2a** is the first reported tetraalkynylated phenylenediamine and, as such, is valuable for the construction of other structures.

Upon treatment of **2a** with dione **3** in ethanol with molecular sieves, the hexaethynylquinoxaline derivative **4** formed in 55% yield.[11] If **2a** was treated with the commercially available quinone **5**, the tetrabromide **6** was isolated (Scheme 1). Pd-catalyzed coupling of **6** to an excess of 3,3-dimethylbutyne gave the octaethynylphenazine representative **7** as a stable, orange, crystalline solid. While spectral data indicated the presence of a peralkynylated phenazine, the attractive topology of **7** was confirmed by single-crystal X-ray structural analysis (Figure 2).[15] The bond lengths and bond angles for **7** are in excellent agreement with the expected values.[1,5,7]

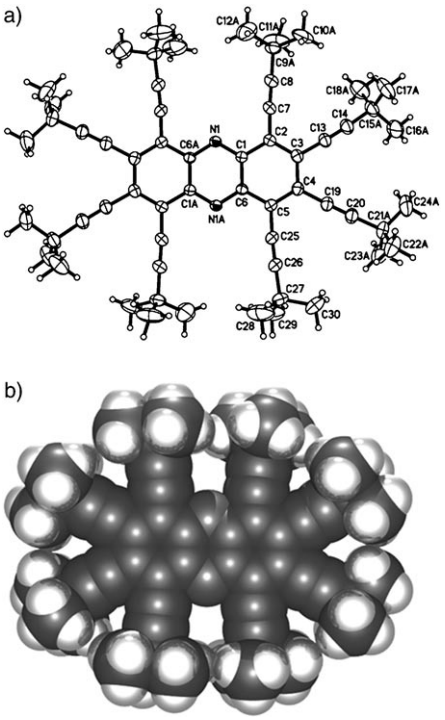


Figure 2. a) ORTEP drawing of **7** at the 50% probability level. b) Space-filling view of **7**. The phenazine nucleus can carry eight alkyne units, as the pyrazine ring creates a void that accommodates the substituents and forms an internal pocket.

Figure 3 shows the packing of **7** in the solid state. The molecules are arranged in tilted stacks that are 0.97-nm apart along the *b* axis in a classic herringbone arrangement. Close π–π contacts are not observed due to the bulky *tert*-butyl groups that encase the aromatic faces of **7**.

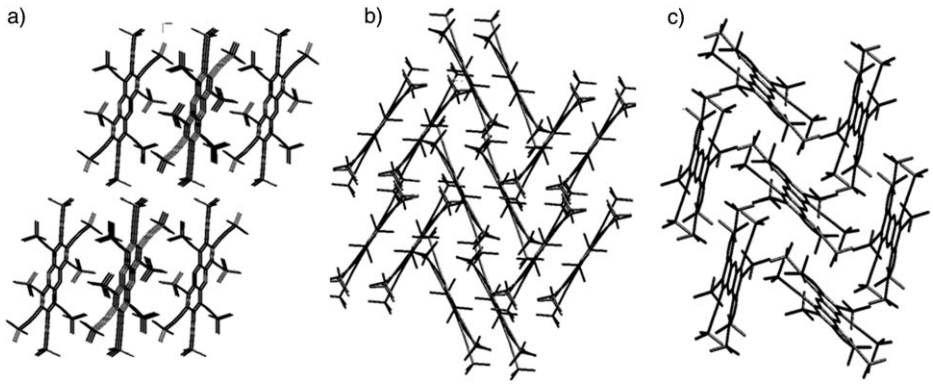


Figure 3. Packing of **7** in the solid state. a, b) View along the *b* and *a* axes, respectively. The stacking distance is 0.97 nm. c) View along the approximate diagonal of *a* and *c* axes. The herringbone pattern is visible in (b) and (c).

Upon going from **4** to **7**, significant red shifts in both the absorption and emission spectra were recorded (Figure 4) which result from the extension of the π system. While the

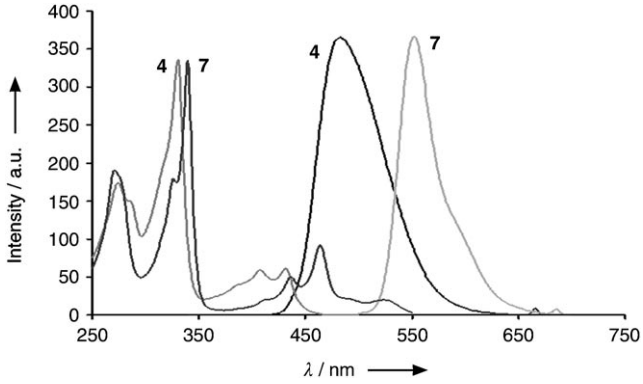


Figure 4. Absorption (left) and emission spectra (right) of **4** (λ_{max} = 434 nm [2.85 eV], λ_{em} = 485 nm) and **7** (λ_{max} = 527 nm [2.35 eV], λ_{em} = 554 nm) in chloroform.

emission spectra of **4** and **7** are unstructured, their absorption spectra feature a similar fine structure as those of anthracene or phenazine; compounds **4** and **7** are obviously "true" acenes, despite their alkyne decoration.[16] When comparing the UV/Vis spectrum of **7** (λ_{max} = 527 nm) to that of phenazine (λ_{max} = 363 nm), a red shift of 162 nm in the absorption is noted. To estimate the band gap and the position of the frontier orbitals of **7**, an ab initio quantum chemical calculation (B3LYP, 6-31G**) was performed (*tert*-butyl groups omitted; HOMO: −5.80 eV; LUMO: −3.19 eV; gap: 2.61 eV). To compare the band gap and position of the frontier orbitals, we also performed quantum chemical calculations (B3LYP, 6-31G**) on anthracene (HOMO: −5.24 eV; LUMO: −1.65 eV; gap: 3.59 eV) and phenazine (HOMO: −6.09 eV; LUMO: −2.43 eV; gap: 3.66 eV). The introduction of the nitrogen atoms into the frame of the acenes lowers the energy of the HOMO and LUMO, but does not significantly decrease the band gap. Alkyne decoration, however, leads to a decrease in the band gap. The calculations

 © 2006 Wiley-VCH Verlag GmbH & Co. KGaA, Weinheim

agree well with the absorption data and reflect the gross electronic differences between phenazine and **7**.

The crystal structure of **7** reveals a rigid binding pocket generated by the alkyne groups and the phenazine nitrogen atom. The three π-basic sites should allow the complexation of metal cations. Phenazine itself forms coordination polymers with copper and silver.[17] Exposure of **4** and of **7** to silver triflate led to a bathochromic shift in their absorption spectra and to quenching of their emission. The shift is larger in **7** than in **4**. Upon exposure to Cu^{I} or Cu^{II}, no chromic changes occurred but slight quenching was observed for both peralkynyls with Cu^{II} triflate. Surprised by the lack of binding to copper ions, we treated **4** and **7** with a series of metal salts (see Figure 5 and Table 1). While alkali and alkaline-earth metals generally do not lead to spectral shifts, Ba^{2+} did cause a shift in the absorption spectrum of **7**. Ag^{+}, As^{3+}, and Hg^{2+} ions, as well as trifluoroacetic acid generated chromic responses in **4** and **7**, while indium and tin triflates induced a bathochromic shift in **7**. According to the shape of the spectra of **7**, In^{3+}, Ba^{2+}, and Sn^{2+} ions can be grouped together as they elicit the same response from **7**, while Ag^{+}, As^{3+}, and Hg^{2+} ions and proton acids show spectral responses that are different from each other and from those of the first group (Table 1). The presence of the second alkynylated fused benzene unit in **7** as compared to **4** seems to significantly increase the binding of the pyrazine motif to metal cations. Changes in emission are much less pronounced, suggesting that **4** and **7** bind less strongly to metal cations in their excited states.

To understand the relationship between molecular structure and metal binding, we performed a titration of **4**, **7**, and **8** with AgOTf and $Hg(OTf)_2$. However, attempts to obtain the binding constants for association of **4**, **7**, and **8** to $Hg(OTf)_2$ were inconclusive; multiple coordination equilibria are present, and various combinations of proposed simple metal-to-ligand stoichiometries did not lead to a reasonable fit of the experimental data to any assumed model using the program SPECFIT.[18]

From the results of titrations with AgOTf, compounds **4** and **7** first form 1:1 and then 2:1 metal–ligand complexes, with $\log\beta_1 = 4.5$ (± 0.2) and $\log\beta_2 = 8.8$ (± 0.1) for **4**, and $\log\beta_1 = 6.5$ (± 0.3) and $\log\beta_2 = 12.8$ (± 0.2) for **7**. The presence of the two alkynylated phenyl arms aligned parallel in structure **7** increases the binding to silver by a factor of 100, as compared to the quinoxaline **4**. A similar effect is apparent for the binding of the second silver ion, which is, in both cases, only slightly less strongly coordinated than the first one, suggesting that the additional positive charge does not significantly affect the binding properties of the second pocket. We have investigated the binding of AgOTf to **8** and found that nonlinear least-squares fitting with the program SPECFIT[18] leads to a different complexation behavior. The spectral data are best interpreted by a 1:2 and a 1:4 ligand-to-metal complex stoichiometry with $\log\beta_2 =$

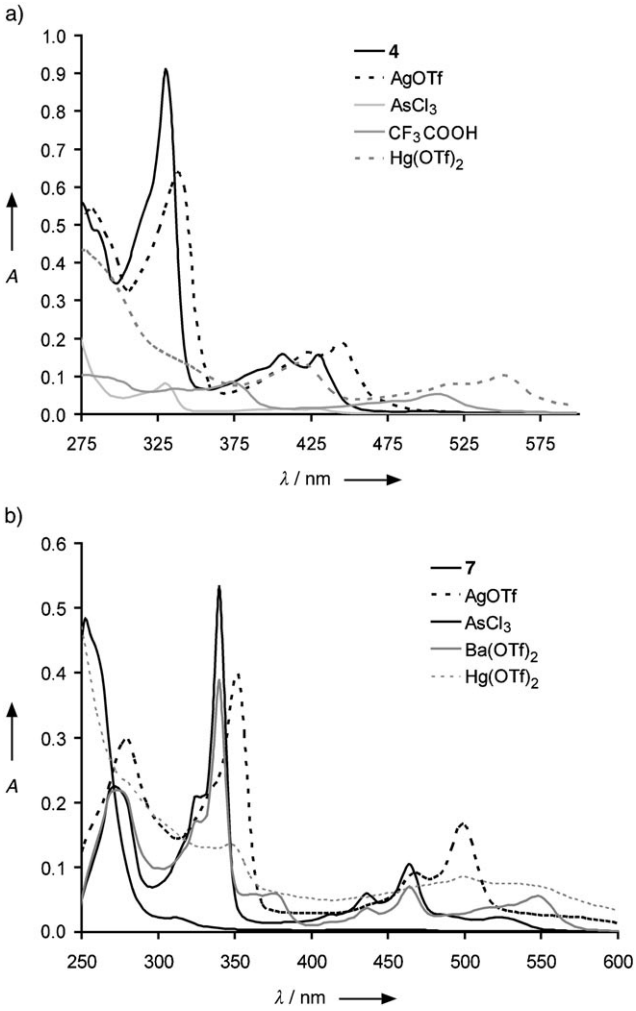


Figure 5. Absorption spectra of a) **4** and b) **7** in the presence of representative metal cations. $OTf = CF_3SO_3^-$.

Table 1: Absorption (λ_{max}) and emission (λ_{em}) data for the interaction of **4** and **7** with metal ions.[a]

	4		**7**	
	λ_{max} [nm]	λ_{em} [nm]	λ_{max} [nm]	λ_{em} [nm]
no metal	331, 409, 432	482	340, 464, 523 sh	553
CF_3CO_2H	376, 509	quenched	376, 510, 548	quenched
AgOTf	340, 420, 446	514 vw	351, 467, 500	quenched
$AsCl_3$	331, 407, 446 vw	quenched	314, 466, 550 vw	quenched
$Ba(OTf)_2$	no change	no change	340, 377, 464, 548	553[b]
$Ca(OTf)_2$, $CdCl_2$, $Cu(OTf)$, CuI, $Eu(OTf)_3$, KOTf, LiOTf, $Mg(OTf)_2$, $Na(OTf)$, $Pb(NO_3)_2$, $Tl(OTf)$, $Zn(OTf)_2$	no change	no change[c]	no change	no change[c]
$Hg(OTf)_2$	278, 418, 552	quenched	348, 449, 543 br	567 w
$In(OTf)_3$	no change	no change	340, 376, 464, 548	546 w
$Sn(OTf)_2$	no change	no change	340, 376, 464, 548	quenched

[a] sh = shoulder; w = weak; vw = very weak; br = broad. [b] Decreased intensity. [c] Slight quenching with $Cu(OTf)_2$.

© 2006 Wiley-VCH Verlag GmbH & Co. KGaA, Weinheim

13.0 (±0.3) and $\log\beta_4 = 22.1$ (±0.3). Not unexpectedly, the presence of the phenyl groups increases the interaction with the silver cations and leads to this somewhat exotic complexation behavior.

The underlying structural principle of alkyne-framed N-heterocycles will be exploited in the future to construct a more general class of rigid receptors **7** by coupling differentiated functional alkynes to **6**. Those starting alkynes would carry auxiliary binding sites and/or modulate the electronic properties of the system to investigate the interaction of these ligands with metal cations in water and in organic solvents.[18]

In conclusion, we have described a facile synthetic approach that yields peralkynylated quinoxalines and phenazines. Both **4** and **7**, which are the first reported peralkynylated heteroacenes, show attractive and quite selective metal-binding properties that will be harnessed in the future. Derivatives of this class of fluorescent molecules might find use as organic n-type semiconductors.

Experimental Section

2: Dry THF (150 mL) was added to a flame-dried 250-mL Schlenk flask charged with **1**, then $LiAlH_4$ (4 equiv) was added to the mixture under a stream of nitrogen over a period of 30 min, and stirring was continued for 4 h. Analytically pure **2** was obtained after aqueous workup.

2a: Prepared from **1a** (1.00 g, 2.18 mmol). Red solid (0.760 g, 81 %); m.p.: 167 °C (decomp); ^{1}H NMR (400 MHz, $CDCl_3$): $\delta = 3.34$ (bs, 4H), 1.42 (s, 18H), 1.40 ppm (s, 18H); $^{13}C\{^1H\}$ NMR (100 MHz, $CDCl_3$): $\delta = 136.89$, 119.38, 112.01, 108.50, 102.97, 77.37, 75.46, 31.25, 31.02, 28.76, 28.52 ppm.

2c: Prepared from **1c** (1.00 g, 1.16 mmol). Red solid (0.706 g, 73 %); m.p.: 185 °C (decomp); ^{1}H NMR (400 MHz, $CDCl_3$): $\delta = 3.22$ (bs, 4H), 1.17–1.13 ppm (m, 84H); $^{13}C\{^1H\}$ NMR (100 MHz, $CDCl_3$): $\delta = 136.45$, 118.97, 112.69, 104.47, 102.25, 101.48, 96.35, 19.14, 12.16, 11.42 ppm.

4: Molecular sieves, **2a** (0.204 g, 0.476 mmol), **3** (0.209 g, 0.500 mmol), and toluene (10 mL) were heated at 80 °C for 4 h. Removal of the solvent and chromatography of the residue (3:1 hexanes/CH_2Cl_2) furnished **4** (0.315 g, 55 %); m.p.: 194–196 °C; ^{1}H NMR (400 MHz, $CDCl_3$): $\delta = 1.43$ (s, 18H), 1.37 (s, 18H) 1.18 ppm (s, 42H); $^{13}C\{^1H\}$ NMR (100 MHz, $CDCl_3$): $\delta = 141.53$, 140.38, 130.29, 126.08, 112.48, 108.94, 104.26, 99.52, 78.46, 75.23, 33.58, 29.16, 18.75, 11.89 ppm; IR (KBr): $\nu = 2966$, 2945, 2866, 2222, 1539, 1462, 1411, 1313 cm^{-1}; MS (70 eV): *m/z* (%): 811 (100) [M^+], 726 (60), 645 (5); HR-MS: *m/z* calcd for $C_{54}H_{78}N_2Si_2$: 810.57036; found: 810.56716.

7: **2a** (0.274 g, 0.639 mmol), **5** (0.273 g, 0.645 mmol), ethanol (10 mL), and a drop of H_2SO_4 were heated at reflux for 14 h. Filtration followed by crystallization from CH_3OH/CH_2Cl_2 yielded **6** (0.250 g, 48 %); ^{1}H NMR (400 MHz, $CDCl_3$): $\delta = 1.41$ (s, 18H), 1.37 ppm (s, 18H); $^{13}C\{^1H\}$ NMR (100 MHz,$CDCl_3$): $\delta = 143.87$, 139.54, 132.67, 131.29, 127.99, 126.09, 113.08, 112.62, 79.46, 75.09, 32.63, 31.15, 28.35, 28.00 ppm. Triethylamine (7 mL), **6** (0.424 g, 0.519 mmol), $[(PPh_3)_2PdCl_2]$ (5 mol %), CuI (5 mol %), and 3,3-dimethylbutyne (5 equiv) were stirred at 120 °C for 18 h in a sealed flask. Aqueous workup and column chromatography (4:1 hexanes/CH_2Cl_2) furnished **7** (0.196 g, 46 %); m.p.: 248 °C (decomp.); ^{1}H NMR (400 MHz, $CDCl_3$): $\delta = 1.46$ (s, 36H), 1.32 ppm (s, 36H); $^{13}C\{^1H\}$ NMR (100 MHz, $CDCl_3$): $\delta = 141.82$, 130.27, 124.71, 111.36, 110.00, 77.46, 75.92, 31.92, 30.84, 28.56, 28.31 ppm; IR (KBr): $\nu =$ 2966, 2923, 2862, 2214, 1728, 1712, 1695, 1548, 1452, 1440, 1390, 1361, 1261 cm^{-1}; MS (70 eV): *m/z* (%): 820 (100) [M^+]; HR-MS: *m/z* calcd for $C_{60}H_{72}N_2$: 820.56955; found: 820.56726.

8: A mixture of 3,6-bis(3,3-dimethylbut-1-ynyl)benzene-1,2-diamine (1.70 g, 6.33 mmol), molecular sieves (1.0 g),and 1,2-diphenylethane-1,2-dione (2.00 g, 9.51 mmol) in dry toluene (50 mL) was heated at reflux for 18 h. Workup and column chromatography (silica gel, 1:1 hexane/CH_2Cl_2) afforded **8** (1.77 g, 63 %); m.p.: 232–234 °C; IR (KBr): $\nu = 3055$, 2966, 2922, 2895, 2864, 2216, 1560, 1466, 1337, 1242, 1097, 841, 700 cm^{-1}; ^{1}H NMR (400 MHz, $CDCl_3$): $\delta = 7.75$–7.72 (m, 6H), 7.38–7.31 (m, 6H), 1.45 ppm (s, 18H); $^{13}C\{^1H\}$ NMR (100 MHz, $CDCl_3$): $\delta = 152.27$, 140.93, 138.94, 132.40, 130.21, 129.04, 128.03, 123.33, 106.84, 75.98, 31.02, 28.52 ppm; HR-MS (70 eV): *m/z* calcd for $C_{32}H_{30}N_2$ [M^+]: 442.24090; found: 442.24153.

Received: June 15, 2005
Revised: October 19, 2005
Published online: December 19, 2005

Keywords: alkynes · cations · fused-ring systems · nitrogen heterocycles

[1] a) R. Diercks, J. C. Armstrong, R. Boese, K. P. C. Vollhardt, *Angew. Chem.* **1986**, *98*, 270–271; *Angew. Chem. Int. Ed. Engl.* **1986**, *25*, 268–269; b) R. Boese, J. R. Green, J. Mittendorf, D. L. Mohler, K. P. C. Vollhardt, *Angew. Chem.* **1992**, *104*, 1643–1645; *Angew. Chem. Int. Ed. Engl.* **1992**, *31*, 1643–1645; c) T. X. Neenan, G. M. Whitesides, *J. Org. Chem.* **1988**, *53*, 2489; d) Y. Tobe, K. Kubota, K. Naemura, *J. Org. Chem.* **1997**, *62*, 3430–3431; e) J. D. Tovar, N. Jux, T. Jarrosson, S. I. Khan, Y. Rubin, *J. Org. Chem.* **1997**, *62*, 3432–3433.

[2] H. W. Marx, F. Moulines, T. Wagner, D. Astruc, *Angew. Chem.* **1996**, *108*, 1842–1845; *Angew. Chem. Int. Ed. Engl.* **1996**, *35*, 1701–1704.

[3] a) H. Hopf, M. Kreutzer, P. G. Jones, *Chem. Ber.* **1991**, *124*, 1471–1475; b) Y. Rubin, C. B. Knobler, F. Diederich, *Angew. Chem.* **1991**, *103*, 708–710; *Angew. Chem. Int. Ed. Engl.* **1991**, *30*, 698–700; c) F. Diederich, Y. Rubin, *Angew. Chem.* **1992**, *104*, 1123–1145; *Angew. Chem. Int. Ed. Engl.* **1992**, *31*, 1101–1123.

[4] a) J. Anthony, C. B. Knobler, F. Diederich, *Angew. Chem.* **1993**, *105*, 437–440; *Angew. Chem. Int. Ed. Engl.* **1993**, *32*, 406–409; b) G. J. Palmer, S. R. Parkin, J. E. Anthony, *Angew. Chem.* **2001**, *113*, 2577–2580; *Angew. Chem. Int. Ed.* **2001**, *40*, 2509–2512.

[5] a) N. Jux, K. Holczer, Y. Rubin, *Angew. Chem.* **1996**, *108*, 2031–2034; *Angew. Chem. Int. Ed. Engl.* **1996**, *35*, 2509–2512; b) U. H. F. Bunz, V. Enkelmann, *Organometallics* **1994**, *13*, 3823–3833; c) W. Steffen, M. Laskoski, J. G. M. Morton, U. H. F. Bunz, *J. Organomet. Chem.* **2004**, *689*, 4345–4356; d) D. M. Zhang, C. A. Tessier, W. J. Youngs, *Chem. Mater.* **1999**, *11*, 3050–3057.

[6] a) M. M. Haley, S. C. Brand, J. J. Pak, *Angew. Chem.* **1997**, *109*, 863–866; *Angew. Chem. Int. Ed. Engl.* **1997**, *36*, 836–838; b) W. B. Wan, S. C. Brand, J. J. Pak, M. M. Haley, *Chem. Eur. J.* **2000**, *6*, 2044–2055; c) M. M. Haley, J. J. Pak, S. C. Brand, *Top. Curr. Chem.* **1999**, *201*, 81–130.

[7] a) U. H. F. Bunz, V. Enkelmann, *Angew. Chem.* **1993**, *105*, 1712–1714; *Angew. Chem. Int. Ed. Engl.* **1993**, *32*, 1653–1655; b) U. H. F. Bunz, G. Roidl, M. Altmann, V. Enkelmann, K. D. Shimizu, *J. Am. Chem. Soc.* **1999**, *121*, 10719–10726; c) M. Laskoski, W. Steffen, J. G. M. Morton, M. D. Smith, U. H. F. Bunz, *Angew. Chem.* **2002**, *114*, 2484–2488; *Angew. Chem. Int. Ed.* **2002**, *41*, 2378–2382; d) U. H. F. Bunz, *J. Organomet. Chem.* **2003**, *683*, 269–287.

[8] a) R. Faust, C. Weber, *J. Org. Chem.* **1999**, *64*, 2571–2573; b) F. Mitzel, S. Fitzgerald, A. Beeby, R. Faust, *Chem. Commun.* **2001**, 2596–2597; c) F. Mitzel, S. Fitzgerald, A. Beeby, R. Faust, *Chem. Eur. J.* **2003**, *9*, 1233–1241; d) S. Ott, R. Faust, *Synlett* **2004**, 1509–1512.

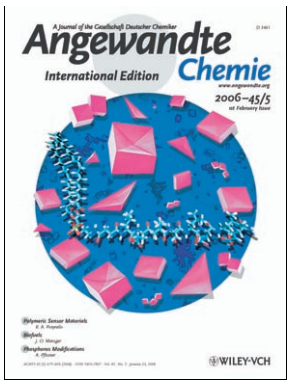
 © 2006 Wiley-VCH Verlag GmbH & Co. KGaA, Weinheim

[9] M. Ohkita, M. Kawano, T. Suzuki, T. Tsuji, *Chem. Commun.* **2002**, 3054 – 3055.
[10] a) J. E. Anthony, J. S. Brooks, D. L. Eaton, S. R. Parkin, *J. Am. Chem. Soc.* **2001**, *123*, 9482 – 9483; b) M. M. Payne, S. R. Parkin, J. E. Anthony, *J. Am. Chem. Soc.* **2005**, *127*, 8028 – 8029; c) J. E. Anthony, D. L. Eaton, S. R. Parkin, *Org. Lett.* **2002**, *4*, 15 – 18.
[11] a) R. Faust, C. Weber, V. Fiandanese, G. Marchese, A. Punzi, *Tetrahedron* **1997**, *53*, 14655 – 14670; b) R. Faust, B. Göbelt, *Tetrahedron Lett.* **1997**, *38*, 8017 – 8020; c) R. Faust, C. Weber, *Liebigs Ann.* **1996**, 1235 – 1238; d) R. Faust, B. Göbelt, C. Weber, *Synlett* **1998**, 64 – 65.
[12] C. G. Bangcuyo, M. D. Smith, U. H. F. Bunz, *Synlett* **2004**, 169 – 172.
[13] Crystallographic data for **2a**: yellow blocks, crystal dimensions $0.44 \times 0.36 \times 0.30\ mm^3$, space group $P2_1/c$ (no. 14, monoclinic), $a = 6.671(3)$ Å, $b = 26.982(9)$ Å, $c = 20.034(7)$ Å, $\beta = 92.721(15)°$, $V = 2751.0(2)$ Å^3, $Z = 4$, $\rho_{calcd} = 1.134\ g\,cm^{-3}$, $\mu(Mo_{K\alpha}) = 0.087\ mm^{-1}$. Data were measured on a Bruker SMART APEX diffractometer ($Mo_{K\alpha}$ radiation, $\lambda = 0.71073$ Å) at 150(1) K, and the structure was solved by direct methods. Of 3309 reflections collected, 2503 were unique reflections ($R_{int} = 0.1251$); data/restraints/parameters 2503/6/422; final R indices [$I > 2\sigma(I)$]: $R_1 = 0.0758$, $wR_2 = 0.1881$; R indices (all data): $R_1 = 0.0891$, $wR_2 = 0.2025$; largest diff. peak and hole: 0.329 and $-0.241\ e\,Å^{-3}$.
[14] a) J. H. Williams, *Acc. Chem. Res.* **1993**, *26*, 593 – 598; b) M. Weck, A. R. Dunn, K. Matsumoto, G. W. Coates, E. B. Lobkovsky, R. H. Grubbs, *Angew. Chem.* **1999**, *111*, 2909 – 2912; *Angew. Chem. Int. Ed.* **1999**, *38*, 2741 – 2745.
[15] Crystallographic data for **7**: irregular orange-red crystals, crystal dimensions $0.52 \times 0.40 \times 0.22\ mm^3$, space group $P2_1/c$ (no. 14, monoclinic), $a = 19.4214(9)$ Å, $b = 9.9650(5)$ Å, $c = 15.4061(7)$ Å, $\beta = 112.6820(10)°$, $V = 2751.0(2)$ Å^3, $Z = 2$, $\rho_{calcd} = 0.991\ g\,cm^{-3}$, $\mu(Mo_{K\alpha}) = 0.056\ mm^{-1}$. Data were measured on a Bruker SMART APEX diffractometer ($Mo_{K\alpha}$ radiation, $\lambda = 0.71073$ Å) at 293(1) K, and the structure was solved by direct methods. Three of the four crystallographically inequivalent *tert*-butyl groups are rotationally disordered. Of 18417 reflections collected, 3950 were unique ($R_{int} = 0.0338$); data/restraints/parameters 3950/19/370; final R indices [$I > 2\sigma(I)$]: $R_1 = 0.0518$, $wR_2 = 0.1420$; R indices (all data): $R_1 = 0.0636$, $wR_2 = 0.1536$; largest diff. peak and hole: 0.195 and $-0.185\ e\,Å^{-3}$. CCDC-275052 (**2a**) and -275053 (**7**) contain the supplementary crystallographic data for this paper. These data can be obtained free of charge from The Cambridge Crystallographic Data Centre via www.ccdc.cam.ac.uk/data_request/cif.
[16] B. Nickel, A. A. Ruth, *J. Phys. Chem.* **1991**, *95*, 2027 – 2036.
[17] a) M. Munakata, S. Kitagawa, N. Ujimaru, M. Nakamura, M. Maekawa, H. Matsuda, *Inorg. Chem.* **1993**, *32*, 826 – 832; b) S. R. Batten, K. S. Murray, *Coord. Chem. Rev.* **2003**, *246*, 103 – 130.
[18] R. A. Binstead, A. D. Zuberbühler, SPECFIT Global Analysis System, Spectrum Software Associates, Marlborough, MA 01752, **2001**.
[19] J. N. Wilson, U. H. F. Bunz, *J. Am. Chem. Soc.* **2005**, *127*, 4124 – 4125.

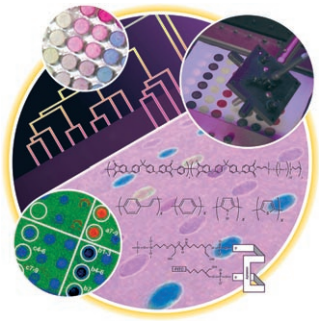
 © 2006 Wiley-VCH Verlag GmbH & Co. KGaA, Weinheim

Cover Picture

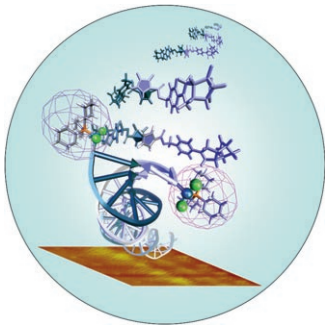
Silvia Cavalli, Daniela C. Popescu, Emily E. Tellers, Matthijn R. J. Vos, Benoît P. Pichon, Mark Overhand, Hanna Rapaport, Nico A. J. M. Sommerdijk,* and Alexander Kros*



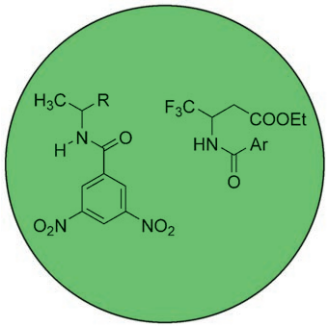
Disclosing the secret of biomineralization can lead to the construction of novel organic–inorganic hybrid materials with unique properties. N. A. J. M. Sommerdijk and A. Kros describe in their Communication on page 739 ff. the importance of the adaptability of self-organized β-sheet lipopeptide monolayers that act as templates for the developing inorganic phase of calcite. (Cover illustration by Hugo Simões shows a lipopeptide and purple "blocks" of calcite.)



Sensor Materials
Polymer-based materials for chemical and biological sensors are being intensively researched by combinatorial methods. In the Review on page 702 ff., R. A. Potyrailo describes the status of these techniques, development trends, and remaining knowledge gaps.



DNA-like Polymers
An artificial polymer prepared from bisnorbornene monomers with a rigid ferrocene bridge forms DNA-like structures. In their Communication on page 727 ff., T.-Y. Luh and co-workers report the synthesis, characterization, and modeling studies of this polymer.



Chirality
In the Communication on page 766 ff, V. A. Soloshonok reports that enantiomers with a trifluoromethyl group at a stereogenic carbon center are prone to self-disproportionation on achiral silica gel columns. Thus, the stereochemical outcome of all asymmetric reactions of fluorine-containing compounds should be reevaluated.

Contents

VIP *The following Communications have been judged by at least two referees to be "very important papers" and will be published online at www.angewandte.org soon:*

*J. Deschamp, O. Chuzel, J. Hannedouche, O. Riant**
Highly Diastereo- and Enantioselective Copper-Catalyzed Tandem Conjugated Reduction/Aldol Reaction to Ketones

J. W. Bode, R. M. Fox, K. D. Baucom*
Chemoselective Amide Ligations by Decarboxylative Condensations of *N*-Alkylhydroxylamines and α-Keto Acids

A. Oleksi, A. G. Blanco, R. Boer, I. Usón, J. Aymamí, A. Rodger, M. J. Hannon, M. Coll**
Molecular Recognition of a Three-Way DNA Junction by a Metallosupramolecular Helicate

J. E. Banham, C. R. Timmel, R. J. M. Abbott, S. M. Lea, G. Jeschke**
A New Tool for Characterization of Weak Protein–Protein Interactions: Evidence from DEER for the Trimerization of a von Willebrand Factor A Domain in Solution

B. H. Lipshutz, B. A. Frieman, A. E. Tomaso, Jr.*
Copper-in-Charcoal (Cu/C): Heterogeneous, Copper-Catalyzed Asymmetric Hydrosilylations

J. T. Shaw, J. M. Mitchell*
A Structurally Diverse Library of Polycyclic Lactams Resulting from the Systematic Placement of Proximal Functional Groups

Obituary

Henry Taube (1915–2005): Electron Transfer — *P. C. Ford, E. I. Solomon* — **692**

Books

Optical Spectroscopy in Chemistry and Life Sciences — Werner Schmidt — *reviewed by M. Volk* — **694**

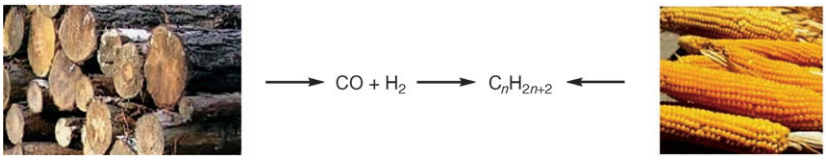
Carbon Nanotubes — M. Meyyappan — *reviewed by D. M. Guldi* — **695**

Highlights

Biofuels

J. O. Metzger* — **696 – 698**

Production of Liquid Hydrocarbons from Biomass



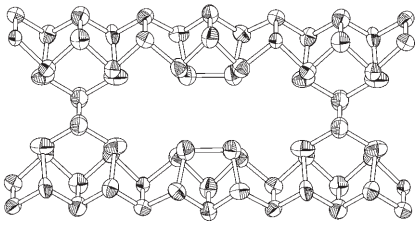
Sugar in the gas tank?! Biomass is the only practical source of renewable liquid fuel (see picture). In research worldwide, new technologies are being developed for the generation of liquid fuels from renewable resources. One example is the reduction of polyols, such as sorbitol, which can be obtained from carbohydrates, into alkanes in an aqueous-phase reforming process.

Phosphorus Modifications

A. Pfitzner* — **699 – 700**

Phosphorus Remains Exciting!

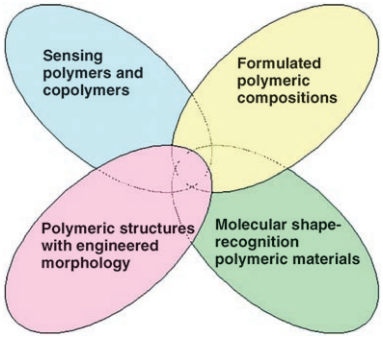
A peep down the pipe: Although phosphorus has been known for about 350 years, it still offers scope for discovery. Thus success has now been achieved in the elucidation of the crystal structure of fibrous phosphorus in which the polymeric phosphorus tubes are present as parallel tubes (see structure) contrary to Hittorf's phosphorous in which these tubes are linked cross-wise. In addition, polymers with the translational unit $[P_{12}]$ have been isolated from their copper iodide adducts.



InterScience

© 2006 Wiley-VCH Verlag GmbH & Co. KGaA, Weinheim

Reviews



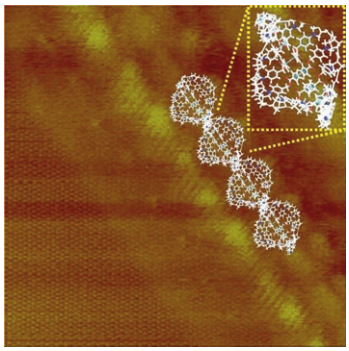
From conception to application: Combinatorial and high-throughput experimentation technologies make important contributions to research in the area of polymeric sensor materials that are based on homo- and copolymers, formulated materials, engineered structures with desired morphologies, and molecular recognition materials (see picture).

Materials Research

R. A. Potyrailo* _____ **702 – 723**

Polymeric Sensor Materials: Toward an Alliance of Combinatorial and Rational Design Tools?

Communications

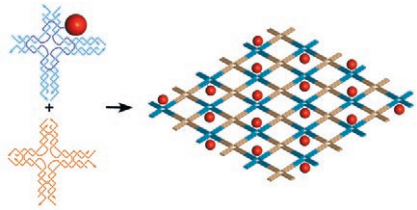


Close to original: A DNA-like double-stranded polymer is synthesized by ring-opening metathesis polymerization of a bisnorbornene derivative containing a rigid ferrocene spacer. The polymer forms helices (see picture), supercoils, and ladders, which are observable by scanning tunneling microscopy.

DNA-like Polymers

H.-C. Yang, S.-Y. Lin, H.-C. Yang, C.-L. Lin, L. Tsai, S.-L. Huang, I. W.-P. Chen, C.-H. Chen, B.-Y. Jin, T.-Y. Luh* **726 – 730**

Molecular Architecture towards Helical Double-Stranded Polymers



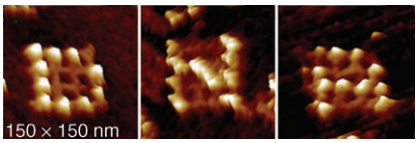
The incorporation of a single gold nanoparticle into a rationally designed DNA nanostructure and the use of the nanoparticle-bearing DNA nanostructure for the templated self-assembly of periodical nanoparticle arrays is presented. This approach allows the opportunity to control the interparticle spacings and hierarchical architectures of nanoparticles.

Nanostructures

J. Sharma, R. Chhabra, Y. Liu, Y. Ke, H. Yan* _____ **730 – 735**

DNA-Templated Self-Assembly of Two-Dimensional and Periodical Gold Nanoparticle Arrays

Decorated tiles: Self-assembling DNA nanostructures can be used to form addressable, size-controlled nanoarrays with a variety of programmed patterns. Arrays of DNA cross-shaped tiles were decorated with pixels of individual protein molecules. The letters "D", "N", and "A" on self-assembled 4×4 arrays (<80-nm square, see picture) were prepared by a minimal-depth strategy.



DNA Nanostructures

S. H. Park, C. Pistol, S. J. Ahn, J. H. Reif, A. R. Lebeck, C. Dwyer,* T. H. LaBean* _____ **735 – 739**

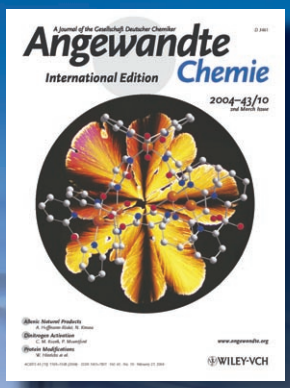
Finite-Size, Fully Addressable DNA Tile Lattices Formed by Hierarchical Assembly Procedures

For the USA and Canada:
ANGEWANDTE CHEMIE International Edition (ISSN 1433-7851) is published weekly by Wiley-VCH PO Box 191161, D 69451 Weinheim, Germany. Air freight and mailing in the USA by Publications Expediting Inc. 200 Meacham Ave., Elmont, NY 11003. Periodicals postage paid at Jamaica NY 11431. US POSTMASTER: send address changes to *Angewandte Chemie*, Wiley-VCH, 111 River Street, Hoboken, NJ 07030. Annual subscription price for institutions: US$ 5685/5168 (valid for print and electronic / print or electronic delivery); for individuals who are personal members of a national chemical society prices are available on request. Postage and handling charges included. All prices are subject to local VAT/sales tax.

© 2006 Wiley-VCH Verlag GmbH & Co. KGaA, Weinheim

The best in chemistry –

for more than a hundred years



A Journal of the Gesellschaft Deutscher Chemiker

Angewandte
International Edition **Chemie**

www.angewandte.org

1888: ***The beginning of a success story***

Constant Innovations

1962: First issue of the International Edition
1976: Graphical abstracts
1979: Cover pictures
1988: Centenary of Angewandte
1989: Routine use of color
1991: New section: Highlights
1992: Computerized editorial tracking system
1995: Internet service for readers
1998: Regular press service; full-text online
2000: New section: Essays; EarlyView: Communications available online ahead of the printed version
2001: New section: Minireviews
2002: Online submission of manuscripts
2003: Weekly publication; new section: News; new layout
2004: Backfiles (1962-1997); ManuscriptXpress: Online system for authors and referees



Angewandte's advisors...

Richard N. Zare
Stanford University

» Size does matter, as well as shape, motion, composition, and chemical complexity. I read **Angewandte Chemie** each week to learn about the latest, most exciting developments in the world of chemistry. «

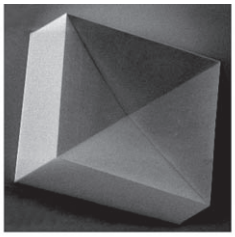
Angewandte Chemie International Edition *is a journal of the German Chemical Society (GDCh)*

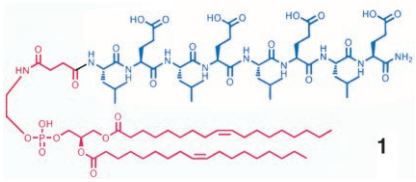
GDCh

WILEY InterScience® DISCOVER SOMETHING GREAT

WILEY-VCH

1192104_gu



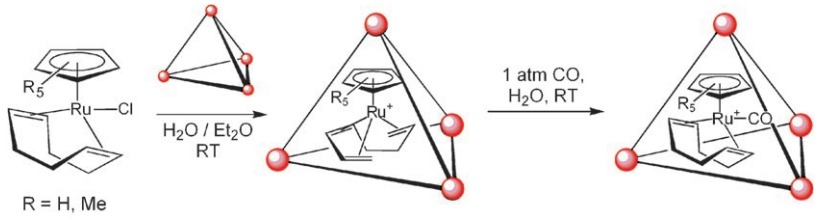


Habit forming: Amphiphilic lipopeptide **1** forms a stable monolayer with an antiparallel β-sheet conformation. This monolayer interacts with calcium ions and can be used as a biomimetic mineralization template for the formation of a new crystal habit of calcite (see SEM image). The nucleation of different crystal faces can be achieved depending on the ability of the template to adapt to the organic phase.

Biomineralization

S. Cavalli, D. C. Popescu, E. E. Tellers, M. R. J. Vos, B. P. Pichon, M. Overhand, H. Rapaport, N. A. J. M. Sommerdijk,* A. Kros* _____ **739 – 744**

Self-Organizing β-Sheet Lipopeptide Monolayers as Template for the Mineralization of $CaCO_3$



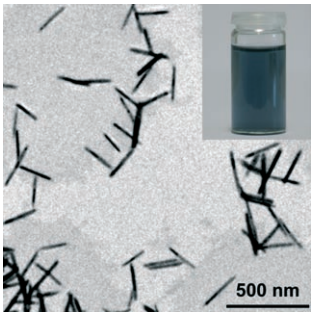
Trapped in a cage: A supramolecular metal–ligand assembly is utilized to stabilize two reactive organometallic intermediates in aqueous solution. While these organometallic complexes decompose in organic solution within hours and in the presence of water within minutes, binding into the supramolecular cage renders them inert for several weeks. Despite their stabilization, the guest molecules are still able to react stoichiometrically with CO.

Host–Guest Systems

D. Fiedler, R. G. Bergman,* K. N. Raymond* _____ **745 – 748**

Stabilization of Reactive Organometallic Intermediates Inside a Self-Assembled Nanoscale Host

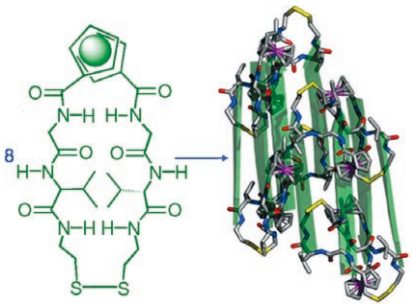
To cap it all off: Colloidally stable hydrophilic 1D CdTe nanostructures (see picture) have been easily prepared under aqueous conditions in the presence of capping thiol ligands. The present methodology shows a strong dependence on the concentration of the precursors and the molecular structure of the ligand.



Nanostructures

H. Zhang, D. Wang,* H. Möhwald _____ **748 – 751**

Ligand-Selective Aqueous Synthesis of One-Dimensional CdTe Nanostructures



Self-assembly of 1,*n*′-disubstituted ferrocene cyclopeptides leads to the first model of β barrels, a ubiquitous structural motif in proteins. The β-barrel model has eight β strands arranged almost parallel to the axis of the channel with an internal pore diameter of 8 Å.

Macrocycles

S. Chowdhury, D. A. R. Sanders, G. Schatte, H.-B. Kraatz* ____ **751 – 754**

Discovery of a Pseudo β Barrel: Synthesis and Formation by Tiling of Ferrocene Cyclopeptides

© 2006 Wiley-VCH Verlag GmbH & Co. KGaA, Weinheim

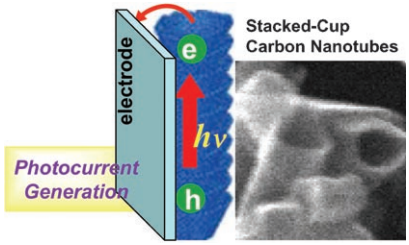
Contents

Charge Separation

T. Hasobe, S. Fukuzumi,*
P. V. Kamat* ——— **755 – 759**

Stacked-Cup Carbon Nanotubes for Photoelectrochemical Solar Cells

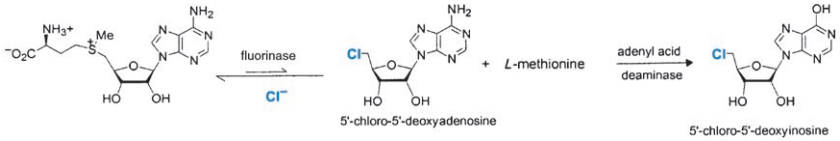
Seeing the light: Stacked-cup carbon nanotubes (SCCNTs) have been electrophoretically deposited on conducting glass electrodes from a suspension in THF by using a dc field (see picture). These SCCNT films undergo charge separation and deliver photocurrent on irradiation with visible light. The photon conversion efficiency of 17% observed with the SCCNT system is two orders of magnitude greater than those obtained with carbon nanotubes.



Enzyme Catalysis

H. Deng, S. L. Cobb, A. R. McEwan, R. P. McGlinchey, J. H. Naismith, D. O'Hagan,* D. A. Robinson, J. B. Spencer ——— **759 – 762**

The Fluorinase from *Streptomyces cattleya* Is Also a Chlorinase

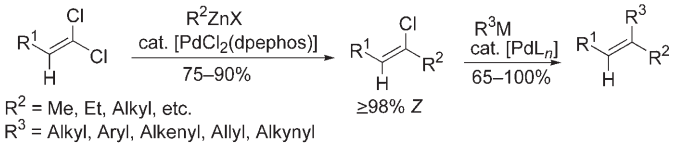


Choices choices: The fluorinase enzyme from *Streptomyces cattleya* (catalyzes the formation of a C–F bond from fluoride ions) also has the capacity to utilize a chloride ion although it has a clear preference for the fluoride ion. The enzyme mediates a nucleophilic chlorination reaction, which is an unusual mechanism for enzymatic chlorination.

Cross-Coupling

Z. Tan, E.-i. Negishi* ——— **762 – 765**

Widely Applicable Pd-Catalyzed *trans*-Selective Monoalkylation of Unactivated 1,1-Dichloro-1-alkenes and Pd-Catalyzed Second Substitution for the Selective Synthesis of *E* or *Z* Trisubstituted Alkenes



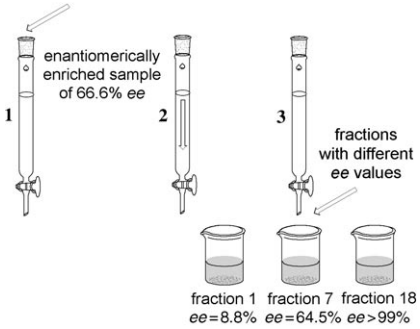
Double substitution: The first selective and widely applicable method for a stepwise alkylation of 1,1-dichloro-1-alkenes involving a cross-coupling double substitution using Pd-catalysis has been developed. This method provides an efficient and highly selective route for the synthesis of *E* or *Z* trisubstituted alkenes. dpephos = bis(*o*-diphenylphosphanylphenyl-ether).

Liquid Chromatography

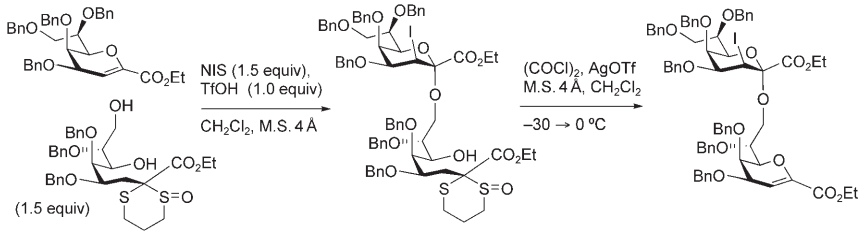
V. A. Soloshonok* ——— **766 – 769**

Remarkable Amplification of the Self-Disproportionation of Enantiomers on Achiral-Phase Chromatography Columns

A phase they're going through: The enantiomers of chiral compounds containing a trifluoromethyl group directly bonded to a stereogenic carbon center are prone to self-disproportionation on columns of achiral silica gel (see picture). Thus, all fluorine-containing chiral reagents and drugs, as well as literature data on the stereochemical outcome of asymmetric transformations involving fluorine-containing compounds, should be reevaluated.



© 2006 Wiley-VCH Verlag GmbH & Co. KGaA, Weinheim



Iodoalkoxylation (see scheme) of a glycal with an acyclic saccharide precursor leads to an efficient stereoselective synthesis of di- and tri-α(2,8)-3-deoxy-D-*manno*-2-octulosonic acid (KDO; see picture). The glycal forms α-linked 3-iodo-KDO derivatives. The opening of the pyran ring improves the reactivity of the C8 hydroxy group. NIS = *N*-iodosuccimide, Tf = triflate, M.S. = molecular sieves

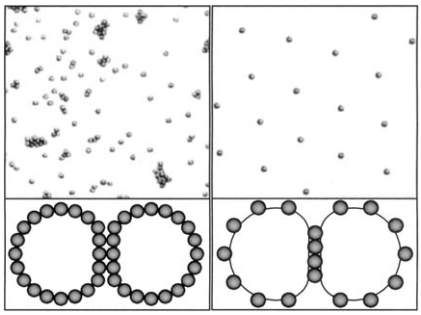
Synthetic Methods

H. Tanaka, D. Takahashi, T. Takahashi* ——— **770 – 773**

Stereoselective Synthesis of Oligo-α(2,8)-3-deoxy-D-*manno*-2-octulosonic Acid Derivatives

---

On suspension: While slightly hydrophobic silica particles can stabilize emulsions by forming dense, close-packed monolayers at the droplet surface that act as a steric barrier against coalescence, strongly repulsive particles can stabilize emulsions as a result of spontaneous particle accumulation in a dense monolayer bridging the emulsion droplets that are sparsely covered with particles (see microscopy images).

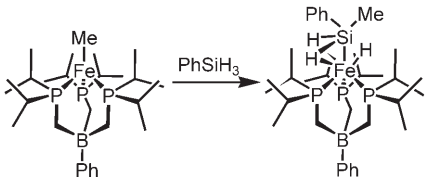


Colloids

T. S. Horozov,* B. P. Binks ——— **773 – 776**

Particle-Stabilized Emulsions: A Bilayer or a Bridging Monolayer?

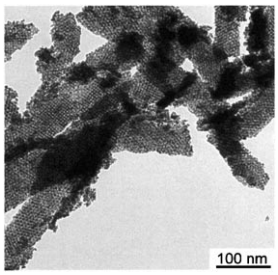
Reaction of the high-spin iron(II) alkyl complex [{PhB(CH_2P*i*Pr_2)$_3$}FeMe] with phenylsilane or mesitylsilane affords unusual diamagnetic silane adducts of the iron(II) hydride [{PhB(CH_2P*i*Pr_2)$_3$}FeH]. An η^3 bonding mode in these silane adducts has been established by NMR spectroscopy, X-ray crystallography, and DFT methods. Rapid interconversion of the hydride positions in solution via a silylene intermediate is proposed.



Silanes

C. M. Thomas, J. C. Peters* ——— **776 – 780**

An η^3-H_2SiR_2 Adduct of [{PhB(CH_2P*i*Pr_2)$_3$}Fe^{II}H]



Keeping order: Mesoporous crystalline iron oxide thin films were prepared by using special block copolymer templates. The optimized templating properties and temperature stability of the porogens allowed a crystal-to-crystal phase transition (from goethite to hematite) within the walls of the porous scaffold without disruption of the mesostructure.

Mesoporous Materials

T. Brezesinski, M. Groenewolt, M. Antonietti, B. Smarsly* ——— **781 – 784**

Crystal-to-Crystal Phase Transition in Self-Assembled Mesoporous Iron Oxide Films

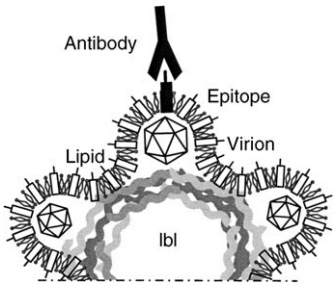
© 2006 Wiley-VCH Verlag GmbH & Co. KGaA, Weinheim

Contents

Biotechnology

M. Fischlechner, L. Toellner, P. Messner, R. Grabherr, E. Donath* ——— **784 – 789**

Virus-Engineered Colloidal Particles—A Surface Display System

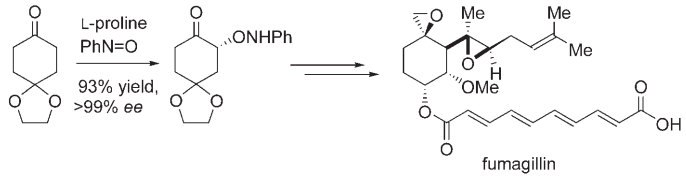


Coat of arms: Combining colloidal particles, whose surfaces have been coated with a polyelectrolyte multilayer by means of the layer-by-layer (lbl) technology, with virus surface display systems enables a variety of biological functions to be added to the particles (see picture). The proteins displayed on the colloidal surface can be monitored by using modern sorting and analytical techniques.

Total Synthesis

J. Yamaguchi, M. Toyoshima, M. Shoji, H. Kakeya, H. Osada, Y. Hayashi* ——— **789 – 793**

Concise Enantio- and Diastereoselective Total Syntheses of Fumagillol, RK-805, FR65814, Ovalicin, and 5-Demethylovalicin



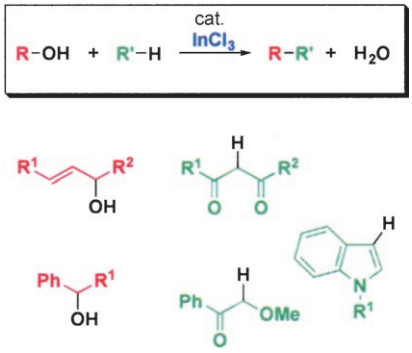
L-Proline-mediated α-aminoxylation is a key step in the enantio- and diastereoselective total syntheses of fumagillin, ovalicin, and related compounds (see scheme). These compounds contain a cyclohexane ring, two epoxides, and five or six contiguous stereogenic centers, and they display anti-angiogenesis or immunosuppressive properties.

C–C Coupling

M. Yasuda, T. Somyo, A. Baba* ——— **793 – 796**

Direct Carbon–Carbon Bond Formation from Alcohols and Active Methylenes, Alkoxyketones, or Indoles Catalyzed by Indium Trichloride

The unsalted variety: The direct coupling reaction of alcohols with active methylenes, alkoxyketones, or indoles catalyzed by $InCl_3$ proceeds without the formation of metal salts (see scheme). As H_2O is the only by-product of this system, the alkylated products are easily isolated in pure form, and the reaction is suitable for large-scale synthesis.

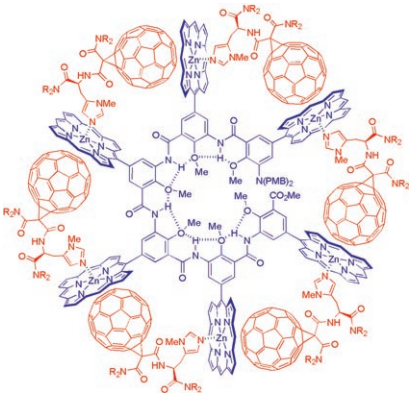


Foldamers

J.-L. Hou, H.-P. Yi, X.-B. Shao, C. Li, Z.-Q. Wu, X.-K. Jiang, L.-Z. Wu, C.-H. Tung, Z.-T. Li* ——— **796 – 800**

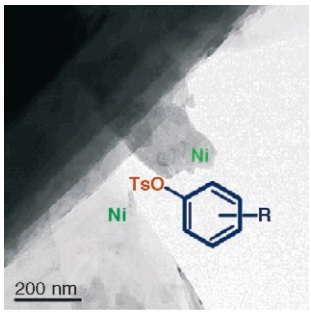
Helicity Induction in Hydrogen-Bonding-Driven Zinc Porphyrin Foldamers by Chiral C_{60}-Incorporating Histidines

High chiral amplification is exhibited by a new series of zinc porphyrin appended, hydrogen-bonded foldamers on binding with C_{60}-incorporating chiral histidines as a result of the cooperation of two discrete noncovalent interactions: zinc porphyrin/imidazole coordination and zinc porphyrin/C_{60} π–π stacking (see picture).



© 2006 Wiley-VCH Verlag GmbH & Co. KGaA, Weinheim

How would you reduce an aryl OH group? Traditionally, a palladium catalyst, a mild source of hydride, and a triflate derivative are used in solution. A more modern alternative is presented that is not only economical but heterogeneous as well. Nickel-on-graphite (Ni/C_g) is introduced as a very inexpensive catalyst that reduces aryl tosylates and mesylates with excellent functional group tolerance.

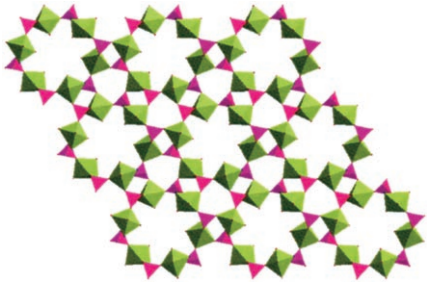


Synthetic Methods

B. H. Lipshutz,* B. A. Frieman, T. Butler, V. Kogan ——— **800 – 803**

Heterogeneous Catalysis with Nickel-on-Graphite (Ni/C_g): Reduction of Aryl Tosylates and Mesylates

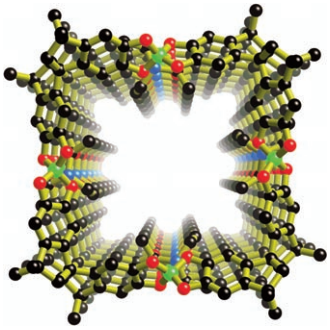
Turning over a new leaf: In the title iron phosphonate compounds, triangles and hexagons fuse together to generate a maple leaf lattice (see polyhedral representation; green Fe, purple P). This lattice is a new type of topologically frustrated antiferromagnetic network. Exotic forms of magnetic behavior are often encountered in such frustrated materials.



Iron Phosphonates

D. Cave, F. C. Coomer, E. Molinos, H.-H. Klauss, P. T. Wood* ——— **803 – 806**

Compounds with the "Maple Leaf" Lattice: Synthesis, Structure, and Magnetism of $M_x[Fe(O_2CCH_2)_2NCH_2PO_3]_6 \cdot n\,H_2O$

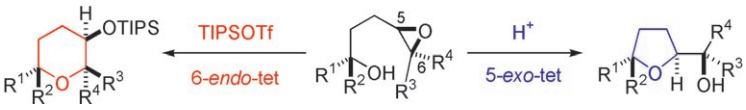


Electrostatic glue: Chiral anionic molecular squares are generated by linking four spiro-biscatecholate ligands with boron centers. Through ionic interactions and hydrogen bonding, substituted ammonium ions facilitate the stacking of the anionic squares into infinite nanotubes (see picture; green B, black C, blue N, red O).

Supramolecular Chemistry

B. F. Abrahams, D. J. Price, R. Robson* ——— **806 – 810**

Tetraanionic Organoborate Squares Glued Together by Cations To Generate Nanotubular Stacks



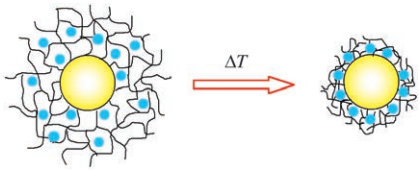
Against the rules: The switching of the usual 5-*exo* cyclizations of epoxide substrates to the 6-*endo* mode, which goes against Baldwin's rule, is demonstrated by treating bishomoepoxy alcohols with triisopropylsilyl triflate (TIPSOTf) in nitromethane (see scheme). This method is different to those previously reported in which elaborate modifications of the epoxide substrate are required to attain 6-*endo* cyclization.

Cyclizations

Y. Morimoto,* Y. Nishikawa, C. Ueba, T. Tanaka ——— **810 – 812**

Reagent-Controlled Switching of 5-*exo* to 6-*endo* Cyclizations in Epoxide Openings

Nanoreactors: Metal nanoparticles must be stabilized with carrier systems against aggregation if they are to have applications in catalysis. One such system, a thermosensitive network of poly(*N*-isopropylacrylamide) that surrounds a polystyrene core, enables control over the catalytic activity of the nanoparticles through a phase transition and leads to applications as a controllable nanoreactor.



Nanoparticles

Y. Lu, Y. Mei, M. Drechsler, M. Ballauff* ——— **813 – 816**

Thermosensitive Core–Shell Particles as Carriers for Ag Nanoparticles: Modulating the Catalytic Activity by a Phase Transition in Networks

© 2006 Wiley-VCH Verlag GmbH & Co. KGaA, Weinheim

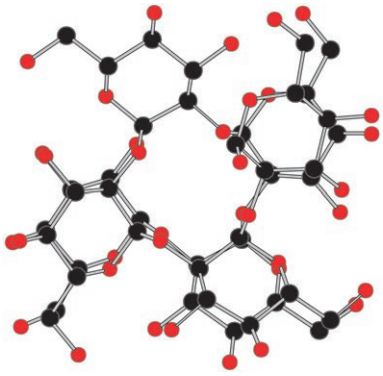
Contents

Sugar Helices

D. Fischer, E. Loos, A. Geyer* . **816 – 819**

Oligo-(1→2)-α-D-glucopyranosyl-(1→2)-β-D-fructofuranosides Form Tight Sugar Coils

The cyanobacterial oligosaccharides [α-D-Glc(1→2)]$_n$-β-D-Fru ($n \leq 9$) form right-handed helices with a tetrasaccharide repeat, a diameter of 12 Å, and a pitch of 5 Å. The vicinal α-(1→2)-glycosidic linkages stabilize this compact helix with a significant energy barrier of unwinding. Kojiheptaose ($n = 7$) with a fructofuranose terminus is the smallest biopolymer with an unfolding barrier observable by NMR spectroscopy.

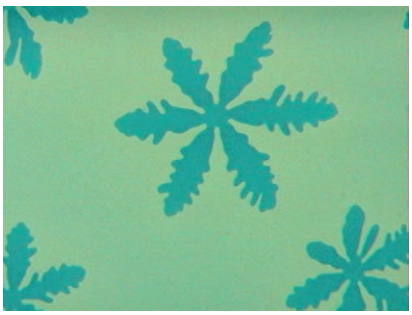


Supramolecular Chemistry

W. Pisula, M. Kastler, D. Wasserfallen, J. W. F. Robertson, F. Nolde, C. Kohl, K. Müllen* _____ **819 – 823**

Pronounced Supramolecular Order in Discotic Donor–Acceptor Mixtures

Mixing a hexa-*peri*-hexabenzocoronene (HBC) derivative and a perylene- or terrylenediimide results in the formation of complex helical arrangements in the columnar superstructures. Weak donor–acceptor interactions between the electron-rich HBC and the electron-poor rylene dye lead to strictly alternating and long-range-ordered stacks. The mixtures display homeotropic orientation on surfaces (picture shows an image from an optical microscope).

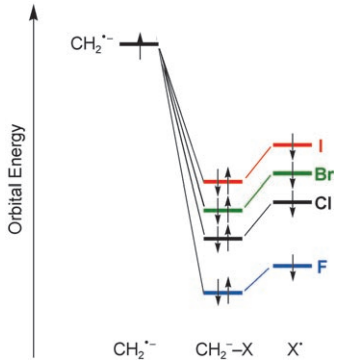


Substituent Effects

F. M. Bickelhaupt,* H. L. Hermann, G. Boche* _____ **823 – 826**

α-Stabilization of Carbanions: Fluorine Is More Effective than the Heavier Halogens

Ready steady go! The basicity of the carbanions CH_2X^- decreases continuously in the series X = F, Cl, Br, I. However, contrary to the common assumption, this occurs *not* because of the increasing α-stabilization of CH_2X^-: F stabilizes CH_2X^- *more* effectively than Cl, Br, and I (see picture). This apparent contradiction results from the usually ignored stabilization of the corresponding acids CH_3X by X.

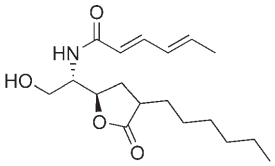


Sphingolactones

V. Wascholowski, A. Giannis* . **827 – 830**

Sphingolactones: Selective and Irreversible Inhibitors of Neutral Sphingomyelinase

Ceramide analogues which act as potent inhibitors of the neutral sphingomyelinase (N-SMase) without needing to contain reactive epoxy groups are the sphingolactones (see picture for an example). Sphingolactones are useful chemical tools for exploring the biological significance of ceramide and N-SMase in, for example, apoptosis and inflammatory processes.



The issues for January 2006 appeared online on the following dates
Issue 1: December 14. · Issue 2: December 21. · Issue 3: January 5. · Issue 4: January 11

© 2006 Wiley-VCH Verlag GmbH & Co. KGaA, Weinheim

Sources

Product and Company Directory

You can start the entry for your company in "Sources" in any issue of *Angewandte Chemie*.

If you would like more information, please do not hesitate to contact us.

Wiley-VCH Verlag – Advertising Department
Tel.: 0 62 01 - 60 65 65
Fax: 0 62 01 - 60 65 50
E-Mail: MSchulz@wiley-vch.de

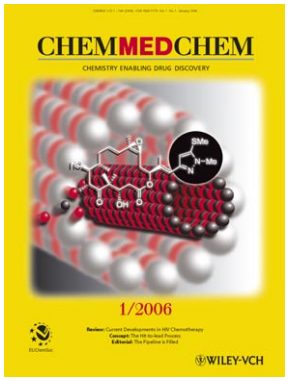
Service

Keywords ____ *832*

Authors ____ *833*

Sources ____ *A5*

Preview ____ *835*



For more information on ChemMedChem see www.chemmedchem.org

Corrigendum

The correct correspondence address for the authors of this Communication is:

State Key Laboratory of Structural Chemistry
Fujian Institute of Research on the Structure of Matter
and Graduate School of the Chinese Academy of Sciences
Fuzhou, Fujian 350002 (P. R. China)

Lanthanide–Transition-Metal Sandwich Framework Comprising $\{Cu_3\}$ Cluster Pillars and Layered Networks of $\{Er_{36}\}$ Wheels

J.-W. Cheng, J. Zhang, S.-T. Zheng, M.-B. Zhang, G.-Y. Yang* ____ **73–77**

Angew. Chem. Int. Ed. **2006**, *45*

DOI 10.1002/anie.200502917

© 2006 Wiley-VCH Verlag GmbH & Co. KGaA, Weinheim

Henry Taube (1915–2005): Electron Transfer

Henry Taube died on November 16, 2005, at his home on the campus of Stanford University. He was born on November 30, 1915, in Neudorf (Saskatchewan, Canada), the son of farmers of German descent who immigrated to Canada from the Ukraine. His first language was low German, and he occasionally referred to himself as "just a farm boy from Saskatchewan", although such a description belied a character of considerable sophistication. In an interview published in 2005,[1] he commented on the influence of his father, known to his community as "Honest Sam Taube", by saying: "*He always kept his word and that had a large influence on my life and science. Although I've often been disappointed by ideas that didn't work out, I learned not to fool myself, not to see things that weren't there, not to disregard the science.*"



Henry attended the University of Saskatchewan, where he received his BS and MS degrees, then moved to the University of California at Berkeley, where he earned his PhD in 1940 while working with William Bray. After faculty positions at Cornell University (1941–1946) and the University of Chicago (1946–1961), he moved to Stanford University, where he became Marguerite Blake Wilbur Professor in 1976. He held the Department Chair between 1972 and 1974 and from 1978 to 1979. In 1986, he became emeritus but continued to carry out active experimental studies until about five years ago.

Henry Taube was "*one of the most creative research workers of our age in the field of coordination chemistry throughout its extent,*" according to the Royal Swedish Academy of Sciences in the citation accompanying the announcement of the 1983 Nobel Prize in Chemistry.[2] He was long interested in oxidation–reduction processes beginning with studies involving ozone and hydrogen peroxide, and during the 1940s his work centered on oxidations of main-group elements by small molecules.

Henry's first publications involving transition metals appeared around 1950 and were concerned largely with defining the labilities of coordination complexes toward ligand-substitution reactions. This led directly to experiments that definitively showed that electrons could be passed between a reductant and an oxidant through a bridging ligand—the first demonstration of an inner-sphere electron-transfer reaction between two transition-metal complexes [Eq. (1)].[3] The genius of the

$$[Co(NH_3)_5Cl]^{2+} + [Cr(H_2O)_6]^{2+} + 5\,H^+ \rightarrow [Co(H_2O)_6]^{2+} + [Cr(H_2O)_5Cl]^{2+} + 5\,NH_4^+ \quad (1)$$

experiment was understanding that, as the cobalt(III) and chromium(III) complexes are "inert" to ligand substitution while the Co^{II} and Cr^{II} ions are labile, the transfer of Cl^- from one center to the other is indicative of a transition state in which the chloride ion bridges both centers at the instant of electron transfer.

Although Henry's contribution to understanding inorganic redox mechanisms was the focus of his Nobel Prize citation, the scope of his research was much broader. He was among the first to determine coordination numbers and stabilities of solvated transition-metal ions and to apply paramagnetic metal complexes as NMR shift reagents. He was also among the first to use isotopes in delving into reaction mechanisms. The synthesis in his laboratory in the 1960s of certain dinuclear ruthenium complexes—the so-called Creutz–Taube ion—led to considerable interest and debate on the nature of mixed-valence compounds. More recent studies concerned with the reactions between osmium amines and various organic ligands were at the interface between coordination and organometallic chemistry. It is difficult to give justice to the full impact of his contributions on modern chemistry and biochemistry. The press release on the 1983 Nobel Prize concluded with "*Henry Taube [...] has for thirty years been at the leading edge of research in several fields [...]*".

Henry's honors included election to the US National Academy of Sciences and the American Academy of Arts and Sciences as well as honorary memberships of the national academies of Australia, Brazil, Canada, Denmark, Finland, Hungary, India, Japan, and the UK. Besides the Nobel Prize and among a much longer list of distinguished awards, he was the recipient of the National Medal of Science in 1977, the Robert A. Welch Award in Chemistry in 1983, and the American Chemical Society Priestley Medal in 1985.

His students, postdoctoral fellows and faculty colleagues valued Henry Taube not only for his extraordinary scientific achievements but also as a really genuine person, a wonderful human being. As a research mentor, he would make several daily rounds through the laboratory to chat with students and postdoctoral researchers, and frequently began a conversation with the question, "*What's new?*". An accepted response might be a comment on politics, world affairs, cultural events, or sports, all of which Henry was comfortable discussing, although he was of course especially open to talking about the science at hand. Group members did not feel that they worked *for* him, they worked *with* him. Often an intellectual debate would be accompanied by a wager on a particular result, a bottle of wine being a common currency. His real talent was making chemistry not only challenging and stimulating to his coworkers but a lot of fun as well. He appealed to one's better instincts and made one want to live up to his expectations.

Henry's interests extended beyond the laboratory. He was an enthusiastic gardener and enjoyed listening to music and reading novels. He was a collector of different items: at one time old recordings of classical and operatic music; at other times antique blowtorches and old bottles. He was a gracious host and loved a good martini.

Several years ago, the Taube Lecture was established at Stanford to honor Henry's seminal contributions to inorganic chemistry. Henry presented the inaugural lecture, an amazingly insight-

WILEY InterScience DISCOVER SOMETHING GREAT
© 2006 Wiley-VCH Verlag GmbH & Co. KGaA, Weinheim

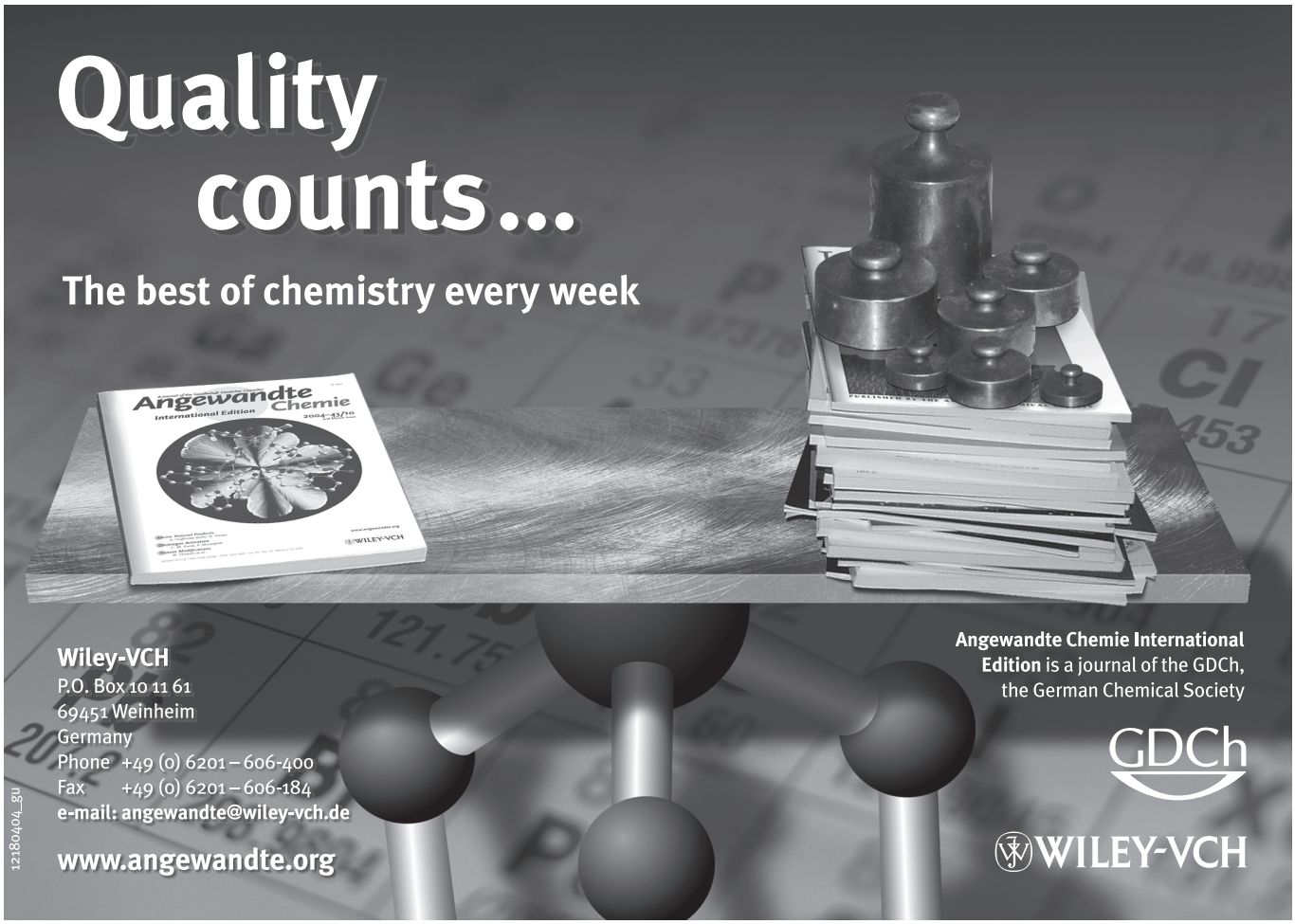
ful overview of his thoughts on back-bonding. This has been followed by annual lectures in his honor by outstanding inorganic chemists. Henry's family requests that any contributions be made to the Taube Lecture Fund.

Henry Taube was a great scientist, mentor, colleague, and person. Speaking collectively for his former co-workers, colleagues, and friends, we will miss him.

Peter C. Ford
University of California, Santa Barbara
Edward I. Solomon
Stanford University

[1] P. C. Ford, *Coord. Chem. Rev.* **2005**, *249*, 275 – 279.
[2] http://nobelprize.org/chemistry/laureates/1983/press.html.
[3] H. Taube, H. J. Myers, *J. Am. Chem. Soc.* **1954**, *76*, 2103 – 2111.

DOI: 10.1002/anie.200504564



 © 2006 Wiley-VCH Verlag GmbH & Co. KGaA, Weinheim

Biofuels

DOI: 10.1002/anie.200502895

Production of Liquid Hydrocarbons from Biomass

*Jürgen O. Metzger**

Keywords:
biomass · carbohydrates · hydrocarbons · lignocelluloses · sustainability

Dedicated to Professor Dieter Lenoir on the occasion of his 70th birthday

Research is being conducted worldwide to develop new technologies for the generation of liquid fuels from renewable resources. In this context, it was stated recently that "biomass is the only practical source of renewable liquid fuel".[1] This is of utmost importance for sustainable development.[2] Currently, biodiesel is produced by transesterification of vegetable oils[3] and ethanol by fermentation of glucose. Processes for the efficient gasification of biomass to produce CO and H_2 (synthesis gas) are being developed.[4,5] The synthesis gas can be further processed to produce methanol or liquid alkanes by Fischer–Tropsch synthesis using well-established industrial processes.

In Agenda 21, Chapter 4.20, the United Nations call for "criteria and methodologies for the assessment of environmental impacts and resource requirements throughout the full life-cycle of products and processes". A simple metric for biofuel production is the overall energy efficiency, that is, the heating value of the biofuel divided by the energy required to produce the biofuel from the respective biomass. Biodiesel production from rapeseed oil in Germany has an overall energy efficiency (not taking into account potential glycerol use) of about 1.9[6] and from soybean oil in the USA of about 3.[7]

The overall energy efficiency for the production of ethanol from corn in the USA equals about 1.1 without energy credits for coproducts.[8] However, Pimentel pointed out quite recently: "In the U.S. ethanol system, considerably more energy, including high-grade fossil fuel, is required to produce ethanol than is available in the energy ethanol output. Specifically about 29% more energy is used to produce a gallon of ethanol than the energy in a gallon of ethanol."[9] Approximately 67% of the energy required for ethanol production is consumed in the fermentation/distillation process, of which over half is used to distill ethanol from water.[8] A process without the energy-consuming distillation step would be most important.

Huber et al. have recently demonstrated that it is possible to produce light alkanes by aqueous-phase reforming (APR) of biomass-derived oxygenates such as sorbitol, which can be obtained from glucose by hydrogenation.[10,11] The production of alkanes from aqueous carbohydrate solutions would be advantageous because of the easy separation of the alkanes from water. Accordingly, it was estimated that the overall energy efficiency for alkane production from corn would be increased to approximately 2.2, assuming that this process eliminates the energy-intensive distillation step but still requires all of the remaining energy input needed for the production of ethanol from corn.[8]

Much hydrogen is needed to reduce biomass-derived oxygenates to alkanes as shown in Equation (1). The main

$$C_6H_{14}O_6 + 6\,H_2 \rightarrow C_6H_{14} + 6\,H_2O \qquad (1)$$

problem arises immediately, as with any hydrogen technology: currently, there is no energy- and cost-efficient method for making hydrogen, let alone burning it as a fuel. Importantly, it was shown in earlier work that hydrogen can be produced in a catalytic process at 500 K in water from biomass-derived polyols having a C/O stoichiometry of 1:1 such as sorbitol [Eq. (2)].[12,13] The equilibrium constant for reaction (2) per mole of CO_2 is of the order of 10^8 at 500 K, indicating that the conversion of sorbitol in the presence of water to H_2 and CO_2 is highly favorable.

$$C_6H_{14}O_6 + 6\,H_2O \rightarrow 13\,H_2 + 6\,CO_2 \qquad (2)$$

Equations (1) and (2) show that it should be feasible to generate from the molecules of the biomass in the presence of an appropriate catalyst the hydrogen needed to reduce them to alkanes, possibly in a one-pot reaction. The overall reaction (3) is an exothermic

$$19\,C_6O_6H_{14} \rightarrow 13\,C_6H_{14} + 36\,CO_2 + 42\,H_2O \qquad (3)$$

process and converts approximately 1.5 mol of sorbitol into 1 mol of hexane. About 95% of the heating value but only 30% of the mass of the biomass-derived reactant is retained in the product. The remaining 70% of the biomass is found as CO_2 and water.

Production of alkanes by aqueous-phase reforming of sorbitol takes place in a one-pot reaction by a bifunctional reaction pathway that involves first the formation of hydrogen and CO_2 on the appropriate metal catalyst (such as Pt/Al_2O_3) and the dehydration of sorbitol on a solid acid catalyst (such as silica–alumina). These initial steps are followed by hydrogenation of the dehydrated reaction intermediates on the metal catalyst. When these steps are balanced properly, the hydrogen produced in the first step is fully consumed by hydrogenation of the dehydrated reaction intermediates, which leads to

[*] Prof. Dr. J. O. Metzger
Institut für Reine und Angewandte Chemie
Carl von Ossietzky Universität Oldenburg
Postfach 2503
26111 Oldenburg (Germany)
Fax: (+49) 441-798-3618
E-mail: juergen.metzger@uni-oldenburg.de

WILEY InterScience DISCOVER SOMETHING GREAT
© 2006 Wiley-VCH Verlag GmbH & Co. KGaA, Weinheim

the overall conversion of sorbitol to alkanes plus CO_2 and water. A rationalization of the reaction pathway is given in Figure 1.

Figure 2 shows that not only hexane but also lighter alkanes from methane to pentane are formed from the C_6-polyol sorbitol. Up to 60% overall yield of alkanes was obtained. Interestingly, the moderate yield of alkanes seems to be limited mainly by the moderate yield of hydrogen. Thus, a maximum yield of 61% of hydrogen with respect to sorbitol was obtained over Pt/Al_2O_3 under optimized reaction conditions.[12] In contrast, the yield of alkanes could be increased up to 98% when hydrogen was co-fed with the aqueous sorbitol stream. Under these reaction conditions sorbitol is converted to alkanes and water without the formation of CO_2 since hydrogen is supplied externally and not produced as an intermediate in the process. However, the weight hourly space velocity seems to be rather low. The mass of 10% sorbitol solution reacted per mass of catalyst per hour was 1.3.

Consequently, high-yielding processes are feasible to produce alkanes from biomass-derived polyols such as sorbitol. A disadvantage would be that sorbitol has to be produced in two reaction steps, for example, from the renewable feedstock starch via glucose, which has to be hydrogenated and already requires one equivalent of hydrogen. It has been demonstrated that glucose can be used as substrate for the APR process to generate hydrogen. The yield of 50% hydrogen is much lower than that with sorbitol.[12] Starch has not been used as a substrate.

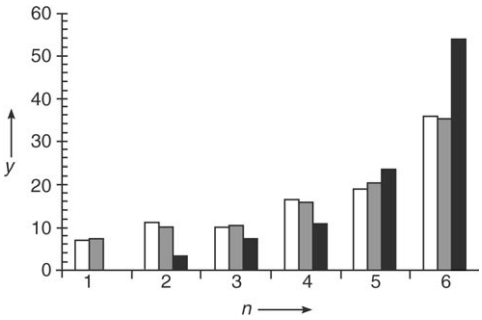


Figure 2. Selectivity y for aqueous-phase reforming of 5 wt% sorbitol over $Pt/SiO_2/Al_2O_3$ versus the number of carbon atoms n in the alkane; white: 498 K and 34.8 bar; gray: 538 K and 60.7 bar; black: co-feeding H_2 at 498 K and 34.8 bar.[10]

Another important problem is the fact that the highest alkane that can be formed by APR from sorbitol is hexane. Unfortunately, the high volatility of hexane makes this compound a poor fuel additive. Thus, the production of high-quality liquid fuels from carbohydrates requires the formation of longer-chain alkanes, which cannot be obtained from biomass-derived carbohydrates consisting predominantly of pentoses and hexoses. Huber et al.[8] proposed to solve this problem by first linking carbohydrate-derived moieties through the formation of C–C bonds before APR processing. They presented a catalytic process for the conversion of biomass-derived carbohydrates to liquid alkanes in the higher mass ranges (from C7 to C15). Furfural and hydroxylmethylfurfural (HMF), which are available from pentoses and hexoses, respectively, by dehydration are key intermediates. An efficient industrial process for the production of HMF must be developed because it is a key intermediate of a biobased chemical industry as well.[14] Furfural and HMF were transformed in two to three reaction steps by well-known reactions, for example the aldol reaction, into molecules containing C_8 to C_{15} chains. An example is given for the condensation of two equivalents of furfural with one equivalent of acetone in Figure 3. These molecules yielded higher alkanes predominantly with the chain length of the substrate by a modified process (four-phase reactor system). The normal APR process could not be used because extensive amounts of coke formed on the catalyst surface.

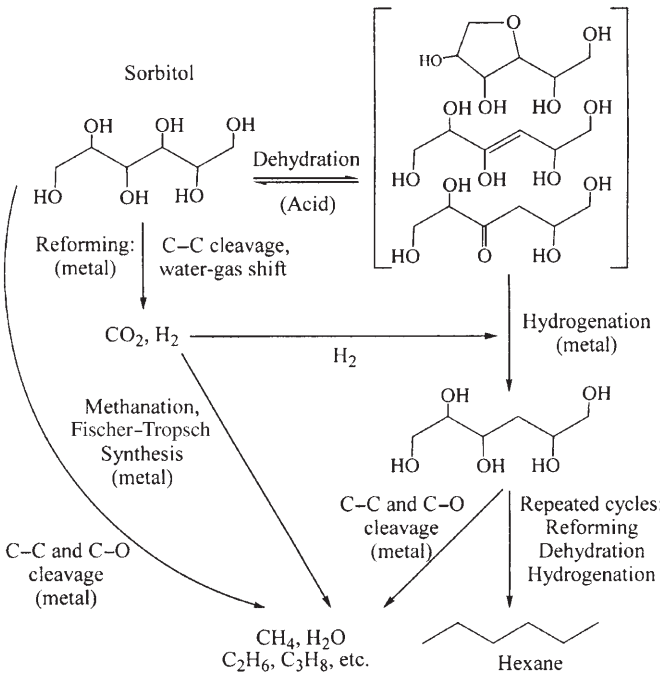


Figure 1. Reaction pathways for the production of alkanes from sorbitol in aqueous solution over a $Pt/SiO_2/Al_2O_3$ catalyst.[10]

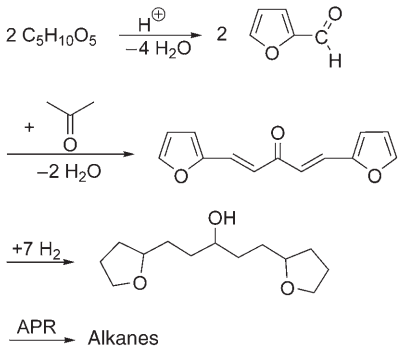


Figure 3. Synthesis of a C_{13} substrate derived from pentoses via furfural followed by aldol condensation with acetone and hydrogenation. In the modified APR process at 523–538 K, a 1% solution of hexadecane with externally supplied hydrogen yielded 79% alkanes with a selectivity of 69% C_{13} and 20% C_{12}.[8]

© 2006 Wiley-VCH Verlag GmbH & Co. KGaA, Weinheim

The encouragement of environmentally sound and sustainable use of renewable natural resources is one aim of Agenda 21 (Chapter 4.18). The main problem of the APR process seems to be that the substrates are carbohydrates and compounds derived therefrom. It is obvious that most plant-derived biomass consists of carbohydrates. But the carbohydrates needed for the APR process can be obtained only from agricultural products such as sugar cane and corn. In contrast, feedstocks used for the production of liquid fuels and hydrogen should preferably be obtained from high-productivity biomass crops that do not require synthetic fertilizers and biocides.[15] This is not the case with corn, sugar cane, and other agricultural crops. In addition, the area based energy yield per year is relatively low compared to that of the lignocellulosic biomass of wood, which can be cultivated largely without synthetic fertilizers and biocides. Unfortunately the APR process cannot be applied to lignocelluloses. Most importantly, lignocelluloses like other types of biomass can be completely gasified to synthesis gas, which can be further processed to produce methanol or liquid alkanes by the Fischer–Tropsch synthesis.[4,5] In addition to the complete gasification, the fast pyrolysis of lignocelluloses has been investigated to give a "bio-oil". This "bio-oil" can be gasified in a second reaction step to synthesis gas or can be separated to give a lignin-derived phenolic fraction. The latter can possibly used for the production of phenolic resins, while the carbohydrate-derived fraction is catalytically steam-reformed to produce hydrogen (Biorefinery[16]).[17]

Remarkably, Olah proposed recently "Beyond Oil and Gas: The Methanol Economy".[18] In the suggested methanol economy, methanol would be used as a convenient energy-storage material, a fuel, and a feedstock for the synthesis of hydrocarbons and their products. A sustainable approach to a methanol economy could be the reforestation of wasteland to supply the necessary quantities of lignocellulosic biomass[19] and their efficient conversion to synthesis gas followed by conversion to methanol and liquid hydrocarbons.[20]

Published online: December 22, 2005

[1] T. E. Bull, *Science* **1999**, *285*, 1209.

[2] M. Eissen, J. O. Metzger, E. Schmidt, U. Schneidewind, *Angew. Chem.* **2002**, *114*, 402 – 425; *Angew. Chem. Int. Ed.* **2002**, *41*, 414 – 436; J. O. Metzger, M. Eissen, *C. R. Chim.* **2004**, *7*, 569 – 581; S. Boschen, D. Lenoir, M. Scheringer, *Naturwissenschaften* **2003**, *90*, 93 – 102.

[3] G. Knothe, J. van Gerpen, J. Krahl, *The Biodiesel Handbook*, AOCS, Champaign, **2005**.

[4] D. L. Klass, *Biomass for Renewable Energy, Fuels, and Chemicals*, Academic Press, San Diego, **1998**.

[5] *Biomasse-Vergasung – Der Königsweg für eine effiziente Strom- und Kraftstoffbereitstellung?* (Ed.: Fachagentur Nachwachsende Rohstoffe e.V.), Landwirtschaftsverlag, Münster, **2004**.

[6] K. Kraus, G. Niklas, M. Tappe, *Aktuelle Bewertung des Einsatzes von Rapsöl/RME im Vergleich zu Dieselkraftstoff*, Umweltbundesamt, Berlin, **1999**.

[7] J. Sheehan, V. Camobreco, J. Duffield, M. Graboski, H. Shapouri, Life Cycle Inventory of Biodiesel and Petroleum Diesel for Use in an Urban Bus, Final Report, May 1998, U.S. Department of Energy's Office of Fuels Development and U.S. Department of Agriculture's Office of Energy, http://www.nrel.gov/docs/legosti/fy98/24089.pdf.

[8] G. W. Huber, J. N. Chheda, C. J. Barrett, J. A. Dumesic, *Science* **2005**, *308*, 1446 – 1450.

[9] D. Pimentel, *Nat. Resour. Res.* **2003**, *12*, 127 – 134.

[10] G. W. Huber, R. D. Cortright, J. A. Dumesic, *Angew. Chem.* **2004**, *116*, 1575 – 1577; *Angew. Chem. Int. Ed.* **2004**, *43*, 1549 – 1551.

[11] R. R. Davda, J. W. Shabaker, G. W. Huber, R. D. Cortright, J. A. Dumesic, *Appl. Catal. B* **2005**, *56*, 171 – 186.

[12] R. D. Cortright, R. R. Davda, J. A. Dumesic, *Nature* **2002**, *418*, 964 – 967.

[13] G. W. Huber, J. W. Shabaker, J. A. Dumesic, *Science* **2003**, *300*, 2075 – 2077.

[14] F. W. Lichtenthaler, *Acc. Chem. Res.* **2002**, *35*, 728 – 737.

[15] E. Chornet, S. Czernik, *Nature* **2002**, *418*, 928 – 929.

[16] B. Kamm, M. Kamm, *Appl. Microbiol. Biotechnol.* **2004**, *64*, 137 – 145.

[17] S. Czernik, R. French, C. Feik, E. Chornet, *Ind. Eng. Chem. Res.* **2002**, *41*, 4209 – 4215.

[18] G. A. Olah, *Angew. Chem.* **2005**, *117*, 2692 – 2696; *Angew. Chem. Int. Ed.* **2005**, *44*, 2636 – 2639.

[19] The current global energy consumption amounts to 400×10^{18} J. The average energy content of wood is 17×10^{9} J per ton. Thirty billion tons of wood per year would be required for the global energy consumption if one assumes an energy conversion efficiency of 80%, which should be possible but is not yet realized. Fast-growing tree species in moderate latitudes produce up to twenty tons of round timber per hectare and year, and tropical dry forests produce even up to 30 tons. An area of one billion hectares of tropical dry forests and 1.5 billion hectares of forests in the moderate latitudes, respectively, would be necessary to provide the global energy demand. Agricultural areas are not available. They are required to produce food for the increasing global population of up to 9 billion. The existing forests can be used only partially. However, there are sufficient areas available globally suited for reforestation. Some billion hectares of formerly wooded areas have been denuded across all continents by human activities. Currently, the desertification is advancing most rapidly. The most important transdisciplinary challenge for science and technology is to stop and reverse the desertification, to reforest the billion hectares of wasteland, and to use the lignocellulose continuously to produce methanol and hydrocarbons, which would meet the global energy demand. The contributions of chemistry to cope with this task will be of utmost importance.

[20] A. Hüttermann, J. O. Metzger, *Nachr. Chem.* **2004**, *52*, 1133 – 1138.

 © 2006 Wiley-VCH Verlag GmbH & Co. KGaA, Weinheim

DOI: 10.1002/anie.200503603

Phosphorus Modifications

Phosphorus Remains Exciting!

*Arno Pfitzner**

Keywords:
element modifications · phosphorus · structure elucidation

Today, the search for new element modifications is basically characterized by work under extreme conditions, in particular, high pressures and very often high temperatures. This situation is not surprising since the discovery of new elements and their characterization under normal conditions is more a topic of chemical-historical literature. Despite this, surprises are still found in the area of the main-group elements, such as the discovery of the fullerenes for which Curl, Kroto, and Smalley were awarded the Nobel Prize in 1996. In addition to carbon, there is another element for which new modifications can be envisaged when kinetic effects are considered, and whose phase diagram still has unexplained features: phosphorus. Initially this notion appears surprising because the element has been known for about 350 years, but when the numerous possibilities for phosphorus atoms to bond with one another are taken into account, the idea seems quite plausible.

In 1995 Böcker and Häser investigated theoretically and systematically the energetic relationships between the many plausible bonding patterns of phosphorus.[1] This work showed that, for example, a whole series of energetically equivalent possibilities exists for the formation of phosphorus polymers. Presumably this situation also explains the difficulties encountered clarifying the structures of different forms of the so-called red phosphorus. As well as the multiatom polymers, there is also tetrahedral P_4, which is a very small phosphorus molecule that is familiar to every chemist.

The discovery of phosphorus lies far in the past but now the time at last appears to be ripe for a whole series of new experimental findings. Thus Ruck et al.[2] have reported the elucidation of the crystal structure of so-called fibrous phosphorus, a form that had been postulated by Thurn und Krebs as early as 1969.[3] Apparently, depending upon the crystallization conditions, the polymeric phosphorus tubes with the familiar pentagonal cross-section are either linked crosswise with one another (Hittorf's or violet phosphorus) or parallel so that double tubes are formed (fibrous phosphorus). According to the current results of Ruck et al., Hittorf's phosphorus is formed from amorphous red phosphorus either from lead melts or by heating with small amounts of iodine. In contrast, the fibrous modification was not obtained from lead; crystals in detectable amounts are formed best in a temperature gradient of approximately 10 K at about 580 K. Ruck et al. conclude from their observations that crystallization of the tubes on the wall of the quartz glass ampoule supports the parallel orientation of the tubes. They were able to determine the crystal structure of the fibrous modification of phosphorus by X-ray diffraction on a single crystal (Figure 1) and demonstrate the clear difference from Hittorf's phosphorus by high-resolution electron diffraction imaging.

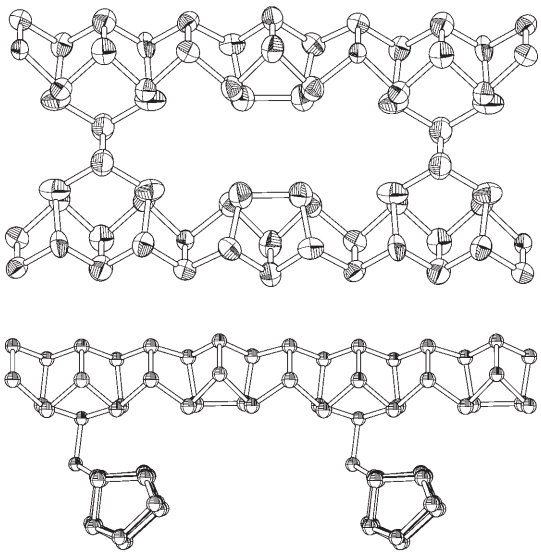


Figure 1. Linkage of the phosphorus strands in fibrous phosphorus (top; data from ref. [2]) and Hittorf's phosphorus (bottom; data from ref. [3]).

The extensive theoretical investigations in ref. [2] showed that unlike Hittorf's phosphorus, in the fibrous form the P–P bond between the strands has no π-bonding component. At this position the fibrous modification has a *trans* conformation, whereas the linkage in Hittorf's phosphorus can be regarded as a *gauche* conformation. In this way the significantly different bond lengths at this position can be explained very well. In contrast to earlier assumptions[3] the density of both forms is the same. It may be concluded from this result that the synthesis conditions are solely responsible for the formation of the one or the other modification, and not, for instance, different thermodynamic stabilities. This situation also explains the simultaneous formation of Hittorf's and fibrous phosphorus from the gas phase. Calculations confirm the energetic equivalence of both allotropes.

According to theoretical investigations by Häser it can be assumed that in addition to these two differently linked tubes of phosphorus with pentagonal cross section, the polymers with the

[*] Prof. Dr. A. Pfitzner
Institut für Anorganische Chemie
Universität Regensburg
93040 Regensburg (Germany)
Fax: (+49) 941-943-4983
E-mail: arno.pfitzner@chemie.uni-regensburg.de

© 2006 Wiley-VCH Verlag GmbH & Co. KGaA, Weinheim

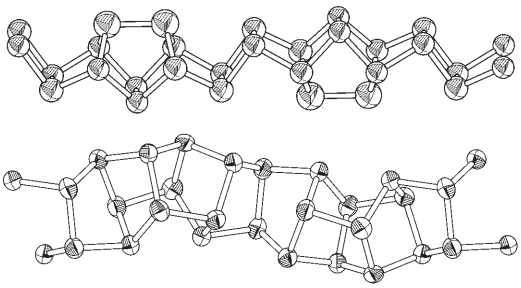


Figure 2. [P_{12}] polymers which according to data in ref. [1] represent energetically equivalent (bottom) or only slightly less favorable alternatives (top) to the pentagonal, linked tubes (from ref. [4]).

translational unit $[P_{12}]$[4] (Figure 2) isolated recently from their copper iodide adducts are also similarly energetically favorable. To date, however, it has not been possible to obtain them in crystalline form, instead, as a result of the synthesis conditions and possibly their poorly packable structures they occur as amorphous, nanoscale rods. Unlike the crystalline modifications that are obtained at relatively high temperatures, the nanoscale, unlinked phosphorus rods are formed at room temperature.

Thus within just one year a whole series of alternatives to Hittorf's phosphorus has been synthesized and characterized. By consideration of the synthetic and investigational methods it becomes clear that only by the combination of the different methods available today (e.g. high-resolution transmission electron microscopy, solid-state NMR spectroscopy, and DFT calculations) was a satisfactory characterization possible. The time is therefore ripe finally to fill in the remaining white patches on the phosphorus phase diagram.

New work on crystalline white phosphorus (P_4) has also been performed. At the beginning of the year, the crystal structure of the γ-phase of P_4 was determined by X-ray diffraction on powder samples.[5] To obtain this phase the phase-transformation behavior of P_4 during rapid temperature change was used. The structure was solved from powder data with the aid of modern methods (simulated annealing and subsequent Rietveld refinement). A more accurate analysis of γ-P_4 with theoretical methods shows that the lone electron pair on the phosphorus atoms influences the crystal structure. In this way the deviations of the structure from the an expected "ideal structure" can be explained very well by an optimization of the van der Waals forces between tetrahedral molecules.[5]

Published online: December 28, 2005

[1] S. Böcker, M. Häser, *Z. Anorg. Allg. Chem.* **1995**, *621*, 258.

[2] M. Ruck, D. Hoppe, B. Wahl, P. Simon, Y. Wang, G. Seifert, *Angew. Chem.* **2005**, *117*, 7788; *Angew. Chem. Int. Ed.* **2005**, *44*, 7616.

[3] H. Thurn, H. Krebs, *Acta Crystallogr. Sect. B* **1969**, *25*, 125.

[4] A. Pfitzner, M. F. Bräu, J. Zweck, G. Brunklaus, H. Eckert, *Angew. Chem.* **2004**, *116*, 4324; *Angew. Chem. Int. Ed.* **2004**, *43*, 4228.

[5] H. Okudera, R. E. Dinnebier, A. Simon, *Z. Kristallogr.* **2005**, *220*, 259.

 © 2006 Wiley-VCH Verlag GmbH & Co. KGaA, Weinheim

R. A. Potyrailo

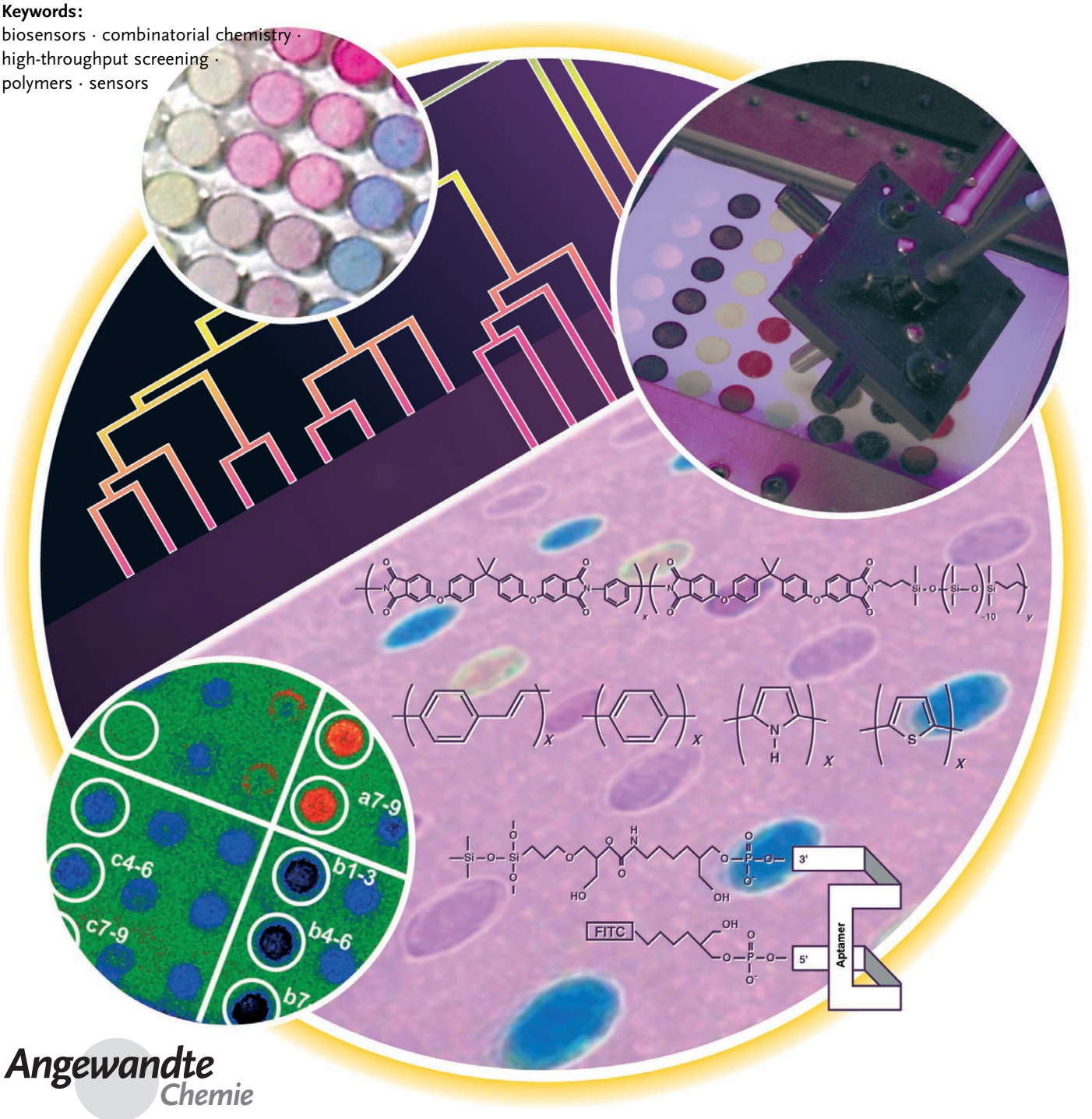
DOI: 10.1002/anie.200500828

Materials Research

Polymeric Sensor Materials: Toward an Alliance of Combinatorial and Rational Design Tools?

*Radislav A. Potyrailo**

Keywords:
biosensors · combinatorial chemistry · high-throughput screening · polymers · sensors



© 2006 Wiley-VCH Verlag GmbH & Co. KGaA, Weinheim

Increased selectivity, response speed, and sensitivity in the chemical and biological determinations of gases and liquids are of great interest. Particular attention is paid to polymeric sensor materials, which are applicable to sensors exploiting various energy transduction principles, such as radiant, electrical, mechanical, and thermal energy. Ideally, numerous functional parameters of sensor materials can be tailored to meet specific needs using rational design approaches. However, increasing the structural and functional complexity of polymeric sensor materials makes it more difficult to predict the desired properties. Combinatorial and high-throughput methods have had an impact on all areas of research on polymer-based sensor materials including homo- and copolymers, formulated materials, polymeric structures with engineered morphology, and molecular shape-recognition materials. Herein we report on the state-of-the-art, the development trends, and the remaining knowledge gaps in the area of combinatorial polymeric sensor materials design.

From the Contents

1. Introduction 703
2. Trends in the Design of Polymeric Sensor Materials 703
3. Sensing Polymers and Copolymers 706
4. Formulated Polymeric Compositions 708
5. Polymeric Structures with Engineered Morphology 712
6. Molecular Shape-Recognition Polymeric Materials 714
7. Combined Techniques 717
8. Summary and Outlook 718

1. Introduction

Designing sensors with new functionalities is currently achieved by interdisciplinary approaches. Innovative sensor ideas originate by coupling new scientific methods, such as combinatorial and high-throughput materials screening,[1,2] with micro- and nanofabrication[3–6] and microfluidics.[7] Such cross-fertilization is driven by the increasing need for chemical and biological monitoring and leads to the creation of sensors with new capabilities.[8–10] Indeed, sensors with greater sensitivity are required today to analyze ultratrace levels of environmental pollutants, pathogens in water, and low-vapor-pressure energetic materials in the air. Sensors with faster response times are desired to monitor transient in vivo events in patients. More-selective sensors are required to analyze specific proteins in vitro or to analyze ambient urban or battlefield air. For these and many other reasons, sensors are being developed based on several energy-transduction principles (radiant, electrical, mechanical, and thermal energy).[11] Polymeric sensor materials bring a desirable diversity in transduction principles for the detection of chemical and biological agents in gases and liquids.[8,9,12–14]

The design of sensor materials is a cornerstone of the sensor development process, which includes discovery, optimization, and commercialization.[5] This design of sensor materials involves many processes, such as evaluation of intrinsic properties (sensitivity, linearity, hysteresis, selectivity, shelf-life) and manufacturability (cost, tolerances), and although no phase can be skipped, the duration of certain material-development phases can be reduced by applying new research methods. The complex nature of the interactions between function and composition, preparation method, and end-use conditions of sensor materials, however, often makes their rational design for "real world" applications difficult.[10,15–19]

Combinatorial and high-throughput techniques, which are the applied use of technologies and automation for the rapid synthesis and performance screening of relatively large number of compounds, have tremendous potential in the rational design of sensor materials.[1,2] Individual techniques for the accelerated development of materials have been known for decades: combinatorial and factorial experimental designs,[20] parallel synthesis of materials on a single substrate,[21] and screening of materials for performance properties.[22] However, it took the innovative scientific vision of Joseph Hanak in 1970 to suggest a sequence of steps to fabricate, test, and analyze multiple materials for desired properties at once.[23] Hanak was truly ahead of his time and "it took 25 years for the world to realize his idea".[2]

Herein, we describe new opportunities in the research of polymer sensor materials that have been opened up through the use of combinatorial and high-throughput methods. We show that polymeric sensor materials are applicable to all known types of sensors because of their extremely broad range of capabilities. It is hoped that this critical analysis of the state-of-the-art and the trends in the development of polymeric sensor materials will stimulate further advances in this area.

[*] Dr. R. A. Potyrailo
General Electric Company
Global Research Center
Niskayuna, New York 12309 (USA)
Fax: (+1) 518-387-6972
E-mail: potyrailo@crd.ge.com

 © 2006 Wiley-VCH Verlag GmbH & Co. KGaA, Weinheim

2. Trends in the Design of Polymeric Sensor Materials

2.1. Strategies in Sensor Development

The first reports on polymeric sensor materials date back to the 1960s.[24] Since then, new knowledge of molecular interactions, micro-/nanoscale fabrication, and analytical characterization tools has resulted in innovative chemical and biological sensing concepts that have been successfully demonstrated and validated for numerous applications. If we consider the predominant mechanisms of sample–sensor recognition interactions, we can identify four broad areas of research into polymer-based sensor materials (Figure 1): 1) homo- or copolymers for sensing without any additional polymer-modification steps; 2) formulated polymers with soluble and insoluble additives; 3) engineered polymeric structures with desired morphology; 4) polymeric materials with molecular shape-induced improvement in sensor selectivity.

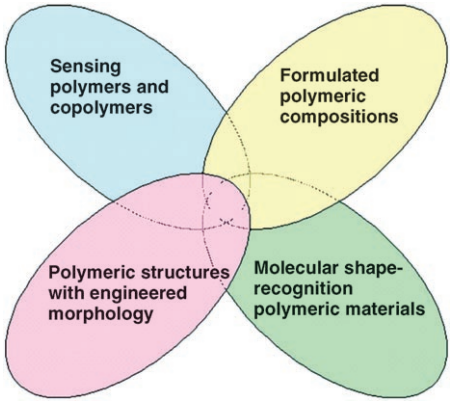


Figure 1. Development trends in the recognition of chemical and biological analytes by polymeric sensor materials.

2.2. Development Challenges

Developing sensor materials is a challenge because it requires extensive experimentation not only to achieve the best short-term performance, but also to address long-term stability, manufacturability, cost, and other practical issues. Of course, the rational design of functional materials based on prior knowledge is a very attractive approach because it avoids time-consuming synthesis and testing. However, to be quantitatively successful, rational design requires detailed knowledge regarding how materials properties relate to materials function.[25–28] This knowledge is often obtained from extensive experimental and simulation data. Some examples of the occasional successful results of the rational design of polymeric sensor materials are presented in Table 1.[27–31] Increasing structural and functional complexity of materials limits the ability to rationally define the precise requirements that lead to a desired set of properties.[32] Thus, in addition to rational design, a variety of sensing materials—such as, dyes and ionophores, biopolymers, organic and hybrid polymers, and nanomaterials—have been discovered by using detailed experimental observations or simply by chance.[33–35]

Table 1: Rational design of polymeric sensor materials.

Rational design	Required knowledge	Reference
prediction of zero-current ion fluxes in ion-selective electrode membranes for trace-level measurements	experimentally determined thermodynamic selectivities of ion-selective electrode polymer sensor membranes	[29]
hydrogen bond acidic polymers for reagent-formulated vapor sensors	experimentally identified hydrogen bond acidic polymers	[30]
cavitand receptors for selective mass sensors	experimentally identified multiple hydrogen-bonding interactions encoded in cavitand receptors	[28]
polymer matrix components for molecular imprinting	measurements of analyte binding on molecularly imprinted sensor materials	[31]
conducting polymeric composites for organic solvent vapor sensors	detailed experimental data on polymer composites characteristics	[27]

2.3. Use of Combinatorial and High-Throughput Techniques in Sensor-Materials Research

It is difficult to predict quantitatively the numerous properties of sensor materials by using rational approaches (Table 2).[15,17,36–43] Relevant descriptors must be determined to understand the details of the design of sensor materials and to establish quantitative structure–function relationships. Although applying combinatorial and high-throughput screening tools can accelerate this process, the number of purely serendipitous combinations of sensor materials components is simply too large to handle even with "ultrahigh-throughput screening". It is not feasible to synthesize all the possible molecules and apply all possible process conditions to characterize the materials function. In this case, a method that allows the most promising candidates to be shortlisted



Radislav A. Potyrailo is a project leader in GE Global Research in Niskayuna, New York and an Industrial Adjunct Professor of Chemistry at Indiana University. He holds an optoelectronics Degree from Kiev Polytechnic Institute, Ukraine and a PhD in Analytical Chemistry from Indiana University. His research focuses on functional materials, microfluidic and solid-state sensors, multivariate data analysis, and combinatorial materials science. He has published over 50 articles, four books, and holds 37 US patents. He is the initiator and a co-chair of the First Gordon Research Conference on Combinatorial Materials Science.

 © 2006 Wiley-VCH Verlag GmbH & Co. KGaA, Weinheim

Table 2: Parameters relevant to sensor applications that are difficult or impossible to quantitatively predict using rational approaches.

Parameter	Reference
chemical response of block copolymers	[36]
design of polymers for selective complexation with desired metal ions	[37]
selectivity of prospective ionophores	[38]
performance of multicomponent formulated sensor materials	[17]
quantum yield of conjugated organic polymers	[39]
emission color of conjugated organic polymers	[40]
collective effects of the preparation method of conducting polymers, their morphology, substrate/film interface, and substrate degree of hydration	[15]
activity of immobilized bioreceptors	[41]
long-term stability of enzyme-containing polymer films	[42]
sensing properties of polymeric nanofibers below 20 nm in diameter	[43]

should be applied. In materials science, focused libraries are often designed, produced, and tested in a high-throughput mode for a subset of a truly "combinatorial" space where the initial subset selection is performed by using rational and intuitive approaches.

The acceptance of combinatorial methods in materials science is illustrated by the growth of scientific publications in this area (Figure 2). The number of publications related to rational and combinatorial methods of materials design has rapidly increased over the last five years, with the growth rate of publications on the combinatorial design of materials exceeding that on the rational design of materials. We believe

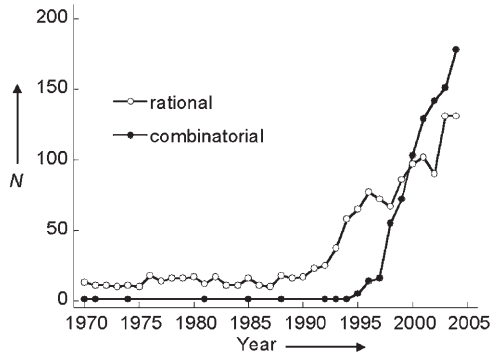


Figure 2. Number of publications associated with rational and combinatorial design of materials as determined from a SciFinder search.

that this data illustrates not only the acceptance of combinatorial methods in materials science but also the demand to apply combinatorial methods to the more rational design of materials.

Discrete and gradient sensor arrays can be applied for exploratory and focused combinatorial screening. Discrete sensor arrays (Figure 3)[10,44,45] can be produced using ink-jet printers,[46] liquid-dispensing robots,[17,47] microarrayers,[48] automated dip-coating,[49] or during in situ polymerizations.[44,50] As was first demonstrated in the early 1970s,[51] spatial gradients in polymers can be generated by varying the chemical nature of the monomers, the molecular constitution of the polymers, and their supramolecular structure or morphology. Additional parameters are needed in polymeric sensor materials to generate gradients, for example, concen-

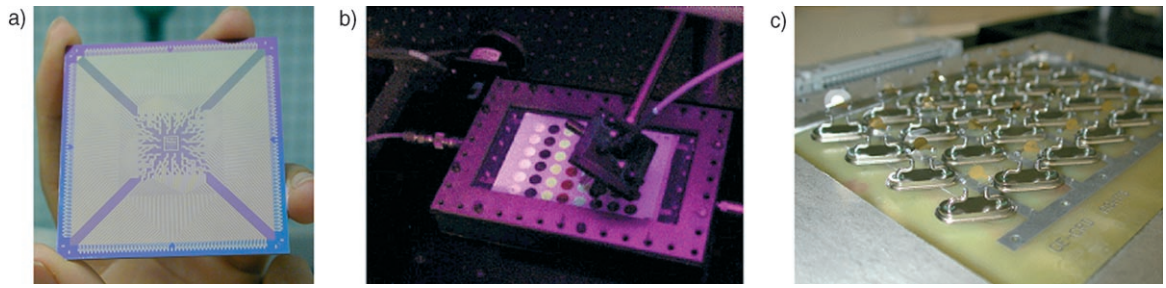


Figure 3. Examples of discrete sensor arrays: a) Interdigital 96-element electrode array for the screening of electropolymerized conductive polymers; b) 48-element array of formulated polymeric compositions for optical sensors; c) 24-element array of acoustic-wave resonant devices for the screening of vapor-sorbing polymers and copolymers. Adapted from refs. [10, 44, 45].

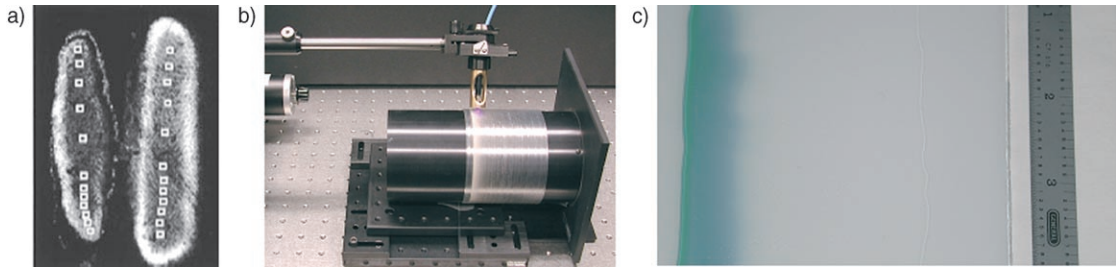


Figure 4. Examples of fabrication methods of composition-gradient arrays of sensor materials: a) In situ photopolymerization. The left stripe is a polymerized gradient array of two siloxanes A and B, beginning at the base with siloxane A alone and ending at a mixture of A and B. The right stripe contains only siloxane A as a control. b) Microextrusion. A coiled 1D polymer fiber array with a gradient concentration of a temperature-sensitive phosphor along its length. c) Solvent casting. Gradient increase in the concentration of a colorimetric reagent from right to left in a formulated optical sensor film. Adapted from refs. [16, 52].

© 2006 Wiley-VCH Verlag GmbH & Co. KGaA, Weinheim

trations of formulation additives and the film thickness. Gradient polymeric sensor arrays (Figure 4)[16,52] can be produced by solvent-assisted polymerization,[16] fiber drawing,[53] draw coating,[19,54,55] ink-jet printing,[56] and potentially by electrospinning.[57,58] If a material requires an additional curing or polymerization, it can be performed using gradient temperature heaters[59] and gradient UV curing setups.[54]

Creating a combinatorial screening process to design and optimize sensor materials involves several key process steps including planning, materials synthesis, characterization of materials response to analytes and interferences, incorporation of results into a database, data analysis, data mining, and scale-up of combinatorial leads (Figure 5). Certain aspects of

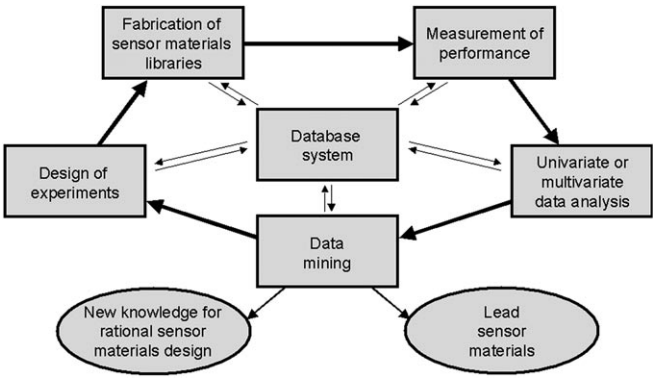


Figure 5. Key process steps in a typical combinatorial screening process map to design and optimize sensor materials.

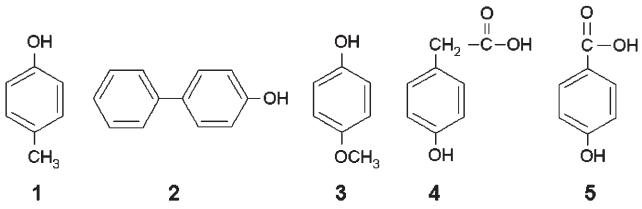
the process will depend on the throughput of materials production and performance testing. As we have shown, when screening 50–100 coating formulations per day, certain aspects of the process can be performed manually.[60] In the pharmaceutical industry automation is more desirable yet should be undertaken with caution.[61] Knowledge generated from combinatorial experimentation can significantly assist in the more rational design of sensor materials. On the other hand, for practical applications, predictive models should also adapt materials development aspects that are less straightforward for combinatorial screening, such as shelf-life and long-term stability of response.

3. Sensing Polymers and Copolymers

Unmodified homo- and copolymers are widely used for sensing. Although rational approaches exist to design polymers with desired properties, such as thermal transitions, thermal expansion coefficients, water uptake, refractive index,[26,62] the rational design of sensing polymers remains rare.

3.1. Ion-Complexing Polymers and Copolymers

The hydroxy groups of phenol units can act as effective chelating ligands for metal ions, and thus polyphenols can be used to detect ionic species in water. The enzymatic synthesis of such polymers benefits from rational polymer design.[63] The intrinsic UV fluorescence of these polymers changes upon complexation of metal ions.[64] However, the origin of the selective response to different metal ions is less well known and difficult to predict quantitatively. Such a knowledge gap inspired a detailed exploration of combinations of a variety of starting monomers to find polymers for the detection of metal ions of environmental importance. An array of fifteen phenolic homopolymers and copolymers was generated from five phenolic monomers **1**–**5** by peroxidase-



catalyzed oxidative polymerization. These polymers were tested for their response to Fe^{3+}, Cu^{2+}, Co^{2+}, and Ni^{2+} ions.[64,65] The polymers demonstrated a significant cross-sensitivity to the studied ions. Thus, combining some of these polymers into a sensor array[66] would be attractive for a more selective ion detection.

The number of polymers in such a sensor array can be significantly reduced by using cluster analysis. This data-mining tool is often used to assess the diversity of materials by compositional or performance properties and to develop structure–property relationship models.[67] For example, the results of cluster analysis of published polymer data[65] are shown in the dendrogram in Figure 6, which displays the diversity between polymers in response to Fe^{3+}, Cu^{2+}, Co^{2+}, and Ni^{2+} ions. Polymers **1**-**1** and **2**-**3** are the most similar in their response to all the studied ions, as demonstrated by a very small diversity D_1 between them. Polymers **1**-**3** and **5**-**5** show the largest diversity in their response to all the studied

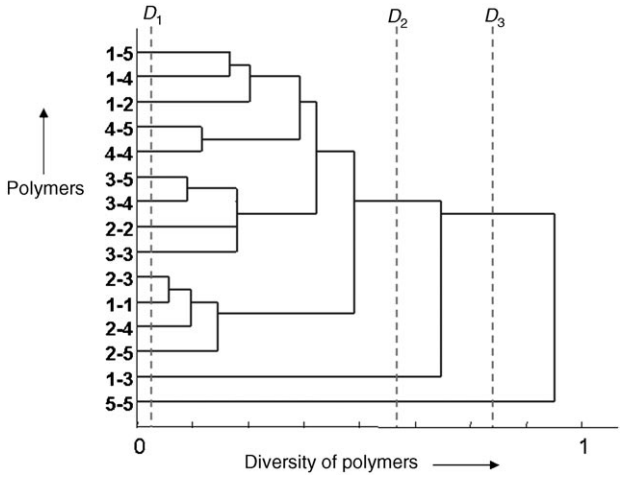


Figure 6. Results of cluster analysis that demonstrate the diversity of the response to Fe^{3+}, Cu^{2+}, Co^{2+}, and Ni^{2+} ions of a 15-member array of homo- and copolymers from the phenolic monomers **1**–**5**. D_1–D_3 are diversity levels between different polymers.

 © 2006 Wiley-VCH Verlag GmbH & Co. KGaA, Weinheim

ions, and thus there is a large diversity D_2 between the two of them and the rest of the polymers. Polymer **5**-**5** is the most different from the rest of the synthesized polymers as indicated by the largest diversity D_3. Such data-mining tools provide a means to further evaluate synthesized polymers to select the best combinations for operation in a sensor array. To confirm such diversity, it is typical to perform replicate polymerizations and characterize which properties of the resulting polymers can also affect sensor response (for example, average molecular weight, amount of residual monomers, trace contaminants). When coupled with quantitative structure–property relationships—simulation tools that incorporate molecular descriptors—new knowledge generated from combinatorial experiments may provide additional insights for the rational design of metal-ion-binding phenolic polymers.

3.2. Vapor-Sorbing Polymers and Copolymers

Several models[62,68–70] can be applied in gas sensing to calculate polymer responses. These models are based on knowledge of the polymer–analyte interaction mechanisms, including dispersion, dipole induction, dipole orientation, and hydrogen-bonding interactions,[14,71] and can be further applied to construct sensors with transducers based on electrical, radiant, mechanical, and thermal energy.[5,6,72–77] One widely accepted model is based on linear solvation energy relationships (LSER).[68] This model calculates polymer/gas partition coefficients for single vapors—this is a thermodynamic parameter which is defined as the ratio of the analyte concentration in the polymer-sensor film to the analyte concentration outside the film.[78] We applied the LSER method to select the best combination of polymers to construct a sensor array to determine isomers of dichloroethylene (DCE).[79] Figure 7 shows our LSER results of

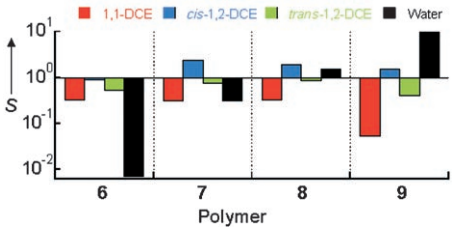
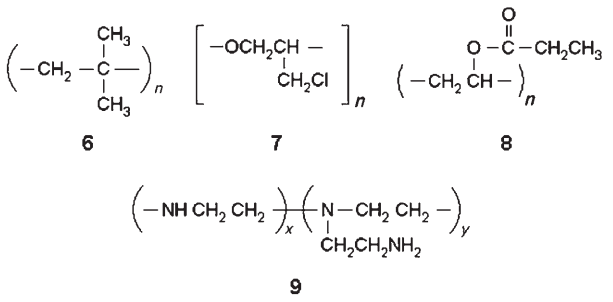


Figure 7. LSER model of the sorption response of polymers **6**–**9** to three isomers of dichloroethylene in the presence of water vapor.

response of polymers **6**–**9** to three isomers of dichloroethylene, which are chlorinated organic solvent vapors of industrial and environmental interest, and to water vapor as a potential interferent.

In practical sensors it is critical to make use of knowledge of the long-term stability of polymeric materials. The aging of base polymers and copolymers as well as their substrate-dewetting effects upon exposure to vapors is difficult or impossible to model.[26,80] To address this aspect and to improve high-throughput evaluation capabilities, we have



developed a three-level, high-throughput screening strategy to screen sensor materials for practical applications (Figure 8). In the primary screen, sensor materials were

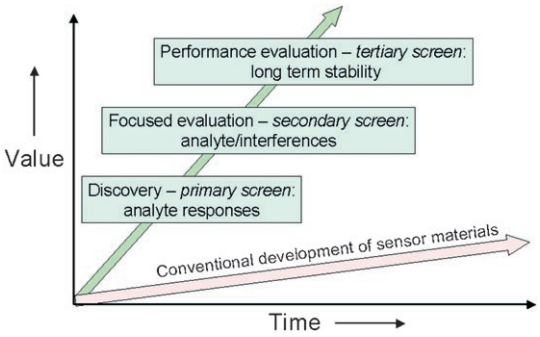
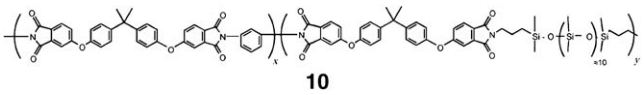


Figure 8. Three-step strategy for combinatorial screening of polymeric sensor materials.

identified for the best analyte response. In the secondary screen, materials were further selected on the basis of the diversity of their response to interferences. The tertiary screen involved evaluation of the performance of the materials under conditions mimicking the long-term application.[77] We demonstrated this approach in the development of materials for resonant sensors to detect chlorinated organic vapors at part-per-billion levels. These materials were based on the silicone-*block*-polyimide **10**[34,81] and are over 100-



times more sensitive in the detection of chlorinated organic solvent vapors than other known polymers. Several of these sensor coatings were tested in the field (Figure 9).[82]

Detailed determination of analyte–polymer interactions using combinatorial experimentation provides the foundation for a better understanding of the materials parameters that affect sensor selectivity. Our efforts in the high-throughput screening of sensing polymers for long-term stability[77] promise to supply additional experimental data for the development of more practical sensor models. Significant uncertainties and inconsistencies between polymer-materials databases have been reported that limit the accuracy of models.[70] It is possible that combinatorial screening may offer a more accurate reference experimental data because of the elimination of discrepancies between laboratory results.

© 2006 Wiley-VCH Verlag GmbH & Co. KGaA, Weinheim

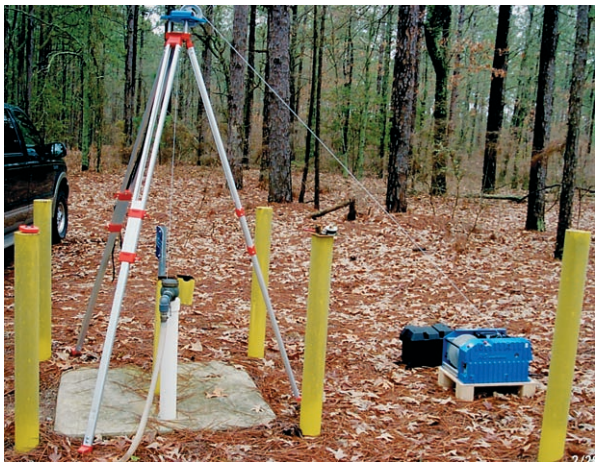


Figure 9. Application of the sensor array system in the field with sensor coatings developed using high-throughput screening. Adapted from Ref. [82].

4. Formulated Polymeric Compositions

The functionality of formulated polymeric materials can be categorized into two broad groups: 1) those expanding the range of types of species detectable by sensors and 2) those expanding the range of transduction principles with polymer materials. These sensor materials are often multicomponent formulations that necessitate careful attention to the concentration of each formulation component and the ratio of components. Table 3 shows the typical complexity of formulation compositions of polymeric coatings for ion-selective electrodes, optical sensors, sensors based on composite conductive polymers, conjugated doped polymers, and polymer-immobilized biomolecules.

4.1. Expansion of Types of Detectable Species

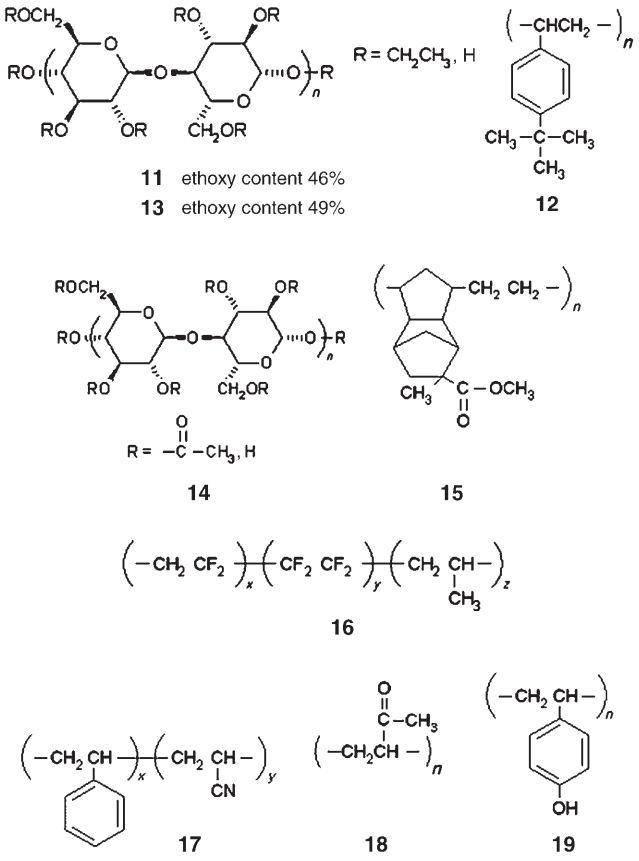
Analyte-complexing reagents are incorporated into polymers to expand the range of detectable species. Depending on the analyte–reagent response mechanism, sensors can be built based on all known detection principles (the conversion of radiant,[9,38,87] electrical,[4,38,88,89] mechanical,[90] or thermal[91,92] energy). Other reagents can also be incorporated into polymers to provide plasticization, modification of electrical conductivity, and improvement of dispersion of additives.[17,18,38,85,89,93–95] These changes in polymeric properties serve to tailor the dynamic range, selectivity, accuracy, sensitivity, long-term stability, and response time of formulated materials.[83,96,97]

Table 3: Typical formulated polymeric sensor materials.

Sensor type	Formulation components	Function	Reference
ion-selective electrode	polyurethane and terpolymer mixture of poly(vinyl chloride), poly(vinyl acetate), and poly(hydroxypropyl acrylate)	polymer matrix	[83]
	dioctyladipate and octyldiphenylphosphate	plasticizer mix	
	methylmonensin	sodium ionophore	
	potassium tetrakis-(4-chlorophenyl) borate	lipophilic anionic additive to facilitate phase transfer	
	thioether-derivatized calix[4]arene (TDC)	free ligand	
	[Ag(tdc)NO_3]	silver complex for improvement of sensor stability	
	tetrahydrofuran	common solvent	
optochemical sensor for ions	copolymer of vinyl chloride, vinyl acetate, and vinyl alcohol	polymer matrix	[84]
	combination of bis(2-ethylhexyl)sebacate and 2-nitrophenyl octyl ether	plasticizer mix	
	valinomycin	potassium ionophore	
	potassium tetrakis-(4-chlorophenyl) borate	lipophilic anionic additive to facilitate phase transfer	
	chromoionophore VI	fluorescent pH indicator	
	nile red	reference fluorophore	
	tetrahydrofuran	common solvent	
composite resistor polymeric film for vapors	poly(vinyl acetate)	polymer matrix	[85]
	carbon black	electrically conductive additive	
	hypermer surfactants	improve dispersion of carbon black	
	tetrahydrofuran	common solvent	
conducting conjugated polymer biosensor	polyaniline (electrochemically polymerized)	conducting polymer matrix	[86]
	glucose oxidase enzyme	sensor moiety	
polymeric biosensor	poly(lactic acid) and poly(glycolic acid)	polymer matrix	[41]
	recombinant human KGF antibodies	sensor moiety	
	sodium bis(ethylhexyl)sulfosuccinate	protein stabilizer in organic solvents	
	dichloromethane, chloroform, *n*-heptane, *n*-octane, *iso*-octane	solvent mixture	

 © 2006 Wiley-VCH Verlag GmbH & Co. KGaA, Weinheim

Optimizing formulated sensor materials is a cumbersome process because theoretical predictions are often negated by practical issues, such as poor solubility and compatibility of formulation components.[17,98,99] These practical issues represent significant knowledge gaps that prevent a more efficient rational design of formulated sensor materials. Thus, combinatorial methods have been used for the development of multicomponent formulated sensor materials for gaseous[17,45,100,101] and ionic[18,19,47,55,102] species. Polymer matrices[16,35,94,103] and plasticizers[94,95,104] are known to affect the response of sensors for gases and liquids, and so an automated screening was applied to determine which polymers and plasticizers were best for the construction of oxygen-sensing materials based on the [Ru(4,7-diphenylphenanthroline)] fluorophore. After the initial screening of polymer matrices **11**–**19** (Figure 10a), focused libraries were constructed with



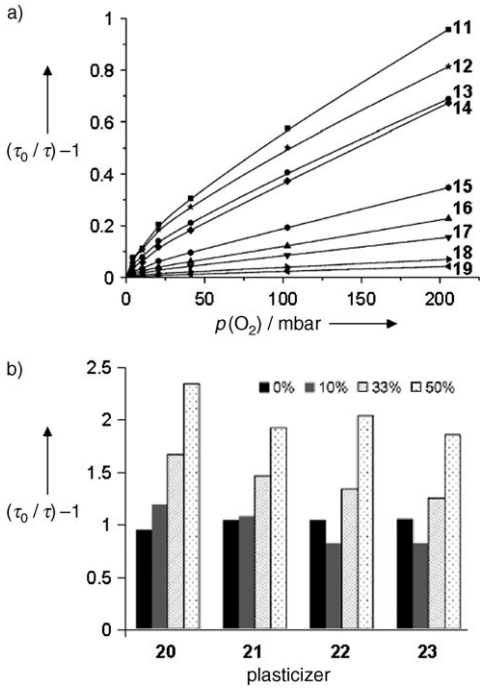
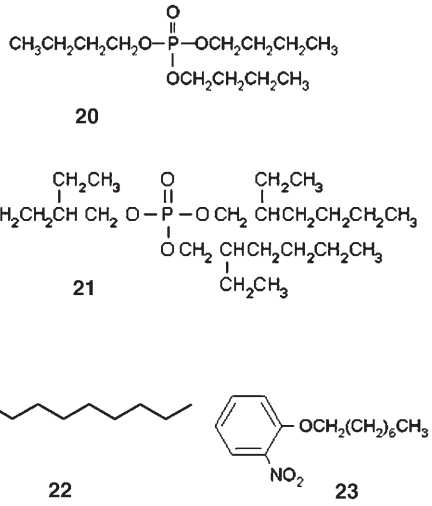


Figure 10. Results of combinatorial screening of steady-state responses of formulated materials for gas sensors. a) Stern–Volmer plots of the quenching of the [Ru(4,7-diphenylphenanthroline)]-based fluorophore in polymers **11**–**19** by oxygen, measured as changes in the fluorescence decay time. b) Effect of type and concentration of plasticizers **20**–**23** on the sensitivity of fluorescent oxygen-sensing materials in polymer **11**. Adapted from ref. [17].



plasticizers **20**–**23** to tune the sensitivity of the sensors (Figure 10b). Although the sensitivity of the sensor coatings generally increased with the plasticizer concentration as a result of an increase in the permeability of the polymer matrix to oxygen, it was unexpectedly found that incorporation of plasticizers **22** and **23** at low concentrations gave an initial decrease in the sensitivity. By combining manual and automated steps in the preparation of discrete sensor-film arrays, it was possible to reduce the time needed to screen sensor materials by a factor of at least 1000.[17]

Optimizing the concentration of the formulation components is also critical and can require a great deal of effort as a result of nonlinear relationships.[16,30,96,97,105,106] A detailed optimization of formulated sensor materials can be performed by using our recently developed approach to the preparation and analysis of libraries of sensor materials.[107] This method combines the fabrication of gradients of materials composition with recording the materials response before and after exposure to the analyte, and taking the ratio or difference of responses. Thus, if the reagent concentration

 © 2006 Wiley-VCH Verlag GmbH & Co. KGaA, Weinheim

is too low in the coating, the signal ratio or difference will be low. However, if the reagent concentration is too high in the coating, the signal ratio or difference will also be diminished relative to the optimum reagent concentration. We applied our method to optimize sensor-material formulations for the analysis of ionic and gaseous species.[107] Figure 11 shows the

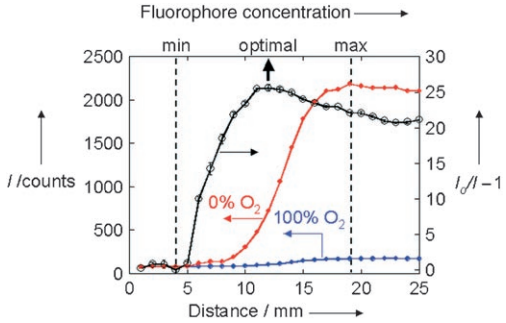
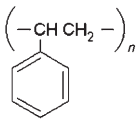


Figure 11. Optimization of formulated sensor materials using gradient films. Variation of fluorescence intensity I at different oxygen concentrations and sensitivity $I_0/I-1$ of an oxygen-sensitive film of polymer **24** with an incorporated platinum octaethylporphyrin fluorophore as a function of the distance along the sensor film; the concentration of the fluorophore follows the gradient.

optimization of the concentration of platinum octaethylporphyrin in a film of polystyrene (**24**) for the detection of oxygen by fluorescence quenching. This data demonstrates the simplicity, yet tremendous value, of such determinations for the rapid assessment of sensor-film formulations. Unlike traditional approaches to optimization of the concentration,[97,106] the new method provides a higher information density and allows time-affordable optimization of the concentration of several formulation components with tertiary and higher gradients.[107]

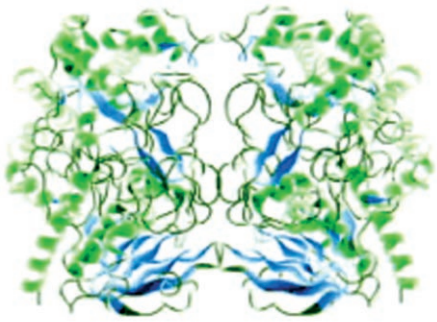


24

Formulated polymer-based sensors can incorporate not only molecular species as soluble additives, but also micro- and nanoparticles, large biomolecules (e.g., enzymes, catalytic antibodies, noncatalytic proteins, nucleic acids), whole microbial, plant and animal cells, and other insoluble functional components.[56,95,99,108–110] Similar to the function of soluble additives, the proper function of these insoluble additives strongly depends on the local microenvironment. Complex interactions with the polymer matrix and other additives further complicate the rational design of these sensors.

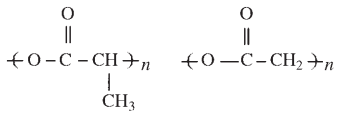
One of the greatest challenges in rational design is achieving a suitable immobilization of biomolecules to preserve their analyte-binding ability and to attain a stable and reproducible biosensor response.[41,111] The difficulties arise from the simultaneous effects of numerous parameters that include polymer hydrophilicity, partition and diffusion coefficients of substrate and products between sample solution and polymer matrix, loading and relative distribution of bioreceptors, and film thickness. Some of these parameters can be optimized meticulously by using a trial-and-error approach. Unfortunately, others (such as drying time and reagent leaching) are less straightforward to improve.[56]

The use of combinatorial screening has led to significant progress in the optimization of immobilization matrices for biosensors. In one application, amperometric glucose biosensor materials were synthesized with immobilized glucose oxidase **25**.[112] The ratio between the different starting monomers defined the pH change that was needed for



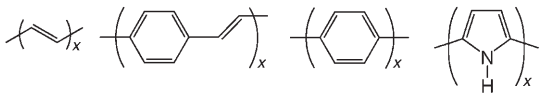
25

precipitation of the polymer and defined the properties of the deposited polymer layer. However, practical limitations once again played a major role, and only one-third of about 150 polymers made were suitable for precipitation at the desired pH value. Nevertheless, from these combinatorial screening experiments, the required types and ratio of hydrophilic and hydrophobic residues were identified.[112] In another application, multicomponent formulations based on biodegradable polymer combinations of poly(lactic acid) (**26**) and poly(glycolic acid) (**27**) with incorporated recombinant human antibodies were identified.[41]

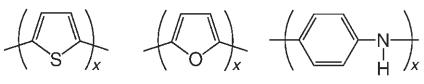


26 **27**

The application of polymers with an intrinsic conductivity also permits development of chemical and biological sensors.[15,113–116] A variety of conjugated organic monomers readily undergo polymerization and form linear polymers, for example, acetylene, *p*-phenylenevinylene, *p*-phenylene, pyrrole, thiophene, furan, and aniline form polymers **28**–**34**



28 **29** **30** **31**



32 **33** **34**

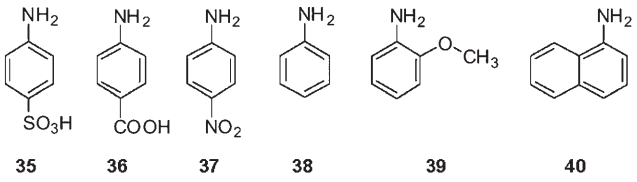
© 2006 Wiley-VCH Verlag GmbH & Co. KGaA, Weinheim

that are widely employed in sensors.[13,114,117,118] However, the resulting conducting polymers lack selectivity and are often unstable. Thus, such polymers are chemically modified to reduce these undesirable effects. Modification methods include side-group substitution of heterocycles, doping of polymers, charge compensation upon polymer oxidation by incorporation of functionalized counterions, formation of organic–inorganic hybrids, and the incorporation of various biomaterials (e.g., enzymes, antibodies, nucleic acids, cells).[109,117] Variation of the polymerization conditions (e.g., oxidation potential, oxidant, temperature, solvent, electrolyte concentration, monomer concentration) can also be employed to produce diverse polymeric materials from the same monomer because polymerization conditions affect the sensor properties of polymers (e.g., morphology, molecular weight, connectivity of monomers, conductivity, band gap).[114,119]

The gas-sensing mechanisms at work in conjugated polymers include changes in the charge-carrier density or charge-carrier mobility of polymers and conformational transitions of the polymer chain from a "compact coil" to an "extended coil". The mechanisms for ion sensing involve ion ligation with individual conjugated polymer chains, interchain interactions of conjugated polymers, conformational changes in the backbone, and shifts in the dopant–anion equilibrium within the conducting polymer.[115] Conducting polymers have been employed in sensors based on electronic,[15,116,120] radiant,[113,121] and mechanical[122] transduction. Changes in electrical conductivity and chemical potential have been employed in electronic transducers. The sensitivity of the band gap to the polymer conformation and energy migration were responsible for the optical responses in radiant transducers.[114] The surface perturbations as a result of analyte interactions with the film caused the changes in the wave velocity in mechanical transducers.[122]

Although the adsorption isotherm can in principle describe the primary interaction with the analyte, the effect of the analyte on the conductivity of the surface layer is very complex. Thus, the relationship between the measured bulk conductivity and the concentration of the analyte species is always empirical,[15] hence the need exists for extensive studies of various conducting materials to build a more fundamental understanding. Such extensive experiments are too time consuming to be practical, unless a fast method can be found. One such opportunity was demonstrated in a system designed for multiple electrochemical polymerization reactions on the individual electrodes of an electronic 96-sensor system.[44,123] Approximately 20 minutes of manual sample handling and around 14 hours of computer controlled experiment time was needed to complete all the reactions, compared to two weeks for conventional experiments.[44] This sensor system has been applied to combinatorial electrochemical copolymerization of monomer mixtures of nonconductive 3- and 4-aminobenzoic acids and conductive aniline at various ratios to study the effects of the nonconductive aniline derivatives. Incorporating different types of aminobenzoic acid in the polymer structure demonstrated quite unexpected differences in the responses of the sensor.[124]

The solubility of polymers in common solvents makes possible the deposition of materials by liquid-handling approaches.[17,46–48] However, unlike other sensor polymers, conducting polymers are often difficult to dissolve, thus limiting the methods that can be used for their deposition.[44,50,125] Conductive polymers were synthesized with improved solubility properties by using combinatorial tools. Reactions to modify polyaniline (**34**) were performed using combinatorial diazonium coupling.[126] The reaction required the coupling of a diazonium salt, produced by diazotization of one of the aromatic amines **35**–**37**, with another aromatic amine **38**, **39**, or **40**. Although **34** is insoluble in common



solvents, these modifications gave polymers that are soluble in several common solvents and which partially retained their conductivity (Figure 12). It was found that the most important factor in the conductivity change was the size of the substituent group, except for strongly electron-withdrawing

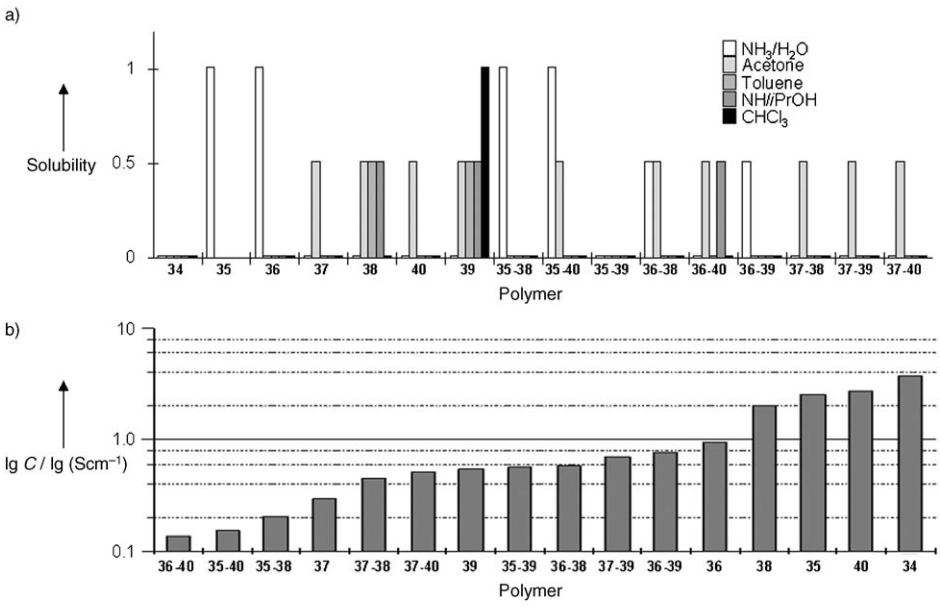


Figure 12. Properties of polyaniline **34** and its derivatives synthesized combinatorially using diazonium coupling of amines **35**–**40**. a) Solubility in common solvents (0, insoluble; 0.5, slightly soluble; 1, highly soluble). b) Electrical conductivity. Adapted from ref. [119]

© 2006 Wiley-VCH Verlag GmbH & Co. KGaA, Weinheim

groups that lowered the conductivity by electronic effects.[119,126]

4.2. Expansion of Transduction Principles

Polymers and copolymers that exhibit volume or phase transitions in response to chemical and biological stimuli permit the development of mechanical-energy transducers, such as microcantilevers and acoustic-wave devices,[69,75–77,127] and radiant-energy transducers whose function is based on white-light interferometry and ellipsometry.[73] Insoluble additives responsible for the signal transduction were incorporated into these polymers to simplify detection and even improve sensor performance. This approach expands the number of applicable transduction concepts. Transducers based on electrical energy (chemoresistors)[5,6,36,74,128–130] and transducers based on radiant energy (colloid diffraction, resonant, and holographic sensors)[131–133] can be prepared from the same base polymers. These relatively new radiant-energy transducers produce a colorimetric response in sensor films that is caused not by chemical changes of the organic reagents but rather by the physical phenomena of light interaction with metal and dielectric nanoparticles in the polymer films. Such polymeric materials were developed for the detection of ionic, non-ionic, and biological species.[131,134]

Chemiresistors are made up of nonconductive polymers and conductive additives (e.g., carbon particles,[36,85,95,135] carbon nanotubes,[130,136] and metal nanoclusters,[110]).[128] Polymer swelling induces a conductivity change in the chemiresistors. The function of conductive composite chemiresistors can be explained by classical percolation theory,[137,138] which assumes the polymer matrix to be a perfect insulator and the conductivity change of the polymer composite to be from a perfect insulator to a conductor. These requirements are not always valid in practical polymer composites employed in chemiresistors.[137,139] It was shown that the performance of chemiresistors made of conductive polymer composites depends on many parameters, including the nature of the sorbing polymer, the geometry, concentration, and dispersion uniformity of the conductive component dispersed in the nonconductive polymer.[140]

One of the most important criteria for chemiresistor materials is their selectivity to the analytes of interest.[13] New models have been reported recently for chemiresistor composites of polymer and carbon black arranged in sensor arrays.[70,141] The experimental resistivity data from seven polymers indicates that the prediction quality of the developed models was different for different polymers.[70] Combinatorial experiments were performed to identify copolymer–carbon-black formulations with improved selectivity.[36] Copolymers were synthesized by using the living-polymerization process[142] with a combination of polar and nonpolar monomers. The response of the synthesized copolymers was typically a linear combination of the responses of the two homopolymers (Figure 13a), as expected for block copolymers.[143] Unexpectedly, however, several block copolymers exhibited sorption behavior that was not a linear combination of the properties of their two homopolymers (Figure 13b).

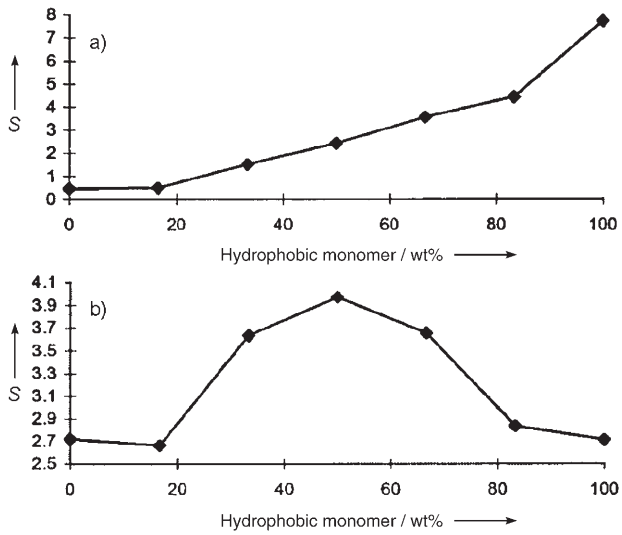


Figure 13. Electrical response of combinatorially synthesized block copolymers with variable loading of hydrophobic monomer to a) hexane and b) acetone. Adapted from Ref. [36].

Thus, this combinatorial effort demonstrated that synthesized copolymers could indeed provide a valuable approach to construct libraries of chemically diverse polymeric sensor materials.

The key feature of formulated sensor materials is the opportunity to tailor responses to a specific need. Several aspects of the development of formulated sensor materials still require attention, for example, the understanding of the compatibility of formulation components and the aging mechanisms. Our tools developed for the combinatorial screening of polymeric coatings[76,77] (see Section 3.2) can also be applied to study these phenomena in formulated coatings[144] that are applicable for sensors.

5. Polymeric Structures with Engineered Morphology

A wide variety of modifications to the surface morphology of polymers exist and can be applied to the development of sensor architectures. These modifications can be induced by many means, including lithographic and soft-lithographic techniques, replication from masters, pattern formation using self-assembly and controlled deposition, nanomachining, emulsion templating, and wetting-assisted templating.[145,146] These morphological modifications enable creation of features on the micrometer to nanometer size scales. Representative examples of sensor polymer materials of these scales are presented in Figure 14.[147–152] Although the engineered features can be as small as only several nanometers, these modifications of the polymer morphology typically have a resolution above the molecular level and should not affect molecular recognition. Approaches to polymer modification that affect molecular recognition are discussed in Section 6.

 © 2006 Wiley-VCH Verlag GmbH & Co. KGaA, Weinheim

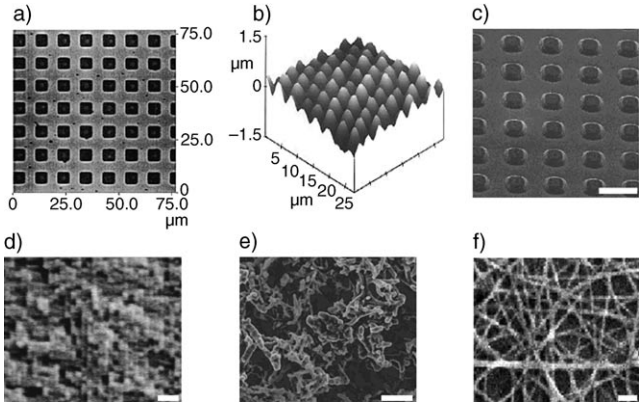


Figure 14. Patterning of polymeric sensor materials on micro- (a–c) and nano- (d–f) scales. a) Polymeric 2D grating as a chemoresponsive diffraction-based sensor;[147] b) photopolymerized sensor array on a tip of a coherent optical fiber bundle;[148] c) structured hydrogel as a chemosensor;[149] d) nanotemplated polymer replica of photonic crystals of porous silicon dioxide;[150] e) polyaniline nanofibers prepared from a formic acid/methanol mixture;[151] f) electrospun polymer nanofibers.[152] The scale bar in (c) is 10 μm, while in (d–f) the scale bars are 1 μm.

5.1. Microscale Modifications

Microscale modifications enable expansion of the transduction principles of polymeric sensors and improvement of sensor performance. Patterning of polymeric films to form a diffraction grating can be used for radiant transduction if the patterned films exhibit changes in the volume or refractive index. This concept enabled the detection of gases by radiant transduction when several types of polymer films were patterned to form 2D gratings.[147] These polymeric gratings ($5 \times 5\,\mu m$ squares separated by 5 μm, see Figure 14a) were responsive to the same vapors as nonpatterned films, and there was a good correlation between response patterns from mechanical-energy (surface-acoustic wave) and radiant-energy (chemical gratings) transducers. The good agreement between polymer-response patterns measured with two types of transducers suggested that the knowledge about vapor-sorbing polymers obtained from transducers based on mechanical energy[14,71] could be used as a guide for the design of polymeric chemoresponsive grating arrays.

Modification of the morphology of the sensor film can also lead to improvements in the performance of the sensor. Naturally, the response speed of micropatterned sensor films is expected to improve because of the preferential radial diffusion of the analyte. The first micropatterned sensors contained several thousand individual elements photodeposited as hemispheres with diameters of 2.8 μm and center-to-center spacings of 3.6 μm (Figure 14b). Radial, rather than linear, diffusion of analyte species into the micropatterned films resulted in a rapid response time of 200 and 300 ms for O_2- and pH-sensitive arrays, respectively.[148]

In addition to the increase in the response speed of the sensor, other sensor performance parameters could also be improved. In particular, known dimensional changes of hydrogels in response to ionic, non-ionic, and biological species[131,134] can be enhanced through biaxial confinement of the hydrogel by patterning, so that expansion only occurs in the unconstrained direction.[149,153] pH-sensitive hydrogel microstructures formed by photoresist lithography and dry etching with features down to 2.5 μm (Figure 14c) were almost twice as sensitive as the bulk structures.[149] In addition, the more favorable diffusion efficiency resulted in a response speed of the patterned hydrogel of several seconds, compared to an equilibrium time of 15 minutes for a reference gel structure.

Interestingly, it was also shown that microscale modifications of the polymer could affect chemical selectivity. Highly porous polymers were produced by polymerization of the continuous phase of highly dispersed emulsions.[146] Many parameters of the initial monomers and the morphology of resulting materials were varied to optimize the polymer proterties. Alterations in the stability of the emulsions controlled the void diameter from 1 to 100 μm. The optimum selection of the monomer phase and nonpolymerizable solvent, cross-link density, and surfactant combination provided a high surface area in excess of $700\,m^2\,g^{-1}$. Porous polymer membranes were soaked in a solution containing an ionophore, a lipophilic anionic additive, and a plasticizer for sensor applications. Unexpectedly, it was found that their selectivity for potassium over other cations was ten-times better than achieved with conventional cast sensor films.

5.2. Nanoscale Modifications

Nanoscale modifications provide an opportunity to develop sensor materials with previously unavailable properties. However, the reproducibility of the fabrication of such materials is challenging. Nanostructured templating is emerging as one technique to fabricate ordered sensing nanostructures in a reproducible manner. The design of sensor materials may be accelerated by evaluating the sensing performance of the template itself and then making a nanotemplated polymeric replica with a similar response. For example, films of polystyrene (**24**) were templated by porous photonic silicon dioxide crystals. After removal of the template, polymeric castings replicated the nanostructure of the master photonic crystals (Figure 14d). These nanotemplated polystyrene films were used as vapor sensors, and their response was identical to the nanotemplate.[150]

Depending on the energy-transduction mechanism and exact transducer design features, the signal intensity produced from a nanostructured film can be larger[152,154] or smaller[151] relative to that of conventional continuous films. Indeed, when nanofibers of polyaniline (**34**) were prepared from formic acid/methanol mixtures (Figure 14e), they had faster responses, but lower sensitivity than conventional thin films because of the poor contact resistance associated with nanofiber films.[151]

Electrospinning has become one of the most popular methods for nanoscale modifications of materials for sensor applications. This process is a cost-effective and efficient approach to fabricate sensor materials by using high static voltages to produce a three-dimensional interconnected network of fibers from polymer solutions or melts with diameters

© 2006 Wiley-VCH Verlag GmbH & Co. KGaA, Weinheim

down to several nanometers and surface area to volume ratios 1000-times larger than that of microfibers.[57,152] The application of almost 50 polymers in approximately 30 different solvents has been reported in polymer electrospinning.[57] The sensitivity of electrospun nanofibrous sensor films (Figure 14 f) in the detection of vapors and metal ions can be two to three orders of magnitude higher than those obtained from thin-film sensors prepared with a properly selected transduction method.[152]

Several approaches can be applied to produce different compositions of nanofibers (Figure 15). A coaxial two-capillary spinneret (Figure 15 a) was employed to generate uniform nanofibers with homogeneously blended polymeric compositions from two polymeric solutions.[155] Interestingly, these solutions were not compatible in the conventional mixing process. Several syringes can also be used at once with a single output and a controlled solution flow to fabricate multicomponent nanofibers (Figure 15 b).[156,157]

Another potentially useful approach to fabricate multicomponent composite nanofibers arrays is presented in Figure 15 c.[158] This approach utilizes an array of capillaries and can be applied for sequential or parallel electrospinning. This array of capillaries can be fabricated with diameters from hundreds of nanometers to tens of micrometers.[159] Connecting each capillary to a different solution enables nanofibers with a range of different compositions to be electrospun simultaneously to produce assemblies of nanofibers with various unique combinations of functionalities. An array of local deposits can be produced by controlling a local electrostatic field that attracts charged products to specified substrate areas. Such a field can be formed by using a dielectric mask with an array of holes to cover a conducting substrate or with an array of addressable electrodes. Applying these arrayed capillaries can increase not only the production throughput,[160] but also considerably expand the compositional and structural diversity of electrospun nanofibers and their assemblies.[159]

Fabricating nanometer-sized structures in polymeric materials can not only bring expected improvements in the performance of sensor materials (response speed and sensor sensitivity), but may result in some less-expected effects and new phenomena.[161] Since an electrified jet of a polymer solution undergoes rapid solvent evaporation during electrospinning, the polymer chains may experience an extremely strong shear force that prevents relaxation of the polymer chain. Thus, the chain conformation and crystallinity of the resulting polymer nanofibers could be different from solution-cast polymers. In addition, strong stretching forces associated with electrospinning may induce orientation of the polymer chains along the axis of a fiber.[155,162] Nanofibers of conjugated polymers aligned by electrospinning may exhibit polarized photoluminescence.[155,163] To discover new effects, it is critical to control the fabrication parameters including solution properties (viscosity, elasticity, conductivity, surface tension), instrumental variables (hydrostatic pressure in the capillary tube, electrical potential at the capillary tip, distance between the capillary tip and collecting screen), and ambient parameters (solution temperature, laboratory humidity, air velocity in the chamber).[57] The proper selection of these parameters can be performed with new experimental designs[164] by using high-throughput screening approaches.

Compared to other directions of research into polymer sensor materials, combinatorial methods are only finding use in modifying the morphology of the polymeric structures. In the near future combinatorial experimentation will likely be used to address the relationship between the size of the nanostructures and the sensitivity, selectivity, and aging of the resulting polymeric materials. The decrease in the size of the features in polymeric materials promises to bring unexpected results in sensor response. Indeed, it was recently discovered that the polyaniline/polyethylene oxide nanofibers with diameters below 15 nm were not electrically conducting but isolating.[43] New knowledge about numerous aspects of behavior of morphology-modified polymers will be generated by using high-throughput techniques.

6. Molecular Shape-Recognition Polymeric Materials

A dramatic improvement in sensor selectivity has been achieved by devising polymeric materials that recognize specific molecular shapes of chemical and biological species of interest. Such analyte–shape recognition is performed by using two broad approaches. In one approach, specific networks of molecular cavities in synthetic highly cross-linked polymers are engineered by a self-organized polymer-

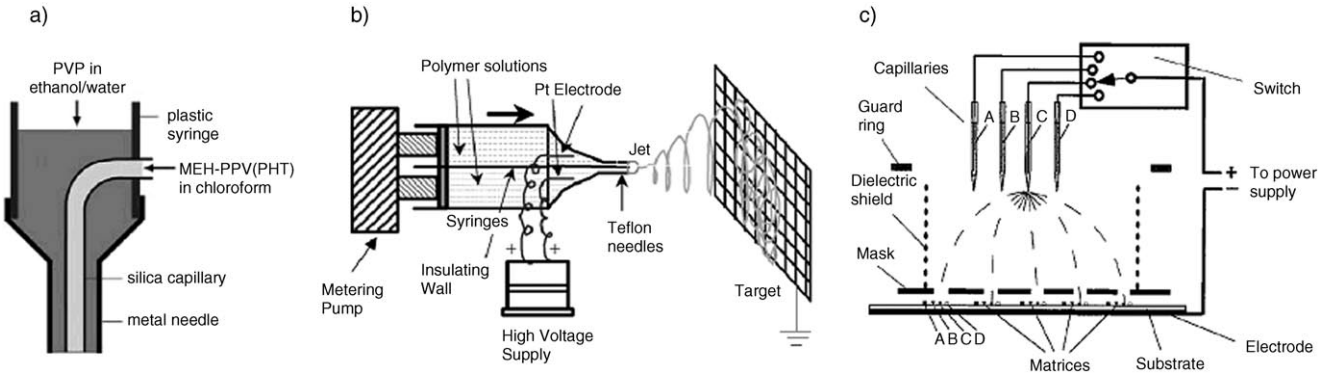


Figure 15. Electrospinning approaches adaptable for combinatorial development of polymer sensor materials. a) Coaxial two-capillary spinneret;[155] b) two-syringe system;[156] c) capillary array for sequential or parallel electrospinning.[158]

 © 2006 Wiley-VCH Verlag GmbH & Co. KGaA, Weinheim

ization to match molecular configurations of analyte species by using molecular imprinting methods.[165–170] In the second approach, desired biopolymer receptors are screened from a pool of receptor candidates using in vitro selection methods.[171,172]

6.1. Molecular Imprinting

In molecular imprinting, first demonstrated in 1972,[165] polymeric materials are synthesized by using a process that includes selection of starting components, formation of a functional monomer–template complex in solution, polymerization, and template removal.[170] Intermolecular forces that develop during polymerization between the template molecule, functional monomer, and developing polymer matrix are responsible for creating a microenvironment for the imprint. The resulting polymer network contains synthetic receptors that are complementary in size, shape, and functional group orientation to the imprint template. Typical templates are small organic molecules, ions, biological molecules, and organisms. The molecularly imprinted polymers can be used in the gas phase as well as in inorganic or organic solvents.[173] The binding sites of molecularly imprinted polymers[167] can have affinities and selectivities approaching those of antibodies.

Cation sensing by molecularly imprinted polymers is achieved by employing cavities equipped with complexing groups arranged to match the charge, coordination number, coordination geometry, and size of a target cation. Anion-complexing molecularly imprinted polymers often employ a coordinatively captured metal ion that has a large affinity for the anion and provides a detectable signature for anion binding.[168] Neutral analytes can be sensed in liquids through steric and hydrophobic/hydrophilic interactions. Polymeric biosensors can be prepared by employing epitope imprinting to create binding sites for peptides and proteins.[174] The detection of gases is less established and relies on a change in the physicochemical properties of molecularly imprinted polymers through selective enrichment by an analyte and formation of a weak complex.[169] Besides sensors, other applications of molecularly imprinted polymers include selective solid-phase extraction for quantitative analysis, sorbents for preparative separations, screening tools in drug discovery, and enzyme-like catalysis.[175]

Numerous parameters affect the selectivity and capacity of molecularly imprinted polymers. The short-range molecular organization at the receptor site is provided by the complementary interactions (hydrogen bonding, electrostatic, and/or van der Waals forces) between the template and the functional and cross-linking monomers. Polymer morphology and selectivity are also affected by the stoichiometry and concentration of the template and monomers. Furthermore, the solvent (porogen) used in the polymerization process not only mediates interactions between functional groups and the template molecule but also determines the timing of the phase separation during polymerization that affects the morphology and porosity of the polymer. The timing of phase separation is also influenced by the polymerization temperature, and the selectivity and capacity of the final polymer are affected by the temperature dependence of the equilibrium between the functional monomers and template. Many parameters that influence the properties of the materials at different length scales significantly hinder the development of detailed design rules,[175] although there are a few reports that discuss rational design efforts.[31,176] Thus high-throughput and combinatorial synthesis techniques,[173,175,177] as well as computational techniques such as chemometric multivariate optimizations,[178] thermodynamic treatment of recognition phenomena,[179] molecular modeling,[180] and conformational analysis[181] have been applied to accelerate development of molecularly imprinted polymers.

Traditional analytical methods to evaluate molecularly imprinted polymers include chromatography, scintillation counting, and mass spectrometry. The analysis of combinatorially synthesized molecularly imprinted polymers is preferably performed with instrumentation designed for combinatorial screening[182] with partial automation.[175,183] Thus similar data quality can be obtained in much shorter times (Figure 16).

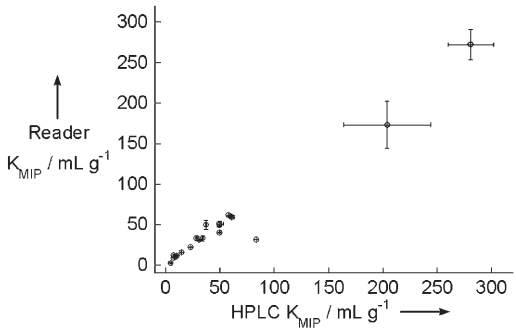
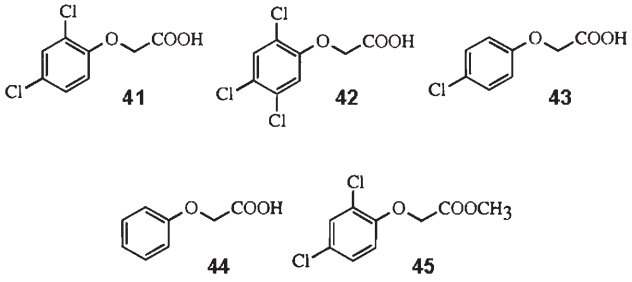


Figure 16. Correlation between the partition coefficients K of the template obtained from the fast parallel assessment of a molecularly imprinted acrylate-based polymer library with a UV microplate reader and a serial analysis by conventional HPLC. Adapted from Ref. [183].

High-throughput screening of molecularly imprinted polymers by optical methods attracts a great deal of research effort because of the possibility of screening highly dense polymer libraries and the potential to apply the same detection principles in radiant sensors. Optical imaging of a molecularly imprinted polymer library was performed in an analogous manner to competitive enzyme immunoassays.[184] The antigen 2,4-dichlorophenoxyacetic acid (**41**) was labeled with tobacco peroxidase, and the chemoluminescence reaction of luminol was used for detection. Microtiter plates were



© 2006 Wiley-VCH Verlag GmbH & Co. KGaA, Weinheim

coated with polymeric microspheres generated from 4-vinylpyridine as the functional monomer and tri(methylol)propane trimethacrylate as the cross-linker imprinted with **41**. Figure 17a shows a typical image of a competitive assay in a 96-well plate. A calibration curve for **41** was obtained by

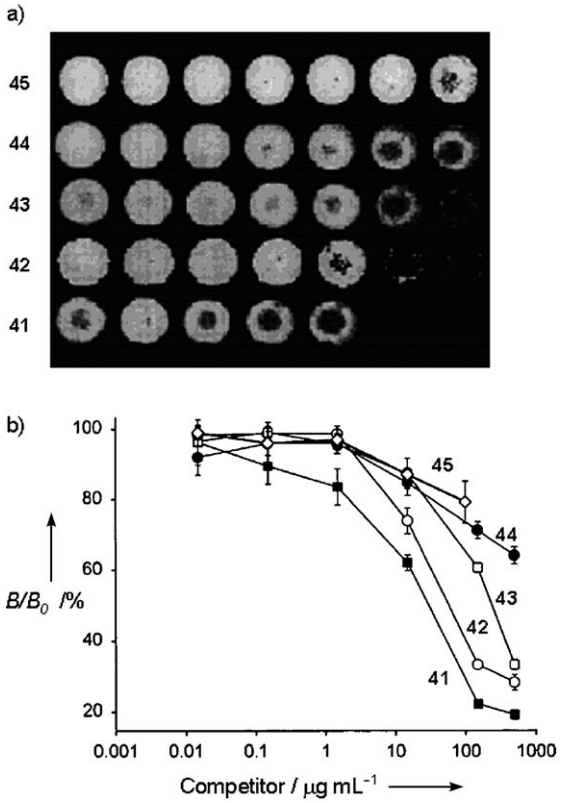
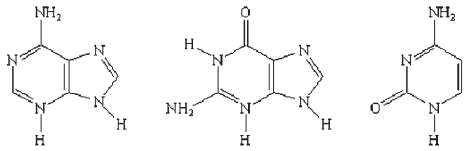


Figure 17. Parallel screening of molecularly imprinted polymers using spectroscopic imaging for the determination of the concentration of **41** and interferences **42**–**45**. a) Typical chemoluminescence image of a competitive assay in a 96-well plate. b) Calibration curves for the determination of **41**–**45** where B/B_0 is the ratio of bound to total ligand. Adapted from ref. [184]

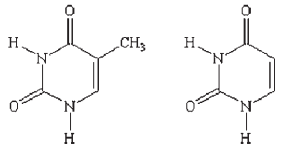
quantifying the intensities of the individual spots (Figure 17b). When compounds structurally related to **41**, namely **42**–**45**, were tested in the competitive assay, their cross-reactivities were in the same range as the ones previously reported for a radioassay with a similar molecularly imprinted polymer.[185] Similar molecularly imprinted polymers were also employed as sensing layers in several types of sensors.[186]

6.2. In Vitro Selection

In vitro selection is used to construct highly selective materials based on nucleic acid biopolymers. From the perspective of organic chemistry, nucleic acids are linear heterocopolymers that consist of several monomers (nucleotides) **46**–**50**.[187] Synthetic single-stranded nucleic acid biopolymers, both DNA and RNA, have been applied in the development of sensor materials. These biopolymer materials,



46 **47** **48**



49 **50**

known as aptamers, range in size from 6 to 40 kDa[188] and are selected combinatorially by iterative isolation and enrichment of the best sequences from a pool of 10^{13}–10^{18} independent nucleic acid sequences with affinity for a defined analyte.[171,189–191] After 8–15 cycles, the pool evolves into a subset of sequences with unique tertiary structures, whose binding motif size for an analyte typically consist of 25–60 nucleotides.[187] The binding constants for these aptamers with analytes are several orders of magnitude greater than the biopolymers from the original pool. As a result, aptamers that are highly selective for their analytes are produced with known sequences for further PCR amplification.[192] The key molecular interactions that provide the high specificity of the aptamer–ligand association include hydrogen bonding, stacking effects, and molecular-shape complementarity.[172]

There are several well-recognized benefits to using aptamers, instead of antibodies, to sense non-nucleic acid analytes.[172,190,193] In theory, aptamer selection is much faster, cheaper, more versatile, and more reliable than antibody preparation. Such selection produces high-affinity sensing biopolymers that can be propagated indefinitely with little risk of losing the stock, at significantly lower cost than antibodies, and without the use of animals. This approach provides the opportunity to generate ligands to antigens that are toxic to humans and animals.[194] The binding constants of aptamers are in the nM range, which are often comparible to or better than those of antibodies.[172] Methods for automated high-throughput selection of aptamers were developed to address the growing needs for selective receptors.[195] Examples of species for which aptamers have been selected range from small molecules (amino acids, metal ions, antibiotics, organic dyes), to large molecules (proteins, biological cofactors), to large biological assemblages (red blood cell membranes, viruses, tissues).[37,172,196,197] Recently, aptamers **51** and **52** were developed for agents such as Bacillus anthracis[198] and ricin,[199,200] respectively.

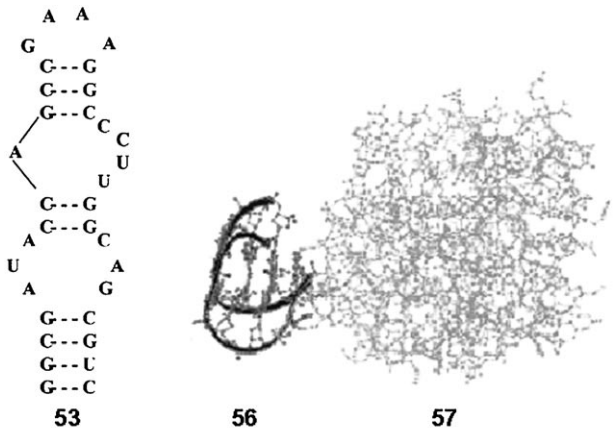
5'-AGAGGAATGTATAAGGATGTTCCGGGCGTGTGGGTAAGTC-3'

51

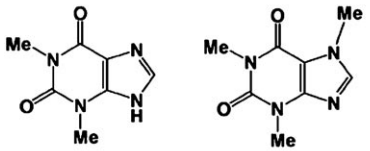
5'GGCGAAUUCAGGGGACGUAGCAAUGACUGCC

52

 © 2006 Wiley-VCH Verlag GmbH & Co. KGaA, Weinheim



53 56 57



54 55

An astonishingly high selectivity has been demonstrated with the theophylline-binding RNA aptamer **53**.[201] Theophylline (**54**) is a drug that differs from caffeine (**55**) by only a single methyl group yet the affinity of **53** for **54** is 10000 times greater than for **55**.[172] Such selectivity is greater than any of the existing theophylline antibodies.[197]

The high selectivity of synthetic aptamers, sometimes even better than antibodies, is a result of the selective demand in the combinatorial selection process that eliminates sequences that bind to closely related analogues of the analyte.[202] The simplicity with which these aptamers are synthetically engineered for sensor applications make them on a par with or superior to the natural antibodies.[203]

For aptamers to be functional in sensors, an immobilization strategy is needed that will preserve their 3D analyte-binding conformation. The first sensor with surface-immobilized aptamers coupled with the detection of analyte binding by fluorescence anisotropy was demonstrated in 1998.[191] The immobilization of antithrombin aptamer **56** onto glass (Figure 18a) provided both high sensitivity and selectivity in the detection of the protein thrombin (**57**, Figure 18b). Several more recent reports describe the applications of aptamers in sensor arrays for the determination of biological and chemical species.[192,200,204]

Combinatorial methodologies will continue to have an impact on the development of polymers that will act as molecular recognition sensor materials. New concepts for selectivity improvement will emerge and, when coupled with combinatorial screening, will expand the range of selectively detected analytes.

7. Combined Techniques

Combining different sensing concepts in one device is a well-practiced approach to improve sensor performance. Improvements can be achieved by employing more than one energy-transduction principle in the sensor (e.g., radiant-mechanical[100,205] and electrical-mechanical sensors[206]) and by designing a sensor material based on more than one analyte-recognition principle (Figure 1). A carefully selected combination of energy-transduction principles in a sensor can provide orthogonal responses from the sensor that can lead to improvements in selectivity and long-term stability. Applying more than one analyte recognition concept in a sensor material opens up opportunities for the design of more diverse materials, such as composites of molecularly imprinted polymers with electrically conducting polypyrrole (**31**)[207] or proteins,[92] combination of molecular imprinting

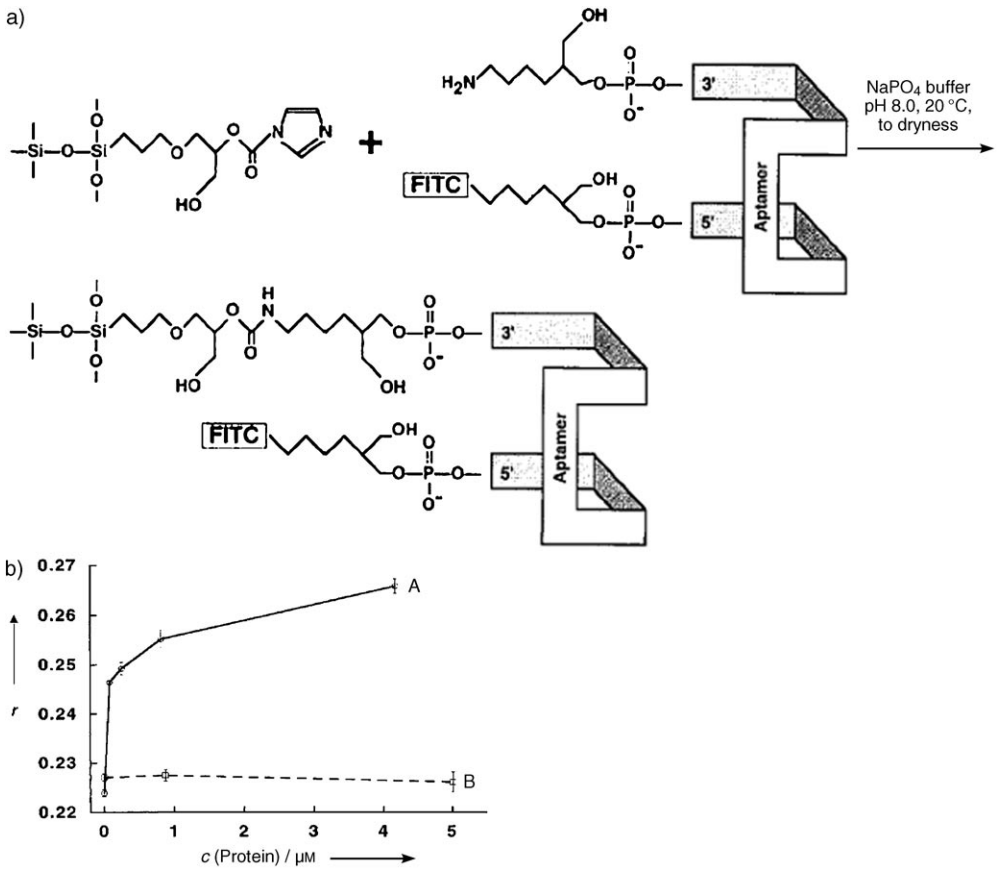


Figure 18. Selective determination of thrombin (**57**) with an immobilized aptamer **56**. a) Immobilization of **56**; b) fluorescence anisotropy of **56** as a function of the concentration of **57** (A, analyte) and elastase (B, interference). Adapted from ref. [191].

© 2006 Wiley-VCH Verlag GmbH & Co. KGaA, Weinheim

and metal or semiconductor optical materials (films, crystals, or nanoparticles),[208] and formulation of polymeric chemoresponsive diffraction gratings with vapochromic reagents.[133,209]

Combining polymeric sorbing coatings with optical sensors based on surface enhanced Raman spectroscopy (SERS) not only enhances the selectivity and sensitivity, but also simplifies spectral analysis.[210] Polymer layers on the SERS substrates can enhance the robustness and shelf-life of the sensor by preventing mechanical wear and chemical deterioration by air oxidation of the metal surface. When such polymers are applied onto the SERS surface, modifications of polymeric films are possible to provide additional sensing capabilities. In one application, molecularly imprinted polymer layers were prepared on SERS surfaces to monitor the uptake and release of substances through the polymer by SERS.[211] In another application, porous polymer beads with a large inner area were used as a stabilizing matrix for SERS-active gold particles.[212] In yet another application, silver-polydimethylsiloxane nanocomposites were fabricated to improve the qualitative and quantitative analysis of aromatic pollutants in water.[213] This approach considerably improved the reproducibility and sensitivity of the technique by minimizing the thermal and photolytic effects inherent in SERS. Combinatorial approaches have been applied to optimize metallic SERS substrates. These approaches include 2D variation of the density of nanoparticles to determine the optimal surface coverage to obtain the most efficient SERS sensors.[214] The roughness of metallic substrates have been explored by combinatorial methods[215] and showed that the performance of the SERS sensors with optimized periodic structures was at least one order of magnitude larger than that of isolated films.

8. Summary and Outlook

The benefits of combinatorial and high-throughput methods in sensor materials research are in the exploration of multidimensional chemical composition and process parameters space at a previously unavailable level of detail at a fraction of the time required for conventional one-at-a-time experiments. When coupled with the prior knowledge, these new tools provide the opportunity for more challenging, yet more rewarding investigations, which previously seemed to be too time consuming to consider. Combinatorial and high-throughput methods have been particularly successful in the areas of molecular shape recognition[171] and formulated[45] sensor materials. The desired selectivity and sensitivity have been achieved in both areas through careful optimization procedures. For practical acceptance, these results should be followed up by detailed evaluation of manufacturability and other practical issues that are less adaptable to new research tools.

Combinatorial and high-throughput screening technologies will continue to have an impact on the development of polymeric sensor materials. Parallel synthesis and high-throughput characterization tools can provide better quality data than conventional one-at-a-time experiments because of the elimination of possible uncontrolled variations in experimental conditions. New combinatorial schemes will be developed where various reaction variables can be altered simultaneously and where important cooperative effects can be carefully probed to provide better understanding of possible sources of variation. This knowledge should lead to the development of new sensor performance models that will relate intrinsic and performance properties of sensor materials and will expand the range of rationally designed sensor materials (see Table 1). Advances in computational chemistry and chemometrics will provide more capabilities for virtual screening and more guided selection of space for experimental screening. Gathered and analyzed data will provide new opportunities for the analysis of structure–property relationships, reduction or elimination of remaining gaps in sensor-development knowledge (see Table 2), and for the more cost- and time-effective design of sensor materials.

The multidisciplinary aspects of combinatorial techniques will continue to have an impact on researchers as well. It is likely that in the future a combinatorial chemist will acquire skills as diverse as experimental planning, automated synthesis, basics of high-throughput materials characterization, chemometrics, and data mining. Perhaps everyone dealing with massive amounts of data will be able to perform standard multivariate statistical and cluster analysis using available tools for rapid assessment of materials trends that are not visually noticeable because of several components being involved in the experimental design. These skills will provide a powerful vision for exploring multicomponent interactions and synergistic effects in sensor materials that was impossible to imagine in the 20th century.

We gratefully acknowledge the NIST ATP, US DOE, and GE components for support of our combinatorial sensor research. We thank Andrew Pris for his valuable comments on the manuscript, and Terry Leib, Greg Chambers, William Flanagan, and Amy Linsebigler for support and encouragement.

Received: March 5, 2005
Revised: September 5, 2005

[1] B. Jandeleit, D. J. Schaefer, T. S. Powers, H. W. Turner, W. H. Weinberg, *Angew. Chem.* **1999**, *111*, 2648–2689; *Angew. Chem. Int. Ed.* **1999**, *38*, 2494–2532; *Combinatorial and Artificial Intelligence Methods in Materials Science* (Eds.: I. Takeuchi, J. M. Newsam, L. T. Wille, H. Koinuma, E. J. Amis), Materials Research Society, Warrendale, **2002**; *High Throughput Analysis: A Tool for Combinatorial Materials Science* (Eds.: R. A. Potyrailo, E. J. Amis), Kluwer Academic/Plenum Publishers, New York, **2003**; *Special Issue: High-Throughput and Combinatorial Methods in Polymer Research* (Ed.: U. S. Schubert), *Macromol. Rapid Commun.* **2003**; *Special Issue: Combinatorial Material Research and High-Throughput Experimentation in Polymer and Material Research* (Eds.: U. S. Schubert, E. J. Amis), *Macromol. Rapid Commun.* **2004**; H. Koinuma, I. Takeuchi, *Nat. Mater.* **2004**, *3*, 429–438; *Combinatorial and Artificial Intelligence Methods in Materials Science II* (Eds.: R. A. Potyrailo, A. Karim, Q. Wang, T. Chikyow), Materials Research Society, Warrendale, **2004**; *Special Feature on Combinatorial and High-Throughput Materials Research* (Eds.:

 © 2006 Wiley-VCH Verlag GmbH & Co. KGaA, Weinheim

R. A. Potyrailo, I. Takeuchi), *Meas. Sci. Technol.* **2005**; *Special Feature on Combinatorial Instruments and Techniques* (Eds.: J. C. Grunlan, A. R. Mehrabi, R. A. Potyrailo), *Rev. Sci. Instrum.* **2005**.

[2] W. Maier, G. Kirsten, M. Orschel, P.-A. Weiß, A. Holzwarth, J. Klein in *Combinatorial Approaches to Materials Development, Vol. 814* (Ed.: R. Malhotra), American Chemical Society, Washington, **2002**, pp. 1–21.

[3] R. D. Piner, J. Zhu, F. Xu, S. Hong, C. A. Mirkin, *Science* **1999**, *283*, 661–663; A. Hierlemann, H. Baltes, *Analyst* **2003**, *128*, 15–28.

[4] H. Suzuki, *Electroanalysis* **2000**, *12*, 703–715.

[5] C. Hagleitner, A. Hierlemann, O. Brand, H. Baltes in *Sensors Update, Vol. 11* (Eds.: H. Baltes, W. Göpel, J. Hesse), VCH, Weinheim, **2002**, pp. 101–155.

[6] C. Hagleitner, A. Hierlemann, O. Brand, H. Baltes in *Sensors Update, Vol. 12* (Eds.: H. Baltes, W. Göpel, J. Hesse), VCH, Weinheim, **2003**, pp. 51–120.

[7] H. Becker, C. Gärtner, *Electrophoresis* **2000**, *21*, 12–26; T. Thorsen, S. J. Maerkl, S. R. Quake, *Science* **2002**, *298*, 580–584; D. Erickson, D. Li, *Anal. Chim. Acta* **2004**, *507*, 11–26; T. Vilkner, D. Janasek, A. Manz, *Anal. Chem.* **2004**, *76*, 3373–3386.

[8] G. Harsanyi, *Polymer Films in Sensor Applications*, Technomic, Lancaster, **1995**; *Polymers in Sensors. Theory and Practice* (Eds.: N. Akmal, A. M. Usmani), American Chemical Society, Washington, **1998**.

[9] R. A. Potyrailo, S. E. Hobbs, G. M. Hieftje, *Fresenius J. Anal. Chem.* **1998**, *362*, 349–373.

[10] R. A. Potyrailo, *Macromol. Rapid Commun.* **2004**, *25*, 77–94.

[11] S. Middelhoek, J. W. Noorlag, *Sens. Actuators* **1981/82**, *2*, 29–41; J. Janata, *Principles of Chemical Sensors*, Plenum, New York, **1989**.

[12] *Fiber Optic Chemical Sensors and Biosensors* (Ed.: O. S. Wolfbeis), CRC, Boca Raton, **1991**; B. Adhikari, S. Majumdar, *Prog. Polym. Sci.* **2004**, *29*, 699–766.

[13] K. J. Albert, N. S. Lewis, C. L. Schauer, G. A. Sotzing, S. E. Stitzel, T. P. Vaid, D. R. Walt, *Chem. Rev.* **2000**, *100*, 2595–2626.

[14] J. W. Grate, *Chem. Rev.* **2000**, *100*, 2627–2648.

[15] J. Janata, M. Josowicz, *Nat. Mater.* **2002**, *2*, 19–24.

[16] T. A. Dickinson, D. R. Walt, J. White, J. S. Kauer, *Anal. Chem.* **1997**, *69*, 3413–3418.

[17] A. Apostolidis, I. Klimant, D. Andrzejewski, O. S. Wolfbeis, *J. Comb. Chem.* **2004**, *6*, 325–331.

[18] P. Chojnacki, T. Werner, O. S. Wolfbeis, *Microchim. Acta* **2004**, *147*, 87–92.

[19] R. A. Potyrailo, *Polym. Mater. Sci. Eng.* **2004**, *90*, 797–798.

[20] G. A. Birina, K. A. Boitsov, *Zavod. Lab.* **1974**, *40*, 855–857.

[21] K. Kennedy, T. Stefansky, G. Davy, V. F. Zackay, E. R. Parker, *J. Appl. Phys.* **1965**, *36*, 3808–3810; R. Hoffmann, *Angew. Chem.* **2001**, *113*, 3439–3443; *Angew. Chem. Int. Ed.* **2001**, *40*, 3337–3340.

[22] R. Hoogenboom, M. A. R. Meier, U. S. Schubert, *Macromol. Rapid Commun.* **2003**, *24*, 15–32.

[23] J. J. Hanak, *J. Mater. Sci.* **1970**, *5*, 964–971.

[24] W. H. King, Jr., *Anal. Chem.* **1964**, *36*, 1735–1739; G. Shaw, *Trans. Faraday Soc.* **1967**, *63*, 2181–2189; I. Bergman, *Nature* **1968**, *218*, 396; E. I. Hormats, F. C. Unterleitner, *J. Phys. Chem.* **1965**, *69*, 3677–3681; A. Shatkay, *Anal. Chem.* **1967**, *39*, 1056–1065.

[25] R. E. Newnham, *Crystallogr. Rev.* **1988**, *1*, 253–280; D. E. Akporiaye, *Angew. Chem.* **1998**, *110*, 2594–2595; *Angew. Chem. Int. Ed.* **1998**, *37*, 2456–2457; D. Lamb, J. F. Anstey, D.-Y. Lee, C. M. Fellows, M. J. Monteiro, R. G. Gilbert, *Macromol. Symp.* **2001**, *174*, 13–27; A. A. Gusev, H. R. Lusti, *Adv. Mater.* **2001**, *13*, 1641–1643; M. R. Caplan, D. A. Lauffenburger, *Ind. Eng. Chem. Res.* **2002**, *41*, 403–412; J. J. Lavigne, E. V. Anslyn, *Angew. Chem.* **2001**, *113*, 3212–3225; *Angew. Chem. Int. Ed.* **2001**, *40*, 3119–3130.

[26] C. W. Ulmer II, D. A. Smith, B. G. Sumpter, D. I. Noid, *Comput. Theor. Polym. Sci.* **1998**, *8*, 311–321.

[27] A. Carrillo, I. R. Martín-Domínguez, A. Rosas, A. Márquez, *Polymer* **2002**, *43*, 6307–6313.

[28] M. Suman, M. Freddi, C. Massera, F. Ugozzoli, E. Dalcanale, *J. Am. Chem. Soc.* **2003**, *125*, 12068–12069.

[29] A. Ceresa, A. Radu, S. Peper, E. Bakker, E. Pretsch, *Anal. Chem.* **2002**, *74*, 4027–4036.

[30] I. Levitsky, S. G. Krivoshlykov, J. W. Grate, *Anal. Chem.* **2001**, *73*, 3441–3448.

[31] S. Marx, A. Zaltsman, I. Turyan, D. Mandler, *Anal. Chem.* **2004**, *76*, 120–126.

[32] P. G. Schultz, *Appl. Catal. A* **2003**, *254*, 3–4; M. E. Eberhart, D. P. Clougherty, *Nat. Mater.* **2004**, *3*, 659–661; J. Kohn, *Nat. Mater.* **2004**, *3*, 745–747.

[33] B. C. McKusick, R. E. Heckert, T. L. Cairns, D. D. Coffman, H. F. Mower, *J. Am. Chem. Soc.* **1958**, *80*, 2806–2815; P. Bühlmann, E. Pretsch, E. Bakker, *Chem. Rev.* **1998**, *98*, 1593–1687; E. D. Steinle, S. Amemiya, P. Bühlmann, M. E. Meyerhoff, *Anal. Chem.* **2000**, *72*, 5766–5773; C. J. Pedersen, *J. Am. Chem. Soc.* **1967**, *89*, 7017–7036; Y. Hu, O. K. Tan, J. S. Pan, X. Yao, *J. Phys. Chem. B* **2004**, *108*, 11214–11218; V. Svetlicic, A. J. Schmidt, L. L. Miller, *Chem. Mater.* **1998**, *10*, 3305–3307; P. D. Martin, T. D. Wilson, I. D. Wilson, G. R. Jones, *Analyst* **2001**, *126*, 757–759.

[34] R. A. Potyrailo, T. M. Sivavec, *Anal. Chem.* **2004**, *76*, 7023–7027.

[35] D. R. Walt, T. Dickinson, J. White, J. Kauer, S. Johnson, H. Engelhardt, J. Sutter, P. Jurs, *Biosens. Bioelectron.* **1998**, *13*, 697–699.

[36] A. J. Matzger, C. E. Lawrence, R. H. Grubbs, N. S. Lewis, *J. Comb. Chem.* **2000**, *2*, 301–304.

[37] Y. Lu, J. Liu, J. Li, P. J. Bruesehoff, C. M.-B. Pavot, A. K. Brown, *Biosens. Bioelectron.* **2003**, *18*, 529–540.

[38] E. Bakker, P. Bühlmann, E. Pretsch, *Chem. Rev.* **1997**, *97*, 3083–3132.

[39] R. Deans, J. Kim, M. R. Machacek, T. M. Swager, *J. Am. Chem. Soc.* **2000**, *122*, 8565–8566.

[40] O. Lavastre, I. Illitchev, G. Jegou, P. H. Dixneuf, *J. Am. Chem. Soc.* **2002**, *124*, 5278–5279.

[41] E. J. Cho, Z. Tao, Y. Tang, E. C. Tehan, F. V. Bright, W. L. Hicks, Jr., J. A. Gardella, Jr., R. Hard, *Appl. Spectrosc.* **2002**, *56*, 1385–1389.

[42] K. Rege, N. R. Raravikar, D.-Y. Kim, L. S. Schadler, P. M. Ajayan, J. S. Dordick, *Nano Lett.* **2003**, *3*, 829–832.

[43] Y. Zhou, M. Freitag, J. Hone, C. Staii, A. T. Johnson, N. J. Pinto, A. G. MacDiarmid, *Appl. Phys. Lett.* **2003**, *83*, 3800–3802.

[44] V. M. Mirsky, V. Kulikov in *High Throughput Analysis: A Tool for Combinatorial Materials Science* (Eds.: R. A. Potyrailo, E. J. Amis), Kluwer Academic/Plenum Publishers, New York, **2003**, chap. 20.

[45] E. J. Amis, *Nat. Mater.* **2004**, *3*, 83–85.

[46] A. V. Lemmo, J. T. Fisher, H. M. Geysen, D. J. Rose, *Anal. Chem.* **1997**, *69*, 543–551; P. Calvert, *Chem. Mater.* **2001**, *13*, 3299–3305; B.-J. de Gans, U. S. Schubert, *Langmuir* **2004**, *20*, 7789–7793.

[47] L. Hassib, R. A. Potyrailo, *Polym. Prepr. Am. Chem. Soc. Div. Polym. Chem.* **2004**, *45*, 211–212.

[48] M. Schena, *Microarray Analysis*, Wiley, Hoboken, **2003**.

[49] R. A. Potyrailo, W. G. Morris, R. J. Wroczynski, P. J. McCloskey, *J. Comb. Chem.* **2004**, *6*, 869–873.

[50] V. M. Mirsky, V. Kulikov, Q. Hao, O. S. Wolfbeis, *Macromol. Rapid Commun.* **2004**, *25*, 253–258.

[51] M. Shen, M. B. Bever, *J. Mater. Sci.* **1972**, *7*, 741–746.

 © 2006 Wiley-VCH Verlag GmbH & Co. KGaA, Weinheim

[52] R. A. Potyrailo, R. J. Wroczynski, *Rev. Sci. Instrum.* **2005**, *76*, 062222.
[53] R. A. Potyrailo, R. J. Wroczynski, J. E. Pickett, M. Rubinsztajn, *Macromol. Rapid Commun.* **2003**, *24*, 123–130; R. A. Potyrailo, A. W. Szumlas, T. L. Danielson, M. Johnson, G. M. Hieftje, *Meas. Sci. Technol.* **2005**, *16*, 235–241.
[54] R. A. Potyrailo, D. R. Olson, M. J. Brennan, J. R. Akhave, M. A. Licon, A. R. Mehrabi, D. L. Saunders, B. J. Chisholm, US Patent 6544334 B1, **2003**.
[55] R. A. Potyrailo, L. Hassib, *Rev. Sci. Instrum.* **2005**, *76*, 062225.
[56] F. Turcu, G. Hartwich, D. Schäfer, W. Schuhmann, *Macromol. Rapid Commun.* **2005**, *26*, 325–330.
[57] Z.-M. Huang, Y.-Z. Zhang, M. Kotaki, S. Ramakrishna, *Compos. Sci. Technol.* **2003**, *63*, 2223–2253.
[58] J. Kameoka, D. Czaplewski, H. Liu, H. G. Craighead, *J. Mater. Chem.* **2004**, *14*, 1503–1505.
[59] R. A. Potyrailo, D. R. Olson, G. F. Medford, M. J. Brennan, *Anal. Chem.* **2002**, *74*, 5676–5680.
[60] R. A. Potyrailo, B. J. Chisholm, D. R. Olson, M. J. Brennan, C. A. Molaison, *Anal. Chem.* **2002**, *74*, 5105–5111; R. A. Potyrailo, B. J. Chisholm, W. G. Morris, J. N. Cawse, W. P. Flanagan, L. Hassib, C. A. Molaison, K. Ezbiansky, G. Medford, H. Reitz, *J. Comb. Chem.* **2003**, *5*, 472–478.
[61] R. Mullin, *Chem. Eng. News* **2004**, *82 (Issue 30)*, 23–32.
[62] C. D. Maranas, *Ind. Eng. Chem. Res.* **1996**, *35*, 3403–3414.
[63] M. N. Patel, D. H. Sutaria, S. D. Patel, *Angew. Makromol. Chem.* **1996**, *234*, 13–20; J. Kim, X. Wu, M. R. Herman, J. S. Dordick, *Anal. Chim. Acta* **1998**, *370*, 251–258.
[64] X. Wu, J. Kim, J. S. Dordick, *Biotechnol. Prog.* **2000**, *10*, 513–516.
[65] D.-Y. Kim, X. Wu, J. S. Dordick in *Biocatalysis in Polymer Science, Vol. 840*, American Chemical Society, Washington, **2003**, pp. 34–49.
[66] K. Persaud, G. Dodd, *Nature* **1982**, *299*, 352–355.
[67] M. Otto, *Chemometrics: Statistics and Computer Application in Analytical Chemistry*, Wiley-VCH, Weinheim, **1999**; R. A. Potyrailo in *Encyclopedia of Materials: Science and Technology, Vol. 2* (Eds.: K. H. J. Buschow, R. W. Cahn, M. C. Flemings, B. Ilschner, E. J. Kramer, S. Mahajan), Elsevier, Amsterdam, **2001**, pp. 1329–1343; J. Scheidtmann, A. Frantzen, G. Frenzer, W. F. Maier, *Meas. Sci. Technol.* **2005**, *16*, 119–127.
[68] J. W. Grate, M. H. Abraham, *Sens. Actuators B* **1991**, *3*, 85–111; M. H. Abraham, *Chem. Soc. Rev.* **1993**, *22*, 73–83.
[69] B. M. Wise, N. B. Gallagher, J. W. Grate, *J. Chemom.* **2003**, *17*, 463–469.
[70] M. Belmares, M. Blanco, W. A. Goddard III, R. B. Ross, G. Caldwell, S.-H. Chou, J. Pham, P. M. Olofson, C. Thomas, *J. Comput. Chem.* **2004**, *25*, 1814–1826.
[71] J. W. Grate, H. Abraham, R. A. McGill in *Handbook of Biosensors and Electronic Noses. Medicine, Food, and the Environment* (Ed.: E. Kress-Rogers), CRC, Boca Raton, **1997**, pp. 593–612.
[72] J. W. Grate, S. N. Kaganove, S. J. Patrash, R. Craig, M. Bliss, *Chem. Mater.* **1997**, *9*, 1201–1207; A. Brecht, G. Gauglitz, *Sens. Actuators B* **1997**, *38–39*, 1–7; R. A. Potyrailo, S. E. Hobbs, G. M. Hieftje, *Anal. Chem.* **1998**, *70*, 1639–1645; C. Phillips, M. Jakusch, H. Steiner, B. Mizaikoff, A. G. Fedorov, *Anal. Chem.* **2003**, *75*, 1106–1115; A. Hierlemann, D. Lange, C. Hagleitner, N. Kerness, A. Koll, O. Brand, H. Baltes, *Sens. Actuators B* **2000**, *70*, 2–11; D. S. Ballantine, Jr., R. M. White, S. J. Martin, A. J. Ricco, G. C. Frye, E. T. Zellers, H. Wohltjen, *Acoustic Wave Sensors: Theory, Design, and Physico-Chemical Applications*, Academic Press, San Diego, **1997**; M. Thompson, D. C. Stone, *Surface-Launched Acoustic Wave Sensors: Chemical Sensing and Thin-Film Characterization*, Wiley, New York, **1997**.
[73] F. Rathgeb, G. Gauglitz, *Anal. Chim. Acta* **1998**, *372*, 333–340.
[74] C. Hagleitner, A. Hierlemann, D. Lange, A. Kummer, N. Kerness, O. Brand, H. Baltes, *Nature* **2001**, *414*, 293–296.
[75] M. J. Sepaniak, P. G. Datskos, N. V. Lavrik, C. Tipple, *Anal. Chem.* **2002**, *74*, 568A–575A; N. V. Lavrik, M. J. Sepaniak, P. G. Datskos, *Rev. Sci. Instrum.* **2004**, *75*, 2229–2253; M. Ward, D. A. Buttry, *Science* **1990**, *249*, 1000–1007.
[76] R. A. Potyrailo, W. G. Morris, R. J. Wroczynski, in *High Throughput Analysis: A Tool for Combinatorial Materials Science* (Eds.: R. A. Potyrailo, E. J. Amis), Kluwer Academic/Plenum, New York, **2003**, chap. 11.
[77] R. A. Potyrailo, W. G. Morris, R. J. Wroczynski, *Rev. Sci. Instrum.* **2004**, *75*, 2177–2186.
[78] J. W. Grate, A. Snow, D. S. Ballantine, Jr., H. Wohltjen, M. H. Abraham, R. A. McGill, P. Sasson, *Anal. Chem.* **1988**, *60*, 869–875; J. W. Grate, S. J. Patrash, M. H. Abraham, *Anal. Chem.* **1995**, *67*, 2162–2169; J. W. Grate, S. J. Patrash, M. H. Abraham, C. M. Du, *Anal. Chem.* **1996**, *68*, 913–917; A. Hierlemann, E. T. Zellers, A. J. Ricco, *Anal. Chem.* **2001**, *73*, 3458–3466.
[79] R. A. Potyrailo, R. J. May, T. M. Sivavec, *Sensor Lett.* **2004**, *2*, 31–36.
[80] J. W. Grate, R. A. McGill, *Anal. Chem.* **1995**, *67*, 4015–4019; J. Zhu, J. Zhao, Y. Liao, W. Jiang, *J. Polym. Sci. B* **2005**, *43*, 2874–2884; J. Peng, Y. Xuan, H. Wang, B. Li, Y. Han, *Polymer* **2005**, *46*, 5767–5772.
[81] T. M. Sivavec, R. A. Potyrailo, US Patent 6357278 B1, **2002**.
[82] R. E. Shaffer, R. A. Potyrailo, J. J. Salvo, T. M. Sivavec, L. Salsman, US DoE Information Bridge, http://www.osti.gov/servlets/purl/834346-tEuKN5/native/, **2003**.
[83] D. Liu, R. K. Meruva, R. B. Brown, M. E. Meyerhoff, *Anal. Chim. Acta* **1996**, *321*, 173–183.
[84] I. Koronczi, J. Reichert, G. Heinzmann, H. J. Ache, *Sens. Actuators B* **1998**, *51*, 188–195.
[85] K. Arshak, E. Moore, L. Cavanagh, J. Harris, B. McConigly, C. Cunniffe, G. Lyons, S. Clifford, *Composites Part A* **2004**, *36*, 487–491.
[86] H. Sangodkar, S. Sukeerthi, R. S. Srinivasa, R. Lal, A. Q. Contractor, *Anal. Chem.* **1996**, *68*, 779–783.
[87] G. Boisde, A. Harmer, *Chemical and Biochemical Sensing With Optical Fibers and Waveguides*, Artech House, Boston, **1996**; O. S. Wolfbeis, *Anal. Chem.* **2004**, *76*, 3269–3284.
[88] E. Bakker, E. Pretsch, *Anal. Chem.* **2002**, *74*, 420A–426A; J. Janata, *Crit. Rev. Anal. Chem.* **2002**, *33*, 109–120.
[89] E. Bakker, *Anal. Chem.* **2004**, *76*, 3285–3298.
[90] R. L. Gunter, W. G. Delinger, K. Manygoats, A. Kooser, T. L. Porter, *Sens. Actuators A* **2003**, *107*, 219–224; A. Kooser, R. L. Gunter, W. D. Delinger, T. L. Porter, M. P. Eastman, *Sens. Actuators B* **2004**, *99*, 474–479.
[91] S. Kröger, B. Danielsson in *Handbook of Biosensors and Electronic Noses. Medicine, Food, and the Environment* (Ed.: E. Kress-Rogers), CRC, Boca Raton, **1997**, pp. 279–298.
[92] J. Rick, T.-C. Chou, *Biosens. Bioelectron.* **2005**, *20*, 1878–1883.
[93] M. S. Freud, N. S. Lewis, *Proc. Natl. Acad. Sci. USA* **1995**, *92*, 2652–2656; E. Wang, H. B. Chen, H. Patel, I. Sadaragani, C. Romero, *Anal. Chim. Acta* **1999**, *397*, 287–294.
[94] N. V. Kolytcheva, H. Müller, J. Marstalerz, *Sens. Actuators B* **1999**, *58*, 456–463.
[95] M. Penco, L. Sartore, F. Bignotti, S. D. Sciucca, V. Ferrari, P. Crescini, S. D'Antone, *J. Appl. Polym. Sci.* **2004**, *91*, 1816–1821.
[96] A. B. Collaudin, L. J. Blum, *Sens. Actuators B* **1997**, *38–39*, 189–194.
[97] B. J. Basu, A. Thirumurugan, A. R. Dinesh, C. Anandan, K. S. Rajam, *Sens. Actuators B* **2005**, *104*, 15–22.
[98] A. Mills, A. Lepre, L. Wild, *Anal. Chim. Acta* **1998**, *362*, 193–202; J. M. Bedlek-Anslow, J. P. Hubner, B. F. Carroll, K. S. Schanze, *Langmuir* **2000**, *16*, 9137–9141.
[99] J. Wang, M. Musameh, Y. Lin, *J. Am. Chem. Soc.* **2003**, *125*, 2408–2409.

 © 2006 Wiley-VCH Verlag GmbH & Co. KGaA, Weinheim

[100] R. A. Potyrailo, US Patent 6567753 B2, **2003**.
[101] R. A. Potyrailo, M. J. Brennan, US Patent 6684683 B2, **2004**.
[102] R. A. Potyrailo, in *Second Dutch Polymer Institute workshop "High Throughput Experimentation/Combinatorial Material Research"*, May 15–16 2003, Eindhoven, The Netherlands, **2003**.
[103] Y. Amao, *Microchim. Acta* **2003**, *143*, 1–12; P. Hartmann, W. Trettnak, *Anal. Chem.* **1996**, *68*, 2615–2620; S. Draxler, M. E. Lippitsch, I. Klimant, H. Kraus, O. S. Wolfbeis, *J. Phys. Chem.* **1995**, *99*, 3162–3167; G. J. Mohr, O. S. Wolfbeis, *Sens. Actuators B* **1996**, *37*, 103–109; V. L. Conway, K. P. Hassen, L. Zhang, W. R. Seitz, T. S. Gross, *Sens. Actuators B* **1997**, *45*, 1–9.
[104] C. Preininger, G. Mohr, I. Klimant, O. S. Wolfbeis, *Anal. Chim. Acta* **1996**, *334*, 113–123; S. Peper, A. Ceresa, Y. Qin, E. Bakker, *Anal. Chim. Acta* **2003**, *500*, 127–136; A. Legin, S. Makarychev-Mikhailov, O. Goryacheva, D. Kirsanov, Y. Vlasov, *Anal. Chim. Acta* **2002**, *457*, 297–303.
[105] A. Mills, *Sens. Actuators B* **1998**, *51*, 60–68; K. Eaton, *Sens. Actuators B* **2002**, *85*, 42–51.
[106] D. B. Papkovsky, G. V. Ponomarev, W. Trettnak, P. O'Leary, *Anal. Chem.* **1995**, *67*, 4112–4117.
[107] R. A. Potyrailo, L. Hassib in *MACRO 2004—World Polymer Congress, the 40th IUPAC International Symposium on Macromolecules*, *July 4–9*, IUPAC, Paris, **2004**.
[108] X. Chen, N. Matsumoto, Y. Hu, G. S. Wilson, *Anal. Chem.* **2002**, *74*, 368–372; M. Mehrvar, M. Abdi, *Anal. Sci.* **2004**, *20*, 1113–1126; S. Reiter, D. Ruhlig, B. Ngounou, S. Neugebauer, S. Janiak, A. Vilkanauskyte, T. Erichsen, W. Schuhmann, *Macromol. Rapid Commun.* **2004**, *25*, 348–354; J. Dumont, G. Fortier, *Biotechnol. Bioeng.* **1996**, *49*, 544–552.
[109] I. Gill, *Chem. Mater.* **2001**, *13*, 3404–3421; I. Gill, A. Ballesteros, *J. Am. Chem. Soc.* **1998**, *120*, 8587–8598.
[110] S. Hrapovic, Y. Liu, K. B. Male, J. H. T. Luong, *Anal. Chem.* **2004**, *76*, 1083–1088.
[111] P. N. Bartlett, K. F. E. Pratt, *Biosens. Bioelectron.* **1993**, *8*, 451–462; P. N. Bartlett, K. F. E. Pratt, *J. Electroanal. Chem.* **1995**, *397*, 61–78.
[112] S. Neugebauer, S. Isik, A. Schulte, W. Schuhmann, *Anal. Lett.* **2003**, *36*, 2005–2020; B. Ngounou, S. Neugebauer, A. Frodl, S. Reiter, W. Schuhmann, *Electrochim. Acta* **2004**, *49*, 3855–3863.
[113] M. Leclerc, *Adv. Mater.* **1999**, *11*, 1491–1498.
[114] D. T. McQuade, A. E. Pullen, T. M. Swager, *Chem. Rev.* **2000**, *100*, 2537–2574.
[115] L. Dai, P. Soundarrajan, T. Kim, *Pure Appl. Chem.* **2002**, *74*, 1753–1772.
[116] J. Bobacka, A. Ivaska, A. Lewenstam, *Electroanalysis* **2003**, *15*, 366–374.
[117] G. Bidan, *Sens. Actuators B* **1992**, *6*, 45–56.
[118] P. Gomez-Romero, *Adv. Mater.* **2001**, *13*, 163–174.
[119] C. Barbero, D. F. Acevedo, H. J. Salavagione, M. C. Miras, *Jornadas Sam/Conamet/Simposio Materia 2003* **2003**, C-12.
[120] R. Singhal, A. Chaubey, K. Kaneto, W. Takashima, B. D. Malhotra, *Biotechnol. Bioeng.* **2004**, *85*, 277–282.
[121] H.-A. Ho, M. Béra-Abérem, M. Leclerc, *Chem. Eur. J.* **2004**, *11*, 1718–1724.
[122] E. Milella, M. Penza, *Thin Solid Films* **1998**, *329*, 694–697.
[123] V. Kulikov, V. M. Mirsky, *Meas. Sci. Technol.* **2004**, *15*, 49–54.
[124] V. Kulikov, V. M. Mirsky, T. L. Delaney, D. Donoval, A. W. Koch, O. S. Wolfbeis, *Meas. Sci. Technol.* **2005**, *16*, 95–99.
[125] K. Tada, M. Onoda, *Adv. Funct. Mater.* **2002**, *12*, 420–424.
[126] C. Barbero, H. J. Salavagione, D. F. Acevedo, D. E. Grumelli, F. Garay, G. A. Planes, G. M. Morales, M. C. Miras, *Electrochim. Acta* **2004**, *49*, 3671–3686.
[127] Y. Zhang, H.-F. Ji, G. M. Brown, T. Thundat, *Anal. Chem.* **2003**, *75*, 4773–4777; G.-G. Bumbu, G. Kircher, M. Wolkenhauer, R. Berger, J. S. Gutmann, *Macromol. Chem. Phys.* **2004**, *205*, 1713–1720.
[128] M. C. Lonergan, E. J. Severin, B. J. Doleman, S. A. Beaber, R. H. Grubbs, N. S. Lewis, *Chem. Mater.* **1996**, *8*, 2298–2312.
[129] S. V. Patel, M. W. Jenkins, R. C. Hughes, W. G. Yelton, A. J. Ricco, *Anal. Chem.* **2000**, *72*, 1532–1542.
[130] J. Wang, M. Musameh, *Anal. Chem.* **2003**, *75*, 2075–2079.
[131] J. H. Holtz, S. A. Asher, *Nature* **1997**, *389*, 829–832; A. J. Marshall, J. Blyth, C. A. B. Davidson, C. R. Lowe, *Anal. Chem.* **2003**, *75*, 4423–4431.
[132] A. Convertino, A. Capobianchi, A. Valentini, E. N. M. Cirillo, *Adv. Mater.* **2003**, *15*, 1103–1105; R. Palkovits, C. Mayer, G. Bauer, H. Winkler, F. Pittner, T. Schalkhammer, *Biopolymers* **2003**, *69*, 333–342.
[133] R. C. Bailey, M. Parpia, J. T. Hupp, *Mater. Today* **2005**, 46–52.
[134] T. Miyata, N. Asami, T. Uragami, *Nature* **1999**, *399*, 766–769; G. Gerlach, M. Guenther, G. Suchaneck, J. Sorber, K.-F. Arndt, A. Richter, *Macromol. Symp.* **2004**, *210*, 403–410; F. J. Arregui, Z. Ciaurriz, M. Oneca, I. R. Matías, *Sens. Actuators B* **2003**, *96*, 165–172; H. J. van der Linden, S. Herber, W. Olthuis, P. Bergveld, *Analyst* **2003**, *128*, 325–331; J. E. Meiring, M. J. Schmid, S. M. Grayson, B. M. Rathsack, D. M. Johnson, R. Kirby, R. Kannappan, K. Manthiram, B. Hsia, Z. L. Hogan, A. D. Ellington, M. V. Pishko, C. G. Willson, *Chem. Mater.* **2004**, *16*, 5574–5580.
[135] S. Srivastava, R. Tchoudakov, M. Narkis, *Polym. Eng. Sci.* **2000**, *40*, 1522–1528; J. F. Feller, I. Linossier, G. Levesque, *Polym. Adv. Technol.* **2002**, *13*, 714–724.
[136] B. Zhang, R. W. Fu, M. Q. Zhang, X. M. Dong, P. L. Lan, J. S. Qiu, *Sens. Actuators B* **2005**, *109*, 323–328.
[137] F. Lux, *J. Mater. Sci.* **1993**, *28*, 285–301.
[138] L. Flandin, J. Y. Cavaillé, G. Bidan, Y. Brechet, *Polym. Compos.* **2000**, *21*, 165–174.
[139] H. Lei, W. G. Pitt, L. K. McGrath, C. K. Ho, *Sens. Actuators B* **2004**, *101*, 122–132.
[140] N. Probst, in *Carbon Black Science and Technology* (Eds.: J.-B. Donnet, R. C. Bansal, M.-J. Wang), Marcel Decker, New York, **1993**.
[141] A. V. Shevade, M. A. Ryan, M. L. Homer, A. M. Manfreda, H. Zhou, K. S. Manatt, *Sens. Actuators B* **2003**, *93*, 84–91.
[142] M. Weck, P. Schwab, R. H. Grubbs, *Macromolecules* **1996**, *29*, 1789–1793.
[143] B. J. Doleman, R. D. Sanner, E. J. Severin, R. H. Grubbs, N. S. Lewis, *Anal. Chem.* **1998**, *70*, 2560–2564.
[144] Y. Feng, A. Karim, R. A. Weiss, J. F. Douglas, C. C. Han, *Macromolecules* **1998**, *31*, 484–493; K. A. Barnes, A. Karim, J. F. Douglas, A. I. Nakatani, H. Gruell, E. J. Amis, *Macromolecules* **2000**, *33*, 4177–4185; S. Sharma, M. H. Rafailovich, D. Peiffer, J. Sokolov, *Nano Lett.* **2001**, *1*, 511–514.
[145] Y. Xia, J. A. Rogers, K. E. Paul, G. M. Whitesides, *Chem. Rev.* **1999**, *99*, 1823–1848; R. M. Crooks, *ChemPhysChem* **2001**, *2*, 644–654; G. M. Whitesides, E. Ostuni, S. Takayama, X. Jiang, D. E. Ingber, *Annu. Rev. Biomed. Eng.* **2001**, *3*, 335–373; I. W. Hamley, *Angew. Chem.* **2003**, *115*, 1730–1752; *Angew. Chem. Int. Ed.* **2003**, *42*, 1692–1712; J. M. Helt, C. M. Drain, J. D. Batteas, *J. Am. Chem. Soc.* **2004**, *126*, 628–634; M. Steinhart, J. H. Wendorff, A. Greiner, R. B. Wehrspohn, K. Nielsch, J. Schilling, J. Choi, U. Gosele, *Science* **2002**, *296*, 1997.
[146] A. Barbetta, R. J. Carnachan, K. H. Smith, C.-t. Zhao, N. R. Cameron, R. Kataky, M. Hayman, S. A. Przyborski, M. Swan, *Macromol. Symp.* **2005**, *226*, 203–212.
[147] R. C. Bailey, J. T. Hupp, *Anal. Chem.* **2003**, *75*, 2392–2398.
[148] B. G. Healey, D. R. Walt, *Anal. Chem.* **1997**, *69*, 2213–2216.
[149] M. Lei, Y. Gu, A. Baldi, R. A. Siegel, B. Ziaie, *Langmuir* **2004**, *20*, 8947–8951.
[150] Y. Y. Li, F. Cunin, J. R. Link, T. Gao, R. E. Betts, S. H. Reiver, V. Chin, S. N. Bhatia, M. J. Sailor, *Science* **2003**, *299*, 2045–2047.

 © 2006 Wiley-VCH Verlag GmbH & Co. KGaA, Weinheim

[151] G. Li, C. Martinez, J. Janata, J. A. Smith, M. Josowicz, S. Semancik, *Electrochem. Solid-State Lett.* **2004**, *7*, H44 – H47.
[152] X. Wang, C. Drew, S.-H. Lee, K. J. Senecal, J. Kumar, L. A. Samuelson, *Nano Lett.* **2002**, *2*, 1273 – 1275.
[153] R. Toomey, D. Freidank, J. Ruhe, *Macromolecules* **2004**, *37*, 882 – 887.
[154] S. Virji, J. Huang, R. B. Kaner, B. H. Weiller, *Nano Lett.* **2004**, *4*, 491 – 496.
[155] D. Li, A. Babel, S. A. Jenekhe, Y. Xia, *Adv. Mater.* **2004**, *16*, 2062 – 2066.
[156] P. Gupta, G. L. Wilkes, *Polymer* **2003**, *44*, 6353 – 6359.
[157] S. Madhugiri, A. Dalton, J. Gutierrez, J. P. Ferraris, K. J. Balkus, Jr., *J. Am. Chem. Soc* **2003**, *125*, 14531 – 14538.
[158] V. N. Morozov, T. Y. Morozova, *Anal. Chem.* **1999**, *71*, 3110 – 3117.
[159] D. Li, Y. Xia, *Adv. Mater.* **2004**, *16*, 1151 – 1170.
[160] J. Bowman, M. Taylor, V. Sharma, A. Lynch, S. Chadha, *Mater. Res. Soc. Symp. Proc.* **2003**, *752*, AA1.5.1.
[161] K. Matyjaszewski in *MACRO 2004—World Polymer Congress, the 40th IUPAC International Symposium on Macromolecules, July 4 – 9*, IUPAC, Paris, France, **2004**.
[162] R. Jaeger, H. Schonherr, G. J. Vancso, *Macromolecules* **1996**, *29*, 7634 – 7636; A. Pedicini, R. J. Farris, *Polymer* **2003**, *44*, 6857 – 6862.
[163] R. J. O. M. Hoofman, M. P. de Haas, L. D. A. Siebbeles, J. M. Warman, *Nature* **1998**, *392*, 54 – 56; T.-Q. Nguyen, J. Wu, V. Doan, B. J. Schwartz, S. H. Tolbert, *Science* **2000**, *288*, 652 – 656.
[164] N. Kattamuri, C. Sung, *Mater. Res. Soc. Symp. Proc.* **2004**, *788*, L8.36.31.
[165] G. Wulff, A. Sarhan, *Angew. Chem.* **1972**, *84*, 267; *Angew. Chem. Int. Ed. Engl.* **1972**, *11*, 341.
[166] D. Kriz, O. Ramstrom, K. Mosbach, *Anal. Chem.* **1997**, *69*, 345A – 349A; A. Merkoçi, S. Alegret, *TrAC Trends Anal. Chem.* **2002**, *22*, 717 – 725.
[167] K. Haupt, K. Mosbach, *Chem. Rev.* **2000**, *100*, 2495 – 2504.
[168] G. M. Murray, O. M. Uy, *Tech. Instrum. Anal. Chem.* **2001**, *23*, 441 – 465.
[169] F. L. Dickert, O. Hayden, *Tech. Instrum. Anal. Chem.* **2001**, *23*, 503 – 525.
[170] K. Haupt, *Analyst* **2001**, *126*, 747 – 756.
[171] A. D. Ellington, J. W. Szostak, *Nature* **1990**, *346*, 818 – 822; C. Tuerk, L. Gold, *Science* **1990**, *249*, 505 – 510; A. D. Ellington, J. W. Szostak, *Nature* **1992**, *355*, 850 – 852.
[172] T. Hermann, D. J. Patel, *Science* **2000**, *287*, 820 – 825.
[173] D. Batra, K. J. Shea, *Curr. Opin. Chem. Biol.* **2003**, *7*, 434 – 442.
[174] J. O. Mahony, K. Nolan, M. R. Smyth, B. Mizaikoff, *Anal. Chim. Acta* **2004**, *534*, 31 – 39.
[175] F. Lanza, B. Sellergren, *Macromol. Rapid Commun.* **2004**, *25*, 59 – 68.
[176] M. Ulbricht, M. Belter, U. Langenhangen, F. Schneider, W. Weigel, *Desalination* **2002**, *149*, 293 – 295.
[177] T. Takeuchi, D. Fukuma, J. Matsui, *Anal. Chem.* **1999**, *71*, 285 – 290; F. Lanza, B. Sellergren, *Anal. Chem.* **1999**, *71*, 2092 – 2096; J. Cederfur, Y. Pei, M. Zihui, M. Kempe, *J. Comb. Chem.* **2003**, *5*, 67 – 72; Q.-Z. Zhu, K. Haupt, D. Knopp, R. Niessner, *Anal. Chim. Acta* **2002**, *468*, 217 – 227.
[178] M. P. Davies, V. De Biasi, D. Perrett, *Anal. Chim. Acta* **2004**, *504*, 7 – 14; F. Navarro-Villoslada, B. San Vicente, M. C. Moreno-Bondi, *Anal. Chim. Acta* **2004**, *504*, 149 – 162.
[179] I. A. Nicholls, *J. Mol. Recognit.* **1998**, *11*, 79 – 82; I. A. Nicholls, K. Adbo, H. S. Andersson, P. O. Andersson, J. Ankarloo, J. Hedin-Dahlström, P. Jokela, J. G. Karlsson, L. Olofsson, J. Rosengren, S. Shoravi, J. Svenson, S. Wikman, *Anal. Chim. Acta* **2001**, *435*, 9 – 18.
[180] I. Chianella, M. Lotierzo, S. A. Piletsky, I. E. Tothill, B. Chen, K. Karim, A. P. F. Turner, *Anal. Chem.* **2002**, *74*, 1288 – 1293.
[181] L. Wu, Y. Li, *J. Mol. Recognit.* **2004**, *17*, 567 – 574.
[182] S. A. Piletsky, E. V. Piletska, B. Chen, K. Karim, D. Weston, G. Barrett, P. Lowe, A. P. F. Turner, *Anal. Chem.* **2000**, *72*, 4381 – 4385.
[183] B. Dirion, Z. Cobb, E. Schillinger, L. I. Andersson, B. Sellergren, *J. Am. Chem. Soc.* **2003**, *125*, 15101 – 15109.
[184] I. Surugiu, B. Danielsson, L. Ye, K. Mosbach, K. Haupt, *Anal. Chem.* **2001**, *73*, 487 – 491.
[185] K. Haupt, A. Dzgoev, K. Mosbach, *Anal. Chem.* **1998**, *70*, 628 – 631.
[186] S. Kröger, A. P. F. Turner, K. Mosbach, K. Haupt, *Anal. Chem.* **1999**, *71*, 3698 – 3702; M. Jakusch, M. Janotta, B. Mizaikoff, K. Mosbach, K. Haupt, *Anal. Chem.* **1999**, *71*, 4786 – 4791.
[187] A. Jäschke, C. Frauendorf, F. Hausch, *Synlett* **1999**, *6*, 825 – 833.
[188] W. James in *Encyclopedia of Analytical Chemistry* (Ed.: R. A. Meyers), Wiley, Chichester, **2000**, pp. 4848 – 4871; E. J. Merino, K. M. Weeks, *J. Am. Chem. Soc.* **2003**, *125*, 12370 – 12371.
[189] K. W. Uphoff, S. D. Bell, A. D. Ellington, *Curr. Opin. Struct. Biol.* **1996**, *6*, 281 – 288.
[190] W. Xu, A. D. Ellington, *Proc. Natl. Acad. Sci. USA* **1996**, *93*, 7475 – 7480.
[191] R. A. Potyrailo, R. C. Conrad, A. D. Ellington, G. M. Hieftje, *Anal. Chem.* **1998**, *70*, 3419 – 3425.
[192] V. Pavlov, Y. Xiao, B. Shlyahovsky, I. Willner, *J. Am. Chem. Soc.* **2004**, *126*, 11768 – 11769.
[193] L. Gold, *J. Biol. Chem.* **1995**, *270*, 13581 – 13584; D. W. Drolet, L. Moon-McDermott, T. S. Romig, *Nat. Biotechnol.* **1996**, *14*, 1021 – 1025.
[194] Q. Yang, I. J. Goldstein, H.-Y. Mei, D. R. Engelke, *Proc. Natl. Acad. Sci. USA* **1998**, *95*, 5462 – 5467.
[195] J. C. Cox, P. Rudolph, A. D. Ellington, *Biotechnol. Prog.* **1998**, *14*, 845 – 850; D. W. Drolet, R. D. Jenison, D. E. Smith, D. Pratt, B. J. Hicke, *Comb. Chem. High Throughput Screening* **1999**, *2*, 271 – 278.
[196] L. B. McGown, M. J. Joseph, J. B. Pitner, G. P. Vonk, C. P. Linn, *Anal. Chem.* **1995**, *67*, 663A – 668A; M. Famulok, G. Mayer, M. Blind, *Acc. Chem. Res.* **2000**, *33*, 591 – 599; S. L. Clark, V. T. Remcho, *Electrophoresis* **2002**, *23*, 1335 – 1340.
[197] M. N. Stojanovic, D. M. Kolpashchikov, *J. Am. Chem. Soc.* **2004**, *126*, 9266 – 9270.
[198] J. G. Bruno, J. L. Kiel, *Biosens. Bioelectron.* **1999**, *14*, 457 – 464; J. Vivekananda, J. L. Kiel, US Patent 6569630 B1, **2003**.
[199] J. R. Hesselberth, D. Miller, J. Robertus, A. D. Ellington, *J. Biol. Chem.* **2000**, *275*, 4937 – 4942.
[200] R. Kirby, E. J. Cho, B. Gehrke, T. Bayer, Y. S. Park, D. P. Neikirk, J. T. McDevitt, A. D. Ellington, *Anal. Chem.* **2004**, *76*, 4066 – 4075.
[201] R. D. Jenison, C. Gill, A. Pardi, B. Polisky, *Science* **1994**, *263*, 1425 – 1429; G. R. Zimmermann, C. L. Wick, T. P. Shields, R. D. Jenison, A. Pardi, *RNA* **2000**, *6*, 659 – 667; H. Gouda, I. D. Kuntz, D. A. Case, P. A. Kollman, *Biopolymers* **2003**, *68*, 16 – 34.
[202] S. D. Jayasena, *Clin. Chem.* **1999**, *45*, 1628 – 1650.
[203] M. Rajendran, A. D. Ellington, *Comb. Chem. High Throughput Screening* **2002**, *5*, 263 – 270.
[204] M. Lee, D. R. Walt, *Anal. Biochem.* **2000**, *282*, 142 – 146; J. R. Epstein, D. R. Walt, *Chem. Soc. Rev.* **2003**, *32*, 203 – 214; C. A. Savran, S. M. Knudsen, A. D. Ellington, S. R. Manalis, *Anal. Chem.* **2004**, *76*, 3194 – 3198.
[205] M. Furuki, L. S. Pu, *Thin Solid Films* **1992**, *210/211*, 471 – 473; A. Hierlemann, A. J. Ricco, K. Bodenhöfer, W. Göpel, *Anal. Chem.* **1999**, *71*, 3022 – 3035.
[206] A. W. Snow, W. R. Barger, M. Klusty, H. Wohltjen, N. L. Jarvis, *Langmuir* **1986**, *2*, 513 – 519.
[207] D. Kriz, L. I. Andersson, M. Khayyami, B. Danielsson, P.-O. Larsson, K. Mosbach, *Biomimetics* **1995**, *3*, 81 – 90.
[208] A.-M. L. Nickel, F. Seker, B. P. Ziemer, A. B. Ellis, *Chem. Mater.* **2001**, *13*, 1391 – 1397; C. I. Lin, A. K. Joseph, C. K.

 © 2006 Wiley-VCH Verlag GmbH & Co. KGaA, Weinheim

Chang, Y. D. Lee, *J. Chromatogr. A* **2004**, *1027*, 259 – 262; J. Matsui, K. Akamatsu, S. Nishiguchi, D. Miyoshi, H. Nawafune, K. Tamaki, N. Sugimoto, *Anal. Chem.* **2004**, *76*, 1310 – 1315.

[209] R. C. Bailey, J. T. Hupp, *J. Am. Chem. Soc.* **2002**, *124*, 6767 – 6774.

[210] T. Mourey, A. P. Carpenter, S. Siggia Jr., A. Lane, *Anal. Chem.* **1976**, *48*, 1592 – 1596; A. Pal, D. L. Stokes, J. P. Alarie, T. Vo-Dinh, *Anal. Chem.* **1995**, *67*, 3154 – 3159; T. Vo-Dinh, D. L. Stokes, *Field Anal. Chem. Technol.* **1999**, *3*, 346 – 356.

[211] S. Kostrewa, M. Emgenbroich, D. Klockow, G. Wulff, *Macromol. Chem. Phys.* **2003**, *204*, 481 – 487.

[212] M. Larsson, J. Lu, J. Lindgren, *J. Raman Spectrosc.* **2004**, *35*, 826 – 834.

[213] M. A. De Jesús, K. S. Giesfeldt, M. J. Sepaniak, *J. Raman Spectrosc.* **2004**, *35*, 895 – 904.

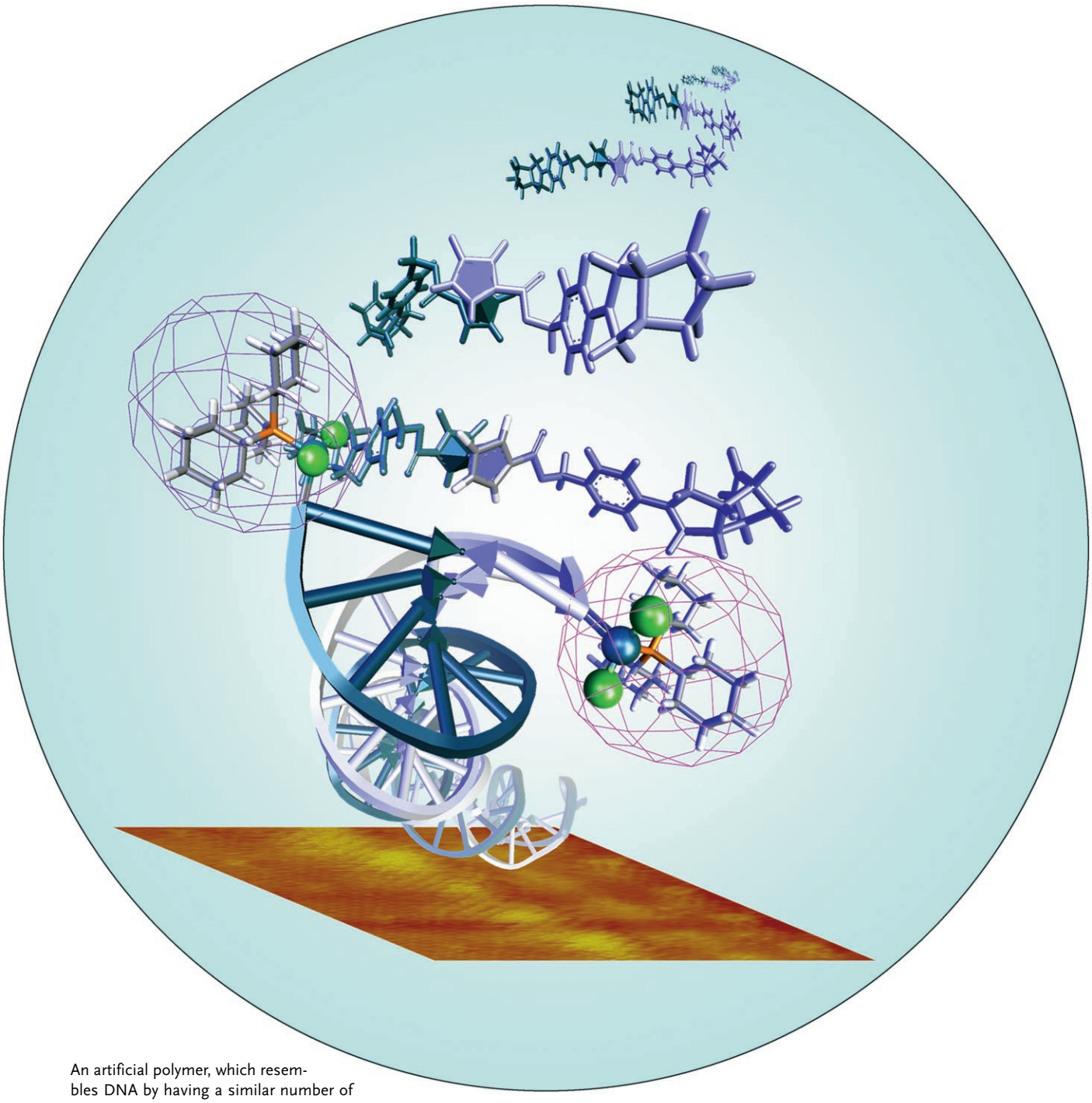
[214] B. E. Baker, N. J. Kline, P. J. Treado, M. J. Natan, *J. Am. Chem. Soc.* **1996**, *118*, 8721 – 8722.

[215] M. Kahl, E. Voges, S. Kostrewa, C. Viets, W. Hill, *Sens. Actuators B* **1998**, *51*, 285 – 291.

© 2006 Wiley-VCH Verlag GmbH & Co. KGaA, Weinheim

Communications

DOI: 10.1002/anie.200503406



An artificial polymer, which resembles DNA by having a similar number of monomeric units per pitch and similar spacing between neighboring monomeric units, was prepared through ring-opening metathesis polymerization and studied by scanning tunneling microscopy. The monomer is a bisnorbornene derivative with a rigid ferrocene bridge. For more details, see the Communication by T.-Y. Luh and co-workers on the following pages.

WILEY InterScience DISCOVER SOMETHING GREAT

© 2006 Wiley-VCH Verlag GmbH & Co. KGaA, Weinheim

DNA-like Polymers

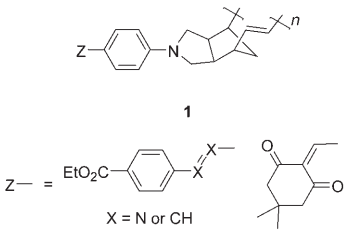
DOI: 10.1002/anie.200503406

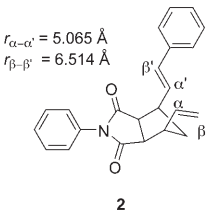
Molecular Architecture towards Helical Double-Stranded Polymers**

*Hui-Chun Yang, Shu-Yi Lin, Hsiao-Ching Yang, Cheng-Lan Lin, Lun Tsai, Shou-Ling Huang, I. Wen-Peter Chen, Chun-hsien Chen, Bih-Yaw Jin, and Tien-Yau Luh**

Biopolymers provide unique structural features and fascinating chemical and biological properties that artificial polymers are still far from matching. In DNA, the linking base pairs are perpendicular to the deoxyribose phosphate backbones and π–π stacking between base-pair layers is characteristic of the double-helical structure. Much effort has focused on the helical double-stranded oligomers in which the two single chains are chelated to metal ions,[1] complexed through hydrogen bonding,[2] π–π stacked,[3] or form inclusion complexes.[4] Ladderlike organic polymers that have two strands connected by covalent dative or ionic bonds have been briefly explored.[5] The synthesis of polymers structurally comparable to those of DNA remains a challenge. Herein we report the molecular architecture of the first helical double-stranded polymer. Our design involves a suitable monomer that contains two polymerizable groups linked by a rigid spacer. The control of the orientation of the linkers during polymerization is indispensable for the synthesis of double-stranded polymers.

It has been shown that polymers **1**, obtained from ring-opening metathesis polymerization (ROMP) of norbornenes with rigid pendant groups by using the Grubbs I catalyst,[6] exhibit second-order nonlinear optical hyperpolarizability





that is molecular-weight dependent.[7] Such a relationship implies that these polymers may adopt a brushlike structure with relatively uniform stereochemistry and conformation. The spacing of each monomeric unit in **1** was 5–6 Å as revealed by the X-ray crystal structure of **2**.[7b] It is envisaged that the introduction of another norbornene moiety at the end of this pendant group may furnish a useful entry for double-stranded polymers.

The bisnorbornene derivative, **3**, was synthesized according to Scheme 1. The ferrocene moiety was incorporated as part of the linker as it has a certain rigidity but is somewhat flexible. It is interesting to note that the closest Fe–Fe interatomic distances in single-crystal ferrocene and its derivatives range from 5.5 to 5.9 Å.[8] This spacing occupied by the ferrocene moiety appears to be within the limit of span for the vinylcyclopentane monomeric unit in polynorbornenes. Moreover the benzylic moiety and the ester linkage in **3** provide additional flexibility in this linker. Treatment of **3** with 10 mol% of the Grubbs I catalyst afforded, in 90% yield, **4**, which is soluble in $CHCl_3$, CH_2Cl_2, and THF. The ^{13}C NMR spectrum of **4** matched nicely that of **3** and the signals of **4** are relatively sharp, which is consistent with it having a double-stranded structure. Temperature-dependent ^1H NMR spectra of **4** in CD_2Cl_2 suggest that the polymer is very fluxional and the barrier for this conformational equilibrium is very low. The UV absorption for **4** is at $\lambda_{max} = 261$ nm ($\varepsilon = 45.9\ g^{-1}\,cm^2$), which is blue-shifted in comparison with that of **3** ($\lambda_{max} = 267$ nm; $\varepsilon = 55.8\ g^{-1}\,cm^2$). In addition, a decrease in ε for **4** suggests that there might be some kind of interaction between the linking chromophores.[9]

Treatment of **3** with 10% NaOH in a mixture of MeOH/$CHCl_3$ at room temperature afforded **5** and **6** in essentially quantitative yield. Under the same conditions, methanolysis of **4** gave the corresponding single-stranded polymer, **7a** ($\bar{M}_n = 7330\ g\,mol^{-1}$, PDI = 1.46; $\bar{M}_n$ is the number-average molecular weight, PDI is the polydispersity index) in 89% yield in addition to **5** in 66% yield. Polymer **7b** ($\bar{M}_n = 3540\ g\,mol^{-1}$, PDI = 1.28) was also obtained from the reaction of **6** with the Grubbs I catalyst in 89% yield. It is interesting to note that **7a** showed the same spectroscopic properties as **7b**. These results imply that **4** has a molecular weight of $\bar{M}_n = 21\,000\ g\,mol^{-1}$ and on average about 29 repetitive units. More-detailed experimental methods and spectroscopic properties are found in the Supporting Information.

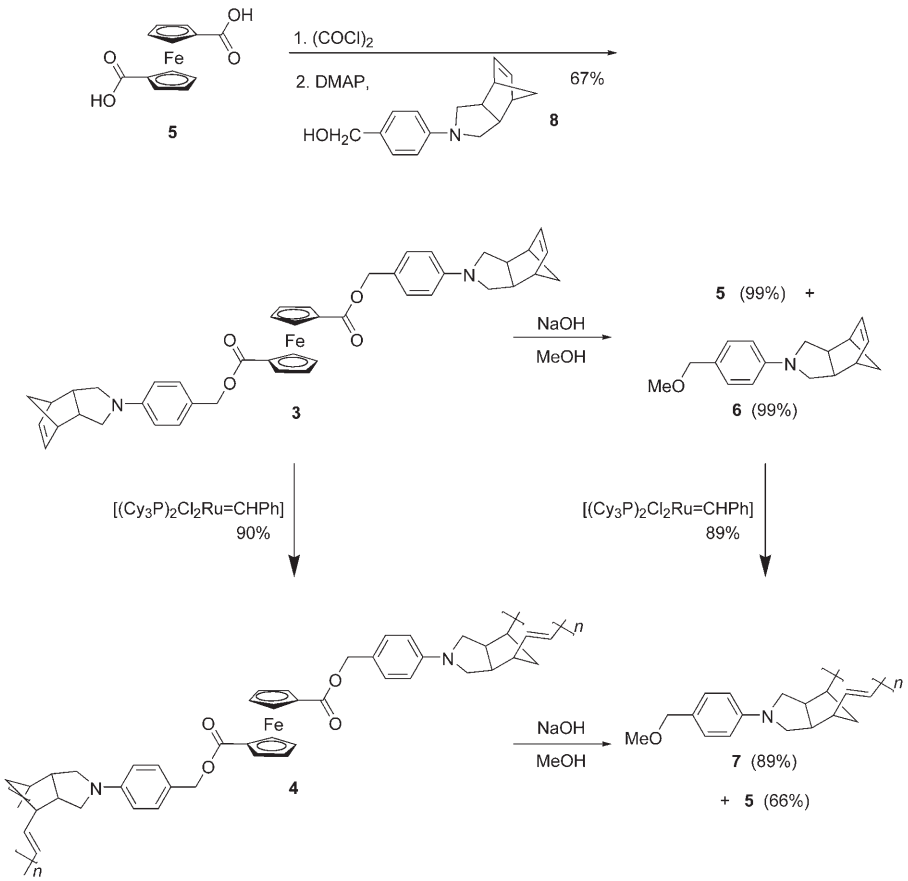
Both **3** and **4** exhibit reversible redox peaks that correspond to the ferrocene moiety. The formal potentials of **3** and **4** were 385 and 439 mV (versus Fc/Fc^+), respectively. There was an additional redox pair with a formal potential of 506 mV for **3** arising from the *para*-substituted aniline moiety. This oxidation was not observed with **4**. Presumably the peak

[*] H.-C. Yang, Dr. H.-C. Yang, Dr. C.-L. Lin, L. Tsai, S.-L. Huang, Prof. B.-Y. Jin, Prof. T.-Y. Luh
Department of Chemistry
National Taiwan University
Taipei 106 (Taiwan)
Fax: (+886) 2-2364-4971
E-mail: tyluh@ntu.edu.tw
H.-C. Yang, Prof. T.-Y. Luh
Institute of Polymer Science and Engineering
National Taiwan University
Taipei 106 (Taiwan)
Dr. S.-Y. Lin, I. W.-P. Chen, Prof. C.-H. Chen
Department of Chemistry
National Tsing Hua University
Hsinchu 300 (Taiwan)
Dr. C.-L. Lin
Institute of Chemistry
Academia Sinica
Nangang, Taipei 115 (Taiwan)

[**] This work was funded by the National Science Council of the Republic of China.

Supporting information for this article is available on the WWW under http://www.angewandte.org or from the author.

 © 2006 Wiley-VCH Verlag GmbH & Co. KGaA, Weinheim



Scheme 1. Synthetic routes of molecules used in this work. DMAP = 4-dimethylaminopyridine.

might merge with the oxidation of the ferrocene moiety in the polymer.

Scanning tunneling microscopy (STM) was employed to characterize the structure of **4**. Helical, supercoil, and ladder structures were observed (Figure 1). The length of these features in Figure 1 is longer than what was estimated based on the average molecular weight. It seems likely that weak adsorbate–substrate interactions may result in only those that have large molecular weights or exhibit strongly lateral attractions were imaged. Figure 1a shows a helical structure **A** on a flat graphite substrate (highly ordered pyrolytic graphite, HOPG). The lengths of the stripes range from 1.2 to 2.4 nm and are shorter for bright stripes (crossover regions) and longer for dim stripes. The average spacing between stripes is 0.45 ± 0.04 nm, the average pitch length is 5.2 ± 0.2 nm, and each pitch consists of twelve or thirteen monomeric units.

For the supercoil structure **B** (Figure 1b) the average spacing per turn, the apparent height, and the nominal width are about 7.1, 3.2, and 3.0 nm, respectively, which is consistent with the structure being a hollow coil. Attempts to observe molecularly resolved images for supercoils were unsuccessful. Presumably, half of the coil per turn is not in contact with the graphite substrate, which results in enhanced thermal motion and makes imaging difficult.

The ladder structures **C** shown in Figure 1c display an apparent uniform width throughout and exhibit parallel lines or bright spots, for example, going from the upper right to the lower left corner in Figure 1c. Vertical to these parallel lines are fine rows; together these lines and rows create a ladderlike image. The width of these ladders ranges from 2.2 to 2.4 nm and the spacing between the rows falls between 0.45 and 0.55 nm, which is consistent with the proposed ladder structure although the ferrocene diester, benzene ring, and the backbone moieties cannot be unambiguously identified at this stage.

The observation of three different images of **4** on HOPG appears to be consistent with the fluxional behavior of **4** as revealed by the variable-temperature NMR spectroscopy study. Molecular-mechanics calculations were carried out to

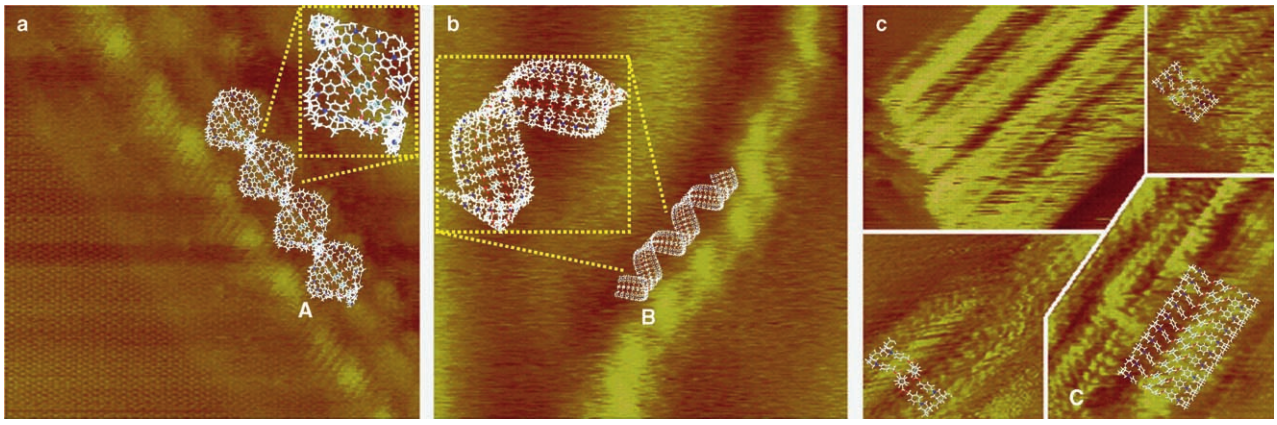


Figure 1. STM images of **4** on HOPG at a flat terrace rather than at a step edge or domain boundaries.[10] The values in parentheses are the corresponding imaging sizes and conditions: a) helical structure (16.8×16.8 nm, $E_{bias} = 0.19$ V, $i_{tunneling} = 200$ pA); b) supercoil (58×58 nm, $E_{bias} = 0.19$ V, $i_{tunneling} = 20$ pA); c) ladder (clockwise from the upper left one: 35×28 nm, 5.0×6.5 nm, 7.0×7.4 nm, 7.2×5.3 nm; $E_{bias} = 0.24$ V, $i_{tunneling} = 20$ pA). E_{bias} is the applied bias potential, $i_{tunneling}$ is the tunneling current.

 © 2006 Wiley-VCH Verlag GmbH & Co. KGaA, Weinheim

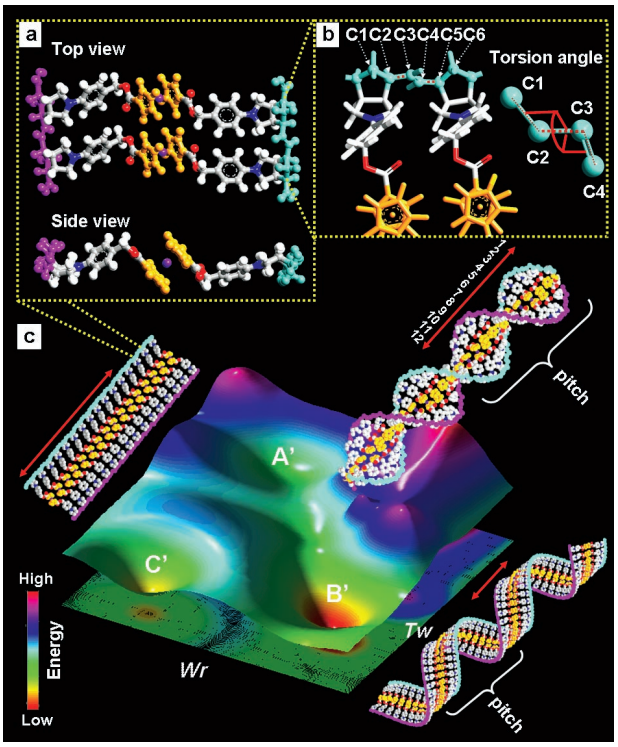


Figure 2. Schematic representation of the molecular modeling. a) Structures of monomer and isotactic dimer. b) Definition of torsion angles on backbone (C1-C2-C3-C4 and C3-C4-C5-C6) related to conformational transition. c) The potential-energy surface based on the simulated energies of three local structures: **A**′ (helical), **B**′ (supercoil), **C**′ (ladder), and transition-energy for interconversions. The two geometrical characteristics, twisting number (*Tw*) and writhing number (*Wr*), define the topology of the secondary structures.

simulate the structures of **4** (with different molecular weights) and **3** by using a modified version of universal force field found in molecular-modeling programs.[11] The 3D topologies of the secondary structures of **4** were established by varying both the conformation of **3** and the tacticity of the backbone of **4**. The two carboxy groups on the cyclopentadienyl moieties in **3** were *anti* relative to the ferrocene moiety and this zigzag structure (Figure 2a) was used as a basis for estimating the secondary structure of **4**. The double bonds in **4** were all *trans* according to the NMR results. With these constraints and extensive exploration of the potential surface by combining geometrical optimization and molecular simulation, we conclude that **4** is more stable in the isotactic than in the syndiotactic form. To account for the STM results described above, three major secondary structures of **4** in the isotactic form were obtained: double-stranded helix **A**′, supercoil **B**′, and ladder **C**′. Local structure **A**′ (Figure 2c) had a diameter of 2.2 nm and 12 monomeric units in a pitch. These data closely matched the results from the STM image of **A**. Structure **B**′ appeared to be more flexible, and the modeled supercoil with 25 monomeric units per pitch had a diameter of 3.1 nm, which is consistent with the experimental structure, **B** (Figure 1b).

Figure 2c shows a schematic map based on the simulated energies of three local structures, **A**′, **B**′, and **C**′. The supercoil form, **B**′, was the most stable whereas the helical structure, **A**′, had the highest energy among these three structures. The most important feature of these structures is the strong coupling between the dihedral angles in the backbone and the space occupied by the linkers. The shear-induced twist–writhe transition (Figure 2c) results in the translation from one form to another.[12] It is interesting to note that a slight change in torsion angles may provoke such a profound influence on the secondary structure. The detailed calculations are described in the Supporting Information.

In summary, we have described an unprecedented synthesis of a DNA-like double-stranded polymer obtained by ROMP of a bisnorbornene derivative. The polymer structurally resembles DNA by having a comparable width, a similar number of monomeric units per pitch, five-membered rings in the polymeric frame, perpendicular linkers to the backbones, and similar spacing between neighboring monomeric units. The fluxional behavior of the polymer and its ability to dissociate hydrolytically into two single-stranded polymers make it further resemble DNA molecules. The oxidation-labile ferrocene linkers in this polymer are aligned coherently along the polymer axis. Insight into the structural features of such a polymer might pave the way to tailor other polymers that simulate biological systems.

Received: September 27, 2005
Published online: December 28, 2005

Keywords: helical structures · metathesis · molecular modeling · ring-opening polymerization · scanning probe microscopy

[1] a) J.-M. Lehn, A. Rigault, J. Siegel, J. Harrowfield, B. Chevrier, D. Moras, *Proc. Natl. Acad. Sci. USA* **1987**, *84*, 2565–2569; b) U. Koert, M. M. Harding, J.-M. Lehn, *Nature* **1990**, *346*, 339–342; c) E. C. Constable, *Pure Appl. Chem.* **1996**, *68*, 253–260; d) C. R. Woods, M. Benaglia, F. Cozzi, J. S. Siegel, *Angew. Chem.* **1996**, *108*, 1977–1980; *Angew. Chem. Int. Ed. Engl.* **1996**, *35*, 1830–1833; e) C. Piguet, G. Bernardinelli, G. Hopfgartner, *Chem. Rev.* **1997**, *97*, 2005–2062; f) A. Williams, *Chem. Eur. J.* **1997**, *3*, 15–19; g) M. Albrecht, *Chem. Rev.* **2001**, *101*, 3457–3497; h) D. J. Hill, M. J. Mio, R. B. Prince, T. S. Hughes, J. S. Moore, *Chem. Rev.* **2001**, *101*, 3893–4011, and references therein; i) A. Orita, T. Nakano, D.-L. An, K. Tanikawa, K. Wakamatsu, J. Otera, *J. Am. Chem. Soc.* **2004**, *126*, 10389–10396.

[2] a) J. Sánchez-Quesada, C. Steel, P. Prados, J. de Mendoza, *J. Am. Chem. Soc.* **1996**, *118*, 277–278; b) B. Gong, Y. Yan, H. Zeng, E. Skrzypczak-Jankunn, Y. W. Kim, J. Zhu, H. Ickes, *J. Am. Chem. Soc.* **1999**, *121*, 5607–5608; c) V. Berl, I. Huc, R. G. Khoury, M. J. Krische, J.-M. Lehn, *Nature* **2000**, *407*, 720–723; d) A. P. Bisson, F. J. Carver, D. S. Eggleston, R. C. Haltiwanger, C. A. Hunter, D. L. Livingstone, J. F. Mccabe, C. Rotger, A. E. Rowan, *J. Am. Chem. Soc.* **2000**, *122*, 8856–8868; e) P. S. Corbin, S. C. Zimmerman, *J. Am. Chem. Soc.* **2000**, *122*, 3779–3780; f) H. Zeng, R. S. Miller, R. A. Flowers II, B. Gong, *J. Am. Chem. Soc.* **2000**, *122*, 2635–2644; g) P. S. Corbin, S. C. Zimmerman, *J. Am. Chem. Soc.* **2000**, *122*, 3779–3780; h) J. S. Nowick, D. M. Chung, K. Maitra, S. Maitra, K. D. Stigers, Y. Sun, *J. Am. Chem. Soc.* **2000**, *122*, 7654–7661; i) V. Berl, I. Huc, R. G. Khoury, J.-M. Lehn, *Chem. Eur. J.* **2001**, *7*, 2810–2820; j) I. Huc, *Eur. J. Org. Chem.* **2004**, 17–29; k) M. Albrecht, *Angew. Chem.* **2005**, *117*, 6606–6609; *Angew. Chem. Int. Ed.* **2005**, *44*, 6448–6451; l) H. Gong, M. J.

 © 2006 Wiley-VCH Verlag GmbH & Co. KGaA, Weinheim

Krische, *J. Am. Chem. Soc.* **2005**, *127*, 1719 – 1725; m) Y. Tanaka, H. Katagiri, Y. Furusho, E. Yashima, *Angew. Chem.* **2005**, *117*, 3925 – 3938; *Angew. Chem. Int. Ed.* **2005**, *44*, 3867 – 3870.

[3] G. J. Gabriel, B. L. Iverson, *J. Am. Chem. Soc.* **2002**, *124*, 15174 – 15175.

[4] a) A. Harada, J. Li, M. Kamachi, *Nature* **1994**, *370*, 126 – 128; b) A. P. Bisson, C. A. Hunter, *Chem. Commun.* **1996**, 1723 – 1724.

[5] a) S. Nagahama, A. Matsumoto, *J. Am. Chem. Soc.* **2001**, *123*, 12176 – 12181; b) T. E. O. Screen, J. R. G. Thorne, R. G. Denning, D. G. Bucknall, H. L. Anderson, *J. Am. Chem. Soc.* **2002**, *124*, 9712 – 9713; c) H. Tang, J. Sun, J. Jiang, X, Zhou, T. Hu, P. Xie, R. Zhang, *J. Am. Chem. Soc.* **2002**, *124*, 10482 – 10488; d) M. M. Green, J.-W. Park, T. Sato, A. Teramoto, S. Lifson, R. L. B. Selinger, J. V. Selinger, *Angew. Chem.* **1999**, *111*, 3328 – 3345; *Angew. Chem. Int. Ed.* **1999**, *38*, 3138 – 3154; e) T. Nakano, Y. Okamoto, *Chem. Rev.* **2001**, *101*, 4013 – 4038; f) J. J. L. M. Cornelissen, A. E. Rowan, R. J. M. Nolte, N. A. J. M. Sommerdijk, *Chem. Rev.* **2001**, *101*, 4039 – 4070; g) L. Brunsveld, B. J. B. Folmer, E. W. Meijer, R. P. Sijbesma, *Chem. Rev.* **2001**, *101*, 4071 – 4097; h) E. Yashima, K. Maeda, T. Nishimura, *Chem. Eur. J.* **2004**, *10*, 42 – 51.

[6] a) P. Schwab, R. H. Grubbs, J. W. Ziller, *J. Am. Chem. Soc.* **1996**, *118*, 100 – 110; b) J. G. Hamilton in *Handbook of Metathesis, Vol. 3* (Ed.: R. H. Grubbs), Wiley-VCH, Weinheim, **2003**, pp. 143 – 179.

[7] a) J. A. Sattigeri, C.-W. Shiau, C.-C. Hsu, F.-F. Yeh, S. Liou, B.-Y. Jin, T.-Y. Luh, *J. Am. Chem. Soc.* **1999**, *121*, 1607 – 1608; b) W.-Y. Lin, M. G. Murugesh, S. Sudhakar, H.-C. Yang, H.-C. Tai, C.-S. Chang, Y.-H. Liu, Y. Wang, Y. I.-W. P. Chen, C.-h. Chen, T.-Y. Luh, *Chem. Eur. J.* **2006**, *12*, 324 – 330.

[8] J. D. Dunitz, L. E. Orgel, A. Rich, *Acta Crystallogr.* **1956**, *9*, 373 – 375;

[9] a) D. M. Shin, I. S. Lee, Y. K. Chung, *Eur. J. Inorg. Chem.* **2003**, 2311 – 2317; b) A. Dirksen, U. Hahn, F. Schwanke, M. Nieger, J. N. H. Reek, F. Vögtle, L. D. Cola, *Chem. Eur. J.* **2004**, *10*, 2036 – 2047.

[10] C. R. Clemmer, T. P. Beebe, Jr., *Science* **1991**, *251*, 640 – 642.

[11] a) D. Frenkel, B. Smit, *Understanding Molecular Simulation: From Algorithms to Applications*, Academic Press, New York, **1996**; b) A. R. Leach, *Molecular Modeling. Principles and Applications*, Longman, Essex, **1997**; c) A. K. Rappé, C. J. Casewit, K. S. Colwell, W. A. Goddard III, W. M. Skiff, *J. Am. Chem. Soc.* **1992**, *114*, 10024 – 10035; d) C. J. Casewit, K. S. Colwell, A. K. Rappé, *J. Am. Chem. Soc.* **1992**, *114*, 10035 – 10046; e) A. K. Rappé, C. J. Casewit, *Molecular Mechanics Across Chemistry*, University Science Books, Sausalito, **1997**; f) J. A. McCammon, S. C. Harvey, *Dynamics of Proteins and Nucleic Acids*, Cambridge University Press, Cambridge, **1988**.

[12] a) F. B. Fuller, *Proc. Natl. Acad. Sci. USA* **1971**, *68*, 815 – 819; b) M. D. Frank-Kamenetskii, *Unraveling DNA*, VCH, Weinheim, **1995**.

 © 2006 Wiley-VCH Verlag GmbH & Co. KGaA, Weinheim

Nanostructures

DOI: 10.1002/anie.200503208

DNA-Templated Self-Assembly of Two-Dimensional and Periodical Gold Nanoparticle Arrays**

*Jaswinder Sharma, Rahul Chhabra, Yan Liu, Yonggang Ke, and Hao Yan**

Nanoparticles (NPs) are being actively developed as building blocks for electronic, photonic, and spintronics devices. When they are organized into well-defined ensembles, their collective properties depend critically on the interparticle spacings and their hierarchical organization. Up to now, methods to control these parameters were scarce. DNA-templated self-assembly provides a unique solution to meet the above challenge, largely because of the following features of DNA and DNA-based nanostructures: DNA has a well-defined geometry and highly predictable, diverse, and programmable intra/intermolecular interactions; DNA can be conveniently modified by different chemical groups, which act as linkers to covalently attach DNA oligomers to the surface of NPs; the design of stiff DNA-based nanostructures and their self-assembly have become a routine method to construct one- and two-dimensional DNA lattices of well-defined patterns.[1–10] More specifically, when NPs are assembled onto self-assembled DNA lattices, the periodicities and interparticle spacings defined by the DNA scaffolds can be readily adjusted, with nanometer spatial precisions. This level of precision provides exquisite control in the construction of rationally defined NP architectures.

Although the generic idea of using DNA to scaffold nanoelectronics was first proposed by Robinson and Seeman 18 years ago,[11] the development of self-assembled DNA nanoscaffolds to organize functional nanomaterials is still in the early stages. There has been a limited number of works reporting developments towards this goal and most of them are focused on the use of flexible and linear DNA as templates.[12–22] To achieve more predictable structural geometries of NP arrays, it is desirable to use more rigid DNA nanostructures as scaffolds to reduce the conformational flexibility. Recently Le et al.[23] used a double-crossover DNA tiling lattice to direct the assembly of 5-nm Au NPs

[*] J. Sharma,[+] R. Chhabra,[+] Dr. Y. Liu, Y. Ke, Prof. H. Yan
Department of Chemistry and Biochemistry and Biodesign Institute
Arizona State University
Tempe, AZ 85287 (USA)
Fax: (+1) 480-965-2747
E-mail: hao.yan@asu.edu

[+] These two authors contributed equally

[**] We thank Dr. Junping Zhang for helpful discussions. This study was supported by grants from the NSF (CCF-0453686, CCF-0453685) and a research grant from the Biodesign Institute at ASU to H.Y.

Supporting information for this article is available on the WWW under http://www.angewandte.org or from the author.

WILEY InterScience DISCOVER SOMETHING GREAT
© 2006 Wiley-VCH Verlag GmbH & Co. KGaA, Weinheim

functionalized with multiple copies of T_{15} sequences. This investigation represents a breakthrough in the use of self-assembled 2D DNA nanostructures as scaffolding for nanoelectronic materials. However, the presence of multiple copies of the same DNA sequence on the NP surface requires first depositing the DNA lattice onto a solid substrate before assembly of the NPs on the DNA lattice. This approach is to prevent the possible cross-linking between multiple layers of DNA lattices mediated by the multiple T_{15} on a single Au NP. Greater precision in controlling the final structure of the NP lattices would require the use of NPs functionalized with a single DNA strand or NPs conjugated with different strands in a stoichiometrically controlled fashion. This functionalization is particularly important in the hierarchical organization of DNA-templated NP arrays.

Herein, we report the first assembly of 5-nm Au NPs functionalized with a single DNA strand on three different patterned structural templates which are constructed from self-assembled DNA tiles. We show that the periodicity and interparticle spacings of the NP nanoarrays can be precisely controlled through variation of the DNA-tile dimensions. In our strategy, the NP-conjugated strand first participates in the formation of a single DNA-tile structure, this Au-NP-bearing DNA tile was subsequently used to assemble with another DNA tile to form three different lattice structures, each with a well-defined periodical pattern.

We have developed a new DNA/NP conjugate system that allows Au NPs to be readily assembled onto a DNA tiling system. This novel system is amenable both to the DNA-tiling-lattice formation and the prevention of nonspecific aggregations between the Au NPs. This development paves the way for the assembly of more complex nanoparticle arrays on DNA nanoscaffolds for future device applications. Previously, there has been two ways to conjugate DNA with Au NPs: 1) one Au NP is linked with many DNA oligomers, as developed by Mirkin et al.[13] and 2) one Au NP is linked with only one DNA oligomer, as developed by Alivisatos and co-workers.[26] Au-NP/DNA conjugates prepared by the method of Mirkin can tolerate high salt concentrations (e.g., 1 mM Mg^{2+}), but it is difficult control the stoichiometry. Au-NP/DNA conjugates prepared by the method of Alivisatos has a well-defined stoichiometry and allows precise structural control, but the particle tends to irreversibly aggregate at high salt concentrations, especially in the presence of Mg^{2+} ions. Unfortunately, high salt concentration (e.g., Mg^{2+}) was proven to be necessary for DNA self-assembly using tiling structures. Therefore, the above two methods alone are not ideal for DNA-tiling-lattice templated organization; as a result, previous Au-NP assemblies were mostly based on linear DNA structures, and the use of 2D DNA lattices to organize nanoparticles was not very successful, though the idea was proposed more than 18 years ago. Herein, we solved this problem by first coating a Au NP with the desired DNA in a 1:1 ratio using the strategy of Alivisatos, then further coating the Au NP with an excess of nonrelated DNA (thiolated T_5 oligomer) using the method of Mirkin. The resultant DNA/Au NP has advantages from both methods: a well-defined stoichiometry and a resistance to high salt concentrations. The new DNA/Au NPs made it possible to program Au NPs into different architectures.

Figure 1 illustrates the design strategy and the three different lattice structures. A detailed description of the construction of DNA-tile structures and lattices can be found elsewhere.[24] In brief, the design of DNA nanostructures

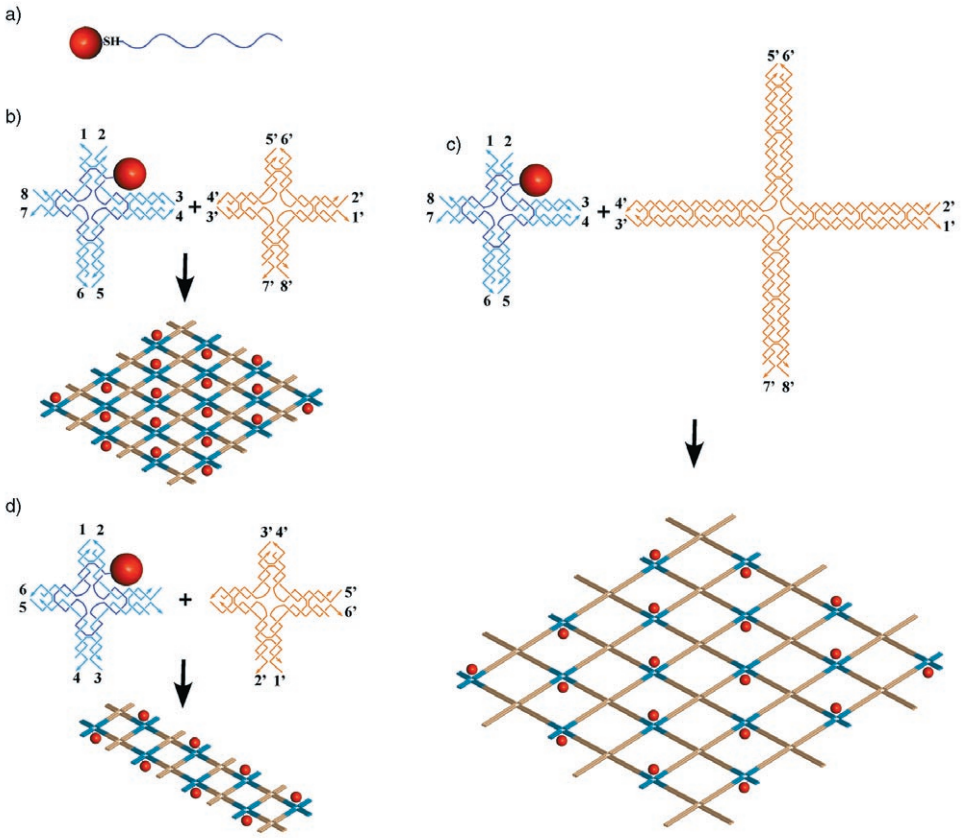


Figure 1. Schematic representations of the DNA-templated assembly of periodical Au-NP nanoarrays. a) A 1:1 conjugate of a Au NP (red ball) with a thiolated DNA strand (dark-blue curved line). b) A Au NP on a NGAB lattice. The DNA strands self-assemble into the cross-shaped A (blue) and B (orange) tiles with sticky ends so that 1 is complemented with 1′, 2 with 2′, and so forth. The central strand on A tile carries the Au NP into the self-assembled 2D nanogrid. c) A Au NP on a NGABL lattice. The A tile remains the same as in (b), and the four arms of the B tiles are each elongated by four DNA helical turns, thus the 2D arrays assembled have a larger cavity. d) A Au NP on a NTAB lattice. They self-assemble into 1D nanotrack by modifying the sticky ends of the A and B tiles. Note: all the A tiles share the same central strand that carries the Au NP.

© 2006 Wiley-VCH Verlag GmbH & Co. KGaA, Weinheim

begins with the self-assembly of a set of single-stranded DNA molecules into branched motifs known as tiles. DNA tiles carry single-stranded overhangs, or "sticky ends", which are encoded to recognize the complementary sticky ends of other DNA tiles, thus facilitating their self-assembly into ordered lattices. Herein, we utilize a family of DNA tiles that resemble a cross structure composed of four four-arm DNA branch junctions to template the assembly of Au NPs. A single unit of the cross structure has been shown to self-assemble into 2D nanogrids that display periodic square cavities.[5] A two-tile system (A and B tiles) has also been developed so that A and B tiles associate with each other alternatively to form 2D nanogrids or 1D nanotracks.[25] Herein, we utilize the A/B tile system and link the 5-nm Au NPs (represented as a red ball) with a 109-base-DNA strand (colored bright blue) that participates in the A tile (colored blue). The A and B tiles and their sticky ends are designed so that they can form three different lattice structures, as illustrated in Figure 1 b–d, respectively. The distance between neighboring A and B tiles in Figure 1 b is 4.5 helical turns of DNA, and the dimension of each cavity from center to center measures approximately 19.3 nm (this lattice structure is termed "NGAB"). We added an extra four turns to each arms of the B tile in Figure 1 c so that the dimension of the cavity becomes larger and measures approximately 33 nm (this lattice structure is termed "NGABL"). Figure 1 d illustrates that a nanotrack can be formed from the A and B tiles used in Figure 1 b by redesigning the sticky-ends matching strategy and blocking the growth of the lattice along the second dimension (this lattice structure is termed "NTAB"). In our design, the Au-NP-conjugated DNA strand participates in the A tile, weaving through the four arms of the cross with an extra T9 region that protrudes out from the side of the tile to prevent potential steric hindrance between the Au NP and the tile itself. The arrangements of the DNA tiles and the relative positions of the Au NPs on the three different DNA lattices are illustrated in Figure 1 as 3D side views. Note that there are relative rotations (in plane rotation and/or flipping over) of the A tiles, thus the positions of the Au NPs within the lattice cavities are controlled and well defined. Detailed schematic representations that show such rotations can be found in the Supporting Information. Overall, the above design provides us an excellent platform to test the DNA/nanostructure templated assembly of Au NPs and the control of interparticle spacings determined by their underneath lattices.

To achieve the above design, we adopted reported methods[26] to first conjugate the 109-base thiolated DNA strand in the A tile (which is shown as the dark-blue strand in Figure 1) to the surface of the 5-nm Au NPs, and the Au NP that contains a single copy of the DNA strand was isolated with 3% agarose gel electrophoresis (see the Experimental Section). Figure 2 a is an agarose gel that shows the separation of Au NPs with different copies of DNA strands conjugated to it. The band that corresponds to the 1:1 ratio of the Au NPs and DNA migrates slower relative to the bare Au NPs and was purified out of the gel for further annealing with other DNA strands to form the A-tile structures shown in Figure 1.

Figure 2 b shows a native agarose gel that demonstrates that the 5-nm Au NP conjugated with a single DNA strand

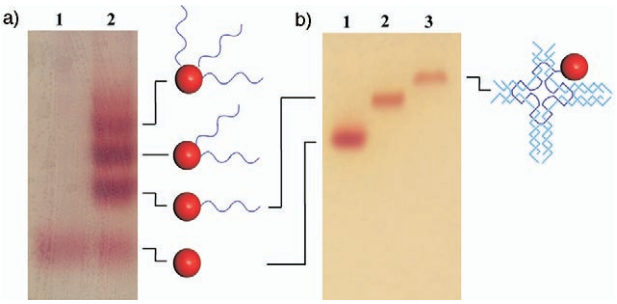


Figure 2. a) The Au NPs conjugated with different numbers of the thiolated ssDNAs are separated by 3% agarose gel electrophoresis. Lane 1: Au NP alone; lane 2: a mixture of Au NP with the thiolated DNA strands. The ratios between Au and DNA for each band are indicated at the side. b) The incorporation of the Au NP into the A tile is confirmed by using 3% native agarose gel. Lane 1: Au NP alone; lane 2: 1:1 conjugate of a Au NP with the 109-base-DNA strand; lane 3: annealed A tile carrying one Au NP.

participates in the formation of the A-tile structure, thus allowing a single Au NP to be incorporated in the tile. Lane 1 contains the 5-nm Au NP with no DNA attached. Lane 2 contains a Au NP conjugated with a single 109-base-DNA strand obtained from the separation protocol shown in Figure 2 a. Lane 3 contains the annealed A tile that is composed of the DNA strand conjugated with a Au NP and all the other strands involved in the A tile. A single and slower migrating pink band relative to the band in lane 2 indicates the successful incorporation of the 5-nm Au NP into the A tile.

It is important to point out again that we have optimized the buffer conditions to be amenable to the formation of the tile structure and also prevent the aggregation of Au NPs. We have observed that the 5-nm Au NPs and their DNA conjugates have the tendency to precipitate when there are Mg^{2+} ions (>1 mM) present in the buffer. However, the presence of Mg^{2+} ions (>1 mM) is usually required for the proper hybridization of the DNA-base pairing in the formation of the DNA-tile structures and lattices. To solve this problem, we replaced the Mg^{2+} ions with a higher concentration of Na^{+} ions in a TBE buffer (Tris–borate ethylenediaminetetraacetic acid (EDTA); 89 mM Tris, 89 mM boric acid, 2 mM EDTA, and 600 mM sodium chloride, pH 8.0). We found that under this buffer condition the A/B tile used can form 2D nanogrids and 1D nanotracks, but the 5-nm Au NPs conjugated with DNA form aggregates. We added thiolated short T5 oligomers to cover the surface of the Au NPs and further stabilize and prevent aggregation between the Au NPs. This approach greatly increases the charge density of the Au-NP surface, thus Au NPs with the thiolated T5 oligomers do not aggregate in 600 mM NaCl buffer.

After the Au NPs conjugated with the 109-base-DNA strand were incorporated into the A tile, the A tiles were mixed with three different B tiles to further self-assemble into the NGAB, NGABL, and NTAB lattices (Figure 1 b–d). The Au-NP lattices formed by the templated assembly were deposited onto the mica surface and observed by atomic force microscopy (AFM). Figure 3 a–c shows AFM images that correspond to the NGAB, NGABL, and NTAB lattice

 © 2006 Wiley-VCH Verlag GmbH & Co. KGaA, Weinheim

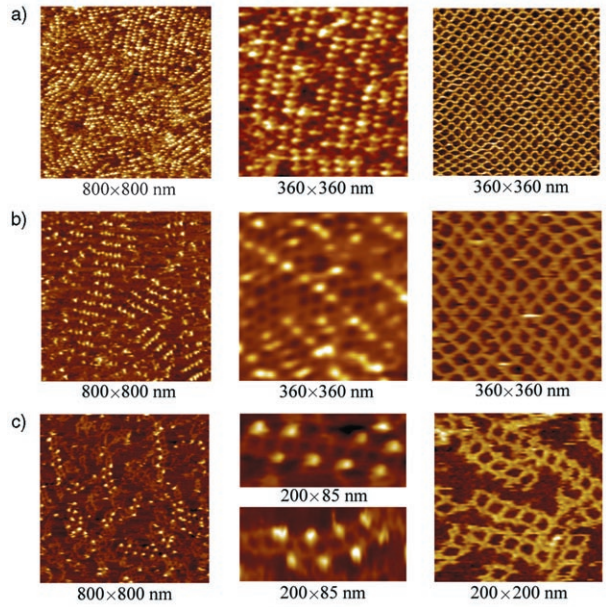


Figure 3. AFM images show the patterning of Au NPs on the self-assembled DNA nanostructures. a) Au NPs on NGAB lattices; b) Au NPs on NGABL lattices; c) Au NPs on NTAB lattices. In each group of images, the right image shows the DNA lattice or arrays without the Au NPs. The height scales for these images are approximately 2 nm. The images on the left are large scan areas that show the regular patterning of AU NPs. The middle images are zoom-in, high-resolution scans which show both the Au NPs and the DNA scaffolds underneath. The height scales for these images are approximately 5 nm.

structures, respectively. The left panels in Figure 3 a–c show a larger scan area, followed by the zoom-in image for a close-up view of both the NPs and their underlying DNA nanogrids and nanotracks. The panels on the right are images that show the control experiments when the Au NPs were not attached to the 109-base-DNA strand. The Au NPs appear as brighter dots with heights measuring 4.3–5.1 nm (Figure 4). The AFM images reveal periodical NP-lattice structures for each design, and the measured repeating distance between the particles are shown in Figure 4, which match the designed parameters. The underlying DNA lattices are revealed clearly in the zoom-in images. The enlargements of the particle–particle distances shown in Figure 3 b confirmed the designed increase in the helical turns between the A and B tiles. The resolution obtained for the zoom-in image shown in Figures 3 c and 4 b can even tell the exact position of the Au NPs relative to each individual tile, thus matching the designed pattern illustrated in Figure 1 c, d (detailed analysis of these patterns is shown in the Supporting Information).

It is notable that the DNA lattices underneath the NPs observed by AFM do not show a perfect square most of the time, but rather a rhombus shape. The flexibility of the cross-shaped tile at the crossing point has been recognized in the bare DNA 2D array formed, in which the acute angle of the cross may range from 90° to as small as 45° under stress. It is also noted that the NPs are always positioned at the corner of the crossing with the obtuse angle. The formation of the obtuse angle at the corner containing the NP possibly results from positioning the NPs at the crossing, which induces steric displacement in the DNA helices, or from the electrostatic repulsion between the highly negative charged NP (with multiple copies of T5 strands on surface) and the DNA bases in the phosphate backbone of the DNA strand. The rhombus-shaped cavity led to a shortened distance between the NPs along one diagonal direction and an elongated distance along the other diagonal direction.

The well-defined periodicity and the AFM image and profile clearly demonstrated that the NPs are sitting on the DNA lattices in a rationally organized fashion. However, it is also noted that there are some tiles in the A-tile position on the DNA lattice lacking the Au NPs. We reasoned that this positioning is because the Au NP and DNA linkage is not strong enough, so some Au NPs become detached from the DNA strands in the processing procedures after the gel-

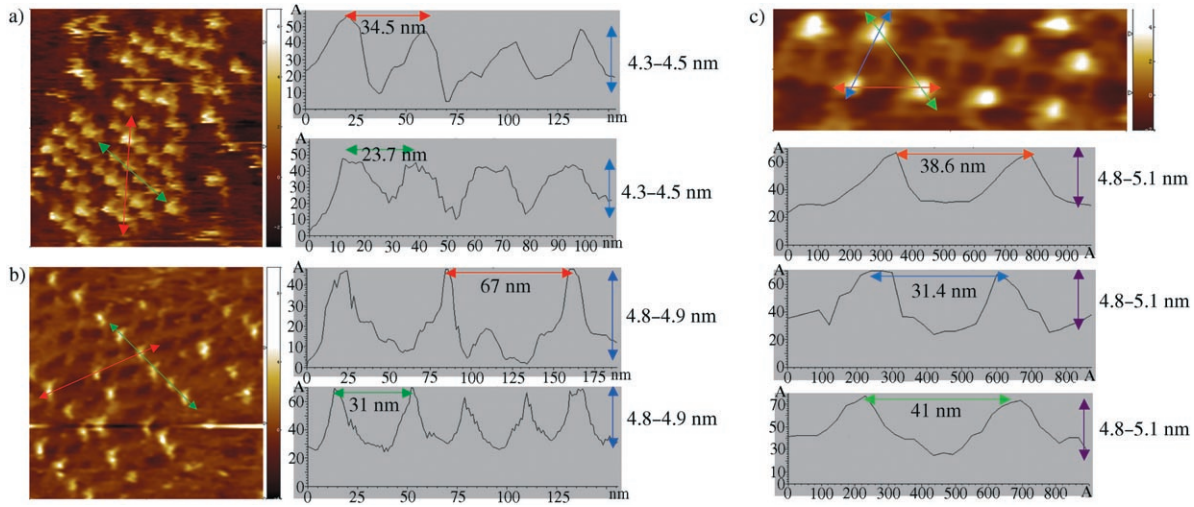


Figure 4. Surface cross-section analysis of the AFM images. a) Au NPs on a NGAB lattice; b) Au NPs on a NGABL lattice; c) Au NPs on a NTAB lattice. The lines with a double arrowhead in the images indicate the range of the cross-section analysis. Their colors correspond to the colors of the arrows on the profile plots. Distance and height measured are labeled in the profile plots. The measured distances are all within ±2 nm to the calculated distances from the design.

 © 2006 Wiley-VCH Verlag GmbH & Co. KGaA, Weinheim

purification step. The DNA strand lacking the Au NP still can be incorporated into the A tile and then grow into the DNA lattice in the following annealing steps. Stable linkages between the DNA strands and NPs need to be developed to achieve a higher yield of the NP assembly on the DNA nanoscaffolds.

In summary, we have successfully demonstrated the incorporation of a single Au NP into an unique rationally designed DNA-nanostructural building block (an unit tile), and used the NP-bearing DNA tile for the directed self-assembly of two-dimensional NP arrays with well-defined periodical patterns and precisely controlled interparticle spacings. This approach opens up great opportunities to control the interparticle spacings and hierarchical architectures of nanoparticles. With the development of DNA nanotechnology, the design of DNA-nanostructural building blocks of different geometries and lattice morphologies is not a formidable task any more. By introducing unique sticky ends to the NP-bearing DNA building blocks, sophisticated patterns can be achieved, opening up opportunities to construct useful nanoscale devices from the well-organized nanoparticles. For example, photonic antenna could be constructed by aligning metallic nanoparticles of different sizes into a chain or parallel chainlike configuration with well-defined interparticle spacings.[27] Precisely controlled organization of Au and other nanoparticles onto patterned DNA lattices could also enable us to study their distance-dependent optical and electronic properties. To maximize the full potential of using DNA nanoarchitecture to scaffold nanoelectronics, it is necessary to develop methods to assemble other type of NPs, such as magnetic, semiconductor NPs onto DNA templates.

Experimental Section

DNA-tile complex and lattice formation: The sequences of all DNA strands used are listed in the Supporting Information. The DNA sequences were designed with the SEQUIN program.[28] DNA strands were synthesized by Integrated DNA Technologies, Inc. (www.idtdna.com) and purified by denaturing polyacrylamide gel electrophoresis (PAGE). DNA-tile complexes (A and B tiles) were formed by mixing an equal quantity of each strand designed in the complex at a concentration of 1 μM, as estimated by OD_{260}, in 1 × TBE/Na^+ buffer (89 mM Tris, 89 mM boric acid, 2 mM EDTA, and 600 mM sodium chloride, pH 8.0).

Phosphination of Au NPs: Au colloids with diameters of 5 nm (purchased from Ted Pella Inc.) were stabilized by complexation with bis(*p*-sulfonatophenyl)phenylphosphine dihydrate dipotassium salt (Strem Chemicals Inc.). This salt (20 mg) was added to the gold-colloid solution (100 mL; ≈1 OD at 520 nm), the mixture was shaken overnight at room temperature. NaCl (solid) was then added slowly to this mixture while stirring until the color changed from deep burgundy to light purple. The supernatant was carefully removed with a pipette after centrifugation, and the Au NPs were resuspended in 1 mM phosphine solution (5 mL). Methanol (5 mL) was added, the mixture centrifuged, the supernatant removed, and the Au NPs were resuspended in 2.5 mM phosphine solution (2 mL). The concentration of the Au NPs was estimated from the optical absorbance at 520 nm. Phosphine coating gives a net negative charge on the particle surface, which stabilizes the Au NPs in high concentrations of particles and electrolytes.

Au/DNA conjugates: The thiolated DNA strand was purchased from IDT and purified by denaturing PAGE. The thiolated DNA strand was incubated overnight with Au NPs capped with phosphine in a ratio of 1.0:1.0 in 0.5 × TBE containing 50 mM NaCl at room temperature. Different combinations of DNA/Au conjugates (particles bearing 1–4 single-stranded DNAs (ssDNAs)) were separated by 3% agarose gel (running buffer 0.5 × TBE, loading buffer 30% glycerol, at 15 $V\,cm^{-1}$). Different bands were clearly visible from the red color of the Au NPs. The band with DNA/Au in a 1:1 ratio was electro-eluted onto the glass fiber filter and a dialysis membrane (MWCO 10000) inserted in front of the band in the gel. The conjugate was recovered using a 0.45-μm centrifugal filter device. The concentration of this Au NP/DNA conjugate was estimated from the optical absorbance at 520 nm.

Further stabilization of Au NPs: The Au particles conjugated with the 109-base-DNA strand were further stabilized by adding thiolated T5 ssDNA oligomers to avoid further coagulation during annealing under high-electrolyte conditions. This stabilization was carried out by incubating a relatively high concentration (T5/Au = 100:1) of ssDNA T5 relative to the concentration of DNA/Au conjugates in 0.5 × TBE buffer containing 50 mM NaCl overnight at room temperature.

Au-NP and DNA-tile assemblies: To form the A-tile structure bearing a single 5-nm Au NP, the Au NP conjugated with the 109-base-DNA strand was heated at 60 °C for 5 min. The other strands of the A tile were also preheated at 90 °C for 5 min. These two solutions were mixed together at 60 °C in an equimolar ratio and were slowly cooled to room temperature in 1 × TBE buffer containing 600 mM NaCl. Another tube contained annealed strands comprising the B tile in 1 × TBE containing 600 mM NaCl. The A and B tiles annealed separately were mixed in 1:1 ratio at 40 °C and cooled slowly to room temperature. Similar procedures were adopted for the NGABL and NTAB systems.

AFM imaging: A mixture of 1 × TAE/Mg (2 μL; 40 mM Tris, 20 mM acetic acid, 2 mM EDTA, 12.5 mM magnesium acetate, pH 8.0) buffer was first dropped onto freshly cleaved mica (Ted Pella, Inc.) and left to adsorb onto the surface for 2 min. A sample of the DNA lattice (2 μL) was deposited on the drop. Mg preadsorbed on mica can help the DNA structure stay on the mica during the AFM scan. Buffer (1 × TAE/Mg; 400 μL) was added to the drop on the mica and imaging was performed in a fluid cell in AAC mode on a Pico-plus atomic force microscope (Molecular Imaging) using NP-S tips (Veeco Inc.).

Received: September 9, 2005
Published online: December 19, 2005

Keywords: DNA · nanoparticles · nanostructures · scanning probe microscopy · templated self-assembly

[1] N. C. Seeman, *Nature* **2003**, *421*, 427–431.
[2] E. Winfree, F. Liu, L. A. Wenzler, N. C. Seeman, *Nature* **1998**, *394*, 539–544.
[3] T. H. Labean, H. Yan, J. Kopatsch, F. R. Liu, E. Winfree, J. H. Reif, N. C. Seeman, *J. Am. Chem. Soc.* **2000**, *122*, 1848–1860.
[4] C. D. Mao, W. Q. Sun, N. C. Seeman, *J. Am. Chem. Soc.* **1999**, *121*, 5437–5443.
[5] H. Yan, S. H. Park, G. Finkelstein, J. H. Reif, T. H. LaBean, *Science* **2003**, *301*, 1882–1884.
[6] P. W. K. Rothemund, N. Papadakis, E. Winfree, *PLoS Biol.* **2004**, *2*, 2041–2053.
[7] B. Q. Ding, R. J. Sha, N. C. Seeman, *J. Am. Chem. Soc.* **2004**, *126*, 10230–10231.
[8] J. C. Mitchell, J. R. Harris, J. Malo, J. Bath, A. J. Turberfield, *J. Am. Chem. Soc.* **2004**, *126*, 16342–16343.
[9] N. Chelyapov, Y. Brun, M. Gopalkrishnan, D. Reishus, B. Shaw, L. Adleman, *J. Am. Chem. Soc.* **2004**, *126*, 13924–13925.

 © 2006 Wiley-VCH Verlag GmbH & Co. KGaA, Weinheim

[10] Y. He, Y. Chen, H. Liu, A. E. Ribbe, C. Mao, *J. Am. Chem. Soc.* **2005**, *127*, 12202 – 12203.
[11] B. H. Robinson, N. C. Seeman, *Protein Eng.* **1987**, *1*, 295 – 300.
[12] For a recent review on this topic, see: C. M. Niemeyer, U. Simon, *Eur. J. Inorg. Chem.* **2005**, *18*, 3641 – 3655.
[13] C. A. Mirkin, R. L. Letsinger, R. C. Mucic, J. J. Storhoff, *Nature* **1996**, *382*, 607 – 609.
[14] A. P. Alivisatos, K. P. Johnsson, X. Peng, T. E. Wilson, C. J. Loweth, M. P. Bruchez, Jr., P. G. Schultz, *Nature* **1996**, *382*, 609 – 611.
[15] C. J. Loweth, W. B. Caldwell, X. Peng, A. P. Alivisatos, P. G. Schultz, *Angew. Chem.* **1999**, *111*, 1925 – 1929; *Angew. Chem. Int. Ed.* **1999**, *38*, 1808 – 1812.
[16] C. M. Niemeyer, W. Bürger, J. Peplies, *Angew. Chem.* **1998**, *110*, 2391 – 2395; *Angew. Chem. Int. Ed.* **1998**, *37*, 2265 – 2268.
[17] H. Li, S. H. Park, J. H. Reif, T. H. LaBean, H. Yan, *J. Am. Chem. Soc.* **2004**, *126*, 418 – 419.
[18] P. Hazarika, B. Ceyhan, C. M. Niemeyer, *Angew. Chem.* **2004**, *116*, 6631 – 6633; *Angew. Chem. Int. Ed.* **2004**, *43*, 6469 – 6471.
[19] Z. Deng, Y. Tian, S. Lee, A. E. Ribbe, C. Mao, *Angew. Chem.* **2005**, *117*, 3648 – 3651; *Angew. Chem. Int. Ed.* **2005**, *44*, 3582 – 3585.
[20] S. A. Claridge, S. L. Goh, J. M. Frechet, S. C. Williams, C. M. Micheel, A. P. Alivisatos, *Chem. Mater.* **2005**, *17*, 1628 – 1635.
[21] B. Zou, B. Ceyhan, U. Simon, C. M. Niemeyer, *Adv. Mater.* **2005**, *17*, 1643 – 1647.
[22] R. Kretschmer, W. Fritzsche, *Langmuir* **2004**, *20*, 11797 – 11801.
[23] J. D. Le, Y. Pinto, N. C. Seeman, K. Musier-Forsyth, T. A. Taton, R. A. Kiehl, *Nano Lett.* **2004**, *4*, 2343 – 2347.
[24] N. C. Seeman, *Methods Mol. Biol.* **2005**, *303*, 143 – 166.
[25] S. H. Park, P. Yin, Y. Liu, J. H. Reif, T. H. LaBean, H. Yan, *Nano Lett.* **2005**, *5*, 729 – 733.
[26] D. Zanchet, C. M. Micheel, W. J. Parak, D. Gerion, A. P. Alivisatos, *Nano Lett.* **2001**, *1*, 32 – 35.
[27] K. Li, M. T. Stockman, D. J. Bergman, *Phys. Rev. Lett.* **2003**, *91*, 227402 – 227402:1 – 4.
[28] N. C. Seeman, *J. Biomol. Struct. Dyn.* **1990**, *8*, 573 – 581.

 © 2006 Wiley-VCH Verlag GmbH & Co. KGaA, Weinheim

DNA Nanostructures

DOI: 10.1002/anie.200503797

Finite-Size, Fully Addressable DNA Tile Lattices Formed by Hierarchical Assembly Procedures**

Sung Ha Park, Constantin Pistol, Sang Jung Ahn, John H. Reif, Alvin R. Lebeck, Chris Dwyer, and Thomas H. LaBean**

The development of a versatile and readily programmable assembly system for the controlled placement of matter at the molecular scale remains a major goal for nanoscience, nanotechnology, and supramolecular chemistry. Herein, we present a significant step toward this goal by using self-assembling DNA nanostructures to construct fully addressable, finite-sized arrays displaying a variety of programmed patterns. We have assembled DNA tile arrays decorated with proteins in the shape of the letters "D", "N", and "A" that are less than 80 nm on a side. We demonstrate procedures that explore two extremes in hierarchical assembly strategies: 1) minimization of the number of unique molecular address labels (DNA sticky-end sequences) required for encoding tile associations, and 2) minimization of the depth (number of sequential steps) of the assembly process. Higher production yields of defect-free assemblies were achieved by procedures that minimize assembly depth (and maximize diversity of address labels). Some observations on scaling of these strategies to larger arrays are also presented.

[*] Dr. C. Dwyer
Department of Electrical and Computer Engineering
Duke University, Durham, NC 27708 (USA)
Fax: (+1) 919-660-1605
E-mail: dwyer@ece.duke.edu

Dr. T. H. LaBean
Departments of Computer Science and Chemistry
Duke University, Durham, NC 27708 (USA)
Fax: (+1) 919-660-1605
E-mail: thomas.labean@duke.edu

Dr. S. H. Park
Physics Department
Duke University, Durham, NC 27708 (USA)

C. Pistol, Dr. J. H. Reif, Dr. A. R. Lebeck
Department of Computer Science
Duke University, Durham, NC 27708 (USA)

Dr. S. J. Ahn
Length Laboratory
Korea Research Institute of Standards and Science
Daejeon, 305-340 (Korea)

[**] We thank H. Yan and P. Yin for helpful discussions and J. Liu for the use of the DI Nanoscope IIIa AFM. This work was supported by grants from the National Science Foundation to T.H.L. (EIA-02-18376), J.H.R. (CCF-04-32038), and A.L. (CCR-03-26157). We are also grateful for support from the Duke University Provost Common Fund and Duke University Graduate School, and for equipment donations from IBM and Intel.

Supporting information for this article is available on the WWW under http://www.angewandte.org or from the author.

© 2006 Wiley-VCH Verlag GmbH & Co. KGaA, Weinheim
InterScience

Fifteen years ago, Eigler and Schweizer made a significant advance in nanoscale construction when they used a scanning tunneling microscope (STM) to position 35 xenon atoms at precise sites on a nickel surface.[1] They wrote "IBM" in letters a mere 5 nm on an edge, thus presaging a variety of research applications such as quantum corrals and single-molecule chemistry. However, nanofabrication by STM requires expensive instruments under low-temperature, ultra-high-vacuum conditions and produces only one or a small number of copies of a desired structure. This last limitation restricts the applicability and scalability of STM and other top-down assembly methods such as e-beam lithography. Bottom-up self-assembly, on the other hand, can be used to fabricate huge numbers of objects simultaneously, but previous demonstrations of molecular-scale self-assembly lacked sufficient programming complexity to form objects as sophisticated as letters. Herein, we report massively parallel fabrication (on the order of 10^{13} copies) of letters less than 80-nm square by DNA-based self-assembly.

Self-assembled nanostructures with DNA as building blocks were proposed by Seeman in 1982[2] and recently have been experimentally demonstrated in a wide variety of forms.[3] DNA nanostructures have been assembled by using carefully designed linear oligonucleotides with complementary base-pairing segments that form branch-junction motifs. These assemblies were produced with various geometrical structures and functionalities: one- and two-dimensional periodically patterned structures,[4–12] three-dimensional polyhedra,[13–15] nanomechanical devices,[16–21] molecular computers,[22–26] and organizations of other functionalized molecules.[27–29] DNA's excellent intrinsic characteristics, which include molecular recognition, programmability, self-organization, and molecular-scale structuring properties, make it an interesting nanoscale building material, although up to now its usefulness in nanotechnology applications has been limited by a lack of finite-size control and unique addressability in the assembled objects. Finite-sized assemblies have been prototyped with cleverly designed RNA puzzle pieces, and have been shown to form objects with the potential for symmetric addressability,[30] although their use for the display of any arbitrary 2D pattern has not yet been demonstrated.

Herein, we report the prototype fabrication of size-controllable, fully addressable, and precisely programmable DNA-based nanoarrays (NAs) consisting of cross-shaped tiles by using a novel stepwise hierarchical assembly technique. We implemented the construction of fully addressable, finite-size "N (row) × M (column)" NAs from DNA tiles with four arms, each of which contains a Holliday junction-like crossover;[7,8] these DNA tiles are referred to here as "cross tiles". DNA nanostructures were visualized by atomic force microscopy (AFM) under buffer solution, and their dimensions were shown to be in excellent agreement with the designs. The fixed-size DNA nanostructures described may find future use as templates for organizing heteromaterials for developing nanotechnologies, especially in nanoelectronics including, but not limited to, fabrication of functionalized nanowires,[31] nanocircuits,[32] quantum cellular automata,[33] and spintronic devices.[34]

Perhaps the simplest strategy for the construction of finite-sized nanostructures with maximal control over the placement of components would be to use unique DNA sequences everywhere throughout the structure. Such a design would necessarily restrict the maximum allowable size of the structure because of limitations on the size of the set of unique DNA sequences available. Herein, we made use of stepwise assembly strategies that involve the sequential buildup of hierarchical superstructures, such that the formation of stable substructures allows the reuse of DNA base sequences that are complemented and sequestered within double-helical domains. We investigated a "minimal sequence set" (MSS) assembly strategy, which makes maximal reuse of sticky-end sequences and requires a four-step procedure for assembly of a 16-tile, 4 × 4 lattice (Figure 1B). We compared this procedure with a "minimal depth" (MD) assembly strategy, which reduces the number of assembly steps by reusing base sequences only at the tile cores and by using unique sequences for all sticky ends encoding tile-to-tile associations. The MD strategy required the redesign of each of the five-base-pair sticky ends (two per arm) to satisfy the constraint that each tile should match perfectly at only one position in the 16-tile lattice.[35] This second strategy allows the construction of a 4 × 4 NA in a two-step process (Figure 1C).

Schematic diagrams of the self-assembling cross tiles are shown in Figure 1A. The drawings show simplified strands as colored lines that represent different DNA strands, with arrowheads marking the 3′ ends. Each tile consists of three kinds of strands: a central loop strand, four shell strands, and four arm strands. The arm strands carry five-base sticky ends at both the 5′ and 3′ ends. Both construction strategies make use of two different core sequences (A and B tile types, see red/blue diagrams in Figure 1B and C), which are defined by the loop and shell strands. Detailed core nucleotide sequences and sets of complementary sticky ends for tile associations are given in the Supporting Information.

Schematics of the strategies and AFM imaging results of the MSS and MD assembly procedures for 16-tile 4 × 4 NAs are given in Figure 1B and C, respectively. The MSS strategy begins with eight test tubes containing two tiles each (Figure 1B, i), then it proceeds to four tubes of four tiles (Figure 1B, ii), two tubes of eight tiles (Figure 1B, iii), and finally one tube containing all 16 tiles (Figure 1B, iv). The MD strategy requires one step of 16 tubes with one tile each (Figure 1C, i), followed immediately by a second step with one tube containing all 16 tiles (Figure 1C, ii).

Our stepwise assembly technique is a general method for the construction of any finite-size $N \times M$ NA. For example, 2 × 2 NAs (Figure 1B, ii) were fabricated in two steps: in the first annealing step, equimolar mixtures of the strands for tiles 1 and 2 were placed in one tube and strands for tiles 3 and 4 were mixed in a separate tube. These were then cooled slowly from 95 to 20 °C, and then in the second step (low-temperature anneal) equal volumes of the two 1 × 2 NAs were mixed and cooled slowly from 42 to 20 °C by floating the microtube in 1 L of water at 42 °C, which was then cooled to room temperature on the bench over ≈4 h. Low-temperature annealing prevents the assembled supertiles and lattices from

 © 2006 Wiley-VCH Verlag GmbH & Co. KGaA, Weinheim

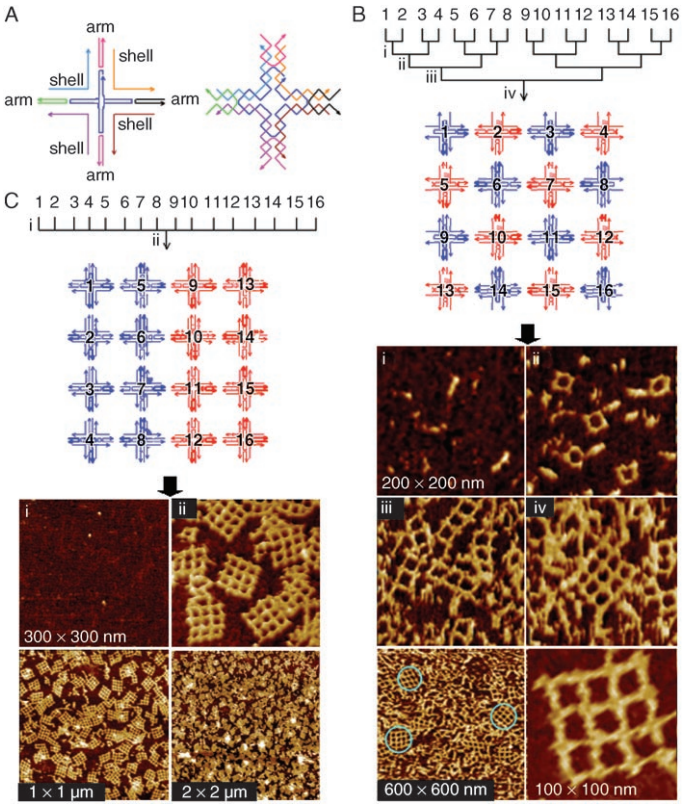


Figure 1. DNA tile and NA structures and assembly schemes. A) Schematic drawings of the strand trace in cross tiles with strand names marked (arm, shell, and loop). B) MSS strategy and constructs. A converging-stream diagram of the four-step assembly process starting with eight tubes of two tiles each (i) and concluding with one tube containing all 16 tiles (iv). The blue and red diagram shows the placement of tiles (1 through 16) in the NA and the identity of loop strands (A-loops are blue and B-loops are red). The bottom six panels are AFM height images with dimensions as labeled and height scale from 0 to 3 nm. Panels i)–iv) correspond to the same labels as in the annealing scheme above; thus, i) 1×2 NA, ii) 2×2 NA, iii) 2×4 NA, and iv) 4×4 NA. The two bottom AFM images are zoom-out and zoom-in pictures of (iv), with error-free NAs in the zoom-out image circled in turquoise. C) MD strategy and constructs. A converging-stream diagram of the two-step assembly starts with 16 tubes with one tile each (i) and goes directly to one tube of 16 tiles (ii). The blue and red diagram shows the placement of A-loop and B-loop tiles in the final NA. The bottom four panels are AFM height images with i) showing single tiles and ii) showing complete 4×4 NAs. The two bottom panels are zoom-out images to show the increased production yield of defect-free assemblies from the two-step method.

dissociating into their component tiles or strands. In this case, the melting temperature for the component cross tiles is ≈60 °C.[7] As the five-base sticky ends average 50 % CG content, their melting temperatures are expected to be ≈30 °C, so reheating them to 42 °C provided sufficient structural motion to facilitate further hybridization to the desired lattice structures. Subsequent assembly steps involved reheating to a moderate temperature (below the expected melting point of any desired substructure), followed by slow cooling back to room temperature. This is the process used in the sequential steps outlined in Figure 1 B. Similarly, the MD assembly (Figure 1 C) also required reheating of the 16-tile mixture to 23 °C and then slow cooling to room temperature over the course of 4 h. Incubation of annealed samples at 4 °C overnight prior to examination by AFM improved the quality of the imaging data.

Comparison of the AFM scans in Figure 1 B and C reveals that the two-step process produces higher yields of properly assembled target structures and fewer partially assembled "waste" products. We define the production yield of defect-free assemblies as the proportion of the total mass of material observed that is found in well-formed target structures. We analyzed the AFM images and counted single tiles, 1×2, 2×2, and all other NAs and lattice fragments. We estimated production yields by tallying the total numbers of target structures and fragments, multiplying each tally by the object size in units of whole tiles (as whole tiles are the smallest observable substructure), and dividing the number of cross tiles found in the target structures by the total number of cross tiles observed in the AFM images. By analyzing several scans of wide areas from several different annealing reactions we can estimate the production yield for each assembly strategy. The first step of the MSS assembly procedure results in a 1×2 NA with average yields of approximately 0.80 ± 0.04. We estimate a production yield of about 0.11 ± 0.03 for the final 4×4 NA in the MSS assembly. On the other hand, the two-step MD assembly strategy results in production yields of approximately 0.34 ± 0.06 for the 4×4 NA structure. To effectively utilize stepwise strategies with multiple assembly steps in the future, and to increase the yield of final products, it is desirable to maximize the yield and purity of the target structure at each step. This may require the adoption of purification steps to remove unassociated and/or misassembled strands that could interfere downstream.

We tested our ability to properly address the NAs by including loop strands modified with biotin at desired points in the assembly process. Binding of individual streptavidin (SA) molecules at biotin sites generates bumps (height ≈5 nm) at the center of the cross tiles. The lattices can be thought of as pixel arrays, and in these experiments the binding of SA protein at a given grid point corresponds to the pixel being turned on, whereas the absence of SA represents a pixel in the off state. Figure 2 A shows high-resolution AFM images of a variety of programmed patterns on 2×2 NAs, which demonstrate the full addressability of the constructs. The images show symmetrically and asymmetrically patterned SA and clearly demonstrate the successful assembly of 2×2 NAs with the MSS system.

The programming of 4×4 NAs was demonstrated by using both MSS and MD assembly schemes. Figure 2 B shows diagrams and high-resolution AFM images of three different 4×4 NAs with programmed deletions produced by the MSS strategy. These partial arrays demonstrate not only the addressability and programmability of the 4×4 NAs, but also the rigidity and robustness of the structure. Another example of MSS-programmed fabrication shown in Figure 2 C is of NAs with biotin–SA conjugates on all eight of its B tiles (the 100-nm scan shows the detail and the 800-nm scan gives an idea of the construction yield). Figure 2 D and E show

 © 2006 Wiley-VCH Verlag GmbH & Co. KGaA, Weinheim

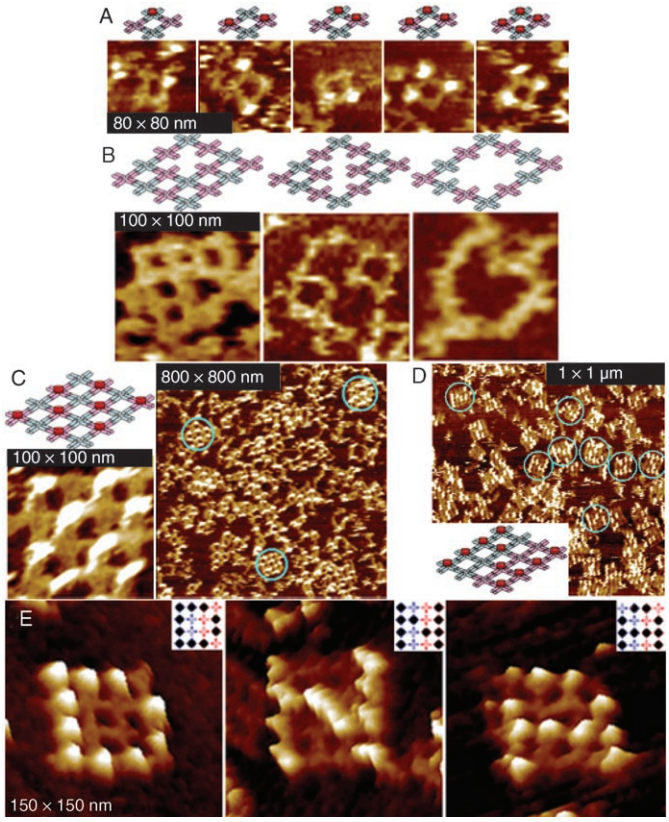


Figure 2. Demonstration of precise programming by self-assembly. A) Diagrams and AFM height images of 2×2 NAs with programmed SA protein attachment. B) Diagrams and AFM images of 4×4 NAs assembled by the MSS strategy and displaying programmed holes. Left: without tile 6; middle: without tiles 6 and 11; and right: without tiles 6, 7, 10, and 11 (see also Supporting Information). C) Diagram and AFM images of a minimal-sequence 4×4 NA programmed with a specific SA protein pattern. The zoom-out scan shows a mixture of final products with error-free arrays circled in turquoise. D) Diagram and AFM image of a 4×4 NA assembled by the MD process and displaying a specific pattern with defect-free arrays circled in turquoise. E) The letters "D", "N", and "A" displayed on self-assembled 4×4 arrays by the two-step MD strategy.

schematics and AFM images of assemblies produced with the MD system and programmed to display specific patterns that resemble the letters D, N, and A. Based on the observed production yields of the letter "D" and the sample volume and concentration, we estimate that the procedure generated on the order of 10^{13} copies of the target nanostructure. The success of these self-assembly procedures lends credence to a wide range of proposed molecular self-assembly fabrication schemes. By balancing the reuse of DNA sequences (MSS strategy) with the number of assembly steps (MD strategy) to achieve an acceptable production yield, we can begin to place bounds on the size of the 2D DNA tile lattices that we can reasonably hope to construct. We also examined the scaling of the required number of sticky-end sequences and the depth (number of sequential steps) of the assembly process with increasing NA dimensions (see the Supporting Information).

In summary, we have designed and assembled size-controlled and fully addressable DNA-based nanoarrays in a hierarchical stepwise manner. The reliability of stepwise assembly and the molecular-level control demonstrated by our system represents a major step toward developing DNA-based nanotechnologies for myriad future applications. Potential uses include fixed-size algorithmic assemblies for DNA computing and complex patterning of nanomaterials for the fabrication of artificial bionanomachines, devices, and sensors. By prototyping the two extremes of assembly strategy—minimal sequence set and minimal process depth—we have begun to experimentally investigate the ranges of production yield and the limits on object size that we can hope to achieve by self-assembly using DNA tile nanofabrication.

Experimental Section

The design of cross-tile types A and B was based on the structure of immobile four-arm branched junctions. The subsequence used for all bulged loops was T4. Sequences were designed with the program SEQUIN[36] to minimize the chance of undesired complementary association and sequence symmetry. Synthetic oligonucleotides were purchased from Integrated DNA Technologies (Coralville, IA) and purified by polyacrylamide gel electrophoresis. Complexes were formed by mixing a stoichiometric quantity of each strand in physiological buffer, 1×TAE/Mg^{2+} (Tris acetate (40 mM, pH 8.0), EDTA (2 mM), and magnesium acetate (12.5 mM)). The final concentration of DNA was between 0.0625 and 1.0 μM. In the first annealing step, equimolar mixtures of strands were heated to 95 °C, cooled slowly to 20 °C by placing the Eppendorf tubes in 2 L of boiled water in a styrofoam box for at least 40 h to facilitate hybridization, and then incubated overnight at 4 °C for structure stabilization. In subsequent steps, moderate-temperature annealing was performed by cooling the DNA tile mixtures slowly from 42 °C (40 °C for the third step and 38 °C for the fourth step) to 20 °C by placing the Eppendorf tubes in 1 L of water on the bench for ≈4 h. The samples were incubated overnight at 4 °C after each annealing step. Biotinylated loop strands and SA interaction were used to demonstrate full addressability. SA was added to the aqueous solution of the assembled NAs for 1 h at room temperature. The final concentration of SA was between 0.0625 and 1.0 μM, and matched the concentration of biotinylated loop strands. The samples were incubated overnight at 4 °C before AFM imaging.

AFM was performed in the tapping mode under 1×TAE/Mg^{2+} buffer. An annealed sample (5 μL) was dropped onto freshly cleaved mica and left for 5 min. A portion of 1×TAE/Mg^{2+} buffer (30 μL) was then placed on the mica and another portion (30 μL) was placed on the AFM tip. AFM images were obtained on a Digital Instruments Nanoscope IIIa instrument with a multimode fluid-cell head by using NP-S oxide-sharpened silicon nitride tips (Vecco).

Received: October 27, 2005
Published online: December 22, 2005

Keywords: DNA structures · nanostructures · nanotechnology · self-assembly · supramolecular chemistry

[1] D. M. Eigler, E. K. Schweizer, *Nature* **1990**, *344*, 524.
[2] N. C. Seeman, *J. Theor. Biol.* **1982**, *99*, 237.
[3] N. C. Seeman, *Nature* **2003**, *421*, 427.
[4] E. Winfree, F. Liu, L. A. Wenzler, N. C. Seeman, *Nature* **1998**, *394*, 539.
[5] C. Mao, W. Sun, N. C. Seeman, *J. Am. Chem. Soc.* **1999**, *121*, 5437.

 © 2006 Wiley-VCH Verlag GmbH & Co. KGaA, Weinheim

[6] T. H. LaBean, H. Yan, J. Kopatsch, F. Liu, E. Winfree, J. H. Reif, N. C. Seeman, *J. Am. Chem. Soc.* **2000**, *122*, 1848.
[7] H. Yan, S. H. Park, G. Finkelstein, J. H. Reif, T. H. LaBean, *Science* **2003**, *301*, 1882.
[8] S. H. Park, P. Yin, Y. Liu, J. H. Reif, T. H. LaBean, H. Yan, *Nano Lett.* **2005**, *5*, 729.
[9] D. Liu, S. H. Park, J. H. Reif, T. H. LaBean, *Proc. Natl. Acad. Sci. USA* **2004**, *101*, 717.
[10] D. Liu, M. Wang, Z. Deng, R. Walulu, C. Mao, *J. Am. Chem. Soc.* **2004**, *126*, 2324.
[11] B. Ding, R. Sha, N. C. Seeman, *J. Am. Chem. Soc.* **2004**, *126*, 10230.
[12] Y. Brun, M. Gopalkrishnan, D. Reishus, B. Shaw, N. Chelyapov, L. Adleman, *Proceedings of the 1st Conference on the Foundations of Nanoscience* **2004**, pp. 2–15.
[13] J. Chen, N. C. Seeman, *Nature* **1991**, *350*, 631.
[14] Y. Zhang, N. C. Seeman, *J. Am. Chem. Soc.* **1994**, *116*, 1661.
[15] W. M. Shih, J. D. Quispe, F. Gerald, G. F. Joyce, *Nature* **2004**, *427*, 618.
[16] C. Mao, W. Sun, Z. Shen, N. C. Seeman, *Nature* **1999**, *397*, 144.
[17] B. Yurke, A. J. Turberfield, A. P. Mills, F. Simmel, J. L. Neumann, *Nature* **2000**, *406*, 605.
[18] H. Yan, X. Zhang, Z. Shen, N. C. Seeman, *Nature* **2002**, *415*, 62.
[19] L. Feng, S. H. Park, J. H. Reif, H. Yan, *Angew. Chem.* **2003**, *115*, 4478; *Angew. Chem. Int. Ed.* **2003**, *42*, 4342.
[20] J. J. Li, W. Tan, *Nano Lett.* **2002**, *2*, 315.
[21] W. U. Dittmer, A. Reuter, F. C. Simmel, *Angew. Chem.* **2004**, *116*, 3634; *Angew. Chem. Int. Ed.* **2004**, *43*, 3550.
[22] L. Adleman, *Science* **1994**, *266*, 1021.
[23] E. Winfree, *J. Biomol. Struct. Dyn.* **2000**, *18*, 263.
[24] C. Mao, T. H. LaBean, J. H. Reif, N. C. Seeman, *Nature* **2000**, *407*, 493.
[25] Y. Benenson, T. Paz-Elizur, R. Adar, E. Keinan, Z. Livneh, E. Shapiro, *Nature* **2001**, *414*, 430.
[26] B. Ravinderjit, N. Chelyapov, C. Johnson, P. Rothemund, L. Adleman, *Science* **2002**, *296*, 499.
[27] C. M. Niemeyer, W. Bürger, J. Peplies, *Angew. Chem.* **1998**, *110*, 2391; *Angew. Chem. Int. Ed.* **1998**, *37*, 2265.
[28] J. J. Storhoff, C. A. Mirkin, *Chem. Rev.* **1999**, *99*, 1849.
[29] S. E. Baker, W. Cai, T. L. Lasseter, K. P. Weidkamp, R. J. Hamers, *Nano Lett.* **2002**, *2*, 1413.
[30] A. Chworos, I. Severcan, A. Koyfman, P. Weinkam, E. Oroudjev, H. Hansma, L. Jaeger, *Science* **2004**, *306*, 2068.
[31] E. Braun, Y. Eichen, U. Sivan, G. Ben-Yoseph, *Nature* **1998**, *391*, 775.
[32] C. Dwyer, L. Vicci, J. Poulton, D. Erie, R. Superfine, S. Washburn, R. Taylor, *IEEE Trans. on VLSI* **2004**, *12*, 1214.
[33] M. Lieberman, S. Chellamma, B. Varughese, Y. Wang, C. Lent, G. Bernstein, G. Snider, F. Peiris, *Ann. N. Y. Acad. Sci.* **2002**, *960*, 225.
[34] M. Zwolak, M. Di Ventra, *Appl. Phys. Lett.* **2002**, *81*, 925.
[35] C. Dwyer, S. H. Park, T. H. LaBean, A. R. Lebeck, *Proceedings of the 2nd Conference on the Foundations of Nanoscience*, *Vol. 2*, **2005**, p. 187.
[36] N. C. Seeman, *J. Biomol. Struct. Dyn.* **1990**, *8*, 573.

 © 2006 Wiley-VCH Verlag GmbH & Co. KGaA, Weinheim

Biomineralization

DOI: 10.1002/anie.200501654

Self-Organizing β-Sheet Lipopeptide Monolayers as Template for the Mineralization of $CaCO_3$**

Silvia Cavalli, Daniela C. Popescu, Emily E. Tellers, Matthijn R. J. Vos, Benoît P. Pichon, Mark Overhand, Hanna Rapaport, Nico A. J. M. Sommerdijk, and Alexander Kros**

The large variation in inorganic structures encountered in biological systems, often with exquisite and unique morphologies, has fascinated researchers in all scientific disciplines for a long time.[1] For materials scientists, an understanding of the principles underlying the process of biomineralization holds great promise for the design and synthesis of new inorganic and hybrid structures with yet unrealized properties. The central concept in biomineralization research is that organized biomacromolecules, which contain well-defined arrays of functional groups, control polymorph selection and the oriented nucleation of crystals by lowering the nucleation energy of specific crystal faces.[2] Control over crystal morphology is then exerted by the interaction of biomolecules in solution with specific crystal planes during growth.

Recently, it has become clear that the classical concept, which proposes that a template containing well-defined arrays of functional groups controls the nucleation of the inorganic crystals by geometric and stereochemical matching, needs expanding.[3] Furthermore, a crucial role for amorphous calcium carbonate as a transient intermediate has been proposed.[4] In the last few years it was demonstrated that specific nucleation of calcite can be achieved without an

[*] D. C. Popescu,[+] M. R. J. Vos, Dr. B. P. Pichon, Dr. N. A. J. M. Sommerdijk
Laboratory of Macromolecular and Organic Chemistry
Eindhoven University of Technology
P.O. Box 513, 5600 MB, Eindhoven (The Netherlands)
Fax: (+31) 40-245-1036
E-mail: n.sommerdijk@tue.nl

S. Cavalli,[+] E. E. Tellers, Dr. M. Overhand, Dr. A. Kros
Leiden Institute of Chemistry, Leiden University
P.O. Box 9502, 2300 RA, Leiden (The Netherlands)
Fax: (+31) 71-527-4397
E-mail: a.kros@chem.leidenuniv.nl

Dr. H. Rapaport
Department of Biotechnology Engineering
Ben Gurion University of the Negev
P.O. Box 653, 84105 Beer-Sheva (Israel)

[+] These authors contributed equally.

[**] We are grateful to Wim Jesse, Hans van den Elst, and Nico Meeuwenoord for their technical assistance. Hugo Simões and Jan-Willem Handgraaf are acknowledged for the graphics. We thank Dr. J. Aizenberg for fruitful discussions. This research was supported by the Netherlands Scientific Organization (NWO) through an open competition grant (D.C.P.) and a VENI grant (A.K.).

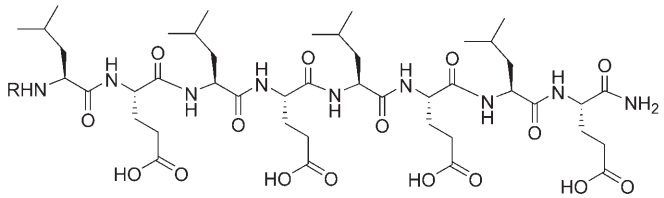
Supporting information for this article is available on the WWW under http://www.angewandte.org or from the author.

© 2006 Wiley-VCH Verlag GmbH & Co. KGaA, Weinheim
InterScience

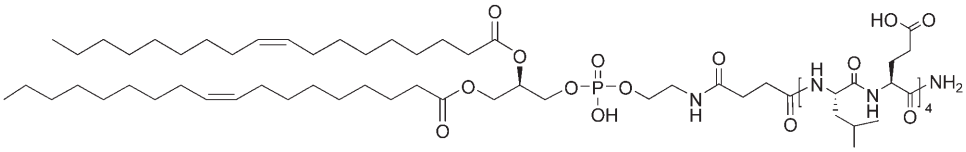
epitaxial match with the exposed crystal planes,[5–7] and it has been suggested that electrostatic interactions play an important role in the control of the orientation of crystal growth.[8,9]

In nature crystal nucleation and growth are often controlled by carboxylate-rich polypeptides (containing, for example, aspartate and glutamate), which are present within a macromolecular matrix with organized β-sheet domains.[10] Although (poly)peptides have been successfully employed as additives that are capable of modifying the growth of calcium carbonate crystals,[11] there have been few reports in which peptides with predefined secondary structures have been studied as templates for mineralization.[9a,12–14] Recently, it was demonstrated that amphiphilic peptides comprising phenylalanine (Phe) and glutamic acid (Glu) residues can form ordered Langmuir monolayers with a β-pleated sheet structure at the air/water interface.[15]

We have modified the water-soluble $(Leu\text{-}Glu)_4$ octapeptide motif **1** with a phospholipid moiety (dioleoyl phosphatidyl ethanolamine, DOPE) to increase its amphiphilicity so that it would form stable monolayers at the air/water interface. We anticipated that the resulting lipopeptide **2** should be able to form a β-sheet structure, thereby exposing an ordered array of carboxylate groups to the aqueous phase. Herein, we report how this monolayer interacts with Ca^{2+} ions and is employed subsequently as a biomimetic mineralization template for the formation of a new crystal habit of calcite.



1: R = H
3: R = C(O)CH$_3$



2

Surface-pressure–surface-area (π–A) isotherms of the resulting lipopeptide **2** were characterized by an apparent condensed liquid phase that was present over a rather large trajectory (Figure 1a). The slope of the isotherm indicated a fluidlike character of the monolayer, most probably provided by the unsaturated lipid chains.[16] Brewster angle microscopy (BAM) images (not shown) revealed that **2** self-assembled into preformed domains with millimeter dimensions. These domains, which were present in the expanded state, fused upon compression to form a continuous film. The compressed monolayer was transferred to quartz plates and ZnSe prisms for CD and FTIR analysis, respectively (see the Supporting Information for details). The β-sheet structure was confirmed by the appearance of a CD signal displaying a maximum at 202 nm and a minimum at 218 nm,[17] as well as by an amide I vibration at 1628 cm^{-1} in the FTIR spectrum. The small IR band at 1694 cm^{-1} indicated an antiparallel organization of the strands (Figure 1c,d).[18] The β-sheet organization of lipopeptide **2** at the air/water interface was further confirmed by in situ grazing incidence X-ray diffraction (GIXD) measurements (see the Supporting Information).[19]

To verify the stability of the lipopeptide secondary structure upon complexation with Ca^{2+} ions, isotherms were recorded with an aqueous $CaCl_2$ solution (10 mM) as the subphase (Figure 1a). An expansion in molecular area from 189 to 202 $Å^2$ molecule^{-1} was observed; however, the CD and IR spectra of the transferred monolayers still revealed the spectroscopic characteristics typical of β-pleated strands (see the Supporting Information). A further expansion of the molecular area to approximately 250 $Å^2$ molecule^{-1} was observed when **2** was spread on a subphase containing $Ca(HCO_3)_2$ (9 mM, Figure 1a), which is the solution used in the crystallization experiments described below.[20] In this case BAM no longer revealed the formation of domains, either before or upon compression. These results indicate that, on account of the DOPE moiety, the lipopeptide **2** forms a monolayer that self-assembles without compression, but is still dynamic and adapts its structure upon complexation of calcium ions to interact efficiently with the nucleating crystals.

Calcium carbonate crystals were grown under self-organized monolayers of **2** ($\pi = 30\ mN\,m^{-1}$) by using the Kitano method[20] and collected after 5, 20, and 48 h. Calcite was produced predominantly in the form of pyramidal crystals together with rhombohedral crystals having a concave central region.[21] The pyramidal crystals were characterized by three thermodynamically stable {10.4} faces that were oriented to the aqueous phase and one face consisting of three facets that was oriented to the monolayer (Figure 2a). Crystals with a similar elevated feature consisting of three inclined facets have been observed before.[6b,9c,22] It was suggested that the apex represented the initial point of attachment to the monolayer, and that the outer edges of the crystal detached in time from the monolayer as a result of gravity. Computer modeling of the crystals based on scanning electron micrographs[23] indicated that, in almost all cases, the facetted faces belonged to the class {01.*l*}, with *l* ranging from 1–2. The formation of this class of crystal faces in solution has been reported frequently for biogenic calcite,[24] and recently also for the octapeptide $(Phe\text{-}Asp)_4$.[9a] In addition, (01.2)-oriented calcite crystals were obtained with different monolayer systems.[5,6a,9b,25,26]

Previously, Lahiri et al. reported the formation of calcite crystals with symmetrical indentation defined by three {01.2} faces around a (00.1) face, which formed the attachment point to a porphyrin monolayer.[27] In the present case the concave indentation of these crystals is defined by four roughened

 © 2006 Wiley-VCH Verlag GmbH & Co. KGaA, Weinheim

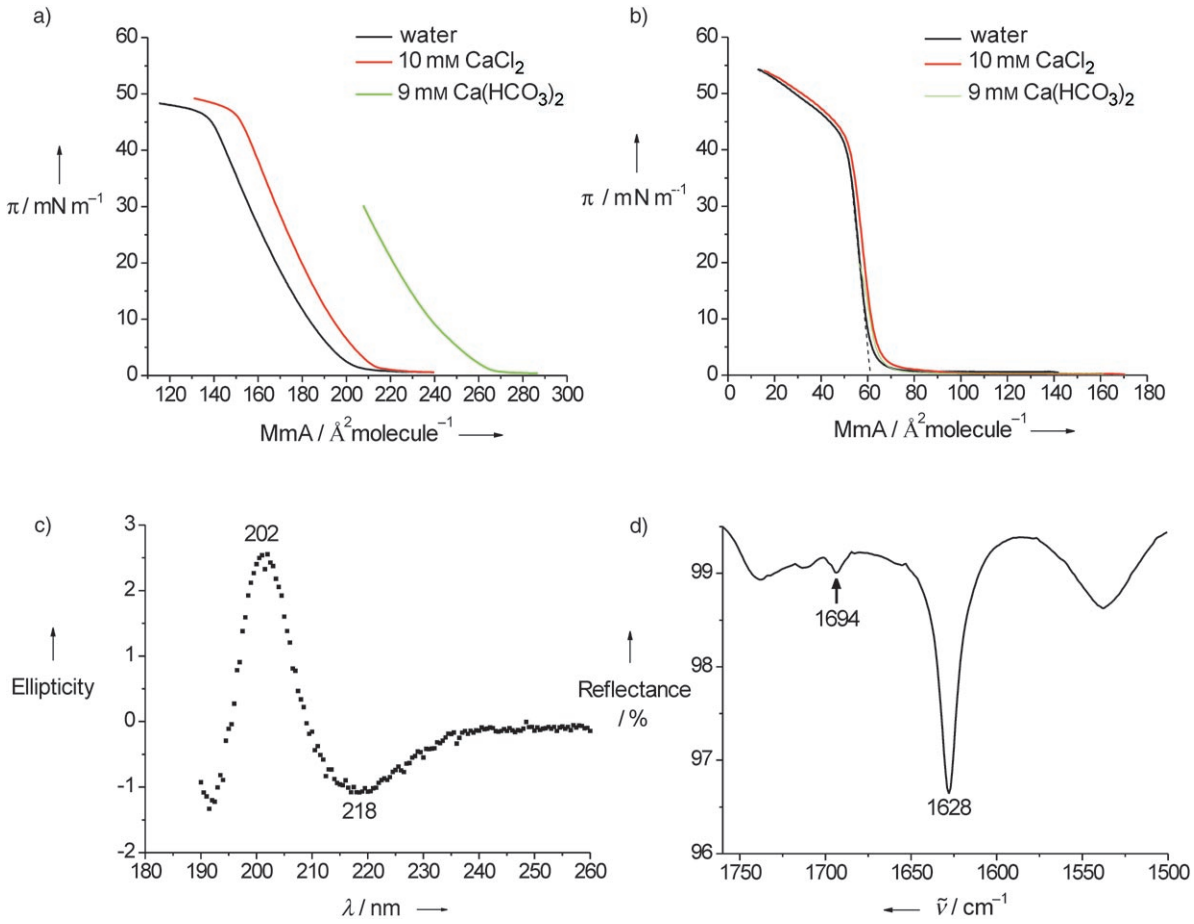


Figure 1. π–A isotherms of the monolayer of a) lipopeptide **2** and b) N-acetylated octapeptide **3** on (——) H_2O, (——) $CaCl_2$ (10 mM), and (——) $Ca(HCO_3)_2$ (9 mM) subphases at 20 °C. The limiting molecular areas for compounds **2** and **3** were determined by extrapolating the slope in the liquid condensed region to zero pressure (see dashed line as an example for **3**).[15] c) CD and d) FTIR spectra of the monolayer of lipopeptide **2** transferred from a water subphase at $\pi = 30\ mN\,m^{-1}$ at 20 °C.

planes (Figure 2b), the outer edges of which form a plane that can be modeled by the $(1\bar{1}.\bar{4})$ face of calcite. However, this morphological appearance of indented rhombohedral crystals has not, to our knowledge, been reported before. Also in the present case, a central patch could be located on several crystals (Figure 2c). The indented crystals were dominant over the pyramidal crystals after 5, 20, and 48 h and this population slightly increased with time (Figure 3a). Selected-area electron diffraction performed on crystals with a rhombohedral shape collected within 20 minutes after the start of the experiment revealed that these crystals had a {10.0} orientation (Figure 2c). This finding suggests that for the indented crystals, crystal nucleation starts from a {10.0} face.

Crystal indentation might be the combined result of gravity and limited Ca^{2+} and HCO_3^{2-} ion transport from the mineralization solution. As the crystal grows it becomes heavier and tends to sink, while still being attached to the monolayer. Being flexible, the monolayer presumably bends to follow the sinking crystal. This will create a gap between the monolayer and the face of the crystal attached to it, toward the edges of the crystal (Figure 3c). Therefore, the hindering effect of the monolayer on ion transport will also be reduced in that region. This allows the outer corners of the crystal facing the monolayer to grow upwards, thus creating an indentation in the crystal.

The N-acetylated octapeptide **3** was also prepared for comparison. The π–A isotherm of **3** revealed a sharp transition from the gaseous to the solid phase (Figure 1b). A molecular area of 61 $Å^2$ molecule^{-1} was determined from this curve, a value which was lower than expected (130 $Å^2$ molecule^{-1} [28]), probably as a result of the high water solubility of **3**. CD and FTIR studies of the transferred monolayers indicated the presence of an antiparallel β-sheet structure (see the Supporting Information). The CD spectrum displayed a maximum at 201 nm and a minimum at 221 nm, while the IR spectra showed a strong band at 1627 cm^{-1} and a weak one at 1694 cm^{-1}.[29] When the isotherm of **3** was recorded on a $CaCl_2$ subphase (10 mM) or on a subphase containing $Ca(HCO_3)_2$ (9 mM) no expansion of the monolayer was observed, which suggests that **3**, in contrast to lipopeptide **2**, does not significantly adapt its structure upon exposure to Ca^{2+} ions (Figure 1b).

Crystals grown under monolayers of **3** again showed both types of modifications. However, in this case predominantly pyramidal crystals were observed after five hours and only a minor (< 5 %) amount of indented crystals was present. The latter population increased to approximately 50 % of the total

 © 2006 Wiley-VCH Verlag GmbH & Co. KGaA, Weinheim

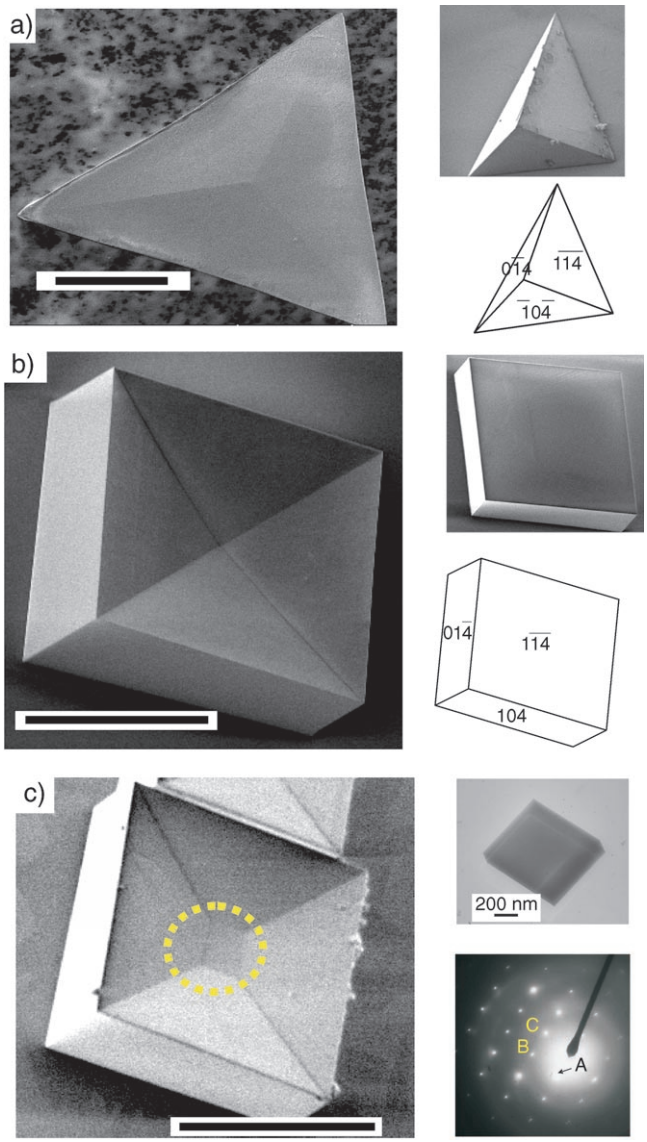


Figure 2. Calcite crystals grown under monolayers of **2**. a) Left: SEM image of a (01.2)-oriented pyramidal crystal as observed from the side attached to the monolayer; right: model[23] and SEM image of a similar crystal viewed from the side exposed to the solution. b) Left: SEM image of a rhombohedral crystal with a concave central region from the side attached to the monolayer; right: model and SEM image of a similar crystal viewed from the side exposed to the solution. c) Left: SEM image of an indented crystal showing a central patch; right: TEM image and electron diffraction pattern of a rhombohedral crystal isolated after 20 min. The pattern corresponds to the [10.0] zone of calcite. Reflections A $(0\bar{1}.\bar{1})$ 4.2 Å; B $(0\bar{1}.4)$ 3.0 Å; C (00.5) 3.4 Å. Angles $(0\bar{1}.\bar{1})\wedge(00.5) = 104°$; $(0\bar{1}.\bar{1})\wedge(0\bar{1}.4) = 59°$. Camera length = 60 cm. Bars represent 20 μm except when indicated otherwise.

number of modified crystals after 20 hours, and only became predominant after 48 hours (65%, Figure 3b). Importantly, most of the pyramidal crystals increased in size rather than in number, which suggests that their nucleation only occurred in the earlier stages of the experiment. In contrast, we observed the appearance of small indented crystals throughout the whole experiment, thus indicating that these crystals also nucleated in the later stages of the experiment.

From the change of the composition of the mineral phase with time, it is apparent that the monolayers of **2** and **3** differ in their ability to nucleate the indented versus pyramidal morphology at the different time points. We propose that in the case of **3**, the nucleation of the face leading to the indented calcite takes place in the later stages of the experiments, probably because the solidlike monolayer needs more time to reorganize and to adapt to the growing crystals.

The {01.1} and {01.2} crystal planes are defined by the same 4.99 Å distance in one direction, but show a gradual change in the orientation of the carbonate groups which are rotated over approximately 10° on going from $l = 1$ to $l = 2$ (Figure 4). The 4.99 Å distance most probably relates to the interstrand distance in the template as defined by the hydrogen bonds in the β-sheet (4.7–4.8 Å; GIXD, see the Supporting Information), which allows an approximate match of the template carboxylate groups with the carbonate ions in the crystal plane. Although there is only a 10° rotation between the planes with $l = 1$ and $l = 2$, significant differences are found in the interion distances in the different nucleation planes. It is therefore likely that in this direction the alignment of the carboxylate groups with respect to the carbonate ions plays a much more important role than the matching of the distances of the two phases.

The more adaptable monolayer of **2** clearly favors the formation of a different set of planes, that is, those belonging to the {10.0} family. Interestingly, these planes are related to the {01.*l*} planes ($l = 1$ or 2) by a further rotation of the carbonate ions (Figure 4). The {10.0} faces are again defined by a distance of 4.99 Å in one direction and have a spacing of 8.53 Å in the other direction. These data suggest that in this case the spacing of 4.99 Å also relates to the interstrand distance of 4.7–4.8 Å in the β-sheet. The interaction of the carboxylate groups of the template with the {10.0} faces along the other direction is most likely related to the ability of the monolayer to adapt to the growing crystal.

The surface-pressure–surface-area isotherms recorded on H_2O and $Ca(HCO_3)_2$ subphases showed an expansion of the mean molecular area from 189 to 250 $Å^2$ molecule^{-1}, respectively. We presume that the expansion in the direction of the backbone of the molecule should account for most of the observed increase in mean molecular area.[30] If a small expansion in the interstrand distance from 4.7–4.8 to 4.99 Å is envisioned, the molecule should then expand from ≈40 to ≈50 Å (that is, by about 25%) along its long axis. It is important to note, however, that stretching of the peptide backbone alone to an all-*trans* configuration yields a maximum distance between the Glu side chains of about 7.6 Å compared to the 8.53-Å spacing of the {10.0} face. Nevertheless, the flexibility of the template should allow it to organize such that the carboxylate groups align with the carbonate ions in the nucleation plane while matching the 4.99 Å distance, similar to the proposal for amide-containing phospholipid derivatives.[6] However, other factors, such as the charge density of the amphiphile and the possible presence of a layer of carbonate ions between the crystal and the monolayer, should not be neglected.[8c,9] We propose that the N-acetylated octapeptide **3** has a limited ability to

 © 2006 Wiley-VCH Verlag GmbH & Co. KGaA, Weinheim

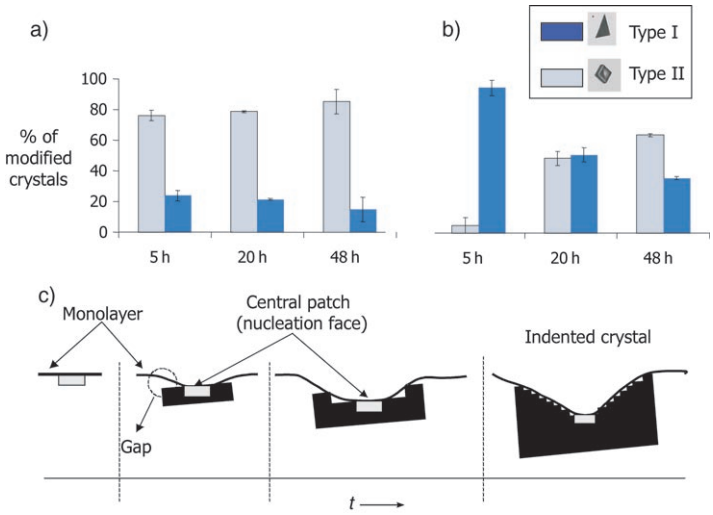


Figure 3. Distribution of the two populations of crystals (Type I: pyramidal shape; Type II: indented crystals) nucleated under monolayers of a) lipopeptide **2** and b) N-acetylated octapeptide **3**, as a percentage of the number of modified crystals (crystals isolated after 5, 20, and 48 h). c) Proposed model for the formation of indented crystals.

adapt to the growing crystal, and hence is responsible for the preferred nucleation of the {01.*l*} faces ($l = 1$ or 2) and the much slower formation of the indented crystals.

In conclusion, we have demonstrated that amphiphilic lipopeptide **2** forms stable monolayers with an antiparallel β-sheet conformation. This finding enabled us not only to study the effect of these monolayers on the crystallization of calcium carbonate, but also to investigate interactions with the developing mineral phase. Indeed, the formation of habit-modified calcite was observed. Apart from a small amount of pyramidal {01.*l*}-oriented crystals ($l = 1$ or 2), the majority of the modifications resulted in a new type of indented calcite crystal, which according to electron diffraction studies nucleated from a {10.0} face. The formation of this morphological form was significantly suppressed when the less adaptable peptide **3** was used.

In previous studies, the formation of crystals with the {01.2}[6a,25,26] and {10.0}[6b,31] orientations was related to geometrical lattice matching and stereochemical complementarity between the functional groups of the template and the positions of ions in the nucleation plane. In other studies, the oriented nucleation of crystals was attributed to nonspecific electrostatic effects rather than to an epitaxial match between the monolayer and the crystal face.[8,9] We have demonstrated that the nucleation of different crystal faces can be achieved depending on the ability of the template to adapt to the structure of the inorganic phase. Although the importance of the flexibility of the template has been known for many years,[32] it is rarely taken into account in reports on crystal nucleation. Furthermore, the results indicate that stretching of the template in only one direction allows the reorientation of its functional groups, so that the

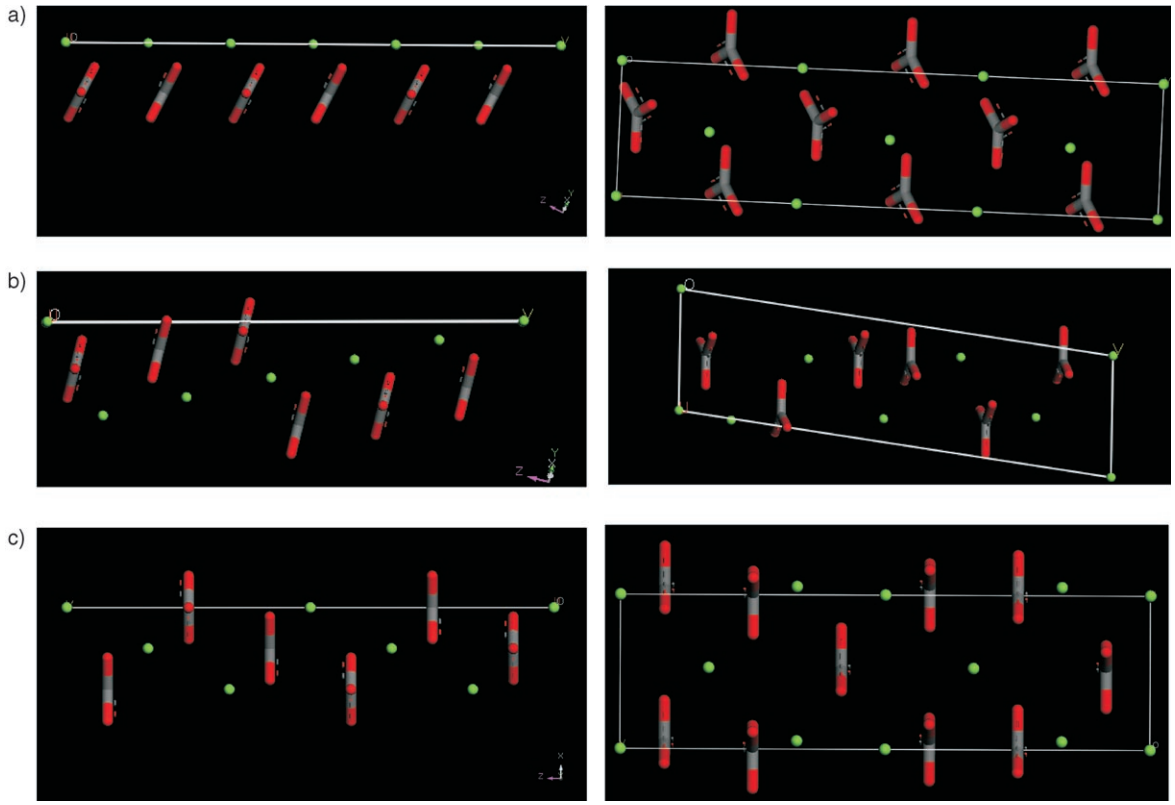


Figure 4. Models of the a) (01.2), b) (01.1), and c) (10.0) planes of calcite with the viewing direction along (left) and perpendicular to (right) the plane.

© 2006 Wiley-VCH Verlag GmbH & Co. KGaA, Weinheim

stabilization of different crystal planes can be achieved without the need for an epitaxial relation between the two components.

Received: May 13, 2005
Revised: August 17, 2005
Published online: October 18, 2005

Keywords: calcium · crystal growth · lipopeptides · monolayers · template synthesis

[1] P. Q. Harting, *Q. J. Microsc. Sci.* **1872**, *12*, 118 – 123.
[2] S. Mann, *Nature* **1988**, *332*, 119 – 124.
[3] H. Cölfen, S. Mann, *Angew. Chem.* **2003**, *115*, 2452 – 2468; *Angew. Chem. Int. Ed.* **2003**, *42*, 2350 – 2365.
[4] a) Y. Politi, T. Arad, E. Klein, S. Weiner, L. Addadi, *Science* **2004**, *306*, 1161 – 1164; b) L. Addadi, S. Raz, S. Weiner, *Adv. Mater.* **2003**, *15*, 959 – 970.
[5] a) J. Aizenberg, A. J. Black, G. M. Whitesides, *Nature* **1999**, *398*, 495 – 498; b) A. M. Travaille, J. J. J. M. Donners, J. W. Gerritsen, N. A. J. M. Sommerdijk, R. J. M. Nolte, H. van Kempen, *Adv. Mater.* **2002**, *14*, 492 – 495.
[6] a) S. Champ, J. A. Dickinson, P. S. Fallon, B. R. Heywood, M. Mascal, *Angew. Chem.* **2000**, *112*, 2828 – 2831; *Angew. Chem. Int. Ed.* **2000**, *39*, 2716 – 2719; b) P. J. J. A. Buijnsters, J. J. J. M. Donners, S. J. Hill, B. R. Heywood, R. J. M. Nolte, B. Zwanenburg, N. A. J. M. Sommerdijk, *Langmuir* **2001**, *17*, 3623 – 3628.
[7] J. J. J. M. Donners, R. J. M. Nolte, N. A. J. M. Sommerdijk, *J. Am. Chem. Soc.* **2003**, *124*, 9700 – 9701.
[8] a) D. M. Duffy, J. H. Harding, *Langmuir* **2004**, *20*, 7630 – 7636; b) D. M. Duffy, J. H. Harding, *Langmuir* **2004**, *20*, 7637 – 7642; c) D. M. Duffy, A. M. Travaille, H. van Kempen, J. H. Harding, *J. Phys. Chem. B* **2005**, *109*, 5713 – 5718.
[9] a) D. Volkmer, M. Fricke, T. Huber, N. Sewald, *Chem. Commun.* **2004**, *16*, 1872 – 1873; b) D. Volkmer, M. Fricke, C. Agena, J. Mattay, *J. Mater. Chem.* **2004**, *14*, 2249 – 2259; c) D. Volkmer, M. Fricke, D. Vollhardt, S. Siegel, *J. Chem. Soc. Dalton Trans.* **2002**, 4547 – 4554.
[10] S. Mann, *Biomineralization: Principles and Concepts in Bioinorganic Materials Chemistry*, Oxford University Press, New York, **2001**.
[11] a) L. Addadi, S. Weiner, *Proc. Natl. Acad. Sci. USA* **1985**, *82*, 4110 – 4114; b) L. A. Gower, D. A. Tirrell, *J. Cryst. Growth* **1998**, *191*, 153 – 160; c) T. Sugawara, Y. Suwa, K. Ohkawa, H. Yamamoto, *Macromol. Rapid Commun.* **2003**, *24*, 847 – 851.
[12] a) L. Addadi, J. Moradian, E. Shay, N. G. Maroudas, S. Weiner, *Proc. Natl. Acad. Sci. USA* **1987**, *84*, 2732 – 2736; b) H. Bekele, J. H. Fendler, J. W. Kelly, *J. Am. Chem. Soc.* **1999**, *121*, 7266 – 7267; c) D. B. DeOliveira, R. A. Laursen, *J. Am. Chem. Soc.* **1997**, *119*, 10627 – 10631; d) G. Falini, S. Fermani, M. Gazzano, A. Ripamonti, *J. Chem. Soc. Dalton Trans.* **2000**, 3983 – 3987; e) J. E. Meegan, A. Aggeli, N. Boden, R. Brydson, A. P. Brown, L. Carrick, A. R. Brough, A. Hussain, R. J. Ansell, *Adv. Funct. Mater.* **2004**, *14*, 31 – 37.
[13] M. Bertrand, A. Brack, *Chem. Eur. J.* **2000**, *6*, 3452 – 3455.
[14] Y. Levi, S. Albeck, A. Brack, S. Weiner, L. Addadi, *Chem. Eur. J.* **1998**, *4*, 389 – 396.
[15] H. Rapaport, K. Kjaer, T. R. Jensen, L. Leiserowitz, D. A. Tirrell, *J. Am. Chem. Soc.* **2000**, *122*, 12523 – 12529.
[16] M. Lindén, J. B. Rosenholm, *Langmuir* **1995**, *11*, 4499 – 4504.
[17] A. Rodger, B. Nordén, *Circular Dichroism and Linear Dichroism*, Oxford University Press, New York, **1997**, p. 21.
[18] M. Jackson, H. H. Mantsch, *Crit. Rev. Biochem. Mol. Biol.* **1995**, *30*, 95 – 120.
[19] Details of the GIXD measurements will be part of a forthcoming publication.
[20] Y. Kitano, K. Park, D. W. Hood, *J. Geophys. Res.* **1963**, *67*, 4873 – 4874.
[21] In the absence of a monolayer only unmodified calcite and some vaterite crystals were isolated.
[22] S. Mann, B. R. Heywood, S. Rajam, J. B. A. Walker, *J. Phys. D* **1991**, *24*, 154 – 164.
[23] Calcite crystals were modeled with SHAPE V7.1.2., Shape Software, Kingsport, USA, **2004**.
[24] a) J. Aizenberg, J. Hanson, T. F. Koetzle, L. Leiserowitz, S. Weiner, L. Addadi, *Chem. Eur. J.* **1995**, *1*, 414 – 422; b) J. Aizenberg, S. Albeck, S. Weiner, L. Addadi, *J. Cryst. Growth* **1994**, *142*, 156 – 164.
[25] a) J. Aizenberg, A. J. Black, G. H. Whitesides, *J. Am. Chem. Soc.* **1999**, *121*, 4500 – 4509; b) D. D. Archibald, S. B. Qadri, B. P. Gaber, *Langmuir* **1996**, *12*, 538 – 546.
[26] A. Berman, D. J. Ahn, A. Lio, M. Salmeron, A. Reichert, D. Charych, *Science* **1995**, *269*, 515 – 518.
[27] J. Lahiri, G. Xu, D. M. Dabbs, N. Yao, I. A. Aksay, J. T. Groves, *J. Am. Chem. Soc.* **1997**, *119*, 5449 – 5450.
[28] The repeat distances of 4.7 and 6.9 Å, which have been observed previously in crystalline β-sheet structures, can be used to estimate the area per molecule. For example, $(4 \times 4.7 \times 6.9)$ Å = 129.7 Å for an eight-residue peptide; see ref. [15].
[29] In aqueous solution the acetylated octapeptide **3** showed a random-coil conformation.
[30] In situ GIXD measurements on water and $CaCl_2$ solution subphases showed that the interstrand distance remained constant upon compression. The strand length, however, appeared to have an elastic behavior, as the conformation of the backbone changed upon compression.
[31] S. Rajam, B. R. Heywood, J. B. A. Walker, S. Mann, R. J. Davey, J. D. Birchall, *J. Chem. Soc. Faraday Trans.* **1991**, *87*, 727 – 734.
[32] a) S. Mann, B. R. Heywood, S. Rajam, J. D. Birchall, *Nature* **1988**, *334*, 692 – 695; b) D. J. Ahn, A. Berman, D. Charych, *J. Phys. Chem.* **1996**, *100*, 12455 – 12461; c) S. J. Cooper, R. B. Sessions, S. D. Lubetkin, *J. Am. Chem. Soc.* **1998**, *120*, 2090 – 2098; d) G. Xu, N. Yao, I. A. Aksay, J. T. Groves, *J. Am. Chem. Soc.* **1998**, *120*, 11977 – 11985.

 © 2006 Wiley-VCH Verlag GmbH & Co. KGaA, Weinheim

Host–Guest Systems

DOI: 10.1002/anie.200501938

Stabilization of Reactive Organometallic Intermediates Inside a Self-Assembled Nanoscale Host**

Dorothea Fiedler, Robert G. Bergman, and Kenneth N. Raymond**

Molecular container compounds provide a new space for reaction chemistry, both literally and figuratively, through the encapsulation of smaller guest molecules.[1] The environment of the host interior may be very different from that of the exterior surroundings, resulting in novel patterns of reactivity. In effect, the energetic landscape within a host may be significantly altered from that of the bulk solution, so that what is "unstable" in solution may become "stable" and vice versa. The stabilization of reactive species within the narrow confines of a host cavity is an intriguing functional property of covalent and self-assembled hosts and has been observed in a number of different systems. Both kinetic and thermodynamic factors can contribute to this stabilization: the tight host portals may kinetically inhibit guest escape and subsequent reactivity, or strong host–guest binding may stabilize an otherwise reactive structure.[2] Cram and Warmuth have used hemicarcerands to isolate the highly unstable intermediates cyclobutadiene, *o*-benzyne, and cycloheptatetraene by preventing them from dimerization or reaction with bulk-phase species.[3–5] Fujita and co-workers observed the formation of an otherwise nonisolable cyclic silanol trimer within the cavity of their M_6L_4 supramolecular host.[6,7] Rebek et al. were able to inhibit homolytic bond cleavage of benzoyl peroxide by encapsulation, even at elevated temperatures for prolonged periods of time.[8] All of these examples involved reactive organic species. Herein, we report the stabilization of reactive organometallic intermediates in aqueous solution through molecular encapsulation. This result augurs well for the further development of encapsulated organometallic chemistry.

[*] D. Fiedler, Prof. R. G. Bergman, Prof. K. N. Raymond
Department of Chemistry
University of California
Berkeley, CA 94720-1460 (USA)
Fax: (+1) 510-642-7714
E-mail: bergman@cchem.berkeley.edu
raymond@socrates.berkeley.edu

[**] Supported by the Director of the Office of Energy Research, Office of Basic Energy Sciences, Chemical Sciences Division (US Department of Energy) under contract DE-AC02-05CH11231. The authors thank Dr. Forrest E. Michael, Dr. Anna V. Davis, and Dennis H. Leung for helpful discussions; Dr. Ulla Andersen, Dr. Robert M. Yeh, and Dr. Georg Seeber for obtaining the MS data; and the Waters Corp. for use of the TOF spectrometer.

Supporting information for this article is available on the WWW under http://www.angewandte.org or from the author.

Over the past years, we have investigated the properties and utilities of an M_4L_6 tetrahedral assembly constructed from metal and ligand components.[9,10] In this structure, the metal atoms are located on the vertices of the tetrahedron and the six bis(bidentate) catechol amide ligands span the edges (Figure 1). The tetrahedron assembles exclusively as the

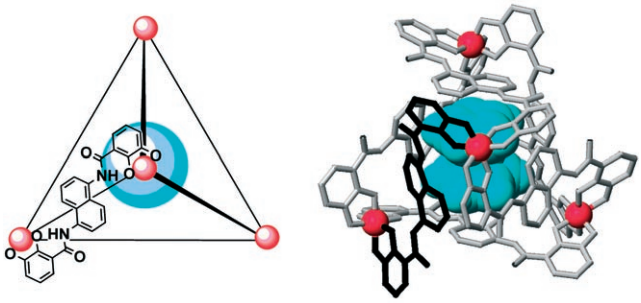


Figure 1. Left: A schematic representation of the [G⊂M_4L_6] supramolecular tetrahedral assembly, with a view down the C_3 axis. One ligand is drawn and the other ligands are represented as sticks for clarity. Right: CAChe model of [CpRu(η^6-C_6H_6)⊂Fe_4L_6]$^{11-}$, with the guest molecule shown in a space-filling view; the hydrogen atoms are omitted for clarity.

homochiral stereoisomer (that is, ΔΔΔΔ or ΛΛΛΛ), with its chirality generated by the tris(bidentate) chelation of each of the four metal centers. The metal–ligand assembly has provided rich host–guest chemistry; it can bind a large variety of monocationic guest molecules, which range from simple alkyl ammonium ions[11,12] to cationic organometallic species, into its hydrophobic cavity.[13] Among the organometallic complexes encapsulated by the supramolecular host are ruthenium sandwich complexes and half-sandwich complexes of the general formula [Cp/Cp*Ru(diene)(H_2O)]$^+$ (Cp = cyclopentadiene, Cp* = pentamethylcyclopentadiene).[14,15] The tetrahedron has also demonstrated its ability to stabilize reactive organic intermediates: a water-sensitive cationic phosphane–acetone adduct—previously synthesized only under anhydrous conditions—was stabilized in aqueous solution for several weeks.[16,17]

The high binding affinity of half-sandwich complexes in the M_4L_6 host prompted us to investigate the structurally related [CpRuCl(cod)] (cod = 1,5-cyclooctadiene), a catalyst employed in many C–C bond-forming reactions, as a guest precursor.[18] In polar media, this complex should undergo halide dissociation to form the cationic solvated species. Under the previously established biphasic reaction conditions,[15] an organometallic complex could be quantitatively encapsulated; however, to our surprise the resulting product did not appear to be [CpRu(cod)(H_2O)⊂Ga_4L_6]$^{11-}$. The ^{1}H NMR spectrum of the host–guest complex displays an apparent doubling of all expected signals (Figure 2).[19] For example, two resonances for the encapsulated Cp fragment at $\delta = 2.07$ and 2.04 ppm are detected; also, all the signals for the cod moiety of the guest molecule are displayed twice. The 2D TOCSY spectrum reveals that two different species with 12 cod resonances each are encapsulated, in an approximate 1:1 ratio, as two independent spin systems are observed (see the

 © 2006 Wiley-VCH Verlag GmbH & Co. KGaA, Weinheim

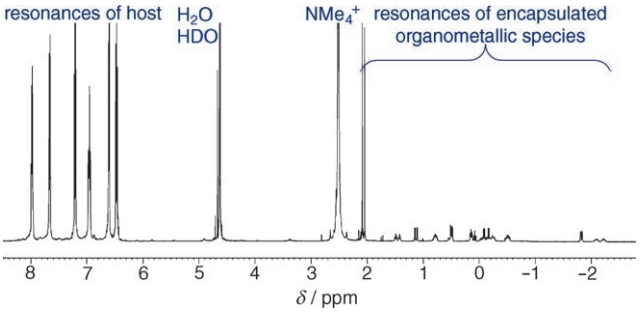


Figure 2. ^{1}H NMR spectrum of $[\mathbf{1}\subset Ga_4L_6](NMe_4)_5K_6$.

Supporting Information). In addition, the electrospray mass spectrum did not corroborate the formation of $[CpRu(cod)(H_2O)\subset Ga_4L_6]^{11-}$ either. Only peaks that correspond to the host–guest complex $[CpRu(cod)\subset Ga_4L_6]^{11-}$ were observed, implying that the metal–ligand assembly incorporated merely the desolvated $[CpRu(cod)]^+$ fragment. Although no such 16-e$^-$ species has been isolated previously, the cluster cavity is known to stabilize reactive species that would not be able to exist outside of the assembly,[16] and the supramolecular structure might function as a very large and non-coordinating counterion.

To explore this possibility, we attempted to prepare the complex $[CpRu(cod)]BF_4$ by treating [CpRuCl(cod)] with $AgBF_4$ in CH_2Cl_2. Unexpectedly, the dominant reaction product turned out to be the novel complex [CpRu(*cis*-1,3,7-octatriene)]BF_4 (**1**-BF_4). This compound showed a complex ^{1}H NMR spectrum with one Cp resonance and 12 different cod signals (Figure 3, top). When the spectrum of **1**-BF_4 is compared with the spectrum of the previously isolated host–guest complex (Figure 3, bottom), it becomes apparent that **1** is the encapsulated guest. Each resonance of **1** is displayed twice in the spectrum of the host–guest complex, confirming that **1** is chiral and its placement into the chiral cavity leads to the formation of two diastereomeric host–guest species.

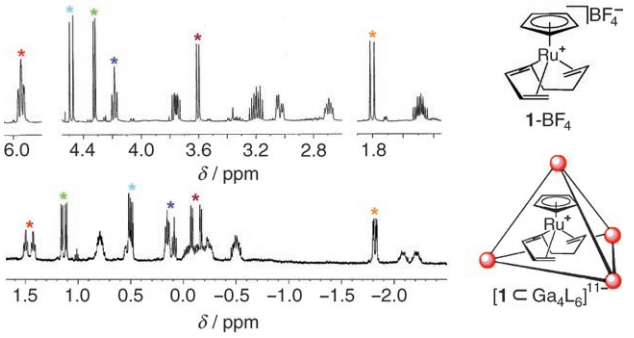


Figure 3. Comparison of the ^{1}H NMR spectra of **1**-BF_4 (top) and $[\mathbf{1}\subset Ga_4L_6](NMe_4)_5K_6$ (bottom). Encapsulation of the chiral ruthenium complex **1** into the chiral cavity leads to the formation of two diastereomers in a 1:1 ratio. Selected resonances are highlighted to illustrate the doubling of signals.

The structure of **1**-BF_4 was elucidated by performing a number of NMR experiments. An HMQC–HMBC sequence defined the C–C bond connectivities and gave evidence for the presence of four =CH- groups and four -CH_2- groups. The final structure of **1**-BF_4 was assigned through coupling-constant analysis (see the Supporting Information) in combination with 2D TOCSY and 2D NOESY NMR studies.[20] Compound **1**-BF_4 is stable for approximately 20 h at room temperature in CD_2Cl_2. Addition of water to the organic solution resulted in fast and irreversible decomposition.[21] The major decomposition product was identified as the cyclooctatriene complex [CpRu(1,3,5-cyclooctatriene)]BF_4, the hexafluorophosphate analogue of which has been reported previously.[22] Importantly, this decomposition does not occur when the complex is encapsulated. Inside the metal–ligand assembly, this reactive intermediate is stable for several weeks at room temperature in aqueous solution. It is protected from the outside chemical environment and sheltered from possible reaction channels that lead to decomposition.

The Cp* analogue of **1** was reported by Itoh and co-workers.[23] They obtained [Cp*Ru(*cis*-1,3,7-octatriene)]OTf (Tf = trifluoromethanesulfonyl) through treatment of [Cp*RuCl(butadiene)] with AgOTf in the presence of excess butadiene and found that addition of CO (one atm) to [Cp*Ru(*cis*-1,3,7-octatriene)]OTf led to the formation of the carbonyl complex [Cp*Ru(cod)(CO)]OTf.[23,24] Complex **1**-BF_4 reacted with CO in CH_2Cl_2 in a similar fashion to yield $[CpRu(cod)(CO)]BF_4$ (**2**-BF_4) as a pale-yellow solid. This carbonyl complex possesses a strong characteristic C=O stretch in the IR spectrum at $\nu = 2023$ cm^{-1} and has previously been described by Crocker et al.[25] Compound **2**-BF_4 was encapsulated in water, and the resulting host–guest complex $[\mathbf{2}\subset Ga_4L_6]^{11-}$ reveals the typical upfield shift in the ^{1}H NMR spectrum for the guest and inclusion into the asymmetric cavity: 12 separate signals are displayed for the cod moiety of the Ru complex. In addition, the IR spectrum shows a strong C=O stretch at $\nu = 2026$ cm^{-1}, confirming encapsulation of the carbonyl complex. More interestingly, the host–guest complex $[\mathbf{2}\subset Ga_4L_6]^{11-}$ could also be generated from $[\mathbf{1}\subset Ga_4L_6]^{11-}$ in water through the addition of CO. This transformation was monitored by ^{1}H NMR spectroscopy (Figure 4). The starting material $[\mathbf{1}\subset Ga_4L_6]^{11-}$ clearly shows two sets of signals for the two diastereomeric host–guest complexes. Upon addition of CO, the formation of the new product $[\mathbf{2}\subset Ga_4L_6]^{11-}$, as well as the disappearance of the starting material, is observed after 1 day; after 5 days, the transformation is complete. Comparison of this product with the independently prepared $[\mathbf{2}\subset Ga_4L_6]^{11-}$ shows that the host–guest complexes are identical.

The corresponding Cp* complexes showed very similar reactivity patterns (see Scheme 1). The cationic octatriene complex [Cp*Ru(*cis*-1,3,7-octatriene)]BF_4 (**3**-BF_4) was formed through halide abstraction from [Cp*RuCl(cod)] with $AgBF_4$. Similar to the Cp complex, **3**-BF_4 completely decomposed in CD_2Cl_2 within 30 hours and in the presence of water within minutes. However, the host–guest complex $[\mathbf{3}\subset Ga_4L_6]^{11-}$, generated through the reaction of [Cp*RuCl(cod)] with $[Ga_4L_6]^{12-}$, was stable in aqueous solution for more than two weeks. Again, the host–guest complex $[\mathbf{3}\subset Ga_4L_6]^{11-}$ was treated with CO, quantitatively yielding

 © 2006 Wiley-VCH Verlag GmbH & Co. KGaA, Weinheim

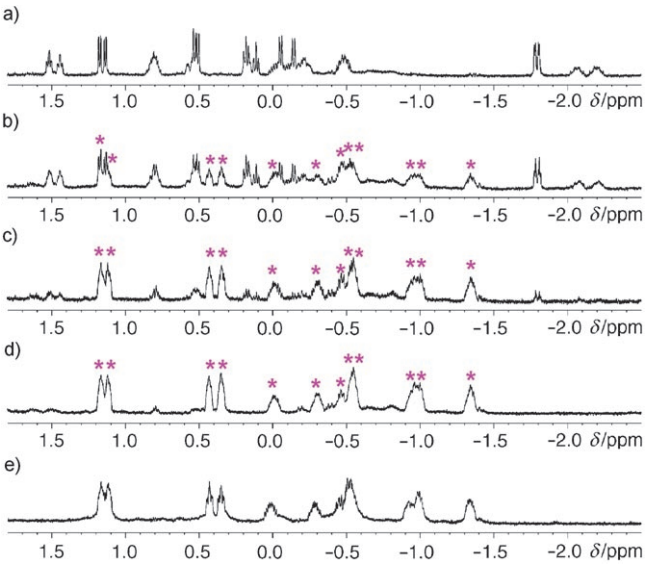
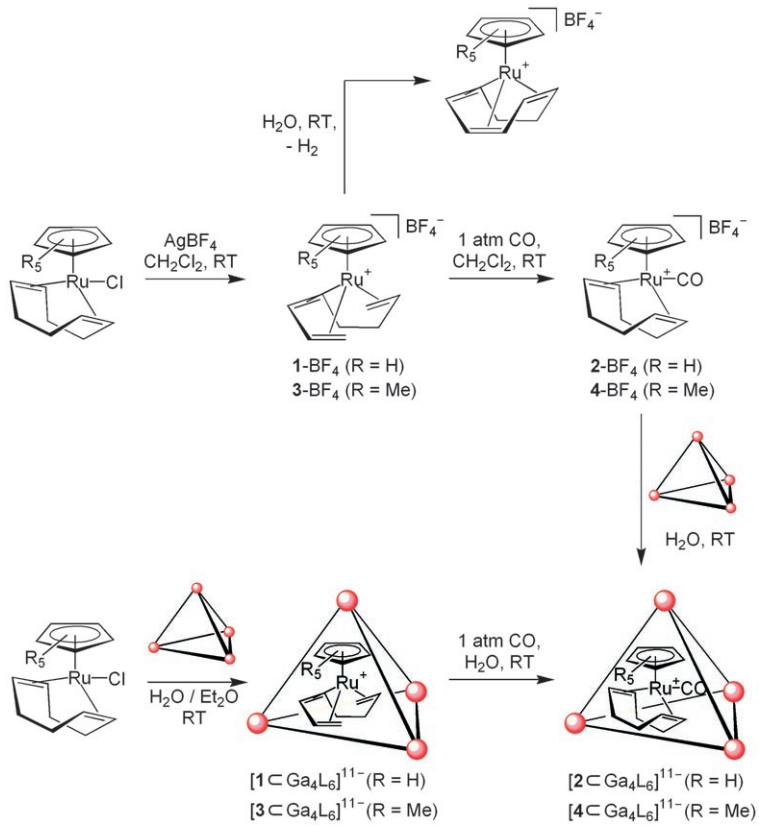


Figure 4. Reaction of [CpRu(*cis*-1,3,7-octatriene)⊂Ga_4L_6]$^{11-}$ ([**1**⊂Ga_4L_6]$^{11-}$) with CO monitored by ^{1}H NMR spectroscopy. Conversion into the carbonyl complex [CpRu(cod)(CO)⊂Ga_4L_6]$^{11-}$ ([**2**⊂Ga_4L_6]$^{11-}$, *) is complete after 5 days. a) [**1**⊂Ga_4L_6]$^{11-}$; b) [**1**⊂Ga_4L_6]$^{11-}$ + CO, 1 day; c) [**1**⊂Ga_4L_6]$^{11-}$ + CO, 2 days; d) [**1**⊂Ga_4L_6]$^{11-}$ + CO, 5 days; e) [**2**⊂Ga_4L_6]$^{11-}$, prepared independently.



Scheme 1. Summary of host–guest reactivity. The reactive intermediates **1** and **3** are stabilized by the presence of the supramolecular host.

the carbonyl complex [Cp*Ru(cod)(CO)⊂Ga_4L_6]$^{11-}$ ([**4**⊂Ga_4L_6]$^{11-}$). As monitored by ^{1}H NMR spectroscopy (see the Supporting Information), the disappearance of the two diastereomeric complexes of [**3**⊂Ga_4L_6]$^{11-}$ is accompanied by the formation of the carbonyl complex [**4**⊂Ga_4L_6]$^{11-}$.

At this point, we are not entirely able to distinguish whether the addition of CO proceeds inside the cavity or if **1** and **3** dissociate from the metal–ligand assembly, undergo reaction in the bulk solution, and then re-enter the cavity. Due to the lack of decomposition of the reactive ruthenium complexes over extended periods of time though (no leaching is observed over several weeks), we can conclude that **1** and **3** reside only transiently, if at all, in the bulk solution. In addition, recent studies on related systems showed that dissociation of the sterically demanding guest molecules [Cp*Ir(PMe_3)(C_2H_4)]$^+$ and [Cp^*_2Co]$^+$ from the host cavity is slow ($t_{1/2}$ = hours to weeks).[13,26] We therefore propose that reactivity takes place within the protective cavity.

In summary, two reactive organometallic intermediates have been stabilized in the inner phase of a chiral metal–ligand assembly. Although these complexes decompose within hours in organic solution and within minutes in water, the corresponding host–guest complexes are stable in aqueous solution for weeks. Encapsulation by the size- and shape-complementary host provides enough binding energy for the guests to prevent their decomposition. Despite their stabilization, the guest molecules are still able to react stoichiometrically with CO. These findings illustrate that supramolecular container molecules may soon find additional use in organometallic chemistry.[27] Not only can encapsulation by a supramolecular host stabilize certain intermediates, but stabilization may also be exploited to alter the chemical reactivity and selectivity of the bound guest molecules. Ideally, novel modes of selectivity or new reactivity can be anticipated by changing the relative stabilities of intermediates along a catalytic cycle, and thus shifting the energy surface of the reaction. In this particular case, we have isolated reactive organometallic species which are intermediates in the catalytic dimerization and oligomerization of substituted butadienes. We are now investigating the catalytic reactivity of these novel host–guest complexes.

Received: June 3, 2005
Revised: October 7, 2005
Published online: December 21, 2005

Keywords: cage compounds · host–guest systems · reactive intermediates · ruthenium

[1] D. J. Cram aptly described the interior of such molecules as an "inner phase"; for example, see: D. J. Cram, *Nature* **1992**, *356*, 29.
[2] Separation of these kinetic and thermodynamic phenomena may be difficult.

 © 2006 Wiley-VCH Verlag GmbH & Co. KGaA, Weinheim

[3] D. J. Cram, M. E. Tanner, R. Thomas, *Angew. Chem.* **1991**, *103*, 1048; *Angew. Chem. Int. Ed. Engl.* **1991**, *30*, 1024.
[4] R. Warmuth, *Angew. Chem.* **1997**, *109*, 1406; *Angew. Chem. Int. Ed. Engl.* **1997**, *36*, 1347.
[5] R. Warmuth, M. A. Marvel, *Angew. Chem.* **2000**, *112*, 1168; *Angew. Chem. Int. Ed.* **2000**, *39*, 1117.
[6] M. Yoshizawa, T. Kusukawa, M. Fujita, K. Yamaguchi, *J. Am. Chem. Soc.* **2000**, *122*, 6311.
[7] M. Yoshizawa, T. Kusukawa, M. Fujita, S. Sakamoto, K. Yamaguchi, *J. Am. Chem. Soc.* **2001**, *123*, 10454.
[8] S. Körner, F. C. Tucci, D. M. Rudkevich, T. Heinz, J. Rebek, Jr., *Chem. Eur. J.* **2000**, *6*, 187.
[9] D. L. Caulder, R. E. Powers, T. N. Parac, K. N. Raymond, *Angew. Chem.* **1998**, *110*, 1940; *Angew. Chem. Int. Ed.* **1998**, *37*, 1840.
[10] D. L. Caulder, K. N. Raymond, *J. Chem. Soc. Dalton Trans.* **1999**, 1185.
[11] D. L. Caulder, C. Brückner, R. E. Powers, S. König, T. N. Parac, J. A. Leary, K. N. Raymond, *J. Am. Chem. Soc.* **2001**, *123*, 8923.
[12] T. N. Parac, D. L. Caulder, K. N. Raymond, *J. Am. Chem. Soc.* **1998**, *120*, 8003.
[13] D. H. Leung, D. Fiedler, R. G. Bergman, K. N. Raymond, *Angew. Chem.* **2004**, *116*, 981; *Angew. Chem. Int. Ed.* **2004**, *43*, 963.
[14] D. Fiedler, D. Pagliero, J. L. Brumaghim, R. G. Bergman, K. N. Raymond, *Inorg. Chem.* **2004**, *43*, 846.
[15] D. Fiedler, D. H. Leung, R. G. Bergman, K. N. Raymond, *J. Am. Chem. Soc.* **2004**, *126*, 3674.
[16] M. Ziegler, J. L. Brumaghim, K. N. Raymond, *Angew. Chem.* **2000**, *112*, 4285; *Angew. Chem. Int. Ed.* **2000**, *39*, 4119.
[17] J. L. Brumaghim, M. Michels, K. N. Raymond, *Eur. J. Org. Chem.* **2004**, 4552.
[18] B. M. Trost, F. D. Toste, A. B. Pinkerton, *Chem. Rev.* **2001**, *101*, 2067.
[19] Encapsulated guests in this M_4L_6 system are readily identified by a strong upfield shift of their resonances.
[20] Regarding the proposed mechanism for the formation of **1** based on variable-temperature NMR studies: at −80 °C an intermediate with C_s symmetry is observed, presumably [CpRu(cod)]F–BF_3] (with one of the four fluorine atoms coordinated to the Ru center). This complex is stable up to 0 °C. At this point, formation of **1** starts, along with decomposition to the cyclooctatriene complex, and a weak hydride signal at $\delta = -12.3$ ppm is also observed. A possible mechanism for the formation of **1** starts with insertion of the metal into a methylene C–H bond; hydride migration gives rise to 9-ruthenal(IV)bicyclo[4.2.1]-2-nonene and reductive decyclization leads to the product (also, see the Supporting Information).
[21] The decomposition to the cyclooctatriene complex is irreversible owing to the formation of H_2.
[22] M. O. Albers, D. J. Robinson, A. Shaver, E. Singleton, *Organometallics* **1986**, *5*, 2199.
[23] K. Masuda, K. Nakano, T. Fukahori, H. Nagashima, K. Itoh, *J. Organomet. Chem.* **1992**, *428*, C21.
[24] K. Itoh, K. Masuda, T. Fukahori, K. Nakano, K. Aoki, H. Nagashima, *Organometallics* **1994**, *13*, 1020.
[25] M. Crocker, M. Green, C. E. Morton, K. R. Nagle, A. G. Orpen, *J. Chem. Soc. Dalton Trans.* **1985**, 2145.
[26] A. V. Davis, K. N. Raymond, *J. Am. Chem. Soc.* **2005**, *127*, 7912.
[27] Hupp and co-workers, for example, demonstrated that encapsulation of a manganese epoxidation catalyst significantly increased the catalyst lifetime: M. L. Merlau, M. P. Mejia, S. T. Nguyen, J. T. Hupp, *Angew. Chem.* **2001**, *113*, 4369; *Angew. Chem. Int. Ed.* **2001**, *40*, 4239.

 © 2006 Wiley-VCH Verlag GmbH & Co. KGaA, Weinheim

Nanostructures

DOI: 10.1002/anie.200502751

Ligand-Selective Aqueous Synthesis of One-Dimensional CdTe Nanostructures**

Hao Zhang, Dayang Wang, and Helmuth Möhwald*

The past decade has witnessed tremendous progress in the wet-chemical preparation of semiconductor nanocrystals with defined size, shape, and surface chemistry, driven by their immensely promising fundamental and technical applications.[1] One current focus lies in establishing methodologies to synthesize one-dimensional (1D) nanostructures such as nanorods and nanowires owing to their increasingly recognized advantages over quasi-spherical nanocrystals, so-called quantum dots (QDs), particularly in view of technical applications.[2] Anisotropic crystal growth is a prerequisite for the formation of 1D nanostructures and necessitates a profound difference in the surface energy between crystallographic facets.[1] In this context, the hexagonal wurtzite structure is favored as a consequence of the large chemical dissimilarity of their facets as compared with the cubic zinc-blende structure.[1,3] To date, 1D nanostructures of various semiconductors have been generated in organic media mainly through decomposition of lipophilic organometallic precursors at high temperatures in the presence of two or more ligands.[4]

Recently, high-quality QDs, particularly of type II/VI semiconductors, have been prepared in aqueous media with the aid of water-soluble thiol ligands. This method offers a number of advantages such as low cost, facility of scale-up, and being environmentally friendly.[5,6] The aqueous synthesis methodology, however, cannot be used to directly generate 1D nanostructures owing to temperature limitations; a crystal growth temperature of around 100 °C is not sufficient to overcome the energy barrier of transforming zinc-blende to wurtzite structures. Most recently, the groups of Kotov and Rogach reported success in transforming preformed zinc-blende QDs of CdTe into wurtzite nanowires by partially removing the capping ligands of thioglycolic acid (TGA).[7] Inspired by these successes, herein, we demonstrate the direct preparation of stable colloidal CdTe nanorods or nanowires in water (by storing dilute aqueous solutions of their precursors) which selectively occurs in the presence of ligands with a

[*] Dr. H. Zhang, Dr. D. Wang, Prof. Dr. H. Möhwald
Max Planck Institute of Colloids and Interfaces
14424 Potsdam (Germany)
Fax: (+49) 331-567-9202
E-mail: dayang.wang@mpikg-golm.mpg.de

[**] H.Z. is grateful to the Alexander von Humboldt Foundation for a research fellowship. A. Rogach (University of Munich) is acknowledged for helpful discussions. R. Pitschke and U. Blöck (Hahn-Meitner-Institute, Berlin) are acknowledged for assistance with TEM studies. We thank the Max Planck Society for financial support.

Supporting information for this article is available on the WWW under http://www.angewandte.org or from the author.

WILEY InterScience DISCOVER SOMETHING GREAT
© 2006 Wiley-VCH Verlag GmbH & Co. KGaA, Weinheim

TGA-like molecular structure. This ligand selectivity should provide a better understanding of the role of the thiol ligands in the growth of crystals in an aqueous synthesis process.

Weller and co-workers recently pioneered the formation of CdTe QDs by refluxing aqueous solutions of their precursors, Cd^{2+} and HTe^-, in the presence of various thiol ligands such as TGA.[5] Usually, a molar ratio of Cd^{2+}/ligand/HTe^- of 1:2.4:0.5 and a concentration of the precursor of 4.8×10^{-2} M is used with respect to the ligand. In this study, we diluted the aqueous solution of the precursors of the CdTe nanocrystals by 20 times to 2.4×10^{-3} M, while maintaining the molar ratio of the precursors. The ligands studied initially were 3-mercaptopropionic acid (MPA), 1-thioglycerol (TG), 2-mercaptoethylamine (MA), and TGA (Scheme 1a). Upon storing the precursor solutions of CdTe nanocrystals at 80 °C for 2 h, the solution that contained TGA turned dark blue (Figure 1a) while those containing MPA, TG, and MA turned

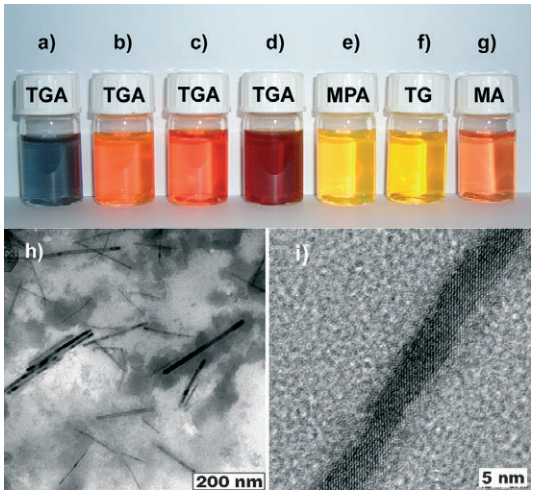


Figure 1. Photographs of aqueous solutions of TGA-stabilized CdTe nanocrystals formed by storing solutions of their precursors at 80 °C for 2 h: a) 2.4×10^{-3} M, b) 9.6×10^{-3} M, c) 2.4×10^{-2} M, and d) 4.8×10^{-2} M. Optical photographs of aqueous solutions of CdTe nanocrystals formed by storing 2.4×10^{-3} M solutions of the precursors at 80 °C for 2 h in the presence of e) MPA, f) TG, and g) MA. h) TEM and i) HRTEM images of TGA-stabilized nanocrystals derived from 2.4×10^{-3} M solutions of the precursors (as shown in part a).

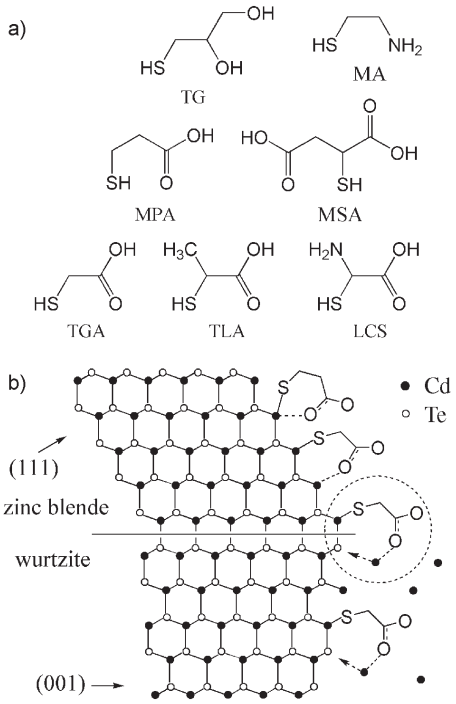
yellow or red (Figure 1e, f, and g, respectively). This difference of the optical behavior may be related to the variation of the shape and/or size of the resulting nanocrystals. Transmission electron microscopy (TEM) studies revealed that the presence of TGA led to the formation of nanorods that were 100–400 nm in length and 4–20 nm in diameter (Figure 1h). This elongation may cause a long-wavelength shift of the optical absorption (see Supporting Information) to give the resulting dark blue color of the suspension (Figure 1a). These nanorods exhibited a weak luminescence owing to the weaker quantum confinement of 1D nanostructures relative to that of 0D nanostructures.[8] X-ray diffraction and selected-area electron diffraction patterns revealed that the lattice structure of the resulting nanorods is wurtzite (see Supporting Information). Their high-resolution TEM (HRTEM) image shows that the long axis of the resulting nanorods is parallel to the (001) direction and perpendicular to the (100) direction of the wurtzite lattice (Figure 1i). In contrast, the presence of TG, MPA, and MA yielded quasi-spherical zinc-blende dots of 3–4 nm in size. These observations demonstrate the selectivity of TGA as a ligand for the formation of CdTe wurtzite nanorods.

Upon increasing the concentration of the TGA-containing solution of the CdTe precursors to 9.6×10^{-3} M, for example, and after 2 h storage at 80 °C, the resultant solution was orange-colored and luminescent (Figure 1b–d). TEM studies indicated the formation of zinc-blende QDs of about 3 nm (see Supporting Information), confirming the crucial role of the concentration of the precursors in the formation of CdTe nanorods. Note that the CdTe QDs obtained from dilute precursor solutions show a poor colloidal stability and agglomerate faster than those from 4.8×10^{-2} M solutions of the precursors, consistent with previous studies.[9] However, the MPA-stabilized QDs were slightly more stable.

Formation of 1D semiconductor nanostructures usually necessitates anisotropic crystal growth along the wurtzite (001) axis by means of Ostwald ripening and oriented attachment.[1d,10] However, the thermodynamically stable structure of CdTe is zinc-blende,[11] thus the growth of CdTe nanocrystals proceeds predominantly in the zinc-blende structure in conventional colloidal synthetic processes.[5,12] With the present strategy, the presence of TGA led to the formation of wurtzite CdTe nanorods even after storing aqueous solutions at 2.4×10^{-3} M of the precursors at room temperature (ca. 4 h). In contrast, the use of TG, MPA, or MA as stabilizers afforded only small amounts of zinc-blende QDs after storing the respective solutions at room temperature for several weeks. This observation strongly suggests that capping by TGA favors the growth of the CdTe nuclei in the wurtzite structure and selectively leads to the growth of nanorods.

As depicted in Scheme 1a, TGA has a different functional terminus and a different chain length compared to TG, MA, and MPA; these structural differences may be used to elucidate the vital effect of TGA on the growth of CdTe nanocrystals. Weller and co-workers reported the possibility of the secondary coordination between the carbonyl oxygen atoms of the capped thiol ligands and the Cd sites on CdTe nanocrystals, enhancing the colloidal stability of CdTe nanocrystals.[13] Such secondary coordination requires the outward carbonyl oxygen of the ligand to bend backwards to link with the Cd site on the nanocrystal, leading to a configuration with a polygonal loop. Both MPA and TGA have a carboxylic acid terminus. As a result of the longer chain in MPA, secondary coordination leads to a hexagonal loop—the most favorable configuration—in which the carbonyl oxygen and the thiol sulfur atoms coordinate with the same Cd site (Scheme 1b). Here, we observed a better colloidal stability of MPA-stabilized CdTe QDs which is likely due to the steric effect of this hexagonal configuration. As TGA is shorter than MPA by one methylene unit, the carbonyl oxygen atom of TGA may coordinate with the Cd site adjacent to that capped by the thiol sulfur atom to achieve the stable hexagonal configuration (Scheme 1b). Hence, one molecule of TGA can cap two Cd sites through the secondary coordination of its

 © 2006 Wiley-VCH Verlag GmbH & Co. KGaA, Weinheim



Scheme 1. a) Summary of the molecular structures of the ligands studied. b) 2D representation of the (111) zinc-blende facet of CdTe nanocrystals with ABCABC stacking and their (001) wurtzite facet with ABAB stacking, in which the secondary coordination of MPA and TGA is also illustrated. The dashed circle highlights that the carbonyl oxygen of TGA may absorb a free Cd^{2+} ion from solution through secondary coordination and place it on the Te site in an ABAB stacking manner, thus allowing growth of a (001) wurtzite facet.

carboxylate group, whereas one molecule of MPA can cap only one Cd site.

Alternatively, secondary coordination could also allow the carbonyl oxygen of TGA to absorb free Cd^{2+} ions from the surroundings and place them on the Te site. Hence, this secondary coordination of TGA may induce the growth of the crystal. It is thought that the carbonyl oxygen could locate the Cd ion on the Te sites at will. The (111) zinc-blende facet is atomically identical to the (001) wurtzite facet, as shown in Scheme 1b, with the former displaying ABCABC stacking while the latter reveals ABAB stacking.[4] As suggested by molecular dynamics calculations,[14] ABAB stacking is kinetically more favorable than ABCABC stacking. During the growth of CdTe nanocrystals which occurs mainly through Ostwald ripening,[5] the secondary coordination of TGA may therefore benefit the growth of the CdTe clusters in an ABAB stacking manner, in turn leading to the anisotropic growth of the wurtzite nanorods along their (001) axis. In the present study, the resulting wurtzite CdTe nanorods show a poor long-term stability. They gradually degraded into luminescent QDs at room temperature over several weeks (see Supporting Information). This demonstrates that the formation of CdTe nanorods with the aid of the secondary coordination of TGA is *kinetically* rather than *thermodynamically* favorable.

To better understand the influence of the secondary coordination of ligands on the growth of CdTe nanocrystals, thiolactic acid (TLA), L-cysteine (LCS), and mercaptosuccinic acid (MSA) were utilized as capping ligands. After storing solutions of the precursors (2.4×10^{-3} M) with added TLA or LCS at 80 °C for 2 h, wurtzite CdTe nanorods were observed in both cases (see Supporting Information). This result can be explained by the similarity of their molecular structures to that of TGA; only one of the side groups bound to the methylene is different (Scheme 1a). The secondary coordination of the carbonyl oxygen atoms of TLA and LCS may also benefit the anisotropic crystal growth along the wurtzite (001) axis. Surprisingly, although TLA is the structural isomer of MPA, the latter does not lead to formation of wurtzite nanorods.

The molecular structure of MSA combines features of both MPA and TGA, as depicted in Scheme 1a. Figure 2b reveals that MSA, with its TGA moiety, induces the

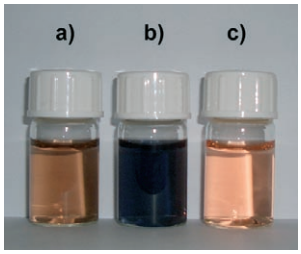


Figure 2. Photographs of freshly prepared aqueous solutions of the precursors (2.4×10^{-3} M) of CdTe nanocrystals in the presence of MSA (a), and those stored at 80 °C for 2 h (b) and 6 h (c).

formation of wurtzite CdTe nanorods upon storing aqueous solutions of the precursors at 2.4×10^{-3} M at 80 °C for 2 h (see also Supporting Information). However, a further 4 h storage rapidly led to degradation of the resulting nanorods into luminescent QDs (see Supporting Information). This fast degradation suggests that the secondary coordination of the MPA moiety of MSA may facilitate the formation of the QDs (see above).

To circumvent the poor structural stability of the resulting CdTe nanorods, we used both TGA-like and non-TGA-like ligands in the solutions of the precursor. As shown in Figure 3, the simultaneous presence of TGA and TG led to the wurtzite CdTe nanowires with uniform sizes and aspect ratios. Their aspect ratios could be well-tuned by storage at 80 °C. In this case, the resulting nanowires exhibited robust colloidal and

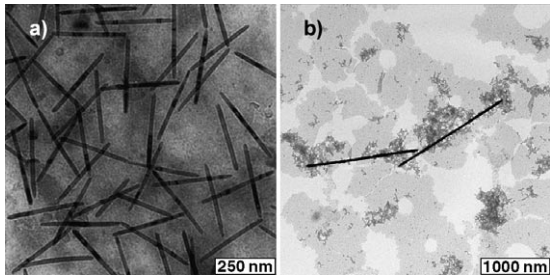


Figure 3. TEM images of CdTe nanorods obtained by storage of 2.4×10^{-3} M solutions of the precursors in the presence of TGA and TG at 80 °C for 8 h (a) and 13 h (b). A 1:1 molar ratio of TGA/TG was used.

 © 2006 Wiley-VCH Verlag GmbH & Co. KGaA, Weinheim

structural stability; precipitates or QDs were hardly detectable even after several weeks. The role of the dual ligands in the growth of wurtzite CdTe nanowires is not yet clear, but studies to this end are currently underway in our laboratory.

In summary, we have demonstrated a direct aqueous method to fabricate 1D CdTe nanostructures. Owing to their unusual secondary coordination, only TGA-like ligands with a molecular structure of HS-CH(R)-COOH (R = H, CH_3, NH_2, etc.) favor the growth of CdTe nanocrystals with a wurtzite structure and indeed lead to anisotropic 1D growth along the wurtzite (001) axis. Besides obtaining CdTe nanowires with defined sizes and aspect ratios, we showed that the simultaneous presence of TGA-like and non-TGA-like ligands provides robust colloidal and structural stability. The formation of 1D wurtzite CdTe nanostructures necessitates a fairly low concentration of the precursors, about 20 times lower than the concentration for the generation of QDs by conventional methods. As a result of the complexity of the effect of the ligand,[13] we are not yet able to completely elucidate the mechanism of formation of CdTe nanorods in the presence of TGA-like ligands. Currently our efforts are directed to more detailed investigations of the mechanism behind the growth of CdTe nanocrystals. As the 1D CdTe nanostructures that we have obtained are functionalized on their surfaces with carboxylic acid groups, for example, they should be easy to conjugate with other molecules which is of great appeal for technical applications.

Experimental Section

Here, we modified the conventional aqueous procedure to produce CdTe nanocrystals with the aid of thiol ligands.[5,6] Freshly prepared solutions of NaHTe were added to N_2-saturated solutions of $CdCl_2$ at pH 9.0 in the presence of one or two thiol ligands. The concentrations of the precursors were varied from 2.4×10^{-3} M to 4.8×10^{-2} M with respect to the ligand, and the molar ratio of Cd^{2+}/ligand/HTe^- used was 1:2.4:0.5. The resulting solutions were stored at a temperature ranging from 25 °C to 80 °C for a certain period to initiate the growth of CdTe nanocrystals. The resulting nanocrystals were visualized by a Zeiss EM 912 Omega microscope at 120 kV. HRTEM studies were peformed on a Philips CM 120 microscope at 300 kV.

Received: August 4, 2005
Revised: September 14, 2005
Published online: December 15, 2005

Keywords: cadmium · ligand effects · nanostructures · synthetic methods · tellurium

[1] a) X. Peng, L. Manna, W. Yang, J. Wickham, E. Scher, A. Kadavanich, A. P. Alivisatos, *Nature* **2000**, *404*, 59 – 61; b) V. I. Klimov, A. A. Mikhailovsky, S. Xu, A. Malko, J. A. Hollingsworth, C. A. Leatherdale, H. J. Eisler, M. G. Bawendi, *Science* **2000**, *290*, 314 – 317; c) J. D. Holmes, K. P. Johnston, R. C. Doty, B. A. Korgel, *Science* **2000**, *287*, 1471 – 1473; d) C. Pacholski, A. Kornowski, H. Weller, *Angew. Chem.* **2002**, *114*, 1234 – 1237; *Angew. Chem. Int. Ed.* **2002**, *41*, 1188 – 1191; e) T. Mokari, E. Rothenberg, I. Popov, R. Costi, U. Banin, *Science* **2004**, *304*, 1787 – 1790.

[2] For a review, see: Y. Xia, P. Yang, Y. Sun, Y. Wu, B. Mayers, B. Gates, Y. Yin, F. Kim, H. Yan, *Adv. Mater.* **2003**, *15*, 353 – 389.

[3] L. Manna, L. W. Wang, R. Cingolani, A. P. Alivisatos, *J. Phys. Chem. B* **2005**, *109*, 6183 – 6192.

[4] a) L. Manna, E. C. Scher, A. P. Alivisatos, *J. Am. Chem. Soc.* **2000**, *122*, 12700 – 12706; b) Z. A. Peng, X. Peng, *J. Am. Chem. Soc.* **2002**, *124*, 3343 – 3353.

[5] N. Gaponik, D. V. Talapin, A. L. Rogach, K. Hoppe, E. V. Shevchenko, A. Komowski, A. Eychmüller, H. Weller, *J. Phys. Chem. B* **2002**, *106*, 7177 – 7185.

[6] H. Zhang, Z. Zhou, B. Yang, M. Y. Gao, *J. Phys. Chem. B* **2003**, *107*, 8 – 13.

[7] a) Z. Tang, N. A. Kotov, M. Giersig, *Science* **2002**, *297*, 237 – 240; b) Y. Volkov, S. Mitchell, N. Gaponik, Y. P. Pakovich, J. F. Donegan, D. Kelleher, A. L. Rogach, *ChemPhysChem* **2004**, *5*, 1600 – 1602.

[8] H. Yu, J. Li, R. Loomis, L. Wang, W. E. Buhro, *Nat. Mater.* **2003**, *2*, 517 – 520.

[9] J. Aldana, Y. A. Wang, X. Peng, *J. Am. Chem. Soc.* **2001**, *123*, 8844 – 8850.

[10] K. Cho, D. V. Talapin, W. Gaschler, C. B. Murray, *J. Am. Chem. Soc.* **2005**, *127*, 7140 – 7147.

[11] S. Wei, S. B. Zhang, *Phys. Rev. B* **2000**, *62*, 6944 – 6947.

[12] S. Kumar, M. Ade, T. Nann, *Chem. Eur. J.* **2005**, *11*, 2220 – 2224.

[13] a) M. Gao, S. Kirstein, H. Möhwald, A. L. Rogach, A. Kornowski, A. Eychmüller, H. Weller, *J. Phys. Chem. B* **1998**, *102*, 8360 – 8363; b) H. Bao, Y. Gong, Z. Li, M. Gao, *Chem. Mater.* **2004**, *16*, 3853 – 3859.

[14] B. J. Alder, B. P. Carter, D. A. Young, *Phys. Rev.* **1969**, *183*, 831 – 833.

 © 2006 Wiley-VCH Verlag GmbH & Co. KGaA, Weinheim

Macrocycles

DOI: 10.1002/anie.200502788

Discovery of a Pseudo β Barrel: Synthesis and Formation by Tiling of Ferrocene Cyclopeptides**

*Somenath Chowdhury, David A. R. Sanders, Gabriele Schatte, and Heinz-Bernhard Kraatz**

Inspired by channel-forming proteins involved in transmembrane transport and controlling biological functions,[1] the construction of porous organic architectures with well-defined shapes and sizes from simple building blocks has

[*] S. Chowdhury, Prof. D. A. R. Sanders, Prof. H.-B. Kraatz
Department of Chemistry
University of Saskatchewan
110 Science Place, Saskatoon, SK, S7N 5C9 (Canada)
Fax: (+1) 306-966-4730
E-mail: kraatz@skyway.usask.ca
Dr. G. Schatte
Saskatchewan Structural Science Centre
University of Saskatchewan
110 Science Place, Saskatoon, SK, S7N 5C9 (Canada)

[**] We acknowledge support from the NSERC in the form of an operating grant. H.-B.K. is the Canada Research Chair in Biomaterials.

Supporting information for this article is available on the WWW under http://www.angewandte.org or from the author.

© 2006 Wiley-VCH Verlag GmbH & Co. KGaA, Weinheim

emerged as an important subject in biological chemistry and materials science.[2–8] In this regard, recently introduced peptide-derived materials are used to mimic biological channels and serve as models for transmembrane pores or as antibacterial pore-forming agents,[9–10] with potential applications in drug delivery or as constrained chiral reaction environments.[2,11–12] These channels are mainly self-assembled from cyclopeptides, which stack on top of each other to give large hollow tubes, with the individual cyclopeptides connected by hydrogen-bonding akin to that found in antiparallel β sheets. The peptide β barrel presents a particular challenge. This ubiquitous structural motif is present in a wide range of proteins, including pore-forming proteins present as membrane proteins of gram-negative bacteria, mitochondria, and chloroplasts, and control many sophisticated biological functions.[13] In a β barrel, the peptide strands are arranged more or less parallel to the axis of the barrel. To date, it has not been possible to synthesize a model for such an ubiquitous biological structural motif.[14] Herein, we report the synthesis and the structure of the first artificial β barrel obtained by self-assembly from smaller bio-organometallic ferrocene–peptide conjugates. In this model, eight β strands are arranged almost parallel to the axis of the channel with an internal-pore diameter of 8 Å. Experimental evidence shows that the pore appears to be filled with water molecules (see below). Our approach offers the potential to exploit such structures for the new design of functional transmembrane channels. Such structures may also find applications in separation science, supramolecular host–guest chemistry, and molecular electronics.

The structure of 1,*n*′-disubstituted ferrocene–peptide conjugates is controlled by a fine balance between inter- and intramolecular hydrogen-bonding, and the attached peptide strands attain a β-sheet conformation.[15–18] In general, *P*- and *M*-helical conjugates with respect to ferrocene are formed if L- and D-amino acids are attached, respectively, to the metallocene and the substituents adopt a flexible *anti* conformation, which is not suitable for the sheetlike intramolecular interactions of the elongated peptide strands. We decided to force the attached strands to align parallel to each other by chemically linking the two pendant peptide chains with cysteamine (CSA), a disulfide linker, thereby restricting the mobility of the strands. We expected this to have a profound consequence in that this chemical modification should foster intermolecular hydrogen bonding, which is akin to that found in antiparallel β sheets.

To optimize intramolecular hydrogen bonding between the two peptide substituents, a small twist of the cyclopentadiene (Cp)/amide planes is required, thus resulting in the peptide strands to turn towards each other.[19] From this observation we predicted that restricting the formation of a "flat" β sheet by tying the two peptide substituents through a cystamine linker will induce additional curving of the peptide strands and thus may allow hollow hydrogen-bonded assemblies based on a β-sheet motif to be created. For this purpose, we designed two ferrocene (Fc) cyclopeptides, Fc(Gly-Val-CSA)$_2$ (**5**) and Fc(Gly-Ile-CSA)$_2$ (**6**; Gly = glycine, Val = valine, Ile = isoleucine), each with a glycine unit as the first amino acid attached to the ferrocene unit, thus giving maximum flexibility to the pendant peptide chains, followed by valine or isoleucine, amino acids with a very high propensity to form β sheets. Compounds **5** and **6** were synthesized by the cyclization of 1,1′-ferrocene dicarboxylic acid and cysteamine peptide conjugates at very high dilution and were characterized spectroscopically (see the Supporting Information). These compounds are poorly soluble in organic solvents, as expected for strongly hydrogen-bonded materials.[21] Compound **5** was readily obtained from solutions of low concentration in a crystalline form suitable for structural analysis by X-ray diffraction studies. The molecular structure of **5**, together with its supramolecular arrangement, is shown in Figure 1.

There are three different types of hydrogen bonding present in **5**. Intramolecular hydrogen bonding is observed between the C=O group and the adjacent (H)N group (N(21)-O(12): 2.7848(4), N(23)-O(13): 2.848(3), N(11)-O(22): 3.013(4) Å). The Fc(Gly-Val-CSA)$_2$ units are linked by intermolecular hydrogen bonding (2.898(4) and 3.036(4) Å). The intermolecular hydrogen-bonding interactions between head-to-tail connected ferrocene peptides results in the formation of a 14-membered ring, as expected for two peptides that interact in an antiparallel β-sheet fashion (see Figure 1b).[16] The β sheets are parallel to the *b*–*c* plane. Additional hydrogen bonding (O23···N13: 2.824(4) Å) between adjacent sheets results in the formation of β barrels with a diameter of approximately 8 Å (measured between adjacent oxygen atoms of the C=O groups, see Figure 1c). Importantly, the structural rigidity allows the molecules to act as tiles that form what can be described as pseudo barrels (Figure 1d).

Figure 2 gives a stereoview of a pseudo barrel formed by tiling of the Fc conjugates and superimposes the direction of the individual β strands. The barrel is formed by eight β strands arranged in a up-up-down-down-up-up-down-down pattern. The axis of the barrel is parallel to the *a*–*c* plane and perpendicular to the *b*–*c* plane. The ϕ/ψ angles for the four residues are (Gly1: −134/194°, Val1: −56/146°, Gly2: −76/161°, Val2: −115/64°). These residues all fit close to the theoretical region of β-sheet conformations (ϕ: −180–−45°, ψ: 45–225°).[22] As is seen with naturally occurring β sheets, there is distortion, but the angles still fall within the "allowed" Ramachandran region associated with β-sheet structures.[23–27] The third "residue" (the cystamine) of one substituent (chain 1) has a ϕ value of approximately −97°, thus making the one substituent of the molecule a fairly close approximation of a β strand.[22]

There is precedence for naturally occurring eight-stranded β barrels. For example, OmpX,[28] OmpA,[29] and PagP[30] are all eight-stranded barrels with various biological functions, which range from toxin binding to controlling enzymatic activity. Another example is NspA from *N. meningitides*, which is involved in cell adhesion and has potential applications in structure-based vaccine design.[31] In these natural β barrels, the β strands are tilted from the barrel axis, whereas the β strands are almost parallel to the barrel axis in our pseudo β barrel.

Figure 3a provides a view of the interior surface of the pseudo barrel, thus showing hydrophilic and hydrophobic

 © 2006 Wiley-VCH Verlag GmbH & Co. KGaA, Weinheim

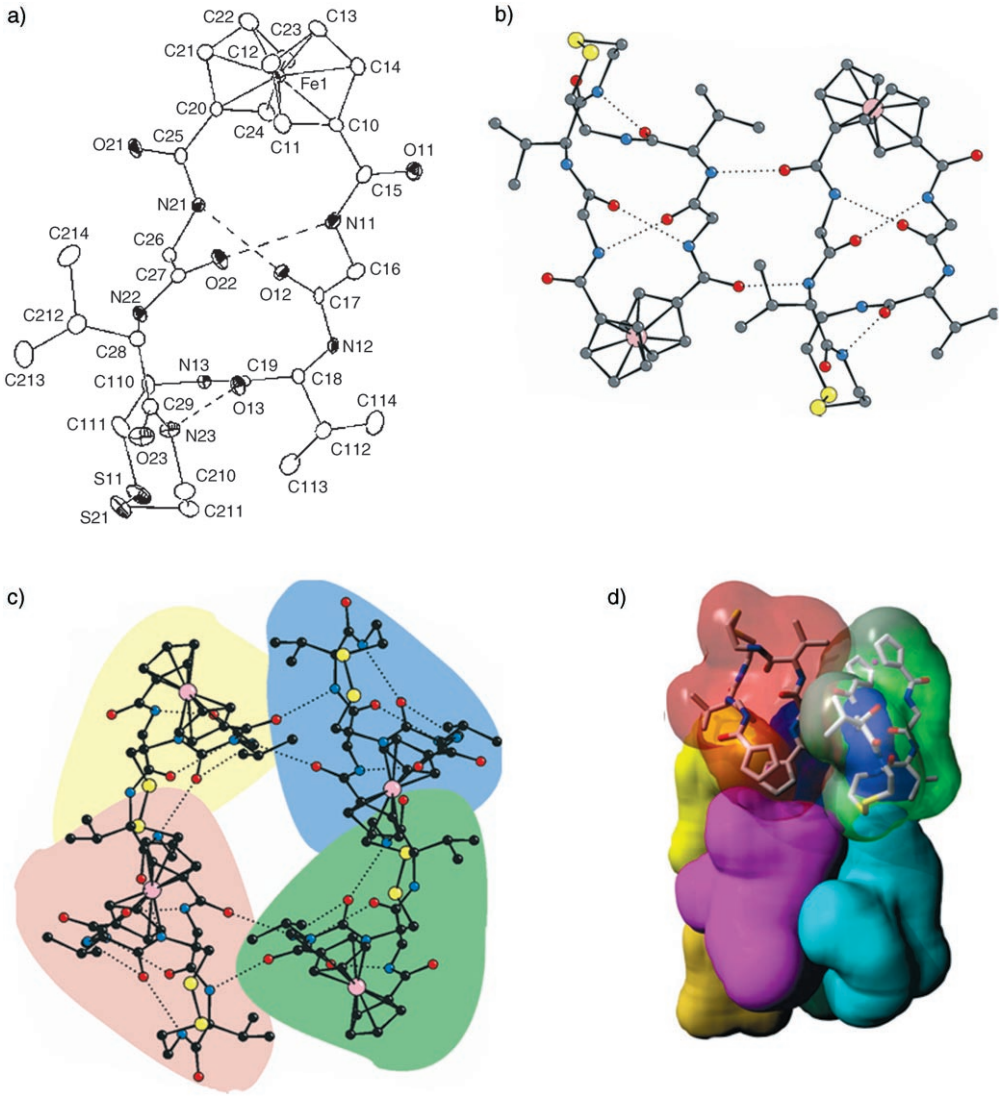


Figure 1. The crystal structure of Fc(Gly-Val-CSA)$_2$ (**5**) and a schematic view of the formation of the pseudo β barrel. a) Molecular structure of **5** showing the *P*-helicity of the ferrocene unit and the intramolecular hydrogen bonding between the two pendant peptide strands. The geometry of the Fc group, the amide substituents, and the bond lengths and angles are well within established parameters for Fc–peptide conjugates.[20] b) Formation of β sheets through intermolecular N(H)···O=C hydrogen bonding. The head-to-tail interaction of the molecules results in an unusual up-up-down-down arrangement of the peptide strands. The arrangement between the two peptide strands on the two Fc conjugates is antiparallel. c) Four molecules interact through hydrogen bonding to form a β barrel; a view down the *c* axis is shown, and the disordered water molecules inside the cavity of the barrel are omitted for clarity. d) Molecular-surface representation showing a side view of the half barrel viewed along the *c* axis formed by tiling of cyclic ferrocene peptides.[35]

characteristics. Some of the peptide carbonyl groups point towards the inside of the pseudo barrel. We assume that this imparts sufficient hydrophilic character on the interior of the barrel to enable water to be inside the pseudo barrels. X-ray analysis shows a significant amount of residual electron density inside the pore, which is best modeled as approximately 12 disordered water molecules, with adjacent water molecules separated from each other by approximately 2.8 Å, which corresponds to strong hydrogen bonding. The closest contact between the water and the interior walls of the pseudo barrel is 3.5 Å, thus indicating weak hydrogen-bonding interactions with the walls. ^{1}H NMR spectroscopic analysis of **5** in solution clearly indicates the presence of water as part of the crystalline solid. The ^{1}H NMR spectra indicate the presence of approximately 1.2–1.5 molecules of water per molecule of Fc–peptide for a total of approximately 9–12 molecules of water per 8-mer or pseudo barrel. As the space within the barrel is 386 Å^3, theoretically 10 water molecules, each occupying 40 Å^3, could fit the pore. Therefore, a model including only water molecules inside the pore best fits all the experimental evidence.

These results compare well with pore-forming cyclopeptides, described before by Ghadiri, who interpreted residual electron density present within the pores of the cylindrical β-sheet peptide as that from water molecules.[32]

FT-IR spectroscopy is also a powerful technique for the examination of the secondary structure of peptides.[33] In particular, the amide-I region offers a characteristic footprint that allows us to distinguish between an α helix, a β sheet, and a random-coil conformation. The FT-IR spectrum of **5** in the solid state exhibits amide-I bands at 1640 and 1682 cm^{-1} and an amide-II band at 1536 cm^{-1}, which are the characteristic peaks for a β sheet.[33,34] Importantly, the IR absorptions are virtually identical for the Ile derivative **6** (1640, 1680, and 1535 cm^{-1}, respectively; see the Supporting Information), thus indicating that the structures of **5** and **6** are similar in the solid state. As expected, the amide N–H bonds are involved in hydrogen bonding, and absorptions are observed in the amide-A region at 3280 and 3282 cm^{-1} for **5** and **6**, respectively. Our observations are closely related to those made by Ghadiri and co-workers who showed that cyclopeptides with alternating D- and L-amino acid sequences, assemble by intermolecular hydrogen bonding into peptide nanotubes, in which the individual building blocks have an antiparallel β-sheet conformation.[5]

In summary, we have outlined a potential strategy for the design of porous peptide materials, in which the barrellike

 © 2006 Wiley-VCH Verlag GmbH & Co. KGaA, Weinheim

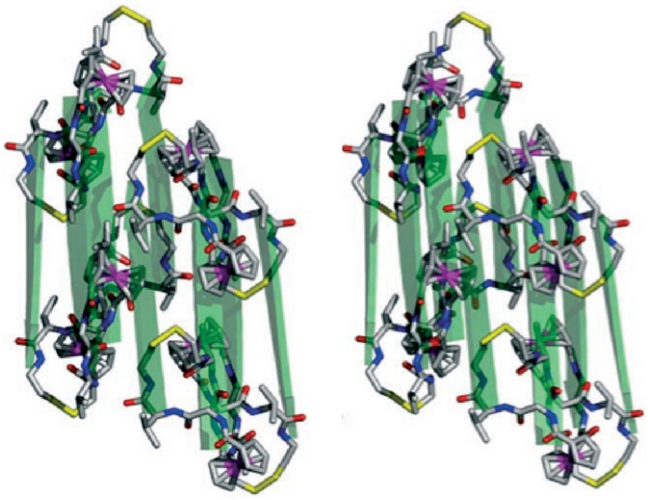


Figure 2. Stereoview of the pseudo barrel formed by tiling of **5**. The individual molecules are indicated as well as the direction of the individual β strands.[22]

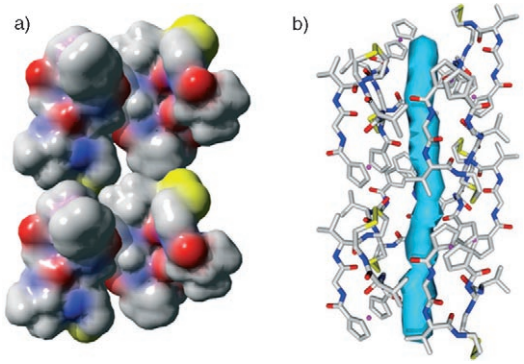


Figure 3. a) Van der Waals surface representation of a cut-away side view of the interior of the pseudo barrel that shows the hydrophilic and hydrophobic characteristics (red: oxygen, blue: nitrogen, yellow: sulfur, gray: carbon). b) The same side view of the pseudo barrel in (a) generated by tiling of **5**. This channel has an interior diameter of approximately 8 Å. The residual electron density within this channel is interpreted as water molecules that are disordered over several positions and only the approximate envelope of the channel content is shown.

pores are formed by the self-assembly of bio-organometallic peptide conjugates. Although solubility of these systems is a challenge at present, the use of hydroxy-containing amino acids, such as serine and threonine, should allow us to study self-assembly in solution. Our approach is promising for the use of readily available starting materials in the assembly of large, porous peptide materials, which may find applications in biological chemistry and materials science. If successful, the strategy described herein should lend itself to the preparation of novel proteins that incorporate the β-barrel motif.[36]

Received: August 6, 2005
Revised: October 19, 2005
Published online: December 27, 2005

Keywords: β barrel · ferrocene · macrocycles · peptides · self-assembly

[1] M. H. Saier, *J. Membr. Biol.* **2000**, 175, 165 – 180.
[2] D. T. Bong, T. D. Clark, J. R. Granja, M. R. Ghadiri, *Angew. Chem.* **2001**, *113*, 1016 – 1041; *Angew. Chem. Int. Edn.* **2001**, 40, 988 – 1011.
[3] D. Venkataraman, S. Lee, J. S. Zhang, J. S. Moore, *Nature* **1994**, *371*, 591 – 593.
[4] A. Harada, J. Li, M. Kamachi, *Nature* **1993**, *364*, 516 – 518.
[5] M. R. Ghadiri, J. R. Granja, R. A. Milligan, D. E. McRee, N. Khazanovich, *Nature* **1993**, *366*, 324 – 327.
[6] M. R. Ghadiri, J. R. Granja, L. K. Buehler, *Nature* **1994**, *369*, 301 – 304.
[7] J. C. Nelson, J. G. Saven, J. S. Moore, P. G. Wolynes, *Science* **1997**, *277*, 1793 – 1796.
[8] D. Ranganathan, C. Lakshmi, I. L. Karle, *J. Am. Chem. Soc.* **1999**, *121*, 6103 – 6107.
[9] J. R. Granja, M. R. Ghadiri, *J. Am. Chem. Soc.* **1994**, *116*, 10785 – 10786.
[10] S. Fernandez-Lopez, H. S. Kim, E. C. Choi, M. Delgado, J. R. Granja, A. Khasanov, K. Kraehenbuehl, G. Long, D. A. Weinberger, K. M. Wilcoxen, M. R. Ghadiri, *Nature* **2001**, *414*, 329 – 329.
[11] J. Sanchez-Quesada, H. S. Kim, M. R. Ghadiri, *Angew. Chem.* **2001**, *113*, 2571 – 2574; *Angew. Chem. Int. Ed.* **2001**, *40*, 2503 – 2506.
[12] B. Eisenberg, *Acc. Chem. Res.* **1998**, *31*, 117 – 123.
[13] W. C. Wimley, *Curr. Opin. Struct. Biol.* **2003** 13, 404 – 411.
[14] N. Sakai, J. Mareda, S. Matile, *Acc. Chem. Res.* **2005**, *38*, 79 – 87.
[15] D. R. van Staveren, N. Metzler-Nolte, *Chem. Rev.* **2004**, *104*, 5931 – 5985.
[16] T. Moriuchi, A. Nomoto, K. Yoshida, A. Ogawa, T. Hirao, *J. Am. Chem. Soc.* **2001**, *123*, 68 – 75.
[17] T. Moriuchi, K. Yoshida, T. Hirao, *Org. Lett.* **2003**, *5*, 4285 – 4288.
[18] A. Nomoto, T. Moriuchi, S. Yamazaki, A. Ogawa, T. Hirao, *Chem. Commun.* **1998**, 1963 – 1964.
[19] S. Chowdhury, G. Schatte, H. B. Kraatz, *Dalton Trans.* **2004**, 1726.
[20] L. Lin, A. Berces, H. B. Kraatz, *J. Organomet. Chem.* **1998**, *556*, 11 – 20.
[21] D. Gauthier, P. Baillargeon, M. Drouin, Y. L. Dory, *Angew. Chem.* **2001**, *113*, 4771 – 4774; *Angew. Chem. Int. Ed.* **2001**, *40*, 4635 – 4638.
[22] G. N. Ramachandran, V. Sasisekharan, *Adv. Protein Chem.* **1968**, 23, 283 – 437.
[23] M. R. Betancourt, J. Skolnick, *J. Mol. Biol.* **2004**, *343*, 635 – 649.
[24] S. Hovmoller, T. Zhou, T. Ohlson, *Acta Crystallogr. Sect. D* **2002**, *58*, 768 – 776.
[25] P. A. Karplus, *Protein Sci.* **1996**, *5*, 1406 – 1420.
[26] A. D. Solis, S. Rackovsky, *Proteins Struct. Funct. Genet.* **2002**, *48*, 463 – 486.
[27] W. Kabsch, C. Sander, *Biopolymers* **1983**, *22*, 2577 – 2637.
[28] J. Vogt, G. E. Schulz, *Struct. Folding Design* **1999**, *7*, 1301 – 1309.
[29] A. Pautsch, G. E. Schulz, *Nat. Struct. Biol.* **1998**, *5*, 1013 – 1017.
[30] P. M. Hwang, R. E. Bishop, L. E. Kay, *Proc. Natl. Acad. Sci. USA* **2004**, *101*, 9618 – 9623.
[31] L. Vandeputte-Rutten, M. P. Bos, J. Tommassen, P. Gros, *J. Biol. Chem.* **2003**, *278*, 24825 – 24830.
[32] T. D. Clark, J. M. Buriak, K. Kobayashi, M. P. Isler, D. E. McRee, M. R. Ghadiri, *J. Am. Chem. Soc.* **1998**, *120*, 8949 – 8962.
[33] S. Krimm, J. Bandekar, *Adv. Protein Chem.* **1986**, *39*, 181 – 364.
[34] A. Barth, C. Zscherp, *Q. Rev. Biophys.* **2002**, *35*, 369 – 430.
[35] Crystal data for **5**: $C_{30}H_{42}Fe_1N_6O_6S_2$, $M_r = 702.67$, orthorhombic, $P2_12_12_1$, $a = 14.4808(4)$, $b = 16.2650(5)$, $c = 16.4770(4)$ Å, $\alpha = \beta = \gamma = 90°$, $Z = 4$; $\mu = 0.543\ mm^{-1}$, $\rho_{calcd} = 1.209\ Mg\,m^{-3}$.
[36] The synthesis and characterization of **5**, **6**, and intermediate species; IR spectra of **5** and **6**; and X-ray structural data for **5** are given in the Supporting Information.

 © 2006 Wiley-VCH Verlag GmbH & Co. KGaA, Weinheim

Charge Separation

DOI: 10.1002/anie.200502815

Stacked-Cup Carbon Nanotubes for Photoelectrochemical Solar Cells**

Taku Hasobe, Shunichi Fukuzumi, and Prashant V. Kamat**

The usefulness of carbon nanotubes in optical, electronic, and catalytic applications has prompted researchers to synthesize carbon nanostructures of different shapes and sizes.[1–4] Stacked-cup carbon nanotubes consisting of truncated conical graphene layers are of particular interest because whereas conventional carbon nanotubes are made up of seamless cylinders of hexagonal carbon networks, the stacked-cup structure provides a hollow tubular morphology.[5] This truncated-cone morphology provides a large portion of exposed and reactive edges in the outer and inner surfaces of the hollow tubes. The availability of the inner and outer edges of these stacked-cups to chemical functionalization or surface modification opens up new avenues in electronic and catalytic applications.[6] The longer stacked cups are broken into smaller units by ball milling, and thus the number of accessible active sites is increased.[7] These smaller stacked cup units are also referred to as nanobarrels. The increased active area along the tubular surface facilitates impregnation of metal nanoparticles quite effectively. By making use of this added feature, carbon stacked cups have been successfully used as supports in fuel cells.[8]

An interesting property of carbon nanostructures is their optical response, and their utilization in light energy conversion devices. Fullerenes, for example, exhibit rich photochemistry and act as electron shuttles in photochemical solar cells.[9] They also play an important role in improving the performance of organic photovoltaic cells. On the other hand, the semiconducting carbon nanotubes undergo charge separation when subjected to bandgap excitation. The exciton annihilation and charge-separation processes have been characterized by transient absorption and emission measurements.[4,10,11] Efforts have also been made to modify the carbon nanotubes with semiconductors for use in photocurrent generation.[12,13] Herein we present the optical properties of stacked-cup carbon nanotubes, and the effectiveness of their semiconducting properties to generate photocurrent in a photoelectrochemical cell with high photoconversion efficiency (Figure 1).

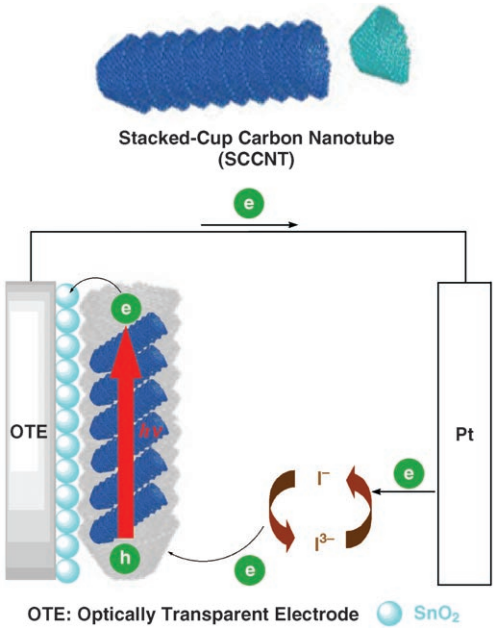


Figure 1. Light-induced charge separation in a photoelectrochemical cell based on stacked-cup carbon nanotubes (SCCNTs).

The ball-milled sample of stacked-cup carbon nanotubes (referred to as SCCNTs or carbon nanobarrels) in the tubular form was a gift from GSI Creos corporation, Japan. These nanotubes can be readily suspended in organic solvents, such as THF, by sonication for 30–60 minutes, and remain in suspension for more than 24 h. The absorption spectrum of the suspension in THF showed broad absorption with no specific absorption peaks (spectrum a in Figure 2 A). The ease of solubilization of these stacked cups allowed us to carry out transient absorption spectroscopy measurements (see below).

We adopted an electrophoretic deposition method to cast the films of SCCNTs onto conducting glass electrodes. The procedure was similar to that employed in assembling films of

[*] Dr. T. Hasobe,[+] Prof. Dr. P. V. Kamat
Radiation Laboratory
Department of Chemistry & Biochemistry and
Department of Chemical & Biomolecular Engineering
University of Notre Dame
Notre Dame, IN 46556 (USA)
Fax: (+1) 574-631-8068
E-mail: pkamat@nd.edu
Dr. T. Hasobe,[+] Prof. Dr. S. Fukuzumi
Department of Material and Life Science
Graduate School of Engineering
Osaka University, SORST
Japan Science and Technology Agency
2-1 Yamada-oka, Suita, Osaka 565-0871 (Japan)
[+] Current address:
School of Materials Science
Japan Advanced Institute of Science and Technology
Ishikawa, 923-1292, Japan

[**] We would like to thank GSI Creos Corporation, Japan for providing the sample of stacked-cup carbon nanotubes, and Tim Hall for his assistance in SEM characterization. This work was partially supported by Grant-in-Aid (No. 16205020) and by the COE program of Osaka University (Integrated Ecochemistry) from the Ministry of Education, Culture, Sports, Science, and Technology, Japan. T.H. acknowledges the support of Research Fellowships from the Japan Society for the Promotion of Science (JSPS) for Young Scientists. P.V.K. acknowledges support from the Office of Basic Energy Science of the U.S. Department of the Energy. This is contribution No. NDRL 4623 from the Notre Dame Radiation Laboratory and from Osaka University.

© 2006 Wiley-VCH Verlag GmbH & Co. KGaA, Weinheim

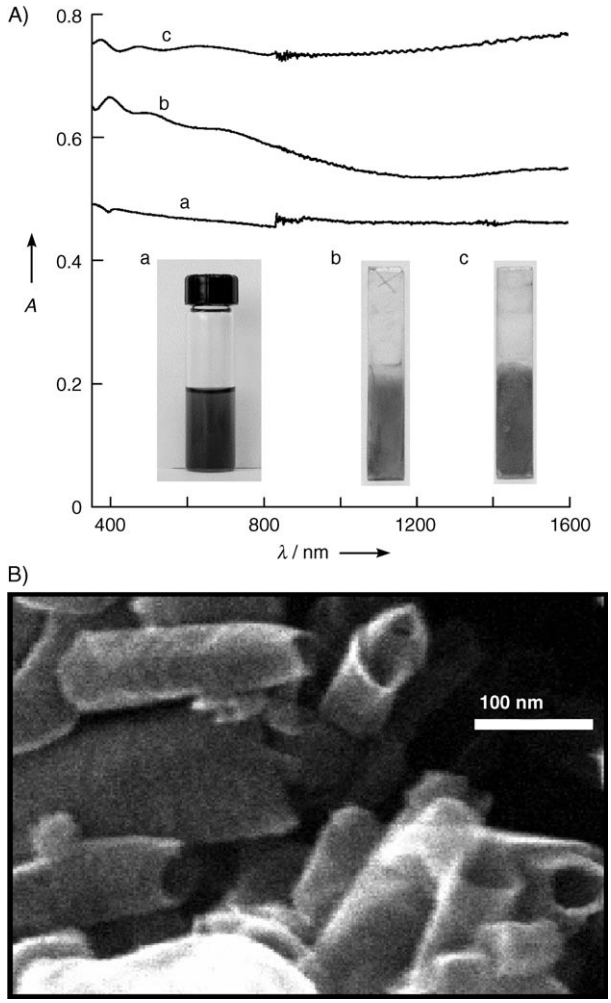


Figure 2. A) Absorption spectra of: a) a suspension of SCCNTs in THF, b) OTE/SCCNT, and c) OTE/SnO_2/SCCNT. B) Transmission electron microscope (TEM) image of SCCNTs.

carbon nanotubes and C_{60} clusters on electrode surfaces.[14,15] A suspension of SCCNTs (3 mL) in THF was transferred to a 1-cm cuvette. Two optically transparent electrodes (OTE) cut from conducting glass were inserted and a dc field (200 $V\,cm^{-1}$) was applied. Within one minute, the SCCNTs were driven to the positive electrode surface and a robust film was deposited (referred to as OTE/SCCNT). A similar procedure was also adopted to deposit SCCNTs onto OTE/SnO_2 and OTE/TiO_2 electrodes (referred to as OTE/SnO_2/SCCNT and OTE/TiO_2/SCCNT, respectively). The absorption spectra and photographs of these two electrodes are shown in Figure 2A. The scanning electron micrograph of these films shows a closed packed assembly of SCCNTs (Figure 2B). The hollow tubes are approximately 50 nm in diameter and 0.2–0.3 μm in length. The assembly of SCCNTs onto the electrode surface provides a porous morphology to the film. The ball-milled samples produce relatively short-length stacked-cup tubes, as expected.[7] Another interesting aspect is that these individual stacked tubes remain separated and are not bundled as we usually see with single-wall or multi-wall carbon nanotubes. Previous studies[5,6] have shown that these hollow tubes possess a significantly higher proportion of exposed outer edges which in turn minimizes van der Waals interactions between the tubes.

To probe the optical activity of these stacked cups we subjected the OTE/SCCNT electrode to laser pulse (387 nm) excitation in a femtosecond transient absorption spectrometer. The transient spectra recorded at different times are shown in Figure 3A. A broad bleaching in the red region was seen immediately following the laser pulse excitation. The bleaching recovers within 2 ps, thus illustrating the reversibility of the system to optical excitation. The reproducibility of the transient recovery at 760 nm is confirmed by the forward and reverse delay scans (Figure 3B). The transient bleaching and its recovery observed in these experiments parallels the behavior of single-wall carbon nanotubes (SWCNTs).[11] The ultra-bandgap excitation of SCCNTs with a laser pulse at 387 nm produces excitons in the C_2-V_2

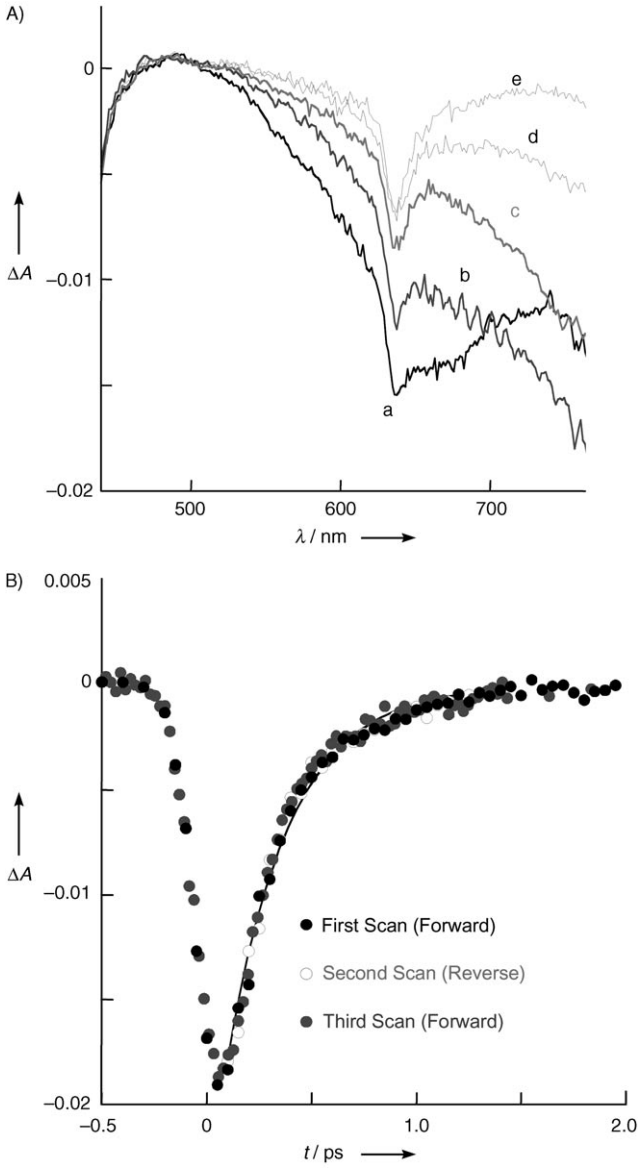


Figure 3. A) Time-resolved transient absorption spectra of OTE/SCCNT recorded using a laser pulse of 387 nm: a) 0 ps, b) 0.1 ps, c) 0.3 ps, d) 0.5 ps, and e) 1.0 ps. B) Time profiles of absorption at 760 nm after first (forward), second (reverse), and third scans (forward).

 © 2006 Wiley-VCH Verlag GmbH & Co. KGaA, Weinheim

level. These excitons quickly migrate to the C_1-V_1 level and undergo deactivation by exciton annihilation. A small fraction of these excitons dissociate to produce a charge-separated state. By comparing these results with those of SWCNTs,[11,15,16] one can conclude that SCCNTs exhibit optical transitions similar to those of SWCNTs, and provide the basis for exploring other semiconducting properties of these materials.

If the optical transitions we observe in Figure 3 were indeed responsible for charge separation, we should be able to harvest these charge carriers for generating photocurrent in a photovoltaic or photoelectrochemical cell. A photoelectrochemical cell consisting of an OTE/SnO_2/SCCNT electrode and a Pt counterelectrode was constructed and the generation of photovoltage and photocurrent, in the presence of the I_3^-/I^- redox couple, were recorded (Figure 4). Visible light (λ>400 nm) was obtained from a 450 W Xenon lamp filtered using a Corning 3–73 filter. When the OTE/SnO_2/SCCNT electrode was subjected to excitation with visible light we observed a rapid generation of photocurrent. The photogenerated electrons in the SCCNTs are collected by the SnO_2 nanocrystallites to generate anodic current. Thus, a steady photocurrent can be delivered using SCCNT-based photoelectrochemical cells. The on-off cycles of illumination confirmed the reproducibility and stability of the photocurrent response of the SCCNT film (Figure 4B).

We recorded the photocurrent action spectrum by employing a monochromatic excitation source. The IPCE (incident photon to charge carrier generation efficiency) response at different excitation wavelengths (trace a in Figure 4A) shows a maximum efficiency value of 4%. These IPCE values are nearly an order of magnitude greater than those obtained for SWCNT electrodes (OTE/SnO_2/SWCNT: trace b in Figure 4A) under similar experimental conditions.[15]

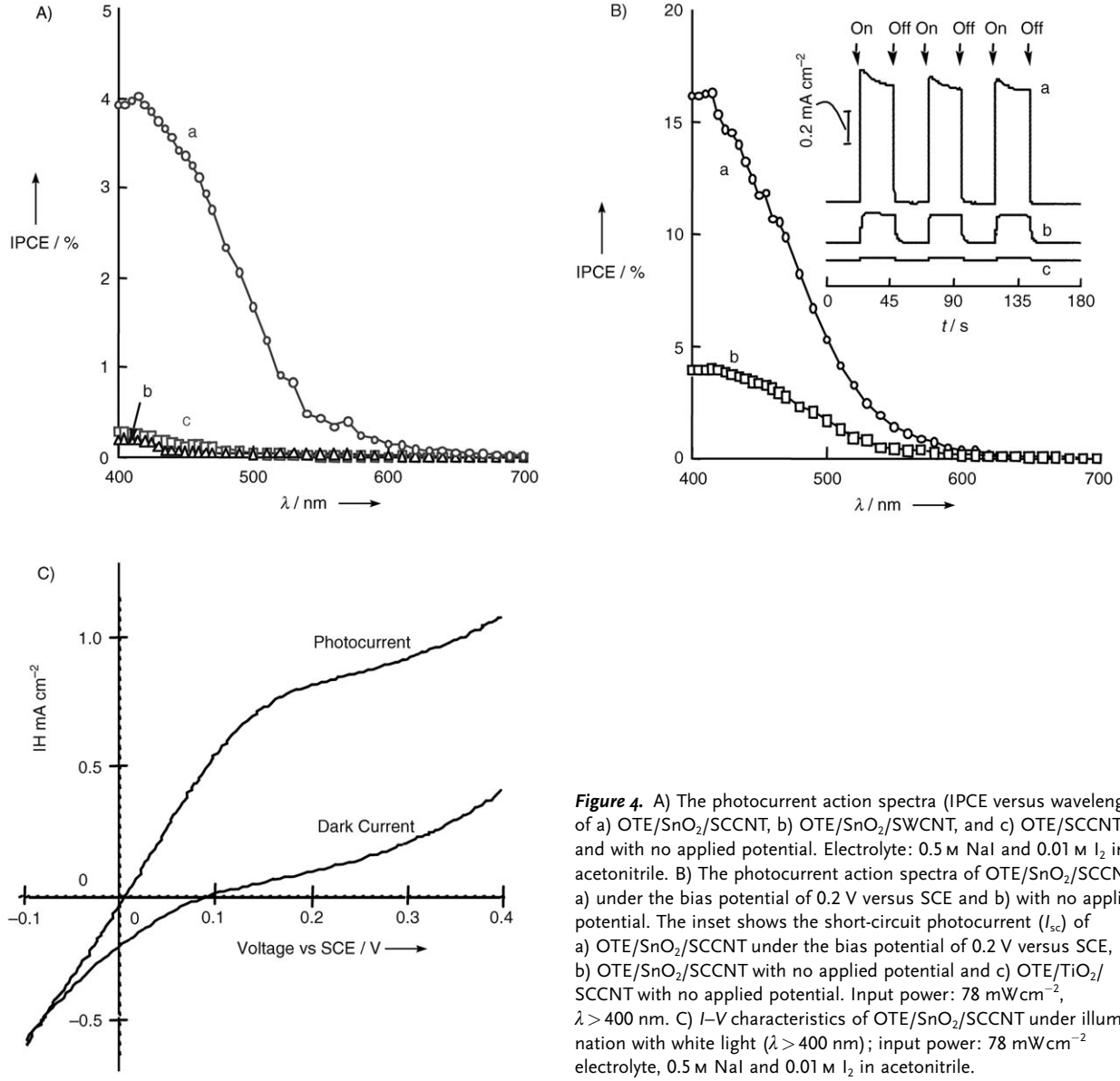


Figure 4. A) The photocurrent action spectra (IPCE versus wavelength) of a) OTE/SnO_2/SCCNT, b) OTE/SnO_2/SWCNT, and c) OTE/SCCNT and with no applied potential. Electrolyte: 0.5 M NaI and 0.01 M I_2 in acetonitrile. B) The photocurrent action spectra of OTE/SnO_2/SCCNT a) under the bias potential of 0.2 V versus SCE and b) with no applied potential. The inset shows the short-circuit photocurrent (I_{sc}) of a) OTE/SnO_2/SCCNT under the bias potential of 0.2 V versus SCE, b) OTE/SnO_2/SCCNT with no applied potential and c) OTE/TiO_2/SCCNT with no applied potential. Input power: 78 mWcm^{-2}, λ > 400 nm. C) *I–V* characteristics of OTE/SnO_2/SCCNT under illumination with white light (λ > 400 nm); input power: 78 mWcm^{-2} electrolyte, 0.5 M NaI and 0.01 M I_2 in acetonitrile.

 © 2006 Wiley-VCH Verlag GmbH & Co. KGaA, Weinheim

The SnO_2 films cast on OTE do not exhibit any photocurrent at wavelengths greater than 350 nm. The presence of SnO_2 nanocrystallites increases the surface area and maximizes the charge collection from excited SCCNTs. Indeed, the increased IPCE of OTE/SnO_2/SCCNT electrodes relative to the OTE/SCCNT electrode (trace c in Figure 4A) confirms the role of SnO_2 nanocrystallites as charge collectors. Further improvements in the efficiency of charge collection can be achieved by applying an external electrochemical bias. Figure 4B compares the performance of the SCCNT electrodes under no bias with those under +0.2 V versus the standard calomel electrode (SCE) bias. A maximum IPCE of 17%, recorded at +0.2 V, is the highest efficiency ever reported for pristine carbon nanostructures. Previous studies, which report the photoelectrochemical effect of carbon nanostructures, do not show photocurrent efficiencies of similar magnitude. For example, C_{60} films exhibit a maximum IPCE value of less than 5%[14,17] and SWCNT films[15] exhibit a maximum IPCE value of less than 0.2%. Furthermore, the photoconversion efficiency of SCCNT films are comparable to those obtained with pristine nanostructured semiconductor films (TiO_2, ZnO, CdS),[18,19] thereby suggesting the effectiveness of SCCNTs to undergo equally efficient charge separation under excitation with visible light.

The short circuit photocurrent (I_{sc}) measurements carried out with the OTE/SnO_2/SCCNT electrode, with and without anodic bias, and the OTE/TiO_2/SCCNT electrode without bias are compared in the inset of Figure 4B. The photocurrent response is sensitive to illumination by visible light and can be reproduced during on-off cycles. Interestingly, the I_{sc} value of OTE/TiO_2/SCCNT (trace c) is much smaller than that of OTE/SnO_2/SCCNT (traces a and b). This result suggests that the electron transfer from excited SCCNTs to SnO_2 nanocrystallites is exergonic, while that from excited SCCNTs to TiO_2 nanocrystallites is endergonic (see below).

The *I–V* characteristics of the OTE/SnO_2/SCCNT electrode are shown in Figure 4C. The increased photocurrent generation at anodic potentials shows that the SCCNT films possess n-type semiconducting behavior, which delivers a maximum photocurrent of about 1 mA cm^{-2} under anodic bias. Another interesting feature of the *I–V* characteristics is the zero current potential which in the present case is close to 0 V versus the SCE. As shown in earlier studies,[20] this value represents the apparent flat band potential as the photogenerated charge carriers recombine at this potential without producing net current. As a result of the n-type behavior seen in SCCNT films, effective charge separation is observed at potentials greater than 0 V versus the SCE.

The mechanism of photocurrent generation (Figure 1) shows photoinduced charge separation within SCCNTs as the primary step, followed by hole transfer to the I_3^-/I^- redox couple in solution, and transfer of electrons to the collecting electrode. If this semiconducting property of SCCNTs is indeed responsible for the generation of photocurrent, we should be able to observe the photovoltage generation even in the absence of the I_3^-/I^- redox couple. The accumulated charges during excitation with visible light will cause a change in the open circuit voltage. Spectra a–c (Figure 5) show the generation of photovoltage with time for OTE/SnO_2/SCCNT and OTE/TiO_2/SCCNT electrodes in an acetonitrile solution (0.1 M *n*-tetrabuthylammonium perchlorate as the electrolyte). Care was taken to prevent excitation below wavelengths of 400 nm, and photovoltage observed with blank OTE/SnO_2 and OTE/TiO_2 electrodes was negligible under these conditions.

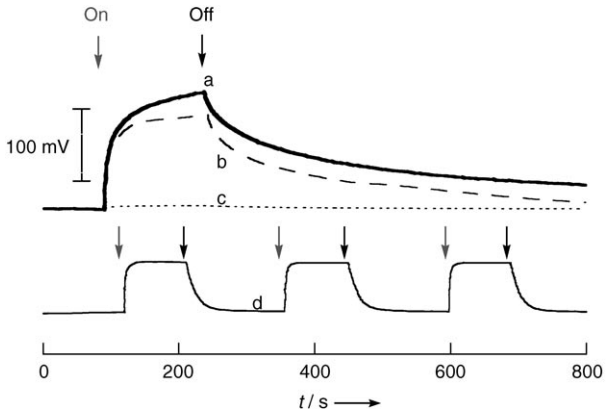


Figure 5. Photovoltage responses of OTE/SnO_2/SCCNT in an acetonitrile solution containing 0.1 M *n*-tetrabuthylammonium perchlorate (TBAP) under a) deaerated and b) air-saturated conditions. c) Photovoltage response of OTE/SnO_2 in an acetonitrile solution containing 0.1 M TBAP under deaerated condition (blank experiment). d) Photovoltage response of OTE/SnO_2/SCCNT in acetonitrile solution containing 0.5 M NaI and 0.01 M I_2; input power: 78 mW cm^{-2}.

The rise in the photovoltage is seen only when SCCNT was deposited on the SnO_2 support. The photovoltage observed with OTE/TiO_2/SCCNT was negligibly small. The reason behind this discrepancy is the conduction band energy of the two supports (E_{CB} for SnO_2 and TiO_2 are 0 and −0.5 V (versus the normal hydrogen electrode (NHE)) respectively). The ability of excited SCCNTs to transfer electrons only to SnO_2 and not TiO_2 shows that the conduction band of the SCCNTs lies between 0 and −0.5 V (versus NHE). This estimate is also in close agreement with the *I–V* characteristics (Figure 4C), which exhibit anodic photocurrents at potentials greater than 0 V. The photovoltage response in the presence of a redox couple I_3^-/I^- (spectrum d, Figure 5) was also rapid, but decayed faster when the illumination was turned off. The electrode quickly attains equilibration in the presence of a redox couple by transferring access charge to the I_3^-/I^- couple.

To date, SWCNTs and MWCNTs (multi-wall carbon nanotubes) have not been fully explored for use in photovoltaic applications because of their poor charge separation efficiency. Superior performance observed in the present study with SCCNTs highlights the usefulness of carbon nanostructures for applications in the conversion of light energy. Our study explores, for the first time, the semiconducting property of SCCNTs and its efficient utilization in the photoelectrochemical conversion of light energy into electricity. We conclude on the basis of the results presented in this study that the SCCNTs exhibit photocurrents two orders of magnitude greater than SWCNTs. It should be noted that the observed maximum photoconversion efficiency (IPCE) of about 17% is lower than the one observed with

 © 2006 Wiley-VCH Verlag GmbH & Co. KGaA, Weinheim

dye-sensitized solar cells (80–90 %).[21] On the other hand, the efficiencies of SCCNT based cells are comparable to the efficiency (5–15 %) of photoelectrochemical cells based on nanostructured semiconductor films (TiO_2, ZnO, CdS etc).[18,19] Modification of SCCNT films with sensitizers or organic semiconductors may provide new avenues to further improve the photoconversion efficiency. Efforts are currently underway to employ SCCNTs in organic solar cells based on polyphenylene vinylene (PPV).

Received: August 9, 2005
Published online: December 21, 2005

Keywords: charge separation · nanotubes · photochemistry · solar cells

[1] H. J. Dai, *Acc. Chem. Res.* **2002**, *35*, 1035.
[2] O. Zhou, H. Shimoda, B. Gao, S. J. Oh, L. Fleming, G. Z. Yue, *Acc. Chem. Res.* **2002**, *35*, 1045.
[3] P. Serp, M. Corrias, P. Kalck, *Appl. Catal. A* **2003**, *253*, 337.
[4] A. Jorio, R. Saito, T. Hertel, R. B. Weisman, G. Dresselhaus, M. S. Dresselhaus, *MRS Bull.* **2004**, *29*, 276.
[5] M. Endo, Y. A. Kim, T. Hayashi, Y. Fukai, K. Oshida, M. Terrones, T. Yanagisawa, S. Higaki, M. S. Dresselhaus, *Appl. Phys. Lett.* **2002**, *80*, 1267.
[6] C. Kim, Y. J. Kim, Y. A. Kim, T. Yanagisawa, K. C. Park, M. Endo, M. S. Dresselhaus, *J. Appl. Phys.* **2004**, *96*, 5903.
[7] Y. A. Kim, T. Hayashi, Y. Fukai, M. Endo, T. Yanagisawa, M. S. Dresselhaus, *Chem. Phys. Lett.* **2002**, *355*, 279.
[8] M. Endo, Y. A. Kim, M. Ezaka, K. Osada, T. Yanagisawa, T. Hayashi, M. Terrones, M. S. Dresselhaus, *Nano Lett.* **2003**, *3*, 723.
[9] P. V. Kamat, M. Haria, S. Hotchandani, *J. Phys. Chem. B* **2004**, *108*, 5166.
[10] M. J. O'Connell, S. M. Bachilo, C. B. Huffman, V. C. Moore, M. S. Strano, E. H. Haroz, K. L. Rialon, P. J. Boul, W. H. Noon, C. Kittrell, J. P. Ma, R. H. Hauge, R. B. Weisman, R. E. Smalley, *Science* **2002**, *297*, 593.
[11] Y. Z. Ma, J. Stenger, J. Zimmermann, S. M. Bachilo, R. E. Smalley, R. B. Weisman, G. R. Fleming, *J. Chem. Phys.* **2004**, *120*, 3368.
[12] L. Sheeney-Haj-Khia, B. Basnar, I. Willner, *Angew. Chem.* **2005**, *117*, 78; *Angew. Chem. Int. Ed.* **2005**, *44*, 78.
[13] I. Robel, B. Bunker, P. V. Kamat, *Adv. Mater.* **2005**, *17*, 2458.
[14] P. V. Kamat, S. Barazzouk, K. G. Thomas, S. Hotchandani, *J. Phys. Chem. B* **2000**, *104*, 4014.
[15] S. Barazzouk, S. Hotchandani, K. Vinodgopal, P. V. Kamat, *J. Phys. Chem. B* **2004**, *108*, 17015.
[16] Y. Z. Ma, L. Valkunas, S. M. Bachilo, G. R. Fleming, *J. Phys. Chem. B* **2005**, *109*, 15671.
[17] T. Hasobe, H. Imahori, S. Fukuzumi, P. V. Kamat, *J. Phys. Chem. B* **2003**, *107*, 12105
[18] S. Hotchandani, P. V. Kamat, *J. Phys. Chem.* **1992**, *96*, 6834.
[19] V. Subramanian, E. Wolf, P. V. Kamat, *J. Phys. Chem. B* **2001**, *105*, 11439.
[20] V. Subramanian, E. E. Wolf, P. V. Kamat, *J. Am. Chem. Soc.* **2004**, *126*, 4943.
[21] M. K. Nazeeruddin, A. Kay, I. Rodicio, B. R. Humphry, E. Mueller, P. Liska, N. Vlachopoulos, M. Graetzel, *J. Am. Chem. Soc.* **1993**, *115*, 6382.

 © 2006 Wiley-VCH Verlag GmbH & Co. KGaA, Weinheim

Enzyme Catalysis

DOI: 10.1002/anie.200503582

The Fluorinase from *Streptomyces cattleya* Is Also a Chlorinase**

Hai Deng, Steven L. Cobb, Andrew R. McEwan, Ryan P. McGlinchey, James H. Naismith, David O'Hagan, David A. Robinson, and Jonathan B. Spencer*

Streptomyces cattleya is unusual in that it elaborates organofluorine metabolites and in particular secretes fluoroacetate and 4-fluorothreonine as secondary metabolites when incubated in a medium supplemented with fluoride ions.[1,2] The first committed step on the biosynthetic pathway to these fluorometabolites involves the enzymatic mediated synthesis of 5′-fluoro-5′-deoxyadenosine (5′-FDA) from S-adenosyl-L-methionine (SAM) and fluoride ions.[3–5] After depurination, 5′-FDA is metabolized first to 5-fluoro-5-deoxyribose-1-phosphate (5′-FRP)[6] and then to fluorocetaldehyde.[7] Fluoroacetaldehyde is converted separately into fluoroacetate[8] and 4-fluorothreonine[9] (Scheme 1).

The fluorination enzyme, which has been the subject of a recent structural study,[10] has been isolated and fully characterized, the gene has been cloned, and the enzyme has been overexpressed. A stereochemical study that involved (5′S)-[5′-^{2}H]-SAM has indicated that the C–F bond of 5′-FDA replaces the C–S bond of SAM with an inversion of configuration.[11,12] This observation, as well as a theoretical study[13] and structural analysis[10] all suggest an S_N2 reaction mechanism for the fluorinase. Despite the high bond-dissociation energy of the C–F bond (the strongest bond in organic chemistry[14]), we herein report that the fluorinase operates in the reverse direction and that it utilizes a chloride ion. Incubation of 5′-FDA with L-(^{13}C-methyl)methionine resulted in the formation of ^{13}C-methyl-SAM, which was identified by HPLC–ES-MS. A similar experiment with L-selenomethionine (L-Se-met) and 5′-FDA resulted in a sixfold more-efficient reaction to generate L-Se-SAM, which was readily identified through the mass-spectrometry fragmentation

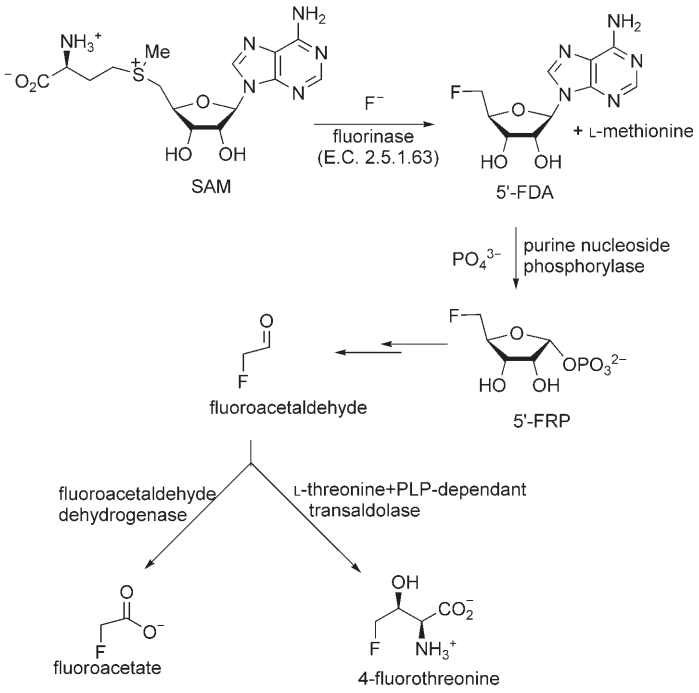
[*] Dr. H. Deng, Dr. S. L. Cobb, A. R. McEwan, R. P. McGlinchey, Prof. Dr. J. H. Naismith, Prof. Dr. D. O'Hagan, Dr. D. A. Robinson
School of Chemistry and
Centre for Biomolecular Science
University of St Andrews
St Andrews, KY16 9ST (UK)
Fax: (+44) 1334-463-808
E-mail: do1@st-and.ac.uk

Dr. J. B. Spencer
Chemistry Laboratories
University of Cambridge
Lensfield Rd, Cambridge, CB2 1EW (UK)

[**] We thank the BBSRC for funding (H.D. and D.A.R.) and GSK and the Pro-Bio-Faraday for a Studentship (R.P.M.).

Supporting information for this article is available on the WWW under http://www.angewandte.org or from the author.

© 2006 Wiley-VCH Verlag GmbH & Co. KGaA, Weinheim
InterScience

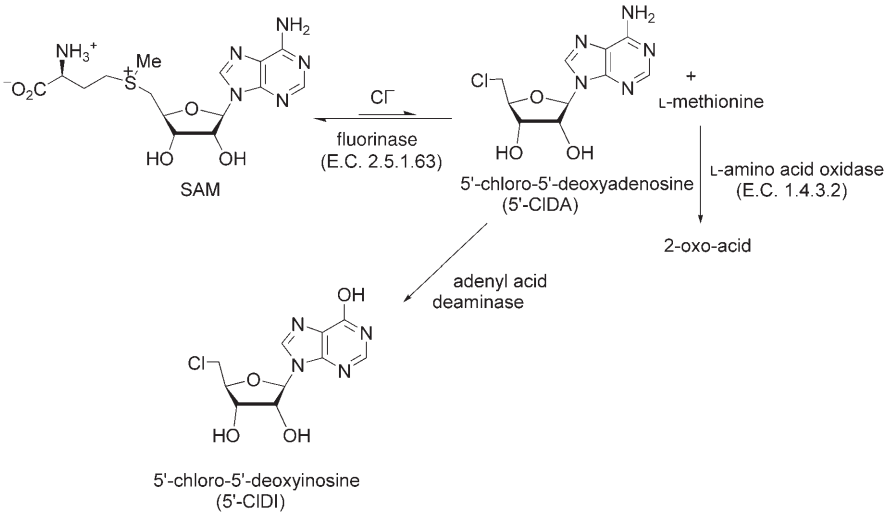


Scheme 1. A summary of the biosynthesis of fluoroacetate and 4-fluorothreonine highlighting the fluorinase and the other characterized enzymes on the pathway.

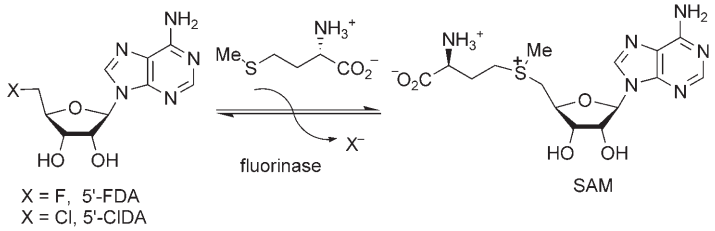
product of methylselenoadenosine (MeSeAdo) by its signature isotope fingerprint in HPLC–ES-MS. Comparison with the V_{max} values that were calculated at saturating kinetics (assays run in each direction) indicated that the equilibrium lies in favor of 5′-FDA by a factor of three (see Scheme 2).

Efforts were made to replace the fluoride ion with a chloride ion as a substrate for the fluorinase by using standard assay protocols. Incubation with chloride ions in the presence of SAM has never resulted in the production of 5′-chloro-5′-deoxyadenosine (5′-ClDA) (by HPLC). It now emerges, however, that the failure to detect 5′-ClDA is due to the equilibrium of the chloride reaction lying significantly in favor of substrates over products rather than an inherent inability of the fluorinase to activate the chloride ions towards nucleophilic attack. This was revealed in two separate coupled-enzyme assays that were designed to shift the equilibrium of the reaction towards the organochlorine product. The first of these involved an assay in which the fluorinase was coupled to an L-amino acid oxidase (*Bothrops atrox* venom; purchased from Sigma Chem. Co. Ltd.). Removal of L-methionine, the coproduct of halide substitution by enzymatic oxidation, inhibits the reverse reaction. This assay therefore generated 5′-ClDA and allowed, for the first time, the detection of this product from SAM and chloride ions (see Scheme 3.)

A related experiment involved a coupled fluorinase/adenyl acid deaminase (*Aspergillus sp.*)[15] assay. In this reaction the resultant 5′-ClDA was converted into 5′-chloro-5′-deoxyinosine (5′-ClDI). The production of 5′-ClDI was readily identified by HPLC–ES-MS against a reference compound.[16] These experiments indicated that the fluorinase can process chloride ions in a manner similar to that of fluoride ions. A set of fluorinase/L-methionine oxidase coupled assay experiments that were conducted at high concentrations of SAM (1 mM) and halide ion (25 mM) indicated a rate preference for F^- over Cl^- by a factor of 120. This preference was also demonstrated in a fluorinase-mediated trans-halogenation reaction as illustrated in Figure 1. Incubation of 5′-ClDA with fluoride ion, L-selenomethionine (catalyst), and the fluorinase resulted in an efficient and progressive conversion of 5′-ClDA to 5′-FDA, a reaction that proceeds through L-Se-SAM as a transient but detectable (by using HLPC) intermediate (see Figure 1).



Scheme 3. Coupled enzyme assays with 5′-ClDA driving organochlorine synthesis.



Scheme 2. The fluorinase operates in reverse with both 5′-FDA and 5′-ClDA.

The increased size of the chloride ion over the fluoride ion raises the legitimate question of the ability of chloride ions or 5′-ClDA to coordinate to the fluoride- and 5′-FDA-binding sites of the protein. To explore this aspect further, 5′-ClDA was cocrystallised with overexpressed fluorinase (without added L-methionine). This resulted in a structure with 5′-ClDA bound to the active site of the enzyme as illustrated in Figure 2. There are three monomers in the asymmetric unit and all three have essentially the same structure although

 © 2006 Wiley-VCH Verlag GmbH & Co. KGaA, Weinheim

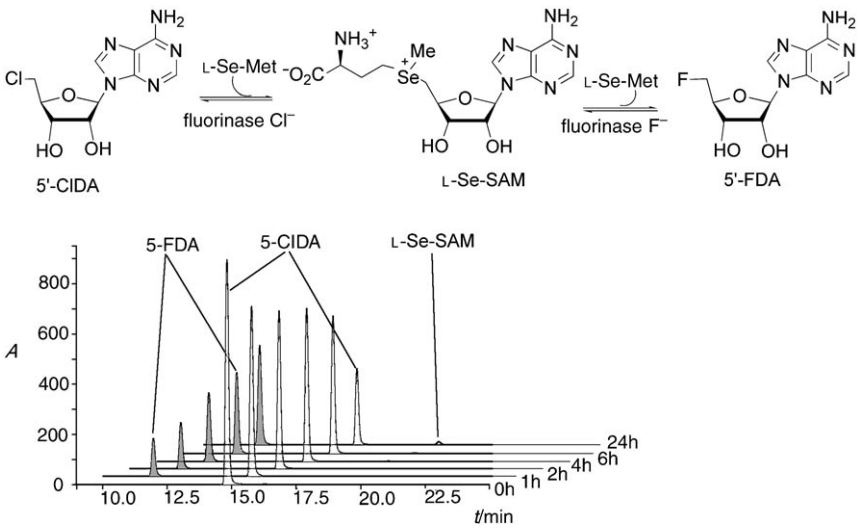


Figure 1. HPLC profile monitoring the fluorinase mediated transhalogenation reaction of 5′-ClDA to 5′-FDA with time and using L-Se-methionine as a co-catalyst. L-Se-SAM accumulates as a minor product.

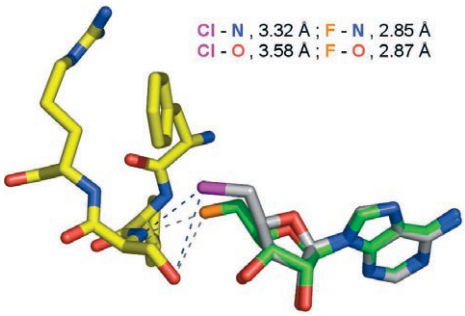


Figure 2. Structure of the 5′-ClDA-fluorinase co-complex with contacts and distances between the halogens and Ser-156 N and O atoms shown. For 5′-ClDA, C = gray, N = blue, O = red, and Cl = purple. The protein is similarly colored except C = yellow. Shown superimposed over 5′-ClDA is 5′-FDA with C = green, F = orange, and N = blue. As can be seen, the Cl atom lies further away from the backbone amide of Ser-156.

there are some small differences owing to crystal packing. Only one subunit of the trimer is discussed.

The difference electron density shows that the C5′–Cl bond adopts two orientations that locate the organochlorine atom in one of two positions. One conformer (shown in Figure 2) is similar to that observed for 5′-FDA when bound to the fluorinase, however, the chlorine atom is displaced by 1.3 Å relative to the location of the fluorine in the 5′-FDA complex. The chlorine atom is anchored to the main chain amide of Ser-156 by a hydrogen bond and a polar contact to the side chain hydroxy group of the same residue. Similar noncovalent contacts are also observed between the fluorine atom and Ser-156 although the distances are shorter for the 5′-FDA structure. We attribute this change in position to be a consequence of the larger van der Waals radius of the Cl atom relative to the F atom. The protein underwent no significant change in response to the larger atom, rather the substrate adjusts its position which perhaps suggests a rigid ligand binding site. The altered position of the halogen does not, however, prevent the enzyme from catalyzing the reaction.

In the second conformation (not shown) the chlorine rotated out of the halogen binding site into the "empty" L-methionine sulfur binding site. Of course in the catalytic situation, L-methionine will occupy the space above the ribose ring and there will be no possibility of chlorine adopting this second orientation.

This study reveals that the fluorinase will catalyze the combination of chloride ions and SAM to generate 5′-ClDA. The reaction is only observed in coupled-enzyme assays that prevent the reverse reaction from occurring. No organohalogen products were detected when Br^- and I^- were used in these reactions. This reaction extends the repertoire of the fluorinase and reveals a novel enzymatic chlorination reaction which operates by nucleophilic substitution rather than through the electrophilic hypochlorite[17] or flavin dependent enzymes[18] or by a recently reported enzymatic chlorine radical process.[19] A combination of nucleophilic chloride ion and SAM is responsible for the production of chloromethane in fungi.[20,21] This is the only other enzymatic reaction we are aware of in which Cl^- acts as a nucleophile, interestingly with a different regiochemistry on the same substrate.

Experimental Section

HPLC and NMR spectroscopy time course: The reaction mixtures for HPLC were incubated at 37 °C with 5′-ClDA (0.3 mM), L-Se-methionine (0.08 mM), KF (75 mM), and fluorinase (6 mg mL^{-1}, 500 μL) in a final volume of 650 μL. Samples for HPLC analysis (60 μL) were boiled at 95 °C (3 min) and the precipitated protein was then removed by centrifugation. An aliquot (20 μL) of the clear supernatant was used for HPLC analysis (Vivian 9012 UV/Vis detector at 260 nm and 9050 solvent delivery module).

Samples for ^{19}F NMR (500 MHz) analysis were incubated at 37 °C with 5′-FDA (0.5 mM), L-methionine (40 mM), D_2O (10 %) and fluorinase (6 mg mL^{-1}, 500 μL) in a final volume of 700 μL.

Preparations of ESI-MS sample: A sample (250 μL) for ESI-MS analysis was incubated at 37 °C overnight with 5′-FDA (0.4 mM), methionine (L-methionine-^{13}C-methyl or selenomethionine; 15 mM) and fluorinase (6 mg mL^{-1}) and then were boiled at 95 °C (3 min) and the precipitated protein was then removed by centrifugation. The supernatant was injected directly into the ESI-MS (MicroMass, Manchester, UK) with MeCN as the solvent. The SAM analogue molecules were detected in positive ion mode. Se-SAM underwent fragmentation to 5′-methylselenoadenosine during ESI-MS analyses (see the Supporting Information).

Crystallization of the 5-ClDA co-complex: FDAS (4 mg mL^{-1}) was incubated overnight with 5′-ClDA (20 mM) at room temperature. The solution was then crystallized by vapor diffusion against a reservoir containing PEG 1000 (32 %), phosphate-citrate buffer solution (0.1 M, pH 4.2), and Li_2SO_4 (0.2 M). A single crystal was selected and flash cooled to 100 K in a nitrogen stream. A data set was recorded at the European synchrotron radiation facility by using the

 © 2006 Wiley-VCH Verlag GmbH & Co. KGaA, Weinheim

ID14 EH2 beamline. The structure was solved by molecular replacement with the original FDAS structure and refined by using Refmac. The final R-factor was 19.0% with an R-free of 24.7%.

Received: October 10, 2005
Published online: December 21, 2005

Keywords: chlorinase · enzyme catalysis · fluorinase · halogenation · S-adenosylmethionine

[1] M. Sanada, T. Miyano, S. Iwadare, J. M. Williamson, B. H. Arison, J. L. Smith, A. W. Douglas, J. M. Liesch, E. Inamine, *J. Antibiot.* **1984**, *39*, 259 – 265.
[2] D. O'Hagan, D. B. Harper, *Nat. Prod. Rep.* **1994**. *11*, 123 – 133.
[3] D. O'Hagan, C. Schaffrath, S. Cobb, J. T. G. Hamilton, C. D. Murphy, *Nature* **2002**, *416*, 279.
[4] C. Schaffrath, H. Deng, D. O'Hagan, *FEBS Lett.* **2003**, *547*, 111 – 114.
[5] C. Schaffrath, S. L. Cobb, D. O'Hagan, *Angew. Chem.* **2002**, *114*, 4069 – 4071; *Angew. Chem. Int. Ed.* **2002**, *41*, 3913 – 3915.
[6] S. L. Cobb, H. Deng, J. T. G. Hamilton, R. P. McGlinchey, D. O'Hagan, *Chem. Commun.* **2004**, 592 – 593.
[7] H. Deng, D. O'Hagan, C. Schaffrath, *Nat. Prod. Rep.* **2004**, *21*, 773 – 784.
[8] C. D. Murphy, S. J. Moss, D. O'Hagan, *Appl. Environ. Microbiol.* **2001**, *67*, 4919 – 4921.
[9] C. D. Murphy, D. O'Hagan, C. Schaffrath, *Angew. Chem.* **2001**, *113*, 4611 – 4613; *Angew. Chem. Int. Ed.* **2001**, *40*, 4479 – 4481.
[10] C. J. Dong, F. L. Huang, H. Deng, C. Schaffrath, J. B. Spencer, D. O'Hagan, J. H. Naismith, *Nature* **2004**, *427*, 561 – 565.
[11] C. D. Cadicamo, J. Courtieu, H. Deng, A. Meddour, D. O'Hagan, *ChemBioChem* **2004**, *5*, 685 – 690.
[12] D. O'Hagan, R. J. M. Goss, A. Meddour, J. Courtieu, *J. Am. Chem. Soc.* **2003**, *125*, 379 – 387.
[13] H. Senn, D. O'Hagan, W. Thiel, *J. Am. Chem. Soc.* **2005**, *127*, 13643 – 13655.
[14] B. E. Smart, *Properties of Fluorinated Organic Compounds, Vol. 1*, ACS, **1995**, pp. 979 – 1010.
[15] A. L. Margolin, D. R. Borcherding, D. Wolfkugel, N. Margolin, *J. Org. Chem.* **1994**, *59*, 7214 – 7218.
[16] S. L. Cobb, Ph.D thesis, University of St Andrews, **2005**.
[17] A. Butler, J. N. Carter-Franklin, *Nat. Prod. Rep.* **2004**, *21*, 180 – 188.
[18] C. Dong, S. Flecks, S. Unversucht, C. Haupt, K.-H. van Pée, J. H. Naismith, *Science* **2005**, *309*, 2216 – 2219.
[19] F. H. Vaillancourt, E. Yeh, D. A. Vosburg, S. E. O'Connor, C. T. Walsh, *Nature* **2005**, *436*, 1191 – 1194.
[20] D. Saxena, S. Aouad, J. Attieh, H. Saini, *Appl. Environ. Microbiol.* **1998**, *64*, 2831 – 2835.
[21] X. Ni, L. P. Hager, *Proc. Natl. Acad. Sci. USA* **1999**, *96*, 3611 – 3615.

 © 2006 Wiley-VCH Verlag GmbH & Co. KGaA, Weinheim

Cross-Coupling

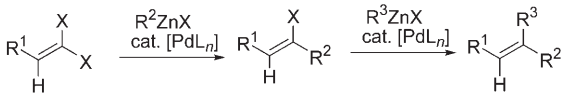
DOI: 10.1002/anie.200503519

Widely Applicable Pd-Catalyzed *trans*-Selective Monoalkylation of Unactivated 1,1-Dichloro-1-alkenes and Pd-Catalyzed Second Substitution for the Selective Synthesis of *E* or *Z* Trisubstituted Alkenes**

*Ze Tan and Ei-ichi Negishi**

Dedicated to Professor P. L. Fuchs on the occasion of his 60th birthday

Since the discovery of the Pd-catalyzed highly *trans*-selective monosubstitution of 1,1-dihalo-1-alkenes and the subsequent second substitution to produce trisubstituted alkenes [Eq. (1)],[1] its development as a method for not only the



(1)

X = Cl, Br, I, so forth

selective synthesis of monosubstitution products[2] but also for disubstitution products[1,2c,e,3–5] has attracted considerable attention from synthetic chemists.

Although the development of the monosubstitution reaction with aryl,[3] alkenyl,[4] and alkynyl metals[5] and related nucleophiles has been reasonably successful, the Pd- or Ni-catalyzed monoalkylation has not been,[6] except in one isolated example, which consists of the Pd-catalyzed stepwise double alkylation of β,β-dichlorostyrene with *n*BuZnCl (81% yield) and then *n*HexMgBr (77% yield).[1] These results were reproducible in our hands but could not be extended to a similar stepwise dialkylation of alkyl-substituted 1,1-dichloro-1-alkenes, such as 1,1-dichloro-1-octene. Under the influence of 5 mol% of [$PdCl_2$(dppb)] (dppb = 1,4-bis(diphenylphosphino)butane), its reaction with *n*OctZnBr produced only a trace amount, if any, of (*Z*)-8-chloro-7-hexadecene, with (*Z*)-8-(*n*-octyl)-7-hexadecene as practically the only product. The tendency to produce dialkylation products is even more pronounced in the corresponding reactions of 1,1-dibromo-1-alkenes. Thus, even β,β-dibromostyrenes would produce only

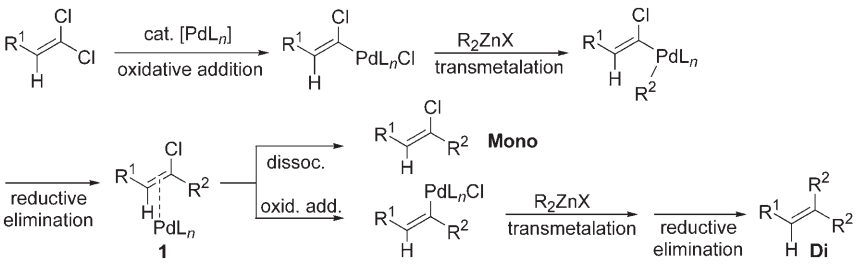
[*] Dr. Z. Tan, Prof. E.-i. Negishi
Herbert C. Brown Laboratories of Chemistry
Purdue University, 560 Oval Drive
West Lafayette, IN 47907-2084 (USA)
Fax: (+1) 765-494-0239
E-mail: negishi@purdue.edu

[**] We thank the National Science Foundation (grant CHE-0309613), the National Institutes of Heath (grant GM36792), and Purdue University for support of this research.

Supporting information for this article is available on the WWW under http://www.angewandte.org or from the author.

InterScience
© 2006 Wiley-VCH Verlag GmbH & Co. KGaA, Weinheim

their dialkylation products. Despite these disappointing results, a systematic screening of Pd catalysts, additives, and solvents was conducted, which led to an optimized set of conditions that involve 5 mol% of [$PdCl_2$(dpephos)] (dpephos = bis(*o*-diphenylphosphanylphenylether))[7] and dimethylformamide (DMF). In some cases, the use of one molar equivalent of *N*-methylimidazole (NMI)[8] relative to an alkyl zinc reagent has been shown to further improve the yields. The results of the *trans*-selective monoalkylation are summarized in Table 1.

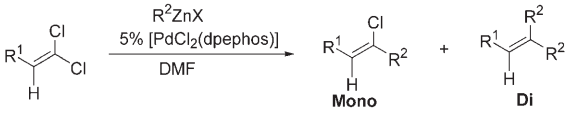


Scheme 1. Putative mechanistic scheme for the competitive formation of the mono- and dialkylation products.

Although the intricate mechanistic details remain unclear, the following features are worth mentioning: First, as long as the combination of [$PdCl_2$(dpephos)] and DMF, along with one molar equivalent of NMI for some cases of monomethylation, is used, various types of 1,1-dichloro-1-alkenes that contain alkyl, aryl, alkenyl, and alkynyl groups as the R^1 group can be satisfactorily monoalkylated for the first time with alkyl zinc compounds containing Me, Et, and higher linear and β-branched primary alkyl groups. Second, the difference between dppb and dpephos ligands in the selective monoalkylation of alkyl-substituted 1,1-dichloro-1-alkenes is striking, and it is clear that competitive formation of the disubstitution products is the major side reaction to be minimized. This goal may be attained by suppressing the second substitution through promotion of catalyst dissociation from the putative monosubstituted alkene–Pd π-complex **1** (Scheme 1).[9] The success observed with 1,1-dichloro-1-alkenes but not with 1,1-dibromo-1-alkenes can also be readily understood in these terms. Third, although unwanted, the formation of the disubstitution product must undoubtedly be responsible for the high stereoselectivity (≥98–99%) attainable by Pd-catalyzed *trans*-selective monosubstitution through kinetic resolution in the second stage of disubstitution, in which the undesired *cis*-monosubstituted isomer of **1** must be significantly more reactive than **1** itself. In this sense, the observed formation of the disubstitution products must be a blessing in disguise to a certain extent.

With the development of a widely applicable and satisfactory protocol for the *trans*-selective monoalkylation of 1,1-dichloro-1-alkenes, the second substitution of relatively unreactive internal *Z* chloroalkenes was investigated. In the only reported case of a stepwise dialkylation using β,β-dichlorostyrene,[1] the second alkylation was achieved by using *n*HexMgBr and 1 mol% [$NiCl_2$(dppp)] (dppp = 1,3-bis(diphenylphosphino)propane). This procedure was very satisfactory for the methylation of (*Z*)-2-chloro-1-phenyl-1-decene with MeMgBr, thus providing the desired methylation product in almost quantitative yield and with >98% stereoisomeric purity. Its application to the methylation of (*Z*)-8-chloro-7-hexadecene was also high yielding, but the product was essentially a 1:1 mixture of the *E* and *Z* isomers (Scheme 2).[10] The use of some other chelating ligands containing the diphenylphosphino group, such as dppf and dpephos, did improve the stereoisomeric ratio, but the highest *E*/*Z* ratio never exceeded 6:1 (Scheme 2). Fortunately, a recent development of satisfactory procedures for the Pd-catalyzed cross-coupling of organochlorides through the use of bulky trialkylphosphines[8,11] and dialkylarylphosphines[12] came to the rescue. Thus, when (7*Z*)-8-chloro-7-hexadecene was treated with MeMgBr in the presence of 5 mol% [Pd(*t*Bu_3P)$_2$] at 50°C for 6 h, the desired product of (7*E*)-8-methyl-7-hexadecene was obtained in 90% yield and with high stereoselectivity (*E*/*Z* = 97:3). Under the

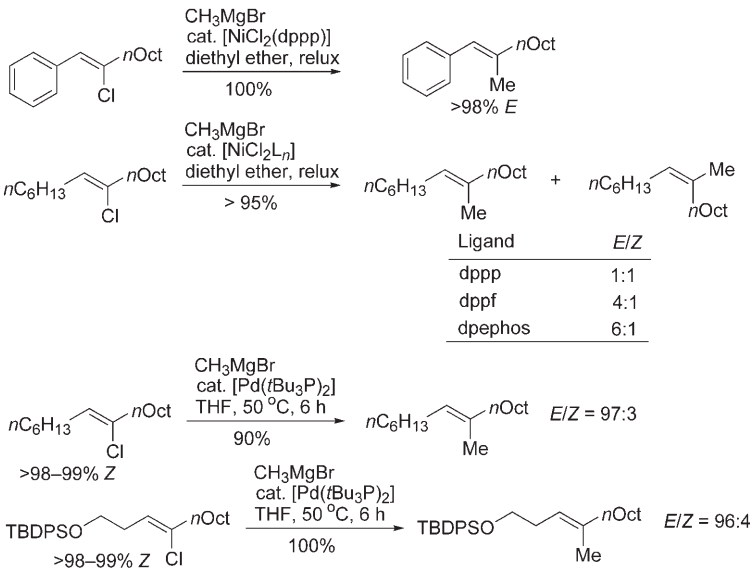
Table 1: Pd-catalyzed *trans*-selective monoalkylation of 1,1-dichloro-1-alkenes with alkyl zinc compounds and a catalytic amount of [$PdCl_2$(dpephos)].



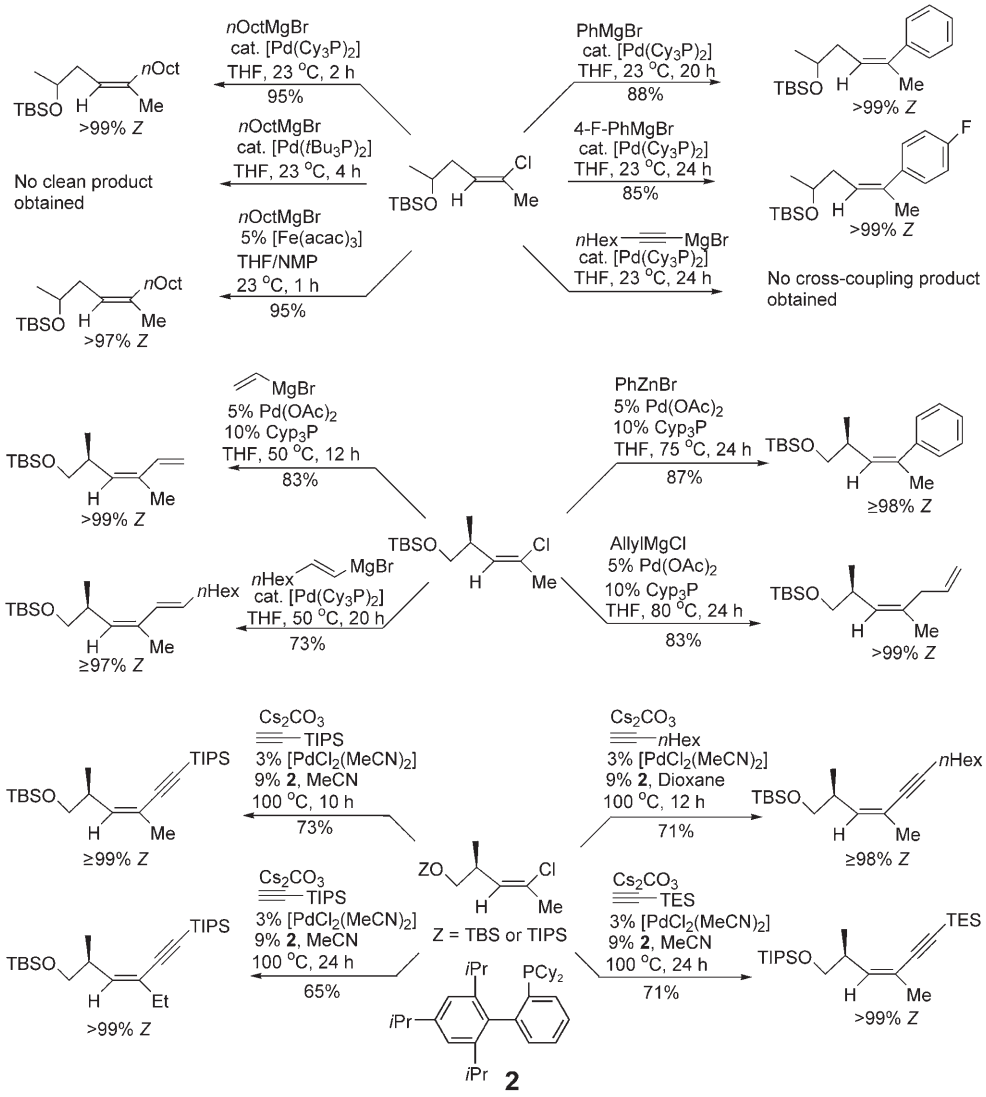
Entry	R^1	R^2ZnX[a] (additive)	Conditions *T* [°C]	Conditions *t* [h]	Yield[b] [%] Mono[c]	Di
1	*n*Hex	Me_2Zn	70	16	50	50
2	*n*Hex	Me_2Zn–NMI[d]	55	10	75	15
3	*n*Hex	Et_2Zn	50	6	76	13
4	*n*Hex	*n*OctZnBr	23	20	85	<3
5	*n*Hex	*n*OctCH(Me)CH_2ZnBr	50	20	70	25
6	TBSOCH$_2$CHMe	Me_2Zn–NMI[d]	60	6	76	15
7	TBSOCH$_2$CHMe	Et_2Zn	23	6	85	5[e]
8	TBDPSO(CH$_2$)$_2$	*n*OctZnBr	50	20	80	12
9	TBSOCH(Me)CH_2	Me_2Zn–NMI[d]	65	16	85	12
10	TBSO(CH$_2$)$_3$	*n*OctZnBr	50	24	83	10
11	TMS–≡–	Me_2Zn	65	7	90	5
12	TMS–≡–/\	Me_2Zn	65	5	82	15
13	Ph	Me_2Zn	70	5	80	10
14	Ph	*n*OctZnBr	50	12	90	3

[a] Me_2Zn and Et_2Zn were purchased from Aldrich, R^2ZnBr were prepared from R^2I by lithiation with *t*BuLi (2 equiv) and zincation with dry $ZnBr_2$. [b] Determined by GLC with an internal standard. [c] All monoalkylated products were >98–99% isomerically pure, and their configurations were determined by a combination of NMR techniques, including NOE interaction studies and chemical-shift analysis. [d] NMI (1 equiv relative to Me_2Zn) was added. [e] In addition to the disubstitution product, another by-product identified as the dechlorinated monosubstitution product was produced in 8% yield.

 © 2006 Wiley-VCH Verlag GmbH & Co. KGaA, Weinheim



Scheme 2. $[Pd(tBu_3P)_2]$-catalyzed cross-coupling of *Z* chloroalkenes with MeMgBr for the synthesis of *trans*-trisubstituted alkenes.



Scheme 3. Cross-coupling of internal *Z* chloroalkenes with Grignard reagents or terminal alkynes in the presence of Pd catalysts containing bulky trialkylphosphines or **2**.

same conditions, (3*Z*)-1-*tert*-butyldiphenylsilyloxy-4-chloro-3-dodecene gave the desired methylation product in quantitative yield as a 96:4 mixture of the *E* and *Z* isomers (Scheme 2).

Even with the use of $[Pd(tBu_3P)_2]$, however, *Z* chloroalkenes could not be alkylated in useful yields with higher alkyl magnesium halides, such as *n*OctMgBr, with β-dehydrometallation and hydrogenolysis of the *Z* chloroalkenes as the major side reactions. On the other hand, the use of Cy_3P or Cyp_3P as ligands (Cy = cyclohexyl and Cyp = cyclopentyl, respectively)[8,11] led to the formation of the desired alkylation products in high yields (Scheme 3). Satisfactory results were also observed with the use of $[Fe(acac)_3]$ (acac = acetylacetonate)[13] as a catalyst. As indicated by the results summarized in Scheme 3, Pd complexes with Cy_3P and Cyp_3P appear to be generally satisfactory catalysts for the second substitution with Grignard reagents containing alkyl, aryl, alkenyl, and allyl groups. In some favorable cases, even organozinc reagents, such as PhZnBr, can successfully couple with the *Z* chloroalkenes in the presence of a Pd–Cyp_3P complex. Despite all these favorable results, the reaction of (*Z*)-TBSOCH(Me)CH_2CH=C(Cl)Me (TBS = *tert*-butyldimethylsilyl) with *n*HexC≡CMgBr in the presence of 5 mol% of $Pd(Cy_3P)_2$ failed to produce the desired alkynylation product. However, the use of $Et_3SiC{\equiv}CH$ or $iPr_3SiC{\equiv}CH$ in MeCN in the presence of 2-dicyclohexylphosphino-2′,4′,6′-triisopropyl-1,1′-biphenyl[12g] (**2**; X-PHOS; purchased from Strem Chemicals) proved to be reasonably satisfactory.

Thus, for the first time, a selective and widely applicable method for the stepwise double substitution of 1,1-dichloro-1-alkenes involving the first *trans*-selective alkylation followed by a second substitution with alkyl-, aryl-, alkenyl-, allyl-, and alkynyl metal compounds has been developed. Although this protocol has not yet been applied to the synthesis of natural products, it promises to be applicable to the synthesis of natural products containing *Z* trisubstituted alkenes, such as hennoxazole A,[14] discodermolide,[15] and ratjadone.[16]

Experimental Section

General procedure for monoalkylation: A flame-dried 25-mL round-bottomed flask under argon was charged with 1,1-dichloro-1-alkene (1 mmol), DMF (3 mL), and $[PdCl_2(dpephos)]$ (35 mg, 0.05 mmol, 5 mol%). After the addition of the organozinc reagent (1.2 mmol), the reaction mixture was stirred at the appro-

 © 2006 Wiley-VCH Verlag GmbH & Co. KGaA, Weinheim

priate temperature until gas–liquid chromatographic (GLC) analysis indicated the disappearance of the starting material. The reaction mixture was then quenched with diluted HCl. After extraction with diethyl ether, the combined organic layers were washed with brine, dried over $MgSO_4$, filtered, and concentrated. The residue was purified by flash column chromatography on silica gel to give the desired product.

General procedure for the cross-coupling of the *Z* chloroalkenes with Grignard reagents: A flame-dried 25-mL three-neck round-bottomed flask under argon was charged with $Pd(OAc)_2$ (11 mg, 0.05 mmol, 5 mol%), Cyp_3P (24 mg, 0.1 mmol, 10 mol%), and THF (2 mL). The mixture was stirred at 23°C for 10 min and a *Z* chloroalkene (1 mmol) was added followed by the Grignard reagent (1.5 mmol). The flask was stirred at the appropriate temperature until GLC analysis indicated the consumption of the starting material. The mixture was allowed to cool to room temperature, quenched with saturated NH_4Cl, and extracted with diethyl ether. The combined organic layers were washed with brine, dried over $MgSO_4$, filtered, and concentrated. The residue was purified by flash column chromatography on silica gel to give the desired product.

General procedure for the cross-coupling of the *Z* chloroalkenes with terminal alkynes: A flame-dried 25-mL three-neck round-bottomed flask with a reflux condenser under argon was charged with $[PdCl_2(MeCN)_2]$ (8 mg, 0.03 mmol, 3 mol%), **2** (43 mg, 0.09 mmol, 9 mol%), and Cs_2CO_3 (812 mg, 2.5 mmol), followed by anhydrous acetonitrile (3 mL) and the appropriate *Z* chloroalkene (1 mmol). The slightly yellow suspension was stirred at 23°C for 25 min. The alkyne (1.5 mmol) was added by syringe, and the reaction mixture was stirred in a heating bath at the desired temperature for the indicated time. The mixture was allowed to cool to room temperature, quenched with saturated NH_4Cl, and extracted with diethyl ether. The combined organic layers were washed with brine, dried over $MgSO_4$, filtered, and concentrated. The residue was purified by flash column chromatography on silica gel to give the desired product.

Received: October 5, 2005
Published online: December 20, 2005

Keywords: cross-coupling · Grignard reagents · homogeneous catalysis · organozinc reagents · phosphanes

[1] A. Minato, K. Suzuki, K. Tamao, *J. Am. Chem. Soc.* **1987**, *109*, 1257.
[2] a) W. R. Roush, K. J. Moriarty, B. B. Brown, *Tetrahedron Lett.* **1990**, *31*, 6509; b) W. R. Roush, K. Koyama, M. L. Martine, K. J. Moriarty, *J. Am. Chem. Soc.* **1996**, *118*, 7502; c) A. Minato, *J. Org. Chem.* **1991**, *56*, 4052; d) C. Xu, E. Negishi, *Tetrahedron Lett.* **1999**, *40*, 431; e) W. Shen, L. Wang, *J. Org. Chem.* **1999**, *64*, 8873; f) M. Ogasawara, H. Ikeda, T. Hayshi, *Angew. Chem.* **2000**, *112*, 1084; *Angew. Chem. Int. Ed.* **2000**, *39*, 1042; g) M. Ogasawara, H. Ikeda, T. Hayashi, *Chem. Lett.* **2000**, 776; h) J. Uenishi, K. Matsui, *Tetrahedron Lett.* **2001**, *42*, 4353; i) J. Uenishi, K. Matsui, H. Ohmiya, *J. Organomet. Chem.* **2002**, *653*,141.
[3] J. Shi, E. Negishi, *J. Organomet. Chem.* **2003**, *687*, 518.
[4] a) X. Zeng, Q. Hu, M. Qian, E. Negishi, *J. Am. Chem. Soc.* **2003**, *125*, 13636; b) X. Zeng, M. Qian, Q. Hu, E. Negishi, *Angew. Chem.* **2004**, *116*, 2309; *Angew. Chem. Int. Ed.* **2004**, *43*, 2259.
[5] J. Shi, X. Zeng, E. Negishi, *Org. Lett.* **2003**, *5*, 1825.
[6] J. S. Panek, T. Hu, *J. Org. Chem.* **1997**, *62*, 4914.
[7] P. W. N. M. van Leeuwen, P. C. J. Kamer, J. N. H. Reek, P. Dierkes, *Chem. Rev.* **2000**, *100*, 2741.
[8] J. Zhou, G. C. Fu, *J. Am. Chem. Soc.* **2003**, *125*, 12527.
[9] It is possible that the ethereal oxygen atom of dpephos may exert a chelation effect to facilitate the dissociation of alkenes.
[10] The high stereoselectivity observed with β-chlorostyrenes could be because of stabilization of the putative alkenyl nickel intermediate through chelation by the phenyl group, which is absent in the case of alkyl-substituted chloroalkenes.
[11] a) C. Dai, G. C. Fu, *J. Am. Chem. Soc.* **2001**, *123*, 2719; b) M. R. Netherton, C. Dai, K. Neuschütz, G. C. Fu, *J. Am. Chem. Soc.* **2001**, *123*, 10099; c) J. H. Kirchhoff, C. Dai, G. C. Fu, *Angew. Chem.* **2002**, *114*, 2025; *Angew. Chem. Int. Ed.* **2002**, *41*, 1945; d) M. R. Netherton, G. C. Fu, *Angew. Chem.* **2002**, *114*, 4066; *Angew. Chem. Int. Ed.* **2002**, *41*, 3910; e) J. H. Kirchhoff, M. R. Netherton, I. D. Hills, G. C. Fu, *J. Am. Chem. Soc.* **2002**, *124*, 13662; f) A. F. Littke, G. C. Fu, *Angew. Chem.* **2002**, *114*, 4350; *Angew. Chem. Int. Ed.* **2002**, *41*, 4176; g) K. Meuzel, G. C. Fu, *J. Am. Chem. Soc.* **2003**, *125*, 3718; h) J. Y. Lee, G. C. Fu, *J. Am. Chem. Soc.* **2003**, *125*, 5616; i) M. Eckhardt, G. C. Fu, *J. Am. Chem. Soc.* **2003**, *125*, 13642; j) J. Zhou, G. C. Fu, *J. Am. Chem. Soc.* **2003**, *125*, 14726.
[12] a) D. W. Old, J. P. Wolfe, S. L. Buchwald, *J. Am. Chem. Soc.* **1998**, *120*, 9722; b) J. P. Wolfe, R. A. Singer, B. H. Yang, S. L. Buchwald, *J. Am. Chem. Soc.* **1999**, *121*, 9550; c) A. Aranyos, D. W. Old, A. Kiyomori, J. P. Wolfe, J. P. Sadighi, S. L. Buchwald, *J. Am. Chem. Soc.* **1999**, *121*, 4369; d) J. Yin, M. P. Rainka, X. Zhang, S. L. Buchwald, *J. Am. Chem. Soc.* **2002**, *124*, 1162; e) H. N. Nguyen, X. Huang, S. L. Buchwald, *J. Am. Chem. Soc.* **2003**, *125*, 11818; f) D. Gelman, S. L. Buchwald, *Angew. Chem.* **2003**, *115*, 6175; *Angew. Chem. Int. Ed.* **2003**, *42*, 5993; g) J. E. Milne, S. L. Buchwald, *J. Am. Chem. Soc.* **2004**, *126*, 13028.
[13] a) A. Fürstner, A. Leitner, M. Mendez, H. Krause, *J. Am. Chem. Soc.* **2002**, *124*, 13856; b) A. Fürstner, M. Méndez, *Angew. Chem.* **2003**, *115*, 5513; *Angew. Chem. Int. Ed.* **2003**, *42*, 5355; c) M. Nakamura, K. Matsuo, S. Ito, E. Nakamura, *J. Am. Chem. Soc.* **2004**, *126*, 3686; d) for Fe-catalyzed dialkylation and reductive monoalkylation of 1,1-dichloro-1-alkenes, see: M. Dos Santos, X. Franck, R. Hocquemiller, B. Figadère, J. F. Peyrat, O. Provot, J. D. Brion, M. Alami, *Synlett* **2004**, 2697.
[14] a) T. Ichiba, W. Y. Yoshida, P. J. Scheuer, T. Higa, *J. Am. Chem. Soc.* **1991**, *113*, 3173; b) P. Wipf, S. Lim, *J. Am. Chem. Soc.* **1995**, *117*, 558; c) D. R. Williams, D. A. Brooks, M. A. Berliner, *J. Am. Chem. Soc.* **1999**, *121*, 4924; d) F. Yokokawa, T. Asano, T. Shiori, *Org. Lett.* **2000**, *2*, 4169.
[15] a) S. P. Gunasekera, M. Gunasekera, R. E. Longley, G. K. Schulte, *J. Org. Chem.* **1990**, *55*, 4912; b) J. B. Nerenberg, D. T. Hung, P. K. Sommers, S. L. Schreiber, *J. Am. Chem. Soc.* **1993**, *115*, 12621; c) S. S. Harried, G. Yang, M. A. Strawn, D. C. Myles, *J. Org. Chem.* **1997**, *62*, 6098; d) J. A. Marshall, B. A. Johns, *J. Org. Chem.* **1998**, *63*, 7885; e) A. B. Smith, T. J. Beauchamp, M. J. LaMarche, M. D. Kaufmann, Y. Qui, H. Arimoto, D. R. Jones, K. Kobayashi, *J. Am. Chem. Soc.* **2000**, *122*, 8654; f) I. Paterson, G. J. Florence, K. Gerlach, J. P. Scott, *Angew. Chem.* **2000**, *112*, 385; *Angew. Chem. Int. Ed.* **2000**, *39*, 377; g) A. Arefolov, J. S. Panek, *J. Am. Chem. Soc.* **2005**, *127*, 5596.
[16] a) D. Schummer, K. Gerth, H. Reichenbach, G. Höfle, *Liebigs Ann.* **1995**, 685; b) U. Bhatt, M. Christmann, M. Quitschalle, E. Claus, M. Kalesse, *J. Org. Chem.* **2001**, *66*, 1885; c) D. R. Williams, D. C. Ihle, S. V. Plummer, *Org. Lett.* **2001**, *3*, 1383.

 © 2006 Wiley-VCH Verlag GmbH & Co. KGaA, Weinheim

Liquid Chromatography

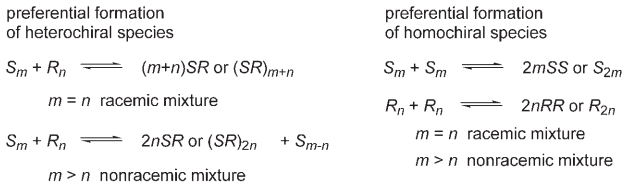
DOI: 10.1002/anie.200503373

Remarkable Amplification of the Self-Disproportionation of Enantiomers on Achiral-Phase Chromatography Columns**

*Vadim A. Soloshonok**

Dedicated to Professor Yuri Nikolaevich Belokon on the occasion of his 67th birthday

Two distinct modes of association can be envisioned when considering the intermolecular interactions between the enantiomers of a chiral compound in solution, namely, modes based on the preferential formation of either heterochiral or homochiral species (Scheme 1). In both cases, the



Scheme 1. Modes of association of the enantiomers of a chiral compound in solution.

formation of dimeric or more complex oligo/polymeric associates can be expected. When the ratio between the amounts of *S* and *R* enantiomers is equal ($m = n$, a racemic mixture), any type of association will give rise to isoenergetic enantiomeric species that display identical chemical and physical properties. However, when a nonracemic mixture is considered ($m > n$), the outcome will be drastically different. Thus, when heterochiral associations are preferred one can expect the formation of racemic species $2n\,S,R$ or $(S,R)_{2n}$ plus an excess of enantiomer *S*, which are different chemical entities and therefore may be separated without the application of any *external element of chirality*. In the case when homochiral associations are preferred, the situation is more subtle as the formation of dimers will result in different numbers of enantiomeric *S*,*S* and *R*,*R* pairs. However, when oligo/polymeric associations are favored, the formation of aggregates of different molecular weight is possible and therefore their separation may be achieved.

The first physical observation of the enantiomer associations discussed above, and therefore a proof of concept,[1] was reported more than 35 years ago by Williams et al.,[1a] who studied the NMR spectra of nonracemic dihydroquinines. They detected two sets of peaks for some protons, with peak areas being proportional to the relative ratio of the enantiomers. These associations are believed to be responsible for several remarkable phenomena observed for nonracemic compounds, such as the nonlinear behavior of optical rotation[2] and UV absorbance,[3] as well as nonlinear effects in asymmetric catalysis.[4]

However, the most fascinating opportunity offered by the enantiomer associations is the possibility of using the *internal chirality* of nonracemic mixtures for their optical purification/separation by achiral-phase chromatography.[5] Thus, in 1983 Cundy and Crooks reported on the separation of an excess of ^{14}C-labeled (*S*)-(−)-nicotine enantiomer (second fraction) from the racemate (first fraction) on an achiral HPLC system.[6] Since that time a handful of sporadic publications on such separations of various organic compounds by HPLC,[7] medium-pressure liquid chromatography (MPLC),[8] and flash[9] and regular[10] chromatography have appeared in the literature. However, this phenomenon still remains virtually unknown[11] to most practitioners in academic and industrial laboratories, and routine column chromatography on silica gel is generally accepted as a safe method for the purification of optically active compounds that does not alter the original enantiomeric composition.

Moreover, authors use different terminology to describe the observed phenomenon, most frequently calling it "enantiomeric enrichment on achiral-phase chromatography".[12] This definition is clearly incorrect and rather misleading, as part of a nonracemic sample does indeed undergo enantiomeric enrichment while the rest of the sample becomes more racemic. Herein, we introduce the term "self-disproportionation of enantiomers" or "enantiomer self-disproportionation" to describe the phenomenon, and report on the truly remarkable amplification of this effect that is induced by a trifluoromethyl group.

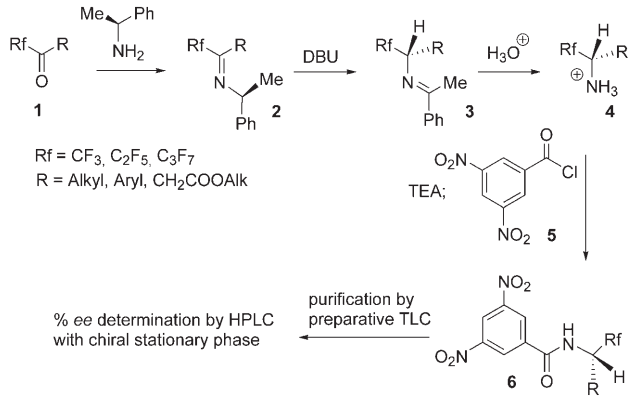
In the course of our studies on the asymmetric biomimetic transamination of perfluoroalkyl keto compounds **1** to amines and amino acids **4** by the DBU-catalyzed isomerization of imine **2** to Schiff base **3** (Scheme 2),[13] we encountered an irritating problem of poor reproducibility in the *ee* values. Thus, for determination of the enantiomeric purity of amino compounds **4** by HPLC analysis on chiral stationary phases, we used a method that required preparation of the dinitrobenzoyl derivatives **6**. As the reaction of highly electrophilic acid chloride **5** with amino compounds **4** generated substantial amounts of by-products, the chromatographic purification of derivatives **6** was inevitable.

Detailed analysis of the research data revealed that, as a consequence of the overlap of target compounds **6** with the by-products, preparative TLC or column chromatography allowed the recovery of 65 to 80% of pure derivatives **6** from the crude reaction mixture. Then we found that the enantiomeric purity of the samples strongly depended on the amount

[*] Prof. V. A. Soloshonok
Department of Chemistry and Biochemistry
The University of Oklahoma
620 Parrington Oval, Room 208, Norman, OK 73019 (USA)
Fax: (+1) 405-325-6111
E-mail: vadim@ou.edu

[**] This work was supported by the Department of Chemistry, University of Oklahoma. The author is grateful to the Central Glass Company (Dr. A. Ishii) for the numerous samples of enantiomerically pure and racemic trifluoromethyl-containing compounds used in this study. The help of graduate students D. Berbasov and H. Iwasaki, and undergraduate students S. Taylor, I. Ojemaye, and A. V. Soloshonok is gratefully acknowledged.

InterScience
© 2006 Wiley-VCH Verlag GmbH & Co. KGaA, Weinheim



Scheme 2. Asymmetric biomimetic transamination of perfluoroalkyl keto compounds. DBU = 1,8-diazabicyclo[5.4.0]undec-7-ene; TEA = triethylamine.

of recovered **6**, and increased with increasing percentage recovery. These observations led us to an experiment in which we loaded a sample of β-amino acid **6** (Rf = CF_3, R = CH_2COOEt) of 66.6% *ee* on a regular silica gel column and subjected the sample to chromatography with hexane/EtOAc = 5:1 as mobile phase.[14] We were expecting to find some effect of self-disproportionation of enantiomers leading to different *ee* percentage values in different fractions. However, the results obtained were truly remarkable (Table 1): the

Table 1: Chromatography of compound (*S*)-**6** (Rf = CF_3, R = CH_2COOEt; 66.6% *ee*) with elution by hexane/EtOAc = 5:1.

Fraction	*ee* [mass%]	Fraction	*ee* [mass%]
1	8.1 (3.3)	11	94.3 (91.9)
2	15.7 (7.9)	12	95.9 (93.5)
3	32.2 (12.1)	13	96.9 (95.2)
4	43.9 (25.3)	14	97.3 (96.3)
5	56.5 (39.2)	15	96.9 (97.9)
6	66.3 (52.6)	16	98.6 (97.9)
7	76.1 (64.5)	17	99.5 (98.5)
8	82.2 (74.0)	18	>99.9 (99.1)
9	86.2 (81.6)	19	>99.9 (99.6)
10	91.0 (87.6)	20	>99.9 (>99.9)

first fraction was substantially more racemic than the later fractions, which afforded virtually enantiomerically pure product of >99.9% *ee*.

The magnitude of this effect, which amounted to an unprecedented[15] 91.8% difference between the lowest and highest *ee* values obtained, was totally unexpected. To investigate the possible application of the observed self-disproportionation of enantiomers on achiral silica gel, for the practical optical purification of optically active samples by using their internal chirality, we conducted a series of experiments in which the starting *ee* value of the samples was varied and different eluents were used. Consideration of the results summarized in Table 2 leads to the following conclusions: to obtain enantiomerically pure samples, at least under the conditions studied so far, the *ee* value of the starting nonracemic mixture should be higher than 61% (Table 2, entries 1 versus 2). Next, very high (95% *ee*; Table 2, entry 1) and low (31.1% *ee*; Table 2, entry 2) *ee* values lead to diminished enantiomer self-disproportionation. Application of a more polar solvent also results in this reduced effect (Table 2, entry 6).

Table 2: Self-disproportionation of enantiomers of compound **6** (Rf = CF_3, R = CH_2COOEt) on achiral silica gel chromatography.

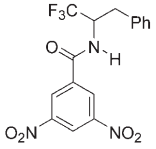


Entry	Starting %*ee* (*S*)	Eluent[a]	%*ee* min	%*ee* max
1	95.0	Hex/EtOAc = 5:1	83.3	99.9
2	31.1	Hex/EtOAc = 5:1	20.9	41.8
3	61.1	Hex/EtOAc = 5:1	12.6	95.5
4	66.6	Hex/EtOAc = 5:1	8.1	99.9
5	66.6	Hex/Et_2O = 1:1	54.8	99.9
6	66.6	$CHCl_3$	65.5	68.2

[a] Hex = hexane.

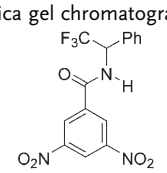
Similar results for the enantiomer self-disproportionation were also obtained for compounds **6** derived from (2-benzyl)trifluoroethylamine (Table 3) and (2-phenyl)trifluoroethylamine (Table 4). The magnitude of the effects observed was less pronounced than that of the β-amino acid derivative

Table 3: Self-disproportionation of enantiomers of compound **6** (Rf = CF_3, R = CH_2Ph) on achiral silica gel chromatography.



Entry	Starting %*ee* (*S*)	Eluent	%*ee* min	%*ee* max
1	95.0	Hex/EtOAc = 5:1	90.8	97.6
2	31.1	Hex/EtOAc = 5:1	27.1	53.4
3	61.1	Hex/EtOAc = 5:1	49.9	92.3
4	66.6	Hex/EtOAc = 5:1	58.4	99.9
5	66.6	Hex/Et_2O = 1:1	55.7	95.2
6	66.6	$CHCl_3$	65.8	68.6

Table 4: Self-disproportionation of enantiomers of compound **6** (Rf = CF_3, R = Ph) on achiral silica gel chromatography.

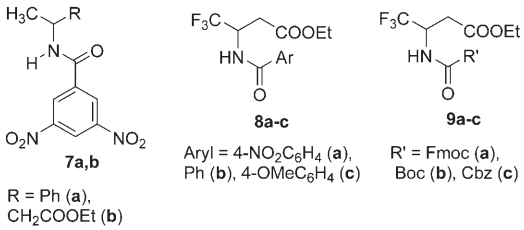


Entry	Starting %*ee* (*S*)	Eluent	%*ee* min	%*ee* max
1	95.0	Hex/EtOAc = 5:1	91.0	99.6
2	31.1	Hex/EtOAc = 5:1	28.9	39.1
3	61.1	Hex/EtOAc = 5:1	55.1	70.3
4	66.6	Hex/EtOAc = 5:1	59.9	78.8
5	66.6	Hex/Et_2O = 1:1	64.8	72.1
6	66.6	$CHCl_3$	66.6	66.6

 © 2006 Wiley-VCH Verlag GmbH & Co. KGaA, Weinheim

6 (Table 1); however, enantiomerically pure samples (99.9% *ee*) were obtained in both cases. It is interesting that in the latter case, the effect was not observed when $CHCl_3$ was used as eluent.

With these results in hand, we next focused our attention on determining what structural feature in **6** might be responsible for the enantiomer self-disproportionation effect. One may agree that the best "suspect" would be a highly polar dinitrobenzoyl moiety. Therefore, we prepared samples of the corresponding derivatives of phenylethylamine (*R*)-**7a** and β-aminobutyric acid (*R*)-**7b** of 66.6% *ee* and subjected them to chromatography under standard conditions (Scheme 3).[14] Surprisingly, the enantiomer self-

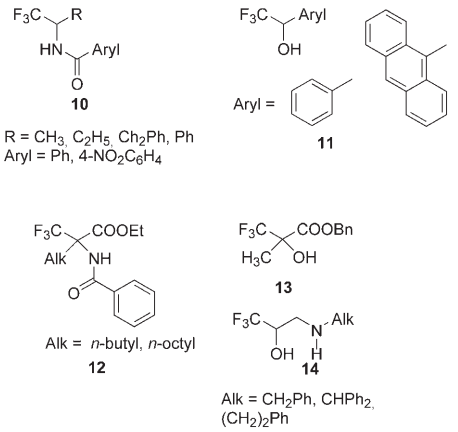


Scheme 3. Compounds used to examine the structural features of **6**. Fmoc = 9-fluorenylmethoxycarbonyl; boc = *tert*-butoxycarbonyl; cbz = benzyloxycarbonyl.

disproportionation effect was not observed for either of these compounds as all the collected fractions showed 66.6 ± 0.05% *ee*. We reasoned that the combination of a polar trifluoromethyl group and a dinitrobenzoyl moiety in the same molecule could explain the chromatographic behavior of **6**. To this end we prepared compounds (*S*)-**8a–c** of 66.6% *ee* bearing *p*-nitrobenzoyl, unsubstituted benzoyl, and *p*-methoxybenzoyl groups, respectively. Again, quite surprisingly, in all three cases we detected a strong enantiomer self-disproportionation effect on achiral silica gel. Moreover, β-amino acid derivatives (*S*)-**9a–c** of 66.6% *ee*, with the typical protection groups Fmoc, Boc, and Cbz, respectively, were also found to undergo enantiomer self-disproportionation.

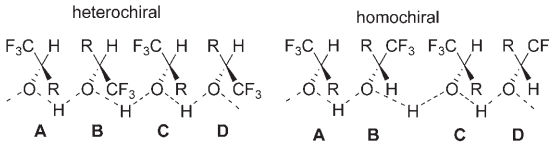
All these data strongly suggest that a trifluoromethyl group directly bonded to a stereogenic carbon center may be solely responsible for the phenomenon observed. To evaluate the generality of this finding we studied the chromatographic behavior[14] of a series of compounds that contained a trifluoromethyl group directly bonded to a stereogenic center, which were either commercially available or readily prepared by synthetic methods. The results were truly impressive, as in all the examples studied so far (Scheme 4) we observed a substantial enantiomer self-disproportionation effect. Considering that these examples include different classes of compounds, such as amines **10**, alcohols **11**, β-amino acids **6**, α-amino acids **12**, α-hydroxy acids **13**, and amino alcohols **14**, the enantiomer self-disproportionation effect should be generally expected for compounds containing a trifluoromethyl group directly bonded to a stereogenic carbon center.

The true nature of the role of a trifluoromethyl group (or, more generally, a perfluoroalkyl group) may be quite



Scheme 4. Compounds with a trifluoromethyl group directly bonded to a stereogenic center. Bn = benzyl.

complicated and awaits a comprehensive study. However, at this point we can suggest a general feature that should be taken into consideration by any plausible model for explaining enantiomer self-disproportionation on trifluoromethyl-containing compounds. It is well documented[16] that in transition states or supramolecular associations a trifluoromethyl group tends to be in a position as far as possible from another trifluoromethyl group or any negatively charged substituents. Therefore, it is reasonable to assume that this principle will also be valid for the formation of the corresponding dimers, trimers, and so on. Thus, by considering the possible arrangements of trifluoromethyl alcohol molecules through hydrogen bonding, one can envision two models that describe heterochiral and homochiral interactions



Scheme 5. Models of heterochiral and homochiral interactions of trifluoromethyl alcohol molecules.

(Scheme 5). As can be clearly seen in Scheme 5, the trifluoromethyl groups point away from each other in the heterochiral *R*,*S*,*R*,*S* arrangement, which minimizes the destabilizing electrostatic repulsive interactions. By contrast, in the homochiral arrangement the trifluoromethyl groups of molecules **B** and **C** point toward each other, thus rendering this association unstable. Therefore, we assume that heterochiral interactions would lead to the formation of macromolecular structures of relatively high molecular weight, whereas only dimers would be expected in the case of homochiral interactions. This assumption is in perfect agreement with the experimental data, which show that the excess enantiomer of alcohol **11** is always eluted first followed by the more racemic fractions.[17]

In summary, we have demonstrated that compounds containing a trifluoromethyl group directly bonded to a stereogenic carbon center are prone to a strong enantiomer

 © 2006 Wiley-VCH Verlag GmbH & Co. KGaA, Weinheim

self-disproportionation effect on achiral silica gel. One of the serious consequences of this finding is that all fluorine-containing chiral reagents and drugs currently on the market, as well as all previously reported literature data on the stereochemical outcome of asymmetric transformations involving fluorine-containing compounds, should be carefully reevaluated. On the basis of the results described herein and the literature data,[6–10] one may conclude that any type of column chromatography is not a safe method for the purification of nonracemic mixtures in the determination of their enantiomeric purity. We would like to suggest that chemists dealing with nonracemic compounds should first run an "enantiomer self-disproportionation test" before using chromatography for any purification steps. As shown herein, an increase in the polarity of an eluent usually leads to elimination of the enantiomer self-disproportionation effect. Once a "safe" eluent has been identified, chromatography can be used for sample purification. The full scope of the enantiomer self-disproportionation induced by trifluoromethyl and other polar groups, and application of this effect to the purification of nonracemic compounds using the internal chirality of a sample, are currently under study.

Received: September 22, 2005
Published online: December 22, 2005

Keywords: asymmetric synthesis · chiral resolution · chirality · disproportionation · liquid chromatography

[1] a) T. Williams, R. G. Pitcher, P. Bommer, J. Gutzwiller, M. Uskokovic, *J. Am. Chem. Soc.* **1969**, *91*, 1871; for other NMR studies, see: b) A. Dobashi, N. Saito, Y. Motoyama, S. Hara, *J. Am. Chem. Soc.* **1986**, *108*, 307; c) B. S. Jursic, S. I. Goldberg, *J. Org. Chem.* **1992**, *57*, 7172.

[2] a) A. Horeau, *Tetrahedron Lett.* **1969**, 3121; b) A. Horeau, J. P. Guette, *Tetrahedron* **1974**, *30*, 1923.

[3] J. Georges, *Spectrochim. Acta A* **1995**, *51*, 985.

[4] a) C. Puchot, O. Samuel, E. Dunach, S. Zhao, C. Agami, H. B. Kagan, *J. Am. Chem. Soc.* **1986**, *108*, 2353; b) M. Kitamura, S. Suga, M. Niwa, R. Noyori, Z.-X. Zhai, H. Suga, *J. Phys. Chem.* **1994**, *98*, 12776; c) M. Kitamura, S. Suga, H. Oka, R. Noyori, *J. Am. Chem. Soc.* **1998**, *120*, 9800; d) C. Girard, H. B. Kagan, *Can. J. Chem.* **2000**, *78*, 816.

[5] Besides the potential practical application of this phenomenon in the development of conceptually new separation techniques, it could lead to models for amplification of the optical activity of chiral compounds under prebiotic conditions. a) S. Bondy, M. Harrington, *Science* **1979**, *203*, 1243; b) J. B. Youatt, R. D. Brown, *Science* **1981**, *212*, 1145.

[6] K. C. Cundy, P. A. Crooks, *J. Chromatogr.* **1983**, *281*, 17.

[7] a) R. Charles, E. Gil-Av, *J. Chromatogr.* **1984**, *298*, 516; b) T.-L. Tsai, K. Herman, E. Hug, B. Rohde, A. S. Dreiding, *Helv. Chim. Acta* **1985**, *68*, 2238; c) A. Dobashi, Y. Motoyama, K. Kinoshita, S. Hara, N. Fukasaku, *Anal. Chem.* **1987**, *59*, 2209; d) R. Matusch, C. Coors, *Angew. Chem.* **1989**, *101*, 624; *Angew. Chem. Int. Ed. Engl.* **1989**, *28*, 626; e) E. Loza, D. Lola, A. Kemme, J. Freimanis, *J. Chromatogr. A* **1995**, *708*, 231; f) R.-M. Nicoud, J.-N. Jaubert, I. Rupprecht, J. Kinkel, *Chirality* **1996**, *8*, 234; g) K. Monde, N. Harada, M. Takasugi, P. Kutschy, M. Suchy, M. Dzurilla, *J. Nat. Prod.* **2000**, *63*, 1312; h) M. Suchy, P. Kutschy, K. Monde, H. Goto, N. Harada, M. Takasugi, M. Dzurilla, E. Balentova, *J. Org. Chem.* **2001**, *66*, 3940.

[8] H. Kosugi, M. Abe, R. Hatsuda, H. Uda, M. Kato, *Chem. Commun.* **1997**, 1857.

[9] P. Diter, S. Taudien, O. Samuel, H. B. Kagan, *J. Org. Chem.* **1994**, *59*, 370.

[10] a) H. Takahata, *Yuki Gosei Kagaku Kyokaishi* **1996**, *54*, 708; b) K. Tanaka, H. Osuga, H. Suzuki, Y. Shogase, Y. J. Kitahara, *J. Chem. Soc. Perkin Trans. 1* **1998**, 935; c) B. V. Ernholt, I. B. Thomsen, A. Lohse, I. W. Plesner, K. B. Jensen, R. G. Hazell, X. Liang, A. Jacobsen, M. Bols, *Chem. Eur. J.* **2000**, *6*, 278.

[11] For instance, in the most recent book (a) and review article (b) on unconventional methods for the resolution of enantiomers, this phenomenon was not even mentioned; a) F. Toda, *Enantiomer Separation*, Springer, Berlin, **2004**; b) E. Fogassy, M. Nogradi, E. Palovics, J. Schindler, *Synthesis* **2005**,1555.

[12] The following definitions are found in the literature: "self-amplification of optical activity",[7a] "enantiomer differentiation",[7b] "autoseparation of enantiomers",[7c] "separation of excess enantiomer",[7d,10a] "enantiomeric enrichment",[7e–h,9,10b,c] and "optical purification".[8]

[13] a) T. Ono, V. P. Kukhar', V. A. Soloshonok, *J. Org. Chem.* **1996**, *61*, 6563; b) V. A. Soloshonok, T. Ono, *J. Org. Chem.* **1997**, *62*, 3030; c) V. A. Soloshonok, T. Ono, I. V. Soloshonok, *J. Org. Chem.* **1997**, *62*, 7538; d) V. A. Soloshonok, I. V. Soloshonok, V. P. Kukhar', V. K. Svedas, *J. Org. Chem.* **1998**, *63*, 1878; for recent publications, see: e) V. A. Soloshonok, H. Ohkura, K. Uneyama, *Tetrahedron Lett.* **2002**, *43*, 5449; f) H. Ohkura, D. O. Berbasov, V. A. Soloshonok, *Tetrahedron Lett.* **2003**, *44*, 2417; g) V. A. Soloshonok, D. O. Berbasov, *J. Fluorine Chem.* **2004**, *125*, 1757.

[14] All experiments were conducted under the same conditions unless otherwise stated. Silica gel (200–300 mesh) was purchased from Natland International Corporation. Temperature: ambient ($T = 21$–$23\,^{\circ}C$); amount of sample: $m = 0.0300 \pm 0.0001$ g; columns: diameter $d = 16$ mm, length $l = 230$ mm; amount of each fraction $V = 7$ mL. The enantiomeric excess was determined by HPLC analysis: Sumichiral OA-4500, $l = 25$ cm, $d = 4.6$ mm.

[15] In three previous examples of self-disproportionation of enantiomers on achiral silica gel, the greatest *ee* percentage differences between the lowest and highest *ee* values obtained were: 83%,[10a] 31%,[10b] and 21%.[10c]

[16] a) V. A. Soloshonok, V. P. Kukhar', S. V. Galushko, N. Y. Svistunova, D. V. Avilov, N. A. Kuzmina, N. I. Raevski, Y. T. Struchkov, A. P. Pisarevsky, Y. N. Belokon, *J. Chem. Soc. Perkin Trans. 1* **1993**, 3143; b) V. A. Soloshonok, A. D. Kacharov, D. V. Avilov, T. Hayashi, *Tetrahedron Lett.* **1996**, *37*, 7845; c) P. Bravo, A. Farina, V. P. Kukhar', A. L. Markovsky, S. V. Meille, V. A. Soloshonok, A. E. Sorochinsky, F. Viani, M. Zanda, C. Zappala, *J. Org. Chem.* **1997**, *62*, 3424; d) V. A. Soloshonok, A. D. Kacharov, D. V. Avilov, K. Ishikawa, N. Nagashima, T. Hayashi, *J. Org. Chem.* **1997**, *62*, 3470; e) V. A. Soloshonok, D. V. Avilov, V. P. Kukhar', L. V. Meervelt, N. Mischenko, *Tetrahedron Lett.* **1997**, *38*, 4671.

[17] The same order of elution was also reported by Matusch and Coors[7d] for the anthracene-derived alcohol **11** under HPLC conditions (LiChrosorb-NH_2 stationary phase, hexane/dichloromethane as eluent).

 © 2006 Wiley-VCH Verlag GmbH & Co. KGaA, Weinheim

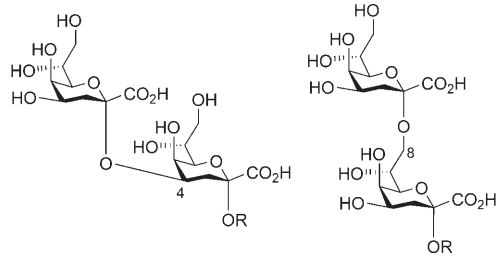
Synthetic Methods

DOI: 10.1002/anie.200503299

Stereoselective Synthesis of Oligo-α(2,8)-3-deoxy-D-*manno*-2-octulosonic Acid Derivatives

*Hiroshi Tanaka, Daisuke Takahashi, and Takashi Takahashi**

3-Deoxy-D-*manno*-2-octulosonic acid (KDO), a unique sugar component of lipopolysaccharides (LPSs), is an important constituent of the outer membrane of Gram-negative bacteria.[1] KDO is frequently present in the form of α(2,4)- and α(2,8)-linked homooligomers **1** and **2** connected to lipid A in

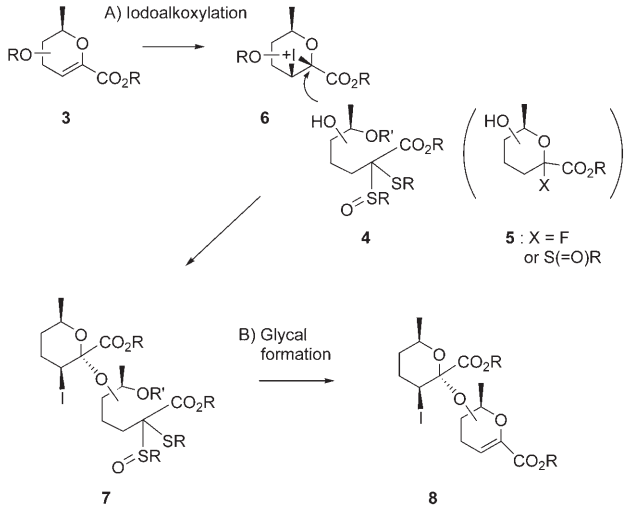


1 **2**

LPSs. These unique di- and oligo-KDO fragments are found only in bacterial cell walls and do not exhibit significant biological activity. Therefore, they could serve as potential antigens in the development of antibacterial vaccines. However, the possibility that such isolated oligosaccharides could be heterogeneous and/or contaminated with antigenic compounds cannot be excluded. Therefore, the chemical synthesis of these ulosonic acid-containing oligosaccharides would circumvent these issues as they relate to vaccine development.

Recent progress in oligosaccharide synthesis has resulted in a number of efficient glycosidation methodologies. However, the glycosidation of ulosonic acids often involves the generation of undesirable β stereoisomers and/or the 2,3-elimination of the donors as a result of the presence of a C1 carboxyl group and the lack of a C3 substituent.[2] In addition, the hydroxy groups, both in the pyran ring and on the endocyclic side chain, are less reactive toward glycosylation. In 1987, Shiba and co-workers reported that α-ketopyranosyl fluoride was an effective donor for the α-selective glycosidation of KDO.[3] Furthermore, in 1989, Achiwa and co-workers reported that the glycal ester underwent glycosyloxyselenation to provide α-linked 3-phenylselenyl-KDO derivatives.[4] The feasibility of these methods was mainly demonstrated by the synthesis of mono-KDO-containing oligosaccharides. However, the coupling of two and three KDO units often resulted in reduced product yields and some loss of selectivity. Notably, the low-nucleophilicity hydroxy groups on KDO units promote significant 2,3-elimination of the donor instead of the coupling reaction. Therefore, an efficient method for the stereoselective synthesis of α-linked KDO dimers and trimers is still needed.

Previously, we investigated the synthesis of oligosaccharides with acyclic glycosyl donors,[5] and reported on the synthesis of 2,3,6-deoxyglycosides by the one-pot cyclization and glycosidation of acyclic glycosyl donors possessing sulfoxide and alkylsulfanyl groups at the pseudo-anomeric position.[6] The acyclic donors were stable to various glycosidation reagents such as Lewis acids and to oxidative reagents. We envisaged that the acyclic saccharide precursors **4** could be used as glycosyl acceptors for iodoalkoxylation of the glycal ester **3**, and could be converted to α-KDO glycosylated products **7** through diaxial opening[4,7] of the iodonium ion **6** without decomposition of the sulfur-based leaving groups (Scheme 1). The hydroxy groups on the acyclic



Scheme 1. Strategy for the synthesis of α-linked oligo-KDO by iodoalkoxylation.

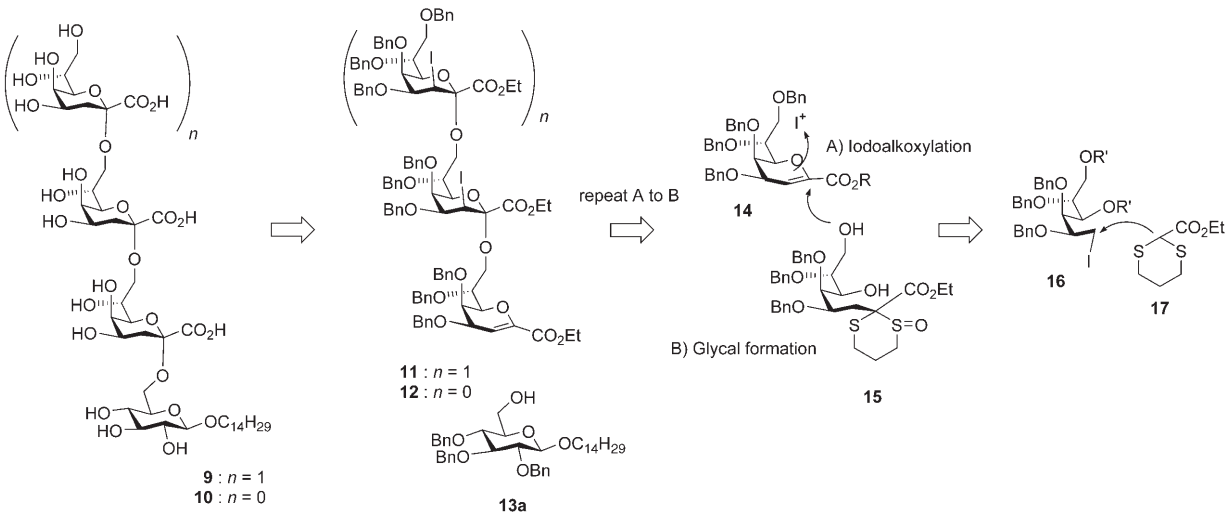
saccharide precursors would be expected to exhibit an enhanced reactivity toward glycosylation in comparison with the corresponding cyclic acceptors **5**, because the opening of the pyran and furan rings of the saccharide units is known to be an effective strategy for improving the reactivity of hydroxy groups toward glycosylation.[8] The coupling products **7** can be converted to the glycal ester **8** for glycosidation. Herein, we describe the synthesis of oligosaccharides containing tri- and di-α(2,8)-KDO units by iodoalkoxylation with an acyclic saccharide precursor.

The strategy developed for the synthesis of α(2,8)-KDO derivatives **9** and **10** is shown in Scheme 2. These compounds

[*] Dr. H. Tanaka, D. Takahashi, Prof. Dr. T. Takahashi
Department of Applied Chemistry
Graduate School of Science and Engineering
Tokyo Institute of Technology
2-12-1 Ookayama, Meguro, Tokyo 152-8552 (Japan)
Fax: (+81) 3-5734-2884
E-mail: ttak@apc.titech.ac.jp

Supporting information for this article is available on the WWW under http://www.angewandte.org or from the author.

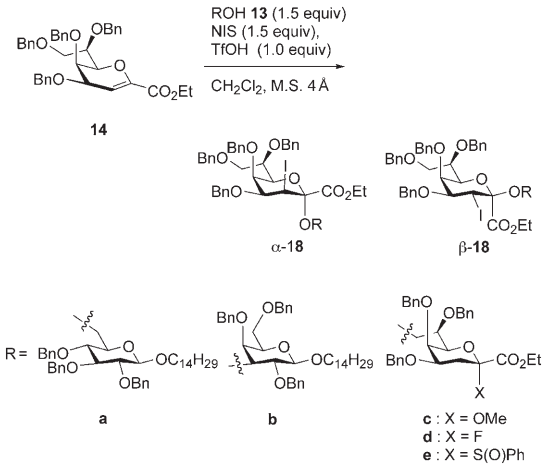
InterScience
© 2006 Wiley-VCH Verlag GmbH & Co. KGaA, Weinheim



Scheme 2. Strategy for the synthesis of tri- and di-α(2,8)-KDO derivatives **9** and **10**. Bn = benzyl.

could be prepared by the glycosylation of acceptor **13a** with the corresponding glycal esters **11** and **12** attached to α(2,8)-KDO units. The synthesis of the glycal ester **12** could be achieved by the regio- and stereoselective iodoalkoxylation of the glycal ester **14** with diol **15**, which contains alkylsulfanyl and sulfoxide groups at the C2 position, followed by subsequent cyclization and β elimination. Trisaccharide **11** was prepared from **12** by the iodoalkoxylation and β elimination protocol. Benzyl ethers were selected as O-protecting groups to improve the reactivity of the glycal esters **11**, **12**, and **14** toward iodoalkoxylation. The resulting iodide and benzyl ethers can be readily removed by hydrogenolysis. Diol **15** can be prepared by alkylation of dithiane **17**[9] with the corresponding alkyl halide **16**.[5,6,10]

We first investigated the iodoalkoxylation of the glycal ester **15** with alcohols **13** (Scheme 3 and Table 1). Treatment of the benzyl-protected glycal ester **14** and primary alcohols **13a** with NIS and TfOH provided the 3-iodo-α-glycoside α-**18a** in 93% yield with excellent selectivity.[11] Notably,



Scheme 3. Iodoalkoxylation of **14** with various acceptors **13** (see also Table 1) NIS = *N*-iodosuccinimide; TfOH = trifluoromethanesulfonic acid; M.S. = molecular sieves.

Table 1: Iodoalkoxylation of **14** with various acceptors **13** (Scheme 3).

Entry	Acceptor	Product	*T* [°C]	Yield [%]	α/β[a]
1	**13a**	**18a**	−50	93	>95:5
2	**13b**	**18b**	−50 to −40	77	>95:5
3	**13c**	**18c**	−50 to −20	73	92:8
4	**13d**	**18d**	–	–	–

[a] The α/β ratio was estimated by HPLC analysis with refractive index detection.

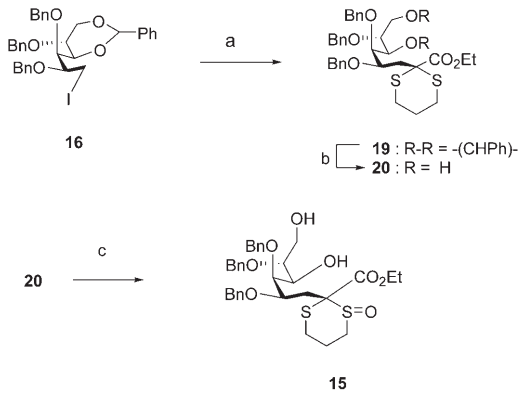
although iodoalkoxylation of glycals in the synthesis of α-linked 2-deoxyglycosides is known to proceed under mildly oxidative conditions,[12] the use of a stoichiometric amount of TfOH was critical for the iodoalkoxylation of glycal ester **14** to proceed. Glycosylation at the C3 secondary alcohol moiety of galactoside **13b** proceeded smoothly to provide disaccharide α-**18b** in excellent yield and selectivity.[13]

Next, the glycosylation of KDO derivatives **13c–e** at the C8 position was examined. The methyl glycoside **13c** was converted to the corresponding α-glycoside α-**18c** in 73% yield with α/β = 92:8.[11] On the other hand, glycosyl sulfoxide **13e** was difficult to prepare because of its instability. The glycosyl fluoride **13d** decomposed under these reaction conditions. These results suggest that, although the iodoalkoxylation of glycal esters would be effective for the synthesis of α-linked KDO derivatives, it would be difficult to design cyclic glycal precursors that are amenable to iodoalkoxylation.

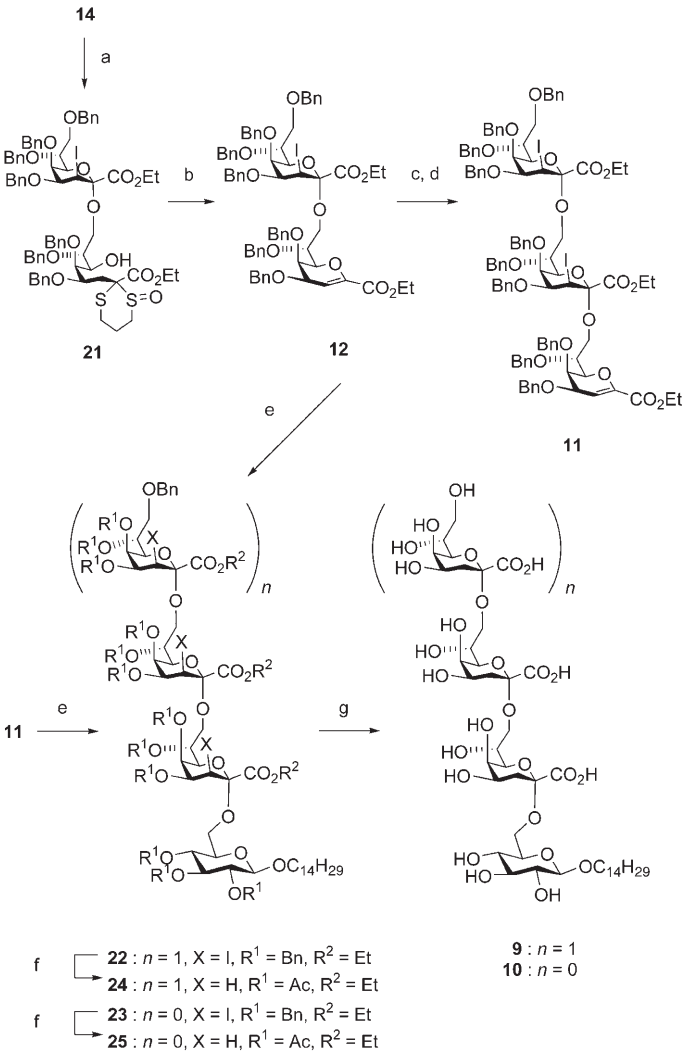
We then examined the synthesis of the α(2,8)-KDO derivatives **9** and **10**. The preparation of the acyclic building blocks **15** is shown in Scheme 4. Treatment of iodide **16**[14] with dithiane **17** in the presence of NaH in DMF provided the alkylated product **19**, which was followed by removal of the acetal of **19** under acidic conditions to afford diol **20** in 71% overall yield. Oxidation of thioether **20** provided sulfoxide **15** in good yield.

Iodoalkoxylation and glycal formation is shown in Scheme 5. Treatment of the glycal ester **14** and 1.5 equivalents of diol **15** in the presence of NIS/TfOH at −50 to −20 °C

 © 2006 Wiley-VCH Verlag GmbH & Co. KGaA, Weinheim



Scheme 4. Reagents and conditions: a) **17**, NaH, *t*BuOH (cat.), DMF; b) CSA, MeOH, THF, 71% (based on **16**); c) *m*-CPBA, CH_2Cl_2, 95%. DMF = *N*,*N*-dimethylformamide; CSA = 10-camphorsulfonic acid; CPBA = chloroperbenzoic acid.



Scheme 5. Reagents and conditions: a) **15** (1.5 equiv), NIS, TfOH, M.S. 4 Å, CH_2Cl_2, −50 to −20°C, 89%; b) $(COCl)_2$, AgOTf, M.S. 4 Å, CH_2Cl_2, −30 to 0°C, 77%, $\alpha/\beta => 95:5$; c) **15** (1.5 equiv), NIS, TfOH, M.S. 4 Å, CH_2Cl_2, −50 to −20°C, 68%; d) $(COCl)_2$, AgOTf, M.S. 4 Å, CH_2Cl_2, −30 to 0°C, 85%, $\alpha/\beta => 95:5$; e) **13a** (1.5 equiv), NIS, TfOH, M.S. 4 Å, CH_2Cl_2, −50°C to room temperature, 80%, $\alpha/\beta => 95:5$ for **23**, 55%, $\alpha/\beta = 86:14$ for **22**; f) 1. $Pd(OH)_2$, *n*-BuOH, MeOH, ethyl acetate; 2. Ac_2O, Py, CH_2Cl_2, DMAP, 71% for **25**, 53% for **24**; g) LiOH, $MeOH/H_2O$, 50°C, quantitative for **10**, 89% for **9**. Py = pyridine; DMAP = 4-dimethylaminopyridine.

provided α-glycoside **21** in 89% yield. These results indicate that the opening of the pyran ring of the KDO derivative effectively improved the coupling yield of the C8 hydroxy group, and that sulfoxide and alkylsulfanyl groups represent suitable protecting groups for the linear building blocks at the pseudo-anomeric position for the iodoalkoxylation. The sequential activation of the two leaving groups with $(COCl)_2$ and AgOTf in CH_2Cl_2 afforded the glycal ester **12** bearing an α-linked KDO unit as a single diastereomer. AgOTf played a crucial role in increasing the yield of the glycal ester **12**. Iodoalkoxylation of **12** with 1.5 equivalents of **15** followed by glycal formation provided the tri-KDO derivative **11** in good total yield with excellent selectivity. Glycosylation of the primary alcohol **13a** with glycal esters **11** and **12** proceeded stereoselectively to provide α-glycosides **22** and **23** in good yields with excellent selectivity. Removal of the iodide and cleavage of all the benzyl ether protecting groups, followed by acetylation, provided the peracetyl-protected tri- and tetrasaccharides **24** and **25** in 53 and 71% yield, respectively. Hydrolysis of the ester groups in **24** and **25** provided tri- and di-α(2,8)-KDO-containing oligosaccharides **9** and **10** in good yields. The α linkages of the KDO units of **24** and **25** were confirmed by analysis of their ^{1}H NMR spectra on the basis of reported empirical rules.[11]

In conclusion, an efficient synthesis of tri-α(2,8)-KDO derivatives based on an iterative glycosidation strategy has been developed. Iodoalkoxylation of the glycal esters **11**, **12**, and **14** proceeded in a stereoselective manner to provide α-linked KDO derivatives in good yields. The acyclic building block **15** was found to be an effective glycosyl acceptor and was converted to the glycal ester for glycosidation. The opening of the pyran ring effectively improved the reactivity of the C8 hydroxy group. The glycal esters **11** and **12** bearing KDO units constitute potentially useful building blocks for the synthesis of α-KDO-conjugated oligosaccharides.

Received: September 16, 2005
Published online: December 22, 2005

Keywords: carbohydrates · glycosides · glycosylation · oligosaccharides · synthetic methods

[1] F. M. Unger, *Adv. Carbohydr. Chem. Biochem.* **1981**, *38*, 324–387.
[2] For reviews on the synthesis of KDO glycosides, see: a) J. Hansson, S. Oscarson, *Curr. Org. Chem.* **2000**, *4*, 535–564; b) L. S. Li, Y. L. Wu, *Curr. Org. Chem.* **2003**, *7*, 447–475.
[3] M. Imoto, S. Kusumoto, T. Shiba, *Tetrahedron Lett.* **1987**, *28*, 6277–6280.
[4] K. Ikeda, S. Akamatsu, K. Achiwa, *Carbohydr. Res.* **1989**, *189*, C1–C4.
[5] T. Takahashi, H. Tsukamoto, H. Yamada, *Org. Lett.* **1999**, *1*, 1885–1887.

 © 2006 Wiley-VCH Verlag GmbH & Co. KGaA, Weinheim

[6] T. Amaya, D. Takahashi, H. Tanaka, T. Takahashi, *Angew. Chem.* **2003**, *115*, 1877 – 1880; *Angew. Chem. Int. Ed.* **2003**, *42*, 1833 – 1836.
[7] P. Kosma, H. Sekljic, G. Balimt, *J. Carbohydr. Chem.* **1996**, *15*, 701 – 704.
[8] a) K. Heins, K. Propp, R. Harrison, H. Paulsen, *Chem. Ber.* **1967**, *100*, 2655 – 2663; b) S. Kusumoto, K. Yamamoto, M. Imoto, M. Inage, *Bull. Chem. Soc. Jpn.* **1986**, *59*, 1411 – 1417.
[9] This compound is commercially available.
[10] a) M. Imoto, S. Kusumoto, T. Shiba, *Tetrahedron Lett.* **1987**, *28*, 6235 – 6238; b) P. A. M. van der Klein, G. J. P. H. Boons, G. H. Veenman, G. A. van der Marel, J. H. Van Boom, *Tetrahedron Lett.* **1989**, *30*, 5477 – 5480; c) H. Tsukamoto, T. Takahashi, *Tetrahedron Lett.* **1997**, *38*, 6415 – 6418; d) T. Takahashi, H. Tsukamoto, M. Kurosaki, H. Yamada, *Synlett* **1997**, *9*, 1065 – 1066.
[11] Structure determination of the α-linked 3-iodo-KDO units was achieved by removal of the iodides and benzyl ether protecting groups followed by acetylation, and subsequent ^{1}H NMR spectroscopic analysis of the acetylated products on the basis of reported empirical rules; P. Kosma, M. Strobl, G. Allmaier, E. Schmid, H. Brade, *Carbohydr. Res.* **1994**, *254*, 105 – 132.
[12] R. W. Frisen, S. J. Danishefsky, *J. Am. Chem. Soc.* **1989**, *111*, 6656 – 6660.
[13] The α linkage of the KDO unit of α-**18b** was confirmed by analysis of the coupling constant $^{3}J_{C1\text{-}H3ax}$ (< 1 Hz) of the corresponding deprotected product; F. M. Unger, D. Stix, G. Schulz, *Carbohydr. Res.* **1980**, *80*, 191 – 195.
[14] Alkyl iodide **16** was prepared by standard methods. All new compounds exhibited satisfactory spectroscopic and analytical data (see Supporting Information).

 © 2006 Wiley-VCH Verlag GmbH & Co. KGaA, Weinheim

Colloids

DOI: 10.1002/anie.200503131

Particle-Stabilized Emulsions: A Bilayer or a Bridging Monolayer?**

Tommy S. Horozov and Bernard P. Binks*

Solid colloidal particles are widely used in many industries, for example, food, cosmetics, paper, paint etc. The fact that they can be irreversibly held at fluid interfaces and stabilize emulsions was realized a long time ago.[1,2] Recently, it was shown that certain solid nanoparticles alone can act as excellent emulsion[3–5] and foam stabilizers.[3,6] It is accepted that the stability of particle-stabilized emulsions is due to the coherent particle layer around the droplets, which acts as a steric (mechanical) barrier against coalescence.[3,7,8] This situation implies that particle interactions at the droplet surface are dominated by attractive forces, which results in the formation of coherent monolayers with significant mechanical strength.[7,8] Recent results have shown that stable emulsions can be formed even if the droplets are barely covered with well-separated particles.[4] However, this does not fit in with the steric barrier mechanism of stabilization and is still enigmatic. Here, we demonstrate for the first time the link between particle behavior and interactions in planar monolayers and the mechanisms of emulsion stabilization. We show why strongly repulsive colloidal particles, which give well-ordered, dilute planar monolayers, can act as very effective emulsion stabilizers. This effect arises from the spontaneous accumulation of particles in a dense monolayer bridging the emulsion droplets sparsely covered with particles, thus preventing coalescence, as revealed by direct in situ microscope observations. Our results imply that two general mechanisms of emulsion stabilization by solid particles thus exist: 1) steric stabilization of emulsion droplets covered by coherent particle layers, and 2) stabilization by particle bridges when the droplets are sparsely covered. This is very important for understanding the fundamentals of solid-stabilized emulsions and designing more efficient particle stabilizers.

Small solid particles can spontaneously attach to air–water or oil–water interfaces to form monolayers. The energy needed for their detachment is usually much greater than the thermal energy; therefore they are irreversibly trapped at the fluid interface.[3] This effect determines the ability of certain colloidal particles to act as very effective emulsion and foam stabilizers.[3–8] In particle-stabilized emulsions, liquid droplets covered with coherent particle layers are dispersed in another immiscible liquid. The particle layers at the drop surface provide steric (mechanical) hindrance to droplet coalescence, thus making these emulsions completely stable for years.[3,7] This well-accepted mechanism of stabilization can be realized if the droplets are covered with sufficiently dense particle layers close to complete surface coverage[7] or if a rigid crust of particles forms around the droplets.[9] Some results, however, do not fit into this picture of emulsion stabilization. For example, Midmore has obtained very stable emulsions even though the estimated coverage of the droplets with silica nanoparticles was as low as around 29 %.[8] Recently, Vignati et al.[4] have reported stable emulsions at about 5 % particle coverage of the droplets, which cannot be explained by steric stabilization. On the basis of microscopy observations performed after dilution of the emulsions, they hypothesized that particles within the contact region may form a monolayer bridging the droplets, thus keeping them at a finite distance, which stabilizes the thin liquid film between the droplets and prevents coalescence.[4] The formation of bridging particle monolayers in isolated liquid films has been reported,[10–12] but direct experimental evidence of their existence in real emulsions is still missing. Hence, the mechanism of stabilization of emulsion droplets sparsely covered with particles remains unclear and enigmatic. This raised the question about the link between the structure of isolated particle monolayers

[*] Dr. T. S. Horozov, Prof. B. P. Binks
Surfactant & Colloid Group
Department of Chemistry
University of Hull
Hull, HU6 7RX (UK)
Fax: (+44) 1482-466-410
E-mail: t.s.horozov@hull.ac.uk

[**] We thank Wacker-Chemie, Burghausen, for financial support.

 © 2006 Wiley-VCH Verlag GmbH & Co. KGaA, Weinheim InterScience

and the mechanism of stabilization in particle-stabilized emulsions. Despite existing theoretical analyses,[7] such a link has not been shown experimentally until now.

Herein we report experimental results that demonstrate, for the first time, the link between the structure of planar monolayers of particles and the mechanism of stabilization of particle-stabilized emulsions. Planar monolayers of micrometer-size silica particles hydrophobized to different extents were formed at an octane–water interface and studied by microscopy. Slightly hydrophobic particles with a contact angle θ of 65° measured through the aqueous layer give aggregated disordered monolayers (Figure 1a). In contrast,

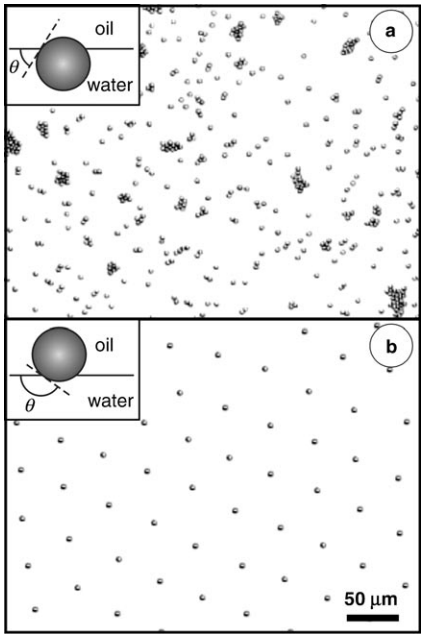


Figure 1. Images of horizontal, planar monolayers of silica particles at an octane–water interface 1 h after their formation by spreading. The particle diameter is 3 μm and particle contact angles θ are a) 65° and b) 152° (see insets). The aqueous phase contains 10 and 100 mM NaCl, respectively.

very hydrophobic particles with $\theta = 152°$ give monolayers with a totally different structure (Figure 1b). The silica particles in the latter case are ordered in a hexagonal array at very large interparticle distances of around 50 μm. These results are consistent with our previous findings concerning the effect of particle hydrophobicity on particle interactions at oil–water interfaces.[13] The weak repulsion between less-hydrophobic particles ($\theta = 65°$) is insufficient to oppose the attraction; therefore, the particles easily aggregate and give disordered monolayers at very low electrolyte concentrations in the aqueous phase (10 mM NaCl). In contrast, the interactions between the most-hydrophobic silica particles ($\theta = 152°$) are dominated by strong, long-range Coulomb repulsion through the oil as a result of charges at the particle–oil interface. This finding is supported by the fact that these particles form well-ordered, stable monolayers with a crystalline structure even at high electrolyte concentration in the aqueous phase (100 mM). The reasons for such a remarkable difference in interactions between particles with different hydrophobicities have been analyzed elsewhere.[13] The question of interest here is whether the observed differences in the monolayer structure affect the way in which particles stabilize emulsions.

To answer the above question we studied emulsions formed by shaking equal volumes of octane and water in the presence of 1 wt% silica particles with different hydrophobicities to those used in the monolayer experiments. We found that an oil-in-water (o/w) emulsion is formed in the presence of less-hydrophobic particles ($\theta = 65°$), whereas a water-in-oil (w/o) emulsion is obtained when the most-hydrophobic particles ($\theta = 152°$) are used. This result is in agreement with previous findings that particles with $\theta < 90°$ can stabilize o/w emulsions, while those with $\theta > 90°$ give w/o emulsions.[2,3,5,7] In both cases the emulsions were unstable just after their formation, and fast creaming of the oil droplets in the o/w emulsion and sedimentation of the water droplets in the w/o emulsion was observed. The respective resolved bulk liquids were very clear, thereby suggesting that almost all the particles are adsorbed at the oil–water interface. This process was accompanied by very fast droplet coalescence during the first 10 s, but gradually slowed down, and after several minutes terminated completely. Further changes in droplet size were not detected and the emulsions were stable against coalescence for several months. This gradual transformation of an initially unstable emulsion into an indefinitely stable one is called a limited coalescence and is typical for particle-stabilized emulsions at low particle concentrations.[14]

Images of o/w and w/o emulsions taken in situ with a horizontal microscope about one hour after their formation are shown in Figure 2. Although the composition of both

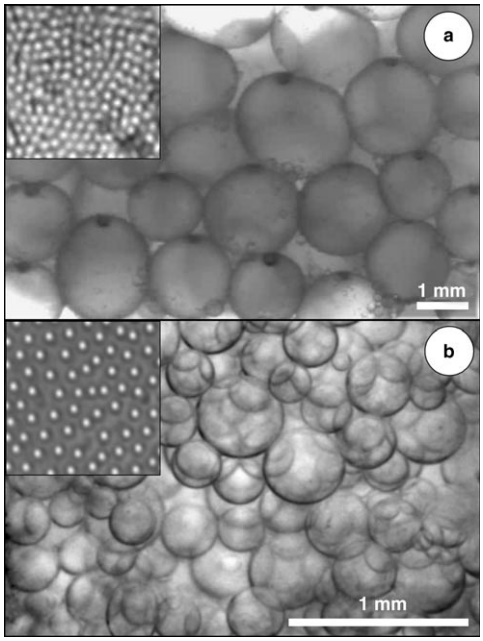


Figure 2. Images of a) an octane-in-water emulsion stabilized by slightly hydrophobic silica particles with a contact angle of 65° and b) a water-in-octane emulsion stabilized by very hydrophobic silica particles with a contact angle of 152°, both taken 1 h after emulsification by shaking. The particle diameter is 3 μm and particle concentration is 1% w/v. The insets ($40 \times 40\ \mu m^2$) show the monolayer structure in situ at the drop surface obtained at higher magnification.

 © 2006 Wiley-VCH Verlag GmbH & Co. KGaA, Weinheim

emulsions is the same, the droplet size is remarkably different. The average diameter of oil droplets determined from the images of the stable o/w emulsion is 1.7 ± 0.2 mm (a), while that of the water droplets in the w/o emulsion is 0.3 ± 0.1 mm (b). Hence, the emulsion droplets stabilized by the most-hydrophobic particles are more than five times smaller than those stabilized by the less-hydrophobic ones. A closer look at the droplet surface at higher magnification reveals another interesting difference, namely that the oil droplets are covered with a dense monolayer of close-packed particles (a, inset), which can act as a steric barrier between the droplets and thus prevent coalescence. Surprisingly, the monolayers of the most-hydrophobic particles on the water droplets are rather dilute (b, inset). Although not perfectly ordered, as in the planar monolayers, the particles are well separated at around 6 μm (ca. two particle diameters). Clearly, these dilute particle monolayers cannot serve as a steric barrier against droplet coalescence, therefore there must be another reason for the prolonged stability of these emulsions.

The magnified in situ images of the w/o emulsion in Figure 3 solve the mystery. Several touching drops are shown in Figure 3a. The circular contact regions (liquid films) between the drops are easily seen as bright spots marked "F". Their structure becomes clear at even higher magnification (Figure 3b), where it can be seen that particles in the oil film between touching water droplets are well ordered in a dense disk with a crystalline structure. Spontaneous formation of similar crystalline disks of bridging particles has previously been observed during thinning of isolated oil films in water when the film surfaces were covered with dilute monolayers of very hydrophobic silica particles.[12] The same should happen when two droplets in the w/o emulsion come into contact: some of the particles become attached to the surface of both water droplets, thus forming stable particle bridges through the oil because θ is greater than 90°. One can conclude that the crystalline disks between touching droplets are, in fact, particle monolayers bridging the droplets. The significant particle density of the bridging monolayer is due to the strong capillary attraction between particles caused by the deformed menisci around them. The dense bridging monolayer ("F" in Figure 3b) stabilizes the liquid film between droplets,[15] thus preventing coalescence, although the droplets are barely covered with particles outside the contact region ("D" in Figure 3b). Therefore, the most-hydrophobic particles can form an emulsion with smaller drops and a larger interfacial area at the same adsorbed amount than that of the less-hydrophobic particles, which have to be closely packed at the drop surface to prevent coalescence.

Our results clearly show that there is a link between the particle interactions, the structure of their dilute planar monolayers, and the mechanism of emulsion stabilization. The lack of long-range repulsion between less-hydrophobic particles ($\theta = 65°$) results in the disordered structure of their dilute monolayers. For the same reason, these particles are easily dragged away from the central, thinnest part of isolated water films in oil and are unable to provide effective film stabilization.[12] Dense, close-packed monolayers are needed for film stabilization[12] and for protection of the emulsion droplets from coalescence (Figure 2a). Hence, these emulsions are stabilized by the steric-hindrance mechanism (Figure 4a). In contrast, the strong Coulomb repulsion

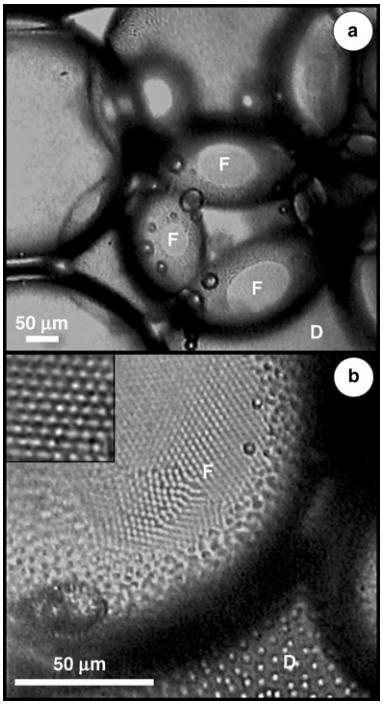


Figure 3. Images of the same water-in-octane emulsion as Figure 2b at a) intermediate and b) higher magnification. The oil films (F) formed between touching water droplets are stabilized by dense, ordered monolayers of bridging particles (b, inset). The particles on the droplet surface outside the films (D) are well separated. The inset corresponds to an area of 25×25 μm^2.

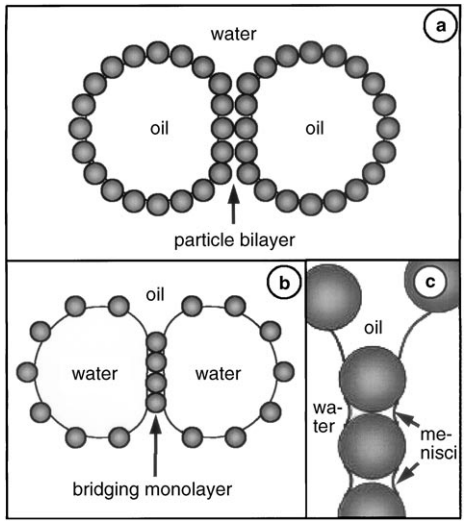


Figure 4. Two mechanisms of emulsion stabilization by colloidal particles: a) steric stabilization of emulsion droplets covered with dense, particle monolayers, and b) bridging stabilization of emulsion droplets covered with dilute particle monolayers. The particles on the emulsion droplets in the contact region form a dense, bridging monolayer as a result of strong capillary attraction caused by the menisci around them (c).

 © 2006 Wiley-VCH Verlag GmbH & Co. KGaA, Weinheim

between the most-hydrophobic particles ($\theta = 152°$) results in the well-ordered structure of their monolayers (Figure 1b). This repulsion keeps these particles in the thinnest region of isolated oil films in water, where they are able to bridge the film surfaces and to spontaneously form a dense, crystalline disk which prevents film rupture.[12] The same process occurs in the w/o emulsion during collisions between water droplets and effectively prevents them from coalescing even though the droplet surface is only partially covered with particles (Figure 2b and Figure 3b). Hence, these emulsions are stabilized by the bridging particle monolayer mechanism (Figure 4b,c). This mechanism could explain some of the existing experimental data for high stability of emulsions at a low surface concentration of particles.[4,8,9]

The link between particle behavior and interactions in planar monolayers and the mechanism of emulsion stabilization by solid colloidal particles is clearly demonstrated by these experiments. Slightly hydrophobic silica particles, which give aggregated, disordered, planar monolayers as a consequence of the lack of strong interparticle repulsion, can stabilize emulsions by forming dense, close-packed monolayers at the droplet surface that act as a steric barrier against coalescence. In contrast, strongly repulsive colloidal particles, which give well-ordered, dilute, planar monolayers, can stabilize emulsions as a result of spontaneous particle accumulation in a dense monolayer bridging the emulsion droplets sparsely covered with particles. These findings are important for understanding the fundamentals of particle-stabilized emulsions. They will also help in designing more effective particle stabilizers by tuning the interactions between colloidal particles in planar monolayers at oil–water interfaces.

Experimental Section

Monodisperse silica particles of diameter 3.00 ± 0.05 μm and density 2 g cm^{-3} were purchased from Tokuyama Corp., Japan. They were hydrophobized to different extents with silanizing agents and the contact angles were determined as described elsewhere.[12] *n*-Octane (99%, Lancaster) was passed several times through basic alumina (BDH) to remove polar impurities. Water was passed through a reverse osmosis unit and then a Milli-Q reagent system. The NaCl used had a purity of 99.9% (from BDH). Planar monolayers of particles were formed by spreading a dilute particle suspension in 70 wt% 2-propanol/water at the octane–water interface in a small petri dish and were observed from above with a microscope, as described previously.[12,13] Emulsions were formed in glass cuvettes ($10 \times 10 \times 45$ mm^3, Helma) with teflon stoppers by mixing equal volumes of octane and water with silica particles. Before mixing, the less-hydrophobic particles were dispersed in water, whereas the most-hydrophobic ones were dispersed in octane. The cuvettes were then shaken vigorously by hand at a frequency of 2–3 Hz for 10 s. The volume of the emulsions formed was 2 mL. The evolution of the emulsions with time was observed from the side with a drop-shape analysis system (DSA 10, Krüss) at low magnification. The structure of stable emulsions over a long time was observed in situ (without dilution) with a horizontal Optiphot 2 microscope (Nikon) supplied with extra-long working-distance objectives.[12,13]

Received: September 2, 2005
Published online: December 15, 2005

Keywords: colloids · emulsions · monolayers · silica

[1] W. Ramsden, *Proc. R. Soc. London* **1903**, 72, 156–164.
[2] S. U. Pickering, *J. Chem. Soc.* **1907**, *91*, 2001–2021.
[3] B. P. Binks, *Curr. Opin. Colloid Interface Sci.* **2002**, *7*, 21–41.
[4] E. Vignati, R. Piazza, T. P. Lockhart, *Langmuir* **2003**, *19*, 6650–6656.
[5] S. Stiller, H. Gers-Barlag, M. Lergenmueller, F. Pflücker, J. Schulz, K. P. Wittern, R. Daniels, *Colloids Surf. A* **2004**, *232*, 261–267.
[6] B. P. Binks, T. S. Horozov, *Angew. Chem.* **2005**, *117*, 3788–3791; *Angew. Chem. Int. Ed.* **2005**, *44*, 3722–3725.
[7] D. E. Tambe, M. M. Sharma, *Adv. Colloid Interface Sci.* **1994**, 52, 1–63.
[8] B. R. Midmore, *Colloids Surf. A* **1998**, *132*, 257–265.
[9] B. P. Binks, M. Kirkland, *Phys. Chem. Chem. Phys.* **2002**, *4*, 3727–3733.
[10] N. P. Ashby, B. P. Binks, V. N. Paunov, *Chem. Commun.* **2004**, 436–437.
[11] E. J. Stancik, M. Kouhkan, G. G. Fuller, *Langmuir* **2004**, *20*, 90–94.
[12] T. S. Horozov, R. Aveyard, J. H. Clint, B. Neumann, *Langmuir* **2005**, *21*, 2330–2341.
[13] T. S. Horozov, R. Aveyard, B. P. Binks, J. H. Clint, *Langmuir* **2005**, *21*, 7405–7412.
[14] S. Arditty, C. P. Whitby, B. P. Binks, V. Schmitt, F. Leal-Calderon, *Eur. Phys. J. E* **2003**, 11, 273–281.
[15] N. D. Denkov, I. B. Ivanov, P. A. Kralchevsky, D. T. Wasan, *J. Colloid Interface Sci.* **1992**, *150*, 589–593.

 © 2006 Wiley-VCH Verlag GmbH & Co. KGaA, Weinheim

Silanes

DOI: 10.1002/anie.200502527

An η^3-H_2SiR_2 Adduct of [{PhB-(CH_2PiPr_2)$_3$}$Fe^{II}H$]**

*Christine M. Thomas and Jonas C. Peters**

The tripodal tris(phosphino)borate ligand $[PhB(CH_2PiPr_2)_3]^-$ (abbreviated $[PhBP^{iPr}_3]$) stabilizes iron complexes in a wide range of oxidation states, including high-valent Fe^{IV}.[1] $[(PhBP^{iPr}_3)FeL_n]$ systems are, moreover, known to mediate a

[*] C. M. Thomas, Professor J. C. Peters
Division of Chemistry and Chemical Engineering
Arnold and Mabel Beckman Laboratories of Chemical Synthesis
California Institute of Technology
Pasadena, CA 91125 (USA)
Fax: (+1) 626-577-4088
E-mail: jpeters@caltech.edu.

[**] This work was supported by the NSF (CHE-01232216) and BP (MC^2 program). Larry Henling and Dr. Mike Day are acknowledged for crystallographic assistance, and Erin J. Daida is acknowledged for executing several preliminary screen reactions. We also thank the referees of this manuscript for several insightful suggestions.

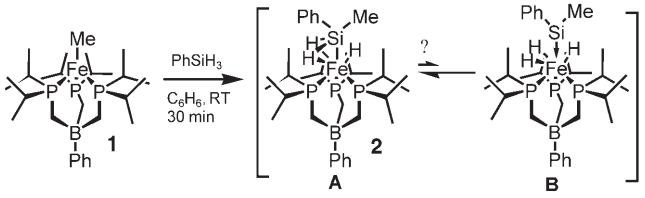
Supporting information for this article is available on the WWW under http://www.angewandte.org or from the author.

WILEY InterScience DISCOVER SOMETHING GREAT
© 2006 Wiley-VCH Verlag GmbH & Co. KGaA, Weinheim

number of two-electron redox transformations, including Fe^{II}/Fe^{IV} oxidative group transfer and oxidative addition/reductive elimination processes.[1a,c] In the latter context, it was recently demonstrated that four-coordinate iron alkyl species of the type $[(PhBP^{iPr}_3)Fe^{II}R]$ undergo facile hydrogenolysis to generate iron(IV) trihydrides of the type $[(PhBP^{iPr}_3)Fe^{IV}(H)_3(PR_3)]$ that can be likewise generated by H_2 addition to $[(PhBP^{iPr}_3)Fe^{II}(H)(PR_3)]$ precursors.[1c] These complexes mediate catalytic olefin hydrogenation, most likely through uncommon Fe^{II}/Fe^{IV} oxidative addition/reductive elimination steps.[1c] Motivated by these findings, we have examined the reactivity of these four-coordinate $[(PhBP^{iPr}_3)Fe^{II}R]$ alkyl species with silane substrates for comparison with their reactivity towards H_2, anticipating that structurally distinctive iron silylene species might be generated. Herein, we report the structural and spectroscopic characterization of unusual η^3-silane adducts of iron(II), namely $[(PhBP^{iPr}_3)Fe^{II}(H)(\eta^3\text{-}H_2SiR_2)]$. As described below, the available structural, spectroscopic, and theoretical data also suggest the possibility that the $[(PhBP^{iPr}_3)Fe^{II}(H)(\eta^3\text{-}H_2SiR_2)]$ systems described herein equilibrate via silylene intermediates of the type $[(PhBP^{iPr}_3)Fe^{IV}(H)_3(SiR_2)]$.[2] Such silylene intermediates would be isoelectronic with the previously reported $[(PhBP^{iPr}_3)Fe^{IV}(H)_3(PR_3)]$ but appear to be too high in energy relative to their ground state $[(PhBP^{iPr}_3)Fe^{II}(H)(\eta^3\text{-}H_2SiR_2)]$ isomers to be directly observed.

Although silicon-containing transition-metal complexes that exhibit η^2-$HSiR_3$ interactions are ubiquitous,[3,4] those that exhibit well-characterized interactions between two or more metal hydrides and a coordinated silicon atom are much less common. These interactions have nevertheless been described in certain cases, such as in the dinuclear complex $[\{(PR_3)_2(H)_2Ru\}_2(\eta^4\text{-}SiH_4)]$ of Sabo-Etienne and co-workers[5] and in the mononuclear complexes $[ReH_4(PPh_3)(\eta^3\text{-}H_2SiR_3)]$,[6] $[(PCy_3)_2Ru(H)(\eta^2\text{-}H_2)(\eta^3\text{-}H_2SiPh_3)]$ (Cy = cyclohexyl),[7] $[Ru(PPh_3)_3H_3SiMeCl_2]$,[8] and $[Cp^*Ru(PPh_3)(\eta^3\text{-}H_2SiMeCl_2)]$ ($Cp^* = C_5Me_5$).[9] Metal hydride/silyl systems of these types are often described as lying somewhere along the continuum to oxidative addition, the limit being full oxidative addition with earlier, "arrested" addition stages also being common.[4a] To the best of our knowledge, the $[(PhBP^{iPr}_3)Fe^{II}(H)(\eta^3\text{-}H_2SiR_2)]$ complexes described here are the first thoroughly characterized examples of arrested silane adducts of iron that exhibit an η^3 binding mode (i.e., $Fe(\eta^3\text{-}H_2SiR_2)$). The only other example of this binding mode for a silane ligand of any transition-metal complex appears to be the aforementioned dinuclear ruthenium system of Sabo-Etienne.[5]

A $[(PhBP^{iPr}_3)Fe^{II}(H)(\eta^3\text{-}H_2SiR_2)]$ species is formed by the reaction between $[(PhBP^{iPr}_3)FeMe]$ (**1**) and $PhSiH_3$ (Scheme 1), which leads to the quantitative formation of a single diamagnetic red product (**2**), as evidenced by ^{1}H NMR spectroscopy. In contrast to the previously reported reaction of **1** with H_2,[1c] no



Scheme 1. Reaction of **1** with phenylsilane.

methane loss is detected by ^{1}H NMR spectroscopy. The $^{31}P\{^1H\}$ NMR spectrum of **2** reveals a broad singlet at $\delta = 76$ ppm, which is consistent with a C_{3v}-symmetric structure. All three phosphorus nuclei remain magnetically equivalent in the $^{31}P\{^1H\}$ NMR spectrum at temperatures as low as $-80\,^\circ$C. The ^{1}H NMR spectrum of **2** reveals a hydride signal at $\delta = -13.5$ ppm with a complicated splitting pattern (see below).

To assess the structure of complex **2** in the solid state, X-ray quality single crystals were grown by cooling a concentrated solution of **2** in diethyl ether to $-35\,^\circ$C. High-resolution X-ray diffraction analysis provided the solid-state structure shown in Figure 1.[10] The structure confirms that a 1,2-methyl migration occurs from the iron center to the silicon center during the transformation. A remarkably short Fe···Si distance of 2.1280(7) Å is present that is very similar to the Fe···Si distance of 2.154(1) Å reported for the only structurally characterized example of an iron silylene species, $[Cp^*Fe(CO)(SiMes_2)SiMe_3]$ ($Mes = 2,4,6\text{-}Me_3C_6H_2$).[11] Moreover, the geometry of the silicon atom of **2** is rigorously

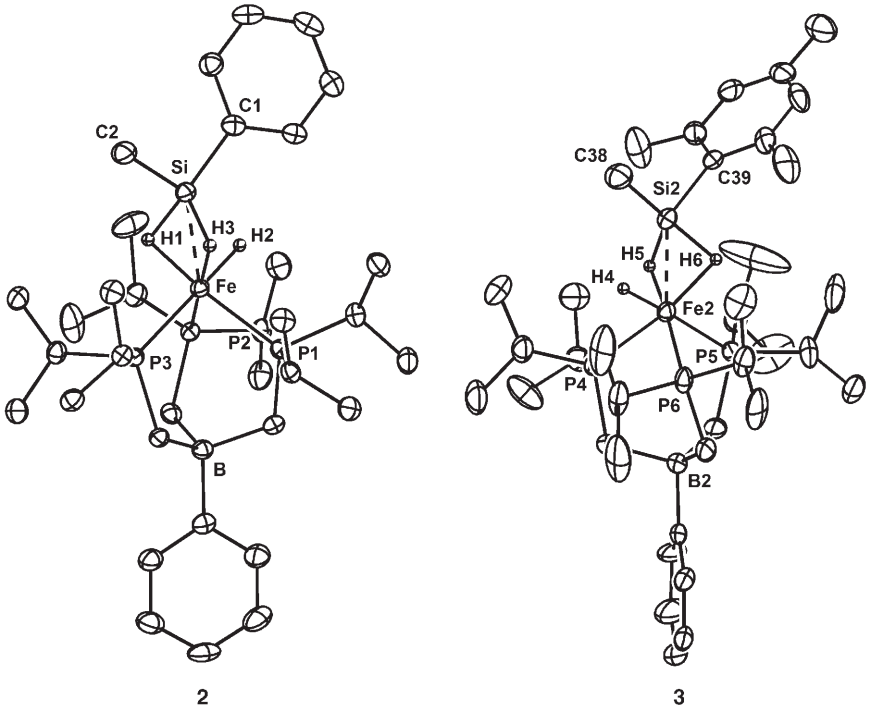


Figure 1. Solid-state molecular structure of $[(PhBP^{iPr}_3)Fe^{II}(H)(H_2SiPhMe)]$ (**2**) and $[(PhBP^{iPr}_3)Fe^{II}(H)(H_2SiMesMe)]$ (**3**) showing 50% displacement ellipsoids. Only one of the two independent molecules present in the asymmetric unit of **3** is shown. Hydrogen atoms other than the hydrides of interest have been omitted for clarity.

 © 2006 Wiley-VCH Verlag GmbH & Co. KGaA, Weinheim

planar ($\sphericalangle$C2-Si-Fe + $\sphericalangle$C2-Si-C1 + $\sphericalangle$C1-Si-Fe = 360°) if one considers its connectivity to the phenyl, methyl, and iron substituents only. These structural data suggested a Si atom with silylene character and led to our initial, but ultimately incorrect, assignment of **2** as a silylene trihydride of structure type **B** (Scheme 1). All three hydride positions could be located in the difference Fourier map and refined, and careful examination reveals that two of the hydrides (H1 and H3) are located within bonding distance of both the iron and the silicon centers (Fe–H1: 1.55 Å; Fe–H3: 1.57 Å; Si–H1: 1.46 Å; Si–H3: 1.55 Å). The third hydride (H2) is located outside the typical bonding radius of the silicon atom (2.00 Å)[4b] and resides appreciably closer to the Fe center (Fe–H2: 1.48 Å). These data are inconsistent with the silylene structure **B**.

As there is inevitable uncertainty in accurately locating the positions of hydrogen atoms close to much heavier atoms such as Si and Fe by X-ray crystallography, a related complex was prepared for additional structural support of the assignment. In an analogous reaction to that shown in Scheme 1, complex **1** reacts with one equivalent of mesitylsilane (H_3SiMes) to generate a diamagnetic red product (**3**) in quantitative yield. Complex **3** displays analogous NMR data to that of **2**, with a $^{31}P\{^1H\}$ shift at $\delta = 79$ ppm and a hydride-type ^1H NMR resonance at $\delta = -13.4$ ppm, which also suggests a highly symmetric structure in solution. X-ray quality crystals could be obtained in a similar way, and one of the two independent molecules present in the asymmetric unit is shown in Figure 1.[12] As in the case of **2**, two of the three hydrides are located within bonding distance of the silicon atom in each molecule (Si–H5: 1.56 and 1.62 Å; Si–H6: 1.67 and 1.74 Å), while the third hydride appears to be outside the bonding radius of the Si atom (Si···H4: 2.14 and 1.97 Å). The Fe···Si distances in both molecules for **3** (2.131(1) and 2.141(1) Å) are essentially identical to that in **2** (2.1280(7) Å). Regardless of the inevitable uncertainty in the specific Fe···H and Si···H distances, the significant similarity between the structures of **2** and **3** strongly suggests the presence of two 3-centered Fe-H-Si interactions in the solid state and one Fe-H(hydride) interaction.

For additional structural examination of the hydride positions, a density functional (DFT) geometry optimization of the structure of **2** was performed using the Jaguar package (B3LYP/LACVP**).[13,14] All of the atoms of **2** were used in the calculation, and the structure was minimized using the experimentally determined crystallographic coordinates as an initial estimate. The resulting Fe–H and Si–H bond lengths were very similar to those determined by crystallography (Table 1). Interestingly, perturbing the crystallographic coordinates to provide a more threefold symmetric structure without Si-H interactions as a starting point led to the same structural minimum. It is gratifying to note that the DFT model locates two short and one much longer Si···H distance, which is in accord with the η^3-H_2SiR_2 adduct formulation. Accordingly, a natural bond orbital (NBO) analysis predicts only two Si–H bonding orbitals (Si–H1, Si–H3).[15] Likewise, only one Fe–H bonding orbital is predicted (Fe–H2) and no bonding orbital is located between Si and Fe. The cutoff energy for locating a bond for donor–acceptor-type interactions is less than 20 kJ mol^{-1}. Interactions below this energy are ignored by NBO analaysis.[13,15] Therefore, the experimentally observed close contact between the iron center and the silicon–hydride bonds Si–H1 and Si–H3 is best characterized as η^3 in character. Likewise, any interaction between the iron hydride H2 and the Si center would also be characterized as an attractive interaction, although likely one of a much weaker nature if it is present at all. Complexes **2** and **3** are therefore best described as η^3 silane adducts of an iron(II) hydride (structure type **A** in Scheme 1) and not as iron(IV) silylene trihydrides (structure type **B**).

Table 1: Interatomic distances for **2** as determined by X-ray crystallography and a DFT (B3LYP/LACVP**) geometry optimization.

	Experimental [Å]	Calculated [Å]
Fe–Si	2.1280(7)	2.166
Fe–H1	1.553(1)	1.555
Fe–H2	1.482(1)	1.484
Fe–H3	1.566(2)	1.569
Si–H1	1.464(1)	1.469
Si–H2	2.001(2)	2.073
Si–H3	1.552(2)	1.554

Further inspection of the solution-state NMR data available for **2** confirms that a significant Si···H interaction is also maintained in the solution phase. A $T_{1\,min}$ measurement of 177 ms (−30 °C, [D_8]toluene) was determined for the hydride resonance of the ^1H NMR spectrum. This large value would appear to rule out the presence of a nonclassical dihydrogen adduct species (η^2-H_2) but does not help to distinguish between a classical hydride formulation versus the η^2-Si–H–Fe interaction suggested by the crystallographic and DFT data.[16,17] Simulation of the hydride signal (Figure 2) reveals that its complicated splitting pattern arises from first-order coupling of each equivalent hydride to one *trans* phosphorus atom ($^2J_{P\text{-}H} = 27$ Hz) and two *cis* phosphorus atoms ($^2J_{P\text{-}H} = 3$ Hz). The coupling pattern is complicated by second-order effects that result from phosphorus–phosphorus coupling ($^2J_{P\text{-}P} = 62$ Hz). Accordingly, the hydride signal appears as a singlet in the $^1H\{^{31}P\}$ NMR spectrum. The second-order splitting pattern of the hydride signal in the

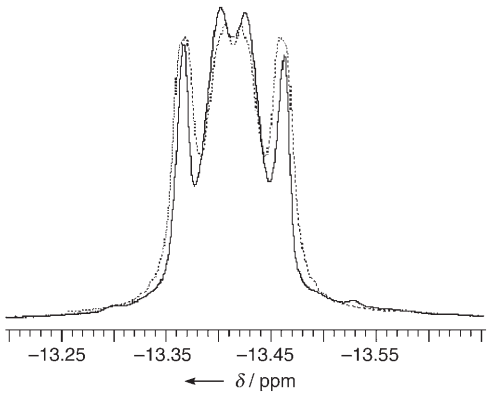


Figure 2. Experimental (solid) and simulated (dotted) ^1H NMR spectrum of **2** (500 MHz, 25 °C, C_6D_6) in the hydride region. See text for discussion.

 © 2006 Wiley-VCH Verlag GmbH & Co. KGaA, Weinheim

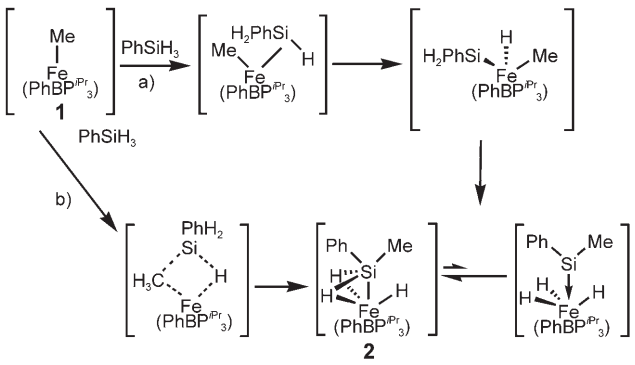
^{1}H NMR spectrum changes as the temperature of the solution decreases, which indicates a fluxional process of some type (see Supporting Information). Decoalescence of the signal, however, likely occurs at temperatures well below those examined (−80 °C).

The ^{29}Si{^{1}H} NMR data obtained for **2** and **3** reveal signals at $\delta = 162$ and 160 ppm,[18] respectively. These values are significantly downfield of known classical transition-metal–silyl adducts ($\delta = -120$ to 90 ppm) but are also upfield of reported transition-metal silylenes ($\delta = > 200$ ppm).[4a,2] Although monomeric complexes containing η^2-HSiR$_3$ interactions display a wide range of chemical shifts in the ^{29}Si{^{1}H} NMR spectrum (from $\delta = -28$ to 55 ppm),[3,4a] the unusually large downfield shifts observed for **2** and **3** are likely reflective of the η^3 nature of the silane ligand and the very close Fe–Si contact that results, as evident from the solid-state structures.

Closer inspection of the hydride signals for both **2** and **3** reveals the presence of ^{29}Si satellites that provide $J_{\text{Si-H}}$ coupling values of 68 and 70 Hz, respectively. The rapid exchange of the hydrides in solution means that the actual ^{29}Si coupling can be determined by the following equation: $J_{\text{obs}} = 1/3[2\times {}^1J_{\text{Si-H}(\eta^2)} + {}^2J_{\text{Si-H(terminal)}}]$.[19] If it is assumed that $^2J_{\text{Si-H(terminal)}}$ is zero, maximum $^1J_{\text{Si-H}(\eta^2)}$ values of 102 and 105 Hz are predicted for **2** and **3**, respectively. An HMQC experiment was undertaken for each species to confirm these coupling constants and to assign the solution structures of **2** and **3** definitively.[20] The data reveal a direct correlation between the ^{29}Si NMR signals of **2** and **3** and their corresponding hydride signals in the ^{1}H NMR spectrum (see Supporting Information). These data further confirm that Si–H interactions exist for **2** and **3** both in solution and in the solid state.

On the basis of the structural, spectroscopic, and DFT data, **2** and **3** are assigned as iron(II) hydride complexes featuring two η^2-Si–H interactions that give rise to η^3-H$_2$SiR$_2$ adducts of [(PhBP$^{i\text{Pr}}_3$)Fe$^{\text{II}}$H]. Although a third, very weak attractive interaction with the hydride ligand cannot be fully dismissed,[4d] such an interaction would need to be regarded as highly distinct from that of the other two H atoms, in which a strong interaction with both Si and Fe is evident. Whereas three-centered, two-electron bonding interactions in **2** and **3** are apparent in their solid-state structures, all three hydrides undergo rapid exchange in solution and appear to be chemically equivalent. It seems plausible to us that an iron(IV) silylene trihydride, shown as structure type **B** in Scheme 1, could be responsible for the rapid interconversion of the hydride positions on the NMR time scale. As noted above, isolobal [(PhBP$^{i\text{Pr}}_3$)Fe$^{\text{IV}}$(H)$_3$(PR$_3$)] species are chemically stable within this system, and the extremely short Fe–Si bond length, together with the planar nature around the Si center with respect to the methyl, phenyl, and iron substituents, suggests that virtually no structural reorganization would be required at the Si center under such a scenario. An alternative mechanism for interconversion concerns an intermediate in which the Si center interacts equivalently with all three H atoms. This would give rise to a [(PhBP$^{i\text{Pr}}_3$)Fe(η^4-H$_3$SiR$_2$)] intermediate. The possibility of a weak interaction between the Si center and the hydride ligand in the ground-state structures of **2** and **3** would set the stage for this type of dynamic pathway.[3g]

Likewise, a number of mechanistic pathways to account for the overall formation of **2** and **3** can be envisioned. Two plausible mechanisms are shown in Scheme 2. In view of the propensity for the [PhBP$^{i\text{Pr}}_3$]Fe scaffold to undergo two-



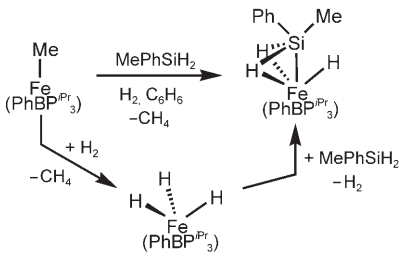
Scheme 2. Two possible mechanisms for the formation of **2**.

electron redox processes, it is perhaps most reasonable to propose an oxidative addition/reductive elimination mechanism as shown in path a.[1] In this scenario, the first step is coordination of silane followed by an oxidative addition to the Fe$^{\text{II}}$ center. Reductive 1,2-methyl migration from iron to silicon then affords an isomer of **2** (or **3**). A sigma-bond metathesis (pathway b) also provides a convenient and potentially low energy methyl-migration pathway. No intermediates could be detected when the reaction between **1** and PhSiH$_3$ was monitored by ^{1}H NMR spectroscopy at low temperature (−50 °C, [D$_8$]toluene).

Methane loss does not occur during the course of the reaction between **1** and phenylsilane or mesitylsilane, whereas such loss occurs readily when **1** is exposed to H$_2$.[1c] To probe the possibility that reversible methane loss and reactivation might be occurring prior to methyl migration, a deuterium-labeling study was undertaken. The deuterated methyl species, [(PhBP$^{i\text{Pr}}_3$)FeCD$_3$] ([CD$_3$]-**1**), is generated by addition of [D$_3$]MeLi to [(PhBP$^{i\text{Pr}}_3$)FeCl]. Reaction between [CD$_3$]-**1** and PhSiH$_3$ results in the formation of [(PhBP$^{i\text{Pr}}_3$)Fe(H)(H$_2$SiPhCD$_3$)] ([CD$_3$]-**2**) as the sole product, as evidenced by ^{1}H NMR data (see Supporting Information). Likewise, the reaction between **1** and PhSiD$_3$ results in the formation of [(PhBP$^{i\text{Pr}}_3$)Fe(D)(D$_2$SiPhMe)] ([D],[D$_2$-silyl]-**2**). These experiments appear to rule out any incipient methane formation prior to methyl migration.

Finally, **1** exhibits selectivity for primary silane substrates. No reaction is observed between **1** and secondary or tertiary silane substrates (e.g., Ph$_2$SiH$_2$ and Et$_3$SiH) over extended periods, presumably because such silanes cannot lead to the thermodynamically stable η^3-silane adduct structures. Secondary silane substrates do react, however, if **1** is exposed to H$_2$ in their presence. For example, **1** reacts with MePhSiH$_2$ to produce **2** quantitatively under a blanket of hydrogen (Scheme 3). Examination of this reaction sequence at low temperature (−20 °C, [D$_8$]toluene) reveals methane loss and the initial formation of the previously reported trihydride species [(PhBP$^{i\text{Pr}}_3$)FeH$_3$] prior to product formation.[1c] [(PhBP$^{i\text{Pr}}_3$)FeH$_3$] gradually decays as **2** appears. This sequence

 © 2006 Wiley-VCH Verlag GmbH & Co. KGaA, Weinheim



Scheme 3. Reaction of **1** with $MePhSiH_2$ under H_2.

suggests that **1** reacts with H_2 to generate a reactive hydride source that is then trapped by silane, analogous to the trapping of such hydride species by the addition of a phosphine donor.[1c]

In conclusion, it has been found that the [(PhBP$^{iPr}_3$)FeMe] complex reacts with primary aryl silanes to mediate Si–H bond activations and 1,2-methyl migrations that generate unusual η^3-H_2SiRMe silane adducts of [(PhBP$^{iPr}_3$)Fe^{II}H] (R = Ph, Mes). These iron complexes serve as relatives to the numerous Group 8 complexes of the general type [L_3M-(ER_3)H_3] (E = Si, Sn; M = Fe, Ru, Os) now known.[21] The key distinction to be drawn is that the complexes described herein feature a less-substituted Si atom that strongly attracts two Fe–H bonds—resulting in the formation of a [(PhBP$^{iPr}_3$)Fe(H)(η^3-H_2SiR_2)] complex with a very short Fe···Si distance that is distinct from, but closely associated with, its silylene isomer [(PhBP$^{iPr}_3$)Fe(H)$_3$(SiR_2)].

Received: July 19, 2005
Revised: October 12, 2005
Published online: December 21, 2005

Keywords: borates · iron · phosphanes · silanes

[1] a) T. A. Betley, J. C. Peters, *J. Am. Chem. Soc.* **2004**, *126*, 6252; b) T. A. Betley, J. C. Peters, *J. Am. Chem. Soc.* **2003**, *125*, 10782; c) E. J. Daida, J. C. Peters, *Inorg. Chem.* **2004**, *43*, 7474.

[2] For relevant examples of transition-metal–silylene complexes, see: a) J. C. Peters, J. D. Feldman, T. D. Tilley, *J. Am. Chem. Soc.* **1999**, *121*, 9871; b) B. V. Mork, T. D. Tilley, *J. Am. Chem. Soc.* **2004**, *126*, 4385; c) J. D. Feldman, J. C. Peters, T. D. Tilley, *Organometallics* **2002**, *21*, 4065; d) P. B. Glaser, P. W. Wanandi, T. D. Tilley, *Organometallics* **2004**, *23*, 693; e) C. Beddie, M. B. Hall, *J. Am. Chem. Soc.* **2004**, *126*, 13564; f) P. Glaser, T. D. Tilley, *J. Am. Chem. Soc.* **2003**, *125*, 13640.

[3] For examples of Group 8 η^2-silane adducts, see: a) S. C. Bart, E. Lobkovsky, P. J. Chirik, *J. Am. Chem. Soc.* **2004**, *126*, 13794; b) Y. Ohki, T. Kojima, M. Oshima, H. Suzuki, *Organometallics* **2001**, *20*, 2654; c) R. S. Simons, C. A. Tessier, *Organometallics* **1996**, *15*, 2604; d) E. Scharrer, M. Brookhart, *J. Organomet. Chem.* **1995**, *497*, 61; e) U. Schubert, S. Gilbert, S. Mock, *Chem. Ber.* **1992**, *125*, 835; f) E. Scharrer, S. Chang, M. Brookhart, *Organometallics* **1995**, *14*, 5686; g) F. Delpech, S. Sabo-Etienne, J.-C. Daran, B. Chaudret, K. Hussein, C. J. Marsden, J.-C. Barthelat, *J. Am. Chem. Soc.* **1999**, *121*, 6668; h) I. Atheaux, F. Delpech, B. Donnadieu, S. Sabo-Etienne, B. Chaudret, K. Hussein, J.-C. Barthelat, T. Braun, S. B. Duckett, R. N. Perutz, *Organometallics* **2002**, *21*, 5347; i) S. Lachaize, S. Sabo-Etienne, B. Donnadieu, B. Chaudret, *Chem. Commun.* **2003**, 214.

[4] For reviews that cover η^2-Si–H interactions, see: a) J. Y. Corey, J. Braddock-Wilking, *Chem. Rev.* **1999**, *99*, 175; b) U. Schubert, *Adv. Organomet. Chem.* **1990**, *30*, 151; c) G. I. Nikonov, *J. Organomet. Chem.* **2001**, *635*, 24; d) Z. Lin, *Chem. Soc. Rev.* **2002**, *31*, 239; e) G. J. Kubas, *Metal Dihydrogen and Sigma Bond Complexes: Structure, Theory, and Reactivity*, Kluwer Academic, New York, **2001**.

[5] a) I. Atheaux, B. Donnadieu, J.-C. Daran, S. Sabo-Etienne, B. Chaudret, K. Hussein, J.-C. Barthelat, *J. Am. Chem. Soc.* **2000**, *122*, 5664; b) R. Ben Said, K. Hussein, J.-C. Barthelat, I. Atheaux, S. Sabo-Etienne, M. Grellier, B. Donnadieu, B. Chaudret, *Dalton Trans.* **2003**, 4139.

[6] X.-L. Luo, D. Baudry, P. Boydell, P. Charpin, M. Nierlich, M. Ephritikhine, R. H. Crabtree, *Inorg. Chem.* **1990**, *29*, 1511.

[7] K. Hussein, C. J. Marsden, J.-C. Barthelat, V. Rodriguez, S. Conejero, S. Sabo-Etienne, B. Donnadieu, B. Chaudret, *Chem. Commun.* **1999**, 1315.

[8] N. M. Yardy, F. R. Lemke, *Organometallics* **2001**, *20*, 5670.

[9] A. L. Osipov, S. M. Gerdov, L. G. Kuzmina, J. A. K. Howard, G. I. Nikonov, *Organometallics* **2005**, *24*, 587.

[10] Crystallographic data for [(PhBP$^{iPr}_3$)Fe^{II}(H)(H_2SiPhMe)] (**2**): M_r = 660.51, red block, collection temperature = 100 K, triclinic, space group $P\bar{1}$, a = 11.3852(12), b = 12.0036(13), c = 16.1029(17) Å, α = 95.172(2), β = 107.352(2), γ = 95.805(2)°, V = 2072.9(4) Å^3, Z = 2, R_1 = 0.0309 [$I > 2\sigma(I)$], GOF = 1.068. CCDC-273356 (**2**) contains the supplementary crystallographic data for this paper. These data can be obtained free of charge from The Cambridge Crystallographic Data Centre via www.ccdc.cam.ac.uk/data_request/cif.

[11] H. Tobita, A. Matsuda, H. Hashimoto, K. Ueno, H. Ogino, *Angew. Chem.* **2004**, *116*, 223; *Angew. Chem. Int. Ed.* **2004**, *43*, 221.

[12] Crystallographic data for [(PhBP$^{iPr}_3$)Fe(H)(H_2SiMesMe)] (**3**): M_r = 702.59, red block, collection temperature = 100 K, orthorhombic, space group $P2_12_12_1$, a = 18.1126(13), b = 20.3251(14), c = 21.6417(16) Å, V = 7967.2(10) Å^3, Z = 8, R_1 = 0.0609 [$I > 2\sigma(I)$], GOF = 1.677. CCDC-27358 (**3**) contains the supplementary crystallographic data for this paper. These data can be obtained free of charge from The Cambridge Crystallographic Data Centre via www.ccdc.cam.ac.uk/data_request/cif.

[13] Jaguar 5.0, Schrodinger, LLC, Portland, Oregon, 2002.

[14] C. Lee, W. Yang, R. G. Parr, *Phys. Rev. B* **1988**, *37*, 785.

[15] NBO 5.0, E. D. Glendening, J. K. Badenhoop, A. E. Reed, J. E. Carpenter, J. A. Bohmann, C. M. Morales, F. Weinhold, Theoretical Chemistry Institute, University of Wisconsin, Madison, 2001; http://www.chem.wisc.edu/≈nbo5.

[16] R. H. Crabtree, M. Lavin, L. Bonneviot, *J. Am. Chem. Soc.* **1986**, *108*, 4032.

[17] For comparison, the recently reported [(PhBP$^{iPr}_3$)Fe(H)$_3$(PMe_3)] complex exhibits a $T_{1\,min}$ of 140 ms.[1c]

[18] The ^{29}Si{^{1}H} signal for **3** appears as a sharp quartet ($^2J_{Si\text{-}P}$ = 61 Hz) while the signal for **2** is a broad singlet.

[19] F. L. Taw, R. G. Bergman, M. Brookhart, *Organometallics* **2004**, *23*, 886–890.

[20] R. M. Silverstein, F. X. Webster, *The Spectrometric Identification of Organic Compounds*, 6th ed., Wiley, New York, **1998**, chap. 6, pp. 262.

[21] For examples, see: a) S. Gilbert, M. Knorr, S. Mock, U. Schubert, *J. Organomet. Chem.* **1994**, *480*, 241; b) L. J. Procopio, D. H. Berry, *J. Am. Chem. Soc.* **1991**, *113*, 4039; c) C. E. F. Rickard, W. R. Roper, S. D. Woodgate, L. J. Wright, *J. Organomet. Chem.* **2000**, *609*, 177; d) K. Hubler, U. Hubler, W. R. Roper, P. Schwerdtfeger, L. J. Wright, *Chem. Eur. J.* **1997**, *3*, 1608–1616.

 © 2006 Wiley-VCH Verlag GmbH & Co. KGaA, Weinheim

Mesoporous Materials

DOI: 10.1002/anie.200502332

Crystal-to-Crystal Phase Transition in Self-Assembled Mesoporous Iron Oxide Films**

*Torsten Brezesinski, Matthijs Groenewolt, Markus Antonietti, and Bernd Smarsly**

In the past years, various types of mesoporous metal oxide films featuring crystalline pore walls have been synthesized by our group,[1] but the preparation of mesoporous crystalline iron oxides has remained a challenge. Magnetic nanoparticles of the iron oxides magnetite (Fe_3O_4) and maghemite (γ-Fe_2O_3) are already used for magnetic data storage[2] and biomedical applications,[3] and similar applications are envisaged for magnetic mesoporous materials. Furthermore, mesoporous iron oxide films offer potential as materials for electrodes,[4] (magneto)optical devices,[5] and catalysts.[6] In particular, interest in hematite (α-Fe_2O_3) has increased, owing to its ferrimagnetic behavior, and catalytic and sensoric activity.[7] For all of these applications, homogeneous mesoporous thin films are desirable.

Although nanocrystalline iron oxide aerogels,[8] as well as mesostructured amorphous iron oxides have been synthesized,[9] mesoporous crystalline films have not been reported to date, for several reasons. Firstly, similar to alumina precursors, iron species feature a complex sol–gel behavior and a strong gelation tendency. Secondly, iron oxides display an intricate crystallization behavior, forming a variety of crystalline phases, including many with nonstoichiometric compositions.[10] Thirdly, the preparation of regular mesopore structures by sol–gel processing is further impeded by the fact that these procedures usually lead to the initial formation of goethite (α-FeOOH). This iron oxide modification has to be transformed into another modification through a crystal-to-crystal phase transition, which can potentially disrupt the mesostructure.

Herein, we report the synthesis of crack-free mesoporous α-Fe_2O_3 and α-FeOOH thin films using the evaporation-induced self-assembly (EISA) process and a subsequent, straightforward heat-treatment step. The problems listed above were overcome through the use of appropriate novel block copolymer templates, namely, poly(isobutylene)-*block*-poly(ethylene oxide) (PIB–PEO),[11] which features an ultrahydrophobic poly(isobutylene) block, and the recently developed poly(ethylene-co-butylene)-*b*-poly(ethylene oxide) (KLE).[12] Both block copolymers tolerate the extreme processing conditions in the EISA process. Additionally, the size of the micelles generated by these block copolymers was selected to be larger than those of the pluronic surfactants that are usually applied. Hence, the micelle/pore size was of a suitable dimension to be mapped by nanocrystals without destruction of the mesostructure at the onset of crystallization. A similar process was successfully applied in the preparation of mesoporous nanocrystalline perovskites.[13] However, in contrast to these oxides, iron oxide undergoes a crystal-to-crystal phase transition from goethite to hematite. We, therefore, investigated the mesostructural changes that occur with the phase transition, and the peculiarities of crystallization behavior within mesoscopic confinement.[14]

Transmission electron microscopy (TEM) images obtained after heat treatment of films at 450 °C depict the well-ordered mesostructure, which is composed of pores with an average diameter of approximately 10 nm (Figure 1 a). Moreover, they reveal that the samples are highly homogeneous. The corresponding selected-area electron diffraction (SAED) pattern displays rings characteristic of a structure composed of small domains with their crystallographic axes randomly oriented with respect to one another (Figure 1 b).

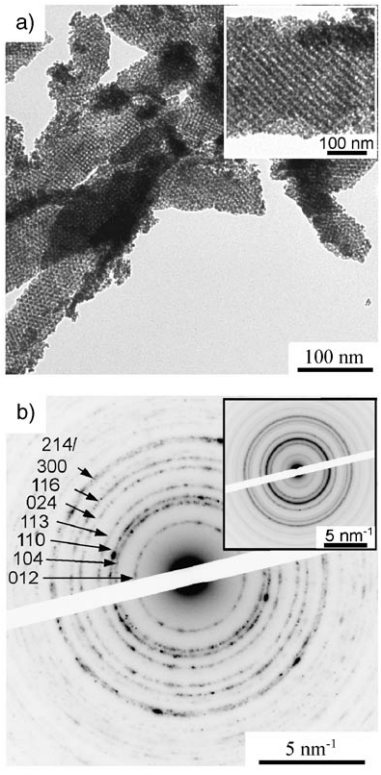


Figure 1. a) TEM images of a mesoporous α-Fe_2O_3 film after heat treatment at 450 °C; the inset is a magnification. b) SAED pattern of the same zone, showing diffraction rings corresponding to the α-phase of Fe_2O_3; the inset depicts the first crystalline modification (α-FeOOH) found at 300 °C.

[*] Dr. T. Brezesinski, Dr. M. Groenewolt, Prof. Dr. M. Antonietti, Dr. B. Smarsly
Max Planck Institute of Colloids and Interfaces
Research Campus Golm
14424 Potsdam (Germany)
Fax: (+49) 331-567-9502
E-mail: bernd.smarsly@mpikg.mpg.de

[**] We thank Prof. Dr. Ken-ichi Iimura for the XPS analyses, Ines Below and Dr. Helmut Schlaad for providing the block copolymers, and Dr. Heinz Amenitsch for help with the in situ 2D-SAXS measurements at the Elettra synchrotron facility in Trieste. Financial support by the Max Planck Society is gratefully acknowledged.

Supporting information for this article is available on the WWW under http://www.angewandte.org or from the author.

 © 2006 Wiley-VCH Verlag GmbH & Co. KGaA, Weinheim

The *d*-spacings could be unambiguously assigned to hematite, the α-phase of Fe_2O_3, which is the most thermodynamically stable form of FeO_x. The crystallite size was determined to be approximately 7–10 nm. At temperatures below 350 °C, SAED revealed that α-FeOOH is formed as the low-temperature modification (Figure 1 b, inset).

Atomic force microscopy (AFM) demonstrated that the pores are accessible from the top and showed the smooth, crack-free surface of the films (see Supporting Information). In addition, Brunnauer–Emmet–Teller (BET) analysis using Krypton as adsorbent (77 K) gave a surface area of 150 $m^2 g^{-1}$, indicating that the majority of the mesopores are accessible.

FeO_x species containing exclusively Fe^{3+} ions were obtained after heat treatment of the films, probably because $FeCl_3$ was employed as the precursor. Various experiments were, therefore, performed in an attempt to generate other species. These experiments involved iron oxide precursors of different valences and thermal treatment of the films under an inert atmosphere. In general, Fe_3O_4, the spinel-type iron oxide, was difficult to obtain by sol–gel processing, as Fe^{2+} tends to oxidize to Fe^{3+}; Fe_3O_4 oxidizes to γ-Fe_2O_3 with preservation of the lattice structure. Because of the poor sol–gel chemistry of Fe^{2+} salts, films of fair optical quality without structuring on the mesoscale were obtained. Interestingly, the use of stoichiometric amounts of Fe^{2+} and Fe^{3+} precursors also resulted in α-Fe_2O_3, demonstrating the distinct sensitivity of Fe^{2+} ions towards oxidation. These findings indicate that the preparation of mesoporous Fe_3O_4 and γ-Fe_2O_3 films by the sol–gel route is substantially more difficult than the synthesis of α-FeOOH and α-Fe_2O_3 films.

To elucidate the influence of mesoscopic confinement on the crystallization behavior, a nonporous powder was prepared without polymer template. Wide-angle X-ray scattering (WAXS) of this reference material revealed that the first crystalline phase formed (goethite) transforms completely into hematite at 300 °C (see Supporting Information).[15] Interestingly, in mesostructured films, this crystal-to-crystal phase transition does not take place below 350 °C, pointing to the retardation of nucleation and crystal growth within the thin walls of the scaffold. The retention of mesostructural order can be attributed to the relatively high thermal stability of the novel block copolymers. Pluronic surfactants, on the other hand, decompose entirely at 350 °C. The PIB–PEO and the KLE porogens were shown to facilitate the preservation of mesoscopic order up to 400–450 °C, that is, during the conversion of the amorphous matrix into its crystalline counterpart.[16]

For direct comparison, thin films were prepared using pluronic F127 to shed more light on the influence of the template stability on mesostructural integrity during the crystal-to-crystal phase transition from α-FeOOH to α-Fe_2O_3. Small-angle X-ray scattering (SAXS) and TEM showed that the use of 30 wt. % porogen, with respect to the amount of α-Fe_2O_3 formed, resulted in films with good optical quality and well-ordered mesostructure (see Supporting Information). Mesostructural collapse was observed at approximately 350 °C, because the complete thermal decomposition of the pluronic template was faster than the recrystallization of the iron oxide matrix. This finding suggests that porogens with higher thermal stability are necessary for the preservation of mesostructure, in the presence of stresses induced by the phase transition.

X-ray photoelectron spectroscopy (XPS) was used to gain further insight into the chemical composition of the mesoporous iron oxide thin films after the onset of crystallization. The XPS data were in good agreement with a reference of almost pure α-Fe_2O_3.[17] Figure 2 demonstrates that the thin

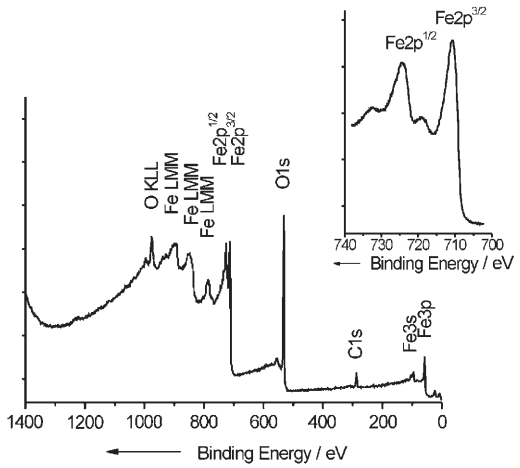


Figure 2. XPS survey spectrum of a mesoporous iron oxide film after heat treatment at 450 °C, confirming the generation of α-Fe_2O_3. The inset is a high-resolution expansion of the Fe2p energy region, showing the complex line shape and the characteristic Fe^{3+} satellite peak.

layers consist of iron, oxygen, and a small amount of contaminating carbon. Moreover, no other impurities, such as chlorides arising from the use of the $FeCl_3$ precursor, could be detected. The $Fe2p^{3/2}$ binding energy of 710.8 eV and the corresponding satellite peak at 718.8 eV, a result of charge transfer screening, can be solely attributed to the presence of Fe^{3+} ions of α-Fe_2O_3. The ratio of atomic concentrations calculated from the O1s and Fe2p peak areas deviates slightly from the theoretical value of 1.5, but it has been reported that quantitative analysis of the XPS data of iron oxides involves certain difficulties (such as, OH groups on the surface and photoreduction of Fe^{3+}).[17]

The temperature-dependent evolution of the mesostructure was also investigated by in situ 2D-SAXS, using a charge-coupled device (CCD) camera (Figure 3), and by 1D-SAXS in symmetric reflection mode, using an energy-dispersive detector (Figure 4). At a temperature of 100 °C, the typical 2D-SAXS scattering pattern of a distorted cubic arrangement of micelles is observed. Similar patterns have been observed for metal oxide systems made with the KLE block copolymer.[1,13] Up to 450 °C, the 2D-SAXS patterns become increasingly ellipsoidal, indicating an anisotropic shrinkage of the mesostructure, in the direction normal to the substrate. Evidently, the transition from α-FeOOH to α-Fe_2O_3 does not affect the mesoscopic order at all, as indicated by the relatively unchanged 2D-SAXS patterns below 450 °C. This finding is remarkable in light of the mechanical stresses that accompany crystal-to-crystal phase transitions. At 600 °C, only broad signals are observed, suggesting degradation of the meso-

 © 2006 Wiley-VCH Verlag GmbH & Co. KGaA, Weinheim

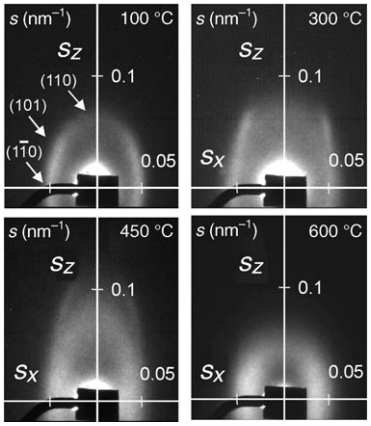


Figure 3. In situ 2D-SAXS measurements, performed during thermal treatment of an iron oxide film, demonstrate the evolution of the bcc arrangement of mesopores as a function of temperature. The scattering patterns are blurred owing to the X-ray fluorescence of iron oxide.

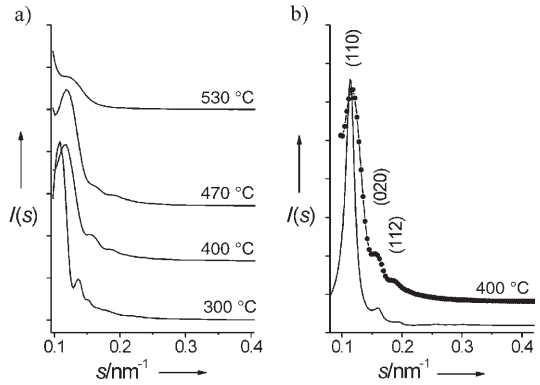


Figure 4. a) 1D-SAXS patterns of mesoporous iron oxide films obtained during various heat-treatment steps. b) Experimental 1D-SAXS pattern of a film treated at 400 °C (circles, line to guide the eye) and the corresponding curve fitting (solid line), which is displaced from the experimental curve for better visualization.

structural order because of diffuse sintering of the nanocrystallites. Thus, the 2D-SAXS patterns demonstrate that an intact cubic mesostructure exists up to temperatures of at least 450 °C.

The 1D-SAXS pattern of a sample heat treated at 400 °C (that is, after the crystal-to-crystal phase transition) displays a sequence of interference maxima, which are attributed to the (110), (020), and (112) reflections of a bcc arrangement of mesopores (Figure 4b). These reflections are in apparent contradiction to the [110] orientation observed in 2D-SAXS, but can be explained by the slit-shaped beam profile of the 1D-SAXS setup used.[18] A recently described procedure was used to quantitatively analyze the lattice parameter and the mesopore size.[12,19] This method provides an average pore diameter of 8 nm and a lattice parameter of 14 nm in the direction normal to the substrate. Note that the reflections are observable up to 470 °C, indicating the regularity of the pore arrangement even at elevated temperatures.

In summary, this study suggests that mesoporous films composed of nanocrystalline phase-pure α-Fe_2O_3 can be obtained by the EISA process using novel block copolymer templates. Porogens featuring a high hydrophilic–hydrophobic contrast and a relatively high thermal stability, such as PIB–PEO and KLE, were able to stabilize the mesostructured scaffold during conversion of the lattice structure from α-FeOOH into α-Fe_2O_3. Hence, the approach described herein could present a general strategy for the preparation of mesoporous films of other metal oxides that undergo crystal-to-crystal phase transitions.

Experimental Section

PIB–PEO (85 mg) was dissolved in EtOH (2 mL) and added to a solution containing $FeCl_3$ (400 mg) and H_2O (300 mg) in a mixture of THF (1 mL) and EtOH (4 mL). The resulting isotropic sol was stirred for 6 h before it was used. Mesostructured thin films were prepared by dip-coating silicon substrates or glass at a constant withdrawal rate (6 mm s^{-1}) and relative humidity (15–20%). Finally, mesoporous crystalline FeO_x films were obtained through controlled nanocrystallization, by heating with a ramp of 5 °C min^{-1} in air. For the in situ 2D-SAXS experiments the heating ramp was adjusted to 10 °C min^{-1} (no significant difference was observed for the different heating rates).

Received: July 4, 2005
Revised: September 29, 2005
Published online: December 21, 2005

Keywords: electron microscopy · iron oxide · mesoporous materials · phase transitions · self-assembly

[1] a) T. Brezesinski, C. Erpen, K. Iimura, B. Smarsly, *Chem. Mater.* **2005**, *17*, 1683–1690; b) M. Kuemmel, D. Grosso, C. Boissière, B. Smarsly, T. Brezesinski, P. A. Albouy, H. Amenitsch, C. Sanchez, *Angew. Chem.* **2005**, *117*, 4665–4668; *Angew. Chem. Int. Ed.* **2005**, *44*, 4589–4592.
[2] Q. A. Pankhurst, R. J. Pollard, *J. Phys. Condens. Matter* **1993**, *5*, 8487–8508.
[3] Q. A. Pankhurst, J. Connolly, S. K. Jones, J. Dobson, *J. Phys. D* **2003**, *36*, R167–R181.
[4] P. Poizot, S. Laruelle, S. Grugeon, L. Dupont, J. M. Tarascon, *Nature* **2000**, *407*, 496.
[5] D. R. Rolison, *Science* **2003**, *299*, 1698.
[6] a) L. Y. Wang, L. Han, J. Luo, C. I. Zhong, *Abstr. Pap. Am. Chem. Soc.* **2004**, *228*, U473–U473; b) B. V. Reddy, S. N. Khanna, *Phys. Rev. Lett.* **2004**, *93*, 068301.
[7] a) D. H. Chen, D. R. Chen, X. L. Jiao, Y. T. Zhao, *J. Mater. Chem.* **2003**, *13*, 2266–2270; b) M. Pelino, C. Colella, C. Canatalini, M. Faccio, G. Ferri, A. Damico, *Sens. Actuators B* **1992**, *7*, 464–469.
[8] J. W. Long, M. S. Logan, C. P. Rhodes, E. E. Carpenter, R. M. Stroud, D. R. Rolison, *J. Am. Chem. Soc.* **2004**, *126*, 16879–16889.
[9] a) F. Jiao, P. G. Bruce, *Angew. Chem.* **2004**, *116*, 6084–6087; *Angew. Chem. Int. Ed.* **2004**, *43*, 5958–5961; b) G. Wirnsberger, K. Gatterer, P. Behrens, *J. Mater. Chem.* **1998**, *8*, 1509–1510.
[10] A. F. Holleman, E. Wiberg, *Lehrbuch der Anorganischen Chemie*, de Gruyter, Berlin, **1995**.
[11] M. Groenewolt, T. Brezesinski, H. Schlaad, M. Antonietti, P. G. Groh, B. Ivan, *Adv. Mater.* **2005**, *17*, 1158–1162.
[12] A. Thomas, H. Schlaad, B. Smarsly, M. Antonietti, *Langmuir* **2003**, *19*, 4455–4459.
[13] D. Grosso, C. Boissière, B. Smarsly, T. Brezesinski, N. Pinna, P. A. Albouy, H. Amenitsch, M. Antonietti, C. Sanchez, *Nat. Mater.* **2004**, *3*, 787–792.

 © 2006 Wiley-VCH Verlag GmbH & Co. KGaA, Weinheim

[14] P. D. Yang, D. Y. Zhao, D. I. Margolese, B. F. Chmelka, G. D. Stucky, *Nature* **1998**, *396*, 152 – 155.
[15] A. F. Gualtieri, P. Venturelli, *Am. Mineral.* **1999**, *84*, 895 – 904.
[16] T. Brezesinski, B. Smarsly, K. Iimura, D. Grosso, C. Boissière, M. Antonietti, C. Sanchez, *Small* **2005**, *1*, 889 – 898.
[17] a) S. Gota, E. Guiot, M. Henriot, M. G. Soyer, *Phys. Rev. B* **1999**, *60*, 14387 – 14395; b) Q. X. Wang, H. B. Pan, B. Z. Song, H. Z. Li, *J. Inorg. Mater.* **2002**, *17*, 782 – 786.
[18] H. Miyata, T. Noma, M. Watanabe, K. Kuroda, *Chem. Mater.* **2002**, *14*, 766 – 772.
[19] B. Smarsly, C. Göltner, M. Antonietti, W. Ruland, E. Hoinkis, *J. Phys. Chem. B* **2001**, *105*, 831 – 840.

 © 2006 Wiley-VCH Verlag GmbH & Co. KGaA, Weinheim

Biotechnology

DOI: 10.1002/anie.200502620

Virus-Engineered Colloidal Particles—A Surface Display System**

*Martin Fischlechner, Lars Toellner, Paul Messner, Reingard Grabherr, and Edwin Donath**

Colloidal particles have become valuable tools in biotechnology and medicine. Even a small sample provides a huge surface which can be engineered in many ways. One of the most versatile ways to engineer the surface of colloidal particles is to coat them with a polyelectrolyte multilayer by means of the layer-by-layer (lbl) technology.[1] Multifunctional composite colloidal devices can be fabricated in this way with nanometer precision in a radial direction. Since most of the important biomolecules—nucleic acids, proteins, and many carbohydrates—are essentially polyelectrolytes, the lbl technology has the potential to generate complex colloidal multilayer composites consisting of biological and artificial building blocks. This technology can thus be seen as a promising platform for the fabrication of bio-nanocomposite systems with inbuilt biological, chemical, and physical functions.[2]

Recently, lbl technology has been extended by fusing a virus membrane with a lipid layer on top of a polyelectrolyte multilayer cushion with the purpose of fabricating particles carrying virions on their surface.[3] Specifically, rubella virus like particles (RLPs) lacking the viral genome were crafted onto the colloidal surface of lipid-coated lbl colloids by employing membrane fusion at decreased pH values. To demonstrate the general aspect of this approach and, especially, to outline the versatility of possible surface modifications by the use of genetically modified virions, baculoviruses displaying foreign peptides on their surface were used as building blocks.

Baculoviruses, here *Autographa californica* nuclear polyhedrosis virus (*Ac*NPV), have been developed to a surface display system for the screening of genetic libraries.[4,16] By displaying foreign peptides fused with the major-envelope glycoprotein gp64 at the surface of the virus,[5] it was possible to select surface-modified virions with a desired binding property. Colocalization of the displayed polypeptide and the corresponding gene makes it possible to propagate the "binders" and to further enrich these viruses, thus leading to a pool or a single clone decorated with a desired functional polypeptide. The fact that no a priori knowledge of the genetic sequence is necessary and that entire pools can be screened explains the impact of the several surface display systems developed in biotechnology[6] and, recently, also in materials science.[7]

Herein, we show how combining the baculovirus surface display system with colloidal particles has a number of advantages. For example, further functions can be added to the particles without interfering with those provided by the virus, by either engineering the multilayers underneath the lipid layer or the particle core in a desired way. This situation would not be possible with the virus display system alone. In particular, it would be hard to add functions to the virus other than those of the displayed peptide, simply because of the lack of available space and engineering possibilities. Furthermore, the handling of colloidal particles by modern sorting and analytical machines is well established.

A lipid bilayer adsorbed to the polyelectrolyte multilayer support[8] provides the starting point for further functionalization. The advantage of this approach is that the versatility of the lbl technology in regards to the composition and properties of the polyelectrolyte multilayer is combined[9] with an interface similar to biological systems.

Given the proper composition of the lipid layer on top one can attempt fusion with enveloped viruses at low pH values, that is, under conditions comparable to those inside endosomes.[3] This approach mimics the second step of the infection mechanism of many lipid-enveloped viruses.[10] After fusion, the virions present their membrane proteins on the colloidal surface. If virions which display engineered polypeptides on their surface are employed, these epitopes are also presented on the colloidal surface.

[*] Dipl.Ing M. Fischlechner, Dr. L. Toellner, Prof. Dr. E. Donath
Institute of Medical Physics and Biophysics
Leipzig University
Härtelstrasse 16–18, 04107 Leipzig (Germany)
Fax: (+49) 341-971-5749
E-mail: done@medizin.uni-leipzig.de
Prof. Dr. P. Messner
Center for NanoBiotechnology
University of Natural Resources and Applied Life Sciences
1180 Vienna (Austria)
Prof. Dr. R. Grabherr
Institute of Applied Microbiology
University of Natural Resources and Applied Life Sciences
1190 Vienna (Austria)

[**] This research was supported by a grant from the Volkswagenstiftung within the framework of the program "Complex Materials" (VW foundation I/78 168). We thank Wolfgang Ernst for advice and discussions, Alexandra Spenger for the construction of *Ac*COIN-3D6, Nicole Borth for help with FACS analysis, and Harald Berger for support with CLSM imaging. Many thanks to Julia Romanova and Boris Ferko for influenza A viruses and Bernhard Benke for designing Figure 1.

InterScience
© 2006 Wiley-VCH Verlag GmbH & Co. KGaA, Weinheim

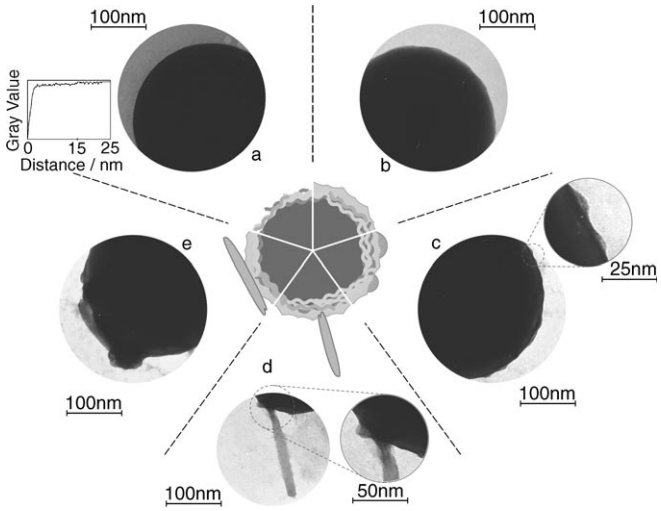


Figure 1. Transmission electron microscopy images of coated silica colloids: a) coated with 5 polyelectrolyte layers (PAH/PSS). A radial intensity scan is shown in the inset. The layer is identified as a slightly less dense outer region. b) Sample (a) with an additional lipid bilayer. c) RLPs fused with sample (b). d) and e): Sample (b) decorated with baculovirions. A virion is fused at its pole with the composite surface in (d), while a virion lies flat on the surface of the colloid in (e).

Figure 1 shows electron microscopy images of virus-decorated silica particles at different stages of the coating protocol. While the presence of the polyelectrolyte supporting layer in Figure 1 a is not directly visible, a closer inspection of the radial intensity distribution (see inset) revealed its presence. A polyelectrolyte layer thickness of about 15 ± 2 nm was inferred from intensity line scans. The layer is rather smooth, probably as a result of drying it under the vacuum in the electron microscope. The heavy staining by the uranyl ions is explained by their strong interaction with the cations of the layer. The presence of the lipid layer in Figure 1 b is immediately evidenced by a less-stained layer with a thickness of about 15–20 nm at the surface of the silica particle. This layer is composed of both the polyelectrolyte support and the adjacent lipid layer. The less-efficient staining in Figure 1 b compared to Figure 1 a is presumably caused by the limited permeability of the uranyl ions through the lipid layer.

If these lipid-coated lbl colloids are incubated with virions in a buffer at low pH values (pH 4.5), fusion between the viral membrane and the lipid layer takes place to give virus-decorated particle surfaces. Baculoviruses can be seen attached to the surface of the colloidal particles in Figure 1 d and e. Interestingly, the baculoviruses are quite often found in an upright position (Figure 1 d), thus indicating the inherent asymmetry of the fusion protein distribution over their surface.[11] The membrane fusion proteins are thought to be preferentially found at one end of the virus, but viruses lying flat on the surface can also be found.

This approach is by no means restricted to baculoviruses. There are many degrees of freedom to subclone engineered polypeptides into other virions or viruslike particles which can subsequently be fused with the lipid layer attached to the colloid.[12] For example, Figure 1 c shows lipid-coated lbl colloids fused with rubella virus like particles (RLPs).[13]

The set of proteins displayed on the colloidal surface can be monitored by immunofluorescence, which is a quantitative measure if analyzed by flow cytometry (fluorescence-assisted cell sorting, FACS). The fluorescence intensities of particles with a diameter of 1 μm displaying wild-type *Ac*NPV are shown in Figure 2 a and b. The presence of the baculovirus

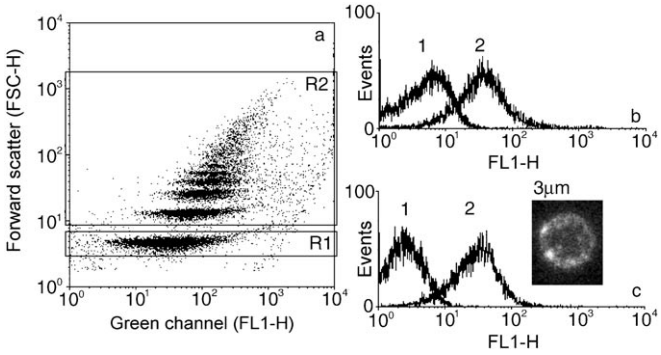


Figure 2. a) and b): Immunofluorescence against 1-μm lipid-coated colloids fused with wild-type baculovirions (wt-*Ac*NPV). a) Dot plot, where each dot provides a measured event, for which the forward scattering (FSC-H) and the fluorescence in the FITC channel (FL1-H) were recorded and used for subsequent analysis. Region R1 is assigned to single colloids, and R2 to particle aggregates. b) Single colloids have been gated and their fluorescence versus particle counts are shown. Curve 1: Lipid-coated lbl colloids, curve 2: lipid-coated lbl colloids fused with wt-*Ac*NPV. c) Inset: CLSM scan of a 3-μm colloid coated with *Ac*NPV displaying an antibody-binding fragment of HIV-1 gp120 (curve 2). Curve 1: colloids with wt-*Ac*NPV; curve 2: colloids displaying the HIV-1 gp120 epitope on their surface.

membrane fusion protein gp64 was detected with B12D5, a monoclonal, mouse-derived anti-gp64 antibody,[14] followed by incubation with a secondary anti-mouse conjugate labeled with fluorescein isothiocyanate (FITC), which actually provided the fluorescence signal in the FL1-H channel. Figure 2 a shows a dot plot of the fluorescence intensity of colloids coated with wild-type *Ac*NPV against the respective forward-scattering intensity. The scatter plot R1 of the FACS signal represents the population of single coated colloids, whereas region R2 summarizes the aggregates of order two and higher. The resolution is sufficient to resolve aggregates up to the sixth order. The quality of the preparations in terms of the presence of aggregates depends largely on the lipid-coating step and decreases slightly as the size of the colloids decrease. Whereas the preparation of 1-μm lbl colloids in Figure 2 a shows 40 % single colloids, the percentage of single particles in the case of 3-μm colloids is about 75 %. Single particles corresponding to R1 in Figure 2 a have been gated and are shown in terms of fluorescence intensity versus particle counts in Figure 2 b. Curve 2 refers to 1-μm lipid lbl colloids coated with wild-type *Ac*NPV. Curve 1 represents the control measured before the virus was added. In Figure 2 c baculoviruses were employed which had a 17 amino acid long epitope of HIV-1 gp120 glycoprotein engineered to their surface. The inset in Figure 2 c shows a confocal laser scanning

 © 2006 Wiley-VCH Verlag GmbH & Co. KGaA, Weinheim

microscopy (CLSM) image obtained with immunofluorescence. Although the resolution of the CLSM device is not sufficient to determine the size and shape of the coated baculoviruses exactly, the fluorescent spots on the colloidal surface indicate the presence of the viral elements. Figure 2c compares the immunofluorescence of particles carrying a virus displaying a HIV-1 gp120 glycoprotein fragment[15] (curve 2) with the fluorescence of particles covered with the wild-type virus (curve 1). The engineered HIV-1 gp120 glycoprotein fragment is clearly detectable.

This presence of the engineered HIV-1 gp120 antibody-binding fragment on the colloidal surface can be regarded as a "proof of principle", which consists of linking a combinatorial surface display strategy, that is, the so-called epitope mapping approach,[16,4] with the engineering of a functional colloidal surface.[1]

The direct use of the viral building elements, which had been previously screened for functional polypeptide, has the major advantage that a loss of the functionality of the screened epitope is rather unlikely to occur. In phage display systems, the functional polypeptide is, for example, selected on a phage. When it is subsequently used attached to another surface there is always a potential risk that functionality is lost, since the latter was provided in part by the phage surface itself or by the peptide–phage interaction and not by the peptide alone.

Fusion of viruses with the lipid-coated lbl composites, which is the key step of coating, is closely related to the infectivity of the virions. This ensures that the virus surface properties can be transferred to the lbl composites as long as the virions can still be produced and propagated in the cell culture despite the introduced surface-protein modifications. Therefore it is possible to equip the lipid-coated colloids with a number of functions if virus populations displaying different epitopes or different virus species are mixed before coating.

To prove this idea, a 1:1 mixture of two different baculovirus populations—one displaying the streptag peptide, a molecular mimic of biotin, the other displaying an epitope derived from HIV-1 gp41[17]—was prepared. Figure 3a shows the results obtained with the colloids coated with only the streptag-displaying baculoviruses, Figure 3c corresponds to colloids coated with viruses displaying only the HIV-1 gp41 epitope, and Figure 3b corresponds to colloids coated with a mixture of both baculo clones. All three samples were incubated with streptavidin labeled with Quantum Red for the detection of the streptag epitope, with the anti HIV-1 gp41 antibody 3D6, and with an anti-human, FITC-labeled antibody conjugate, respectively. The dot plots shown in Figure 3a, b, and c demonstrate the specific binding of the fluorescent conjugates on the three different colloidal surfaces. The streptag epitope carrying colloids show up as the right-most fluorescence distribution in the red channel (FL3-H) and as the left-most distribution in the green FITC channel (FL1-H). The appearance of the HIV-1 gp41 epitope carrying colloids is the opposite way round. Colloids carrying both epitopes, which were prepared from the mixture, show an intermediate distribution in both channels, thus indicating that sample b indeed displays both engineered epitopes on its surface, however, as expected, at a diminished frequency.

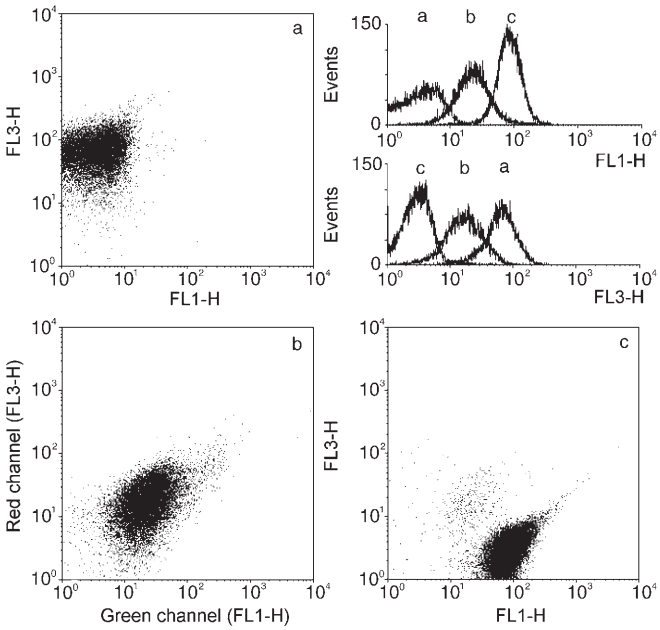


Figure 3. Dot plots of 3-μm colloids fused with two different genetically engineered baculoviruses: a) with baculoviruses displaying streptag, c) with virions displaying an HIV-1 gp41 epitope, b) with a mixture of both. Whereas in (a) and (c) only one epitope is evident, both epitopes show up in (b). The FITC-channel (FL1-H) was used for antibody detection, while the Quantum Red fluorescence sensitive channel (FL3-H) was used for streptag detection.

Baculoviruses displaying the streptag peptide were chosen since they substantially extend the display possibilities of the system. The streptag peptide binds with great specificity to streptavidin which, as a result of its four biotin binding sites, can be used as a molecular linker between the viruslike surface of the lbl composite and biotinylated species. If a desired sequence, for example, cannot be displayed, because it interferes with fusion, it can nevertheless be added afterwards by utilizing the streptag linker.

When using viruses as modules for the colloidal display system, it is of great interest as to whether they can still be propagated after they have become part of the colloidal composite. On one hand virus viability is crucial in regards to the issue of biological safety,[18] while on the other hand it has a large impact on the technology itself. For example, if viruses attached to colloids can be propagated, this would allow screening of the engineered functionalities at the level of the composites themselves. Thus, experiments were performed with baculoviruses which contain an expression cassette on their genome encoding for the green fluorescent protein (GFP).[19] They were coated onto 3-μm particles and added to *Spodoptera frugiperda* (*Sf*9) cells. The coated colloids were readily endocytosed and could be detected inside the cells. Particles inside endosomes and also free particles in the cytoplasma have been observed. The possibility of propagation is closely connected to the stability of the composite within a biological environment. Two different samples were prepared, one carrying rather stable poly(allylamine hydrochloride) and poly(sodium 4-styrenesulfonate) (PAH/PSS) layers and the other containing the biologically degradable

 © 2006 Wiley-VCH Verlag GmbH & Co. KGaA, Weinheim

protamine/dextrane sulfate couple. Protamine release has been shown previously for the latter sample.[20] The cells were tested after 72 h for GFP expression by means of FACS analysis. The CLSM image in Figure 4 indeed shows a virus-infected, GFP-expressing *Sf*9 cell with one visible particle appearing as a dark sphere in the bottom right region of the cell. The image recorded in the transmission mode shows that not all cells express GFP. GFP expression is quantified in Figure 4 (panels 1–4). The control images 1, 2a, and 3a show no transfection, thus proving the absence of viruses in the supernatant. Only a small rate of transfection (2.3%) was observed when lbl colloids with a PAH/PSS support were applied. Baculoviruses on colloids with protamine/dextrane sulfate layers underneath the lipid layer, however, led to considerable transfection of 18.9%, which is about ten times more than with PAH/PSS. The transfection rate achieved by adding free virus to the cell culture reached a value of 64.6%. Although more insight into the mechanism of decomposition of such composites is needed, the stability of the polyelectrolytes used for the assembly seems to play an important role for the decomposition of the viruslike surface. It cannot be excluded either that the lipid polyelectrolyte interaction may contribute to the difference in transfection efficiencies.

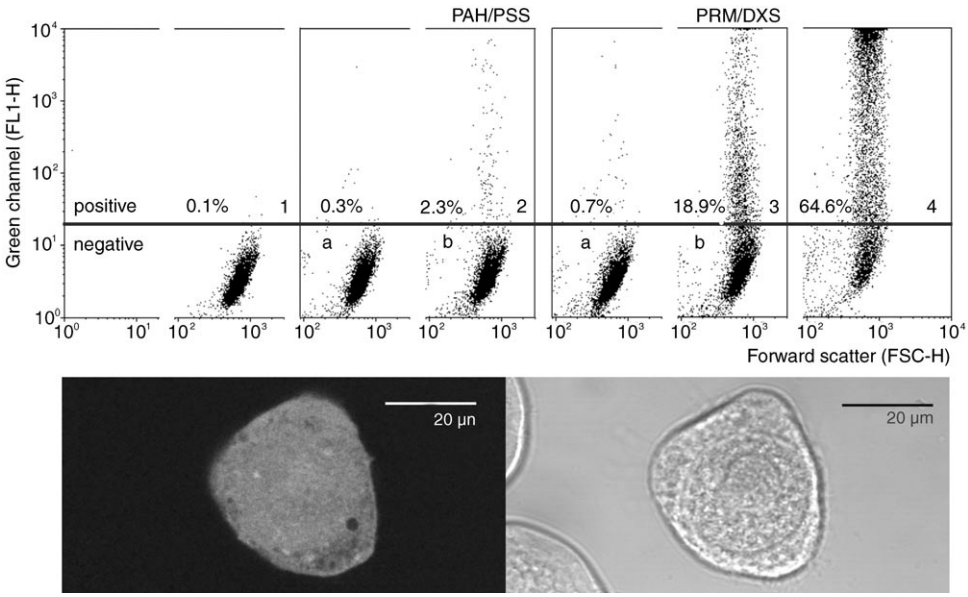


Figure 4. FACS dot plots (FL1-H versus FSC) of *Sf*9 cells incubated for 72 h with baculovirus-coated 3-µm colloids. The baculoviruses contained a GFP-expression cassette to monitor infection. GFP is recorded in FL1-H. Panel 1: control cells, panel 2b: cells incubated with virus-coated colloids carrying a PAH/PSS multilayer support; panel 3b: with protamine/dextrane sulfate support; panel 4: cells inoculated with free baculoviruses; panels 2a and 3a: controls, cells incubated with supernatants of the colloidal samples. The CLSM image shows a GFP-expressing *Sf*9 cell with an incorporated 3-µm colloid. The transmission image demonstrates the presence of two other cells which have not been transfected.

Experiments are currently under way to explore the technological potential of these engineered systems in diagnostics and other fields. For example, a bead array with four particle populations of different fluorescence intensity carrying *Ac*NPV with the HIV-1 gp120 epitope, wild-type *Ac*NPV, UV-inactivated influenza A/PR8, and influenza A type Singapore were prepared, mixed, and added to sera containing antibodies to either one of these antigenes. Figure 5 shows that the presence of the antibodies can be verified. The advantage of the bead array approach is that very small sample volumes are required. The virus-decorated lbl particles can be easily prepared and provide a great versatility in regard to the use of antigenes given the possibilities of the display approach. It is worth mentioning that the lipid layer serves not only as a means for virus fusion during the process of fabrication, but, most importantly, inhibits in a universal manner nonspecific interactions with the antibodies, a major problem associated with surface-bound antigenes.

Although there are many challenging questions left, the suggested colloid/lbl/lipid layer/virus composite may have considerable technological potential. It provides flexibility, is

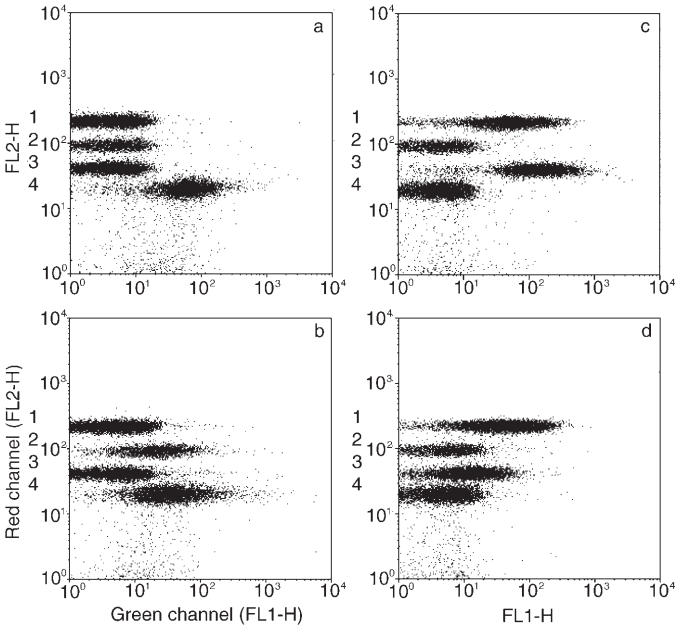


Figure 5. FACS dot plots of virus-decorated lbl colloids used as a bead array for antibody detection. Particles carrying different amounts of fluorescent polyelectrolyte layers in the red channel (FL2-H) and four different virus species, respectively. 1: influenza A/Singapore, 2: wild-type *Ac*NPV, 3: influenza A/PR8, 4: *Ac*NPV with HIV-1 gp120 epitope. In a) ARP 360 (directed against the engineered HIV-1 gp120 epitope), b) B12D5 (directed against gp64, the major envelope protein of *Ac*NPV), c) polyclonal sera against influenza A/PR8, and d) influenza A/Singapore was added to the samples. The different colloidal populations display corresponding fluorescence signals with respect to the bound antigens on the colloidal surface.

 © 2006 Wiley-VCH Verlag GmbH & Co. KGaA, Weinheim

easy to prepare, and fits well to the currently available analysis techniques. We hope it will find its way toward applications in the interdisciplinary field of nanobiotechnology, thus offering highly versatile possibilities in the engineering of proteinogenic surfaces.

Experimental Section

Materials: Silica particles with diameters of 3 μm, 1 μm, and 500 nm were purchased from microparticles GmbH (Berlin, Germany). Poly(allylamine hydrochloride) (PAH; M.W. ca. 70000) and poly(sodium 4-styrenesulfonate) (PSS; M.W. ca. 70000) were obtained from Aldrich. Protamine sulfate (PRM) from herring and dextrane sulfate sodium salt (DXS; M.W. ca. 500000) were obtained from Sigma. L-α-Phosphatidylserine (PS; porcine brain, sodium salt; 20 mg mL^{-1} in chloroform) and L-α-phosphatidylcholine (PC; egg, chicken; 20 mg mL^{-1} in chloroform) were purchased from Avanti Polar Lipids, Inc. Quantum Red labeled streptavidin, anti-mouse IgG-FITC, and anti-human IgG-FITC (γ-chain specific) were purchased from Sigma. ARP 360[21] was obtained from *The Aids Reagent Project*. The hmAb 3D6[17] was kindly provided by H. Katinger (IAM, Vienna, Austria). B12D5[14] was provided by L. Volkman (University of California Berkeley, USA).

RLP preparation: RLPs were isolated according to Fischlechner et al.[3]

Baculoviruses and insect cells: All baculoviral constructs were derived from wild-type *Ac*NPV (*Autographa californica* nuclear polyhedrosis virus, ATCC). Standard protocols for virus propagation as were applied described by O'Reilly et al.[22] The baculoviral clone *Ac*COPS-PCR-LIB-Frg10 (Frg10), which displays a fragment of HIV-1 (IIIB) gp120 on its surface, was constructed as described in the literature.[16]

The baculoviral clone *Ac*COIN-3D6 was constructed in a similar fashion.[5] The construction of *Ac*Omega-GFP and *Ac*COIN-streptag is described by Ernst et al.[5]

The total protein content of ultracentrifuged baculoviruses was determined by using the Bio-Rad Protein Assay. *Sf*9 cells (*Spodoptera frugiperda*, ATCC) were grown in modified IPL-41 (Sigma–Aldrich, Munich, Germany) as described by Toellner.[16]

Particle preparation: Silica particles were coated with 5 polyelectrolyte layers. PAH and PSS were dissolved in 0.5 M NaCl in a concentration of 1 mg mL^{-1} for the coating of 3-μm particles (3 mg mL^{-1} and 6 mg mL^{-1} for 1 μm and 500 nm particles, respectively). After each adsorption step (10 min at room temperature) the colloidal suspension was washed by centrifuging 3 times in 0.1 M NaCl. Coating with the PRM/DXS couple (first layer PAH) was performed in an analogous manner, except that PRM was dissolved in 0.1 M NaCl and 7 multilayers were adsorbed.

Addition of the lipid layer: Small unilamellar liposomes consisting of PS and PC (75% PS, 25% PC (mol mol^{-1}), in 0.1 M NaCl) were prepared by extrusion through a polycarbonate membrane with a pore diameter of 50 nm. The lipid bilayer was formed by adsorption of unilamellar vesicles onto multilayer-coated colloids with PAH or PRM as the top layer. The vesicles and the substrates were stirred for 30 min in 0.1 M NaCl at room temperature. After incubation, the samples were washed 3 times with 0.1 M NaCl or phosphate-buffered saline (PBS). Liposomes made from 1 mg phospholipids were used for the coating with (100 μL, 5% (v/v) stock solution) 3-μm lbl colloids (3 mg and 6 mg for 1-μm and 500-nm particles, respectively).

Fusion procedure: The fusion of baculovirions onto the lipid-coated colloids was conducted in 0.2 M phosphate/0.1 M citrate buffer at pH 4.5 by incubation of lipid-coated colloids with the virions for 10 mins at room temperature followed by 3 washings with PBS. Typically, viral protein (8 μg) was used for coating the lipid-coated 3-μm LbL colloids (10 μL, 5% (v/v) stock solution; 25 μg and 50 μg viral protein were used for 1-μm and 500-nm particles, respectively).

Electron microscopy: Colloids of 500 nm size were prepared as described before and suspended in PBS. Colloids were adsorbed onto the microscope grid by floating it on a drop of sample suspension for 1 min. The adsorbed colloids were then negatively stained by floating the grid on a drop of 1% aqueous uranyl acetate solution for another minute. Images were taken on a Philips CM12 electron microscope, operated at 80 keV acceleration voltage.

Immunofluorescence testing: Typically, colloidal sample (10 μL; 5% (v/v)) was incubated with the primary antibody, diluted 1:50 in PBS/5% FCS for 1 h followed by two washings with PBS. The secondary antibody was added in similar fashion. After washing the samples twice with PBS, they were analyzed by flow cytometry (FACSCalibur (Becton Dickinson)), with 10000 single colloids measured. The data were analyzed using the WinMDI software written by J. Trotter.

Confocal laser scanning microscopy (CLSM): CLSM images were obtained using a Leica TCS SP2 microscope. Images were analyzed using ImageJ software (Rasband, W.S., ImageJ, U.S. National Institutes of Health, Bethesda, Maryland, USA).

Viability assay: 3-μm lipid-coated colloids, one sample made up of 5 layers of PAH/PSS, the other made up of PAH following 6 layers PRM/DXS, were fused with *Ac*Omega-GFP as explained above. The colloids were incubated with *Sf*9 cells for 72 h in a ratio of 5 colloids per cell, then analyzed by means of FACS. As negative controls, the supernatants of the last washing steps of the colloidal samples were given to *Sf*9 cells. As a positive control, native *Ac*Omega-GFP (0.02 μg total protein) was applied.

Received: July 26, 2005
Published online: December 15, 2005

Keywords: antibodies · biotechnology · colloids · sensors · viruses

[1] a) E. Donath, G. B. Sukhorukov, F. Caruso, S. A. Davis, H. Möhwald, *Angew. Chem.* **1998**, *110*, 2324; *Angew. Chem. Int. Ed.* **1998**, *37*, 2202; b) F. Caruso, R. A. Caruso, H. Möhwald, *Science* **1998**, *282*, 1111; c) G. Decher, *Science* **1997**, *277*, 1232.

[2] a) C. S. Peyratout, L. Dähne, *Angew. Chem.* **2004**, *116*, 3850; *Angew. Chem. Int. Ed.* **2004**, *43*, 3762; b) G. B. Sukhorukov, A. L. Rogach, B. Zebli, T. Liedl, A. G. Skirtach, K. Köhler, A. A. Antipov, N. Gaponik, A. S. Susha, M. Winterhalter, W. J. Parak, *Small* **2005**, *1*, 194.

[3] M. Fischlechner, O. Zschörnig, J. Hofmann, E. Donath, *Angew. Chem.* **2005**, *117*, 2952; *Angew. Chem. Int. Ed.* **2005**, *44*, 2892.

[4] a) R. Grabherr, W. Ernst, C. Oker-Blom, I. Jones, *Trends Biotechnol.* **2001**, *19*, 231; b) R. Grabherr, W. Ernst, *Comb. Chem. High Throughput Screening* **2001**, *4*, 185.

[5] a) W. Ernst, R. Grabherr, D. Wegner, N. Borth, A. Grassauer, H. Katinger, *Nucleic Acids Res.* **1998**, *26*, 1718; b) W. J. Ernst, A. Spenger, L. Toellner, H. Katinger, R. M. Grabherr, *Eur. J. Biochem.* **2000**, *267*, 4033; c) A. Spenger, R. Grabherr, L. Töllner, H. Katinger, W. Ernst, *Eur. J. Biochem.* **2002**, *269*, 4458.

[6] a) J. F. Smothers, S. Henikoff, P. Carter, *Science* **2002**, *298*, 621; b) I. Benhar, *Biotechnol Adv.* **2001**, *19*, 1.

[7] a) M. Sarikaya, C. Tamerler, A. K. Y. Jen, K. Schulten, F. Baneyx, *Nat. Mater.* **2003**, *2*, 577; b) S. W. Lee, C. Mao, C. E. Flynn, A. M. Belcher, *Science* **2002**, *296*, 892; c) C. Mao, C. E. Flynn, A. Hayhurst, R. Qi, J. Sweeney, G. Georgiou, B. Iverson, A. M. Belcher, *Proc. Natl. Acad. Sci. USA* **2003**, *100*, 6946.

[8] a) S. Moya, E. Donath, G. B. Sukhorukov, M. Auch, H. Bäumler, H. Lichtenfeld, H. Möhwald, *Macromolecules* **2000**, *33*, 4538; b) S. Moya, W. Richter, S. Leporatti, H. Bäumler, E. Donath, *Biomacromolecules* **2003**, *4*, 808.

 © 2006 Wiley-VCH Verlag GmbH & Co. KGaA, Weinheim

[9] a) F. Caruso, C. Schüler, *Langmuir* **2000**, *16*, 9595; b) C. S. Peyratout, L. Dähne, *Angew. Chem.* **2004**, *116*, 3850; *Angew. Chem. Int. Ed.* **2004**, *43*, 3762.
[10] T. S. Jardetzky, R. A. Lamb, *Nature* **2004**, *427*, 307.
[11] S. D. J. Chapple, I. M. Jones, *J. Biotechnol.* **2002**, *95*, 269.
[12] a) J. A. G. Briggs, T. Wilk, S. D. Fuller, *J. Gen. Virol.* **2003**, *84*, 757; b) M. J. Schnell, L. Buonocore, E. Kretzschmar, E. Johnson, J. K. Rose, *Proc. Natl. Acad. Sci. USA* **1996**, *93*, 11359.
[13] T. C. Hobman, M. L. Lundstrom, C. A. Mauracher, L. Woodward, S. Gillam, M. G. Farquhar, *Virology* **1994**, *202*, 574.
[14] B. A. Keddie, G. W. Aponte, L. E. Volkman, *Science* **1989**, *243*, 1728.
[15] In brief, a library consisting of 60 overlapping PCR-derived DNA fragments of the HIV-1 gp120 sequence was cloned into the baculovirus genome in a way that the corresponding polypeptides were presented as part of an additional gp64 membrane-fusion protein. Baculovirus-infected cells containing the binding sequence for a selected antibody at their membrane were identified by their immunofluorescence and sorted by means of FACS. Subsequent virus propagation yielded a monoclonal virus population displaying the selected epitope sequence.
[16] L. Toellner, Establishment of a baculovirus surface display library using the major envelope protein gp120 from human immunodeficiency virus 1 as a model; *PhD Thesis*, University of Natural Resources and Applied Life Sciences, Vienna, Austria **2002**, http://edocs.tu-berlin.de/diss/2002/toellner_lars.htm.
[17] a) R. Grunow, S. Jahn, T. Porstmann, S. S. Kiessig, H. Steinkellner, F. Steindl, D. Mattanovich, L. Gurtler, F. Deinhardt, H. Katinger, *J. Immunol. Methods* **1988**, 106, 257; b) A. Spenger, R. Grabherr, L. Töllner, H. Katinger, W. Ernst, *Eur. J. Biochem.* **2002**, *269*, 4458.
[18] a) Viruses with pathogenic features probably can also be used as building blocks, because fusion mechanisms appear to be quite general; b) D. S. Dimitrov, *Nat. Rev. Microbiol.* **2004**, *2*, 109.
[19] W. Ernst, R. Grabherr, D. Wegner, N. Borth, A. Grassauer, H. Katinger, *Nucleic Acids Res.* **1998**, *26*, 1718.
[20] S. Hiller, S. Leporatti, A. Schnäckel, E. Typlt, E. Donath, *Biomacromolecules* **2004**, *5*, 1580–1587.
[21] J. P. Moore, Q. J. Sattenau, H. Yoshiyama, M. Thali, M. Charles, N. Sullivan, S. W. Poon, M. S. Fung, F. Traincard, M. Pinkus, *J. Virol.* **1993**, *67*, 6136.
[22] D. R. O'Reilly, L. K. Miller, V. A. Luckow, *Baculovirus expression vectors: a laboratory manual*, W. H. Freeman, New York, **1992**.

 © 2006 Wiley-VCH Verlag GmbH & Co. KGaA, Weinheim

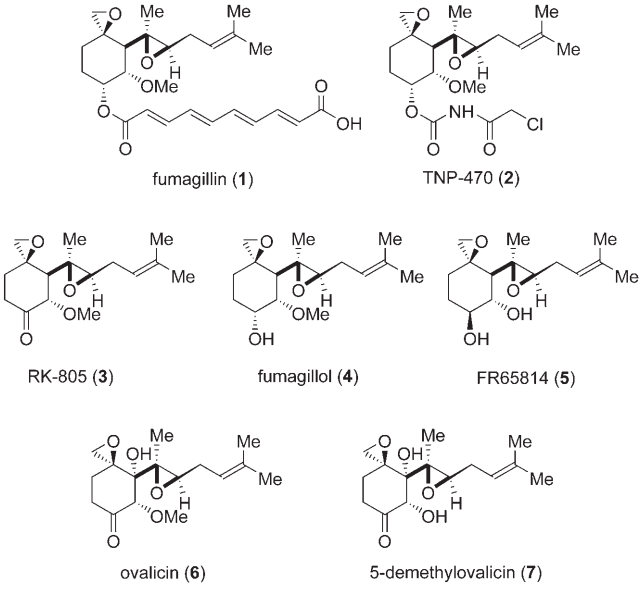
Total Synthesis

DOI: 10.1002/anie.200502826

Concise Enantio- and Diastereoselective Total Syntheses of Fumagillol, RK-805, FR65814, Ovalicin, and 5-Demethylovalicin**

*Junichiro Yamaguchi, Maya Toyoshima, Mitsuru Shoji, Hideaki Kakeya, Hiroyuki Osada, and Yujiro Hayashi**

The inhibition of angiogenesis is a promising method of treating diseases in which this process is involved, such as cancer and rheumatoid arthritis.[1] During our continuing research on angiogenesis inhibitors, we have identified and synthesized several novel compounds with such activity, including epoxyquinols A and B,[2] and azaspirene.[3] Recently, we also isolated RK-805 (**3**) from the fungus *Neosartorya* sp.[4] RK-805 is structurally similar to fumagillin (**1**)[5] and TNP-470 (**2**),[6] a synthetic derivative of fumagillin, which are both inhibitors of angiogenesis. Ovalicin (**6**)[7] is another inhibitor



[*] J. Yamaguchi, M. Toyoshima, Dr. M. Shoji, Prof. Dr. Y. Hayashi
Department of Industrial Chemistry
Faculty of Engineering
Tokyo University of Science
Kagurazaka, Shinjuku-ku, Tokyo 162-8601 (Japan)
Fax: (+81) 3-5261-4631
E-mail: hayashi@ci.kagu.tus.ac.jp
Dr. H. Kakeya, Prof. Dr. H. Osada
Antibiotics Laboratory
Discovery Research Institute, RIKEN
Wako, Saitama 351-0198 (Japan)

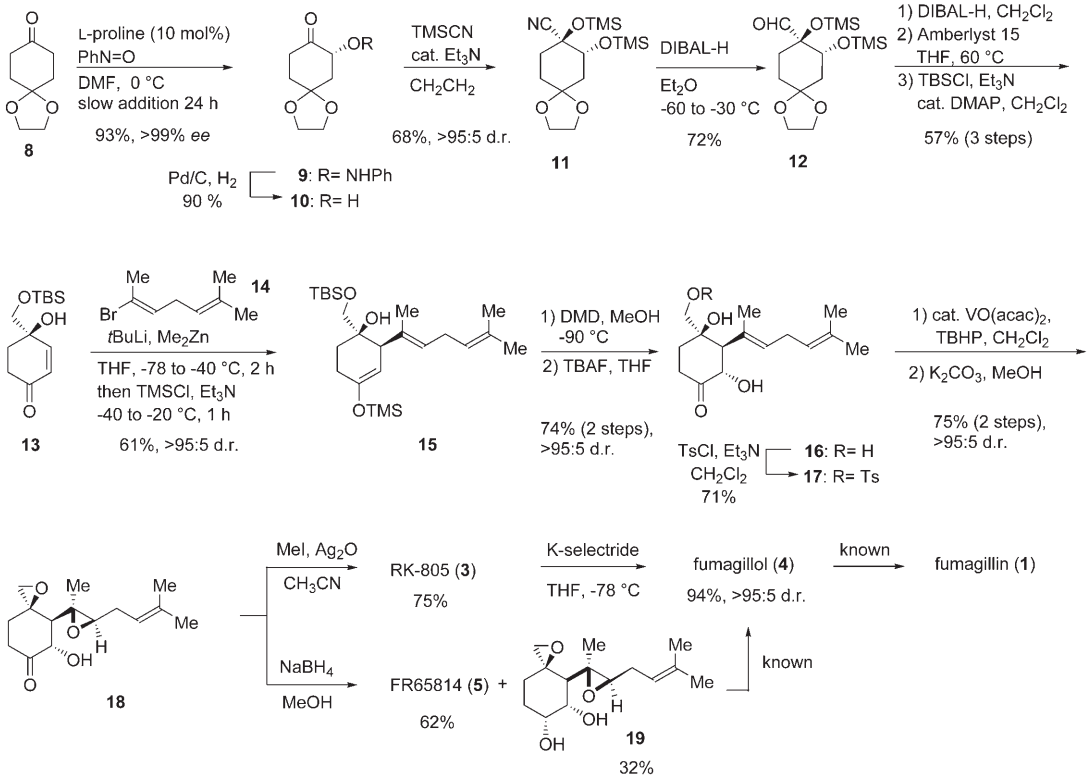
[**] This paper is dedicated to Prof. E. J. Corey for his elegant total syntheses of the fumagillin and ovalicin families. This work was partially supported by a Grant-in-Aid for Scientific Research on Priority Areas 16073219 from The Ministry of Education, Culture, Sports, Science, and Technology (MEXT).

© 2006 Wiley-VCH Verlag GmbH & Co. KGaA, Weinheim

of angiogenesis and is more stable than fumagillin and TNP-470, while 5-demethylovalicin (**7**)[8] was isolated recently and found to be as potent an angiogenesis inhibitor as ovalicin. While these natural products are anti-angiogenesis agents, FR65814 (**5**),[9] which has a similar structure, displays completely different biological activity and is an immunosuppressant.

Systematic comparison of the biological properties of these natural products and their derivatives is highly desirable.[10] These compounds comprise a cyclohexane framework, two epoxides, and five or six contiguous stereogenic centers, three or four of which are situated on the cyclohexane ring. As a result of their unique structure and important biological properties, they have proved attractive synthetic targets. Four racemic syntheses[11] including Corey's first excellent total syntheses of fumagillin (**1**)[11a] and ovalicin (**6**) have been reported.[11b] The optically active compounds have been prepared from a chiral pool, starting from quinic acid[12] and quebrachitol[13] for ovalicin, glycidol[14] for fumagillin, allose[15] and mannitol[16] for fumagillin, and glucose[17] for FR65814, while diastereoselective syntheses of fumagillin using chiral auxiliaries have been reported by Sorensen[18] and Eustache[19] and their respective co-workers. However, only one catalytic asymmetric synthesis has been reported for any of these compounds, namely, Corey's synthesis of ovalicin (**6**)[20] through substrate-enhanced asymmetric dihydroxylation. Moreover, there is no single, flexible method to access both families. Herein, we disclose the concise, flexible, and highly diastereoselective asymmetric, catalytic total syntheses of compounds of both families, including RK-805 (**3**), fumagillol (**4**), FR65814 (**5**), ovalicin (**6**), and 5-demethylovalicin (**7**) using our recently developed proline-mediated α-aminoxylation of carbonyl compounds[21] as a key step.

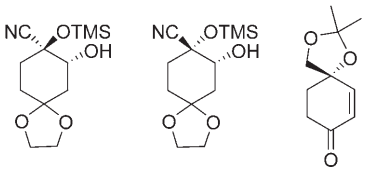
Synthesis of the fumagillin family started from 1,4-cyclohexanedione monoethylene ketal (**8**; Scheme 1). α-Aminoxylation of **8** (1.2 equiv) using 10 mol% of L-proline with slow addition of nitrosobenzene (1.0 equiv) over 24 h proceeded efficiently at 0°C to afford nearly optically pure *R*-α-aminoxylated cyclohexanone **9** (>99% *ee*) in 93% yield, in a reaction that can be scaled up to 25 g of **8** without compromising the yield or enantioselectivity.[21b,c] Reductive cleavage of the N–O bond was performed under an atmosphere of H_2 in the presence of Pd/C[21e] for 3 h in THF (90%). Diastereoselective construction of the epoxide moiety from the ketone carbonyl was found to be troublesome because of easy racemization and low selectivity: Racemic epoxide was obtained, albeit in good yield, when **10** was treated at room temperature with a sulfur ylide such as dimethylsulfonium methylide.[22] The epoxide was generated with low diastereoselectivity (2.5:1–3.4:1) by conventional two-step procedures such as vinylidene formation with $Ph_3P{=}CH_2$ and successive epoxidation with either TBHP in the presence of VO(acac)$_2$[23] at room temperature or MCPBA at 0°C. After some experimentation, it was found that cyano bis(trimethyl-



Scheme 1. Total syntheses of fumagillol (**4**), RK-805 (**3**), FR65814 (**5**), and the formal total synthesis of fumagillin (**1**). DMF = *N*,*N*-dimethylformamide; TMS = trimethylsilyl; DIBAL-H = diisobutylaluminum hydride; TBS = *tert*-butyldimethylsilyl; DMAP = 4-(dimethylamino)pyridine; DMD = dimethyldioxirane; TBAF = tetra-*n*-butylammonium fluoride; Ts = *p*-toluenesulfonyl; acac = acetylacetonate; TBHP = *tert*-butylhydroperoxide; selectride = tri-*sec*-butylborohydride.

 © 2006 Wiley-VCH Verlag GmbH & Co. KGaA, Weinheim

silyl) ether **11** could be obtained with high diastereoselectivity in moderate yield, although the diastereoselectivity of the initial cyanation was low. When hydroxy ketone **10** was treated with TMSCN (2.5 equiv) in the presence of Et_3N (0.1 equiv)[24] at 0 °C, cyano mono(trimethylsilyl) ethers **20** and **21** were obtained in low diastereoselectivity (3.5:1) after



20 **21** **22**

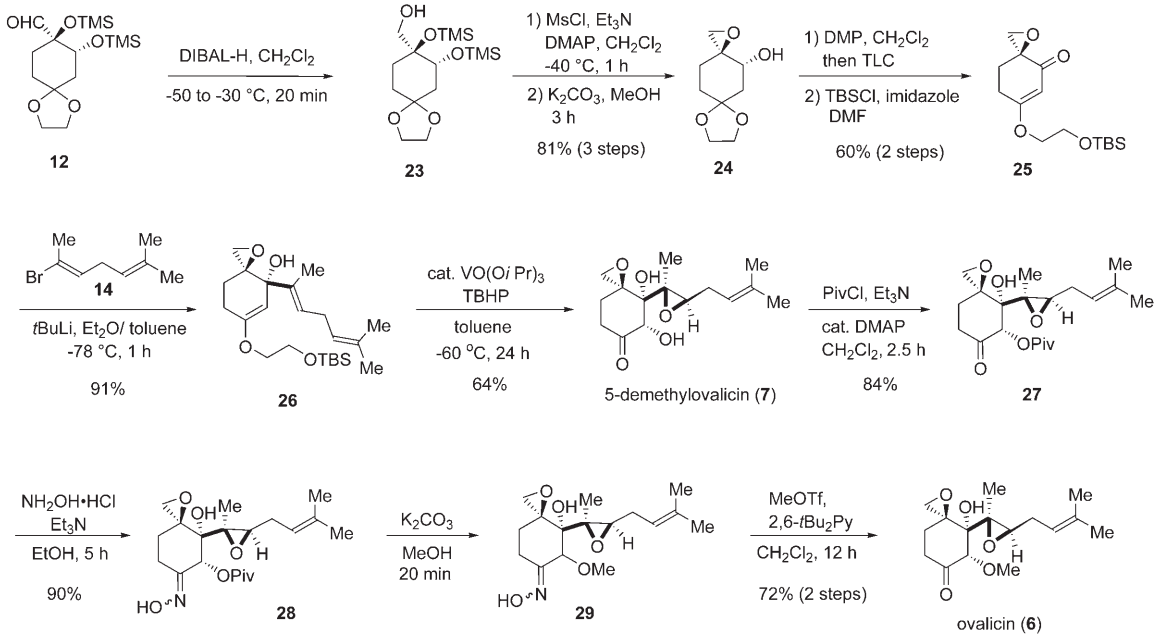
0.5 h. After 2.5 h, however, bis(trimethylsiloxy) cyanocyclohexane **11** was obtained with high diastereoselectivity (> 95:5) in 68 % yield along with cyano mono(trimethylsilyl) ether **21** in 20 % yield because of kinetic discrimination between the diastereomers during the formation of the second TMS ether. The two-step transformation of the cyanide to the alcohol was cleanly performed by repeated reductions with DIBAL-H. Acid treatment with Amberlyst in THF/H_2O at 60 °C for 2 days led to removal of all the protecting groups, with concomitant dehydration affording a cyclohexenone diol. Selective protection of the primary alcohol with TBSCl using Et_3N at room temperature for 12 h afforded TBS ether **13** in 57 % yield over three steps. The optical purity (> 99 % *ee*) of **13** was checked by chiral HPLC analysis of its acetate, which indicated that no racemization had occurred during these transformations. The absolute stereochemistry was confirmed by the conversion of **13** into the enantiomer of Taber's intermediate **22**.[14]

The next task was diastereoselective introduction of the side chain which was also found to be troublesome. The choice of protecting group for the cyclohexenone and the metal cation of the nucleophile are both important for achieving the desired conjugate addition: The tertiary alcohol should be free,[25] and vinyl zincate was found to be the reagent of choice.[26] Thus, α,β-enone **13** reacted with vinyl zincate prepared from **14**[27] at −78 °C to afford the Michael addition product, which was trapped with TMSCl as its trimethylsilyl enol ether **15**. This ether was obtained in 61 % yield as a single isomer, in which the side chain had been introduced stereoselectively from the same side as the hydroxy group. Protection of the tertiary alcohol or use of divinyl cuprate instead of vinyl zincate led to unsatisfactory results. Epoxidation[28] of the silyl enol ether with dimethyldioxirane (DMD) at low temperature (−90 °C) in acetone proceeded diastereoselectively without oxidation of the other trisubstituted double bonds and α-hydroxy cyclohexanone **16** was obtained after treatment with TBAF as a single isomer in 74 % yield over two steps. Though the reaction sequence of conjugate addition, silyl trapping, and Rubottom oxidation was also employed in Taber's synthesis of fumagillin to install a side chain and the hydroxy group at the C5 position, the stereochemistry of the conjugate addition was completely different.[14] Taber et al. reported that intermediate **22** containing an acetal group reacted stereoselectively with a divinyl cuprate derivative in the undesired fashion, that is, *anti* to the oxygen atom of the spirocyclic ether, necessitating several additional steps to correct the stereochemistry. In our synthesis, direct introduction of the side chain with the correct stereochemistry by exploiting the free hydroxy group in combination with a zincate makes the total synthesis efficient and straightforward.

During epoxidation at the side chain, the order of the next two procedures was very important to obtain high diastereoselectivity (Scheme 1). The diastereoselectivity of epoxidation of dihydroxy tosylate **17** with TBHP in the presence of $VO(acac)_2$[23] was excellent, and bis(epoxide) **18** was obtained as a single isomer after treatment with K_2CO_3 in MeOH, whereas reversal of the order of reaction led to low diastereoselectivity (2:1).[29] Formation of the methyl ether with MeI and Ag_2O in CH_3CN gave RK-805, which was stereoselectively reduced with K-selectride at −78 °C to give fumagillol as a single isomer in good yield. The conversion of fumagillol into fumagillin in a single step is known,[11a,14] thus, the formal total synthesis of fumagillin was also accomplished. When **18** was reduced with $NaBH_4$ in MeOH at −50 °C to −10 °C, FR65814 was obtained predominantly in 62 % yield along with **19** in 32 % yield. The conversion of **19** into fumagillol in a single step is known.[11c,18]

Next, the syntheses of 5-demethylovalicin and ovalicin were examined (Scheme 2). The intermediate **12** used in our synthesis of the fumagillin family was employed here also, first to generate the epoxide **24**. Oxidation of **24** with the Dess–Martin periodinane (DMP),[30] followed by acid treatment with thin layer chromatography (TLC) to generate a 3-(2-hydroxyethyloxy)cyclohex-2-enone derivative, and treatment with TBSCl afforded cyclohexenone **25**. The side chain was introduced in a highly diastereoselective manner by using a vinyllithium reagent.[20] As the side chain, the 6-methylhepta-2,5-dien-2-yl substituent was found to be unstable, easy to isomerize, and prone to decomposition, thus its epoxidation had to be carried out immediately.[31] Though conventional epoxidation with $VO(acac)_2$ and TBHP,[23] or *m*-chloroperbenzoic acid gave a complex mixture owing to the instability of the side chain, and the other double bond of the side chain was selectively epoxidized with DMD, $VO(OiPr)_3$[32] was found to be an efficient catalyst, promoting the epoxidation of both the silyl enol ether and the desired side chain alkene at low temperature (−60 °C) to afford 5-demethylovalicin (**7**) as a single isomer with the creation of three chiral centers. The last task necessary to convert 5-demethylovalicin into ovalicin (**6**) was transformation of the alcohol to its methyl ether. Although conventional reagents[33] such as NaH and MeI, Ag_2O and MeI, or MeOTf and 2,6-di-*tert*-butylpyridine, failed, a modification of Corey's method[11b] through the corresponding oxime gave ovalicin stereoselectively. Thus, protection of the alcohol as an ester, formation of the oxime, treatment with base in MeOH, and conversion of the oxime into a ketone gave ovalicin (**6**) as a single isomer, with the ovalicin intermediates **28** and **29** each obtained also as single isomers.[34] Note that oxime **29** was converted into ovalicin (**6**) in good yield without affecting the two epoxides or the trisubstituted alkene under alkylation conditions, when this conversion is usually performed under

 © 2006 Wiley-VCH Verlag GmbH & Co. KGaA, Weinheim



Scheme 2. Total syntheses of ovalicin (**6**) and 5-demethylovalicin (**7**). Ms = methanesulfonyl; DMP = Dess–Martin periodinane; Piv = pivaloyl; OTf = trifluoromethanesulfonate, Py = pyridine.

oxidative, reductive, or acid-hydrolysis conditions.[33] Though the synthetic scheme from **25** is similar to that in Corey's elegant synthesis,[11b] in which introduction of the side chain followed by various functional group manipulations are key transformations, there is an important difference; namely, the effective epoxidation catalyst ($VO(OiPr)_3$), which allows diastereoselective double epoxidation without affecting the labile side chain, saves a couple of steps and improves the efficiency of the synthesis.

The ^1H and ^{13}C NMR spectra, IR spectra, and optical rotations of the synthetic samples of **3**,[4] **4**,[14] **5**,[9] **6**,[13b,35] and **7**[8] are in complete agreement with those previously reported.

In summary, the concise enantio- and diastereoselective total syntheses of fumagillol, RK-805, FR65814, 5-demethylovalicin, and ovalicin in 11–15 steps from commercially available compounds have been demonstrated. These are some of the shortest syntheses reported for these chiral natural products and demonstrate clearly the power of the proline-mediated asymmetric catalytic α-aminoxylation. The initial aminoxylation reaction controls both the absolute and the relative stereochemistry of the subsequently generated stereogenic centers, which are formed by the following transformations: 1) a highly diastereoselective formation of bis(trimethylsilyl ether) cyanide **11** involving kinetic discrimination; 2) a diastereoselective Michael reaction by the use of vinyl zincate (**13**→**15**); 3) a stereoselective double epoxidation catalyzed by $VO(OiPr)_3$ at low temperature (**26**→**7**); and 4) an alkylative deprotection of an oxime (**29**→**6**). Corey's asymmetric total synthesis of ovalicin (**6**)[20] using asymmetric dihydroxylation is a landmark chiral synthesis of a member of the fumagillin and ovalicin families. The present route using an α-aminoxylation catalyzed by inexpensive proline is as efficient as Corey's synthesis;[20] it allows the synthesis to be performed on a large scale and allows easy derivatization, as well as being the first strategy applied to both fumagillin and ovalicin families, thus demonstrating the flexibility of the present synthetic method.

Received: August 9, 2005
Published online: December 20, 2005

Keywords: asymmetric synthesis · inhibitors · natural products · organocatalysis · total synthesis

[1] a) J. Folkman, *J. Natl. Cancer Inst.* **1990**, *82*, 4; b) W. Risau, *Nature* **1997**, *386*, 671; c) M. Klagsbrun, M. A. Moses, *Chem. Biol.* **1999**, *6*, R217; d) G. Gasparini, *Drugs* **1999**, *58*, 17.

[2] a) H. Kakeya, R. Onose, H. Koshino, A. Yoshida, K. Kobayashi, S.-I. Kageyama, H. Osada, *J. Am. Chem. Soc.* **2002**, *124*, 3496; b) H. Kakeya, R. Onose, A. Yoshida, H. Koshino, H. Osada, *J. Antibiot.* **2002**, *55*, 829; c) M. Shoji, J. Yamaguchi, H. Kakeya, H. Osada, Y. Hayashi, *Angew. Chem.* **2002**, *114*, 3324; *Angew. Chem. Int. Ed.* **2002**, *41*, 3192; d) M. Shoji, S. Kishida, M. Takeda, H. Kakeya, H. Osada, Y. Hayashi, *Tetrahedron Lett.* **2002**, *43*, 9155; e) M. Shoji, H. Imai, I. Shiina, H. Kakeya, H. Osada, Y. Hayashi, *J. Org. Chem.* **2004**, *69*, 1548.

[3] a) Y. Asami, H. Kakeya, R. Onose, A. Yoshida, H. Matsuzaki, H. Osada, *Org. Lett.* **2002**, *4*, 2845; b) Y. Hayashi, M. Shoji, J. Yamaguchi, K. Sato, S. Yamaguchi, T. Mukaiyama, K. Sakai, Y. Asami, H. Kakeya, H. Osada, *J. Am. Chem. Soc.* **2002**, *124*, 12078.

[4] Y. Asami, H. Kakeya, R. Onose, Y.-H. Chang, M. Toi, H. Osada, *Tetrahedron* **2004**, *60*, 7085.

[5] M. C. McCowen, M. E. Callender, J. F. Lawlis, *Science* **1951**, *113*, 202.

[6] D. Ingber, T. Fujita, S. Kishimoto, K. Sudo, T. Kanamaru, H. Brem, J. Folkman, *Nature* **1990**, *348*, 555.

[7] H. Sigg, H. P. Weber, *Helv. Chim. Acta* **1968**, *51*, 1395.

 © 2006 Wiley-VCH Verlag GmbH & Co. KGaA, Weinheim

[8] K.-H. Son, J.-Y. Kwon, H.-W. Jeong, H.-K. Kim, C.-J. Kim, Y.-H. Chang, J.-D. Choi, B.-M. Kwon, *Bioorg. Med. Chem.* **2002**, *10*, 185.
[9] H. Hatanaka, T. Kino, M. Hashimoto, Y. Tsurumi, A. Kuroda, H. Tanaka, T. Goto, M. Okuhara, *J. Antibiot.* **1988**, *41*, 999.
[10] a) G. Zhou, C. W. Tsai, J. O. Liu, *J. Med. Chem.* **2003**, *46*, 3452; b) V. Rodeschini, J.-G. Boiteau, P. V. de Weghe, C. Tarnus, J. Eustache, *J. Org. Chem.* **2004**, *69*, 357; c) R. Maztischek, A. Huwe, A. Giannis, *Org. Biomol. Chem.* **2005**, *3*, 2150, and references therein.
[11] a) E. J. Corey, B. B. Snider, *J. Am. Chem. Soc.* **1972**, *94*, 2549; b) E. J. Corey, J. P. Dittami, *J. Am. Chem. Soc.* **1985**, *107*, 256; c) D. A. Vosburg, S. Weiler, E. J. Sorensen, *Angew. Chem.* **1999**, *111*, 1022; *Angew. Chem. Int. Ed.* **1999**, *38*, 971; d) M. Hutchings, D. Moffat, N. S. Simpkins, *Synlett* **2001**, *661*.
[12] A. Barco, S. Benetti, C. D. Risi, P. Marchetti, G. P. Pollini, V. Zanirato, *Tetrahedron: Asymmetry* **1998**, *9*, 2857.
[13] a) S. Bath, D. C. Billington, S. D. Gero, B. Quiclet-Sire, M. Samadi, *J. Chem. Soc. Chem. Commun.* **1994**, 1495; b) D. H. R. Barton, S. Bath, D. C. Billington, S. D. Gero, B. Quiclet-Sire, M. Samadi, *J. Chem. Soc. Perkin Trans. 1* **1995**, 1551.
[14] D. F. Taber, T. E. Christos, A. L. Rheingold, I. A. Guzei, *J. Am. Chem. Soc.* **1999**, *121*, 5589.
[15] D. Kim, S. K. Ahn, H. Bae, W. J. Choi, H. S. Kim, *Tetrahedron Lett.* **1997**, *38*, 4437.
[16] O. Bedel, A. Haudrechy, Y. Langlois, *Eur. J. Org. Chem.* **2004**, 3813.
[17] a) S. Amano, N. Ogawa, M. Ohtsuka, S. Ogawa, N. Chida, *Chem. Commun.* **1998**, 1263; b) S. Amano, N. Ogawa, M. Ohtsuka, N. Chida, *Tetrahedron* **1999**, *55*, 2205.
[18] D. A. Vosburg, S. Weiler, E. J. Sorensen, *Chirality* **2003**, *15*, 156.
[19] J.-G. Boiteau, P. Van de Weghe, J. Eustache, *Org. Lett.* **2001**, *3*, 2737.
[20] E. J. Corey, A. Guzman-Perez, M. C. Noe, *J. Am. Chem. Soc.* **1994**, *116*, 12109.
[21] a) Y. Hayashi, J. Yamaguchi, K. Hibino, M. Shoji, *Tetrahedron Lett.* **2003**, *44*, 8293; b) Y. Hayashi, J. Yamaguchi, T. Sumiya, M. Shoji, *Angew. Chem.* **2004**, *116*, 1132; *Angew. Chem. Int. Ed.* **2004**, *43*, 1112; c) Y. Hayashi, J. Yamaguchi, T. Sumiya, K. Hibino, M. Shoji, *J. Org. Chem.* **2004**, *69*, 5966; d) Y. Hayashi, J. Yamaguchi, K. Hibino, T. Sumiya, T. Urushima, M. Shoji, D. Hashizume, H. Koshino, *Adv. Synth. Catal.* **2004**, *346*, 1435; e) G. Zhong, *Angew. Chem.* **2003**, *115*, 4379; *Angew. Chem. Int. Ed.* **2003**, *42*, 4247; f) S. P. Brown, M. P. Brochu, C. J. Sinz, D. W. C. MacMillan, *J. Am. Chem. Soc.* **2003**, *125*, 10808; g) A. Bøgevig, H. Sundeen, A. Córdova, *Angew. Chem.* **2004**, *116*, 1129; *Angew. Chem. Int. Ed.* **2004**, *43*, 1109; h) A. Córdova, H. Sunden, A. Bøgevig, M. Johansson, F. Himo, *Chem. Eur. J.* **2004**, *10*, 3673; i) N. Momiyama, H. Torii, S. Saito, H. Yamamoto, *Proc. Natl. Acad. Sci. USA* **2004**, *101*, 5374; j) W. Wang, J. Wang, H. Li, L. Liao, *Tetrahedron Lett.* **2004**, *45*, 7235; k) H. Sunden, N. Dahlin, I. Ibrahem, H. Adolfsson, A. Córdova, *Tetrahedron Lett.* **2005**, *46*, 3385; for a review, see: l) P. Merino, T. Tejero, *Angew. Chem.* **2004**, *116*, 3055; *Angew. Chem. Int. Ed.* **2004**, *43*, 2995.
[22] E. J. Corey, M. Chaykovsky, *J. Am. Chem. Soc.* **1965**, *87*, 1353.
[23] K. B. Sharpless, R. C. Michaelson, *J. Am. Chem. Soc.* **1973**, *95*, 6136.
[24] S. Kobayashi, Y. Tsuchiya, T. Mukaiyama, *Chem. Lett.* **1991**, 537.
[25] For hydroxy-directed Michael reaction, see: a) K. A. Swiss, D. C. Liotta, C. A. Maryanoff, *J. Am. Chem. Soc.* **1990**, *112*, 9393; b) K. A. Swiss, W. Hinkley, C. A. Maryanoff, D. C. Liotta, *Synthesis* **1992**, 127; c) M. Solomon, W. C. L. Jamison, M. MaCormick, D. Liotta, D. A. Cherry, J. E. Mills, R. D. Shah, J. D. Rodgers, C. A. Maryanoff, *J. Am. Chem. Soc.* **1988**, *110*, 3702.
[26] For Michael reactions of zincate, see: a) M. Suzuki, Y. Morita, H. Koyano, M. Koga, R. Noyori, *Tetrahedron* **1990**, *46*, 4809; b) A. Fürstner, K. Grela, C. Mathes, C. W. Lehmann, *J. Am. Chem. Soc.* **2000**, *122*, 11799.
[27] Vinyl bromide **14** was prepared by Sorensen's modified route[11c,18] of a synthetic procedure originally reported by Corey et al.; see: E. J. Corey, J. Lee, B. E. Roberts, *Tetrahedron Lett.* **1997**, *38*, 8915.
[28] G. M. Rubottom, M. A. Vazquez, D. R. Pellagrina, *Tetrahedron Lett.* **1974**, 4319.
[29] When the spiro epoxide is formed first, the diastereoselectivity of the epoxidation of the side chain is not high. See also reference [11c].
[30] a) D. B. Dess, J. C. Martin, *J. Org. Chem.* **1983**, *48*, 4155; b) D. B. Dess, J. C. Martin, *J. Am. Chem. Soc.* **1991**, *113*, 7277; c) R. E. Ireland, L. Liu, *J. Org. Chem.* **1993**, *58*, 2899.
[31] Epoxidation of the side chain was performed as the last step of Corey's synthesis;[11b] however, we thought it was better to oxidize much earlier owing to the instability of the precursor.
[32] D. R. Pesiri, D. K. Morita, T. Walker, W. Tumas, *Organometallics* **1990**, *18*, 4916.
[33] T. W. Greene, P. G. M. Wuts, *Protective Groups in Organic Synthesis*, 3rd ed., Wiley, New York, **1999**.
[34] The stereochemistry of **28** and **29** was not determined.
[35] D. E. Cane, R. H. Levin, *J. Am. Chem. Soc.* **1975**, *97*, 1282.

 © 2006 Wiley-VCH Verlag GmbH & Co. KGaA, Weinheim

C–C Coupling

DOI: 10.1002/anie.200503263

Direct Carbon–Carbon Bond Formation from Alcohols and Active Methylenes, Alkoxyketones, or Indoles Catalyzed by Indium Trichloride**

*Makoto Yasuda, Toshio Somyo, and Akio Baba**

To construct C–C bonds, coupling reactions between reactive nucleophiles such as organometallic compounds (R′M) and halides or a related species (RX) are undoubtedly a useful process. The species RX and R′M are often prepared from alcohols (ROH) and active methylenes (R′H), respectively. However, the coupling reaction intrinsically produces a salt (MX) alongside the desired product (R–R′). The direct

[*] Dr. M. Yasuda, T. Somyo, Prof. Dr. A. Baba
Department of Applied Chemistry and
Handai Frontier Research Center
Graduate School of Engineering
Osaka University
2-1 Yamadaoka, Suita, Osaka 565-0871 (Japan)
Fax: (+81) 6-6879-7387
E-mail: baba@chem.eng.osaka-u.ac.jp

[**] This work was supported by a Grant-in-Aid for Scientific Research from the Ministry of Education, Culture, Sports, Science, and Technology, Japan, and the Sumitomo Foundation. Thanks are due to Mr. H. Moriguchi, Faculty of Engineering, Osaka University, for assistance in obtaining mass spectra.

Supporting information for this article is available on the WWW under http://www.angewandte.org or from the author.

© 2006 Wiley-VCH Verlag GmbH & Co. KGaA, Weinheim
InterScience

reaction between ROH and R′H would be an ideal process for C–C bond formation because preparation of the reactive materials would not be required and only H_2O would be generated as a side product (Figure 1). This process would

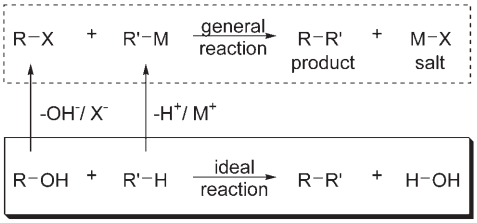


Figure 1.

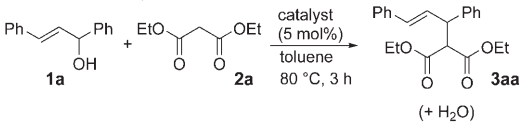
significantly save energy during multistep transformations and separation of the product from the salt. Thus, a catalyst for the reaction is required that activates either ROH or R′H and has low oxophilicity and insensitivity to water.

The Tsuji–Trost coupling reaction between allylic acetate or its derivatives with a carbanion derived from active methylenes[1] is an important synthetic tool. Recently, direct use of allylic alcohols and active methylenes for the Tsuji–Trost-type reactions has been intensively studied using palladium complexes in the presence of a base or acid cocatalyst.[2,3] Copper(I) can accelerate the reaction in the absence of a cocatalyst but an equimolar amount is required.[4] Although the catalytic reaction using a cobalt species was reported,[5] active methylenes were limited to β-diketones or keto esters, while diesters, which display a much lower reactivity owing to lower acidity (enolizable ability), could not be used. Those reactions based on transition-metal chemistry involve only allylic alcohols because the key intermediates are a π-allylic species. In this context, expansion of substrates for this type of reaction to a wide range of active methylenes and other classes of alcohols is desired.

Catalytic activation of alcohols is generally difficult because of the inefficient leaving-group ability of the hydroxy group. We have been studying catalytic activation with silyl nucleophiles and found that indium catalysts are quite effective.[6] We now report the indium-catalyzed reaction of allylic and benzylic alcohols with various active methylenes, alkoxyketones, and indoles, in the absence of a cocatalyst/activator.

First, we examined the reaction of the allylic alcohol **1a** with diethyl malonate **2a** using various catalysts (Table 1). Neither a palladium catalyst nor HCl gave the product (entries 1 and 2). Gratifyingly, $InCl_3$ was found to act as a catalyst to give **3aa** in 52% yield (entry 3, Table 1). $InBr_3$ also led to formation of the product (entry 4), while no products were observed using $In(OAc)_3$, $In(OH)_3$, $In(acac)_3$ (acac = acetylacetonate), or In as a catalyst. Other Group 13 Lewis acids such as $BF_3{\cdot}OEt_2$, $AlCl_3$, and $GaCl_3$ gave lower yields (entries 5–7, Table 1). When $Sc(OTf)_3$ was used as a catalyst, the product was contaminated with that of a redox side reaction (entry 8).[7] A large-scale synthesis of **3aa** was successful using $InCl_3$ without the need for a solvent

Table 1: Effect of catalysts on the reaction of **1a** with **2a**.[a]



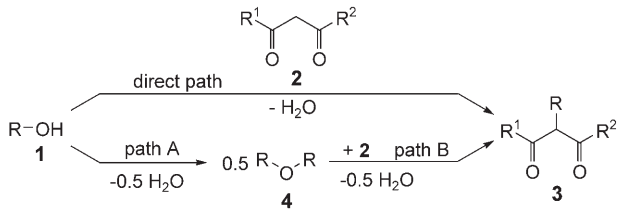
Entry	Catalyst	Yield [%]	Entry	Catalyst	Yield [%]
1	$[Pd(PPh_3)_4]$	0	5	$BF_3{\cdot}OEt_2$	0
2	HCl[b]	0	6	$AlCl_3$	6
3	$InCl_3$	52 (49)[c]	7	$GaCl_3$	18
4	$InBr_3$	45	8	$Sc(OTf)_3$	25[d]

[a] All reactions were performed using **1a** (1 mmol), **2a** (1 mmol), and catalyst (0.05 mmol) in toluene (2 mL). OTf = trifluoromethanesulfonate. [b] HCl in dioxane. [c] Isolated yield (8.6 g) after distillation from a synthesis performed on a large scale (50 mmol scale, 15 h). [d] $PhCOCH_2CHPhCH(CO_2Et)_2$ was obtained in 25% alongside the desired product **3aa** (25%).

(entry 3, Table 1). The product was easily isolated by distillation as there was no contamination by salt side-products.

We then explored the generality of the $InCl_3$-catalyzed reaction by varying the alcohol and active methylene substrates (Table 2). The reaction of allylic alcohol **1a** with active methylenes **2a–c** including diesters, keto esters, and diketones smoothly proceeded to give the corresponding alkylated products (entries 1–3, Table 2). The primary allylic alcohol **1b** afforded a regioisomeric mixture (entry 4). The cyclic allylic alcohol **1c** gave the desired product **3cc** in high yield (entry 6, Table 2). Interestingly, the benzylic alcohols **1d** and **1e** were applicable in this system as electrophiles (entries 7–11, Table 2),[8] while such benzylic species are not suitable in the Tsuji–Trost reaction based on π-allyl chemistry.[9] When simple monoketones such as acetophenone or propiophenone were used as nucleophiles, no desired product was obtained. Surprisingly, the reaction using α-methoxyketone **2d** gave the alkylated product **3ad** (entry 12, Table 2). Higher loadings of **2** improved the yield for the reactions that initially gave low yields (entries 5 and 13). In all cases, selective monoalkylation was accomplished without dialkylation.[3] Thus, the present system has potential for a wide range of nucleophiles and electrophiles.

Scheme 1 shows plausible pathways for the $InCl_3$-catalyzed reaction,[10] with the most probable being a direct path through alkylation of indium-activated alcohol.[6] We also

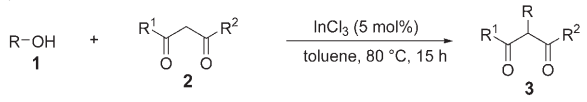


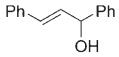
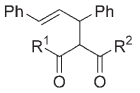
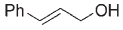
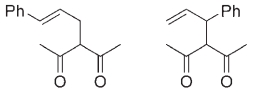
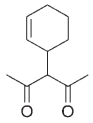
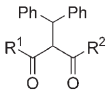
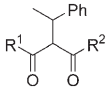
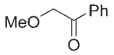
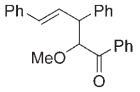
Scheme 1. Plausible reaction courses for the catalyzed reaction.

propose paths A and B from the observation of bis(diphenylmethyl) ether **4d** by NMR spectroscopy during the formation of **3dc** in the $InCl_3$-catalyzed reaction of **1d** with **2c**. A dimeric ether **4** could be an intermediate of the reaction

 © 2006 Wiley-VCH Verlag GmbH & Co. KGaA, Weinheim

Table 2: $InCl_3$-catalyzed direct reaction of **1** with **2**.[a]



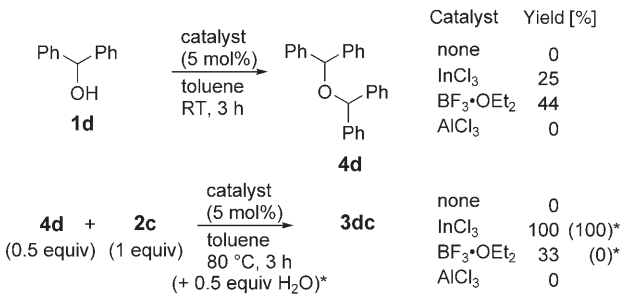
Entry	Alcohol		Nucleophile	Product		Yield [%]
1		**1a**	**2a**		**3aa**	69
2			**2b**		**3ab**	85[b]
3			**2c**		**3ac**	95
4		**1b**	**2c**		**3bc**	35
5					(85[c]:15)	75[d]
6		**1c**	**2c**		**3cc**	81
7			**2a**		**3da**	61[e]
8		**1d**	**2b**		**3db**	99
9			**2c**		**3dc**	99
10		**1e**	**2b**		**3eb**	46[f]
11			**2c**		**3ec**	87
12		**1a**			**3ad**	50[f]
13						82[f,g]

2d

[a] The reactions were performed with alcohols (1 mmol), nucleophile (1.0 mmol), and $InCl_3$ (5 mol%) in toluene (2 mL) at 80°C for 15 h. **2a**: R^1 = OEt, R^2 = OEt; **2b**: R^1 = Me, R^2 = OEt; **2c**: R^1 = Me, R^2 = Me. [b] Mixture of diastereomers (55:45) [c] Enol-type compound is involved. [d] **2c** (5 mmol). [e] Dichloroethane was used as solvent. [f] Mixture of diastereomers (ca. 1:1). [g] **2d** (2 mmol).

that proceeds in two steps: A) dimerization and B) alkylation. A catalyst that accelerates both steps is necessary to complete the reaction.

Paths A and B were independently examined with $InCl_3$ or other Lewis acids (Scheme 2). While both reactions

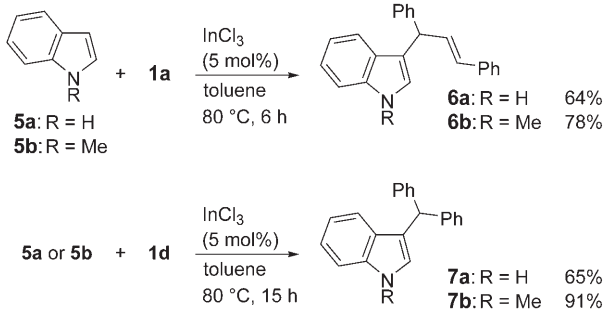


Scheme 2. Effect of the catalyst on paths A and B.

corresponding to paths A and B were catalyzed by $InCl_3$ and $BF_3{\cdot}OEt_2$, $InCl_3$ showed significant activity for alkylation relative to $BF_3{\cdot}OEt_2$. Furthermore, $BF_3{\cdot}OEt_2$ showed no catalytic activity for the alkylation step in the presence of H_2O, in contrast to the effective activity of $InCl_3$. Interestingly, $InCl_3$-catalyzed reaction of **4d** with **2c** is faster in the presence of H_2O than in its absence, as reflected by the yields of **3dc** (59% and 39%, respectively; 80°C, 3 min). An interaction between $InCl_3$ and the active methylenes is possible,[11] even though our NMR study did not show any evidence for this. Although the exact reaction mechanism is not known at this stage, the activation of alcohols through two possible pathways (Scheme 1) and that of active methylenes by $InCl_3$ leads to effective C–C bond formation.

The modification of indoles[12] is an important subject, and some reports have recently appeared in which equimolar promoters[13] or transition-metal catalysts were used.[14,15] Application of the present strategy to indoles gave 3-alkylated products in high yield and with high selectivity using allylic or benzylic alcohols (Scheme 3). No regioisomers through *N*- or 2-alkylation were obtained. Tamaru and co-workers recently reported the Pd-catalyzed reaction of allylic alcohol with indoles in the presence of Et_3B.[16] Although *N*-methylindole (**5b**) was not a good substrate therein, in our system **5b** gave the alkylated products **6b** or **7b** in high yields.

In summary, we have developed a mild and direct process for C–C bond formation from alcohols and active methylenes, alkoxyketones, or indoles in the presence of an indium catalyst, with the formation of water only as a side product. This reaction can be carried out in a very simple operation, by just mixing the substrates with $InCl_3$, followed



Scheme 3. $InCl_3$-catalyzed alkylation of indoles.

by extraction and/or distillation. This method is energy-saving and "green" and provides a straightforward and practical route to alkylated compounds.

Received: September 14, 2005
Revised: October 7, 2005
Published online: December 21, 2005

Keywords: alcohols · C–C coupling · indium · synthetic methods

 © 2006 Wiley-VCH Verlag GmbH & Co. KGaA, Weinheim

[1] a) *Palladium Reagents and Catalysts* (Ed.: J. Tsuji), Wiley, Chichester, **1995**; b) J. Tsuji, I. Minami, *Acc. Chem. Res.* **1987**, *20*, 140 – 145; c) S. A. Godleski, *Comprehensive Organic Synthesis, Vol. 4* (Eds.: B. M. Trost, I. Fleming), Pergamon, Oxford, **1991**, chap. 3.3; d) B. M. Trost, *Acc. Chem. Res.* **1980**, *13*, 385 – 393.

[2] a) F. Ozawa, H. Okamoto, S. Kawagishi, S. Yamamoto, T. Minami, M. Yoshifuji, *J. Am. Chem. Soc.* **2002**, *124*, 10968 – 10969; b) K. Manabe, S. Kobayashi, *Org. Lett.* **2003**, *5*, 3241 – 3244; c) H. Kinoshita, H. Shinokubo, K. Oshima, *Org. Lett.* **2004**, *6*, 4085 – 4088; d) M. Kimura, R. Mukai, N. Tanigawa, S. Tanaka, Y. Tamaru, *Tetrahedron* **2003**, *59*, 7767 – 7777.

[3] Allylations in the absence of a base or acid have been reported, but do not show selectivity for monoallylation; see: Y. Kayaki, T. Koda, T. Ikariya, *J. Org. Chem.* **2004**, *69*, 2595 – 2597.

[4] J. B. Baruah, A. G. Samuelson, *J. Organomet. Chem.* **1989**, *361*, C57 – 60.

[5] M. Mukhopadhyay, J. Iqbal, *Tetrahedron Lett.* **1995**, *36*, 6761 – 6764.

[6] a) M. Yasuda, S. Yamasaki, Y. Onishi, A. Baba, *J. Am. Chem. Soc.* **2004**, *126*, 7186 – 7187; b) M. Yasuda, Y. Onishi, M. Ueba, T. Miyai, A. Baba, *J. Org. Chem.* **2001**, *66*, 7741 – 7744; c) M. Yasuda, T. Saito, M. Ueba, A. Baba, *Angew. Chem.* **2004**, *116*, 1438 – 1440; *Angew. Chem. Int. Ed.* **2004**, *43*, 1414 – 1416; d) T. Saito, M. Yasuda, A. Baba, *Synlett* **2005**, 1737 – 1739.

[7] The oxidative product $PhCOCH_2CHPhCH(CO_2Et)_2$ was presumably derived from 1,4-addition to a chalcone that was generated in situ.

[8] For the cobalt-catalyzed reaction using excess acetylacetone and benzylic alcohols, see: J. Marquet, M. Moreno-Manas, *Chem. Lett.* **1981**, 173 – 176.

[9] R. Kuwano, Y. Kondo, Y. Matsuyama, *J. Am. Chem. Soc.* **2003**, *125*, 12104 – 12105.

[10] When a catalytic amount of 2,6-di-*tert*-butylpyridine (5 mol%) was introduced to the $InCl_3$-catalyzed reaction of **1a** with **2c**, the yield of the coupled product **3ac** (76%) was not suppressed compared to that for the pyridine-free reaction which gave **3ac** in 80%. It suggests that the presence of a Brønsted acid is not important even if a small amount of the acid is generated in situ. Only indium trichloride can be considered as a catalyst in this system.

[11] M. Nakamura, K. Endo, E. Nakamura, *J. Am. Chem. Soc.* **2003**, *125*, 13002 – 13003.

[12] M. Bandini, A. Melloni, S. Tommasi, A. Umani-Ronchi, *Synlett* **2005**, 1199 – 1222.

[13] For a recent example of the allylation of indole, see: X. Zhu, A. Ganesan, *J. Org. Chem.* **2002**, *67*, 2705 – 2708.

[14] a) B. S. Lane, M. A. Brown, D. Sames, *J. Am. Chem. Soc.* **2005**, *127*, 8050 – 8057; b) M. Bandini, A. Melloni, A. Umani-Ronchi, *Org. Lett.* **2004**, *6*, 3199 – 3202.

[15] Propargylic alcohols directly react with indole with the ruthenium/NH_4BF_4 system; see: Y. Nishibayashi, M. Yoshikawa, Y. Inada, M. Hidai, S. Uemura, *J. Am. Chem. Soc.* **2002**, *124*, 11846 – 11847.

[16] M. Kimura, M. Futamata, R. Mukai, Y. Tamaru, *J. Am. Chem. Soc.* **2005**, *127*, 4592 – 4593.

 © 2006 Wiley-VCH Verlag GmbH & Co. KGaA, Weinheim

Foldamers

DOI: 10.1002/anie.200502465

Helicity Induction in Hydrogen-Bonding-Driven Zinc Porphyrin Foldamers by Chiral C_{60}-Incorporating Histidines**

*Jun-Li Hou, Hui-Ping Yi, Xue-Bin Shao, Chuang Li, Zong-Quan Wu, Xi-Kui Jiang, Li-Zhu Wu, Chen-Ho Tung, and Zhan-Ting Li**

Helical biomacromolecules such as DNA and polypeptides or proteins play important roles in living systems. Extensive efforts have been devoted to helicity induction in unnatural oligomers, polymers, and dendrimers to explore new properties and functions.[1–3] In many cases, chiral amplification has been observed, which has found applications in molecular recognition,[4] light harvesting,[5] and catalysis.[6] We are motivated to explore new applications of hydrogen-bonding-driven aromatic oligoamide foldamers in chiral recognition.[7–9] Herein we report a new efficient strategy for helicity induction based on porphyrin-appended hydrogen-bonded foldamers and chiral C_{60}-incorporating histidines.

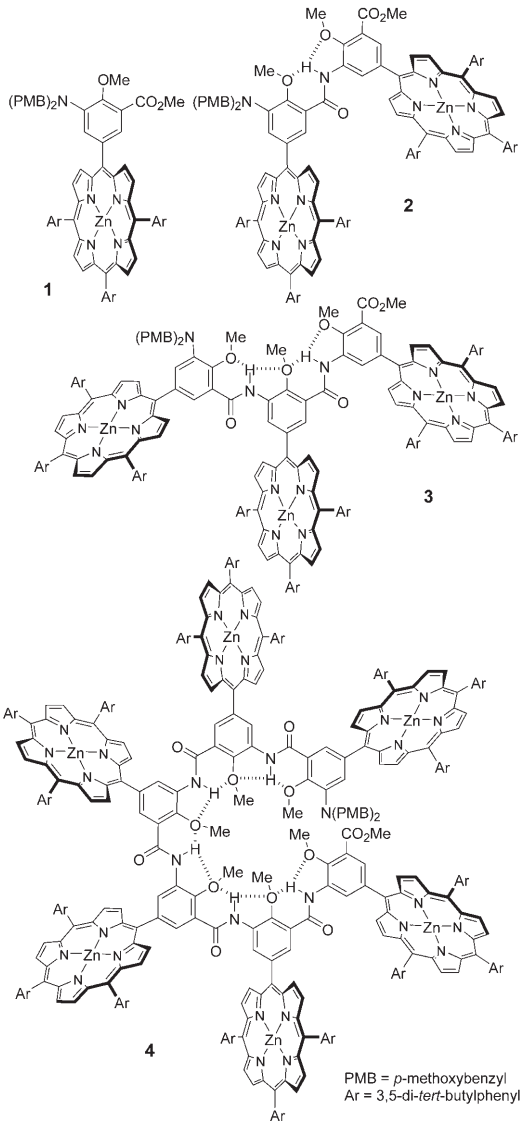
It is well established that zinc porphyrin is coordinated by N ligands such as pyridine and imidazole,[10,11] and also spontaneously attracted to C_{60} by π–π interaction.[12] Since zinc porphyrin is five-coordinate, we envisioned that rationally designed zinc porphyrin-appended foldamers might complex N ligand–C_{60} adducts through cooperation of the two discrete noncovalent interactions. Therefore, receptors **1**–**4** were synthesized and characterized. Previously,[13] we demonstrated that the repeating oligoamide skeletons in **2**–**4** adopt rigid, planar folding conformations due to intramolecular three-centered hydrogen bonding.[14] Indeed, the ^{1}H NMR spectra of **2**, **3**, and **4** in $CDCl_3$ revealed that all the signals of their NH protons appear in the downfield region, indicating the existence of intramolecular hydrogen binding and folding conformation for these molecules. The appended

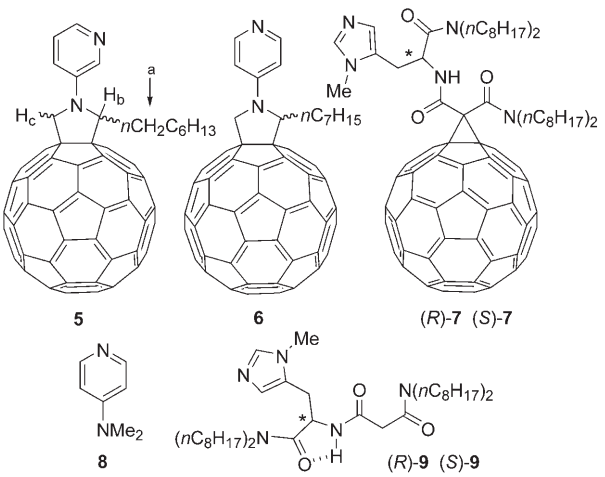
[*] J.-L. Hou, H.-P. Yi, Dr. X.-B. Shao, C. Li, Z.-Q. Wu, Prof. X.-K. Jiang, Prof. Z.-T. Li
State Key Laboratory of Bio-Organic and Natural Products Chemistry
Shanghai Institute of Organic Chemistry
Chinese Academy of Sciences
354 Fenglin Lu, Shanghai 200032 (China)
Fax: (+86) 21-6416-6128
E-mail: ztli@mail.sioc.ac.cn
Prof. L.-Z. Wu, Prof. C.-H. Tung
Technical Institute of Physics and Chemistry
Chinese Academy of Science
Beijing 100101 (China)

[**] We thank the Ministry of Science and Technology (G2000078101), the National Natural Science Foundation (20321202, 90206005, 20372080, 20332040, 20425208) of China, and the Chinese Academy of Sciences for financial support.

Supporting information for this article is available on the WWW under http://www.angewandte.org or from the author.

WILEY InterScience DISCOVER SOMETHING GREAT
© 2006 Wiley-VCH Verlag GmbH & Co. KGaA, Weinheim





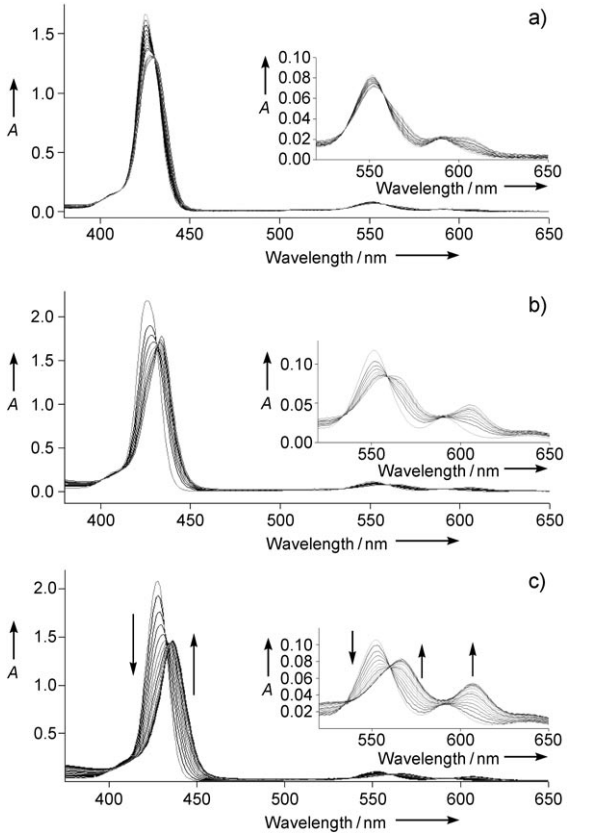


Figure 1. Absorption spectral changes of a) **2** (3.6×10^{-6} M), b) **3** (2.4×10^{-6} M), and c) **4** (1.2×10^{-6} M) on titration with (*R*)-**7** (0–7.2×10^{-4} M) in $CHCl_3$ at 25 °C.

zinc porphyrin units should adopt a conformation that is on average perpendicular to the folding skeleton.[4a] Such an arrangement would facilitate cooperative, "domino" interaction with structurally matching C_{60}–ligand adducts. Receptors **1**–**4** have good solubility in $CHCl_3$, and their absorption and ^{1}H NMR spectra in this solvent showed no evidence of intermolecular aggregation of the oligoamide skeletons or inter- or intramolecular aggregation of the porphyrin units.

With **1**–**4** in hand, guests **5**–**7** were synthesized. Upon addition of **5**–**7**, the UV/Vis spectra of **1**–**4** in $CHCl_3$ changed substantially, indicative of strong complexation. The UV/Vis titration results of **2**, **3**, and **4** with (*R*)-**7** are presented in Figure 1. The λ_{max} of the Soret and Q bands of **4** were red-shifted from 427.6 and 552.4 nm to 436.8 and 556.8 nm, respectively, with tight isosbestic points at 433.1 and 560.0 nm. In contrast, the shorter oligomers **2** and **3** exhibited smaller red shifts. Interestingly, a clear isosbestic point is observed for the Soret band in the UV/Vis spectra of all complexes. This result may reflect that the zinc porphyrin units in the foldamers have very similar binding affinities due to their ordered arrangement. The apparent association constants K_a between the zinc porphyrin unit of the receptors and **5**–**9** in $CHCl_3$ were determined on the basis of the titration experiments (Table 1).[15,16]

For a given guest, the K_a value increases pronouncedly with elongation of the foldamer. This increased binding affinity is clearly the result of increased π–π stacking between zinc porphyrin and C_{60}.[12,17] This increasing π–π interaction in the longer oligomers may be attributed to the enhanced

 © 2006 Wiley-VCH Verlag GmbH & Co. KGaA, Weinheim

Table 1: Apparent association constants K_a [M^{-1}] for the complexes of the zinc porphyrin unit of receptors **1**–**4** with guests **5**–**9** in $CHCl_3$ at 25 °C, measured by UV/Vis titration.[a]

1:**5**	3.8×10^4	**1**:**6**	3.7×10^4	**1**:(*R*)-**7**	5.9×10^3				
2:**5**	1.4×10^5	**2**:**6**	1.6×10^5	**2**:(*R*)-**7**	1.1×10^4	**2**:**8**	8.7×10^3	**2**:(*R*)-**9**	9.7×10^2
3:**5**	2.8×10^5	**3**:**6**	1.6×10^5	**3**:(*R*)-**7**	2.1×10^4	**3**:**8**	8.5×10^3	**3**:(*R*)-**9**	3.4×10^3
4:**5**	2.0×10^5	**4**:**6**	1.5×10^6	**4**:(*R*)-**7**	3.5×10^4	**4**:**8**	1.1×10^4	**4**:(*R*)-**9**	5.4×10^3
4:**5**[b]	2.1×10^5	**4**:**6**[b]	1.7×10^6	**4**:(*R*)-**7**[b]	2.3×10^4			**4**:(*S*)-**7**	3.6×10^4

[a] With error of $\leq$15%. [b] Determined by fluorescence titration method (excitation wavelength 559 nm, emission wavelength 600 nm).

spatial matching between the C_{60} and porphyrin units due to warping of the porphyrin units in one direction. The larger **6** and **7** exhibit even greater binding ability than their C_{60}-free counterparts **8** and **9**, and this clearly shows the important contribution of π–π stacking to complexation. Although imidazole is a stronger ligand to zinc porphyrin than pyridine,[11] **7** has lower binding capability than both **5** and **6**, which may be rationalized by considering the greater structural flexibility of **7**.

The stoichiometry of the complexes was also estimated. For example, the ^{1}H NMR spectra for [**2**]/[**5**] ([**5**] = 11 mM) in $CDCl_3$ revealed a clear inflexion point for the change in the chemical shift of H_a of **5** at [**2**]/[**5**] = 0.5. This value indicates that these two compounds form a stable complex with 1:2 stoichiometry. Due to signal overlap, association constants could not be obtained from the ^{1}H NMR titration experiments. The Job plot for the **4**:**7** system, based on the UV/Vis experiments, revealed maximum change in absorbance at [**4**]/([**4**] + [(*R*)-**7**]) ≈ 0.17, which corresponds to 1:5 stoichiometry and is smaller than the value of 0.14 expected for 1:6 stoichiometry. This result may indicate that with both compounds being at low concentration for the UV/Vis measurement, the maximum stoichiometry was not achieved. Nevertheless, Job plots revealed a 1:6 stoichiometry for the complexes of **4** with **5** and **6** due to increased binding affinity (see Supporting Information).

Fluorescence studies revealed that the emissions of the zinc porphyrin units of **1**–**4** could be quenched significantly by the guests.[18] The quenching data for their fluorescent emission at 600 nm (excitation wavelength: 559 nm at the isosbestic point of the Q band) is presented in Table 2. Quenching efficiency increases remarkably with elongation of the oligomers. This result is consistent with the above UV/Vis study and also supports the existence of cooperativity for the complexation of the oligomers with the guests. Based on the fluorescence quenching experiments,[17a,19] the apparent association constants of the complexes of **4** with **5**–**7** were also determined (Table 1), which are quite comparable with those evaluated by UV/Vis titration. As an example, the titration spectra of **4** with (*R*)-**7** are shown in Figure 2.

Chirality amplification was then investigated for the new porphyrin-appended foldamers. When (*R*)-**7** or (*S*)-**7** was added to solutions of **2**–**4** in $CHCl_3$, mirror-image Cotton effects resulted (Figure 3, the CD spectrum of the guest has been subtracted). In contrast, **1** is completely silent under identical conditions. The second Cotton effect is noticeably stronger than the first and increased substantially with elongation of the oligomers. The maximum CD amplitude $\Delta\varepsilon$ is 162, 1098, and

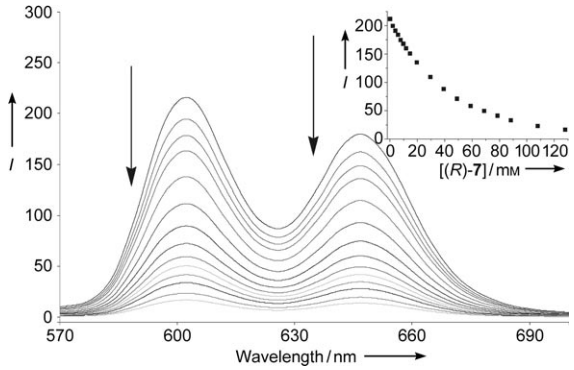


Figure 2. Fluorescence spectral changes of **4** (1.2×10^{-6} M) on addition of (*R*)-**7** (0–1.3×10^{-4} M) in $CHCl_3$ at 25 °C. Inset: plot of emission intensity of **4** at 600 nm versus [(*R*)-**7**].

2346 $M^{-1}cm^{-1}$ for **2**, **3**, and **4**, respectively, and the ability of **4** for chiral amplification is about 14.5 and 2.1 times as large as those of **2** and **3**. Because the total concentration (20 μM) of porphyrin units is identical for all oligomers, the results clearly indicate a remarkably large cooperativity in **4** for transferring the chirality of the histidine unit to the whole supramolecular architecture. In contrast, the chiral induction of C_{60}-free **9** is much smaller (Figure 4). Compared to those of **2** and **3**, the CD signal of **4** in the region of the porphyrin Soret band is also shifted remarkably on complexation with **7**. The CD band between 500 and 580 nm in Figure 3 should be produced from the chiral C_{60} unit of **7**, since similar signals were not observed when **7** was replaced by C_{60}-free **9** (Figure 4). Interestingly, another strong Cotton effect was also displayed between 580 and 640 nm in the assembly of **4** and **7**,[20] which is not observed in the assembly of **2** or **3**. The chiral amplification, signal shifting, and new additional Cotton effect in the region of long wavelength displayed by the longer foldamers on complexation with the chiral C_{60} derivatives may be explained by considering that the increased binding affinity of the chiral

Table 2: Fluorescent quenching data of receptors **1**–**4** by adducts **5**–**7** in $CHCl_3$ at 25 °C.

	I_0[a]	I[b] $[(I_0-I)/I_0]$[c]			[**5**] [M][d]	[**6**] [M][d]	[(*R*)-**7**] [M][d]
		5	**6**	(*R*)-**7**			
1	179	173 (0.04)	161 (0.10)	163 (0.09)	–[e]	–[e]	–[e]
2	213	129 (0.39)	107 (0.50)	195 (0.08)	1.2×10^{-5}	8.6×10^{-6}	–[e]
3	214	117 (0.45)	90 (0.58)	188 (0.12)	8.2×10^{-6}	5.7×10^{-6}	3.7×10^{-5}
4	210	51 (0.76)	21 (0.90)	174 (0.17)	3.6×10^{-6}	2.9×10^{-6}	3.0×10^{-5}

[a] Values of pure receptors at [porphyrin] = 7.2×10^{-6} M. [b] Values when 1 equiv of guest (7.2×10^{-6} M) was added. [c] Quenching efficiency. [d] Guest concentration at $[I_0-I]/I_0 = 0.5$. [e] $[I_0-I]/I_0 > 0.5$ in the concentration range investigated.

 © 2006 Wiley-VCH Verlag GmbH & Co. KGaA, Weinheim

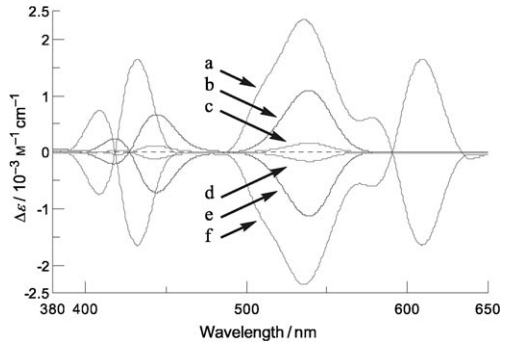


Figure 3. CD spectra of **4** (3.3×10^{-6} M) in the presence of (*R*)-**7** (a) and (*S*)-**7** (f), **3** (6.7×10^{-6} M) in the presence of (*R*)-**7** (b) and (*S*)-**7** (e), and **2** (1.0×10^{-5} M) in the presence of (*R*)-**7** (c) and (*S*)-**7** (d) in $CHCl_3$ at 25 °C ($[(R)\text{-}7]=[(S)\text{-}7]=5.0\times10^{-3}$ M).

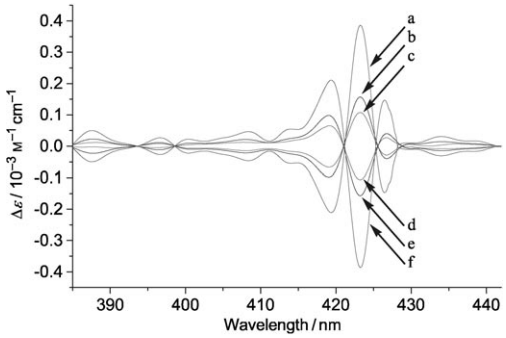


Figure 4. CD spectra of **4** (3.3 μM) in the presence of (*S*)-**9** (a) and (*R*)-**9** (f), **3** (6.6 μM) in the presence of (*S*)-**9** (b) and (*R*)-**9** (e), and **2** (10 μM) in the presence of (*S*)-**9** (c) and (*R*)-**9** (d) in $CHCl_3$ at 25 °C ($[(R)\text{-}9]=[(S)\text{-}9]=5.0\times10^{-3}$ M).

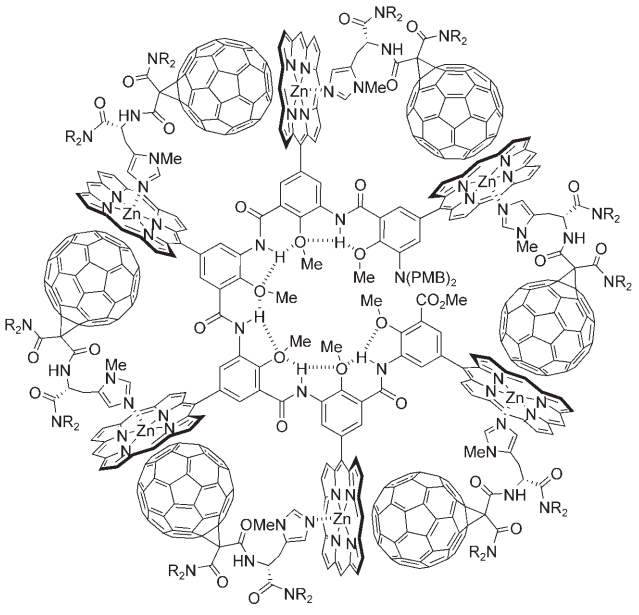


Figure 5. Proposed binding mode for the complex between **4** and (*R*)-**7**.

guest to the longer receptors would lead to more ordered chiral assembling architecture in which all the porphyrin and C_{60} units are warped in one direction. Based on these spectral investigations, we propose that for the complexation of the porphyrin-appended foldamer receptors, a clockwise or anticlockwise one-direction binding mode should be of lowest energy. Figure 5 presents a plausible binding mode for the system of **4** with (*R*)-**7**.

Chiral induction or amplification of nonnatural oligomers and polymers has been the subject of intensive research in recent years.[4,20] In this work, we demonstrated that foldamers are suitable skeletons for achieving this target. In principle, the chiral-recognition subunits can also be incorporated into one folding skeleton, which would lead to increased chiral amplification, while chiral induction based on rigid, unfolding architectures might also exhibit new interesting features.

Received: July 14, 2005
Revised: September 7, 2005
Published online: December 15, 2005

Keywords: asymmetric amplification · foldamers · fullerenes · hydrogen bonds · porphyrins

[1] a) A. E. Rowan, R. J. M. Nolte, *Angew. Chem.* **1998**, *110*, 65; *Angew. Chem. Int. Ed.* **1998**, *37*, 63; b) F. Diederich, M. Gómez-López, *Chem. Soc. Rev.* **1999**, *28*, 263; c) E. Yashima, K. Maeda, T. Nishiumura, *Chem. Eur. J.* **2004**, *10*, 42.

[2] a) E. Yashima, K. Maeda, Y. Okamoto, *Nature* **1999**, *399*, 449; b) J. H. K. Hirschberg, L. Brunsveld, A. Ramzi, J. A. J. M. Vekemans, R. P. Sijbesma, E. W. Meijer, *Nature* **2000**, *407*, 167; c) H. Fenniri, B.-L. Deng, A. E. Ribbe, *J. Am. Chem. Soc.* **2002**, *124*, 11064.

[3] a) A. Petitjean, L. A. Cuccia, J.-M. Lehn, H. Nierengarten, M. Schmutz, *Angew. Chem.* **2002**, *114*, 1243; *Angew. Chem. Int. Ed.* **2002**, *41*, 1195; b) R. B. Prince, S. A. Barnes, J. S. Moore, *J. Am. Chem. Soc.* **2000**, *122*, 2758.

[4] a) C. Ikeda, Z. S. Yoon, M. Park, H. Inoue, D. Kim, A. Osuka, *J. Am. Chem. Soc.* **2005**, *127*, 534; b) W.-S. Li, D.-L. Jiang, Y. Suna, T. Aida, *J. Am. Chem. Soc.* **2005**, *127*, 7700.

[5] M.-Y. Choi, T. Yamazaki, I. Yamazaki, T. Aida, *Angew. Chem.* **2004**, *116*, 152; *Angew. Chem. Int. Ed.* **2004**, *43*, 150.

[6] E. Delort, T. Darbre, J.-L. Reymond, *J. Am. Chem. Soc.* **2004**, *126*, 15642.

[7] For recent reviews, see a) C. Schmuck, *Angew. Chem.* **2003**, *115*, 2552; *Angew. Chem. Int. Ed.* **2003**, *42*, 2448; b) I. Huc, *Eur. J. Org. Chem.* **2004**, 17; c) R. P. Cheng, *Curr. Opin. Struct. Biol.* **2004**, *14*, 512; d) A. Sanford, K. Yamato, X. W. Yang, L. H. Yuan, Y. H. Han, B. Gong, *Eur. J. Biochem.* **2004**, *271*, 1416.

[8] a) J.-L. Hou, X.-B. Shao, G.-J. Chen, Y.-X. Zhou, X.-K. Jiang, Z.-T. Li, *J. Am. Chem. Soc.* **2004**, *126*, 12386; b) Z.-Q. Wu, X.-K. Jiang, S.-Z. Zhu, Z.-T. Li, *Org. Lett.* **2004**, *6*, 229; c) J. Zhu, X.-Z. Wang, Y.-Q. Chen, X.-K. Jiang, X.-Z. Chen, Z.-T. Li, *J. Org. Chem.* **2004**, *69*, 6221.

[9] For recent examples of other aromatic amide foldamers, see a) E. Kolomiets, V. Berl, I. Odriozola, A.-M. Stadler, N. Kyritsakas, J.-M. Lehn, *Chem. Commun.* **2003**, 2868; b) B. Huang, M. A. Prantil, T. L. Gustafson, J. R. Parquette, *J. Am. Chem. Soc.* **2003**, *125*, 14518; c) H. Jiang, J.-M. Léger, I. Huc, *J. Am. Chem. Soc.* **2003**, *125*, 3448; d) L. H. Yuan, H. Q. Zeng, K. Yamato, A. R. Sanford, W. Feng, H. Atreya, D. K. Sukumaran, T. Szyperski, B. Gong, *J. Am. Chem. Soc.* **2004**, *126*, 16528; e) D.

 © 2006 Wiley-VCH Verlag GmbH & Co. KGaA, Weinheim

Kanamori, T. Okamura, H. Yamamoto, N. Ueyama, *Angew. Chem.* **2005**, *117*, 995; *Angew. Chem. Int. Ed.* **2005**, *44*, 969; f) J. Garric, J.-M. Léger, I. Huc, *Angew. Chem.* **2005**, *117*, 1990; *Angew. Chem. Int. Ed.* **2005**, *44*, 1954.
[10] J. K. M. Sanders in *The Porphyrin Handbook, Vol. 3* (Eds.: K. M. Kadish, K. M. Smith, R. Guilard), Academic Press, New York, **2000**, pp. 347–368.
[11] A. Satake, Y. Kobuke, *Tetrahedron* **2005**, *61*, 13.
[12] P. D. Boyd, C. A. Reed, *Acc. Chem. Res.* **2005**, *38*, 235.
[13] H.-P. Yi, C. Li, J.-L. Hou, X.-K. Jiang, Z.-T. Li, *Tetrahedron* **2005**, *61*, 7974.
[14] B. Gong, *Chem. Eur. J.* **2001**, *7*, 4337.
[15] K. A. Connors, *Binding Constants*, Wiley, New York, **1987**.
[16] The association constant is the averaged value of the K_{assoc} of the discrete zinc porphyrin units when the receptor contains more than one zinc porphyrin unit; see ref. [4b] and: T. Hasobe, H. Imahori, P. C. Kamat, T. K. Ahn, S. K. Kim, D. Kim, A. Fujimoto, T. Hirakawa, S. Fukuzumi, *J. Am. Chem. Soc.* **2005**, *127*, 1216.
[17] UV/Vis experiments in $CHCl_3$ revealed very weak spectral change for all the receptors when an excess of pure C_{60} was added. The π–π stacking should be facilitated by intermolecular coordination between the zinc porphyrin and N ligand units: a) N. Armaroli, F. Diederich, L. Echegoyen, T. Habicher, L. Flamigni, G. Marconi, J.-F. Nierengarten, *New J. Chem.* **1999**, *23*, 77; b) T. Da Ros, M. Prato, D. Guldi, E. Alessio, M. Ruzzi, L. Pasimeni, *Chem. Commun.* **1999**, 635; c) F. D'Souza, G. R. Deviprasad, M. S. Rahman, J.-P. Choi, *Inorg. Chem.* **1999**, *38*, 2157; d) S. R. Wilson, S. MacMahon, F. T. Tat, P. D. Jarowski, D. I. Schuster, *Chem. Commun.* **2003**, 226; e) F. D'Souza, S. Gadde, M. E. Zandler, M. Itou, Y. Araki, O. Ito, *Chem. Commun.* **2004**, 2276; f) F. D'Souza, R. Chitta, S. Gadde, M. E. Zandler, A. S. D. Sandanayaka, Y. Araki, O. Ito, *Chem. Commun.* **2005**, 1279; g) F. D'Souza, R. Chitta, S. Gadde, M. E. Zandler, A. L. McCarty, A. S. D. Sandanayaka, Y. Araki, O. Ito, *Chem. Eur. J.* **2005**, *11*, 4416.
[18] N. Solladié, M. E. Walther, M. Gross, T. M. F. Duarte, C. Bourgogne, J.-F. Nierengarten, *Chem. Commun.* **2003**, 2412.
[19] F. Hauke, A. Swartz, D. M. Guldi, A. Hirsch, *J. Mater. Chem.* **2002**, *12*, 2088.
[20] R. Kessinger, C. Thilgen, T. Mordasini, F. Diederich, *Helv. Chim. Acta* **2000**, *83*, 3069.

 © 2006 Wiley-VCH Verlag GmbH & Co. KGaA, Weinheim

Synthetic Methods

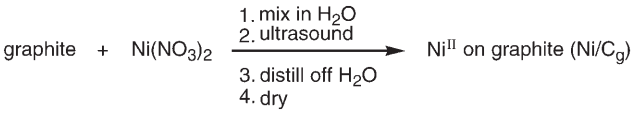
DOI: 10.1002/anie.200502887

Heterogeneous Catalysis with Nickel-on-Graphite (Ni/C_g): Reduction of Aryl Tosylates and Mesylates**

Bruce H. Lipshutz, Bryan A. Frieman, Tom Butler, and Vladimir Kogan*

Graphite, one of four allotropic forms of carbon, occurs in well-ordered sheets and in a relatively pure state.[1] With approximately 3.3 Å between two-dimensional layers of carbon atoms, nickel atoms can be readily impregnated,[2] akin to alkali-metal atoms that form well-known graphite intercalation compounds.[3] In the appropriate oxidation state, valuable yet inexpensive metal-catalyzed cross-couplings could be anticipated. Herein, we describe a new preparation of this active species, nickel-on-graphite (Ni/C_g), as well as the first study of its manipulation and use as a catalyst for synthetic purposes. For this initial investigation, we chose the challenging and valuable transformation involving reduction of an aromatic tosylate or mesylate,[4] for which there is no generally recognized technology to our knowledge.[5]

Ni/C_g (3–5% by weight) is conveniently prepared by mixing nickel nitrate and graphite in water (Scheme 1).



Scheme 1. Preparation of Ni/C_g.

Maximum distribution is obtained by ultrasonication at ambient temperatures over the course of an hour. Distillation of the water at atmospheric pressure drives off oxides of nitrogen to lead to Ni^{II}/C_g (presumably in the form of NiO/C_g). Drying this material under vacuum affords the catalyst, which can be generated in multigram quantities and is best stored in a dry, inert environment.

Reduction of a phenolic OH moiety in the presence of a multitude of functionality, in general, is a nontrivial operation.[4] Most often, as highlighted by Larock,[6] one relies on a chemoselective insertion of Pd^0 into a derived triflate in the

[*] Prof. B. H. Lipshutz, B. A. Frieman, T. Butler, Dr. V. Kogan
Department of Chemistry and Biochemistry
University of California
Santa Barbara, CA 93106 (USA)
Fax: (+1) 805-893-8265
E-mail: lipshutz@chem.ucsb.edu

[**] We warmly thank the NIH (GM 40287) for financial support and Dr. Louise Weaver of the Microscopy and Microanalysis Facility at the University of New Brunswick for the surface analyses (cf. http://www.unb.ca/fredericton/science/emunit/).

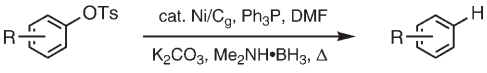
Supporting information for this article is available on the WWW under http://www.angewandte.org or from the author.

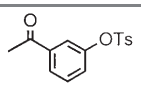
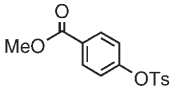
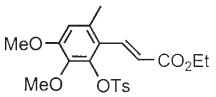
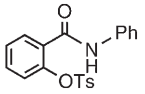
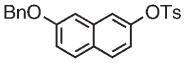
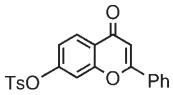
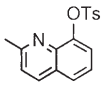
WILEY InterScience DISCOVER SOMETHING GREAT
© 2006 Wiley-VCH Verlag GmbH & Co. KGaA, Weinheim

presence of a mild source of hydride (e.g., Bu_3SnH, formate, etc.).[7] No recommendations are offered for the corresponding, far more common, and economically attractive tosylate or mesylate,[5c] let alone under heterogeneous conditions.

The combination of Ni/C_g and preformed dimethylamide borane (1.1 equiv; used in its kaliated form and prepared from $Me_2NH{\cdot}BH_3$[8] + K_2CO_3) in hot dimethylformamide (DMF; 120 °C) is very effective for the reduction of aryl tosylates. Switching to Cs_2CO_3 results in a much faster generation of the amide, although the rates and efficiencies of the subsequent reductions of sulfonates are unaffected. Reactants bearing ketone, ester, enoate, and amide functionalities are untouched (Table 1, entries 1–4, respectively).

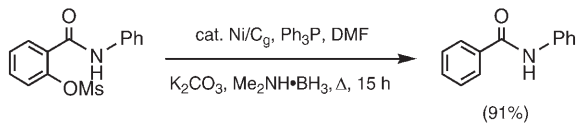
Table 1: Reduction of aryl tosylates catalyzed by Ni/C_g.



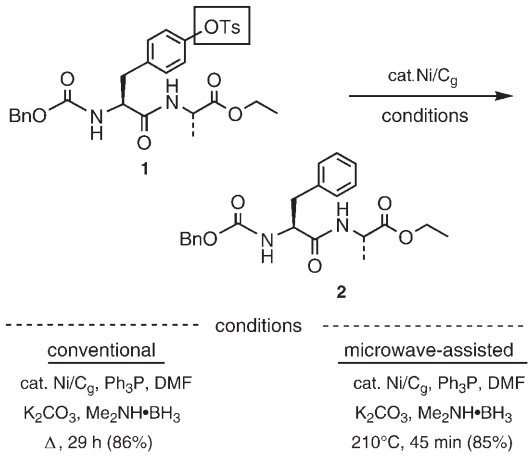
Entry	Substrate	*t* [h]	Yield [%][a]
1		9	quant[b]
2		6	quant[b]
3		14	88
4		14	91
5	 **9**	6	92
6		9	92
7		6	93

[a] Yield of the isolated products as purified by chromatography. [b] Quantitative yield indicated by quantitative GC. Ts = *p*-toluenesulfonate.

Also worthy of note is that benzyl protecting groups on aromatic alcohols (e.g., entry 5) remain intact, and conjugate reduction does not take place under these conditions. Reactions performed at approximately 0.33 M tended to require 6–15 h, with longer times likely reflecting both steric and electronic factors in the substrates. Mesylates behave akin to tosylates (Scheme 2). The reduction of nonracemic tyrosine derivative **1** to the corresponding phenylalanine-containing dipeptide **2** occurs smoothly using conventional heating without loss of stereochemical integrity (Scheme 3; "conventional").

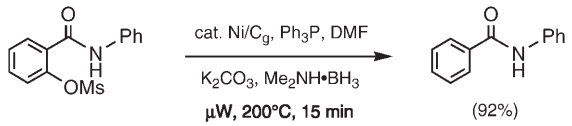


Scheme 2. Ni/C_g-catalyzed reduction of an aryl mesylate (Ms).



Scheme 3. Conversion of a tyrosine-containing dipeptide into the corresponding phenylalanine derivative under conditions of conventional and microwave heating.

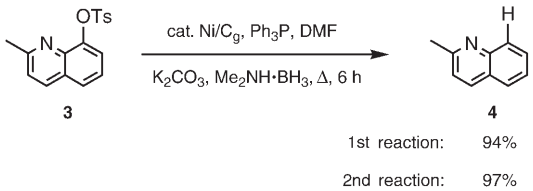
One approach to increasing the pace at which these heterogeneous reductions take place is to apply microwave irradiation.[9,10] While uncommonly employed for heterogeneous catalysis,[11] it has been found that Ni/C_g is indeed amenable to such cross-couplings. Reactions that otherwise take several hours with conventional heating (cf. Table 1) can be effected in minutes (Schemes 3 ("microwave-assisted") and 4).



Scheme 4. Rapid reduction of an aryl mesylate assisted by microwave irradiation.

Although $Ni(NO_3)_2$ and graphite are both of low cost, opportunities nonetheless exist for catalyst recycling. Following conversion of tosylate **3** into the reduced aromatic compound **4**, reuse of the filtered and collected Ni/C_g in a second and otherwise identical reduction afforded similar results (Scheme 5).

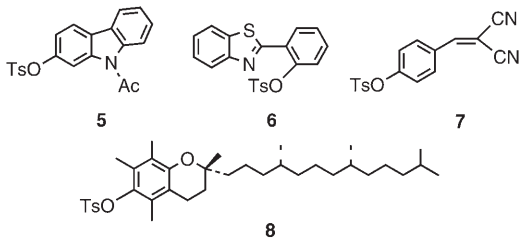
Not all of the tosylates examined were successfully reduced by Ni/C_g. Those reactions attempted that failed, notwithstanding considerable effort under modified condi-



Scheme 5. Recycling of Ni/C_g.

 © 2006 Wiley-VCH Verlag GmbH & Co. KGaA, Weinheim

tions (e.g., higher amounts of catalyst, more electron-rich ligands, microwave heating, rigorously dried solvent, etc.), are illustrated in Scheme 6. For carbazole **5**, *N*-deprotection was observed, whether the nitrogen atom was masked as the acetyl derivative or otherwise (e.g., pivaloyl, etc.). Both the



Scheme 6. Substrates that were not susceptible to reduction.

benzthiazole **6** and dicyanostyrene **7** cases led to net hydrolysis of the tosylate (with or without the presence of drying agents, molecular sieves, etc.), and the vitamin E derivative **8** appears to be too hindered and/or deactivated to react even at elevated temperatures (up to 210 °C under microwave irradiation).

To gauge the level of bleed of nickel from graphite under conventional heating conditions, inductively coupled plasma (ICP) analyses[12] were conducted on a sample reaction mixture. Thus, following the conversion of tosylate **9** (cf. Table 1, entry 5) into the corresponding reduced aromatic compound,[13] hot filtration of the crude mixture was followed by solvent removal and digestion in refluxing aqua regia. The data indicated that 4.99 % of the 5 % Ni/C_g (or 0.155 mg nickel for the amount of catalyst used) in the reaction mixture could be determined to be in solution. Thus, only 0.0025 equivalents of nickel relative to substrate were detected, an amount insufficient to effect the observed chemistry.

Transmission electron microscopy (TEM) was used to examine the physical nature of Ni-on-graphite.[14] There appears to be no visible sign of extensive clustering of nickel atoms, presumably due to the use of ultrasonication during the preparation of the catalyst. From Figure 1 a, scaled at 100 nm, two graphite sheets can be distinguished that indicate independent nickel clusters. A cross section of the catalyst at 200 nm (Figure 1 b), taken from a different perspective, shows that nickel is indeed impregnated within the sheets. In conjunction with our ICP-atomic emission spectrometric (AES) data indicating that only approximately 0.25 % nickel relative to substrate is in solution, these data suggest that reactions of Ni/C_g primarily take place on the surface of the graphite layers. Thus, as is the case with nickel-in-charcoal (Ni/C),[15] the hydrocarbon appears to support, retain, and maintain the metal in a catalytically active state.

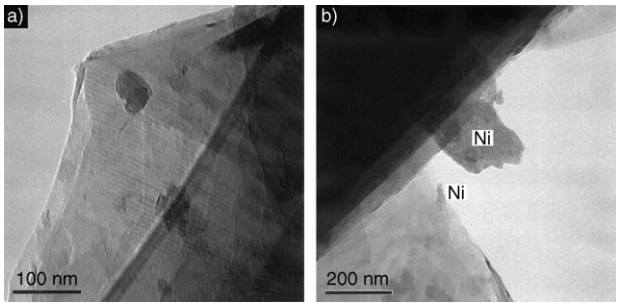


Figure 1. TEM images of Ni/C_g. a) Nickel clusters on graphite sheets; b) cross section showing exposed nickel atoms on the support.

In summary, a readily available, very inexpensive catalyst in the form of nickel-on-graphite has been prepared and shown to afford chemoselective reductions of aryl tosylates and mesylates. This heterogeneous material is amenable to use under either conventional heating conditions, or microwave irradiation which greatly enhances reaction rates. Catalyst reisolation and recycling can be effected without loss of activity. New additional chemistry associated with Ni/C_g will be reported in due course.

Experimental Section

Preparation of Ni^{II}/C_g: Graphite powder (3.75 g, 1–2 μm) was added to a 100-mL round-bottomed flask containing a stirring bar. A solution of $Ni(NO_3)_2{\cdot}6H_2O$ (727 mg, 2.30 mmol; Aldrich, 24,407-4, Ni content determined by ICP analysis: 92 %;) in deionized H_2O (35 mL) was added to the graphite, and deionized H_2O (40 mL) was added to wash down the sides of the flask. The flask was purged under argon and stirred vigorously for 1 min. The flask was submerged in an ultrasonic bath under a positive argon flow for 60 min. The flask was attached to an argon-purged distillation setup and placed in a sand bath preheated at 175–180 °C with a stirring plate. As the distillation ended, the flask temperature rises automatically, but should be kept below 210 °C for an additional 15 min. Upon cooling to room temperature, the black solid was washed with H_2O (2×50 mL) under argon into an in vacuo predried 150-mL course-fritted funnel. The H_2O used to wash the Ni/C was removed with a rotatory evaporator and analyzed for remaining nickel. The fritted funnel was inverted under vacuum and allowed to stand for 3 h until the Ni/C_g fell from the frit into a collection flask. Any Ni/C_g that remained on the fritted funnel was scraped off with a spatula and collected. The collection flask was then dried in vacuo at 100 °C for 18 h. Using these specific amounts, all of the nickel, which corresponded to 0.552 mmol Ni^{II} g^{-1} catalyst or 3.2 % Ni/catalyst by weight, was mounted on the support.

Representative procedure for Ni/C_g-catalyzed reductions of aryl tosylates: Ni/C_g (96 mg, 0.05 mmol), PPh_3 (70 mg, 0.27 mmol), K_2CO_3 (150 mg, 1.10 mmol), and borane–dimethylamine complex (68 mg, 1.10 mmol) were added to an argon-purged, flame-dried long-necked 10-mL round-bottomed flask in a glove box. Dry DMF (2 mL) was added to the reaction mixture and allowed to stir at room temperature for 2 h. The tosylate (1.00 mmol) was added to the reaction mixture and washed down the sides of the flask with additional DMF (1 mL). The flask was then equipped with a reflux condenser and placed into a preheated oil bath at 120 °C. The reaction was followed by TLC until complete disappearance of the starting material was observed. The flask was then allowed to cool to room temperature and filtered to remove Ni/C_g. The flask was washed with methanol (3×10 mL) and CuCl (27 mg, 0.27 mmol) was added to sequester PPh_3.[16] The solvent was evaporated under reduced pressure, and the reduced material was afforded by column chromatography on silica gel of the residue.

Received: August 14, 2005
Published online: December 21, 2005

 © 2006 Wiley-VCH Verlag GmbH & Co. KGaA, Weinheim

Keywords: aryl tosylates · graphite · heterogeneous catalysis · nickel · reduction

[1] W. Ruedorff, *Adv. Inorg. Chem. Radiochem.* **1959**, *1*, 223.
[2] A. Furstner, F. Hofer, H. Weidmann, *Carbon* **1991**, *29*, 915; D. Savoia, C. Trombini, A. Umani-Ronchi, *Pure Appl. Chem.* **1985**, *57*, 1887.
[3] H. Shioyama, *Synth. Met.* **2000**, *114*, 1.
[4] For an example that involves the aglycon of vancomycin, see D. A. Evans, C. J. Dinsmore, D. A. Evrard, K. M. DeVries, *J. Am. Chem. Soc.* **1993**, *115*, 6426; D. A. Evans, C. J. Dinsmore, *Tetrahedron Lett.* **1993**, *34*, 6029.
[5] a) K. Sasaki, T. Kubo, M. Sakai, Y. Kuroda, *Chem. Lett.* **1997**, 617; b) A. J. Barlett, J. S. E. Holker, E. O'Brien, T. J. Simpson, *J. Chem. Soc. Perkin Trans. 1* **1983**, 667; c) W. Cabri, S. De Bernardis, F. Francalanci, S. Penco, *J. Org. Chem.* **1990**, *55*, 350.
[6] R. C. Larock, *Comprehensive Organic Reactions*, 2nd ed., Wiley-VCH, New York, **1999**.
[7] J. Saa, M. Dopico, G. Martorell, A. Garcia-Raso, *J. Org. Chem.* **1990**, *55*, 991.
[8] The quality of $Me_2NH{\cdot}BH_3$ appears to have an important influence on the extent of conversion; use of fresh hydride, therefore, is strongly recommended.
[9] a) *Microwave Assisted Organic Synthesis* (Eds.: J. P. Tierney, P. Lidstrom), Blackwell Publishing, **2005** (cf. http://www.blackwell-publishing.com/book.asp?ref=1405115602andsite=1); b) A. K. Bose, M. S. Manhas, S. N. Ganguly, A. H. Sharma, B. K. Banik, *Synthesis* **2002**, 1578.
[10] A Personal Chemistry Emrys Optimizer was used in this study and has recently been replaced by the Biotage Initiator; cf. http://www.biotagedcg.com/DynPage.aspx?id=4193andmn1=919andmn2=1149.
[11] For example, see R. K. Arvela, N. E. Leadbeater, *Org. Lett.* **2005**, *7*, 2101; for a review, see: B. Desai, C. O. Kappe in *Top. Curr. Chem.* (Ed.: A. Kirschning), Springer, **2004**, pp. 177–207.
[12] A. W. Varnes, *Handbook of Instrumental Techniques for Analytical Chemistry* (Ed.: F. Settle), Prentice Hall, Upper Saddle River, NJ, **1997**, p. 395; *Inductively Coupled Plasma Mass Spectrometry* (Ed.: A. Montaser), Wiley-VCH, New York, **1998**.
[13] Although all examples in Table 1 were run with 1 mmol of reactant, the scale was increased to 5 mmol for the case of tosylate **9**; under otherwise identical conditions (albeit for 12 vs. 6 h), the reaction led to a 90% yield of isolated product of the reduced material.
[14] Data was acquired using a JEOL 2011 STEM operated at 200 keV; the EDX detector is an EDAX Genesis.
[15] B. H. Lipshutz, S. Tasler, W. Chrisman, B. Spliethoff, B. Tesche, *J. Org. Chem.* **2003**, *68*, 1177.
[16] B. H. Lipshutz, B. A. Frieman, H. Birkedal, *Org. Lett.* **2004**, *6*, 2305.

 © 2006 Wiley-VCH Verlag GmbH & Co. KGaA, Weinheim

Iron Phosphonates

DOI: 10.1002/anie.200502847

Compounds with the "Maple Leaf" Lattice: Synthesis, Structure, and Magnetism of $M_x[Fe(O_2CCH_2)_2NCH_2PO_3]_6 \cdot n\,H_2O$**

*Dale Cave, Fiona C. Coomer, Eduardo Molinos, Hans-Henning Klauss, and Paul T. Wood**

Compounds in which geometric frustration is present in an extended lattice are attracting a great deal of attention,[1] because the degeneracy of the spin ground state in such materials can lead to exotic magnetic behavior, such as the formation of spin liquid[2,3] and spin ice[4,5] phases. To prepare new frustrated lattices, methods must be developed to construct materials based on odd-sided polygons with antiferromagnetic coupling. Since antiferromagnetic exchange interactions are common, the second requirement is easily fulfilled. As the triangle is the only odd-sided polygon which can be packed into an extended array, this is the only building block we need to consider. Possible triangular bridges include TO_4^{n-} ions such as phosphate, sulfate, or selenate. When the T atom sits on a site of tetrahedral crystallographic symmetry, three-dimensional frustrated lattices, such as those belonging to the pyrochlore family, may be produced.[2] Location of the T atom on a three-fold axis can produce a two-dimensional frustrated lattice, such as the kagomé net.[6] Many more frustrated topologies are possible in two dimensions. Some, such as the kagomé lattice, may be derived from the triangular lattice by removal of a fraction of the nodes. Others are the result of combining triangles with other shapes, such as squares.[7] In practice, the T atom may lie somewhere other than a high-symmetry site; this will lead to lattice distortions and deviations from ideal physical behavior. However, some topologies have few real-life examples. In fact, many frustrated topologies have been envisioned, for which predictions of magnetic behavior have been made,[7] but for which there are no model compounds. One example can be derived from the triangular lattice by removal of 1/7 of the nodes. This approach produces a lattice with connectivity five that has been referred to as the "maple leaf" lattice.[8] Herein, we

[*] Dr. D. Cave, F. C. Coomer, E. Molinos, Dr. P. T. Wood
University Chemical Laboratory
Lensfield Rd, Cambridge, CB21EW (UK)
Fax: (+44) 1223-336-017
E-mail: ptw22@cam.ac.uk
Dr. H.-H. Klauss
Institut für Physik der Kondensierten Materie
Technische Universität Braunschweig (Germany)

[**] We wish to thank Prof. Dieter Fenske (Universität Karlsruhe) for collecting some of the X-ray diffraction data, and Dr. John E. Davies and Dr. Andrew D. Bond (University of Southern Denmark) for help with crystallography in Cambridge. This work was supported by the EPSRC. M = Na, $x = 11$; M = K, $x = 11$, M = Rb, $x = 10$.

Supporting information for this article is available on the WWW under http://www.angewandte.org or from the author.

 © 2006 Wiley-VCH Verlag GmbH & Co. KGaA, Weinheim InterScience

report the synthesis of a family of iron coordination solids which have this topology.

Reaction of anhydrous iron(III) chloride with alkali-metal salts of the ligand *N*-phosphinomethyliminodicarboxylic acid, $H_2O_3PCH_2N(CH_2CO_2H)_2$ (PMIDA) in superheated methanol yields $M_x[Fe(O_2CCH_2)_2NCH_2PO_3]_6 \cdot n\,H_2O$ (**1** M = Na, x = 11; **2** M = K, x = 11; **3** M = Rb, x = 10) as green-yellow octahedra (**1**) and green hexagonal plates (**2** and **3**), respectively. In all cases, the compounds are formed along with colorless crystals of alkali metal halide, which must be removed by sieving. The connectivity of the network in all three compounds is the same, but the average oxidation state of the iron and the space group of the crystals is different. Compound **1** is the most symmetrical, crystallizing[9] in space group $R\bar{3}$ with one FeL fragment (L = $(O_2CCH_2)_2NCH_2PO_3$) in the asymmetric unit (Figure 1).

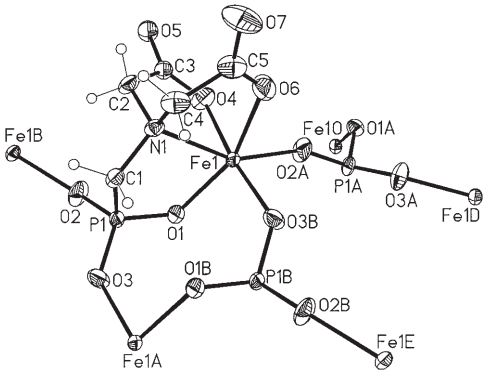


Figure 1. View of the asymmetric unit of **1** with attached symmetry equivalent phosphonate groups and iron ions. Thermal ellipsoids are set at 50 % probability. Selected bond lengths are given in the Supporting Information.

One ligand occupies four coordination sites around the iron atom, and two additional oxygen atoms from the phosphonate groups of other ligands occupy another two sites, completing a distorted octahedral coordination sphere. Hence, the iron atom is bridged to five equivalent metal centers by three phosphonate groups. Four of the iron atoms are linked by simple Fe-O-P-O-Fe bridges, whilst the fifth is linked by two such bridges to form an (-Fe-O-P-O-)$_2$ eight-membered ring. There are also two types of (-Fe-O-P-O-)$_6$ rings formed around three-fold axes in the structure, one of which is centered on the $\bar{3}$ site (Figure 2). These rings link together to generate a two-dimensional lattice, as shown in Figure 3. We can consider the topology of the lattice by joining the iron centers linked by phosphonate bridges. This generates a defect variant of the triangular lattice, in which 1/7 of the nodes are missing (Figure 4). The magnetic ground-state structure of $S = 1/2$ ions on this lattice has recently been considered from a theoretical perspective,[8] but, to our knowledge, no other real examples of this topology have been described.

The structures of **2** and **3** have the same connectivity, but lower symmetry, crystallizing in space groups $P3_1$ and $C2/c$, respectively.[9] In both cases, there are six FeL moieties in the asymmetric unit, along with many alkali-metal sites. The Fe sites are all fully occupied but some of the K/Rb sites appear to have fractional occupancies. We have investigated the correct stoichiometry of the Rb site in **3** by performing full elemental analysis and by modeling the Fe^{II}/Fe^{III} ratio from the Mössbauer spectrum. These methods give broad agreement for an Rb/Fe ratio of 10:6 and an Fe^{II}/Fe^{III} ratio of 4:2. This result is similar to that obtained by refinement of the

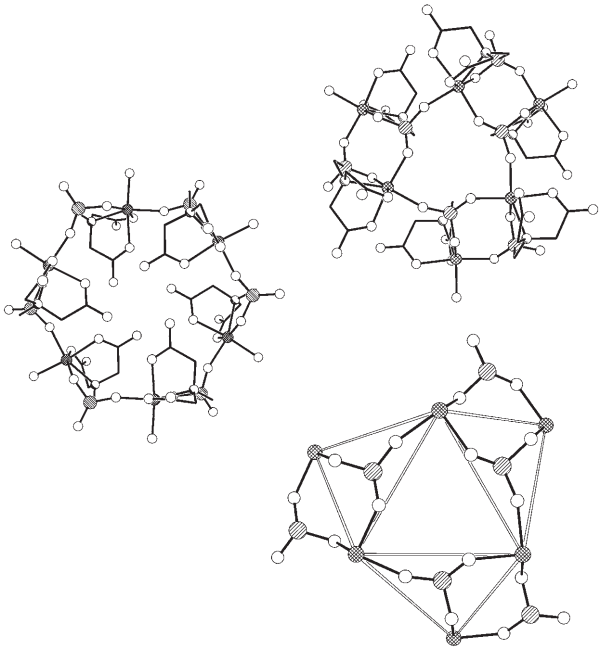


Figure 2. Hexagonal (left) and triangular (right) building blocks in compound **1**; Fe crosshatched circles, P striped circles, O open circles. In the bottom right picture, only the Fe, P, and O atoms are illustrated to emphasize the four fused-triangle motif.

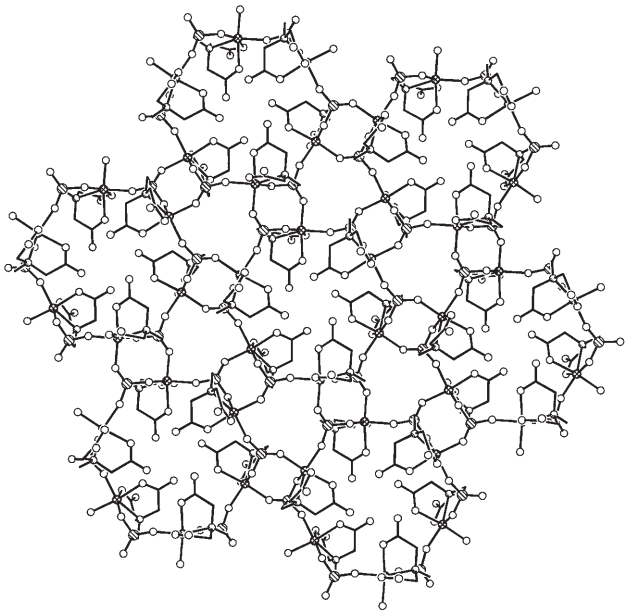


Figure 3. A packing diagram showing part of a layer in compound **1**; Fe crosshatched circles, P striped circles, O open circles.

 © 2006 Wiley-VCH Verlag GmbH & Co. KGaA, Weinheim

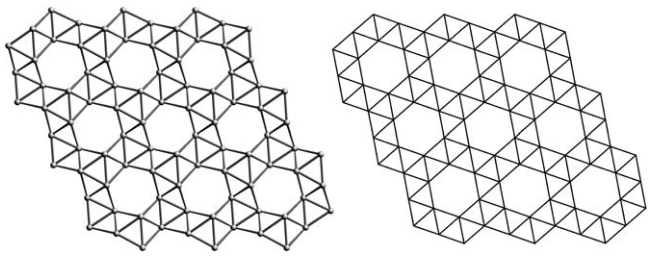


Figure 4. The superexchange lattice in compound **1** (left; Fe circles) and the idealized maple leaf lattice (right).

rubidium-site occupancy in the X-ray structure determination. Refinement of the occupancies of the K sites in **2** gives a K/Fe ratio of 11:6, which requires an Fe^{II}/Fe^{III} ratio of 5:1. For both compounds there is a wide variation in the metal–ligand bond lengths, which is consistent with a variety of average oxidation states for the six crystallographically distinct Fe sites in each structure (see Supporting Information).

The magnetic behavior of **1**–**3** was investigated using a Quantum Design MPMS5 SQUID magnetometer. Field-cooled magnetization measurements were recorded between 5 and 300 K at 100 G, and isothermal magnetization measurements were recorded between 0 and 5 T at 5 K. There is no indication of long-range order in the temperature-dependent susceptibility measurements (Figure 5), nor is there any sign

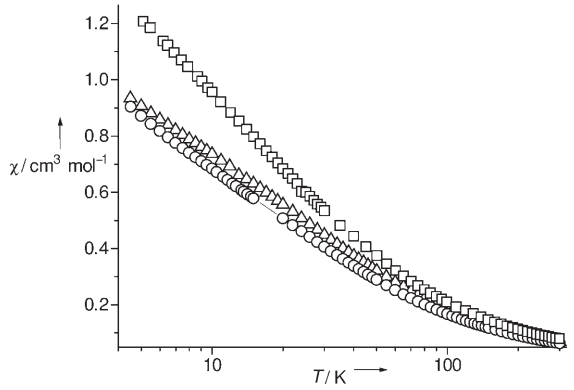


Figure 5. Temperature dependence of the magnetic susceptibility of compounds **1** (□), **2** (○), and **3** (△).

of a broad maximum characteristic of short-range antiferromagnetic order. Plots of χ^{-1} versus T obey the Curie–Weiss law at all temperatures. The Weiss constants Θ are suggestive of moderate antiferromagnetic coupling (−21(1), −20.5(2), and −17.2(2) K for compounds **1**, **2**, and **3**, respectively) and the Curie constants C are consistent with the Fe oxidation-state assignments (25.3(1), 20.21(3), and 21.73(3) $cm^3 mol^{-1} K$ for compounds **1**, **2**, and **3**, respectively). The Fe-O-P-O-Fe superexchange pathway is clearly quite weak, but the extent of magnetic frustration in these lattices is sufficient to prevent order down to the low-temperature limit of our measurements ($T_N < |\Theta|/4$) and the interlayer separation is sufficient to prevent long-range order mediated by dipolar coupling.

A recent article encourages the development of new strategies for preparing frustrated lattices.[10] The use of ligands incorporating triangular templates that are also superexchange pathways, such as the one employed herein, is one approach. However, it is difficult to control the topology of the lattices generated in this way. If we consider the case of the ligand employed herein, nitrogen and carboxylate donors account for three of the six coordination sites around the metal, and the phosphonate oxygen atoms take up the remaining three. Since each phosphonate group can link the central metal atom to two others, each iron center could, in theory, be linked to six neighbors, giving a triangular lattice. In practice, the steric demands of linking the central metal atom to six neighboring FeL moieties is too great. The steric pressure is, therefore, reduced by forming two phosphonate bridges to one adjacent FeL moiety, thereby reducing the connectivity of the lattice to five. This five-fold connectivity could also produce the trellis lattice, which is a much more anisotropic arrangement than the maple leaf lattice, or the T6 lattice, which is a much more compact arrangement (Figure 6). Serendipity is, therefore, involved, not only in the

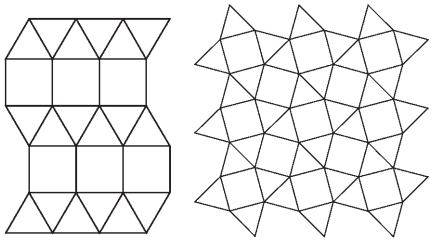


Figure 6. Other lattices with five-fold connectivity: the trellis lattice (left) and the T6 lattice (right).

resultant connectivity, but also in the "choice" of topology. The role of chance is further illustrated by the work of Clearfield and co-workers, who have studied this, and other, phosphonate ligands extensively.[11] They have found many other interesting coordination modes that compete with the formation of frustrated networks.

Experimental Section

1: Anhydrous $FeCl_3$ (0.25 g, 1.54 mmol) and NaI (2 g, 13.3 mmol) were added to a stirred solution of $H_2O_3PCH_2N(CH_2CO_2H)_2$ (0.440 g, 1.94 mmol) and NaOH (0.308 g, 7.7 mmol) in methanol (10 mL). The resulting yellow slurry was placed in a 23-mL teflon-lined autoclave and heated at 200 °C for 43 h, and then cooled to room temperature over 5 h. The resulting green-yellow octahedral crystals were removed from the solution by pipette, washed with methanol, sonicated, and sieved through a 63-micron sieve. The resulting crystals were then dried under vacuum. Yield: 94 mg (18 % based on Fe). Elemental analysis calcd (%) for $C_{30}Fe_6H_{48}N_6Na_{11}O_{48}P_6$: C 17.1, H 2.4, N 4.1, P 9.1; found C 16.9, H 2.3, N 4.0, P 8.9.

2: The reaction between $H_2O_3PCH_2N(CH_2CO_2H)_2$ (0.440 g, 1.94 mmol), KOH (0.425 g, 7.57 mmol), and anhydrous $FeCl_3$ (0.25 g, 1.54 mmol) was carried out in the manner described for compound **1**. Compound **2** was isolated in a similar manner to compound **1**, but with the omission of the sieving, as green hexagonal plate-like crystals. Yield: 253 mg (46 % based on Fe). Elemental analysis calcd (%) for $C_{30}Fe_6H_{40}K_{11}N_6O_{44}P_6$: C 16.8, H 1.9, N 3.9, P 8.7; found C 16.7, H 1.9, N 3.6, P 8.4.

 © 2006 Wiley-VCH Verlag GmbH & Co. KGaA, Weinheim

3: $H_2O_3PCH_2N(CH_2CO_2H)_2$ (0.440 g, 1.94 mmol), RbOH (0.776 g, 7.57 mmol), and anhydrous $FeCl_3$ (0.25 g, 1.54 mmol) were treated in an identical manner to **2** to give green hexagonal plates of compound **3**. Isolated yield: 359 mg (54% based on Fe). Elemental analysis calcd (%) for $C_{30}Fe_6H_{40}N_6O_{44}P_6Rb_{10}$: C 14.1, H 1.6, N 3.3, Fe 13.1, Rb 33.3; found C 14.0, H 1.7, N 3.0, Fe 14.7(±0.9), Rb 30.1(±1.3).

Received: August 10, 2005
Published online: December 21, 2005

Keywords: geometric frustration · hydrothermal synthesis · iron · magnetic properties · phosphonates

[1] J. E. Greedan, *J. Mater. Chem.* **2001**, *11*, 37, and references therein.
[2] S. H. Lee, C. Broholm, C. Ratcliff, G. Gasparovic, Q. Huang, T. H. Kim, S. W. Cheong, *Nature* **2002**, *418*, 856.
[3] V. Fritsch, J. Hemberger, N. Buttgen, E. W. Scheidt, H. A. K. von Nidda, A. Loidl, V. Tsurkan, *Phys. Rev. Lett.* **2004**, *92*, 116401.
[4] S. T. Bramwell, M. J. P. Gingras, *Science* **2001**, *294*, 1495.
[5] J. Snyder, J. S. Slusky, R. J. Cava, P. Schiffer, *Nature* **2001**, *413*, 48.
[6] A. S. Wills, A. Harrison, C. Ritter, R. I. Smith, *Phys. Rev. B* **2000**, *61*, 6156.
[7] J. Richter, J. Schulenberg and A. Honecker in *Quantum Magnetism* (Eds.: U. Schollwöck, J. Richter, D. J. J. Farnell, R. F. Bishop), Springer, Berlin, **2004**.
[8] D. Schmalfuss, P. Tomczak, J. Schulenburg, J. Richter, *Phys. Rev. B* **2002**, *65*, 224405; Z. F. Wang, B. W. Southern, *Phys. Rev. B* **2003**, *68*, 094419.
[9] Data were collected using a Stoe IPDS diffractometer at the Institut für Anorganische Chemie der Universität Karlsruhe, for compound **1**, and an Enraf-Nonius KappaCCD diffractometer at the University of Cambridge for compounds **2** and **3**. CCDC-279857, CCDC-279858, and CCDC-279859 (compounds **1** to **3**) contain the supplementary crystallographic data for this paper. These data can be obtained free of charge from The Cambridge Crystallographic Data Centre via www.ccdc.cam.ac.uk/data_request/cif. Crystal data for **1**: rhombohedral, $R\bar{3}$, $a = 14.074(2)$, $c = 27.515(6)$ Å, $V = 4719.9(19)$ Å^3, $\theta_{max} = 31.63°$, $\lambda = 0.71073$ Å, $T = 200(2)$ K, 11821 measured reflections of which 2615 were unique ($R_{int} = 0.0312$), 2518 reflections had $I > 2\sigma(I)$. The structure was solved by direct methods and refined against F^2 using SHELXTL software. All non-hydrogen atoms were refined anisotropically, and hydrogen atoms were allowed to ride on their parent atoms. 168 parameters, $R1 = 0.0367$ (for reflections with $I > 2\sigma(I)$), $wR2 = 0.0917$ (all data), $S = 1.040$, largest peak (hole) 1.101(−0.848). Crystal data for **2**: trigonal, $P3_1$, $a = 14.3858(3)$, $c = 29.1666(7)$ Å, $V = 5227.4(2)$ Å^3, $\theta_{max} = 25.03°$, $\lambda = 0.71073$ Å, $T = 180(2)$ K, 12765 measured reflections of which 9489 were unique ($R_{int} = 0.0307$), 8580 reflections had $I > 2\sigma(I)$. The structure was solved by direct methods and refined against F^2 using SHELXTL software. All non-hydrogen atoms were refined anisotropically, and hydrogen atoms were allowed to ride on their parent atoms. 956 parameters, $R1 = 0.0553$ (for reflections with $I > 2\sigma(I)$), $wR2 = 0.1423$ (all data), $S = 1.068$, largest peak (hole) 1.248(−0.629). Crystal data for **3**: monoclinic, $C2/c$, $a = 24.3559(12)$, $b = 13.6490(5)$, $c = 27.515(6)$ Å, $\beta = 96.722(2)°$, $V = 13718.7(11)$ Å^3, $\theta_{max} = 22.44°$, $\lambda = 0.71073$ Å, $T = 180(2)$ K, 19048 measured reflections of which 7290 were unique ($R_{int} = 0.0678$), 5396 reflections had $I > 2\sigma(I)$. The structure was solved by direct methods and refined against F^2 using SHELXTL software. The Rb, Fe, P, and N atoms were refined anisotropically, the C and O atoms were refined isotropically, and the hydrogen atoms were allowed to ride on their parent atoms. 562 parameters, $R1 = 0.0797$ (for reflections with $I > 2\sigma(I)$), $wR2 = 0.2055$ (all data), $S = 1.035$, largest peak (hole) 1.527(−1.023).
[10] A. Harrison, *J. Phys. Condens. Matter* **2004**, *16*, S553.
[11] See, for example, J. G. Mao, A. Clearfield, *Inorg. Chem.* **2002**, *41*, 2319.

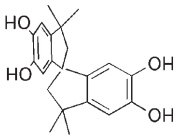
 © 2006 Wiley-VCH Verlag GmbH & Co. KGaA, Weinheim

Supramolecular Chemistry

DOI: 10.1002/anie.200503156

Tetraanionic Organoborate Squares Glued Together by Cations To Generate Nanotubular Stacks**

*Brendan F. Abrahams, David J. Price, and Richard Robson**



1

3,3,3′,3′-Tetramethyl-1,1′-spirobisindane-5,5′,6,6′-tetrol (**1**; hereafter LH_4), which is easily obtained in racemic form, is an attractive building block for the construction of functional solids, because of its ready availability, its rigid angularity, and its chirality. Shea and co-workers have reported that reaction of LH_4 with phenyltriethoxysilane under basic conditions generates tetraanionic molecular squares of composition $[(C_6H_5Si)_4L_4]^{4-}$, in which the silicon centers have five-coordinate environments that are probably close to square pyramidal with a square O_4 base defined by two L^{4-} units.[1] Although no X-ray crystallographic data are available, NMR spectroscopy indicates that a single diastereoisomer with C_{2h} symmetry containing the two L^{4-} enantiomers in equal numbers is selectively formed. Duhme and co-workers isolated $Na_4[(MoO_2)_2L_2]$ from the reaction of LH_4 with sodium molybdate.[2] In this case, X-ray crystallography revealed a macrocycle with a 2:2 rather than a 4:4 ligand/metal ratio, the two L^{4-} units being of the same chirality. Herein, we describe some organoborate solids containing $[B_4L_4]^{4-}$ molecular squares, in which all four of the L^{4-} components are of the same chirality. These squares, which contain a large central hole, are stacked one on top of another

[*] Dr. B. F. Abrahams, Dr. D. J. Price, Prof. R. Robson
School of Chemistry
University of Melbourne
Victoria 3010 (Australia)
Fax: (+61) 393-475-180
E-mail: r.robson@unimelb.edu.au

[**] The authors gratefully acknowledge support from the Australian Research Council.

Supporting information for this article is available on the WWW under http://www.angewandte.org or from the author.

WILEY InterScience DISCOVER SOMETHING GREAT
© 2006 Wiley-VCH Verlag GmbH & Co. KGaA, Weinheim

and "glued" together by cations to form infinite columns. Large channels of roughly square cross section and of roughly nanometer dimensions run through the centers of the columns.

Reaction of LH_4 with $B(OMe)_3$ and triethylamine (Et_3N) in methanol in a sealed tube at 160 °C generates crystals of solvated $(Et_3NH)_4[B_4L_4]$.[3a,4a] The crystal structure contains discrete molecular $[B_4L_4]^{4-}$ squares, shown in Figure 1, in

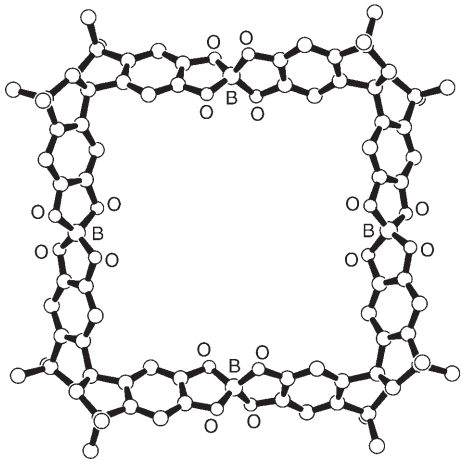


Figure 1. A $[B_4L_4]^{4-}$ square in the structure of solvated $(Et_3NH)_4[B_4L_4]$. Hydrogen atoms are omitted for clarity.

which all four L^{4-} units have the same handedness. The B···B separation across the center of the squares is 13.22 Å. The organoborate squares, all of the same chirality, stack one on top of another in the direction perpendicular to the B_4 plane (that is, the *c* direction), with the negatively charged boron centers of one square vertically above and below those of adjacent squares. The $[Et_3NH]^+$ ions are located between pairs of anionic boron centers. A combination of electrostatic anion–cation attraction (Figure 2a) and hydrogen bonding (Figure 2b) aligns the components of the stack to produce a tubular structure. As is indicated in Figure 2b, all the N–H vectors point in the same direction and form significant hydrogen bonds to two ligand oxygen atoms (N–H···O 2.939(4) and 3.018(4) Å).

All the columns in the structure are parallel and are packed as shown in Figure 3. Any column of a given chirality makes contact with four columns of opposite chirality. The tubes contain disordered solvent, which is very easily removed without disruption of the tubular structure (see below). This structure is reminiscent of the cyclic peptide nanotubes described by Ghadiri et al.,[5] which also consist of stacks of macrocycles hydrogen bonded together to generate tubular structures. However, in the present example of $(Et_3NH)_4[B_4L_4]$, anion–cation attraction provides a powerful additional tube-forming influence.

Reactions under conditions similar to those above, but with benzyldiethylamine ($BzEt_2N$) replacing triethylamine, yield crystals of composition $(BzEt_2NH)_4[B_4L_4]\cdot 4\,MeOH$.[3b,4b] The crystal structure is very similar to that of solvated $(Et_3NH)_4[B_4L_4]$. Stacks of $[B_4L_4]^{4-}$ squares, all of the same

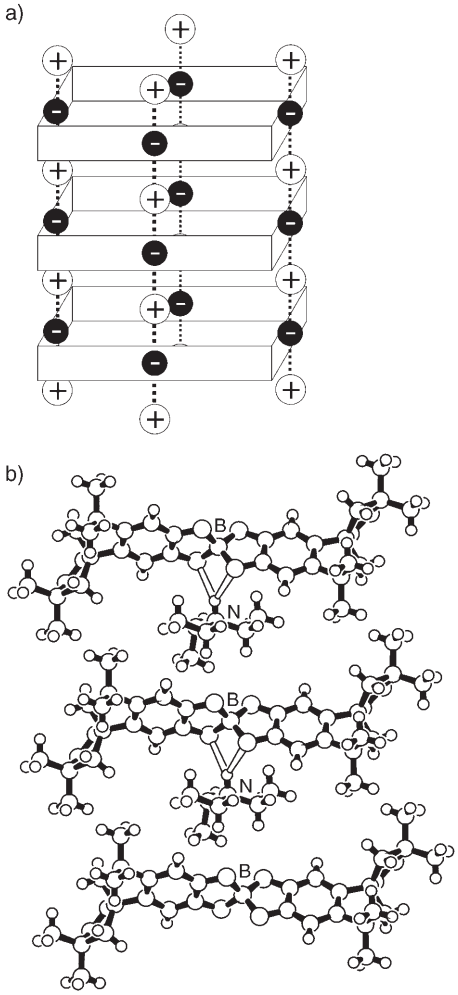


Figure 2. a) Schematic representation of the stacking of tetraanionic squares, electrostatically glued together by monocations. Negative charges correspond to boron centers. b) Section of the crystal structure of solvated $(Et_3NH)_4[B_4L_4]$, showing the location of the $[Et_3NH]^+$ ions between anionic boron centers. Hydrogen bonds are indicated by the open connections.

chirality, are glued together by the $[BzEt_2NH]^+$ ions in much the same way. However, in $(BzEt_2NH)_4[B_4L_4]\cdot 4\,MeOH$, the benzyl groups project into the channels, as was our intention, making edge-to-face phenyl contacts, as shown in Figure 4. Four methanol molecules, trapped in the spaces above and below the quartets of benzyl groups, are securely imprisoned, as indicated by thermogravimetric measurements described below.

We wondered if it might also be possible to use appropriate diamines in place of triethylamine. When doubly protonated, the diamines could potentially tether column to column, in addition to binding square to square. Reaction of LH_4 with $B(OMe)_3$ and 1,3-di(aminomethyl)-benzene (amb) under conditions similar to those employed above with triethylamine, yields crystals of solvated $(Me_2ambH_2)_2[B_4L_4]$ (in which $[Me_2ambH_2]^{2+}$ represents the diprotonated form of 1,3-di(methylaminomethyl)benzene, that is, $(MeNH_2{}^+CH_2)_2C_6H_4$).[3c,4c] Evidently, N-methylation of the amino groups of amb by methanol has occurred under

 © 2006 Wiley-VCH Verlag GmbH & Co. KGaA, Weinheim

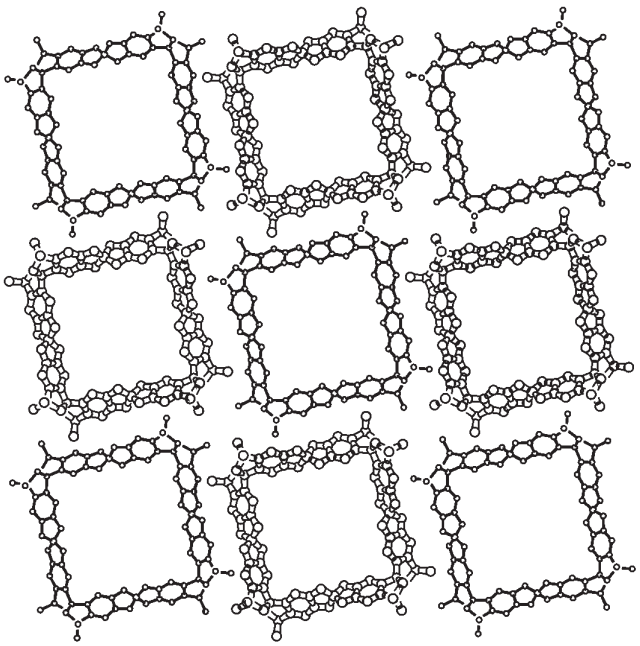


Figure 3. Packing of the "square stacks" in solvated $(Et_3NH)_4[B_4L_4]$. The stacks represented using small circles and thin closed bonds are all of the same chirality; the stacks represented using large circles and thick open bonds have the opposite chirality. Hydrogen atoms are omitted for clarity.

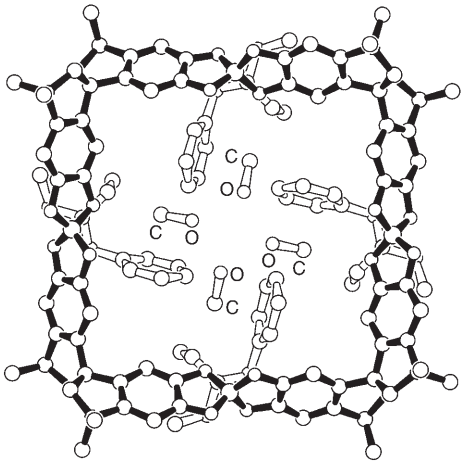


Figure 4. A $[B_4L_4]^{4-}$ square and four associated $[BzEt_2NH]^+$ ions in the structure of $(BzEt_2NH)_4[B_4L_4]\cdot 4\,MeOH$. The major orientations of the disordered methanol molecules are shown. Hydrogen atoms are omitted for clarity.

the forcing conditions used (160 °C in a sealed tube). Similar methylation reactions have been reported previously.[6] The presence of the $[Me_2ambH_2]^{2+}$ ion was independently indicated by electrospray mass spectrometry (ES/MS) on the solution obtained by decomposing the crystals of $(Me_2ambH_2)_2[B_4L_4]$ in aqueous acid. In the crystal structure of solvated $(Me_2ambH_2)_2[B_4L_4]$, $[B_4L_4]^{4-}$ squares, in which all the L^{4-} units have the same chirality, are again present. Again, the squares stack one on top of another to generate tubelike columns, but now squares of opposite chirality alternate within a column, as shown in Figure 5a. Each square is

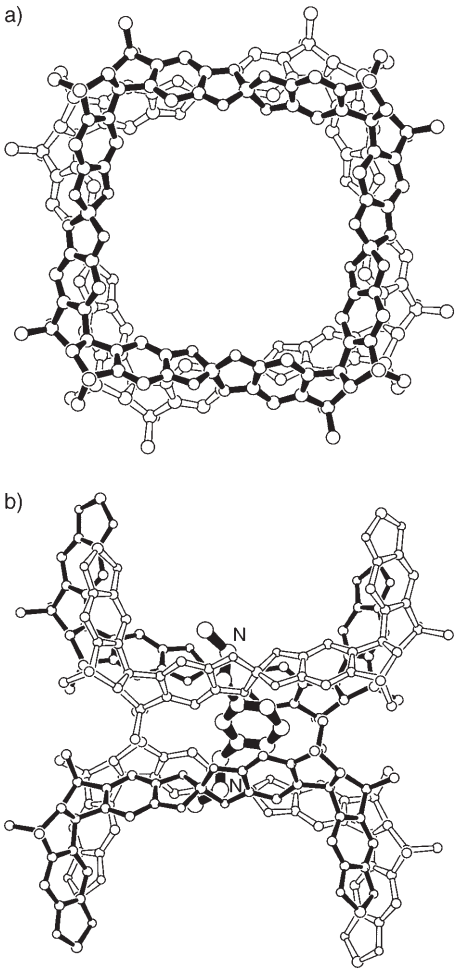


Figure 5. a) Two neighboring molecular squares of opposite chirality (represented by open or closed bonds) in the structure of solvated $(Me_2ambH_2)_2[B_4L_4]$. b) One orientation of the disordered $[Me_2ambH_2]^{2+}$ ion (large circles and thick closed bonds) and parts of the two neighboring columns that it tethers (small circles and thin open or closed bonds). Hydrogen atoms are omitted for clarity.

rotated by approximately 20° around the tetragonal axis relative to its two nearest-neighbor squares of opposite chirality. This alternation within the stack leads to an approximate doubling of the *c* parameter, compared to those of the other compounds,[4] in which all squares in a stack have the same chirality. As is shown in Figure 5b, the $[Me_2ambH_2]^{2+}$ ions are located between columns, as intended, where they do indeed serve as tethers. The two cationic nitrogen centers are electrostatically bonded to separate columns. The cation is disordered over two overlapping sets of sites related by a twofold axis. The two nitrogen atoms are hydrogen bonded to catechol oxygen atoms (N–H···O 2.983(8) Å at one nitrogen and 2.788(9) Å at the other).

If the channels in the structures of solvated $(Et_3NH)_4[B_4L_4]$ and $(Me_2ambH_2)_2[B_4L_4]$ are regarded as tubes of constant square section, the edges of the squares, taking van der Waals surfaces into account, are estimated to be 7.5 and 9.8 Å, in each of the compounds, respectively.

When a sample of solvated $(Et_3NH)_4[B_4L_4]$ on the pan of the thermogravimetric instrument is exposed to a stream of

 © 2006 Wiley-VCH Verlag GmbH & Co. KGaA, Weinheim

nitrogen, it loses all its solvent, prior to any heating. The resulting mass of the sample remains essentially unchanged when the sample is subsequently heated to 270 °C, beyond which decomposition occurs (see Supporting Information). Thermogravimetric analysis of $(BzEt_2NH)_4[B_4L_4]\cdot 4\,MeOH$ indicates insignificant weight loss up to 270 °C; evidently, the methanol molecules remain trapped in the structure. Thermogravimetric analysis of solvated $(Me_2ambH_2)_2[B_4L_4]$ reveals relatively slow weight loss up to approximately 150 °C, whereafter little weight loss occurs until 270 °C; evidently, in this case, the solvent is held more tenaciously than in $(Et_3NH)_4[B_4L_4]$.

When suspended in water, ethanol, or chloroform for one week, crystals of solvated $(Et_3NH)_4[B_4L_4]$ and $(Me_2ambH_2)_2$-$[B_4L_4]$ show no signs of either dissolution or deterioration. After the compounds are collected, dried under vacuum, and exposed to the atmosphere, their powder X-ray diffraction (XRD) patterns remain unchanged. Their powder XRD patterns also remain unchanged after the compounds are held at 200 °C for 90 minutes in a stream of nitrogen. Such stability to solvent loss is not rare in coordination polymers, but the present cases are exceptional in that electrostatic anion–cation attractive forces, in concert with secondary bonding interactions, are responsible for preserving the crystallinity.

It is interesting to consider how the rigid angularity and chirality of the L^{4-} ligand, together with the stereochemical preferences of the associated metal or metalloid center (for example, molybdenum,[2] silicon,[1] or boron, herein) influence the composition and geometrical features of the aggregates they form. The strong preference of the $\{MoO_2\}^{2+}$ moiety for a *cis* dioxo arrangement imposes a *cis* configuration upon the two chelating catechol donors, which strongly inclines them towards one another, predisposing the system to form a "small ring" 2:2 association. When the two locally chiral doubly chelated molybdenum centers in $[(MoO_2)_2L_2]^{4-}$ have the same absolute configuration, and when the two L^{4-} units are of the same chirality, a relatively strain-free 2:2 association is formed.[2] On the other hand, the two catechol units associated with each silicon center in $[(C_6H_5Si)_4L_4]^{4-}$ and with each boron center in $[B_4L_4]^{4-}$ are nearly diametrically opposed to each other. The two catechol groups are essentially coplanar in the case of $[(C_6H_5Si)_4L_4]^{4-}$, thereby providing the O_4 base of a square pyramidal coordination environment, and are essentially orthogonal in the case of $[B_4L_4]^{4-}$, forming a tetrahedral coordination environment. As can be seen in Figure 1, boron's requirement for a tetrahedral environment is nicely satisfied in the 4:4 association $[B_4L_4]^{4-}$, when all four L^{4-} units have the same chirality. In contrast, the square pyramidal coordination geometry of the silicon centers in the $[(C_6H_5Si)_4L_4]^{4-}$ squares is more easily attained by two L^{4-} units of one chirality and two of the other.[1]

Preliminary synthetic and structural exploration indicates that many nitrogen bases, upon reaction with LH_4 and $B(OMe)_3$, yield tetragonal crystalline products, in which either all squares in a column have the same chirality (given by Et_3N, Me_3N, $Me_2NCH_2CH_2NH_2$, $Et_2NCH_2CH_2OH$, $BzEt_2N$, and piperazine) or squares of opposite chirality alternate within a column (given by $NH_2(CH_2)_nNH_2$ ($n = 2$, 3, or 6), NH_3, N_2H_4, Et_2NOH, and triethylenetetramine). Thus, the basic structure, consisting of chiral squares electrostatically cemented together by cations to form nanotubes that are packed parallel to one another, appears to be strongly preferred. Similar tubular structures are expected to be obtainable with a wide range of other nitrogen bases.

In summary, we report herein the first members of an extended family of easily accessible solids with spacious tubular structures. In the structures, chiral anionic macrocycles containing a large square central hole are cemented together by cations. The basic tubular structure is preserved after solvent removal, and these compounds have the potential to show interesting sorption properties. The fact that no atom within the structure is heavier than oxygen may be beneficial in practical applications where low density is important, for example, the storage of gases, such as hydrogen.

Received: September 6, 2005
Revised: November 2, 2005
Published online: December 15, 2005

Keywords: boron · crystal engineering · nanotubes · spiro compounds · supramolecular chemistry

[1] D. J. McCord, J. H. Small, J. Greaves, Q. N. Van, A. J. Shaka, E. B. Fleischer, K. J. Shea, *J. Am. Chem. Soc.* **1998**, *120*, 9763.

[2] A.-K. Duhme, S. C. Davies, D. L. Hughes, *Inorg. Chem.* **1998**, *37*, 5380.

[3] a) Preparation of $(Et_3NH)_4[B_4L_4]\cdot 12\,H_2O$: $B(OMe)_3$ (0.0296 g, 0.293 mmol) in methanol (2.5 mL) was added to a solution of LH_4 (0.0870 g, 0.256 mmol) in methanol/Et_3N (2.5 mL/1 mL). The solution was heated in a sealed tube at 160 °C for two days. Colorless crystals were collected, washed with methanol, and allowed to air dry. Yield: 0.0673 g, 53 %. Elemental analysis (%) calcd for $(Et_3NH)_4[B_4L_4]\cdot 12\,H_2O$ ($C_{108}H_{168}B_4N_4O_{28}$): C 64.4, H 8.4, N 2.8; found for air-dried sample: C 64.3, H 7.8, N 2.9; calcd for $(Et_3NH)_4[B_4L_4]\cdot 5\,H_2O$ ($C_{108}H_{154}B_4N_4O_{21}$): C 68.7, H 8.2, N 3.0; found for room-temperature vacuum-dried sample: C 68.9, H 8.1, N 3.0. b) Preparation of $(BzEt_2NH)_4[B_4L_4]\cdot 4\,MeOH$: $B(OMe)_3$ (0.0170 g, 0.169 mmol) in methanol (0.5 mL) was added to a solution of LH_4 (0.05 g, 0.1 mmol) in methanol/$BzEt_2N$ (0.5 mL/0.3 mL). The solution was heated in a sealed tube at 160 °C for two days. Colorless crystals were collected, washed with methanol, and allowed to air dry. Yield: 0.0347 g, 62 %. Elemental analysis (%) calcd for $C_{132}H_{168}B_4N_4O_{20}$: C 72.9, H 7.8, N 2.6; found: C 72.8, H 7.4, N 2.8. c) Preparation of $(Me_2ambH_2)_2[B_4L_4]\cdot 10\,H_2O$: $B(OMe)_3$ (0.25 g, 2.5 mmol) was added to a solution of LH_4 (0.86 g, 2.5 mmol) and amb (0.08 g, 0.6 mmol) in methanol (5 mL). The solution was heated in a sealed tube at 160 °C for two days. Colorless crystals were collected, washed with methanol, and allowed to air dry. Yield: 0.468 g, 41 %. Elemental analysis (%) calcd for $C_{104}H_{146}B_4N_4O_{26}$: C 65.7, H 7.2, N 2.9; found: C 65.8, H 6.8, N 3.3.

[4] a) Crystal data for $(Et_3NH)_4[B_4L_4]\cdot 6\,MeOH$: $0.03\times0.03\times0.15$ mm, tetragonal, $P4/n$, $a = 26.559(2)$, $c = 8.297(2)$ Å, $V = 5853(1)$ Å^3, $\rho_{calcd} = 1.129$ g cm^{-3}, $\theta_{max} = 27.7°$, $Mo_{K\alpha}$ radiation, $\lambda = 0.71073$ Å, $T = 130$ K, no absorption correction applied, $\mu(Mo_{K\alpha}) = 0.076$ mm^{-1}, 35805 reflections measured, 6761 unique, 372 parameters, $wR2$ (all data) = 0.1863, $R1$ [$I > 2\sigma(I)$] = 0.0760, max./min. residual electron density = 0.494/−0.336 e Å^{-3}; b) Crystal data for $(BzEt_2NH)_4[B_4L_4]\cdot 4\,MeOH$: $0.13\times0.15\times0.50$ mm, tetragonal, $P4/n$, $a = 26.762(1)$, $c = 8.4339(8)$ Å, $V = 6040.5(7)$ Å^3, $\rho_{calcd} = 1.195$ g cm^{-3}, $\theta_{max} = 27.5°$, $Mo_{K\alpha}$ radiation, $\lambda = 0.71073$ Å,

 © 2006 Wiley-VCH Verlag GmbH & Co. KGaA, Weinheim

$T = 130$ K, no absorption correction applied, $\mu(Mo_{K\alpha}) = 0.079\ mm^{-1}$, 35117 reflections measured, 6865 unique, 394 parameters, $wR2$ (all data) = 0.2398, $R1$ $[I > 2\sigma(I)] = 0.0759$, max./min. residual electron density = 0.598/−0.525 e Å^{-3}; c) Crystal data for $(Me_2ambH_2)_2[B_4L_4]\cdot 5\,MeOH$: $0.30 \times 0.30 \times 0.55$ mm, tetragonal, $P4/ncc$, $a = 26.812(1)$, $c = 16.792(1)$ Å, $V = 12072(1)$ Å^3, $\rho_{calcd} = 1.035\ g\,cm^{-3}$, $\theta_{max} = 27.6°$, $Mo_{K\alpha}$ radiation, $\lambda = 0.71073$ Å, $T = 130$ K, no absorption correction applied, $\mu(Mo_{K\alpha}) = 0.070\ mm^{-1}$, 70228 reflections measured, 6949 unique, 373 parameters, $wR2$ (all data) = 0.3113, $R1$ $[I > 2\sigma(I)] = 0.0981$, max./min. residual electron density = 1.188/−0.494 e Å^{-3}. All structures were solved by direct methods and refined against F^2 using *SHELX*97.[7] CCDC-281956 ($(Et_3NH)_4[B_4L_4]\cdot 6\,MeOH$), CCDC-281957 ($(BzEt_2NH)_4[B_4L_4]\cdot 4\,MeOH$), and CCDC-281958 ($(Me_2ambH_2)_2[B_4L_4]\cdot 5\,MeOH$) contain the supplementary crystallographic data for this paper. These data can be obtained free of charge from The Cambridge Crystallographic Data Centre via www.ccdc.cam.ac.uk/data_request/cif.

[5] M. R. Ghadiri, J. R. Granja, R. A. Milligan, D. E. McRee, N. Khazanovich, *Nature* **1993**, *366*, 324.

[6] For example: T. Y. Oku, H. Arita, T. Tsuneki, T. Ikariya, *J. Am. Chem. Soc.* **2004**, *126*, 7368.

[7] G. M. Sheldrick, *SHELX*97 (Release 97-2), University of Göttingen, Germany, **1998**.

 © 2006 Wiley-VCH Verlag GmbH & Co. KGaA, Weinheim

Cyclizations

DOI: 10.1002/anie.200503143

Reagent-Controlled Switching of 5-*exo* to 6-*endo* Cyclizations in Epoxide Openings**

Yoshiki Morimoto, Yoshihiro Nishikawa, Chigusa Ueba, and Takeshi Tanaka*

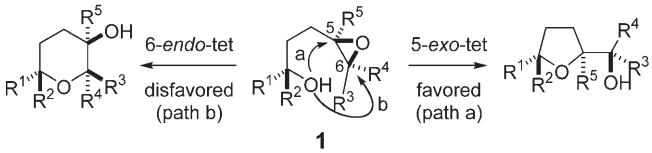
Tetrahydrofuran (THF) and tetrahydropyran (THP) rings are ubiquitous structural units that are extensively encountered in a number of biologically active natural products and functional molecules. Therefore, the development of synthetic methods for constructing THF and THP ether rings has attracted much attention from synthetic organic chemists.[1]

[*] Prof. Dr. Y. Morimoto, Y. Nishikawa, C. Ueba, T. Tanaka
Department of Chemistry
Graduate School of Science
Osaka City University
Sumiyoshi-ku, Osaka 558-8585 (Japan)
Fax: (+81) 6-6605-2522
E-mail: morimoto@sci.osaka-cu.ac.jp

[**] We thank Prof. M. Hashimoto, Hirosaki University, for providing us with a chance to begin this research. This work was supported by the Novartis Foundation (Japan) for the Promotion of Science, the Saneyoshi Scholarship Foundation, and a Grant-in-Aid for Scientific Research on Priority Areas 17035071 from the Ministry of Education, Culture, Sports, Science, and Technology (MEXT).

Supporting information for this article is available on the WWW under http://www.angewandte.org or from the author.

Among the possibilities, the intramolecular cyclization of bishomoepoxy alcohols is intriguing from the point of view of regioselectivity as well as it being one of the most practical and effective methods for the synthesis of both THF and THP cyclic ethers. In general, 5-*exo*-tet cyclizations are preferred to the 6-*endo*-tet variant because of a dominant stereoelectronic effect, which is known as Baldwin's rule.[2] However, the exact mode of cyclization depends on the substrates employed (Scheme 1). Thus, to observe 6-*endo* regioselectivity in opposition to Baldwin's rule a wide variety of methods have been devised, particularly over the last two decades. However, they almost all involve elaborate modifications of the epoxide substrate, for example, by the introduction of a π orbital[3] adjacent to the epoxide or sulfonyl[4] or trimethylsilyl (TMS)[5] substituents on the epoxide to activate the C6 position. There have hitherto been only two exceptions, namely, antibody catalysis[6] and $La(OTf)_3$-catalyzed cyclizations,[7] which overcome the normal preference for 5-*exo*-tet ring formation without the need for modification of the substrate, although in the latter case the substrates are limited to unusual methoxymethyl-substituted epoxides **1** ($R^5 = CH_2OMe$; Scheme 1). Herein, we report the non-enzymatic



1

Scheme 1. 5-*Exo* versus 6-*endo* cyclizations of bishomoepoxy alcohols to give THF (path a) and THP derivatives (path b).

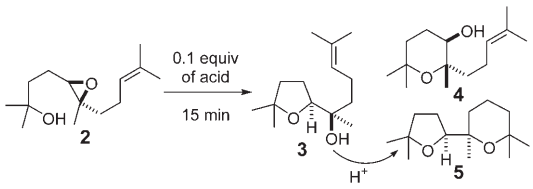
reagent-controlled switching of 5-*exo* to 6-*endo* cyclizations using the epoxide substrate **1** (R^1–R^4 = alkyl, R^5 = H), which usually demonstrates 5-*exo* regioselectivity.

In view of our interests in the synthesis of structurally and bioactively unique triterpene polyethers (oxasqualenoids),[8] we chose bishomoepoxy alcohol **2**[9] as the substrate for our investigation of the effective 6-*endo* cyclization. Alcohol **2** was prepared by the Sharpless epoxidation[10] of the corresponding bishomoallylic alcohol precursor.[11] In practice, acid-catalyzed cyclizations of bishomoepoxy alcohols such as **2** predominantly afford 5-*exo*-cyclized products[12] in a stereospecific and stereoselective manner (entry 1, Table 1).[13] First, we examined the solvent effect of the reaction catalyzed by (±)-10-camphorsulfonic acid (CSA). As the polarity of the solvents increased, the ratio of 6-*endo* cyclization increased (entries 2–4, Table 1). A stronger acid than CSA, such as trifluoromethanesulfonic acid (TfOH), further increased the yield of the 6-*endo* product **4** (entries 5–7). Bicyclic ether **5**, which could be generated by further cyclization of **3**,[14] was isolated in 13% yield as a by-product alongside **3** and **4** (entry 7, Table 1). However, we could not alter the preference for 5-*exo*-tet ring formation.

Next, we investigated the use of silyl triflates in the presence of 2,6-lutidine to activate the epoxide (Table 2).[15] Although treatment of **2** with TMSOTf in dichloromethane yielded only undesired diene **8a** (entry 1, Table 2), we were delighted to find that the reaction in acetonitrile provided 6-

InterScience
© 2006 Wiley-VCH Verlag GmbH & Co. KGaA, Weinheim

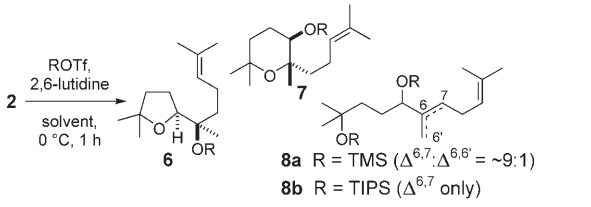
Table 1: Cyclizations of bishomoepoxy alcohol **2** catalyzed by Brønsted acids.



Entry	Acid	Solvent	*T*	Yield [%][a]		Ratio[b]
				3	**4**	5-*exo*/6-*endo*
1	CSA	CH_2Cl_2	0 °C	86	2	36:1
2	CSA	CH_2Cl_2	RT	77	4	22:1
3	CSA	CH_3CN	RT	70	20	3.5:1
4	CSA	CH_3NO_2	RT	59	18	3.2:1
5	TfOH	CH_2Cl_2	0 °C	76	6	13.3:1
6	TfOH	CH_3CN	0 °C	55	22	2.5:1
7	TfOH	CH_3NO_2	0 °C	33	25	1.9:1[c]

[a] Isolated yield. [b] Based on the isolated yield. [c] The ratio 5-*exo*/6-*endo* is equivalent to **(3+5)/4**.

Table 2: Cyclizations of bishomoepoxy alcohol **2** promoted by silyl triflates ROTf.[a]



Entry	ROTf (equiv)	Solvent	Yield [%][b]		Ratio[c]
			6+7	**8**	5-*exo*/6-*endo*
1	TMS (5)	CH_2Cl_2		70	
2	TMS (2)	CH_3CN	63		1:2.6
3	TMS (2)	CH_3NO_2	54		1:3.3
4	TES (2)	CH_3NO_2	59		1:5.8
5	TBS (5)	CH_3NO_2	82		1:12
6	TIPS (5)	CH_3NO_2	83		1:15
7[d]	TIPS (5)	CH_2Cl_2	34	38	1:2.7
8	TIPS (5)	CH_3CN	78		1:6.8

[a] The reaction was carried out at 0 °C for 1 h under a nitrogen atmosphere in the presence of 2,6-lutidine (1.4 equiv based on ROTf). [b] Isolated yield. [c] The ratio was determined by integration of the ^{1}H NMR spectra of the mixture of **6** and **7**. [d] The reaction was performed for 3.5 h. TES = triethylsilyl; TBS = *tert*-butyldimethylsilyl; TIPS = triisopropylsilyl.

endo-cyclized THP **7** in preference to 5-*exo* THF **6** (entry 2, Table 2).[16] The employment of nitromethane as solvent increased the 6-*endo* regioselectivity (entry 3, Table 2). Thus, other commercially available silyl triflates were further examined in nitromethane (entries 4–6, Table 2). The 6-*endo* regioselectivity was found to increase according to the steric bulkiness of the R group in ROTf (TMS < TES < TBS < TIPS). The best result was obtained by treating **2** with 5 equivalents of TIPSOTf in the presence of 7 equivalents of 2,6-lutidine in nitromethane at 0 °C for 1 h to give THP **7** (R = TIPS) in a ratio of 15:1 6-*endo*/5-*exo*. The TIPSOTf-promoted reaction in less-polar solvents led to a decrease in the 6-*endo* regioselectivity (entries 7 and 8, Table 2).

These results may be rationalized as follows: As these reactions are acidic epoxide openings, both S_N1 and S_N2 properties could be incorporated in the transition state (Figure 1). In terms of a stereoelectronic effect, 5-*exo* prod-

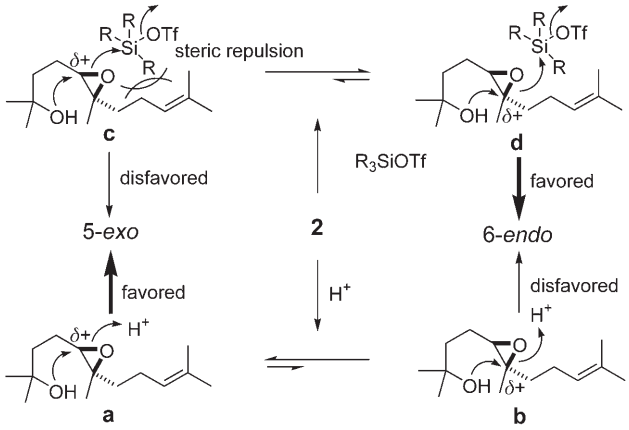


Figure 1. Possible transition states **a**–**d** with both S_N1 and S_N2 properties leading to 5-*exo* and 6-*endo* products.

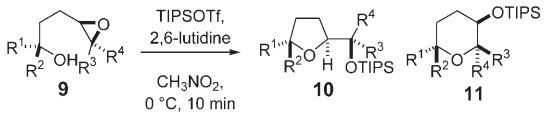
ucts would predominate by way of transition states **a** and **c** (Baldwin's rule). On the other hand, if an incipient partial positive charge upon the epoxide opening is considered, then 6-*endo* products would predominate because tertiary carbocations **b** and **d** are more stable than the secondary ones **a** and **c**. In the case of Brønsted acids as shown in Table 1, the stereoelectronic effect overcomes the electrostatic one; therefore, 5-*exo* THF **3** was overwhelmingly produced in dichloromethane (entry 1, Table 1). However, the factors that favored transition state **b**, namely, more-polar solvents and a stronger acid, relatively increased the production of 6-*endo* THP **4** (entry 7, Table 1). In the case of trialkylsilyl triflates (Table 2), steric repulsion between alkyl groups on the silicon and in the substrate occurs in transition state **c** leading to 5-*exo* THF **6** with a sterically encumbered acyclic tertiary silyl ether. Then, as the disadvantageous steric repulsion overcomes the advantageous stereoelectronic effect, 6-*endo* THP **7** with a cyclic secondary silyl ether would predominate by way of transition state **d** without such a steric repulsion. In practice, the factors that destabilize **c** and stabilize **d**, that is, sterically bulkier silyl triflates and more-polar solvents, respectively, impart a greater 6-*endo* regioselectivity.

The TIPSOTf-promoted cyclization was also investigated for substrates **9a**–**f** (Table 3). Good 6-*endo* regioselectivities were observed for all except **9d** (entry 4, Table 3). It was also seen that the cyclization proceeds in a stereospecific manner (entry 6, Table 2; and entries 1–3, Table 3) and displays 6-*endo* regioselectivity regardless of the relative configuration of the tertiary alcohol and epoxide substrates (entry 5, Table 3).

In conclusion, we have demonstrated the TIPSOTf-promoted switching of 5-*exo* to 6-*endo* cyclizations in nitro-

 © 2006 Wiley-VCH Verlag GmbH & Co. KGaA, Weinheim

Table 3: Cyclizations of bishomoepoxy alcohols **9a–f** promoted by TIPSOTf.[a]



Entry	9	R^1, R^2, R^3, R^4	Yield [%][b] 10 + 11	Ratio[c] 5-*exo*/6-*endo*
1	**a**	$R^1 = R^2 = R^4 = Me$, $R^3 = (CH_2)_2CH{=}CMe_2$	9 + 71	1:8
2	**b**	$R^1 = R^2 = R^3 = Me$, $R^4 = (CH_2)_3CHMe_2$	72	1:17
3	**c**	$R^1 = R^2 = R^4 = Me$, $R^3 = (CH_2)_3CHMe_2$	7 + 60	1:8
4	**d**	$R^1 = R^2 = R^3 = R^4 = Me$	86	1:3
5	**e + f**[d]	$R^1 = Ph$, $R^2 = R^3 = R^4 = Me$ (**e**), $R^2 = Ph$, $R^1 = R^3 = R^4 = Me$ (**f**)	79	1:8

[a] The reaction of **9** with TIPSOTf (5 equiv) in CH_3NO_2 was carried out in the presence of 2,6-lutidine (7 equiv) at 0 °C for 10 min under a nitrogen atmosphere. [b] Isolated yield. [c] Ratios were either determined by integration of the ^{1}H NMR spectra of the mixture of **10** and **11** or based on isolated yields. [d] As a mixture in a ratio of 1:1.4.

methane without the need for modification of the substrate, which normally shows a preference for 5-*exo*-tet ring formations. It is noteworthy that this sterically controlled switching by TIPSOTf (Figure 1) forms a contrast to the chelation-controlled switching in $La(OTf)_3$-catalyzed cyclizations.[7] Thus, a THF or THP ring can be formed from the same substrate by changing only the reagent, which would make possible the straightforward approach to bioactive oxasqualenoids.[8] Clarification of the details of the reaction mechanism and applications of this cyclization to natural products synthesis are in progress.

Received: September 5, 2005
Published online: December 15, 2005

Keywords: cyclization · oxygen heterocycles · regioselectivity · solvent effects

[1] For reviews, see: a) J.-C. Harmange, B. Figadère, *Tetrahedron: Asymmetry* **1993**, *4*, 1711–1754; b) U. Koert, *Synthesis* **1995**, 115–132.
[2] J. E. Baldwin, *J. Chem. Soc. Chem. Commun.* **1976**, 734–736.
[3] a) K. C. Nicolaou, M. E. Duggan, C.-K. Hwang, P. K. Somers, *J. Chem. Soc. Chem. Commun.* **1985**, 1359–1362; b) K. C. Nicolaou, C. V. C. Prasad, P. K. Somers, C.-K. Hwang, *J. Am. Chem. Soc.* **1989**, *111*, 5330–5334; c) T. Suzuki, O. Sato, M. Hirama, *Tetrahedron Lett.* **1990**, *31*, 4747–4750; d) C. Mukai, Y. Ikeda, Y. Sugimoto, M. Hanaoka, *Tetrahedron Lett.* **1994**, *35*, 2179–2182; e) C. Mukai, Y. Sugimoto, Y. Ikeda, M. Hanaoka, *Tetrahedron Lett.* **1994**, *35*, 2183–2186; f) H. Matsukura, M. Morimoto, T. Nakata, *Chem. Lett.* **1996**, 487–488; g) H. Matsukura, M. Morimoto, H. Koshino, T. Nakata, *Tetrahedron Lett.* **1997**, *38*, 5545–5548; h) J. D. Ha, E. Y. Shin, S. K. Kang, J. H. Ahn, J.-K. Choi, *Tetrahedron Lett.* **2004**, *45*, 4193–4195.
[4] a) Y. Mori, K. Yaegashi, H. Furukawa, *J. Am. Chem. Soc.* **1996**, *118*, 8158–8159; b) Y. Mori, H. Furuta, T. Takase, S. Mitsuoka, H. Furukawa, *Tetrahedron Lett.* **1999**, *40*, 8019–8022; c) H. Furuta, T. Takase, H. Hayashi, R. Noyori, Y. Mori, *Tetrahedron* **2003**, *59*, 9767–9777.
[5] a) G. Adiwidjaja, H. Flörke, A. Kirchning, E. Schaumann, *Tetrahedron Lett.* **1995**, *36*, 8771–8774; b) T. P. Heffron, T. F. Jamison, *Org. Lett.* **2003**, *5*, 2339–2342.
[6] a) K. D. Janda, C. G. Shevlin, R. A. Lerner, *Science* **1993**, *259*, 490–493; b) J. Na, K. N. Houk, C. G. Shevlin, K. D. Janda, R. A. Lerner, *J. Am. Chem. Soc.* **1993**, *115*, 8453–8454.
[7] a) K. Fujiwara, T. Tokiwano, A. Murai, *Tetrahedron Lett.* **1995**, *36*, 8063–8066; b) T. Tokiwano, K. Fujiwara, A. Murai, *Synlett* **2000**, 335–338.
[8] a) M. L. Souto, C. P. Manríquez, M. Norte, J. J. Fernández, *Tetrahedron* **2002**, *58*, 8119–8125; b) M. L. Souto, C. P. Manríquez, M. Norte, F. Leira, J. J. Fernández, *Bioorg. Med. Chem. Lett.* **2003**, *13*, 1261–1264.
[9] All new compounds were satisfactorily characterized by ^{1}H and ^{13}C NMR and IR spectroscopy and by low- and high-resolution mass spectrometry (see Supporting Information).
[10] a) K. B. Sharpless, R. C. Michaelson, *J. Am. Chem. Soc.* **1973**, *95*, 6136–6137; b) T. Fukuyama, B. Vranesic, D. P. Negri, Y. Kishi, *Tetrahedron Lett.* **1978**, 2741–2744.
[11] Y. Morimoto, T. Iwai, *J. Am. Chem. Soc.* **1998**, *120*, 1633–1634.
[12] The structures of 5-*exo*-cyclized products **3** and **14** generated by treatment of **2** and **9a**, respectively, with CSA in CH_2Cl_2 were identical to those obtained for authentic samples.[11] See Supporting Information.
[13] For other similar examples that undergo stereospecific 5-*exo* cyclizations, see: a) S. Hanessian, N. G. Cooke, B. DeHoff, Y. Sakito, *J. Am. Chem. Soc.* **1990**, *112*, 5276–5290; b) M. Hashimoto, H. Harigaya, M. Yanagiya, H. Shirahama, *J. Org. Chem.* **1991**, *56*, 2299–2311; c) K. Ujihara, H. Shirahama, *Tetrahedron Lett.* **1996**, *37*, 2039–2042; d) T. B. Towne, F. E. McDonald, *J. Am. Chem. Soc.* **1997**, *119*, 6022–6028; e) Y. Morimoto, T. Iwai, T. Yoshimura, T. Kinoshita, *Bioorg. Med. Chem. Lett.* **1998**, *8*, 2005–2010; f) Z. Xiong, E. J. Corey, *J. Am. Chem. Soc.* **2000**, *122*, 4831–4832; g) Y. Morimoto, T. Iwai, T. Kinoshita, *J. Am. Chem. Soc.* **2000**, *122*, 7124–7125; h) Y. Morimoto, T. Iwai, T. Kinoshita, *Tetrahedron Lett.* **2001**, *42*, 6307–6309; i) Y. Morimoto, M. Takaishi, T. Iwai, T. Kinoshita, H. Jacobs, *Tetrahedron Lett.* **2002**, *43*, 5849–5852.
[14] K. Nacro, M. Baltas, C. Zedde, L. Gorrichon, J. Jaud, *Tetrahedron* **1999**, *55*, 5129–5138.
[15] a) M. E. Jung, D. C. D'Amico, *J. Am. Chem. Soc.* **1997**, *119*, 12150–12158; b) M. E. Jung, B. Hoffmann, B. Rausch, J.-M. Contreras, *Org. Lett.* **2003**, *5*, 3159–3161.
[16] Desilylation of the mixture of silyl ethers **6** and **7** with tetrabutylammonium fluoride provided THF **3** and THP **4**, respectively, in almost the same ratios as those reported in Table 2.

 © 2006 Wiley-VCH Verlag GmbH & Co. KGaA, Weinheim

Nanoparticles

DOI: 10.1002/anie.200502731

Thermosensitive Core–Shell Particles as Carriers for Ag Nanoparticles: Modulating the Catalytic Activity by a Phase Transition in Networks**

*Yan Lu, Yu Mei, Markus Drechsler, and Matthias Ballauff**

Metal nanoparticles have properties that are significantly different from the bulk properties of the metals.[1–4] Moreover, their high surface-to-volume ratio renders them ideal candidates for application as catalysts.[5–9] However, the pronounced tendency of nanoparticles to aggregate must be overcome by using suitable carrier systems. Recently, a number of systems have been discussed that are suitable for applications in aqueous environments. These include polymers,[10–14] dendrimers,[15,16] microgels,[17,18] and other colloidal systems.[19,20] In all the cases studied so far, these carrier systems only provide a suitable support for the nanoparticles and prevent them from aggregating. In this way the carrier system of, for example, dendrimers or microgels acts much in the same way as a "nanoreactor" that immobilizes the particles and leads to their more convenient handling.

Here we report on the first system that allows us to modulate the activity of nanoparticles through a thermodynamic transition that takes place within the carrier system. Figure 1 displays the principle. Metallic nanoparticles are embedded in a polymeric network attached to a colloidal core particle. In all the cases discussed here the core consists of poly(styrene) (PS) while the network consists of poly(*N*-isopropylacrylamide) (PNIPA) cross-linked with *N*,*N*′-methylenebisacrylamide (BIS). The particles are suspended in water, which swells the PNIPA at room temperature. The PNIPA network, however, undergoes a phase transition around 30 °C, during which most of the water is expelled. Previous experiments[21] have demonstrated that this transition is perfectly reversible and the process of shrinking and reswelling can be repeated without degradation or coagulation of the particles.

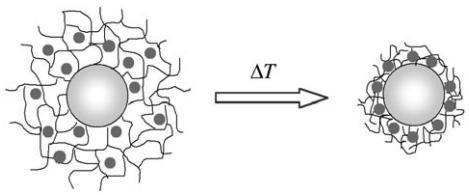


Figure 1. PS-NIPA-Ag composite particles consisting of thermosensitive core–shell particles in which Ag nanoparticles are embedded. The composite particles are suspended in water which swells the thermosensitive network attached to the surface of the core particles. In this state the reagents can diffuse freely to the nanoparticles that act as catalysts. At higher temperatures ($T > 30$ °C) the network shrinks and the catalytic activity of the nanoparticles is strongly diminished.

Metallic nanoparticles embedded in such a network are fully accessible to reactants at low temperature. Above the phase transition, however, the marked shrinkage of the network should be followed by a concomitant slowing down of the diffusion of the reactants within the network. The rate of reactions catalyzed by the nanoparticles should thus be slowed down considerably. In this way, the network could act as a "nanoreactor" that can be opened or closed to a certain extent.

Herein we demonstrate that thermosensitive core–shell networks may indeed be used as such a nanoreactor. The activity of the catalyst can be modulated by temperature over a wide range. As the model reaction we chose the reduction of 4-nitrophenol to 4-aminophenol by sodium borohydride. The reaction was repeatedly performed to check the catalytic activity of the metal nanoparticles, and the results obtained in the present study can be directly compared to literature data.[8,22]

The carrier particles having a PS core and a PNIPA shell were prepared as described recently.[23,24] Figure 2 shows a schematic representation of the silver nanoparticles being

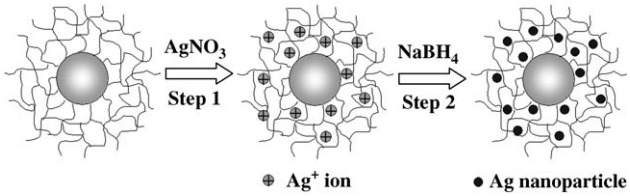


Figure 2. Formation of silver nanoparticles in the PS–NIPA core–shell system. The cross-linked PNIPA chains absorb Ag ions (step 1) which are reduced to produce Ag nanoparticles immobilized in the thermosensitive network (step 2).

generated directly in the network of the carrier particles. To this end, a dilute suspension of the carrier particles is treated with a 0.1 M $AgNO_3$ solution and the reduction is achieved through addition of an aqueous solution of $NaBH_4$. The suspension of the composite particles is subsequently cleaned by ultrafiltration with pure water.

Figure 3 shows an image of several particles obtained by cryogenic transmission electron microscopy (cryo-TEM; additional micrographs can be found in the Supporting

[*] Dr. Y. Lu, Y. Mei, Prof. Dr. M. Ballauff
Physikalische Chemie I
Universität Bayreuth
Universitätsstrasse 30, 95440 Bayreuth (Germany)
Fax: (+49) 921-55-2780
E-mail: matthias.ballauff@uni-bayreuth.de
Dr. M. Drechsler
Makromolekulare Chemie II
University of Bayreuth
95440 Bayreuth (Germany)

[**] We thank the Deutsche Forschungsgemeinschaft (SFB 481), Bayreuth, BASF, and the Fonds der Chemischen Industrie for financial support.

Supporting information for this article is available on the WWW under http://www.angewandte.org or from the author.

 © 2006 Wiley-VCH Verlag GmbH & Co. KGaA, Weinheim

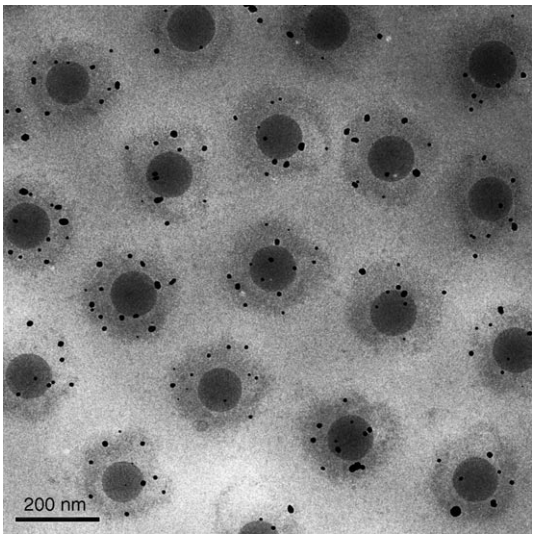


Figure 3. Cryo-TEM image for the silver nanocomposite particles.

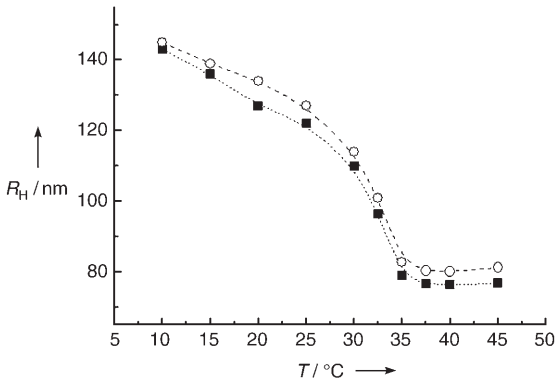


Figure 4. Hydrodynamic radii versus temperature plot for PS-NIPA-Ag particles. ■: hydrodynamic radii for the PS–NIPA particles, ○: PS-NIPA-Ag particles.

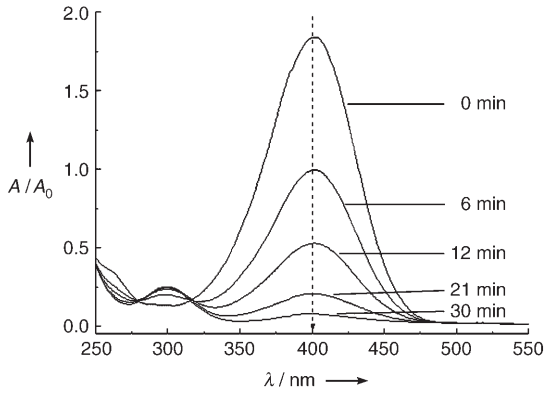


Figure 5. Reduction of 4-nitrophenol by $NaBH_4$: UV/Vis spectra of solutions of 4-nitrophenol measured at different times *t*.

Information).[25] The formation of the Ag nanoparticles is also seen from the suspension becoming yellow after the reduction which corresponds to a maximum in the UV/Vis spectrum (see Supporting Information) at 410 nm. The Ag nanoparticles generated by this method have diameters of 8.5 nm (±1.5 nm; Figure 3). Thermogravimetric analysis measurements indicate that 10.4 wt% Ag had been embedded. Moreover, it shows that all the particles are immobilized within the network and none are located outside of the PNIPA shells of the carriers. This observation indicates a strong localization of the Ag^+ ions within the network, most probably caused by a complexation of the Ag^+ ions by the nitrogen atoms of the PNIPA. This proposal was confirmed by the slight shrinkage of the PNIPA network after the addition of $AgNO_3$ to the system, as shown by dynamic light scattering measurements (see the Supporting Information). Figure 3 also indicates that the nanoparticles are truly immobilized in the mesh of the PNIPA network, fixed to the surface of the core particles. Hence, the composite particles consisting of the carrier and the Ag nanoparticles are expected to present a stable system; thus, no loss of Ag particles should occur during the reaction.

Dynamic light scattering measurements of composite particles at different temperatures indicate that the thermosensitive properties of the PNIPA network are not hindered by the incorporation of silver particles into the network. The silver nanoparticles do not disturb the phase transition within the network. Figure 4 displays the hydrodynamic radii of the carrier particles (squares) and the composite particles (circles). Both sets of data agree more or less, thus showing that the thermosensitive shell undergoes a phase transition at 32 °C. This result is in excellent agreement with previous findings.[21,23]

Only small amounts of the composite particles are needed to catalyze the reduction of 4-nitrophenol by $NaBH_4$ (ca. 6 mg L^{-1}). Hence, the adsorption of the composite particles can be disregarded and the reduction can be followed by monitoring the UV/Vis spectra as a function of time (Figure 5). The degree of conversion can be directly read off these curves, and the ratio of the concentration c_t of 4-nitrophenol at time t to its value c_0 at $t = 0$ is given directly by the ratio of the respective absorbance A/A_0.

Since the concentration of borohydride largely exceeds the concentration of 4-nitrophenol, the reaction should be of first order with regard to this reactant. Figure 6 shows that this is the case for temperatures ranging from 10 to 40 °C. Linear relationships between $\ln[c_t/c_0]$ and the reaction time t are obtained in all cases at low conversions. Deviations from linearity is only seen for low temperatures and high degrees of conversion. However, for the present purpose it suffices to discuss the initial rates of reaction. It must be noted that there is an induction period t_0, which is obtained by extrapolation to zero conversion (see Figure 6). This finding is in accord with other studies on the catalysis of this reaction by metal nanoparticles.[8]

The rate constants $k(T)$ obtained from these plots are shown in Figure 7, and it is interesting to note that the constants k obtained at different temperatures do not exhibit the typical dependence on temperature. Instead of a simple linear relationship between $\ln k$ and T^{-1}, the change of k with temperature can be divided into three regions. When the reaction temperature is low, the PNIPA network is totally swollen with water. In this case the silver nanoparticles which have been embedded in the network are fully accessible to the

 © 2006 Wiley-VCH Verlag GmbH & Co. KGaA, Weinheim

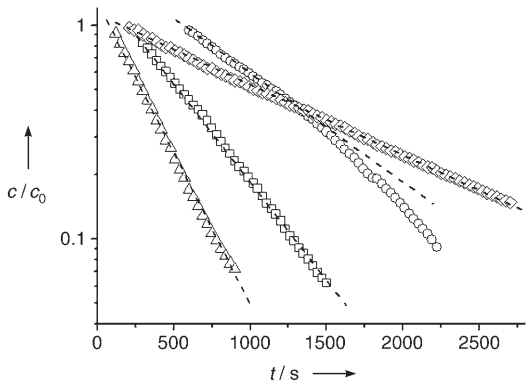


Figure 6. Influence of temperature on the kinetic constant k measured with PS-NIPA-Ag particles. The concentrations are as follows: [4-nitrophenol] = 0.1 mM, [$NaBH_4$] = 10 mM, [PS-NIPA-Ag] = 6.3×10^{-3} g L^{-1}. ○: 283 K; □: 293 K; ◇: 305.5 K; △: 313 K.

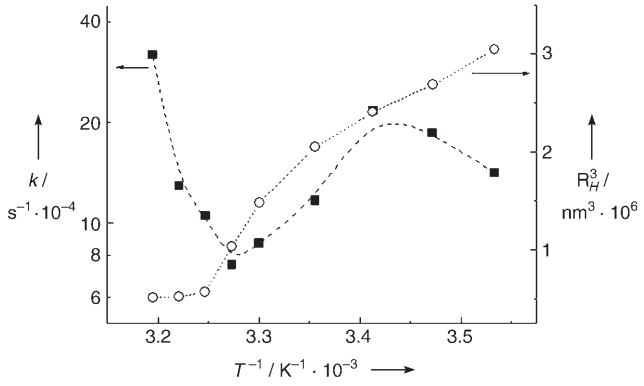


Figure 7. Arrhenius plot of the reaction rate k. ■: reaction rate k measured in the presence of PS-NIPA-Ag particles at different temperatures. ○: volume change of the particles with temperature.

reactants for the catalytic reduction. Here the rate constant k will exhibit a conventional Arrhenius-type dependence on temperature. However, when the reaction temperature is higher than 25 °C, the PNIPA network shrinks markedly with an increase in temperature. The shrinking of the network resulting from the expulsion of water is followed by a concomitant slowing down of the diffusion of reactants within the network. This process will in turn lower the rate of the reaction catalyzed by the silver nanoparticles. It is clear that the increase in k by the rise in temperature is overcompensated by the diffusional barrier. Hence, the reaction rate must reach its minimum at the transition temperature. Figure 7 demonstrates this through the plot of the cube of the hydrodynamic radius R_H (see Figure 4) as a function of $1/T$. R_H^3 is inversally proportional to the density of the network, which increases considerably with temperature, thus impeding the diffusion within the network. If the temperature is increased further, the density of the network stays constant; the strong increase in k with T dominates and the reaction rate rises again.

In conclusion, the thermosensitive PNIPA network can act as a "nanoreactor" that can be opened or closed to a certain extent: As shown in Figure 7, the catalytic activity of the silver nanoparticles can be modulated by temperature in a nonmonotonous way over a wide range.

Experimental Section

N-Isopropylacrylamide (NIPA, Aldrich), *N,N'*-methylenebisacrylamide (BIS, Fluka), sodium dodecyl sulfate (SDS, Fluka), and potassium peroxodisulfate (KPS, Fluka) were used as received. Styrene (BASF) was destabilized on Al_2O_3 and stored in the refrigerator. Silver nitrate ($AgNO_3$, Aldrich), sodium borohydride ($NaBH_4$, Aldrich), and 4-nitrophenol (Aldrich) were used as received. Water was purified by reverse osmosis (MilliRO, Millipore) and ion exchange.

The core–shell-type PS–NIPA particles were synthesized and characterized as described in Ref. [20,22] The PS core latex was prepared by conventional emulsion polymerization using styrene (253.2 g) and NIPA (13.75 g) as the monomers, SDS (2.34 g dissolved in 925 g water) as the surfactant, and KPS (0.50 g dissolved in 20 g of water) as the initiator. The reaction was run at 80 °C for 8 h. Purification was done by ultrafiltration with 10 times the volume of water.

The core–shell system was prepared by seeded emulsion polymerization. PS core latex (347.67 g) was diluted with water (500 g) together with NIPA (40.07 g) and BIS (1.37 g). After this stirred mixture had been heated to 80 °C, the reaction was started with the addition of KPS (0.40 g, dissolved in 15 g water), and the reaction was run for 4.5 h. The latex was purified by ultrafiltration against purified water (membrane: cellulose nitrate with 100 nm pore size supplied by Schleicher & Schuell).

The preparation of the silver nanoparticles in an aqueous solution was carried out by addition of silver nitrate to a suspension of PS–NIPA particles and subsequent reduction with sodium borohydride. For a typical experiment, an aqueous solution of $AgNO_3$ (0.1 M, 0.575 mL) was added to an aqueous solution of PS–NIPA (2 g PS–NIPA latex diluted with 98 g water), and the mixture was stirred for 30 minutes under N_2. A solution of sodium borohydride (0.043 g) in water (5 g) was then quickly added to the solution with stirring for one hour. After that, silver nanocomposite particles were cleaned by ultrafiltration against purified water (membrane: cellulose nitrate with 100 nm pore size supplied by Schleicher & Schuell).

Catalytic reduction of 4-nitrophenol: An aqueous solution of sodium borohydride (10 mM, 0.05 mL) was added to a solution of 4-nitrophenol (0.1 mM, 2.95 mL). A definite amount of silver nanoparticles (6.3×10^{-3} g L^{-1}) was then added to this solution. Immediately after the addition of silver nanoparticles, UV spectra of the mixture were recorded with a UV/VIS spectrometer. The kinetic study of the reaction was performed by measuring the change in intensity of the absorbance at 400 nm with time. The spectra were recorded every 1.5 minutes in the range 250–550 nm.

Cryo-TEM samples were prepared by vitrification of thin liquid films supported on a TEM copper grid (600 mesh, Science Services, Munich, Germany) in liquid ethane. The sample was inserted into a cryotransfer holder (CT3500, Gatan, Munich, Germany) and transferred to a Zeiss EM922 EFTEM microscope (Zeiss NTS GmbH, Oberkochen, Germany). Examinations were carried out at around 90 K. The electron microscope was operated at an acceleration voltage of 200 kV. All images were recorded digitally by a bottom-mounted CCD camera system (UltraScan 1000, Gatan, Munich, Germany) and processed with a digital imaging processing system (Digital Micrograph 3.9 for GMS 1.4, Gatan, Munich, Germany).[25] Dynamic light scattering measurements were performed with an ALV 4000 goniometer (Peters) at different temperatures at 90°. The UV spectra were measured on a Lambda 25 spectrometer (Perkin Elmer).

Received: August 3, 2005
Published online: December 19, 2005

Keywords: heterogeneous catalysis · nanoparticles · nanoreactors · thermochemistry

 © 2006 Wiley-VCH Verlag GmbH & Co. KGaA, Weinheim

[1] F. Frederix, J. M. Friedt, K. H. Choi, W. Laureyn, A. Campitelli, D. Mondelaers, G. Maes, G. Borghs, *Anal. Chem.* **2003**, *75*, 6894 – 6900.

[2] M. Brust, C. J. Kiely, *Colloids Surf. A* **2002**, *202*, 175 – 186.

[3] C. H. Ho, J. Tobis, C. Sprich, R. Thomann, J. C. Tiller, *Adv. Mater.* **2004**, *16*, 957 – 961.

[4] H. R. Moon, J. H. Kim, M. P. Suh, *Angew. Chem.* **2005**, *117*, 1287 – 1291; *Angew. Chem. Int. Ed.* **2005**, *44*, 1261 – 1265.

[5] C. T. Campbell, S. C. Parker, D. E. Starr, *Science* **2002**, *298*, 811 – 814.

[6] A. B. R. Mayer, J. E. Mark, S. H. Hausner, *Angew. Makromol. Chem.* **1998**, *259*, 45 – 53.

[7] M. Zhao, R. M. Crooks, *Angew. Chem.* **1999**, *111*, 375 – 377; *Angew. Chem. Int. Ed.* **1999**, *38*, 364 – 366.

[8] a) N. Pradhan, A. Pal, T. Pal, *Colloids Surf. A* **2002**, *196*, 247 – 257; b) S. Praharaj, S. Nath, S. K. Ghosh, S. Kundu, T. Pal, *Langmuir* **2004**, *20*, 9889 – 9892.

[9] C. Shi, M. Cheng, Z. Qu, X. Bao, *Appl. Catal. B* **2004**, *51*, 171 – 181.

[10] a) C. W. Chen, M. Q. Chen, T. Serizawa, M. Akashi, *Adv. Mater.* **1998**, *10*, 1122- 1126; b) C. W. Chen, T. Serizawa, M. Akashi, *Langmuir* **1999**, *15*, 7998 – 8006; c) Q. Sun, Y. Deng, *Langmuir* **2005**, *21*, 5812 – 5816.

[11] a) G. Carotenuto, *Appl. Organomet. Chem.* **2001**, *15*, 344 – 351; b) G. Garotenuto, G. P. Pepe, L. Nicolais, *Eur. Phys. J. B* **2000**, *16*, 11 – 17.

[12] K. P. Velikov, G. E. Zegers, A. Blaaderen, *Langmuir* **2003**, *19*, 1384 – 1389.

[13] J. W. Jim, J. Lee, J. H. Ryu, J. S. Lee, S. J. Kim, S. H. Han, I. S. Chang, H. H. Kang, K. D. Suh, *J. Polym. Sci. Part A* **2004**, *42*, 2551 – 2557.

[14] O. Siiman, A. Burshteyn, *J. Phys. Chem. B* **2000**, *104*, 9795 – 9810.

[15] Z. Liu, X. Wang, H. Wu, C. Li, *J. Colloid Interface Sci.* **2005**, *287*, 604 – 611.

[16] a) K. Esumi, A. Suzuki, A. Yamohira, K. Torigoe, *Langmuir* **2000**, *16*, 2604 – 2608; b) T. Endo, T. Yoshimura, K. Esumi, *J. Colloid Interface Sci.* **2005**, *286*, 602 – 609; c) K. Esumi, R. Isono, T. Yoshimura, *Langmuir* **2004**, *20*, 237 – 243.

[17] a) A. Pich, S. Bhattacharya, Y. Lu, V. Boyko, H.-J. Adler, *Langmuir* **2004**, *20*, 10706 – 10711; b) A. Pich, J. Hain, Y. Lu, V. Boyko, Y. Prots, H.-J. Adler, *Macromolecules* **2005**, *38*, 6610 – 6619.

[18] a) A. Biffis, N. Orlandi, B. Corain, *Adv. Mater.* **2003**, *15*, 1551 – 1555; b) A. Biffis, E. Sperotto, *Langmuir* **2003**, *19*, 9548 – 9550.

[19] G. Sharma, M. Ballauff, *Macromol. Rapid Commun.* **2004**, *25*, 547 – 552.

[20] a) A. A. Antipov, G. B. Sukhorukov, Y. A. Fedutik, J. Hartmann, M. Giersig, H. Moehwald, *Langmuir* **2002**, *18*, 6687 – 6693; b) D. G. Shchukin, I. L. Radtchenko, G. B. Sukhorukov, *ChemPhysChem* **2003**, *4*, 1101 – 1103.

[21] a) N. Dingenouts, Ch. Norhausen, M. Ballauff, *Macromolecules* **1998**, *31*, 8912 – 8917; b) J.-H. Kim, M. Ballauff, *Colloid Polym. Sci.* **1999**, *277*, 1210 – 1214; c) M. Ballauff, *Macromol. Chem. Phys.* **2003**, *204*, 220 – 234.

[22] T. Vincent, E. Guibal, *Langmuir* **2003**, *19*, 8475 – 8483.

[23] a) N. Dingenouts, M. Ballauff, *Acta Polym.* **1998**, *49*, 178 – 183; b) N. Dingenouts, Ch. Norhausen, M. Ballauff, *Macromolecules* **1998**, *31*, 8912 – 8917; c) S. Seelenmeyer, I. Deike, N. Dingenouts, S. Rosenfeldt, Ch. Norhausen, M. Ballauff, T. Narayanan, *J. Appl. Crystallogr.* **2000**, *33*, 574 – 576; d) N. Dingenouts, S. Seelenmeyer, I. Deike, S. Rosenfeldt, M. Ballauff, P. Lindner, T. Narayanan, *Phys. Chem. Chem. Phys.* **2001**, *3*, 1169 – 1174; e) S. Seelenmeyer, I. Deike, S. Rosenfeldt, Ch. Norhausen, M. Ballauff, T. Narayanan, *J. Chem. Phys.* **2001**, *114*, 10471 – 10478; f) I. Deike, M. Ballauff, N. Willenbacher, A. Weiss, *J. Rheol.* **2001**, *45*, 709 – 720.

[24] a) D. Duracher, F. Sauzedde, A. Elaissari, A. Perrin, C. Pichot, *Colloid Polym. Sci.* **1998**, *276*, 219 – 231; b) D. Duracher, F. Sauzedde, A. Elaissari, C. Pichot, L. Nabzar, *Colloid Polym. Sci.* **1998**, *276*, 920 – 929; c) K. Kratz, T. Hellweg, W. Eimer, *Colloids Surf. A* **2000**, *170*, 137 – 149; d) T. Hellweg, C. D. Dewhurst, E. Bruckner, K. Kratz, W. Eimer, *Colloid Polym. Sci.* **2000**, *278*, 972 – 978.

[25] A. Wittemann, M. Drechsler, Y. Talmon, M. Ballauff, *J. Am. Chem. Soc.* **2005**, *127*, 9688 – 9689.

 © 2006 Wiley-VCH Verlag GmbH & Co. KGaA, Weinheim

Sugar Helices

DOI: 10.1002/anie.200503145

Oligo-(1→2)-α-D-glucopyranosyl-(1→2)-β-D-fructofuranosides Form Tight Sugar Coils**

*Daniela Fischer, Eckhard Loos, and Armin Geyer**

Dedicated to Professor Horst Kunz on the occasion of his 65th birthday

The conformational dynamics of glucooligosaccharides is generally fast without significant energy barriers between rotational isomers about the glycosidic bond. The new class of glucans described here exhibits an energy barrier large enough to result in line-broadening in the ^{1}H NMR spectra from the slow equilibrium between a folded helix and a partially unfolded structure. α-D-Glucooligosaccharides and glucans are ubiquitous saccharides connected by either (1→3)-, (1→4)-, or (1→6)- linkages. Beside their role as storage sugars, certain oligosaccharides are important bioprotectants of cellular membranes and proteins (vide infra). The oligosaccharides isolated from *Nostoc* sp. and *N. ellipsosporum* extend this class of carbohydrates by the (1→2)-linked oligomers of α-D-glucose with the highest degrees of polymerization known so far. In contrast to the widespread

[*] Prof. Dr. A. Geyer
Fachbereich Chemie
Philipps-Universität Marburg
35032 Marburg (Germany)
Fax: (+49) 6421-28-22021
E-mail: geyer@staff.uni-marburg.de

Dr. D. Fischer
Fachbereich Chemie und Pharmazie
Universität Regensburg
93040 Regensburg (Germany)

Dr. E. Loos
Lehrstuhl für Zellbiologie und Pflanzenphysiologie
Universität Regensburg
93040 Regensburg (Germany)

[**] This work was supported by the Deutsche Forschungsgemeinschaft. The authors thank Edelgard Herold for help in the preparation of the oligosaccharides.

WILEY InterScience DISCOVER SOMETHING GREAT
© 2006 Wiley-VCH Verlag GmbH & Co. KGaA, Weinheim

inulins,[1] where a single pyranose ring terminates a fructan oligomer, α-D-Glc(1→2)[-β-D-Fru(1→2)]$_n$, the cyanobacterial oligosaccharides described here have an inverted composition with a single fructofuranose terminating a linear chain of glucopyranoses, [α-D-Glc(1→2)]$_n$-β-D-Fru. The individual oligomers could be separated up to the decasaccharide ($n = 9$). They form right-handed helices with a tetrasaccharide repeat, a diameter of 12 Å, and a pitch of 5 Å. Although any glucan can assume helical conformations in solution, only the vicinal α-(1→2)-glycosidic linkages of the cyanobacterial oligosaccharides induce a compact helix which—in the presence of appropriate helix-capping fructofuranose—exhibits a relevant energy barrier of unwinding. Kojiheptaose with a fructofuranose end-capping, [α-D-Glc-(1→2)]$_7$-β-D-Fru, is the smallest biopolymer with an NMR-observable unfolding barrier (^{1}H NMR, 300 K, 600 MHz), thus demonstrating the cooperative stabilizing effect of helix capping and helix pitch. The secondary structure of the native oligosaccharide collapses upon selective hydrolysis of the helix-capping fructofuranose.

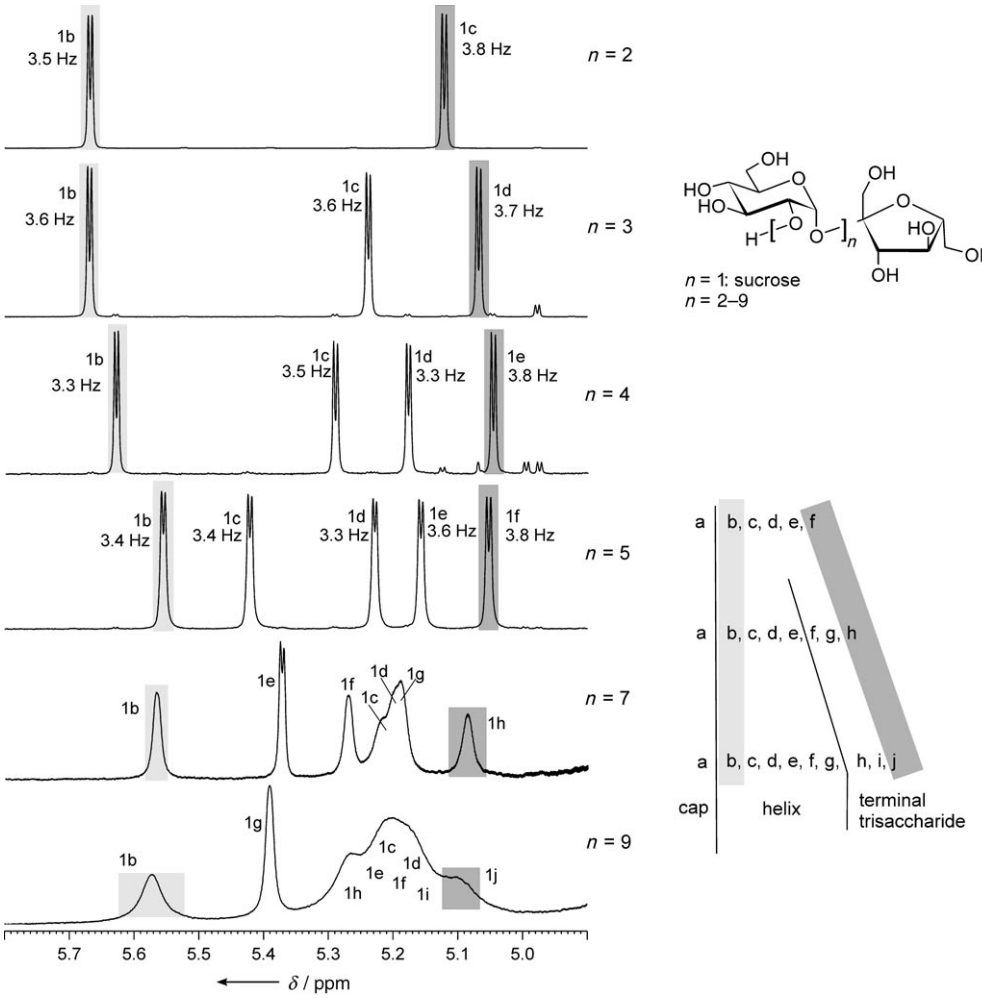


Figure 1. Expansion of the anomeric region from the ^{1}H NMR spectra (D_2O, 300 K, 600 MHz) of the α-D-glucooligosaccharides [α-D-Glc(1→2)]$_n$-β-D-Fru isolated from *N. ellipsosporum*. The signal assignments are based on homo- (DQF-COSY) and heteronuclear (HMQC, HMBC) correlations and additionally on dipolar contacts (ROESY) in the fast-exchange regime (320 K) for the octa- and decasaccharide. In all compounds studied, the anomeric proton of the pyranose b (gray) is resonant at lowest field (highest ppm value), while the glucopyranose on the opposite end of the oligomer appears at highest field (dark gray).

The amount and composition of cyanobacterial intracellular saccharides varies in response to environmental stress. Total intracellular carbohydrate levels of the investigated *Nostoc* species rise up to tenfold in response to salt (75 mM NaCl, 2 days) and temperature (40 °C, 1 day), respectively. Especially under heat stress, sucrose and the lower glucooligosaccharides in *N. ellipsosporum* are displaced by higher oligomers up to the decasaccharide. The quality of this new class of nonreducing sugars to act as bioprotectants[2,3] is described elsewhere.[4]

Oligo-(1→2)-α-D-glucopyranosyl-(1→2)-β-D-fructofuranosides were isolated and characterized up to the decasaccharide, thus exceeding previously known koji oligomers obtained from either in vitro synthesis[5] or natural sources[6] and establishing a complete series of α(1→2)-glucans with a fructofuranoside capping on the reducing-end terminus. Transglycosidic heteronuclear $^3J_{CH}$ couplings identify α(1→2)-linkages and assign the fructofuranoside on the reducing end of the α(1→2)-glucan chain. Well-separated anomeric resonances in the ^{1}H NMR spectra (Figure 1) with ^3J coupling constants of around 3.5 Hz are observed even for the hexasaccharide [α-D-Glc(1→2)]$_5$-β-D-Fru.[4] The assignments of the homo- and heteronuclear NMR spectra are obtained in a completeness that cannot be achieved for other glucans which exhibit the minimal dispersions of ^{1}H NMR chemical shifts typical of homooligomers. The signals of the anomeric protons of the α-(1→2)-linked hexasaccharide (Figure 1) are at least 0.1 ppm (^{1}H NMR, 600 MHz) separated from each other, while, for comparison, the signals of the anomeric protons of the three glycosidic linkages of the α-(1→4)-glucan maltotetraose are not at all separated in the ^{1}H NMR spectrum. The unexpectedly large chemical-shift dispersion is a consequence of the limited conformational flexibility of the vicinal progression of glycosidic linkages. One helix turn is formed by four glucose rings, and hydrophobic stacking between neighboring helix turns stabilizes the overall secondary structure. The characteristic NOEs are discussed in Figure 2, and a model is shown in Figure 3.

The glycosidic torsions of each Glcα(1→2)-Glc disaccharide moiety of the right-handed helix assume values of approximately $\phi = -30°$ (ϕ = H1-C1-O2-C2) and $\psi = +30°$ (ψ = C1-O2-C2-H2), which are well within the global energy

 © 2006 Wiley-VCH Verlag GmbH & Co. KGaA, Weinheim

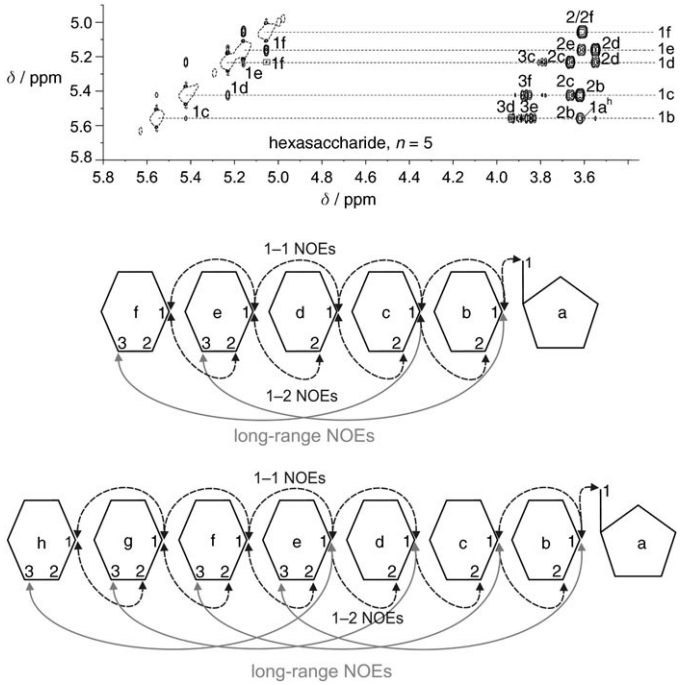


Figure 2. Top: Expansion of the anomeric region from the rotating-frame NOESY spectrum (ROESY) of the hexasaccharide [α-D-Glc(1→2)]$_5$-β-D-Fru including the NOE assignments. Bottom: Schematic representation of two capped α(1→2)-glucans with the NOEs defining the helix structure. Average distances for NOEs: $H1_i$–$H1_{i+1}$ = 2.9–3.4 Å, $H2_i$–$H1_{i+1}$ = 2.1–2.2 Å; long-range NOEs: $H1_i$–$H3_{i+3}$ = 2.4–2.5 Å. The NOE pattern of the octasaccharide (320 K) is a logical extension of the hexasaccharide. Long-range NOEs are absent after acidolysis of the fructofuranoside bond and the average interglycosidic NOEs shorten ($H1_i$–$H1_{i+1}$ = 2.3 Å for the α epimer and 2.4–2.8 Å for the β epimer) as a result of conformational flexibility.

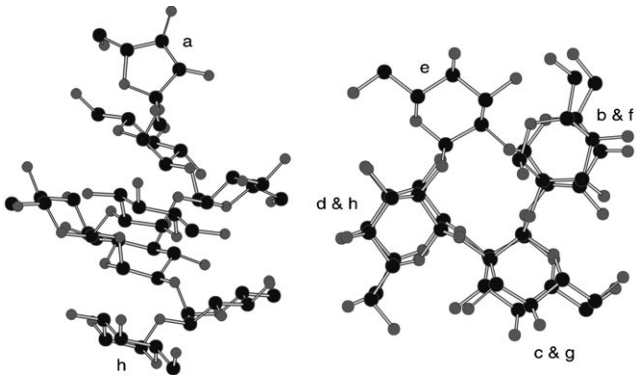


Figure 3. Left: Side view of the energy-minimized average structure of the octasaccharide including NOE-derived distance restraints. The plane of the fructofuranose ring is perpendicular to the planes of the pyranose rings of the helix. Right: Top view along the helix axis showing the tetrasaccharide repeat (ring a is not shown in this representation). Molecules were constructed in HyperChem and minimized in vacuo to 0.01 kcal mol^{-1} Å^{-1}. The MM2+ parameter set was used for the minimization procedure in conjunction with the Polak–Ribiere conjugate gradient method implemented in HyperChem.

minimum of the Ramachandran plot of an isolated kojibiose disaccharide encompassing values for ϕ between 0 and −60° and ψ between −60 and +60°.[7] In contrast to an isolated kojibiose disaccharide, the ϕ/ψ plots of the longer α(1→2)-glucans are much more restricted because the borderline between *P* and *M* helicity divides the global energy minimum of the ϕ/ψ plots along a line where the sum of ϕ and ψ equals −60°. Together with the +60° (O2-C2-C1-O1) added by each pyranose, a preference for an overall zero helicity (ring) results. In other words, the combination of glycosidic torsions preferred by an individual α(1→2)-glycosidic bond is not accessible for α(1→2)-glucans which evade the zero-pitch region towards the neighboring tight helical conformations. Both helix senses are accessible by only minor changes of the glycosidic torsions, and the preference for either helix sense is controlled by secondary effects. These can be minor structural variations on the termini of the α(1→2)-glucan which suffice to induce either *P* or *M* helix sense or an equilibrium of both. Fructofuranose is a modification of the reducing end of the kojioligosaccharides. The fructofuranose acts as a helix-cap for a right-handed helix by coordinating to the terminal trisaccharide moiety (Figure 3, HyperChem,[8] $n = 7$). Selective acidolysis of the single ketosidic bond of the pentasaccharide ($n = 4$) causes the collapse of the secondary structure apparent from significant overall changes in the chemical shifts and the altered NOE pattern. The kojitetraose [α-D-Glc(1→2)]$_4$-OH appears as two separate ^{1}H NMR signal sets, one for the α and one for the β anomer of the reducing glucose. Both differ significantly from the fructose-capped α-(1→2)-glucan; even the anomeric proton of the terminal glucose on the opposite end of the homooligomer senses a low-field shift of 0.17 ppm (α-anomer) and 0.66 ppm (β-anomer), respectively, compared to [α-D-Glc(1→2)]$_4$-β-D-Fru. Such large chemical-shift variations document how the fructofuranose helix-cap influences the entire chain of the α(1→2)-glucan. The cooperative collapse of the helical secondary structure upon cleavage of the fructofuranose is evident even in the NMR spectra of the highest oligomers studied here, although only the shorter ones can be fully assigned in the ^{1}H NMR spectra.

The line-broadening observed for the larger octa- and decasaccharide (Figure 1) could be nearly resolved in the fast-exchange regime at 320 K, but the slow-exchange regime with separate signal sets for the exchanging isomers was not accessible. At 300 K, the fourth-to-last anomeric proton (pyranose e of the octasaccharide and pyranose g of the decasaccharide, respectively) and the anomeric protons of the terminal pyranoses are the only resolved anomeric protons. The anomeric proton of the fourth-to-last pyranose is resonant at a chemical shift of approximately 5.4 ppm, baseline-separated from all other resonances. The discrete chemical environment of a single pyranose within the α-(1→2)-glucan chain is caused by different secondary structures of the reducing end and the nonreducing end moieties. These opposing helix senses accessible by the α(1→2)-glucans are bridged by the fourth-to-last pyranose forming the saddle required between *P* and *M* helix. The right-handed helix induced by the helix-capping fructofuranose is opposed by the terminal trisaccharide moiety (f–h of the octa- and h–j of the decasaccharide) of the larger oligomers forcing the fourth-to-last pyranose into the saddle position between the two opposing helix senses. The energy barrier does not further increase for higher oligomers, a phenomenon which is

 © 2006 Wiley-VCH Verlag GmbH & Co. KGaA, Weinheim

observed also for racemization barriers of achiral homooligomers.[9] Macroscopic examples of saddle structures are found in leaf tendrils of bryony (*Bryonia alba)* or vine tendrils which adopt both helix senses to relieve torsion during curling. Selective acidolysis of the single ketosidic bond in the decasaccharide ($n = 9$), again, as in the case of the defructosylated [α-D-Glc(1→2)]$_4$-OH, results in a complete reshaping of the ^{1}H NMR spectrum. Yet, no signal assignment is feasible because of the insufficient chemical-shift dispersion, as expected for a homooligomer with fraying ends.

Taken together, α-(1→2)-glucans have a strong tendency to form helical secondary structures with structural modifications on the reducing end of the α(1→2)-glucooligosaccharide exerting a long-range conformational effect. The fructofuranose cap on the reducing-end terminus stabilizes a right-handed helix which is independent of the length of the attached homooligomer, ending, however, at the fourth-to-last pyranose. The unique conformational properties of oligo-(1→2)-α-D-glucopyranosyl-(1→2)-β-D-fructofuranosides challenge the general view of oligosaccharides as flexible biomolecules. Current studies are focused on the correlation between the molecular architecture and the bioprotective properties of the fructose-capped kojioligosaccharides.

Received: September 5, 2005
Published online: December 20, 2005

Keywords: carbohydrates · conformation analysis · glucans · helical structures · NMR spectroscopy

[1] C. V. Stevens, A. Meriggi, K. Booten, *Biomacromolecules* **2001**, *2*, 1–16.
[2] G. Brumfiel, *Nature* **2004**, *428*, 14–15.
[3] G. Byrant, K. L. Koster, J. Wolfe, *Seed Sci. Res.* **2001**, *11*, 17–25.
[4] D. Fischer, A. Geyer, E. Loos, *FEBS J.*, in press.
[5] H. Chaen, T. Nishimoto, T. Nakada, F. Tetsuya, S. Fukuda, M. Kurimoto, Y. Tsujisaka, *J. Biosci. Bioeng.* **2001**, *92*, 177–182.
[6] T. Watanabe, Y. Kamo, M. Yoshihiro, K. Matsuda, W. F. Dudman, *Carbohydr. Res.* **1982**, *110*, 170–175.
[7] This data was taken from the databank http://www.glycosciences.de.
[8] *HyperChem*; Hypercube, Inc., Gainesville, FL 32601.
[9] R. H. Janke, G. Haufe, E.-U. Würthwein, J. H. Borkent, *J. Am. Chem. Soc.* **1996**, *118*, 6031–6035.

 © 2006 Wiley-VCH Verlag GmbH & Co. KGaA, Weinheim

Supramolecular Chemistry

DOI: 10.1002/anie.200500669

Pronounced Supramolecular Order in Discotic Donor–Acceptor Mixtures**

*Wojciech Pisula, Marcel Kastler, Daniel Wasserfallen, Joseph W. F. Robertson, Fabian Nolde, Christopher Kohl, and Klaus Müllen**

Dedicated to the memory of Tadeusz Pakula

An approach to tuning the properties of materials is the blending of two different discotic compounds. In analogy to the mixing of two linear polymers, various effects can be expected, ranging from a phase separation in the blend to the formation of a homogenous one-phase system. In the case of two polymers, the blending enthalpy determines whether the mixture will be homogenous or phase separated.[1] The mixing of two macromolecules that self-assemble into superstructures is complex, since additional interactions between the different components complicate the description of the system.[2] As illustrated in Figure 1, several different supramolecular assemblies can be formed in the mixture. For discotic molecules, which self-assemble in columnar super-

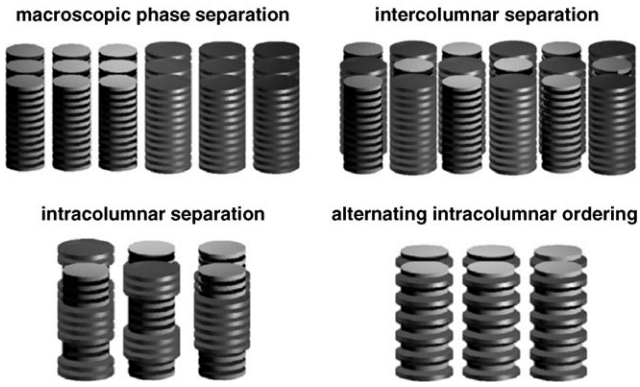


Figure 1. Different possible supramolecular organizations in a mixture of two discotic compounds with different molecular architectures.

[*] Dr. W. Pisula, M. Kastler, D. Wasserfallen, Dr. J. W. F. Robertson, F. Nolde, Dr. C. Kohl, Prof. Dr. K. Müllen
Max-Planck Institut für Polymerforschung
55128 Mainz (Germany)
Fax: (+49) 6131-379-350
E-mail: muellen@mpip-mainz.mpg.de

[**] This research was supported by the EU through the NAIMO (integrated project no. NMP4-CT-2004-500355) and by the Deutsche Forschungsgemeinschaft (Schwerpunkt Feldeffekttransistoren). M.K. thanks the Fonds der Chemischen Industrie and the Bundesministerium für Bildung und Forschung for financial support.

Supporting information for this article is available on the WWW under http://www.angewandte.org or from the author.

© 2006 Wiley-VCH Verlag GmbH & Co. KGaA, Weinheim

structures by π stacking, this ranges from a heterogeneous phase to micro- and even nanoseparation.

Intensive investigations of mixtures containing triphenylene as the donor compound have been carried out, whereby trinitrofluorenone,[2,3] azatriphenylenes,[4,5] and mellitic trimides[6] have been used as acceptor molecules. For equimolar mixtures, alternating stacking of the acceptor and donor molecules has been observed, leading to an enhanced columnar stability. Time-of-flight experiments verified an enhanced columnar organization and revealed considerably higher charge-carrier mobilities for the blends.[7–9]

In this study, the effect of blending two discotic materials, which differ significantly in their electronic properties, was examined. While hexa-*peri*-hexabenzocoronene substituted by long, branched alkyl chains (HBC-$C_{10,6}$, **1**; Figure 2) is an electron-donating agent, perylenediimide[10] (PDI, **2**) and terrylenediimide derivatives (TDI, **3**) are strong acceptors. Semiemperical calculations (AM1) indicate that there is a weak electronic interaction between the two components, which should lead to alternating stacking in the columnar structure and therefore to increased stabilization and a higher level of order in this donor–acceptor mixture. In addition, the blended molecules are compatible in size, permitting matched intracolumnar packing and leading to a different self-assembly on surfaces.

The substitution of the HBC aromatic core with bulky, branched side chains led to a considerable lowering of the isotropization temperature (T_i) to 93 °C for **1** in comparison to those of HBC derivatives with linear side chains. Two-dimensional wide-angle X-ray diffraction (2D-WAXS) experiments indicated a herringbone arrangement (Figure 3a) of the HBC discs in the room-temperature plastic crystalline phase, whereby heating beyond the phase transition at 24 °C (second differential calorimetry scan at a rate of 10 °C min^{-1}) resulted in a disordered columnar liquid-crystalline (LC) phase. Highly birefringent dendritic structures appeared when the material was cooled from the isotropic phase between glass slides, implying defect structures with columns predominately parallel to the surface (Figure 2a). During crystallization of **2** from the isotropic phase (T_i = 130 °C), optical textures with pseudofocal conical fan shapes (Figure 2b) were observed, indicating the formation of a mesophase in which the molecules are orthogonally arranged with respect to the stacking axis. Such intracolumnar

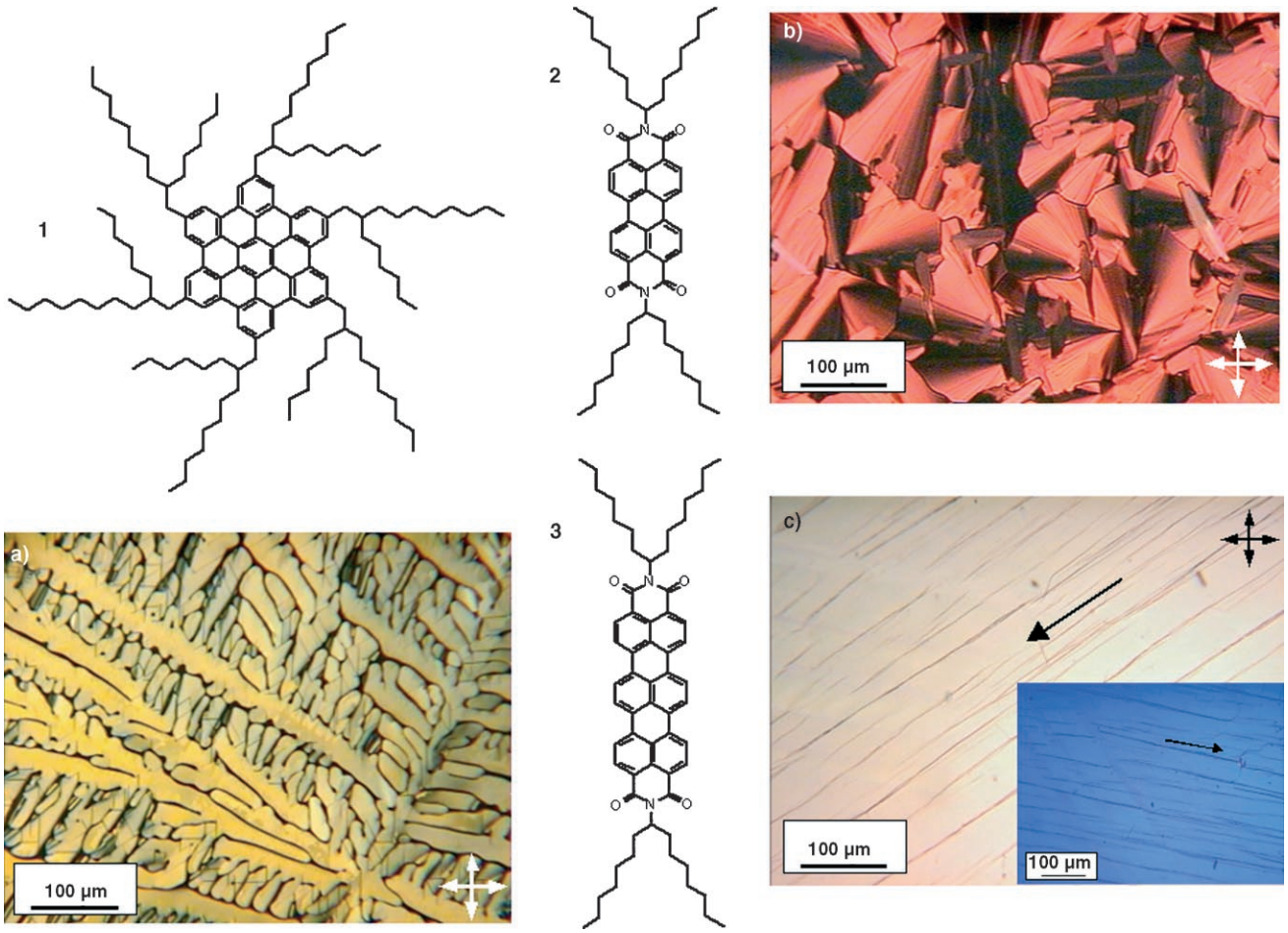


Figure 2. Chemical structures and polarized optical microscopic images of a) **1**, b) **2**, and c) **3** (the arrow indicates the columnar orientation); in the inset the same section of the sample was rotated relative to the direction of polarization of the light, and it indicates a high level of optical anisotropy. The crossed arrows indicate the orientation of the polarization filters in the optical microscope. The images were recorded during crystallization from the isotropic phase at the cooling rate of 1 °C min^{-1}.

 © 2006 Wiley-VCH Verlag GmbH & Co. KGaA, Weinheim

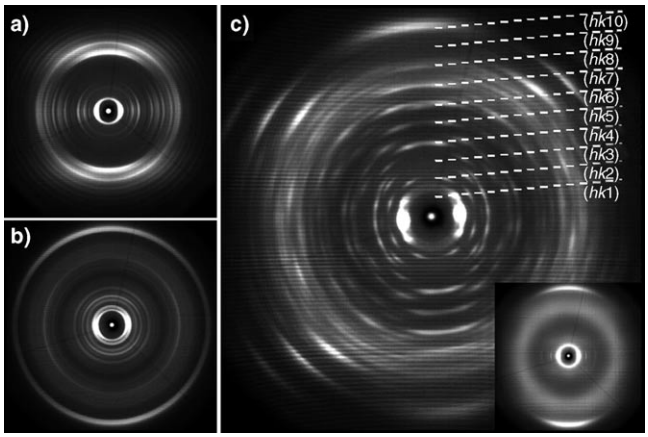


Figure 3. Room-temperature 2D-WAXS patterns of a) **1** b) **2**, and c) and an equimolar mixture of **1** and **2** (inset shows the sample directly after extrusion). The Miller's indexes describe the periodicity along the columnar structures. All samples were prepared by filament extrusion, and the filament axis was oriented vertically in the diffraction experiment.

packing of **2** was also confirmed by the 2D-WAXS experiments.

Mixtures of **1** with **2** or **3** were first prepared at set molar ratios in solution and afterwards blended in the isotropic phase to avoid demixing due to different solubilities. The investigation of the thermal behavior by differential scanning calorimetry (DSC) revealed that all prepared mixtures formed a macroscopic, homogeneous phase.

Photoluminescence excitation spectra for an equimolar mixture of **1** and **2** in solution showed a superposition of the spectra of the pure components. In contrast, drop-cast films of the blend showed a shift of the fluorescence signal of **2** by 60 nm accompanied by a strong quenching, which was expected because of energy-transfer processes. The significant change of the electronic environment of the chromophore was supported by the differential pulse voltammetry measurements. These displayed an additional peak for the mixture which was shifted by 0.18 eV in comparison to measurements with pure **2**.

The 2D-WAXS pattern of the equimolar mixture of **1** and **2** indicated a considerable difference of the supramolecular arrangement in the blend (Figure 3c). The X-ray pattern changed significantly when the extruded sample was annealed for 48 h at ambient conditions, whereby the number of distinct reflections increased dramatically. A set of new higher order reflections appeared, indicating an exceptional long-range order and a complex helical arrangement of the two discotic species within the columnar stacks. The transformation of the first equatorial reflection, which converted from an isotropic shape (Figure 3c) to three sharp peaks, was particularly impressive. This implied not only a simple intracolumnar reorganization but also a rearrangement of entire columnar segments.

The layered distribution of the reflections in the meridional direction in the WAXS pattern in Figure 3c was identified by the Miller's indices (*hkl*), which were assigned to the intracolumnar packing.[11] The smallest intracolumnar repeating distance between single building blocks is 0.34 nm. This distance is in relation to the (*hkl*) reflection lines indicating strong correlations over long ranges between ten molecules per helical pitch (helical pitch distance: 3.4 nm). The suggested model for the supramolecular arrangement is illustrated in Figure 4. It is assumed that an alternating molecular packing results in the helical organization. In this

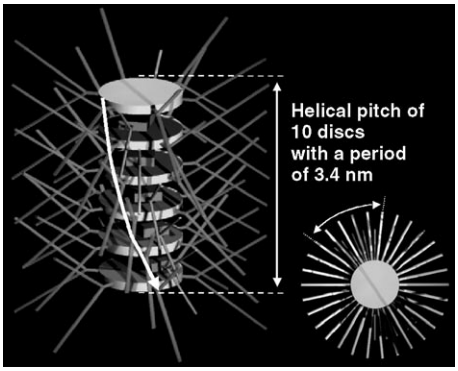


Figure 4. Schematic packing model of an alternating intracolumnar arrangement for the binary mixture. Molecules of **2** are intercalated between units of **1**, which are displaced by 12° with respect to each other, resulting in a helical pitch of 3.4 nm.

structure, PDI (**2**) is intercalated between the HBC discs (**1**), which are rotated with respect to each other by 12° thus providing the necessary repeat unit for the helical arrangement. This rotation is induced by the space demand of the alkyl side chains in both derivatives. In 2003 helical columnar arrangements were observed for HBC derivatives with rigid substituents.[12] Electronic donor–acceptor interactions were thought to cause the observed pronounced alternating intracolumnar ordering. A similar situation was reported for single crystals consisting of hexafluorobenzene and fullerene; the interactions were confirmed by fluorescence and differential pulse voltammetry measurements.[13]

To gain more detailed insight into the supramolecular arrangement of other mixtures, complementary compositions with ratios of 1:2 and 2:1 were investigated. All extruded samples showed significantly higher order after annealing. The 2D-WAXS pattern of both blends displayed reflections at positions identical to those observed for the 1:1 blend, but with different reflection intensities, which depended on the composition ratio. The additional reflections reached their maximum intensity for the 1:1 molar ratio, possibly due to sequences of identical molecules of the excess components in the nonequimolar mixtures.

The new supramolecular structure in the blends significantly affected the thermal behavior and the morphology. When a 2:1 mixture of HBC (**1**) and PDI (**2**) was cooled down from the isotropic phase between two glass slides, a homogenous film was obtained that did not display significant birefringence in polarized light; this would be characteristic for a homeotropic phase (Figure 5a). The transmission 2D-WAXS pattern of the film confirmed the proposed orientation (Figure 5b), whereby the lateral arrangement of the lattice differed considerably between the domains. This

 © 2006 Wiley-VCH Verlag GmbH & Co. KGaA, Weinheim

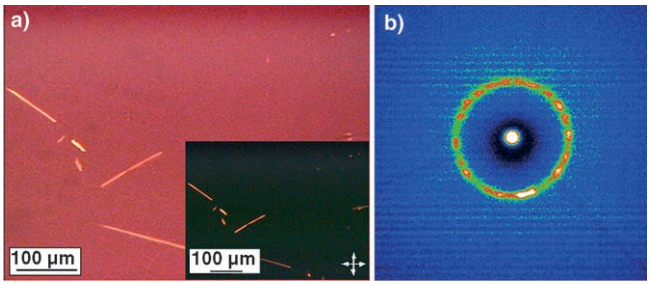


Figure 5. Example for a homeotropically aligned sample based on the 2:1 mixture of **1** and **2**. a) Image from the optical microscope (polarizer and analyzer at a 45° angle with respect to each other; inset recorded with crossed polarizers). b) Characteristic 2D-WAXS pattern of the film with homeotropic order (identical hexagonal lattice in different small domains leads to the appearance of multiple reflections).

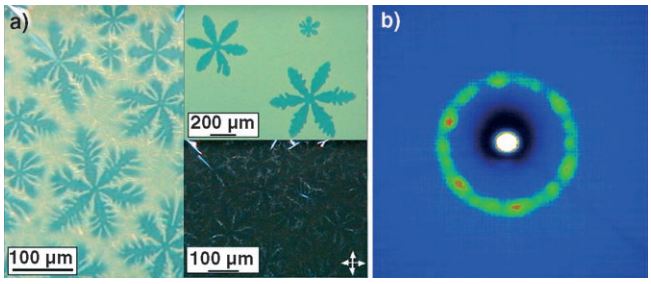


Figure 6. Example of a homeotropically aligned sample based on the 2:1 mixture of **1** and **3**. a) Image from the optical microscope (polarizer and analyzer at a 45° angle with respect to each other; lower inset recorded with crossed polarizers, upper inset image recorded during crystallization of the dendritic structure). b) Characteristic 2D-WAXS pattern of the film with homeotropic order.

morphology stands in contrast to those of the individual components. A similar morphology was also obtained for mixtures of other compositions; however, the number of birefringent defects increased significantly.

In general, HBCs with nonbulky alkyl substituents align homeotropically when cooled down from the isotropic phase. When the π-stacking interactions between the aromatic cores are significantly reduced in the isotropic phase, the molecules arrange with their planes parallel to the surface. This arrangement is assumed to be the most thermodynamically favored, since interactions (e.g. van der Waals interactions) between the molecule and the surface are maximized. On the other hand, the high steric demand of the alkyl chains close to the aromatic core might hinder the approach the disc to the surface, as seen for HBC-$C_{10,6}$ **1** and previously for HBC-$C_{14,10}$.[14] In both cases, the high degree of rotational freedom at the β position of the side chains results in the increase of the steric requirements, which lead the formation of defect structures

The steric influence of the substituents on the columnar packing can be reduced synthetically[15] or, as described in this work, by packing effects of the donor–acceptor molecules. The electronic interaction between **1** and **2** resulted in the strictly alternating stacking of the donor and acceptor species. The distance between the HBC discs in the columns increased, whereby the steric influence of the long, branched $C_{10,6}$ alkyl chains on the stacking was significantly reduced. Consequently, the mixture formed a homeotropic phase. Additionally, the intracolumnar packing was enhanced by the helical arrangement of the molecules. Analogous behavior was observed for mixtures of **1** and **3** with molar ratios of 1:1 and 2:1 (Figure 6). Both blends revealed a homeotropic alignment suggesting an identical intracolumnar packing of the two discotics as described above.

In conclusion, we have shown that supramolecular organization in a binary mixture differs strongly from that of the individual components. Strictly alternating stacks formed spontaneously when the mixture was cooled from the isotropic state, because of the weak donor–acceptor interactions between the electron-rich **1** and the electron-poor rylene dyes **2** and **3**. These interactions, proved by photoluminescence and differential pulse voltammetry, lead to a significantly higher level of order within the self-assembled columnar stacks. The molecules in the mixture assume a homeotropic orientation, due to an auxiliary effect of the smaller aromatic molecule, while forming the first monolayer of the sterically demanding HBCs on the surface.

Experimental Section

The blends were first prepared in tetrachlormethane and were then used in the isotropic phase. To ensure an intermixture of both compounds, the blends were processed in an ultrasonic bath under nitrogen atmosphere.

The 2D-WAXS experiments were performed by means of a rotating anode (Rigaku 18 kW) X-ray beam with a pinhole collimation and a Siemens 2D detector. A double graphite monochromator for the $Cu_{K\alpha}$ radiation ($\lambda = 0.154$ nm) was used. The samples were oriented by filament extrusion. The optical textures were investigated using a Zeiss microscope with polarizing filters equipped with a Hitachi KP-D50 color digital CCD camera. The samples were sandwiched between two glass slides and then thermally treated (first heated to the isotropic phase and then slowly cooled down) on a Linkam hotstage regulated with a Linkam TMS 91 temperature controller.

Electrochemical measurements were performed on a voltametric analyzer (AutoLab PGSTAT-30, potentiostat/galvanostat) in a three-electrode cell with a gold working electrode (3 mm diameter), a silver quasi-reference electrode (AgQRE, calibrated with the Fc/Fc^+ redox couple $E° = 4.8$ eV) and a platinum counterelectrode. Films were dropcast from a solution of toluene. Tetrabutylammonium perchlorate ($TBAClO_4$, 0.1 M) and acetonitrile were used as electrolyte and solvent, respectively. Differential pulse voltammetry was measured with 15-mV, 50-ms pulses at 100-ms intervals.

The photoluminescence was recorded on a SPEX Fluorolog 2 type 212 steady-state fluorometer at a concentration of 10^{-3} M and dropcast films on quartz substrates. DSC was measured with a Mettler DSC 30 at a heating rate of 10 K min^{-1} from −100 °C to 200 °C. The electronic potential density distribution was calculated by means of Spartan for Windows (AM1 of ground state). The synthesis of HBC-$C_{10,6}$ **1** has been described elsewhere;[12] the syntheses of PDI **2** and TDI **3** are described in the Supporting Information.

Received: February 22, 2005
Revised: July 7, 2005
Published online: December 19, 2005

 © 2006 Wiley-VCH Verlag GmbH & Co. KGaA, Weinheim

Keywords: dyes/pigments · helical structures · homeotropic phases · supramolecular chemistry

[1] R. L. Scott, *J. Chem. Phys.* **1949**, *17*, 279.
[2] W. Kranig, C. Boeffel, H. W. Spiess, O. Karthaus, H. Ringsdorf, R. Wustefeld, *Liq. Cryst.* **1990**, *8*, 375.
[3] V. V. Tsukruk, J. H. Wendorff, O. Karthaus, H. Ringsdorf, *Langmuir* **1993**, *9*, 614.
[4] N. Boden, R. J. Bushby, Z. B. Lu, O. R. Lozman, *Liq. Cryst.* **2001**, *28*, 657.
[5] E. O. Arikainen, N. Boden, R. J. Bushby, O. R. Lozman, J. G. Vinter, A. Wood, *Angew. Chem.* **2000**, *112*, 2423; *Angew. Chem. Int. Ed.* **2000**, *39*, 2333.
[6] L. Y. Park, D. G. Hamilton, E. A. McGehee, K. A. McMenimen, *J. Am. Chem. Soc.* **2003**, *125*, 10586.
[7] B. R. Wegewijs, L. D. A. Siebbeles, N. Boden, R. J. Bushby, B. Movaghar, O. R. Lozman, Q. Liu, A. Pecchia, L. A. Mason, *Phys. Rev. B* **2002**, 65.
[8] A. Pecchia, O. R. Lozman, B. Movaghar, N. Boden, R. J. Bushby, K. J. Donovan, T. Kreouzis, *Phys. Rev. B* **2002**, 65.
[9] T. Kreouzis, K. Scott, K. J. Donovan, N. Boden, R. J. Bushby, O. R. Lozman, Q. Liu, *Chem. Phys.* **2000**, *262*, 489.
[10] H. Langhals, I. R. O. Yürük, *Tetrahedron* **2000**, *56*, 5435.
[11] H. C. Holst, T. Pakula, H. Meier, *Tetrahedron* **2004**, *60*, 6765.
[12] J. H. Wu, M. D. Watson, K. Müllen, *Angew. Chem.* **2003**, *115*, 5487; *Angew. Chem. Int. Ed.* **2003**, *42*, 5329.
[13] Z. H. Wang, F. Dotz, V. Enkelmann, K. Müllen, *Angew. Chem.* **2005**, *117*, 1273; *Angew. Chem. Int. Ed.* **2005**, *44*, 1247.
[14] W. Pisula, M. Kastler, D. Wasserfallen, T. Pakula, K. Müllen, *J. Am. Chem. Soc.* **2004**, *126*, 8074.
[15] W. Pisula, Ž. Tomović, B. El Hamaoui, M. D. Watson, T. Pakula, K. Müllen, *Adv. Funct. Mater.* **2005**, *15*, 893.

 © 2006 Wiley-VCH Verlag GmbH & Co. KGaA, Weinheim

Substituent Effects

DOI: 10.1002/anie.200501633

α-Stabilization of Carbanions: Fluorine Is More Effective than the Heavier Halogens**

F. Matthias Bickelhaupt, Holger L. Hermann, and Gernot Boche**

Dedicated to Professor Rolf Huisgen on the occasion of his 85th birthday

"Carbanions", more precisely organometallic compounds, are among the most important reagents in organic synthesis.[1–3] Gas-phase experimental[4] and theoretical[5] investigations have contributed much to our knowledge of how the basicity and stability of carbanions CH_2X^- depend intrinsically, that is, in the absence of solvent and counterions, on their structure, in particular, on the nature of the α-substituent X. Thus, it has been established that third- and higher-period substituents X (e.g., Cl, SH) substantially decrease the proton affinity (PA) of CH_2X^-, whereas second-row substituents (e.g., F, OH) are significantly less effective in reducing the basicity of these species. This follows from the trend in the energy change $\Delta E_{isod}(X)$ associated with the isodesmic reaction in Equation (1) of the proton transfer from CH_3X to CH_3^-.

$$CH_3^- + CH_3X \rightarrow CH_4 + CH_2X^- \quad \Delta E_{isod}(X) \tag{1}$$

This reaction energy is equal to the difference in the proton affinities of CH_3^- and CH_2X^- [Eq. (2)].

$$\Delta E_{isod}(X) = PA(CH_2X^-) - PA(CH_3^-). \tag{2}$$

It becomes some 10–20 kcal mol^{-1} more exothermic if one goes from second- to higher-period substituents X, which implies that the basicity of CH_2X^-, as measured by the proton affinity $PA(CH_2X^-)$, decreases. The common explanation is that, compared to substituents of the second period, third- and higher-period substituents stabilize the carbanion more effectively, that is, the strength of their C–X bond leads to more stabilization. This has been ascribed to the fact that

[*] Dr. F. M. Bickelhaupt
Afdeling Theoretische Chemie
Scheikundig Laboratorium der Vrije Universiteit
De Boelelaan 1083, 1081 HV Amsterdam (The Netherlands)
Fax: (+31) 20-598-7629
E-mail: fm.bickelhaupt@few.vu.nl
Dr. H. L. Hermann, Prof. Dr. G. Boche
Fachbereich Chemie
Philipps-Universität
Hans-Meerwein-Strasse, 35032 Marburg (Germany)
Fax: (+49) 6421-282-8917
E-mail: boche@chemie.uni-marburg.de

[**] We thank the Netherlands Organization for Scientific Research (NWO-CW), the Fonds der Chemischen Industrie (FCI), and the Deutsche Forschungsgemeinschaft (DFG), Sonderforschungsbereich 260, for financial support.

 © 2006 Wiley-VCH Verlag GmbH & Co. KGaA, Weinheim

Table 1: Homolytic C–X bond energies $\Delta E_A(X)$ and $\Delta E_N(X)$ of CH_2X^- and CH_3X (in kcal mol^{-1}) and SOMO energies $\varepsilon_{SOMO}(X)$ of X (in eV).[a]

X	$\varepsilon_{SOMO}(X)$	$\Delta E_A(X)$	$\Delta E_N(X)$	$\Delta E_A(X)-\Delta E_N(X)$	$\Delta E_{isod}(X)$[b]	$\Delta E_{isod}(X)$, MP2[b]
F	−13.8	−117.0	−119.2	2.2	−6.5	−7.1
Cl	−10.1	−97.4	−85.6	−11.8	−20.5	−19.1
Br	−9.2	−91.5	−75.3	−16.2	−24.9	−22.5
I	−8.3	−86.4	−64.1	−22.3	−31.0	−27.5
H	−7.6	−103.2	−111.9	8.7	0.0	0.0
OH	−10.1[c]	−91.0[d]	−97.2	6.2	−2.5	−1.4
SH	−7.9[c]	−93.3[d]	−75.9	−17.4	−26.1	−19.5
NH_2	−7.6[c]	−76.7[d]	−89.1	12.4	3.7	0.2
PH_2	−6.1[c]	−91.0[d]	−71.9	−19.1	−27.8	−22.6
CH_3	−5.5[c]	−83.2	−93.2	10.0	1.3	1.9
SiH_3	−5.4[c]	−107.3	−86.1	−21.2	−29.9	−24.8

[a] Computed at BP86/TZ2P,[6,7] except for the last column which was computed at the MP2(full) level and includes ZPE corrections.[8] [b] Isodesmic reaction energy, see Equations (1), (2), and (6). [c] SOMO energy for the equilibrium structure of X•. [d] Based on the most stable conformers (Y for CH_2OH^-, W for CH_2SH^-, Ψ for $CH_2NH_2^-$, Ψ for $CH_2PH_2^-$). The results differ by only 2–3 kcal mol^{-1} for the less stable conformers (W for CH_2OH^-, Y for CH_2SH^-, X for $CH_2NH_2^-$, X for $CH_2PH_2^-$).

third- and higher-period substituents are more electropositive and have a greater polarizability (e.g., Cl compared to F).[4,5] In the case of, for example, SH and OH, the former is considered to stabilize the carbanion more effectively also because of the σ* effect, that is, a more effective hyperconjugation caused by the low energy of the σ^*_{S-H} orbital compared to the σ^*_{O-H} orbital.[5c,d,f,g]

Herein, we show, based on quantum-chemical computations, that the picture of stronger α-stabilization of the carbanion by third- and higher-period elements is not correct for halogen substituents, and that, on the contrary, α-stabilization of the carbanion CH_2X^- is *strongest* for fluorine and becomes *less so* along the series X = F, Cl, Br, and I. This is shown not to be in contradiction with the observed decrease in basicity of CH_2X^- along this series. To this end, we computed and analyzed the C–X bond energy $\Delta E_A(X)$, which is a direct measure of the effect of the various substituents X on the stability of the corresponding anion CH_2X^-. We also studied the α-stabilization of CH_2X^-, and the role of the σ* effect therein, for substituents X of Groups 14 (CH_3, SiH_3), 15 (NH_2, PH_2), and 16 (OH, SH). Our computations were carried out with the Amsterdam density functional (ADF) program at the BP86/TZ2P level of the generalized gradient approximation (GGA) to density functional theory (DFT).[6,7] The results are collected in Table 1 and Figures 1 and 2.

In agreement with previous experimental and theoretical evidence,[4,5] the proton affinity of CH_2X^- decreases along the series X = F, Cl, Br, and I, as is reflected by the increase in exothermicity of $\Delta E_{isod}(X)$ (see [Eq. (2)]) from −6.5 (F) to −20.5 (Cl), −24.9 (Br), and −31.0 kcal mol^{-1} (I) at the BP86/TZ2P level of theory (Table 1). For comparison, we find the same trend at the MP2 level of theory (Table 1).[8] This trend is, however, not the result of an increase in α-stabilization, that is, an increasingly stable C–X bond between the radical anion $CH_2^{\bullet-}$ and the substituent X• in CH_2X^- along the series F, Cl. Br, I. Quite to the contrary, the C–X bond strength $\Delta E_A(X)$ in the anion CH_2X^- displays exactly the opposite trend: it *weakens* along the series from −117.0 (F) to −97.4 (Cl), −91.5 (Br), and −86.4 kcal mol^{-1} (I) (Table 1). In other words, α-stabilization of CH_2X^- *decreases* along the series F, Cl, Br, I. Bonding analyses[7] reveal that this trend originates primarily from the decreasing stabilization associated with forming the C–X electron-pair bond as the energy of the halogen *n*p atomic orbital carrying the radical electron rises (i.e., as the electronegativity decreases) from F to I.[9] This finding is shown schematically in Figure 1, in which the situations for X = F and X = I are labelled **1a** and **1b**; the situations for X = Cl and Br lie between these two extremes.

Why, then, does CH_2X^- become less basic along the series F, Cl, Br, and I? As pointed out by Brauman and co-workers, the carbanion stability can only be deduced from its basicity by means of isodesmic reactions

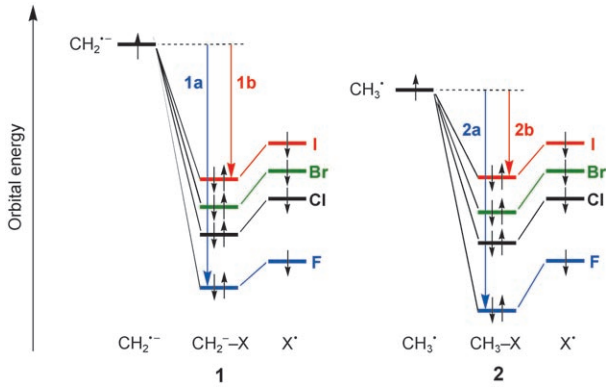


Figure 1. Orbital interaction diagram for the formation of the C–X electron-pair bond in CH_2X^- (**1**) and CH_3X (**2**) with X = F (blue), Cl (black), Br (green), and I (red).

[see Eqs. (1) and (2)] "if we assume that the substituents [X] primarily influence these reactions by their effect on the anions".[4a] This assumption, however, can not be made for the halogen substituents X. In fact, to understand why CH_2X^- becomes less basic along the series F, Cl, Br, I, it is even crucial to take into account that $PA(CH_2X^-)$ does *not*, as generally presumed, depend *only* on the stabilization of the radical anion $CH_2^{\bullet-}$ by X• (i.e., the C–X bond strength $\Delta E_A(X)$ in CH_2X^-) but *also* on the stabilization of the methyl radical $CH_3^{\bullet}$ by X• (i.e., the C–X bond strength $\Delta E_N(X)$ in CH_3X). This becomes obvious if the dissociation reaction (3) of the conjugate acid CH_3X is broken down into the three partial reactions (4a–c).

$$CH_3X \rightarrow CH_2X^- + H^+ \quad PA(CH_2X^-) \tag{3}$$

$$CH_3X \rightarrow CH_3^{\bullet} + X^{\bullet} \quad -\Delta E_N(X) \tag{4a}$$

$$CH_3^{\bullet} \rightarrow CH_2^{\bullet-} + H^+ \quad PA(CH_2^{\bullet-}) \tag{4b}$$

$$CH_2^{\bullet-} + X^{\bullet} \rightarrow CH_2X^- \quad \Delta E_A(X) \tag{4c}$$

 © 2006 Wiley-VCH Verlag GmbH & Co. KGaA, Weinheim

Thus, the PA of CH_2X^- depends on the PA of the $CH_2^{\bullet-}$ radical anion and on the difference in the stabilization of $CH_2^{\bullet-}$ by X$^\bullet$ versus that of $CH_3^\bullet$ by X$^\bullet$, that is, the C–X bond strengths $\Delta E_A(X)$ *and* $\Delta E_N(X)$ in CH_2X^- and CH_3X, respectively [Eq. (5)].

$$PA(CH_2X^-) = PA(CH_2^{\bullet-}) + \Delta E_A(X) - \Delta E_N(X) \quad (5)$$

Likewise, $\Delta E_{isod}(X)$ depends not only on the difference in the stabilization of the radical anion $CH_2^{\bullet-}$ by H$^\bullet$ versus that by X$^\bullet$ in CH_2X^- (i.e., the C–H and C–X bond strengths $\Delta E_A(H)$ and $\Delta E_A(X)$ in CH_3^- and CH_2X^-, respectively) but *also* on the difference in stabilization of the methyl radical $CH_3^\bullet$ by H$^\bullet$ versus that by X$^\bullet$ in CH_3X (i.e., the C–H and C–X bond strengths $\Delta E_N(H)$ and $\Delta E_N(X)$ in CH_4 and CH_3X, respectively) [Eq. (6)].

$$\Delta E_{isod}(X) = [\Delta E_A(X) - \Delta E_N(X)] - [\Delta E_A(H) - \Delta E_N(H)] \quad (6)$$

Note that $\Delta E_A(H) - \Delta E_N(H)$ is a constant in our series of compounds (it amounts to $+8.7$ kcal mol^{-1}). The trend in $\Delta E_{isod}(X)$ is therefore determined by $\Delta E_A(X) - \Delta E_N(X)$ and it depends critically on how both the C–X bond strengths, $\Delta E_A(X)$ in the anion and $\Delta E_N(X)$ in the corresponding acid, vary relative to one another along the series X = F, Cl, Br, I. As can be seen from Table 1, the C–X bond strength $\Delta E_N(X)$ in CH_3X shows exactly the same trend as $\Delta E_A(X)$ discussed above. Importantly, however, $\Delta E_N(X)$ changes more pronouncedly with each step along the series X: from -119.2 (F) to -85.6 (Cl), -75.3 (Br), and -64.1 kcal mol^{-1} (I) (see also the $\Delta E_A(X) -$ $\Delta E_N(X)$ values in Table 1).[10] Again, the dominant mechanism behind this trend is that the stabilization associated with dropping the radical electron of $CH_3^\bullet$ into the C–X electron-pair bonding combination is weakened continuously as the halogen *n*p atomic orbital rises in energy on going from the highly electronegative F (labeled **2a** in Figure 1) via Cl and Br to the less electronegative I (labelled **2b** in Figure 1).[10] In Figure 2, $\Delta E_{isod}(X)$, $\Delta E_A(X)$, and $\Delta E_N(X)$ are plotted as a function of the energy of the halogen SOMO, $\varepsilon_{SOMO}(X)$. All three energies display nearly (but not exactly) linear correlations with $\varepsilon_{SOMO}(X)$. It is also evident from Figure 2 that the PA of CH_2X^- decreases along the series F, Cl, Br, I *not* because the α-stabilization of the anion $\Delta E_A(X)$ increases, but because it *decreases more slowly* along this series than the C–X bond strength $\Delta E_N(X)$ of CH_3X.[11]

In addition to Group 17 substituents F, Cl, Br, and I, we studied trends in basicity and α-stabilization of CH_2X^- for substituents X of Groups 16, 15, and 14. In all groups, the PA of CH_2X^- decreases if one goes from second- to third-row substituents X, as reflected by the corresponding increase in exothermicity of $\Delta E_{isod}(X)$ [kcal mol^{-1}]: -6.5 (F), -20.5 (Cl; see above); -2.5 (OH), -26.1 (SH); 3.7 (NH_2), -27.8 (PH_2); 1.3 (CH_3), -29.9 kcal mol^{-1} (SiH_3) (see Table 1). While the σ* effect ("hyperconjugation") is, of course, absent for Group 17 substituents, it becomes increasingly important along the Groups 16–14. As outlined above, the trend in $\Delta E_{isod}(X)$ from second- to third-period substituents X is determined by the term $\Delta E_A(X) - \Delta E_N(X)$ in Equation (6). For the halogens,

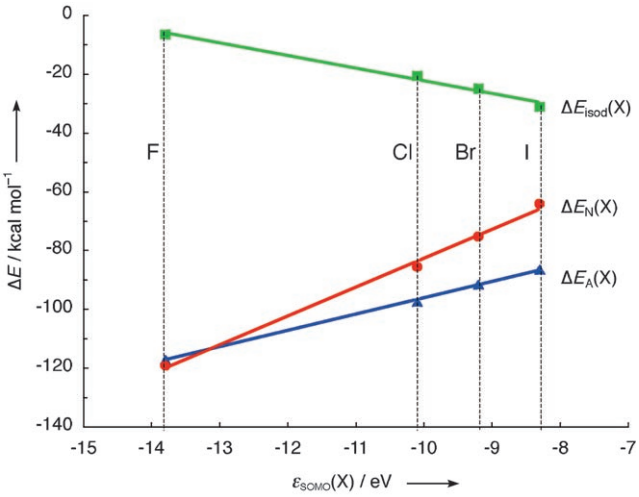


Figure 2. Isodesmic reaction energy $\Delta E_{isod}(X)$ [see Eq. (6)] and C–X bond energies $\Delta E_N(X)$ in CH_3X and $\Delta E_A(X)$ in CH_2X^- as a function of the energy of the singly occupied molecular orbital (SOMO) of the halogens X = F, Cl, Br, and I.

both, $\Delta E_A(X)$ and $\Delta E_N(X)$, *decrease* from X = F to Cl but they do so at different rates (see above). Likewise, the C–X bond strengths $\Delta E_N(X)$ in the neutral compounds CH_3X also decrease as one descends the Groups 16, 15, and 14: -97.2 (X = OH), -75.9 (SH); -89.1 (NH_2), -71.9 (PH_2); -93.2 (CH_3), -86.1 kcal mol^{-1} (SiH_3) (see Table 1). However, in contrast to the situation for the halogen-substituted anions CH_2X^-, the C–X bond strength $\Delta E_A(X)$ for the carbanion CH_2X^- becomes *stronger* as one descends the Groups 16, 15, and 14: -91.0 (X = OH), -93.3 (SH); -76.7 (NH_2), -91.0 (PH_2); -83.2 (CH_3), -107.3 kcal mol^{-1} (SiH_3) (see Table 1).

The bonding analyses show that this increase in $\Delta E_A(X)$ for X = SH, PH_2, and SiH_3 originates from the σ* effect. Thus, if one goes from the second to the third period (e.g., from CH_3 to SiH_3), $\Delta E_A(X)$ becomes more stabilizing due to the increase in charge donation from the lone-pair MO and SOMO of the $CH_2^{\bullet-}$ radical anion into the unoccupied $\sigma^*_{X\text{-}H}$ orbitals of the substituent X$^\bullet$ as the energy of these σ* orbitals decreases. Furthermore, the σ* effect becomes increasingly important along the Groups 16, 15, and 14 as the σ* orbitals are more localized on the central atom (instead of H), and as their number increases from 1 to 3. Note that, from X = OH to SH, the trend in $\Delta E_{isod}(X)$ is primarily determined by the weakening of $\Delta E_N(X)$ but, from CH_3 to SiH_3, the dominant contribution stems from the σ* effect-driven strengthening of $\Delta E_A(X)$.

In conclusion, the basicity of the anion CH_2X^-, as a function of X, decreases in Groups 16 (from OH to SH), 15 (from NH_2 to PH_2), and 14 (from CH_3 to SiH_3), because the α-stabilization of CH_2X^- increases. The reason is the stronger hyperconjugation with the $\sigma^*_{S\text{-}H}$, $\sigma^*_{P\text{-}H}$, and $\sigma^*_{Si\text{-}H}$ orbitals compared with $\sigma^*_{O\text{-}H}$, $\sigma^*_{N\text{-}H}$, and $\sigma^*_{C\text{-}H}$ orbitals, respectively. In contrast, the basicity of CH_2X^- along the series X = F, Cl, Br, I does not decrease, as commonly assumed, because of an increasing α-stabilization ($\Delta E_A(X)$) of CH_2X^-. Rather, $\Delta E_A(X)$ *decreases* along the halogen series, however *more*

 © 2006 Wiley-VCH Verlag GmbH & Co. KGaA, Weinheim

slowly than the α-stabilization ($\Delta E_N(X)$) of the conjugate acid CH_3X.

Received: May 12, 2005
Revised: September 6, 2005
Published online: December 19, 2005

Keywords: α-stabilization · bond theory · carbanions · density functional calculations · substituent effects

[1] a) F. A. Carey, R. J. Sundberg, *Advanced Organic Chemistry*, Part A, 4th ed., Kluwer Academic/Plenum, New York, **2001**; b) J. March, *Advanced Organic Chemistry*, 4th ed., Wiley-Interscience, New York, **1992**; c) *Lithium Chemistry: A Theoretical and Experimental Overview* (Eds.: A.-M. Sapse, P. von R. Schleyer), Wiley, New York, **1995**.

[2] See also, for example: a) M. Shimizu, T. Hiyama, *Angew. Chem.* **2005**, *117*, 218; *Angew. Chem. Int. Ed.* **2005**, *44*, 214; b) D. M. Hodgson, Y. K. Chung, J. M. Paris, *J. Am. Chem. Soc.* **2004**, *126*, 8664; c) P. Knochel, W. Dohle, N. Gommermann, F. F. Kneisel, F. Kopp, T. Korn, I. Sapountzis, V. A. Vu, *Angew. Chem.* **2003**, *115*, 4438; *Angew. Chem. Int. Ed.* **2003**, *42*, 4302; d) M. Schlosser, *Angew. Chem.* **1998**, *110*, 1538; *Angew. Chem. Int. Ed.* **1998**, *37*, 1496; e) D. Seebach, *Angew. Chem.* **1990**, *102*, 1363; *Angew. Chem. Int. Ed. Engl.* **1990**, *29*, 1320; f) G. Boche, *Angew. Chem.* **1989**, *101*, 286; *Angew. Chem. Int. Ed. Engl.* **1989**, *28*, 277; g) D. Seebach, H. Siegel, J. Gabriel, R. Hässig, *Helv. Chim. Acta* **1980**, *63*, 2046; h) D. Seebach, H. Siegel, K. Müllen, K. Hiltbrunner, *Angew. Chem.* **1979**, *91*, 844; *Angew. Chem. Int. Ed. Engl.* **1979**, *18*, 784; i) H. Siegel, K. Hiltbrunner, D. Seebach, *Angew. Chem.* **1979**, *91*, 845; *Angew. Chem. Int. Ed. Engl.* **1979**, *18*, 785.

[3] a) G. Boche, J. C. W. Lohrenz, *Chem. Rev.* **2001**, *101*, 697. This article deals in detail with the structure and reactivity of carbenoids $LiCH_2X$ and $XZnCH_2X$ (X = F, Cl, Br, I, NR_2, OR, SR), as well as with calculations of appropriate model compounds. It explores the strong significance of the cation (e.g., Li^+ or XZn^+) for both, structure and reactivity, of these species. b) Details of the calculations: H. Hermann, J. C. W. Lohrenz, A. Kühn, G. Boche, *Tetrahedron* **2000**, *56*, 4109.

[4] See, for example: a) B. Römer, G. G. Gatev, M. Zhong, J. I. Brauman, *J. Am. Chem. Soc.* **1998**, *120*, 2919; b) S. Ingemann, N. M. M. Nibbering, *J. Chem. Soc. Perkin Trans. 2* **1985**, 837; c) S. Ingemann, N. M. M. Nibbering, *Can. J. Chem.* **1984**, *62*, 2273; d) J. E. Bartmess, R. L. Hays, H. N. Khatri, R. N. Misra, S. R. Wilson, *J. Am. Chem. Soc.* **1981**, *103*, 4747; e) NIST Computational Chemistry Comparison and Benchmark Database, NIST Standard Reference Database Number 101, Release 11, May 2005 (Ed.: R. D. Johnson III), http://srdata.nist.gov/cccbdb.

[5] See, for example: a) P. M. Mayer, L. Radom, *J. Phys. Chem. A* **1998**, *102*, 4918; b) H. J. Castejon, K. B. Wiberg, *J. Org. Chem.* **1998**, *63*, 3937; c) K. B. Wiberg, H. Castejon, *J. Am. Chem. Soc.* **1994**, *116*, 10489; d) A. M. El-Nahas, P. v. R. Schleyer, *J. Comput. Chem.* **1994**, *15*, 596; e) C. F. Rodriquez, S. Sirois, A. C. Hopkinson, *J. Org. Chem.* **1992**, *57*, 4869; f) F. Bernardi, A. Bottoni, A. Venturini, A. Mangini, *J. Am. Chem. Soc.* **1986**, *108*, 8171; g) P. v. R. Schleyer, T. Clark, A. J. Kos, G. W. Spitznagel, C. Rohde, D. Arad, K. N. Houk, N. G. Rondan, *J. Am. Chem. Soc.* **1984**, *106*, 6467; h) J. R. Larson, N. D. Epiotis, *J. Am. Chem. Soc.* **1981**, *103*, 410.

[6] a) G. te Velde, F. M. Bickelhaupt, S. J. A. van Gisbergen, C. Fonseca Guerra, E. J. Baerends, J. G. Snijders, T. Ziegler, *J. Comput. Chem.* **2001**, *22*, 931; b) C. Fonseca Guerra, J. G. Snijders, G. te Velde, E. J. Baerends, *Theor. Chem. Acc.* **1998**, *99*, 391; c) The TZ2P basis set consists of Slater-type orbitals (STOs) and is of triple-ζ quality, augmented with two sets of polarization functions on H (2p and 3d), C, N, O, F, Si, P, S, Cl, Br, and I (3d and 4f).

[7] F. M. Bickelhaupt, E. J. Baerends in *Rev. Comput. Chem, Vol. 15* (Eds.: K. B. Lipkowitz, D. B. Boyd), Wiley-VCH, New York, **2000**, pp. 1 – 86.

[8] a) Basis sets for ab initio MP2(full)//MP2(full) computations: 6-311++G(d,p) for H, C, N, O, F, Si, P, S, Cl, and (4111/3111/1) with relativistic effective core potential for Br, I, see: A. Bergner, M. Dolg, W. Küchle, H. Stoll, H. Preuß, *Mol. Phys.* **1993**, *80*, 1431; b) ab initio computations were carried out with Gaussian 98 (Revision A.7), M. J. Frisch, G. W. Trucks, H. B. Schlegel, G. E. Scuseria, M. A. Robb, J. R. Cheeseman, V. G. Zakrzewski, J. A. Montgomery, R. E. Stratmann, J. C. Burant, S. Dapprich, J. M. Millam, A. D. Daniels, K. N. Kudin, M. C. Strain, O. Farkas, J. Tomasi, V. Barone, M. Cossi, R. Cammi, B. Mennucci, C. Pomelli, C. Adamo, S. Clifford, J. Ochterski, G. A. Petersson, P. Y. Ayala, Q. Cui, K. Morokuma, D. K. Malick, A. D. Rabuck, K. Raghavachari, J. B. Foresman, J. Cioslowski, J. V. Ortiz, B. B. Stefanov, G. Liu, A. Liashenko, P. Piskorz, I. Komaromi, R. Gomperts, R. L. Martin, D. J. Fox, T. Keith, M. A. Al-Laham, C. Y. Peng, A. Nanayakkara, C. Gonzalez, M. Challacombe, P. M. W. Gill, B. G. Johnson, W. Chen, M. W. Wong, J. L. Andres, M. Head-Gordon, E. S. Replogle, J. A. Pople, Gaussian, Inc., Pittsburgh, PA, **1998**.

[9] In fact, this is exactly what one would expect based on qualitative molecular orbital theory. For an excellent introduction into and overview of molecular orbital theory, see, for example: a) R. Hoffmann, *Angew. Chem.* **1982**, *94*, 725; *Angew. Chem. Int. Ed. Engl.* **1982**, *21*, 711; b) T. A. Albright, J. K. Burdett, M.-H. Whangbo, *Orbital Interactions in Chemistry*, Wiley-Interscience, New York, **1985**.

[10] This agrees nicely with the following studies: a) A. Shurki, P. C. Hiberty, S. Shaik, *J. Am. Chem. Soc.* **1999**, *121*, 822; b) L. Deng, V. Branchadell, T. Ziegler, *J. Am. Chem. Soc.* **1994**, *116*, 10645; See also c) F. M. Bickelhaupt, T. Ziegler, P. v. R. Schleyer, *Organometallics* **1996**, *15*, 1477.

[11] One factor causing $\Delta E_A(X)$ to weaken more slowly along the series X = F, Cl, Br, I than $\Delta E_N(X)$ is the bond overlap, which along this series increases more steeply (and thus counteracts more strongly the trend in electronegativity difference across the C–X bond) in CH_2^-–X than in CH_3–X.

 © 2006 Wiley-VCH Verlag GmbH & Co. KGaA, Weinheim

Sphingolactones

DOI: 10.1002/anie.200501983

Sphingolactones: Selective and Irreversible Inhibitors of Neutral Sphingomyelinase

*Veit Wascholowski and Athanassios Giannis**

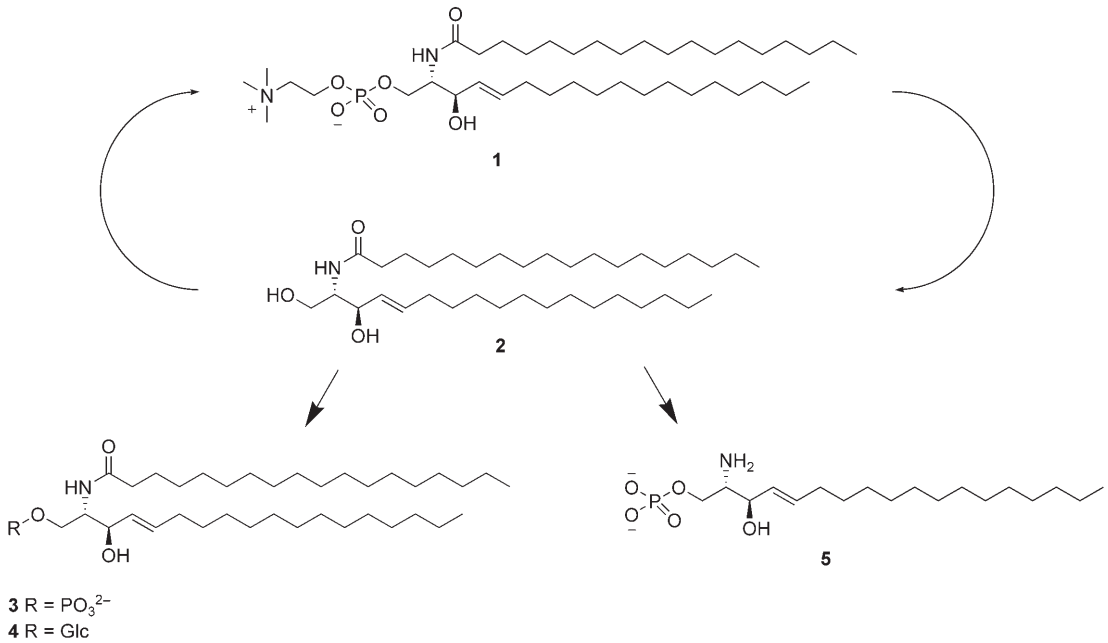
Sphingolipids are important components of the plasma membranes of eukaryotic cells. In the last few years increasing attention has been focussed on sphingolipid metabolites, because of their numerous biological effects and particularly because of their possible function as second messengers.

The primary catabolite of sphingomyelin (**1**) is ceramide (**2**), which is generated through the enzymatic activity of sphingomyelinases and is assumed to be involved in cell regulation, modulation of inflammatory processes, and also in programmed cell death (apoptosis).[1–5] Ceramide is also able to activate different signal-transduction cascades, both directly and indirectly.[1] Control of these biological effects is reached through regulation of the intracellular ceramide concentration by enzymes of the ceramide biosynthesis and by the formation of other sphingolipids, such as ceramide-1-phosphate (**3**), more complex glycosphingolipids (**4**), and sphingosine-1-phosphate (**5**).[1]

It has been assumed for a few years that the hydrolysis of sphingomyelin is the major process for the formation of biological active ceramide. In the tightly regulated sphingomyelin cycle[1–3,6] (Scheme 1) ceramide is generated through the action of either an acid sphingomyelinase (A-SMase) or a membrane-bound neutral sphingomyelinase (N-SMase). Different cytokines, such as TNF-α, interleukin-1β, interferon-γ, as well as radiation, heat, oxidative agents, vitamin D_3, and NO are all able to activate sphingomyelinases.[3,4]

However, various aspects of ceramide-mediated signal transduction, particularly its role in apoptosis, are controversial.[3–7] Additionally, the question as to which of the sphingomyelinases is important for stimulus-induced ceramide production is still a point of controversy.[3,8–11] The membrane-located neutral sphingomyelinase, which underlies physiological regulation through glutathione and arachidonic acid, is believed to play a relevant role in signal transduction.[1,3]

Potent, and above all, selective inhibitors are necessary to understand the biological function of ceramide and the sphingomyelinases. Although some inhibitors of N-SMase are known,[12,13] only scyphostatin (**6**),[12b,c,g] spiroepoxide **7**,[13a,b] and manumycin A (**8**),[12a] as well as its simple analogues have been used to examine the precise roles of these enzymes (Scheme 2).[14] However, all these compounds contain reactive epoxy groups, which are able to modify different cellular proteins through covalent interactions. Therefore, it is difficult to interpret the results of biological cell experiments. Here, we present the development of a new class of potent, selective and epoxy-free inhibitors of neutral sphingomyelinase, which we term sphingolactones.

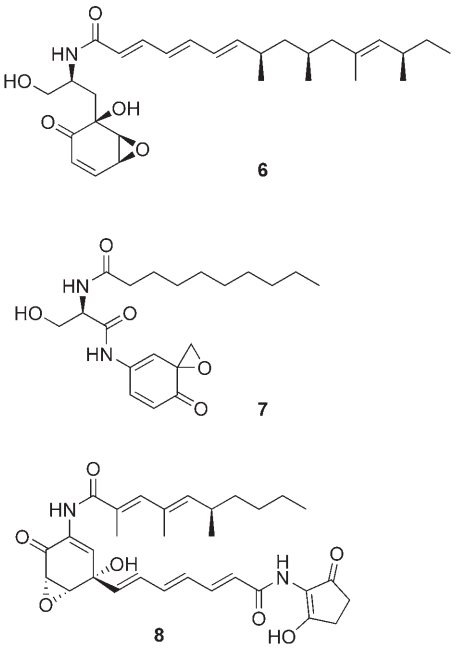


Scheme 1. The sphingomyelin cycle. Ceramide **2** is generated from spingomyelin (**1**) through the action of sphingomyelinases. This competes in a metabolic equilibrium with ceramide-1-phosphate (**3**), more complex glycosphingolipids (e.g., **4**, Glc = glucose), and sphingosine-1-phosphate (**5**).

[*] Dipl.-Chem. V. Wascholowski, Prof. Dr. A. Giannis
University of Leipzig
Institute of Organic Chemistry
04103 Leipzig (Germany)
Fax: (+49) 341-973-6599
E-mail: giannis@chemie.uni-leipzig.de

Supporting information for this article is available on the WWW under http://www.angewandte.org or from the author.

 © 2006 Wiley-VCH Verlag GmbH & Co. KGaA, Weinheim



Scheme 2. Scyphostatin (**6**), spiroepoxide **7**, and manumycin (**8**).

The conception of the inhibitors is based on the following facts: Both, scyphostatin (**6**) as well as manumycin A (**8**) contain a polyunsaturated fatty acid residue as a common structural element. Furthermore, synthetic manumycin analogues with unsaturated carboxylic acids in the amide moiety possess a higher affinity to N-SMase relative to those with saturated fatty acid chains.[12a] Moreover, it is known from our own research, that the primary hydroxy group of **7** is essential for the inhibitory activity.[13c] As a replacement for the reactive epoxy groups we chose the γ-butyrolactone scaffold, a privileged structure, which is a recurrent structural motif[15] present in many biological active molecules. Figure 1 shows the structural features of the desired inhibitor.

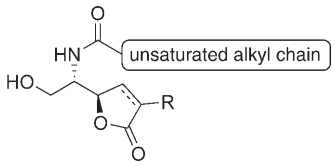
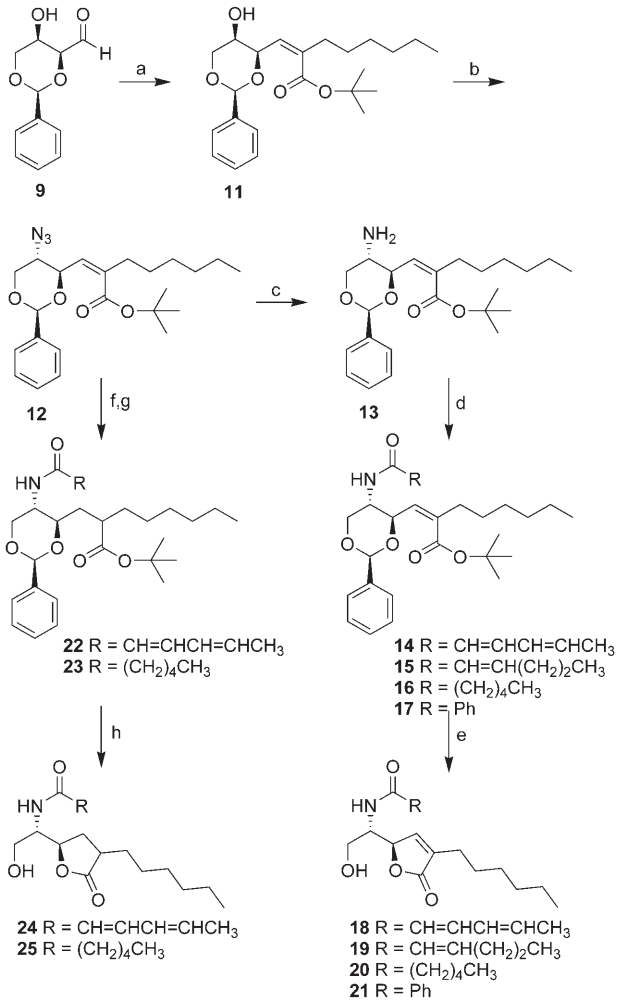


Figure 1. Structural features of the desired inhibitor.

The synthesis of the targeted inhibitor (Scheme 3) starts with the reaction of 2,4-*O*-benzylidene-D-threose (**9**), which is readily accessible by periodate cleavage of 4,6-*O*-benzylidene-D-galactose,[16,17] with the appropriate modified aryl phosphonate **10**[18] in an Ando variant[19] of the Horner–Wadsworth–Emmons (HWE) reaction[20] at −78 °C. The desired *Z* isomer **11** was obtained together with the corresponding *E* isomer in a ratio of 20:1. After azide exchange and reduction, amine **13** was modified with different carboxylic acid chlorides to obtain the amides **14**–**17**. Cleavage of the protecting groups with catalytic amounts of *para*-toluenesulfonic acid and in situ lactonization yielded the desired lactones **18**–**21**. The syntheses of **24** and **25** were completed by catalytic hydrogenolysis of compound **12** with Pd on charcoal (Scheme 3). The reaction results in an inseparable mixture of diastereomers in a ratio of 4:1. Further conversion into the desired compounds **24** and **25** was carried out in analogy to the described synthesis above.



Scheme 3. Synthesis of sphingolactones. a) 1.2 equiv LiCl, 1.2 equiv $(PhO)_2P(O)CH((CH_2)_5CH_3)COOtBu$ (**10**), 1.1 equiv DBU, THF, 67%; b) 1. 1.5 equiv Py, 1.3 equiv TfO_2, CH_2Cl_2, 2. 4 equiv NaN_3, DMF, 62%; c) 1.6 equiv Ph_3P, THF, H_2O, 60 °C, 94%; d) 1.5 equiv NEt_3, 1.1 equiv RCOCl, THF, 87–98%; e) cat. *p*-TsOH, DMF, 1,2-ethandiol, 76–85%; f) cat. Pd/C, H_2, ethanol, quant.; g) 1.5 equiv NEt_3, 1.1 equiv RCOCl, THF, 94–97%; h) cat. *p*-TsOH, DMF, 1,2-ethandiol, 72–79%. DBU = 1,8-diazabicyclo[5.4.0]undec-7-ene, Py = pyridine, Tf = trifluoromethanesulfonyl, Ts = toluene-4-sulfonyl.

The synthesized compounds were then evaluated regarding their inhibitory effect against N-SMase, for which a microsome preparation containing Mg^{2+}-dependent N-SMase from rat brain was used. Indeed, lactone **18**, as well as **24** and **25** proved to be time-dependent (irreversible) inhibitors of the N-SMase (Figure 2). Derivatives **19**–**21** also proved to be effective (irreversible inhibition, data not shown).

Subsequently, we investigated the inhibitors to determine which functional group is crucial for irreversible inhibition. In this context, the reduced derivative **24**, which contains a more

 © 2006 Wiley-VCH Verlag GmbH & Co. KGaA, Weinheim

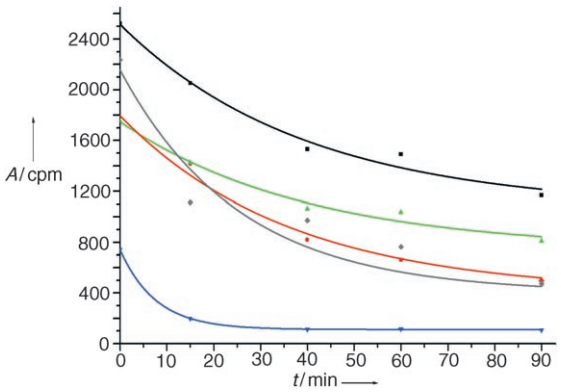


Figure 2. Time-dependence of the inhibition of the neutral sphingomyelinase by **18** (◆), **24** (▼), and **25** (●) (final concentration 350 μM). Hypothetical curve through a reversible competitive inhibition by **25**: ▲; control: ■; *A* = activity; cpm = counts per minute; *t* = preincubation time.

electrophilic lactone group, was identified as a better inhibitor than compound **18**. Therefore, it seems apparent that the inhibitory activity correlates directly with the lactone and is not accomplished by a 1,4-addition to the Michael system of compound **18**. This hypothesis is supported by the fact that N-SMase is also irreversibly inhibited by the saturated lactone **25**, as well as by derivative **21**. Moreover, increasing concentrations of sphingomyelin in the assay attenuate the inhibitory effect of **24** (Figure 3). This result indicates that inhibitor **24**

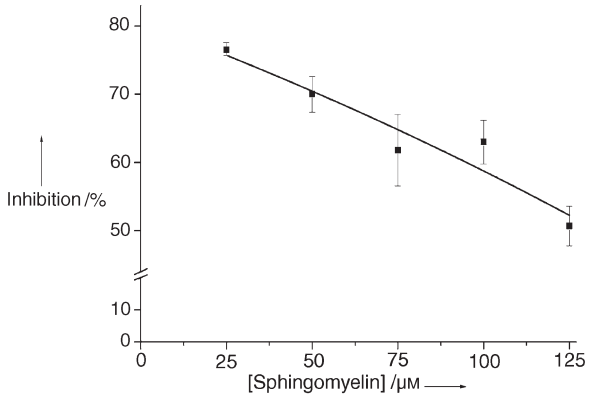


Figure 3. Inhibition of N-Smase by **24** at different concentrations of sphingomyelin. (final concentration 350 μM, no preincubation).

directly binds at the active site of N-SMase. The acid sphingomyelinase was only weakly competitive and only slightly dependent on the concentration of compound **24** (Figure 4).

The *N*-acyl chain exerts a decisive influence on the inhibitory effect of the synthesized lactones. In particular, the conjugated system of (2*E*,4*E*)-hexadienic acid seems to be able to adjust the inhibitor **24** at the active site of N-SMase, thus allowing an as yet unidentified nucleophile of the enzyme to attack the lactone.

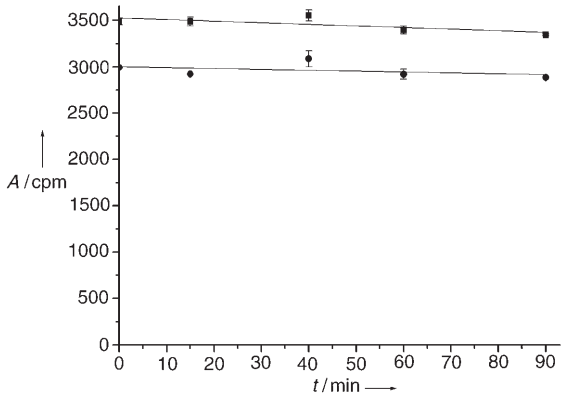


Figure 4. Effect of **24** (●) on A-SMase (final concentration 350 μM). control: ■.

The selective N-SMase inhibitors describe, which we term sphingolactones, are characterized by their high potency, with compound **24** possessing the highest inhibitory activity. In contrast to the previously described N-SMase inhibitors such as scyphostatin (**6**), spiroepoxide **7**, and manumycin A (**8**), the sphingolactones are stable and contain no epoxy function. Therefore, they represent useful chemical tools to explore the biological significance of ceramide and N-SMase in apoptosis, inflammation responses, malignant processes, and neurodegenerative diseases, such as Alzheimer's disease or multiple sclerosis.[1,21]

Received: June 8, 2005
Published online: December 19, 2005

Keywords: ceramide · inhibitors · lactones · signal transduction · sphingomyelinase

[1] a) V. Wascholowski, A. Giannis, *Drug News Perspect.* **2001**, *14*, 581–590; b) B. Ogretmen, Y. A. Hannun, *Nat. Rev. Cancer* **2004**, *4*, 604–616; c) A. Huwiler, T. Kolter, J. Pfeilschifter, K. Sandhoff, *Biochim. Biophys. Acta* **2000**, *1485*, 63–99; d) T. Kolter, K. Sandhoff, *Angew. Chem.* **1999**, *111*, 1632–1670; *Angew. Chem. Int. Ed.* **1999**, *38*, 1532–1568.
[2] D. K. Perry, Y. A. Hannun, *Biochim. Biophys. Acta* **1998**, *1463*, 233–243.
[3] N. Marchesini, Y. A. Hannun, *Biochem. Cell Biol.* **2004**, *82*, 27–44.
[4] M. E. Venable, L. M. Obeid, *Biochim. Biophys. Acta* **1999**, *1439*, 291–298.
[5] G. Liu, L. Oleine, R. L. Hébert, *Crit. Rev. Clin. Lab. Sci.* **1999**, *36*, 511–573.
[6] Y. Hannun, R. Bell, *Science* **1989**, *243*, 500–507.
[7] R. N. Kolesnick, M. Kronke, *Annu. Rev. Physiol.* **1998**, *60*, 643–665.
[8] K. Hoffmann, V. M. Dixit, *Trends Biochem. Sci.* **1998**, *23*, 374–377.
[9] R. Kolesnick, Y. A. Hannun, *Trends Biochem. Sci.* **1999**, *24*, 224–225.
[10] D. K. Perry, Y. A. Hannun, *Trends Biochem. Sci.* **1999**, *24*, 226–227.
[11] K. Hoffmann, V. M. Dixit, *Trends Biochem. Sci.* **1999**, *24*, 227.
[12] a) C. Arenz, M. Thutewohl, O. Block, H. Waldmann, H.-J. Altenbach, A. Giannis, *ChemBioChem* **2001**, *2*, 141–143; b) F.

 © 2006 Wiley-VCH Verlag GmbH & Co. KGaA, Weinheim

Nara, M. Tanaka, S. Madsuda-Inoue, *J. Antibiot.* **1999**, *52*, 531 – 535; c) M. Inoue, W. Yokota, G. Murugesh, T. Izuhara, T. Katho, *Angew. Chem.* **2004**, *116*, 4303 – 4305; *Angew. Chem. Int. Ed.* **2004**, *43*, 4207 – 4209; d) R. Uchida, H. Tomoda, Y. Dong, S. Omura, *J. Antibiot.* **1999**, *52*, 572 – 574; e) M. Tanaka, F. Nara, Y. Yamasato, S. Masuda-Inoue, H. Doi-Yoshioka, S. Kumakura, R. Enokita, T. Ogita, *J. Antibiot.* **1999**, *52*, 670 – 673; f) M. Tanaka, F. Nara, Y. Yamasato, Y. Ono, T. J. Ogita, *J. Antibiot.* **1999**, *52*, 827 – 830; g) F. Nara, M. Tanaka, T. Hosoya, K. Suzuki-Konagai, T. Ogita, *J. Antibiot.* **1999**, *52*, 525 – 530; h) R. Uchida, H. Tomoda, M. Arai, S. Omura, *J. Antibiot.* **2001**, *54*, 882 – 889; i) S. F. Martin, C. Gómez-Díaz, P. Navas, J. M. Villalba, *Biochem. Biophys. Res. Commun.* **2002**, *297*, 581 – 586; j) Q. Zhou, M. R. Band, A. Hernandez, Z. L. Liu, F. A. Kummerow, *Life Sci.* **2004**, *75*, 1567 – 1577.

[13] a) C. Arenz, A. Giannis, *Angew. Chem.* **2000**, *112*, 1498 – 1500; *Angew. Chem. Int. Ed.* **2000**, *39*, 1440 – 1442; b) C. Arenz, A. Giannis, *Eur. J. Org. Chem.* **2001**, 137 – 140; c) C. Arenz, M. Gartner, V. Waschołowski, A. Giannis, *Bioorg. Med. Chem.* **2001**, *9*, 2901 – 2904; d) E. N. Pitsinos, V. Waschołowski, S. Karaliota, C. Rigou, E. A. Couladouros, A. Giannis, *ChemBioChem* **2003**, *4*, 1223 – 1225; e) C. Luberto, D. F. Hassler, P. Signorelli, Y. Okamoto, H. Sawai, E. Boros, D. J. Hazen-Martin, L. M. Obeid, Y. A. Hannun, G. K. Smith, *J. Biol. Chem.* **2002**, *277*, 41 128 – 41 139; f) R. A. Claus, A. Wüstholz, S. Müller, C. L. Bockmeyer, N. H. Riedel, R. Kinscherf, H.-P. Deigner, *ChemBioChem* **2005**, *6*, 726 – 737; g) T. Hakogi, Y. Monden, S. Iwama, S. Katsumura, *Org. Lett.* **2000**, *2*, 2627 – 2630; h) T. Yokomatsu, H. Takechi, T. Akiyama, S. Shibuya, T. Kominato, S. Soeda, H. Shimeno, *Bioorg. Med. Chem. Lett.* **2001**, *11*, 1277 – 1280; i) T. Hakogi, Y. Monden, M. Taichi, S. Iwama, S. Fujii, K. Ikeda, S. Katsumura, *J. Org. Chem.* **2002**, *67*, 4839 – 4846; j) C. C. Lindsey, C. Gomez-Diaz, J. M. Villalba, T. R. Pettus, *Tetrahedron* **2002**, *58*, 4559 – 4565; k) T. Yokomatsu, T. Murano, T. Akiyama, J. Koizumi, S. Shibuya, Y. Tsuji, S. Soeda, H. Shimeno, *Bioorg. Med. Chem. Lett.* **2003**, *13*, 229 – 236; l) M. Taguchi, K. Sugimoto, K.-I. Goda, T. Akama, K. Yamamoto, T. Suzuki, Y. Tomishima, M. Nishiguchi, K. Arai, K. Takahashi, T. Kobori, *Bioorg. Med. Chem. Lett.* **2003**, *13*, 1963 – 1966; m) M. Taguchi, K.-I. Goda, K. Sugimoto, T. Akama, K. Yamamoto, T. Suzuki, Y. Tomishima, M. Nishiguchi, K. Arai, K. Takahashi, T. Kobori, *Bioorg. Med. Chem. Lett.* **2003**, *13*, 3681 – 3684.

[14] a) T. Numakawa, H. Nakayama, S. Suzuki, T. Kubo, F. Nara, Y. Numakawa, D. Yokomaku, T. Araki, T. Ishimoto, A. Ogura, T. Taguchi, *J. Biol. Chem.* **2003**, *278*, 41 259 – 41 269; b) K. Hanada, N. M. Palacpac, P. A. Magistrado, K. Kurokawa, G. Rai, D. Sakata, T. Hara, T. Horii, M. Nishijima, T. Mitamura, *J. Exp. Med.* **2002**, *195*, 23 – 34; c) M. Czarny, J. Liu, P. Oh, J. E. Schnitzer, *J. Biol. Chem.* **2003**, *278*, 4424 – 4430; d) M. Czarny, J. E. Schnitzer, *Am. J. Physiol. Heart Circ. Physiol.* **2004**, *287*, H1344 – H1352; e) R. Ramer, U. Weinzierl, B. Schwind, K. Brune, B. Hinz, *Mol. Pharmacol.* **2003**, *64*, 1189 – 1198; f) S. Falcone, C. Perrotta, C. De Palma, A. Pisconti, C. Sciorati, A. Capobianco, P. Rovere-Querini, A. A. Manfredi, E. Clementi, *J. Immunol.* **2004**, *173*, 4452 – 4463; g) R. Barsacchi, C. Perrotta, S. Bulotta, S. Moncada, N. Borgese, E. Clementi, *Mol. Pharmacol.* **2003**, *63*, 886 – 895; h) L. M. Frago, S. Cañón, E. J. de la Rosa, Y. León, I. Varela-Nieto, *J. Cell Sci.* **2003**, *116*, 475 – 486; i) S. F. Martín, C. Gómez-Díaz, P. Navas, J. M. Villalba, *Biochem. Biophys. Res. Commun.* **2002**, *297*, 581 – 586.

[15] a) H. M. R. Hoffmann, J. Rabe, *Angew. Chem.* **1985**, *97*, 96 – 112; *Angew. Chem. Int. Ed. Engl.* **1985**, *24*, 94 – 110; b) A. G. González, M. H. Silva, J. I. Padrón, F. Léon, E. Reyes, M. Álvarez-Mon, J. P. Pivel, J. Quintana, F. Estévez, J. Bermejo, *J. Med. Chem.* **2002**, *45*, 2358 – 2361; c) F. P. Kuhajda, E. S. Pizer, J. N. Li, N. S. Mani, G. L. Frehywot, C. A. Townsend, *Proc. Natl. Acad. Sci. USA* **2000**, *97*, 3450 – 3454; d) H. M. Ogmundsdottir, G. M. Zoega, S. R. Gissurarson, K. Ingolfsdottir, *J. Pharm. Pharmacol.* **1998**, *50*, 107 – 115; e) A. Randazzo, C. Debitus, L. Minale, P. P. Garcia, M. J. Alcaraz, M. Paya, L. Gomez-Paloma, *J. Nat. Prod.* **1998**, *61*, 571 – 575; f) A. E. Mitchell, J. Zheng, B. D. Hammcock, M. Lo Bello, A. D. Jones, *Biochemistry* **1998**, *37*, 6752 – 6759; g) A. Huwe, R. Mazitschek, A. Giannis, *Angew. Chem.* **2003**, *115*, 2170 – 2187; *Angew. Chem. Int. Ed.* **2003**, *42*, 2122 – 2138; h) M. Hirao, J. Posakony, M. Nelson, H. Hruby, M. Jung, J. A. Simon, A. Bedalow, *J. Biol. Chem.* **2003**, *278*, 52 773 – 52 782; i) J. Posakony, M. Hirao, S. Stevens, J. A. Simon, A. Bedalow, *J. Med. Chem.* **2004**, *47*, 2635 – 2644; j) M. Biel, A. Kretsovali, E. Karatzali, J. Papamatheakis, A. Giannis, *Angew. Chem.* **2004**, *116*, 4065 – 4067; *Angew. Chem. Int. Ed.* **2004**, *43*, 3974 – 3976; k) A. Kar, S. Gogoi, N. P. Argade, *Tetrahedron* **2005**, *61*, 5297 – 5302.

[16] E. G. Gros, V. Deulofeu, *J. Org. Chem.* **1964**, *29*, 3647 – 3656.

[17] P. Zimmermann, R. R. Schmidt, *Liebigs Ann. Chem.* **1988**, 663 – 667.

[18] K. Ando, *J. Org. Chem.* **2000**, *65*, 4745 – 4749.

[19] K. Ando, *J. Org. Chem.* **1999**, *64*, 6815 – 6821.

[20] B. E. Maryanoff, A. B. Reitz, *Chem. Rev.* **1989**, *89*, 863 – 927.

[21] M. P. Mattson, *Nature* **2004**, *430*, 631 – 639.

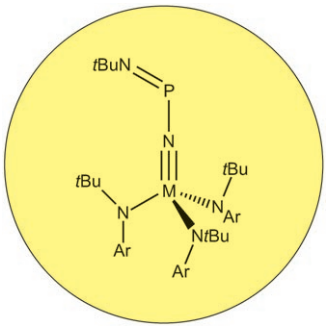
 © 2006 Wiley-VCH Verlag GmbH & Co. KGaA, Weinheim

Cover Picture

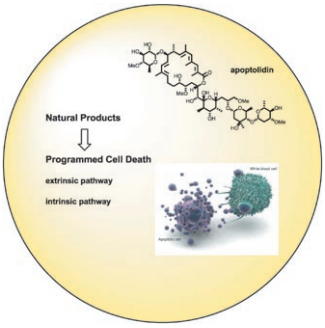
Tommaso Marcelli, Richard N. S. van der Haas, Jan H. van Maarseveen, and Henk Hiemstra*



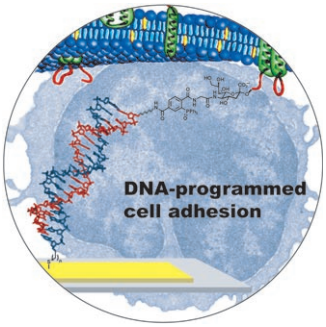
Alkaloids extracted from the Quinine tree bark are a privileged scaffold for the development of asymmetric organocatalysts. In their Communication on page 929 ff., H. Hiemstra and co-workers describe a novel *Cinchona*-derived thiourea compound able to catalyze the Henry (nitroaldol) reaction of aromatic aldehydes with high enantioselectivities. The cover picture shows *Cinchona pubescens* (courtesy of Forest and Kim Starr, USA) and a typical Henry product.



Low-Coordinate Phosphorus Compounds
In his Minireview on page 862 ff., C. C. Cummins presents a synthesis of low-coordinate phosphorus compounds that relies on anionic complexes with terminal nitride, phosphide, and carbide ligands as the starting materials.



Programmed Cell Death
Natural products such as apoptolidin can selectively control the programmed cell death (apoptosis) of cancer cells. U. Koert et al. describe in their Review on page 872 ff. the biochemical sequences of apoptosis as well as the total synthesis of apoptolidin.



Sequence-Specific Attachment
Short DNA strands linked to the surfaces of living cells mediate the sequence-specific attachment of the cells to substrates. This programmable adhesion technology, is described by M. B. Francis and co-workers in their Communication on page 896 ff.

Contents

VIP *The following Communications have been judged by at least two referees to be "very important papers" and will be published online at www.angewandte.org soon:*

*J. Deschamp, O. Chuzel, J. Hannedouche, O. Riant**
Highly Diastereo- and Enantioselective Copper-Catalyzed Tandem Conjugated Reduction/Aldol Reaction to Ketones

J. W. Bode, R. M. Fox, K. D. Baucom*
Chemoselective Amide Ligations by Decarboxylative Condensations of *N*-Alkylhydroxylamines and α-Keto Acids

A. Oleksi, A. G. Blanco, R. Boer, I. Usón, J. Aymamí, A. Rodger, M. J. Hannon, M. Coll**
Molecular Recognition of a Three-Way DNA Junction by a Metallosupramolecular Helicate

J. E. Banham, C. R. Timmel, R. J. M. Abbott, S. M. Lea, G. Jeschke**
A New Tool for Characterization of Weak Protein–Protein Interactions: Evidence from DEER for the Trimerization of a von Willebrand Factor A Domain in Solution

B. H. Lipshutz, B. A. Frieman, A. E. Tomaso, Jr.*
Copper-in-Charcoal (Cu/C): Heterogeneous, Copper-Catalyzed Asymmetric Hydrosilylations

J. T. Shaw, J. M. Mitchell*
A Structurally Diverse Library of Polycyclic Lactams Resulting from the Systematic Placement of Proximal Functional Groups

Meeting Reviews

Mechanically Induced Chemistry: New Perspectives on the Nanoscale — *I. Frank* — **852**

Books

Comprehensive Organic Functional Group Transformations II — Alan R. Katritzky, Richard J. K. Taylor — *reviewed by E. Haak, H. Hopf, U. Jahn* — **855**

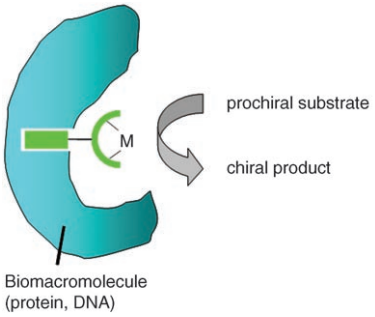
Highlights

Asymmetric Catalysis

R. Krämer* — **858 – 860**

Supramolecular Bioinorganic Hybrid Catalysts for Enantioselective Transformations

Biomacromolecules (proteins, DNA) provide a chiral second sphere for achiral or racemic metal-complex catalysts. Such supramolecular hybrids have recently been optimized for high enantioselectivity by structural variation of both the chemical and the biological component, and provide the products with ≥90% *ee* for specific reactions.

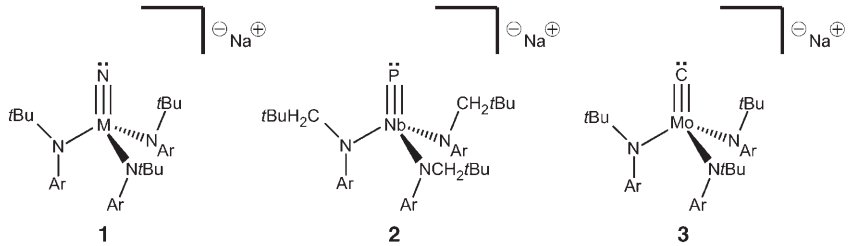


Minireviews

Coordination Chemistry

C. C. Cummins* — **862 – 870**

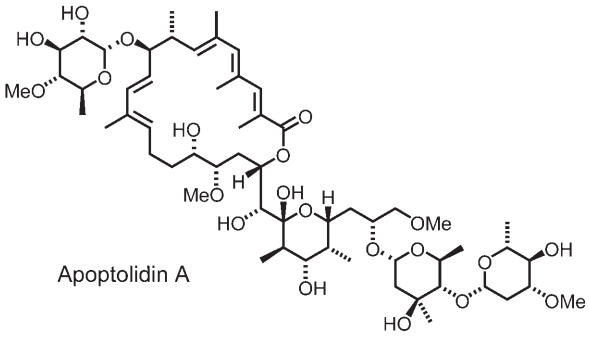
Terminal, Anionic Carbide, Nitride, and Phosphide Transition-Metal Complexes as Synthetic Entries to Low-Coordinate Phosphorus Derivatives



Atoms to get attached to: Anionic terminal nitride (**1**), phosphide (**2**), and carbide complexes (**3**) function as excellent platforms for the construction of systems containing low-coordinate phosphorus centers. The N, P, or C atomic substituents respectively are expanded into new or rare bound ligands: CPPh, NPN*t*Bu, and $PPPh_2$.

WILEY InterScience DISCOVER SOMETHING GREAT
© 2006 Wiley-VCH Verlag GmbH & Co. KGaA, Weinheim

Reviews



Apoptolidin A

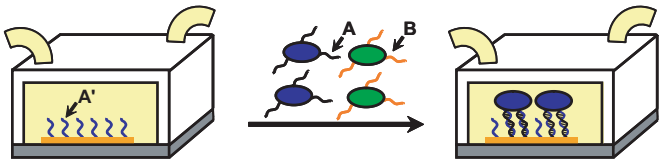
Lethal drugs: Natural products such as apoptolidin can selectively induce the programmed cell death (apoptosis) of cancer cells. This ability makes them interesting lead structures for antitumor therapy. This Review describes the biochemical mechanism of apoptosis and compares known syntheses of apoptolidin.

Drug Research

P. T. Daniel, U. Koert,*
J. Schuppan ——— **872 – 893**

Apoptolidin: Induction of Apoptosis by a Natural Product

Communications



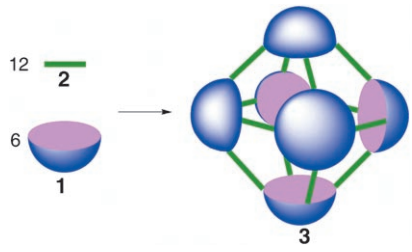
Stuck-on genes: Live cells functionalized with single-stranded DNA oligonucleotides bind, independent of native adhesion mechanisms, to substrates that bear complementary DNA strands in a sequence-specific manner. This strategy has been successfully utilized with several common mammalian cell lines and device platforms.

DNA Recognition

R. A. Chandra, E. S. Douglas, R. A. Mathies, C. R. Bertozzi, M. B. Francis* ——— **896 – 901**

Programmable Cell Adhesion Encoded by DNA Hybridization

A whole in one! The octahedral nanocontainer **3** composed of six cavitands **1** that are connected together by 12 diamino bridging units **2** through 24 imine bonds was synthesized in nearly quantitative yield in a one-pot reaction. Molecular mechanics calculations and NMR experiments suggest that this container has a diameter of 3.2 Å and an inner cavity volume of about 1700 Å^3.



Supramolecular Chemistry

X. Liu, Y. Liu, G. Li, R. Warmuth* ——— **901 – 904**

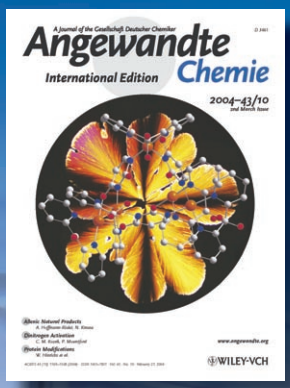
One-Pot, 18-Component Synthesis of an Octahedral Nanocontainer Molecule

For the USA and Canada:
ANGEWANDTE CHEMIE International Edition (ISSN 1433-7851) is published weekly by Wiley-VCH PO Box 191161, D 69451 Weinheim, Germany. Air freight and mailing in the USA by Publications Expediting Inc. 200 Meacham Ave., Elmont, NY 11003. Periodicals postage paid at Jamaica NY 11431. US POSTMASTER: send address changes to *Angewandte Chemie*, Wiley-VCH, 111 River Street, Hoboken, NJ 07030. Annual subscription price for institutions: US$ 5685/5168 (valid for print and electronic / print or electronic delivery); for individuals who are personal members of a national chemical society prices are available on request. Postage and handling charges included. All prices are subject to local VAT/sales tax.

© 2006 Wiley-VCH Verlag GmbH & Co. KGaA, Weinheim

The best in chemistry –

for more than a hundred years



A Journal of the Gesellschaft Deutscher Chemiker

Angewandte
International Edition **Chemie**

www.angewandte.org

1888: ***The beginning of a success story***

Constant Innovations

1962: *First issue of the International Edition*
1976: *Graphical abstracts*
1979: *Cover pictures*
1988: *Centenary of Angewandte*
1989: *Routine use of color*
1991: *New section: Highlights*
1992: *Computerized editorial tracking system*
1995: *Internet service for readers*
1998: *Regular press service; full-text online*
2000: *New section: Essays; EarlyView: Communications available online ahead of the printed version*
2001: *New section: Minireviews*
2002: *Online submission of manuscripts*
2003: *Weekly publication; new section: News; new layout*
2004: *Backfiles (1962-1997); ManuscriptXpress: Online system for authors and referees*



Angewandte's advisors...

Ulrich Stilz
Aventis, Frankfurt/Main

» With its interdisciplinary and international orientation ***Angewandte Chemie*** *has set the benchmark for publishing innovative results. The editorial team is acknowledged for the success of this renowned journal, that provides scientists with a unique forum, in which to discuss their discoveries. «*

Angewandte Chemie International Edition *is a journal of the German Chemical Society (GDCh)*

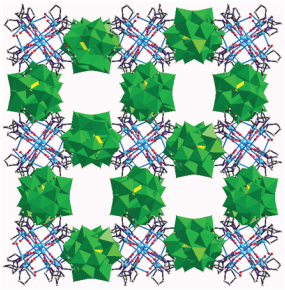
GDCh

WILEY InterScience® DISCOVER SOMETHING GREAT

WILEY-VCH

1198404_gu

A twist to the right, or to the left: Both enantiomers of a new chiral material were synthesized by a rational approach, using enantiopure proline ligands, copper cations, and Keggin polyoxometalate anions as building blocks. The compounds have open-framework structures containing helical channels.



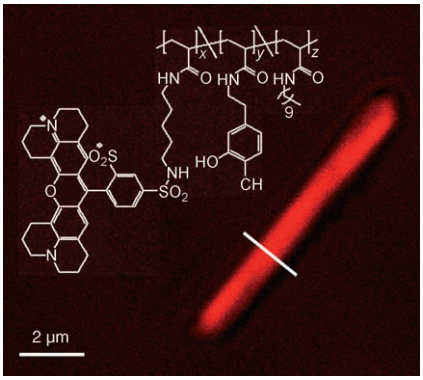
Chiral Frameworks

H.-Y. An, E.-B. Wang,* D.-R. Xiao, Y.-G. Li, Z.-M. Su,* L. Xu ——— **904 – 908**

Chiral 3D Architectures with Helical Channels Constructed from Polyoxometalate Clusters and Copper–Amino Acid Complexes

---

Three in one: TiO_2 nanoparticles have been functionalized with reactive polymeric ligands that incorporate chelating dopamine anchor groups, a modifying unit to allow the binding of functional molecules such as fluorescent dyes (see picture), as well as groups to tailor the solubility of the inorganic nanocrystals in different solvents.

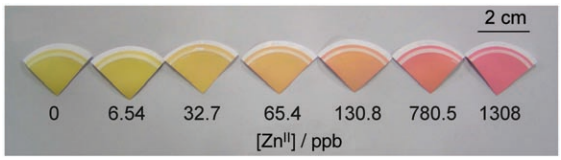


Functional Nanoparticles

M. N. Tahir, M. Eberhardt, P. Theato, S. Faiß, A. Janshoff, T. Gorelik, U. Kolb, W. Tremel* ——— **908 – 912**

Reactive Polymers: A Versatile Toolbox for the Immobilization of Functional Molecules on TiO_2 Nanoparticles

---



Sensitive indicators: Test strips for metal ions were obtained simply by filtering dispersions of hydrophobic indicator dyes in the form of nanoparticles or nanofibers through cellulose ester membrane filters, which gave firm and uniform coatings on the surface. The picture shows the detection of ppb concentrations of Zn^{II} with azo-dye-loaded test strips.

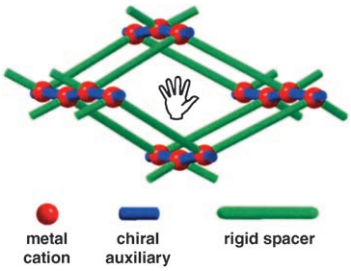
Metal Indicators

Y. Takahashi,* H. Kasai, H. Nakanishi, T. M. Suzuki* ——— **913 – 916**

Test Strips for Heavy-Metal Ions Fabricated from Nanosized Dye Compounds

---

A handy approach: A new synthetic approach starting from readily available chemicals successfully produces a robust homochiral metal–organic microporous framework. The material exhibits size- and enantioselective guest-sorption properties (see picture), as well as remarkable catalytic activity with size- and chemoselectivity, and high conversion in the oxidation of thioethers to sulfoxides.



Microporous Frameworks

D. N. Dybtsev, A. L. Nuzhdin, H. Chun, K. P. Bryliakov, E. P. Talsi, V. P. Fedin,* K. Kim* ——— **916 – 920**

A Homochiral Metal–Organic Material with Permanent Porosity, Enantioselective Sorption Properties, and Catalytic Activity

© 2006 Wiley-VCH Verlag GmbH & Co. KGaA, Weinheim

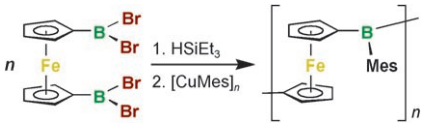
Contents

Ferrocene-Based Polymers

J. B. Heilmann, M. Scheibitz, Y. Qin, A. Sundararaman, F. Jäkle,* T. Kretz, M. Bolte, H.-W. Lerner, M. C. Holthausen,* M. Wagner* ——— **920 – 925**

A Synthetic Route to Borylene-Bridged Poly(ferrocenylene)s

Iron chains: The highly soluble, ferrocene-containing polymer [-fc-B(Mes)-]$_n$ (fc = Fe(C_5H_4)$_2$, Mes = mesityl), with an average chain length of about 16 repeat units (n = 16), is readily accessible by a novel polycondensation reaction starting from fc(BBr_2)$_2$ and $HSiEt_3$ (see scheme). The polymer contains three-coordinate

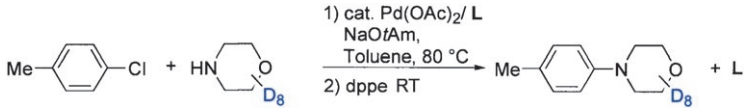


boron centers, which are well-suited for the promotion of electron delocalization along the polymer chain.

Palladium Catalysis

E. R. Strieter, S. L. Buchwald* **925 – 928**

Evidence for the Formation and Structure of Palladacycles during Pd-Catalyzed C–N Bond Formation with Catalysts Derived from Bulky Monophosphinobiaryl Ligands

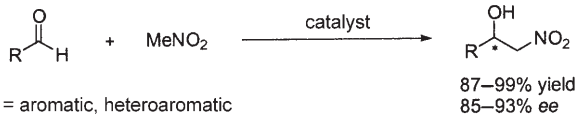


The structural origins of the differences in catalytic activity observed between catalysts containing 2′-substituted and 2′,6′-disubstituted biaryl monophosphane ligands for a Pd-catalyzed C–N bond-forming reaction are discussed. It is shown that palladacycle formation is avoided and optimal catalyst activity is achieved through the use of the 2′,6′-disubstituted ligands. (*t*Am = *tert*-amyl, dppe = 1,2-bis(diphenylphosphanyl)-ethane).

Cinchona Alkaloids

T. Marcelli, R. N. S. van der Haas, J. H. van Maarseveen, H. Hiemstra* ——— **929 – 931**

Asymmetric Organocatalytic Henry Reaction

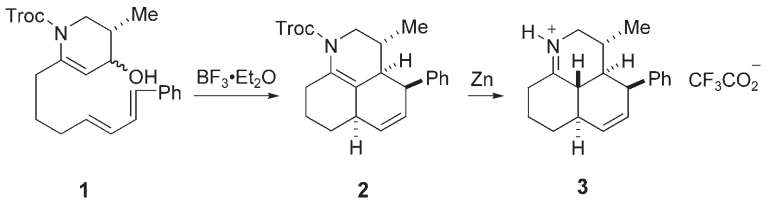


The nitroaldol (Henry) reaction between aromatic aldehydes and nitromethane can be carried out in high yields and enantiomeric excess by using a novel *Cinchona*-derived thiourea catalyst. Hydrogen-bond donors at the C6′ position in these organocatalysts are shown to induce preferential formation of one enantiomer.

Cycloaddition Reactions

B. B. Snider,* Q. Che ——— **932 – 935**

Synthesis of (±)-Deoxysymbioimine Using an Intramolecular Diels–Alder Reaction with an *N*-Alkoxycarbonyl 2,3-Dihydropyridinium Cation as the Dienophile



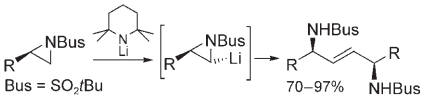
Three rings: Treatment of an *N*-2,2,2-trichloroethoxycarbonyl (Troc)-substituted tetrahydropyridinol (**1**) with BF_3·Et_2O in CH_2Cl_2 gave a tricyclic adduct **2** (31% yield) through an intramolecular Diels–Alder reaction. Reduction with zinc gave deoxysymbioimine (**3**), a potential antiresorptive and anti-inflammatory drug.

Synthetic Methods

D. M. Hodgson,* S. M. Miles **935 – 938**

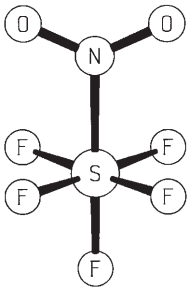
Dimerization of Lithiated Terminal Aziridines

Let's get together: Dimerization of enantiopure terminal aziridines by lithiation gives efficiently N-protected 2-ene-1,4-diamines with complete selectivity for the *E* olefin (see scheme). The usefulness of the method was demonstrated in a concise synthesis of (*R*,*S*,*S*,*R*)-2,5-diamino-



1,6-diphenylhexane-3,4-diol, the core unit of many extremely potent HIV protease inhibitors and also asymmetric catalysts.

© 2006 Wiley-VCH Verlag GmbH & Co. KGaA, Weinheim

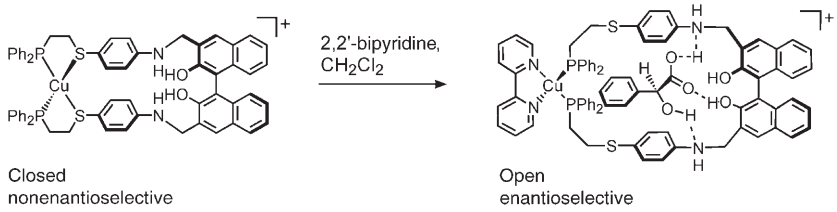


Call off the search: Photolysis of a mixture of SF_5Br and NO_2 results in the synthesis of gram quantities of pentafluoronitrosulfane, SF_5NO_2 (see picture), whose preliminary structure was obtained by gas-phase electron diffraction studies and reveals the longest S^{VI}—N bond reported (1.903(7) Å).

Fluoro–Sulfur Compounds

N. Lu,* H. P. S. Kumar, J. L. Fye, J. Sun Blanks, J. S. Thrasher,* H. Willner, H. Oberhammer ——— 938 – 940

Synthesis of the Long Sought After Compound Pentafluoronitrosulfane, SF_5NO_2

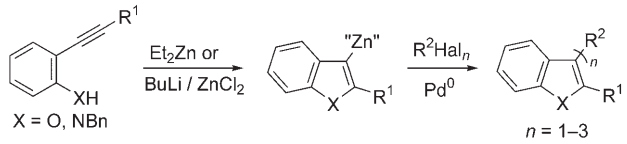


The weak-link approach is used to synthesize a four-coordinate Cu^I complex for the chiral recognition of mandelic acid. The chelation through 2,2′-bipyridine in a reaction that concomitantly breaks weak Cu—S links and opens the condensed structure into a 27-membered macrocycle switches on the complex so it acts as an enantioselective fluorescent receptor.

Host–Guest Systems

J. Heo, C. A. Mirkin* ——— 941 – 944

Pseudo-Allosteric Recognition of Mandelic Acid with an Enantioselective Coordination Complex

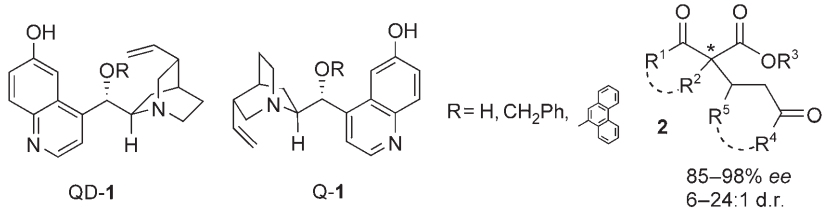


Closing the ring: Thermally stable but reactive 3-zinciobenzofurans and indoles were synthesized by metalative cyclization of 2-ynyl phenols or anilines. Furthermore, a variety of extended π-conjugated molecules were obtained by Pd-catalyzed cross-coupling reactions of these heterocycles with mono- or polyhalo-substituted arenes and alkenes (R^2Hal_n; see scheme; Bn = benzyl).

Heterocycles

M. Nakamura,* L. Ilies, S. Otsubo, E. Nakamura* ——— 944 – 947

3-Zinciobenzofuran and 3-Zincioindole: Versatile Tools for the Construction of Conjugated Structures Containing Multiple Benzoheterole Units



Added value: The conjugate addition of cyclic or acyclic α-substituted β-ketoesters to α,β-unsaturated ketones using a chiral organic catalyst (**1**) can be achieved with good enantioselectivity, diastereoselectivity, and yield. This asymmetric C—C bond formation strategy provides a range of chiral building blocks **2** that contain an all-carbon quaternary stereocenter.

Conjugate Addition

F. Wu, H. Li, R. Hong, L. Deng* ——— 947 – 950

Construction of Quaternary Stereocenters by Efficient and Practical Conjugate Additions to α,β-Unsaturated Ketones with a Chiral Organic Catalyst

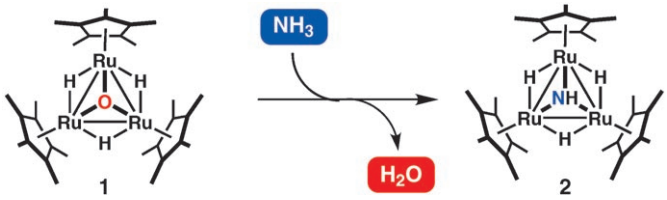
© 2006 Wiley-VCH Verlag GmbH & Co. KGaA, Weinheim

Contents

N–H Activation

Y. Nakajima, H. Kameo, H. Suzuki* ——— 950 – 952

Cleavage of Nitrogen–Hydrogen Bonds of Ammonia Induced by Triruthenium Polyhydrido Clusters

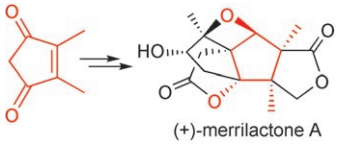


More cleavage: The complex $[(Cp^*Ru)_3(\mu_3\text{-}H)_2(\mu\text{-}H)_3]$ ($Cp^* = \eta^5\text{-}C_5Me_5$) promotes N–H bond cleavage of ammonia to yield the mono-μ_3-imido complex $[(Cp^*Ru)_3(\mu_3\text{-}NH)(\mu\text{-}H)_3]$ (**2**), probably via μ-amido complex $[(Cp^*Ru)_3(\mu\text{-}NH_2)(\mu\text{-}H)_4]$. Introduction of a triply bridging oxo ligand into the Ru_3 core (→**1**) makes the reaction kinetically and thermodynamically favorable and gives **2** within 1 h at 80 °C.

Natural Product Synthesis

G. Mehta,* S. R. Singh ——— 953 – 955

Total Synthesis of (±)-Merrilactone A

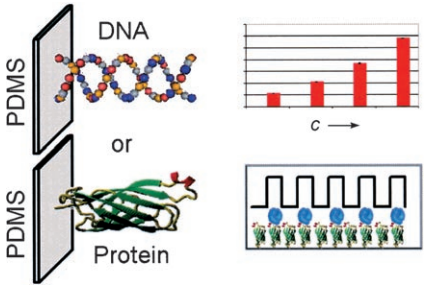


Merrily, merrily: A total synthesis of the pentacyclic sesquiterpenoid merrilactone A starting from 2,3-dimethyl-2-cyclopentene-1,4-dione has been achieved with good stereo- and regioselectivity. Merrilactone A exhibits impressive neurotrophic activity and may be important for the development of therapeutic drugs for neurodegenerative disorders.

Label-Free Biosensors

J. C. Latham, D. A. Markov, H. S. Sørensen, D. J. Bornhop* ——— 955 – 958

Photobiotin Surface Chemistry Improves Label-Free Interferometric Sensing of Biochemical Interactions

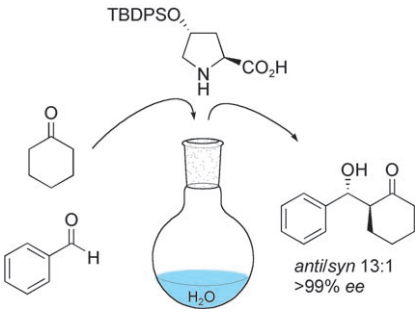


A highly sensitive and cost-effective biosensor: Simple surface chemistry of photobiotin, bound with a layer of avidin, allows convenient immobilization of any biotinylated molecule of interest onto microfluidic channels molded in poly(dimethylsiloxane) (PDMS). The biosensor obtained this way is capable of monitoring biomolecular interactions in label-free situations and in small (picoliter) volumes.

Asymmetric Synthesis

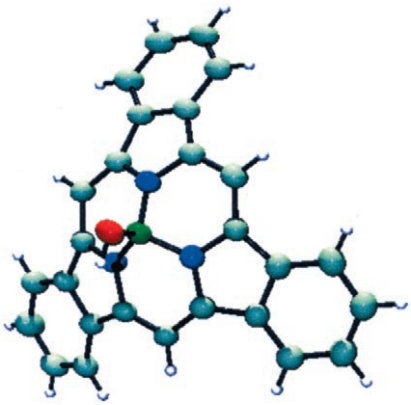
Y. Hayashi,* T. Sumiya, J. Takahashi, H. Gotoh, T. Urushima, M. Shoji ——— 958 – 961

Highly Diastereo- and Enantioselective Direct Aldol Reactions in Water



Going green: The synthetically very important aldol reaction can proceed in water without a metal catalyst with excellent enantioselectivity. The key to the reaction is a small, synthetic organic catalyst based on *trans*-hydroxyproline with a siloxy group. Thus, this method is an environmentally friendly process for the synthesis of chiral molecules.

© 2006 Wiley-VCH Verlag GmbH & Co. KGaA, Weinheim

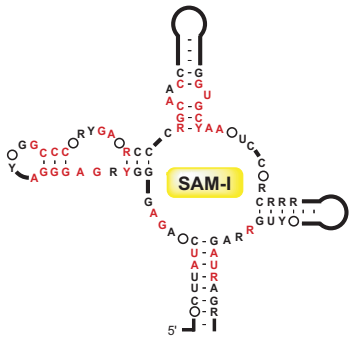


Keeping it in the family: A one-pot condensation with a boric acid template leads to the synthesis of subporphineboron(III) complexes (see example; B green, O red, N blue, C turquoise, H white), ring-contracted congeners of porphyrins. Facile axial ligand exchange reactions provide alkoxy- and carboxy-coordinated subporphyrins, which have bowl-shaped structures with a bowl depth that depends on the axial group.

Template Synthesis

Y. Inokuma, J. H. Kwon, T. K. Ahn, M.-C. Yoo, D. Kim,* A. Osuka* **961 – 964**

Tribenzosubporphines: Synthesis and Characterization

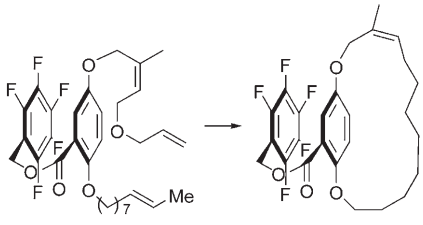


A series of analogues of *S*-adenosylmethionine (SAM) have been used to examine the molecular-recognition characteristics of an RNA genetic element or riboswitch. Biochemical assays indicate that the riboswitch of the SAM-I class is highly selective for SAM and exhibits a pattern of molecular recognition that is distinct from that of the SAM-II class of riboswitches.

RNA

J. Lim, W. C. Winkler, S. Nakamura, V. Scott, R. R. Breaker* **964 – 968**

Molecular-Recognition Characteristics of SAM-Binding Riboswitches



Correct orientation: Macrocyclic paracyclophanes of multiple ring sizes and diverse functionality are prepared by olefin metathesis (see scheme for an example), through the exploitation of solution-phase quadrupolar interactions between the core arene and pendant pentafluoroarene units. This approach reverses the tendency for dimeric products to be formed during macrocyclizations.

Cyclophanes

Y. El-azizi, A. Schmitzer, S. K. Collins* **968 – 973**

Exploitation of Perfluorophenyl–Phenyl Interactions for Achieving Difficult Macrocyclizations by Using Ring-Closing Metathesis



The tides are turning: Kalata B1 (KB1) is the prototypical member of an exceptionally stable and resistant family of plant-derived miniproteins called cyclotides. The biosynthesis of KB1 and a small library of KB1-based cyclotides (variation occurs in five solvent-exposed loops) in *E. coli* has been performed by using recombinant-DNA expression techniques and protein splicing.

Biosynthesis

R. H. Kimura, A.-T. Tran, J. A. Camarero* **973 – 976**

Biosynthesis of the Cyclotide Kalata B1 by Using Protein Splicing

© 2006 Wiley-VCH Verlag GmbH & Co. KGaA, Weinheim

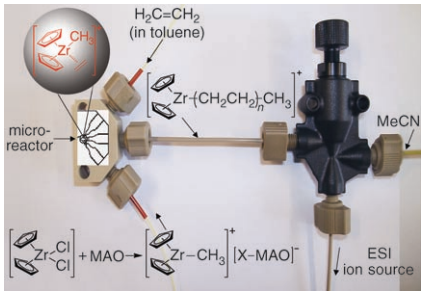
Contents

Reaction Mechanisms

L. S. Santos, J. O. Metzger* — **977 – 981**

Study of Homogeneously Catalyzed Ziegler–Natta Polymerization of Ethene by ESI-MS

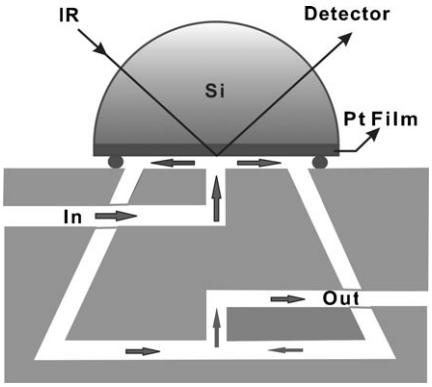
Direct evidence: An ESI mass spectrometer coupled online to a microreactor was used to intercept the catalytically active cationic intermediates of the Ziegler–Natta polymerization of ethene with the homogeneous catalyst system $[Cp_2ZrCl_2]$/MAO (see picture; MAO = methylaluminoxane, Cp = cyclopentadienyl, X = CH_3, Cl). For the first time these intermediates were studied directly from the solution and their catalytic activity proved.



Electrocatalysis

Y. X. Chen,* M. Heinen, Z. Jusys, R. J. Behm* — **981 – 985**

Kinetics and Mechanism of the Electrooxidation of Formic Acid—Spectroelectrochemical Studies in a Flow Cell

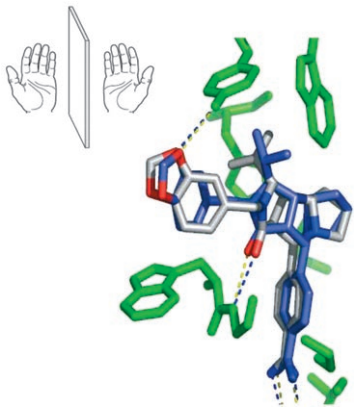


Go with the flow: A novel spectroelectrochemical flow cell with well-defined mass transport allows time-resolved electrochemical and in situ FTIR spectroscopy measurements under continuous electrolyte flow (e.g. during electrolyte exchange). Its potential for mechanistic and kinetic studies was demonstrated in studies on the electrooxidation of formic acid.

Protein Binding

J. Fokkens, G. Klebe* — **985 – 989**

A Simple Protocol To Estimate Differences in Protein Binding Affinity for Enantiomers without Prior Resolution of Racemates

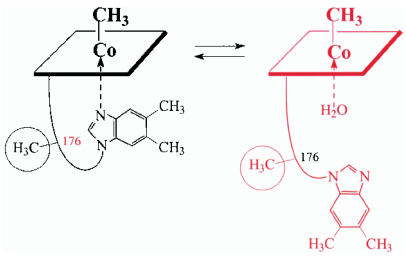


Like hand in glove: A simple protocol that uses isothermal titration calorimetry to semiquantitatively determine the difference in binding affinity of two enantiomers to a protein without requiring prior resolution of the racemates has been developed. Affinity differences can been explained in terms of differences in the structural fit of the enantiomers into the binding pocket of the protein (see picture).

Molecular Switch

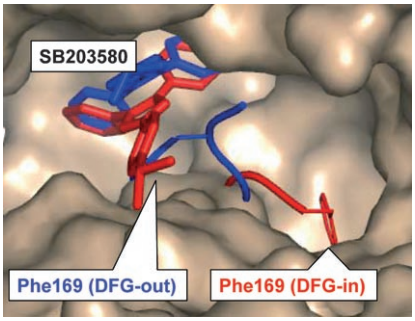
P. Butler, M.-O. Ebert, A. Lyskowski, K. Gruber, C. Kratky, B. Kräutler* — **989 – 993**

Vitamin B_{12}: A Methyl Group without a Job?



At a record distance: The methyl group at C176 of the nucleotide loop of vitamin B_{12} derivatives has a significant effect on their characteristic "base-on"/"base-off" switch (see scheme), the constitutional result of which is a remarkable 11 bonds away from C176.

© 2006 Wiley-VCH Verlag GmbH & Co. KGaA, Weinheim



In its apo state kinase p38 effects slow motions that can be detected in the NMR spectrum. One of the affected parts is the pharmacologically interesting DFG motif. Diarylurea inhibitors that bind to the DFG-out conformation lock this motif in a defined state, whereas DFG-in inhibitors that bind to the adjacent hinge region leave the flexibility of the DFG motif unaffected (see crystal structure of the complex of p38 with the inhibitor SB203580).

Drug Design

M. Vogtherr, K. Saxena, S. Hoelder, S. Grimme, M. Betz, U. Schieborr, B. Pescatore, M. Robin, L. Delarbre, T. Langer, K. U. Wendt, H. Schwalbe* ——— **993 – 997**

NMR Characterization of Kinase p38 Dynamics in Free and Ligand-Bound Forms

Sources

Product and Company Directory

You can start the entry for your company in "Sources" in any issue of ***Angewandte Chemie***.

If you would like more information, please do not hesitate to contact us.

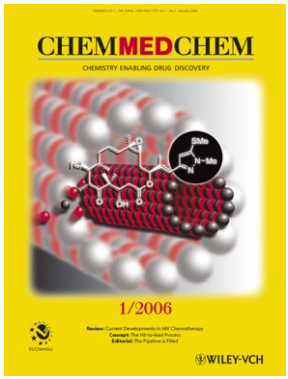
Wiley-VCH Verlag – Advertising Department
Tel.: 0 62 01 - 60 65 65
Fax: 0 62 01 - 60 65 50
E-Mail: MSchulz@wiley-vch.de

Service

Keywords ——— ***998***

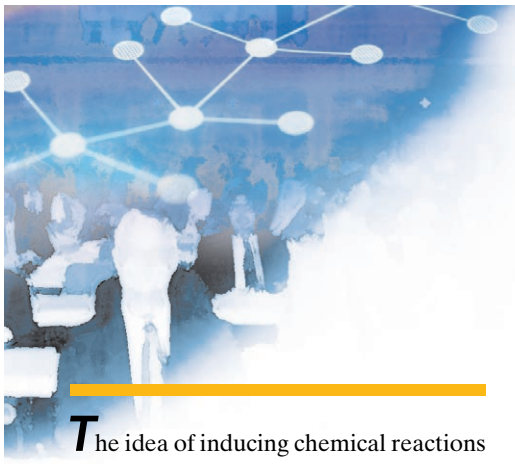
Authors ——— ***999***

Preview ——— ***1001***



For more information on ChemMedChem see www.chemmedchem.org

© 2006 Wiley-VCH Verlag GmbH & Co. KGaA, Weinheim



Mechanically Induced Chemistry: New Perspectives on the Nanoscale**

*Irmgard Frank**

The idea of inducing chemical reactions by exerting mechanical force dates back to the beginning of the twentieth century, when Ostwald developed the concept of mechanochemistry.[1] Mechanically induced chemistry thus has a long history and it continues to be of high importance for industrial applications such as the preparation of electrode materials.[2] New aspects of this field have emerged from recent developments in the nanosciences. With atomic force and scanning tunneling microscopy (AFM and STM, respectively) techniques, it is meanwhile possible to manipulate single molecules and to eventually induce chemical reactions. Of particular importance in this context is the work done by the group of Hermann Gaub (Munich), who succeeded in detecting the breaking of a single chemical bond and measuring the corresponding force. In parallel to this experimental progress, molecular dynamics methods have been developed that allow such processes to be explained in full detail. Besides classical molecular dynamics approaches, Car–Parrinello molecular dynamics has become very important and allows the quantum mechanical nature of chemical bonds to be taken into account during a molecular dynamics simulation. At the 87th International Bunsen Discussion Meeting that took place in Tutzing near Munich during October 3–6, 2005, the whole spectrum of theoretical approaches were brought together with recent experimental developments.

Michael Klein (Philadelphia) gave an impressive overview of the different aspects of this topic in the introductory talk. Klein's own contributions to the field cover a broad range: He performed the first Car–Parrinello molecular dynamics simulations in the field of mechanically induced chemistry. This work showed the behavior of a molecular knot under strong tension up to bond breaking.[3] Additionally, consecutive reactions were observed, such as the formation of a ring from the fragments. Classical molecular dynamics has been used for the investigation of phenomena on larger scales, while for the investigation of significantly larger molecular systems, Klein and co-workers have developed coarse-grain methods. Here, the atomic approach is abandoned and thus it becomes possible to simulate, for example, the intrusion of macromolecules into biological membranes.[4]

In general, the simulation of biosystems under mechanical load is particularly important. Klaus Schulten (Urbana) presented simulations of highly complex biological systems. His group uses a broad range of methods depending on the nature of the problem, and of special importance is NAMD or NAMD2 ("not (just) another molecular dynamics" program), the code developed by Schulten for classical molecular dynamics simulations of extremely large systems. With this approach, systems such as α-hemolysin and its membrane environment (about 3×10^5 atoms) was studied.[5] In connection with the SMD (steered molecular dynamics) approach that was also developed by Schulten and co-workers, and endorsed by the versatile graphics program VMD, a mighty package is now available for the simulation of large systems under mechanical load.

A general problem not only to the investigation of the dynamics of proteins but also especially to the simulation of chemical reactions is the limited timescale that is accessible to molecular dynamics simulations. Hence, several groups are currently developing approaches to accelerate rearrangements or chemical reactions in a simulation. In several of the studies presented, metadynamics was applied, a method that was recently developed by Alessandro Laio and Michele Parrinello.[6] Metadynamics represents an alternative approach to the "chemical flooding" method by Helmut Grubmüller (Göttingen), who impressively demonstrated the efficiency of his approach with simulations of chemical reactions of strained ring systems. "Chemical flooding" thus complements "conformational flooding", which allows the study of rearrangements in larger systems. In part with Paul Tavan (Munich), Grubmüller also conducted simulations of strained systems with classical molecular dynamics and characterized the fundamental phenomena many years ago. Applications ranged from simple polymers to the simulation of the unbinding of the streptavidin–biotin complex.[7]

Since many years, the work of Grubmüller is closely connected to the experiments performed by Matthias Rief (Munich), who has performed strain experiments for diverse systems such as polysaccharides and DNA.[8] Together with Hermann Gaub, he answered the question how strong are the forces that arise from the breaking of a single covalent bond. Rief presented current results on the unfolding of green fluorescent protein (GFP). Here, two metastable states have been found as intermediates of the unfolding process. On the basis of the experiments, the free-energy landscape could be characterized in full detail.[9]

A further highlight of the meeting was the talk by Peter Hamm (Zürich) about photoswitchable peptides. By means of a photoreaction, it is possible

[*] Dr. I. Frank
Ludwig-Maximilians-Universität München
Department Chemie
Butenandtstrasse 5–13, Haus E
81377 München (Germany)
Fax: (+49) 89-2180-77568
E-mail: frank@cup.uni-muenchen.de

[**] 87th International Bunsen Discussion Meeting, October 3–6, 2005, Tutzing (Germany).

InterScience
© 2006 Wiley-VCH Verlag GmbH & Co. KGaA, Weinheim

in these systems to induce mechanical tension in a peptide chain. By using infrared spectroscopy with femtosecond time resolution, the consecutive fast dynamics in the peptide backbone can be studied on the timescale of a few picoseconds. Particularly prominent is the experiment using azobenzene as a photoswitch[10] which has also been investigated theoretically by the groups of Gerhard Stock and Paul Tavan. Hamm also discussed the use of alternative chromophores.

At present, several groups are working on the spectroscopic investigation of single dye molecules under tensile stress, the results of which may lead to new possibilities in the development of local stress sensors. The studies presented by the groups of Claus Seidel (Düsseldorf) and Christoph Bräuchle (Munich) lead one to expect that this aim will be reached in the near future.

The meeting closed with two more theoretical sessions, starting with a lecture by Dominik Marx (Bochum), whose Car–Parrinello molecular dynamics simulations on the formation of gold nanowires under tensile stress are known beyond the theoretical chemistry community[11] (Figure 1). These systems, which have been investigated experimentally by the group of Harald Fuchs, demonstrate most impressively that remarkable phenomena can be triggered by mechanical stress on the nanoscale.

Gotthard Seifert (Dresden) then presented the results of simulations with tight-binding density functional theory (DFT). His investigations of, for example, molybdenum sulfide nanotubes,[12] convincingly demonstrated the high potential of the method in the field of inorganic systems (Figure 2). The simulations showed in detail which processes occur if nanotubes are broken under extreme tensile stress.

In the concluding talk, Schulten pointed out how multifaceted and broad the field of mechanically induced chemistry is, even if one restricts the discussion to phenomena on the atomic scale. With the range of different molecular dynamics methods (Car–Parrinello, tight-binding, force-field, coarse-grained) and with methods from statistical mechanics, it is nowadays possible to explain highly complex processes on different scales from a theoretical point of view. In combination with exciting

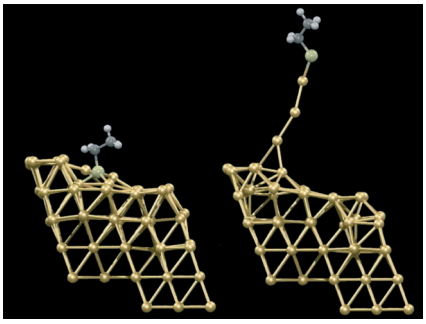


Figure 1. Formation of a gold nanowire under tensile stress, modeled with Car–Parrinello molecular dynamics. A sufficiently strong covalent attachment to the gold surface is achieved with sulfur (light yellow; courtesy of D. Marx).

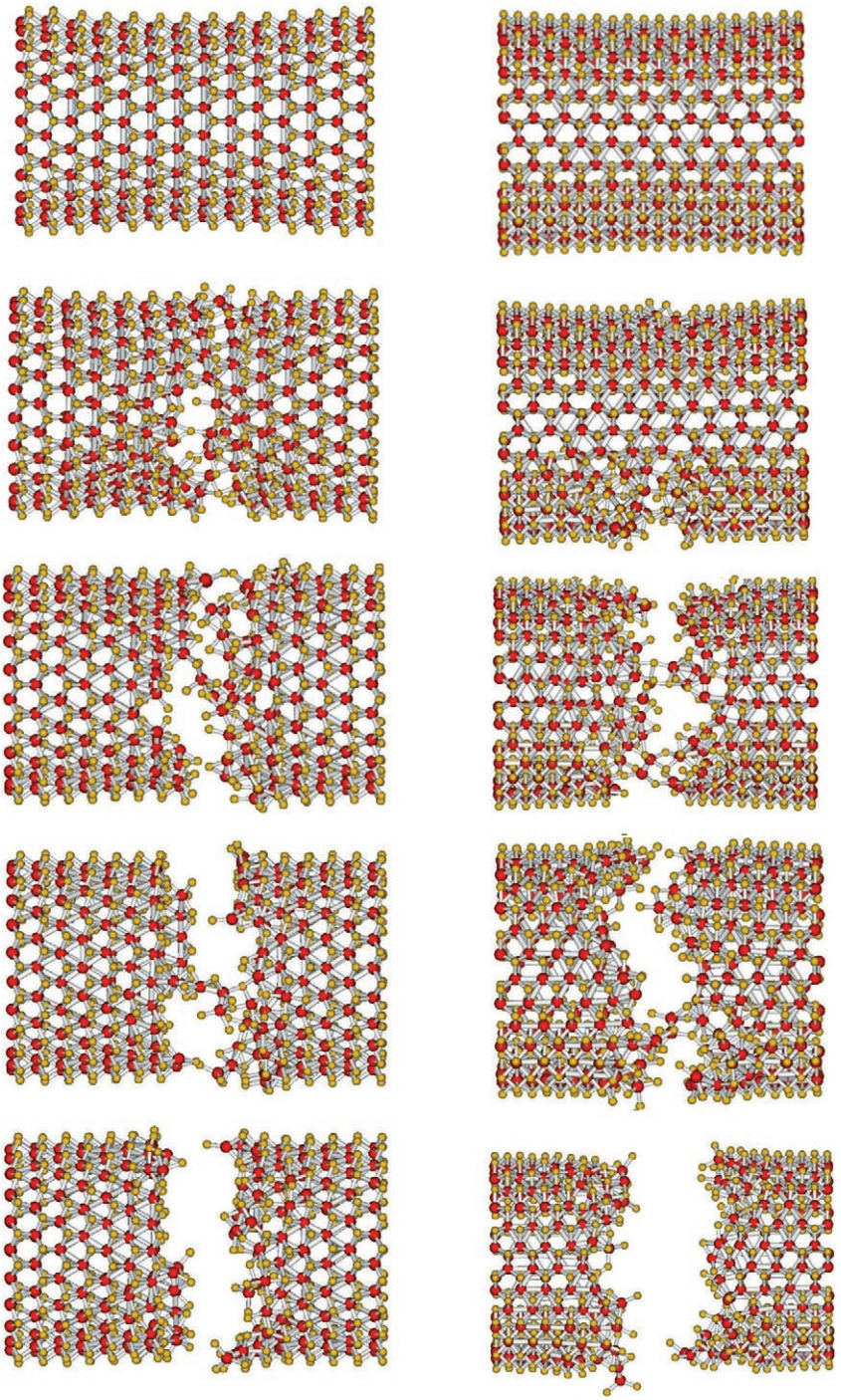


Figure 2. Tight-binding DFT simulation of the breaking of MoS_2 nanotubes under mechanical load (courtesy of I. Ivanovskaya, T. Heine, and G. Seifert).

© 2006 Wiley-VCH Verlag GmbH & Co. KGaA, Weinheim

developments concerning single-molecule methods and time-resolved spectroscopy, novel insights will be gained in the near future into the processes that occur in materials under extreme conditions on the shortest length and timescales.

[1] W. Ostwald, *Handbuch der allgemeinen Chemie, Bd. 1*, Akademische Verlagsgesellschaft mbH, Leipzig, **1919**, 70.

[2] S. Kipp, V. Sepelak, K. D. Becker, *Chem. Unserer Zeit* **2005**, *39*, 384.

[3] A. M. Saitta, P. D. Soper, E. Wasserman, M. L. Klein, *Nature* **1999**, *399*, 46.

[4] G. Srinivas, D. E. Discher, M. L. Klein, *Nat. Mater.* **2004**, *3*, 638.

[5] A. Aksimentiev, K. Schulten, *Biophys. J.* **2005**, *88*, 3745.

[6] A. Laio, M. Parrinello, *Proc. Natl. Acad. Sci. USA* **2002**, *99*, 12562.

[7] H. Grubmüller, B. Heymann, P. Tavan, *Science* **1996**, *271*, 997.

[8] M. Rief, H. Grubmüller, *ChemPhysChem* **2002**, *3*, 255.

[9] H. Dietz, M. Rief, *Proc. Natl. Acad. Sci. USA* **2004**, *101*, 16192.

[10] J. Bredenbeck, J. Helbing, A. Sieg, T. Schrader, W. Zinth, C. Renner, R. Behrendt, L. Moroder, J. Wachtveitl, P. Hamm, *Proc. Natl. Acad. Sci. USA* **2003**, *100*, 6452.

[11] D. Krüger, H. Fuchs, R. Rousseau, D. Marx, *Angew. Chem.* **2003**, *115*, 2353; *Angew. Chem. Int. Ed.* **2003**, *42*, 2251.

[12] G. Seifert, H. Terrones, M. Terrones, G. Jungnickel, T. Frauenheim, *Phys. Rev. Lett.* **2000**, *85*, 146.

DOI: 10.1002/anie.200504567

 © 2006 Wiley-VCH Verlag GmbH & Co. KGaA, Weinheim

Asymmetric Catalysis

DOI: 10.1002/anie.200502907

Supramolecular Bioinorganic Hybrid Catalysts for Enantioselective Transformations

*Roland Krämer**

Keywords:
asymmetric catalysis · DNA · hybrid catalysts · proteins

Dedicated to Prof. Günther Helmchen on the occasion of his 65th birthday

The efficient preparation of enantiopure compounds is of primary importance for the production of pharmaceuticals, vitamins, agrochemicals, and flavorants and is a major endeavor in modern organic chemistry. Metal-catalyzed homogeneous enantioselective transformations (e.g. hydrogenations, epoxidations, hydroformylations, allylic substitutions) have proven useful and versatile, and the achievements in this field were recognized in 2001 with the Nobel Prize in Chemistry.[1] Despite these efforts, it remains difficult to tailor the second coordination sphere of metal complexes and predict stereoselectivity, and the impact of enantioselective catalysis for the production of fine chemicals remains modest.[2]

Biocatalysis has emerged as an alternative tool for the synthesis of enantiopure compounds. The efficiency as well as chemo-, region-, and stereoselectivity of enzymatic reactions are often unsurpassed. While specific enzymes have broad substrate spectra and function in organic solvents, the substrate scope of most enzymes is narrower than that of synthetic metal-complex catalysts. Enzymes are often more useful with polar substrates in aqueous media where product isolation can be a serious problem, and their operational stability can be rather limited.

These problems have been addressed by "genetic" sequence variation of the protein.[3] "Directed evolution" combines the generation of millions of mutants with efficient high-throughput-screening procedures for enantioselectivity, and is a particular promising concept for the optimization of protein-based catalysts.[4] Also, a considerable number of interesting transformations has been accomplished by directed evolution of nucleic acid based biocatalysts (ribozymes, DNAzymes),[5] although their potential for enantioselective reactions has hardly been explored.[6,7] Despite a great deal of progress, the engineering of biocatalysts for specific reactions by sequence variation remains very challenging.

In some respects, metal-complex catalysts and biocatalysts are complementary. This has prompted chemists to develop hybrids from inorganic catalysts and biomacromolecules that provide a well-defined, chiral microenvironment.[8] Both covalent and noncovalent strategies have been applied successfully to the site-specific anchoring of a catalytically active metal complex to the biomolecule.

In view of catalyst optimization, the noncovalent approach (Figure 1) seems more appealing since it avoids the potential complications associated with chemical modification of the biomacromolecule. Since the host molecule's binding pocket was by no means optimized by nature to support the enantioselectivity of a specific metal-catalyzed reaction, the success of the approach critically depends on the efficient optimization of catalyst performance. As early as 1978, Wilson and Whitesides[9] showed that an achiral rhodium(I) diphosphine complex is converted into an enantioselective hydrogenation catalyst

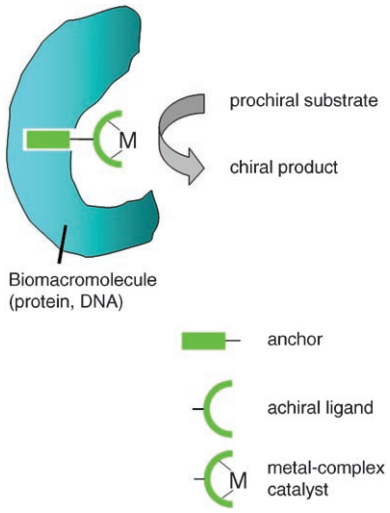


Figure 1. Supramolecular hybrid catalyst of a metal complex and a biomacromolecule.

(39% *ee*) by noncovalent, supramolecular embedding into the protein avidin.

This article highlights two very recent, important contributions to the field that demonstrate how such bioinorganic hybrid catalysts can be optimized to yield enantioselectivies greater than or equal to 90% *ee*:

- Ward and co-workers[10] have substantially improved the performance of metal-complex/protein hybrids by a combined chemogenetic approach.
- Rolfes and Feringa[11] could for the first time efficiently transfer the chiral information of the DNA double helix to a metal-catalyzed, enantioselective reaction.

By structural variations, Ward et al. have improved the enantioselectivity of Whiteside's rhodium–avidin hybrid to 96% *ee*.[12] But the strength of the chemogenetic approach is more impressively demonstrated by exploration of a novel organometallic ruthenium(II)

[*] Prof. Dr. R. Krämer
Anorganisch-Chemisches Institut
Universität Heidelberg
Im Neuenheimer Feld 270
69120 Heidelberg (Germany)
Fax: (+49) 6221-548-599
E-mail:
roland.kraemer@urz.uni-heidelberg.de

InterScience
© 2006 Wiley-VCH Verlag GmbH & Co. KGaA, Weinheim

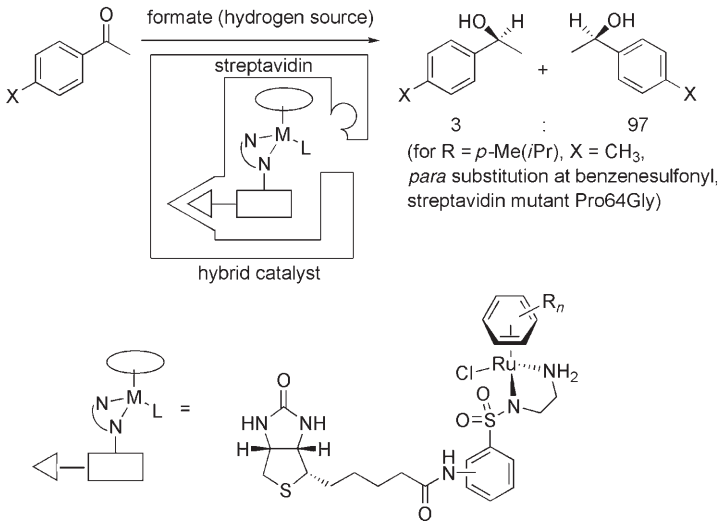


Figure 2. Hydrogenation of acetophenones catalyzed by a supramolecular hybrid composed of a biotin-modified Ru^{II} complex and the protein streptavidin.

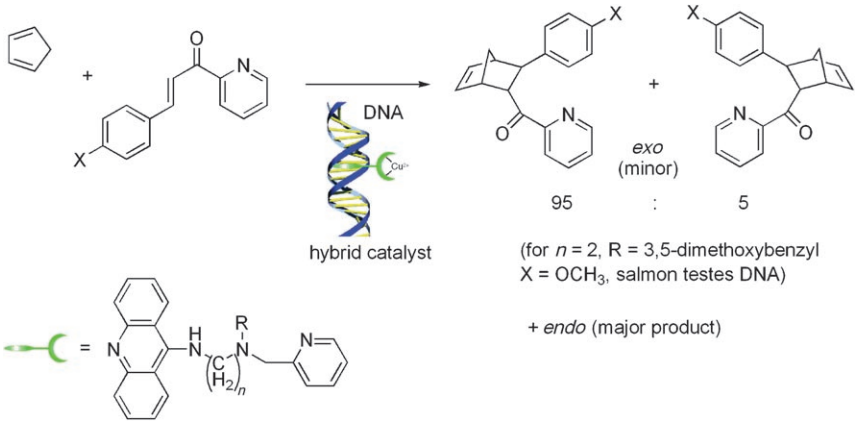
complex/streptavidin hybrid (Figure 2).[10] The η^6-arene complex catalyzes the reduction of acetophenone to 1-phenylethanol by transfer hydrogenation, using formate as the hydrogen source. A biotin conjugate of the complex (Figure 2) forms a 1:1 mixture of epimers at ruthenium; alone, this catalyst produces a racemic mixture of the alcohol.

Remarkably, the choice of the capping arene (η^6-benzene or η^6-*p*-cymene) determines which enantiomer of the product is produced preferentially (Table 1). In addition, several streptavidin point mutants were screened to "genetically" optimize the performance of the system. Mutant Pro64Gly (i.e. proline at position 64 in the wild-type protein is replaced by glycine) reduces the enantioselectivity of the η^6-benzene complex but increases the *R* selectivity of the *p*-cymene complex from 66 to 85%, and up to 94% *ee* with the substrate *p*-methylacetophenone ($X = CH_3$). Chemical and genetic methodologies have been combined efficiently to optimize the activity and enantioselectivity of the hybrid catalyst (Table 1). Very recently, the substrate specificity of hybrid hydrogenation catalysts could also be tuned in this way.[13]

Table 1: Effect of structural variation of the Ru complex/streptavidin hybrid on catalyst performance.[10][a]

R_n	X	Streptavidin	Conv. [%]	*ee* [%]
H	H	wild type	30	63 (*S*)
p-Me(*i*Pr)	H	wild type	82	68 (*R*)
H	H	Pro64Gly	30	58 (*S*)
p-Me(*i*Pr)	H	Pro64Gly	90	85 (*R*)
p-Me(*i*Pr)	CH_3	Pro64Gly	92	94 (*R*)

[a] Water, pH 6.3, 1% catalyst, 45–55°C.



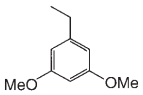
Scheme 1. Diels–Alder reaction catalyzed by supramolecular hybrid of a 9-aminoacridine-modified Cu^{II} complex and ds-DNA.

In a remarkably simple, supramolecular approach, Roelfes and Feringa could demonstrate the potential of hybrid DNAzymes in asymmetric catalysis.[11] A catalytically active copper(II) complex was attached to DNA through a 9-aminoacridine unit, a small aromatic molecule that efficiently intercalates into the DNA double helix. The copper(II) complex catalyzes a Diels–Alder reaction between the diene cyclopentadiene and a prochiral dienophile that binds the metal ion through a pyridyl group (Scheme 1). Both *endo* and *exo* cycloaddition products are formed, each as a mixture of two enantiomers. The Cu^{II} complex of the achiral ligand alone forms the *endo* product in excess, but both the *endo* and *exo* forms are essentially generated as racemic mixtures. In the presence of salmon testes DNA, the complex anchors to the DNA double helix through the acridine intercalator, and DNA is expected to create a chiral "second sphere" and control the enantioselectivity of the reaction. The reactions were performed in water and followed to >80% completion (three days at 5°C), and the Cu complex completed up to 22 turnovers.

As already observed for the metal–protein hybrids, variations in the chemical structure of the Cu complex have a dramatic influence on catalytic selectivity. First, the length of the $(CH_2)_n$ spacer between the bidentate chelating ligand and the aminoacridine moiety is crucial for both the enantioselectivity and the enantiopreference (Table 2). Second, the choice of substitutent R at the aliphatic N donor of the ligand significantly influences chirality transfer. For $n = 2$ the enantioselectivity is improved significantly from −37% *ee* (R = 1-naphthylmethyl) to −78% *ee* (R = 3,5-dimethoxybenzyl). (Positive and negative *ee* values indicate the two enantiomers.) The highest selectivity (−90% *ee* for the *exo* form) was observed for $n = 2$

© 2006 Wiley-VCH Verlag GmbH & Co. KGaA, Weinheim

Table 2: Effect of structural variation of the Cu^{II} complex/DNA hybrid on catalyst performance.[12][a]

n	R	X	DNA	*endo*/*exo*	*ee*(*exo*)[b] [%]
3		H	salmon testes	98:2	18
2		H	salmon testes	96:4	−37
5		H	salmon testes	97:3	< 5
2		H	salmon testes	92:8	−78
2		OMe	salmon testes	91:9	−90
2		H	16-mer duplex	82:18	−80

[a] Water, pH 6.5, 5 °C, 3 days, > 80% conversion. [b] Positive and negative *ee* values indicate the two enantiomers.

and R = 3,5-dimethoxybenzyl with a methoxy derivative of the dienophile substrate (Scheme 1, $X = OCH_3$).

The effect of sequence variation of the DNA host remains to be explored. A first indication for the influence of DNA sequence on catalytic selectivity is the observation that a synthetic 16-mer ds-DNA increases the ratio of the *exo* product (from 8% with salmon testes DNA to 18% with 16-mer DNA), although enantioselectivity is nearly unchanged. In contrast to the protein hybrids discussed above in which the localization of metal catalyst is well defined, intercalation of acridine into DNA is not sequence specific. Using a selective DNA binding moiety tethered to the catalyst would open the possibility to address specific DNA sequences and create a well-defined second sphere.

In summary, supramolecular hybrid catalysts of achiral or racemic metal complexes and biomacromolecules (proteins, DNA) have recently been optimized for high enantioselectivity (≥ 90% *ee* for specific reactions) by combined structural variation of both the chemical and the biological component. It will be interesting to apply the concept to a broader range of reactions and to add the potential of directed-evolution methods with a more extensive structural variation of the biomolecular part for creating highly enantioselective hybrid catalysts.

Published online: December 22, 2005

[1] a) W. S. Knowles, *Angew. Chem.* **2002**, *114*, 2096 – 2107; *Angew. Chem. Int. Ed.* **2002**, *41*, 1998 – 2007; b) R. Noyori, *Angew. Chem.* **2002**, *114*, 2108 – 2123; *Angew. Chem. Int. Ed.* **2002**, *41*, 2008 – 2022; c) K. B. Sharpless, *Angew. Chem.* **2002**, *114*, 2126 – 2135; *Angew. Chem. Int. Ed.* **2002**, *41*, 2024 – 2032.

[2] H.-U. Blaser, *Chem. Commun.* **2003**, 293 – 296.

[3] D. H. Moffet, M. H. Hecht, *Chem. Rev.* **2001**, *101*, 3191 – 3203.

[4] a) M. T. Reetz, A. Zonta, K. Schimossek, K. Liebeton, K.-E. Jaeger, *Angew. Chem.* **1997**, *109*, 2961 – 2963; *Angew. Chem. Int. Ed. Engl.* **1997**, *36*, 2830 – 2832; b) M. T. Reetz, *Proc. Natl. Acad. Sci. USA* **2004**, *101*, 5716 – 5722; Extension of the methodology to the development of hybrid catalysts was proposed: M. T. Reetz, M. Rentzsch, A. Pletsch, M. Maywald, *Chimia* **2002**, *56*, 721 – 723.

[5] R. R. Breaker, *Chem. Rev.* **1997**, *97*, 371 – 390; A. Jenne, M. Famulok, *Top. Curr. Chem.* **1999**, *202*, 101 – 131.

[6] B. Seelig, S. Keiper, F. Stuhlmann, A. Jäschke, *Angew. Chem.* **2000**, *112*, 4764 – 4768; *Angew. Chem. Int. Ed.* **2000**, *39*, 4576 – 4579.

[7] P. Ordukhanian, G. F. Joyce, *J. Am. Chem. Soc.* **2002**, *124*, 12499 – 12506.

[8] D. Qi, C. M. Tann, D. Haring, M. D. Distefano, *Chem. Rev.* **2001**, *101*, 3081; C. M. Thomas, T. R. Ward, *Chem. Soc. Rev.* **2005**, *34*, 337 – 346; Directed evolution of hybrid catalysts has been suggested: M. T. Reetz, *Chimia* **2002**, *56*, 721 – 723.

[9] M. E. Wilson, G. M. Whitesides, *J. Am. Chem. Soc.* **1978**, *100*, 306 – 307.

[10] C. Letondor, N. Humbert, T. R. Ward, *Proc. Natl. Acad. Sci. USA* **2005**, *102*, 4683 – 4687.

[11] G. Roelfes, B. L. Feringa, *Angew. Chem.* **2005**, *117*, 3294 – 3296; *Angew. Chem. Int. Ed.* **2005**, *44*, 3230 – 3232.

[12] M. Skander, N. Humbert, J. Collot, J. Gradinaru, G. Klein, A. Loosli, J. Sauser, A. Zocchi, F. Gilardoni, T. R. Ward, *J. Am. Chem. Soc.* **2004**, *126*, 14411 – 14418; T. R. Ward, *Chem. Eur. J.* **2005**, *11*, 3798 – 3804; M. Skander, C. Malan, A. Ivanova, T. T. Ward, *Chem. Commun.* **2005**, *38*, 4815 – 4817.

[13] G. Klein, N. Humbert, J. Gradinaru, A. Ivanova, F. Gilardoni, U. E. Rusbandi, T. R. Ward, *Angew. Chem.* **2005**, *117*, 7942 – 7945; *Angew. Chem. Int. Ed.* **2005**, *44*, 7764 – 7767.

 © 2006 Wiley-VCH Verlag GmbH & Co. KGaA, Weinheim

Coordination Chemistry

DOI: 10.1002/anie.200503327

Terminal, Anionic Carbide, Nitride, and Phosphide Transition-Metal Complexes as Synthetic Entries to Low-Coordinate Phosphorus Derivatives**

*Christopher C. Cummins**

Keywords:
carbides · low-coordinate compounds · multiple bonds · nitrides · phosphide

Dedicated to Professor Richard R. Schrock

Anionic terminal one-atom nitride, phosphide, and carbide complexes are excellent starting materials for the synthesis of ligands containing low-coordinate phosphorus centers in the protecting coordination sphere of the metal complex. Salt-elimination reactions with chlorophosphanes lead to phosphaisocyanide, iminophosphinimide, and diorganophosphanylphosphinidene complexes in which the unusual phosphorus ligands are stabilized by coordination. X-ray structure analyses and density-functional calculations illuminate the bonding in these compounds.

1. Introduction

While the metal–ligand multiple-bond chemistry of single-atom ligands to date has featured most prominently the terminal oxo and nitrido functional groups,[1] recent developments have added terminal carbide[2–8] and phosphide[9–18] (alternatively carbido, phosphido) functional groups to the list of such available units. Terminal arsenic complexes were added to this list through the independent contributions of Schrock and Scheer.[9,14] The outer limit so far for triple bonds between trivalent Group 6 metal fragments and heavier Group 15 single atoms was reached recently with the report from Scheer et al. describing the remarkable tungsten–antimony complex $[(N_3N)W{\equiv}Sb]$, where $N_3N = N(CH_2CH_2NSiMe_3)_3$.[19]

Introduced herein is the idea that terminal, single-atom ligands constitute an attractive platform for the synthetic building up of interesting or unusual ligands within the protective coordination sphere of a metal complex. To demonstrate this idea we have focused to date on the construction of bound ligands containing low-coordinate phosphorus. The twin notions of multiple bonds involving phosphorus and low-coordination in phosphorus chemistry[20] find a pleasing and natural nexus in this research. Moreover, this research underscores the myriad advantages to be had in blending transition-metal chemistry with objectives in main-group element science.

The coverage herein is focused by using the further constraint that the terminal carbide, nitride, or phosphide complexes carry an overall single negative charge. This charge is typically balanced by a single alkali-metal counterion, either associated in an intimate ion pair or sequestered separately by a cryptand or by a pair of appropriate crown-ether macrocycles. Either way, this state of affairs permits simple salt-elimination to be employed in the bond-forming process that affixes a new moiety atop the metal–ligand multiple-bond platform.

2. Terminal Carbide Complexes: Methine Group Transfer and Phosphaisocyanide Complexes[5]

In the general area of all-carbon ligands,[2] and in the realm of the molybdenum alkylidyne complexes useful for alkyne metathesis,[21,22] the terminal carbide moiety holds a special position. Defined as having a one-coordinate carbon atom bonded solely to a transition-metal center, terminal carbide complexes were first discovered in a stepwise synthesis entailing deoxygenation of bound carbon monoxide.[3] The neutral carbonyl complex $[(OC)Mo(N\mathit{t}BuAr)_3]$ was accordingly reduced by one electron and pivaloylated to

[*] Prof. Dr. C. C. Cummins
Department of Chemistry
Massachusetts Institute of Technology
77 Massachusetts Avenue, Cambridge, MA 02139-4307 (USA)
Fax: (+1) 617-258-5700
E-mail: ccummins@mit.edu

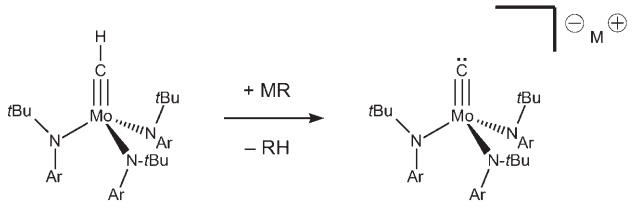
[**] This work was supported by the United States National Science Foundation (CHE-0316823).

InterScience

© 2006 Wiley-VCH Verlag GmbH & Co. KGaA, Weinheim

provide [*t*BuC(O)OCMo(N*t*BuAr)$_3$], which itself was subsequently converted in a reductive C–O bond cleavage process into the desired ionic terminal carbide complex [CMo(N*t*BuAr)$_3$]$^-$. This species was obtained as its potassium salt, either as an intimate ion-pair dimer or as discrete ions with sandwiching of the potassium counterion as [K(benzo-[15]crown-5)$_2$]$^+$.

As part of the procedure for purifying the [CMo(N*t*BuAr)$_3$]$^-$ salts, the anion was protonated to provide the methylidyne complex [HCMo(N*t*BuAr)$_3$] in high yield. After recrystallization of the methylidyne complex, deprotonation with benzylpotassium[23] led smoothly to the desired potassium salts in pure form (Scheme 1).

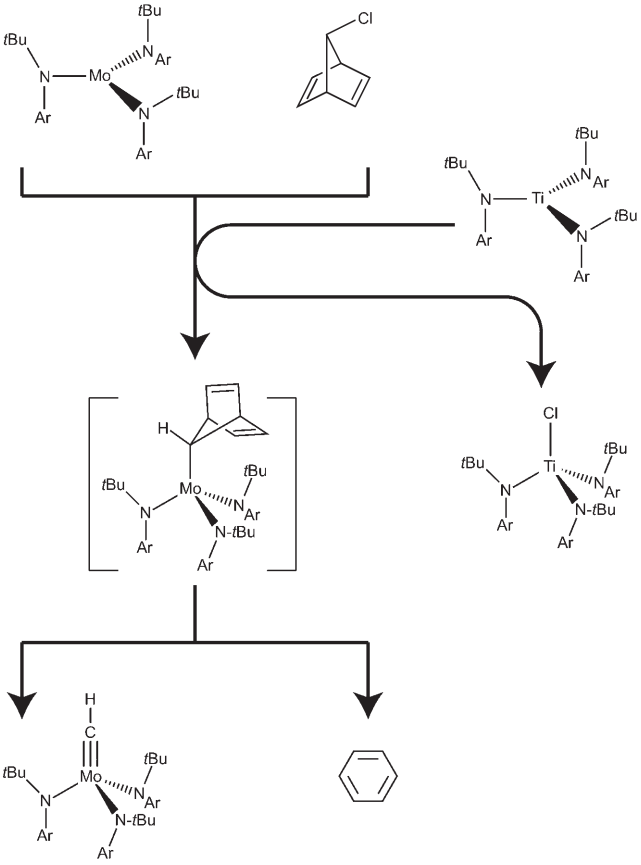


Scheme 1. Deprotonation of methylidine [HCMo(N*t*BuAr)$_3$] yields pure [CMo(N*t*BuAr)$_3$]$^-$, for example, MR = KCH$_2$Ph.

Relevant to the use of [Mo(N*t*BuAr)$_3$] and derived alkylidyne complexes as precursors to alkyne metathesis catalysts,[21,22] it should be noted that methylidyne [HCMo(N*t*BuAr)$_3$] has been generated and identified as one component of the mixture that results upon treatment of [Mo(N*t*BuAr)$_3$] with dichloromethane.[24]

Because the carbon atom of interest in the [CMo(N*t*BuAr)$_3$]$^-$ ion was derived from carbon monoxide, it was possible, without modifying the synthetic procedure, to obtain it in ^{13}C-labeled form. The NMR spectroscopic properties of terminal carbide complexes are of particular interest: $\delta =$ 501 ppm for the signal of the carbide carbon atom in [^{13}CMo(N*t*BuAr)$_3$]$^-$ as compared with $\delta = 282$ ppm for this anion's conjugate acid, the methylidyne complex [H^{13}CMo(N*t*BuAr)$_3$]. The origin of the extreme downfield ^{13}C NMR shift in carbide ion [^{13}CMo(N*t*BuAr)$_3$]$^-$ was investigated with a combination of solid-state ^{13}C NMR spectroscopic methods and density-functional theory (DFT) calculations, with the resulting understanding that there is an unusually large chemical shielding anisotropy (CSA = 806 ppm) associated with the metal–carbon multiple bond in this system.[4]

A one-pot synthesis has been developed for a high-yield conversion of [Mo(N*t*BuAr)$_3$] into its methylidyne counterpart (Scheme 2).[5] In this methine (CH) transfer reaction, 7-chloronorbornadiene[25–27] is used as the methine source, while the three-coordinate titanium(III) complex [Ti(N*t*BuAr)$_3$] is used as a specific chlorine-atom abstractor. It is well documented that [Ti(N*t*BuAr)$_3$] is potent for the one-electron reduction of metal oxo groups,[28,29] carbonyl groups,[30] metal–halogen bonds,[31] and carbon–halogen bonds.[30] For the latter two substrate types, and for chlorine in particular, formation of [ClTi(N*t*BuAr)$_3$] ensues, and this highly crystalline orange compound can frequently be isolated with comparative ease, and reduced by sodium amalgam back to [Ti(N*t*BuAr)$_3$]. In the new synthesis of the methylidyne [HCMo(N*t*BuAr)$_3$], 7-chloronorbornadiene is added to a solution of [Mo(N*t*BuAr)$_3$] with no reaction; subsequent addition of [Ti(N*t*BuAr)$_3$] effects chlorine-atom abstraction giving [ClTi(N*t*BuAr)$_3$] along with (presumably) the 7-norbornadienyl radical. Facile and selective trapping of the latter 7-norbornadienyl radical, and subsequent cleavage of benzene from a putative molybdenum(IV) 7-norbornadienyl intermediate, accounts for the observed smooth CH-transfer reaction. Note that the success of this unusual one-pot CH transfer reaction relies on the



Scheme 2. Synthesis of the methylidyne complex [HCMo(N*t*BuAr)$_3$] as a starting point for the construction of phosphaisocyanide complexes.



Christopher C. Cummins ("Kit") carried out inorganic and organometallic synthesis graduate studies under the direction of Prof. Richard R. Schrock at the Massachusetts Institute of Technology (MIT), from which he obtained his doctorate in 1993. Also in 1993 he joined the chemistry faculty at MIT as an Assistant Professor, and in 1996 he was promoted to his current rank of Professor. His awards include the ACS Pure Chemistry Award, the NSF Alan T. Waterman award, and an Alexander von Humboldt research award. Among his research interests are inorganic syntheses, small-molecule activation, and the stabilization of unusual ligands.

© 2006 Wiley-VCH Verlag GmbH & Co. KGaA, Weinheim

orthogonal specificities of the molybdenum versus the titanium three-coordinate complexes. While molybdenum prefers to form bonds to carbon and thus serves as a facile organic radical trap, titanium instead pursues reactivity modes that result in bonds to electronegative halogen or oxygen atoms. It may well be the case that enhanced Lewis acidity of the d^1 Ti complex with its two low-lying empty d orbitals, in contrast with the high-spin d^3 Mo system, accounts for the relative facility with which $[Ti(NtBuAr)_3]$ attacks reducible substrates that have lone pairs of electrons (e.g. on R–Cl or $R_2C{=}O$) for coordination.

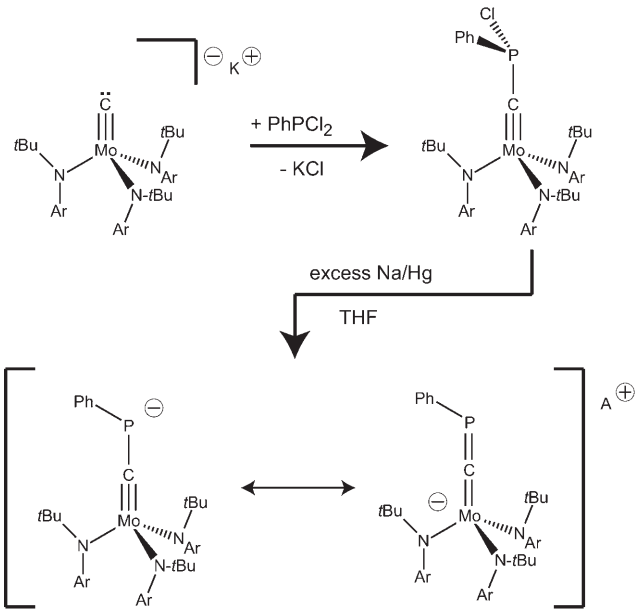
While terminal carbide $[CMo(NtBuAr)_3]^-$ is an anionic system, with nucleophilic properties that are enhanced accordingly by the presence of the negative charge, the synthesis and characterization of terminal ruthenium carbide complexes that are charge neutral is a recent development of great significance.[7] The chemistry used to prepare such complexes is again related to the metathesis reactivity of metal–carbon double and triple bonds. In particular, Grubbs' ruthenium benzylidene catalysts were found to react with *trans*-2,3-dicarbomethoxymethylenecyclopropane to provide $[CRuCl_2\{P(C_6H_{11})_3\}_2]$ in 54% yield as air-stable yellow crystals.[7] The ^{13}C NMR spectroscopy shift for the carbide carbon atom in this system was observed at $\delta = 471.5$ ppm, reminiscent of the large downfield shifts observed both for $[^{13}CMo(NtBuAr)_3]^-$, as discussed above, and for the anionic tungsten terminal carbide complex $Li[CWTp'(CO)_2]$ (Tp′ = hydridotris(3,5-dimethylpyrazolyl)borate) which is generated and observed in situ ($\delta = 556$ ppm).[6]

One of the most exciting prospects for terminal carbide complexes is their employment in the rational construction of new carbon-containing ligands or carbide complexes. The neutral ruthenium carbide system has some promise as a σ-donor ligand, as it has been shown to coordinate to $\{Mo(CO)_5\}$, and to $\{PdCl_2(SMe_2)\}$ fragments.[8]

Electrophiles $SiMe_3Cl$, PhC(O)Br, I_2, RC(=O)Ph (R = H, Ph), and CH_3I all were shown to furnish functionalized carbynes upon reaction with the anionic tungsten terminal carbide complex $Li[CWTp'(CO)_2]$.[6] The formation of WC–X (X = Si, C, I) bonds in this fashion reveals the carbide intermediate to be versatile in the construction of a variety of carbynes in a process that erects the coordinated carbyne ligand atop the already present WC multiple bond functionality.

The terminal carbide ion $[CMo(NtBuAr)_3]^-$ likewise has a substantial chemistry stemming from its reactivity towards electrophiles. Perhaps most interesting has been its intermediacy in the construction of the coordinated phosphaisocyanide ligand PhPC in the anionic complex $[(PhPC)Mo(NtBuAr)_3]^-$ (Scheme 3), structurally characterized as its ion-pair salt dimer with $[Na(Et_2O)(thf)]^+$ (Figure 1).[5]

Phosphaisocyanide is a term synonymous with "isophosphaalkyne", and it should be pointed out that this molecular class of general formula R-PC is one that has been the subject of an as-yet-unfulfilled quest.[32] While $[(PhPC)Mo(NtBuAr)_3]^-$ can be construed as the first example of a terminal phosphaisocyanide complex, its very short molybdenum–carbon interatomic distance of only 1.759(7) Å suggests that this complex can also be described as a substituted



Scheme 3. Synthesis of a phosphaisocyanide complex from carbide anion $[CMo(NtBuAr)_3]^-$. A = counterion.

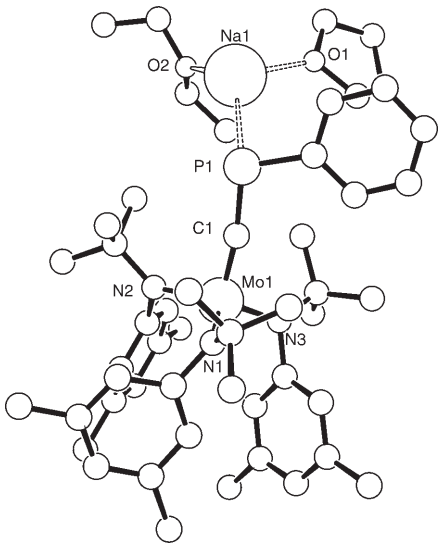


Figure 1. Crystal structure of $[Na(Et_2O)(thf)]^+[(PhPC)Mo(NtBuAr)_3]^-$. One-half of the centrosymmetric, dimeric structure is depicted.

alkylidyne complex. The question may be summarized as follows: to what extent are the resonance forms $[Mo{\equiv}C\text{-}P\text{-}Ph]^- \leftrightarrow [Mo\text{-}C{\equiv}P\text{-}Ph]^-$ appropriate descriptors of the bonding in this anionic system? To put this in perspective, the neutral paramagnetic ($S = 1/2$) carbonyl complex $[(OC)Mo(NtBuAr)_3]$ has a low CO stretching frequency of 1840 cm^{-1},[3] but on reduction to $Na^+[(OC)Mo(NtBuAr)_3]^-$ the observed ν_{CO} drops even further to the very low value of 1617 cm^{-1}.[33] Clearly, the ability of the anionic, formally molybdenum(II) fragment $[Mo(NtBuAr)_3]^-$ to backbond is substantially enhanced relative to neutral $[Mo(NtBuAr)_3]$. While the neutral carbonyl complex $[(OC)Mo(NtBuAr)_3]$ has

© 2006 Wiley-VCH Verlag GmbH & Co. KGaA, Weinheim

not been structurally characterized, the related isocyanide complex [(*t*BuNC)Mo(N*t*BuAr)$_3$] has been so studied,[34] and found to have a Mo–C distance of 1.936(6) Å together with a C–N distance of 1.184(8) Å.

The above suggests that if a neutral complex of formula [(RPC)Mo(N*t*BuAr)$_3$] can be obtained, it will have considerably greater phosphaisocyanide character, and less alkylidyne character, than the [(PhPC)Mo(N*t*BuAr)$_3$]$^-$ anion.[5]

3. Phosphorus-Substituted Organic Azide Complexes: Iminophosphinimides

The number of instances in which an organic azide (RN_3) complexed terminally to a transition metal has been observed or isolated is small to date. Structurally characterized examples include [$Cp_2TaMe(N_3Ph)$] ($Cp = C_5H_5$),[35] [$Cp_2TaMe(N_3$-4-$NMe_2C_6H_4)$],[36] [$(MesN_3)V(I)(NRAr^F)_2$],[37] where $R = C(CD_3)_2CH_3$ and $Ar^F = 2,5$-$FMeC_6H_3$, [{(μ-calix[4]-$(O)_4$)$W(N_3Ph)$}$_2$].[38] The V and W complexes contain d^2 early-transition-metal fragments. In the case of the tantalum system, it was pointed out that such complexes can be considered as intermediates en route to organoimido complexes,[39] a favorable transformation benefiting from the loss of the stable dinitrogen molecule.[40] Accordingly, the structurally characterized vanadium and tantalum systems both were observed to transform into the corresponding imido complexes under mild conditions. The tungsten phenylazide complex was obtained by using [(μ-calix[4]-$(O)_4$)$W(\eta^2$-$C_6H_{10})$] as a synthon for the d^2 fragment, cyclohexene being lost in the reaction. Also known is an example of a structurally characterized terminal organoazide complex of a d^{10} metal fragment. In particular, [{HB[3,5-$(CF_3)_2Pz]_3$}Cu(N_3-1-Ad)] was characterized and found to exhibit little perturbation in the bond lengths of the complexed relative to the free 1-adamantylazide ligand.[41] This situation is in contrast to that for organoazide binding to the d^2 metal fragments, in which the M–N bond is an imido-like multiple bond, the M-N-N group is near linear, and the MN–N bond is substantially elongated. Effectively, terminal complexation of an organic azide by an early-transition-metal d^2 fragment proceeds with two-electron reduction of the organic azide to a [N-N=N-R]$^{2-}$ "diazenidimido" form.

Substitution of the central nitrogen atom in an organic azide for phosphorus, together with coordination to a d^2 metal fragment, may be expected to afford an analogous [N-P=N-R]$^{2-}$ "iminophosphinimido" entity. No such complexes, with consecutive two-coordination at N, P, and N, are currently to be found in a search of the Cambridge structural database. Such complexes are an attractive target as there is the possibility to observe their transformation to organoimido complexes with loss of the intriguing PN molecule.[42]

The anionic niobium nitride complex [NNb(N*t*BuAr)$_3$]$^-$ (Scheme 4), obtained as its sodium salt by reductive decarbonylation of neutral niobium(IV) isocyanate [(OCN)Nb(N*t*BuAr)$_3$],[43] was deemed a potential starting point for the synthesis of an iminophosphinimide complex. It should be noted that anionic niobium(V) nitride complexes have also been obtained by dinitrogen cleavage reactions.[44–47]

Treatment of dimeric Na$^+$[NNb(N*t*BuAr)$_3$]$^-$ with PCl_3 established the first P–N linkage in the new construct, providing dichlorophosphinimido [(Cl_2PN)Nb(N*t*BuAr)$_3$] in 86% yield as a pale yellow solid (^{31}P NMR, $\delta = 158$ ppm).[48] This was converted in two steps and good overall yield into the desired iminophosphinimide precursor, [{(*t*BuHN)(Cl)P}NNb(N*t*BuAr)$_3$] which was to be subjected to dehydrohalogenation in the ultimate synthetic step. Dehydrohalogenation was effected by treatment with Li[$N(SiMe_3)_2$], producing the desired *tert*-butyliminophosphinimide complex [(*t*BuN=PN)Nb(N*t*BuAr)$_3$] isolated in 66% yield as bright yellow microcrystals. An indication of the presence of two-coordinate phosphorus in the *tert*-butyliminophosphinimide complex was the observed triplet at $\delta =$ 318 ppm ($^1J_{^{14}N,^{31}P} = 61$ Hz) in the ^{31}P NMR spectrum.

Unfortunately, crystals of [(*t*BuN=PN)Nb(N*t*BuAr)$_3$] suitable for an X-ray diffraction study were not obtained. In fact, the prospect for obtaining X-ray structural data on the *tert*-butyliminophosphinimide complex was complicated owing to its ready conversion into an orange dimer (^{31}P NMR, $\delta =$ 240 ppm) over 24 h at 23 °C. This dimer was shown by single-crystal X-ray crystallography (Figure 2) to be the product of [2+2] head-to-tail cycloaddition of the P=N double bond component. The dimer exhibits crystallographic inversion symmetry, a planar P_2N_2 ring, and pyramidal phosphorus atoms.

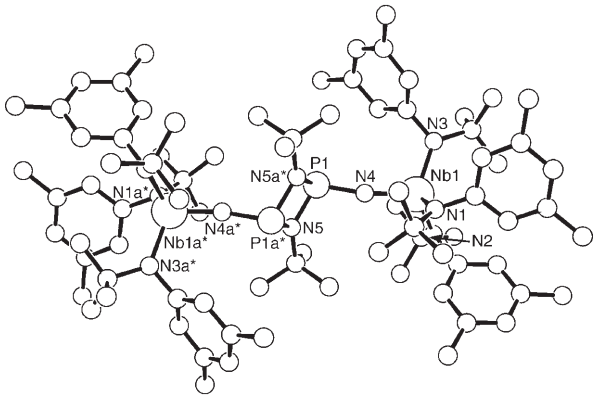
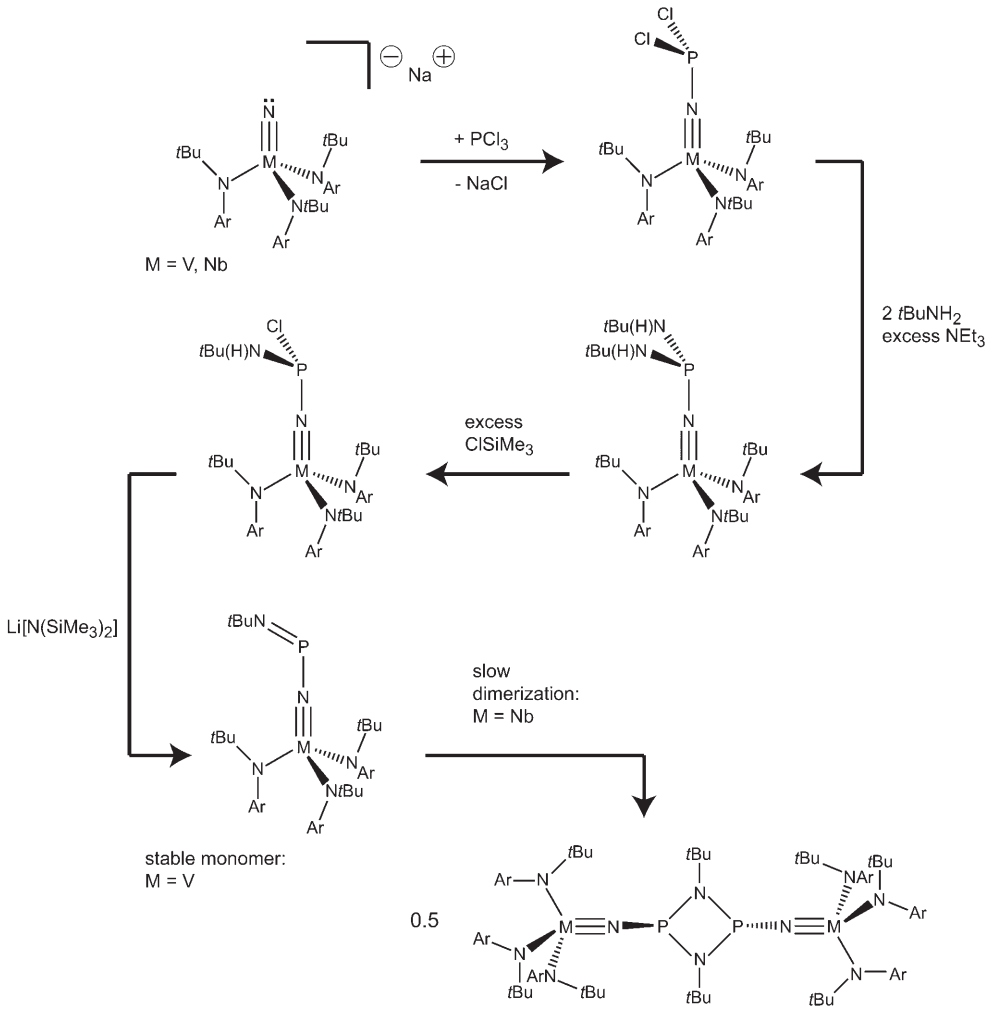


Figure 2. Crystal structure of the [(*t*BuN=PN)Nb(N*t*BuAr)$_3$] dimer.

A precedent for the aforementioned [2+2] head-to-tail dimerization is $(Me_3Si)_2$N-P=N$SiMe_3$ which dimerizes slowly at 25 °C, with crystals of the dimer depositing from the neat liquid monomer, note that the closely related system $(Me_3Si)_2$N-P=N*t*Bu is immune to dimerization.[49] The extensive chemistry of iminophosphanes has been reviewed.[50] Both $(Me_3Si)_2$N-P=NR systems have ^{31}P NMR spectroscopy chemical shifts ($\delta = 330$ ppm, R = *t*Bu;[51] 325 ppm, R = $SiMe_3$[52]) similar to that observed for the monomeric iminophosphinimide complex [(*t*BuN=PN)Nb(N*t*BuAr)$_3$]. The lack of dimerization of $(Me_3Si)_2$N-P=N*t*Bu has been attributed to the enhanced steric protection afforded by the *t*Bu substituent, relative to $SiMe_3$.[49] It was speculated accordingly that a vanadium iminophosphinimide complex,

© 2006 Wiley-VCH Verlag GmbH & Co. KGaA, Weinheim



Scheme 4. Niobium(v) and vanadium(v) iminophosphinimide complexes have different dimerization behavior.

analogous to that described above for niobium, might offer greater steric protection to the P=N functional group. The rationale in this case being, that the closer contact between smaller vanadium and the *t*BuN=PN terminus ought to pull the *t*BuN=PN ligand deeper into the protection of the trigonal pocket afforded by the {M(N*t*BuAr)$_3$} platform. Imido V–N bond lengths are typically 0.10–0.15 Å shorter than the corresponding imido Nb–N bond lengths for four-coordinate complexes of the type considered here.

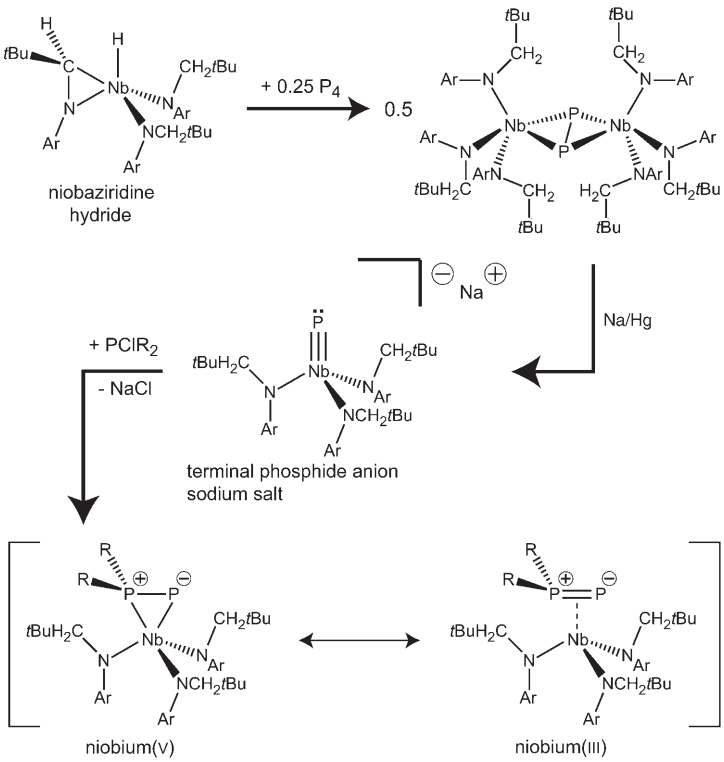
The synthesis of [(*t*BuN=PN)V(N*t*BuAr)$_3$] was carried out using the same method as in the niobium case.[48] This vanadium iminophosphinimide complex was obtained as red crystals, and had a ^{31}P NMR spectroscopy signal ($\delta =$ 341 ppm) consistent with its formulation as a monomer. In addition, DFT calculations on a model vanadium iminophosphinimide predicted a very similar value for the ^{31}P NMR chemical shift to that observed experimentally.[48] While a crystal structure determination on [(*t*BuN=PN)V(N*t*BuAr)$_3$] proved problematic owing to *tert*-butyl group disorder, the fact that this system was stable to mild heating (60 °C, hexane, 18 h) indicates that complexes of this type should be amenable to further study.

4. Diorganophosphanylphosphinidenes: Phosphinidenes with a PR$_2$ Substituent

Phosphinidene complexes, especially those of the terminal variety, were long sought by synthetic chemists prior to the first reports of their successful isolation.[53,54] Representative substituents on terminal phosphinidene ligands include Mes* (2,4,6-*t*Bu$_3$C$_6$H$_2$),[55–59] 2,6-dimesitylphenyl (dmp),[60] cyclohexyl,[61] phenyl,[62] and trimethylsilyl.[63] An intriguing possibility was that the availability of a terminal phosphide anion, for example, [PNb(NNpAr)$_3$]$^-$ where Np = neopentyl, would permit the synthesis of phosphinidenes with more exotic substituents through substitution reactions. That a terminal phosphide anion of a Group 5 metal was likely to be attainable was suggested by known phosphinidene substituent-exchange reactions that were based on Ph–P bond cleavage with Li^0 in THF.[63]

The niobaziridine hydride complex [HNb(η^2-*t*BuHC=NAr)(NNpAr)$_2$] (Scheme 5) was developed as a synthon for the three-coordinate[64] {Nb(NNpAr)$_3$} fragment.[65] Accordingly, reaction of the niobaziridine hydride complex with elemental phosphorus (as P$_4$, white phosphorus) provided

 © 2006 Wiley-VCH Verlag GmbH & Co. KGaA, Weinheim



Scheme 5. P–P bond cleavage and formation at the {Nb(NNpAr)$_3$} fragment.

quantitatively the dark green bridging-P_2 complex [(μ_2:η^2,η^2-P_2){Nb(NNpAr)$_3$}$_2$].[65] Structural characterization of the diniobium μ_2:η^2,η^2-P_2 complex revealed a butterfly disposition of the core atoms with a Nb-P-P-Nb dihedral angle of 135.61(5)°. Some degree of multiple P–P bonding in this complex is indicated by the relatively short P–P interatomic distance of 2.160 Å; the P–P single-bond length in P_4 is 2.21 Å.[66] A related reaction of a metal complex with P_4 to produce a μ_2:η^2,η^2-P_2 complex is that which leads to [(μ_2:η^2,η^2-P_2){CpCr(CO)$_2$}$_2$],[67] while a reaction producing [(μ_2:η^2,η^2-P_2){Cp*Re(CO)$_2$}$_2$] (Cp* = C_5Me_5) is even more closely related owing to the lack of metal–metal bonding in this P_2-bridged system.[68]

A key finding is that the P_2 complex [(μ_2:η^2,η^2-P_2)-{Nb(NNpAr)$_3$}$_2$] could be cleaved reductively by sodium amalgam in THF to provide the desired terminal phosphide ion [PNb(NNpAr)$_3$]$^-$, as its [Na(OEt$_2$)]$^+$ salt, in 65 % yield as yellow-orange blocks.[17] We note that the aforementioned μ-P_2 complex is analogous to the known d^2–d^2 diniobium dinitrogen complex [(μ:η^1,η^1-N_2){Nb(NCy$_2$)$_3$}$_2$],[69] in which the dinitrogen ligand bridges the two niobium atoms in the typical linear, end-on fashion. The related d^3–d^3 dimolybdenum dinitrogen complex [(μ:η^1,η^1-N_2){Mo(N*t*BuAr)$_3$}$_2$] undergoes facile N–N bond homolysis with formation of two equivalents of the terminal nitridomolybdenum(VI) complex, [NMo(N*t*BuAr)$_3$].[70] Reductive cleavage of the P_2 complex [(μ_2:η^2,η^2-P_2){Nb(NNpAr)$_3$}$_2$] upon addition of two electrons can be understood in terms of converting a formal d^2–d^2 system into the d^3–d^3 state required to effect the complete six-electron reductive scission of the diphosphorus molecule. A further analogy can be made as follows: the heterodinuclear μ-dinitrogen complex [{(Ar*i*PrN)$_3$Nb}(μ-N_2){Mo(N*t*BuAr)$_3$}], a formal d^2–d^3 system, undergoes reductive cleavage upon treatment with KC_8[71] in THF to provide a 1:1 mixture of neutral [NMo(N*t*BuAr)$_3$] and ionic [NNb(N*i*PrAr)$_3$]$^-$ (potassium salt) nitrido complexes.[44] These complexes are separable and isolable in pure form owing to their different states of charge.

Terminal phosphide ion [PNb(NNpAr)$_3$]$^-$ was structurally characterized as its [Na([12]crown-4)$_2$]$^+$ salt, such that one-coordination at phosphorus was not augmented by any close contacts to the alkali-metal counterion.[17] Of particular interest is the very short Nb–P bond of 2.186(2) Å, the shortest contact on record between these two elements. This situation is in keeping with the formulation of [PNb(NNpAr)$_3$]$^-$ as having a niobium–phosphorus triple bond; note that the sum of proposed Nb and P triple-bond covalent radii is 2.10 Å.[72] Also supporting this formulation is the large downfield chemical shift observed for [PNb(NNpAr)$_3$]$^-$ ($\delta = 1020$ ppm) in the ^{31}P NMR spectrum in THF solution, such a shift being characteristic of the terminal phosphide functional group.[13] The electronic origin of the large downfield chemical shifts in the ^{13}C, ^{15}N, and ^{31}P NMR spectra of terminal carbide,[4] nitride,[73] and phosphide[13] complexes, respectively, is in the mixing of a high-lying filled σ-symmetry molecular orbital (A_1 in the C_{3v} point group) with a low-lying virtual π^* molecular orbital (E in C_{3v} point symmetry, doubly degenerate) in the presence of the applied magnetic field.[13] Solid-state NMR spectroscopy investigations of such axially symmetric systems are particularly advantageous, because the $\delta_{11} = \delta_{22}$ principal components of the shielding tensor can be studied independently of the δ_{33} term,[4,13,73] which is desirable because the δ_{33} term contains no information pertaining to the aforementioned orbital interaction.

A DFT-derived representation of niobium–phosphorus triple bonding is provided for the model ion [PNb(NH$_2$)$_3$]$^-$ (Figure 3). Indicated with an arrow in Figure 3 is the midpoint of the niobium–phosphorus triple bond. The accumulation of electron density midway between the Nb and P nuclei is an indication of substantial covalent character to the NbP triple bond.

1,1-Diorganophosphanylphosphinidenes (PPR$_2$), when considered as free ligands, are isomers of diphosphenes RP=PR. The parent system PPH$_2$ along with isomer HP=PH has been the focus of several theoretical studies.[74–77] The *tert*-butyl substituted variant, *t*Bu$_2$PP, is known in complexes to electronically mimic olefins and in trapping experiments to have singlet phosphinidene character.[78] Singlet phosphinidenes are being sought, and the phosphino substituent has been proposed as one of the most viable for their stabilization.[79] Recently the terminally bonded phosphinophosphinidene complex [(η^1-PP*t*Bu$_2$){Cp$_2$Zr(PPhMe$_2$)}] was reported as the product of reaction between zirconocene dichloride and the reagent *t*Bu$_2$P-P(SiMe$_3$)Li in the presence of excess

 © 2006 Wiley-VCH Verlag GmbH & Co. KGaA, Weinheim

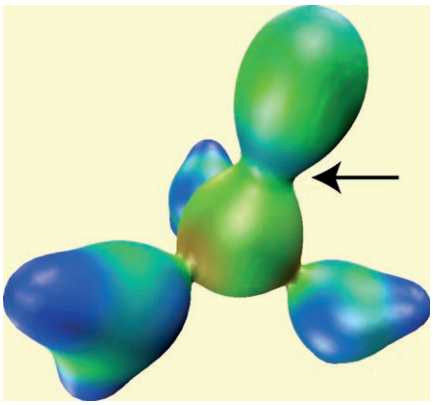


Figure 3. Calculated electron-density isosurface for the $[PNb(NH_2)_3]^-$ ion shows the Nb–P triple bond (arrow). Colors reflect the values of the electron localization function (ELF): Blue corresponds to high ELF, red to low ELF.

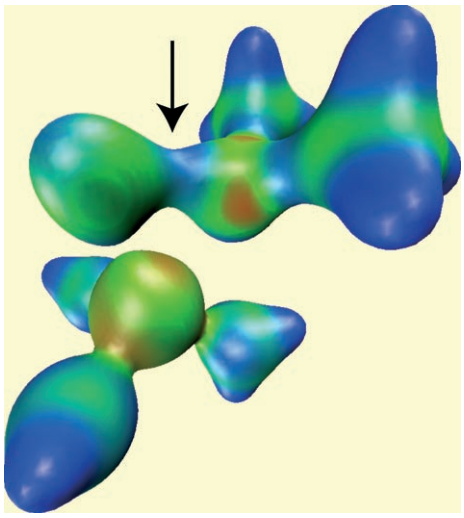


Figure 4. Calculated electron-density isosurface for the $[(\eta^1\text{-}PPMe_2)Nb(NH_2)_3]$ model system: The P–P bond (arrow) and the lone pair on the two-coordinate phosphorus (top left) are both blue, and thus are distinguished clearly from the four-coordinate phosphorus which is partly red (low ELF value; colors as for Figure 3).

$PPhMe_2$.[80] The reagent $tBu_2P\text{-}P(SiMe_3)Li$ joins the $tBu_2P\text{-}P{=}P(X)tBu_2$ (X = Br or Me) family as agents effective for the delivery of the $PPtBu_2$ unit to metal centers, in what has been termed "phosphinophosphinidene transfer".[81–83]

While earlier reported syntheses proceed by the delivery of an intact $\{P\text{-}PR_2\}$ fragment to a metal center, our method provides an alternative in that the P–P bond of the complexed diorganophosphanylphosphinidene ligand is formed by the reaction of the terminal phosphide ion $[PNb(NNpAr)_3]^-$ with the desired chlorodiorganophosphane, $ClPR_2$.[17] The reaction takes place with salt elimination as shown in the final step of Scheme 5. An exciting prospect for future extension of this chemistry is the use of small or functional substituents R on the $ClPR_2$ reagent. As shown in Scheme 5, this new method for the construction of complexed 1,1-diorganophosphanylphosphinidene units atop the terminal phosphide moiety provides an example of the previously unknown $\eta^2\text{-}PPPh_2$ ligand. That the PPR_2 ligands bind in an η^2 fashion to the formally d^2 $\{Nb(NNpAr)_3\}$ fragment is interesting, and contrasts with the observed η^1-binding of the valence-isoelectronic NPR_2 ligand to the more crowded $\{Nb(NtBuAr)_3\}$ fragment.[43]

Figure 4 shows an electron-density isosurface for the model system $[(\eta^1\text{-}PPMe_2)Nb(NH_2)_3]$; the isosurface is colored according to the corresponding electron localization function (ELF) value.[84,85] Note that the electron density is low near the midpoint of bond paths that connect ligand atoms to the electropositive niobium center. Indicated with an arrow is the midpoint of the P–P bond in the molecule; note that in relation to the terminal phosphide anion (compare electron-density isosurface in Figure 3) P–P multiple bond character has been obtained at the expense of Nb–P multiple bonding. Consideration of the ELF has been exceptionally enlightening with regard to bonding patterns in main-group systems,[86] and is equally informative in the present case of the complexed $PPMe_2$ model ligand. Multiple bonds between heavier main-group elements is an area of current intense interest to experimentalists and theoreticians alike,[87,88] and it is an area to which the methods proposed herein may contribute generously.

5. Summary

The above vignettes have illustrated how elusive ligands may be synthesized by elaboration of anionic, terminal, single-atom metal–ligand multiply bonded substituents. In the described processes, the terminal multiply bonded single-atom substituent becomes incorporated as the terminus of a new complexed entity. The limits are boundless for the application of this idea to the creation of new thought-provoking ligands and bound molecules.

Received: September 19, 2005
Published online: December 30, 2005

[1] W. A. Nugent, J. M. Mayer, *Metal–Ligand Multiple Bonds: The Chemistry of Transition Metal Complexes Containing Oxo, Nitrido, Imido, Alkylidene, or Alkylidyne Ligands*, Wiley, New York, **1988**.
[2] M. I. Bruce, P. J. Low in *Advances in Organometallic Chemistry, Vol. 50*, **2004**, p. 179.
[3] J. C. Peters, A. L. Odom, C. C. Cummins, *Chem. Commun.* **1997**, 1995.
[4] J. B. Greco, J. C. Peters, T. A. Baker, W. M. Davis, C. C. Cummins, G. Wu, *J. Am. Chem. Soc.* **2001**, *123*, 5003.
[5] T. Agapie, P. L. Diaconescu, C. C. Cummins, *J. Am. Chem. Soc.* **2002**, *124*, 2412.
[6] A. E. Enriquez, P. S. White, J. L. Templeton, *J. Am. Chem. Soc.* **2001**, *123*, 4992.
[7] R. G. Carlson, M. A. Gile, J. A. Heppert, M. H. Mason, D. R. Powell, D. Vander Velde, J. M. Vilain, *J. Am. Chem. Soc.* **2002**, *124*, 1580.
[8] A. Hejl, T. M. Trnka, M. W. Day, R. H. Grubbs, *Chem. Commun.* **2002**, 2524.
[9] M. Scheer, J. Müller, M. Haser, *Angew. Chem.* **1996**, *108*, 2637; *Angew. Chem. Int. Ed. Engl.* **1996**, *35*, 2492.
[10] B. P. Johnson, G. Balazs, M. Scheer in *New Aspects In Phosphorus Chemistry IV, Vol. 232*, **2004**, p. 1.

© 2006 Wiley-VCH Verlag GmbH & Co. KGaA, Weinheim

[11] C. E. Laplaza, W. M. Davis, C. C. Cummins, *Angew. Chem.* **1995**, *107*, 2181; *Angew. Chem. Int. Ed. Engl.* **1995**, *34*, 2042.
[12] N. C. Zanetti, R. R. Schrock, W. M. Davis, *Angew. Chem.* **1995**, *107*, 2184; *Angew. Chem. Int. Ed. Engl.* **1995**, *34*, 2044.
[13] G. Wu, D. Rovnyak, M. J. A. Johnson, N. C. Zanetti, D. G. Musaev, K. Morokuma, R. R. Schrock, R. G. Griffin, C. C. Cummins, *J. Am. Chem. Soc.* **1996**, *118*, 10654.
[14] N. C. Mösch-Zanetti, R. R. Schrock, W. M. Davis, K. Wanninger, S. W. Seidel, M. B. Odonoghue, *J. Am. Chem. Soc.* **1997**, *119*, 11037.
[15] F. H. Stephens, J. S. Figueroa, P. L. Diaconescu, C. C. Cummins, *J. Am. Chem. Soc.* **2003**, *125*, 9264.
[16] M. J. A. Johnson, P. M. Lee, A. L. Odom, W. M. Davis, C. C. Cummins, *Angew. Chem.* **1997**, *109*, 110; *Angew. Chem. Int. Ed. Engl.* **1997**, *36*, 87.
[17] J. S. Figueroa, C. C. Cummins, *Angew. Chem.* **2004**, *116*, 1002; *Angew. Chem. Int. Ed.* **2004**, *43*, 984.
[18] J. S. Figueroa, C. C. Cummins, *J. Am. Chem. Soc.* **2004**, *126*, 13916.
[19] G. Balazs, M. Sierka, M. Scheer, *Angew. Chem.* **2005**, *44*, 4999; *Angew. Chem. Int. Ed.* **2005**, *44*, 4920.
[20] M. Regitz, O. J. Scherer, *Multiple Bonds and Low Coordination in Phosphorus Chemistry*, Thieme, Stuttgart, **1990**.
[21] W. Zhang, S. Kraft, J. S. Moore, *Chem. Commun.* **2003**, 832.
[22] W. Zhang, S. Kraft, J. S. Moore, *J. Am. Chem. Soc.* **2004**, *126*, 329.
[23] D. Hoffmann, W. Bauer, F. Hampel, N. Hommes, P. von R. Schleyer, P. Otto, U. Pieper, D. Stalke, D. S. Wright, R. Snaith, *J. Am. Chem. Soc.* **1994**, *116*, 528.
[24] A. Fürstner, C. Mathes, C. W. Lehmann, *J. Am. Chem. Soc.* **1999**, *121*, 9453.
[25] S. C. Clarke, B. L. Johnson, *Tetrahedron* **1968**, *24*, 5067.
[26] P. R. Story, *J. Org. Chem.* **1961**, *26*, 287.
[27] P. R. Story, S. R. Fahrenholtz, *Org. Synth.* **1964**, *44*, 12.
[28] P. W. Wanandi, W. M. Davis, C. C. Cummins, M. A. Russell, D. E. Wilcox, *J. Am. Chem. Soc.* **1995**, *117*, 2110.
[29] J. C. Peters, A. R. Johnson, A. L. Odom, P. W. Wanandi, W. M. Davis, C. C. Cummins, *J. Am. Chem. Soc.* **1996**, *118*, 10175.
[30] T. Agapie, P. L. Diaconescu, D. J. Mindiola, C. C. Cummins, *Organometallics* **2002**, *21*, 1329.
[31] E. Kim, A. L. Odom, C. C. Cummins, *Inorg. Chim. Acta* **1998**, *278*, 103.
[32] L. Weber, *Eur. J. Inorg. Chem.* **2003**, 1843.
[33] J. C. Peters, PhD Thesis, Massachusetts Institute of Technology, **1998**.
[34] F. H. Stephens, J. S. Figueroa, C. C. Cummins, O. P. Kryatova, S. V. Kryatov, E. V. Rybak-Akimova, J. E. McDonough, C. D. Hoff, *Organometallics* **2004**, *23*, 3126.
[35] G. Proulx, R. G. Bergman, *J. Am. Chem. Soc.* **1995**, *117*, 6382.
[36] G. Proulx, R. G. Bergman, *Organometallics* **1996**, *15*, 684.
[37] M. G. Fickes, W. M. Davis, C. C. Cummins, *J. Am. Chem. Soc.* **1995**, *117*, 6384.
[38] G. Guillemot, E. Solari, C. Floriani, C. Rizzoli, *Organometallics* **2001**, *20*, 607.
[39] D. E. Wigley, *Prog. Inorg. Chem.* **1994**, *42*, 239.
[40] T. A. Hanna, A. M. Baranger, R. G. Bergman, *Angew. Chem.* **1996**, *108*, 693; *Angew. Chem. Int. Ed. Engl.* **1996**, *35*, 653.
[41] H. V. R. Dias, S. A. Polach, S. K. Goh, E. F. Archibong, D. S. Marynick, *Inorg. Chem.* **2000**, *39*, 3894.
[42] H. S. Plitt, H. Schnöckel, M. Bar, R. Ahlrichs, *Z. Anorg. Allg. Chem.* **1992**, *607*, 45.
[43] M. G. Fickes, A. L. Odom, C. C. Cummins, *Chem. Commun.* **1997**, 1993.
[44] D. J. Mindiola, K. Meyer, J. P. F. Cherry, T. A. Baker, C. C. Cummins, *Organometallics* **2000**, *19*, 1622.
[45] H. Kawaguchi, T. Matsuo, *Angew. Chem.* **2002**, *114*, 2916; *Angew. Chem. Int. Ed.* **2002**, *41*, 2792.
[46] A. Zanotti-Gerosa, E. Solari, L. Giannini, C. Floriani, A. Chiesi-Villa, C. Rizzoli, *J. Am. Chem. Soc.* **1998**, *120*, 437.
[47] A. Caselli, E. Solari, R. Scopelliti, C. Floriani, N. Re, C. Rizzoli, A. Chiesi-Villa, *J. Am. Chem. Soc.* **2000**, *122*, 3652.
[48] J. K. Brask, M. G. Fickes, P. Sangtrirutnugul, V. Dura-Vila, A. L. Odom, C. C. Cummins, *Chem. Commun.* **2001**, 1676.
[49] E. Niecke, W. Flick, S. Pohl, *Angew. Chem.* **1976**, *88*, 305; *Angew. Chem. Int. Ed. Engl.* **1976**, *15*, 309.
[50] E. Niecke, D. Gudat, *Angew. Chem.* **1991**, *103*, 251; *Angew. Chem. Int. Ed. Engl.* **1991**, *30*, 217.
[51] O. J. Scherer, N. Kuhn, *J. Organomet. Chem.* **1974**, *82*, C3.
[52] E. Niecke, W. Flick, *Angew. Chem.* **1973**, *85*, 586; *Angew. Chem. Int. Ed. Engl.* **1973**, *12*, 585.
[53] A. H. Cowley, A. R. Barron, *Acc. Chem. Res.* **1988**, *21*, 81.
[54] A. H. Cowley, *Acc. Chem. Res.* **1997**, *30*, 445.
[55] A. H. Cowley, B. Pellerin, J. L. Atwood, S. G. Bott, *J. Am. Chem. Soc.* **1990**, *112*, 6734.
[56] D. S. J. Arney, R. C. Schnabel, B. C. Scott, C. J. Burns, *J. Am. Chem. Soc.* **1996**, *118*, 6780.
[57] F. Basuli, B. C. Bailey, J. C. Huffman, M. H. Baik, D. J. Mindiola, *J. Am. Chem. Soc.* **2004**, *126*, 1924.
[58] F. Basuli, L. A. Watson, J. C. H. Man, D. J. Mindiola, *Dalton Trans.* **2003**, 4228.
[59] F. Basuli, J. Tomaszewski, J. C. Huffman, D. J. Mindiola, *J. Am. Chem. Soc.* **2003**, *125*, 10170.
[60] R. Melenkivitz, D. J. Mindiola, G. L. Hillhouse, *J. Am. Chem. Soc.* **2002**, *124*, 3846.
[61] C. C. Cummins, R. R. Schrock, W. M. Davis, *Angew. Chem.* **1993**, *105*, 758; *Angew. Chem. Int. Ed. Engl.* **1993**, *32*, 756.
[62] J. B. Bonanno, P. T. Wolczanski, E. B. Lobkovsky, *J. Am. Chem. Soc.* **1994**, *116*, 11159.
[63] J. S. Freundlich, R. R. Schrock, W. M. Davis, *J. Am. Chem. Soc.* **1996**, *118*, 3643.
[64] C. C. Cummins, *Prog. Inorg. Chem.* **1998**, *47*, 685.
[65] J. S. Figueroa, C. C. Cummins, *J. Am. Chem. Soc.* **2003**, *125*, 4020.
[66] N. N. Greenwood, A. Earnshaw, *Chemistry of the Elements*, 2nd Ed., Butterworth-Heinemann, Oxford, **1997**.
[67] L. Y. Goh, C. K. Chu, R. C. S. Wong, T. W. Hambley, *J. Chem. Soc. Dalton Trans.* **1989**, 1951.
[68] O. J. Scherer, M. Ehses, G. Wolmershäuser, *Angew. Chem.* **1998**, *110*, 530; *Angew. Chem. Int. Ed.* **1998**, *37*, 507.
[69] P. Berno, S. Gambarotta, *Organometallics* **1995**, *14*, 2159.
[70] C. E. Laplaza, M. J. A. Johnson, J. C. Peters, A. L. Odom, E. Kim, C. C. Cummins, G. N. George, I. J. Pickering, *J. Am. Chem. Soc.* **1996**, *118*, 8623.
[71] M. A. Schwindt, T. Lejon, L. S. Hegedus, *Organometallics* **1990**, *9*, 2814.
[72] P. Pyykkö, S. Riedel, M. Patzschke, *Chem. Eur. J.* **2005**, *11*, 3511.
[73] E. L. Sceats, J. S. Figueroa, C. C. Cummins, N. M. Loening, P. van der Wel, R. G. Griffin, *Polyhedron* **2004**, *23*, 2751.
[74] T. L. Allen, A. C. Scheiner, H. F. Schaefer III, *J. Phys. Chem.* **1990**, *94*, 7780.
[75] T. L. Allen, A. C. Scheiner, Y. Yamaguchi, H. F. Schaefer III, *J. Am. Chem. Soc.* **1986**, *108*, 7579.
[76] T. L. Allen, A. C. Scheiner, Y. Yamaguchi, H. F. Schaefer III, *Chem. Phys. Lett.* **1985**, *121*, 154.
[77] M. W. Schmidt, M. S. Gordon, *Inorg. Chem.* **1986**, *25*, 248.
[78] J. Olkowska-Oetzel, J. Pikies, *Appl. Organomet. Chem.* **2003**, *17*, 28.
[79] M. T. Nguyen, A. VanKeer, L. G. Vanquickenborne, *J. Org. Chem.* **1996**, *61*, 7077.
[80] J. Pikies, E. Baum, E. Matern, J. Chojnacki, R. Grubba, A. Robaszkiewicz, *Chem. Commun.* **2004**, 2478.
[81] H. Krautscheid, E. Matern, J. Pikies, G. Fritz, *Z. Anorg. Allg. Chem.* **2000**, *626*, 2133.
[82] H. Krautscheid, E. Matern, I. Kovacs, G. Fritz, J. Pikies, *Z. Anorg. Allg. Chem.* **1997**, *623*, 1917.

 © 2006 Wiley-VCH Verlag GmbH & Co. KGaA, Weinheim

[83] H. Krautscheid, E. Matern, G. Fritz, J. Pikies, *Z. Anorg. Allg. Chem.* **1998**, *624*, 501.
[84] A. Savin, R. Nesper, S. Wengert, T. F. Fässler, *Angew. Chem.* **1997**, *109*, 1892; *Angew. Chem. Int. Ed. Engl.* **1997**, *36*, 1808.
[85] B. Silvi, A. Savin, *Nature* **1994**, *371*, 683.
[86] H. Grützmacher, T. F. Fässler, *Chem. Eur. J.* **2000**, *6*, 2317.
[87] P. P. Power, *Chem. Commun.* **2003**, 2091.
[88] P. P. Power, *Chem. Rev.* **1999**, *99*, 3463.

Life's Simple Pleasures!



13280407_gu

No need to waste precious time looking for the right information – Register now for the free **Wiley-VCH Alerting Service.**

It's simple – and it's fast.

To receive regular news per e-mail tailored precisely to your needs and interests, just fill in the registration form at **www.wiley-vch.de/home/pas/**

WILEY-VCH

© 2006 Wiley-VCH Verlag GmbH & Co. KGaA, Weinheim

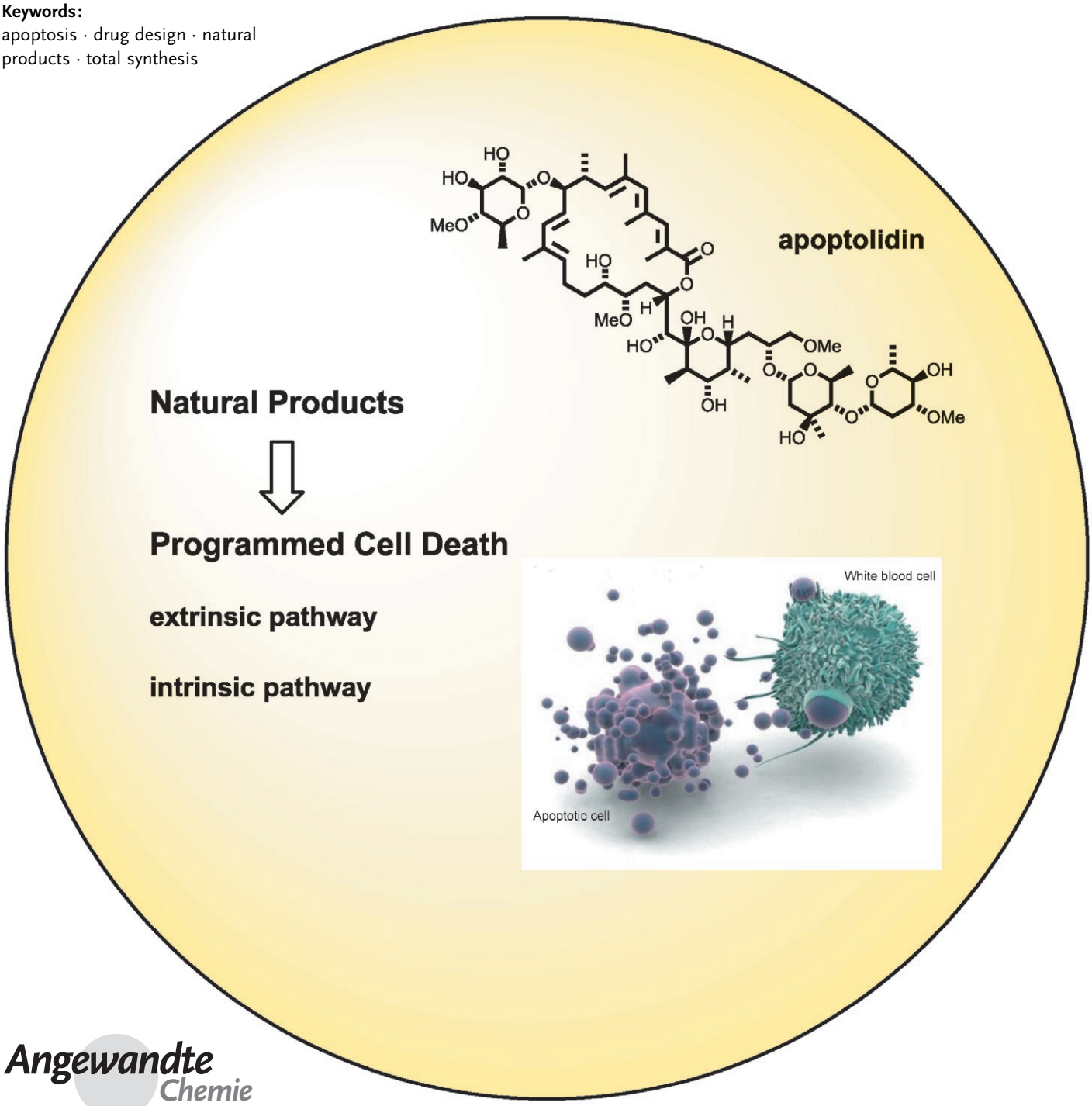
Drug Research

DOI: 10.1002/anie.200502698

Apoptolidin: Induction of Apoptosis by a Natural Product

Peter T. Daniel, Ulrich Koert, and Julia Schuppan*

Keywords:
apoptosis · drug design · natural products · total synthesis



© 2006 Wiley-VCH Verlag GmbH & Co. KGaA, Weinheim

Apoptolidin is a natural product that selectively induces apoptosis in several cancer cell lines. Apoptosis, programmed cell death, is a biological key pathway for regulating homeostasis and morphogenesis. Apoptotic misregulations are connected with several diseases, in particular cancer. The extrinsic way to apoptosis leads through death ligands and death receptors to the activiation of the caspase cascade, which results in proteolytic degradation of the cell architecture. The intrinsic pathway transmits signals of internal cellular damage to the mitochondrion, which loses its structural integrity, and forms an apoptosome that initiates the caspase cascade. Compounds which regulate apoptosis are of high medical significance. Many natural products regulate apoptotic pathways, and apoptolidin is one of them. The known synthetic routes to apoptolidin are described and compared in this Review. Selected further natural products which regulate apoptosis are introduced briefly.

From the Contents

1. Introduction	873
2. Biochemical Pathways for Apoptosis	874
3. Apoptolidin	876
4. Other Natural Products which Regulate Apoptosis	885
5. Concluding Remarks	890

1. Introduction

Adult multicellular organisms continuously encounter the need to regenerate differentiated, aging, or damaged cells. This situation requires the propensity of tissue stem cells to divide and to differentiate. However, it is important to keep the number of growing cells constant in a living organism (homeostasis). For this reason, eukaryotic cells have developed a genetically encoded program that controls cell death. This regulated type of cell death is called apoptosis.[1] The term apoptosis is derived from the Greek word for the falling down of the colored leaves in autumn. Multicellular organisms utilize this program during embryonal development to eliminate superfluous cells and to shape out parts of the body (morphogenesis). A prominent example of morphogenesis by apoptosis is the redevelopment of the interdigital tissue of the human embryo between day 51 and day 60 after conception (Figure 1). Another example is the involution of the tadpole tail.

During apoptosis the cell undergoes a shrinking and decomposition into vesicles, which are finally eliminated by the immune system (Figure 2A). The role of apoptosis in the development of an organism has been well studied for the nematode *Caenorhabditis elegans* (*C. elegans*). This organism develops 1090 cells from which 131 are eliminated by apoptosis (Figure 2B). The Nobel Prize in medicine and physiology was awarded to Sydney Brenner, Robert Horvitz, and John E. Solston in 2002 for their contributions to our

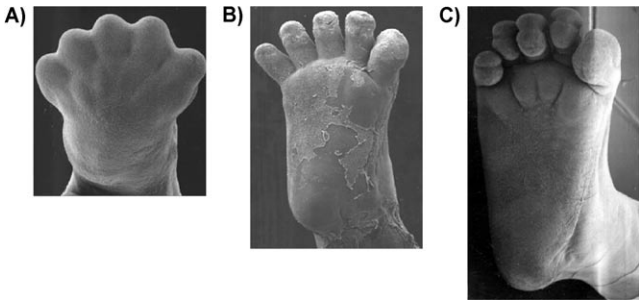


Figure 1. Morphogenesis by apoptosis: redevelopment of the interdigital tissue of a human embryo between day 51 (**A**), 54 (**B**), and 60 (**C**) after conception.

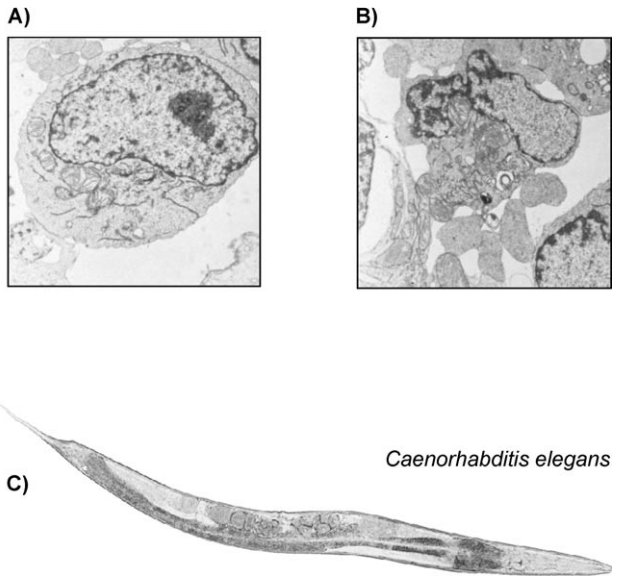


Figure 2. Normal (**A**) and apoptotic (**B**) lymphoma cell; picture of *C. elegans* (**C**).

[*] Prof. Dr. U. Koert
Fachbereich Chemie
Philipps-Universität Marburg
35032 Marburg (Germany)
Fax: (+49) 6421-282-5677
E-mail: koert@chemie.uni-marburg.de
Prof. Dr. P. T. Daniel
Department of Hematology, Oncology and Tumor Immunology
University Medical Center Charité
Humboldt University of Berlin (Germany)
Dr. J. Schuppan
Chiracon GmbH
Biotechnology Park, Luckenwalde (Germany)

© 2006 Wiley-VCH Verlag GmbH & Co. KGaA, Weinheim

understanding of apoptosis and its role in the life of *C. elegans*.[2] Although this use of *C. elegans*, *Drosophila*, and other alternative model organisms[3] has facilitated research on some basic aspects of cell-death regulation, most recent insights originate, however, from studies on mice and humans. This has been helped by the great progress made in functional genomics and the cloning of whole genomes.

Today, research in the area of apoptosis contributes to the understanding and treatment of diseases, in particular cancer.[4–10] Compounds which regulate apoptosis and overcome the apoptosis deficiency of cancer cells are therefore of high medical significance. An important goal is to develop low-molecular-weight compounds that selectively induce apoptosis in cancer cells, and this may lead to new antitumor drugs. Natural products are privileged structures which have evolved for functional reasons, for example, in response to selection pressure by antibiotics.[11] Numerous natural products are known that induce or inhibit apoptosis. Representative examples are apoptolidin, okadaic acid, cerulenin, lactacystin, bryostatin, staurosporine, taxanes, colchicine, laulimalide, geldanamycin, and betulinic acid. Notably, plants have evolved very different ways to regulate, induce, and execute cell death that show no equivalent with regard to apoptotic signal transduction in the animal kingdom.[12] This situation may explain the impressive potency of naturally occurring compounds to induce apoptosis in mammalian cells, since plants have evolved chemical weapons against parasites that may now be utilized, for example, for immune suppression or treatment of hyperproliferative diseases. This Review summarizes biochemical pathways for apoptosis and their modulation by naturally occurring compounds with an emphasis on apoptolidin.

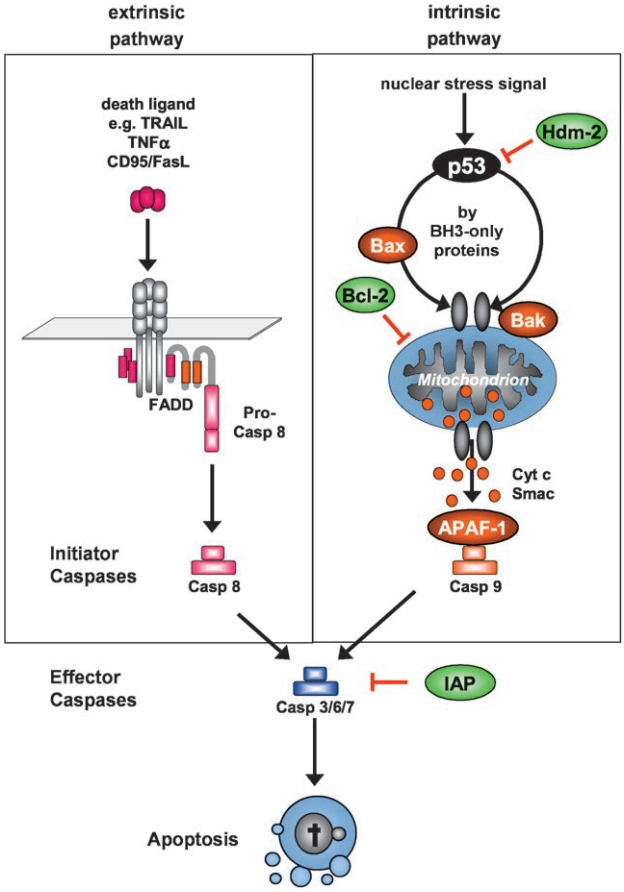


Figure 3. The extrinsic and intrinsic apoptotic pathways.

2. Biochemical Pathways for Apoptosis

2.1. The Cell Death Programs

Apoptosis of a cell can be induced by external signals or be internal pathways (Figure 3). The extrinsic pathway is often utilized in case a whole organism intends to eliminate a superfluous cell. Surrounding cells then send a death signal via death ligands such as CD95 (APO-1, Fas), TRAIL, or TNFα that bind to the respective death receptor. This process initiates recruitment of adapter proteins such as FADD or TRADD to the cytosolic death domain of the receptor. This, in turn triggers recruitment of the caspase-8 or -10 initiator caspases that are activated and initiate cell death through the caspase cascade.[13]

In contrast, the intrinsic pathway is triggered from within a cell following, for example, DNA damage or genotoxic stress. If the cell detects such internal damage is beyond repair it addresses a very important apoptotic actuating mechanism, which resides at the mitochondrion.[14] This mechanism is regulated by balanced equilibria between proapoptotic Bax-like and antiapoptotic Bcl-2-like proteins. To tightly control



Peter Daniel was born in 1960 and studied human medicine at the University of Tübingen (Germany), where he received his PhD in 1987. He carried out postdoctoral studies at the Deutsche Krebsforschungszentrum (German Cancer Institute) in Heidelberg until 1993, and subsequently moved to the Robert-Rössle-Klinik der Charité at the Humboldt University in Berlin, where he headed a research group. He completed his habilitation in 2003 with his work on the deregulation of the cell cycle and apoptosis as a molecular basis for the therapy resistance of tumors.



Ulrich Koert was born in Hanau in 1961, and obtained his PhD in 1988 with G. Quinkert at Frankfurt University. After postdoctoral research with J.-M. Lehn in Strasbourg (1988–1990), he moved to the Philipps-University, Marburg, and completed his habilitation in 1994. He was associate professor at Munich University (1996) and full professor at the Humboldt university, Berlin (1996–2001). Since 2001 he has been professor for organic chemistry at the Philipps-University, Marburg. His reseach interests include natural product synthesis, medicinal chemistry, and function-oriented synthesis.

 © 2006 Wiley-VCH Verlag GmbH & Co. KGaA, Weinheim

Bax and its homologous killer proteins, Bax must be activated by pro-apoptotic BH3-only proteins that trigger a conformational switch in Bax. This process results in translocation from the cytosol into the outer mitochondrial membrane, oligomerization, and formation of channels that mediate release of cytotoxic factors that trigger caspase-dependent and independent cell death. These factors include cytochrome C that, once in the cytosol, binds to the adapter protein APAF-1 which then binds the initiator caspase-9. Smac, the second mitochondrial activator of cell death, interferes with the binding of IAP proteins to active caspases. This process interferes with the proteasomal degradation of active caspases and is sufficient to trigger cell death in human cancer cells.[15a]

The two apoptosis mechanisms, the extrinsic and the intrinsic, are interconnected. For example, the BH3-only protein Bid[14, 15b,c] is cleaved by caspase-8 and -3 to a truncated Bid (t-Bid) protein that triggers activation of Bax or the Bax homologue Bak. This may result in sensitization of the mitochondrial pathway for intrinsic death signals.[16, 17a] Likewise, Smac may facilitate caspase processing by the extrinsic pathway. Examples of synthetic antagonists of the BH3/Bcl-xL complex have been desribed recently.[17b]

Thus, regardless of the induction phase, a cascade of caspase activations results that converge at the level of the executioner caspases-3, -6, and -7.[18,19a] Caspases are cystein proteases which cleave the target peptide at an aspartic acid position. This basic principle of apoptosis promoters acting in a cascade leading to activation of executing enzymes, for example, the caspases, is conserved through evolution and can be traced back to archaic organisms such as *Caenorhabditis elegans* and possibly even simpler organisms such as facultative multicellular organisms like the slime molds (*Dictyostelium*) that express a paracaspase.[3] Subsequent to caspase activation, nuclear endonucleases are activated and a disassembly of the cellular biopolymers occurs.[20a] The cellular waste is deposited in apoptotic vesicles (apoptotic bodies) and these or whole apoptotic cells are quickly disposed of by phagocytes.[20b] In contrast to necrosis, no inflammatory reaction results upon apoptosis.

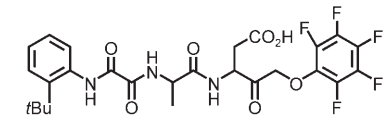
In intact cells the proapoptotic pathways are countercontrolled by multiple layers of antiapoptotic pathways which address the various signaling events. At the level of the death receptors, FLIP proteins interfere with caspase recruitment to the ligand/ receptor signaling complexes. IAP proteins bind to active caspases through a conserved motif and act as E3-ubiquitin ligases to sequester active caspases through the proteasome. Antiapoptotic Bcl-2 family members, including Bcl-x_L, interfere with Bax activation either by binding directly to bax or by sequestering BH3-only proteins.



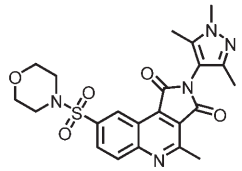
Julia Schuppan was born in 1973, and studied chemistry at the Humboldt University in Berlin. She joined the research group of Prof. Koert in 1998 as a graduate student, where she worked on the total synthesis of apoptolidin. After postdoctoral research with Prof. Feringa in Groningen, The Netherlands, she returned to Germany and since 2004 she has worked in the R&D department of Chiracon GmbH in Luckenwalde, Germany.

2.2. Caspases as Drug Targets

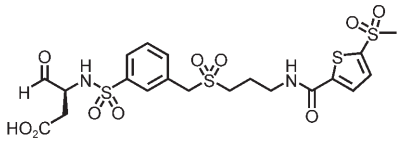
The central role of caspases and, in particular caspase-3, in apoptotic pathways make them a promising drug target for the treatment of diseases that are characterized by cell loss through an excess of apoptotic cell death.[19b,c] These include, for example, neurodegenerative disorders such as Alzheimer's disease or spinal muscular atrophy and also impaired blood perfusion in myocardial infarction or strokes, where apoptotic death plays a major role in the hypoxic penumbra (oxygen defficiency) and during reperfusion.[20c] There, caspase inhibition may interfere with tissue loss. Caspases are cysteine proteases and any inhibitor has to address the strong nucleophilicity of the thiol group in the active site. Therefore, most of the inhibitors reported so far contain a strong electrophilic group and bind irreversibly.[20d] Selected caspase inhibitors are shown in Scheme 1. IDN-6556 is a liver-targeted



IDN-6556



Ivatchenko's caspase 3 inhibitor



Sunesis' caspase 3 inhibitor

Scheme 1. Selected caspase inhibitors.

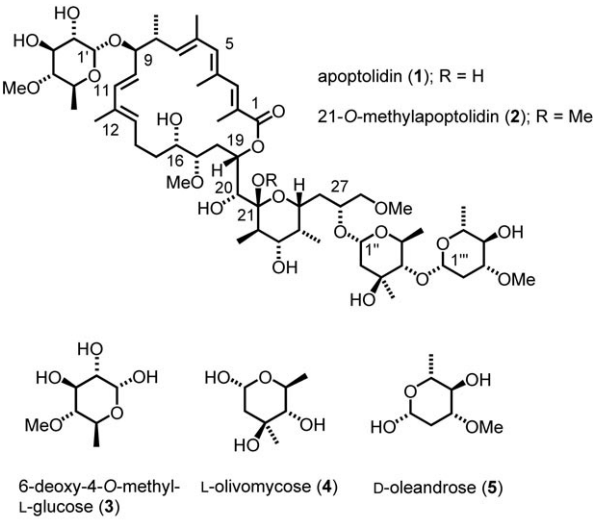
caspase inhibitor in clinical development for the treatment of acute hepatitis or inflammatory liver degeneration following allotransplantation.[20e] Examples of caspase-3 inhibitors have been reported, including by Ivatchenko and co-workers.[20f] Sunesis Pharmaceuticals has developed a caspase-3 inhibitor by use of in situ assembly and dynamic combinatorial chemistry.[20g,h]

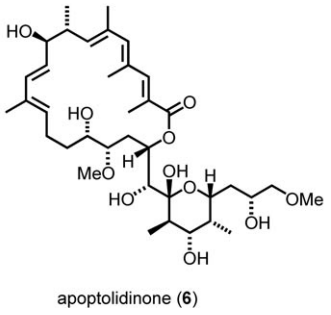
© 2006 Wiley-VCH Verlag GmbH & Co. KGaA, Weinheim

3. Apoptolidin

3.1. Structure and Properties of the Synthetic Target

In the course of screening for specific apoptosis inducers, the novel 20-membered macrolide apoptolidin (**1**; Scheme 2)



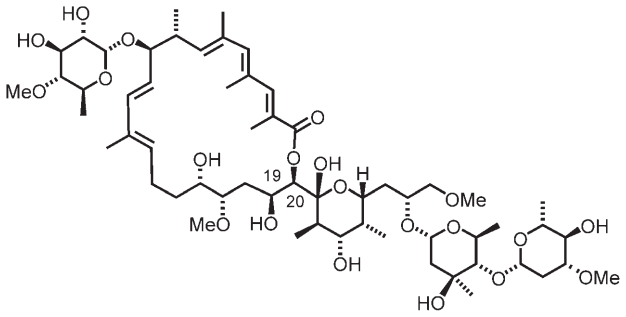


Scheme 2. Structures of the natural product apoptolidin, the sugar residues, and the aglycon apoptolidinone.

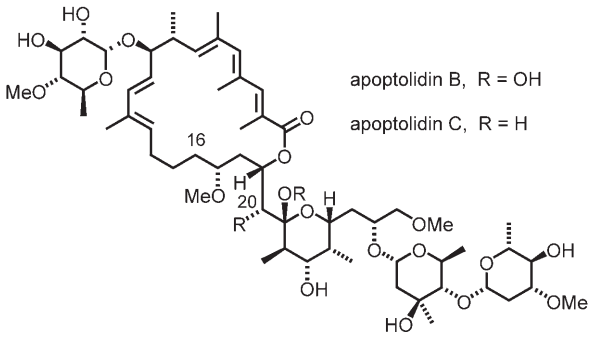
was isolated from *Nocardiopsis* sp. The molecular structure of **1** was elucidated by combined spectroscopic techniques.[21,22] It was shown that apoptolidin induces apoptotic cell death in rat glia cells transformed with the adenovirus E1A oncogene ($IC_{50} = 11\ ng\,mL^{-1}$). In a test carried out by the National Cancer Institute against human cancer cell lines, **1** proved to be among the top 0.1 % most selective cytotoxic agents of the 37000 substances tested. The apoptotic activity of **1** was correlated with its inhibition of mitochondrial F_0-F_1-ATPase.[23] Apoptolidin shares this target with structurally related macrolides such as oligomycin and ossamycin. Furthermore, apoptolidin-mediated apoptosis is independent of the p53 status of the cell, inhibited by Bcl-2, and dependent on the action of caspase-9.[23b] Taken together, these results reflect the major role of the mitochondrial pathway in apoptolidin-induced apoptosis.

Apoptolidin (**1**) is a 20-membered macrolide with a side chain containing a cyclic 6-membered hemiketal. 6-Deoxy-4-O-methyl-L-glucose (**3**; Scheme 2) is attached to O9 and a disaccharide consisting of L-olivomycose (**4**) and D-oleandrose (**5**) is linked to O27. The sugar residues are a prerequisite for the potent bioactivity of the natural product.[23c] Treatment of **1** with MeOH/Amberlyst-15 gives 21-*O*-methylapoptolidin (**2**).[24] The aglycone of apoptolidin is called apoptolidinone (**6**).

Apoptolidin (**1**) can rearrange into the 21-membered macrolactone isoapoptolidin (**7**) by a O19→O20 acyl shift.[25a,b] Treatment of **1** with pH 7 buffer at 37 °C for 20 h leads to a mixture consisting of 62 % **1** and 38 % **2**.



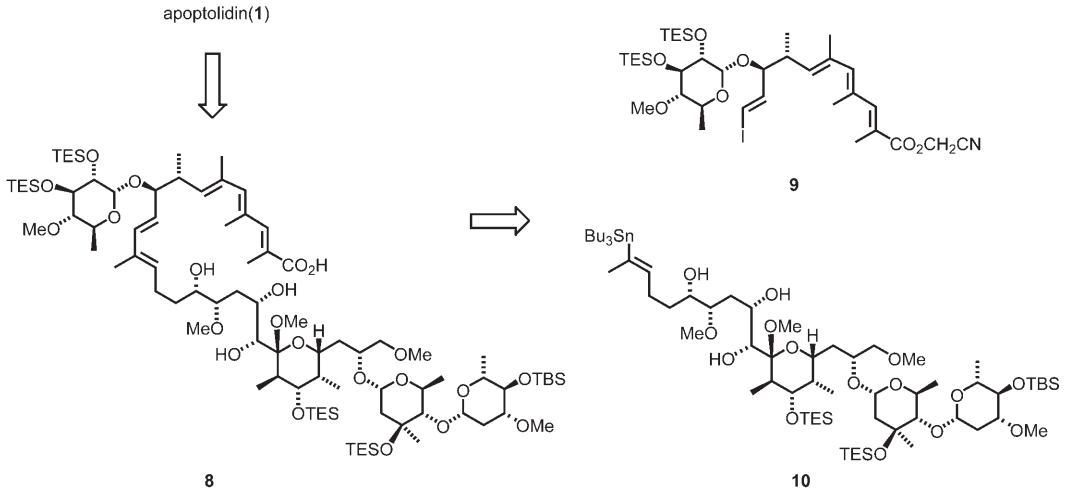
Recently, two analogues of apoptolidin were isolated and structurally characterized: Apoptolidin B and apoptolidin C differ from apoptolidin (**1** = apoptolidin A) by the absence of the OH group at C16 and different substituents at C20.[25c]



3.2. The Marburg Synthesis of Apoptolidin

Most of the syntheses of glycosylated macrolides involve attachment of the sugar moieties to the complete aglycon at the end of the synthesis. This strategy can cause problems with the selective addressing of a particular OH group among many at a late stage of the synthesis. Furthermore, it is a linear approach which weakens the overall synthetic efficiency. Koert and co-workers developed a retrosynthetic analysis to introduce the sugar moieties at a very early stage of the synthesis (Scheme 3).[26–28] A macrolactonization of a fully glycosylated precursor **8** to give **1** could constitute the last part of the synthesis. No protective groups at O16, O19, and O20 would be necessary if a ring-size-selective macrolactonization

 © 2006 Wiley-VCH Verlag GmbH & Co. KGaA, Weinheim

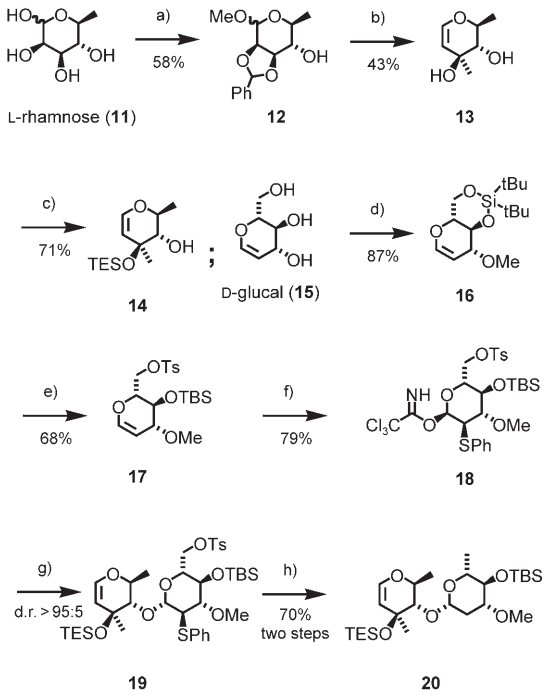


Scheme 3. Retrosynthetic analysis of apoptoldin according to Koert and co-workers.

of **8** could be achieved. The cross-coupling of a fully glycosylated southern half **10** with a glycosylated northern half **9** should be suitable for the assembly of **8**.

Two sugar moieties are required in an apoptolidin synthesis: a disaccharide from L-olivomycose and D-oleandrose at O27 and 6-deoxy-4-*O*-methyl-L-glucose at O9. The glycal **20** (Scheme 4) was chosen as the disaccharide precursor to achieve a stereocontrolled α-glycosidiation.[26] The starting point for the synthesis of **20** was L-rhamnose (**11**), which was converted into the benzylidene-protected methyl acetal **12**. Treatment of **12** with six equivalents of methyl lithium[29] gave, via a cyclohexenone intermediate, glycal **13**, which was protected as the olivomycal building block **14**. D-glucal (**15**) was protected at the O4 and O6 atoms with silyl groups and methylated at O3 to give **16**. Desilylation followed by tosylation of the primary OH group and protection of the secondary alcohol function as a TBS (*tert*-butyldimethylsilyl)[*] ether gave **17**. An auxiliary thiophenyl substituent was then introduced at C2 of the D-oleandrose building block in preparation for a β-selective glycosylation.[30] Towards this end, **17** was treated first with PhSCl, then with Ag_2CO_3 in H_2O/CH_3CN, and the resulting α-anomeric hemiacetal was converted into trichloroacetimidate **18**. The TMSOTf-mediated (trimethylsilyl triflate) glycosylation of **14** and **18** produced disaccharide **19** with a very high β selectivity. The substitution of the tosylate by an iodide and the radical removal of the iodo and the thiophenyl groups completed the preparation of the protected disaccharide building block **20**.

L-Rhamnose is a suitable starting material for the synthesis of the sugar residue at O9 of apoptolidin. In both the syntheses of apoptolidin by Nicolaou et al.[31] and by Koert and co-workers[26] the acetonide-protected L-rhamnose thioglycoside **21**[32] was used as a readily available building block (Scheme 5). The secondary alcohol of **21** was methylated to give **22**. Cleavage of the acetonide group, protection of O3 as a TBS ether, and a subsequent oxidation of the remaining alcohol provided ketone **23**. A highly stereoselective reduction of **23** with $NaBH_4$ gave the corresponding alcohol, which

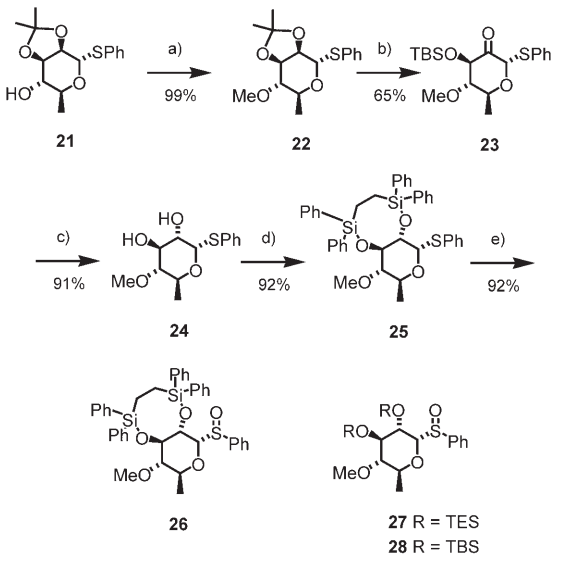


Scheme 4. a) 1. MeOH, Dowex 50WX-8-200; 2. $PhCH(OMe)_2$, *p*TsOH, DMF; b) 6 equiv MeLi, THF, 20 °C, 30 h; c) 1. Ac_2O, pyridine, DMAP, CH_2Cl_2; 2. TESOTf, lutidine; 3. DIBAH, CH_2Cl_2, −60 °C; d) 1. $tBu_2Si(OTf)_2$, lutidine, DMF/CH_2Cl_2 (1:1), −50 °C; 2. MeI, Ag_2O; e) 1. TBAF, THF; 2. *p*TsCl, pyridine, CH_2Cl_2, 0 °C; 3. TBSOTf, lutidine, CH_2Cl_2; f) 1. PhSCl, CH_2Cl_2; 2. Ag_2CO_3, CH_3CN/H_2O (9:1); 3. Cl_3CCN, NaH; g) **14**, TMSOTf, Et_2O, −60→−40 °C, 1 h; h) 1. NaI, DMF, 90 °C, 2 h; 2. Bu_3SnH, AIBN, toluene, 100 °C, 7 h, 70% over three steps. DMAP = 4-dimethylaminopyridine, DIBAH = diisobutylaluminium hydride, TBAF = tetrabutylammonium fluoride, AIBN = azobis(isobutyronitrile), d.r. = diastereomeric ratio.

was desilylated to diol **24**. The choice of the right O2/O3 protecting groups was crucial for the successful glycosylation of the northern half. An α-selective glycosylation demanded a passive protecting group at O2 which could be removed at the end without affecting the highly unsaturated and acid-

[*] A list of abbreviations can be found at the end of the Review.

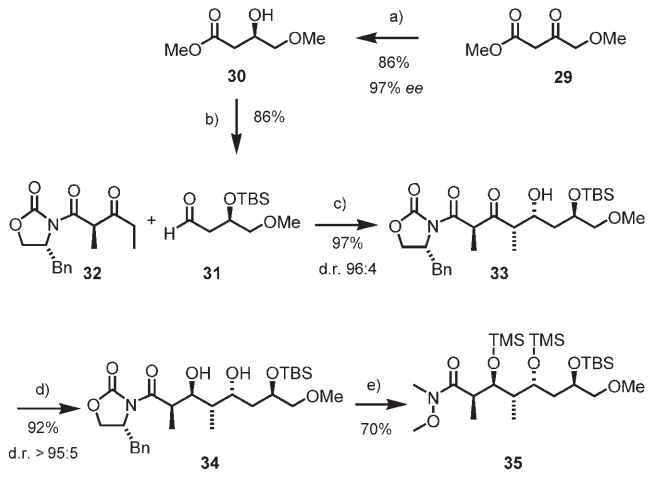
 © 2006 Wiley-VCH Verlag GmbH & Co. KGaA, Weinheim



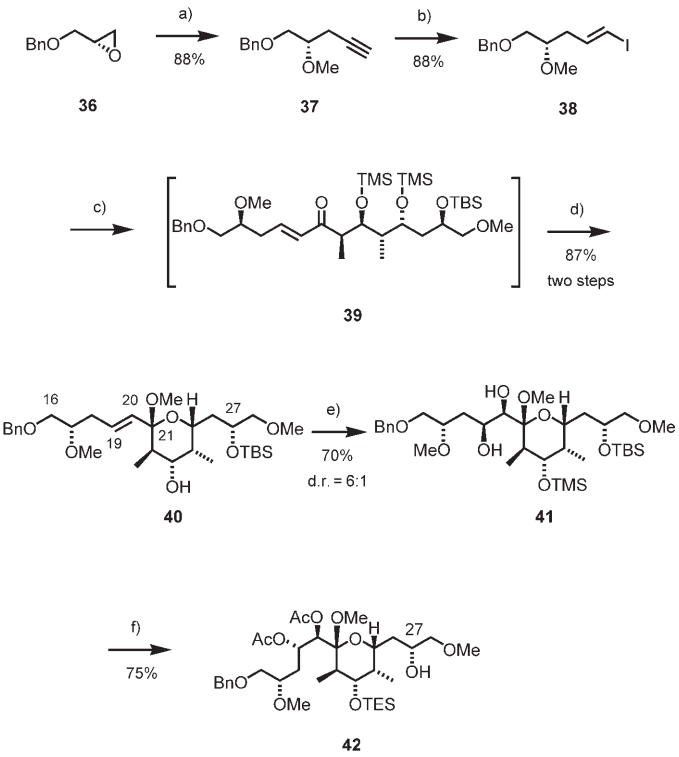
Scheme 5. a) MeI, KOH, DMF, 0 °C; b) 1. *p*TsOH, MeOH; 2. TBSCl, imidazole, DMAP, CH_2Cl_2; 3. Dess–Martin periodinane; c) 1. $NaBH_4$, MeOH, 0 °C, 15 min; 2. TBAF, THF; d) $Ph_2Si(Cl)CH_2CH_2Si(Cl)Ph_2$, imidazole, DMF, 0 °C, 1 h; e) *m*CPBA, CH_2Cl_2, −78 → −20 °C, 2 h, 2:1 epimeric mixture. *m*CPBA = *meta*-chloroperbenzoic acid.

sensitive target molecule. Silyl ethers should be the best choice. After several unsuccessful glycosylation attempts (trichloroacetimidate, glycosyl fluoride, thioglycoside activation by PhSOTf) focus turned to the Kahne glycosylation to activate the gycosyl donor as a sulfoxide.[33] The doubly TES- and doubly TBS-protected sulfoxides **27** and **28** gave unsatisfying glycosylation results, which led to the development of a new protecting group, 1,1,4,4-tetraphenyl-1,4-disilabutyl (SIBA). Treatment of diol **24** with 1,4-dichloro-1,1,4,4-tetraphenyl-1,4-disilabutane ($SIBACl_2$)[34] gave the disilyl ether **25** in 92% yield. Oxidation of **25** with *m*CPBA led to the desired SIBA-protected glycosyl sulfoxide **26**.

After the preparation of both sugar moieties, attention was drawn to the synthesis of the glycosylated southern and northern halves. The starting point for the synthesis of the southern half was the β-ketoester **29** (Scheme 6).[26–28] A Rubinap-catalyzed hydrogenation of **29** gave the β-hydroxyester **30** (97% *ee* determined by HPLC). The latter was protected as a TBS ether and then reduced to aldehyde **31**. A stereocontrolled aldol reaction[35] of **31** with the β-keto imide dipropionyl building block **32**[36] mediated by stannous triflate provided the aldol product **33** in 97% yield with a diastereomer ratio of 96:4. The configuration of the two new stereocenters was later confirmed by X-ray structure analysis.[28] The *anti*-selective reduction[37] of the 1,3-hydroxyketone functionality in **33** with $NaBH(OAc)_3$ gave the 1,3-diol **34** in 92% yield with high stereoselectivity. A transamidation provided the corresponding Weinreb amide in 81% yield, and the two OH groups were protected as TMS ethers to give compound **35**.



Scheme 6. a) [Ru{(S)-binap}], H_2, MeOH, DMF, 95 °C; b) 1. TBSCl; 2. DIBAH, hexane, −78 °C; c) $Sn(OTf)_2$, Et_3N, CH_2Cl_2; d) $NaBH(OAc)_3$, HOAc, CH_3CN, −20 °C → 25 °C; e) 1. $AlMe_3$, Me(MeO)NH HCl, HOAc, CH_2Cl_2, −10 °C; 2. TMSCl.



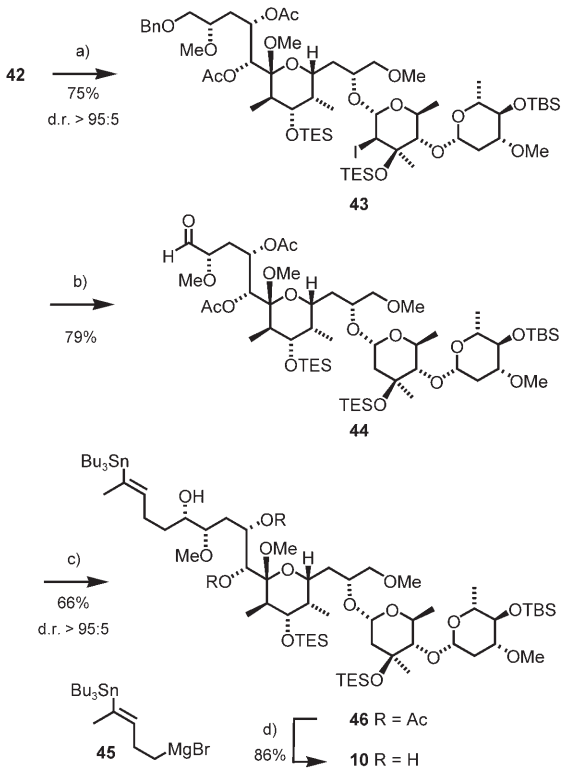
Scheme 7. a) 1. $LiCCSiMe_3$, $BF_3{\cdot}OEt_2$, THF, −78 °C; 2. LiHMDS, MeI, THF, 0 → 20 °C; 3. TBAF; b) $[Cp_2ZrCl_2]$, $LiEt_3BH$, NIS, THF, 20 °C; c) *t*BuLi, Et_2O, −78 °C; **35**; d) PPTS, MeOH, 0 °C; e) 1. TMSCl; 2. $K_2OsO_2(OH)_4$, NMO; *t*BuOH/H_2O; 20 °C, 9 days, 78%; f) 1. Ac_2O, pyridine; 2. TBAF; 3. TESCl; 4. TBAF, 0 °C. Cp = cyclopentadienyl, NIS = *N*-iodosuccinimide, PPTS = pyridinium *p*-toluenesulfonate, NMO = *N*-methylmorpholine *N*-oxide.

A further C_5 building block **38** of the southern half was obtained by epoxide opening of the benzyl-protected (*R*)-glycidol **36** (Scheme 7).[26–28] Subsequent O-methylation and cleavage of the TMS group gave alkyne **37**, which was transformed by hydrozirconation/iodination into the (*E*)-alkenyl iodide **38**. The latter was converted through an iodine–lithium exchange into the corresponding organolithium compound, which was treated with Weinreb amide

 © 2006 Wiley-VCH Verlag GmbH & Co. KGaA, Weinheim

35 to yield ketone **39**. Protodesilylation of the two TMS groups in MeOH/CH_2Cl_2 led through a spontaneous cyclization to ketal **40**. After protection of the alcohol group at C23 as a TES ether a subsequent dihydroxylation (d.r. 6:1) gave diol **41**. The diastereomeric ratio arose from substrate control and attempts to improve the stereoselectivity by various asymmetric versions of dihydroxylation were not successful. Diol **41** was diacetylated and the TMS ether at C27 was cleaved to give alcohol **42**.

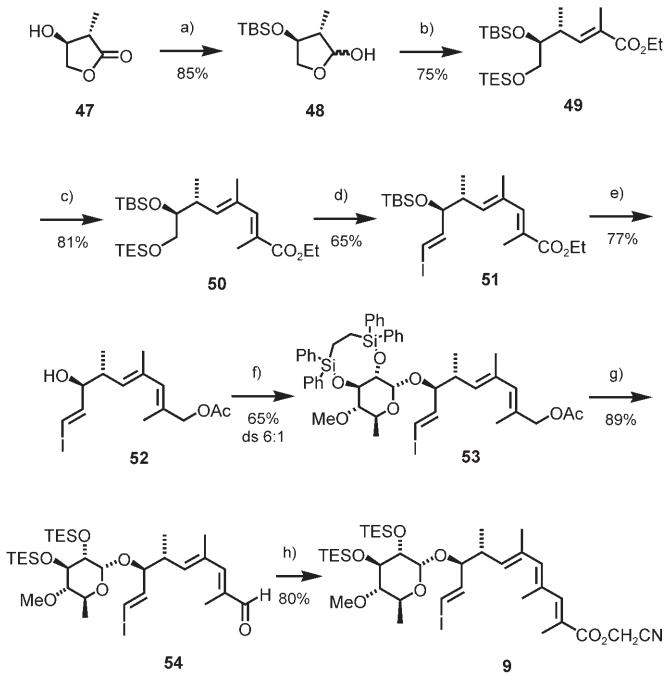
The glycosyl acceptor **42** was treated with the disaccharide glycal **20** to produce the glycoconjugate **43** with a high α selectivity (> 95:5; Scheme 8).[38] Reductive removal of the



Scheme 8. a) 1.2 equiv NIS, MS (4Å), CH_3CN, 0→20 °C, 70 h; b) 1. Bu_3SnH, AIBN; then 1 M KF in H_2O; 2. H_2/$Pd(OH)_2$; 3. Dess–Martin periodinane; c) Et_2O, 7 equiv $MgBr_2$, −78 °C; d) KCN, MeOH, 40 °C, 16 h.

auxiliary iodide, cleavage of the resulting benzyl ether, followed by a Dess–Martin oxidation gave aldehyde **44**. A chelation-controlled addition of Grignard reagent **45** to aldehyde **44** produced the fully glycosylated southern half **46**. The tolerance of the organotin group in the presence of the organomagnesium group is particularly noteworthy in this reaction. A cyanide-mediated cleavage of the acetate groups in **46** afforded the desired building block **10**.

The starting point for the northern half **9** was the β-hydroxylactone **47**, which was protected as a TBS ether and subsequently reduced to lactol **48** (Scheme 9).[26,27] The twofold use of an *E*-selective Wittig reaction led via **49** to diene **50**. Selective cleavage of the TES ether followed by a Dess–Martin oxidation gave an aldehyde which could be

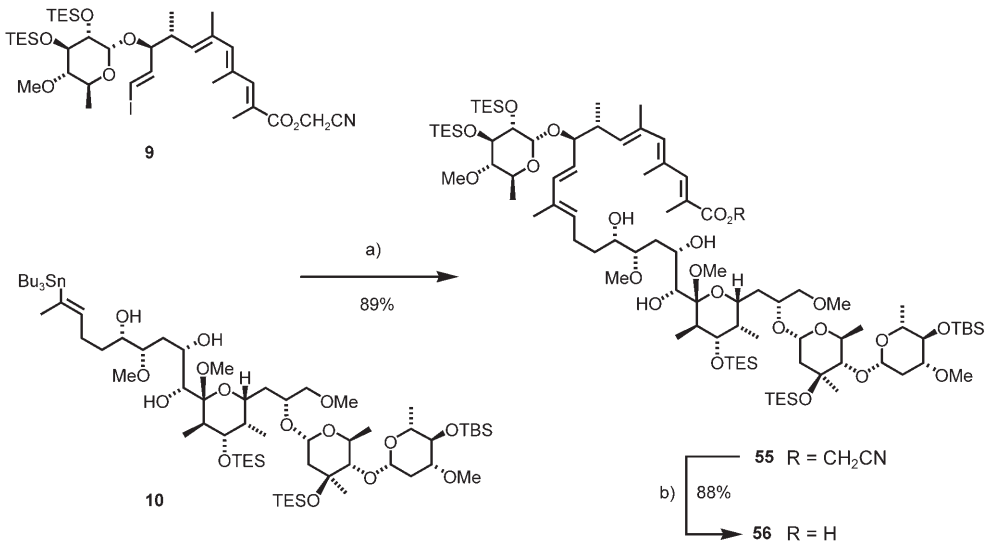


Scheme 9. a) 1. TBSOTf; 2. DIBAH; b) 1. $Ph_3P{=}CCH_3CO_2Et$; 2. TESCl; c) 1. DIBAH; 2. MnO_2; 3. $Ph_3P{=}CCH_3CO_2Et$; d) 1. CSA, MeOH/CH_2Cl_2; Dess–Martin periodinane; $CrCl_2$, CHI_3; THF, dioxane; e) 1. DIBAH, −78 °C; 2. Ac_2O; 3. TBAF, THF, 0 °C; f) **26**, Tf_2O, DTBMP, −80 °C, 10 min; then **52**, MS (4 Å), Et_2O; −78→−30 °C, 30 min; g) 1. TBAF; 2. TESCl, 3. LiOH; 4. MnO_2; h) 1. $(EtO)_2POCH(CH_3)CO_2H$, NaH, THF, 0→35 °C, 30 min; 2. $ClCH_2CN$, Et_3N, MeCN, 0→25 °C, 14 h. DTBMP = 2,6-di-*tert*-butyl-4-methylpyridine, CSA = camphorsulfonic acid.

converted through a Takai reaction into the (*E*)-alkenyl iodide **51**. Reduction of the ester, subsequent protection of the alcohol as an acetate followed by cleavage of the TBS group provided the glycosyl acceptor **52**. Initial attempts to use the doubly TES-protected glycosylsulfoxide **27** as the glycosyl donor failed because of loss of the TES groups under the reaction conditions (Tf_2O, DTBMP, −80→−35 °C). The more stable doubly TBS-protected glycosylsulfoxide **28** gave the desired glycoside in 50% yield but with an unacceptable low stereoselectivity (α/β = 66:33). In contrast, the reaction of the SIBA-protected glycosylsulfoxide **26** with **52** gave the expected product **53** in 65% yield with an acceptable stereoselectivity (α/β = 85:15). The final task for the completion of the northern half was the introduction of the C1–C3 unsaturated ester fragment. The protective groups were adjusted for the final deprotection, with the SIBA group changed to a TES group. Finally the allylic acetate was converted into aldehyde **54**. A Wittig–Horner–Emmons reaction and esterfication sequence gave the complete glycosylated northern half of apoptolidin, the cyanomethyl ester **9**.

Cross-coupling of the northern half with the southern half (**9** + **10**→**55**) was possible using Cu^I/thiophene-2-carboxylate (Cu-Tc) in NMP (Scheme 10).[39] Palladium-mediated coupling conditions required higher temperatures and gave lower yields. The cyanomethyl ester in **55** could be hydrolyzed under very mild conditions (LiOH, 20 °C, 2 h) to acid **56** without

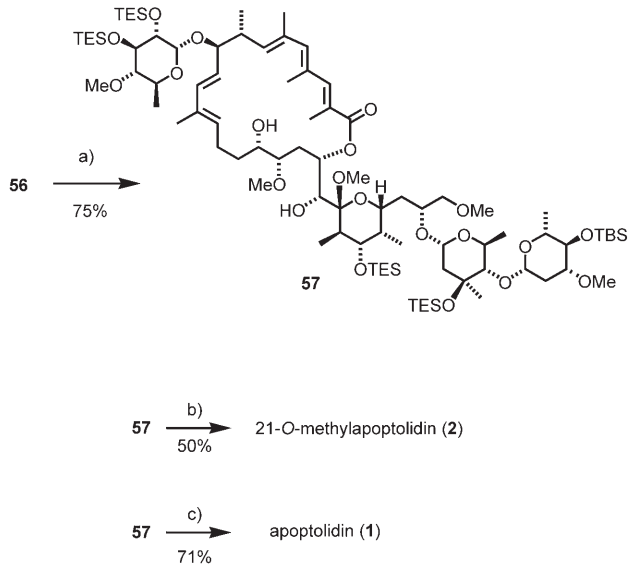
 © 2006 Wiley-VCH Verlag GmbH & Co. KGaA, Weinheim



Scheme 10. a) CuTC, NMP, −5 °C; b) LiOH, THF, MeOH; 20 °C, 2 h.

affecting the triene system or the TES ether groups. The methyl ester, which worked well in the aglycon synthesis,[27] could not been used in the synthesis of **55** because its hydrolysis led to unwanted side-products.

A ring-size-selective macrolactonization of **56** produced the 20-membered lactone **57** in 75% yield (Scheme 11). The final deprotection step required a careful choice of reagents and optimization of the reaction conditions. The use of HF·pyridine in THF/pyridine at room temperature for five days cleaved all the silyl ethers but left the methyl ketal intact and thus gave synthetic 21-*O*-methylapoptolidin (**2**). A complete deprotection of **57** leading to apoptolidin (**1**) was possible with 25% aqueous H_2SiF_6 in CH_3CN at −40→−10 °C.



Scheme 11. a) 2,4,6-Trichlorobenzoyl chloride, Et_3N, THF, 6 h; toluene, DMAP, $c = 3\ 10^{-4}$ M; b) HF, pyridine, THF, 20 °C, 5 days; c) H_2SiF_6 25% in H_2O, CH_3CN, −40→−20 °C, 2 days, −10 °C, 1 day.

3.3. Synthesis of Apoptolidin by Nicolaou et al.

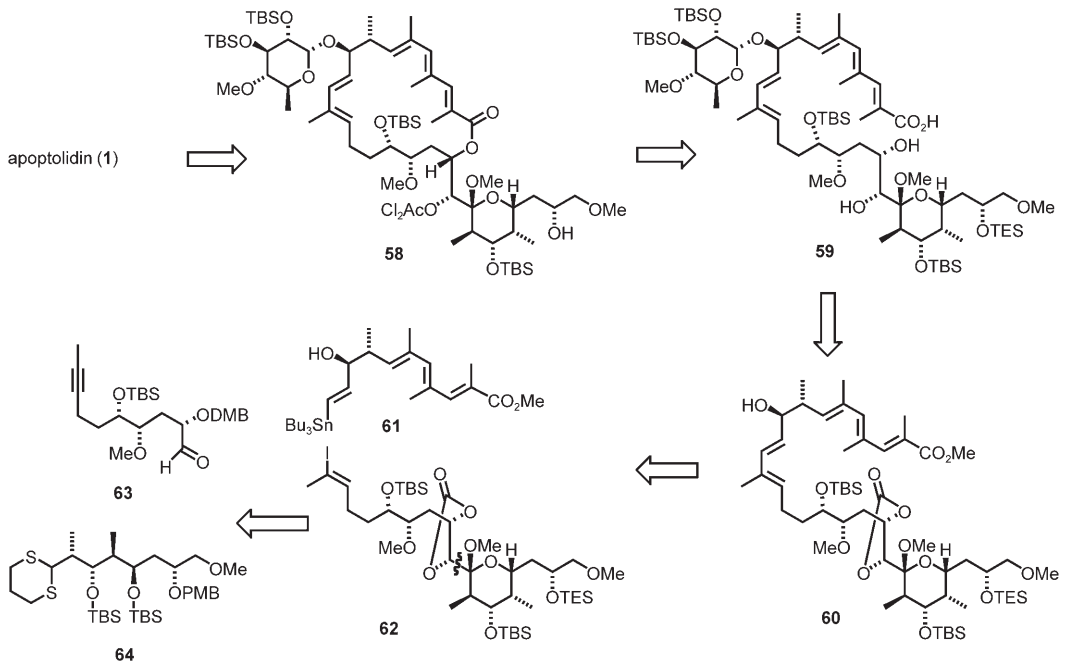
The strategy used by Nicoloau et al. for the synthesis of apotolidin is based on the final attachment of the labile disaccharide moiety at O27 (Scheme 12).[31] Thus, the final part of the synthesis would consist of the stereoselective glycosylation of the glycosyl acceptor **58**. The macrolide **58** is transformed to the dihydroxy acid **59**. At this stage Nicolaou et al. planned to attach the sugar to the O9 position of precursor **60**. A Stille coupling of the alkenylstannane **61** and the alkenyl iodide **62** could be used to assemble **60**. The alkenyl iodide **62** should be accessible by the reaction of aldehyde **63** with dithiane **64**.

The synthesis of the C1–C11 fragment **61** started with the asymmetric crotylation of aldehyde **65** with Brown's (*Z*)-(+)-crotyldisopinocampheylborane to produce the *syn* adduct **66** as a single stereoisomer (Scheme 13).[31] Protection of the alcohol groups of **66** as TBS ethers and a chemoselective ozonolysis of the terminal alkene provided aldehyde **67**. From here, Nicolaou et al. developed a linear and a convergent route to the desired alkenylstannane **61**. The more efficient convergent route is considered here. Treatment of aldehyde **67** with the Ohira–Bestmann reagent gave a terminal acetylene which was methylated to give **68**. This compound was chemoselectively hydroborated with catecholborane in the presence of catalytic amounts of 9-BBN to deliver vinyl boronate **69**. Remarkably, only the desired regioisomer was observed in this hydroboration. Hydrolysis of **69** led to boronic acid **70**, which was subjected to a Suzuki coupling with alkenyl bromide **71** to obtain the conjugate methyl ester **73**. The alkenyl bromide **71** was readily available from the known allylic alcohol **72** by a three-step sequence. A fluoride-mediated removal of the silyl groups in **73** followed by a Pd-catalyzed hydrostannylation gave the (*E*)-alkenylstannane **61** in 68% yield. The regioisomeric hydrostannylation product was not observed, but **61** proved to be thermally labile at ambient temperature.

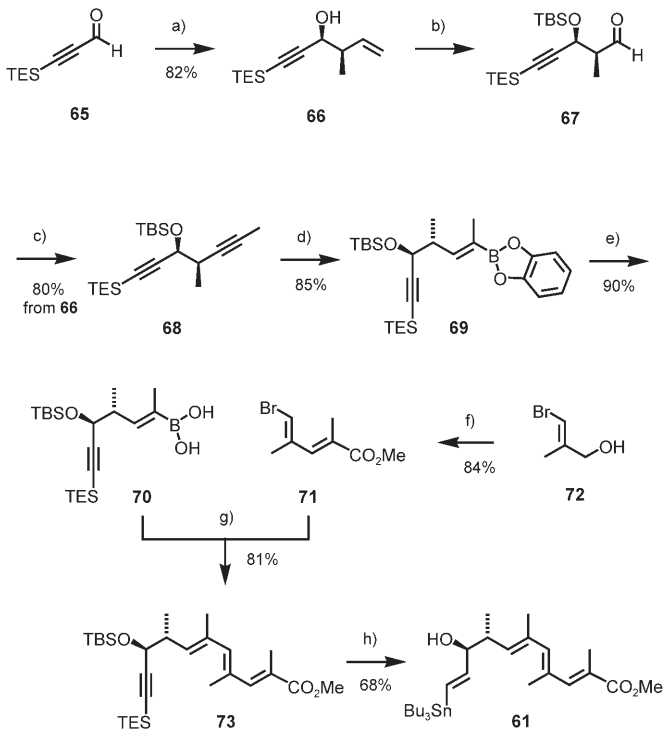
The construction of aldehyde **63** started with the opening of epoxide **74** with allenylmagnesium bromide to deliver alcohol **75**, which was transformed via the TBS ether **76** to aldehyde **77** (Scheme 14). Stereoselective allylation of **77** and subsequent methylation of the alcohol afforded **78**, the terminal double bond of which was asymmetrically dihydroxylated to **79** with a self-mixed AD mix. Formation of the 3,4-dimethoxybenzylidene derivative led to **80**. A DIBAH-induced regioselective ring opening of the acetal followed by a Parikh–Doering oxidation generated aldehyde **63**.

The opening of epoxide **81** to form a lithiated thioketal **82** gave entry to the synthesis of thioketal **64** (Scheme 15).[31] Cleavage of the thioketal in **82** provided aldehyde **83**, which was subjected to an asymmetric Brown crotylation to give

 © 2006 Wiley-VCH Verlag GmbH & Co. KGaA, Weinheim

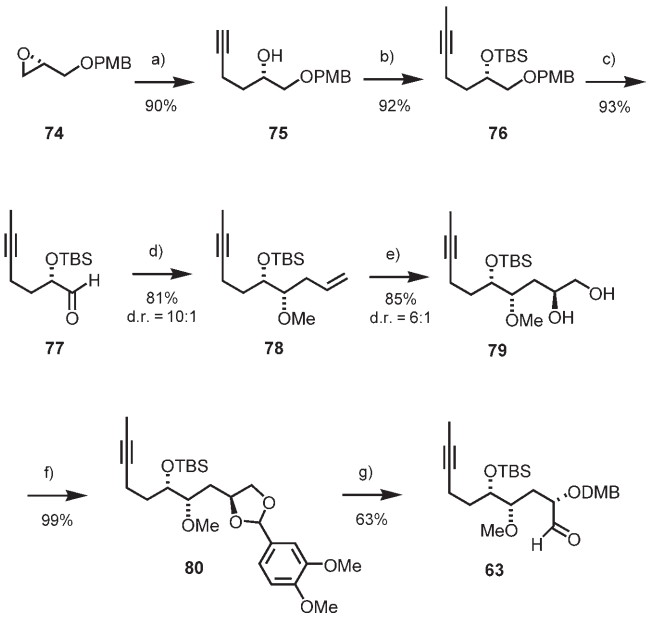


Scheme 12. Retrosynthetic analysis of apoptolidin according to Nicolaou et al.



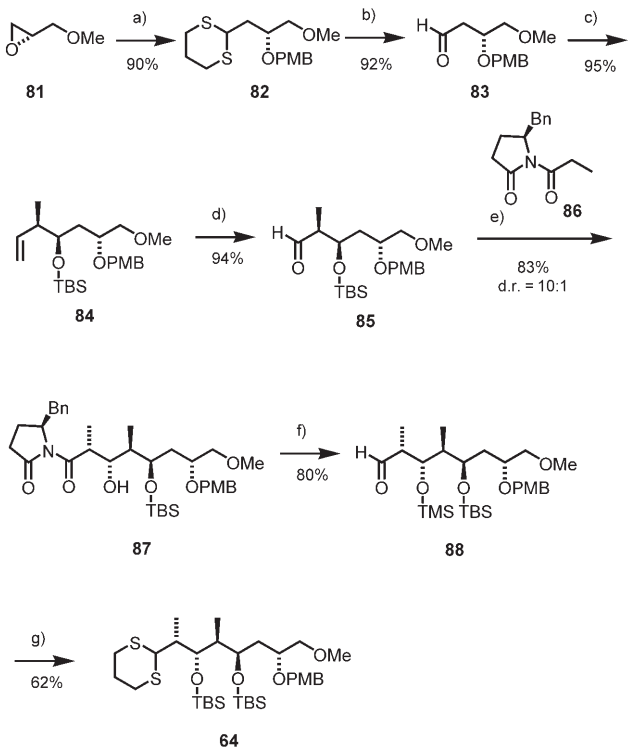
Scheme 13. a) (Z)-(+)-Crotyldiisopinocampheylborane, $BF_3{\cdot}OEt_2$, THF, −78 °C, 6 h; $NaBO_3{\cdot}4H_2O$, THF, H_2O; b) 1. TBSOTf, 2,6-lutidine, CH_2Cl_2, 0 °C, 2 h; 2. O_3, Sudan red 7B, CH_2Cl_2, −78 °C; then PPh_3, −78→25 °C, 12 h; c) 1. $(OMe)_2POC(=N_2)COCH_3$, NaOMe, THF, −78→25 °C, 1 h; 2. *n*BuLi, MeI, −78→25 °C, 2 h; d) catecholborane, 9-BBN, neat, 80 °C; e) phosphare buffer (pH 7), THF, 25 °C, 2 h; f) 1. MnO_2, $Ph_3P{=}C(CH_3)CO_2Et$, CH_2Cl_2, 25 °C, 42 h; 2. LiOH, THF, H_2O, 25 °C, 12 h; 3. CH_2N_2, Et_2O, 0 °C, 30 min; g) $[PdCl_2(Ph_3P)_2]$, NaOAc, MeOH, 70 °C, 5 h; h) 1. TBAF, THF, 0→25 °C, 1 h; 2. *n*Bu_3SnH, $[PdCl_2(Ph_3P)_2]$, THF, 0 °C, 30 min. 9-BBN = 9-borabicyclononane.

alkene **84** as a single stereoisomer. The latter was transformed through dihydroxylation/periodate cleavage to aldehyde **85**. An Evans aldol reaction of **85** with **86** gave the *syn* aldol

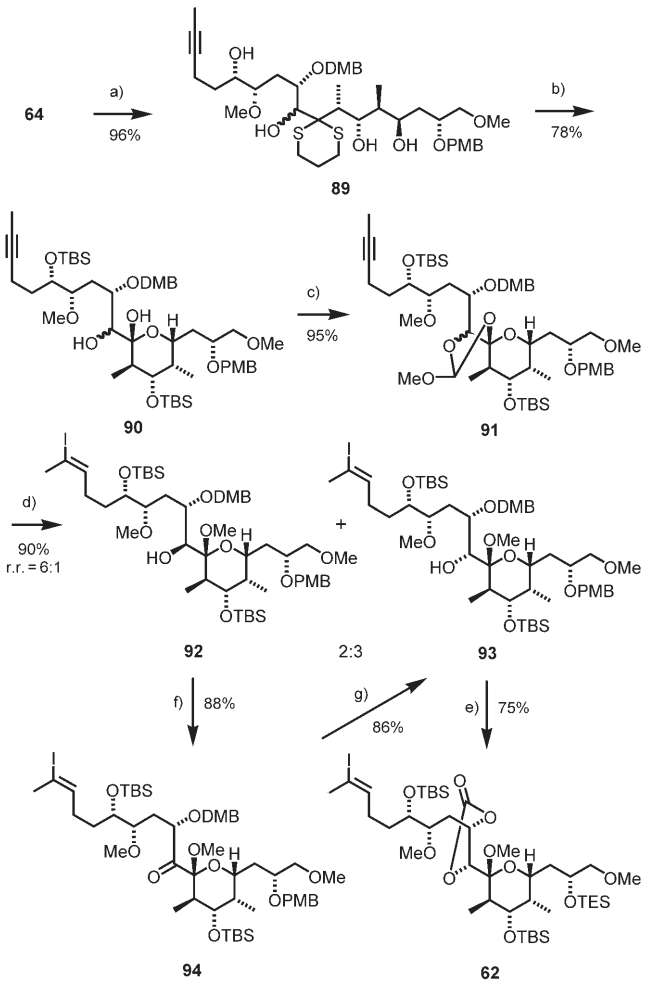


Scheme 14. a) Allenylmagnesium bromide, Et_2O, −78 °C, 1 h; b) 1. TBSOTf, 2,6-lutidine, CH_2Cl_2; 2. *n*BuLi, MeI, THF; c) 1. DDQ, CH_2Cl_2/H_2O; 2. SO_3·py, Et_3N, DMSO/CH_2Cl_2, 0 °C, 3 h; d) 1. (+)-allyldiisopinocampheylborane, Et_2O, −100 °C, 2 h; H_2O_2, NaOH; 2. MeOTf; e) $K_3[Fe(CN)_6]$, K_2CO_3, $(DHQ)_2$-PYR, OsO_4, *t*BuOH/H_2O, 0 °C, 12 h; f) 3,4-dimethoxybenzaldehyde, CSA, toluene, 110 °C; g) 1. DIBAH, CH_2Cl_2, −78 °C, 2. SO_3·py, Et_3N, DMSO/CH_2Cl_2. DDQ = 2,3-dichloro-5,6-dicyano-1,4-benzoquinone, $(DHQ)_2$-PYR = 2,5-diphenyl-4,6-bis(9-*O*-dihydroquinyl)pyrimidine, DMSO = dimethylsulfoxide.

 © 2006 Wiley-VCH Verlag GmbH & Co. KGaA, Weinheim



Scheme 15. a) 1. 1,3-Dithiane, *n*BuLi, THF, −78→25 °C; 2. PMBCl, NaH, DMF; b) MeI, K_2CO_3, MeCN/H_2O, 45 °C, 4 h; c) (*Z*)-(+)-crotyldiisopinocampheylborane, $BF_3{\cdot}OEt_2$, THF, −78 °C, 6 h; $NaBO_3{\cdot}4\,H_2O$, THF, H_2O; TBSOTf, 2,6-lutidine, CH_2Cl_2; d) OsO_4, NMO, *t*BuOH/THF/H_2O; $NaIO_4$, phosphate buffer pH 7; e) **86**, Bu_2BOTf, Et_3N, CH_2Cl_2, −78→0 °C, 2 h; H_2O_2/H_2O; f) 1. HNMe(OMe) HCl, $AlMe_3$, CH_2Cl_2; 2. TMSOTf, 2,6-lutidine; CH_2Cl_2, −30 °C; 3. DIBAH, CH_2Cl_2, −78 °C; g) 1. $HS(CH_2)_3SH$, $BF_3{\cdot}OEt_2$, CH_2Cl_2, −30 °C; 2. TBSOTf, 2,6-lutidine; CH_2Cl_2, 0→25 °C. PMB = *p*-methoxybenzyl.



Scheme 16. a) 1. *t*BuLi, HMPA, THF, −78 °C, 1 h; **63**, −100 °C, 2 h; 2. TBAF, THF; b) 1. $PhI(OCOCF_3)_2$, MeCN, phosphate buffer pH 7, 0 °C, 10 min; 2. TBSOTf, 2,6-lutidine, −78 °C; c) $(MeO)_3CMe$, PPTS, CH_2Cl_2, 25 °C, 12 h; d) $[(Cp)_2ZrHCl]$, THF, 65 °C; I_2, THF, −25 °C, 2 min; e) 1. DDQ, CH_2Cl_2, phosphate buffer pH 7, 0–25 °C, 4 h; 2. triphosgene, pyridine, CH_2Cl_2, −78→0 °C, 30 min; 3. TESOTf, 2,6-lutidine; f) DMP, $NaHCO_3$, CH_2Cl_2; g) $NaBH_4$, MeOH/Et_2O, 0→25 °C. HMPA = hexamethylphosphoramide, DMP = Dess–Martin periodinane, r.r. = regioisomeric ratio.

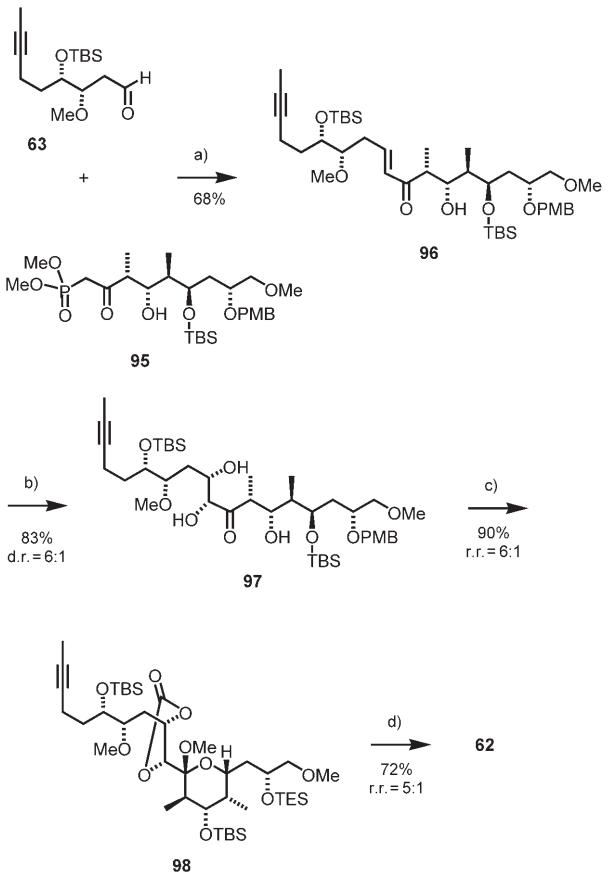
product **87**. The oxazolidinone in **87** was converted into the corresponding Weinreb amide and reduced to aldehyde **88**. A final formation of a thioketal then led to **64**.

The reaction of the lithiated thioketal **64** with aldehyde **63** led to alcohol **89** as an epimeric mixture (3:2, Scheme 16). Cleavage of the thioketal group in **89** resulted in the formation of the six-membered hemiketal. A subsequent chemoselective TBS-protection led to **90**, which was converted into the orthoester **91**. The following regioselective hydrozirconation gave, after iodine treatment, the two separable alkenyl iodides **92** and **93**. The cleavage of the orthoester under the hydrozirconation conditions and the formation of the methyl glycoside are noteworthy and unforeseen. The desired epimer **93** was converted after oxidative cleavage of the PMB ether into carbonate **62**. An oxidation/reduction sequence brought the undesired epimer **92** back to the main route (**92**→**94**→**93**).

The synthetic route to **62** shown in Scheme 16 suffered from low stereoselectivity in the formation of **89** and prompted the developement of a better synthesis for this building block (Scheme 17). A Horner–Wadsworth–Emmons reaction of aldehyde **63** and phosphonate **95** gave enone **96**. The asymmetric dihydroxylation of **96** with AD-mix-α introduced the C19/20 diol functionality in **97** with a 6:1 stereoselectivity. A comparison of the substrate-controlled dihydroxylation from the synthesis developed by Koert and co-workers (**40**→**41**, Scheme 7) with the reagent-controlled dihydroxylation of the synthesis described by Nicolaou et al. reveals a similar degree of stereoselectivity was achieved. Nicolaou et al. finish the synthesis of **62** by a protective-group manipulating sequence (**97**→**98**) followed by hydrozirconation/treatment with iodine to give **62**.

Coupling of alkenylstannane **61** with alkenyl iodide **62** under Stille conditions provided the product **60** in very good yield (Scheme 18). It is instructive to compare this cross-coupling step with the related reaction from the synthesis used by Koert and co-workers (**9** + **10**→**55**, Scheme 10). The Pd coupling works fine for the combination of disubstituted alkenylstannane/trisubstituted alkenyl iodide in the route used by Nicolaou et al. In the system used by Koert and co-workers, a Cu-Tc coupling is required for the combination of

 © 2006 Wiley-VCH Verlag GmbH & Co. KGaA, Weinheim



Scheme 17. a) $Ba(OH)_2$, THF/H_2O, 0→25 °C, 30 min; b) $K_3[Fe(CN)_6]$, K_2CO_3, $MeSO_2NH_2$, $(DHQ)_2$-PHAL, OsO_4, *t*BuOH/H_2O, 0 °C, 12 h; c) 1. TBAF/SiO_2, THF; 2. TsOH, MeOH, 25 °C, 2 h; 3. triphosgene, pyridine, CH_2Cl_2, −78→0 °C; 4. TBSOTf, 2,6-lutidine, CH_2Cl_2; d) 1. $[(Cp)_2ZrHCl]$, THF, 65 °C; I_2, THF, −25 °C, 2 min; 2. triphosgene, pyridine, CH_2Cl_2, −78→0 °C, 30 min; 3. DDQ, CH_2Cl_2, phosphate buffer pH 7, 0→25 °C, 1 h; 4. TESOTf, 2,6-lutidine, CH_2Cl_2, −78 °C. $(DHQ)_2$-PHAL = hydroquinone 1,4-phthalazinediyl ether.

disubstituted alkenyl iodide/trisubstituted alkenylstannane. A Stille coupling was also used successfully by Nicolaou et al. in an earlier synthesis of the macrocyclic core of apoptolidinone.[40] The glycosylation of **60** with the glycosyl sulfoxide **28** following the Kahne protocol and a subsequent base hydrolysis gave dihydroxy acid **59**. Nicolaou et al. mastered the problems with the hydrolysis of the methyl ester in **59**, which forced Koert and co-workers to choose a cyanomethyl ester. A ring-size-selective macrolactonization of **59** led to **99** in an overall yield for the glycosylation/macrolactonization sequence of 24%.

Selective cleavage of the TES ether at O27 in **99** paved the way for the introduction of the disaccharide moiety (Scheme 19). Reaction of the resulting alcohol **58** with the glycosyl fluoride **100** gave α-glycoside **101** as the exclusive stereoisomer. The use of the glycosyl fluoride is advantageous compared with the glycal method used by Koert and co-workers, because the removal of the iodide in the glycal method requires an extra step.

The global deprotection of **101** to apoptoldin (**1**) proved problematic. After careful optimization, all the silyl ethers and the ester at O20 were removed first (**101**→**102**), before using TsOH in THF/H_2O to cleave the methyl glycoside and give apoptolidin (**1**).

3.4. Syntheses of Apoptolidinone

The synthesis of apoptolidinone (**6**) by Sulikowski and co-workers[41] uses a strategy different from those used by Nicolaou et al. and Koert and co-workers. Difficulties with deprotection of a methylglycoside at C21 are avoided by the formation of the six-membered hemiketal in the last step of the synthesis. A Suzuki cross-coupling between C5 and C6 was chosen as the key step for the closure of the 20-membered macrolide ring. This convergent approach minimized the number of steps and the use of protective groups.

The starting point of the synthesis was aldehyde **103**, which gave the secondary alcohol **104** in a chelation-controlled reaction with the Grignard reagent **45** (Scheme 20).[41] Tin–iodine exchange, protection of the alcohol as a TES ether, and cleavage of the thioacetal delivered aldehyde **105**, which was coupled with boronic ester **106** under Suzuki conditions to yield the highly unsaturated aldehyde **107**. A Mukaiyama aldol reaction of **107** with the silyl enol ether **108** gave the β-hydroxy ketone **109** with a stereoselectivity of 4:1 which could be converted in the presence of acid **110** into ester **111** under Yamaguchi conditions.

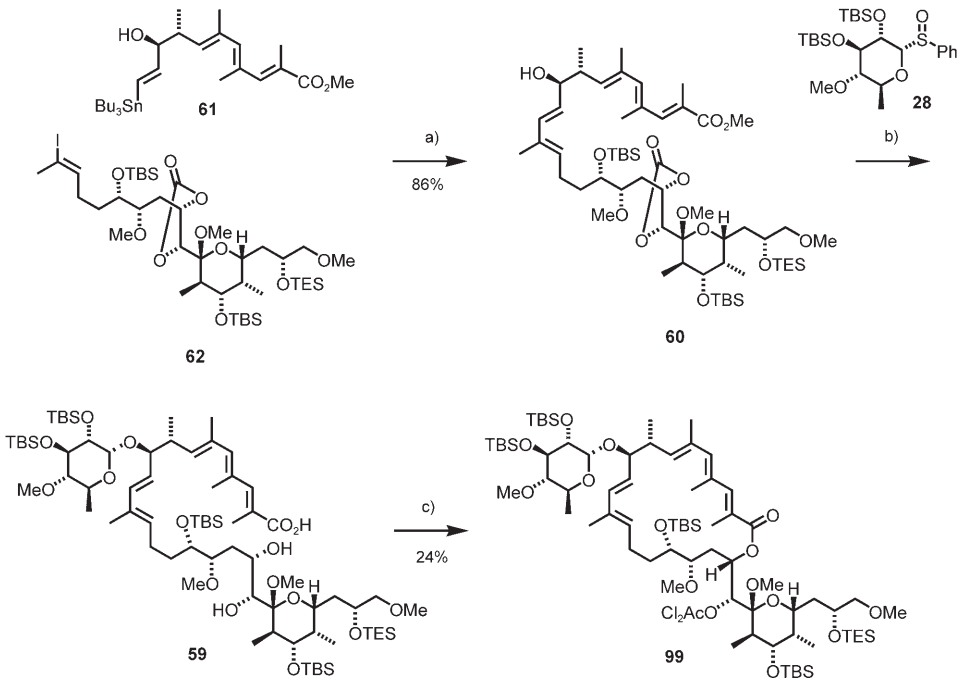
A stereoselective aldol reaction of ketone **111** with aldehyde **112** provided the corresponding *syn* aldol product, which was protected as a TES ether to yield **113** (Scheme 21).[41] A cross-metathesis reaction of **113** with propenylboronate catalyzed by **114** gave the alkenyl boronate **115**, which was used directly for the intramolecular Suzuki coupling to produce the 20-membered ring in **116**. The sequence **113**→**115**→**116** powerfully demonstrates the potential of modern cross-coupling chemistry. Finally, a fluoride-mediated cleavage of all the silyl ethers in **116** resulted in the formation of the six-membered hemiketal and gave apoptolidinone (**6**).

A related approach to the C1–C15 segment using three consecutive Suzuki coupling reactions has been reported.[41c] Crimmins et al. reported very recently the synthesis of apoptolidinone using cross-metathesis and thiazolidinone chiral auxiliaries.[41d]

3.5. Synthetic Studies on Apoptolidin

A synthesis of the C1–C21 macrolide fragment **124** was described by Toshima et al. (Scheme 22).[42a] The addition of a lithium acetylide to aldehyde **117** introduced the C9 stereocenter (**117**→**118**). Aldehyde **118** was converted into **119** by two *E*-selective Wittig reactions. A Horner–Wadsworth–Emmmons reaction generated the C1–C3 fragment (**119**→**120**), and after hydrostannylation of the triple bond and subsequent hydrolysis of the ethyl ester, the acid **121** was obtained. Esterfication of **121** with alcohol **122** according to the Yamaguchi protocol gave compound **123**. A final intramolecular Stille coupling led to the 20-membered macrolide

 © 2006 Wiley-VCH Verlag GmbH & Co. KGaA, Weinheim



Scheme 18. a) $[PdCl_2(MeCN)_2]$, DMF, 25 °C, 15 h; b) 1. **28**; Tf_2O, DTBMP, Et_2O, −90 °C, 1.5 h; 2. KOH, dioxane/H_2O, 65 °C, 24 h; c) 1. 2,4,6-trichlorobenzoyl chloride, Et_3N, THF; DMAP, toluene, 25 °C, 12 h; 2. $(Cl_2Ac)_2O$, pyridine, 0 °C, 5 min.

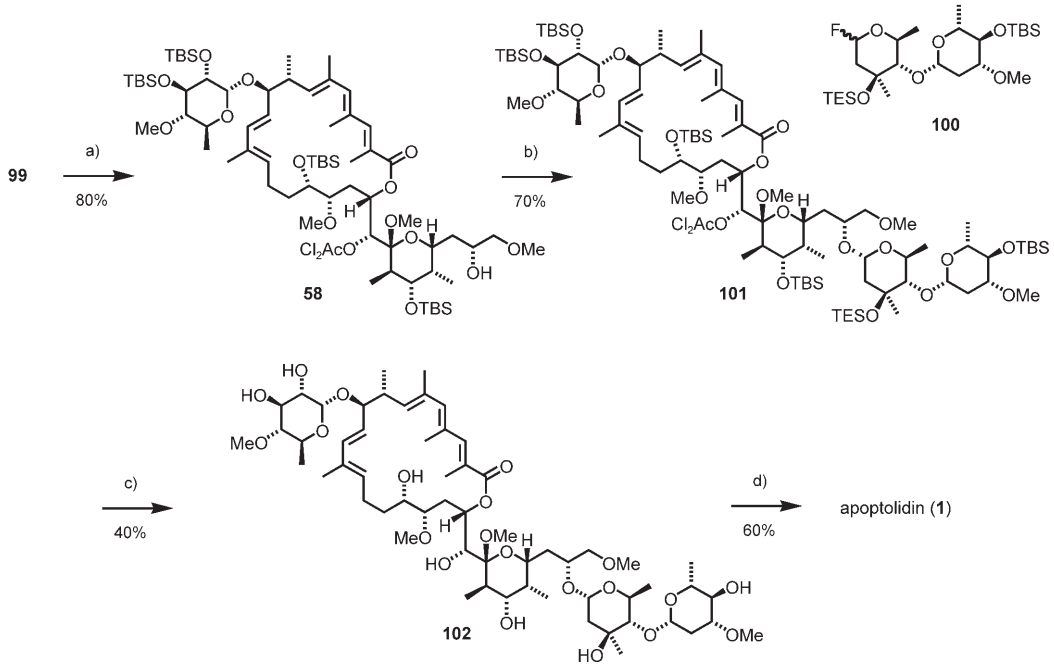
124 in 30% yield. Toshima's research group achieved the synthesis of the C12–C28 fragment **125** through a highly stereoselective aldol reaction.[42b]

Paquette and Taylor reported a stereoselective synthesis of the C1–C11 fragment **134** (Scheme 23).[43] An Evans aldol reaction of aldehyde **126** with **127** was used for the generation of the stereocenters at C8 and C9. The resulting aldol addition product could be transformed into the aldehyde **128**, and addition of isopropenyllithium gave alcohol **129**. Treatment of **129** with thionyl chloride afforded the *E*-allyl chloride **130** stereoselectively. Oxidation of the allyl chloride with trimethylamine *N*-oxide (TMNO) gave the unsaturated aldehyde **131**. A repeat of the former sequence transformed aldehyde **131** via the allylic alcohol **132** into the unsaturated aldehyde **133**. The C1–C3 fragment was finally introduced by a Horner–Wadsworth–Emmons reaction (**133**→**134**).

An alkylative oxidation strategy for the preparation of the C21–C26 segment of apoptolidin was reported by the Fuchs and co-workers.[44a] Crimmins, Long et al. have achieved the enantioselective synthesis of the apoptolidin sugars.[44b]

3.6. Structure–Function Relationship of Apoptolidin and its Derivatives

Khosla and co-workers have identified the mitochondrial F_0F_1-ATPase as a target for apoptolidine. Scheme 24 summarizes experimental data for the binding of apoptolidin and some derivatives to mitochondrial F_0F_1-ATPase.[23c,24,45] The natural product showed strongest



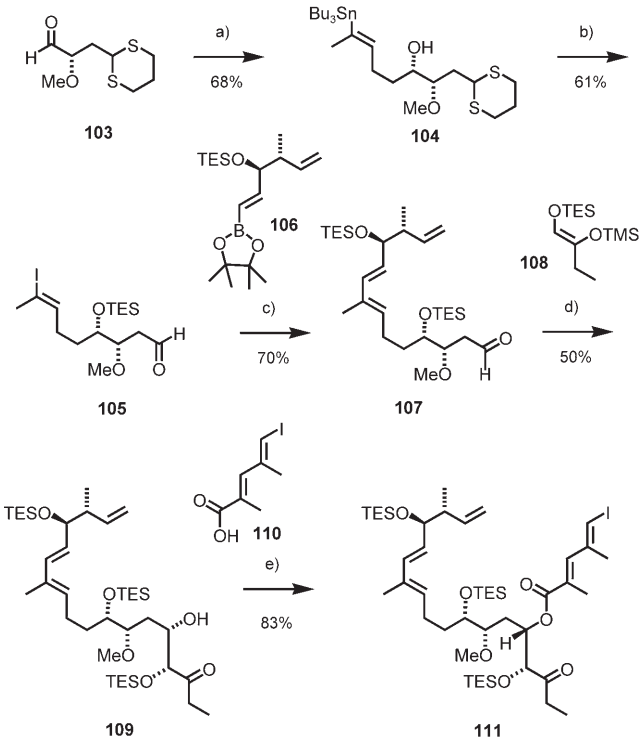
Scheme 19. a) PPTS, $MeOH/CH_2Cl_2$, 0 °C, 1.5 h; b) **100**, $SnCl_2$, Et_2O, 25 °C, 12 h; c) 1. HF·pyridine, THF, −25 °C, 96 h; 2. Et_3N/MeOH, 25 °C, 3.5 h; d) TsOH, THF/H_2O, 0 °C, 2.5 h.

 © 2006 Wiley-VCH Verlag GmbH & Co. KGaA, Weinheim

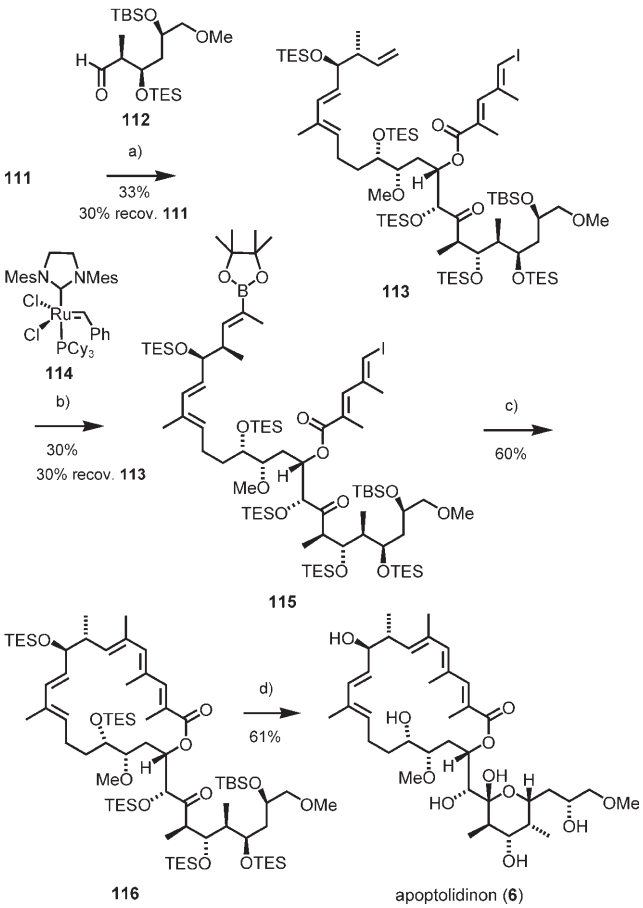
binding. Removal of the disaccharide at O27 and the six-membered hemiketal leads to a slight reduction in the enzyme inhibition. Derivative **135** was accessible from the natural product by acid hydrolysis[23c] and compound **136** by oxidative cleavage.[45]

The cyctotoxicity of apoptolidin and its derivatives was investigated by several research groups (Scheme 25).[21,23,31,46,47] The natural product **1** kills selected tumor cells in the nanomolar range. It is noteworthy that some cancer cell lines are very sensitive to apoptolidin, while others are not. As seen from the IC_{50} value of **2**, the methyl glycoside at C21 has no considerable effect on the cyctoxicity. The aglycone apoptolidinone (**6**) loses all activity.[47] This observation shows that the sugar moieties are crucial for the antitumor activity. Removal of the disaccharide portion at O27 reduced the activity strongly (**137**),[31d,46] while without the six-membered hemiketal only a slight activity is retained (**138**).[31d] The β anomer of the L-glucose at O9 exhibits no activity (**139**).[46] A growth inhibition assay with H292 cells showed similar potencies for apoptolidin (**1** = apoptolidinA), apoptolidin B, and apoptolidin C.[25c]

A possible explanation for the differences of the F_0F_1-ATPase data and the cytotoxicities is that the macrolide part is crucial for binding to the enzyme while the disaccharide portion at O27 facilitates transport to the mitochondrial target. The loss of activity for the L-glucose anomer **139** indicates that this sugar may be involved in target recognition too.



Scheme 20. a) **45**, Et_2O, −78 °C; b) 1. I_2, CH_2Cl_2, 0 °C; 2. TESCl, imidazole; 3. MeI, K_2CO_3, MeCN/pH 7 buffer; c) **106**, [$Pd(Ph_3P)_4$], TlOH, THF/H_2O, 20 °C; d) **108**, $BF_3{\cdot}OEt_2$, CaH_2, CH_2Cl_2, −94 °C; e) **110**, 2,4,6-trichlorobenzoyl chloride, Et_3N, DMAP, toluene, −78→28 °C.



Scheme 21. a) 1. LHMDS, **112**, THF, HMPA, −78 °C, 2 h; 2.1 TESOTf, 2,6-lutidine, CH_2Cl_2, 0 °C; b) isopropenylpinacol boronic ester, **114**, CH_2Cl_2, reflux, 6 h; c) [$Pd(Ph_3P)_4$], TlOEt, THF/H_2O, 28 °C, 30 min; d) HF·pyridine, THF, −10 °C, 12 h, then −5 °C, 5 h. LHMDS = lithium hexamethyldisylazide.

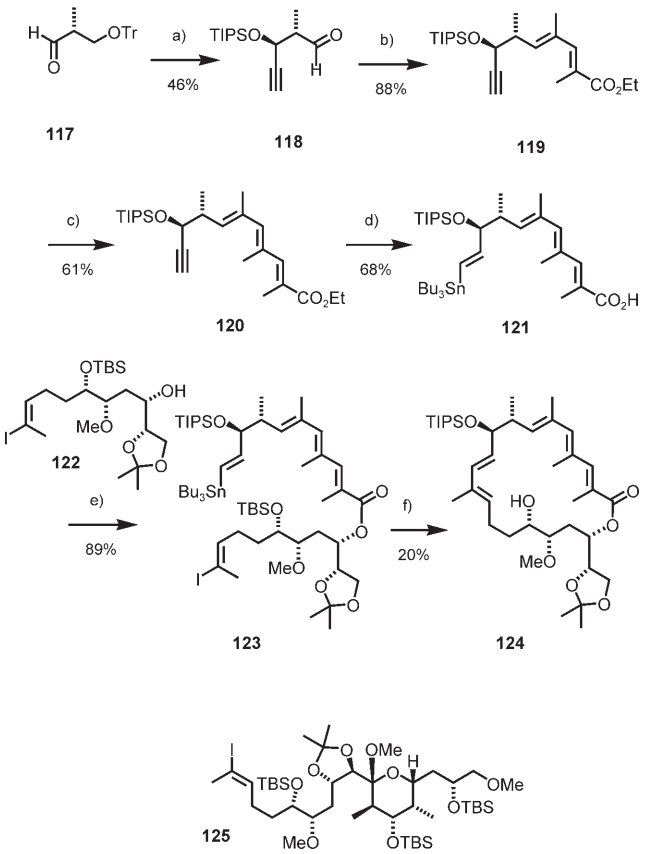
4. Other Natural Products which Regulate Apoptosis

4.1. Phosphataseinhibitors: Calyculin A and Okadaic acid

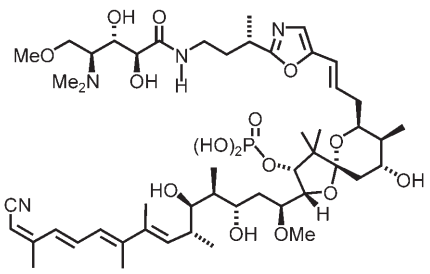
Calyculin A (**140**) and okadaic acid (**141**) are potent inhibitors of protein phosphatases type 1 (PP1) and type 2A (PP2A).[48] Both compounds induce apoptosis in several cancer cell lines through a caspase-3-dependent mechanism.[49] This result demonstrates the importance of caspase regulators as drug targets. Calyculin A was isolated in 1986 from the marine sponge *Discodermia calyx*.[50] The total syntheses of *ent*-**140**,[51] **140**,[52] and related calyculins[53] have been reported.

Okadaic acid (**141**) is produced by various species of dinoflagellate microalgae,[54] which frequently accumulate in sponges, and have been shown to be the cause of diarrhetic shellfish poisoning.[55] It was first isolated as a potent antitumor agent from the sponges *Halichondria okadai* and *H. melanodocia*. Its structure was elucidated in 1981 by an X-ray analysis[56] and several total syntheses of okadaic acid (**141**) have been reported.[57–59]

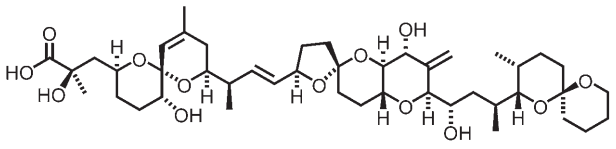
© 2006 Wiley-VCH Verlag GmbH & Co. KGaA, Weinheim



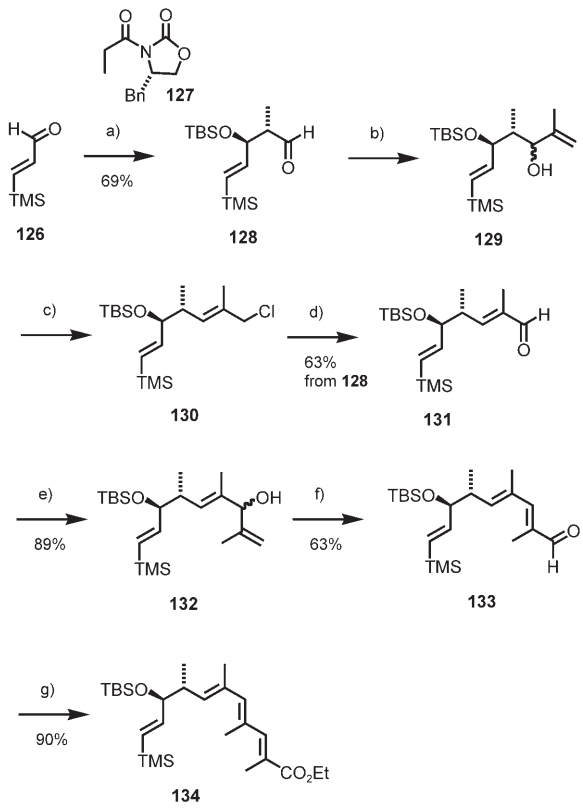
Scheme 22. a) 1. *n*BuLi, HCCTMS, THF, −78 °C; 2. K_2CO_3, MeOH; 3. TIPSOTf, pyridine; 4. CSA, MeOH/CH_2Cl_2; 5. Swern oxidation; b) 1. $Ph_3P{=}C(Me)CO_2Et$, toluene, 110 °C; 2. DIBAH, toluene, −78 °C; 3. MnO_2, CH_2Cl_2, 25 °C; 4. $Ph_3P{=}C(Me)CO_2Et$, toluene, 110 °C; c) 1. DIBAH, toluene, −78 °C; 2. MnO_2, CH_2Cl_2, 25 °C; 3. $(EtO)_2OPCH(Me)CO_2Et$, *n*BuLi, THF, 0 °C; d) 1. Bu_3SnH, $[PdCl_2(PPh_3)_2]$, toluene, 0 °C, 45 min; 2. LiOH, dioxane/H_2O, 80 °C, 10 h; e) 2,4,6-trichlorobenzoyl chloride, Et_3N, THF, DMAP, toluene 25 °C; f) 1. TBAF, THF, 25 °C; 2. $[PdCl_2(PPh_3)_2]$, $Ph_2PO_2NBu_4$, LiCl, DMF, 25 °C, 3 h. TIPS = triisopropylsilyl.



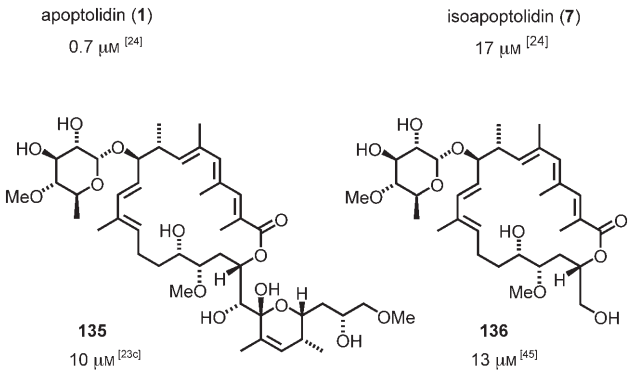
calyculin A (**140**)



okadaic acid (**141**)



Scheme 23. a) 1. Bu_2BOTf, Et_3N, CH_2Cl_2, d.r. > 20:1; 2. TBSOTf, 2,6-lutidine, CH_2Cl_2; 3. $LiBH_4$, Et_2O/H_2O; 4. DMP, CH_2Cl_2; b) isopropenyllithium, THF, −78 °C; c) $SOCl_2$, pentane/Et_2O, 0→25 °C; d) TMNO, DMSO; e) 1. isopropenyllithium, THF, −78 °C; f) 1. $SOCl_2$, pentane/Et_2O, 0→25 °C; 2. TMNO, DMSO; g) $(EtO)_2OPCH(Me)CO_2Et$, *n*BuLi, THF, 0→25 °C.

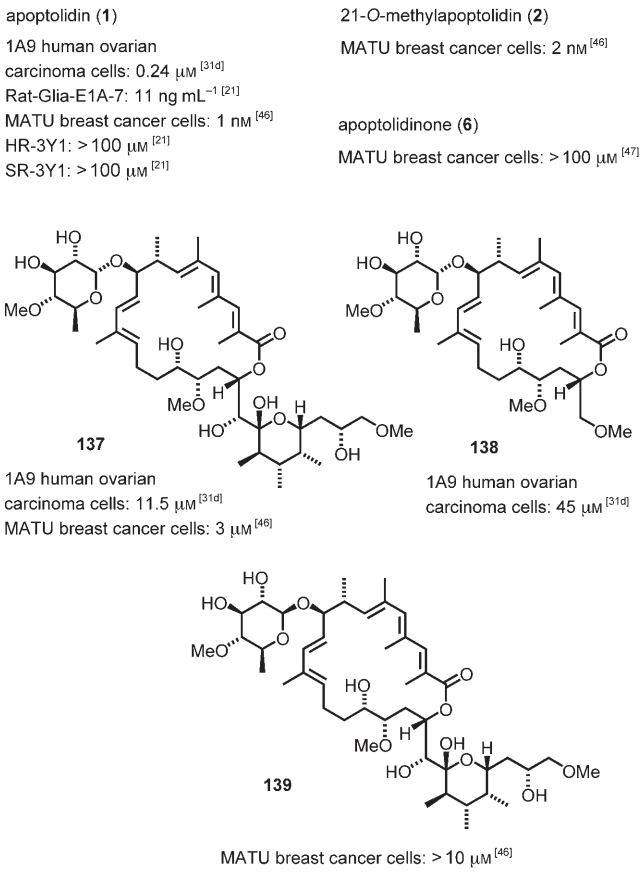


Scheme 24. Inhibition of mitochondrial F_0F_1-ATPase by apoptolidin and selected derivatives. The IC_{50} values are shown.

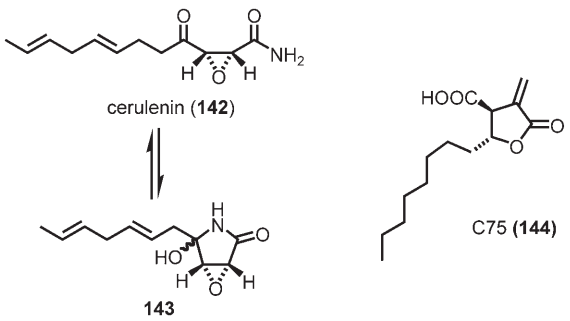
4.2. Inhibitors of Fatty Acid Synthase: Cerulenin

Besides their ability to maintain a high level of anaerobic carbon metabolism (the Warburg effect), a substantial subset of human cancer cells, for example, breast and colorectal cancer cells, express elevated levels of fatty acid synthase. Thus, fatty acid biosynthesis was reasoned to be a valuable target for antitumor drugs.[60] Indeed, it was shown that cerulenin (**142**), a noncompetitive inhibitor of fatty acid

 © 2006 Wiley-VCH Verlag GmbH & Co. KGaA, Weinheim



Scheme 25. Activity of apoptolidin and selected derivatives against different cancer cell lines. The IC_{50} values are shown.

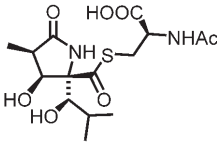


synthase, induced DNA fragmentation and morphological features characteristic of apoptosis in human breast cancer cells.[61] Interestingly, it was shown that inhibition of fatty acid synthesis by cerulenin results in a biphasic stress response: an early accumulation in the S and G2 phase and a late growth arrest in G1 and G2 with an accumulation of p53 and p21 proteins.[62] The p53 function in these cells was probably important in protecting the cells from cerulenin-induced apoptosis, since cells expressing a dominant negative mutant p53 gene underwent extensive apoptosis after exposure to this fatty acid synthesis inhibitor.[62] Thus, it was speculated that cerulenin and other synthetic compounds of this class of cytostatics, for example, C75, might be clinically useful against malignancies carrying p53 mutations. The significance of the mitochondrial pathway for the cerlulenin-meditiated apoptosis was confirmed by the rapid release of cytochrome C.[63]

(+)-Cerulenin (**142**) was first isolated from *Cephalosporium caerulens* by Hata et al. in 1960.[64] Cerulenin was found to exist as a mixture of diastereomeric hydroxylactams **143** in protic solvents, but the nature of the actual active species has been a matter of speculation[65] The natural product has been the target of numerous "racemic" and enantioselective total syntheses.[66], The in vivo activity of cerulenin turned out to be limited because of its chemical instability, and a synthetic, chemically stable analogon C75 (**144**) was developed and synthesized.[67]

4.3. Proteasome Inhibitors: Lactacystin

Experimental evidence has been provided that transcription factor NFκB plays an important role in preventing apoptotic cell death in some cancers by a proteasome-dependent mechanism. Proteasome inhibitors are therefore potential enhancers of apoptotic cell death. It was shown that the potent proteasome inhibitor lactacystin (**145**) in conjunction with the tumor necrosis factor (TNF) induced apoptosis in human lung adenocarcinoma cells.[68]



lactacystin (**145**)

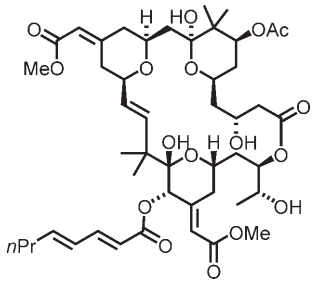
Furthermore, data were presented about the synergistic induction of apoptosis by minimally toxic concentrations of the protein kinase C (PKC) activator and downregulator bryostatin 1 and the proteasom inhibitor lactacystin.[69] These data suggest that leukemic cell apoptosis is modulated by dysregulation of the PKC/mitogen-activated protein kinase cascade following exposure to lactacystin. In Jurkat and Namalwa cells, however, treatment with lactacystin (**145**) alone was shown to be sufficient to induce apoptosis. In these cells, proteasome inhibition modulated the balance among proapoptotic and antiapoptotic Bcl-2 family members, and proapoptotic Bik/Nbk accumulated in the mitochondria thereby influencing the electron-transport chain.[70] The stabilizing effect of lactacystin on activate caspase-3 subunits was identified as the proapoptotic factor.[71] Lactacystin (**145**) was isolated from a streptomyces bacterial strain (OM-6519) found in a Japanese soil sample,[72] and this natural product has been the target of several total syntheses.[73]

4.4. Proteinkinase C Inhibitors: Bryostatin and Staurosporine

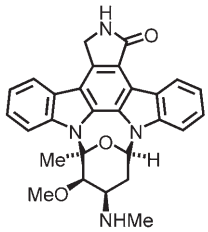
The important role of protein kinase C (PKC) in cellular processes relevant to neoplastic transformation, carcinogenesis, and tumor-cell invasion renders this enzyme a suitable target for anticancer therapy.[74]

Bryostatin 1 (**146**) is a naturally occuring PKC activator that has already reached clinical phase II trials, although first results only showed marginal efficacy in the treatment of metastatic colorectal cancer.[75] In accordance with the anti-apoptotic properties of PKC,[76] it was reported that bryosta-

 © 2006 Wiley-VCH Verlag GmbH & Co. KGaA, Weinheim



bryostatin 1 (**146**)



staurosporine (**147**)

tin 1 acts as an inhibitor of apoptosis in U937 cells.[77] Similarly, treatment of human THP-1 monocytic leukemic cells with bryostatin 1 rendered these cells refractory to proteasome-inhibitor-induced apoptosis.[78] However, in the acute lymphoblastic pre-B leukemia cell-line REH, bryostatin 1 induced a downregulation of Bcl-2, thereby sensitizing the cells for antitubulin agents and drug-induced apoptosis.[79]

A synergistic effect of bryostatin 1 and the proteasome inhibitor lactacystin on apoptosis of human leukemia cells was also observed in U937 cells.[69] These results might be explained by the fact that long-term exposure to bryostatin 1 does not only lead to activation of PKC but also to complete downregulation of the enzyme.

Since the first description of bryostatin 1 (**146**) by Pettit et al. in 1982,[80] the bryostatin family has increased to 18 members, all of them being 20-membered macrolactones which differ mainly in the C7 and C20 substitution pattern.[81] Bryostatin 7 was synthesized by Masamune and co-workers,[82] bryostatin 2 by Evans et al.,[83] and bryostatin 3 by Nishiyama, Yamamura, and co-workers.[84] Wender et al. developed an approach to a series of simplified bryostatin analogues to obtain readily accessible clinical candidates. These were used in further investigation of the PKC binding mode.[85]

The inhibition of PKC by staurosporine (**147**) leads to induction of apoptotic cell death. Interestingly, mechanistic studies revealed that staurosporine-induced apoptosis originates from different points in the cell cycle, depending on the human papilloma virus (HPV) and p53 status of the cells; whereas HPV positive, wild-type p53 cells triggered cell death from G2/M exclusively, G1 cytoplasmic extracts from HPV negative, mutated p53 cells were efficient at inducing hallmarks of apoptosis of isolated cell nuclei.[86] Detailed analysis of apoptosis signaling in staurosporine-induced cell death showed that staurosporine uses distinct pathways of apoptosis and caspase activation which are at least in part different from the pathways triggered by DNA-damaging anticancer drugs or death receptors. For example, it was shown that overexpression of a dominant negative caspase-9 mutant abolished the activation of the caspase-9-dependent caspase cascade after treatment with an anticancer drug but not after treatment with staurosporine.[87] The staurosporine-induced apoptosis in Chang liver cells is associated with down-regulation of BCl-2 and BCl-X_L.[88] Thus, these unique features of staurosporine may allow the chemoresistance of tumor cells to be by-passed, and further encourages clinical trials of derivatives of this PKC inhibitor in antitumor therapy.

Staurosporine (**147**) belongs to the class of indolcarbazole alkaloids and was isolated from *Streptomyces staurosporeus* by Omura et al. in 1977.[89] Its structure was established by X-ray structure analysis,[90,91] and the absolute configuration was initially assigned from CD measurements.[92] The structure and configuration later had to be revised,[93] with chemical synthesis furnishing the final structural proof.[94,95]

4.5. Microtubule-Interfering Natural Products

Microtubule-interfering agents can disrupt the formation and degradation of microtubule dynamics, which results in the destruction of the mitotic spindle in dividing cells, cell-cycle arrest at the M phase, and finally apoptosis.[96] For this reason, microtubules are among the most successful targets for anticancer therapy.[97] There are several tubulin-binding sites known for antimitotic natural products: the vinca domain (for example, for vinblastine, halichondrins, dolastatins) as well as the colchicine domain and the taxane site (for example, for taxol, epothilones, discodermolide). Typical microtubule-interfering natural products are colchicine (**148**),[98] taxol (**149**),[99] epothilones A (**150**) and B (**151**),[100] laulimalide (**152**),[101] eleutherobin (**153**),[102] and discodermolide (**154**).[103] The intense synthetic efforts in the field of microtubule-interfering natural products are beyond the scope of the article.[104]

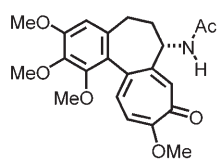
4.6. Heat-Shock Protein Inhibitors: Geldanamycin

The heat-shock protein 90 (HSP90) is a chaperone that interacts with various client proteins and is an emerging target for breast-cancer therapy.[105] Inhibition of HSP90 by geldanamycin (**155**) initiates apoptosis.[106] Geldanamycin was isolated from *Streptomyces hygroscopicus var. geldanus* in 1970.[107] So far, only one total synthesis has been reported.[108] Derivatives of geldanaymcin with increased clinical efficacy and water solubility have been synthesized and evaluated.[109]

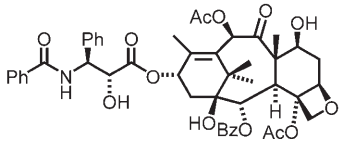
4.7. MAP-Kinases: Betulinic Acid

Betulinic acid (**156**), a triterpene found in the bark of the white birch, induces programmed cell death in melanoma tumor cells.[110] Its mode of action involves activation of

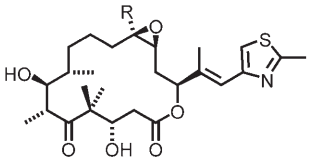
 © 2006 Wiley-VCH Verlag GmbH & Co. KGaA, Weinheim



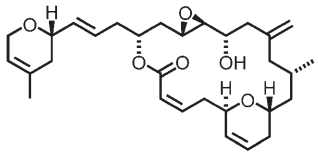
colchicine (**148**)



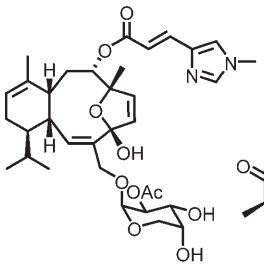
taxol (**149**)



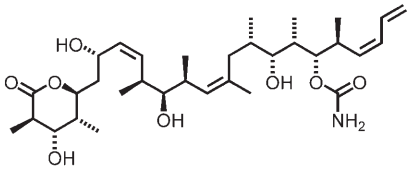
epothilone A (**150**) R = H
epothilone B (**151**) R = CH_3



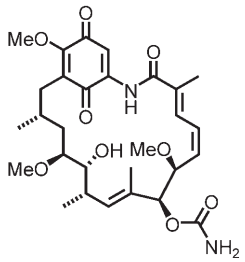
laulimalide (**152**)



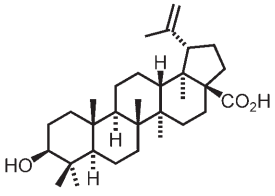
eleutherobin (**153**)



discodermolide (**154**)



geldanamycin (**155**)

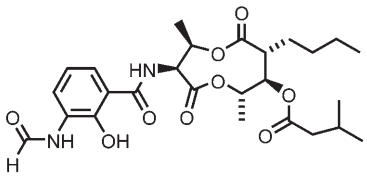


betulinic acid (**156**)

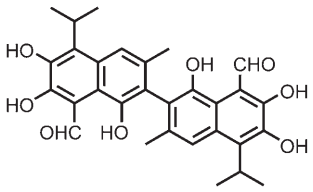
mitogen-activated protein kinases (MAPKs) and gradual depolarization of the mitochondrial membrane potential.[111] Betulinic acid potently induces apoptosis in leukemia cells and is currently being further evaluated for the treatment of leukemia.[112]

4.8. Bcl-2 Inhibitors: Antimycin A, Gossypol, and Tetrocarcin A

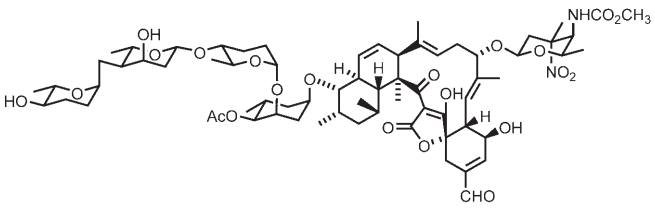
Inhibitors of the antiapoptotic BCl-2 protein are a new class of promising compounds to break down tumor defenses through induction of apoptosis.[113] Representative natural products with Bcl-2-inhibiting action are antimycin A_3 (**157**), gossypol (**158**), and tetrocarcin A (**159**).



antimycin A_3 (**157**)



gossypol (**158**)



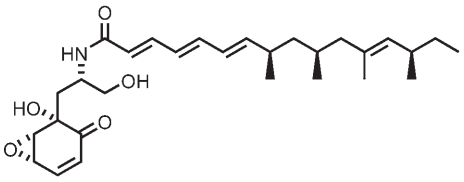
tetrocarcin A (**159**)

Antimycin A_3 (**157**) mimics a peptide containing a BH3 domain and inhibits Bcl-2, which induces apoptosis through the mitochondrial intinsic pathway.[114] The antimycins were first isolated in 1949 from *Streptomyces sp.*[115] The total synthesis of antimycin A has been described.[116] (−)-Gossypol (**158**) acts on the mitochondria to overcome Bcl-2-mediated apoptosis resistance;[117] it is found in cottonseed and its chemistry has been extensively studied.[118] Gossypol (**158**) exhibits atropisomerism and can be separated into its enantiomers.[119] Tetrocarcin A (**159**) was identified as an inhibitor of the antiapoptotic function of Bcl-2, and could serve as a new lead for antitumor therapy.[120] It was reported that the tetrocarcin A induced ER (endoplasmatic reticulum) stress in B-CLL cells mediates apoptosis through a Bcl-2 independent pathway.[121] Tetrocarcin A (**159**) was isolated in 1980 as an antibiotic,[122] and synthetic activities on this compound have been very limited so far.[123]

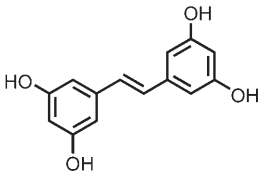
© 2006 Wiley-VCH Verlag GmbH & Co. KGaA, Weinheim

4.9. Other Inhibitors

Ceramide, the product of spingomyelin cleavage, is connected through the extrinsic apoptotic pathway to apoptosis. This makes sphingomyelinase an interesting target for the control of apoptosis and drug targeting.[124] Scyphostatin (**160**)[125] and its synthetic analogues[126] are potent inhibitors of sphingomyelinase, and are currently under investigation.



scyphostatin (**160**)



piceatannol (**161**)

Polyunsaturated fatty acids have been reported as apoptosis-inducing natural products found in the uterus during murine pregnancy.[127] Piceatannol (**161**) from rhubarb roots induces apoptosis in lymphoma cancer cells through the intrinsic pathway.[128]

5. Concluding Remarks

Now that the biochemical pathways of apoptosis are better understood, a controlled intervention becomes more predictable. Apoptotic misregulations are responsible for several diseases, in particular cancer, and there is a strong need for a selective induction of apoptosis in cancer cells. The search for low-molecular-weight compounds has highest priority with regard to inducing apoptosis. There are already numerous natural products known, which control apoptotic pathways at different points. Progress in this field will depend on the cooperation of natural product chemistry, synthesis, and medicinal chemistry.

Natural products are potential lead structures for future drugs to cure apoptotic misregulations. The case of apoptolidin shows the importance of glycoconjugation for biological function. Synthetic strategies that involve an early introduction of the sugar residues are now available and can be very efficient.

Appendix

List of Abbreviations

9-BBN	9-borabicyclononane
Ac	acetyl
AIBN	azobis(isobutyronitrile)
binap	2,2′-bis(diphenylphosphanyl)-1,1′-binaphthyl
Bn	benzyl
Cp	cyclopentadienyl
CSA	camphorsulfonic acid
DDQ	2,3-dichloro-5,6-dicyano-1,4-benzoquinone
$(DHQ)_2$-PHAL	hydroquinine 1,4-phthalazinediyl ether
$(DHQ)_2$-PYR	2,5-diphenyl-4,6-bis(9-*O*-dihydroquinyl)-pyrimidine
DIBAH	diisobutylaluminium hydride
DMAP	4-dimethylaminopyridine
DMP	Dess–Martin periodinane
DMSO	dimethylsulfoxide
d.r.	diastereomeric ratio
DTBMP	2,6-di-*tert*-butyl-4-methylpyridine
HMPA	hexamethylphosphoramide
LHMDS	lithium hexamethyldisilazide
*m*CPBA	*meta*-chloroperbenzoic acid
NIS	*N*-iodosuccinimide
NMO	*N*-methylmorpholine *N*-oxide
PMB	*p*-methoxybenzyl
PPTS	pyridinium-*p*-toluenesulfonate
r.r.	regioisomeric ratio
SIBA	1,1,4,4-tetraphenyl-1,4-disilabutyl
TBAF	tetrabutylammoniumfluoride
TBS	*tert*-butyldimethylsilyl
Tc	thiophene-2-carboxylate
TES	triethylsilyl
TIPS	triisopropylsilyl
TMNO	trimethylamine *N*-oxide
TMS	trimethylsilyl
Tf	trifluoromethanesulfonyl
Ts	*p*-toluenesulfonyl

P.T.D. and U.K. thank all the co-workers cited in the references for their valuable contributions. Dr. D. Mumberg (Schering AG) is acknowledged for the biological evaluation of apoptolidin and its derivatives. Financial support by the Fonds der Chemischen Industrie and Schering AG Berlin is gratefully acknowledged. P.T.D. thanks the Deutsche Krebshilfe and Deutsche José Carreras Leukämie-Stiftung.

Received: August 1, 2005
Published online: January 11, 2006

[1] J. F. Kerr, A. H. Wyllie, A. R. Currie, *Br. J. Cancer* **1972**, *26*, 239–257.
[2] E. Check, *Nature* **2002**, *419*, 548–549.
[3] P. Golstein, L. Aubry, J. P. Levraud, *Nat. Rev. Mol. Cell Biol.* **2003**, *4*, 798–807.
[4] a) J. M. Brown, L. D. Attardi, *Nat. Rev. Cancer* **2005**, *5*, 231–237; b) A. Mrozek, H. Petrowsky, I. Sturm, J. Krauss, S. Hermann, S. Hauptmann, M. Lorenz, P. T. Daniel, *Cell Death Differ.* **2003**, *10*, 461–467.

 © 2006 Wiley-VCH Verlag GmbH & Co. KGaA, Weinheim

[5] A. Prokop, T. Wieder, I. Sturm, F. Essmann, K. Seeger, C. Wuchter, W.-D. Ludwig, G. Henze, B. Dörken, P. T. Daniel, *Leukemia* **2000**, *14*, 1606 – 1613.
[6] B. Rau, I. Sturm, H. Lage, S. Berger, U. Schneider, S. Hauptmann, P. Wust, H. Riess, P. M. Schlag, B. Dörken, P. T. Daniel, *J. Clin. Oncol.* **2003**, *18*, 3391 – 3401.
[7] K. Schelwies, I. Sturm, P. Grabowski, H. Scherübl, I. Schindler, S. Hermann, H. Stein, H. J. Buhr, E. O. Riecken, M. Zeitz, B. Dörken, P. T. Daniel, *Int. J. Cancer* **2002**, *99*, 589 – 596.
[8] I. Sturm, A. G. Bosanquet, S. Hermann, D. Güner, B. Dörken, P. T. Daniel, *Cell Death Differ.* **2003**, *10*, 477 – 484.
[9] I. Sturm, C. H. Kohne, G. Wolff, H. Petrowsky, T. Hillebrand, S. Hauptmann, M. Lorenz, B. Dörken, P. T. Daniel, *J. Clin. Oncol.* **1999**, *17*, 1364 – 1374.
[10] I. Sturm, H. Petrowsky, R. Volz, M. Lorenz, S. Radetzki, T. Hillebrand, G. Wolff, S. Hauptmann, B. Dörken, P. T. Daniel, *J. Clin. Oncol.* **2001**, *19*, 2272 – 2281.
[11] a) K. C. Nicolaou, C. N. Boddy, *Sci. Am.* **2001**, *284*, 54; b) K. C. Nicolaou, J. A. Pfefferkorn, A. J. Roecker, G. Q. Cao, S. Barluenga, H. J. Mitchell, *J. Am. Chem. Soc.* **2000**, *122*, 9939 – 9953.
[12] W. G. van Doorn, E. J. Woltering, *Trends Plant Sci.* **2005**, *10*, 117 – 122.
[13] a) N. A. Thornberry, Y. Lazebnik, *Science* **1998**, *281*, 1312 – 1316; b) C. Garrido, G. Kroemer, *Curr. Opin. Cell Biol.* **2004**, *16*, 639 – 646; c) M. E. Peter, P. H. Krammer, *Cell Death Differ.* **2003**, *10*, 26 – 35.
[14] a) D. R. Green, J. C. Reed, *Science* **1998**, *281*, 1309 – 1312; b) E. Finkel, *Science* **2001**, *292*, 624 – 626; c) P. T. Daniel, K. Schulze-Osthoff, C. Belka, D. Güner, *Essays Biochem.* **2003**, *39*, 73 – 88.
[15] a) A. Hasenjäger, B. Gillissen, A. Müller, G. Normand, P. G. Hemmati, M. Schuler, B. Dörken, P. T. Daniel, *Oncogene* **2004**, *23*, 4523 – 4535; b) D. Tang, J. M. Lahti, V. J. Kidd, *J. Biol. Chem.* **2000**, *275*, 9303 – 9307; c) G. Kulik, J. P. Carson, T. Vomastek, K. Overman, B. D. Gooch, S. Srinivasula, E. Alnemri, G. Nunez, M. J. Weber, *Cancer Res.* **2001**, *61*, 2713 – 2719.
[16] J. Wendt, C. von Haefen, P. G. Hemmati, C. Belka, B. Dörken, P. T. Daniel, *Oncogene* **2005**, *24*, 4052 – 4064.
[17] a) C. von Haefen, B. Gillissen, P. G. Hemmati, J. Wendt, D. Güner, A. Mrozek, C. Belka, B. Dörken, P. T. Daniel, *Oncogene* **2004**, *23*, 8320 – 8332; b) J. T. Ernst, J. Becerril, H. S. Park, H. Yin, A. D. Hamilton, *Angew. Chem.* **2003**, *115*, 553 – 557; *Angew. Chem. Int. Ed.* **2003**, *42*, 535 – 539.
[18] D. W. Nicholson, *Cell Death Differ.* **1999**, *6*, 1028 – 1042.
[19] a) D. W. Nicholson, *Nature* **2000**, *407*, 810 – 816; b) J. R. Reed, *Nat. Rev. Drug Discovery* **2002**, *1*, 111 – 121; c) A. D. Schimmer, *Cancer Res.* **2004**, *64*, 7183 – 7190.
[20] a) S. Nagata, H. Nagase, K. Kawane, N. Mukae, H. Fukuyama, *Cell Death Differ.* **2003**, *10*, 108 – 116; b) K. Lauber, S. G. Blumenthal, M. Waibel, S. Wesselborg, *Mol. Cell* **2004**, *14*, 277 – 287; c) G. S. Robertson, S. J. Crocker, D. W. Nicholson, J. B. Schulz, *Brain Pathol.* **2000**, *10*, 283 – 292; d) R. V. Talanian, K. D. Brady, V. L. Cryns, *J. Med. Chem.* **2000**, *43*, 3351 – 3371; e) F. F. Poordad, *Curr. Opin. Invest. Drugs* **2004**, *5*, 1198 – 1204; f) D. V. Kravchenko, Y. A. Kuzovkova, V. M. Kysil, S. E. Tkachenko, S. Maliarchouk, I. M. Okun, K. V. Balakin, A. V. Ivachtchenko, *J. Med. Chem.* **2005**, *48*, 3680 – 3683; g) D. A. Erlanson, J. W. Lam, C. Wiesmann, T. N. Luong, R. L. Simmons, W. L. DeLano, I. C. Choong, M. T. Burdett, W. M. Flanagan, D. Lee, E. M. Gordon, T. O'Brien, *Nat. Biotechnol.* **2003**, *21*, 308 – 314; h) O. Ramstrom, J.-M. Lehn, *Nat. Rev. Drug Discovery* **2002**, *1*, 26 – 36.
[21] J. W. Kim, H. Adachi, K. Shin-ya, Y. Hayakawa, H. Seto, *J. Antibiot.* **1997**, *50*, 628 – 630.
[22] Y. Hayakawa, J. W. Kim, H. Adachi, K. Shin-ya, K. Fujita, H. Seto, *J. Am. Chem. Soc.* **1998**, *120*, 3524 – 3525.
[23] a) A. R. Salomon, D. W. Voehringer, L. A. Herzenberg, C. Khosla, *Proc. Natl. Acad. Sci. USA* **2000**, *97*, 14766 – 14771; b) A. R. Salomon, D. W. Voehringer, L. A. Herzenberg, C. Khosla, *Chem. Biol.* **2001**, *8*, 71 – 80; c) A. R. Salomon, Y. Zhang, H. Seto, C. Khosla, *Org. Lett.* **2001**, *3*, 57 – 59.
[24] P. A. Wender, O. D. Jankowski, E. A. Tabet, H. Seto, *Org. Lett.* **2003**, *5*, 487 – 490.
[25] a) P. A. Wender, A. V. Gulledge, O. D. Jankowski, H. Seto, *Org. Lett.* **2002**, *4*, 3819 – 3822; b) J. D. Pennington, H. J. Williams, A. R. Salomon, G. A. Sulikowski, *Org. Lett.* **2002**, *4*, 3823 – 3825; c) P. A. Wender, M. Sukopp, K. Longcore, *Org. Lett.* **2005**, *7*, 3025 – 3028.
[26] H. Wehlan, M. Dauber, M. T. Mujica Fernaud, J. Schuppan, M. E. Juarez Garcia, R. Mahrwald, U. Koert, *Angew. Chem.* **2004**, *116*, 4698 – 4702; *Angew. Chem. Int. Ed.* **2004**, *43*, 4597 – 4601.
[27] J. Schuppan, H. Wehlan, S. Keiper, U. Koert, *Angew. Chem.* **2001**, *113*, 2125 – 2128; *Angew. Chem. Int. Ed.* **2001**, *40*, 2063 – 2066.
[28] J. Schuppan, B. Ziemer, U. Koert, *Tetrahedron Lett.* **2000**, *41*, 621 – 624.
[29] G. Jung, A. Klerner, *Chem. Ber.* **1981**, *114*, 740 – 745.
[30] a) R. Preuss, R. R. Schmidt, *Synthesis* **1988**, 694 – 697; b) W. R. Roush, X. F. Lin, *J. Org. Chem.* **1991**, *56*, 5740 – 5742.
[31] a) K. C. Nicolaou, Y. Li, K. C. Fylaktakidou, H. J. Mitchell, H. X. Wei, B. Weyershausen, *Angew. Chem.* **2001**, *113*, 3968 – 3972; *Angew. Chem. Int. Ed.* **2001**, *40*, 3849 – 3854; b) K. C. Nicolaou, Y. Li, K. C. Fylaktakidou, H. J. Mitchell, K. Sugita, *Angew. Chem.* **2001**, *113*, 3972 – 3976; *Angew. Chem. Int. Ed.* **2001**, *40*, 3854 – 3857; c) K. C. Nicolaou, K. C. Fylaktakidou, H. Monenschein, Y. Li, B. Weyershausen, H. J. Mitchell, H. X. Wei, P. Guntupalli, D. Hepworth, K. Sugita, *J. Am. Chem. Soc.* **2003**, *125*, 15433 – 15442; d) K. C. Nicolaou, Y. Li, K. Sugita, H. Monenschein, P. Guntupalli, H. J. Mitchell, K. C. Fylaktakidou, D. Vourloumis, P. Giannakakou, A. O'Brate, *J. Am. Chem. Soc.* **2003**, *125*, 15443 – 15454.
[32] I. Bajza, A. Liptak, *Carbohydr. Res.* **1990**, *205*, 435 – 439.
[33] D. Kahne, S. Walker, Y. Cheng, D. VanEngen, *J. Am. Chem. Soc.* **1989**, *111*, 6881 – 6882.
[34] $SIBACl_2$ was prepared by reaction of 1,2-bis(trichlorosilyl)-ethane with phenylmagnesium bromide.
[35] a) D. A. Evans, J. S. Clark, R. Metternich, V. J. Novack, G. S. Sheppard, *J. Am. Chem. Soc.* **1990**, *112*, 866 – 868; b) D. A. Evans, A. S. Kim, R. Metternich, V. J. Novack, *J. Am. Chem. Soc.* **1998**, *120*, 5921 – 5942.
[36] D. A. Evans, H. P. Ng, J. S. Clark, D. L. Rieger, *Tetrahedron* **1992**, *48*, 2127 – 2142.
[37] a) D. A. Evans, K. T. Chapman, E. M. Carreira, *J. Am. Chem. Soc.* **1988**, *110*, 3560 – 3578; b) D. A. Evans, A. H. Hoveyda, *J. Am. Chem. Soc.* **1990**, *112*, 6447 – 6449.
[38] J. Thiem, J. Elvers, *Chem. Ber.* **1980**, *113*, 3049 – 3057.
[39] G. D. Allred, L. S. Liebeskind, *J. Am. Chem. Soc.* **1996**, *118*, 2748 – 2749.
[40] K. C. Nicolaou, Y. Li, B. Weyershausen, H.-X. Wei, *Chem. Commun.* **2000**, 307 – 308.
[41] a) B. Wu, Q. Liu, G. A. Sulikowski, *Angew. Chem.* **2004**, *116*, 6841 – 6843; *Angew. Chem. Int. Ed.* **2004**, *43*, 6673 – 6675; b) G. A. Sulikowski, W.-M. Lee, B. Jin, B. Wu, *Org. Lett.* **2000**, *2*, 1439 – 1442; c) B. Jin, Q. Liu, G. A. Sulikowski, *Tetrahedron* **2005**, *61*, 401 – 408; d) M. T. Crimmins, H. S. Christie, K. Chaudhary, A. Long, *J. Am. Chem. Soc.* **2005**, *127*, 13810-13812.
[42] a) K. Toshima, T. Arita, K. Kato, D. Tanaka, S. Matsumura, *Tetrahedron Lett.* **2001**, *42*, 8873 – 8876; b) K. Abe, K. Kato, T. Arai, M. A. Rahim, I. Sultana, S. Matsumura, K. Toshima, *Tetrahedron Lett.* **2004**, *45*, 8849 – 8853.
[43] W. D. Paquette, R. E. Taylor, *Org. Lett.* **2004**, *6*, 103 – 106.

© 2006 Wiley-VCH Verlag GmbH & Co. KGaA, Weinheim

[44] a) Y. Chen, J. B. Evarts, E. Torres, P. L. Fuchs, *Org. Lett.* **2002**, *4*, 3571 – 3574; b) M. T. Crimmins, A. Long, *Org. Lett.* **2005**, *7*, 4157 – 4160.
[45] P. A. Wender, O. D. Jankowski, E. A. Tabet, H. Seto, *Org. Lett.* **2003**, *5*, 2299 – 2302.
[46] Hermut Wehlan, PhD Thesis, Philipps university, Marburg, **2004**.
[47] Julia Schuppan, PhD Thesis, Humboldt university, Berlin, **2002**.
[48] H. Ishihara, B. L. Martin, D. L. Brautigan, H. Karaki, H. Ozaki, Y. Kato, N. Fusetani, S. Watabe, K. Hashimoto, D. Uemura, D. J. Hartshorne, *Biochem. Biophys. Res. Commun.* **1989**, *159*, 871 – 877.
[49] a) H. W. Ko, K. S. Han, E. Y. Kim, B. R. Ryu, W. J. Yoon, J. K. Jung, S. U. Kim, B. J. Gwag, *J. Neurochem.* **2000**, *74*, 2455 – 2461; b) H. Okamura, K. Yoshida, H. Morimoto, T. Haneji, *J. Cell. Biochem.* **2005**, *94*, 117 – 125.
[50] Y. Kato, N. Fusetani, S. Matsunaga, K. Hashimoto, S. Fujita, T. Furuya, *J. Am. Chem. Soc.* **1986**, *108*, 2780 – 2781.
[51] a) D. A. Evans, J. R. Gage, J. L. Leighton, *J. Am. Chem. Soc.* **1992**, *114*, 9434 – 9453; b) F. Yokokawa, Y. Hamada, T. Shioiri, *Chem. Commun.* **1996**, 871 – 872; c) A. B. Smith III, G. K. Friestad, J. J.-W. Duan, J. Barbosa, K. G. Hull, M. Iwashima, Y. Qiu, P. G. Spoors, E. Bertonesque, B. A. Salvatore, *J. Org. Chem.* **1998**, *63*, 7596 – 7597; d) P. O. Andersen, A. G. M. Barrett, J. J. Edmunds, J. Jeremy, S. I. Hachiya, J. A. Hendrix, K. Horita, J. W. Malecha, C. J. Parkinson, A. VanSickle, *Can. J. Chem.* **2001**, *79*, 1562 – 1592.
[52] a) N. Tanimoto, S. W. Gerritz, A. Sawabe, T. Noda, S. A. Filla, S. Masamune, *Angew. Chem.* **1994**, *106*, 674 – 677; *Angew. Chem. Int. Ed. Engl.* **1994**, *33*, 673 – 676.
[53] a) A. K. Ogawa, R. W. Armstrong, *J. Am. Chem. Soc.* **1998**, *120*, 12435 – 12442; b) A. B. Smith III, G. K. Friestad, J. Barbosa, E. Bertounesque, J. J.-W. Duan, K. G. Hull, M. Iwashima, Y. Qiu, P. G. Spoors, B. A. Salvatore, *J. Am. Chem. Soc.* **1999**, *121*, 10478 – 10486.
[54] Y. Murakami, Y. Oshima, Y. Yasumoto, *Bull. Jpn. Soc. Sci. Fish.* **1982**, *48*, 69 – 72.
[55] T. Yasumoto, M. Murata, Y. Oshima, M. Sano, *Tetrahedron* **1985**, *41*, 1019 – 1025.
[56] K. Tachibana, P. J. Scheuer, Y. Tsukitani, H. Kikuchi, D. Van Engen, J. Clardy, Y. Gopichand, F. J. Schmitz, *J. Am. Chem. Soc.* **1981**, *103*, 2469 – 2471.
[57] a) M. Isobe, Y. Ichikawa, T. Goto, *Tetrahedron Lett.* **1986**, *27*, 963 – 966; b) M. Isobe, Y. Ichikawa, D. L. Bai, H. Masaki, T. Goto, *Tetrahedron* **1987**, *43*, 4767 – 4776.
[58] a) C. J. Forsyth, S. F. Sabes, R. A. Urbanek, *J. Am. Chem. Soc.* **1997**, *119*, 8381 – 8382; b) R. A. Urbanek, S. F. Sabes, C. J. Forsyth, *J. Am. Chem. Soc.* **1998**, *120*, 2523 – 2533; c) S. F. Sabes, R. A. Urbanek, C. J. Forsyth, *J. Am. Chem. Soc.* **1998**, *120*, 2534 – 2542; d) A. B. Dounay, R. A. Urbanek, S. F. Sabes, C. J. Forsyth, *Angew. Chem.* **1999**, *111*, 2403 – 2406; *Angew. Chem. Int. Ed.* **1999**, *38*, 2258 – 2262.
[59] S. V. Ley, A. C. Humphries, H. Eick, R. Downham, A. R. Ross, R. J. Boyce, J. B. J. Pavey, J. Pietruszka, *J. Chem. Soc. Perkin Trans. 1* **1998**, 3907 – 3911.
[60] S. Lu, M. Archer, *Carcinogenesis* **2005**, *26*, 153 – 157.
[61] E. S. Pizer, C. Jackisch, F. D. Wood, G. R. Pasternack, N. E. Davidson, F. P. Kuhajda, *Cancer Res.* **1996**, *56*, 2745 – 2747.
[62] J. N. Li, M. Gorospe, F. J. Chrest, T. S. Kumaravel, M. K. Evans, W. F. Han, S. E. Pizer, *Cancer Res.* **2001**, *61*, 1493 – 1499.
[63] S. J. Heiligtag, R. Bredehorst, K. A. David, *Cell Death Differ.* **2002**, *9*, 1017 – 1025.
[64] T. Hata, Y. Sano, A. Matsumae, Y. Kanio, S. Nomura, R. Sugawara, *Jpn. J. Bacteriol.* **1960**, *15*, 1075.
[65] R. Shimazawa, Y. Ogawa, N. Morisaki, H. Funabashi, A. Kawaguchi, S. Iwasaki, *Chem. Pharm. Bull.* **1992**, *40*, 2954 – 2957.
[66] H. Yoda in *Cerulenin—Chemistry Reviewed, Vol. 2* (Ed.: G. Lukacs), Springer, Berlin **1993**, pp. 939 – 970; and references therein.
[67] F. Kuhajda, E. S. Pizer, J. N. Li, N. S. Mani, G. L. Frehywot, C. A. Townsend, *Proc. Natl. Acad. Sci. USA* **2000**, *97*, 3450 – 3454.
[68] S. A. Milligan, C. Nopajaroonsri, *Anticancer Res.* **2001**, *21*, 39 – 44.
[69] J. A. Vrana, S. Grant, *Blood* **2001**, *97*, 2105 – 2114.
[70] V. Marshansky, X. Wang, R. Bertrand, H. Luo, W. Duguid, G. Chinnadurai, N. Kanaan, M. D. Vu, J. Wu, *J. Immunol.* **2001**, *166*, 3130 – 3142.
[71] L. Chen, L. Smith, Z. Wang, J. B. Smith, *Mol. Pharm.* **2003**, *64*, 334 – 345.
[72] S. Omura, K. Matsuzaki, T. Fujimoto, K. Kosuge, T. Furuya, S. Fujita, A. Nakagawa, *J. Antibiot.* **1991**, *44*, 117 – 118.
[73] For reviews of the chemistry and biology of lactacystin: see a) E. J. Corey, W. Li, *Chem. Pharm. Bull.* **1999**, *47*, 1 – 10; b) C. E. Masse, A. J. Morgan, J. Adams, J. S. Panek, *Eur. J. Org. Chem.* **2000**, 2513 – 2528; total syntheses: c) E. J. Corey, G. A. Reichard, *J. Am. Chem. Soc.* **1992**, *114*, 10677 – 10678; d) J. S. Panek, C. E. Masse, *Angew. Chem.* **1999**, *111*, 1161 – 1163; *Angew. Chem. Int. Ed.* **1999**, *38*, 1093 – 1095; e) F. Soucy, L. Grenier, M. L. Behnke, A. T. Destree, T. A. McCormack, J. Adams, L. Plamondon, *J. Am. Chem. Soc.* **1999**, *121*, 9967 – 9976; f) T. Nagamitsu, T. Sunazuka, H. Tanaka, S. Omura, P. A. Sprengeler, I. A. B. Smith, *J. Am. Chem. Soc.* **1996**, *118*, 3584 – 3590; g) H. Uno, J. E. Baldwin, A. T. Russell, *J. Am. Chem. Soc.* **1994**, *116*, 2139 – 2140; h) N. Chida, J. Takeoka, N. Tsutsumi, S. Ogawa, *J. Chem. Soc. Chem. Commun.* **1995**, 793 – 794; i) H. Ooi, N. Ishibashi, Y. Iwabuchi, J. Ishihara, S. Hatakeyama, *J. Org. Chem.* **2004**, *69*, 7765 – 7768.
[74] a) F. Caponigro, C. R. French, S. B. Kaye, *Anti-Cancer Drugs* **1997**, *8*, 26 – 33; b) D. W. Jarvis, S. Grant, *Invest. New Drugs* **1999**, *17*, 240 – 277.
[75] J. A. Zonder, A. F. Shields, M. Zalupski, R. Chaplen, L. K. Heilbrun, P. Arlauskas, P. A. Philip, *Clin. Cancer Res.* **2001**, *7*, 38 – 42.
[76] J. Hofmann, *Curr. Cancer Drug Targets* **2004**, *4*, 125 – 146.
[77] G. Meinhardt, J. Roth, G. Totok, *Eur. J. Cell Biol.* **2000**, *79*, 824 – 833.
[78] C. Chen, H. Lin, C. Karanes, G. R. Pettit, B. D. Chen, *Cancer Res.* **2000**, *60*, 4377 – 4385.
[79] N. R. Wall, R. M. Mohammad, A. M. Al-Katib, *Leuk. Res.* **1999**, *23*, 881 – 888.
[80] G. R. Pettit, C. L. Herald, D. L. Doubek, D. L. Herald, E. Arnold, J. Clardy, *J. Am. Chem. Soc.* **1982**, *104*, 6846 – 6848.
[81] a) G. R. Pettit in *The Bryostatins, Vol. 57* (Eds.: W. Herz, G. W. Kirby, W. Steglich, C. Tamm), Springer, New York, **1991**, pp. 153 – 195; b) G. R. Pettit, F. Gao, P. M. Blumberg, C. L. Herald, J. C. Coll, Y. Kamano, N. E. Lewin, J. M. Schmidt, J.-C. Chapuis, *J. Nat. Prod.* **1996**, *59*, 286 – 289; c) G. R. Petitt, *J. Nat. Prod.* **1996**, *59*, 812 – 821.
[82] M. Kageyama, T. Tamura, M. H. Nantz, J. C. Roberts, P. Somfai, D. C. Whritenour, S. Masamune, *J. Am. Chem. Soc.* **1990**, *112*, 7407 – 7408.
[83] D. A. Evans, P. H. Carter, E. M. Carreira, J. A. Prunet, A. B. Charette, M. Lautens, *Angew. Chem.* **1998**, *110*, 2526 – 2530; *Angew. Chem. Int. Ed.* **1998**, *37*, 2354 – 2359.
[84] K. Ohmori, Y. Ogawa, T. Obitsu, Y. Ishikawa, S. Nishiyama, S. Yamamura, *Angew. Chem.* **2000**, *112*, 2376 – 2379; *Angew. Chem. Int. Ed.* **2000**, *39*, 2290 – 2294.
[85] a) P. A. Wender, J. DeBrabander, P. G. Harran, J.-M. Jimenez, M. F. T. Koehler, B. Lippa, C. M. Park, M. Shiozaki, G. R. Pettit, *J. Am. Chem. Soc.* **1998**, *120*, 4534 – 4535; b) P. A. Wender, J. DeBrabander, P. G. Harran, J.-M. Jimenez, M. F. T. Koehler, B. Lippa, C. M. Park, C. Siedenbiedel, G. R. Pettit,

 © 2006 Wiley-VCH Verlag GmbH & Co. KGaA, Weinheim

Proc. Natl. Acad. Sci. USA **1998**, *95*, 6624 – 6631; c) P. A. Wender, B. Lippa, *Tetrahedron Lett.* **2000**, *41*, 1007 – 1011; d) P. A. Wender, K. W. Hinkle, *Tetrahedron Lett.* **2000**, *41*, 6725 – 6729.

[86] B. Bernard, T. Fest, J. L. Pretet, C. Mougin, *Cell Death Differ.* **2001**, *8*, 234 – 244.

[87] A. Stepczynska, K. Lauber, I. H. Engels, O. Janssen, D. Kabelitz, S. Wesselborg, K. Schulze-Osthoff, *Oncogene* **2001**, 1193 – 1202.

[88] M. Giuliano, G. Bellavia, M. Lauricella, A. Danneo, B. Vassallo, R. Vento, G. Tesoriere, *Int. J. Mol. Med.* **2004**, *13*, 565 – 571.

[89] S. Omura, Y. Iwai, A. Hirano, A. Nakagawa, J. Awaya, H. Tsuchiya, Y. Takahashi, R. Masuma, *J. Antibiot.* **1977**, *43*, 275 – 282.

[90] A. Furusaki, N. Hashiba, T. Matsumoto, A. Hirano, Y. Iwai, S. Omura, *J. Chem. Soc. Chem. Commun.* **1978**, 800 – 801.

[91] A. Furusaki, N. Hashiba, T. Matsumoto, A. Hirano, Y. Iwai, S. Omura, *Bull. Chem. Soc. Jpn.* **1982**, *5*, 3681 – 3685.

[92] H. Takahashi, H. Osada, M. Uramoto, K. Isono, *J. Antibiot.* **1990**, *43*, 168 – 173.

[93] N. Funato, H. Takayanagi, Y. Konda, Y. Toda, Y. Hariyage, Y. Iwai, S. Omura, *Tetrahedron Lett.* **1994**, *35*, 1251 – 1254.

[94] a) J. T. Link, S. Raghavan, S. J. Danishefsky, *J. Am. Chem. Soc.* **1995**, *117*, 552 – 553; b) J. T. Link, S. Raghavan, M. Gallant, S. J. Danishefsky, T. C. Chou, L. M. Ballas, *J. Am. Chem. Soc.* **1996**, *118*, 2825 – 2842.

[95] a) J. L. Wood, B. M. Stoltz, S. N. Goodman, *J. Am. Chem. Soc.* **1996**, *118*, 10656 – 10657; b) J. L. Wood, B. M. Stoltz, S. N. Gooman, K. Onwueme, *J. Am. Chem. Soc.* **1997**, *119*, 9652 – 9661.

[96] F. Mollinedo, C. Gajate, *Apoptosis* **2003**, *8*, 413 – 450.

[97] M. A. Jordan, L. Wilson, *Nat. Rev. Cancer* **2004**, *4*, 253 – 265.

[98] T. Graening, H. H. Schmalz, *Angew. Chem.* **2004**, *116*, 3292 – 3318; *Angew. Chem. Int. Ed.* **2004**, *43*, 3230 – 3256.

[99] K. C. Nicolaou, W. M. Dai, R. K. Guy, *Angew. Chem.* **1994**, *106*, 38 – 69; *Angew. Chem. Int. Ed. Engl.* **1994**, *33*, 15 – 44.

[100] a) K. H. Altmann, *Mini-Rev. Med. Chem.* **2003**, *3*, 149 – 158; b) A. Rivkin, T. C. Chao, S. J. Danishefsky, *Angew. Chem.* **2005**, *117*, 2898 – 2910; *Angew. Chem. Int. Ed.* **2005**, *44*, 2838 – 2850; c) D. Schinzer, *Modern Aldol React.* **2004**, *1*, 311 – 328; d) U. Klar, B. Roehr, F. Kuczynski, W. Schwede, M. Berger, W. Skuballa, B. Buchmann, *Synthesis* **2005**, 301 – 305.

[101] J. Mulzer, E. Oehler, *Chem. Rev.* **2003**, *103*, 3753 – 3786.

[102] a) K. C. Nicolaou, J. Pfefferkorn, J. Y. Xu, N. Winssiger, T. Oshima, S. Kim, S. Hosokawa, D. Vourloumis, F. van Delft, T. Li, *Chem. Pharm. Bull.* **1999**, *47*, 1199 – 1213; b) D. Castoldi, L. Caggiano, L. Panigada, O. Sharon, A. M. Costa, C. Gennari, *Angew. Chem.* **2005**, *117*, 594 – 597; *Angew. Chem. Int. Ed.* **2005**, *44*, 588 – 591.

[103] a) S. J. Mickel, *Curr. Opin. Drug Discovery Dev.* **2004**, *7*, 869 – 881; b) I. Paterson, G. J. Florence, *Eur. J. Org. Chem.* **2003**, 2193 – 2208; c) M. Kalesse, *ChemBioChem* **2000**, *1*, 171 – 175.

[104] References [98–103] give selected review articles concerning the chemistry and biology of compounds **148**–**154**.

[105] J. Beliakoff, L. Whitesell, *Anti-Cancer Drugs* **2004**, *15*, 651 – 662.

[106] M. V. Blagosklonny, *Leukemia* **2002**, *12*, 455 – 462.

[107] a) C. De Boer, P. A. Meulman, R. J. Wnuk, D. H. Peterson, *J. Antibiot.* **1970**, *23*, 442 – 447; b) K. L. Rinehart, K. Sasaki, G. Slomp, M. F. Grostic, E. C. Olson, *J. Am. Chem. Soc.* **1970**, *92*, 7591 – 7593.

[108] a) M. B. Andrus, E. L. Meredith, E. J. Hicken, B. L. Simmons, R. R. Glancey, W. Ma, *J. Org. Chem.* **2003**, *68*, 8162 – 8169.

[109] H. Cheng, X. Cao, M. Xian, L. Fang, T. B. Cai, J. J. Ji, J. B. Tunac, D. Sun, P. G. Wang, *J. Med. Chem.* **2005**, *48*, 546 – 652.

[110] E. Pisha, H. Chai, I. S. Lee, T. E. Chagwedera, N. R. Farnsworth, G. A. Cordell, C. W. Beecher, H. H. Fong, A. D. Kingshorn, D. M. Brown, M. C. Wani, M. E. Wall, T. J. Hieken, T. K. Das Gupta, J. M. Pezzuto, *Nat. Med.* **1995**, *1*, 1046 – 1051.

[111] Y. M. Tan, R. Yu, J. M. Pezzuto, *Clin. Cancer Res.* **2003**, *9*, 2866 – 2875.

[112] H. Ehrhardt, S. Fulda, M. Führer, K. M. Debatin, I. Jeremias, *Leukemia* **2004**, *18*, 1406 – 1412.

[113] a) D. Hockenbery, *Chem. Biol.* **2004**, *11*, 417 – 425; b) D. Liu, Z. Huang, *Apoptosis* **2001**, *6*, 453 – 462; c) P. Juin, O. Geneste, E. Raimbaud, J. A. Hickman, *Biochim. Biophys. Acta* **2004**, *1644*, 251 – 260.

[114] S. P. Tzung, K. M. Kim, G. Basanez, C. D. Giedt, J. Simon, J. Zimmerberg, K. Y. J. Zhang, D. M. Hockenbery, *Nat. Cell Biol.* **2001**, *3*, 183 – 191.

[115] B. R. Dunshee, C. Leben, G. W. Keitt, F. M. Strong, *J. Am. Chem. Soc.* **1949**, *71*, 2436 – 2437.

[116] a) M. Kinoshita, M. Wada, S. Aburagi, S. Umezawa, *J. Antibiot.* **1971**, *24*, 724 – 726; b) T. Nishii, S. Suzuki, K. Yoshida, K. Arakaki, T. Tsunoda, *Tetrahedron Lett.* **2003**, *44*, 7829 – 7832.

[117] a) S. Kitada, M. Leone, S. Sareth, D. Thai, J. C. Reed, M. Pellecchia, *J. Med. Chem.* **2003**, *46*, 4259 – 4264; b) C. L. Oliver, M. B. Miranda, S. Shangary, S. Land, S. Wang, D. E. Johnson, *Mol. Cancer Ther.* **2005**, *4*, 23 – 31; c) R. M. Mohammad, S. Wang, A. Aboukameel, B. Chen, X. Wu, J. Chen, A. Al-Katib, *Mol. Cancer Ther.* **2005**, *4*, 13 – 21.

[118] "Gossypol": L. C. Berardi, L. A. Goldblatt in *Toxic Constitutents of Plant Foodstuffs* (Ed.: I. E. Liener), Academic Press, New York, **1980**, pp. 183 – 237.

[119] M. D. Shelley, L. Hartley, R. G. Fish, P. Groundwater, J. J. G. Morgan, D. Mort, M. Mason, A. Evans, *Cancer Lett.* **1999**, *135*, 171 – 180.

[120] T. Nakashima, M. Miura, M. Hara, *Cancer Res.* **2000**, *60*, 1229 – 1235.

[121] G. Anether, I. Tinhofer, M. Senfter, R. Greil, *Blood* **2003**, *101*, 4561 – 4568.

[122] F. Tomita, T. Tamaoki, K. Shirahata, M. Kasai, M. Morimoto, S. Ohkubo, K. Mineura, S. Ishii, *J. Antibiot.* **1980**, *33*, 668 – 670.

[123] M. Kaneko, T. Nakashima, Y. Uosaki, M. Hara, S. Ikeda, Y. Kanda, *Bioorg. Med. Chem. Lett.* **2001**, *11*, 887 – 890.

[124] a) V. Waschowlowski, A. Giannis, *Drug News Perspect.* **2001**, *14*, 581 – 590; b) C. Luberto, D. F. Hassler, P. Signorelli, Y. Okamoto, H. Sawai, E. Boros, D. J. Hazen-Martin, L. M. Obeid, Y. A. Hannun, G. K. Smith, *J. Biol. Chem.* **2002**, *277*, 41128 – 41139.

[125] M. Tanaka, F. Nara, K. Suzuki-Konagai, T. Hosoya, T. Ogita, *J. Am. Chem. Soc.* **1997**, *119*, 7871 – 7872.

[126] a) C. Arenz, M. Gartner, V. Waschowlowski, A. Giannis, *Bioorg. Med. Chem. Lett.* **2001**, *11*, 2901 – 2904; b) C. Arenz, A. Giannis, *Angew. Chem.* **2000**, *112*, 1498 – 1500; *Angew. Chem. Int. Ed.* **2000**, *39*, 1440 – 1442.

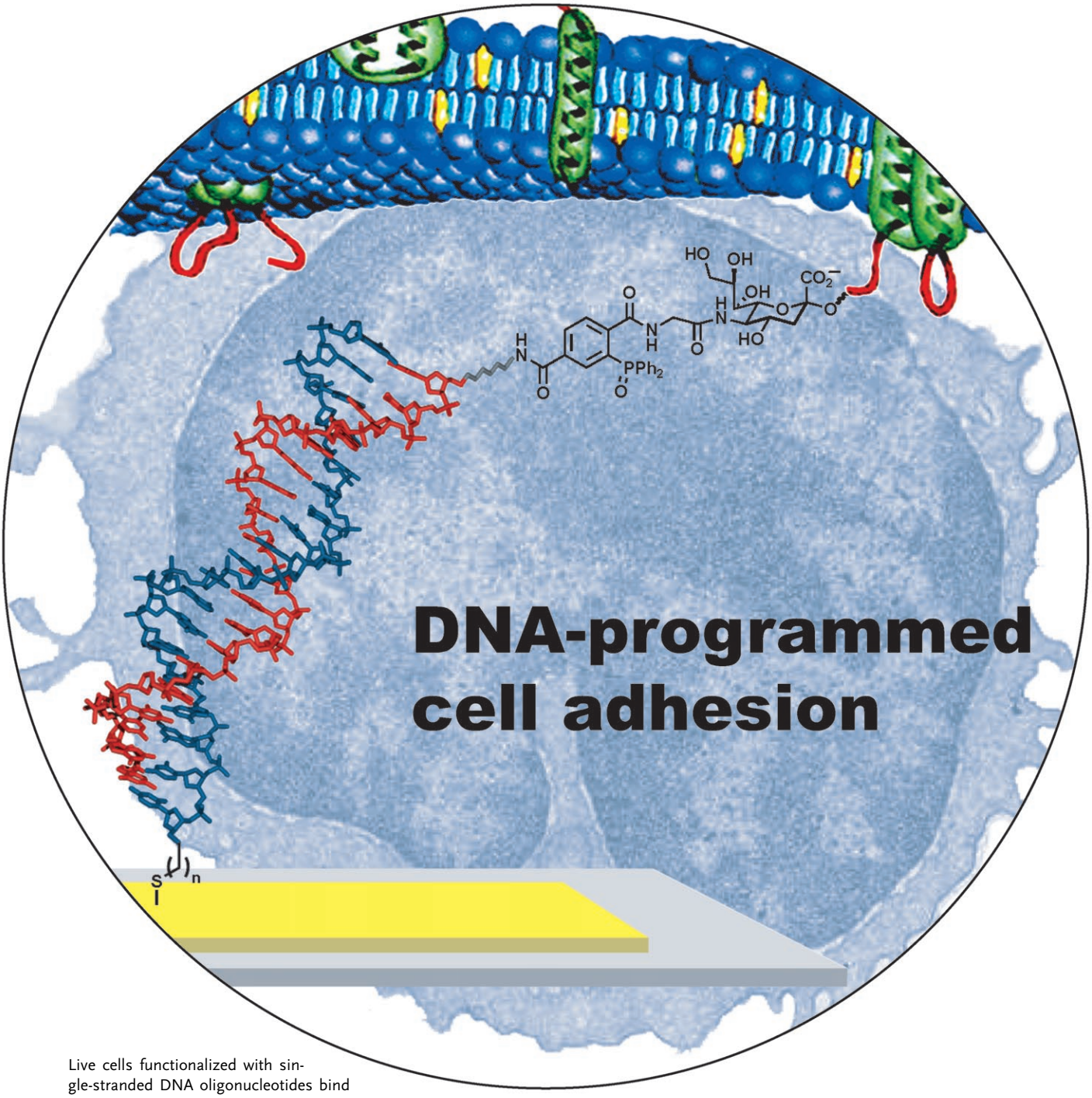
[127] S. D. Liberles, S. L. Schreiber, *Chem. Biol.* **2000**, *7*, 365 – 372.

[128] T. Wieder, A. Prokop, B. Bagci, F. Essmann, D. Bernicke, K. Schulze-Osthoff, B. Dorken, H. G. Schmalz, P. T. Daniel, G. Henze, *Leukemia* **2001**, *15*,1735 – 1742.

© 2006 Wiley-VCH Verlag GmbH & Co. KGaA, Weinheim

Communications

DOI: 10.1002/anie.200502421



Live cells functionalized with single-stranded DNA oligonucleotides bind to substrates that bear complementary DNA strands in a sequence-specific manner. This binding is independent of the native adhesion mechanisms. The strategy has been successfully utilized with several common mammalian cell lines and device platforms. For more information see the Communication by M. B. Francis and co-workers on the following pages.

WILEY InterScience DISCOVER SOMETHING GREAT
© 2006 Wiley-VCH Verlag GmbH & Co. KGaA, Weinheim

DNA Recognition

DOI: 10.1002/anie.200502421

Programmable Cell Adhesion Encoded by DNA Hybridization**

*Ravi A. Chandra, Erik S. Douglas, Richard A. Mathies, Carolyn R. Bertozzi, and Matthew B. Francis**

Microfabrication and patterning techniques from the semiconductor industry have yielded promising new tools for the study of cell biology,[1] foreshadowing future opportunities for cell-based devices, including biosensors,[2] drug-screening platforms,[3] artificial tissues,[4] and designed networks of neurons.[5] To date, the attachment of cells to surfaces has been achieved by exploiting the cell's natural repertoire of adhesion receptors, with a particular emphasis on the integrins.[6] To achieve cell adhesion in these systems, cognate surfaces have typically been patterned with integrin-binding ligands, such as laminin or fibronectin, or synthetic RGD-containing peptides (RGD = arginine, glycine, and aspartic acid) that are derived from them.[1,6] A particular advantage of this approach is its generality as most adherent cell types use integrins as their primary adhesion receptors.[7] However, the commonality of this mechanism makes it difficult to form patterns in which multiple types of cells are arrayed with precision on a single surface. As a result, considerable attention has been directed toward the development of new technologies for the programmable attachment of cells to material surfaces.[8,9]

Herein we show that cell adhesion events can be programmed through the attachment of synthetic single-stranded DNA (ssDNA) strands to the surfaces of living cells. These strands are then used to anchor cells to specified locations on surfaces in a sequence-dependent fashion. This provides an attractive means by which to control the adhesion properties of living cells without a dependence on the

[*] Prof. M. B. Francis
Department of Chemistry
University of California, Berkeley
and
Materials Sciences Division
Lawrence Berkeley National Laboratory
Berkeley, CA 94720 (USA)
Fax: (+1) 510-643-3079
E-mail: francis@cchem.berkeley.edu

R. A. Chandra
Department of Chemistry
University of California, Berkeley
Berkeley, CA 94720 (USA)

E. S. Douglas
UCB/UCSF Joint Graduate Group in Bioengineering
University of California, Berkeley
Berkeley, CA 94720 (USA)

Prof. R. A. Mathies
Department of Chemistry and
UCB/UCSF Joint Graduate Group in Bioengineering
University of California, Berkeley
and
Physical Biosciences Division
Lawrence Berkeley National Laboratory
Berkeley, CA 94720 (USA)

Prof. C. R. Bertozzi
Departments of Chemistry & Molecular and Cell Biology
and
Howard Hughes Medical Institute
University of California, Berkeley
and
Materials Sciences Division
Lawrence Berkeley National Laboratory
Berkeley, CA 94720 (USA)

[**] The authors thank H. Lee, J. Prescher, M. Hangauer, and N. Toriello for helpful discussions and assistance. R.A.C. and E.S.D. were supported by National Science Foundation Predoctoral Fellowships. This work was supported by generous financial support from the Nanoscale Science, Energy, and Technology (NSET) Program of the Department of Energy.

Supporting information for this article is available on the WWW under http://www.angewandte.org or from the author.

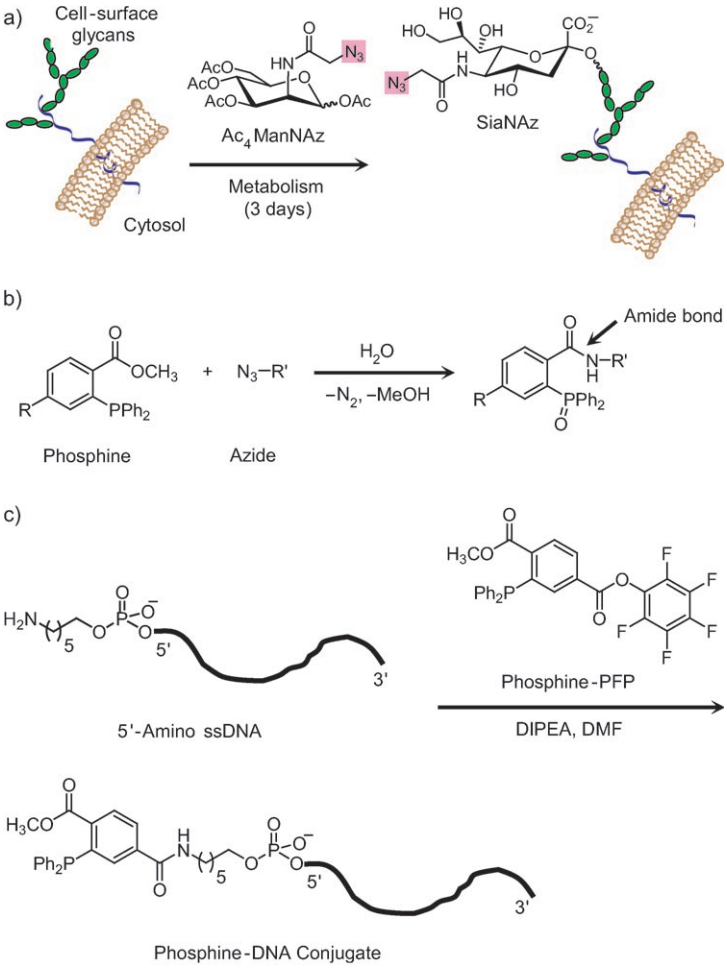


Figure 1. Covalent attachment of ssDNA to cell surfaces. a) Azides can be delivered to cell-surface glycans thorough metabolism of Ac_4ManNAz to SiaNAz. b) The Staudinger ligation of a functionalized phosphine and an azide results in the formation of an amide bond. c) Phosphine-bearing ssDNA strands are synthesized from amino ssDNA and phosphine–PFPs. Ac_4ManNAz = acetylated-*N*-α-azidoacetylmannosamine, SiaNAz = *N*-α-azidoacetyl sialic acid, PFP = pentafluorophenyl.

 © 2006 Wiley-VCH Verlag GmbH & Co. KGaA, Weinheim

receptors that they possess. An advantage of DNA-based systems is the virtually unlimited number of possible coding specificities as was demonstrated in previous studies that have directed synthetic lipid vesicles to supported lipid bilayers with complementary sequences.[10] It is envisioned that, when combined with DNA-patterning techniques developed for microarray platforms,[11] this strategy will allow increasingly complex networks of living cells to be created through self-assembly.

Although there are well-established methods for the functionalization of devices with ssDNA,[11,12] the attachment of ssDNA to the surface of living cells has not yet been reported. To do this,[13] we have developed a synthetic method based on the introduction of specific chemical handles onto cell surfaces by using metabolic oligosaccharide engineering. Briefly, this was achieved though the incorporation of azides into cell surface glycoconjugates by the administration of peracetylated *N*-α-azidoacetylmannosamine (Ac_4ManNAz). Previous studies have shown that this unnatural sugar is metabolized to the corresponding *N*-α-azidoacetyl sialic acid (SiaNAz) within membrane-associated glycans (Figure 1a).[14]

We have reported previously the use of the Staudinger ligation (Figure 1b) as a bioorthogonal reaction for the modification of cell-surface azides with phosphine reagents, yielding stable amide linkages.[15] For these studies, we have expanded this technique to include oligonucleotide attachment.[16] We prepared modified ssDNA with a phosphine group through the reaction of a 5′-amine-modified ssDNA with a phosphine pentafluorophenyl (PFP) ester, as shown in Figure 1c. Model studies conducted with simple azides confirmed that the phosphine–ssDNA conjugate undergoes the Staudinger ligation to form the expected amide-linked product (see Supporting Information). Little or no oxidation of the phosphine–DNA conjugates was observed during handling or storage.

To verify the ability of the phosphine–DNA conjugates to undergo ligation to cell surfaces, human embryonic kidney (HEK) cells were first treated with Ac_4ManNAz in culture media for three days to introduce the azide groups. The cells were then reacted with phosphine–DNA conjugates that were prehybridized with complementary strands that bore a biotin reporter tag for a period of 1–2 h (Figure 2a). After the unreacted phosphine–DNA was removed through rinsing, the cells were treated with fluorescein isothiocyanate-labeled avidin (avidin-FITC). Flow cytometry analysis established the presence of DNA bound to the cell surface (Figure 2b). From these data, we estimate the number of surface DNA conjugates to be approximately 270000 per cell under the conditions used. This value represents a lower limit as it is unlikely that each step of the detection assay (prehybridization, cell-surface conjugation, and avidin-FITC labeling) proceeded with a quantitative yield.[15] Similar results were obtained for Jurkat (human T-cell line) cells. Control experiments, carried out by using DNA strands that lack reactive phosphines, showed no detectable binding above background levels. Similarly, experiments conducted using azide-free cells, but with

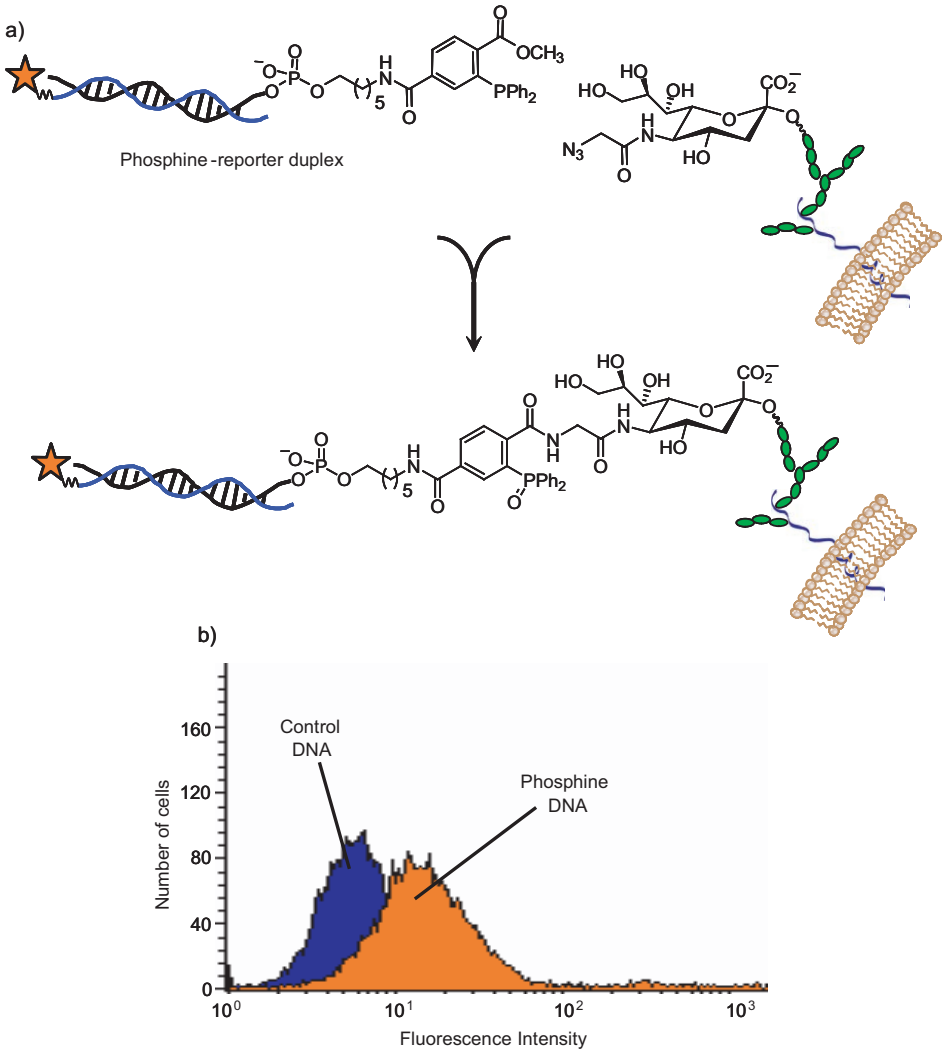


Figure 2. dsDNA complexes are covalently attached to the surface of live cells. a) Experimental overview for the quantification of exogenous DNA on the cell surface. Complementary biotinylated reporter strands are hybridized to the phosphine-bearing DNA. Biotinylated DNA strands are detected after binding to avidin-FITC. b) Flow cytometry analysis of human embryonic kidney (HEK) cells treated with biotinylated DNA strands that lack (blue) or bear (orange) reactive phosphine groups.

© 2006 Wiley-VCH Verlag GmbH & Co. KGaA, Weinheim

phosphine–DNA, showed detectable but greatly reduced labeling efficiency.

In parallel, experiments were carried out by using phosphine–ssDNA conjugates. Although these species are likely to react with surface azides with rates similar to those observed for double stranded DNA (dsDNA), attempts to quantify these groups through subsequent hybridization to biotinylated DNA were unsuccessful. This is likely due to the slow hybridization kinetics associated with the low concentrations of DNA on the plasma membrane, resulting in incomplete labeling. As noted by others,[17] the kinetics of DNA hybridization are substantially different at material surfaces owing to the dramatically higher local DNA concentration. Thus, we chose instead to confirm the presence of ssDNA on the cell membranes through surface attachment.

As an experimental platform, microfluidic devices were constructed to create controlled environments for the introduction of cells and rinsing solutions (Figure 3a).[18] First, a series of Au pads was patterned on glass surfaces by using standard photolithographic techniques (see Supporting Information). After treatment of the pads with commercially obtained 5′-thiolated ssDNA strands, a prefabricated channel layer of (poly)-dimethylsiloxane (PDMS) was affixed on top to form enclosed chambers. The resultant channels were 6 cm long, 600 μm wide, and 32 μm deep, which corresponds to a total volume of 1.5 μL. An external syringe pump was attached to control solution delivery at rates between 1–100 $\mu L\,min^{-1}$, and a mounted epifluorescence microscope with a digital camera was used for analysis. Two complementary 20-mer DNA-sequence pairs (**A**/**A**′ and **B**/**B**′) were chosen such that they possessed an identical overall base composition, but no appreciable affinity for each other. Strands **A**′ and **B**′ were bound to the Au surfaces within the channels, and strands **A** and **B** were attached to the cells by using the Staudinger ligation method described above. The presence and hybridization ability of the surface-immobilized DNA strands in the devices were determined through incubation with fluorescently labeled probe strands (Figure 3b).

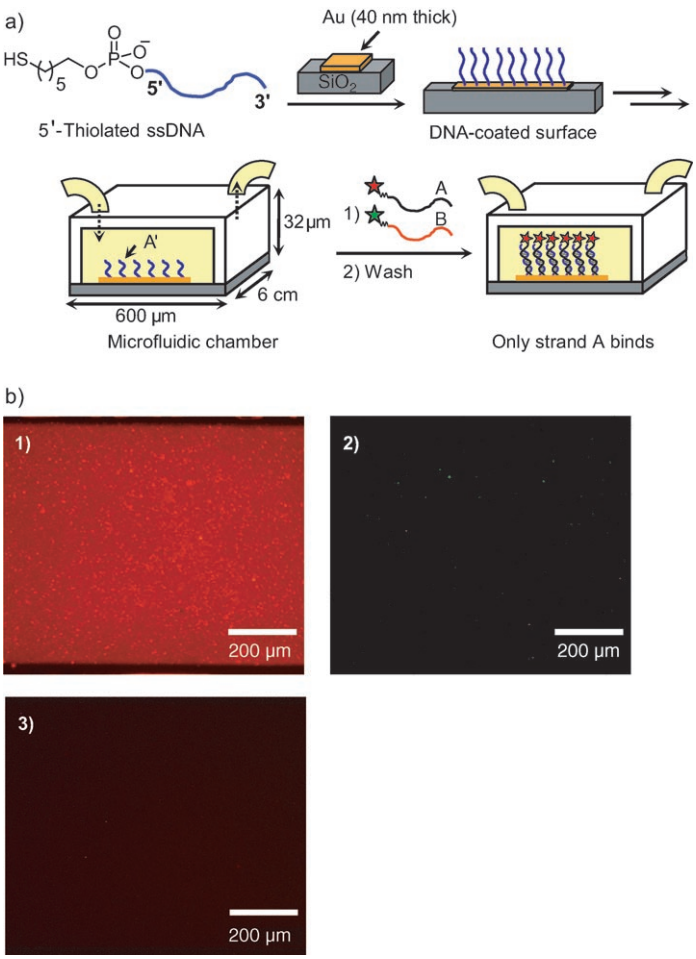


Figure 3. Construction of a microfluidic device for DNA display. a) Thiolated ssDNA strands are bound to patterned Au pads located in microfluidic chambers, solution delivery and washing can be controlled. Coating DNA strands were **A**′: 5′-AGT GAC AGC TGG ATC GTT AC-3′ and **B**′: 5′-CCC TAG AGT GAG TCG TAT GA-3′. The presence of DNA was detected by using matched (**A**, red) and mismatched (**B**, green) probe strands. b) Fluorescence images of 1) Probe **A** incubated with **A**′-coated surface; 2) Probe **B** incubated with **A**′-coated surface; 3) Probe **A** incubated with **B**′-coated surface.

To test the system, we introduced azides onto the surface of Jurkat cells, a naturally non-adherent cell type. The labeled cells were then divided into two subsets and each of these was modified with either DNA sequence **A** or **B**. For tracking purposes, the two subsets of cells were also labeled with either blue (7-amino-4-chloromethylcoumarin) or green (5-chloromethylfluorescein diacetate) cytosolic dyes. Equal numbers of each labeled subpopulation were then mixed and introduced into the device through the syringe pump. The cells were incubated for 35 min under static conditions to allow hybridization, and then unbound cells were flushed from the system with excess phosphate-buffered saline (PBS) solution.

Representative fluorescence microscopy data for these experiments are shown in Figure 4. Only cells bearing ssDNA strands that were complementary to the immobilized DNA were observed to bind to the surface (Figure 4b), whereas otherwise identical cells bearing mismatched sequences were washed away. Quantitative binding data obtained from three device regions are shown in Figure 4c. We found that 95% and 91% of the bound cells had recognized the appropriate complementary sequence for the **A**′ and **B**′ pads, respectively. Control experiments with cells that lack surface DNA showed no binding.

As further confirmation of the DNA dependence of our immobilization method, DNA-coated pads were blocked with complementary DNA sequences prior to the introduction of labeled cells. Although many cells bearing complementary DNA strands were exposed to the pads, virtually no binding was observed following the standard rinsing procedure (Figure 4d).

A particular advantage of this method is the ability to immobilize naturally non-adherent cells as well as adherent ones. This is because metabolic engineering can be used to introduce azide functional groups on virtually any cell type that displays sialic acid residues on its surface.[14] We have explored the generality of this

 © 2006 Wiley-VCH Verlag GmbH & Co. KGaA, Weinheim

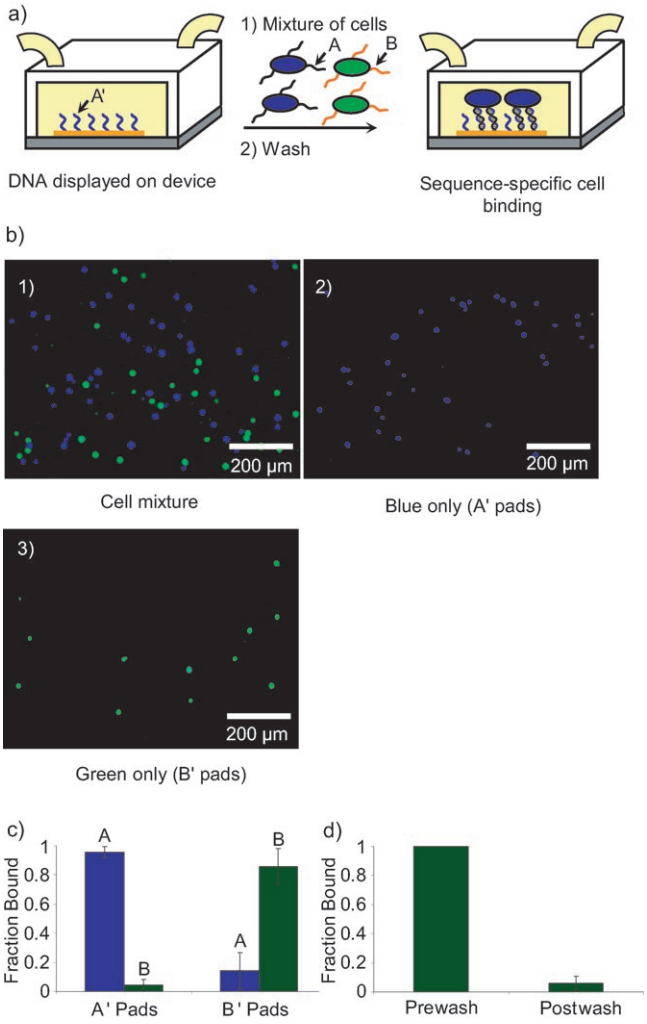


Figure 4. Immobilization of cells is DNA sequence-specific. a) Blue and green dye-labeled Jurkat cell populations were functionalized with DNA sequence **A** or **B**, respectively. An equal number of cells were combined and the mixture was introduced into the microfluidic device (as in Figure 3). b) Fluorescence images of: 1) the cell mixture prewash; 2) an **A**′-coated pad postwash; 3) a **B**′-coated pad postwash. c) Summary data for the fraction of the bound cells with either sequence **A** (blue), or sequence **B** (green) under each pad condition. d) **B**′-coated pads were pre-exposed to excess soluble strand **B**; these data summarize the fraction of green (sequence **B** bound) cells bound before and after washing. Error bars represent the standard deviation of three separate areas of the device.

technique through the immobilization of several additional cell lines, including Chinese Hamster Ovary (CHO) and HEK cells. Both CHO and HEK cells are naturally adherent cell types and each was successfully immobilized through this approach. Furthermore, we have found that this attachment method can be utilized on micropatterned Au pads that possess the same spatial dimensions as the cells (Figure 5).

The strength of DNA-mediated binding was determined by subjecting immobilized cells to increasing lateral shear force. PBS solution was introduced at increasing flow rates (1–50 $\mu L\,min^{-1}$ over a period of 10 min) and the bound HEK cells were observed. In almost every instance, the bound cells were not washed away. Through the use of the Navier-Stokes

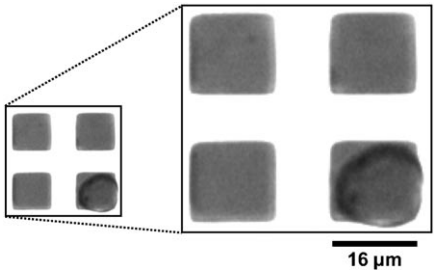


Figure 5. A single human embryonic kidney (HEK) cell immobilized on a 16-μm by 16-μm square Au pad. Cells bearing surface DNA strands were bound to Au pads decorated with complementary strands. Bright field microscopy was used to visualize the cells (magnified portion, 40×). Adhesion of cells lacking DNA or bearing noncomplementary DNA was not observed. Immobilized cells appeared morphologically similar to unbound cells.

method,[19] we calculated that bound cells are stable to shear forces that exceed 31 $dyn\,cm^{-2}$, which is far greater than that needed for most applications.[20] Similar results were noted for Jurkat and CHO cells.

For this method to be broadly useful, the longevity of cell surface–DNA complexes must extend beyond the time scale of the experiment.[1] Although it might be expected that there would be a loss of surface DNA owing to cell membrane recycling or secreted nuclease activity,[21] the cells have remained bound to the surfaces for periods exceeding 25 h despite the fact that we have taken no measures to avoid these degradation pathways.

Finally, we evaluated the prolonged loyalty of bound cells to the surface and their long-term viability though two additional studies conducted in parallel. In the first, Jurkat cells labeled with sequence **A** were immobilized as previously described, and a gentle flow of Jurkat culture medium was continuously applied to the device for 25 h. Cells were visualized by using light microscopy at several time points to determine their positions. Virtually all of the bound cells remained at their initial locations for the entire duration of the experiment. Secondly, we investigated cell viability and membrane integrity by using redoxsensor red CC-1, a fluorescent dye that is retained and activated in live cells. To more closely approximate typical culture conditions, the PDMS channel layer was removed from the device prior to introduction of the cells. After the cells had been allowed to bind for 35 min, Jurkat culture medium was added and the device was incubated at 37 °C for 25 h. The cells in the device were then treated with redoxsensor red CC-1 for 30 min, and the device was gently rinsed to identify the unbound cells. Analysis of both the bound and unbound cells indicated that 79 % of the DNA-bound cells remained viable after the 25 h period. This percentage was identical to that observed for the unbound Jurkat cells. We therefore believe that this method will be useful for applications that require extended cell immobilization.[1] More detailed studies of the physiological effects of DNA-based cell immobilization are currently underway.

In summary, we have described a new approach for engineering cell-adhesion events. This DNA-based strategy is sequence specific and applicable to a variety of devices and

 © 2006 Wiley-VCH Verlag GmbH & Co. KGaA, Weinheim

cell types. Current work is focused on tuning the adhesive properties and studying the long-term behavior of DNA-immobilized cells, and ongoing efforts are capitalizing on the programmability of this method to form complex, multicellular patterns for sensing applications.

Received: July 12, 2005
Revised: November 7, 2005
Published online: December 21, 2005

Keywords: cell adhesion · chemical biology · DNA recognition · glycoproteins · Staudinger ligation

[1] a) R. Singhvi, A. Kumar, G. P. Lopez, G. N. Stephanopoulos, D. I. C. Wang, G. M. Whitesides, D. E. Ingber, *Science* **1994**, *264*, 696; b) C. S. Chen, M. Mrksich, S. Huang, G. M. Whitesides, D. E. Ingber, *Science* **1997**, *276*, 1425; c) C. Roberts, C. S. Chen, M. Mrksich, V. Martichonok, D. E. Ingber, G. M. Whitesides, *J. Am. Chem. Soc.* **1998**, *120*, 6548; d) A. M. P. Turner, N. Dowell, S. W. P. Turner, L. Kam, M. Isaacson, J. N. Turner, H. G. Craighead, W. Shain, *J. Biomed. Mater. Res.* **2000**, *51*, 430; e) N. M. Toriello, E. S. Douglas, R. A. Mathies, *Anal. Chem* **2005**, *77*, 6935.

[2] a) J. B. Shear, H. A. Fishman, N. L. Allbritton, D. Garigan, R. N. Zare, R. H. Scheller, *Science* **1995**, *267*, 74; b) T. H. Rider, M. S. Petrovick, F. E. Nargi, J. D. Harper, E. D. Schwoebel, R. H. Mathews, D. J. Blanchard, L. T. Bortolin, A. M. Young, J. Chen, M. A. Hollis, *Science* **2003**, *301*, 213.

[3] a) J. Ziauddin, D. M. Sabatini, *Nature* **2001**, *411*, 107; b) O. E. Beske, S. Goldbard, *Drug Discovery Today* **2002**, *7*, S131.

[4] a) A. Revzin, P. Rajagopalan, A. W. Tilles, F. Berthiaume, M. L. Yarmush, M. Toner, *Langmuir* **2004**, *20*, 2999; b) E. Cukierman, R. Pankov, D. R. Stevens, K. M. Yamada, *Science* **2001**, *294*, 1708.

[5] D. Kleinfeld, K. H. Kahler, P. E. Hockberger, *J. Neurosci.* **1988**, *8*, 4098.

[6] a) C. S. Chen, M. Mrksich, S. Huang, G. M. Whitesides, D. E. Ingber, *Biotechnol. Prog.* **1998**, *14*, 356; b) M. Mrksich, *Curr. Opin. Chem. Biol.* **2002**, *6*, 794.

[7] a) R. O. Hynes, *Cell* **1992**, *69*, 11; b) F. G. Giancotti, E. Ruoslahti, *Science* **1999**, *285*, 1028.

[8] M. Kato, M. Mrksich, *J. Am. Chem. Soc.* **2004**, *126*, 6504.

[9] C. C. Co, Y.-C. Wang, C.-C. Ho, *J. Am. Chem. Soc.* **2005**, *127*, 1598.

[10] a) C. Yoshina-Ishii, G. P. Miller, M. L. Kraft, E. T. Kool, S. G. Boxer, *J. Am. Chem. Soc.* **2005**, *127*, 1356; b) C. Yoshina-Ishii, S. G. Boxer, *J. Am. Chem. Soc.* **2003**, *125*, 3696.

[11] A. C. Pease, D. Solas, E. J. Sullivan, M. T. Cronin, C. P. Holmes, S. P. A. Fodor, *Proc. Natl. Acad. Sci. USA* **1994**, *91*, 5022.

[12] L. M. Demers, D. S. Ginger, S.-J. Park, Z. Li, S.-W. Chung, C. A. Mirkin, *Science* **2002**, *296*, 1836.

[13] All materials and methods may be found in the Supporting Information.

[14] D. H. Dube, C. R. Bertozzi, *Curr. Opin. Chem. Biol.* **2003**, *7*, 616.

[15] E. Saxon, C. R. Bertozzi, *Science* **2000**, *287*, 2007.

[16] For a related study that utilizes oligonucleotides and the Staudinger ligation, see: C. C.-Y. Wang, T. S. Seo, Z. Li, H. Ruparel, J. Ju, *Bioconjugate Chem.* **2003**, *14*, 697.

[17] For an example, see: M. F. Hagan, A. K. Chakraborty, *J. Chem. Phys.* **2004**, *120*, 4958.

[18] D. C. Duffy, J. C. McDonald, O. J. A. Schueller, G. M. Whitesides, *Anal. Chem.* **1998**, *70*, 4974.

[19] R. B. Bird, W. E. Stewart, E. N. Lightfoot, *Transport Phenomena*, Wiley, New York, **1966**, pp. 80–81.

[20] a) M. Takagi, K. Shiwaku, T. Inoue, T. Shirakawa, Y. Sawa, H. Matsuda, T. Yoshida, *J. Artif. Organs* **2003**, *6*, 222; b) B. T. Marshall, M. Long, J. W. Piper, T. Yago, R. P. McEver, C. Zhu, *Nature* **2003**, *423*, 190.

[21] a) D. A. Nauman, C. R. Bertozzi, *Biochim. Biophys. Acta* **2001**, *1568*, 147; b) K.-C. Hsia, C.-L. Li, H. S. Yuan, *Curr. Opin. Struct. Biol.* **2005**, *15*, 126.

 © 2006 Wiley-VCH Verlag GmbH & Co. KGaA, Weinheim

Supramolecular Chemistry

DOI: 10.1002/anie.200504049

One-Pot, 18-Component Synthesis of an Octahedral Nanocontainer Molecule**

*Xuejun Liu, Yong Liu, Gina Li, and Ralf Warmuth**

The investigation and application of molecular container compounds is a main focus in host–guest chemistry.[1] Molecular containers permit the room-temperature stabilization of otherwise fleeting intermediates,[2] accelerate reactions, and change regio- and stereochemistry.[3,4] The development of self-assembly processes for the synthesis of molecular capsules involving hydrogen bonding or metal coordination has tremendously spurred the growth of this field.[5–8] The power of these supramolecular approaches is their ease and efficiency, best demonstrated in the quantitative synthesis of nanoscale capsules that are large enough to accommodate multiple guests.[9–12] Even though similar sized covalent container molecules, constructed from five or six cavitands, have been prepared in multiple steps,[13,14] an approach for their synthesis with efficiencies that are comparable to those of supramolecular approaches remains elusive. Herein, we report the nearly quantitative one-pot synthesis of a nanoscale container molecule by making use of dynamic covalent chemistry.[15,16] In a thermodynamically driven reaction, 18 components condense to form a nanocontainer with an inner cavity of approximately 1700 $Å^3$ that is suitable for encapsulation of biomolecules or multiple organic species. Our approach is not only very efficient stepwise but also atom-efficient, which should facilitate applications of this nanocontainer in medicinal, analytical, chemical, and material sciences.

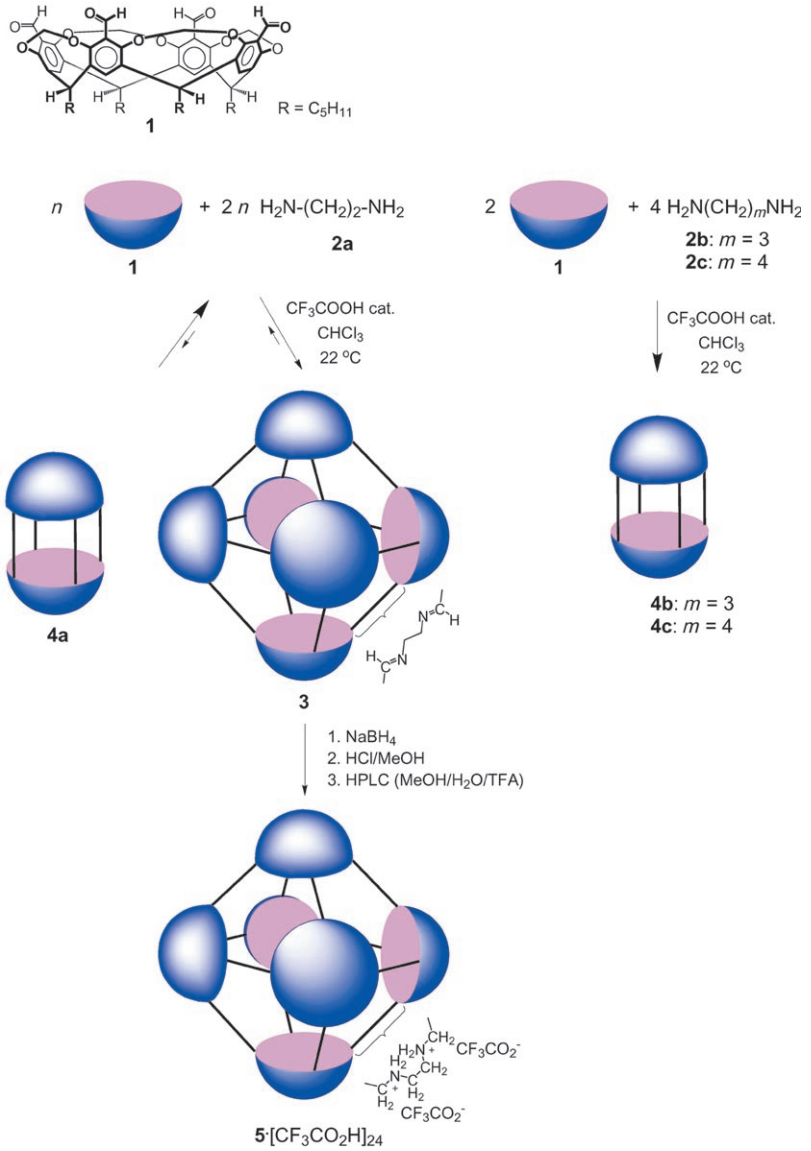
[*] X. Liu, Y. Liu, G. Li, Dr. R. Warmuth
Department of Chemistry and Chemical Biology
Rutgers, The State University of New Jersey
Piscataway, NJ 08854 (USA)
Fax: (+1) 732-445-5312
E-mail: warmuth@rutchem.rutgers.edu

[**] This research is supported by the NSF (grants CHE-0431749 and CHE-0518351). We warmly thank Dr. Seho Kim for assistance with PFG-SE NMR experiments.

Supporting information for this article is available on the WWW under http://www.angewandte.org or from the author.

© 2006 Wiley-VCH Verlag GmbH & Co. KGaA, Weinheim

In an investigation of the condensation reaction between the tetraformylcavitand **1** and various diamines, we discovered the spontaneous formation of an octahedral nanocontainer **3** composed of six cavitands that are connected together with 12 diamino bridging units through 24 newly formed imine bonds (Scheme 1). Earlier work showed that the reaction of two equivalents of **1** with four equivalents of 1,3-phenylenediamine is under thermodynamic control and quantitatively yields an octaiminohemicarcerand.[17]



Scheme 1. The thermodynamically controlled condensation of cavitand **1** with diamines **2a–c** leading to nanocontainer **3** or octaiminohemicarcerands **4b** ($m = 3$) and **4c** ($m = 4$), and reduction of **3** to **5**.

Likewise, the trifluoroacetic acid catalyzed condensation of **1** with 1,3-diaminopropane (**2b**) or 1,4-diaminobutane (**2c**) gave hemicarcerands **4b** and **4c**, respectively, in over 95% yield as supported by NMR and IR spectroscopy, gel permeation chromatography (GPC), and mass spectrometric analysis (Scheme 1). However, when we carried out the same reaction with ethylendiamine (**2a**), the ^{1}H NMR spectrum of the reaction mixture indicated the slow formation of a major product in up to 82% yield with a molecular weight of approximately 6000 Da (GPC; Figure 1a–c). The simplified ^{1}H and ^{13}C NMR spectra are consistent with the octahedrally symmetric **3** being the product of this 18-component condensation reaction (Figure 1c).

The electrospray ionization (ESI) mass spectrum of **3** further supports this conclusion and shows signals for ions $[M+3\,H]^{3+}$, $[M+4\,H]^{4+}$, $[M+5\,H]^{5+}$, and $[M+6\,H]^{6+}$ at m/z 1956.1, 1460.3, 1167.4, and 967.7, respectively. Isolation and purification of **3** proved impossible as a result of the instability of the imine bonds towards normal-phase chromatography. However, after reduction of all the imine bonds of **3** with $NaBH_4$, reversed-phase HPLC purification was possible and nanocontainer **5** was isolated as the trifluoroacetate salt in 63% yield based on **1** (Scheme 1). Again, the ^{1}H and ^{13}C NMR spectra were consistent with the octahedral symmetry of **5**·24 CF_3COOH (Figure 1d).

Furthermore, the ESI mass spectrum of a solution of **5**·24 CF_3COOH in methanol containing 0.1% TFA showed signals at the expected mass-to-charge ratio for ions $[\mathbf{5}+4\,H+n\,CF_3CO_2H]^{4+}$ with $n = 0$–8 and for ions $[\mathbf{5}+5\,H+m\,CF_3CO_2H]^{5+}$ with $m = 0$–7, which result from the addition of up to 12 CF_3CO_2H units to **5** and the loss of four or five trifluoroacetate anions, respectively, during electrospray ionization. Strong charge repulsions might explain the absence of higher than 12-fold protonated ions, in which at least one linker would be doubly charged.

Unfortunately, crystals suitable for X-ray structure determination could not be obtained. Thus, we probed the size and shape of **3** and **5** by molecular mechanics calculations (Amber* force field; Figure 2).[18,19] From these modeling studies we estimated a cavity volume for **5** of approximately 1700 Å^3, which is large enough to encapsulate multiple guest molecules. That **5** adapts a comparable structure in solution was demonstrated by diffusivity measurements. Pulsed field gradient spin echo (PSG-SE) NMR experiments in CD_3OD containing 0.4% CF_3CO_2D provided a diffusion rate $D = (2.28 \pm 0.09) \times 10^{-6}$ cm^2 s^{-1}.[20] Application of the Stokes–Einstein equation yields a solvodynamic diameter of 3.2 nm, which is consistent with estimates from molecular models.

The vast number of products that the reaction of **1** with **2a** theoretically might lead to and the necessity to correctly form 24 new covalent bonds demands for a greater than 99% yield in each bond-forming step, in order for **3** to be the dominant product of the reaction. Such efficiency in one-pot syntheses of molecular containers is only achievable if an ideal template preorganizes the reactants[21] or, as in this case, if bonds form reversibly, thus allowing for error correction and ultimately furnishing the thermodynamically most stable product.[5,6,8–12,15–17] Our force-field calculations provide some insight into the thermodynamics of this reaction. They show that the spatial arrangement of the cavitands of hypothetical **4a** forces each ethylenediamine unit into a *gauche* conforma-

 © 2006 Wiley-VCH Verlag GmbH & Co. KGaA, Weinheim

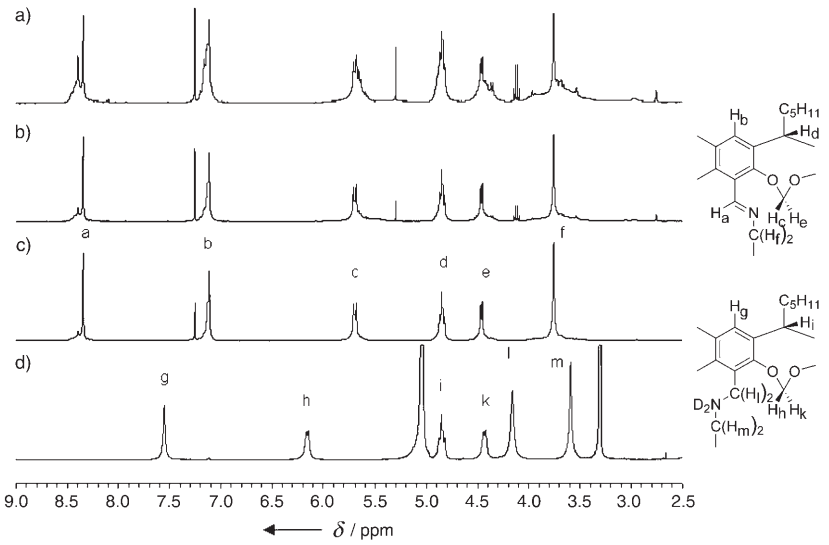


Figure 1. a–c) Partial ^{1}H NMR spectra (400 MHz, 22 °C, $CDCl_3$) of products formed upon mixing **1** with two equivalents of **2a** in $CHCl_3$ containing catalytic amounts of CF_3CO_2H, after a) 0.5 h, b) 3 h, and c) 70 h. d) Partial ^{1}H NMR spectra of **5** (300 MHz, 7 °C, CD_3OD, 0.4 % CF_3CO_2D).

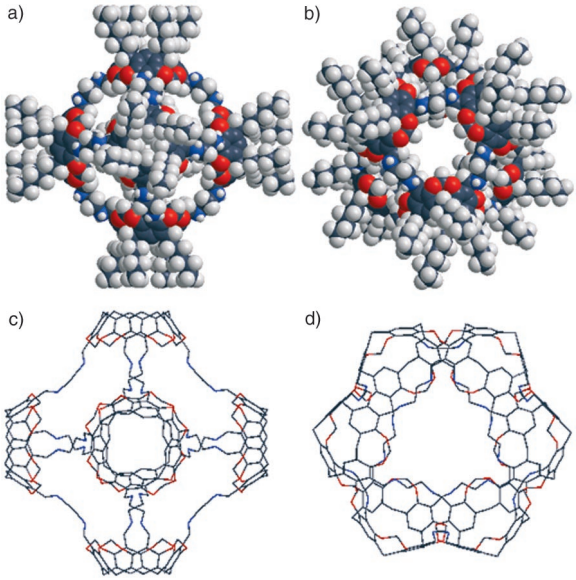


Figure 2. Views along the C_4 (a, c) and C_3 axes (b, d) of energy-minimized structures: a, b) **5**·24 H^+ (space-filling models; Amber* force field,[18] GB/SA water-solvation model[19]); c, d) **3** (stick representation; hydrogen atoms and pentyl groups are omitted; Amber*; vacuum). C gray; H white; O red; N blue.

tion, whereas they are *anti* in **3**, thus minimizing strain within each linker. The fact that condensation of **1** with two equivalents of (*R*,*R*)-1,2-diaminocyclohexane gave polymeric products with molecular weights of greater that 25 000 Da (GPC) rather than the 2:4 hemicarcerand condensation product, which would have been expected based on the preferred conformation of this diamine, suggests that rim-to-rim and/or rim-to-linker interactions might also contribute to the higher stability of **3** versus **4a**. Unfavorable interactions of this kind should increase with decreasing portal size in the host structure, consistent with only the shortest among the investigated diaminoalkanes **2a–c** yielding a hexameric nanocontainer. The fact that nanocontainer **5** is not observed if **1** is treated with two equivalents of **2a** in CH_2ClCH_2Cl or only observed in 17 % yield in $CHCl_2CHCl_2$ shows that the nature of the solvent has a strong influence on the stability of **5** relative to the myriad of other possible oligomeric condensation products. This large solvent effect cannot solely arise from better occupancy of inner space,[22] as part of a solvent molecule can easily protrude through one of the larger openings in the host shell, which have diameters of approximately 8 Å. It suggests that perhaps specific interactions between the solvent and the surface of the host, for which crystallographic studies provide some evidence,[23] are important too and are more favorable for $CHCl_3$ as compared to the other two chlorinated solvents.

We have demonstrated the possibility to synthesize nanosized container molecules from almost 20 components in a single step, which strongly surpasses earlier multistep syntheses in its simplicity and efficiency.[13,14] Our synthesis produces a spherical host that is large enough to encapsulate multiple guests, with portals that should permit polyaromatic compounds easy entrance into its hydrophobic cavity and with functionality that allows derivatization to tailor **5** for specific applications. We see potential uses of **5** and analogues in drug- or pesticide-delivery systems, wastewater detoxification, separation technology, and as molecular reactors for controlled oligomerizations of organic and inorganic monomers. The large variety of reversible bond-forming reactions suitable for dynamic covalent chemistry[15] suggests that other covalent nano-assemblies with spherical or tubular shapes and different properties are accessible through such multicomponent syntheses. The versatility of this approach and the binding properties of **5** are currently being explored in our laboratory.

Experimental Section

Synthesis and characterization of **3** and **5**: A solution of **1**[17] (85.8 mg, 92.3 μmol), ethylene-1,2-diamine (11.1 mg, 184.6 μmol), and CF_3CO_2H (TFA; 0.45 μL, 1 μmol) in $CHCl_3$ (7 mL) was stirred at room temperature under argon for 70 h. A small sample was removed from the reaction mixture, and the solvent was evaporated under high vacuum to yield a yellow solid that contained **3** (82 % by integration of ^{1}H NMR spectra): ^{1}H NMR (400 MHz, $CDCl_3$, 22 °C): $\delta = 8.34$ (s, 24 H; C*H*N), 7.12 (s, 24 H; H_{aryl}), 5.70 (d, ^3J (H,H) = 7.5 Hz, 24 H; $OCH_{out}HO$), 4.83 (t, ^3J (H,H) = 8 Hz, 24 H; $CH(CH_2)_4CH_3$), 4.46 (d, ^3J (H,H) = 7.5 Hz, 24 H; $OCH_{in}HO$), 3.75 (br s, 48 H; NCH_2), 2.25–2.15 (m, 48 H; $CHCH_2(CH_2)_3CH_3$), 1.5–1.3 (m, 144 H; $CHCH_2(CH_2)_3CH_3$), 0.91 ppm (t, ^3J (H,H) = 7.1 Hz, 72 H; CH_3); ^{13}C NMR (100 MHz, $CDCl_3$, 22 °C): $\delta = 157.7$, 153.6, 138.8, 124.5, 121.7, 100.5, 63.2, 36.7, 32.3, 30.1, 27.9, 23.0, 14.4 ppm; IR ($CHCl_3$): $\tilde{\nu} = 2956.8$, 2929.6, 2872.1, 2855.6, 1641.5 (C = N), 1602.6, 1587, 1361.3, 1112.3, 1088.9, 980 cm^{-1}; ESI-MS (CH_2Cl_2/CH_3CN 1:5): *m*/*z* (%): 1954.9 (100) $[M+3H]^{3+}$, 1466.9 (13) $[M+4H]^{4+}$, 1173.7 (3) $[M+5H]^{5+}$.

 © 2006 Wiley-VCH Verlag GmbH & Co. KGaA, Weinheim

Nanocontainer **3** was used in the next step without further purification. $NaBH_4$ (150 mg; 4 mmol) and CH_3OH (0.5 mL) were added to a vigorously stirred solution of crude **3** (90 mg) in $CHCl_3$ (7 mL). After 30 min, excess $NaBH_4$ was destroyed by the addition of water (1 mL). The solvent was removed at reduced pressure, and the residue was dissolved in CH_3OH/conc. HCl (10:1). After 3.5 days at room temperature, the solvent was removed. The crude product was purified by reversed-phase HPLC (Vydac RP-18; 10μ; 300 Å; 21 × 250 mm^2; CH_3OH/H_2O/TFA (gradient 85:15:0.1 to 98:2:0.1, 15 min, then hold for 10 min), 15 mL min^{-1}, 280 nm, t_R(**5**) = 13.4 min) to give **5**·24 CF_3COOH as a white solid (84 mg; 63% yield based on **1**): ^{1}H NMR (300 MHz, CD_3OD, 0.4% CF_3COOD, 7°C): δ = 7.55 (s, 24H; H_{aryl}), 6.16 (d, ^3J (H,H) = 6.9 Hz, 24H; $OCH_{out}HO$), 4.85 (t, ^3J (H,H) = 7.6 Hz, 24H; $CH(CH_2)_4CH_3$), 4.43 (d, ^3J (H,H) = 6.9 Hz, 24H; $OCH_{in}HO$), 4.16 (br s, 48H; NCH_2Ar), 3.59 (br s, 48H, $N(CH_2)_2N$), 2.38 (br s, 48H, $CHCH_2(CH_2)_3CH_3$), 1.6–1.2 (m, 144H; $CHCH_2(CH_2)_3CH_3$), 0.92 ppm (t, ^3J (H,H) = 7.1 Hz, 72H; CH_3); ^{13}C NMR (75 MHz, CD_3OD, 0.4% CF_3COOD, 22°C): δ = 160.5 (q, ^2J (C,F) = 37.8 Hz), 155.1, 139.9, 124.6, 119.9, 101.2, 44.4, 42.7, 38.5, 33.1, 30.9, 29.1, 24.0, 14.6 ppm; ESI-MS (CH_3OH/H_2O/TFA 98:2:0.1) *m/z*: 1478.9 $[M+4H]^{4+}$, 1507.3 $[M+4H+TFA]^{4+}$, 1535.5 $[M+4H+2TFA]^{4+}$, 1564.1 $[M+4H+3TFA]^{4+}$, 1592.5 $[M+4H+4TFA]^{4+}$, 1620.7 $[M+4H+5TFA]^{4+}$, 1649.1 $[M+4H+6TFA]^{4+}$, 1677.4 $[M+4H+7TFA]^{4+}$, 1706.0 $[M+4H+8TFA]^{4+}$; elemental analysis (%) calcd for $C_{408}H_{522}F_{72}N_{24}O_{105}$ (**5**·24 CF_3CO_2H·9 H_2O): C 55.62, H 5.97, N 3.82; found C 55.63, H 6.17, N 3.84.

Received: November 15, 2005
Published online: December 30, 2005

Keywords: cavitands · host–guest systems · multicomponent reactions · supramolecular chemistry

[1] a) D. J. Cram, J. M. Cram, *Container Molecules and their Guests*, Royal Society of Chemistry, Cambridge, UK, **1994**; b) A. Jasat, J. C. Sherman, *Chem. Rev.* **1999**, *99*, 931; c) R. Warmuth, J. Yoon, *Acc. Chem. Res.* **2001**, *34*, 95.
[2] a) D. J. Cram, M. E. Tanner, R. Thomas, *Angew. Chem.* **1991**, *103*, 1048; *Angew. Chem. Int. Ed. Engl.* **1991**, *30*, 1024; b) P. Roach, R. Warmuth, *Angew. Chem.* **2003**, *115*, 3147; *Angew. Chem. Int. Ed.* **2003**, *42*, 3039.
[3] a) J. Kang, J. Rebek, Jr., *Nature* **1997**, *385*, 50; b) D. Fiedler, R. G. Bergman, K. N. Raymond, *Angew. Chem.* **2004**, *116*, 6916; *Angew. Chem. Int. Ed.* **2004**, *43*, 6748.
[4] M. Yoshizawa, Y. Takeyama, T. Kusukawa, M. Fujita, *Angew. Chem.* **2002**, *114*, 1403; *Angew. Chem. Int. Ed.* **2002**, *41*, 1347.
[5] J. Rebek, Jr., *Chem. Soc. Rev.* **1996**, *25*, 255.
[6] M. A. Mateos-Timoneda, M. Crego-Calama, D. N. Reinhoudt, *Chem. Soc. Rev.* **2004**, *33*, 363.
[7] L. R. MacGillivray, J. L. Atwood, *Angew. Chem.* **1999**, *111*, 1080; *Angew. Chem. Int. Ed.* **1999**, *38*, 1018.
[8] a) M. Fujita, M. Tominaga, A. Hori, B. Therrien, *Acc. Chem. Res.* **2005**, *38*, 371; b) S. R. Seidel, P. J. Stang, *Acc. Chem. Res.* **2002**, *35*, 972.
[9] N. Takeda, K. Umemoto, K. Yamaguchi, M. Fujita, *Nature* **1999**, *398*, 794.
[10] B. Olenyuk, J. A. Whiteford, A. Fechtenkoetter, P. J. Stang, *Nature* **1999**, *398*, 796.
[11] a) L. R. MacGillivray, J. L. Atwood, *Nature* **1997**, *389*, 469; b) A. Shivanyuk, J. Rebek, Jr., *Chem. Commun.* **2001**, 2424.
[12] a) L. J. Prins, J. Huskens, F. De Jong, P. Timmerman, D. N. Reinhoudt, *Nature* **1999**, *398*, 498; b) L. J. Prins, F. De Jong, P. Timmerman, D. N. Reinhoudt, *Nature* **2000**, *408*, 181.
[13] E. S. Barrett, J. L. Irwin, A. J. Edwards, M. S. Sherburn, *J. Am. Chem. Soc.* **2004**, *126*, 16747.
[14] D. A. Makeiff, J. C. Sherman, *J. Am. Chem. Soc.* **2005**, *127*, 12363.
[15] a) S. J. Rowan, S. J. Cantrill, G. R. L. Cousins, J. K. M. Sanders, J. F. Stoddart, *Angew. Chem.* **2002**, *114*, 938; *Angew. Chem. Int. Ed.* **2002**, *41*, 898; b) J.-M. Lehn, *Chem. Eur. J.* **1999**, *5*, 2455.
[16] a) R. T. S. Lam, A. Belenguer, S. L. Roberts, C. Naumann, T. Jarrosson, S. Otto, J. K. M. Sanders, *Science* **2005**, *308*, 667; b) K. C.-F. Leung, F. Aricó, S. J. Cantrill, J. F. Stoddart, *J. Am. Chem. Soc.* **2005**, *127*, 5808; c) K. R. West, K. D. Bake, S. Otto, *Org. Lett.* **2005**, *7*, 2615; d) K. S. Chichak, S. J. Cantrill, A. R. Pease, S.-H. Chiu, G. W. V. Cave, J. L. Atwood, J. F. Stoddart, *Science* **2004**, *304*, 1308; e) A. F. M. Kilbinger, S. J. Cantrill, A. W. Waltman, M. W. Day, R. H. Grubbs, *Angew. Chem.* **2003**, *115*, 3403; *Angew. Chem. Int. Ed.* **2003**, *42*, 3281.
[17] a) S. Ro, S. J. Rowan, A. R. Pease, D. J. Cram, J. F. Stoddart, *Org. Lett.* **2000**, *2*, 2411; b) M. L. C. Quan, D. J. Cram, *J. Am. Chem. Soc.* **1991**, *113*, 2754.
[18] D. Q. McDonald, W. C. Still, *Tetrahedron Lett.* **1992**, *33*, 7743.
[19] W. C. Still, A. Tempczyk, R. C. Hawley, T. Hendrickson, *J. Am. Chem. Soc.* **1990**, *112*, 6127.
[20] W. S. Price, *Concepts Magn. Reson.* **1997**, *9*, 299.
[21] J. Sherman, *Chem. Commun.* **2003**,1617.
[22] S. Mecozzi, J. Rebek, Jr., *Chem. Eur. J.* **1998**, *4*, 1016.
[23] a) T. A. Robbins, C. B. Knobler, D. R. Bellew, D. J. Cram, *J. Am. Chem. Soc.* **1994**, *116*, 111; b) M. Yoshizawa, T. Kusukawa, M. Kawano, T. Ohhara, I. Tanaka, K. Kurihara, N. Niimura, M. Fujita, *J. Am. Chem. Soc.* **2005**, *127*, 2798; c) G. W. V. Cave, J. Antesberger, L. J. Barbour, R. M. McKinlay, J. L. Atwood, *Angew. Chem.* **2004**, *116*, 5375; *Angew. Chem. Int. Ed.* **2004**, *43*, 5263; d) S. J. Dalgarno, S. A. Tucker, D. B. Bassil, J. L. Atwood, *Science* **2005**, *309*, 2037.

 © 2006 Wiley-VCH Verlag GmbH & Co. KGaA, Weinheim

Chiral Frameworks

DOI: 10.1002/anie.200503657

Chiral 3D Architectures with Helical Channels Constructed from Polyoxometalate Clusters and Copper–Amino Acid Complexes**

Hai-Yan An, En-Bo Wang, Dong-Rong Xiao, Yang-Guang Li, Zhong-Min Su,* and Lin Xu*

Chiral inorganic–organic materials have received much attention, not only because of their numerous potential applications in nonlinear optics, enantioselective catalysis,

[*] Dr. H.-Y. An, Prof. E.-B. Wang, Dr. D.-R. Xiao, Dr. Y.-G. Li, Prof. Z.-M. Su, Prof. L. Xu
Institute of Polyoxometalate Chemistry
Department of Chemistry
Northeast Normal University
Changchun 130024 (China)
Fax: (+86) 431-509-8787
E-mail: wangenbo@public.cc.jl.cn
zmsu@nenu.edu.cn

[**] This work was financially supported by the National Natural Science Foundation of China (No. 20371011).

Supporting information for this article is available on the WWW under http://www.angewandte.org or from the author.

InterScience
© 2006 Wiley-VCH Verlag GmbH & Co. KGaA, Weinheim

and medicine, but also owing to their intriguing variety of architectures and topologies.[1–3] In recent years, much progress has been made in the design of zeolite and metal–phosphate systems with chiral structures.[4] In contrast, only a few compounds containing polyoxoanions and organic ligands/metal coordination complexes have been reported to have chiral features.[5] Polyoxometalates (POMs),[6,7] as anionic early-transition-metal oxide clusters, bear many properties that make them attractive for applications in catalysis, biology, magnetism, optics, and medicine.[8] Because of their importance in the areas of medicine and asymmetric catalysis, in particular, there has been increasing interest in the construction of enantiomerically pure architectures from POM clusters.[9] Two main approaches have been developed for the formation of chiral POM-based frameworks. The first method is based on the direct connection of POM clusters with chiral organic ligands. A few interesting studies on this approach have been performed by the groups of Pope, Yamase, and Kortz.[10] The second method, which is far less developed than the first, uses a chiral metal–organic complex as a template, which can transfer the chirality of the organic ligands to the whole framework through the bonding of the metal centers to the POM cluster. Using this approach, Hill's group has synthesized a fascinating, enantiomerically pure polytungstate that consists of two units of lacunary $[P_2W_{15}O_{56}]^{12-}$ ion bridged by a chiral zirconium–tartrate coordination complex.[11] However, the preparation of enantiomerically pure high-dimensional frameworks constructed from POM units remains largely unexplored, although they may be of practical use in catalysis and separation. Therefore, the search for suitable chiral organic molecules, metal cations, and POM building units to be applied in the construction of chiral 3D open frameworks is one of the most challenging issues in synthetic chemistry and material science.

The remarkable, chiral multidentate ligand, proline, first seized our attention because: 1) it can act as an enantioselective catalyst in many reactions, and as an amino acid, it is a basic building unit in proteins for study in medical applications;[12] 2) it has a relatively small volume and has versatile coordination behavior,[13] which allows extensive cross-linking between the metal–organic moieties and the oxygen-rich POM units to yield high-dimensional architectures.

Among the many different types of POMs, the most well known are the Keggin heteropolyanions.[14] Although it has been amply demonstrated that these clusters can be linked into low-dimensional (0D, 1D, or 2D) structures by using metal cations or their coordination complexes as linkers,[15] the process of assembling Keggin POMs into 3D frameworks is still in its infancy,[16] perhaps owing to the steric demands of the POMs and the deficient charge density at their surface oxygen atoms. Furthermore, reports of enantiomerically pure assemblies of Keggin POMs are rare.[17] Therefore, our focus is the production of 3D chiral networks based on metal–proline coordination complexes as linkers and Keggin polyoxoanions as achiral building units. Herein, we choose the Keggin cluster $[BW_{12}O_{40}]^{5-}$ as the building block, because of its high charge density and its potential applications.[18] We describe two new enantiomerically pure 3D POM-based frameworks with helical channels, D-**1** and L-**1**. The frameworks are built up from homochiral intertwined double helices. The circular dichroism (CD) spectra of compounds D-**1** and L-**1** in the solution state show significant induced optical activity in the POM moieties, as a result of chirality transfer from the chiral proline molecules to the whole framework.

$KH_2[(D\text{-}C_5H_8NO_2)_4(H_2O)Cu_3][BW_{12}O_{40}]\cdot 5H_2O$ D-**1**

$KH_2[(L\text{-}C_5H_8NO_2)_4(H_2O)Cu_3][BW_{12}O_{40}]\cdot 5H_2O$ L-**1**

We adopted standard synthetic techniques for the preparation of compound D-**1** by the reaction of $K_5[BW_{12}O_{40}]\cdot 15H_2O$[19] with copper(II) and D-proline in a molar ratio of 1:2:2 in water. Compound L-**1** was prepared from L-proline under similar synthetic conditions. Single-crystal X-ray diffraction analyses revealed that compounds D-**1** and L-**1** are enantiomers;[20] their unit-cell dimensions, volumes, related bond distances, and angles are only slightly different. The structures of D-**1** and L-**1** exhibit a unique 3D chiral open framework assembled from $[BW_{12}O_{40}]^{5-}$ polyoxoanions and copper–proline coordination polymer chains. D-**1** crystallizes in the chiral space group $P4_32_12$, and L-**1** in the space group $P4_12_12$, each with one $[BW_{12}O_{40}]^{5-}$ unit, three copper atoms, four proline ligands, one potassium atom, two protons, and six water molecules in the asymmetric unit. The $[BW_{12}O_{40}]^{5-}$ cluster is a classic Keggin structure, which consists of a central BO_4 tetrahedron surrounded by four vertex-sharing W_3O_{13} trimers (Figure 1). Each W_3O_{13} group is composed of three WO_6 octahedra linked in a triangular arrangement by sharing edges. There are four types of oxygen atoms with different coordination modes in the cluster: terminal oxygen atoms Ot, terminal oxygen atoms linked to copper(II) Ot′, bridging oxygen atoms Ob, and central oxygen atoms Oc. Thus, the W–O bond lengths fall into four classes: W–Ot 1.667(13)–1.731(9), W–Ot′ 1.694(12)–1.738(12), W–Ob 1.853(13)–1.970(12), and W–Oc 2.318(8)–2.410(8) Å. The central B–O distances vary from 1.463(16) to 1.591(16) Å, and the O-B-O angles are in the range of 106.4(9)–111.7(10)°, indicating that the BO_4 tetrahedra are distorted.

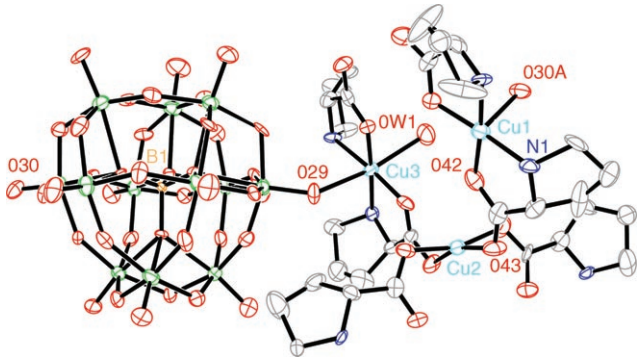


Figure 1. ORTEP drawing of D-**1** with thermal ellipsoids set at 50% probability; B yellow, C gray, N dark blue, O red, Cu blue, W green. Hydrogen and potassium atoms, and solvated water molecules are omitted for clarity. Atom O30A is generated through the symmetry transformation: *y*, *x*−1, −+1.

 © 2006 Wiley-VCH Verlag GmbH & Co. KGaA, Weinheim

There are three crystallographically independent copper(II) centers, each having a different coordination sphere (Figure 1). Cu1 centers a distorted square pyramid, defined by two carboxy oxygen atoms and two nitrogen atoms from two different proline molecules, and one terminal oxygen atom from a Keggin polyoxoanion [Cu1–O30A 2.508(10) Å in D-**1**; 2.470(12) Å in L-**1**]. Cu2 is coordinated by four carboxy oxygen atoms from four different proline molecules in a square-planar geometry. Cu3 has a slightly distorted octahedral coordination environment, formed by two carboxy oxygen atoms and two nitrogen atoms from two different proline molecules, one oxygen atom from a water molecule [Cu3–OW1 2.337(10) Å in D-**1**; 2.364(16) Å in L-**1**], and one terminal oxygen atom from a polyoxoanion [Cu3–O29 2.560(7) Å in D-**1**; 2.515 (12) Å in L-**1**]. Each of the four crystallographically independent proline molecules acts as a tridentate chelating ligand, coordinating to two neighboring copper atoms using its carboxy oxygen atoms and nitrogen atom.

As shown in Figure 2, the copper(II) centers are linked together by proline ligands to yield a 1D coordination

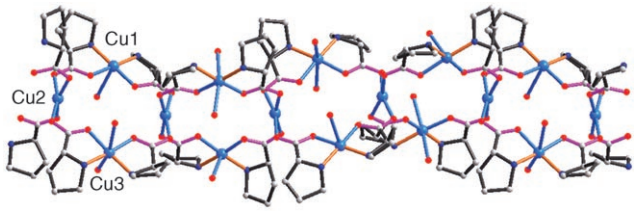


Figure 2. View of the one-dimensional copper–proline coordination polymer chain in D-**1**, showing the carboxylate-bridged tetracopper moieties; C gray, N dark blue, O red, Cu blue.

polymer chain. Each chain consists of moieties in which four copper atoms are bridged by four carboxylate groups from four different proline ligands. The planes of adjacent tetracopper units are nearly perpendicular to one another (see Supporting Information). The copper–proline polymer chains are further covalently bonded to terminal oxo groups of the Keggin clusters by the Cu1 and Cu3 sites of each tetracopper moiety, to form a unique 3D open framework (Figure 3). Each Keggin unit acts as a bidentate ligand, coordinating to two adjacent polymer chains through its terminal oxygen atoms (see Supporting Information). This kind of connection mode results in the formation of channels along the *c* axis. Interestingly, each channel is enclosed by two intertwined helices of the same handedness (Figure 4). Each of these double helices in D-**1** is built up from two identical right-handed single-helical chains with a pitch of 26.201 Å. The helical chains, which are generated around the crystallographic 4_3 axis, are composed of copper–proline subunits bridging four-coordinate boron and six-coordinate tungsten atoms. Differing from D-**1**, the channels of L-**1** are enclosed by two intertwined left-handed helices with a pitch of 26.124 Å, which are generated around the crystallographic 4_1 axis. Such chiral intertwined double helices are rare in inorganic–organic materials. The dimensions of the channels are

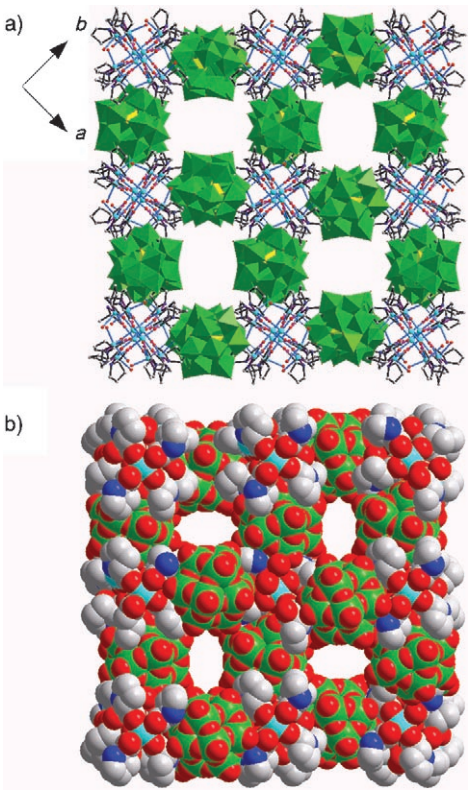


Figure 3. The 3D open-framework structure of D-**1**, which is composed of copper–proline polymer chains covalently linked to Keggin polyoxoanions, viewed along the *c* axis, a) as a polyhedral and ball-and-stick representation, and b) as a space-filling diagram; B yellow, C gray, N dark blue, O red, Cu blue, W green. Hydrogen and potassium atoms, and solvated water molecules are omitted for clarity.

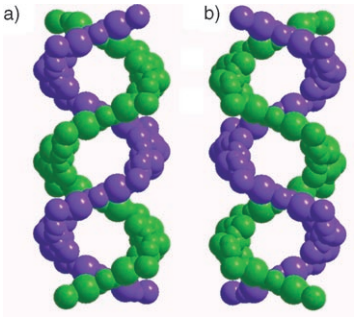


Figure 4. Space-filling diagrams of a) the two intertwined right-handed helices that enclose the channels in D-**1**, and b) the two intertwined left-handed helices in L-**1**.

approximately 10.6 × 7.2 Å in cross section in both compounds (Figure 3b). Water molecules fill the channels and participate in extensive hydrogen-bonding interactions with the polyoxoanions and ligands. The observed chirality of D-**1** and L-**1**, indicated by their chiral space groups, can be understood in terms of chirality transfer from the small chiral proline molecules to the whole framework.

To examine the chiroptical and stable activities of both enantiopure compounds in the solution state, the CD spectra of compounds D-**1** and L-**1** in water were investigated

 © 2006 Wiley-VCH Verlag GmbH & Co. KGaA, Weinheim

(Figure 5). The CD spectra of D-**1** and L-**1** are mirror images of one another, and conclusively demonstrate that D-**1** and L-**1** are enantiomers. Compared with the CD spectra of D-proline (Figure 5, inset), that of D-**1** shows different Cotton effects in

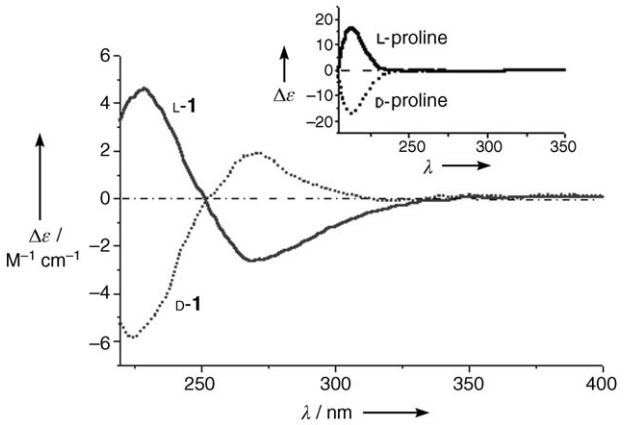


Figure 5. CD spectra in water of D-**1** and L-**1**, and their precursors, D- and L-proline (inset).

the wavelength range of 200–400 nm. The spectrum of the D-proline molecule exhibits only a single negative Cotton effect at 213 nm, while the spectrum of D-**1** exhibits Cotton effects at 225 and 272 nm. In fact, the spectrum of D-**1** displays strong Cotton effects up to 272 nm, the spectral region characteristic of the oxygen-to-tungsten charge-transfer bands of Keggin polyoxoanions.[21] The induced circular dichroism (ICD) in the POM clusters can be clearly seen in the CD spectra,[22] because the chirality transfer from the chiral proline ligands to the POM clusters through the copper bridges leads to a lowering of the symmetry of the Keggin polyoxoanion. The CD and UV/Vis spectra of compounds D-**1** and L-**1** are virtually unchanged with time, indicating that both compounds are enantiomerically stable in aqueous solution.

In summary, we have developed a rational approach to the synthesis of chiral POM-based materials utilizing enantiopure proline ligands, copper cations, and Keggin-type $[BW_{12}O_{40}]^{5-}$ polyoxoanions as building blocks. To our knowledge, compounds D-**1** and L-**1** represent the first examples of homochiral 3D open-framework POM-based compounds with helical channels. The CD spectra of D-**1** and L-**1** in water reveal significant induced optical activity in the POM moieties. It is believed that chirality transfer from the small chiral ligands to the achiral POM units occurs through the copper centers that link them. The successful synthesis of both compounds not only provides novel examples of enantiomerically pure architectures, but also may open up possibilities for the design of new chiral POM-based materials with particular functions.

Experimental Section

D-**1**: D-Proline (0.0576 g, 0.5 mmol) and $CuCl_2{\cdot}2H_2O$ (0.0852 g, 0.5 mmol) were dissolved in water (30 mL). The pH value of the mixture was carefully adjusted with a dilute NaOH solution (1M) to approximately 4.50 and then stirred for 2 h. Then a solution of $K_5[BW_{12}O_{40}]{\cdot}15H_2O$ (0.8306 g, 0.25 mmol) in water (30 mL) was added, and the resulting solution was heated for 2 h at 80 °C. The filtrate was kept for one month at ambient conditions, and blue block crystals of compound D-**1** were isolated in 18% yield (0.110 g, based on copper). Elemental analysis (%) calcd for $C_{20}H_{46}BCu_3KN_4O_{54}W_{12}$: C 6.57, H 1.26, Cu 5.22, K 1.07, N 1.53, W 60.39; found: C 6.83, H 1.01, Cu 5.07, K 0.98, N 1.64, W 60.49. IR (KBr pellet): $\tilde{\nu}=3441$(m), 3260(m), 1561(s), 1451(w), 1325(w), 1185(w), 999(m), 955(s), 904 (s), 821(vs), 532(m), and 424 cm^{-1}(w). $[\alpha]_D^{20}=+43.3$ ($c=1.0$ M, H_2O). $[M]_D=+1581.9$. UV/Vis ($c=1.26\times10^{-5}$ M, H_2O): $\lambda_{max}=256$ nm. CD ($c=5.0\times10^{-4}$ M, H_2O): 225 ($\Delta\varepsilon=-5.9$), 272 nm ($\Delta\varepsilon=1.9$).

L-**1**: The synthesis of compound L-**1** was carried out as described above for compound D-**1**, but starting with L-proline. Yield: 20% (based on copper). Elemental analysis (%) calcd for $C_{20}H_{46}BCu_3KN_4O_{54}W_{12}$: C 6.57, H 1.26, Cu 5.22, K 1.07, N 1.53, W 60.39; found: C 6.78, H 1.03, Cu 5.01, K 1.00, N 1.64, W 60.55. IR (KBr pellet): $\tilde{\nu}=3468$(m), 3260(m), 1560(s), 1455(w), 1377(w), 1326(w), 1184(w), 999(m), 955(s), 904 (s), 821(vs), 533(m), and 423 cm^{-1}(w). $[\alpha]_D^{20}=-44.6$ ($c=1.0$ M, H_2O). $[M]_D=-1629.4$. UV/Vis ($c=1.31\times10^{-5}$ M, H_2O): $\lambda_{max}=256$ nm. CD ($c=4.9\times10^{-4}$ M, H_2O): 229 ($\Delta\varepsilon=4.6$), 269 nm ($\Delta\varepsilon=-2.6$).

Received: October 15, 2005
Published online: December 30, 2005

Keywords: amino acids · chirality · copper · helical structures · polyoxometalates

[1] a) V. Soghomonian, Q. Chen, R. C. Haushalter, J. Zubieta, C. J. O'Connor, *Science* **1993**, *259*, 1596; b) L. J. Prins, J. Huskens, F. D. Jong, P. Timmerman, *Nature* **1999**, *398*, 498; c) J. Chin, S. S. Lee, K. J. Lee, S. Park, D. H. Kim, *Nature* **1999**, *401*, 254.

[2] a) X. H. Bu, H. Liu, M. Du, L. Zhang, Y. M. Guo, M. Shionoya, J. Ribas, *Inorg. Chem.* **2002**, *41*, 5634; b) X. L. Wang, C. Qin, E. B. Wang, L. Xu, Z. M. Su, C. W. Hu, *Angew. Chem.* **2004**, *116*, 5146; *Angew. Chem. Int. Ed.* **2004**, *43*, 5036; c) Y. Cui, H. L. Ngo, P. S. White, W. B. Lin, *Chem. Commun.* **2002**, 1666.

[3] a) X. M. Chen, G. F. Liu, *Chem. Eur. J.* **2002**, *8*, 4811; b) R. G. Xiong, X. Z. You, B. F. Abrahams, Z. L. Xue, C. M. Che, *Angew. Chem.* **2001**, *113*, 4554; *Angew. Chem. Int. Ed.* **2001**, *40*, 4422.

[4] a) M. E. Davis, *Acc. Chem. Res.* **1993**, *26*, 111; b) S. Neeraj, S. Natarajan, C. N. R. Rao, *Chem. Commun.* **1999**, 165; c) Z. Shi, S. Feng, S. Gao, L. Zhang, G. Yang, J. Hua, *Angew. Chem.* **2000**, *112*, 2415; *Angew. Chem. Int. Ed.* **2000**, *39*, 2325; d) Y. Wang, J. H. Yu, M. Guo, R. R. Xu, *Angew. Chem.* **2003**, *115*, 4223; *Angew. Chem. Int. Ed.* **2003**, *42*, 4089; e) L. E. Gordon, W. T. A. Harrison, *Inorg. Chem.* **2004**, *43*, 1808; f) Z. E. Lin, J. Zhang, J. T. Zhao, S. T. Zheng, C. Y. Pan, G. M. Wang, G. Y. Yang, *Angew. Chem.* **2005**, *117*, 7041; *Angew. Chem. Int. Ed.* **2005**, *44*, 6881.

[5] a) T. A. Sullens, R. A. Jensen, T. Y. Shvareva, T. E. Albrecht-Schmitt, *J. Am. Chem. Soc.* **2004**, *126*, 2676; b) S. Bareyt, S. Piligkos, B. Hasenknopf, P. Gouzerh, E. Lacôte, S. Thorimbert, M. Malacria, *Angew. Chem.* **2003**, *115*, 3526; *Angew. Chem. Int. Ed.* **2003**, *42*, 3404; c) M. Sadakane, M. H. Dickman, M. T. Pope, *Inorg. Chem.* **2001**, *40*, 2715; d) H. Y. An, D. R. Xiao, E. B. Wang, Y. G. Li, L. Xu, *New J. Chem.* **2005**, *29*, 854.

[6] a) M. T. Pope, *Heteropoly and Isopoly Oxometalates*, Springer, Berlin, **1983**; b) C. L. Hill, *Chem. Rev.* **1998**, *98*, 1; c) K. Fukaya, T. Yamase, *Angew. Chem.* **2003**, *115*, 678; *Angew. Chem. Int. Ed.* **2003**, *42*, 654; d) C. D. Wu, C. Z. Lu, H. H. Zhuang, J. S. Huang, *J. Am. Chem. Soc.* **2002**, *124*, 3836; e) M. I. Khan, E. Yohannes, R. J. Doedens, *Angew. Chem.* **1999**, *111*, 1374; *Angew. Chem. Int. Ed.* **1999**, *38*, 1292.

[7] a) P. J. Hagrman, D. Hagrman, J. Zubieta, *Angew. Chem.* **1999**, *111*, 2798; *Angew. Chem. Int. Ed.* **1999**, *38*, 2638; b) E. Burkholder, J. Zubieta, *Chem. Commun.* **2001**, *20*, 2056.

 © 2006 Wiley-VCH Verlag GmbH & Co. KGaA, Weinheim

[8] a) A. Müller, S. Q. N. Shah, H. Bögge, M. Schmidtmann, *Nature* **1999**, *397*, 48; b) P. Kögerler, L. Cronin, *Angew. Chem.* **2005**, *117*, 866; *Angew. Chem. Int. Ed.* **2005**, *44*, 844; c) D. Drewes, E. M. Limanski, B. Krebs, *Dalton Trans.* **2004**, *14*, 2087; d) L. Xu, M. Lu, B. B. Xu, Y. G. Wei, Z. H. Peng, D. R. Powell, *Angew. Chem.* **2002**, *114*, 4303; *Angew. Chem. Int. Ed.* **2002**, *41*, 4129.

[9] D. A. Judd, J. H. Nettles, N. Nevins, J. P. Snyder, D. C. Liotta, J. Tang, J. Ermolieff, R. F. Schinazi, C. L. Hill, *J. Am. Chem. Soc.* **2001**, *123*, 886.

[10] a) F. B. Xin, M. T. Pope, *J. Am. Chem. Soc.* **1996**, *118*, 7731; b) M. Inoue, T. Yamase, *Bull. Chem. Soc. Jpn.* **1995**, *68*, 3055; c) M. Inoue, T. Yamase, *Bull. Chem. Soc. Jpn.* **1996**, *69*, 2863; d) U. Kortz, M. G. Savelieff, F. Y. A. Ghali, L. M. Khalil, S. A. Maalouf, D. I. Sinno, *Angew. Chem.* **2002**, *114*, 4246; *Angew. Chem. Int. Ed.* **2002**, *41*, 4070.

[11] a) X. K. Fang, T. M. Anderson, C. L. Hill, *Angew. Chem.* **2005**, *117*, 3606; *Angew. Chem. Int. Ed.* **2005**, *44*, 3540; b) X. K. Fang, T. M. Anderson, Y. Hou, C. L. Hill, *Chem. Commun.* **2005**, *40*, 5044.

[12] a) R. O. Duthaler, *Angew. Chem.* **2003**, *115*, 1005; *Angew. Chem. Int. Ed.* **2003**, *42*, 975; b) S. M. Hu, W. X. Du, J. C. Dai, L. M. Wu, C. P. Cui, Z. Y. Fu, X. T. Wu, *J. Chem. Soc. Dalton Trans.* **2001**, 2963.

[13] a) A. A. H. Abu-Nawwas, J. Cano, P. Christian, T. Mallah, G. Rajaraman, S. J. Teat, R. E. P. Winpenny, Y. Yukawa, *Chem. Commun.* **2004**, 314; b) J. Torres, C. Kremer, E. Kremer, H. Pardo, L. Suescun, A. Mombrú, S. Domínguez, A. Mederos, R. Herbst-Irmer, J. M. Arrieta, *J. Chem. Soc. Dalton Trans.* **2002**, 4035.

[14] a) E. Coronado, C. Giménez-saiz, C. J. Gómez-García, S. C. Capelli, *Angew. Chem.* **2004**, *116*, 3084; *Angew. Chem. Int. Ed.* **2004**, *43*, 3022; b) Y. Ishii, Y. Takenaka, K. Konishi, *Angew. Chem.* **2004**, *116*, 2756; *Angew. Chem. Int. Ed.* **2004**, *43*, 2702.

[15] a) M. Nyman, F. Bonhomme, T. M. Alam, M. A. Rodriguez, B. R. Cherry, J. L. Krumhansl, T. M. Nenoff, A. M. Sattler, *Science* **2002**, *297*, 996; b) A. Dolbecq, P. Mialane, L. Lisnard, J. Marrot, F. Sécheresse, *Chem. Eur. J.* **2003**, *9*, 2914; c) P. Q. Zheng, Y. P. Ren, L. S. Long, R. B. Huang, L. S. Zheng, *Inorg. Chem.* **2005**, *44*, 1190.

[16] a) N. Honma, K. Kusaka, T. Ozeki, *Chem. Commun.* **2002**, 2896; b) F. X. Liu, C. Marchal-Roch, P. Bouchard, J. Marrot, J. P. Simonato, G. Hervé, F. Sécheresse, *Inorg. Chem.* **2004**, *43*, 2240.

[17] a) U. Kortz, S. Matta, *Inorg. Chem.* **2001**, *40*, 815; b) L. S. Felices, P. Vitoria, J. M. Gutiérrez-Zorrilla, S. Reinoso, J. Etxebarria, L. Lezama, *Chem. Eur. J.* **2004**, *10*, 5138.

[18] J. T. Rhule, C. L. Hill, D. A. Judd, R. F. Schinazi, *Chem. Rev.* **1998**, *98*, 327.

[19] C. R. Deitcheff, M. Fournier, R. Franck, R. Thouvenot, *Inorg. Chem.* **1983**, *22*, 207.

[20] Crystal data for D-**1** ($KH_2[(D\text{-}C_5H_8NO_2)_4(H_2O)Cu_3][BW_{12}O_{40}]\cdot 5H_2O$): $M_r = 3653.34$, tetragonal, space group $P4_32_12$, $a = 23.944(3)$, $b = 23.944(3)$, $c = 26.201(5)$ Å, $V = 15022(4)$ Å^3, $Z = 8$, $\rho_{calcd} = 3.227\ g\,cm^{-3}$, $R_{int} = 0.0660$, final $R_1 = 0.0288$ ($wR_2 = 0625$) for 11833 independent reflections [$I > 2\sigma(I)$]. Crystal data for L-**1** ($KH_2[(L\text{-}C_5H_8NO_2)_4(H_2O)Cu_3][BW_{12}O_{40}]\cdot 5H_2O$): $M_r = 3653.34$, tetragonal, space group $P4_12_12$, $a = 23.897(3)$, $b = 23.897(3)$, $c = 26.124(5)$ Å, $V = 14919(4)$ Å^3, $Z = 8$, $\rho_{calcd} = 3.253\ g\,cm^{-3}$, $R_{int} = 0.1208$, final $R_1 = 0.0401$ ($wR_2 = 0.0783$) for 11783 independent reflections [$I > 2\sigma(I)$]. Data were collected on a Bruker Smart-Apex CCD diffractometer with $Mo_{K\alpha}$ ($\lambda = 0.71073$ Å) at 293 K using the ω-scan technique. Empirical absorption corrections were applied. The structures were solved by direct methods and refined by full-matrix least squares on F^2 using the SHELXTL-97 software. The Flack parameters of $-0.014(9)$ and $0.003(13)$ for D-**1** and L-**1** indicate that the absolute configurations are correct. In both compounds, one achiral carbon atom of a proline molecule (C9 in D-**1**; C4 in L-**1**) is disordered. CCDC-285623 (D-**1**) and CCDC-285624 (L-**1**) contain the supplementary crystallographic data for this paper. These data can be obtained free of charge from The Cambridge Crystallographic Data Centre via www.ccdc.cam.ac.uk/data_request/cif.

[21] The UV/Vis spectra of Keggin polyanions exhibit a characteristic absorption band at approximately 260 nm, assigned to O→W charge transfers in the polyanionic structure (see Supporting Information). A. Tézé, J. Canny, L. Gurban, R. Thouvenot, G. Hervé, *Inorg. Chem.* **1996**, *35*, 1001.

[22] S. Allenmark, *Chirality* **2003**, *15*, 409.

 © 2006 Wiley-VCH Verlag GmbH & Co. KGaA, Weinheim

Functional Nanoparticles

DOI: 10.1002/anie.200502517

Reactive Polymers: A Versatile Toolbox for the Immobilization of Functional Molecules on TiO_2 Nanoparticles**

*Muhammad Nawaz Tahir, Marc Eberhardt, Patrick Theato, Simon Faiß, Andreas Janshoff, Tatiana Gorelik, Ute Kolb, and Wolfgang Tremel**

The nanoengineering of particle surfaces is a key for the design and tailored construction of innovative nanomaterials.[1] To have control of the inorganic nanoparticle surfaces allows one to tailor the particle size[2] and solubility.[3] Moreover, the surface characteristics of nanomaterials influence the broad range of properties and the performance of a large variety of devices. For instance, the charge-transport process across the interface between a semiconductor metal oxide and an organic dye[4] or a biomolecule[5] forms the basis for improving the performance of many optoelectronic devices, photovoltaic cells,[6] and light-emitting diodes (LEDs).[7] Oligonucleotides can also be linked to the surfaces of nanoparticles, which may become a new tool for gene

[*] M. N. Tahir, Prof. Dr. W. Tremel
Institut für Anorganische Chemie und Analytische Chemie
Johannes Gutenberg-Universität
Duesbergweg 10–14, 55099 Mainz (Germany)
Fax: (+49) 6131-39-25605
E-mail: tremel@uni-mainz.de

M. Eberhardt, Dr. P. Theato
Institut für Organische Chemie
Johannes Gutenberg-Universität
Duesbergweg 10–14, 55099 Mainz (Germany)

S. Faiß, Prof. Dr. A. Janshoff, Dr. T. Gorelik, Dr. U. Kolb
Institut für Physikalische Chemie
Johannes Gutenberg-Universität
Welderweg 11, 55099 Mainz (Germany)

[**] This work was supported by the Deutsche Forschungsgemeinschaft (DFG) through SFB 625.

Supporting information for this article is available on the WWW under http://www.angewandte.org or from the author.

WILEY InterScience DISCOVER SOMETHING GREAT
© 2006 Wiley-VCH Verlag GmbH & Co. KGaA, Weinheim

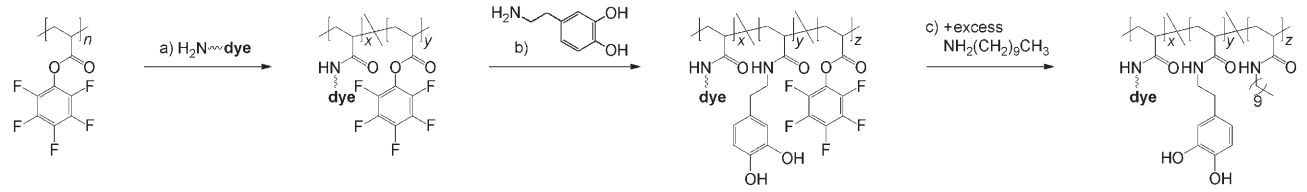
therapy.[8] To conjugate inorganic nanomaterials to organic moieties in hybrid materials by strong covalent or ionic interactions, reactive organic groups have to be attached on the surface of the inorganic component.[9] Surface modification of nanomaterials can be achieved by two methods: by grafting organic groups to the surface of nanomaterials after synthesis (post-functionalization)[10] or by the modification of nanomaterials in situ by organic compounds (in situ functionalization).[11]

Nanocrystalline TiO_2 is particularly attractive for several applications, such as photocatalysis,[12] solar cells,[13] membranes,[14] sensors,[15] nanoceramics,[16] and the degradation of environmental hazardous chemicals.[17] Herein, we introduce a new versatile polymeric ligand that can be used for both the post- and in situ functionalization of TiO_2 as well as other metal oxide nanomaterials.[18] The multifunctional polymeric ligand combines three features: 1) a robust anchor group based on dopamine which is capable of binding to many metal oxides (e.g. TiO_2, Fe_2O_3),[19] 2) a functional molecule (e.g. fluorescent dye, catalyst, biomolecule), and 3) a group that provides solubility of the nanoparticle in different solvents and thereby allows various applications of the inorganic nanomaterial (e.g. solubility of TiO_2 pigments, directed binding to biological targets). The architecture of the polymeric ligand is of major importance because it provides the basis of a comprehensive toolbox to construct supramolecular assemblies of organic–inorganic hybrid nanomaterials. Moreover, this strategy of functionalization can be extended by introducing suitable anchor groups for nanomaterials other than metal oxides.[20a]

The fact that active ester polymers react fast and quantitatively with amines to form the corresponding polyacrylamides opens the possibility to obtain multifunctional polymeric materials.[19] Active ester polymers based on pentafluorophenylacrylates exhibit some outstanding features compared to the commonly used poly(*N*-hydroxysuccinimideacrylates), such as better solubility and higher reactivity, as described elsewhere.[20b] The synthesis of the multifunctional polymeric ligand starting from the precursor pentafluorophenylacrylate polymer is shown in Scheme 1. The active ester ligand was prepared by free-radical polymerization to yield a polymer with a number-average molecular mass $M_n = 29.7\ kg\,mol^{-1}$ and weight-average molecular mass $M_w = 58.5\ kg\,mol^{-1}$ (polydispersity index, PDI = 1.96). This prepolymer was then transformed into the multifunctional polymeric ligand by substituting with amine-containing functionalities. Polymers **P1**, **P2**, and **P3** were prepared by a stepwise substitution of the active ester groups, first, by addition of fluorescent dyes (1-pyrenemethylamine (PyMA), piperazinyl-4-chloro-7-nitrobenzofurazane (pipNBD), and Texas Red, respectively), second, by reaction with 3-hydroxytyramine anchor groups, and last, by quenching with decylamine. The resulting polymer thus incorporates three different features: 1) a fluorescent dye as a functional demonstrator molecule, 2) 3-hydroxytyramine as anchor groups for attachment onto the metal oxide nanoparticles, and 3) a long alkyl chain to increase solubility in nonpolar solvents. The multifunctional polymers thus obtained were analyzed by ^1H NMR and FTIR spectroscopy and GPC to determine the composition of the polymers. The amount of dye and 3-hydroxytyramine, respectively, within the polymers **P1**, **P2**, and **P3** was determined as 10 mol% each. The remaining 80 mol% of the polymers comprised *N*-decylacrylamide repeating units.

For the in situ functionalization of the TiO_2 nanocrystals, $TiCl_4$ was injected into the solution of the polymeric ligand in benzyl alcohol. The solution was stirred for two days at 80°C under argon atmosphere. Post-functionalization was achieved by sealing a mixture of TiO_2 nanowires (synthesized from conc. NaOH and titanium 2-propoxide) and 10 mL of polymeric ligand in benzyl alcohol. In both cases, the product was repeatedly washed with CH_2Cl_2 to remove any unconverted ligand. The functionalized TiO_2 nanocrystals were characterized by transmission electron microscopy (TEM), X-ray diffraction (XRD), ^1H NMR spectroscopy, confocal laser scanning microscopy, and fluorescence spectrophotometry.

TEM images of the synthesized TiO_2 nanowires and TiO_2 nanoparticles are shown in Figure 1. An overview of the nanowires, which were used for post-functionalization, is given in Figure 1a. Figure 1b and c show the TEM images of the in situ functionalized TiO_2 nanoparticles (using **P1**, **P2**, and **P3**) at low magnification and high resolution, respectively. At low magnification (Figure 1b) it can be seen that the sample consists almost exclusively of nanometer-sized TiO_2 particles arranged in a partly agglomerated fashion on a TEM grid.[21] Although it is difficult to identify individual isolated TiO_2 particles because of the presence of the polymeric ligand, a high-resolution (HR)TEM image of an isolated particle is presented in Figure 1c. The crystallinity and phase of the as-synthesized TiO_2 nanoparticles were confirmed by XRD (Figure 2) and TEM (see inset of Figure 1c), which revealed the characteristic diffraction patterns of anatase. Figure 1c shows the HRTEM image of a nanoparticle (diameter $d \approx 2$ nm, length $l \approx 12$ nm) along the [100] view together with the fast Fourier transform (FFT) in the lower right corner. The distances calculated are in good agreement



Scheme 1. Stepwise synthesis of the multifunctional polymeric ligands, which contain 3-hydroxytyramine as anchors for the nanoparticles, alkyl chains for solubility, and fluorescent dye molecules. The active ester units of the polymers were exchanged by 1-pyrenemethylamine in **P1**, pipNBD in **P2**, and Texas Red in **P3**.

 © 2006 Wiley-VCH Verlag GmbH & Co. KGaA, Weinheim

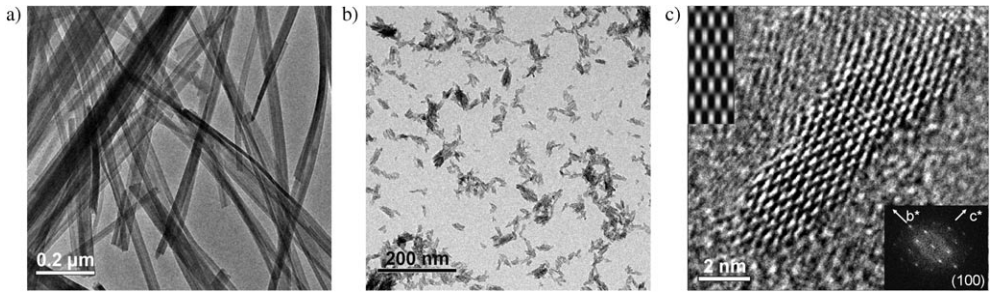


Figure 1. Transmission electron micrographs of a) synthesized TiO_2 nanowires, b) nanoparticles (overview image), and c) an individual nanoparticle (high resolution). The Fourier transform (FFT) and a theoretical HRTEM image of the [100] zone are shown in the lower right and upper left corners, respectively, of part (c).

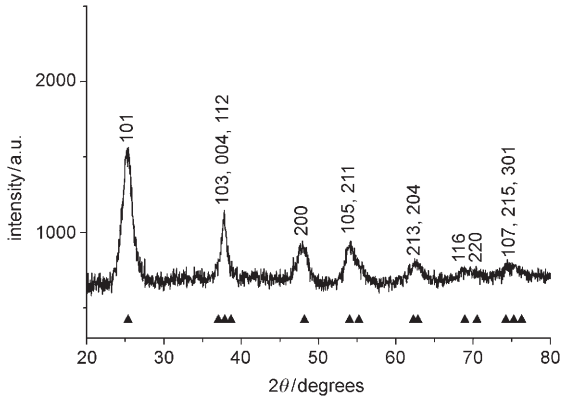


Figure 2. X-ray diffraction pattern of in situ functionalized TiO_2 nanoparticles. The pattern can be fully indexed to anatase. Indices of the reflections are provided, and calculated positions of the anatase reflections are indicated (▲).

with the theoretical values of anatase reflection of the [100] zone (d_{exp}/d_{theo} [Å]: (011) = 3.57/3.51; (004) = 2.40/2.38; (020) = 1.94/1.89). The theoretical HRTEM image of the [100] zone (shown in the upper left corner) was calculated by a multislice method for a thickness of 2 nm at the Scherzer focus and resembles well the experimentally derived image. The crystallinity and the morphology of the TiO_2 nanoparticles are independent of the polymeric ligand **P1**, **P2**, or **P3** used in the synthesis.

The XRD pattern of the as-synthesized polymer-functionalized TiO_2 nanoparticles is shown in Figure 2. All reflections could be indexed to anatase with (101) as the strongest reflection (the calculated reflection positions are highlighted with ticks on the abscissa for comparison). The width of the (004) peak in comparison to the (101) reflection is indicative of the preferred growth of the particle along the *c* direction. In the powder pattern, no traces of other TiO_2 polymorphs could be detected; that is, the crystalline material can be considered a single phase. The peak broadening is due to the nanosized particles. Pawley fitting[22] of the XRD data combined with Scherrer's formula[23] delivered a particle size of 2 nm in both the *a* and *b* directions and 12 nm in the *c* direction. This is in good agreement with the particle shown in Figure 1c. Note that all particles exhibit a good crystallinity, despite the low reaction temperature of 80 °C and the presence of the chelating ligand (10 % dopamine).

Figure 3 shows the confocal laser scanning microscopy images of TiO_2 nanowires and nanoparticles after functionalization of the surface with **P2** and **P3**, respectively. Overview images of as-functionalized TiO_2 nanowires with polymeric ligands **P2** and **P3** are shown in Figure 3a and e, while a single isolated nanowire can be seen in Figure 3b and f. The corresponding nanoparticles functionalized in situ with polymeric ligands **P2** and **P3** are shown in Figure 3d and h, respectively. It is clear from the fluorescence profiles (Figure 3c and g) and images that the nanowires are fully coated by polymer ligands covalently bound to TiO_2 nanowires. The in situ functionalized TiO_2 nanoparticles shown in Figure 3d and h also exhibit the corresponding fluorescence. It is difficult to comment on the actual size of the in situ functionalized nanoparticles because it was beyond the resolution limits of confocal laser scanning microscopy. TiO_2 nanocrystals with surface-bound dopamine have been used for biotin–avidin functionalization coupling. Dopamine binding is a standard method for the surface functionalization of metal oxides[20] where the dopamine group preferentially binds to the edges of the TiO_2 nanocrystals (which have a higher surface energy).[5a] In contrast, full surface coverage, protection, and concomitant functionalization can be achieved by using the novel copolymer ligand which contains a large number of dopamine groups covalently linked to the polymer backbone, whereby the nanoparticles are sheathed partly by surface-bound anchor groups and partly by steric shielding through the polymeric ligand.

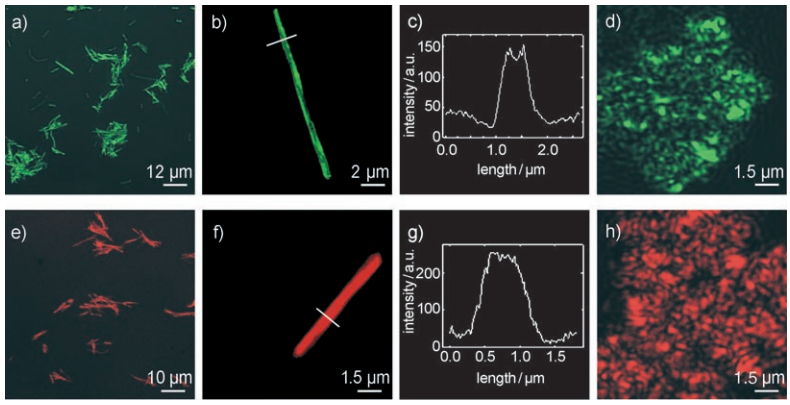


Figure 3. Confocal laser scanning microscopy images and fluorescence profiles of TiO_2 nanowires and nanoparticles. a, b) Post-functionalized TiO_2 nanowires coated with **P2** (NBD), c) the corresponding fluorescence profile for an individual nanowire, and d) TiO_2 nanoparticles functionalized in situ with **P2**. e, f) Post-functionalized TiO_2 nanowires coated with **P3** (Texas Red), g) the corresponding fluorescence profile for an individual nanowire, and h) TiO_2 nanoparticles in situ functionalized with **P2**.

 © 2006 Wiley-VCH Verlag GmbH & Co. KGaA, Weinheim

The versatile use of the functional polymeric ligands as immobilizers for metal oxide nanowires and nanoparticles was demonstrated by the attachment of the three different fluorescent dyes: pyrene in **P1**, NBD in **P2**, and Texas Red in **P3**. To detect the immobilization of the functional polymers on the TiO_2 surfaces, fluorescence spectra were measured. Figure 4a shows the fluorescence spectra of TiO_2 nanoparticles coated with **P1** (solid line), **P2** (dashed line), or **P3** (dotted line). All samples were dissolved in $CHCl_3$ for measurement of their emission spectra (see Supporting Information). TiO_2 nanoparticles carrying the **P1** pyrene fluorophore were excited at 345 nm, those coated with **P2** were excited at 460 nm, and those derivatives with **P3** were excited at 488 nm. Clearly, the expected emission spectra of the respective dye can be seen which proves the flexible application of the functional polymeric ligands.

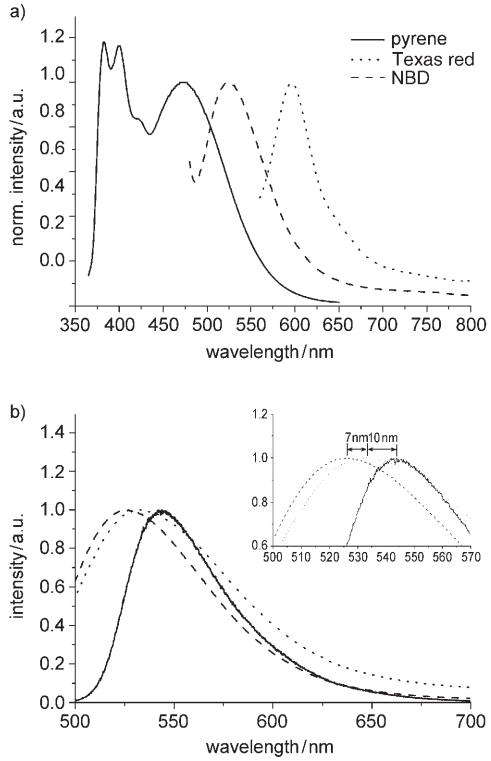


Figure 4. a) Fluorescence spectra of TiO_2 nanoparticles coated with **P1** (pyrene; $\lambda_{ex} = 345$ nm), **P2** (NBD; $\lambda_{ex} = 460$ nm), or **P3** (Texas red; $\lambda_{ex} = 488$ nm). b) Fluorescence spectra of NBD depending on the preparation conditions: post-functionalization (red dotted line); in situ functionalization (blue dashed line); the emission spectrum of **P2** dissolved in $CHCl_3$ (black solid line) was used as a reference. The inset shows the extent of the blue shifts of the maxima relative to that of the reference.

As the functional polymeric ligands were used for both post- and in situ functionalization of TiO_2 nanoparticles, we investigated the fluorescence of **P2** depending on the synthetic procedure (Figure 4b). The solid line in Figure 4 shows the emission spectrum of **P2** dissolved in $CHCl_3$ as a reference. TiO_2 nanowires that were coated with **P2** show a fluorescence spectrum whose maximum is blue-shifted by 10 nm relative to that of the reference, whereas the emission maximum of TiO_2 nanoparticles that were synthesized in the presence of the polymeric ligand **P2** revealed a blue shift of 17 nm with respect to **P2**. This can be understood as follows: The nanoparticles are coated with the polymer which results in a non-uniform environment for the dye molecules. As a result, the hydrophilic TiO_2 surface induces a slight blue shift. This also explains the larger blue shift for the in situ functionalized nanoparticles than for the post-functionalized nanowires, as the nanoparticles exhibit a larger surface-to-volume ratio.

In conclusion, we have demonstrated for the first time that reactive polymer ligands containing dopamine serve as a robust anchor on the surface of titanium dioxide nanoparticles. Compared to the binding of molecules to the surface of oxide particles using dopamine, the novelty and superiority of the polymeric ligand system presented here is based on its multifunctionality, as it incorporates metal-chelating ligands, a functional molecule (pyrene, NBD, or Texas Red), and additional entities that allow the solubility of inorganic nanocrystals in different organic solvents to be tailored according to various potential applications. As a possible extension of the work presented, we envisage the immobilization of proteins to metal oxide surfaces using nitrilotriacetic acid as an anchor ligand;[24] that is, our simple strategy should provide a useful way to link biofunctional molecules in almost any solvent to the surface of metal oxide particles that display a high affinity toward dopamine or toward any other linker group that can replace the dopamine ligand in the polymer. This strategy is extremely versatile and offers new opportunities for optoelectronic and/or biological applications of metal oxide nanoparticles. Finally, this strategy allows the construction of supramolecular structures through the arrangement of inorganic nanoparticles, for example, by introducing biotin/streptavidin linker units as the functional molecules.

Experimental Section

Piperazinyl-NBD (pipNBD) was synthesized according to a reported procedure[1] by reaction of NBD chloride (Fluka) with an excess of piperazine in THF. 1-Pyrenemethylamine hydrochloride (PyMA) and Texas Red are commercially available (Aldrich).

The active ester polymer, poly(pentafluorophenylacrylate) (PFA) was prepared as reported previously.[20b] GPC analysis of the obtained polymer (THF, light-scattering detection) gave the values $M_n = 29.7\ kg\,mol^{-1}$ and $M_w = 58.5\ kg\,mol^{-1}$; the number of repeating units (246) is based on the M_w value.

For the synthesis of the multifunctional poly(acrylamide)s, PFA (700 mg, 2.94 mmol repeating units) was dissolved in a mixture of dry DMF (9 mL) and triethylamine (0.7 mL). The calculated amount of dye dissolved in dry DMF was added, and the resulting solution was stirred for 4 h at 50 °C. 3-Hydroxytyramine hydrochloride (57 mg, 0.3 mmol) in DMF (3 mL) and triethylamine (1 mL) were added, and the clear solution was kept for 2 h at 50 °C. The remaining active ester groups were then quenched with an excess of decylamine (500 mg, 3.2 mmol). The polymer was isolated by precipitation in methanol and finally dried in a vacuum oven at 40 °C for 1 h.

A sample of the functional polymer ligand (100 mg) was dissolved in benzyl alcohol (20 mL) in a glovebox, and the vial was sealed and removed from the glovebox. $TiCl_4$ (0.8 mL) was slowly injected through the septum to the solution of ligand in benzyl alcohol under vigorous stirring at room temperature. With continuous stirring the

 © 2006 Wiley-VCH Verlag GmbH & Co. KGaA, Weinheim

solution was heated to 80 °C for 24 h. The resulting brown suspension was centrifuged, and the precipitate was thoroughly washed twice with CH_2Cl_2. The product was dried in air at room temperature.

Analytical grade ethanol (99.8 %; 6 mL) was added to titanium 2-propoxide (ACROS; 1 g) in a teflon vessel, and the vessel was placed in a desiccator. The precipitation of TiO_2 was initiated under a moist atmosphere, induced by placing a petri dish filled with water at the bottom of the desiccator. The diffusion experiment was stopped after 12 h, and was followed by the addition of 10 M aqueous NaOH solution (25 mL). The reaction vessel was then sealed into a stainless steel hydrothermal bomb, which was placed in an oven maintained at 160 °C for 20 h. After the autoclave was allowed to cool to room temperature, the obtained sample was filtered and repeatedly washed with 0.1 M HNO_3, 1 N HCl, and deionized water. The product was dried under vacuum for 3 h. Finally a soft, fibrous white powder was obtained. Then, TiO_2 nanowires (10 mg) were dispersed in benzyl alcohol (10 mL), and the mixture was sonicated for 15 min. In a separate vial, the polymer ligand (10 mg) was dissolved in benzyl alcohol (10 mL). Both the suspension and solution were mixed under inert conditions, and the mixture was stirred at 60 °C for 4 h. The polymer-functionalized nanowires were isolated and purified by repeated washings with CH_2Cl_2 using centrifugation.

For confocal laser scanning microscopy 10 μL of the sample was placed and dispersed carefully on a thin glass slide washed in piranha solution, and the solvent was evaporated. NBD-functionalized nanowires were imaged using an argon laser with an excitation wavelength of 488 nm, whereas those functionalized with Texas Red were excited with the 543 nm line of a helium/neon laser. A 40× (NA: 1.25) oil immersion objective was used for the imaging of all samples.

Instrumentation: The resulting products were characterized by an inverted laser scanning microscope (Leica TCS SL, Leica Microsystems, Bensheim, Germany), X-ray powder diffraction in reflection geometry (Siemens D8 powder diffractometer, $Cu_{K\alpha}$ radiation), HRTEM (Philips TECNAI F30 electron microscope; field-emission gun, 300 kV extraction voltage) equipped with a high-angle annular dark-field detector (HAADF), a Gatan imaging filter, and an energy dispersive X-ray analysis system.

Received: July 19, 2005
Revised: August 24, 2005
Published online: December 28, 2005

Keywords: fluorescence · nanostructures · organic–inorganic hybrid composites · polymers · titanium

[1] S. Banerjee, M. G. C. Kahn, S. S. Wong, *Chem. Eur. J.* **2003**, *9*, 1898 – 1908.
[2] P. D. Cozzooli, A. Kornowski, H. Weller, *J. Am. Chem. Soc.* **2003**, *125*, 14539 – 14548.
[3] K. Ausman, R. Piner, O. Lourie, R. S. Ruoff, M. D. Korobov, *J. Phys. Chem. B* **2000**, *104*, 8911 – 8915.
[4] a) R. Nudelman, O. Ardon, Y. Hadar, Y. Chen, J. Libman, A. Shanzer, *J. Med. Chem.* **1998**, *41*, 1671 – 1678.
[5] a) N. M. Dimitrijevic, Z. V. Saponjic, B. M. Rabatic, T. Rajh, *J. Am. Chem. Soc.* **2005**, *127*, 1344 – 1345; b) O. V. Salata, *J. Nanobiotechnology* **2004**, *2–3*, 1 – 6.
[6] a) G. Ramakrishna, H. N. Ghosh, *J. Phys. Chem. B* **2001**, *105*, 7000 – 7008; b) W. J. E. Beek, R. A. J. Janssen, *J. Mater. Chem.* **2004**, *14*, 2795 – 2800; c) E. W. McFarland, J. Tang, *Nature* **2003**, *421*, 6, 616 – 618.
[7] J.-W. Huang, S. J Bai, *Nanotechnology* **2005**, *16*, 1406 – 1410.
[8] T. Paunesku, T. Rajh, G. Wiederrecht, J. Maser, T. Vogt, N. Stojicevic, M. Protic, B. Lai, J. Oryhon, M. Thurnauer, G. Woloschak, *Nat. Mater.* **2003**, *2*, 343 – 346.
[9] C. Xu, K. Xu, G. Gu, R. Zheng, H. Liu, X. Zhang, Z. Guo, B. Xu, *J. Am. Chem. Soc.* **2004**, *126*, 9938 – 9939.
[10] G. Kickelbick, U. Schubert in *Synthesis, Functionalization and Surface Treatment of Nanoparticles* (Ed.: M.-I. Baraton), American Scientific, Stevenson Ranch, CA, **2003**.
[11] a) C. Sanchez, G. Soler-Illia, F. Ribot, T. Lalot, C. R. Mayer, V. Cabuil, *Chem. Mater.* **2001**, *13*, 3061 – 3083; b) M. Anderson, L. Österlund, S. Ljungström, A. Palmqvist, *J. Phys. Chem. B* **2002**, *106*, 10674 – 10679; c) S. Yin, Y. Aita, M. Komatsu, J. Wang, Q. Tang, S. Sato, *J. Mater. Chem.* **2005**, *15*, 674 – 682.
[12] S. Hore, E. Palomares, H. Smit, N. J. Bakker, P. Comte, P. Liska, K. R. Thampi, J. M. Karoon, A. Hinsh, J. R. Durrant, *J. Mater. Chem.* **2005**, *15*, 412 – 418.
[13] A. Hagfeldt, M. Grätzel, *Acc. Chem. Res.* **2000**, *33*, 269 – 277.
[14] B. S. Lele, A. J. Russell, *Biomacromolecules* **2004**, *5*, 1947 – 1955.
[15] E. Palomares, R. Vilar, A. Green, J. R. Durrant, *Adv. Funct. Mater.* **2004**, *14*, 111 – 115.
[16] "Nanocrystalline Ceramics, Synthesis and Structure": M. Winterer, *Springer Series in Materials Science, Vol. 53*, Springer, Heidelberg, **2002**.
[17] a) J. H. Schattka, D. G. Shchukin, J. G. Jia, M. Antonietti, R. A. Carusa, *Chem. Mater.* **2002**, *14*, 5103 – 5108; b) L. X. Chen, T. Rajh, Z. Y. Wang, M. C. Thurnauer, *J. Phys. Chem. B* **1997**, *101*, 10688 – 10697.
[18] a) J. L. Dalsin, L. Lin, S. Tosatti, J. Vörös, M. Textor, P. B. Messersmith, *Langmuir* **2005**, *21*, 640 – 646; b) H. Gu, Z. Yang, J. Gao, C. K. Chang, B. Xu, *J. Am. Chem. Soc.* **2005**, *127*, 34 – 35.
[19] N. M. Dimitrijevic, Z. V. Saponjic, B. M. Rabatic, T. Rajh, *J. Am. Chem. Soc.* **2005**, *127*, 1344 – 1345.
[20] a) I. Potavova, R. Mruk, S. Prehl, R. Zentel, T. Basche, A. Mews, *J. Am. Chem. Soc.* **2003**, *125*, 320 – 321; b) M. Eberhardt, R. Mruk, P. Theato, R. Zentel, *Eur. Polym. J.* **2005**, *41*, 1569 – 1575.
[21] TiO_2 nanoparticles that were functionalized in a similar manner have been shown by light-scattering experiments to have a hydrodynamic radius of approximately 80 nm, which is indicative of a partial agglomeration in solution and compatible with the slight agglomeration observed in the TEM image in Figure 1b.
[22] Cerius2, Version 4.2 MS, Accelrys Software Inc..
[23] P. Scherrer, *Gött. Nachr.* **1918**, *2*, 98.
[24] a) M. N. Tahir, P. Théato, W. E. G. Müller, H. C. Schröder, A. Janshoff, J. Zhang, J. Huth, W. Tremel, *Chem. Commun.* **2004**, 2848 – 2849; b) M. N. Tahir, P. Théato, W. E. G. Müller, H. C. Schröder, A. Borejko, S. Faiß, A. Janshoff, J. Huth, W. Tremel, *Chem. Commun.* **2005**, 5533 – 5535.

 © 2006 Wiley-VCH Verlag GmbH & Co. KGaA, Weinheim

Metal Indicators

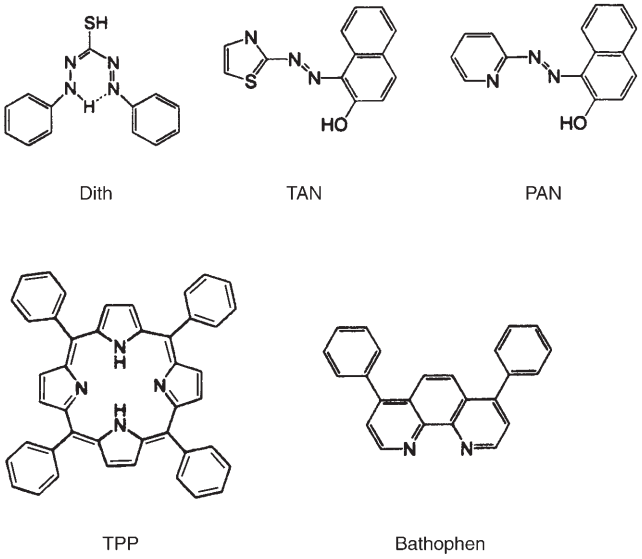
DOI: 10.1002/anie.200503015

Test Strips for Heavy-Metal Ions Fabricated from Nanosized Dye Compounds**

Yukiko Takahashi, Hitoshi Kasai, Hachiro Nakanishi, and Toshishige M. Suzuki**

Analytical test strips for heavy-metal ions can provide simple and convenient procedures for on-site analysis and daily monitoring of water quality without using costly instruments. However, since the standard limit values of heavy metals in the environment and drinking water are remarkably low (ppb level), the detection limits of commercial test strips (ppm level) are insufficient to satisfy the required criteria. In addition, since they are generally prepared by soaking paper in the signaling reagent, leakage of reagent is facile, and hence reliability and sensitivity of detection are poor. Firm fixation of colorimetric and fluorometric reagents for metals on solid substrates has been attempted by incorporation into PVC-based liquid membranes,[1] covalent anchoring with cross-linked copolymers,[2] and layer-by-layer accumulation methods such as Langmuir–Blodgett films[3,4] and alternate deposition of oppositely charged polyelectrolytes.[5,6] A wealth of information on optical sensors and probes for simple determination of heavy metals has been reviewed.[7] However, drawbacks include complicated synthetic procedures, insufficient sensitivity, requirements for auxiliary additives, and difficulty in controlling the concentration of the reagent and its uniformity. Hence, we sought a simple procedure for firm and uniform coating of signaling reagents on an appropriate substrate without any additional matrix.

Recently, a simple and versatile process known as the "reprecipitation method" was proposed for the preparation of aqueous dispersions of organic nanoparticles.[8] The process involves injection of a water-miscible organic solution into water with vigorous stirring. We found that various organic nanoparticles can be uniformly coated onto a membrane filter (cellulose ester type) to form a thin layer simply by filtration of the nanoparticle dispersion. We attempted to apply this simple procedure to the fabrication of analytical test strips from a selection of signaling reagents. We examined popular indicator dyes having an aromatic conjugated system: dithizone (Dith), 1-(2-thiazolylazo)-2-naphthol (TAN), 1-(2-pyridylazo)-2-naphthol (PAN), tetraphenylporphin (TPP), and bathophenanthroline (Bathophen).



Optimized preparative conditions for aqueous dispersions of the indicator dyes are listed in Table 1. Water-miscible acetone and THF were used for dissolution of the dyes. The pH of the aqueous phase was controlled to maintain electroneutrality of the dye species by considering the pK_a values of the respective compounds. Smaller particles are formed with increasing temperature of the aqueous phase and with decreasing dye concentration in the organic phase.[9] Figure 1 shows scanning electron microscopy (SEM) images of TPP nanoparticles and PAN nanofibers. Round particles (50–100 nm) were mainly formed from TPP and Bathophen. In contrast, fibrous products were formed in the case of PAN, TAN, and Dith. These dyes commonly have dissociative protons capable of forming intermolecular hydrogen bonds which assist formation of three-dimensional fibers.

These dye particles/fibers were firmly coated onto the membrane filter as a thin layer simply by filtering the dispersion. Figure 2A shows membrane filters loaded with typical analytical dye particles/fibers. It is noteworthy that the present membranes were prepared without any additives such as coating polymers or modifiers. The color intensity was almost constant across the membrane according to linear scanning of the dye zone by a TLC scanner (Figure 2B), and this indicated uniform dispersion of the reagent (PAN) on the membrane surface. On the contrary, 1–2-μm crystals of PAN prepared by milling formed irregular patches that gave a rough surface on the filter and were easily removed by rubbing with a finger (Figure 2B).

The cross-sectional SEM image (Figure 3A) indicates that the thickness of the dye particle/fiber layer is less than 1 μm. Thus, the membrane provides a remarkably concentrated signaling surface composed of 100% pure indicator dye. In

[*] Dr. Y. Takahashi, Dr. T. M. Suzuki
AIST-Tohoku
National Institute of Advanced Industrial Science and Technology (AIST)
4-2-1, Nigatake, Miyagino-ku, Sendai, 983-8551 (Japan)
Fax: (+81) 22-237-5217
E-mail: yukiko-takahashi@aist.go.jp
H. Kasai, H. Nakanishi
Institute of Multidisciplinary Research for Advanced Materials
Tohoku University
2-1-1 Katahira, Aoba-ku, Sendai 980-8577 (Japan)

[**] Y.T. gratefully thanks the New Energy and Industrial Technology Development Organization (NEDO) for the fellowship support.

Supporting information for this article is available on the WWW under http://www.angewandte.org or from the author.

 © 2006 Wiley-VCH Verlag GmbH & Co. KGaA, Weinheim

Table 1: Preparation conditions and properties of nanosized dyes.

Dye	pH buffer[a]	Organic solvent (concentration)	Target ions	Properties of nanosized dye
Dith	0.01 M HCl (pH 2)	acetone (2 mM)[b]	Hg^{II}, Ag^{I}	fibers: width 25–70 nm, length >1 μm
TAN	MES (pH 6.15)	acetone (2 mM)[b]	Cu^{II}, Ni^{II}, Pd^{II}	mixture of fibers and particles fibers: width 50–150 nm, length >1 μm particles: 25–70 nm
PAN	TAPS (pH 8.4)	acetone (2 mM)[c]	Zn^{II}, Ni^{II}, Co^{III}	mixture of fibers and particles fibers: width 50–150 nm, length >1 μm particles: 25–70 nm
TPP	TAPS (pH 8.4)	THF (5 mM)[b]	Zn^{II}, Cu^{II}	round particles 50–100 nm
Bathophen	TAPS (pH 8.4)	acetone (5 mM)[b]	Fe^{II}	round particles 50–200 nm

[a] MES = 2-morpholinoethanesulfonic acid, TAPS = *N*-tris(hydroxymethyl)methyl-3-aminopropanesulfonic acid. [b] 100 μL of organic solvent was injected into 10 mL of water containing pH buffer. [c] 200 μL of organic solvent was injected into 20 mL of water containing pH buffer

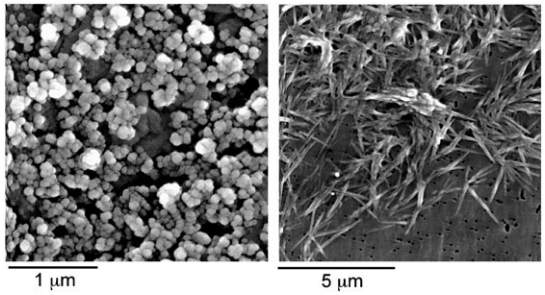


Figure 1. SEM images of TPP nanoparticles and PAN nanofibers on a flat polycarbonate membrane.

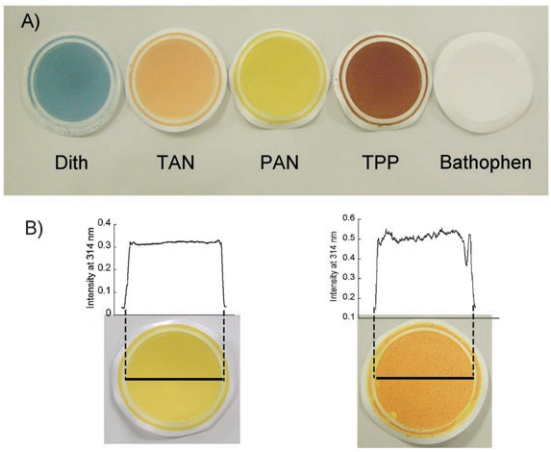


Figure 2. A) Photographs of dye-loaded membranes. B) Color intensity profiles by linear TLC scanning across a PAN nanofiber membrane prepared by the present method (left) and a membrane prepared from PAN microcrystals (right).

addition, reagents are not removed from the support membrane even by rubbing with a finger or by immersion in water. As shown in the top-view SEM image of the membrane (Figure 3B), the Bathophen nanoparticles stick to the cellulose fiber network of the support. Nanofibers of PAN, TAN, and Dith were also firmly captured on the membrane by clinging to cellulose fiber. Since more than 99.5% of dye particles/fibers are retained on the membrane, the present method permits simple control of dye concentration on the filter surface.

The membranes are primarily useful as dip test strips for screening of metal ions. In addition, they are water-permeable, and hence trace metals are enriched on them by filtration of the sample, so that much lower detection limits are achieved. Dissolution of reagents in the sample solution was practically negligible during dip testing and sample filtration, presumably because the dyes are firmly retained on the fiber network of the membrane filter.

We used the PAN-coated membrane as test strip for the detection of Zn^{II}. The pH of

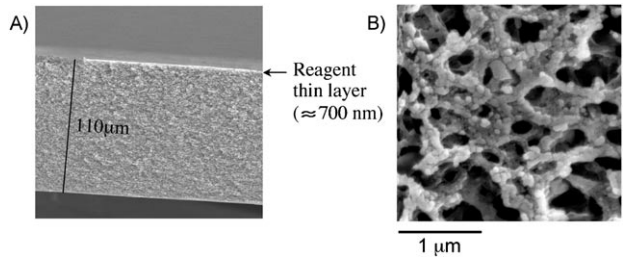


Figure 3. SEM images of Bathophen nanoparticles retained on a mixed cellulose ester membrane filter. A) Cross section. B) Top view.

the test solution was optimized to 8.4, at which the most intense red color is developed and the reaction rate is optimum.[10] We monitored the color change and the relative color intensity (Figure 4) with reflectance-absorption spectrometry. The peak at $\lambda_{max} = 550$ nm indicates that neutral $[Zn(PAN)_2]$ is formed on the membrane filter as the major species. The increasing peak intensity with increasing Zn^{II} concentration enables quantitative determination of test samples by comparison with the calibration curve (inset). Figure 5A shows the color changes of the PAN strip in dip testing. Notably, as little as 65 ppb (1×10^{-7} mol dm^{-3}) of Zn^{II} was detected by naked-eye color test after dipping the test strip for 15 min. Alternatively, sub-ppb concentrations of Zn^{II} were successfully detected by filtration enrichment of 100 mL of sample solution at a filtration rate of about 6.9 mL min^{-1} (Figure 5B).

Dithizone forms a remarkably stable Hg^{II} complex and gives the intense orange-yellow color of $[Hg(HDith)_2]$ under slightly acidic conditions.[11] By simple filtration of the sample solution (100 mL) at 9 mL min^{-1}, detection down to 10 ppb was successfully achieved (see Supporting Information). Interference was studied by filtration of simulated wastewater containing 780 ppm of Na^+, 1000 ppm of K^+, 400 ppm of Ca^{II}, 5.6 ppm of Fe^{II}, 6.4 ppm of Cu^{II}, 6.5 ppm of Zn^{II}, 0.5 ppm of Cd^{II}, 0.5 ppm of Pb^{II}, and 20 ppb of Hg^{II} at pH 2. Addition of ethylenediaminetetraacetic acid (10^{-4} mol dm^{-3}) to the sample solution effectively masked interferences from these ions in the detection of 20 ppb of Hg^{II}.

 © 2006 Wiley-VCH Verlag GmbH & Co. KGaA, Weinheim

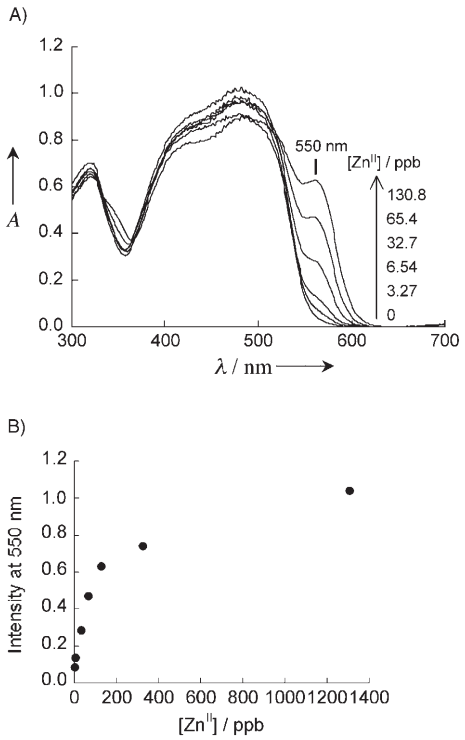


Figure 4. A) Change in reflectance-absorption spectra of a PAN-coated membrane on dipping into Zn^{II} solutions of various concentrations (pH 8.4). B) Calibration curve obtained by plotting the intensity at 550 nm.

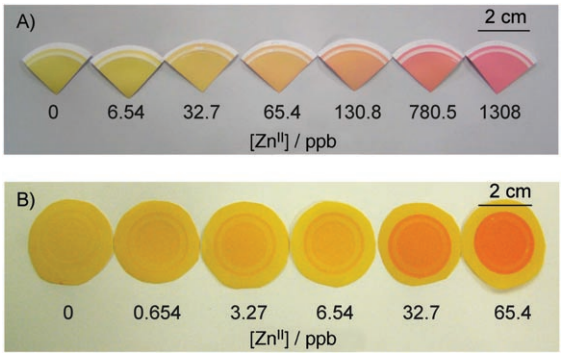


Figure 5. Detection of Zn^{II} by PAN-loaded membrane by the dip and filtration methods. A) Dip method: a test strip was dipped into 10 mL of aqueous Zn^{II} solution at pH 8.4 for 15 min. B) Filtration method: 100 mL of aqueous Zn^{II} solution at pH 8.4 was filtered through the PAN-coated membrane at a flow rate of 6.9 mL min^{-1}.

We also examined a Bathophen-coated membrane for Fe^{II} detection. The test strip showed a marked red color in dip testing of Fe^{II} that was detectable by the naked eye down to 5.6 ppb (see Supporting Information).

In summary, firmly attached and uniform coatings of organic dye nanoparticles/nanofibers on a membrane filter were obtained without using an additional matrix. Key features of this method are its simplicity and applicability to a wide variety of hydrophobic organic dyes. Very thin and pure dye membranes provide a highly concentrated signaling surface, which leads to high sensitivity of this system. Moreover, water-permeable dye-coated membranes allowed naked-eye detection down to ppb concentrations of metal ions by combining filtration enrichment of samples with color signaling.

Experimental Section

Distilled and deionized water was used throughout this work. All analytical reagents were converted to homogeneously dispersed nanoparticles by the reprecipitation method. Typically, 100 μL of a 2 mmol dm^{-3} solution of TAN in acetone was injected into vigorously stirred (1000 rpm) water (10 mL). The pH of the aqueous phase was adjusted to 6.15 with MES buffer. The detection membranes were fabricated by filtration of the aqueous dispersion through a mixed cellulose ester type membrane filter (pore size: 0.1 μm, thickness: 150 μm, ∅ 47 mm, Advantec Co.) under suction. Then the membrane was washed with water and air-dried. The surface concentration of the dye was estimated to be 7×10^{-7} mol cm^{-2}. The concentration of dye can be adjusted in the range of 5×10^{-9} to 7×10^{-7} mol cm^{-2}. The particle size of the aqueous dispersion was analyzed by dynamic light scattering (DLS) before filtration. SEM observation was carried out after loading on a flat polycarbonate membrane filter (pore size: 0.1 μm, Advantec or pore size: 0.05 μm, Millipore).

Dip tests: The detection membranes were cut into 4–10 pieces, and then the test strips were immersed in a buffered (0.01 mol dm^{-3}) solution of appropriate pH. After change in color, the absorption spectra were measured by reflection-absorption spectrophotometry.

Filtration method tests: The detection membrane (∅ 25 mm) was sandwiched between separable filter holders (effective area: 3.14 cm^2). Sample solution (100 mL) containing pH-buffered metal ions was passed through the filter under suction. The color change was monitored by spectroscopy.

The size of nanosized dyes in dispersed solution was determined by DLS (Zetasizer Nano-S, Malvern). The size and morphology were observed by SEM (S-800, Hitachi) and XRD (M18XHF22, Mac Science). Reflection-absorption spectra were measured by a multichannel spectrophotometer (MCPD-3000, Photal Co.) equipped with an optical fiber as light source and signal receiver. The reflection absorbance A is defined by $A=-\log R/R_o$, where R is the reflectance of the colored sample and R_o is that of colorless substrate.[12] The relative intensity of the reflectance signal was determined by scanning the wavelength at appropriate sample point.

Received: August 24, 2005
Revised: November 7, 2005
Published online: December 29, 2005

Keywords: colorimetry · dyes/pigments · membranes · nanostructures · trace analysis

[1] K. Seiler, *Ion-selective Optode Membranes*, Fluka, Buchs, Switzerland, **1993**, pp. 91–97.
[2] G. Orellana, A. M. Gomez-Carneros, C. D. Dios, A. A. Garcia-Martinez, M. C. Moreno-Bondi, *Anal. Chem.* **1995**, *67*, 2231.
[3] G. Caminati, E. Margheri, G. Gabrielli, *Thin Solid Films* **1994**, *244*, 905.
[4] Y. Zheng, J. Orbulescu, X. Ji, M. F. Andreopoulos, M. S. Pham, M. R. Leblanc, *J. Am. Chem. Soc.* **2003**, *125*, 2680.
[5] S.-H. Lee, J. Kumar, S. K. Tripathy, *Langmuir* **2000**, *16*, 10482.
[6] C. Pearson, J. Nagel, M. C. Petty, *J. Phys. D: Appl. Phys.* **2001**, *34*, 285.
[7] I. Oehme, O. S. Wolfbeis, *Mikrochim. Acta* **1997**, *126*, 177–192.
[8] H. Kasai, H. S. Nalwa, H. Oikawa, S. Okada, H. Matsuda, N. Minami, A. Kakuta, K. Ono, A. Mukoh, H. Nakanishi, *Jpn. J. Appl. Phys.* **1992**, *31*, L1132.

 © 2006 Wiley-VCH Verlag GmbH & Co. KGaA, Weinheim

[9] H. Oikawa, H. Kasai, H. Kamatani, H. S. Nalwa, S. Okada, H. Matsuda, N. Minami, A. Kakuta, K. Ono, A. Mukoh, H. Nakanishi, *Chemistry of Functional Dyes, Vol. 2* (Eds.: Z. Yoshida, Y. Shirota), Mita Press, Tokyo, **1993**, pp. 755 – 758.
[10] K. Ueno, T. Imamura, K. L. Cheng, *Handbook of Organic Analytical reagents*, 2nd ed., CRC, Boca Raton, **1992**, pp. 209 – 214.
[11] K. Ueno, T. Imamura, K. L. Cheng, *Handbook of Organic Analytical Reagents*, 2nd ed., CRC, Boca Raton, **1992**, pp. 431 – 439.
[12] H. Yamamoto, T. Kurita, J. Suzuki, R. Hira, K. Nakano, H. Makabe, *J. Chromatogr.* **1976**, *116*, 29.

 © 2006 Wiley-VCH Verlag GmbH & Co. KGaA, Weinheim

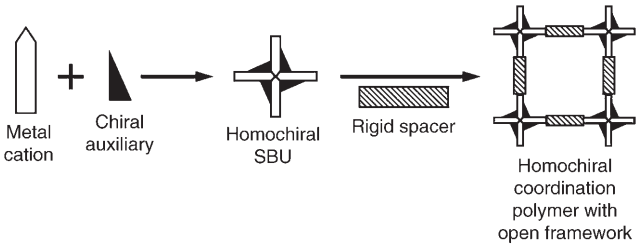
Microporous Frameworks

DOI: 10.1002/anie.200503023

A Homochiral Metal–Organic Material with Permanent Porosity, Enantioselective Sorption Properties, and Catalytic Activity**

Danil N. Dybtsev, Alexey L. Nuzhdin, Hyungphil Chun, Konstantin P. Bryliakov, Evgeniy P. Talsi, Vladimir P. Fedin, and Kimoon Kim**

Metal–organic porous materials are receiving growing attention[1] because of their potential applications in gas storage,[2] separation,[3] and many other areas.[4] Although catalysis is one of the most promising applications of such materials, only a handful of examples have been reported to date.[5] Furthermore, despite considerable efforts, attempts to synthesize robust, homochiral metal–organic porous materials capable of enantioselective separation and/or catalysis have met with only limited success.[6,7] Most homochiral metal–organic frameworks are not robust enough to show permanent porosity, nor porous enough to be useful for selective sorption or catalytic transformation of organic molecules. Therefore, the synthesis of robust homochiral metal–organic frameworks with potential for application is still challenging. For the synthesis of homochiral metal–organic open frameworks, two general approaches have been taken: 1) use of a rigid homochiral organic ligand as a spacer to link adjacent metal centers or secondary building units (SBUs),[5b–d,7] and 2) use of a homochiral ligand as an auxiliary pendant which does not directly participate in the formation of a framework backbone, but forces the framework to adopt a specific chiral topology.[3d] Herein, we introduce another rational approach to the synthesis of homochiral metal–organic frameworks. A metal ion and a readily available homochiral organic ligand are used to form homochiral SBUs, which in turn, are linked together by rigid spacers to build a network structure, in a one-pot reaction (Scheme 1).[8] With a judicious choice of metal ion, homochiral organic molecule, and rigid polytopic linker (that is, a connector with more than one metal coordination site), this approach allows us to synthesize metal–organic open frameworks with stable chiral pores. Herein, we report a new homochiral metal–organic material that has permanent porosity, size- and enantioselective sorption properties, and catalytic activity.[9]



Scheme 1. Our approach to the synthesis of homochiral metal–organic frameworks.

A dimethylformamide (DMF) solution of $Zn(NO_3)_2$, L-lactic acid (L-H_2lac), and 1,4-benzenedicarboxylic acid (H_2bdc) in a 2:1:1 ratio was heated in a teflon-lined stainless steel vessel at 110 °C for 2 days to produce large rod-shaped colorless crystals. Single-crystal X-ray analysis of these crystals revealed a 3D metal–organic framework structure formulated as $[Zn_2(bdc)(L\text{-}lac)(dmf)]\cdot(DMF)$ (**1**·DMF). The phase purity of the bulk product was independently confirmed by powder X-ray diffraction (XRD) and elemental analysis.

The lactate ligand in **1** coordinates to the Zn^{2+} ions in the framework as a dianion owing to the deprotonation of the hydroxy group;[10] therefore, the whole framework is charge neutral. There are two crystallographically independent Zn^{2+}

[*] Dr. D. N. Dybtsev, Dr. H. Chun, Prof. Dr. K. Kim
National Creative Research Initiative Center for Smart Supramolecules
and
Department of Chemistry
Division of Molecular and Life Sciences
Pohang University of Science and Technology
San 31 Hyojadong, Pohang 790-784 (Republic of Korea)
Fax: (+82) 54-279-8129
E-mail: kkim@postech.ac.kr
Dr. D. N. Dybtsev, Prof. Dr. V. P. Fedin
Nikolaev Institute of Inorganic Chemistry
Siberian Branch of the Russian Academy of Sciences
Pr. Lavrentieva 3, Novosibirsk 630090 (Russia)
Fax: (+7) 383-330-9489
E-mail: cluster@che.nsk.su
A. L. Nuzhdin, Dr. K. P. Bryliakov, Prof. Dr. E. P. Talsi
Boreskov Institute of Catalysis
Siberian Branch of the Russian Academy of Sciences
Pr. Lavrentieva 5, Novosibirsk 630090 (Russia)

[**] This work was supported by the Creative Research Initiative Program of the Korean Ministry of Science and Technology and the BK 21 Program of the Korean Ministry of Education (KK). D.N.D. is grateful to the Young Scientist Candidate Fellowship of the President of the Russian Federation (MK-3842.2004.3). A.L.N., K.P.B., and E.P.T. acknowledge the Russian Foundation of Basic Research for financial support (grant 03-03-32009). We also thank Dr. A. V. Golovin for his kind assistance in NMR spectroscopy experiments.

Supporting information for this article is available on the WWW under http://www.angewandte.org or from the author.

InterScience
© 2006 Wiley-VCH Verlag GmbH & Co. KGaA, Weinheim

ions in the polymeric structure, and both of them have a coordination number five and an uncommon trigonal-bipyramidal coordination environment (Figure 1). The first Zn^{2+} ion is coordinated by a deprotonated hydroxy group of a

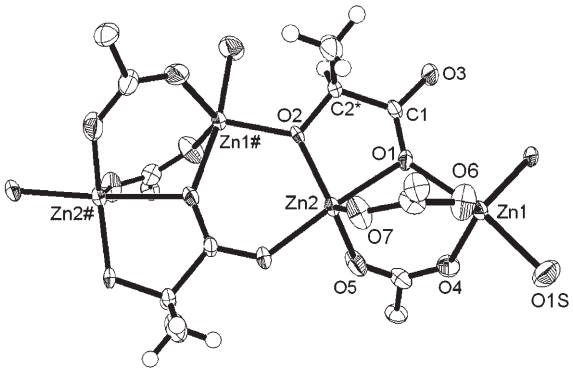


Figure 1. Section of the X-ray crystal structure of **1**·DMF, showing the coordination environments of the Zn^{2+} ions and their connectivity with lactate anions. Thermal ellipsoids are set at 50% probability. The chiral C atom of the lactic acid is marked by an asterisk. The following translation was applied: #) $-0.5+x$, $0.5-y$, $2-z$.

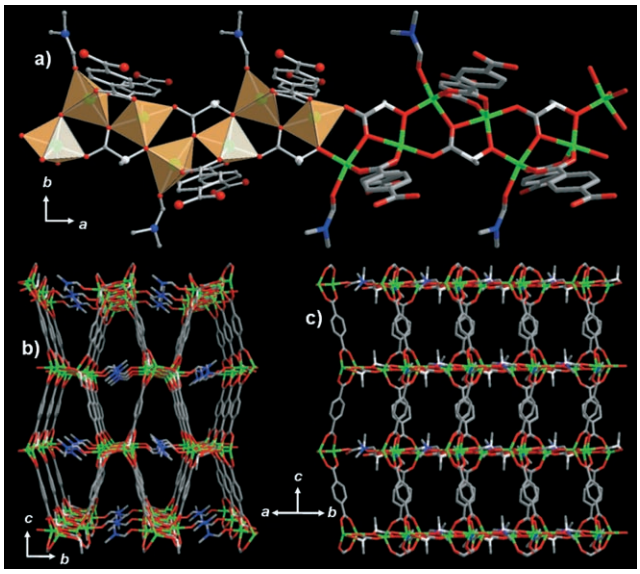


Figure 2. a) A view of the 1D chiral chains (as both ball-and-stick/polyhedra and wire models; polyhedra represent the Zn coordination environments) in the structure of **1**·DMF. b) Perspective view of the structure of **1**·DMF along the *a* axis. c) Projection of the structure of **1**·DMF in the (110) plane. Hydrogen atoms and guest molecules are omitted for clarity. Zn green, N blue, O red, C gray; chiral C atoms of the lactic acid ligand are shown in white.

lactate ligand, a carboxylate oxygen atom of another lactate ligand, and the oxygen atom of a DMF molecule. The second Zn^{2+} ion is chelated by one lactate ligand (by the carboxylic and hydroxy oxygen atoms) and coordinated to a carboxylic oxygen atom of another lactate ligand. In addition, the two Zn^{2+} ions are linked to each other by two bridging benzenedicarboxylate ligands (Figure 1). Overall, each lactate dianion connects four Zn^{2+} ions.

The Zn^{2+} ions and lactate ligands form 1D chiral chains running along the *a* axis (Figure 2). These chains act as SBUs, which are further interlinked by benzenedicarboxylate spacers in the other two directions to form a 3D coordination polymer of **1** with an open architecture.[11] The pores of roughly 5 Å diameter are interconnected in three directions. The chiral centers of the L-lactate moieties are exposed within the voids. In short, the pores in **1** have a homochiral environment.

In the as-synthesized material, the pores are occupied by coordinated DMF ligands, as well as guest DMF molecules that can readily be removed at elevated temperatures. A thermogravimetric analysis on the crystalline product of **1**·DMF indicates an approximately 30% loss of weight between 110–200°C, which is roughly equivalent to the total weight of the coordinated and uncoordinated solvent DMF molecules. Heating the as-synthesized material at a lower temperature (for example, 90°C) in vacuo for 3 h leads to a 10% weight loss, which corresponds to a partial removal of the guest molecules from the pores. The crystalline nature of the partially evacuated material **1**·$(DMF)_x$ ($x \approx 0.4$) was confirmed by powder XRD measurements, in which no significant shift or broadening of peaks was observed compared to the diffractogram of the as-synthesized form. However, heating **1** above 90°C for a prolonged period of time (several days) induces partial collapse of the framework, judging from the peak broadening and appearance of new peaks in powder XRD patterns. This outcome is probably due to the slow detachment of coordinated DMF ligands. These results suggest that the coordinated DMF molecules do not play a direct role in the formation of the metal–organic architecture, but do prevent the porous structure from collapsing.[12]

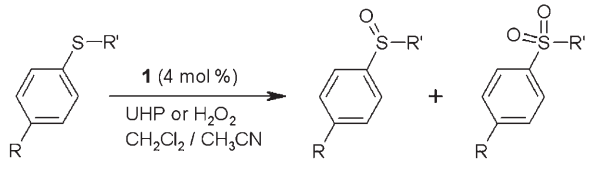
The permanent porosity of the partially evacuated material (**1**·$(DMF)_{0.4}$) was established by reversible gas-sorption experiments using H_2 at 78 K, which revealed an unsaturated type I isotherm characteristic of microporous materials (see Supporting Information). The corresponding Langmuir surface area was estimated to be 190 $m^2 g^{-1}$, which is similar to typical microporous zeolites, but rather small compared to other metal–organic porous materials.[13] This low surface area may be attributed to the incomplete evacuation of guest DMF molecules from the pores in **1**. Nevertheless, the sustainability of the open architecture of **1** is unambiguously demonstrated by the gas-sorption experiments.[7] The guest DMF molecules in **1**·DMF can be smoothly exchanged with other solvent or guest molecules in solution without causing structural collapse, demonstrating the porosity of **1** with respect to guest exchange. The corresponding solvent-accessible volume of the microporous metal–organic framework in **1** was estimated to be as high as 41%, assuming the guest-free structure $[Zn_2(bdc)(L\text{-lac})(dmf)]$.[14]

The most valuable properties of the homochiral porous material **1** arise from the unique combination of its porosity and chirality. Having the importance of enantiopure sulfoxides both as efficient synthetic auxiliaries and as valuable

 © 2006 Wiley-VCH Verlag GmbH & Co. KGaA, Weinheim

pharmaceuticals in mind,[15] we examined the enantioselective sorption of several substituted thioether oxides (**3a**–**d**, see Scheme 2) in the homochiral porous material **1**. The crystalline, partially evacuated material **1**·$(DMF)_{0.4}$ was stirred in a CH_2Cl_2 solution containing a racemic mixture of sulfoxides for 16 h, collected, and thoroughly washed with methanol to extract adsorbed guest molecules. Material **1** showed a remarkable sorption capability towards the sulfoxides with smaller substituents, such as H, Me (**3a**), and Me, Br (**3b**)—0.68 and 0.18 molecules, respectively, per formula unit of $[Zn_2(bdc)(L\text{-}lac)(dmf)]$. The enantiomeric excess (*ee*) values for the adsorbed guests were found to be 20% for **3a** and 27% for **3b**, with the *S* enantiomer in excess for both cases. However, sulfoxides with larger substituents (**3c** and **3d**) were not included in the pores of **1** in any significant amount. Such size- and enantioselective guest inclusion clearly indicates that **1** has a robust framework structure with pores of uniform size and chiral environment.[17] After the sorption experiments, the porous matrix of **1** could be regenerated by extracting the adsorbed guest molecules and reused in the next cycles of sorption experiments, without appreciable loss of its sorption capability.[18] Although the enantioselectivity is modest, these results suggest that **1** may be useful for the separation or purification of such compounds.

The metal–organic porous material **1** is also capable of mediating highly size- and chemoselective catalytic oxidation of thioethers **2** to sulfoxides **3** by urea hydroperoxide (UHP) or H_2O_2 (Scheme 2, Table 1). Paralleling the sorption behavior described above, thioethers **2a** and **2b** with smaller substituents exhibited reasonable conversion (64 and 58%, respectively; Table 1, entries 1 and 2) and high selectivity (92 and 83%, respectively) after 16 h of catalytic reaction, whereas thioethers **2c** and **2d** with bulkier substituents exhibited very poor conversion (only a few percent; Table 1, entries 3 and 4). The remarkable size selectivity in the catalytic reaction implies that the reaction primarily occurs inside the uniform micropores of the framework solid **1** and, therefore, attests to the heterogeneous nature of the catalysis.[19] Furthermore, upon using H_2O_2 instead of UHP and varying the solvent composition, the conversion and selectivity reached a quantitative level (Table 1, entries 5–8).[20] We also found that each formula unit of **1** can perform at least 30 catalytic cycles without loss of oxidation selectivity. To our knowledge, the metal–organic porous material **1** is the first example of its kind that exhibits such a remarkable catalytic activity in sulfoxidations. The mechanism of the catalytic reaction is currently under investigation.[21]



a: R = H, R' = Me;
b: R = Br, R' = Me;
c: R = NO_2, R' = Me;
d: R = H, R' = CH_2Ph

Scheme 2. Oxidation of sulfides catalyzed by **1**.

Table 1: Oxidation of sulfides **2a**–**d** catalyzed by **1**.[a]

Entry	Sulfide	Oxidant (equiv)	**1**/Sulfide	Solvent	Conversion [%][b]	Selectivity [%][c]
1	**2a**	UHP (2)	1:2	CH_2Cl_2	64	92
2	**2b**	UHP (2)	1:2	CH_2Cl_2	58	83
3	**2c**	UHP (2)	1:2	CH_2Cl_2	7	90
4	**2d**	UHP (2)	1:2	CH_2Cl_2	3	[d]
5	**2a**	H_2O_2 30% (3)	1:3	CH_3CN	92	100
6	**2a**	H_2O_2 90% (3)	1:3	CH_2Cl_2/CH_3CN 10:1	100	87
7	**2b**	H_2O_2 90% (3)	1:3	CH_2Cl_2/CH_3CN 10:1	85	100
8	**2b**	H_2O_2 90% (3)	1:50	CH_2Cl_2/CH_3CN 10:1	58	100

[a] Reaction conditions: sulfide concentration 0.05 mol L^{-1}, room temperature, 16 h. [b] Calculated as ([sulfone]+[sulfoxide])/([sulfide]+[sulfoxide]+[sulfone]). [c] Calculated as [sulfoxide]/([sulfoxide]+[sulfone]). [d] Not measured.

Despite the good conversion we, unfortunately, failed to observe any asymmetric induction in the catalytic sulfoxidations. The origin of the failure remains to be investigated in conjunction with the reaction mechanism. However, enantioenriched sulfoxides can be obtained by enantioselective sorption of the resulting racemic mixture by the chiral pores of **1**, which occurs simultaneously with the catalytic process. For example, after catalytic oxidation of **2a** using a comparable amount of **1** (Table 1, entry 1), we observed that (*S*)-**3a** was preferentially adsorbed with 20% *ee* in the pores of crystalline **1**, leaving the corresponding *R* enantiomer in excess in the solution phase. Thus, the homochiral metal–organic microporous material **1** provides a unique opportunity to produce enantioenriched sulfoxides in a one-pot process, through the size-selective catalytic oxidation of thioethers, using cheap and environment-friendly H_2O_2, and the enantioselective separation of the products. With improved enantioselectivity, this method may offer promise for the synthesis of enantiopure sulfoxides, as an alternative to the traditional asymmetric oxidation methods using soluble transition-metal catalysts.[15,22]

In conclusion, we have described a new approach to the synthesis of homochiral metal–organic porous materials starting from readily available chemicals. We successfully produced a 3D homochiral microporous framework that has permanent porosity, size- and enantioselective guest-sorption properties, as well as remarkable catalytic activity with size- and chemoselectivity, and high conversion in the oxidation of thioethers to sulfoxides. Studies to elucidate the mechanism of the catalytic reaction and the origin of the enantioselectivity in guest-sorption are in progress.

Experimental Section

Synthesis: A DMF solution (10 mL) containing $Zn(NO_3)_2{\cdot}6H_2O$ (300 mg, 1 mmol), H_2bdc (83 mg, 0.5 mmol), and L-H_2lac (49 mg, 0.5 mmol) in a teflon-lined steel bomb was heated at 110°C for 2 days. Colorless rod-shaped crystals were collected, washed with DMF, and Et_2O, and dried in vacuo for 3 min to yield **1**·DMF (240 mg, 86%). Elemental analysis (%) calcd for $[Zn_2(bdc)(L\text{-}lac)$-

 © 2006 Wiley-VCH Verlag GmbH & Co. KGaA, Weinheim

(dmf)]·0.9 DMF·0.1 H_2O: C 38.31, H 4.14, N 5.08; found: C 38.38, H 4.23, N 5.08. X-ray data for **1**·DMF: $C_{17}H_{22}N_2O_9Zn_2$, $M_r = 529.11$, orthorhombic, $P2_12_12_1$ (No. 19), $a = 10.299(2)$, $b = 11.824(2)$, $c = 20.372(4)$ Å, $V = 2480.81(90)$ Å^3, $Z = 4$, $T = 223$ K, $\rho_{calcd} = 1.417$ g cm^{-3}, $\mu(Mo_{K\alpha}) = 1.977$ mm^{-1}, $R_1 = 0.0474$, $wR_2 = 0.1339$ ($I > 2\sigma(I)$), GoF = 1.116, Flack = 0.06(2). See Supporting Information for further details. CCDC-281753 (**1**·DMF) contains the supplementary crystallographic data for this paper. These data can be obtained free of charge from The Cambridge Crystallographic Data Centre via www.ccdc.cam.ac.uk/data_request/cif.

Enantioselective sorption experiments: A racemic sulfoxide (**3a–d**, 0.1 mmol) was dissolved in CH_2Cl_2 (2 mL), and the partially evacuated material **1**·$(DMF)_{0.4}$ (heated at 90 °C for 3 h in vacuo before use, 40 mg, 0.17 mmol of zinc atoms) was added to the solution. After stirring the mixture for 16 h at room temperature, the crystalline adsorbent was collected by filtration and flushed with hexane (1 mL), which does not wash out the adsorbed compounds. After the adsorbed sulfoxide was extracted with methanol (2 × 5 mL), the solvent was removed in vacuo, and the resulting sulfoxide was purified by passing it through a short column (SiO_2, hexane/EtOAc) to remove DMF. The enantiomeric excess was measured by ^{1}H NMR spectroscopy with the chiral shift reagent Eu(hfc)$_3$ (hfc = 3-(heptafluoropropylhydroxymethylene)-(+)-camphorate) in CCl_4, as described in reference [16].

Typical catalytic sulfoxidation experiment: A mixture of a sulfide (**2a–d**,0.1 mmol), the partially evacuated material **1**·$(DMF)_{0.4}$ (0.004 to 0.1 mmol zinc atoms), and an oxidant (UHP or H_2O_2, 1–3 equiv with respect to the sulfide) dissolved in CH_2Cl_2 (2 mL) or CH_2Cl_2:CH_3CN (10:1, 2 mL) was stirred at room temperature for 16 h. Then, the solid catalyst was collected by filtration, and the adsorbed sulfoxide was extracted with methanol (2 × 5 mL). The extract and filtrate were combined, the volatiles were removed in vacuo, and the sulfide, sulfoxide, and sulfone were purified by column chromatography (SiO_2, hexane/EtOAc). The composition of the reaction products and the enantiomeric excess were measured by ^{1}H NMR spectroscopy with the chiral shift reagent Eu(hfc)$_3$ in CCl_4, as described in reference [16].

Received: August 24, 2005
Revised: October 10, 2005
Published online: December 30, 2005

Keywords: chirality · heterogeneous catalysis · metal–organic frameworks · microporous materials · sorption

[1] Recent reviews on porous metal–organic frameworks: a) S. Kitagawa, R. Kitaura, S.-i. Noro, *Angew. Chem.* **2004**, *116*, 2388–2430; *Angew. Chem. Int. Ed.* **2004**, *43*, 2334–2375; b) C. N. R. Rao, S. Natarajan, R. Vaidhyanathan, *Angew. Chem.* **2004**, *116*, 1490–1521; *Angew. Chem. Int. Ed.* **2004**, *43*, 1466–1496; c) O. M. Yaghi, M. O'Keeffe, N. W. Ockwig, H. K. Chae, M. Eddaoudi, J. Kim, *Nature* **2003**, *423*, 705–714; d) S. L. James, *Chem. Soc. Rev.* **2003**, *32*, 276–288; e) C. Janiak, *Dalton Trans.* **2003**, 2781–2804; f) I. Goldberg, *Chem. Commun.* **2005**, 1243–1254; g) J. L. C. Rowsell, O. M. Yaghi, *Angew. Chem.* **2005**, *117*, 4748–4758; *Angew. Chem. Int. Ed.* **2005**, *44*, 4670–4679; h) R. J. Hill, D.-L. Long, N. R. Champness, P. Hubberstey, M. Schröder, *Acc. Chem. Res.* **2005**, *38*, 335–348; i) N. W. Ockwig, O. Delgado-Friedrichs, M. O'Keeffe, O. M. Yaghi, *Acc. Chem. Res.* **2005**, *38*, 176–182; j) D. Bradshaw, J. B. Claridge, E. J. Cussen, T. J. Prior, M. J. Rosseinsky, *Acc. Chem. Res.* **2005**, *38*, 273–282; k) G. Férey, C. Mellot-Draznieks, C. Serre, F. Millange, *Acc. Chem. Res.* **2005**, *38*, 217–225; l) Special issue of *J. Solid State Chem.* **2005**, *178*, 2409–2573.

[2] a) S. Noro, S. Kitagawa, M. Kondo, K. Seki, *Angew. Chem.* **2000**, *112*, 2161–2164; *Angew. Chem. Int. Ed.* **2000**, *39*, 2081–2084; b) M. Eddaoudi, J. Kim, N. Rosi, D. Vodak, J. Wachter, M. O'Keeffe, O. M. Yaghi, *Science* **2002**, *295*, 469–472; c) K. Seki, W. Mori, *J. Phys. Chem. B* **2002**, *106*, 1380–1385; d) G. Férey, M. Latroche, C. Serre, F. Millange, T. Loiseau, A. Percheron-Guégan, *Chem. Commun.* **2003**, 2976–2977; e) J. L. C. Rowsell, A. R. Millward, K. S. Park, O. M. Yaghi, *J. Am. Chem. Soc.* **2004**, *126*, 5666–5667; f) D. N. Dybtsev, H. Chun, K. Kim, *Angew. Chem.* **2004**, *116*, 5143–5146; *Angew. Chem. Int. Ed.* **2004**, *43*, 5033–5036; g) H. Chun, D. N. Dybtsev, H. Kim, K. Kim, *Chem. Eur. J.* **2005**, *11*, 3521–3529; h) B. Chen, N. W. Ockwig, A. R. Millward, D. S. Contreras, O. M. Yaghi, *Angew. Chem.* **2005**, *117*, 4823–4827; *Angew. Chem. Int. Ed.* **2005**, *44*, 4745–4749; i) E. Y. Lee, S. Y. Jang, M. P. Suh, *J. Am. Chem. Soc.* **2005**, *127*, 6374–6381; j) R. Matsuda, R. Kitaura, S. Kitagawa, Y. Kubota, R. V. Belosludov, T. C. Kobayashi, H. Sakamoto, T. Chiba, M. Takata, Y. Kawazoe, Y. Mita, *Nature* **2005**, *436*, 238–241; k) X. Zhao, B. Xiao, A. J. Fletcher, K. M. Thomas, D. Bradshaw, M. J. Rosseinsky, *Science* **2004**, *306*, 1012–1015; l) G. Férey, C. Serre, C. Mellot-Draznieks, F. Millange, S. Surblé, J. Dutour, I. Margiolaki, *Angew. Chem.* **2004**, *116*, 6456–6461; *Angew. Chem. Int. Ed.* **2004**, *43*, 6296–6301.

[3] a) K. S. Min, M. P. Suh, *Chem. Eur. J.* **2001**, *7*, 303–313; b) K. Uemura, S. Kitagawa, M. Kondo, K. Fukui, R. Kitaura, H.-C. Chang, T. Mizutani, *Chem. Eur. J.* **2002**, *8*, 3587–3600; c) D. N. Dybtsev, H. Chun, S. H. Yoon, D. Kim, K. Kim, *J. Am. Chem. Soc.* **2004**, *126*, 32–33; d) D. Bradshaw, T. J. Prior, E. J. Cussen, J. B. Claridge, M. J. Rosseinsky, *J. Am. Chem. Soc.* **2004**, *126*, 6106–6114; e) M. Dincă, J. R. Long, *J. Am. Chem. Soc.* **2005**, *127*, 9376–9377; f) T. K. Maji, K. Uemura, H.-C. Chang, R. Matsuda, S. Kitagawa, *Angew. Chem.* **2004**, *116*, 3331–3334; *Angew. Chem. Int. Ed.* **2004**, *43*, 3269–3272; g) K. S. Suslick, P. Bhyrappa, J.-H. Chou, M. E. Kosal, S. Nakagaki, D. W. Smithenry, S. R. Wilson, *Acc. Chem. Res.* **2005**, *38*, 283–291; h) R.-G. Xiong, X.-Z. You, B. F. Abrahams, Z. Xue, C.-M. Che, *Angew. Chem.* **2001**, *113*, 4554–4557; *Angew. Chem. Int. Ed.* **2001**, *40*, 4422–4425.

[4] For other applications, including magnetism, nonlinear optics, luminescence, sensors, conductivity, ion-exchange, see comprehensive reviews [1a,e], and selected recent papers: a) M. J. Rosseinsky, *Microporous Mesoporous Mater.* **2004**, *73*, 15–30; b) S. Bonhommeau, G. Molnár, A. Galet, A. Zwick, J.-A. Real, J. J. McGarvey, A. Bousseksou, *Angew. Chem.* **2005**, *117*, 4137–4141; *Angew. Chem. Int. Ed.* **2005**, *44*, 5472–5475; c) N. Guillou, C. Livage, M. Drillon, G. Férey, *Angew. Chem.* **2003**, *115*, 4137–4141; *Angew. Chem. Int. Ed.* **2003**, *42*, 5314–5317; d) S.-Y. Wan, Y.-T. Huang, Y.-Z. Li, W.-Y. Sun, *Microporous Mesoporous Mater.* **2004**, *73*, 101–108; e) M. Viertelhaus, P. Adler, R. Clérac, C. E. Anson, A. K. Powell, *Eur. J. Inorg. Chem.* **2005**, 692–703; f) G. J. Halder, C. J. Kepert, B. Moubaraki, J. D. Cahion, *Science* **2003**, *298*, 1762–1765.

[5] a) M. Fujita, Y.-J. Kwon, S. Washizu, K. Ogura, *J. Am. Chem. Soc.* **1994**, *116*, 1151–1152; b) J. S. Seo, D. Wand, H. Lee, S. I. Jun, J. Oh, Y. Jeon, K. Kim, *Nature* **2000**, *404*, 982–986; c) C.-D. Wu, A. Hu, L. Zhang, W. Lin, *J. Am. Chem. Soc.* **2005**, *127*, 8940–8941; d) O. R. Evans, H. L. Ngo, W. Lin, *J. Am. Chem. Soc.* **2001**, *123*, 10395–10396; e) T. Dewa, T. Saiki, Y. Aoyama, *J. Am. Chem. Soc.* **2001**, *123*, 502–503; f) O. Ohmori, M. Fujita, *Chem. Commun.* **2004**, 1586–1587.

[6] a) B. Kesanli, W. Lin, *Coord. Chem. Rev.* **2003**, *246*, 305–326; b) M. E. Davis, *Nature* **2002**, *417*, 813–821.

[7] For some homochiral metal–organic frameworks, the porosity has been demonstrated either by reversible gas sorption or guest inclusion; see refs. [3d,h], [5b–d], and a) C.-D. Wu, W. Lin, *Chem. Commun.* **2005**, 3673–3675; b) C.-D. Wu, W. Lin, *Angew. Chem.* **2005**, *117*, 1994–1997; *Angew. Chem. Int. Ed.* **2005**, *44*, 1958–1961; c) Y. Cui, S. J. Lee, W. Lin, *J. Am. Chem. Soc.* **2003**,

 © 2006 Wiley-VCH Verlag GmbH & Co. KGaA, Weinheim

125, 6014 – 6015; d) C. J. Kepert, T. J. Prior, M. J. Rosseinsky, *J. Am. Chem. Soc.* **2000**, *122*, 5158 – 5168.

[8] Our approach is based on the concept of the SBU, which was developed by Yaghi, O'Keeffe, and co-workers (see reference [1c]), and has been widely used in the synthesis of metal–organic frameworks. Note that the framework-forming reaction does not necessarily proceed in a stepwise manner as it appears in Scheme 1. The strategy itself may not be novel, but this is the first time that it has been successfully applied in the synthesis of 3D homochiral metal–organic porous materials.

[9] Recently, a similar scheme has been used to produce a 2D homochiral coordination polymer which, however, does not withstand guest removal and, therefore, is not permanently porous: Y. V. Mironov, N. G. Naumov, K. A. Brylev, O. A. Efremova, V. E. Fedorov, K. Hegetschweiler, *Angew. Chem.* **2004**, *116*, 1317 – 1321; *Angew. Chem. Int. Ed.* **2004**, *43*, 1297 – 1300.

[10] The Zn–O distances between Zn^{2+} ions and the hydroxy oxygen atom of the lactate anion in **1** (1.969 and 1.939 Å) clearly support the deprotonation of the OH group.

[11] A number of porous metal–organic frameworks based on 1D SBUs have been described. For recent examples, see: N. L. Rosi, J. Kim, M. Eddaoudi, B. Chen, M. O'Keeffe, O. M. Yaghi, *J. Am. Chem. Soc.* **2005**, *127*, 1504 – 1518, and references therein.

[12] Similar collapse of porous structures was observed upon removal of coordinated DMF ligands in: H. Chun, D. Kim, D. N. Dybtsev, K. Kim, *Angew. Chem.* **2004**, *116*, 989 – 992; *Angew. Chem. Int. Ed.* **2004**, *43*, 971 – 974.

[13] Typically, the specific surface areas of metal–organic microporous materials are in the range of 1000–3000 $m^2 g^{-1}$; see ref. [2] for recent examples. However, the highest Langmuir surface area obtained to date for metal–organic frameworks is 5650 $m^2 g^{-1}$; see ref. [1k] and H. K. Chae, D. Y. Siberio-Pérez, J. Kim, Y. Go, M. Eddaoudi, A. J. Matzger, M. O'Keeffe, O. M. Yaghi, *Nature* **2004**, *427*, 523 – 527.

[14] A. L. Spek, PLATON, a multipurpose crystallographic tool, Utrecht University, Utrecht, The Netherlands, **2001**.

[15] Recent reviews on chiral sulfoxides: a) H. B. Kagan in *Catalytic Asymmetric Synthesis* (Ed.: I. Ojima), 2nd ed., Wiley-VCH, New. York, **2000**, chap. 6, p. 327; b) I. Fernandez, N. Khiar, *Chem. Rev.* **2003**, *103*, 3651 – 3706, and references therein; c) H. J. Federsel, *Chirality* **2003**, *15*, S128 – S142.

[16] K. P. Bryliakov, E. P. Talsi, *Angew. Chem.* **2004**, *116*, 5340 – 5342; *Angew. Chem. Int. Ed.* **2004**, *43*, 5228 – 5230.

[17] The material $[Zn_2(bdc)(L\text{-lac})(dmf)_x]$ $(x < 1)$ with partially removed coordinating DMF ligands showed poorer sorption of **3b** (about 0.05 molecules per formula unit of $[Zn_2(bdc)(L\text{-lac})(dmf)]$), along with a lower *ee* value (12% in favor of the *S* enantiomer).

[18] After the sorption experiment, the crystalline material **1** was washed thoroughly with CH_2Cl_2 (5 portions, 4–5 mL each) to remove traces of sorbed sulfoxide, collected by filtration, and dried in air for 1 h, before use in the next cycles of sorption experiments. The amount of sorbed **3b** in **1** in the second cycle was found to be the same, 0.18 molecules per formula unit of $[Zn_2(bdc)(L\text{-lac})(dmf)]$.

[19] The heterogeneous nature of the catalysis was further confirmed in that no conversion was observed in the reaction of **2b** with UHP in the supernatant solution, removed after stirring with **1** in CH_2Cl_2 for 16 h.

[20] Without a catalyst, H_2O_2 and UHP do not oxidize the sulfides into sulfoxides or sulfones, as no conversion was observed after 18 h of reaction of **2b** (10 mg, 0.05 mmol) with UHP (10 mg, 2 equiv) in CH_2Cl_2, or with H_2O_2 (90%, 3 equiv) in CH_2Cl_2:CH_3CN (10:1). Also see: M. Palucki, P. Hanson, E. N. Jacobsen, *Tetrahedron Lett.* **1992**, *33*, 7111 – 7114.

[21] To better understand the mechanism of the catalytic reaction with **1**, we are also investigating the same reaction using an analogous homogeneous catalyst.

[22] a) J. Legros, C. Bolm, *Angew. Chem.* **2003**, *115*, 5645 – 5647; *Angew. Chem. Int. Ed.* **2003**, *42*, 5487 – 5489; b) J. Legros, C. Bolm, *Angew. Chem.* **2004**, *116*, 4321 – 4324; *Angew. Chem. Int. Ed.* **2004**, *43*, 4225 – 4228.

 © 2006 Wiley-VCH Verlag GmbH & Co. KGaA, Weinheim

Ferrocene-Based Polymers

DOI: 10.1002/anie.200503515

A Synthetic Route to Borylene-Bridged Poly(ferrocenylene)s**

Julia B. Heilmann, Matthias Scheibitz, Yang Qin, Anand Sundararaman, Frieder Jäkle, Tonia Kretz, Michael Bolte, Hans-Wolfram Lerner, Max C. Holthausen,* and Matthias Wagner**

Dedicated to Professor Herbert W. Roesky on the occasion of his 70th birthday

The chemistry of metal-containing polymers is receiving increasing attention in the search for new materials that possess useful optical, electronic, and magnetic properties.[1–4] Among the compounds developed so far, organometallic macromolecules have become particularly attractive targets ever since the ring-opening polymerization (ROP) of strained

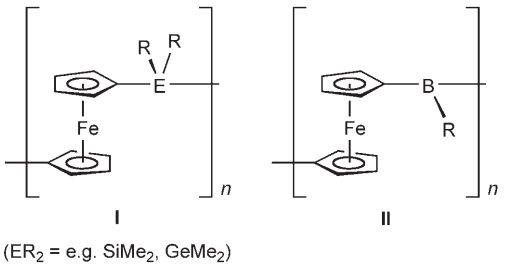
[*] Y. Qin, A. Sundararaman, Prof. Dr. F. Jäkle
Department of Chemistry
Rutgers University Newark
73 Warren Street, Newark, NJ 07102 (USA)
Fax: (+1) 973-353-5064
E-mail: fjaekle@andromeda.rutgers.edu
J. B. Heilmann, Dr. M. Scheibitz, T. Kretz, Dr. M. Bolte, Dr. H.-W. Lerner, Prof. Dr. M. C. Holthausen, Prof. Dr. M. Wagner
Institut für Anorganische Chemie
Johann Wolfgang Goethe-Universität Frankfurt
Marie-Curie-Strasse 11, 60439 Frankfurt (Main) (Germany)
Fax: (+49) 69-798-29260
E-mail: max.holthausen@chemie.uni-frankfurt.de
matthias.wagner@chemie.uni-frankfurt.de

[**] The authors thank Prof. Dr. Rainer Winter and Dipl.-Chem. Jörg Maurer, Universität Regensburg, for helpful discussions. Financial support through PhD grants from the Hessisches Ministerium für Wissenschaft und Kunst (J.B.H.), the Fonds der Chemischen Industrie, and the Bundesministerium für Bildung und Forschung (M.S.) is gratefully acknowledged. M.C.H. wishes to thank Prof. Dr. Gernot Frenking for his helpful discussions. Computer time was provided by the CSC Frankfurt and the HHLR Darmstadt. This work was supported by the Deutsche Forschungsgemeinschaft, and the GPC and light-scattering instrumentation was in part provided by the National Science Foundation.

Supporting information for this article is available on the WWW under http://www.angewandte.org or from the author.

WILEY InterScience DISCOVER SOMETHING GREAT
© 2006 Wiley-VCH Verlag GmbH & Co. KGaA, Weinheim

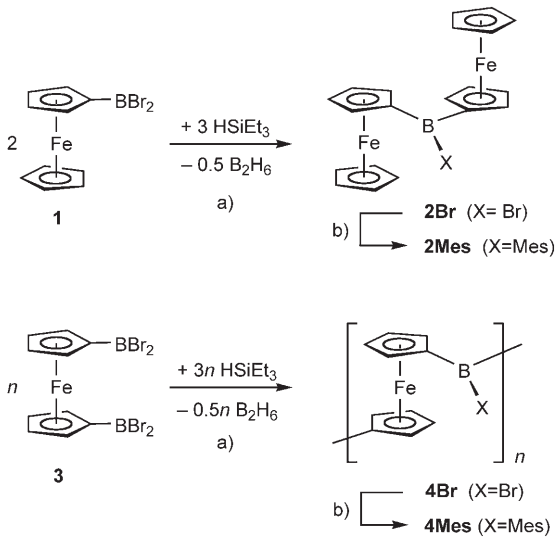
ring-tilted [1]ferrocenophanes[5] was used to synthesize the first high-molecular-weight poly(ferrocenylene)s (**I**, Scheme 1) with skeletal iron atoms. Within this particular class of compounds, boranediyl-bridged poly(ferrocenylene)s



Scheme 1. Poly(ferrocenylene)s **I** generated by ring-opening polymerization of [1]ferrocenophanes; the boron-bridged target polymer **II**.

(**II**, Scheme 1) are of paramount interest because the three-coordinate boron spacer offers a vacant p orbital for conjugative interaction with the cyclopentadienyl π-systems. Boranediyl bridges should therefore be capable of mediating electronic interactions between the iron centers very efficiently.[6,7] The degree of electronic communication via the boron atom can be fine-tuned by modifying the π-donor ability of its substituent R, thereby offering a way for the rational design of novel materials with potentially useful electronic properties. Attempts to polymerize boron-bridged [1]ferrocenophanes using the ROP approach have so far been restricted to boron moieties bearing amino substituents. Moreover, the products obtained proved to be mainly insoluble in organic solvents and the minor soluble fraction was shown by NMR spectroscopy and mass spectrometry to consist primarily of small, cyclic oligomers ($n = 2, 3$).[8,9] The purpose of this paper is to present a new synthetic strategy that provides convenient access to the first soluble ferrocenylborane polymers containing electron-deficient, three-coordinate boron spacers in the polymer main chain. Our key discovery in this context is the facile and quantitative coupling reaction that occurs upon treatment of $FcBBr_2$ with $HSiEt_3$ to yield the diferrocenylborane Fc_2BBr ($Fc = (C_5H_5)Fe(C_5H_4)$). We show here that the same synthetic protocol can successfully be applied to the preparation of the corresponding polymers $[\text{-fc-B(Br)-}]_n$ starting from the difunctional monomer $fc(BBr_2)_2$ ($fc = Fe(C_5H_4)_2$).

We began our study with a detailed investigation of the key coupling step. As mentioned above, Fc_2BBr (**2Br**, Scheme 2) can be obtained by treating two equivalents of $FcBBr_2$ (**1**)[10] with three equivalents of $HSiEt_3$ in toluene;[11] in addition, half an equivalent of B_2H_6 and three equivalents of $BrSiEt_3$ are liberated in the course of the reaction. The NMR spectra of **2Br** agree with those of a structurally authenticated sample of Fc_2BBr that was synthesized independently from $FcSnMe_3$ and $FcBBr_2$.[12] Since there is no indication of the presence of Fc_2BH[13] in the crude reaction mixture, ferrocenyl transfer obviously proceeds not only with practically quantitative yield but also with excellent selectivity towards the formation of BBr bridges. A series of NMR

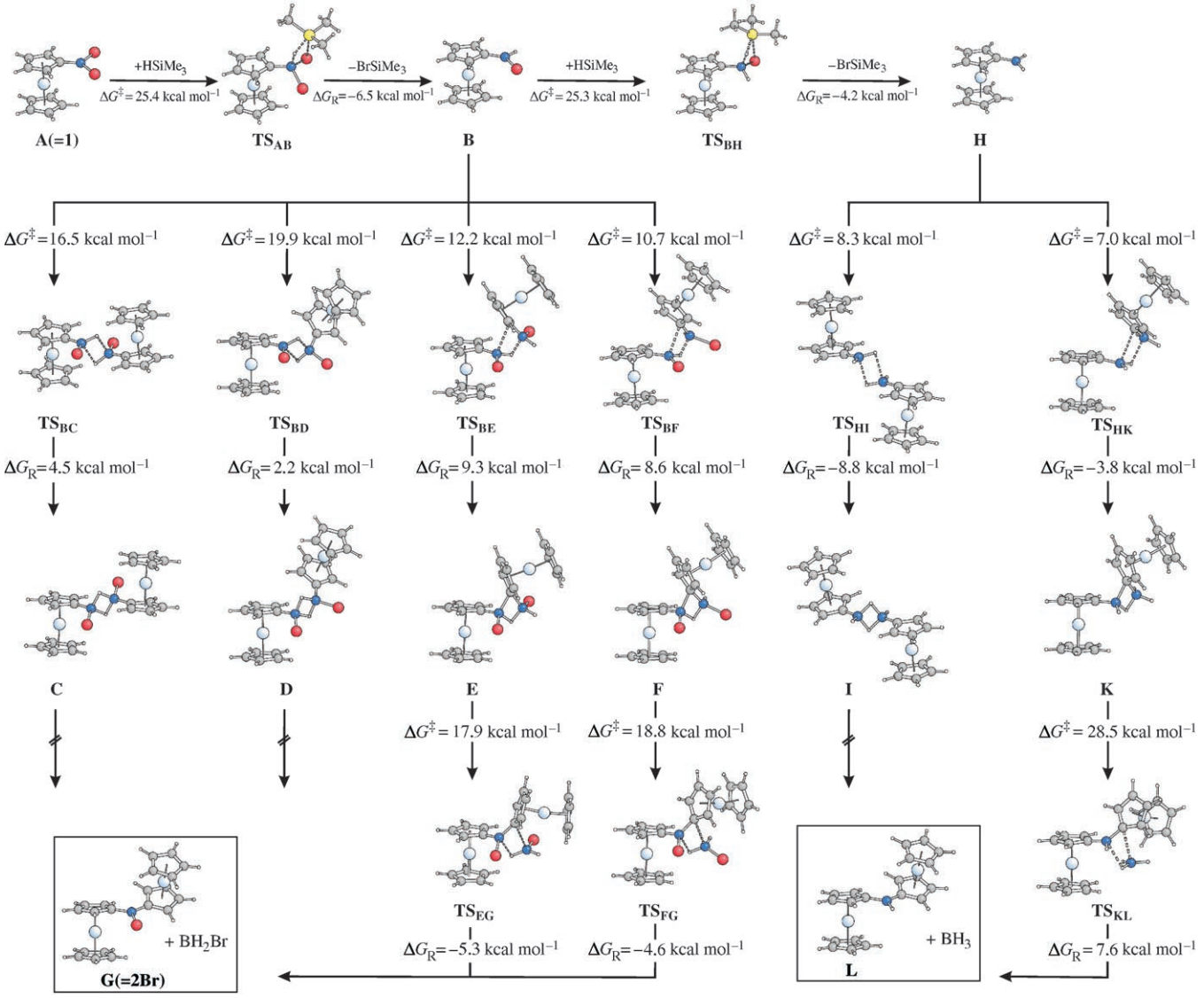


Scheme 2. Synthesis of **2Br**, **4Br**, **2Mes**, and **4Mes**. a) toluene, −78 °C to RT; b) $[CuMes]_n$, toluene, 80 °C; Mes = mesityl.

experiments showed that the reaction of $FcBBr_2$ with $HSiEt_3$ in a molar ratio of 2:1 leads to a mixture of $FcBBr_2$, Fc_2BBr, and B_2H_6. For quantitative conversion, a minimum of 1.5 equivalents of $HSiEt_3$ is required.

Details of the reaction mechanism for the formation of **2Br** (**G** in Scheme 3) were elucidated by means of quantum chemical calculations employing the ONIOM extrapolation scheme (see Supporting Information[11] for details). These calculations were performed with the real molecular models, except for the use of $HSiMe_3$ instead of $HSiEt_3$ as the hydride source. In line with the experimental finding that $FcBBr_2$ does not dimerize under any experimental conditions, we were unable to locate a doubly bromide-bridged dimer of **1** (**A** in Scheme 3). Instead, the reaction commences with formation of FcBHBr (**B**) from $FcBBr_2$ (**A**) via $\mathbf{TS_{AB}}$, the transition structure of a concerted Br/H exchange by $HSiMe_3$ (Scheme 3). $\mathbf{TS_{AB}}$ is connected with an energy barrier of $\Delta G^{\neq} = 25.4\ \text{kcal mol}^{-1}$, and formation of **B** is exergonic by $\Delta G_R = -6.5\ \text{kcal mol}^{-1}$. **B** can dimerize to the doubly hydride-bridged *cis*/*trans* isomers **C** and **D**. We did not find reaction pathways leading from **C** or **D** to the experimentally characterized final product **G**. Instead, we identified alternative routes via the two isomeric (μ-H)(μ-C)-bridged dimers **E** and **F**. Both are higher in energy than their doubly hydride-bridged counterparts, but are formed with significantly lower barriers. Subsequent product formation from **E** and **F** is an exergonic process and occurs with elimination of BH_2Br. Assuming fast pre-equilibria between **B** and **E** and **B** and **F**, the effective activation barriers for the formation of **G** from **B** amount to $\Delta G^{\neq} = 27.2$ and $27.4\ \text{kcal mol}^{-1}$, respectively. Yet another reaction pathway opens up for **B** after consumption of a second equivalent of $HSiMe_3$ to yield $FcBH_2$ (**H**). With $\Delta G^{\neq} = 25.3$ and $\Delta G_R = -4.2\ \text{kcal mol}^{-1}$, the energetic characteristics of this process are very similar to those of the initial step **A**→**B**. Dimerization of **H** to **I** closely resembles the corresponding elementary steps **B**→**C** and **B**→**D** and is kinetically and thermodynamically feasible, but represents a

 © 2006 Wiley-VCH Verlag GmbH & Co. KGaA, Weinheim



Scheme 3. Computed reaction pathways leading to the formation of **G** (=**2Br**); gray C, light blue Fe, blue B, red Br, yellow Si.

dead end for the reaction cascade as well. Thus, also in this region of the potential-energy surface, the productive pathway (now leading to diferrocenylborane **L** with $\Delta G^{\ddagger} = 28.5$ kcal mol^{-1}) proceeds via a (μ-H)(μ-C)-bridged dimer (**K**).

With the scenario outlined in Scheme 3, key elementary steps leading to diferrocenylboranes **G** (=**2Br**) and **L** have been unveiled. The experimentally observed exclusive formation of **G** can be explained by a H/Br exchange reaction according to $\mathbf{L} + {}^1/_2\,(BH_2Br)_2 \rightarrow \mathbf{G} + {}^1/_2\,B_2H_6$, for which we compute a thermodynamic driving force of $\Delta G_R = -7.9$ kcal mol^{-1}. In addition, we found a thermodynamically viable shunt pathway that competes for the formation of **L** via regeneration of **B** from **H** according to $\mathbf{H} + {}^1/_2\,(BH_2Br)_2 \rightarrow \mathbf{B} + {}^1/_2\,B_2H_6$ ($\Delta G_R = -7.7$ kcal mol^{-1}). In conclusion, theory indicates that the overall reaction $2\mathbf{A} + 3\,HSiMe_3 \rightarrow \mathbf{G} + {}^1/_2\,B_2H_6 + 3\,BrSiMe_3$ is highly exothermic (by $\Delta G_R = -26.2$ kcal mol^{-1}) and that competing alternative reaction pathways converge to the sole product **G**, which is fully in line with the experimental observations. Hence, this condensation reaction meets all the requirements for an efficient polymerization process.

Accordingly, the bromo-substituted polymer **4Br** was prepared from $fc(BBr_2)_2$ (**3**)[14] and three equivalents of $HSiEt_3$ in a very clean reaction. This polymer is highly sensitive to air and moisture and does not dissolve in common inert solvents. It was therefore transformed into the corresponding mesityl-substituted polymer **4Mes** by treating a slurry of **4Br** in toluene with $[CuMes]_n$ ($n = 4, 5$).[15–17] The mesityl substituent was chosen because it aids in the solubilization of the material and also provides steric protection to the boron sites (Scheme 2).[18] This new polymer is only moderately sensitive to air and has a high thermal stability, according to thermogravimetric analysis (TGA) under nitrogen. A single-step weight loss of 72%, with an inflection point at 403 °C, gave a brown ceramic material in 28% yield. Differential scanning calorimetry[11] revealed a glass-transition temperature, T_g, of 110 °C, which is similar to that reported for poly(ferrocenylphenylphosphane)

 © 2006 Wiley-VCH Verlag GmbH & Co. KGaA, Weinheim

([-fcP(Ph)-]$_n$, 126 °C), which also contains tricoordinate bridging units.[19] The molecular weight and dispersity of **4Mes** were analyzed by gel permeation chromatography (GPC) on a chromatograph equipped with refractive index (RI) and multi-angle laser light scattering (MALLS) detectors, and further studied by MALDI TOF mass spectrometry.[11] The mesityl-stabilized polymer **4Mes** was found to be well compatible with GPC separation in THF. The GPC trace shows a monomodal distribution with an average molecular weight, M_n, of 5160 and a polydispersity index (PDI) of 1.45 based on in-line static light scattering detection. In order to investigate the structure of these low-molecular-weight polymers further, and to determine the nature of the end-groups, a MALDI TOF–TOF mass spectrum of **4Mes** was acquired in reflectron (+) mode with benzo[*a*]pyrene as the matrix.[20] The spectrum is characterized by three series of peaks (Figure 1), which, by comparison with the peak patterns of

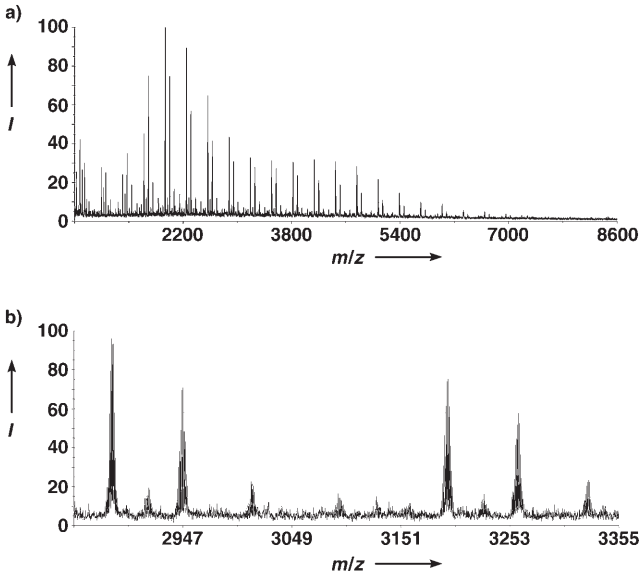


Figure 1. a) MALDI TOF-TOF MS of **4Mes** (reflectron (+) mode with benzo[*a*]pyrene as matrix); b) region between *m*/*z* 2845 and 3355 enlarged.

the respective calculated molecular ion peaks, can confidently be assigned to polymers bearing two -BMes$_2$ termini, one -BMes$_2$ and one -Fc end group, and two -Fc caps, respectively (see Figure 1b: *m*/*z* 2880, [Mes$_2$B{-fc-B(Mes)-}$_8$Mes]$^+$; *m*/*z* 2946, [H{-fc-B(Mes)-}$_9$Mes]$^+$; *m*/*z* 3012, [H{-fc-B(Mes)-}$_9$-Fc]$^+$). The series of peaks representing polymers with two ferrocenyl end groups possesses by far the lowest intensity, while Mes$_2$B[-fc-B(Mes)-]$_n$Mes molecules bearing two boryl end groups are clearly the most abundant ones. Within each series the difference between adjacent peaks, $\Delta(m/z)$, is always 314, which corresponds to one [-fc-B(Mes)-] repeat unit. The highest molecular weight peak that was unambiguously detectable appears at *m*/*z* 6962 and belongs to a polymer containing 21 ferrocenylene fragments (Mes$_2$B[-fc-B(Mes)-]$_{21}$Mes).

To facilitate the analysis of the NMR and UV/Vis spectra as well as the electrochemical data of **4Mes** we prepared two model systems representing different segments of the polymer chain, the dinuclear compound **2Mes** and the 1,1′-diborylated ferrocene fc(BMes$_2$)$_2$ (**5Mes**). While **2Mes** is readily available using the synthesis protocol developed for **4Mes** (Scheme 2), compound **5Mes** is best prepared from 1,1′-dilithioferrocene[21] and Mes$_2$BF.[11]

In the temperature range between 25 and 70 °C, the ^{11}B NMR resonances of **2Mes**, **4Mes** and **5Mes** are broadened beyond detection. The proton NMR spectrum of **2Mes** shows a singlet at $\delta = 6.81$ ppm (C_6H_2), two virtual triplets at $\delta = 4.58$ and $\delta = 4.42$ ppm (C_5H_4), and resonances for the *para* and *ortho* methyl groups at $\delta = 2.31$ and 2.23 ppm, respectively. The ^{1}H NMR spectrum of **5Mes** is characterized by the following resonances: $\delta = 6.75$ (s, C_6H_2), 4.73/4.41 (2 × vtr, C_5H_4), 2.27 ppm (*o*,*p*-CH_3). Correspondingly, five major NMR signals [$\delta(^1H) = 6.79$, 4.48/4.28, 2.30/2.14 ppm] are found in the spectrum of **4Mes** and assigned to internal [-(C_5H_4)Fe(C_5H_4)-B(Mes)-] fragments constituting the polymer chain. These major signals are accompanied by several smaller resonances attributable to the chain end groups [-(Mes)B-Fc] and [-BMes$_2$]. For an infinitely long polymer, the ratio between the cyclopentadienyl protons and aromatic mesityl protons would be 4:1. In the case of **4Mes**, the ratio between the integral values of all cyclopentadienyl signals on one hand and all aromatic mesityl resonances on the other is 4:1.14.

One of the key questions with regard to the electronic properties of **4Mes** is whether a conformation is possible that allows for efficient π-conjugation of the ferrocenes via the empty p orbital of the boron bridge. To this end, the model compound **2Mes** was investigated by X-ray crystallography (Figure 2).[11] An inspection of the dihedral angles between the cyclopentadienyl rings and the B1 C1 C11 C31 plane

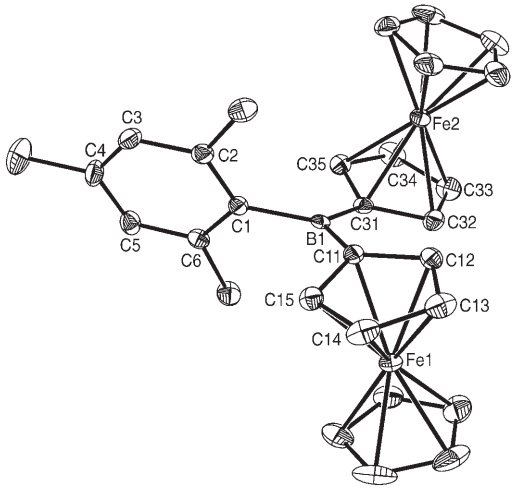


Figure 2. Molecular structure and numbering scheme of compound **2Mes**; thermal ellipsoids shown at the 50% probability level; hydrogen atoms omitted for clarity. Selected bond lengths [Å], angles [°], torsion angles [°], and dihedral angles [°]: B1–C1 1.590(4), B1–C11 1.554(4), B1–C31 1.555(4); C1-B1-C11 119.3(2), C1-B1-C31 117.3(2), C11-B1-C31 123.4(2); C1-B1-C11-C12 −163.2(2), C1-B1-C31-C32 −173.2(2), C11-B1-C31-C32 7.0(4), C31-B1-C11-C12 16.7(4), C11-B1-C1-C6 −119.8(3), C31-B1-C1-C6 60.4(3); C1 to C6 ring//C1 B1 C11 C31 plane 61.2, C11 to C15 ring//C31 to C35 ring 23.4.

 © 2006 Wiley-VCH Verlag GmbH & Co. KGaA, Weinheim

revealed values of 21.8° [C11 to C15] and 14.1° [C31 to C35] in line with a substantial overlap of the corresponding π-electron clouds.

π-Overlap between the p orbital on boron and the ferrocene units is expected to influence the UV/Visible spectra, and the ensuing electronic communication between the ferrocene moieties should be reflected in the redox properties of **4Mes**. Parent ferrocene has its longest wavelength absorption maximum at $\lambda = 440$ nm in the UV/Vis spectrum. This band is pronouncedly shifted to the red upon going to diferrocenylborane **2Mes** ($\lambda = 490$ nm) and experiences a further bathochromic shift in polymeric **4Mes** ($\lambda = 505$ nm), in agreement with an increasing degree of π-delocalization within this series of compounds. Cyclic voltammograms were recorded in CH_2Cl_2 with $[NBu_4][B(C_6F_5)_4]$ (0.1 M) as supporting electrolyte and are referenced against the FcH/FcH^+ couple.[11] The mononuclear model system **5Mes** is reversibly oxidized at a potential of $E^{\circ\prime} = 196$ mV. This anodic shift with respect to parent ferrocene may be explained by the π-electron withdrawing nature of the $BMes_2$ substituents. In the case of the dinuclear compound **2Mes**, two well resolved redox waves of equal intensity and features of chemical reversibility appear at $E^{\circ\prime} = 45$ mV and 467 mV. These transitions are assigned to the successive one-electron oxidations of the two iron centers. The large separation of $\Delta(E^{\circ\prime}) = 422$ mV between the two redox waves indicates pronounced electronic communication between the two ferrocenyl moieties in **2Mes**.[22] The first oxidation event of polymer **4Mes** (one ferrocenylene donor per BMes acceptor) is reversible on the CV timescale and occurs at 140 mV (Figure 3). This value lies between the first redox potential of

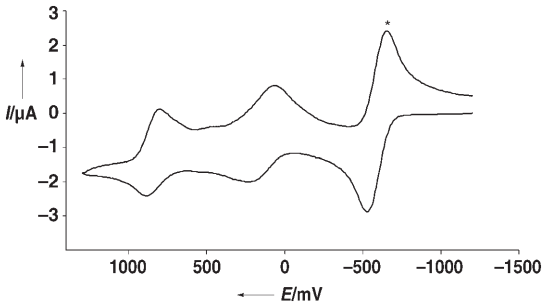


Figure 3. Cyclic voltammogram of **4Mes** (CH_2Cl_2, 0.1 M $[NBu_4][B(C_6F_5)_4]$, $\nu = 0.2$ V s^{-1}, vs. FcH/FcH^+; starred wave: $(C_5Me_5)_2Fe/(C_5Me_5)_2Fe^+$).

2Mes possessing two donors/one acceptor (45 mV) and the redox potential of **5Mes** with one donor/two acceptors (196 mV). A second redox wave with features of chemical reversibility is recorded for **4Mes** at $E^{\circ\prime} = 845$ mV. This transition is absent in the cyclic voltammograms of the model systems and tentatively assigned to a second Fe^{II}/Fe^{III} oxidation. This second redox event is observed at a much higher potential than that of the diferrocene **2Mes** (467 mV), which is probably due to the presence of two neighboring ferrocenium moieties adjacent to each neutral ferrocene in the polymer chain -fc^+-B(Mes)-fc-B(Mes)-fc^+-B(Mes)- following oxidation of alternating ferrocenylene moieties ([Fc-B(Mes)-Fc^+] in the case of the dimer).[23] The large splitting $\Delta(E^{\circ\prime}) = 705$ mV for **4Mes** further suggests very pronounced electronic interactions in this polymer.

In summary, borylene-bridged poly(ferrocenylene)s [-fc-B(Br)-]$_n$ are readily prepared from $fc(BBr_2)_2$ and $HSiEt_3$ via a novel polycondensation reaction. Treatment with $[CuMes]_n$ gives a highly soluble polymer [-fc-B(Mes)-]$_n$ with three-coordinate boron centers, which, due to their empty p orbital, are well-suited for the promotion of electron delocalization along the polymer chain.

Experimental Section

Synthesis of **4Br**: To **3** (3.990 g, 7.60 mmol) in toluene (20 mL) was added neat $HSiEt_3$ (3.888 g, 33.44 mmol) at −78 °C with stirring (note: even though 3 equiv of $HSiEt_3$ are sufficient for full conversion, we found it convenient to use the hydride transfer reagent in some excess when working on a preparative scale). The resulting red solution was allowed to warm to room temperature and stirred overnight, whereupon a red precipitate gradually formed. The microcrystalline solid was collected on a frit, triturated with toluene (10 mL) and dried in vacuo. Yield: 1.914 g (92 % repeat units).

Synthesis of **4Mes**: A solution of $[CuMes]_n$ (0.162 g, 0.89 mmol) in toluene (10 mL) was added slowly at room temperature to a slurry of **4Br** (0.255 g, 0.93 mmol repeat units) in toluene (20 mL). The resulting mixture was stirred overnight and then heated to 80 °C for 8 h, whereupon its color changed from red to purple accompanied by the formation of a greyish precipitate. After filtration and evaporation of solvent under reduced pressure, a purple microcrystalline solid was obtained. The crude product was dissolved in toluene and repeatedly precipitated from toluene into hexanes. Yield: 0.404 g (81 % repeat units).

^{1}H NMR (250.1 MHz, $CDCl_3$): $\delta =$ **6.79** (2H, C_6H_2), 6.76, 4.63, 4.57, **4.48** (4H, C_5H_4), 4.42, **4.28** (4H, C_5H_4), 4.23, 4.08, 2.36, 2.34, **2.30** (6H, o-CH_3), 2.26, 2.24, 2.18, **2.14** (3H, p-CH_3), 2.09 ppm. Note: The five major peaks are printed boldface. UV/Vis (0.1 mM, CH_2Cl_2): $\lambda_{max} = 300$, 380, 505 nm. GPC-RI (THF, PS Standards): $M_w = 3880$, $M_n = 2890$, PDI = 1.34; GPC-MALLS (THF; dn/dc = 0.167): $M_w = 7480$, $M_n = 5160$; PDI = 1.45.

Received: October 4, 2005
Published online: December 30, 2005

Keywords: boranes · density functional calculations · ferrocene · organic–inorganic hybrid composites · polymers

[1] C. U. Pittman, C. E. Carraher, M. Zeldin, J. E. Sheats, B. M. Culbertson, *Metal-Containing Polymeric Materials*, Plenum, New York, **1996**.
[2] R. D. Archer, *Inorganic and Organometallic Polymers*, Wiley-VCH, Weinheim, **2001**.
[3] A. S. Abd-El-Aziz, C. E. Carraher, C. U. Pittman, J. E. Sheats, M. Zeldin, *Macromolecules Containing Metal and Metal-like Elements, Vol. 1*, Wiley, Hoboken, NJ, **2003**.
[4] I. Manners, *Synthetic Metal-Containing Polymers*, Wiley-VCH, Weinheim, **2004**.
[5] I. Manners, *Adv. Organomet. Chem.* **1995**, *37*, 131.
[6] C. Elschenbroich, M. Wolf, O. Burghaus, K. Harms, J. Pebler, *Eur. J. Inorg. Chem.* **1999**, 2173.
[7] For organoboron polymers with organic π-conjugated bridging systems see: a) N. Matsumi, K. Naka, Y. Chujo, *J. Am. Chem. Soc.* **1998**, *120*, 5112; b) N. Matsumi, M. Miyata, Y. Chujo, *Macromolecules* **1999**, *32*, 4467; c) M. Miyata, Y. Chujo, *Polym.*

 © 2006 Wiley-VCH Verlag GmbH & Co. KGaA, Weinheim

Bull. **2003**, *51*, 9; d) R. J.-P. Corriu, T. Deforth, W. E. Douglas, G. Guerrero, W. S. Siebert, *Chem. Commun.* **1998**, 963.
[8] H. Braunschweig, R. Dirk, M. Müller, P. Nguyen, R. Resendes, D. P. Gates, I. Manners, *Angew. Chem.* **1997**, *109*, 2433; *Angew. Chem. Int. Ed. Engl.* **1997**, *36*, 2338.
[9] A. Berenbaum, H. Braunschweig, R. Dirk, U. Englert, J. C. Green, F. Jäkle, A. J. Lough, I. Manners, *J. Am. Chem. Soc.* **2000**, *122*, 5765.
[10] T. Renk, W. Ruf, W. Siebert, *J. Organomet. Chem.* **1976**, *120*, 1.
[11] The Supporting Information contains the syntheses and spectroscopic data of **2Br**, **2Mes**, and **5Mes**, together with details of the theoretical calculations as well as of the DSC- and GPC measurements, the MALDI mass spectrometry, the electrochemical measurements, and the X-ray crystal structure analysis of **2Mes**. CCDC 284797 (**2Mes**) contains the supplementary crystallographic data for this paper. These data can be obtained free of charge from The Cambridge Crystallographic Data Centre via www.ccdc.cam.ac.uk/data_request/cif.
[12] M. Scheibitz, M. Bolte, J. W. Bats, H.-W. Lerner, I. Nowik, R. H. Herber, A. Krapp, M. Lein, M. C. Holthausen, M. Wagner, *Chem. Eur. J.* **2005**, *11*, 584.
[13] M. Scheibitz, J. W. Bats, M. Bolte, H.-W. Lerner, M. Wagner, *Organometallics* **2004**, *23*, 940.
[14] W. Ruf, T. Renk, W. Siebert, *Z. Naturforsch. B* **1976**, *31*, 1028.
[15] T. Tsuda, T. Yazawa, K. Watanabe, T. Fujii, T. Saegusa, *J. Org. Chem.* **1981**, *46*, 192.
[16] H. Eriksson, M. Håkansson, *Organometallics* **1997**, *16*, 4243.
[17] A. Sundararaman, F. Jäkle, *J. Organomet. Chem.* **2003**, *681*, 134.
[18] Steric protection has proven highly useful in the stabilization of other organoboron polymers.[7,24]
[19] T. J. Peckham, J. A. Massey, C. H. Honeyman, I. Manners, *Macromolecules* **1999**, *32*, 2830.
[20] R. Roesler, B. J. N. Har, W. E. Piers, *Organometallics* **2002**, *21*, 4300.
[21] M. D. Rausch, D. J. Ciappenelli, *J. Organomet. Chem.* **1967**, *10*, 127.
[22] It is important to note in this context that both the absolute $E^{\circ\prime}$ values and the splitting $\Delta(E^{\circ\prime})$ are strongly dependent on the supporting electrolyte anion employed (cf. ref. [25]). For example, cyclic voltammetry on **2Mes** in $CH_2Cl_2/[NBu_4][PF_6]$ gives $E^{\circ\prime}$ values of 3 and 266 mV with $\Delta(E^{\circ\prime}) = 263$ mV. For electrochemical studies on related polymers **I** ($ER_2 = SiMe_2$) see: R. Rulkens, A. J. Lough, I. Manners, *J. Am. Chem. Soc.* **1994**, *116*, 797 as well as ref. [23].
[23] R. Rulkens, A. J. Lough, I. Manners, S. R. Lovelace, C. Grant, W. E. Geiger, *J. Am. Chem. Soc.* **1996**, *118*, 12683.
[24] C. D. Entwistle, T. B. Marder, *Chem. Mater.* **2004**, *16*, 4574, and references therein.
[25] R. J. LeSuer, C. Buttolph, W. E. Geiger, *Anal. Chem.* **2004**, *76*, 6395.

 © 2006 Wiley-VCH Verlag GmbH & Co. KGaA, Weinheim

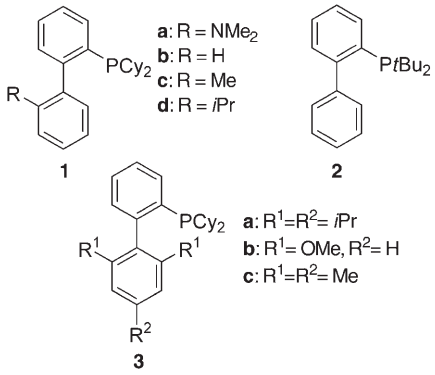
Palladium Catalysis

DOI: 10.1002/anie.200502927

Evidence for the Formation and Structure of Palladacycles during Pd-Catalyzed C–N Bond Formation with Catalysts Derived from Bulky Monophosphinobiaryl Ligands**

*Eric R. Strieter and Stephen L. Buchwald**

One of the most general catalyst systems, in terms of their efficacy in C–C, C–N, and C–O bond-forming reactions, are those based on the bulky, electron-rich monophosphinobiaryl ligands (Scheme 1).[1] First introduced in 1998, the Pd^0 catalyst



Scheme 1. Bulky, electron-rich monophosphinobiaryl ligands used in Pd-catalyzed C–C, C–N, and C–O bond-forming reactions. Cy = cyclohexyl.

based on **1a** demonstrated exceptionally high activity, thereby allowing room-temperature Suzuki–Miyaura couplings of aryl bromides and chlorides as well as room-temperature aminations of aryl bromides, including the first room-temperature amination of an aryl chloride.[2] While searching for catalysts that display higher turnover numbers (TONs) than those observed with **1a**, ligand **2** was discovered, thus further expanding the scope of these cross-coupling reactions.[3] More recently, with the introduction of **3a** and **3b** into this class of ligands, the most general and active catalyst systems to date for Suzuki–Miyaura couplings, C–N bond-forming reactions, and Sonogashira reactions with aryl chlorides and tosylates have been revealed.[4]

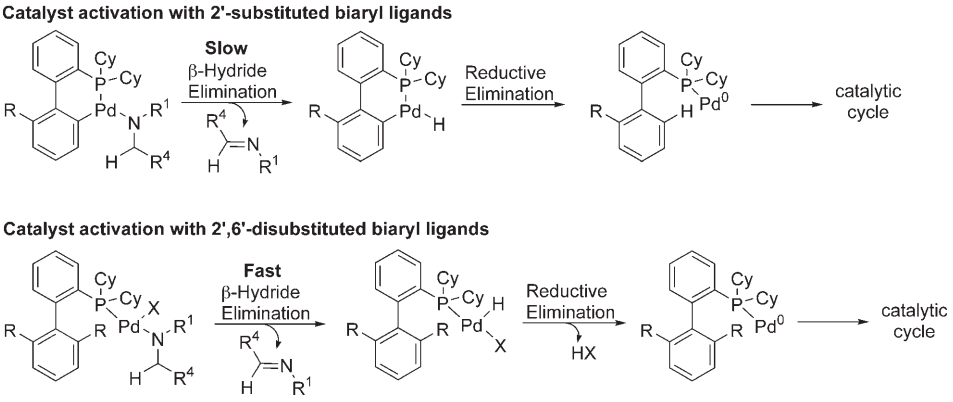
[*] Dr. E. R. Strieter, Prof. Dr. S. L. Buchwald
Department of Chemistry
Room 18-490, Massachusetts Institute of Technology
Cambridge, MA 02139 (USA)
Fax: (+1) 617-253-3297
E-mail: sbuchwal@mit.edu

[**] Support has been provided by the National Institutes of Health (GM 58160), the American Chemical Society (Organic Division Fellowship to E.R.S., sponsored by Albany Molecular Research) and Merck.

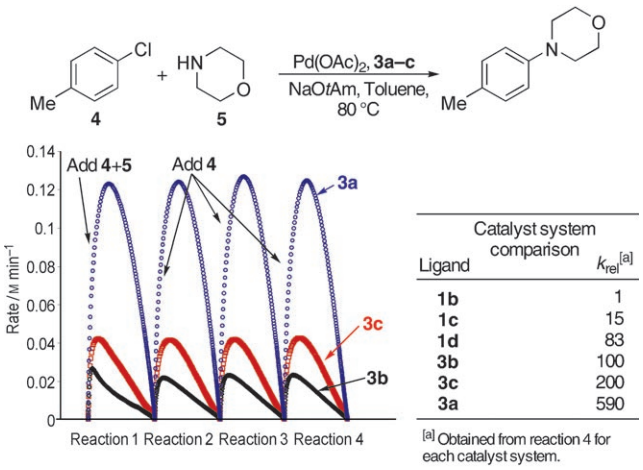
Supporting information for this article is available on the WWW under http://www.angewandte.org or from the author.

© 2006 Wiley-VCH Verlag GmbH & Co. KGaA, Weinheim

A recent mechanistic investigation of the Pd-catalyzed C–N bond formation has indicated that substituents at the *ortho* position of the bottom ring of the monophosphinobiaryl ligand play a critical role in the determination of both the activity and stability of the catalyst.[5] More specifically, the size of the substituent dictates catalyst activity, with larger substituents (namely, *i*Pr) leading to the most active catalysts.[6] Interestingly, catalysts derived from ligands with only one *ortho* substituent on the non-phosphorus-containing ring (that is, **1a–d**) exhibit remarkably different activities relative to those based on **3a**. Using the former catalyst systems, the reaction rate increases with TON, whereas in the latter case the reaction maintains a constant rate for each consecutive reaction. Although this difference in behavior was attributed to a slow activation process with catalysts based on **1a–d**, the structural origins of this discrepancy were not investigated. Our hypothesis is that Pd^{II} precatalysts have a tendency to form palladacycles when complexed with **1a–d**, which have previously been shown to result in a slow activation process (Figure 1).[7] In contrast, palladacycle formation would be prevented with ligands that lack *ortho* hydrogen atoms (2′,6′-disubstituted ligands) on the non-phosphorus-containing ring of the biaryl moiety (for example, **3a–c**), thus leading to the rapid formation of an active Pd^0 complex. The differences in the rate of activation may, in part, arise from the difference in the rate of β-hydride elimination (Scheme 2).[8] This process may be much faster in the case of catalysts derived from 2′,6′-disubstituted ligands than those based on 2′-substituted ligands, in which palladacycles may form. This reasoning is based on the observation that a small primary kinetic isotope effect is observed during the activation process with catalysts based on 2′-substituted ligands.[5]



Scheme 2. Catalyst activation with 2′-substituted and 2′,6′-disubstituted biaryl ligands.



Catalyst system comparison

Ligand	k_{rel}[a]
1b	1
1c	15
1d	83
3b	100
3c	200
3a	590

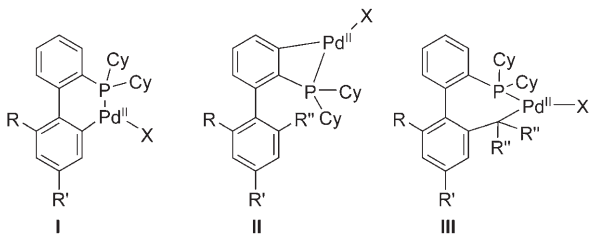
[a] Obtained from reaction 4 for each catalyst system.

Figure 1. Sequential reaction experiment for the amination of *p*-chlorotoluene (**4**) ($4\times[\mathbf{4}]_o = 0.15$ M) with morpholine (**5**) ($[\mathbf{5}]_o = 0.74$–0.78 M). Conditions: $[NaOtAm]_o = 0.8$ M; blue data points: $[Pd(OAc)_2] = 4.2$ mM, $[\mathbf{3a}] = 12.7$ mM; red data points: $[Pd(OAc)_2] = 8.3$ mM, $[\mathbf{3c}] = 25$ mM; black data points: $[Pd(OAc)_2] = 8.3$ mM, $[\mathbf{3b}] = 25$ mM. Note: the L/Pd ratio is 3:1 for all of these reactions. *t*Am = *tert*-amyl.

The differences in reaction rates for catalytic systems generated from biaryl ligands **3a–c**, all of which are 2′,6′-disubstituted ligands, were determined by monitoring sequential reactions by reaction calorimetry to examine whether it is the size, substitution pattern, or both that controls the rate of catalyst activation. The coupling of *p*-chlorotoluene (**4**) with morpholine (**5**) in toluene at 80 °C was used as a model system.[5] The reactions were carried out with four consecutive injections of the reactants into a solution containing $Pd(OAc)_2$, biaryl ligand, and NaO*t*Am equilibrated at 80 °C for 1 h. The first injection contained a mixture of **5** (0.78 M) and **4** (0.15 M), whereas the subsequent injections contained an aliquot of **4** (0.15 M). The activity of catalysts based on **3a–c** is compared in Figure 1, in which the reaction rate is plotted as a function of reaction progress for a four-reaction sequence. The reaction rates follow a similar trend seen before, in which the larger the substituent on the bottom ring the more active the catalyst. Furthermore, each of these catalyst systems are more active than those based on **1a–d**, as evidenced by the k_{rel} values obtained for each catalyst system (also shown in Figure 1). Most importantly, however, the reaction maintains a constant rate for each consecutive reaction, consistent with a rapid catalyst-activation process. This behavior is in direct contrast to that observed for the catalysts derived from **1a–d**, in which the reaction rate increases with each consecutive reaction. Thus, not only does the size of the substituent on the bottom ring of the biaryl unit dictate the activity of the catalyst, but the substitution pattern also controls the rate at which the catalyst is activated.

As the two classes of ligands afford two distinct patterns in their reaction-rate profiles, we sought to test whether the origin of this divergence arises from the formation of palladacycle intermediates.[7] The possible palladacycles that may form with these ligands are shown in Scheme 3. In the first case, a six-membered palladacycle **I** is formed through an attack on the coordinated Pd^{II} center by the bottom ring of the biaryl ligand. Significantly, a similar palladacycle has been successfully employed as a single-component catalyst for Pd-

 © 2006 Wiley-VCH Verlag GmbH & Co. KGaA, Weinheim

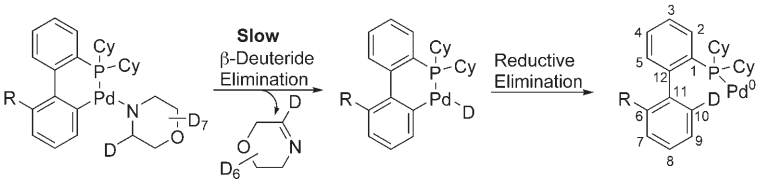


Scheme 3. Structures of potential palladacycles.

catalyzed amination processes.[9] In the second case, the top ring of the biaryl ligand attacks the Pd^{II} center in a similar fashion to that described for **I**, thus generating a four-membered ring palladacycle **II**.[10] Furthermore, on the basis of several studies that demonstrate the potential of Pd^{II}-mediated cleavage of sp^3 C–H bonds, **III** is also a potential intermediate.[11] Taking into consideration the substitution pattern of the two ligand classes, it would appear that the 2′,6′-disubstituted ligands are incapable of forming the first type of palladacycle, whereas all three types of complexes are possible with the 2′-substituted ligands.

To probe the existence and nature of the palladacycle intermediate, [D$_8$]morpholine ([D$_8$]**5**) was employed as the substrate and the extent of deuterium incorporation into the bottom ring of the monophosphinobiaryl was determined. If palladacycle formation occurs and the mechanism is consistent with an amine-induced pathway, then deuterium incorporation into the ligand should be observed with the 2′-substituted ligands (Scheme 4; a similar mechanism can be proposed for the four-membered ring palladacycles). With the use of 2′,6′-disubstituted ligands, however, deuterium incorporation should not occur as palladacycles are absent in this case. Importantly, Louie and Hartwig postulated a similar mechanism for the formation of Pd^0 from palladacycles derived from P(*o*-tolyl)$_3$; however, the relevance of these palladacycles to the catalytic process was not established.[12] The N-arylation of [D$_8$]morpholine was performed under the standard conditions. However, 1,2-bis(diphenylphosphino)ethane (dppe) was added at the end of the reaction to sequester the Pd and facilitate the separation of the monophosphinobiaryl ligand to investigate the isotopic incorporation.

^{2}H NMR, ^{13}C NMR, and ^{1}H NMR spectroscopic analysis was used upon isolation to analyze the free ligand. As indicated by ^{2}H NMR spectroscopy, **3a–c**, all of which are 2′,6′-disubstituted ligands, did not contain deuterium.[13] This observation was subsequently validated by mass-spectrometric analysis. In contrast, the ^{2}H NMR spectroscopic and mass-spectrometric analysis for both **1c** (6% ^{2}H-labeled)[14] and **1d** (15% ^{2}H-labeled)[14] displayed the presence of deuterium, thus confirming our original hypothesis that palladacycles do form with these precatalysts. Furthermore, the presence of a single resonance in the ^{2}H NMR spectrum indicates that a single carbon atom had been isotopically labeled. The chemical shift of this atom ($\delta =$ 7.07 ppm) rules out the possible formation of palladacycle **III**.



Scheme 4. Mechanism for deuterium incorporation into the monophosphinobiaryl ligands.

Two additional pieces of information allowed us to deduce which carbon atom was isotopically labeled. The first was the observation that the doublet ($J_{C\text{-}P} = 6.3$ Hz) at $\delta = 144$ ppm and the singlet at $\delta = 125$ ppm in the ^{13}C{^{1}H} NMR spectrum of the labeled material split into two sets of new peaks approximately 0.1 ppm upfield from the unlabeled resonances (Figure 2, labeled C11 w/C10-H/D and C9 w/C10-H/D). The appearance of these peaks is common with ^{13}C NMR isotope effects for the carbon atom two bonds away from the deuterium label.[17] The second piece of evidence was

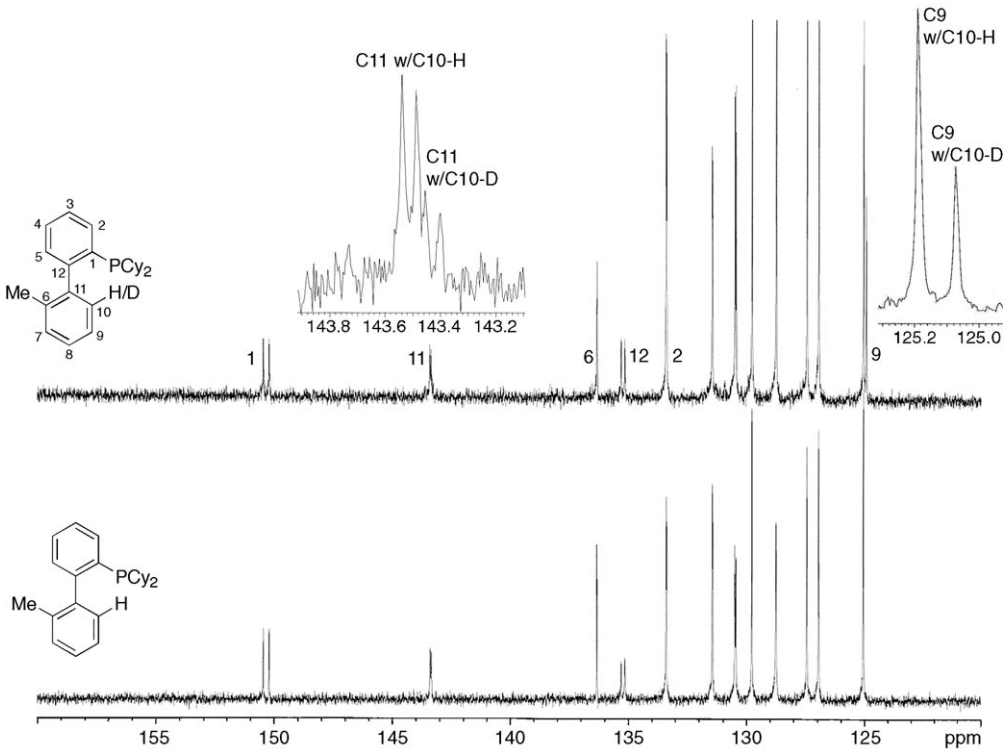


Figure 2. ^{13}C NMR spectroscopic data for ^{2}H-labeled **1c** (top) and unlabeled **1c** (bottom).

© 2006 Wiley-VCH Verlag GmbH & Co. KGaA, Weinheim

provided by 2D NMR experiments, in which the combination of HMQC and TOCSY experiments established that the carbon atoms experiencing an isotope effect reside on the same ring as the proton that decreases in intensity upon ^{2}H labeling ($\delta = 7.05$ ppm in the ^{1}H NMR spectrum). Similar results were obtained with **1d** (see the Supporting Information). Taken together, these data demonstrate that palladacycle formation occurs with the biaryl ligands containing *ortho* hydrogen atoms on the non-phosphorus-containing ring, whereas with the ligands lacking *ortho* hydrogen atoms it does not. Furthermore, the data support the formation of a palladacycle of type **I**.

In summary, we have provided evidence that palladacycles can form during the course of a Pd-catalyzed C–N bond-forming reaction through the use of isotope-labeling studies. This study provides insight into the structural origins of the differences in the catalytic activities observed between the catalysts containing 2′-substituted and 2′,6′-disubstituted biaryl ligands. Specifically, through the use of 2′,6′-disubstituted biaryl ligands palladacycle formation is avoided and optimal catalyst activity is achieved.

Received: August 17, 2005
Revised: October 18, 2005
Published online: December 28, 2005

Keywords: aminations · cross-coupling · palladium · phosphanes

[1] a) A. de Meijere, *Metal-Catalyzed Cross-Coupling Reactions*, 2nd ed., Wiley-VCH, Weinheim, **2004**; b) J. Tsuji, *Palladium Reagents and Catalysts, New Perspectives For the 21st Century*, Wiley, West Sussex, **2004**; for other reviews on C–N and C–O bond-forming reactions, see: c) A. R. Muci, S. L. Buchwald, *Top. Curr. Chem.* **2002**, *219*, 131; d) J. F. Hartwig in *Handbook of Organopalladium Chemistry for Organic Synthesis* (Ed.: E. Negishi), Wiley-Interscience, New York, **2002**, p. 1051; e) A. F. Littke, G. C. Fu, *Angew. Chem.* **2002**, *114*, 4350; *Angew. Chem. Int. Ed.* **2002**, *41*, 4176; f) "Palladium-Catalyzed Aromatic Carbon–Nitrogen Bond Formation": L. Jiang, S. L. Buchwald in *Metal-Catalyzed Cross-Coupling Reactions*, 2nd ed. (Eds.: A. de Meijere, F. Diederich), Wiley-VCH, Weinheim, **2004**, p. 699; g) B. Schlummer, U. Scholz, *Adv. Synth. Catal.* **2004**, *346*, 1599; h) V. Farina, *Adv. Synth. Catal.* **2004**, *346*, 1553; i) U. Christmann, R. Vilar, *Angew. Chem.* **2005**, *117*, 370; *Angew. Chem. Int. Ed.* **2005**, *44*, 366.

[2] D. W. Old, J. P. Wolfe, S. L. Buchwald, *J. Am. Chem. Soc.* **1998**, *120*, 9722; for other important contributions regarding the initial use of bulky electron-rich ligands in Pd-catalyzed cross-coupling reactions, see reference [1e].

[3] a) J. P. Wolfe, S. L. Buchwald, *Angew. Chem.* **1999**, *111*, 2570; *Angew. Chem. Int. Ed.* **1999**, *38*, 2413; b) J. P. Wolfe, R. A. Singer, B. H. Yang, S. L. Buchwald, *J. Am. Chem. Soc.* **1999**, *121*, 9550; c) J. P. Wolfe, H. Tomori, J. P. Sadighi, J. Yin, S. L. Buchwald, *J. Org. Chem.* **2000**, *65*, 1158.

[4] a) X. Huang, K. W. Anderson, D. Zim, L. Jiang, A. Klapars, S. L. Buchwald, *J. Am. Chem. Soc.* **2003**, *125*, 6653; b) H. N. Nguyen, X. Huang, S. L. Buchwald, *J. Am. Chem. Soc.* **2003**, *125*, 11818; c) D. Gelman, S. L. Buchwald, *Angew. Chem.* **2003**, *115*, 6175; *Angew. Chem. Int. Ed.* **2003**, *42*, 5993; d) S. D. Walker, T. E. Barder, J. R. Martinelli, S. L. Buchwald, *Angew. Chem.* **2004**, *116*, 1907; *Angew. Chem. Int. Ed.* **2004**, *43*, 1871; e) T. E. Barder, S. D. Walker, J. R. Martinelli, S. L. Buchwald, *J. Am. Chem. Soc.* **2005**, *127*, 4685.

[5] E. R. Strieter, D. G. Blackmond, S. L. Buchwald, *J. Am. Chem. Soc.* **2003**, *125*, 13978.

[6] For other studies reporting on the impact of ligand structure on the reactivity of Pd complexes in cross-coupling reactions, see: a) E. Galardon, S. Ramdeehul, J. M. Brown, A. Cowley, K. K. Hii, A. Jutand, *Angew. Chem.* **2002**, *114*, 1838; *Angew. Chem. Int. Ed.* **2002**, *41*, 1760; b) I. D. Hills, M. R. Netherton, G. C. Fu, *Angew. Chem.* **2003**, *115*, 5927; *Angew. Chem. Int. Ed.* **2003**, *42*, 5749; c) I. D. Hills, G. C. Fu, *J. Am. Chem. Soc.* **2004**, *126*, 13178.

[7] For a comprehensive review on palladacycles, see: a) J. Dupont, C. S. Consorti, J. Spencer, *Chem. Rev.* **2005**, *105*, 2527; for mechanistic studies concerning palladacycle precatalysts, see: b) M. Beller, T. H. Riermeier, *Eur. J. Inorg. Chem.* **1998**, 29; c) M. Nowotny, U. Hanefield, H. van Koningsveld, T. Maschmeyer, *Chem. Commun.* **2000**, 1877; d) T. Rosner, A. Pfaltz, D. G. Blackmond, *J. Am. Chem. Soc.* **2001**, *123*, 1848; e) T. Rosner, A. Pfaltz, D. G. Blackmond, *J. Am. Chem. Soc.* **2001**, *123*, 4621.

[8] In addition to β-hydride elimination, the slow rate of catalyst activation observed with catalysts based on the 2′-substituted ligands **1a–d** may be because of the slow formation of a Pd^{II} amido complex.

[9] a) D. Zim, S. L. Buchwald, *Org. Lett.* **2003**, *5*, 2413; b) R. B. Bedford, C. S. J. Cazin, S. J. Coles, T. Gelbrich, P. N. Horton, M. B. Hursthouse, M. E. Light, *Organometallics* **2003**, *22*, 987.

[10] X-ray crystallographic analysis of two complexes between both **1a** and $PdCl_2$ and **2** and $PdCl_2$ indicates that a four-membered-ring palladacycle forms, see: X.-X. Zhang, S. L. Buchwald, unpublished results.

[11] a) G. Dyker, *Angew. Chem.* **1999**, *111*, 1808; *Angew. Chem. Int. Ed.* **1999**, *38*, 1698; b) A. E. Shilov, G. B. Shul'pin, *Activation and Catalytic Reactions of Saturated Hydrocarbons in the Presence of Metal Complexes*, Kluwer, Dordrecht, **2000**.

[12] J. Louie, J. F. Hartwig, *Angew. Chem.* **1996**, *108*, 2531; *Angew. Chem. Int. Ed. Engl.* **1996**, *35*, 2359.

[13] The sensitivity of ^{2}H NMR spectroscopy is approximately 1%: N. N. Greenwood, A. Earnshaw, *Chemistry of the Elements*, 2nd ed., Elsevier, Oxford, **1997**.

[14] Determined by analysis of the molecular-ion peaks, which were corrected for the natural abundance of $[M+1]$ and $[M+2]$.

[15] a) G. C. Levy, R. L. Lichter, G. L. Nelson, *Carbon-13 Nuclear Magnetic Resonance Spectroscopy*, 2nd ed., Wiley-Interscience, New York, **1980**; b) S.-K. Chung, K. Sasamoto, *J. Org. Chem.* **1981**, *46*, 4590; c) R. Aydin, H. Günther, *J. Am. Chem. Soc.* **1981**, *103*, 1301.

[16] Although the resonance corresponding to C10 should also split into an observable 1:1:1 triplet, the intensity and $T1$ value may prevent its resolution.

[17] If C2 is ^{2}H labeled, which would result if palladacycle **II** formed, then the doublets at $\delta = 150.5$ (J(C-P) = 31.2 Hz) and 130.6 ppm (J(C-P) = 5.8 Hz) would also be split into two new sets of doublets approximately 0.1 ppm upfield from the unlabeled material; however, this splitting was not observed.

 © 2006 Wiley-VCH Verlag GmbH & Co. KGaA, Weinheim

Cinchona Alkaloids

DOI: 10.1002/anie.200503724

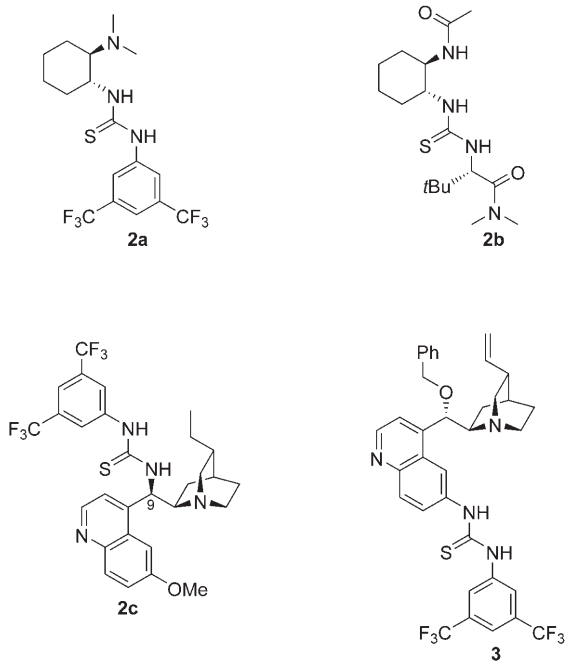
Asymmetric Organocatalytic Henry Reaction**

*Tommaso Marcelli, Richard N. S. van der Haas, Jan H. van Maarseveen, and Henk Hiemstra**

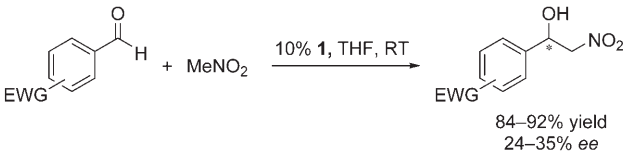
Dedicated to Professor Goffredo Rosini on the occasion of his 65th birthday

The reaction between a carbonyl compound and a nitroalkane, known as the Henry (or nitroaldol) reaction, is a powerful synthetic tool for the construction of complex molecules.[1] In recent years, several efficient catalytic enantioselective methods to perform this reaction have been described.[2] Typically, an aldehyde[3–7] (or an activated ketone)[8,9] is treated with a nitroalkane (mainly nitromethane or nitroethane) in the presence of a chiral metal complex and other additives, such as tertiary amines or molecular sieves, to obtain nitroalcohols with good to excellent optical purities. In the last decade, asymmetric organocatalysis has proven to be a robust and valid alternative to traditional metal-based catalysis for a number of reactions.[10] High enantiomeric excesses have been achieved in the reaction between nitroalkanes and imines (aza-Henry reaction) using chiral, enantiopure organic catalysts. Remarkable results were obtained in particular by Takemoto and co-workers[11] and Yoon and Jacobsen,[12] who employed thioureas **2a** and **2b**, respectively. To date, the use of metal-free catalysts in the parent nitroaldol reaction has never resulted in enantioselectivities exceeding 54% *ee*.[13]

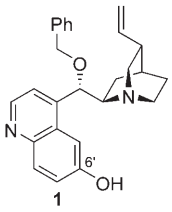
We recently reported the use of *Cinchona* derivatives as asymmetric catalysts for the reaction between activated aromatic aldehydes and nitromethane (Scheme 1).[14] The scope and enantioselectivities were modest, but we proved that a hydrogen-bond donor at the C6′ position of an appropriate *Cinchona* derivative is required to induce preferential formation of one enantiomer. Because the phenol moiety and the basic quinuclidine nitrogen atom can be in reasonable proximity in solution, the enantioselectivity could arise from a double activation of both the nucleophile and electrophile.[15] We envisaged that replacement of the phenol moiety with a better hydrogen-bond donor could result in a more powerful and more enantioselective catalyst.[16] Triggered by a recent report by Soos and co-workers on the introduction of an activated thiourea at the C9 position of the *Cinchona* scaffold **2c**,[17] we decided to functionalize **1** with the same moiety (Scheme 2). Catalyst **3**, a bench-stable crystalline solid, was synthesized on a multigram scale by a reliable and high-yielding sequence (see Supporting Information).



Scheme 2. Thiourea catalysts. **2a**: Takemoto and co-workers[11]; **2b**: Yoon and Jacobsen[12]; **2c**: Soos and co-workers.[17]



Scheme 1. Reaction between activated aromatic aldehydes and nitromethane. EWG = electron-withdrawing group.



Our initial experiments were performed using benzaldehyde (**4a**) as a model substrate with 10 equivalents of nitromethane and 20% of **3** (Table 1). We were delighted to observe that reaction of **4a** in dimethylformamide (DMF) at room temperature afforded the corresponding nitroalcohol **5a** after 6 h in 67% *ee* (Table 1, entry 4). The use of solvents other than DMF or THF mostly led to products with surprisingly low optical purity. Reaction in methanol afforded **5a** in a noteworthy 49% *ee*, whereas reaction in nitromethane, dichloromethane, and toluene essentially gave the racemic product. These results were somewhat puzzling because methanol is generally considered a poor solvent in

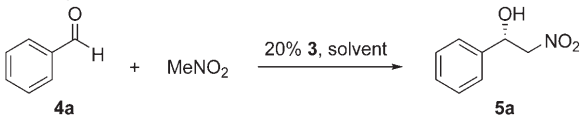
[*] T. Marcelli, R. N. S. van der Haas, Dr. J. H. van Maarseveen, Prof. Dr. H. Hiemstra
Van't Hoff Institute of Molecular Sciences
University of Amsterdam, Nieuwe Achtergracht 129
1018 WS Amsterdam (Netherlands)
Fax: (+31) 20-525-5670
E-mail: hiemstra@science.uva.nl

[**] This research was financially supported by the National Research School Combination Catalysis (NRSC-C).

Supporting information for this article is available on the WWW under http://www.angewandte.org or from the author.

 © 2006 Wiley-VCH Verlag GmbH & Co. KGaA, Weinheim

Table 1: Optimization of the reaction conditions.[a]

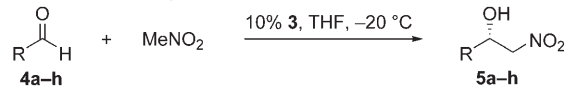


4a **5a**

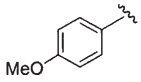
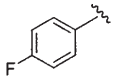
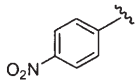
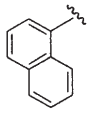
Entry	Solvent	T [°C]	t [h]	Conversion [%][b]	*ee* [%][c]
1	THF	25	6	90	62
2	CH_2Cl_2	25	6	97	6
3	MeCN	25	6	99	42
4	DMF	25	6	96	67
5	$MeNO_2$[d]	25	6	92	7
6	MeOH	25	6	91	49
7	Et_2O	25	6	99	30
8	toluene	25	6	83	5
9	DMF	−20	48	90	82
10	THF	−20	48	99	89

[a] Reactions were carried out with **4a** (0.1 mmol), $MeNO_2$ (1.0 mmol), and **3** (0.02 mmol) in 100 μL of solvent. [b] Determined by ^{1}H NMR spectroscopic analysis. [c] Determined by HPLC analysis using a Chiralcel OD-H column. [d] $MeNO_2$ (100 μL) was used as the solvent/reactant.

Table 2: Substrate scope.[a]

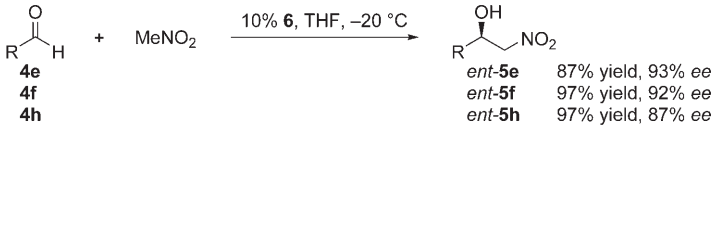


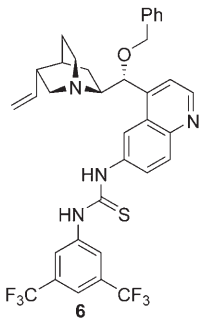
4a–h **5a–h**

Entry	Substrate	R	t [h]	Yield [%][b]	*ee* [%][c]
1	**4a**		48	90	92
2	**4b**		96	97	91
3	**4c**		168	94	89
4	**4d**		24	99	85
5	**4e**		4	91	86
6	**4f**		48	99	92
7	**4g**		24	91	86
8	**4h**		24	95	91

[a] Reactions were carried out with **4** (1.0 mmol), $MeNO_2$ (10.0 mmol), and **3** (0.1 mmol) in 1.0 mL of solvent at −20°C. [b] Yield of isolated product. [c] Determined by HPLC analysis using a Chiralcel OD-H column. Boc = *tert*-butoxycarbonyl.

hydrogen-bond-controlled organocatalysis. On the other hand, Wittkopp and Schreiner demonstrated that a similar thiourea can retain its catalytic activity in protic solvents.[18] Lowering the temperature provided synthetically useful levels of asymmetric induction at a still reasonable reaction rate (Table 1, entry 10). Further optimization revealed that these reactions could be carried out on a 1-mmol scale with only 10% catalyst: under these conditions **5a** was obtained after 48 h in 90% yield of isolated product and with 92% *ee*. Unfortunately, these conditions did not prove suitable for the reaction of aliphatic aldehydes: cyclohexanecarboxaldehyde and isobutyraldehyde were not completely converted into the corresponding nitroalcohols after 1 week and the enantiomeric excess of the products was disappointingly low (<20% *ee*). Nevertheless, a variety of aromatic aldehydes could be transformed into nitroalcohols **5b–h** in consistently high yields and enantiomeric excess (Table 2). Unactivated aromatic aldehydes required long reaction times but the reactions were clean, and we did not observe dehydration to the corresponding nitroalkenes (Table 2, entries 2 and 3). Not surprisingly, activated aldehydes typically furnished the nitroaldol product in one day or less (Table 2, entries 4 and 5). The protocol proved to be also compatible with heterocyclic aldehydes (Table 2, entries 7 and 8). Quinine-derived catalyst **6** (the pseudo enantiomer of **3**) gave access to nitroalcohols with the opposite configuration and comparable enantiomeric excess, as shown by three examples in Scheme 3.

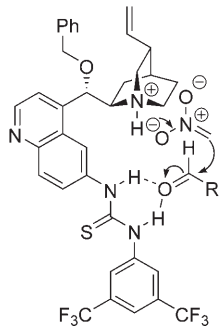




Scheme 3. The use of quinine-derived catalyst **6** (the pseudo-enantiomer of **3**) to prepare nitroalcohols with the opposite configuration.

Although the reasons for the observed enantioselectivity are still not clear, we believe that the aldehyde is activated by the thiourea moiety through double hydrogen bonding,[16] while the nitromethane is activated by the basic quinuclidine nitrogen atom (Scheme 4). Besides providing control over the stereochemical outcome of the reaction, this behavior may also serve to increase the reactivity (catalyst **3** yields faster conversion than **1** under the same conditions). We also believe that the observed solvent dependency of the enantioselectivity may be because of the high conformational freedom of

 © 2006 Wiley-VCH Verlag GmbH & Co. KGaA, Weinheim



Scheme 4. Proposed mode of action of catalyst **3**.

3,[19] because our results cannot be rationalized on the basis of the polarity of the reaction medium.

In conclusion, we have developed a new organocatalyst capable of promoting the direct enantioselective nitroaldol reaction of aromatic and heteroaromatic aldehydes with nitromethane in high yields and enantiomeric excess. To the best of our knowledge, this is the first example of a highly enantioselective organocatalytic Henry reaction of aromatic aldehydes.[20] Although not general, we believe that our protocol constitutes an important step forward in this field. A study aimed at the understanding of the mechanism and the reasons for the observed enantioselectivity is currently underway. We envision that this will allow us to design new catalysts and widen the scope of this transformation.

Received: October 20, 2005

Keywords: alkaloids · asymmetric catalysis · Henry reaction · hydrogen bonds · organocatalysis

[1] For recent reviews, see: a) G. Rosini in *Comprehensive Organic Synthesis, Vol. 2* (Eds.: B. M. Trost, I. Fleming, C. H. Heatcock), Pergamon, New York, **1991**, pp. 321 – 240; b) F. A. Luzio, *Tetrahedron* **2001**, *57*, 915 – 945.

[2] For an excellent short review, see: C. Palomo, M. Oiarbide, A. Mielgo, *Angew. Chem.* **2004**, *116*, 5558 – 5560; *Angew. Chem. Int. Ed.* **2004**, *43*, 5442 – 5444.

[3] a) H. Sasai, T. Suzuki, S. Arai, M. Shibasaki, *J. Am. Chem. Soc.* **1992**, *114*, 4418 – 4420; b) M. Shibasaki, N. Yoshikawa, *Chem. Rev.* **2002**, *102*, 2187 – 2209.

[4] a) B. M. Trost, V. S. C. Yeh, *Angew. Chem.* **2002**, *114*, 889 – 891; *Angew. Chem. Int. Ed.* **2002**, *41*, 861 – 863; b) B. M. Trost, V. S. C. Yeh, H. Ito, N. Bremeyer, *Org. Lett.* **2002**, *4*, 2621 – 2623.

[5] D. A. Evans, D. Seidel, M. Rueping, H. W. Lam, J. T. Shawn, C. V. Downey, *J. Am. Chem. Soc.* **2003**, *125*, 12692 – 12693.

[6] a) Y. Kogami, T. Nakajima, T. Ashizawa, S. Kezuka, T. Ikeno, T. Yamada, *Chem. Lett.* **2004**, 33, 614 – 615; b) Y. Kogami, T. Nakajima, T. Ikeno, T. Yamada, *Synthesis* **2004**, 1947 – 1950.

[7] C. Palomo, M. Oiarbide, A. Laso, *Angew. Chem.* **2005**, *117*, 3949 – 3952; *Angew. Chem. Int. Ed.* **2005**, *44*, 3881 – 3884.

[8] a) C. Christensen, K. Juhl, K. A. Jørgensen, *Chem. Commun.* **2001**, 2222 – 2223; b) C. Christensen, K. Juhl, R. G. Hazell, K. A. Jørgensen, *J. Org. Chem.* **2002**, *67*, 4875 – 4881.

[9] a) S.-F. Lu, D.-M. Du, S.-W. Zhang, J. Xu, *Tetrahedron: Asymmetry* **2004**, *15*, 3433 – 3441; b) D.-M. Du, S.-F. Lu, T. Fang, J. Xu, *J. Org. Chem.* **2005**, *70*, 3712 – 3715.

[10] For comprehensive reviews about asymmetric organocatalysis, see: P. I. Dalko, L. Moisan, *Angew. Chem.* **2001**, *113*, 3840 – 3864; *Angew. Chem. Int. Ed.* **2001**, *40*, 3726 – 3748; and P. I. Dalko, L. Moisan, *Angew. Chem.* **2004**, *116*, 5248 – 5286; *Angew. Chem. Int. Ed.* **2004**, *43*, 5138 – 5175.

[11] a) T. Okino, S. Nakamura, T. Furukawa, Y. Takemoto, *Org. Lett.* **2004**, *6*, 625 – 627; b) X. Xu, T. Furukawa, T. Okino, H. Miyabe, Y. Takemoto, *Chem. Eur. J.* **2005**, in press.

[12] T. P. Yoon, E. N. Jacobsen, *Angew. Chem.* **2005**, *117*, 470 – 472; *Angew. Chem. Int. Ed.* **2005**, *44*, 466 – 468.

[13] a) Y. Misumi, R. A. Bulman, K. Matsumoto, *Heterocycles* **2002**, *56*, 599 – 605; b) R. Chinchilla, C. Najera, P. Sanchez-Agullo, *Tetrahedron: Asymmetry* **1994**, *5*, 1393 – 1402; c) M. T. Allingham, A. Howard-Jones, P. J. Murphy, D. A. Thomas, P. W. R. Caulkett, *Tetrahedron Lett.* **2003**, *44*, 8677 – 8680.

[14] T. Marcelli, R. N. S. van der Haas, J. H. van Maarseveen, H. Hiemstra, *Synlett* **2005**, 2817 – 2819.

[15] Selected applications of this concept to asymmetric organocatalysis: a) Y. Iwabuchi, M. Nakatani, N. Yokoyama, S. Hatakeyama, *J. Am. Chem. Soc.* **1999**, *121*, 10219 – 10220; b) M. Shi, Y.-M. Xu, *Angew. Chem.* **2002**, *114*, 4689 – 4692; *Angew. Chem. Int. Ed.* **2002**, *41*, 4507 – 4510; c) S. Saaby, M. Bella, K. A. Jørgensen, *J. Am. Chem. Soc.* **2004**, *126*, 8120 – 8121; d) X. Liu, H. Li, L. Deng, *Org. Lett.* **2005**, *7*, 167 – 169; e) H. Li, J. Song, X. Liu, L. Deng, *J. Am. Chem. Soc.* **2005**, *127*, 13774 – 13775.

[16] For reviews discussing hydrogen bonding in organocatalysis, see: a) P. R. Schreiner, *Chem. Soc. Rev.* **2003**, *32*, 289 – 296; b) P. M. Pihko, *Angew. Chem.* **2004**, *116*, 2110 – 2113; *Angew. Chem. Int. Ed.* **2004**, *43*, 2062 – 2064.

[17] a) B. Vakulya, S. Varga, A. Csampai, T. Soos, *Org. Lett.* **2005**, *7*, 1967 – 1969; during the preparation of this communication, others reported enantioselective organocatalytic reactions using an analogous catalyst: b) S. H. McCooey, S. J. Connon, *Angew. Chem.* **2005**, *117*, 6525 – 6528; *Angew. Chem. Int. Ed.* **2005**, *44*, 6367 – 6370; c) J. Ye, D. J. Dixon, P. S. Hines, *Chem. Commun.* **2005**, 4481 – 4483.

[18] A. Wittkopp, P. R. Schreiner, *Chem. Eur. J.* **2003**, *9*, 407 – 414.

[19] In solution, *Cinchona* alkaloids exist as a mixture of conformers mainly arising from rotation along the C8–C9 and C4′–C9 bonds: G. D. H. Dijkstra, R. M. Kellogg, H. Wynberg, J. S. Svendsen, I. Marko, K. B. Sharpless, *J. Am. Chem. Soc.* **1989**, *111*, 8069 – 8076; moreover, the flexible thiourea moiety adds further conformational complexity to the molecule.

[20] After submission of this manuscript, Nagasawa and co-workers reported the use of a guanidine thiourea catalyst for the asymmetric Henry reaction of aliphatic aldehydes: Y. Sohtome, Y. Hashimoto, K. Nagasawa, *Adv. Synth. Catal.* **2005**, *347*, 1643 – 1648.

 © 2006 Wiley-VCH Verlag GmbH & Co. KGaA, Weinheim

Cycloaddition Reactions

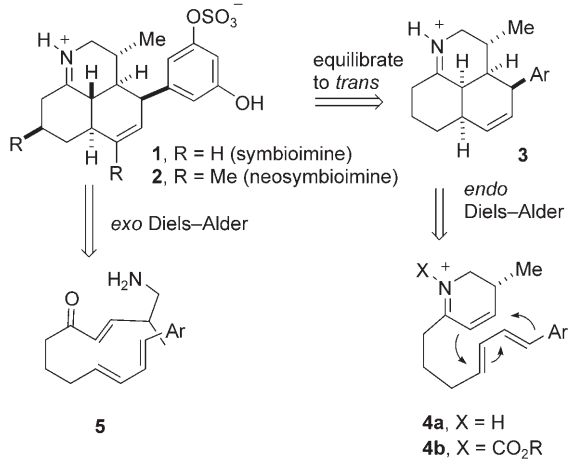
DOI: 10.1002/anie.200503467

Synthesis of (±)-Deoxysymbioimine Using an Intramolecular Diels–Alder Reaction with an *N*-Alkoxycarbonyl 2,3-Dihydropyridinium Cation as the Dienophile**

Barry B. Snider and Qinglin Che*

Uemura et al. recently reported the isolation of the novel tricyclic iminium sulfate symbioimine (**1**) from a cultured symbiotic marine dinoflagellate *Symbiodinium* sp.[1a,b] Symbioimine (**1**) inhibits the differentiation of RAW264 cells into osteoclasts ($EC_{50} = 44\ \mu M$) and significantly inhibits cyclooxygenase-2 activity at 10 μM, thus indicating that **1** is a potential antiresorptive and anti-inflammatory drug.[1c] More recently, Uemura et al. isolated the dimethyl homologue neosymbioimine (**2**) from the same source.[1c]

Uemura et al. originally suggested that the biogenesis of **1** might involve an intramolecular Diels–Alder (IMDA) reaction of enone **5** through an *exo* transition state followed by cyclization to generate the imine (see Scheme 1).[1a,b] While our investigation was in progress, he suggested that the IMDA reaction of dihydropyridinium cation **4a** through an *endo* transition state would give **3** with a *cis* ring fusion, which could readily epimerize to give **1** with a *trans* ring fusion.[1c]



Scheme 1. Retrosynthetic intramolecular Diels–Alder routes to symbioimine (**1**).

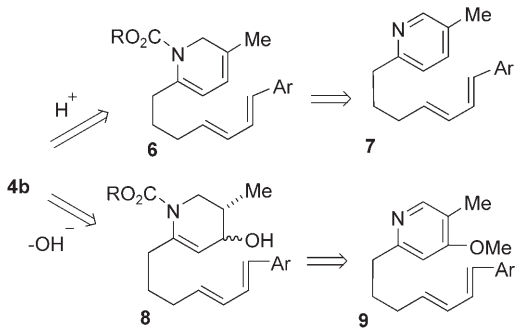
[*] Prof. Dr. B. B. Snider, Q. Che
Department of Chemistry
MS 015, Brandeis University
Waltham, MA 02454-9110 (USA)
Fax: (+1) 781-736-2516
E-mail: snider@brandeis.edu

[**] We thank the National Institute of Health (GM-50151) for financial support and Olga V. Barykina for experimental support.

Supporting information for this article is available on the WWW under http://www.angewandte.org or from the author.

We considered both of these routes for the synthesis of **1**. IMDA reactions of *trans*-enones analogous to **5** give mainly the *endo* adduct,[2] rather than the *exo* adduct needed for the preparation of **1**. Furthermore, it did not appear likely that the methyl substituent of **5** would control the facial selectivity of the IMDA reaction, so mixtures of isomers would be obtained. *cis*-Enones analogous to **4** are known to give *endo* adducts analogous to **3**.[3] Furthermore, the methyl group of **4** will block the bottom face of the dihydropyridinium cation so that the IMDA reaction should occur selectively on the desired top face. Sammakia and co-workers very recently developed a related IMDA reaction of a cyclic oxocarbenium ion for the synthesis of (−)-dihydrocompactin.[4]

Dihydropyridinium cation **4a** is a plausible intermediate in the biosynthesis of **1**, but is not an attractive synthetic intermediate. Although dihydropyridinium cations have seen limited use as dienophiles,[5] they disproportionate readily to give pyridines and tetrahydropyridines.[6] *N*-Alkoxycarbonyl dihydropyridinium cation **4b** will not disproportionate and is more electron deficient, and therefore a more reactive dienophile. Cation **4b** might be available by protonation of dihydropyridine **6**, which can be prepared from pyridine **7** by a Fowler reduction with a chloroformate ester and $NaBH_4$ or $NaBH_3CN$ (see Scheme 2).[7] Alternatively, cation **4b** might be accessible by loss of the hydroxide moiety from tetrahydropyridinol **8**, which can be prepared by Fowler reduction of pyridine **9**, hydrolysis of the enol ether, and reduction of the ketone.

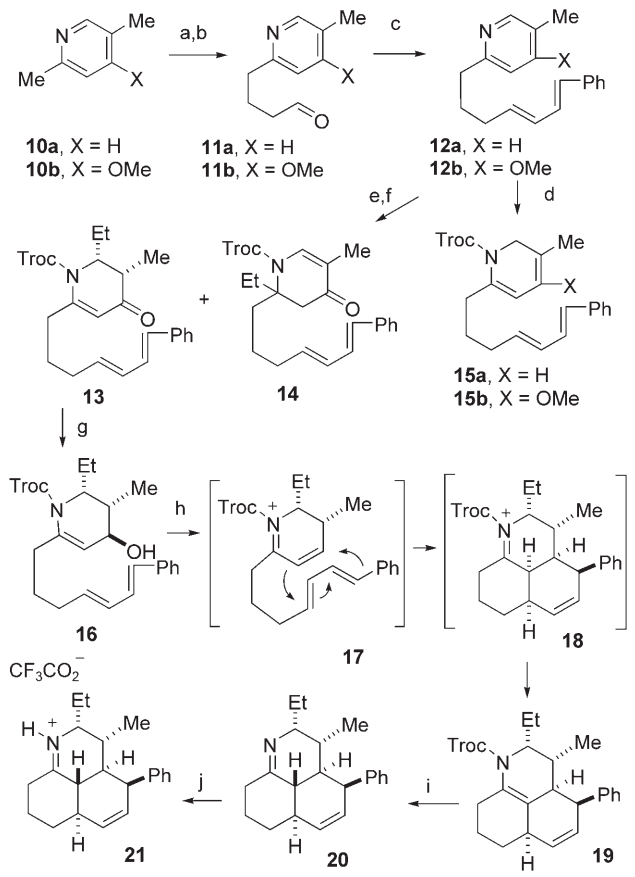


Scheme 2. Retrosynthetic routes to *N*-alkoxycarbonyl dihydropyridinium cation **4b** from pyridines **7** and **9**.

Deprotonation[8] of the 2-methyl group of 2,5-dimethylpyridine (**10a**) with *n*BuLi in THF at 0 °C, alkylation with 2-(2-bromoethyl)-1,3-dioxolane, and hydrolysis of the acetal afforded aldehyde **11a** (88%; see Scheme 3). A Horner–Emmons Wittig reaction with diethyl cinnamylphosphonate afforded **12a** as a 20:1 mixture of the *E*/Z isomers (95%). Treatment of pyridine **12a** with TrocCl and $NaBH_3CN$ afforded an inseparable 2:1 mixture of the desired dihydropyridine **15a** and the 1,4-dihydro isomer. Unfortunately, treatment of this mixture with acid under a variety of conditions did not generate any IMDA adduct, thus suggesting that protonation of dihydropyridine **15a** on the carbon atom bearing the methyl group to generate the *N*-alkoxycarbonyl dihydropyridinium cation is not facile.

We therefore turned our attention to the preparation of tetrahydropyridinol **8**. Deprotonation[9] of the 2-methyl group

InterScience
© 2006 Wiley-VCH Verlag GmbH & Co. KGaA, Weinheim



Scheme 3. a) *n*BuLi (1 equiv), THF; then 2-(2-bromoethyl)-1,3-dioxolane (1 equiv), 4 h; b) 1 M HCl, 25 °C, 1 h (**11a**: 88%, **11b**: 84%; two steps); c) LDA (1 equiv), diethyl (*E*)-cinnamylphosphonate (1 equiv), THF, 0 °C, 1 h; then aldehyde **11**, −78 °C, 1 h, 25 °C, 12 h (**12a**: 95%, **12b**: 82%); d) $NaBH_3CN$ (3 equiv), TrocCl (3 equiv), THF, 25 °C, 30 min (**15a**: 40% and 1,4-dihydropyridine: 20%, **15b**: 0%); e) TrocCl (2 equiv), THF, −78 °C, 1 h; then EtMgBr (2 equiv), −78 °C, 30 min; 25 °C, 1 h; f) 1 M HCl, 30 min (**13**: 67%, **14**: 18%; two steps); g) $NaBH_4$ (1 equiv) $CeCl_3 \cdot 7H_2O$ (1.25 equiv), MeOH, −78 °C, 30 min; 0 °C, 30 min (91%); h) $BF_3 \cdot Et_2O$ (1.2 equiv), CH_2Cl_2, −78 °C, 10 min; 25 °C, 30 min (87%); i) activated Zn dust, 1:1 MeOH/AcOH, 60 °C, 30 min; then K_2CO_3 (83%); j) TFA (1 equiv) (100%). LDA = lithium diisopropylamide, Troc = 2,2,2-trichloroethoxycarbonyl.

of 4-methoxy-2,5-dimethylpyridine (**10b**)[10] with *n*BuLi in THF at −20 °C, alkylation with 2-(bromoethyl)-1,3-dioxolane, and hydrolysis of the acetal afforded aldehyde **11b** (84%). A Horner–Emmons Wittig reaction with diethyl cinnamylphosphonate afforded **12b** (82%). Unfortunately, all attempts to effect Fowler reduction of **12b** to give **15b** were unsuccessful. Although **12b** is not useful for the preparation of deoxysymbioimine, it was useful for the preparation of the ethyl-substituted analogue **16** of tetrahydropyridinol **8**, which allowed us to validate this IMDA approach to symbioimine.

The addition of Grignard reagents to pyridines and chloroformate esters is more facile and general than the Fowler reduction.[11] We therefore treated **12b** with EtMgBr and TrocCl in THF at −78 °C to give a mixture of dienyl ethers that were hydrolyzed with 1 M HCl to give the desired enone **13** (67%) and the regioisomer **14** (18%). Only the *cis* isomer of **13**[12] was isolated, thus suggesting that protonation of the dienyl ether occurs selectively from the face opposite the ethyl group. Luche reduction[13] of enone **13** gave a single stereoisomeric tetrahydropyridinol **16**[12] in 91% yield.

Treatment of alcohol **16** with $BF_3 \cdot Et_2O$ in CH_2Cl_2 at −78–25 °C cleanly afforded the desired tricyclic adduct **19** (87%).[12] Loss of the hydroxide moiety provided the *N*-alkoxycarbonyl dihydropyridinium cation **17**, which underwent the desired IMDA reaction through an *endo* transition state from the face opposite the two alkyl substituents to give adduct **18**. Loss of a proton gave ene carbamate **19**.[12] Reductive cleavage of the Troc group with activated Zn[14] in MeOH/AcOH at 60 °C for 30 min and neutralization with K_2CO_3 afforded imine **20** (83%), which slowly tautomerized to give a 2.5:1 mixture of imine **20** and the enamine corresponding to **19**. Treatment of this mixture with one equivalent of trifluoroacetic acid (TFA) afforded symbioimine analogue **21**[12] quantitatively.

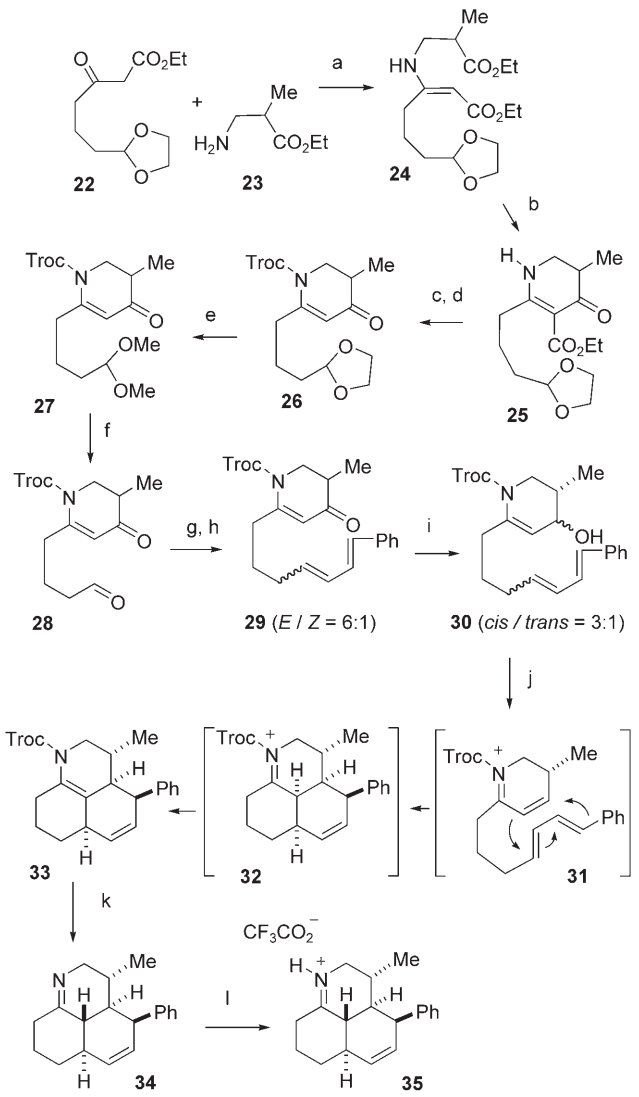
The efficient conversion of **16** into **21** established that the IMDA reaction of **17** gave exclusively *endo* adduct **18**, in which the diene added to the unhindered face of the dihydropyridinium cation. Epimerization occurred readily on deprotection to give exclusively **21** with symbioimine stereochemistry. This behavior suggests that loss of the hydroxide moiety from tetrahydropyridinol **8** will give **4b**, which will undergo the desired IMDA reaction to give the symbioimine skeleton. We therefore turned our attention to alternate routes to tetrahydropyridinol **8**.

Condensation of β-keto ester **22**[15] with β-amino ester **23**[16] in toluene containing acetic acid at reflux afforded enamine **24** (96%; see Scheme 4). Dieckmann condensation of **24** with NaH in THF at reflux provided dihydropyridinone **25** (97%).[17] Hydrolysis[18] of the ethyl ester with aqueous NaOH in MeOH at reflux followed by decarboxylation on neutralization proceeded in 94% yield. Treatment of the dihydropyridinone with *n*BuLi and TrocCl afforded the desired *N*-Troc dihydropyridinone **26** in 96% yield.[19]

Direct deprotection of **26** to give aldehyde **28** was unsuccessful. The acidic conditions needed to cleave the dioxolane also effected an intramolecular aldol reaction of **28**.[20,21] Fortunately, treatment of **26** with pyridinium *p*-toluenesulfonate (PPTS) in MeOH at 65 °C afforded the more easily cleaved dimethyl acetal **27** (95%), which was cleaved to form the desired aldehyde **28** (87%) with PPTS in wet acetone at 55 °C. Aldehyde **28** decomposed on attempted Horner–Emmons Wittig reaction with diethyl cinnamylphosphonate. Fortunately, reaction with the less basic cinnamylidinetriphenylphosphorane[22] afforded **29**, albeit as a 2:1 mixture of the *E*/*Z* isomers. Isomerization with I_2 in CH_2Cl_2 afforded **29** as a 6:1 mixture of the *E*/*Z* isomers in 83% yield from **28**. Luche reduction afforded the requisite tetrahydropyridinol **30**[12] as an inseparable 3:1 mixture of *cis*/*trans* isomers in 95% yield.

Treatment of tetrahydropyridinol **30** with $BF_3 \cdot Et_2O$ in CH_2Cl_2 at −78 °C formed dihydropyridinium cation **31**, which gave the desired tricyclic adduct **33** in 31% yield based on the *E* isomer of **30**.[12] It is not clear why the IMDA reaction of **31** to give **32** proceeded in much lower yield than that of the ethyl homologue **17**. The unstable by-products that were formed from **30** were difficult to characterize. Deprotection of **33** with

 © 2006 Wiley-VCH Verlag GmbH & Co. KGaA, Weinheim



Scheme 4. a) **22** (1 equiv), **23** (1 equiv), toluene, HOAc, reflux, 2 h (96%); b) NaH (3 equiv), THF, reflux, 3 h (97%); c) 1:1 MeOH/25% aqueous NaOH, reflux, 12 h (94%); d) *n*BuLi (1.1 equiv), THF, −78 °C, 30 min; then TrocCl (1.05 equiv), −78 °C, 30 min; 25 °C, 20 min (96%); e) PPTS (0.25 equiv), MeOH, 65 °C, 12 h (95%); f) PPTS (0.3 equiv), wet acetone, 55 °C, 3 h (87%); g) cinnamyltriphenylphosphonium chloride (1 equiv), *n*BuLi (1 equiv), THF, 0 °C, 1 h, cool to −78 °C; then aldehyde **28**, −78 °C, 30 min; 25 °C, 2 h (83%, *E*/*Z* = 2:1); h) I_2 (cat.), CH_2Cl_2, 25 °C, 1 h (100%, *E*/*Z* = 6:1); i) $NaBH_4$ (1 equiv) $CeCl_3 \cdot 7H_2O$ (1.25 equiv), MeOH, −78 °C, 30 min; 0 °C, 30 min (95%, *cis*/*trans* = 3:1); j) $BF_3 \cdot Et_2O$ (1.1 equiv), CH_2Cl_2, −78 °C, 10 min; 25 °C, 20 min (31% based on *E* isomer); k) activated Zn dust, MeOH/AcOH (1:1), 60 °C, 30 min; then K_2CO_3 (75%); l) TFA (1 equiv; 100% yield).

Zn in MeOH/AcOH at 60 °C followed by neutralization with K_2CO_3 afforded imine **34** (75%). Addition of TFA (1 equiv) afforded deoxysymbioimine (**35**) quantitatively. The ^1H and ^{13}C NMR spectral data of **35** correspond very closely to those of **1** except for the expected differences in the aromatic region.[12]

The convergent sequence from **22** and **23** to deoxysymbioimine (**35**) proceeds in 13% overall yield despite the 31% yield of the key IMDA reaction. We are currently optimizing the IMDA reaction of **31**, using the dienes obtained from aldehyde **28** and other Wittig reagents for the synthesis of symbioimine and oxygenated analogues, and exploring whether enantiomerically pure products can be obtained starting with optically pure amino ester **23**.[16c]

Received: September 30, 2005
Published online: December 30, 2005

Keywords: cycloaddition · Diels–Alder reaction · heterocycles · imines

[1] a) M. Kita, M. Kondo, T. Koyama, K. Yamada, T. Matsumoto, K.-H. Lee, J.-T. Woo, D. Uemura, *J. Am. Chem. Soc.* **2004**, *126*, 4794–4795; b) M. Kita, D. Uemura, *Chem. Lett.* **2005**, *34*, 454–459; c) M. Kita, N. Ohishi, K. Washida, M. Kondo, T. Koyama, K. Yamada, D. Uemura, *Bioorg. Med. Chem.* **2005**, *13*, 5253–5258.

[2] a) J.-L. Gras, *J. Org. Chem.* **1981**, *46*, 3738–3741; b) Y. Araki, T. Konoike, *J. Org. Chem.* **1997**, *62*, 5299–5309; c) M. Nörret, M. S. Sherburn, *Angew. Chem.* **2001**, *113*, 4198–4200; *Angew. Chem. Int. Ed.* **2001**, *40*, 4074–4076.

[3] D. F. Taber, S. Kong, S. C. Malcolm, *J. Org. Chem.* **1998**, *63*, 7953–7956.

[4] T. Sammakia, D. M. Johns, G. Kim, M. A. Berliner, *J. Am. Chem. Soc.* **2005**, *127*, 6504–6505.

[5] a) J. E. Baldwin, D. R. Spring, R. C. Whitehead, *Tetrahedron Lett.* **1998**, *39*, 5417–5420; b) K. Jakubowicz, K. Ben Abdeljelil, M. Herdemann, M.-T. Martin, A. Gateau-Olesker, A. Al-Mourabit, C. Marazano, B. C. Das, *J. Org. Chem.* **1999**, *64*, 7381–7387; c) J. E. Baldwin, T. D. W. Claridge, A. J. Culshaw, F. A. Heupel, V. Lee, D. R. Spring, R. C. Whitehead, *Chem. Eur. J.* **1999**, *5*, 3154–3161; d) M. Herdemann, A. Al-Mourabit, M.-T. Martin, C. Marazano, *J. Org. Chem.* **2002**, *67*, 1890–1897.

[6] a) R. F. Francis, C. D. Crews, B. S. Scott, *J. Org. Chem.* **1978**, *43*, 3227–3230; b) R. J. Sundberg, D. S. Grierson, H.-P. Husson, *J. Org. Chem.* **1984**, *49*, 2400–2404; c) N. Naiman, H. Rollema, E. Johnson, N. Castagnoli, Jr., *Chem. Res. Toxicol.* **1990**, *3*, 133–138.

[7] a) F. W. Fowler, *J. Org. Chem.* **1972**, *37*, 1321–1323; b) S. Raucher, J. E. MacDonald, *Synth. Commun.* **1980**, *10*, 325–331; c) R. J. Sundberg, J. D. Bloom, *J. Org. Chem.* **1981**, *46*, 4836–4842; d) R. J. Sundberg, G. Hamilton, C. Trindle, *J. Org. Chem.* **1986**, *51*, 3672–3679; e) G. Zhao, U. C. Deo, B. Ganem, *Org. Lett.* **2001**, *3*, 201–203.

[8] a) H. Sonnenschein, T. Kreher, E. Gründemann, R.-P. Krüger, A. Kunath, V. Zabel, *J. Org. Chem.* **1996**, *61*, 710–714; b) M. B. Leitner, T. Kreher, H. Sonnenschein, B. Costisella, J. Springer, *J. Chem. Soc. Perkin Trans. 2* **1997**, 377–381.

[9] C. H. Heathcock, R. C. D. Brown, T. C. Norman, *J. Org. Chem.* **1998**, *63*, 5013–5030.

[10] W. Chu, S. Kamitori, M. Shinomiya, R. G. Carlson, F. Takusagawa, *J. Am. Chem. Soc.* **1994**, *116*, 2243–2253; 2,5-dimethyl-4-nitropyridine *N*-oxide was converted into 4-methoxy-2,5-dimethylpyridine *N*-oxide in a single step in 83% yield by treatment with K_2CO_3 in MeOH at reflux for 2 h; see: C. Xie, M. T. C. Runnegar, B. B. Snider, *J. Am. Chem. Soc.* **2000**, *122*, 5017–5024.

[11] a) R. S. Al-awar, S. P. Joseph, D. L. Comins, *J. Org. Chem.* **1993**, *58*, 7732–7739; b) D. L. Comins, R. S. Al-awar, *J. Org. Chem.* **1995**, *60*, 711–716.

[12] Stereochemical assignments based on coupling constants and NOE interaction studies are presented in detail in the Supporting Information.

[13] a) A. P. Kozikowski, P.-u. Park, *J. Org. Chem.* **1990**, *55*, 4668–4682; b) D. L. Comins, M. O. Killpack, E. Despagnet, E. Zeller, *Heterocycles* **2002**, *58*, 505–519.

 © 2006 Wiley-VCH Verlag GmbH & Co. KGaA, Weinheim

[14] S. M. Hannick, Y. Kishi, *J. Org. Chem.* **1983**, *48*, 3833 – 3835.
[15] M. Kato, V. P. Kamat, A. Yoshikoshi, *Synthesis* **1988**, 699 – 701.
[16] a) P. Krogsgaard-Larsen, K. Thyssen, K. Schaumburg, *Acta Chem. Scand. Ser. B* **1978**, *32*, 327 – 334; b) M. Solymár, A. Liljeblad, L. Lázár, F. Fülöp, L. T. Kanerva, *Tetrahedron: Asymmetry* **2002**, *13*, 1923 – 1928; c) U. Eilitz, F. Lessmann, O. Seidelmann, V. Wendisch, *Tetrahedron: Asymmetry* **2003**, *14*, 189 – 191.
[17] a) D. Ma, H. Sun, *Org. Lett.* **2000**, *2*, 2503 – 2505; b) N. Leflemme, P. Dallemagne, S. Rault, *Synthesis* **2002**, 1740 – 1746; c) D. Ma, Z. Zhu, *Tetrahedron Lett.* **2003**, *44*, 8609 – 8612.
[18] J. P. Michael, A. S. Howard, R. B. Katz, M. I. Xwane, *Tetrahedron Lett.* **1992**, *33*, 4751 – 4754.
[19] a) D. L. Comins, A. B. Fulp, *Tetrahedron Lett.* **2001**, *42*, 6839 – 6841; b) D. L. Comins, M. J. Sandelier, T. A. Grillo, *J. Org. Chem.* **2001**, *66*, 6829 – 6832.
[20] Details of the aldol reaction are provided in the Supporting Information.
[21] For similar examples, see: a) C. E. Masse, M. Yang, J. Solomon, J. Panek, *J. Am. Chem. Soc.* **1998**, *120*, 4123 – 4134; b) C. A. Maier, B. Wünsch, *Eur. J. Org. Chem.* **2003**, 714 – 720.
[22] J. R. Beadle, S. H. Korzeniowski, D. E. Rosenberg, B. J. Garcia-Slanga, G. W. Gokel, *J. Org. Chem.* **1984**, *49*, 1594 – 1603.

 © 2006 Wiley-VCH Verlag GmbH & Co. KGaA, Weinheim

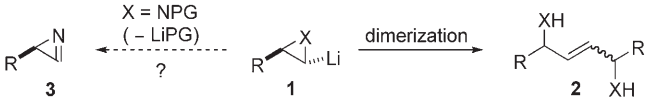
Synthetic Methods

DOI: 10.1002/anie.200503303

Dimerization of Lithiated Terminal Aziridines**

David M. Hodgson and Steven M. Miles*

It has been known for a long time that lithiated epoxides **1** (Scheme 1, X = O) can display carbenoid-type reactivity, including dimerization.[1] Such dimerizations have been developed recently by our research group as a synthetic method for the preparation of symmetric 2-ene-1,4-diols **2** (X = O) from terminal epoxides.[2] Although a useful entry to this valuable class of compounds, this method unfortunately displayed only a 2:1 selectivity in favor of the *E* isomer of the newly formed alkene when using epoxides with primary (R = C_5H_{11}) or secondary (R = cyclohexyl) alkyl substituents (62% and 77% yield of 2-ene-1,4-diol olefin isomer mixtures, respectively).



Scheme 1. Possible reactions of lithiated epoxides or aziridines.

Following on from this, we considered the possibility that lithiated terminal aziridines **1** (X = NPG, PG = protecting group)[3] might undergo similar dimerization, thus leading to synthetically useful (protected) 2-ene-1,4-diamines **2** (X = NPG).[4] At the outset of our studies we were not aware of any examples of such dimerizations in the literature,[5] and it was not known whether the method would yield dimer compounds in useful efficiencies or whether other pathways such as formation of 2*H*-azirines **3**[6] (Scheme 1) would be favored. Although certain lithiated aziridines fused to 5- to 8-membered rings undergo carbenoid transformations,[7] formation of 2*H*-azirines in these cases would be significantly disfavored because of additional ring strain. There is little precedent for lithiated aziridines having carbenoid reactivity when the aziridine is not fused to a second ring.[7b]

One additional variable for aziridines (relative to epoxides) is the choice of the protecting/activating group at the aziridine nitrogen atom. In our initial studies we attempted to dimerize alkyl substituted terminal aziridines bearing the groups Boc (butyloxycarbonyl), tosyl, or Bus (*tert*-butylsulfonyl),[8] by using lithium 2,2,6,6-tetramethylpiperidide (LTMP) as the base.[3] Upon treatment with this base, the N-Boc- and N-tosyl-protected aziridines gave complex mixtures of products with no dimers observed, but the lithiated N-Bus-protected aziridine **1a** (X = NBus; R = C_5H_{11}) formed and underwent dimerization in 90% yield to give the protected 2-ene-1,4-diamine **2a** (X = NBus; R = C_5H_{11}) as a mixture of three discernible diastereoisomers.

There are only two possible isomers (alkene *E* and *Z* isomers) that could arise upon dimerization of an enantiopure terminal aziridine, and so this method seems better suited to enantiopure substrates. With this in mind, we examined the scope of the dimerization reaction with a range of enantiopure (99% *ee*) N-Bus-protected terminal aziridines[9] (Table 1).

The enantiopure aziridines (entries 1–5) all dimerized in high efficiency under the same straightforward reaction conditions (aziridine 0.32 mol dm^{-3} in THF/hexanes (2:3), 3 equiv LTMP, −78 °C to 0 °C, total reaction time 80 min; see Experimental Section).[10] Crucially, all these reactions proceeded with complete *E* selectivity for the alkene bond formed, with no traces of the *Z* alkene detectable in either the crude or purified products. The *E* geometry of the alkene was determined unambiguously in the case of **5b** (single-crystal X-ray structure, see Supporting Information), with the other products **5a** and **5c–e** assigned as *E* isomers by analogy. Other possible reaction pathways for the lithiated aziridines such as azirine formation, reaction with excess LTMP to give enamines/aldehydes,[11] or intramolecular cyclopropanation[12] (entry 4) did not feature significantly. Even when aziridine **4a** was added to LTMP in THF at RT with no cooling, dimer **5a**

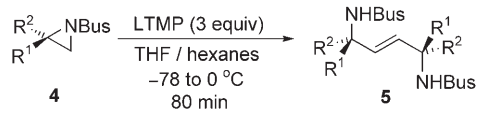
[*] Dr. D. M. Hodgson, Dr. S. M. Miles
Department of Chemistry
University of Oxford
Chemistry Research Laboratory
Mansfield Road, Oxford, OX1 3TA (UK)
Fax: (+44) 186-528-5002
E-mail: david.hodgson@chem.ox.ac.uk

[**] We thank the EPSRC for a Research Grant (GR/S46789/01), the EPSRC National Mass Spectrometry Service Centre for providing mass spectra, Dr. A. Cowley for X-ray crystallographic analyses, and P. Humphreys for preliminary observations and samples of aziridines **4d** and **4g**.

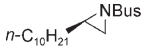
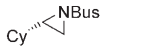
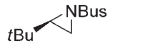
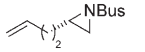
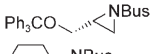
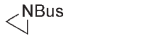
Supporting information for this article is available on the WWW under http://www.angewandte.org or from the author.

 © 2006 Wiley-VCH Verlag GmbH & Co. KGaA, Weinheim

Table 1: Dimerization of lithiated N-Bus aziridines.



4 5

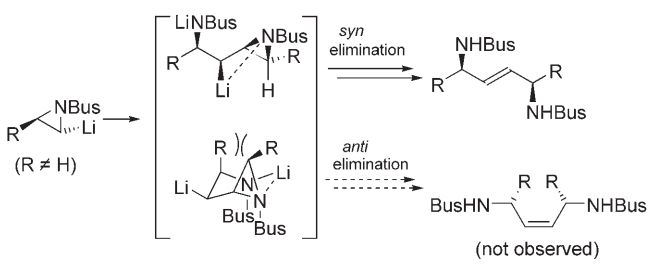
Entry	Aziridine **4**		Yield of dimer **5** [%]
1		(*R*)-**4a**	97
2		(*S*)-**4b**	97
3		(*R*)-**4c**	81
4		(*R*)-**4d**	88
5		(*R*)-**4e**	70
6		**4f**	86[a]
7		**4g**	41[b]

[a] Mixture of olefin isomers obtained (ratio 93:7). [b] Reaction quenched after 10 min at −78 °C and yielded a mixture of olefin isomers (ratio 57:43). Cy = cyclohexyl.

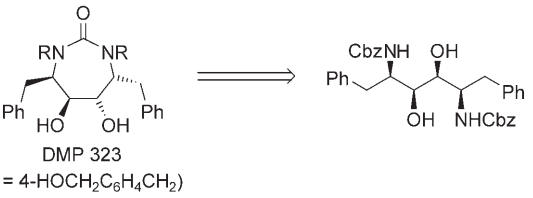
was isolated in 84 % yield and as a single alkene isomer after reaction for 30 minutes, thus demonstrating the inherent robustness and selectivity of the method. Enantiomeric aziridine (*S*)-**4a** also underwent dimerization in 97 % yield (entry 1), thus showing the methodology to be equally applicable to the preparation of either enantiomeric series of dimers **5**. The reaction was also efficient for an achiral 2,2-disubstituted aziridine **4f** and to a lesser extent with the nonsubstituted aziridine **4g** (entries 6 and 7, respectively). In both these latter cases heterochiral as well as homochiral dimerization pathways are possible, and the products were isolated as mixtures of *E* and *Z* isomers.

Formation of the *E* isomer from enantiopure substrates is consistent with an inital *trans*-lithiation of the aziridine at the terminal position,[3] followed by reaction of one lithiated aziridine as a nucleophile with a second acting as an electrophile, and finally *syn* elimination.[2] One possible reason for the superior alkene stereoselectivity seen with aziridines relative to their epoxide counterparts may be a further disfavoring of the *anti*-elimination pathway as a result of steric hindrance between the N-Bus groups (Scheme 2).

1,4-Diamine derivatives, especially cyclic ureas such as the parent DuPont Merck compound DMP 323 (Scheme 3), have



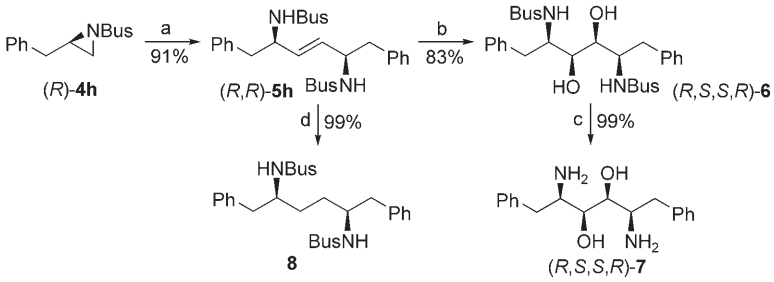
Scheme 2. Possible elimination pathways in dimer formation.



Scheme 3. DMP 323 and its derivation from a 1,4-diamine-2,3-diol unit.[13b]

received considerable attention in recent years as peptidomimetic HIV protease inhibitors.[13] A common structural feature of these inhibitors is a 1,4-diamine-2,3-diol unit with *R*,*S*,*S*,*R* configuration, often with flanking (1,4-) benzyl groups.

We decided to see if our new methodology could be applied in a concise synthesis of such a desirable structural motif, starting with the benzyl-substituted aziridine (*R*)-**4h** (Scheme 4). We found that treatment of aziridine **4h**[9] with LTMP gave the N-Bus-protected 2-ene-1,4-diamine **5h** in



Scheme 4. Applications of the dimerization methodology. Reagents and conditions: a) LTMP (3 equiv), THF/hexanes, −78 °C to 0 °C, 80 min; b) OsO_4 (2.5 mol %), NMO (1.4 equiv), THF/H_2O, RT, 2 days; c) F_3CSO_3H (0.1 N in CH_2Cl_2), anisole, 0 °C to RT, 16 h; d) H_2 (1 atm), Pd on C (5 mol %), EtOH, RT, 24 h.

91 % yield and with complete *E* selectivity. Importantly, potential side products arising from benzylic deprotonation rather than deprotonation at the aziridine were not observed to any significant extent.[14] Simple treatment of alkene **5h** with OsO_4/NMO (*N*-methylmorpholine-*N*-oxide) yielded the *R*,*S*,*S*,*R* diol **6** with high diastereoselectivity (ca. 7:1) over the *R*,*R*,*R*,*R* diol (83 % yield for **6**).[15] The *R*,*S*,*S*,*R* configuration of **6** (and also indirectly the *E* geometry of **5h** prior to *syn*-dihydroxylation) was confirmed by X-ray crystallographic analysis (see Supporting Information).

Removal of the N-Bus group[8a] of diol (*R*,*S*,*S*,*R*)-**6** gave the free diaminodiol (*R*,*S*,*S*,*R*)-**7** in 99 % yield; this is a core C_2-symmetric unit of a number of extremely potent HIV protease inhibitors. (*R*,*S*,*S*,*R*)-**7** has been prepared in a previous HIV protease inhibitor study[16] and has also found use as a ligand or ligand precursor in various enantioselective transformations.[17] The efficiency of deprotection to give the functionalized diaminodiol (*R*,*S*,*S*,*R*)-**7** is of particular note. Benzyl aziridine (*S*)-**4h** was also prepared and dimerized (94 % yield), thus demonstrating that the opposite enantiomeric series can also be accessed.[18] Finally, hydrogenation of

 © 2006 Wiley-VCH Verlag GmbH & Co. KGaA, Weinheim

the alkene bond in the dimeric compound (*R*,*R*)-**5h** was also achieved under mild conditions (1 atm H_2, 5 mol% Pd on C, RT) to give the saturated analogue **8** in 99% yield. This result further highlights the utility of the dimerization methodology, and demonstrates efficient access to saturated protected enantiopure C_2-symmetric 1,4-diamines.

In summary, we have developed a dimerization pathway of terminal aziridines by lithiation to give N-protected 2-ene-1,4-diamines with complete *E*-olefin selectivity when starting with enantiopure substrates. The dimerization proved highly efficient for a range of alkyl-substituted and functionalized aziridines, by using the same straightforward reaction conditions in each case. The usefulness of the method was demonstrated by the efficient and selective synthesis of diaminodiol (*R*,*S*,*S*,*R*)-**7**, the core unit of a number of extremely potent HIV protease inhibitors.

Experimental Section

Representative procedure for dimerization of terminal aziridine **4**: *n*BuLi (1.6 M in hexanes, 1.88 mL, 3.0 mmol) was added dropwise to a solution of 2,2,6,6-tetramethylpiperidine (0.51 mL, 3.0 mmol) in THF (0.4 mL) at −78 °C. The mixture was warmed to 0 °C over 15 min, then cooled to −78 °C before dropwise addition of the aziridine **4** (1.0 mmol) in THF (0.8 mL). The mixture was stirred at −78 °C for 20 min, then at 0 °C for 1 h, before the addition of MeOH (0.8 mL), saturated aqueous NH_4Cl (8 mL), and Et_2O (16 mL). The layers were separated, and the aqueous phase was extracted with Et_2O (16 mL). The combined organic phase was dried ($MgSO_4$) and concentrated under reduced pressure. Flash chromatography of the residue (SiO_2, petroleum ether/diethyl ether) gave the protected 2-ene-1,4-diamine **5**.

Received: September 16, 2005
Published online: December 27, 2005

Keywords: aziridines · lithiation · small ring systems · synthetic methods

[1] a) K. L. Dhawan, B. D. Gowland, T. Durst, *J. Org. Chem.* **1980**, *45*, 922–924; b) P. Lohse, H. Loner, P. Acklin, F. Sternfeld, A. Pfaltz, *Tetrahedron Lett.* **1991**, *32*, 615–618; c) for a review, see: D. M. Hodgson, C. D. Bray in *Aziridines and Epoxides in Organic Synthesis* (Ed.: A. K. Yudin), Wiley-VCH, Weinheim, **2006**, pp. 143–184.

[2] D. M. Hodgson, C. D. Bray, N. D. Kindon, *Org. Lett.* **2005**, *7*, 2305–2308.

[3] The electrophile trapping of lithiated terminal aziridines has been developed recently, see: D. M. Hodgson, P. G. Humphreys, J. G. Ward, *Org. Lett.* **2005**, *7*, 1153–1156.

[4] For a review of the utility of diamine derivatives in asymmetric catalysis, see: F. Fache, E. Schulz, M. L. Tommasino, M. Lemaire, *Chem. Rev.* **2000**, *100*, 2159–2231; for the utility of 1,4-diamine derivatives as HIV protease inhibitors, see Ref. [13].

[5] Dimerization of a lithiated methylene aziridine to give a cyclopentene has been reported, see: H. Quast, C. A. W. Vélez, *Angew. Chem.* **1974**, *86*, 380–381; *Angew. Chem. Int. Ed. Engl.* **1974**, *13*, 342–343; dimerization of N-unprotected aziridines under Lewis acid catalysis to give aminoaziridines is known, see: A. Caiazzo, S. Dalili, A. K. Yudin, *Synlett* **2003**, 2198–2202.

[6] a) F. A. Davis, H. Liu, C.-H. Liang, G. V. Reddy, Y. Zhang, T. Fang, D. D. Titus, *J. Org. Chem.* **1999**, *64*, 8929–8935; b) V. K. Aggarwal, E. Alonso, M. Ferrara, S. E. Spey, *J. Org. Chem.* **2002**, *67*, 2335–2344; c) R. Luisi, V. Capriati, S. Florio, R. Ranaldo, *Tetrahedron Lett.* **2003**, *44*, 2677–2681; d) R. Luisi, V. Capriati, S. Florio, P. Di Cunto, B. Musio, *Tetrahedron* **2005**, *61*, 3251–3260.

[7] a) P. Müller, P. Nury, *Helv. Chim. Acta* **2004**, *87*, 227–239; b) D. M. Hodgson, B. Štefane, T. J. Miles, J. Witherington, *Chem. Commun.* **2004**, 2234–2235; c) C. M. Rosser, S. C. Coote, J. P. Kirby, P. O'Brien, D. Caine, *Org. Lett.* **2004**, *6*, 4817–4819.

[8] a) P. Sun, S. M. Weinreb, M. Shang, *J. Org. Chem.* **1997**, *62*, 8604–8608; b) A. V. Gontcharov, H. Liu, K. B. Sharpless, *Org. Lett.* **1999**, *1*, 783–786.

[9] Enantiopure aziridines were prepared in a straightforward manner and in excellent yield from the corresponding epoxides of opposite configuration (available commercially or according to: S. E. Schaus, B. D. Brandes, J. F. Larrow, M. Tokunaga, K. B. Hansen, A. E. Gould, M. E. Furrow, E. N. Jacobsen, *J. Am. Chem. Soc.* **2002**, *124*, 1307–1315) using the following sequence: a) *t*$BuSO_2NH_2$, $BnEt_3NCl$, K_2CO_3; b) $(MeSO_2)_2O$, 4-dimethylaminopyridine, pyridine; c) K_2CO_3 (see Ref. [3] and also: D. M. Hodgson, M. J. Fleming, S. J. Stanway, *Org. Lett.* **2005**, *7*, 3295–3298).

[10] In studies with substrate **4a**, the use of fewer equivalents of LTMP or extended reaction times at −78 °C led to incomplete reaction.

[11] D. M. Hodgson, C. D. Bray, N. D. Kindon, *J. Am. Chem. Soc.* **2004**, *126*, 6870–6781.

[12] a) D. M. Hodgson, Y. K. Chung, J.-M. Paris, *J. Am. Chem. Soc.* **2004**, *126*, 8664–8665; b) D. M. Hodgson, Y. K. Chung, J.-M. Paris, *Synthesis* **2005**, 2264–2266.

[13] a) P. Y. S. Lam, P. K. Jadhav, C. J. Eyermann, C. N. Hodge, Y. Ru, L. T. Bacheler, J. L. Meek, M. J. Otto, M. M. Rayner, Y. N. Wong, C.-H. Chang, P. C. Weber, D. A. Jackson, T. R. Sharpe, S. Erickson-Viitanen, *Science* **1994**, *263*, 380–384; b) M. E. Pierce, G. D. Harris, Q. Islam, L. A. Radesca, L. Storace, R. E. Waltermire, E. Wat, P. K. Jadhav, G. C. Emmet, *J. Org. Chem.* **1996**, *61*, 444–450; c) D. A. Nugiel, K. Jacobs, T. Worley, M. Patel, R. F. Kaltenbach III, D. T. Meyer, P. K. Jadhav, G. V. De Lucca, T. E. Smyser, R. M. Klabe, L. T. Bacheler, M. M. Rayner, S. P. Seitz, *J. Med. Chem.* **1996**, *39*, 2156–2169; d) P. Y. S. Lam, Y. Ru, P. K. Jadhav, P. E. Aldrich, G. V. DeLucca, C. J. Eyermann, C.-H. Chang, G. Emmett, E. R. Holler, W. F. Daneker, L. Li, P. N. Confalone, R. J. McHugh, Q. Han, R. Li, J. A. Markwalder, S. P. Seitz, T. R. Sharpe, L. T. Bacheler, M. M. Rayner, R. M. Klabe, L. Shum, D. L. Winslow, D. M. Kornhauser, D. A. Jackson, S. Erickson-Viitanen, C. N. Hodge, *J. Med. Chem.* **1996**, *39*, 3514–3525; e) A. M. Davis, S. J. Teague, G. J. Kleywegt, *Angew. Chem.* **2003**, *115*, 2822–2841; *Angew. Chem. Int. Ed.* **2003**, *42*, 2718–2736; f) W. A. Loughlin, J. D. A. Tyndall, M. P. Glenn, D. P. Fairlie, *Chem. Rev.* **2004**, *104*, 6085–6117.

[14] Conversely, when 2,3-epoxypropylbenzene was subjected to dimerization conditions (see Experimental Section) the major product was cinnamyl alcohol (arising from benzylic deprotonation and eliminative rearrangement), and no significant 2-ene-1,4-diol was observed.

[15] Similar dihydroxylation of the analogous N-Boc-protected 2-ene-1,4-diamine displayed poor diastereoselectivity (2:3) and favored the opposite (less desirable for HIV protease inhibition) diastereoisomer to that seen in our case, see: a) A. V. R. Rao, M. K. Gurjar, S. Pal, R. J. Pariza, M. S. Chorghade, *Tetrahedron Lett.* **1995**, *36*, 2505–2508; b) M. K. Gurjar, S. Pal, A. V. R. Rao, R. J. Pariza, M. S. Chorghade, *Tetrahedron* **1997**, *53*, 4769–4778.

[16] A. Dondoni, D. Perrone, M. Rinaldi, *J. Org. Chem.* **1998**, *63*, 9252–9264.

[17] a) A. Zhang, Y. Feng, B. Jiang, *Tetrahedron: Asymmetry* **2000**, *11*, 3123–3130; b) J. Zhao, X. Bao, X. Liu, B. Wan, X. Han, C.

 © 2006 Wiley-VCH Verlag GmbH & Co. KGaA, Weinheim

Yang, J. Hang, B. Jiang, *Tetrahedron: Asymmetry* **2000**, *11*, 3351 – 3359; c) B. Jiang, Y. Feng, J.-F. Hang, *Tetrahedron: Asymmetry* **2001**, *12*, 2323 – 2329.

[18] Derivatization of (*S*,*R*,*R*,*S*)-**7** has been used to produce arrays of HIV protease inhibitors for biological evaluation and has yielded a number of highly active compounds, see: a) D. J. Kempf, L. Codacovi, X. C. Wang, W. E. Kohlbrenner, N. E. Wideburg, A. Saldivar, S. Vasavanonda, K. C. Marsh, P. Bryant, H. L. Sham, B. E. Green, D. A. Betebenner, J. Erickson, D. W. Norbeck, *J. Med. Chem.* **1993**, *36*, 320 – 330; b) K.-H. Budt, A. Peyman, J. Hansen, J. Knolle, C. Meichsner, A. Paessens, D. Ruppert, B. Stowasser, *Bioorg. Med. Chem.* **1995**, *3*, 559 – 571; c) S. F. Martin, G. O. Dorsey, T. Gane, M. C. Hillier, H. Kessler, M. Baur, B. Mathä, *J. Med. Chem.* **1998**, *41*, 1581 – 1597.

 © 2006 Wiley-VCH Verlag GmbH & Co. KGaA, Weinheim

Fluoro–Sulfur Compounds

DOI: 10.1002/anie.200503320

Synthesis of the Long Sought After Compound Pentafluoronitrosulfane, SF_5NO_2**

Norman Lu, H. P. Sampath Kumar, James L. Fye, Jian Sun Blanks, Joseph S. Thrasher,* Helge Willner, and Heinz Oberhammer*

The chemistry of SF_5-containing molecules[1–3] is no longer just of interest to sulfur and fluorine chemists. Recently, this class of compounds has become a very important issue in the area of atmospheric chemistry. According to a recent report, more than 4000 tons of the super greenhouse gas SF_5CF_3 are present in the stratosphere.[4–6] In addition, scientists have also proposed the use of molecules such as SF_5CF_3, SF_6, fluoroalkanes, and so on to terraform Mars.[7]

[*] Prof. Dr. N. Lu
Department of Molecular Science and Engineering
National Taipei University of Technology
Taipei 106 (Taiwan)
Fax: (+886) 227-317-174
E-mail: normanlu@ntut.edu.tw
Dr. H. P. S. Kumar, J. L. Fye, Dr. J. Sun Blanks, Prof. Dr. J. S. Thrasher
Department of Chemistry
The University of Alabama
Tuscaloosa, AL 35487 (USA)
Fax: (+1) 205-348-9104
E-mail: fluorine@bama.ua.edu
Prof. Dr. H. Willner
FB C Anorganische Chemie
Universität Wuppertal
Gaussstrasse 20, 42119 Wuppertal (Germany)
Prof. Dr. H. Oberhammer
Institut für Physikalische und Theoretische Chemie
Universität Tübingen
72076 Tübingen (Germany)

[**] The authors gratefully acknowledge the support of The University of Alabama. N.L. thanks Dr. J. C. Jiang (Institute of Atomic and Molecular Sciences, Academia Sinica, Taiwan) for MP2 calculations.

As a number of simple SF_5-containing compounds are still unknown although the corresponding CF_3 analogues have been well documented, we undertook the preparation of the long sought after molecule SF_5NO_2.[8] Both the thermal and photochemical reactions of SF_5 radical sources such as SF_5Cl, SF_5Br, and S_2F_{10} have been reviewed recently by Lentz and Seppelt;[9] however, we had to make use of either a new SF_5 radical source in $(SF_5)_3N$ or a different light source to the more commonly used mercury immersion lamp, namely, diazo or superblue lamps ($\lambda_{max} = 420$ nm). Thus, SF_5NO_2 was successfully prepared by two independent methods: A) the thermal reaction of $(SF_5)_3N$ with nitrogen dioxide, NO_2 [Eq. (1)], and B) the photochemical reaction between SF_5Br and NO_2 [Eq. (2)]. Herein, we provide an overview of the

$$(SF_5)_3N + NO_2\,(\text{excess}) \rightarrow SF_5NO_2 + \text{side products} \quad (1)$$

$$SF_5Br + NO_2\,(\text{excess}) \xrightarrow{\lambda_{max}=420\,nm} SF_5NO_2 + \text{side products} \quad (2)$$

spectroscopic and physical properties and structure of SF_5NO_2, as this molecule has the longest S^{VI}–N bond reported to date.

Two methods were used to prepare SF_5NO_2, starting either from the novel amine, $(SF_5)_3N$ (method A), or from SF_5Br (method B).[10] Owing to its elongated and weak N–S bonds, $(SF_5)_3N$ readily forms $(SF_5)_2N$[11,12] and SF_5 radicals, which in turn react with NO_2 (or with NO_2Cl) at room temperature to generate SF_5NO_2. By method A, SF_5NO_2 was prepared for the first time by taking advantage of the weak N–S bonds in $(SF_5)_3N$ in its reaction with NO_2.[13] The ^{19}F NMR spectrum of the SF_5NO_2 thus obtained displayed a typical AB_4 pattern, which is characteristic of the SF_5 group. Furthermore, the IR spectrum of SF_5NO_2 showed the diagnostic stretches and bends for both the SF_5 and NO_2 moieties. The SF_5 group usually displays three strong vibrational peaks below 1000 cm^{-1}; in SF_5NO_2, these appeared at 908, 801, and 594 cm^{-1}. The two NO_2 stretching bands in SF_5NO_2 were unambiguously assigned as $\tilde{\nu}_{as}NO_2 = 1654$ cm^{-1} and $\tilde{\nu}_{s}NO_2 = 1303$ cm^{-1}, respectively.

As a result of the limited availability of $(SF_5)_3N$, SF_5Br was tested as an alternative source of the SF_5 radical in method B. The photochemical reaction between SF_5Br and NO_2 successfully yielded SF_5NO_2 as shown in Equation (2). It is thought that during the photolysis, first, SF_5 and Br radicals are formed during the irradiation, which then react with NO_2 individually. Both $BrNO_2$ and BrONO can be formed from the Br radical.[14] The N-bonded product, $BrNO_2$, is the thermodynamically more stable product, while the O-bonded product, BrONO, is favored kinetically. The N-bonded product can also be formed by attack at the rear side on BrONO by the nitrogen atom of another NO_2 molecule, with elimination of NO_2 as described by Broske and Zabel.[15] The SF_5 radical behaves similarly. Both SF_5NO_2 and SF_5ONO are presumed to be formed during the photochemical reaction. (SF_5ONO is a short-lived species that is thought to have been observed by FTIR spectroscopy during the reaction of $(SF_5)_3N$ with NO_2 at room temperature.) However, in this case attack by NO_2 on SF_5ONO from the rear side is impossible owing to the bulkiness of the SF_5 group. SF_5NO_2

© 2006 Wiley-VCH Verlag GmbH & Co. KGaA, Weinheim

was isolated in only 3% yield based on SF_5Br used in this reaction. Presumably, a large proportion of SF_5 radicals that were generated during the reaction decomposed before having the opportunity to react. CsF was used to ease the purification of SF_5NO_2 through the concept of fluoride ion affinity. As shown in Equations (3) and (4), CsF is used to

$$CsF + SOF_4 \rightarrow Cs^+SOF_5^- \quad (3)$$

$$CsF + SF_4 \rightarrow Cs^+SF_5^- \quad (4)$$

remove SF_4 and SOF_4 by salt formation. The use of CsF also helps to remove Br_2 and converts NO_2 into FNO. Some of these side products are almost impossible to remove by distillation from SF_5NO_2 without such treatment with CsF. The crude SF_5NO_2 was then purified by low-temperature trap-to-trap distillation.

The ^{19}F NMR spectrum of SF_5NO_2 revealed an AB_4 pattern. The simulated NMR data are $\delta = 46.79$ ppm (F_{ax}), $\delta = 43.02$ ppm (F_{eq}), and coupling constant $^2J(F_{ax}–F_{eq}) = 144.3$ Hz. In addition, the ^{14}N NMR spectrum of SF_5NO_2 was recorded and is shown in Figure 1. The spectrum does not reveal perfect quintet splitting because of the quadrupolar effects of the ^{14}N nucleus (^{14}N NMR (versus external reference NO_3^- at $\delta = 383$ ppm): $\delta = 283.8$ ppm; $^2J(F–N) = 8$ Hz).

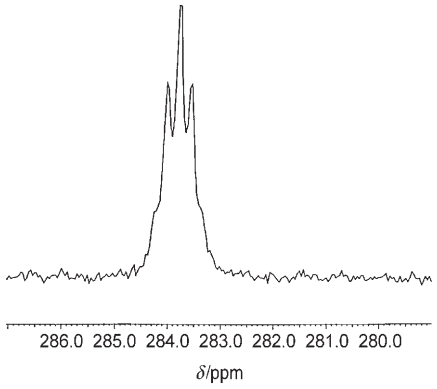


Figure 1. ^{14}N NMR spectrum of SF_5NO_2.

The IR spectrum of SF_5NO_2 is shown in Figure 2. In Table 1, the $\tilde{\nu}_{as}NO_2$ and $\tilde{\nu}_sNO_2$ vibrational frequencies of NO_2 are compared to XNO_2 (X = F, CF_3, and SF_5). As a result of the inductive effects of the strong electron-withdrawing substituents (F, CF_3, and SF_5), the $\tilde{\nu}_{as}NO_2$ and $\tilde{\nu}_sNO_2$ stretching frequencies of these three compounds are all shifted to higher frequencies relative to those for the NO_2 molecule.

A mass spectrum of SF_5NO_2 was obtained and shows the fragmentation pattern, m/z 127 (SF_5^+, 100%), 108 (SF_4^+, 6.7%), 89 (SF_3^+, 51.0%), 81 ($SFNO^+$, 1.5%), 70 (SF_2^+, 11.5%), 64 (SO_2^+, 12.1%), 51 (SF^+, 5.9%), 46 (NO_2^+, 69.3%). Although the molecular ion was not observed, the mass spectrum did reveal fragments at m/z 46 and 127 that indicate the presence of NO_2^+ and SF_5^+, respectively. In addition, the

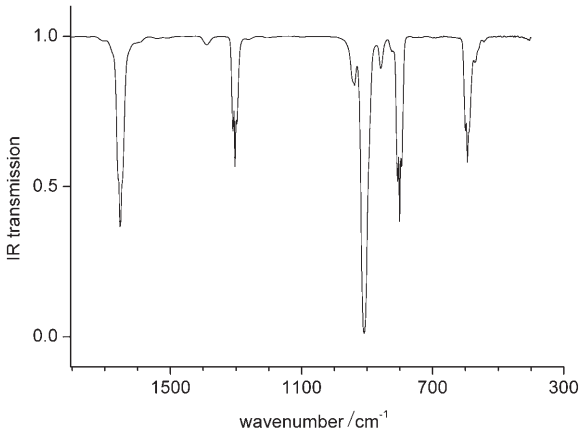


Figure 2. IR spectrum of SF_5NO_2.

Table 1: IR spectral data for the NO_2 moiety in XNO_2 (X = F, CF_3, SF_5) versus the NO_2 molecule.[a]

Compound	$\tilde{\nu}_{as}NO_2$ [cm^{-1}]	$\tilde{\nu}_sNO_2$ [cm^{-1}]	δNO_2 [cm^{-1}]
NO_2	1613	1261	751
FNO_2[16]	1792	1310	822
SF_5NO_2[b] (this work)	1654	1303	801
CF_3NO_2[17,18]	1627	1310	751

[a] $\tilde{\nu}_{as}$ asymmetric stretch; $\tilde{\nu}_s$ symmetric stretch; δ bending mode. [b] For $SF_5{}^{15}NO_2$, the $^{15}NO_2$ frequencies are $\tilde{\nu}_{as}NO_2 = 1618$, $\tilde{\nu}_sNO_2 = 1287$, and $\delta NO_2 = 793$ cm^{-1}.

peak at m/z 81, which corresponds to $SFNO^+$, provided evidence that the two previously mentioned fragments are originally bonded together. By gas density measurements, the relative molecular mass was determined as $M_r = 173.0 \pm 0.5$. The equation derived from the vapor pressure curve is $\ln(p/p_o) = -3788/T + 13.33$. The normal extrapolated boiling point for SF_5NO_2 was determined as 9°C, its heat of vaporization is approximately 29.3 kJ mol^{-1}, and it melts at -78 ± 2°C. Thermal studies of SF_5NO_2 indicate that it mainly decomposes to SOF_4 and FNO at a rate of 3% a day at room temperature, but when heated at 80°C total decomposition took place within minutes.

A gas-phase electron diffraction study of SF_5NO_2 was carried out. The preliminary data, as shown in Figure 3, reveal the longest reported S^{VI}–N bond at 1.903(7) Å, which is some 0.2 Å longer than a normal S^{VI}–N single bond. Quantum chemical calculations (HF/6-31 G* and B3LYP/6-311 + G*) predict rather different values for the S^{VI}–N bond from 1.844 Å to 2.049 Å. Further details of this structure[19] will be reported at a later date.

The goal of this research was to synthesize both SF_5NO_2 and SF_5NO. Here, SF_5NO_2 was successfully prepared by two independent methods but SF_5NO remains unknown. Of the two routes used to prepare SF_5NO_2, one employed the novel amine $(SF_5)_3N$ as a starting material while the other started from SF_5Br. Because $(SF_5)_3N$ is extremely difficult to prepare, the second route was the preferred method for preparing gram quantities of SF_5NO_2. Along the way, a modified procedure for preparing SF_5Br on a 500-gram scale was developed.

 © 2006 Wiley-VCH Verlag GmbH & Co. KGaA, Weinheim

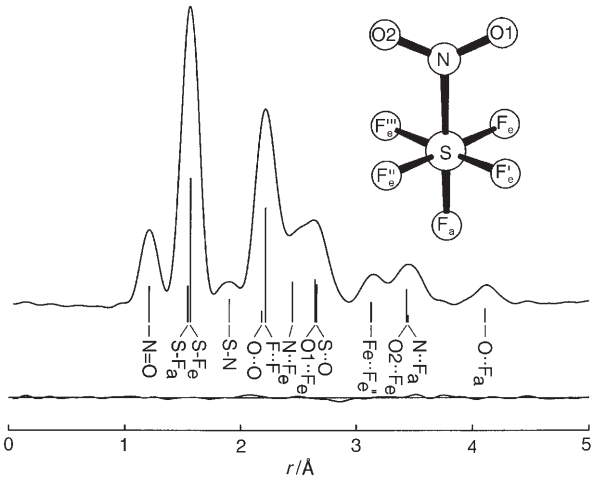


Figure 3. The structure of SF_5NO_2 obtained from gas-phase electron diffraction studies.

The success of the photochemical preparative method for SF_5NO_2 is based on the use of blue light from a diazo lamp ($\lambda_{max} = 420$ nm), as the molecule NO_2 photodissociates at wavelengths shorter than 395 nm as associated with the use of a mercury immersion lamp. The former source of irradiation excites the NO_2 molecule, and the excited NO_2 molecule is believed to further participate in the formation of SF_5 radicals. The molecule SF_5NO_2 has also been studied as a ^{15}N-labeled compound. The IR spectrum of $SF_5{}^{15}NO_2$ shows the expected mass effects of the ^{15}N isotope. The ^{15}N NMR spectrum of $SF_5{}^{15}NO_2$ shows a clear quintet splitting (^{15}N NMR (vs external reference NO_3^- at $\delta = 383$ ppm): $\delta =$ 283.4 ppm (quintet), $^2J(F–N) = 11.6$ Hz), and its ^{19}F NMR spectrum shows additional multiplicities in the equatorial fluorines (AB_4X spin system). The structural data obtained from gas-phase electron diffraction studies indicate the longest S^{VI}-N single bond reported. Further details concerning this study will appear in due course.

Experimental Section

Preparation of SF_5NO_2: Method A: The amine $(SF_5)_3N$ (0.36 g, 0.90 mmol) was transferred under vacuum into a fluorinated ethylene propylene (FEP) tube equipped with a metal valve. Nitrogen dioxide (0.12 g, 2.60 mmol) was then condensed into the FEP tube at −196 °C, and the reaction vessel was allowed to gradually warm to room temperature. After 4 h, all of the $(SF_5)_3N$ crystals had disappeared. The volatile products were subjected to a series of distillations through −105, −130, and −196 °C traps. The −130 °C trap stopped the crude SF_5NO_2. The percentage yield was not calculated owing to the difficult purification of the product.

Method B: SF_5Br (3.9 g, 18.8 mmol) and NO_2 (0.9 g, 19.6 mmol) were transferred to a 4-L or 20-L pyrex reactor. A photolysis chamber with 12 diazo lamps (TL40W/03; each 40 W, 48 inches (ca. 122 cm) long) was used to photolyze this mixture. After 12 h irradiation, the resulting products were condensed into a 300-mL stainless-steel cylinder held at −196 °C. This cylinder was then warmed to dry-ice temperature (−78 °C), and all the materials that are volatile at this temperature were then transferred under vacuum into another cylinder cooled to −196 °C containing 400 grams (large excess) of CsF, which was used to easily remove Br_2, SOF_4, and SF_4 and also to convert NO_2 into FNO. Then, a trap-to-trap distillation through traps at −78 °C, −130 °C, and −196 °C was carried out to separate SF_5NO_2 from impurities such as FNO and SF_6. The product SF_5NO_2 (0.09 g, 0.56 mmol; 3 % yield) was recovered in the trap at −130 °C.

Received: September 19, 2005
Published online: December 30, 2005

Keywords: atmospheric chemistry · fluorine · nitro compounds · photolysis · sulfur

[1] A. Senning, *Sulfur in Organic and Inorganic Chemistry, Vol. 4*, Dekker, New York, **1982**.
[2] O. Lösking, H. Willner, *Angew. Chem.* **1989**, *101*, 1283; *Angew. Chem. Int. Ed. Engl.* **1989**, *28*, 1255.
[3] J. S. Thrasher, K. V. Madappat, *Angew. Chem.* **1989**, *101*, 1285; *Angew. Chem. Int. Ed. Engl.* **1989**, *28*, 1256.
[4] W. T. Sturges, T. J. Wallington, M. D. Hurley, K. P. Shine, K. Sihra, A. Engel, D. E. Oram, S. A. Penkett, R. Mulvaney, C. A. M. Brenninkmeijer, *Science* **2000**, *289*, 611.
[5] M. A. Santoro, *Science* **2000**, *290*, 935.
[6] D. Grossman, *Greenhouse Gas Demystified*, http://www.glrc.org/story.php3?story_id=1100 (accessed July 2001).
[7] M. F. Gerstell, J. S. Francisco, Y. L. Yung, C. Boxe, E. T. Aaltonee, *Proc. Natl. Acad. Sci. USA* **2001**, *98*, 2154.
[8] M. D. Vorb'ev, A. S. Filatov, M. A. Englin, *Zh. Obshch. Khim.* **1974**, *44*, 2724.
[9] "The SF_5, SeF_5, and TeF_5 Groups in Organic Chemistry": D. Lentz, K. Seppelt in *Chemistry of Hypervalent Compounds* (Ed.: K. Akiba), Wiley-VCH, New York, **1999**, pp. 295–325, and reference therein.
[10] R. Winter, R. Terjeson, G. L. Gard, *J. Fluorine Chem.* **1998**, *89*, 105.
[11] "Synthesis of New Amines Containing Pentafluorosulfur Groups": J. B. Nielsen, PhD Dissertation, University of Alabama, Tuscaloosa, **1988**.
[12] a) J. S. Thrasher, J. B. Nielsen, *J. Am. Chem. Soc.* **1986**, *108*, 1108; b) M. R. Choudhury, J. W. Harrell, Jr., J. B. Nielsen, J. S. Thrasher, *J. Chem. Phys.* **1988**, *89*, 5353.
[13] "Preparation, Characterization, and Properties of SF_5NO_2, and Related Compounds": N. Lu, PhD Dissertation, University of Alabama, Tuscaloosa, **2001**.
[14] D. Scheffler, H. Grothe, H. Willner, A. Frenzel, C. Zetzsch, *Inorg. Chem.* **1997**, *36*, 335.
[15] R. Broske, F. Zabel, *J. Phys. Chem. A* **1998**, *102*, 8626.
[16] K. Nakamoto, *Infrared and Raman Spectra of Inorganic and Coordination Compounds*, Wiley, New York, **1986**.
[17] *Gmelin Handbuch, F perfluorhalogenoorgano-Verbindungen, Vol. 8*, Springer, Berlin, **1980**, pp. 2–18, and references therein.
[18] N. Lu, J. S. Thrasher, *J. Fluorine Chem.* **2002**, *117*, 181.
[19] N. Lu, J. S. Thrasher, S. von Ahsen, H. Willner, D. Hnyk, H. Oberhammer, unpublished results.

 © 2006 Wiley-VCH Verlag GmbH & Co. KGaA, Weinheim

Host–Guest Systems

DOI: 10.1002/anie.200503343

Pseudo-Allosteric Recognition of Mandelic Acid with an Enantioselective Coordination Complex**

*Jungseok Heo and Chad A. Mirkin**

Allosteric regulation is a powerful tool utilized efficiently and elegantly in biological systems to control substrate binding and catalysis.[1] Recently, major advances have been made in the design of abiotic supramolecular structures that exhibit allosteric or pseudo-allosteric behavior analogous to their biological counterparts. Sensors capable of signal amplification[2] and asymmetric catalysts with activities and enantioselectivities that can be controlled with allosteric regulators have been designed.[2c,d] Thus far, macrocyclic recognition induced by an allosteric regulator has not been demonstrated. This capability, however, would be a first step towards a system with recognition properties that could be selectively turned on or off with small-molecule coordination chemistry at an allosteric regulatory site.

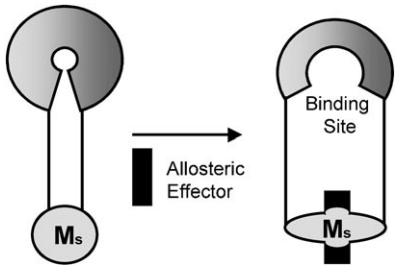
We have developed the weak-link approach (WLA) to supramolecular coordination chemistry.[3–6] This approach utilizes condensed intermediates templated by hemilabile ligands that strategically form both strong and weak coordination bonds with metal centers. Such structures can be selectively and often reversibly opened into flexible macrocycles by reaction with small molecules that break the weak coordination bonds. This ability to use small molecules to interconvert rigid, condensed structures with flexible open macrocycles is ideal for the creation of allosterically regulated systems. A significant advance would be the development of allosteric coordination complexes with chiral recognition elements that could be turned on and off. Such a capability would open avenues for the development of receptors for chemical sensors and separation materials that could selectively recognize, transport, and chemically release target chiral agents. Herein, we report the use of the WLA to synthesize a four-coordinate Cu^{I} complex with chiral recognition for mandelic acid that can be turned on by the chelation of 2,2′-bipyridine (bpy) to the Cu^{I} center in a reaction that concomitantly breaks weak Cu–S links and opens the condensed structure into a 27-membered macrocycle.

[*] Dr. J. Heo, Prof. C. A. Mirkin
Department of Chemistry
and the International Institute for Nanotechnology
2145 Sheridan Road, Evanston, IL, 60208-3113 (USA)
Fax: (+1) 847-467-5123
E-mail: chadnano@northwestern.edu

[**] We are very grateful for support of this work from the NSF and KOSEF and a NIH Director's Pioneer Award for C.A.M.

Supporting information for this article is available on the WWW under http://www.angewandte.org or from the author.

The binaphthyl metallocyclophanes (*S*)-**3** and (*S*)-**4** have been designed for the allosteric recognition of chiral α-hydroxy carboxylic acids (Scheme 1). Compound (*S*)-**4** has two different binding sites, whereas (*S*)-**3** only has one



Scheme 1. The allosteric-effector-mediated shape change of a macrocycle. The structure on the right is capable of the recognition and binding of a target that fits within the cavity. M_s = structural transition-metal center.

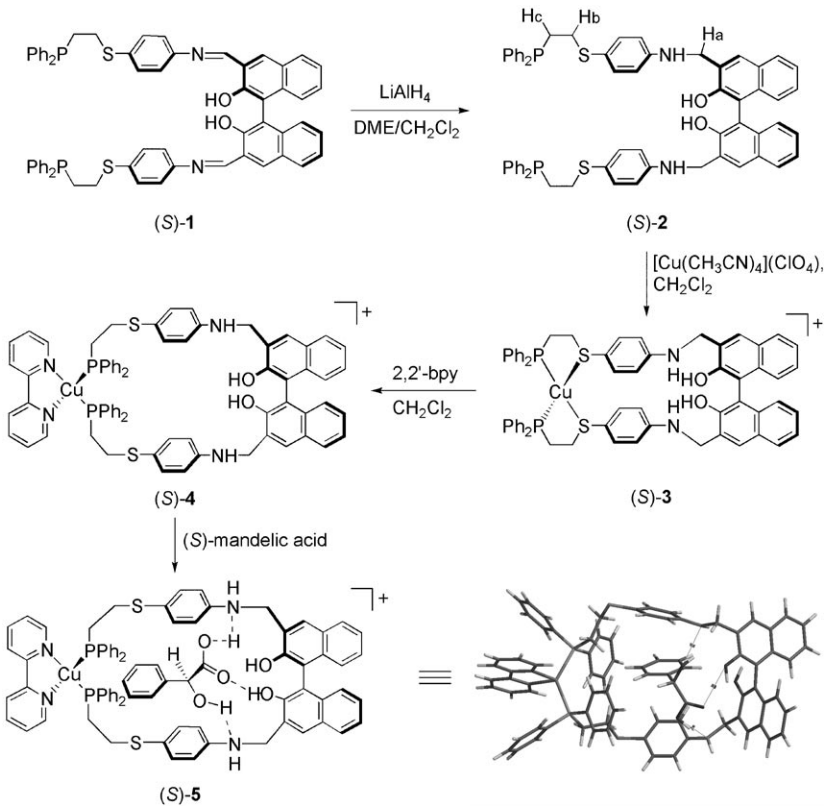
because of its condensed nature. In the case of (*S*)-**4**, one binding site is a $Cu(P,S)_2$ site that allows for allosteric regulation by reaction with 2,2′-bpy. The other is a hydrogen-bonding site for chiral guest molecules, such as mandelic acid derivatives. Therefore, as (*S*)-**3** is converted into (*S*)-**4** by reaction between 2,2′-bpy and the allosteric Cu^{I} regulatory site, a chiral recognition pocket is generated. This structure was designed based upon its resemblance to a bis(binaphthyl) macrocycle, an organic structure known to selectively recognize enantiomers of mandelic acid.[10d]

Enantiomerically pure (*S*)-binol-3,3′-dicarbaldehyde (binol = binaphthol) and 4-(2-diphenylphosphanylethylthio)-phenylamine were coupled by imine condensation (95%) to give (*S*)-**1**, which was reduced with $LiAlH_4$ to give the new amine compound (*S*)-**2** in moderate yield (63%). One equivalent of ligand (*S*)-**2** was treated with one equivalent of $[Cu(CH_3CN)_4](ClO_4)$ in CH_2Cl_2 to form the condensed intermediate (*S*)-**3** in quantitative yield. Compound (*S*)-**3** reacts with 2,2′-bpy (1 equiv) in CH_2Cl_2 to yield (*S*)-**4** cleanly (Scheme 2).

The formation of (*S*)-**4** was evidenced by an upfield shift of the ^1H NMR resonances for the methylene groups of the chelating arms of the tetradentate ligand -$SCH_2CH_2PPh_2$ (Figure 1). These resonances shift from $\delta = 3.00$ and 2.53 ppm to $\delta = 1.86$ and 1.83 ppm, respectively. The binol-CH_2NH_2- resonances exhibit peak splitting[2e,f] that is highly diagnostic of a chiral macrocycle (from a singlet at $\delta =$ 4.46 ppm to two doublets at $\delta = 4.80$ and 4.43 ppm). The $^{31}P\{^1H\}$ NMR spectroscopy of (*S*)-**4** is also consistent with that of a symmetric $[CuP_2(phenanthroline)]$ complex with a singlet at $\delta = -6.4$ ppm.[6b] All other data including ESI mass-spectrometric and elemental analyses are consistent with the proposed structures.

The CD spectrum of (*S*)-**2** exhibits a characteristic positive couplet, which is similar to that of (*S*)-binol, because of the exciton coupling between the long-axis polarized ^1B_b transition, with a positive maximum at 237 nm and a negative minimum at 226 nm (Figure 2). A further negative band at 205 nm was observed and corresponds to a higher energy ^1B_a

 © 2006 Wiley-VCH Verlag GmbH & Co. KGaA, Weinheim InterScience



Scheme 2. Synthesis of chiral macrocycles (*S*)-**3** and (*S*)-**4**. Proposed structure for mandelic acid complexed macrocycle (*S*)-**5**.[13]

pocket is closed and the multiple hydrogen-bonding sites required to complex mandelic acid are not accessible.

In contrast, open complex (*S*)-**4** can accommodate mandelic acid, and the fluorescence intensity of (*S*)-**4** increases in the presence of (*S*)- or (*R*)-mandelic acid. This increase in fluorescence is due to the suppressed photoinduced electron-transfer fluorescence quenching as the amine nitrogen atom of (*S*)-**4** is protonated by the acid (Figure 3b).[7–9] In solution with CH_2Cl_2 (containing 2% of 1,2-dimethoxyethane (DME)), the fluorescence intensity of (*S*)-**4** (1.0×10^{-4} M) was increased 3.1-fold upon treatment of (*S*)-mandelic acid (5.0×10^{-3} M), but only 1.9-fold for (*R*)-mandelic acid (5.0×10^{-3} M). The net fluorescence intensity increase of (*S*)-**4** by (*S*)-mandelic acid was 2.33 times that by (*R*)-mandelic acid.[14] When (*S*)-**4** (1.0×10^{-4} M) was treated with mandelic acid in the concentration range of 5.0×10^{-3} to 2.0×10^{-2} M, the fluorescence enhancement of the open complex exhibits a Benesi–Hildebrand-type relationship.[12] Thus, the association constant of (*S*)-**4**/(*S*)-mandelic acid was found to be 764 M^{-1}, whereas that of (*S*)-**4**/(*R*)-mandelic acid was 367 M^{-1}. This result indicates that the complex (*S*)-**4**/(*S*)-mandelic acid is more stable than (*S*)-**4**/(*R*)-mandelic acid by approximately 0.43 kcal mol^{-1} ($\Delta\Delta G$).

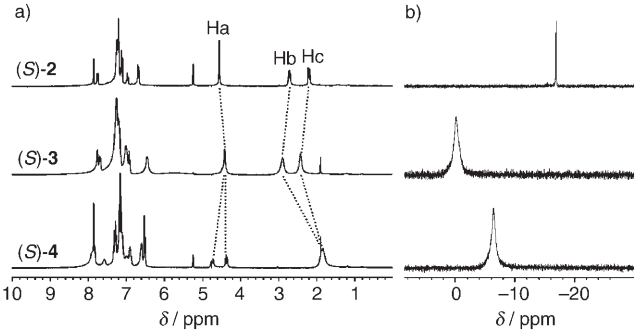


Figure 1. a) ^{1}H NMR spectra of (*S*)-**2**, (*S*)-**3**, and (*S*)-**4**; b) corresponding $^{31}P\{^1H\}$ NMR spectra.

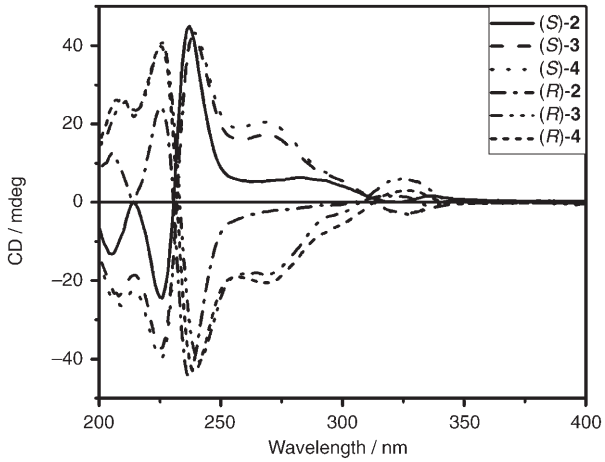


Figure 2. Circular dichroism (CD) spectra of **2**–**4** in acetonitrile.

transition.[11] Compounds (*S*)-**3** and (*S*)-**4** displayed additional positive maxima at 270 nm which can be attributed to a chiral arrangement of the PPh_2 group at the Cu^I center. The CD spectra of (*S*)-**3** and (*S*)-**4** are very similar, thus suggesting that there is very little change in the chirality and dihedral angle of the binol center.

To study the allosteric effect, closed complex (*S*)-**3** and open complex (*S*)-**4** were independently treated with both enantiomers of mandelic acid and monitored by fluorometric analysis.[10] First, (*S*)-**3** (1.0×10^{-4} M) was treated with a 50-fold excess of (*S*)- or (*R*)-mandelic acid (5.0×10^{-3} M). In both cases, no significant changes in the fluorescence intensities were observed (Figure 3a), which is because the binding

Enantiomerically pure (*R*)-binol macrocycles also were synthesized and analyzed for the binding of mandelic acid. Closed complex (*R*)-**3** and open complex (*R*)-**4** were independently treated with both enantiomers of mandelic acid and monitored by fluorometric analysis. In accordance with the titration study of (*S*)-**3** with mandelic acid, no enhanced fluorescence for (*R*)-**3** was observed with the addition of excess mandelic acid. Open macrocycle (*R*)-**4** demonstrated selectivity opposite to that of (*S*)-**4**. The association constant of (*R*)-**4**/(*R*)-mandelic acid was found to be 763 M^{-1}, whereas

 © 2006 Wiley-VCH Verlag GmbH & Co. KGaA, Weinheim

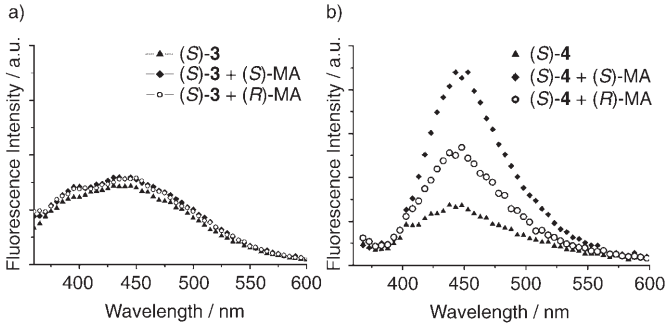


Figure 3. Fluorescence spectra of a) (*S*)-**3** (1.0×10^{-4} M) with/without mandelic acid (MA; 5.0×10^{-3} M, $\lambda_{ex}=360$ nm) and b) (*S*)-**4** (1.0×10^{-4} M) with/without mandelic acid (5.0×10^{-3} M, $\lambda_{ex}=360$ nm).

that of (*R*)-**4**/(*S*)-mandelic acid was 376 M^{-1}. This result indicates that the complex (*R*)-**4**/(*R*)-mandelic acid is more stable than (*R*)-**4**/(*S*)-mandelic acid by approximately 0.42 kcal mol^{-1} ($\Delta\Delta G$).

The chiral ligand (*S*)-**2** shows no selectivity for either (*S*)- or (*R*)-mandelic acid as evidenced by a 3.1-fold fluorescence enhancement for both enantiomers at 373 nm ($\lambda_{ex}=330$ nm). This lack of enantioselectivity is due to the flexible nature of the ligand and demonstrates the importance of macrocycle formation.

In conclusion, a novel synthetic strategy for the construction of an enantioselective fluorescent receptor that features heterotropic positive pseudo-allosterism has been demonstrated. This type of receptor design could be useful in the development sensors and materials that can be used in facilitated transport or molecular mixture separations.

Experimental Section

(*S*)-**1**: 2,2′-Dihydroxy-[1,1′]binaphthalenyl-3,3′-dicarbaldehyde (700 mg, 2.04 mmol), 4-(2-diphenylphosphanylethylthio)phenylamine (1.38 g, 4.10 mmol), CH_2Cl_2 (30 mL), and methanol (50 mL) were added to a Schlenk flask. The resulting solution was heated to reflux for 24 h. The reaction mixture was dried in vacuo, and the resulting orange solid was purified by column chromatography (eluent: CH_2Cl_2), yield = 1.94 g (95 %). ^{1}H NMR (300 MHz, CD_2Cl_2): $\delta=13.11$(s, 2H, OH), 8.85 (s, 2H, N=CH), 8.09 (s, 2H, aromatic), 7.87 (m, 2H, aromatic), 7.35–7.11 (m, 34H, aromatic), 2.89 (m, 4H, H_2C-S), 2.30 ppm (m, 4H, H_2C-P); ^{13}C{^{1}H} NMR (75.5 MHz, CD_2Cl_2): $\delta=162.57$ (s), 154.74 (s), 146.12 (s), 138.01 (d, J(P-C) = 13.5 Hz), 135.75 (d, J(P-C) = 15.8 Hz), 132.96 (br, m), 130.02 (br, m), 128.82 (br, m), 127.93 (s), 124.77 (br, m), 123.80 (br, m), 121.99 (br, m), 121.54 (s), 117.01 (s), 30.31 (d, J(P-C) = 24.0 Hz), 28.28 ppm (d, J(C-P) = 16.5 Hz); ^{31}P{^{1}H} NMR (121.4 MHz, CD_2Cl_2): $\delta=-16.3$ ppm (s); EI MS (*m*/*z*) calcd: 980.28; found: 981.4; elemental analysis (%) calcd for $C_{62}H_{50}N_2O_2P_2S_2\cdot H_2O$: C 74.53, H 5.25, N 2.80; found: C 74.43, H 5.00, N 2.78.

(*S*)-**2**: $LiAlH_4$ (3.0 equiv) was suspended in a solution of (*S*)-**1**·H_2O (3.477 g, 3.48 mmol) in CH_2Cl_2/DME (30 mL/30 mL) at 0 °C. The reaction mixture was stirred overnight at room temperature and quenched with water (20 mL). Volatiles were evaporated under reduced pressure, more water (100 mL) was added, and the reaction mixture extracted with CH_2Cl_2 (3 × 100 mL). The combined organic layers were washed with brine and water. The separated organic layer was concentrated under reduced pressure and dried over Na_2SO_4. Filtration and purification by column chromatography gave the monohydrated amine ligand as a yellow microcystalline solid (eluent: CH_2Cl_2), yield = 2.19 g (63 %). ^{1}H NMR (300 MHz, CD_2Cl_2): $\delta=7.86$ (s, 2H, aromatic), 7.76 (d, 2H, aromatic), 7.27–7.11 (m, 28H, aromatic), 6.98 (d, 2H, aromatic), 6.66 (d, 4H, aromatic), 4.54 (s, 4H, H_2C-NH), 2.76 (m, 4H, H_2C-S), 2.20 ppm (m, 4H, H_2C-P); ^{13}C{^{1}H} NMR (CD_2Cl_2): $\delta=152.03$ (s), 147.39 (s), 138.23 (d, J(P-C) = 14.3 Hz), 133.91 (br, m), 133.34 (s), 132.89 (br, m), 129.25 (br, m), 128.80 (br, m), 126.93 (s), 124.40 (br, m), 123.51 (s), 115.04 (br, m), 113.39 (s), 46.20 (s), 32.81 (s), 28.41 ppm (s); ^{31}P{^{1}H} NMR (121.4 MHz, CD_2Cl_2): $\delta=-16.9$ ppm (s); EI-MS (*m*/*z*) calcd: 985.2; found: 985.2; elemental analysis (%) calcd for $C_{62}H_{54}N_2O_2P_2S_2\cdot H_2O$: C 74.23, H 5.63, N 2.79; found: C 74.22, H 5.44, N 2.68.

(*S*)-**3**: In a Schlenk flask, (*S*)-**2** (295 mg, 0.299 mmol) was dissolved in CH_2Cl_2 (10 mL), and a solution of $[Cu(MeCN)_4](ClO_4)$ (98 mg, 0.300 mmol) in CH_2Cl_2 (10 mL) was added through a cannula to give a colorless solution. The solvent was removed under reduced pressure after stirring for 12 h, and the resulting white solid was dried at 150 °C under vacuum to give a yellowish sticky solid. Recrystallization from CH_2Cl_2/Et_2O afforded an analytically pure compound (as determined by NMR spectroscopy) in quantitative yield (322 mg, 94 %). ^{1}H NMR (300 MHz, CD_2Cl_2): $\delta=7.75$(s, 2H, aromatic), 7.68 (d, 2H, aromatic), 7.25–6.92 (m, 28H, aromatic), 6.45 (s, 4H, aromatic), 4.41 (br, 4H, H_2C-NH), 2.89 (br, 4H, H_2C-S), 2.42 ppm (br, 4H, H_2C-P); ^{13}C{^{1}H} NMR (CD_2Cl_2): $\delta=151.71$ (s), 149.50 (s), 134.49 (br, m), 133.07 (s), 132.50 (br, m), 130.88 (br, m), 129.29 (br, m), 127.05 (s), 126.76 (m), 124.19 (br, m), 116.32 (m), 114.47 (br, m), 112.85 (s), 100.09 (s), 44.99 (br, m), 38.15 (br, m), 28.56 ppm (br, m); ^{31}P{^{1}H} NMR (121.4 MHz, CD_2Cl_2): $\delta=-0.2$ ppm (s); ESI MS (*m*/*z*) calcd: 1047.2; found: 1047.2; elemental analysis (%) calcd for $C_{62}H_{54}N_2O_6P_2S_2ClCu\cdot H_2O$: C 63.85, H 4.84, N 2.40; found: C 64.07, H 4.77, N 2.40.

(*S*)-**4**: In a Schlenk flask, the copper complex (*S*)-**3** (103 mg, 0.0897 mmol) and 2,2′-bipyridine (14 mg, 1 equiv) were dissolved in CH_2Cl_2 (5.0 mL) to give a yellow solution. The solvent was removed after stirring for 1 h to yield an analytically pure yellow solid in quantitative yield (114 mg, 97 %). ^{1}H NMR (300 MHz, CD_2Cl_2): $\delta=$ 7.86 (m, br, 8H, aromatic), 7.57 (s, br, 2H, aromatic), 7.31–7.11 (m, 22H, aromatic), 6.99 (s, br, 2H, aromatic), 6.90 (s, br, 4H, aromatic), 6.52–6.49 (m, 4H, aromatic), 4.74 (d, 2H, ^3J(H-H) = 13.8 Hz, H_2C-NH), 4.36 (d, 2H, ^3J(H-H) = 14.4 Hz, H_2C-NH), 1.86 (br, 4H, H_2C-S), 1.82 ppm (br, 8H, H_2C-P); ^{13}C{^{1}H} NMR (CD_2Cl_2): $\delta=153.19$ (s), 148.75 (s), 139.95 (br, m), 135.76 (br, m), 134.41 (s), 132.87 (br, m), 132.34 (br, m), 129.68 (br, m), 127.84 (s), 126.72 (br, m), 124.12 (br, m), 121.31 (s), 115.31 (br, m), 46.74 (br, m), 32.41 (br, m), 28.19 ppm (br, m). ^{31}P{^{1}H} NMR (121.4 MHz, CD_2Cl_2): $\delta=-6.4$ (s); ESI MS (*m*/*z*) calcd: 1203.3; found: 1203.4; elemental analysis (%) calcd for $C_{72}H_{62}N_4O_6P_2S_2ClCu\cdot H_2O$: C 65.40, H 4.88, N 4.24; found: C 65.67, H 4.87, N 4.30.

Fluorescence measurements: Both enantiomers of mandelic acid were purchased from Aldrich and purified according to literature procedures.[10c] A stock solution of mandelic acid (0.1 M in CH_2Cl_2 containing 10 % DME), a stock solution of fluorophore (2.0 mM in CH_2Cl_2), and DME were mixed and diluted to the desired concentration in a volumetric flask. DME was used to enhance the solubility of mandelic acid, and the concentration was adjusted to 2 %. All of the samples were prepared under air-free conditions, and air-free cuvettes were used to prevent oxidation of the sensor molecule.

Received: September 20, 2005
Published online: December 30, 2005

Keywords: allosterism · coordination modes · enantioselectivity · fluorescence · host–guest systems

[1] a) A. W. Lim, *Curr. Opin. Struct. Biol.* **2002**, *12*, 61–68; b) B. Kobe, B. E. Kemp, *Nature* **1999**, *402*, 373–376.

 © 2006 Wiley-VCH Verlag GmbH & Co. KGaA, Weinheim

[2] a) L. Kovbasyuk, R. Krämer, *Chem. Rev.* **2004**, *104*, 3161 – 3187; b) A. Saghatelian, K. M. Guckian, D. A. Thayer, M. R. Ghadiri, *J. Am. Chem. Soc.* **2003**, *125*, 344 – 345; c) N. C. Gianneschi, P. A. Bertin, S. T. Nguyen, C. A. Mirkin, L. N. Zakharov, A. L. Rheingold, *J. Am. Chem. Soc.* **2003**, *125*, 10508 – 10509; d) N. C. Gianneschi, S. H. Cho, S. T. Nguyen, C. A. Mirkin, A. L. Rheingold, *Angew. Chem.* **2004**, *116*, 5619 – 5623; *Angew. Chem. Int. Ed.* **2004**, *43*, 5503 – 5507; e) T. Nabeshima, Y, Yoshihira, T. Saiki, S. Akine, E. Horn, *J. Am. Chem. Soc.* **2003**, *125*, 28 – 29; f) T. Nabeshima, T. Imaba, N. Furukawa, T. Hosoya, Y. Yano, *Inorg. Chem.* **1993**, *32*, 1407 – 1416; g) M. J. E. Resendiz, J. C. Noveron, H. Disteldorf, S. Fischer, P. J. Stang, *Org. Lett.* **2004**, *6*, 651 – 653; h) M. Yoshizawa, M. Tamura, M. Fujita, *J. Am. Chem. Soc* **2004**, *126*, 6846 – 6847.

[3] a) J. R. Farrell, C. A. Mirkin, I. A. Guzei, L. M. Liable-Sands, A. L. Rheingold, *Angew. Chem.* **1998**, *110*, 484 – 487; *Angew. Chem. Int. Ed.* **1998**, *37*, 465 – 467; b) B. J. Holliday, J. R. Farrell, C. A. Mirkin, K.-C. Lam, A. L. Rheingold, *J. Am. Chem. Soc.* **1999**, *121*, 6316 – 6317; c) M. V. Ovchinnikov, B. J. Holliday, C. A. Mirkin, L. N. Zakharov, A. L. Rheingold, *Proc. Natl. Acad. Sci. USA* **2002**, *99*, 4927 – 4931; d) N. C. Gianneschi, M. S. Marsar, III, C. A. Mirkin, *Acc. Chem. Res.* **2005**, *38*, 825–837.

[4] J. R. Farrell, A. H. Eisenberg, C. A. Mirkin, I. A. Guzei, L. M. Liable-Sands, C. D. Incarvito, A. L. Rheingold, C. L. Stern, *Organometallics* **1999**, *18*, 4856 – 4868.

[5] a) A. H. Eisenberg, F. M. Dixon, C. A. Mirkin, C. L. Stern, C. D. Incarvito, A. L. Rheingold, *Organometallics* **2001**, *20*, 2052 – 2058; b) X. Liu, A. H. Eisenberg, C. L. Stern, C. A. Mirkin, *Inorg. Chem.* **2001**, *40*, 2940 – 2941; c) C. S. Slone, D. A. Weinberger, C. A. Mirkin, *Prog. Inorg. Chem.* **1999**, *48*, 233 – 350.

[6] a) F. M. Dixon, A. H. Eisenberg, J. R. Farrell, C. A. Mirkin, L. M. Liable-Sands, A. L. Rheingold, *Inorg. Chem.* **2000**, *39*, 3432 – 3433; b) M. S. Masar III, C. A. Mirkin, C. L. Stern, L. N. Zakharov, A. L. Rheingold, *Inorg. Chem.* **2004**, *43*, 4693 – 4701.

[7] a) S. S. Peacock, D. M. Walba, F. C. A. Caeta, R. C. Helgeson, D. J. Cram, *J. Am. Chem. Soc.* **1980**, *102*, 2043 – 2052; b) Y. Naruta, F. Tani, N. Ishihara, K. Maruyama, *J. Am. Chem. Soc.* **1991**, *113*, 6865 – 6872; c) Y. Kubo, Y. S. Maeda, S. Tokita, M. Kubo, *Nature* **1996**, *382*, 521 – 524.

[8] a) A. Hu, H. L. Ngo, W. Lin, *J. Am. Chem. Soc.* **2003**, *125*, 11490 – 11491; b) S. J. Lee, A. Hu, W. Lin, *J. Am. Chem. Soc.* **2002**, *124*, 12948 – 12949; c) S. J. Lee, W. Lin, *J. Am. Chem. Soc.* **2002**, *124*, 4554 – 4555; d) J. Hua, W. Lin, *Org. Lett.* **2004**, *6*, 861 – 864.

[9] T. D. James, K. R. A. S. Sandanayake, S. Shinkai, *Nature* **1995**, *374*, 345 – 347.

[10] a) L. Pu, *Chem. Rev.* **2004**, *104*, 1687 – 1716; b) M.-H. Xu, J. Lin, Q.-S. Hu, L. Pu, *J. Am. Chem. Soc.* **2002**, *124*, 14239 – 14246; c) J. Lin, J. Q.-S. Hu, M.-H. Xu, L. Pu, *J. Am. Chem. Soc.* **2002**, *124*, 2088 – 2089; d) J. Lin, H.-C. Zhang, L. Pu, *Org. Lett.* **2002**, *4*, 3297 – 3300.

[11] a) G. Pescitelli, L. Di Bari, P. Salvadori, *Organometallics* **2004**, *23*, 4223 – 4229; b) C. Rosini, C. S. Stefano, H. W. I. Peering, E. W. Meijer, *Eur. J. Org. Chem.* **2000**, 61 – 71; c) W. Hug, F. Ciardelli, Jr., I. Tinoco, *J. Am. Chem. Soc.* **1974**, *96*, 3407 – 3410.

[12] H. A. Benesi, J. H. Hildebrand, *J. Am. Chem. Soc.* **1949**, *71*, 2703 – 2707.

[13] JAGUAR program was used for calculations of the structure optimization; Jaguar 4.1, Schrodinger, Inc., Portland, OR, **2000**.

[14] $ef = (I_S - I_0)/(I_R - I_0) = 2.33$.

 © 2006 Wiley-VCH Verlag GmbH & Co. KGaA, Weinheim

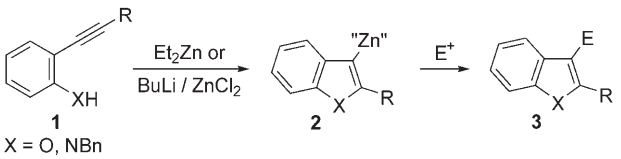
Heterocycles

DOI: 10.1002/anie.200502920

3-Zinciobenzofuran and 3-Zincioindole: Versatile Tools for the Construction of Conjugated Structures Containing Multiple Benzoheterole Units**

Masaharu Nakamura, Laurean Ilies, Saika Otsubo, and Eiichi Nakamura**

Functionalized benzoheteroles, such as benzofuran and indole, form the core of natural products and serve as promising units in materials science.[1] In the latter applications, conjugated compounds containing one or more benzoheterole units are attracting particular attention.[2] A potentially general approach to this class of compounds is the cyclization of a metal 2-ynyl phenolate or 2-ynyl anilide **1** to a 3-metallobenzoheterole intermediate **2** that reacts further with an electrophile to produce the corresponding heterole **3** (Scheme 1). We report herein the virtually quantitative



Scheme 1. Cyclization of a 2-alkynyl phenol or aniline to a 3-zinciobenzoheterole. Bn = benzyl; E^+ = electrophile.

cyclization of **1** into a zinc compound **2** and its use in the concise synthesis of a variety of new benzoheterole conjugated systems (cf. Table 2). Such a cyclization has been known for the synthesis of some 3-metallobenzofuran intermediates (metal = Li, Hg,[3] and Pd[4]), but not in the indole series.[5] The value of the present zinc-mediated chemistry resides in the high yield of the cyclization and the versatility of the resulting zinc compounds **2** in synthesis of a library of new multiple benzoheterole conjugated systems.

The incorporation of a zinc atom to obtain **2**, which is stable yet reactive in the presence of a catalyst, was critical to

[*] Prof. Dr. M. Nakamura, L. Ilies, S. Otsubo, Prof. Dr. E. Nakamura
Department of Chemistry
The University of Tokyo
and Nakamura Functional Carbon Cluster Project ERATO
Japan Science and Technology Agency
Hongo, Bunkyo-ku, Tokyo 113-0033 (Japan)
Fax: (+81) 3-5800-6889
E-mail: masaharu@chem.s.u-tokyo.ac.jp
nakamura@chem.s.u-tokyo.ac.jp

[**] We thank the Ministry of Education, Culture, Sports, Science, and Technology of Japan for financial support, a scholarship (L.I.) and for the 21st Century COE Program for Frontiers in Fundamental Chemistry.

Supporting information for this article is available on the WWW under http://www.angewandte.org or from the author.

InterScience
© 2006 Wiley-VCH Verlag GmbH & Co. KGaA, Weinheim

success, as it was for the addition of a zinc enamide and enolate to an unactivated alkene or alkyne.[6] Deprotonation of a 2-alkynyl phenol **1a–f** with 0.5 equivalents of Et_2Zn followed by heating in the presence of a catalytic amount of *N*,*N*,*N*′,*N*′-tetramethylethylenediamine (TMEDA) in refluxing toluene effected smooth cyclization into 2-substituted benzofurans **3a–f** (E = H), which were isolated after quenching the reaction mixture with aqueous ammonium chloride. We observed 97% deuterium incorporation (R = Ph) after quenching the reaction mixture with deuterium chloride. The reaction afforded 2-aryl, heteroaryl, vinyl, and alkoxymethyl benzofurans in almost quantitative yields (Table 1, entries 1–6), except sterically hindered 2-*tert*-butylbenzofuran (**3c**), which was obtained in 50% yield. Zinc phenoxides are known to form oligomeric aggregates,[7] and therefore TMEDA is thought to activate the aggregate by partially breaking the coordination between the oxygen and zinc atoms. We have so far been unable to cyclize either phenol **1**, in which R = H, likely because of the high acidity of the free acetylenic proton, or the phenol in which R = Me_3Si, as it resists cyclization and premature loss of the silyl group results. We have previously shown that a silicon group retards the reaction taking place with such regiochemistry.[8]

Table 1: Cyclization of a 2-alkynyl phenol or aniline to form a benzoheterole **3** (E = H).

Entry	X	R	**1**	*t*	Yield [%][a]	Product
1	O	Ph	**1a**	1 h	94	**3a**
2	O	*n*Bu	**1b**	1 h	99	**3b**
3	O	*t*Bu	**1c**	3 days	50	**3c**[b]
4	O	*E*-styryl	**1d**	1 h	99	**3d**
5	O	2-thienyl	**1e**	3 h	93	**3e**
6	O	CH_2OMOM[c]	**1f**	1 h	98	**3f**
7	NBn	Ph	**1g**	1 h	99	**3g**

[a] Yield of the isolated product. [b] Starting material **1c** was recovered in 31% yield. [c] MOM = methoxymethyl.

A slightly modified method was found to be useful for the indole synthesis. Deprotonation of *N*-benzyl-protected alkynyl aniline **1g** with butyllithium,[9] followed by treatment with zinc chloride and heating for one hour in toluene quantitatively generated 2-substituted 3-zincioindole, which was quenched with ammonium chloride to give 2-phenylindole in 99% yield (Table 1, entry 7). When the reaction mixture was quenched with deuterium chloride, 95% deuterium incorporation at the mechanistically expected 3 position was observed. TMEDA was not necessary for the cyclization of indoles, presumably because the corresponding zinc anilides tend not to form unreactive aggregates like the related zinc phenoxides.[10]

The zinc intermediate **2** is a useful building block for the construction of various conjugated structures with 2,3-disubstituted benzoheteroles as a key structural motif. After screening several catalyst systems, we found that various aryl and alkenyl halides readily couple with **2** in the presence of $[Pd_2(dba)_3]\cdot CHCl_3$ (dba = dibenzylideneacetone; 5 mol%) and $P(tBu)_3$ (20 mol%; Table 2).[11] The reactions of the 3-zinciobenzofuran intermediate are described first: The reaction with iodobenzene and (*E*)-bromostyrene took place quantitatively to give 2,3-diphenylbenzofuran (**4**)[12] and 2-phenyl-3-(*E*)-phenylethenylbenzofuran (**10**; entries 1 and 7, respectively). The synthetic merit of the zinc methodology is demonstrated in the reactions with polyhaloarenes, which afforded compounds inaccessible by known methods. For example, two or three benzofuran moieties can be introduced in a single step to a benzene ring to yield molecules containing seven and ten aromatic rings (**5** and **7**, 87 and 74% yield of the isolated products, respectively; entries 2 and 4). Molecular-modeling studies suggest intrinsic nonplanarity of these compounds owing to the steric repulsion of substituents on the benzofuran rings, which makes a chiral propeller conformation for tribenzofuran **7** favorable (see the Supporting Information). The present method provides easy access to asymmetrically substituted compounds, such as **6**, by using two different zinc benzofuran compounds. Thus, zinc intermediates **2a** and **2e** were treated sequentially with 1-bromo-4-iodobenzene to give a mixed-furan compound **6** in 82% yield (entry 3). Similarly, we synthesized **8** and **9** with benzofuran-thiophene-benzofuran alternating units in 89 and 67% yield, respectively (entries 5 and 6) by starting with 2,5-diiodothiophene. 1,2-Dibromoethene afforded an ethylene-linked benzofuran **11** and a highly conjugated benzofuran **12** in high yield (entries 8 and 9). The olefin geometry in the starting dibromide was retained in the product. Some of these compounds show intense fluorescence both in solution and in the solid state because of the extended conjugation and nonplanarity; this property will be an interesting future subject of materials-related studies.

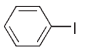
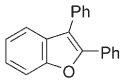
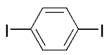
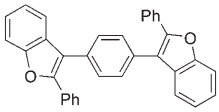
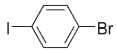
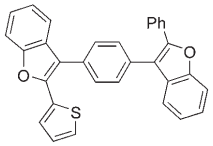
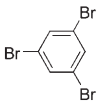
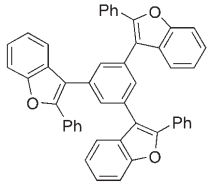
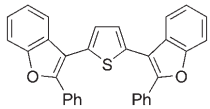
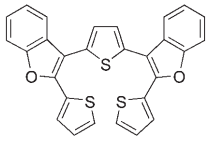
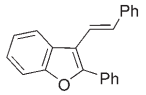
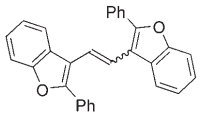
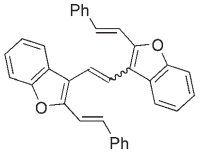
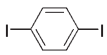
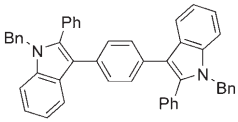
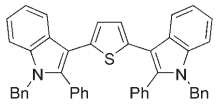
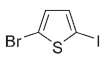
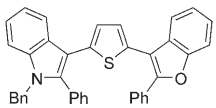
Next, we examined the scope of this coupling protocol for the 3-zincioindole reagent (Table 2, entries 10–12). Coupling of the zinc intermediate **2g** with 1,4-diiodobenzene and 2,5-diiodothiophene in the presence of the Pd^0 catalyst gave the conjugated bisindoles **13** and **14** in excellent yield. We could also synthesize a indole-thiophene-benzofuran ternary compound **15** by allowing zinciobenzofuran **2a** and zincioindole **2g** to react sequentially in one pot with 2-bromo-5-iodothiophene (entry 12).

In conclusion, we have developed an efficient and general synthetic method for 3-metallated 2-substituted benzoheteroles and their use in the preparation of molecules containing multiple benzofuran and indole units. The rather low reactivity of the zinc phenoxides in the absence of TMEDA is probably due to the propensity of zinc phenoxides to form coordinatively saturated oxygen-bridged aggregates, in contrast to the corresponding zinc anilides. The high reactivity of the 3-metallobenzoheterole reported above suggests that other the standard techniques in organozinc chemistry[13] could contribute to expanding the utility of our heteroaromatic zinc reagents. The nonplanar, multiaromatic ring systems suggest their potential as new chiral scaffolds to be exploited in asymmetric synthesis. We expect the present methodology to be applicable to other heterocyclic systems, such as benzothiophenes and benzosiloles, and to provide a variety of new compounds for various applications.

Received: August 17, 2005
Published online: December 30, 2005

 © 2006 Wiley-VCH Verlag GmbH & Co. KGaA, Weinheim

Table 2: Conjugated compounds obtained by Pd-catalyzed coupling with halides.

Entry	Phenol	Electrophile	Coupling product		Yield [%][a]
1	**1a**			**4**	99
2	**1a**			**5**	87
3	**1a** **1e**			**6**	82[b]
4	**1a**[c]			**7**	74
5	**1a**			**8**	89
6	**1e**			**9**	67
7	**1a**			**10**	94
8	**1a**			**11**	92
9	**1d**			**12**	88
10	**1g**			**13**	93
11	**1g**			**14**	91
12	**1a** **1g**			**15**	48

[a] Yield of the isolated products. [b] Symmetric coupling products were obtained in about 15% yield (GC analysis). [c] 10 mol% of palladium and 40 mol% of $P(tBu)_3$ were used. [d] $E/Z = 43:57$, as determined by ^1H NMR spectroscopic analysis.

Keywords: benzoheterole · conjugation · cyclization · heterocycles · palladium · zinc

[1] a) A. R. Katritzky, *Comprehensive Heterocyclic Chemistry, Vol. 4*, Part 3, Pergamon, Oxford, **1984**, pp. 658–712; b) A. Williams, *Furans, Synthesis and Applications*, Noyes Data Corporation, Park Ridge, NJ, **1973**, pp. 1–303.

[2] a) S. Anderson, P. N. Taylor, G. L. B. Verschoor, *Chem. Eur. J.* **2004**, *10*, 518–527; b) K. Nozaki, K. Takahashi, K. Nakano, T. Hiyama, H.-Z. Tang, M. Fujiki, S. Yamaguchi, K. Tamao, *Angew. Chem.* **2003**, *115*, 2097–2099; *Angew. Chem. Int. Ed.* **2003**, *42*, 2051–2053; c) C. Xu, A. Wakamiya, S. Yamaguchi, *Org. Lett.* **2004**, *6*, 3707–3710; d) R. de Bettignies, Y. Nicolas, P. Blanchard, E. Levillain, J.-M. Nunzi, J. Roncali, *Adv. Mater.* **2003**, *15*, 1939–1943.

[3] a) M. Inoue, M. W. Carson, A. J. Frontier, S. J. J. Danishefsky, *J. Am. Chem. Soc.* **2001**, *123*, 1878–1889; b) C. R. Larock, L. W. Harrison, *J. Am. Chem. Soc.* **1984**, *106*, 4218–4227; c) H. Gilman, D. S. Melstrom, *J. Am. Chem. Soc.* **1948**, *70*, 1655–1657.

[4] For example: a) Y. Hu, Y. Zhang, Z. Yang, R. J. Fathi, *Org. Chem.* **2002**, *67*, 2365–2368; b) A. Arcadi, S. Cacchi, G. Fabrizi, F. Marinelli, L. Moro, *Synlett* **1999**, 1432–1434; c) A. Arcadi, S. Cacchi, M. Del Rosario, G. Fabrizi, F. Marinelli, *J. Org. Chem.* **1996**, *61*, 9280–9288; d) Y. Kondo, F. Shiga, N. Murata, T. Sakamoto, H. Yamanaka, *Tetrahedron* **1994**, *50*, 11803–11812.

[5] a) M. Amat, S. Sathyanarayana, S. Hadida, J. Bosch, *Heterocycles* **1996**, *43*, 1713–1718; b) C. E. Reck, A. Bretschneider-Hurley, M. J. Heeg, C. H. Winter, *Organometallics* **1998**, *17*, 2906–2911; c) J. I. DeGraw, J. G. Kennedy, W. A. Skinner, *J. Heterocycl. Chem.* **1966**, *3*, 67–69; d) P. G. Ciattini, E. Morera, G. Ortar, *Tetrahedron Lett.* **1997**, *38*, 2405–2408; e) M. Amat, S. Hadida, J. Bosch, *Tetrahedron Lett.* **1994**, *35*, 793–796.

[6] a) M. Nakamura, T. Fujimoto, K. Endo, E. Nakamura, *Org. Lett.* **2004**, *6*, 4837–4840; b) M. Nakamura, C. Liang, E. Nakamura, *Org. Lett.* **2004**, *6*, 2015–2017; c) M. Nakamura, T. Hatakeyama, E. Nakamura, *J. Am. Chem. Soc.* **2004**, *126*, 11820–11825; d) M. Nakamura, K. Endo, E. Nakamura, *J. Am. Chem. Soc.* **2003**, *125*, 13002–13003; e) M. Nakamura, T. Hatakeyama, K. Hara, E. Nakamura, *J. Am. Chem. Soc.* **2003**, *125*, 6362–6363.

[7] a) M. Nakamura, A. Hirai, E. Nakamura, *J. Am. Chem. Soc.* **2003**, *125*, 2341–2350; b) A. B. Charette, C. Molinaro, C. Brochu, *J. Am. Chem. Soc.* **2001**, *123*, 12160–12167; c) M. M. Olmstead, P. P. Power, S. C. Shoner, *J. Am. Chem. Soc.* **1991**, *113*, 3379–3385.

[8] E. Nakamura, Y. Miyachi, N. Koga, K. Morokuma, *J. Am. Chem. Soc.* **1992**, *114*, 6686–6692.

[9] Diethylzinc is too weak as a base to deprotonate the amine.

[10] A. Erxleben, *Inorg. Chem.* **2001**, *40*, 208–213.

 © 2006 Wiley-VCH Verlag GmbH & Co. KGaA, Weinheim

[11] a) C. Dai, G. C. Fu, *J. Am. Chem. Soc.* **2001**, *123*, 2719–2724; b) T. Yamamoto, M. Nishiyama, Y. Koie, *Tetrahedron Lett.* **1998**, *39*, 2367–2370.
[12] Y. Hu, K. J. Nawoschik, Y. Liao, J. Ma, R. Fathi, Z. Yang, *J. Org. Chem.* **2004**, *69*, 2235–2239.
[13] a) P. Knochel, P. Jones, *Organozinc Reagents*, Oxford University Press, New York, **1999**; b) E. Erdik, *Organozinc Reagents in Organic Synthesis*, CRC, New York, **1996**.

 © 2006 Wiley-VCH Verlag GmbH & Co. KGaA, Weinheim

Conjugate Addition

DOI: 10.1002/anie.200502658

Construction of Quaternary Stereocenters by Efficient and Practical Conjugate Additions to α,β-Unsaturated Ketones with a Chiral Organic Catalyst**

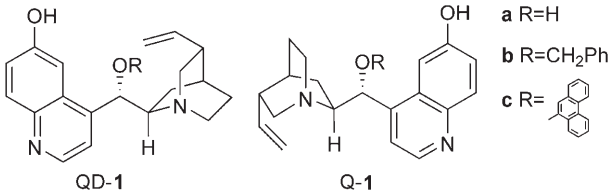
*Fanghui Wu, Hongming Li, Ran Hong, and Li Deng**

The conjugate addition of α-substituted β-ketoesters to α,β-unsaturated ketones represents a highly versatile strategy for the creation of all-carbon quaternary stereocenters, because of the accessibility of a wide range of these Michael donors and acceptors and the proven wide utility of the 1,4-adducts. The successful coupling of the strategic power of this C–C bond formation process with an operationally simple protocol for efficient and reliable enantioselective/diastereoselective control will lead to a direct and exceptionally versatile approach for the stereocontrolled construction of all-carbon quaternary stereocenters.[1] Consequently, this task has captured the attention of synthetic chemists since Wynberg's seminal report on the cinchona alkaloid-catalyzed addition of cyclic β-ketoesters to methyl vinyl ketone (MVK), which is the first documented catalytic enantioselective conjugate addition.[2–8] In spite of the numerous great strides made since then in catalytic asymmetric synthesis,[9] this task remains a formidable challenge of undiminished synthetic significance.

A breakthrough in the development of a highly enantioselective catalytic conjugate addition of α-substituted β-ketoesters to vinyl ketones was reported by Shibasaki and co-workers in 1994.[4a] A bifunctional chiral La–Na–binol complex (binol = 2,2′-dihydroxy-1,1′-binaphthyl) allowed the addition of cyclic and acyclic α-substituted β-ketoesters to MVK to proceed in 62–91% *ee*. More recently, Sodeoka and co-workers reported a Pd–binap complex (binap = 2,2′-bis-(diphenylphosphanyl)-1,1′-binaphthyl) that afforded 86–93% *ee* for the conjugate addition of α-substituted β-ketoesters to methyl and ethyl vinyl ketones.[5] These chiral metal-complex-mediated reactions, which demonstrated substantial scope with respect to ketoester donors, gave greater than 90% *ee* only with MVK as the Michael acceptor. While representing remarkable progress, these results also underscore the importance as well as the challenge of the development of an operationally simple and efficient enantioselective catalytic conjugate addition of broad substrate scope for both α-substituted β-ketoesters and α,β-unsaturated ketones.

Herein, we report the first efficient and general conjugate addition of α-substituted β-ketoesters to α,β-unsaturated ketones catalyzed by a chiral organic catalyst. The reaction affords excellent enantioselectivity, diastereoselectivity, and yield, not only for a wide variety of α-substituted β-ketoesters but also, importantly, for a wide range of α,β-unsaturated ketones. Furthermore, the high stereoselectivity is often achieved at or near room temperature in air with as little as 1.0 mol% of the chiral organic catalyst.

Although 6′-hydroxy cinchona alkaloids **1** (Scheme 1) were shown to be efficient bifunctional chiral organic catalysts for the conjugate addition of various carbon nucleophiles to nitroalkenes and vinyl sulfones,[10] our initial attempts to apply **1** to promote the enantioselective addition of α-substituted β-ketoesters **2** to vinyl ketones **3** were unsuccessful. The reaction of ketoester **2A** and MVK (**3a**) with catalysts **1a–c** in toluene went to completion at room temperature after 0.5–2 h, but the 1,4-adduct **4Aa** was formed in only moderate enantioselectivity (Table 1, entries 1–3). The enantioselectivity could be improved by performing the reaction in either dichloromethane or diethyl ether[11] and by decreasing the reaction temperature. However, even at −78 °C, the enantioselectivity did not reach a synthetically useful level (Table 1, entry 6).



Scheme 1. Structures of the 6′-hydroxy cinchona alkaloid catalysts **1** used.

We then investigated the effect of modifying the ester group[12] of ketoesters **2** on the enantioselectivity. The conjugate addition of *tert*-butyl ketoester **2B** to **3a** with QD-**1b** and Q-**1b** proceeded to completion in 30 min and 1 h, respectively. Significantly, these reactions occurred in a highly enantioselective fashion even at room temperature (Table 1, entries 7 and 8). The enantioselectivity could be further increased with catalyst **1c**, generating the 1,4-adduct **4Ba** in up to 97% *ee* (Table 1, entry 10). A rapid, complete, and highly enantioselective conjugate addition could even be

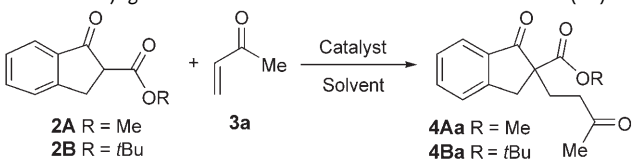
[*] F. Wu, H. Li, Dr. R. Hong, Prof. L. Deng
Department of Chemistry
Brandeis University
Waltham, MA 02454-9110 (USA)
Fax: (+1) 781-736-2516
E-mail: deng@brandeis.edu

[**] This work was financially supported by the National Institutes of Health (GM-61591).

Supporting information for this article is available on the WWW under http://www.angewandte.org or from the author.

 © 2006 Wiley-VCH Verlag GmbH & Co. KGaA, Weinheim

Table 1: Conjugate addition of ketoesters **2A** and **2B** to MVK (**3a**).[a,b]



2A R = Me
2B R = *t*Bu

3a

4Aa R = Me
4Ba R = *t*Bu

Entry	Ketoester	Catalyst	Solvent	*T* [°C]	*t* [h]	*ee* [%][c]
1	**2A**	QD-**1a**	toluene	23	1	40
2	**2A**	QD-**1b**	toluene	23	0.5	59
3	**2A**	QD-**1c**	toluene	23	2	58
4	**2A**	QD-**1b**	Et_2O	23	0.5	64
5	**2A**	QD-**1b**	CH_2Cl_2	23	0.5	66
6	**2A**	QD-**1b**	CH_2Cl_2	−78	12	80
7	**2B**	QD-**1b**	CH_2Cl_2	23	0.5	91
8	**2B**	Q-**1b**	CH_2Cl_2	23	1	92
9	**2B**	QD-**1c**	CH_2Cl_2	23	1	94
10	**2B**	Q-**1c**	CH_2Cl_2	23	1	97
11	**2B**	Q-**1c**[d]	CH_2Cl_2	23	3	96

[a] Unless otherwise specified, the reaction was run with **2** (0.5 M in the indicated solvent) and **3** (2.5 equiv) in the presence of **1** (10 mol%). [b] All the reactions went to completion at the indicated time. [c] Determined by HPLC analysis. [d] 1.0 mol% of the catalyst was used.

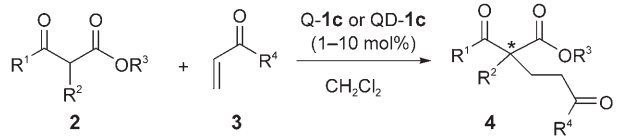
secured with a catalyst loading of only 1.0 mol% (Table 1, entry 11). As shown by a preparative-scale reaction that employed 24 mg of catalyst QD-**1c** (see Experimental Section), gram quantities of the chiral 1,4-adduct **4Ba** could be produced within 3 h in high optical purity. Furthermore, QD-**1c** could be easily recovered in high yield. Thus, this gram-scale reaction consumed only 1.0 mg of the 6′-hydroxy cinchona alkaloid.

We subsequently investigated the scope of the reaction. The addition of cyclic aromatic β-ketoesters **2B–D** to methyl, ethyl, and aryl vinyl ketones (**3a–d**) proceeded rapidly to completion in excellent enantioselectivity and 93–100% yield (Table 2, entries 1–5). Similarly, high enantioselectivity and yield could also be obtained with **2E**, an aliphatic ketoester (Table 2, entry 6). However, relative to the addition of **2B** to **3a**, the reaction rate decreased noticeably for the addition of **2E** to **3a** (Table 2, entry 6 versus entry 1). Guided by the hypothesis that the significantly decreased acidity of the α proton of **2E** relative to that of **2B** could be the cause of the dramatically reduced rate, we attempted the addition of **2F**, an aliphatic ketoester bearing a strong electron-withdrawing hexafluoroisopropyl ester group, to **3a.** Gratifyingly, the reaction with 10 mol% of Q-**1c** and QD-**1c** proceeded to completion in 30 min to afford the 1,4-adduct **4Fa** with 96 and 95% *ee*, respectively, and excellent yields (Table 2, entry 7). Again, both the enantioselectivity and yield remained high when the catalyst loading was reduced to 1.0 mol% (Table 2, entry 8). The addition reactions of the six-membered cyclic ketoester **2G** and the acyclic ketoester **2H** to **3a** with **1c** as catalyst were also found to be highly enantioselective (Table 2, entries 9 and 10).

Our study establishes a rapid, clean, and highly enantioselective conjugated addition of a wide range of substrates that include cyclic and acyclic β-ketoesters as donors and vinyl ketones bearing alkyl and aryl substituents of varying steric and electronic properties as acceptors. The ability of **1c** to afford consistently excellent enantioselectivity for various vinyl ketones is particularly noteworthy, as excellent enantioselectivity (>90% *ee*), to our knowledge, had not been achieved for catalytic conjugate additions of α-substituted ketoesters to vinyl ketones other than **3a**.

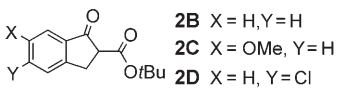
We next explored the possibility of using **1** to promote a conjugate addition of ketoesters **2** to β-substituted enones. The achievement of high enantioselectivity and diastereose-

Table 2: Asymmetric conjugate addition of α-substituted β-ketoesters to vinyl ketones with bifunctional cinchona alkaloid catalyst **1c**.[a]

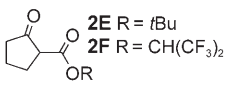


2 **3** **4**

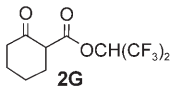
Cyclic α-substituted ketoester:



2B X = H, Y = H
2C X = OMe, Y = H
2D X = H, Y = Cl

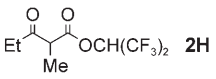


2E R = *t*Bu
2F R = $CH(CF_3)_2$



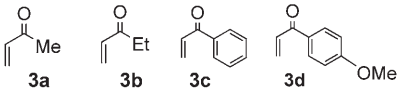
2G

Acyclic α-substituted ketoester:



2H

Vinyl ketone:



3a **3b** **3c** **3d**

Entry	Ketoester	Vinyl ketone	Catalyst loading [mol%]	*T* [°C]	*t* [h]	Yield [%][b]	*ee* [%][c]
1	**2B**	**3a**	1	23	3	96(100)	96[d](97[e])
2	**2B**	**3b**	1	23	5	94	94
3	**2C**	**3a**	1	23	5	98(99)	96(96)
4	**2B**	**3c**	10	−24	0.5	94(94)	96(93)
5[f]	**2D**	**3d**	10	−27	8	94(93)	96(93)
6	**2E**	**3a**	10	23	84	95	96[g]
7	**2F**	**3a**	10	23	0.5	93(90)	96(95)
8	**2F**	**3a**	1	23	24	92	94
9	**2G**	**3a**	10	23	24	89(86)	98(96)
10	**2H**	**3a**	10	−24	20	82(85[h])	90(90)

[a] Unless otherwise specified, the reaction was performed by treatment of **2** (0.3 mmol) with **3** (0.75 mmol, 2.5 equiv) and the catalyst in CH_2Cl_2 (0.6 mL). The data in parentheses are for the enantiomer obtained with QD-**1c** instead of Q-**1c**. [b] Yield of isolated product. [c] Determined by HPLC analysis. [d] The absolute configuration was determined to be *R*; see Supporting Information for details. [e] The reaction was performed based on gram scale of **2B** (1.16 g, 5.0 mmol); see Experimental Section and Supporting Information for details. [f] The reaction was started with a solution of **2** (0.2 mmol) and **1c** (0.02 mmol, 10 mol%) in CH_2Cl_2 (0.4 mL), then a solution of **3** (0.5 mmol, 2.5 equiv) in CH_2Cl_2 (0.4 mL) was added at 0.07 mL h^{-1}. [g] The absolute configuration was determined to be *S*; see Supporting Information for details. [h] The reaction was run for 40 h.

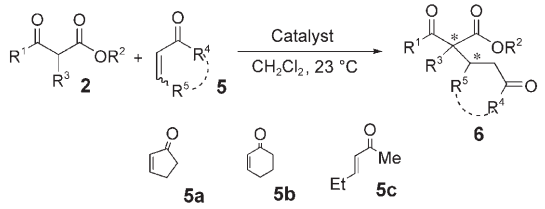
 © 2006 Wiley-VCH Verlag GmbH & Co. KGaA, Weinheim

lectivity for such a conjugate addition, which involves a sterically highly hindered Michael donor and a sterically hindered and electronically relatively weak Michael acceptor, has proven to be a significant challenge. In spite of its synthetic potential for the direct enantioselective creation of adjacent all-carbon quaternary and tertiary stereocenters, to our knowledge there were only three examples of conjugate additions of trisubstituted carbon nucleophiles to β-substituted enones in synthetically useful stereoselectivity. All three literature examples, reported by Sodeoka[5] and Jacobsen,[7] used a *trans*-acyclic enone as the Michael acceptor and were promoted by chiral metal complexes.

Table 3 summarizes the results obtained for the conjugate addition of ketoesters **2** to β-substituted enones **5a–c** catalyzed by cinchona alkaloids **1b** and **1c**. High enantioselectivity and diastereoselectivity as well as excellent yields could be attained for conjugate additions with both five- and six-membered cyclic enones (Table 3, entries 1–3). To the best of our knowledge, these represent the first examples of a highly enantioselective and diastereoselective catalytic conjugate addition of a trisubstituted carbon nucleophile to a cyclic enone. Remarkably, excellent enantioselectivity and useful diastereoselectivity could also be attained with the *trans*-acyclic enone **5c**. Relative to the conjugate additions with vinyl ketones **3**, these reactions require a longer reaction time and higher catalyst loading (Table 3, entry 4). Importantly, the reaction can be conveniently performed at room temperature and the catalysts are easily recyclable in greater than 95% yield.[13]

In conclusion, we have demonstrated the feasibility of using a chiral organic catalyst to mediate a highly efficient and general conjugate addition of α-substituted β-ketoesters to α,β-unsaturated ketones. By giving high stereoselectivity with easily accessible catalysts under operationally simple conditions for a wide range of α-substituted β-ketoesters as well as an unprecedented wide range of enones, the current reaction represents an advance of both conceptual and synthetic significance for the development of catalytic asymmetric conjugate additions. Investigations are currently under way to fully define the scope and understand the mechanism of the reaction.

Table 3: Construction of adjacent quaternary–tertiary stereocenters by enantioselective and diastereoselective conjugate addition of β-ketoester to β-substituted α,β-unsaturated ketones.[a]



Entry	Ketoester	Enone	Catalyst (mol%)	*t* [h]	Yield [%][b]	d.r.[c]	*ee* [%][d]
1[e]	**2B**	**5a**	QD-**1b** (10)	12	99	96:4[f]	98
2	**2F**	**5a**	Q-**1c** (20)	2	95	93:7	95
3[g]	**2B**	**5b**	QD-**1b** (20)	120	87	93:7	85
4	**2F**	**5c**	Q-**1c** (20)	20	83	86:14	99 (94[h])

[a] Unless otherwise specified, the reaction was performed by treatment of **2** (0.3 mmol) with **5** (0.75 mmol, 2.5 equiv) and catalyst (20 mol%) in CH_2Cl_2 (0.3 mL). [b] Yield of isolated product. [c] Unless otherwise specified, d.r. values were determined by HPLC. [d] For the major diastereomer of **6**. [e] The reaction was performed with **2B** (0.3 mmol) and **5a** (0.7 mmol, 2.5 equiv). [f] Determined by ^{1}H NMR analysis of crude products. [g] The reaction was performed with **2B** (0.3 mmol) and **5b** (0.7 mmol, 2.5 equiv). [h] For the minor diastereomer of **6**.

Experimental Section

Preparative-scale synthesis of *tert*-butyl 1-oxo-2-(3-oxobutyl)-2-indancarboxylate **4Ba**: α,β-Unsaturated ketone **3a** (1.02 mL, 12.5 mmol) was added dropwise to a solution of QD-**1c** (24.0 mg, 0.05 mmol) and β-ketoester **2B** (1.16 g, 5.0 mmol) in CH_2Cl_2 (10.0 mL) at room temperature. The resulting clear solution was stirred at room temperature for 3 h, when **2B** was completely consumed as indicated by TLC analysis. The reaction mixture was concentrated under vacuum and subjected to chromatography (SiO_2, hexanes/EtOAc 10:1) to give the desired 1,4-adduct **4Ba** as a colorless oil (1.51 g, >99% yield, 97% *ee*). The enantiomeric excess was determined by HPLC (Daicel Chiralcel OJ, hexanes/isopropyl alcohol (90:10), 1.00 mL min^{-1}, λ = 220 nm, t_r(major) = 27.9 min, t_r(minor) = 33.8 min). ^{1}H NMR (400 MHz, $CDCl_3$): δ = 7.76 (d, J = 8.0 Hz, 1H), 7.62 (td, J = 7.2 Hz, 1.2 Hz, 1H), 7.47 (d, J = 8.0 Hz, 1H), 7.40 (t, J = 7.2 Hz, 1H), 3.61 (d, J = 17.2 Hz, 1H), 3.01 (d, J = 17.2 Hz, 1H), 2.68–2.47 (m, 2H), 2.21–2.16 (m, 2H), 2.13 (s, 3H), 1.39 ppm (s, 9H); ^{13}C NMR (100 MHz, $CDCl_3$): δ = 207.6, 202.7, 170.1, 152.6, 135.2, 127.7, 126.3, 124.6, 81.9, 59.8, 38.8, 37.9, 29.8, 28.3, 27.2 ppm; IR ($CHCl_3$): $\tilde{\nu}$ = 2978, 2932, 1733, 1715, 1607, 1368, 1153 cm^{-1}.

After the 1,4-adduct was collected, the column was washed with methanol to allow the recovery of QD-**1c** in NMR spectroscopically pure form (23 mg, 96%).

Received: July 28, 2005
Published online: December 30, 2005

Keywords: alkaloids · conjugate addition · diastereoselectivity · enantioselectivity · enones

[1] For reviews covering catalytic enantioselective conjugate additions of β-ketoesters to enones, see: a) M. Yamaguchi in *Comprehensive Asymmetric Catalysis* (Eds.: E. N. Jacobsen, A. Pfaltz, H. Yamamoto), Springer, Heidelberg, **2003**, Suppl. 1 to Chap. 31.2, p. 151; b) M. Shibasaki, N. Yoshikawa, *Chem. Rev.* **2002**, *102*, 2187–2209; c) N. Krause, A. Hoffmann-Röder, *Synthesis* **2001**, 171–196; d) M. P. Sibi, S. Manyem, *Tetrahedron* **2000**, *56*, 8033–8061; for reviews on an enantioselective construction of all-carbon quaternary stereocenters, see: e) C. J. Douglas, L. E. Overman, *Proc. Natl. Acad. Sci. USA* **2004**, *101*, 5363–5367; f) J. Christoffers, A. Baro, *Angew. Chem.* **2003**, *115*, 1726–1728; *Angew. Chem. Int. Ed.* **2003**, *42*, 1688–1690; g) J. Christoffers, *Chem. Eur. J.* **2003**, *9*, 4862–4867; h) J. Christoffers, A. Mann, *Angew. Chem.* **2001**, *113*, 4725–4732; *Angew. Chem. Int. Ed.* **2001**, *40*, 4591–4597; i) E. J. Corey, A. Guzman-Perez, *Angew. Chem.* **1998**, *110*, 402–415; *Angew. Chem. Int. Ed.* **1998**, *37*, 388–401.

[2] H. Wynberg, R. Helder, *Tetrahedron Lett.* **1975**, 4057–4060.

[3] For an example of enantioselective conjugate addition of α-methyl α-cyanoacetate to vinyl ketones or acrolein, see: M.

 © 2006 Wiley-VCH Verlag GmbH & Co. KGaA, Weinheim

Sawamura, H. Hamashima, Y. Ito, *J. Am. Chem. Soc.* **1992**, *114*, 8295 – 8296.
[4] a) H. Sasai, T. Arai, M. Shibasaki, *J. Am. Chem. Soc.* **1994**, *116*, 1571 – 1572; b) H. Sasai, E. Emori, T. Arai, M. Shibasaki, *Tetrahedron Lett.* **1996**, *37*, 5561 – 5564.
[5] Y. Hamashima, D. Hotta, M. Sodeoka, *J. Am. Chem. Soc.* **2002**, *124*, 11240 – 11241.
[6] For a recent report of enantioselective addition of cyclic α-substituted β-diketones to alkynones catalyzed by a cinchona alkaloid-based catalyst, see: M. Bella, K. A. Jørgensen, *J. Am. Chem. Soc.* **2004**, *126*, 5672 – 5673.
[7] For chiral Al–salen complex-catalyzed conjugate addition of α-phenyl α-cyanoacetate to acyclic α,β-unsaturated ketones, see: M. S. Taylor, D. N. Zalatan, A. M. Lerchner, E. N. Jacobsen, *J. Am. Chem. Soc.* **2005**, *127*, 1313 – 1317.
[8] For an example of highly enantioselective Michael addition of cyclic β-ketoesters to MVK catalyzed by a phase-transfer catalyst, see: T. Ooi, T. Miki, M. Taniguchi, M. Shiraishi, M. Takeuchi, K. Maruoka, *Angew. Chem.* **2003**, *115*, 3926 – 3928; *Angew. Chem. Int. Ed.* **2003**, *42*, 3796 – 3798.
[9] For a special issue focusing on asymmetric catalysis, see: a) *Proc. Natl. Acad. Sci. USA* **2004**, *101*, 5347 – 5850; for a thematic issue on enantioselective catalysis, see: b) *Chem. Rev.* **2003**, *103*, 2761 – 3400; c) *Comprehensive Asymmetric Catalysis, Vol. 1–3* (Eds.: E. N. Jacobsen, A. Pfaltz, H. Yamamoto), Springer, Berlin, **1999**.
[10] a) H. Li, Y. Wang, L. Tang, L. Deng, *J. Am. Chem. Soc.* **2004**, *126*, 9906 – 9907; b) H. Li, Y. Wang, L. Tang, F. Wu, X. Liu, C. Guo, B. M. Foxman, L. Deng, *Angew. Chem.* **2005**, *117*, 107 – 110; *Angew. Chem. Int. Ed.* **2005**, *44*, 105 – 108; c) H. Li, J. Song, X. Liu, L. Deng, *J. Am. Chem. Soc.* **2005**, *127*, 8948 – 8949.
[11] Ethyl acetate, tetrahydrofuran, dimethylformamide, chloroform, *tert*-butyl methyl ether, diethyl ether, methanol, and toluene were screened, and reactions in these solvents proceeded in 16–63% *ee*.
[12] Sodeoka and co-workers also observed a dramatic effect of changing the ester group of the ketoester donor on the enantioselectivity of the Pd–binap complex-catalyzed conjugate addition; for details see reference [5].
[13] See the Supporting Information for details.

 © 2006 Wiley-VCH Verlag GmbH & Co. KGaA, Weinheim

N–H Activation

DOI: 10.1002/anie.200503222

Cleavage of Nitrogen–Hydrogen Bonds of Ammonia Induced by Triruthenium Polyhydrido Clusters**

*Yumiko Nakajima, Hajime Kameo, and Hiroharu Suzuki**

N–H bond activation of amines has attracted increasing attention owing to its applicability to the synthesis of various amino compounds, and the development of a new and effective reaction system for the activation of ammonia must be one of the most important research targets in connection with the transformation of abundant and inexpensive ammonia into a useful amino compound.[1] However, successful examples of activation of the N–H bond of ammonia are still rare because of both the high N–H bond dissociation energy ($\approx 104 \pm 2$ kcal mol^{-1})[2] and the difficulty in forming an N–H σ complex.[3]

The groups of Milstein[1g,i,j] and Hartwig[1k,q] showed independently that some mononuclear iridium(I) complexes exhibited activity towards oxidative addition of ammonia. A highly unsaturated 14 e species with T-shaped geometry was proposed as a reactive intermediate for the N–H bond cleavage on the basis of kinetic studies.[1q] Some complexes containing a d^0 metal center, such as $[Cp^*_2MH_2]$ (M = Zr, Hf; Cp^* = pentamethylcyclopentadiene),[1b,c,e] $[Cp^*_2ScR]$,[1f] and $[(neopentyl)_3Ta=C(H)(tBu)]$,[1h] also activated ammonia to generate amido and nitrido complexes. There have, thus far, been examples of bimetallic oxidative addition to ammonia. A trinuclear carbonyl cluster, $[Os_3(CO)_{11}(L)]$ (L = *c*-C_6H_8 or CH_3CN), effectively activates ammonia with the participation of the two osmium centers to produce the μ-amido complex $[Os_3(CO)_{10}(\mu\text{-}H)(\mu\text{-}NH_2)]$.[1a,d]

A multimetallic system may work more efficiently for bond activation than a monometallic complex owing to the cooperative action of the metal centers. Each metal center would be allotted a part as a binding site and an activation site, and the transition state of the bond-activation step may, therefore, be stabilized.

[*] Y. Nakajima, H. Kameo, Prof. H. Suzuki
Department of Applied Chemistry
Graduate School of Science and Engineering
Tokyo Institute of Technology
O-okayama, Meguro-ku, Tokyo 152-8552 (Japan)
Fax: (+81) 3-5734-3913
E-mail: hiroharu@n.cc.titech.ac.jp

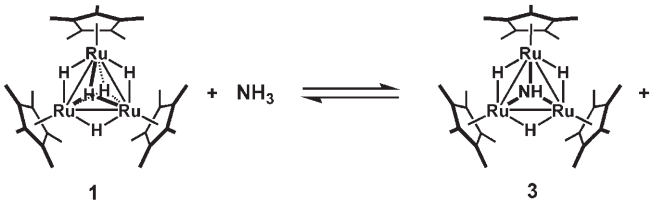
[**] The authors are grateful to Kanto Chemical Co., Inc., for a generous supply of pentamethylcyclopentadiene. This work was supported by grants from the Ministry of Education, Culture, Sports, Science, and Technology, Japan (Nos. 15205009 and 14078210 "Reaction Control of Dynamic Complexes") and by a Grant-in-Aid from the JSPS. This work was partly supported by the 21st Century COE Program.

Supporting information for this article is available on the WWW under http://www.angewandte.org or from the author.

InterScience
© 2006 Wiley-VCH Verlag GmbH & Co. KGaA, Weinheim

We have thus far demonstrated that a trinuclear pentahydrido complex of ruthenium, $[(Cp^*Ru)_3(\mu_3\text{-}H)_2(\mu\text{-}H)_3]$ (**1**) [Eq. (1)], effectively activates a wide spectrum of chemical bonds, such as the C–H bond of alkanes and the N–H and N–N bonds of hydrazines.[4] Herein we report the first example of trinuclear oxidative addition of ammonia to form a μ_3-imido cluster in the reaction of **1** with ammonia. We also demonstrate acceleration of the oxidative addition of ammonia in the reaction with a μ_3-oxo complex, $[(Cp^*Ru)_3(\mu_3\text{-}O)(\mu\text{-}H)_3]$ (**2**) [Eq. (4)].[5]

Complex **1** reacts with ammonia to produce a known μ_3-imido complex, $[(Cp^*Ru)_3(\mu_3\text{-}NH)(\mu\text{-}H)_3]$ (**3**),[4h] and dihydrogen as a result of activation of the two N–H bonds [Eq. (1)].



1 + NH_3 ⇌ 3 + $2\,H_2$ (1)

The reaction is reversible, and treatment of **3** with dihydrogen quantitatively affords **1** and ammonia as reported recently.[4h] Therefore, the reaction reaches a stationary equilibrium when it is carried out in a closed reaction vessel. When the reaction of **1** (8.5×10^{-3} mmol) with ammonia (0.10 mmol) in $[D_8]$THF (0.4 mL) in a sealed tube was monitored by ^{1}H NMR spectroscopy at 80 °C, the reaction reached its equilibrium, **1**/**3** = 70:30, after standing for 3 days. As anticipated, the **1**/**3** ratio improved to 11:89 by reevacuation and recharging with ammonia.

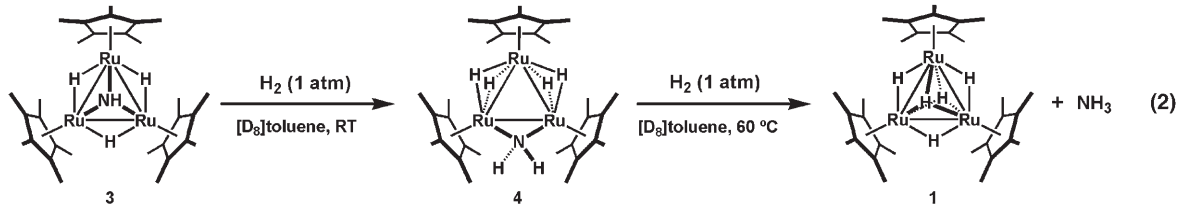
The reaction of **1** with ammonia likely proceeds via an intermediary μ-amido complex, $[(Cp^*Ru)_3(\mu\text{-}NH_2)(\mu\text{-}H)_4]$ (**4**), which would be formed in a sequence of steps, namely, ammonia coordination, N–H bond cleavage, and liberation of dihydrogen. Although no intermediate was detected upon monitoring the reaction by ^{1}H NMR spectroscopy, one plausible intermediate was prepared by partial hydrogenation of **3**.

When the reaction of **3** with dihydrogen (1 atm) in $[D_8]$toluene was monitored by ^{1}H NMR spectroscopy, signals assignable to the newly formed μ-amido complex were observed. The ^{1}H NMR spectrum recorded at −80 °C exhibits two broad signals of the amido hydrogen atoms protons at δ = 2.88 (1H) and 5.09 ppm (1H) and two singlets at $\delta = -17.71$ (2H) and −5.48 ppm (2H) for the metal-bound hydrogen atoms. This clearly indicates the formation of the μ-amido-μ-tetrahydrido complex **4** as a result of the partial hydrogenation of **3**. Two of the four hydrido ligands in **4** probably position on the same side of the μ-amido group with respect to the Ru_3 plane and the rest lies on the opposite side. Upon heating at 60 °C in $[D_8]$toluene, μ-amido complex **4** reacted further with dihydrogen to generate **1** quantitatively [Eq. (2)].

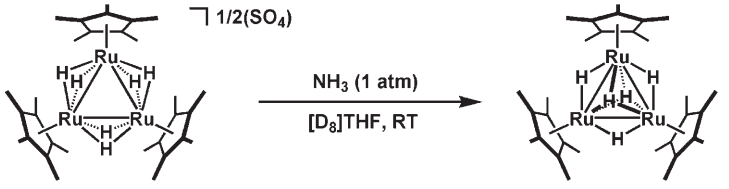
This result suggests that complex **4** is an intermediate species for the formation of μ_3-imido complex **3** from **1** and ammonia through N–H bond activation.

As shown in the reaction of hydrazine with triruthenium polyhydrido complexes **1** and $[(Cp^*Ru)_3(\mu\text{-}H)_6]^1/_2(SO_4)$ (**5**), a decrease in the electron density at the ruthenium center accelerates nucleophilic attack of the hydrazine molecule.[4g,h] On the basis of this observation, we examined the reaction of cationic **5** with ammonia. However, deprotonation to give **1** predominated over nucleophilic attack of ammonia at the metal center because of the protonic character of the hydrido ligand in **5** [Eq. (3)].

A neutral complex that has electron-deficient metal centers would, therefore, be suitable for the promotion of nucleophilic attack of ammonia. Hence we examined the reaction of ammonia with μ_3-oxo complex, $[(Cp^*Ru)_3(\mu_3\text{-}O)(\mu\text{-}H)_3]$ (**2**), in which the electron density of the metal



3 → 4 → 1 + NH_3 (2)

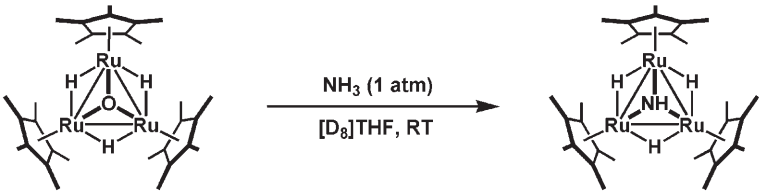


5 → 1 quant + $1/2(NH_4)_2SO_4$ (3)

 © 2006 Wiley-VCH Verlag GmbH & Co. KGaA, Weinheim

centers should be lower owing to the polarization between the oxygen and the ruthenium atoms, and the hydrido ligands should be less protonic than those in **5**.

The reaction of **2** with ammonia (1 atm) proceeded smoothly even at room temperature to yield **3** quantitatively [Eq. (4)]. Notably, the formation of the water stemming from the μ_3-oxo ligand was confirmed by ^{1}H NMR spectroscopy ($\delta = 2.53$ ppm). The reactivity of **2** is remarkably higher than that of **1**, and the reaction is completed within 1 h at 80 °C.



2 **3**

$$+ \; H_2O \qquad (4)$$

We pursued a kinetic study by means of ^{1}H NMR spectroscopy to gain insight into the reaction paths. The entropy and the enthalpy of activation were estimated at -23.0 cal K^{-1} mol^{-1} and 16.7 kcal mol^{-1}, respectively. The relatively large and negative value of the entropy of activation implies that the reaction proceeds through an associative mechanism, and the initial step, namely incorporation of ammonia into the reaction site, is probably the rate-determining step. This is consistent with what we mentioned for the reaction of **1** with 1,1-dimethylhydrazine (-23.0 cal K^{-1} mol^{-1}) and phenylhydrazine (-22.7 cal K^{-1} mol^{-1}):[4g] these hydrazine molecules would be captured into the Ru_3 core from the less bulky $-NH_2$ terminus. The fact that no intermediate was observed when the reaction was monitored at room temperature by ^{1}H NMR spectroscopy also indicates that the initial step of the reaction, namely capture of the ammonia molecule, is the rate-determining step.

In contrast to the reaction with **2**, the reaction of ammonia with a bis(μ_3-oxo) complex, [(Cp*Ru)$_3$(μ_3-O)$_2$(μ-H)] (**6**),[5] resulted in the recovery of the starting complex **6**. This result implies that protonation of the bridging oxygen atom does not take place in the initial step of the reaction and that the presence of the vacant space on the opposite face of the μ_3-oxo ligand with respect to the Ru_3 plane is essential for the promotion of the reaction.

A key feature of this reaction system is that complex **2** is coordinatively unsaturated (46 e) and has a triply bridging oxo ligand. The ammonia molecule would be easily accessible to the reaction site owing to the coordinative unsaturation. The bridging oxo ligand induces polarization of charge between the ruthenium and the oxygen atoms and, as a result, accelerates the nucleophilic attack of ammonia at the ruthenium atom. Furthermore, formation of water would make the reaction exothermic and irreversible.[2] Thus, introduction of the μ_3-oxo ligand into the Ru_3 core makes the reaction not only kinetically but also thermodynamically favorable.

In summary, we have shown that triruthenium pentahydrido complex **1** exhibits considerable activity towards N–H bond cleavage of ammonia and that the introduction of a triply bridging oxo ligand into the Ru_3 core significantly enhances the activity. Although there have been, thus far, several successful examples of the activation of ammonia, this is to our knowledge the first example of "double activation" of ammonia. We are currently investigating a new catalytic process that takes full advantage of this feasible N–H bond cleavage of ammonia.

Received: September 10, 2005
Published online: December 28, 2005

Keywords: cluster compounds · hydride ligands · N–H activation · oxo ligands · ruthenium

[1] a) E. G. Bryan, B. F. G. Johnson, K. Lewis, *J. Chem. Soc. Dalton Trans.* **1977**, 1328–1331; b) J. N. Armor, *Inorg. Chem.* **1978**, *17*, 203–213; c) J. N. Armor, *Inorg. Chem.* **1978**, *17*, 213–218; d) G. Z. Süss-Fink, *Z. Naturforsch. B* **1980**, *35*, 454–457; e) G. L. Hillhouse, J. E. Bercaw, *J. Am. Chem. Soc.* **1984**, *106*, 5472–5478; f) J. E. Bercaw, D. L. Davies, P. T. Wolczanski, *Organometallics* **1986**, *5*, 443–450; g) A. L. Casalnuovo, J. C. Calabrese, D. Milstein, *Inorg. Chem.* **1987**, *26*, 973–976; h) M. M. B. Holl, P. T. Wolczanski, G. V. Duyne, *J. Am. Chem. Soc.* **1990**, *112*, 7989–7994; i) V. R. Koelliker, D. Milstein, *Angew. Chem.* **1991**, *103*, 724–726; *Angew. Chem. Int. Ed. Engl.* **1991**, *30*, 707–709; j) M. Schulz, D. Milestein, *J. Chem. Soc. Chem. Commun.* **1993**, 318–319; k) M. Kanzelberger, X. Zhang, T. J. Emge, A. S. Goldman, J. Zhao, C. Incarvito, J. F. Hartwig, *J. Am. Chem. Soc.* **2003**, *125*, 13644–13645; l) A. M. Winter, K. Eichele, H.-G. Mack, S. Potuznik, H. A. Mayer, W. C. Kaska, *J. Organomet. Chem.* **2003**, *682*, 149–154; m) L.-C. Liang, J.-M. Lin, C.-H. Hung, *Organometallics* **2003**, *22*, 3007–3009; n) D. Conner, C. T. R. Jayaprakash, T. B. Gunnoe, *Organometallics* **2004**, *23*, 2724–2733; o) L. Fan, B. M. Foxman, O. V. Ozerov, *Organometallics* **2004**, *23*, 326–328; p) F. Xia, J. Chen, K. Zeng, Z. Cao, *Organometallics* **2005**, *24*, 1845–1851; q) J. Zhao, A. S. Goldman, J. F. Hartwig, *Science* **2005**, *307*, 1080–1082.

[2] H_2NNH_2 ($D_{NH} = 76 \pm 2$ kcal mol^{-1}), NH_3 ($D_{NH} = 104 \pm 2$ kcal mol^{-1}), H_2O ($D_{OH} = 119.2 \pm 0.2$ kcal mol^{-1}): *Lange's Handbook of Chemistry*, *13th ed.* (Eds.: N. A. Lange, J. A. Dean), McGraw-Hill, New York, **1985**, pp. 3–131.

[3] W. YaO, O. Eisenstein, R. H. Crabtree, *Inorg. Chim. Acta* **1997**, *254*, 99–104.

[4] a) Y. Ohki, H. Suzuki, *Angew. Chem.* **2000**, *112*, 3605–3607; *Angew. Chem. Int. Ed.* **2000**, *39*, 3463–3465; b) T. Takemori, A. Inagaki, H. Suzuki, *J. Am. Chem. Soc.* **2001**, *123*, 1762–1763; c) H. Suzuki, *Eur. J. Inorg. Chem.* **2002**, 1009–1023; d) T. Takao, S. Kakuta, R. Tenjinbayashi, T. Takemori, E. Murotani, H. Suzuki, *Organometallics* **2004**, *23*, 6090–6093; e) A. Inagaki, T. Takemori, M. Tanaka, H. Suzuki, *Angew. Chem.* **2000**, *112*, 411–414; *Angew. Chem. Int. Ed.* **2000**, *39*, 404–406; f) T. Takemori, A. Inagaki, H. Suzuki, *J. Am. Chem. Soc.* **2001**, *123*, 1762–1763; g) Y. Nakajima, H. Suzuki, *Organometallics* **2003**, *22*, 959–969; h) Y. Nakajima, A. Inagaki, H. Suzuki, *Organometallics* **2004**, *23*, 4040–4046.

[5] H. Suzuki, T. Kakigano, K. Tada, M. Igarashi, K. Matsubara, A. Inagaki, M. Oshima, T. Takao, *Bull. Chem. Soc. Jpn.* **2005**, *78*, 67–87.

 © 2006 Wiley-VCH Verlag GmbH & Co. KGaA, Weinheim

Natural Product Synthesis

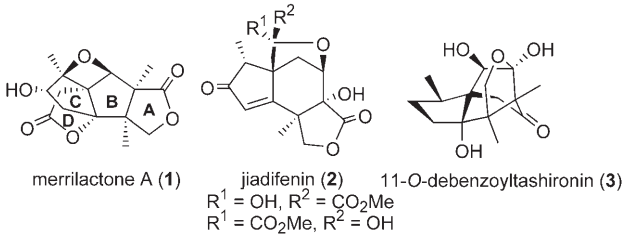
DOI: 10.1002/anie.200503618

Total Synthesis of (±)-Merrilactone A**

Goverdhan Mehta and S. Robindro Singh*

As a consequence of the advancing age profile of the global population, particularly in developed nations, neurodegenerative disorders such as Alzheimer's and Parkinson's diseases have emerged as a major public health concern. In this regard, neurotrophic agents, which have been implicated in the maintenance and growth of neurons as well as prevention of neuronal death, are being considered as potential leads for therapeutic development.[1] While earlier efforts in the area have focused on the naturally occurring polypeptides, pharmacokinetics and bioavailability considerations have kindled interest in exploring small-molecule-based natural product entities as neurotrophic factors.[1b]

Recent pioneering efforts from Fukuyama and co-workers[2] have unraveled a series of densely oxygenated, neurotrophically active polycyclic sesquiterpenoid natural products from a variety of exotic *Illicium* species, thus making available enchanting platforms and opportunities for chemical explorations. These include merrilactone A (**1**),[2a] jiadifenin (**2**),[2b] and 11-*O*-debenzoyltashironin (**3**)[2d] to name a few (Scheme 1). The isolation of merrilactone A (**1**) from the

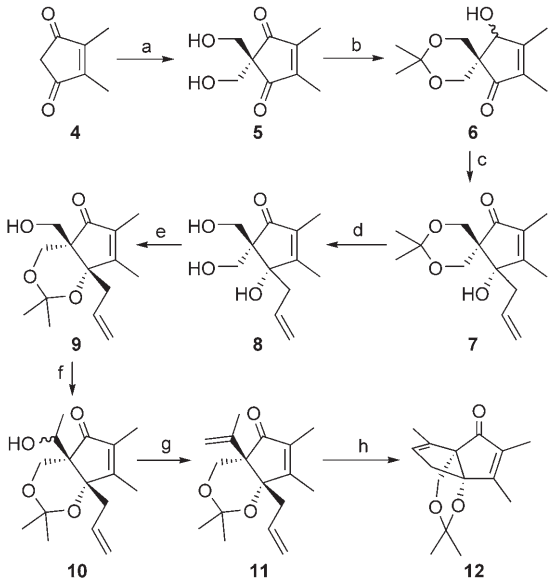


Scheme 1. a) Neurotrophic natural products isolated from *Illicium* sp.

pericarps of *Illicium merrillianum* was reported a few years ago, and in addition to the determination of its crystal structure (X-ray) and absolute configuration (Mosher), **1** was shown to significantly promote neurite outgrowth in the primary cultures of fetal rat cortical neurons at concentrations from 0.1 to 10 μM.[2a] This novel bioactivity profile coupled with the compact pentacyclic caged architecture of merrilactone A, which comprises two γ-lactone moieties, an oxetane ring, an oxa[3.3.3]propellane moiety, and seven contiguous stereogenic centers, make it an alluring synthetic target that has captivated widespread attention. Indeed, two elegant total synthesis of merrilactone A by Danishefsky and co-workers[3a] and Hirama and co-workers[3b] have appeared along with several model synthetic studies[3c,d] including our own[3e] in the past few years. More recently, Meng and Danishefsky have also unveiled an asymmetric approach to **1**.[3f] Herein, we report a total synthesis of **1** that follows a very different conceptual design, embedded in a flexible and diversity-oriented mould.

In our approach towards the synthesis of merrilactone A (**1**), we recognized the centrality of the choice of the starting synthon, keeping in mind the prime importance of setting up the key five-membered ring B of the natural product which includes four contiguous quaternary centers and much of the stereochemistry of the molecule. After screening several candidates, we opted for the readily available 2,3-dimethyl-2-cyclopentene-1,4-dione (**4**)[4] as its symmetry was readily exploitable for stereocontrol and it was intrinsically poised towards an asymmetric adaptation.[5]

Double hydroxymethylation of **4**, mediated by DBU, was nearly quantitative to furnish **5**, whose 1,3-diol moiety was then protected as the acetonide (Scheme 2). Luche reduction[6] of **5** furnished **6** as a single hydroxyenone. Careful addition of the in situ generated allylcerium reagent to **6** followed by MnO_2 oxidation of the allylic secondary hydroxy group led to the hydroxyenone **7** as a single isomer.



Scheme 2. a) DBU, 40% HCHO (aq.), THF, 0°C, 95%; b) i) acetone, 4 Å MS, Amberlyst-15, 92% (based on recovered starting material); ii) $NaBH_4$, $CeCl_3 \cdot 7H_2O$, 0°C, 90%; c) i) $CeCl_3$, allyl magnesium chloride, −78°C, 85%; ii) MnO_2, CH_2Cl_2, 98%; d) THF/H_2O (5:1), 2 N HCl, 90%; e) acetone, 4 Å MS, Amberlyst-15, 94% (**7**/**9** 1:1); f) i) PDC, CH_2Cl_2; ii) MeLi, Et_2O, 62% (2 steps); g) i) PDC, CH_2Cl_2, 85%; ii) Ph_3PCH_2Br, *t*BuOK, Et_2O, 68%; h) Grubbs' catalyst (25 mol%), CH_2Cl_2, reflux, 76%. DBU = 1,8-diazabicyclo[5.4.0]undec-7-ene; MS = molecular sieves; PDC = pyridinium dichromate.

[*] Prof. G. Mehta, S. R. Singh
Department of Organic Chemistry
Indian Institute of Science
Bangalore 560012 (India)
Fax: (+91) 80-2360-0936
E-mail: gm@orgchem.iisc.ernet.in

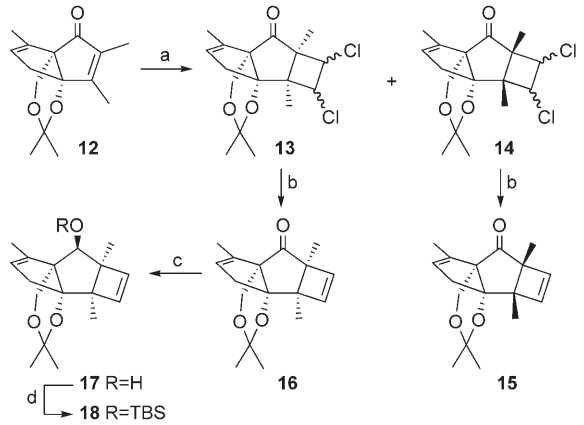
[**] G.M. and S.R.S. thank the CSIR for the award of the Bhatnagar Fellowship and a Senior Research Fellowship, respectively. We thank the CCD and Mr. Saikat Sen for the X-ray crystallographic data, and the JNCASR for research support.

Supporting information for this article is available on the WWW under http://www.angewandte.org or from the author.

 © 2006 Wiley-VCH Verlag GmbH & Co. KGaA, Weinheim

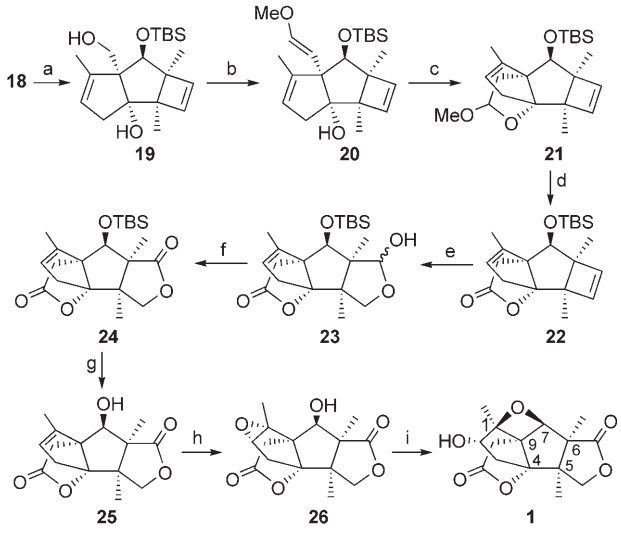
At this stage, a key acetonide deprotection–protection step positioned the four side arms on ring B for sequential annulation of the five-membered ring C and the γ-lactone ring D. Thus, acetonide deprotection in **7** led to the triol **8**, reprotection of which under equilibrating conditions furnished a readily separable (1:1) mixture of the desired acetonide **9** along with **7**, which could be readily recycled (Scheme 2). For the construction of ring C, the primary hydroxy group in **9** was oxidized to the aldehyde followed by addition of methyllithium to give **10**. PDC oxidation of **10** to the corresponding α-methylketone and further Wittig methylenation furnished **11**. The *cis*-oriented allyl and propenyl chains in **11** were suitably positioned towards a ring-closing metathesis reaction, and exposure to Grubbs' first-generation catalyst[7] delivered the diquinane **12** in satisfactory yield.

We then turned our attention towards establishing the γ-lactone-bearing ring A and in particular the quaternization of the two vicinal methyl groups. For this purpose, a cyclobutene ring was identified as an appropriate chemical equivalent. Photochemical [2+2] cycloaddition of *trans*-1,2-dichloroethylene to **12** proceeded with a moderate degree of β-facial selectivity, directed by the steric bulk of the acetonide methyl groups positioned on the α-face, to deliver a readily separable mixture (2:1) of **13** and **14** (Scheme 3). Eliminative dehalogenation of **13** and **14** generated the tricyclic cyclobutene-containing derivatives **15** and **16**, respectively. Reduction of **16** with DIBAL-H exclusively delivered the desired β-hydroxy epimer **17**, whose formulation was confirmed through determination of its X-ray crystal structure (Scheme 3). Stereoselectivity in this reduction reaction could be attributed to the cooperative effect of the intrinsic convex-face steric bias present in **16**, with the added possibility of intramolecular hydride delivery from the α-face, mediated through the coordination of DIBAL with the acetonide oxygen atoms. The hydroxy group in **17** was subsequently protected as its TBS derivative to give **18**.



Scheme 3. a) *trans*-Dichloroethylene, *hν* (pyrex, 400 W), 65% (**13**/**14** 2:1); b) Sodium naphthalenide, −60°C, 70% (**13**), 75% (**14**); c) DIBAL-H, −78°C, 95%; d) TBSOTf, CH_2Cl_2, Et_3N, 86%. DIBAL-H = diisobutylaluminum hydride; TBS = *tert*-butyldimethylsilyl; Tf = trifluoromethanesulfonyl.

After numerous attempts, we devised a route to elaborate **18** into the natural product merrilactone A (Scheme 4).



Scheme 4. a) THF/H_2O (5:1), 2 N HCl, 95%; b) i) TPAP, CH_2Cl_2; ii) $Ph_3PCH_2OCH_3$, *t*BuOK, THF, 54% (2 steps); c) CH_2Cl_2/THF (10:1), $HClO_4$; d) PCC, CH_2Cl_2, 62% (combined yield for steps c and d); e) i) O_3, MeOH, −78°C; ii) $NaBH_4$, MeOH, −78°C, 45%; f) PCC, CH_2Cl_2, 80%; g) TBAF, AcOH, THF, 85%; h) DMDO, 95%; i) *p*TsOH, CH_2Cl_2, 80%. TPAP = tetra-*n*-propylammonium perruthenate; PCC = pyridinium chlorochromate; TBAF = tetra-*n*-butylammonium fluoride; DMDO = dimethyl dioxirane; *p*TsOH = *p*-toluenesulfonic acid.

Acetonide deprotection in **18** led to the diol **19**, oxidation of which with TPAP furnished an intermediate aldehyde that was directly homologated through Wittig methoxymethylenation to the enol ether **20** (Scheme 4). Acid-mediated hydrolysis in **20** led to **21** with concomitant intramolecular hemiacetal formation. Direct oxidation of **21** using PCC delivered the γ-lactone-bearing ring D in **22**. The next stage was the elaboration of the cyclobutene ring in **22** to the second γ-lactone moiety; to this end, ozonolysis and in situ reduction with borohydride of **22** led to lactol **23** as the only characterizable product. The regioselective formation of **23** was somewhat anticipated, as the presence of the bulky TBS group at C7 was expected to cause steric shielding of the neighboring aldehyde group at C6 and allow borohydride to selectively attack the aldehyde group at C5 to give **23**. Oxidation of **23** with PCC delivered the second γ-lactone ring A in **24** (Scheme 4). The final stages in the synthesis of merrilactone A were implemented by following the earlier established protocols.[2c] Deprotection of the alcohol in **24** led to **25**, and epoxidation of the methyl cyclopentene double bond in the latter with DMDO furnished the α-epoxide **26** stereoselectively to set up the homo-Payne rearrangement. Brief exposure of **26** to *p*TsOH led to the target compound merrilactone A (**1**), whose ^1H and ^{13}C NMR spectra were identical to those of the natural product.[2a,3a,b]

 © 2006 Wiley-VCH Verlag GmbH & Co. KGaA, Weinheim

In summary, we have delineated a total synthesis of the neurotrophic sesquiterpenoid merrilactone A (**1**) in a stereo- and regioselective diversity-oriented approach. The overall strategy is also amenable to accessing both the enantiomers of the natural product and is well poised for extension to the total synthesis of other related neurotrophic agents from *Illicium* species.

Received: October 13, 2005
Published online: December 28, 2005

Keywords: diastereoselectivity · natural products · neurotrophic agents · terpenoids · total synthesis

[1] a) For a review on neurotrophic activity, see: F. Hefti, *Annu. Rev. Pharmacol. Toxicol.* **1997**, *37*, 239; b) B. Luu, J.-L. G. de Aguilar, C. Girlanda-Junges, *Molecules* **2000**, *5*, 1439.
[2] a) J.-M. Huang, R. Yokoyama, C.-S. Yang, Y. Fukuyama, *Tetrahedron Lett.* **2000**, *41*, 6111; b) J.-M. Huang, R. Yokoyama, C.-S. Yang, Y. Fukuyama, *J. Nat. Prod.* **2001**, *64*, 428; c) J.-M. Huang, C.-S. Yang, M. Tanaka, Y. Fukuyama, *Tetrahedron* **2001**, *57*, 4691; d) J.-M. Huang, R. Yokoyama, C.-S. Yang, Y. Fukuyama, *J. Nat. Prod.* **2002**, *65*, 527.
[3] a) V. B. Birman, S. J. Danishefsky, *J. Am. Chem. Soc.* **2002**, *124*, 2080; b) M. Inoue, T. Sato, M. Hirama, *J. Am. Chem. Soc.* **2003**, *125*, 10772; c) J. Iriondo-Alberdi, J. E. Perea-Buceta, M. F. Greaney, *Org. Lett.* **2005**, *7*, 3969; d) K. Harada, H. Kato, Y. Fukuyama, *Tetrahedron Lett.* **2005**, *46*, 7407; e) G. Mehta, S. R. Singh, *Tetrahedron Lett.* **2005**, *46*, 2079; f) Z. Meng, S. J. Danishefsky, *Angew. Chem.* **2005**, *117*, 1535; *Angew. Chem. Int. Ed.* **2005**, *44*, 1511.
[4] I. Papoutsis, S. Spyroudid, A. Varvoglis, *Tetrahedron Lett.* **1994**, *35*, 8449.
[5] In a separate effort, we have observed that the *cis*-1,4-enediol derived from **4** can be enzymatically desymmetrized to provide access to both the enantiomers (unpublished results). Alternatively, enzymatic desymmetrization of **5** or enzymatic resolution of the keto-alcohol **6** can also provide chiral precursors for the asymmetric synthesis of merrilactone A.
[6] J. L. Luche, *J. Am. Chem. Soc.* **1978**, *100*, 2226.
[7] R. H. Grubbs, H. Chang, *Tetrahedron* **1998**, *54*, 4413.

 © 2006 Wiley-VCH Verlag GmbH & Co. KGaA, Weinheim

Label-Free Biosensors

DOI: 10.1002/anie.200502418

Photobiotin Surface Chemistry Improves Label-Free Interferometric Sensing of Biochemical Interactions**

*Joey C. Latham, Dmitry A. Markov, Henrik S. Sørensen, and Darryl J. Bornhop**

To accurately characterize molecular interactions, determinations should be done in a label-free manner.[1,2] Furthermore, in order to have the capability to fully evaluate the molecular diversity that exists in nature, it would be most advantageous to make these determinations with micro-total-analysis systems (μ-TAS)[3,4] configured for high throughput.[5,6] Yet, conventional detection methods are difficult to implement in μ-TAS and are often volume- or sensitivity-limited, both impediments to performing systems-biology analyses.

Investigators have developed various detection methods for use with microfluidic devices that have promise for label-free nanoscale detection. These include the nanoelectrode,[7] the porous Si (p-Si) sensor,[8,9] the surface plasmon resonance (SPR) detector,[10–13] and backscattering interferometry.[14–16] However, nanoelectrodes foul easily in real-world applications and require multistep manufacturing procedures for the integration into microfluidic chips. The SPR and p-Si methods are sensitive (detection limits of $\approx$10–50 nM for protein interactions[8,9,17]) and capable of sensing label-free biochemical interactions, yet neither technique is inherently compatible with μ-TAS. Integration or immobilization of p-Si into the fluidic network and long solute-diffusion times hinder the use of this method in μ-TAS. Since SPR relies on the excitation of plasmons—collective oscillations of free electrons that occur predominantly in metals—SPR surfaces are coated with a thin metal layer (for example, gold). This makes integration of SPR sensors into plastics challenging and relatively expensive as a result of the deposition process. Additionally, the

[*] J. C. Latham, D. A. Markov, Prof. Dr. D. J. Bornhop
Vanderbilt University
Department of Chemistry
4226 Stevenson Center, Nashville, TN 37235 (USA)
Fax: (+1) 615-343-1234
E-mail: darryl.bornhop@vanderbilt.edu

H. S. Sørensen
RISØ National Laboratory
Department of Optics and Plasma Research
Building 130, Frederiksborgvej 399, 4000 Roskilde (Denmark)

[**] This work was supported by the National Science Foundation, National Eye Institute, BioP graduate school, Applied Biosystems, and NASA. Affiliations include the Vanderbilt Institute of Nanoscience and Engineering, Vanderbilt Institute of Chemical Biology, and Vanderbilt Institute for Integrative Biosystem Research and Education.

Supporting information for this article is available on the WWW under http://www.angewandte.org or from the author.

© 2006 Wiley-VCH Verlag GmbH & Co. KGaA, Weinheim

elaborate surface chemistry used to immobilize targets on SPR surfaces has been shown to lose as much as 20% of binding capacity over a 24-hour period.[10] Backscattering interferometry in rectangular channels (BIRC)[15] was recently shown to be applicable to label-free assays, can be used to study reversible molecular interactions in poly(dimethylsiloxane) (PDMS) chips, and is compatible with μ-TAS. Although promising, BIRC has been limited by tedious immobilization chemistry and, owing to less than optimum transduction-scheme concentration detection limits, has bordered on relevance to biological systems.

Herein we address many of these problems through the use of simple and robust surface immobilization chemistry on polymer chips and an improved BIRC instrument based on charge-coupled-device (CCD) transduction and fringe-pattern Fourier analysis. For the first time, it is shown that simple photoactivatable surface chemistry[18,19] can be used for the immobilization of substrates onto PDMS-facilitated, label-free, reversible-binding assays. This simplified approach to surface immobilization is a significant alteration to our earlier binding studies and those methods commonly used for surface activation/immobilization chemistry.[12,20]

A two-step biotin/avidin reaction (Figure 1) with a carbene-generating form of photobiotin consisting of a biotin moiety, spacer arm, and photoactivatable group was used to immobilize target molecules of interest. A solution (7 μL) of carbene-generating photobiotin (0.5 mg mL^{-1}) containing 0.02% Tween 20 and 50% (v/v) acetone was introduced into the PDMS channels and allowed to dry. Irradiation of the photobiotin molecule caused photolysis of the diazirine group, thereby producing an electronically excited np* state. Formation of an excited-state diradical was followed by internal conversion and production of a carbene. The highly reactive carbene was then inserted into the oxidized substrate. As a result, a homogeneous layer of biotin molecules was strongly bound to the channel surface.

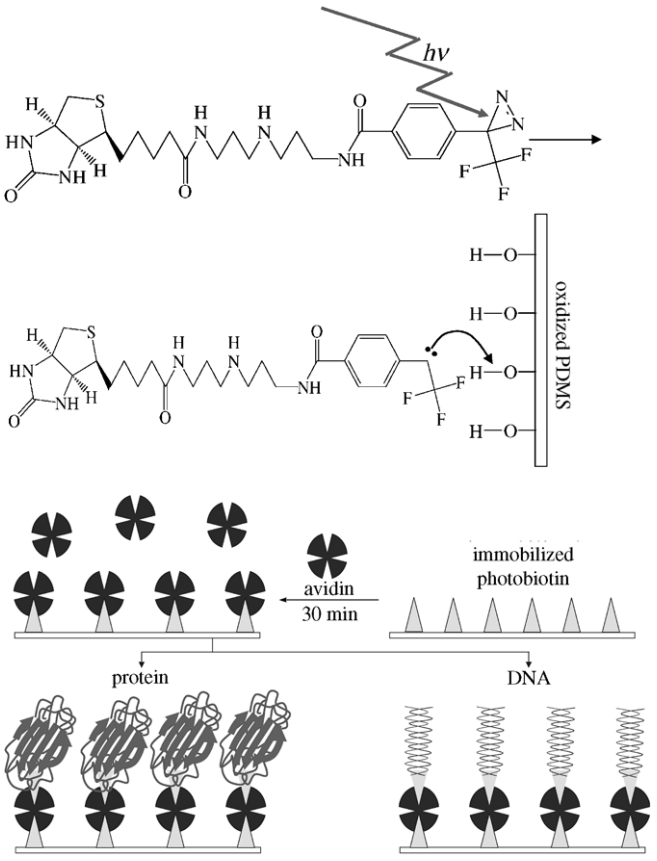


Figure 1. Top: Photobiotin is activated upon exposure to UV light and this promotes insertion into the oxidized PDMS substrate. Center: Avidin binds strongly to the immobilized layer of biotin. The tetrameric nature of avidin signifies that it can simultaneously bind the surface-bound biotin as well as any biotinylated target molecule that passes through the channel (bottom).

A solution of extravidin (0.5 mg mL^{-1}) was injected into the same channels and allowed to incubate for 30 min. Extravidin recognizes the imidazole ring that is *cis* fused to a tetrahydrothiophene ring, and binds to biotin with high affinity (association constant, $K_a = 2.5 \times 10^{11}\,\text{M}^{-1}$).[21] The resulting biotin/avidin complex is very stable to changes in temperature, pH value, and denaturing agents, unlike the lysine/glutaraldehyde/streptavidin/ethanolamine sandwich described in our earlier binding experiments.[15] Fluorescence images (not shown) of fluorescein isothiocyanate (FITC) labeled avidin were used to confirm that the surface chemistry used for immobilization was successful. Thus, biotinylated targets can be immobilized onto the PDMS-molded channel surface to result in a cost-effective, disposable chip that is applicable to the analysis of a variety of reversible biochemical interactions.

As described in detail elsewhere,[14,15,22,23] BIRC (Figure 2) employs a connected light source that illuminates a microfluidic channel, thereby creating a series of high-contrast interference fringes in the backscattered direction that shift with the optical pathlength. Herein we show that the overall performance of BIRC can be improved 100-fold through proper design and implementation of the photo-transduction method.

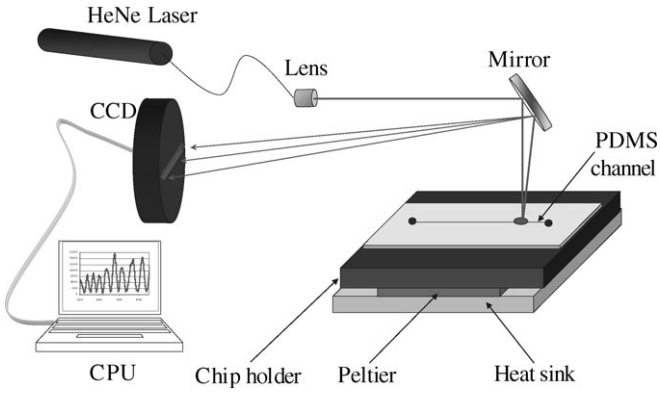


Figure 2. Schematic diagram of BIRC showing the simple optical train consisting of a connected light source, a microfluidic channel, and a phototransducer.

The use of a CCD combined with spatial Fourier analysis[14] for signal transduction, rather than an avalanche photodiode detector, facilitates improved sensitivity and reproducibility, while greatly simplifying alignment. Direction

 © 2006 Wiley-VCH Verlag GmbH & Co. KGaA, Weinheim

of multiple fringes onto the CCD array promotes signal averaging and enhanced signal-to-noise (S/N) results. A fringe-pattern Fourier transformation (FFT) algorithm is inherently insensitive to laser-intensity fluctuations[14] and allows spatial phase determination. Since the CCD is a large-area device, three to upwards of eight fringes from the interference pattern can be used, thereby eliminating the need to align the slit-photodetector with respect to $1/e^2$ intensity on a particular fringe.

To evaluate the new immobilization chemistry and transduction method, two reversibly binding pairs were studied, protein A (P_A) linked to immunoglobulin G (IgG) and a 30-mer DNA–DNA pair. P_A, containing four high-affinity ($K_a = 2\times10^8$–$4.54\times10^8\,M^{-1}$) binding sites capable of interacting with the F_c region of IgG from several species, including human and rabbit, was immobilized onto a PDMS chip by using the chemistry shown in Figure 1. The reversible-binding assay of P_A with IgG was repeated five times (Figure 3). The non-

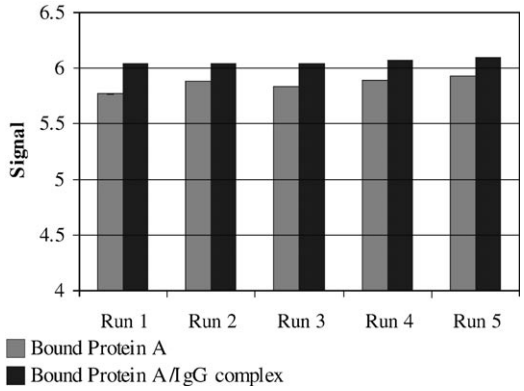


Figure 3. Biotinylated P_A was immobilized on the channel surface. Unreacted P_A was washed out with phosphate-buffered saline (PBS)/Tween 20. A human IgG F_c solution (0.5 mg mL^{-1}) in PBS was introduced into the microfluidic channel and allowed to bind to the P_A for 5 min. The channel was then rinsed with PBS/Tween 20 to remove any unbound IgG. Removal of the bound IgG from P_A was performed by using an acetic acid wash.

complementary fragment, F_{ab}, served as the control and showed no signal (change in refractive index/phase; data not shown) when introduced into the P_A-coated channel. As seen in Figure 3, reversible-binding events can be monitored with an excellent S/N ratio (pooled standard deviation = 0.0017). If it is assumed that complete reaction between the binding pair took place, and on the basis of the target-surface coverage, the 3σ detection limit is 4×10^{-17} mol (40 attomol) in a 500-pL probe volume. These results represent an increase in sensitivity of two orders of magnitude when they are compared to the P_A/IgG experiments performed previously.[15]

The use of microfluidic chips to perform nucleic acid analysis has allowed the detection and discrimination of multiple DNA sequences[24,25] and can eventually facilitate high-throughput screening techniques.[26] As further demonstration of the utility of BIRC, a label-free reversible DNA assay was performed (Figure 4). Immobilization of a biotinylated 30-mer of mActin (5′-ACTCATCGTACTCCTGCTTGCTGATCCACA-3′; $M_W = 9622.5$; melting temperature,

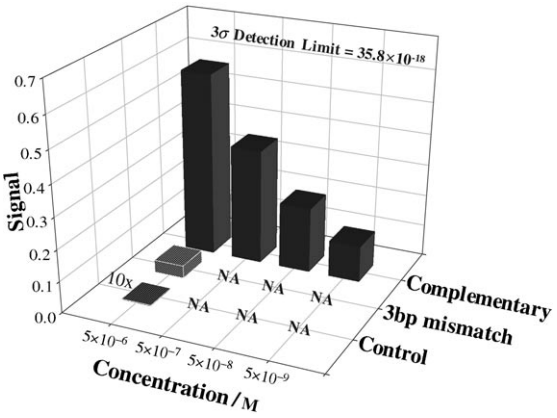


Figure 4. The binding affinity of a complementary DNA strand to an immobilized target over a multiple complementary strand. The complementary strand is also compared to a 3-bp mismatch and control strands at high concentration. All probe strands were allowed 20 min for hybridization. The control signal is shown at ten times its actual signal to allow visualization.

$T_M = 68.7\,°C$) onto the PDMS channel was possible with the biotin/avidin surface chemistry described above. Nonlabeled complementary DNA strands were successively hybridized to the immobilized mActin 30-mer and then removed with an NaOH wash. Binding events of complementary DNA followed exponential growth for BIRC over concentrations ranging from 5 nM up to roughly 500 mM with excellent convergence ($R^2 = 0.988$). A noncomplementary probe strand, according to the Watson–Crick model, served as the control and showed no appreciable signal. If it is assumed that hybridization went to completion and 100% channel-surface coverage was attained, at 3σ, 36 attomol DNA were quantifiable in a 500-pL detection volume.

Ultimately, it would be desirable to screen for an array of different sequences in a label-free manner to avoid perturbations due to the signaling fluorophore or derivation chemistry. A step toward this requires the determination of the discrimination that is possible with BIRC. We used an oligomer consisting of a three-base-pair mismatch (at positions 5, 15, and 25) from that of the complementary mActin strand as an initial test of specificity. The experiment consisted of immobilizing the mActin 30-mer as noted above and a subsequent repetitive hybridization test with a 5-μM solution of the mismatch strand. Figure 4 shows the typical output from one of the binding evaluations. Three trials of these experiments produced an average signal corresponding to greater than 140% of that for the control and approximately 7% of the signal for the complementary strand.

In conclusion, the biotin/avidin surface chemistry significantly simplified substrate preparation, was compatible with PDMS, and facilitated free-solution assays with BIRC. Combination of this new surface chemistry with the CCD FFT transduction has allowed improved detection for P_A/IgG binding by two orders of magnitude.[15] BIRC was also used to monitor DNA hybridization over a wide range of concentrations and allowed discrimination in binding of a three-base-pair mismatch. The use of PDMS microfluidic

 © 2006 Wiley-VCH Verlag GmbH & Co. KGaA, Weinheim

chips and the exceedingly simple optical train of BIRC represents a cost-effective platform for label-free molecular-interaction determinations as well as for the investigation of reversible biological interactions within subnanoliter volumes and at the attomole level. The methodology and technology are compatible with large-scale integration and should facilitate high-throughput assays.

Received: July 11, 2005
Published online: December 30, 2005

Keywords: biosensors · interferometry · nucleic acids · proteins · surface chemistry

[1] M. A. Cooper, *Anal. Bioanal. Chem.* **2003**, *377*, 834.
[2] F. E. Torres, P. Kuhnt, D. De Bruyker, A. G. Bell, M. V. Wolkin, E. Peeters, J. R. Williamson, G. B. Anderson, G. P. Schmitz, M. I. Recht, S. Schweizer, L. G. Scott, J. H. Ho, S. A. Elrod, P. G. Schultz, R. A. Lerner, R. H. Bruce, *Proc. Natl. Acad. Sci. USA* **2004**, *101*, 9517.
[3] C. Hansen, S. R. Quake, *Curr. Opin. Struct. Biol.* **2003**, *13*, 538.
[4] S. K. Sia, G. M. Whitesides, *Electrophoresis* **2003**, *24*, 3563.
[5] J. R. Heath, M. E. Phelps, L. Hood, *Mol. Imaging Biol.* **2003**, *5*, 312.
[6] M. Ferrari, *Nat. Rev. Cancer* **2005**, *5*, 161.
[7] J. Hahm, C. M. Lieber, *Nano Lett.* **2004**, *4*, 51.
[8] V. S. Y. Lin, K. Motesharei, K. P. S. Dancil, M. J. Sailor, M. R. Ghadiri, *Science* **1997**, *278*, 840.
[9] K.-P. S. Dancil, D. P. Greiner, M. J. Sailor, *J. Am. Chem. Soc.* **1999**, *121*, 7925.
[10] R. L. Rich, Y. S. N. Day, T. A. Morton, D. G. Myszka, *Anal. Biochem.* **2001**, *296*, 197.
[11] E. A. Smith, W. D. Thomas, L. L. Kiessling, R. M. Corn, *J. Am. Chem. Soc.* **2003**, *125*, 6140.
[12] J. M. Brockman, A. G. Frutos, R. M. Corn, *J. Am. Chem. Soc.* **1999**, *121*, 8044.
[13] G. J. Wegner, N. J. Lee, G. Marriott, R. M. Corn, *Anal. Chem.* **2003**, *75*, 4740.
[14] D. Markov, D. Begari, D. J. Bornhop, *Anal. Chem.* **2002**, *74*, 5438.
[15] D. A. Markov, K. Swinney, D. J. Bornhop, *J. Am. Chem. Soc.* **2004**, *126*, 16659.
[16] K. Swinney, D. Markov, D. J. Bornhop, *Anal. Chem.* **2000**, *72*, 2690.
[17] T. Sakai, K. Shinahara, A. Torimaru, H. Tanaka, Y. Shoyama, K. Matsumoto, *Anal. Sci.* **2004**, *20*, 279.
[18] S. A. Brooks, W. P. Ambrose, W. G. Kuhr, *Anal. Chem.* **1999**, *71*, 2558.
[19] S. A. Brooks, N. Dontha, C. B. Davis, J. K. Stuart, G. O'Neill, W. G. Kuhr, *Anal. Chem.* **2000**, *72*, 3253.
[20] G. M. Whitesides, E. Ostuni, S. Takayama, X. Y. Jiang, D. E. Ingber, *Annu. Rev. Biomed. Eng.* **2001**, *3*, 335.
[21] A. Chilkoti, P. S. Stayton, *J. Am. Chem. Soc.* **1995**, *117*, 10622.
[22] H. S. Sorensen, H. Pranov, N. B. Larsen, D. J. Bornhop, P. E. Andersen, *Anal. Chem.* **2003**, *75*, 1946.
[23] K. Swinney, D. Markov, D. J. Bornhop, *Rev. Sci. Instrum.* **2000**, *71*, 2684.
[24] A. J. Thiel, A. G. Frutos, C. E. Jordan, R. M. Corn, L. M. Smith, *Anal. Chem.* **1997**, *69*, 4948.
[25] Y. W. C. Cao, R. C. Jin, C. A. Mirkin, *Science* **2002**, *297*, 1536.
[26] F. Vinet, P. Chaton, Y. Fouillet, *Microelectron. Eng.* **2002**, *61–62*, 41.

 © 2006 Wiley-VCH Verlag GmbH & Co. KGaA, Weinheim

Asymmetric Synthesis

DOI: 10.1002/anie.200502488

Highly Diastereo- and Enantioselective Direct Aldol Reactions in Water**

Yujiro Hayashi, Tatsunobu Sumiya, Junichi Takahashi, Hiroaki Gotoh, Tatsuya Urushima, and Mitsuru Shoji*

Reactions in which water is used as the solvent have attracted a great deal of attention because water is an environmentally friendly, safe medium, which avoids the problems of pollution that are inherent with organic solvents.[1] The synthesis of enantiopure molecules is another important issue, and the development of enantioselective reactions in water is an extensively investigated topic,[2] although it was long thought to be mainly confined to the realm of enzymes. Successful catalytic versions of enantioselective reactions have mostly employed transition-metal complexes,[3] and may require toxic, rare, and expensive metals, and suffer from possible contamination of the products by metal. Organocatalysts,[4] however, are free from these problems, and moreover are inexpensive and stable to moisture and air. Thus, the development of small organic molecules that catalyze enantioselective reactions in water is currently a highly sought-after goal in chemistry.

The aldol condensation is a key carbon–carbon bond-forming reaction, which creates the β-hydroxy carbonyl structural unit found in many natural products and drugs.[5] In nature, type I and II aldolases catalyze this reaction in water with perfect enantiocontrol through an enamine mechanism and by using a zinc cofactor, respectively.[6] The Mukaiyama aldol reaction proceeds in aqueous organic solvent, but this is an indirect method that requires preformation of a silyl enol ether as a nucleophile.[7] A Zn-proline-catalyzed aldol reaction occurs in aqueous media with moderate enantiomeric excess.[8] However, proline can catalyze direct aldol reactions in polar organic solvents with high enantioselectivity,[4,9] but it affords the racemate in water.[10] Although several chiral organocatalysts have been developed for the aldol reaction,[4,11] and some of them provide aldols enantioselectively in aqueous organic solvents,[12] they still require the use of an organic solvent.[13] As far as we are aware, only enzymes and antibodies of very high molecular

[*] Prof. Dr. Y. Hayashi, T. Sumiya, J. Takahashi, H. Gotoh, T. Urushima, Dr. M. Shoji
Department of Industrial Chemistry
Faculty of Engineering
Tokyo University of Science
Kagurazaka, Shinjuku-ku, Tokyo 162-8601 (Japan)
Fax: (+81) 3-5261-4631
E-mail: hayashi@ci.kagu.tus.ac.jp

[**] This work was partially supported by a Grant-in-Aid for Scientific Research on Priority Areas 16073219 from The Ministry of Education, Culture, Sports, Science, and Technology (MEXT).

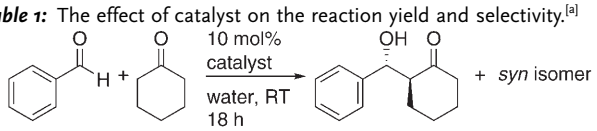
Supporting information for this article is available on the WWW under http://www.angewandte.org or from the author.

WILEY InterScience DISCOVER SOMETHING GREAT
© 2006 Wiley-VCH Verlag GmbH & Co. KGaA, Weinheim

weight have been able to catalyze the direct aldol reaction in water with high enantioselectivity.[5,6] Moreover, a rather large catalyst loading is usually required for the aldol reactions mediated by organocatalysts. Herein we describe a synthetic small organic molecule that promotes highly diastereo- and enantioselective aldol reactions in the presence of water.

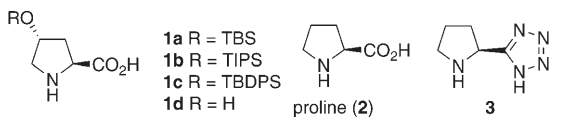
We have previously reported that 4-*tert*-butyldimethylsiloxyproline (**1a**), which is easily prepared from commercially available *trans*-4-hydroxyproline, is a highly active proline surrogate in the α-aminoxylation of carbonyl compounds and the Mannich reaction.[14] Application of this siloxyproline as a catalyst to the aldol reaction of cyclohexanone and benzaldehyde led to an unexpected result, namely, the asymmetric aldol reaction proceeded efficiently in the presence of water and the anti-aldol product was obtained with excellent diastereoselectivity in a nearly optically pure form (Table 1, entry 1).[15] This is the first highly diastereoselective and enantioselective aldol reaction carried out in the presence of water without using an organic solvent. Screening the reaction (Table 1) demonstrated that not only TBS-protected proline **1a** (Scheme 1) but also TIPS- and TBDPS-protected prolines **1b** and **1c**[16] were excellent catalysts, and in all cases the *anti* isomer was obtained in good yield with excellent diastereoselectivity in a nearly optically pure form (entries 1, 6, and 7). Although the amount of water had little effect on the yield and selectivities, with the reaction proceeding in a two-phase system, the reactions without a solvent or in an organic solvent (DMSO)[17] resulted in lower enantioselectivity, with formation of nearly equal amounts of *anti* and *syn* isomers (entries 1–5). These results indicate that water is indispensable for the high diastereo- and enantioselectivities.[18] The reaction scarcely proceeded with the tetrazole catalyst **3** in the presence of water; this catalyst, however, promoted the aldol reaction of chloral in the presence of water (entry 10).[12a] As proline (**2**) and hydroxyproline (**1d**) did not promote the reaction in the presence of water, the siloxy group of catalyst **1** is clearly essential for the success of this reaction (entries 8, 9).

Table 1: The effect of catalyst on the reaction yield and selectivity.[a]



Entry	Catalyst	Yield [%][b]	*anti*:*syn*[c]	*ee* [%][d]
1	**1a**	61	19:1	>99
2[e]	**1a**	66	20:1	>99
3[f]	**1a**	69	20:1	>99
4[g]	**1a**	61	1.8:1	89
5[h]	**1a**	65	1:1	80
6	**1b**	71	14:1	>99
7	**1c**	78	13:1	>99
8	**1d**	<5	–	–
9	**2**	<5	–	–
10	**3**	<5	–	–

[a] Unless otherwise shown, the reaction was performed with benzaldehyde (0.4 mmol), cyclohexanone (207 μL, 2.0 mmol), catalyst (0.04 mmol), and H_2O (0.13 mL) at room temperature for 18 h. [b] Yield refers to the combined yield of isolated diastereomers. [c] Diastereoselectivity was determined by ^{1}H NMR analysis of the reaction mixture. [d] Optical yield refers to that of the *anti* isomer and was determined by HPLC analysis on a chiral phase (chiralcel OD-H). [e] H_2O (72 μL) was employed. [f] H_2O (36 μL) was employed. [g] The reaction was performed neat. [h] The reaction was performed in DMSO (0.4 mL).



Scheme 1. Organocatalysts examined in this study. TBS = *tert*-butyldimethylsilyl, TIPS = triisopropylsilyl, TBDPS = *tert*-butyldiphenylsilyl.

The generality of the reaction was examined in detail using catalyst **1c**, and the results are summarized in Table 2. The reaction has broad applicability with respect to the aldehyde: Both excellent enantioselectivity (over 95% *ee*) and *anti* selectivity were obtained when cyclohexanone and cyclopentanone were employed. Not only reactive, electron-deficient aldehydes, but neutral aldehydes are also excellent electrophilic partners in this reaction. Excellent *ee* values were obtained in the case of electron-rich aldehydes, although the yield was only moderate (entry 4). Both aromatic and aliphatic aldehydes could be employed. Heteroaromatic aldehydes such as furfural and *para*-pyridinecarbaldehyde were also excellent substrates (entries 6 and 7). 2,2-Dimethyl-1,3-dioxan-5-one can be employed successfully as the nucleophilic ketone, and affords a polyoxy compound with excellent selectivity (entry 11).[12f,19] A water-soluble aldehyde such as formaldehyde can also be employed successfully (entry 12).[12a,d] The method has its limitations, however: Although the aldol reaction of acetone and hydoxyacetone proceeded in water, the enantioselectivity was moderate.

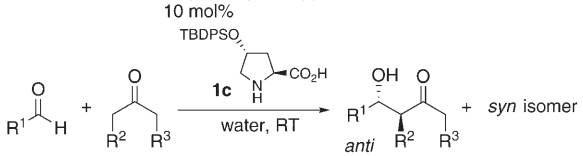
The effectiveness of the siloxyproline catalysts compared to proline and hydroxyproline can be attributed to the solubility of the catalysts. Although proline and hydroxyproline dissolve in water, siloxyproline is only partially soluble in water and forms an organic phase with the aldehyde and ketone in which the aldol reaction proceeds efficiently.

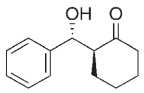
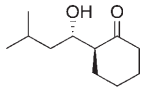
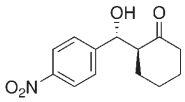
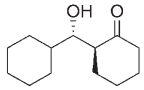
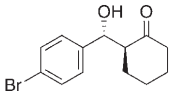
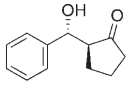
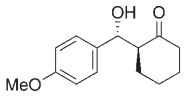
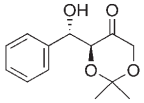
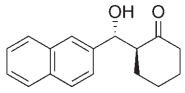
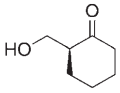
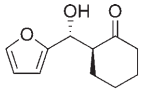
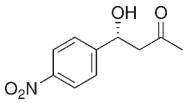
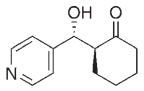
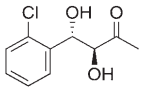
A preliminary study showed that the catalyst loading can be reduced to as low as 1 mol% without compromising the enantioselectivity, and 300 mol% of water is enough for the reaction to be effected in a diastereo- and enantioselective manner, although a longer reaction time is needed (2 days). These reaction conditions are suitable for a preparative-scale synthesis. After the reaction, filtration of the reaction mixture through a short pad of silica gel removed the water and the organocatalyst **1c**, and only a small amount of extra solvent was needed. The direct distillation of the filtrate afforded the product in 78% yield with excellent enantioselectivity on a 6-mmol scale [Eq. (1)].[20] It should be noted that this is the first organocatalyst-mediated aldol reaction, in which only 1 mol% of organocatalyst can promote the reaction with high diastereoselectivity and excellent enantioselectivity.

Our results show that the synthetic compounds **1** are the first asymmetric organocatalysts that promote the aldol

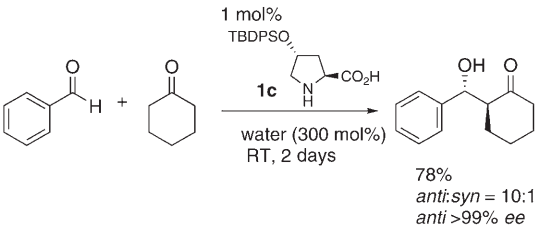
 © 2006 Wiley-VCH Verlag GmbH & Co. KGaA, Weinheim

Table 2: The catalytic asymmetric aldol reaction in water catalyzed by siloxyproline **1c**.[a]



Entry	Product	*t* [h]	Yield [%][b]	*anti*:*syn*[c]	*ee* [%][d]	Entry	Product	*t* [h]	Yield [%][b]	*anti*:*syn*[c]	*ee* [%][d]
1		18	78	13:1	>99	8		20	54	>20:1	>99
2		5	86	20:1	>99	9		24	76	>20:1	>99
3		28	80	20:1	97	10[e]		18	74	9:1	>99
4		50	21	5:1	96	11		18	48	25:1	95
5		40	89	19:1	97	12[f]		90	37	–	96
6[e]		28	79	4.7:1	97	13[g]		18	63	–	67
7		2.5	92	12:1	95	14		72	61	1:1	64, 61[h]

[a] The reaction was performed with aldehyde (0.4 mmol), ketone (2.0 mmol), **1c** (0.04 mmol), and H_2O (0.13 mL) at room temperature. [b] Combined yield of isolated diastereomers. [c] Diastereoselectivity was determined by ^1H NMR analysis of the reaction mixture. [d] Optical yield refers to that of the *anti* isomer and was determined by HPLC analysis on a chiral phase. [e] Catalyst **1a** was used instead of **1c**. [f] Aqueous formalin (35%, 35 μL, 0.4 mmol) and NaCl (47 mg) were employed. [g] Acetone (10.8 mmol) was employed. [h] Optical yield of the *syn* isomer.



(1)

reaction in the presence of water without organic solvent, a process that has hitherto belonged to the realm of enzyme chemistry. The reaction catalyzed by these siloxy catalysts has the following notably features: 1) It proceeds in the presence of water without organic solvent; 2) very high enantioselectivity is attained in most cases; 3) both diastereo- and enantioselectivities are higher than for the reaction performed in an organic solvent; 4) the catalysts themselves can be easily prepared in large quantities from *trans*-hydroxyproline, both enantiomers of which are commercially available; 5) a low catalyst loading (1 mol%) can be utilized. As the synthetic catalysts can be easily modified, their selectivity and reactivity may be tunable, and hence the findings reported herein may open up a new avenue for the design of catalysts that possess even better properties and are effective in water.

Experimental Section

Experimental procedure of Equation (1): Catalyst **1c** (22.2 mg, 0.06 mmol) was added to a suspension of benzaldehyde (0.60 mL, 6.0 mmol), cyclohexanone (3.1 mL, 30 mmol), and water (0.32 mL, 18 mmol) at room temperature. The reaction mixture was stirred for 48 h, and silica gel (220 mg) was added to the reaction mixture. The mixture was filtered through silica gel using ethyl acetate (10 mL), and the crude organic materials were purified by distillation to afford 2-(hydroxyphenylmethyl)cyclohexanone (954.3 mg, 78%) as a colorless oil: *anti*:*syn* = 10:1 (by ^1H NMR spectroscopy of the crude mixture), >99% *ee* (by HPLC on a chiralcel OD-H column, λ = 213 nm, *i*PrOH/hexane 1:100, 1.0 mL min^{-1}; t_R = 19.4 min (major), 25.9 min (minor)).

Received: July 17, 2005
Published online: December 30, 2005

Keywords: aldol reaction · asymmetric synthesis · diastereoselectivity · organocatalysis · solvent effects

 © 2006 Wiley-VCH Verlag GmbH & Co. KGaA, Weinheim

[1] a) *Organic Synthesis in Water* (Ed.: P. A. Grieco), Blackie A & P, London, **1998**; b) U. M. Lindstrom, *Chem. Rev.* **2002**, *102*, 2751; c) C.-J. Li, *Chem. Rev.* **2005**, *105*, 3095.

[2] D. Sinou, *Adv. Synth. Catal.* **2002**, *344*, 221.

[3] *Comprehensive Asymmetric Catalysis I–III* (Eds.: E. N. Jacobsen, A. Pfaltz, H. Yamamoto), Springer, Berlin, **1999**.

[4] a) A. Berkssel, H. Groger, *Asymmetric Organocatalysis*, Wiley-VCH, Weinheim, **2005**; b) P. I. Dalko, L. Moisan, *Angew. Chem.* **2004**, *116*, 5248; *Angew. Chem. Int. Ed.* **2004**, *43*, 5138; c) Y. Hayashi, *J. Syn. Org. Chem. Jpn.* **2005**, *63*, 464.

[5] *Modern Aldol Reactions, Vols. 1, 2* (Ed.: R. Mahrwald), Wiley-VCH, Weinheim, **2004**.

[6] T. D. Machajewski, C.-H. Wong, *Angew. Chem.* **2000**, *112*, 1406; *Angew. Chem. Int. Ed.* **2000**, *39*, 1352.

[7] T. Hamada, K. Manabe, S. Ishikawa, S. Nagayama, M. Shiro, S. Kobayashi, *J. Am. Chem. Soc.* **2003**, *125*, 2989.

[8] T. Darbre, M. Machuqueiro, *Chem. Commun.* **2003**, 1090.

[9] For representative reports, see; a) Z. G. Hajos, D. R. Parrish, *J. Org. Chem.* **1974**, *39*, 1615; b) U. Eder, G. Sauer, R. Wiechert, *Angew. Chem.* **1971**, *83*, 492; *Angew. Chem. Int. Ed. Engl.* **1971**, *10*, 496; c) B. List, R. A. Lerner, C. F. Barbas III, *J. Am. Chem. Soc.* **2000**, *122*, 2395; d) A. B. Northup, D. W. C. MacMillan, *J. Am. Chem. Soc.* **2002**, *124*, 6798.

[10] A. Cordova, W. Notz, C. F. Barbas III, *Chem. Commun.* **2002**, 3024.

[11] Z. Tang, Z.-H. Yang, X.-H. Chen, L.-F. Cun, A.-Q. Mi, Y.-Z. Jiang, L.-Z. Gong, *J. Am. Chem. Soc.* **2005**, *127*, 9285, and references therein.

[12] a) H. Torii, M. Nakadai, K. Ishihara, S. Saito, H. Yamamoto, *Angew. Chem.* **2004**, *116*, 2017; *Angew. Chem. Int. Ed.* **2004**, *43*, 1983; b) A. I. Nyberg, A. Usano, P. M. Pihko, *Synlett* **2004**, 1891; c) Z. Tang, Z.-H. Yang, L.-F. Cun, L.-Z. Gong, A.-Q. Mi, Y.-Z. Jiang, *Org. Lett.* **2004**, *6*, 2285; d) J. Casas, H. Sunden, A. Cordova, *Tetrahedron Lett.* **2004**, *45*, 6117; e) D. E. Ward, V. Jheengut, *Tetrahedron Lett.* **2004**, *45*, 8347; f) I. Ibrahem, A. Cordova, *Tetrahedron Lett.* **2005**, *46*, 3363; g) M. Amedjkouh, *Tetrahedron: Asymmetry* **2005**, *16*, 1411; h) A. Cordova, W. Zou, I. Ibrahem, E. Reyes, M. Engqvist, W.-W. Liao, *Chem. Commun.* **2005**, 3586.

[13] Nornicotine was reported to promote the aldol reaction in water, but low asymmetric induction (ca. 20% *ee*) was observed: a) T. J. Dickerson, K. D. Janda, *J. Am. Chem. Soc.* **2002**, *124*, 3220; b) C. J. Rogers, T. J. Dickerson, A. P. Brogan, K. D. Janda, *J. Org. Chem.* **2005**, *70*, 3705.

[14] Y. Hayashi, J. Yamaguchi, K. Hibino, T. Sumiya, T. Urushima, M. Shoji, D. Hashizume, H. Koshino, *Adv. Synth. Catal.* **2004**, *346*, 1435.

[15] The absolute configuration of the *anti* isomer was determined by comparison of the optical rotation with that reported in the literature: S. E. Denmark, R. A. Stavenger, K.-T. Wong, X. Su, *J. Am. Chem. Soc.* **1999**, *121*, 4982.

[16] K. Inomata, M. Barrague, L. A. Paquette, *J. Org. Chem.* **2005**, *70*, 533.

[17] The other organic solvents gave poor results.

[18] In some reactions,[12] the *ee* value was increased in the presence of water.

[19] D. Enders, C. Grondal, *Angew. Chem.* **2005**, *117*, 1235; *Angew. Chem. Int. Ed.* **2005**, *44*, 1210.

[20] The reaction could be also performed on a 70-mmol scale.

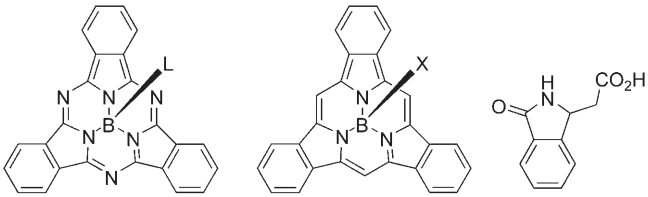
 © 2006 Wiley-VCH Verlag GmbH & Co. KGaA, Weinheim

DOI: 10.1002/anie.200503426

Tribenzosubporphines: Synthesis and Characterization**

Yasuhide Inokuma, Jung Ho Kwon, Tae Kyu Ahn, Min-Chul Yoo, Dongho Kim, and Atsuhiro Osuka**

Subphthalocyanines **1** possess a unique position in the chemistry of phthalocyanines as a ring-contracted congener of phthalocyanine. Since the first synthesis of subphthalocya-



1 **2a** (X = OH) **2b** (X = OMe) **2c** (X = O*i*Pr) **3**

nines by Meller and Ossko in 1972,[1] they have continued to gather much interest in light of their 14π-electron aromatic circuit, triangular bowl-shaped structures, intense fluorescence, and nonlinear optical properties.[2] In sharp contrast, subporphyrin, which is a porphyrinic counterpart of **1**, remains a missing player, thus leaving its study totally untouched, despite recent extensive reports of various ring-expanded and ring-contracted porphyrins.[3] Subporphyrins are expected to be promising macrocycles from both basic and

[*] J. H. Kwon, T. K. Ahn, M.-C. Yoo, Prof. Dr. D. Kim
Center for Ultrafast Optical Characteristics Control and
Department of Chemistry
Yonsei University
Seoul 120-749 (Korea)
Fax: (+82) 2-2123-2434
E-mail: dongho@yonsei.ac.kr
Y. Inokuma, Prof. Dr. A. Osuka
Department of Chemistry
Graduate School of Science
Kyoto University
and
Core Research for Evolutional Science and Technology (CREST)
Japan Science and Technology Agency
Sakyo-ku, Kyoto 606-8502 (Japan)
Fax: (+81) 75-753-3970
E-mail: osuka@kuchem.kyoto-u.ac.jp

[**] This work was partly supported by a Grant-in-Aid from the Ministry of Education, Culture, Sports, Science, and Technology, Japan, (No. 15350022) and the 21st Century COE on Kyoto University Alliance for Chemistry (to A.O.), as well as the National Creative Research Initiatives Program of the Ministry of Science and Technology of Korea (to D.K.).

Supporting information for this article is available on the WWW under http://www.angewandte.org or from the author.

 © 2006 Wiley-VCH Verlag GmbH & Co. KGaA, Weinheim InterScience

applied viewpoints, as judged from the various interesting attributes of subphthalocyanines.[2] Thus, a reliable synthetic route to subporphyrins is highly desirable. Herein we report the synthesis and characterizations of [14]tribenzosubporphine(1.1.1)boron(III) complexes **2a–f**. To the best of our knowledge, this is the first report on the synthesis of subporphyrins.

The hydroxyboron complex of tribenzosubporphine **2a** was synthesized by a modified protocol developed by Gouterman and co-workers[4] for the synthesis of a tetrabenzoporphine using 2-(3-oxo-2,3-dihydro-1*H*-isoindol-1-yl)acetic acid (**3**) and with replacement of the template from a Zn^{II} to a B^{III} ion.[1,2] Compound **3** and boric acid were mixed, ground into a fine powder, and subsequently heated to 350 °C in an N_2 atmosphere for 3.5 h. TLC analysis of the resulting black melt indicated formation of many products, from which a fraction eluting at $R_f = 0.30$ on a silica gel TLC plate with a 1:2:2 mixture of diethyl ether/hexane/dichloromethane was isolated. This product was identified as **2a** on the basis of its parent ion signal by MALDI-TOF mass analysis and its characteristic strong green fluorescence. Repeated separations by chromatography on silica gel gave **2a** as an orange solid in 1.4% yield. Phenylboronic acid or 4-methoxyphenylboronic acid can also be used as the template and give **2a** in comparable yields. The subporphyrin **2a** can also be prepared in 1.2% yield under irradiation with a domestic microwave oven (output: 500 W) for 30 minutes. Although the yields are low, the syntheses of **2a** is quite reproducible.

Reflecting its C_3 symmetry, the subporphyrin **2a** exhibits a very simple ^{1}H NMR spectrum that consists of a singlet at $\delta =$ 9.44 ppm for the *meso* positions, a pair of double doublets for the benzo protons at $\delta = 8.86$ and 7.88 ppm, and a signal at $\delta =$ −2.60 ppm for the hydroxy proton. The observed chemical shifts indicate a diatropic ring current in line with its 14π-electronic network. The ^{13}C NMR spectrum also supports the structure of **2a**, with signals observed at $\delta = 137.0$ and 131.6 ppm for the pyrrolic carbon atoms, signals at $\delta = 127.2$ and 121.5 ppm for the fused benzo carbon atoms, and a signal at $\delta = 97.3$ ppm for the *meso* carbon atom. The ^{11}B NMR spectrum exhibits a singlet at $\delta = -14.6$ ppm, which is slightly less shielded relative to those of subphthalocyanines which appear in the range of $\delta = -17.7$ to −19.6 ppm.[2a] The high resolution electrospray ionization time-of-flight (HRESI-TOF) mass spectrum of **2a** also supports the structure, with a signal at *m*/*z* 409.1387 (calcd for $[C_{27}H_{16}BN_3O]^+$: *m*/*z* 409.1386). The structure of **2a** has been confirmed by X-ray diffraction analysis to be a bowl-shaped tribenzosubporphine structure (Figure 1a).[5]

A solution of **2a** in diethyl ether was stirred in the presence of $H_2{}^{18}O$ for 6 h at room temperature. ESI-TOF mass analysis of this reaction mixture detected two main signals at *m*/*z* 409.14 and 411.14, thus suggesting a facile replacement of the axial hydroxy group. A similar exchange reaction has also been observed on dissolving **2a** in methanol, which immediately gave rise to the appearance of a new spot of **2b** on the TLC plate which became the single product upon refluxing the solution. The methoxy protons of **2b** are observed at $\delta = 0.81$ ppm in the ^{1}H NMR spectrum because of the diatropic ring current. Similarly, refluxing **2a** in 2-propanol afforded isopropoxyboron complex **2c**, which gives rise to signals corresponding to the isopropoxy protons at $\delta =$ 0.63 (1H) and −0.42 ppm (6H) in the ^{1}H NMR spectrum. The subporphyrin **2c** is easily hydrolyzed to **2a** by a small amount of adventitious water in solution, while **2b** is rather stable under basic or neutral conditions, but is readily hydrolyzed in acidic aqueous solution.

The axial hydroxy group of **2a** can be also exchanged by a carboxy group by stirring it in the presence of an excess amount of carboxylic acid, thus providing **2d**, **2e**, and **2f** through the equilibrium shown in Scheme 1. The equilibrium between **2a** and **2d**–**f** could be easily followed by ^{1}H NMR spectroscopy and allowed for the determination of an equilibrium constant of 3.2 (Supporting Information). Stirring a solution of **2a** in the presence of an excess amount of carboxylic acid or continuous removal of water from the reaction mixture gave the carboxyboron complexes in high yields. The ^{11}B NMR spectra of **2d–f** exhibit characteristic, extremely broad signals in the range of $\delta = -13.7$ to −14.6 ppm, and contrast the relatively sharp signals of the hydroxy- and alkoxyboron complexes **2a–c**.

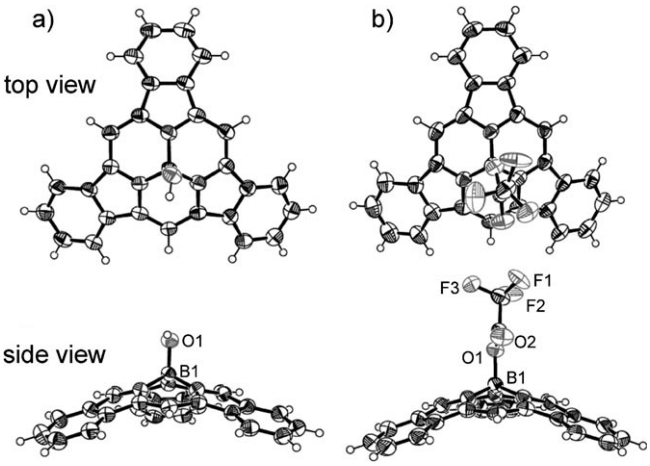
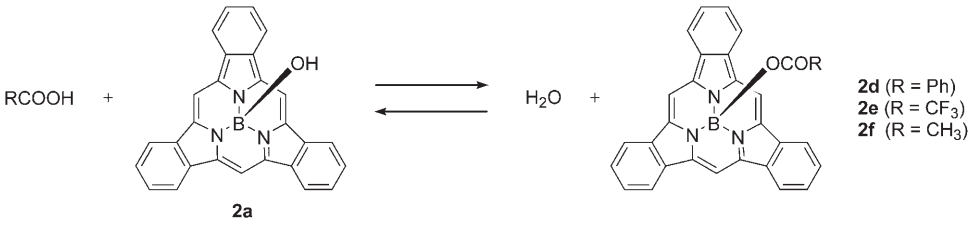


Figure 1. Crystal structures of a) **2a** and b) **2e** at 50% probability of thermal ellipsoids.



Scheme 1. Equilibria between **2a** and **2d–f**.

 © 2006 Wiley-VCH Verlag GmbH & Co. KGaA, Weinheim

Furthermore, X-ray diffraction analysis shows that in the solid-state the macrocycles **2b**, **2c**, and **2e** have bowl-shaped structures, with a variable curvature that depends on the axial group (see Figure 1b and the Supporting Information).[5] The degree of curvature can be characterized by the depth of the bowl, which is defined as the distance from the lowest edge of the macrocycle (the mean plane of the peripheral six carbon atoms of the benzene rings) to the boron atom and is 2.33 Å for **2a**, 1.70 Å for **2b**, 2.10 Å for **2c**, and 2.02 Å for **2e**. The bowl depths of the subporphyrins are less than that (2.55 Å) of subphthalocyanine **1** (L = OH),[2c] and **2b** is the shallowest bowl in the series.[6] The average N-B-N angles are 105.1° for **2a**, 105.5° for **2b**, 105.2° for **2c**, and 108.4° for **2e**, and the average B–N bond lengths are 1.51 Å for **2a**, 1.50 Å for **2b**, 1.51 Å for **2c**, and 1.48 Å for **2e**, and the B–O bond lengths are 1.446(4) Å for **2a**, 1.445(5) Å for **2b**, 1.435(3) Å for **2c**, and 1.506(5) Å for **2e**, respectively. These structural parameters suggest **2e** has a different electronic nature from those of **2a–c**. A possible explanation may be that the B–O bond for **2e** has a larger ionic character than those of **2a–c**. Overall the bowl-shaped structures of the subporphyrins are similar to those of subphthalocyanines.[7]

The absorption spectrum of **2a** exhibits a sharp Soret band at 355 nm with a shoulder at 337 nm, and Q bands at 480 and 514 nm, which are blue-shifted relative to those of metalloporphyrins mainly because of the reduced π-conjugation pathway (Figure 2). The Q bands show a vibronic structure

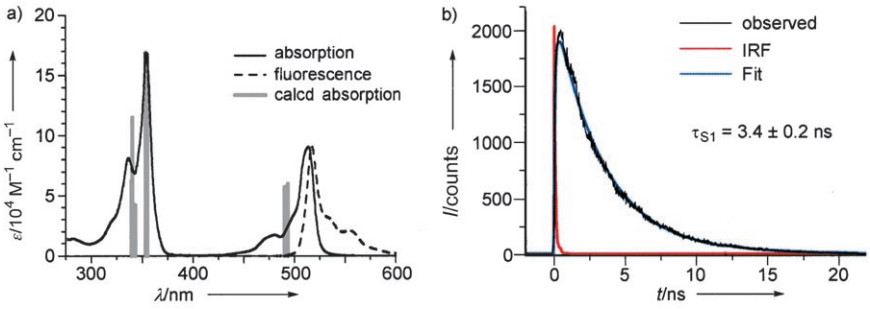


Figure 2. a) Absorption and fluorescence spectra of **2a** in CH_2Cl_2, and calculated absorption bands, and b) the fluorescence decay of **2a**.

similar to those of subphthalocyanines and benzoporphyrins with large molar extinctions of the Q band of $9 \times 10^4\,M^{-1}\,cm^{-1}$, which is more than three times larger than the value ($2.97 \times 10^4\,M^{-1}\,cm^{-1}$) of $Zn^{II}TPP$ (TPP = tetraphenylporphyrin). The strong and sharp Soret bands with an extinction coefficient of $1.64 \times 10^5\,M^{-1}\,cm^{-1}$ differ significantly from the rather broad Soret bands of subphthalocyanines around 300 nm and are similar to the Soret bands of porphyrins. This similarity has been confirmed by calculation of the molecular orbitals (MOs) at the B3LYP/6-31G* level (see the Supporting Information). The π–π* transitions calculated by time-dependent density functional theory (TD-DFT) match well with the absorption spectrum of **2a** (indicated by vertical bars in Figure 2).[8] Interestingly, **2a** exhibits intense green fluorescence at 517 nm with $\Phi_F = 0.41$,[9] whose decay has been found to obey a single exponential function with $\tau = 3.4 \pm 0.2$ ns, as determined by the time-correlated single-photon counting technique. The lowest triplet excited state (T_1) of **2a** has been detected in CH_2Cl_2 by nanosecond time-resolved transient absorption spectroscopy to have a broad absorbance in the range 350–700 nm whose decay follows a single exponential function with $\tau = 54$ μs. Furthermore, femtosecond time-resolved transient absorption anisotropy measurements revealed that the anisotropy value is initially about 0.12 and decays with $\tau = 46 \pm 0.5$ ps. This decay has been assigned to its rotational diffusion time which is distinctly shorter than that (130 ps) of $Zn^{II}TPP$,[10] thus reflecting the smaller molecular size of **2a** compared with that of $Zn^{II}TPP$. Overall, the optical properties of the 14π-electron conjugated aromatic subporphyrins can be regarded as analogous to those of 18π-electron conjugated porphyrins, despite differences that reflect the structural difference in the molecular symmetry and molecular size.

The electrochemical properties of **2a** and **2b** in acetonitrile have been examined by cyclic voltammetry using tetraethylammonium perchlorate as a supporting electrolyte. The first and second one-electron oxidation potentials were determined to be 0.30 and 0.92 V and 0.31 and 0.93 V, as reversible and irreversible waves, versus the ferrocene/ferrocenium ion couple for **2a** and **2b**, respectively, while the reduction-associated waves could not be detected up to −2.0 V. Thus, it may be concluded that subporphyrins are better electron donors than subphthalocyanines.[2a,11]

In summary, the first synthesis of tribenzosubporphyrin **2** has been achieved through the one-pot condensation of **3** in the presence of boric acid as a template. Detailed comparative studies of the optical and electrochemical properties of **2** with those of porphyrins, phthalocyanines, and subphthalocyanines will generate a deeper understanding of the electronic nature of porphyrins and phthalocyanines, and possible applications of **2** to dye-based devices will be worthy of further investigations.

Received: September 28, 2005
Published online: December 28, 2005

Keywords: aromaticity · boron · macrocycles · porphyrinoids · template synthesis

[1] A. Meller, A. Ossko, *Monatsh. Chem.* **1972**, *103*, 150.
[2] a) C. G. Claessens, D. González-Rodríguez, T. Torres, *Chem. Rev.* **2002**, *102*, 835; b) N. Kobayashi, *J. Chem. Soc. Chem. Commun.* **1991**, 1203; c) R. Potz, M. Göldner, H. Hückstädt, U. Cornelissen, A. Tutaß, H. Z. Homborg, *Z. Anorg. Allg. Chem.* **2000**, 626, 588; d) N. Kobayashi, *J. Porphyrins Phthalocyanines* **1999**, *3*, 453.
[3] a) A. Jasat, D. Dolphin, *Chem. Rev.* **1997**, *97*, 2267; b) T. D. Lash, *Angew. Chem.* **2000**, *112*, 1833; *Angew. Chem. Int. Ed.* **2000**, *39*, 1763; c) H. Furuta, H. Maeda, A. Osuka, *Chem. Commun.* **2002**, 1795; d) J. L. Sessler, D. Seidel, *Angew. Chem.* **2003**, *115*, 5292;

 © 2006 Wiley-VCH Verlag GmbH & Co. KGaA, Weinheim

Angew. Chem. Int. Ed. **2003**, *42*, 5134; e) T. K. Chandrashekar, S. Venkatraman, *Acc. Chem. Res.* **2003**, *36*, 676; f) A. Ghosh, *Angew. Chem.* **2004**, *116*, 1952; *Angew. Chem. Int. Ed.* **2004**, *43*, 1918; g) J.-Y. Shin, H. Furuta, K. Yoza, S. Igarashi, A. Osuka, *J. Am. Chem. Soc.* **2001**, *123*, 7190; h) E. Pacholska, L. Latos-Grazynski, Z. Ciunik, *Chem. Eur. J.* **2002**, *8*, 5403; i) A. Berlicka, L. Latos-Grazynski, T. Lis, *Angew. Chem.* **2005**, *117*, 5422; *Angew. Chem. Int. Ed.* **2005**, *44*, 5288; j) A. Krivokapic, A. R. Cowley, H. L. Anderson, *J. Org. Chem.* **2003**, *68*, 1089; k) Z. Hu, J. L. Atwood, M. P. Cava, *J. Org. Chem.* **1994**, *59*, 8071.

[4] L. Edwards, M. Gouterman, C. B. Rose, *J. Am. Chem. Soc.* **1976**, *98*, 7638.

[5] Crystallographic data for **2a**: $C_{27}H_{16}BN_3O\cdot H_2O$, $M_r = 409.24$, monoclinic, space group $C2/c$ (no. 15), $a = 24.535(5)$, $b = 11.708(3)$, $c = 13.940(3)$ Å, $\beta = 91.192(14)°$, $V = 4003.5(15)$ Å^3, $T = 123$ K, $\rho_{calcd} = 1.358$ g cm^{-3}, $Z = 8$; $R_1 = 0.0681$ ($I > 2\sigma(I)$), $R_w = 0.2176$ (all data), GOF = 1.181. Crystallographic data for **2b**: $C_{28}H_{18}BN_3O$, $M_r = 423.26$, orthorhombic, space group P_{nma} (no. 62), $a = 16.272(2)$, $b = 17.852(2)$, $c = 6.8503(9)$ Å, $V = 1990.0(4)$ Å^3, $T = 90$ K, $\rho_{calcd} = 1.413$ g cm^{-3}, $Z = 4$; $R_1 = 0.0947$ ($I > 2\sigma(I)$), $R_w = 0.1970$ (all data), GOF = 1.335. Crystallographic data for **2c**: $C_{30}H_{22}BN_3O$, $M_r = 451.32$, monoclinic, space group $P2_1/c$ (no. 14), $a = 9.8657(11)$, $b = 13.8409(15)$, $c = 17.1556(18)$ Å, $\beta = 104.831(7)°$, $V = 2264.6(4)$ Å^3, $T = 123$ K, $\rho_{calcd} = 1.324$ g cm^{-3}, $Z = 4$; $R_1 = 0.0584$ ($I > 2\sigma(I)$), $R_w = 0.1765$ (all data), GOF = 1.005. Crystallographic data for **2e:** $C_{29}H_{15}BN_3O_2F_3$, $M_r = 505.25$, monoclinic, space group $P2_1/n$ (no. 14), $a = 9.5441(11)$, $b = 15.8360(17)$, $c = 15.4303(18)$ Å, $\beta = 102.245(7)°$, $V = 2279.1(4)$ Å^3, $T = 123$ K; $\rho_{calcd} = 1.473$ g cm^{-3}, $Z = 4$; $R_1 = 0.0722$ ($I > 2\sigma(I)$), $R_w = 0.2223$ (all data), GOF = 1.242; CCDC-281754–281757 contains the supplementary crystallographic data for this paper. These data can be obtained free of charge from The Cambridge Crystallographic Data Centre via www.ccdc.cam.ac.uk/data_request/cif.

[6] Crystal-packing diagrams are pairwise dimeric forms for **2a**, **2c**, and **2e**, whereas J-aggregation-type packing is seen for **2b** (see the Supporting Information). This situation may lead to the shallowest bowl depth in **2b**.

[7] In **1** (L = OH), the average N-B-N angle, B–N bond length, and B–O bond length are reported in Ref. [2c] to be 102.9°, 1.49 Å, and 1.438(14) Å, respectively.

[8] K. A. Nguyen, R. Pachter, *J. Chem. Phys.* **2001**, *114*, 10757.

[9] Relative to $\Phi_F = 0.37$ for 8-amino-1-naphthalenesulfonic acid in ethanol; G. Weber, L. B. Young, *J. Biol. Chem.* **1964**, *239*, 1415.

[10] H. S. Cho, H. Rhee, J. K. Song, C.-K. Min, M. Takase, N. Aratani, S. Cho, A. Osuka, T. Joo, D. Kim, *J. Am. Chem. Soc.* **2003**, *125*, 5849.

[11] B. del Ray, U. Keller, T. Torres, G. Rojo, F. Agulló-López, S. Nonell, C. Martí, S. Brasselet, I. Ledoux, J. Zyss, *J. Am. Chem. Soc.* **1998**, *120*, 12808.

 © 2006 Wiley-VCH Verlag GmbH & Co. KGaA, Weinheim

RNA

DOI: 10.1002/anie.200503198

Molecular-Recognition Characteristics of SAM-Binding Riboswitches**

*Jinsoo Lim, Wade C. Winkler, Shingo Nakamura, Valerie Scott, and Ronald R. Breaker**

Riboswitches are highly structured domains that typically reside within noncoding regions of certain messenger RNAs (mRNAs).[1] These RNAs are genetic control elements that monitor the level of specific metabolites by selective binding without the need for intermediary protein factors. Metabolite binding controls gene expression by several different mechanisms that involve allosteric changes in RNA folding. Riboswitches typically consist of two functional domains, an aptamer domain and an expression platform, which respectively bind metabolite and trigger gene-expression changes. A number of riboswitch classes have been discovered that recognize a variety of important compounds, such as coenzymes, amino acids, and nucleobases, thus indicating that these metabolite-sensing RNAs serve as important components of genetic control circuitry in some organisms.[2] An understanding of the interactions between riboswitches and their metabolite ligands should provide greater insight into the capabilities of RNA as a genetic switch. Furthermore, this knowledge might empower future efforts to design novel antimetabolites that bind to riboswitches, inhibit the expression of key metabolic genes, and thus be selectively toxic to bacteria that carry these RNAs.[3]

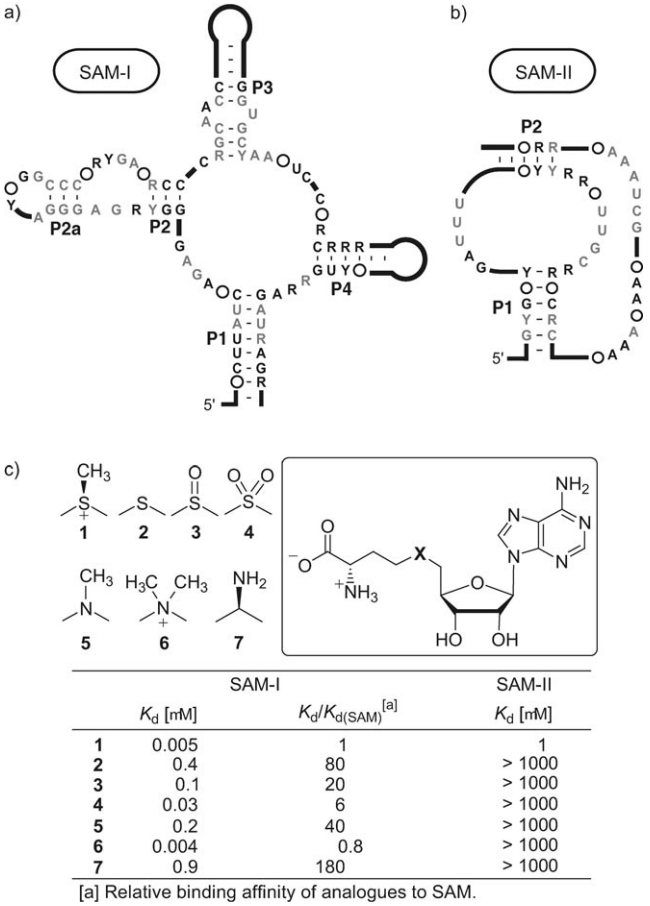
S-adenosyl-L-methionine (SAM; **1**; Figure 1) is an important enzyme cofactor in many biosynthetic pathways.[4] In bacteria of the *Bacillus*/*Clostridium* group, SAM-binding riboswitches (SAM-I; originally termed "S-box" RNAs)[5] control multiple different genes involved in SAM biosynthe-

[*] Dr. J. Lim, V. Scott, Prof. R. R. Breaker
Department of Molecular, Cellular, and Developmental Biology
Yale University
New Haven, CT 06520 (USA)
Fax: (+1) 203-432-0753
E-mail: ronald.breaker@yale.edu
Dr. W. C. Winkler
Department of Biochemistry
University of Texas Southwestern Medical Center at Dallas
Dallas, TX 75390 (USA)
Dr. S. Nakamura
Takeda Pharmaceutical Co. Ltd.
Chuo-ku, Osaka 540-8645 (Japan)

[**] We thank Prof. G. Michael Blackburn (University of Sheffield) for generous gifts of compounds **5** and **6** and Dr. Gail Emilsson and other members of the Breaker laboratory for helpful comments. This study was supported by the grants from the US National Institutes of Health, the US National Science Foundation, DARPA, and the David and Lucile Packard Foundation. SAM = *S*-adenosylmethionine.

Supporting information for this article is available on the WWW under http://www.angewandte.org or from the author.

WILEY InterScience DISCOVER SOMETHING GREAT
© 2006 Wiley-VCH Verlag GmbH & Co. KGaA, Weinheim



	SAM-I		SAM-II
	K_d [nM]	$K_d/K_{d(SAM)}$[a]	K_d [nM]
1	0.005	1	1
2	0.4	80	> 1000
3	0.1	20	> 1000
4	0.03	6	> 1000
5	0.2	40	> 1000
6	0.004	0.8	> 1000
7	0.9	180	> 1000

[a] Relative binding affinity of analogues to SAM.

Figure 1. Consensus sequence and structure for a) aptamers of SAM-I riboswitches found in Gram-positive bacteria and b) aptamers of the SAM-II riboswitches found in alpha proteobacteria. The black and gray letters denote nucleotides that are conserved in 80 and 95%, respectively, of the representatives identified.[6,7] c) Molecular recognition of SAM and its analogues by the SAM-I and -II motifs.

sis, amino acid biosynthesis, and the general metabolism of sulfur.[6] More recently,[7] we have identified a second class of SAM-dependent riboswitches (SAM-II) in alpha proteobacteria. Representatives of this riboswitch class have sequence and structural elements that are distinct from SAM-I riboswitches even though they control genes involved in similar metabolic processes. The existence of two distinct riboswitch classes for SAM provides the first opportunity to compare the molecular-recognition capabilities of two natural aptamers for the same ligand.

Herein, we established the molecular-recognition characteristics of the aptamer domain of a SAM-I riboswitch from the *yitJ* gene of *Bacillus subtilis*.[6c] This data is compared with the molecular-recognition characteristics of a SAM-II riboswitch aptamer from the *metA* gene of *Agrobacterium tumefaciens*.[7] We conclude from these results that the two RNAs indeed form distinct binding pockets for SAM. However, both classes of SAM riboswitches strongly discriminate against most analogues of SAM, which is a requisite for any metabolite-binding receptor that serves as a precision gene-control element.

To uncover determinants of molecular recognition for these RNAs, a series of thioether-modified SAM analogues were tested for their ability to serve as ligands (Figure 1).[8] Values for the dissociation constant (K_d) were determined by conducting in-line probing assays[9,10] in the presence of various concentrations of ligand (Figure 2). These assays can be used to establish the apparent dissociation constant for RNA–ligand complexes. As reported earlier,[6c] **2**, which lacks both a methyl group and the positive charge at the sulfur atom, loses affinity for the SAM-I motif by a factor of 80. In contrast, sulfoxide **3** and sulfone **4** derivatives,[11] although lacking the methyl group, are far better ligands for SAM-I relative to **2**. For example, SAM is bound by the SAM-I motif only sixfold better than **4**. The aza analogue[12] of SAM (**5**) is more isosteric but largely uncharged under in-line probing-assay conditions[13] and therefore is more similar to **2**. Furthermore, sinefungin **7**, a SAM isoster with the same chirality as SAM, drops by more than two orders of magnitude in affinity. The most potent ligand for SAM-I is an aza analogue[12] of SAM (**6**) that carries an extra methyl group and a higher positive charge density.

We conclude that SAM-I RNAs are unlikely to require the methyl group or a specific stereochemistry of the thioether for binding. Moreover, the net positive charge density at the sulfur atom appears to be a key recognition determinant for SAM-I RNAs. This position might form an electrostatic interaction with an anionic or electronegative group of the RNA.

This charge-density correlation is supported by the chemical shifts of both H5′ and Hγ in the ^{1}H NMR spectrum (Figure 3). As the thioether region is located in between H5′ and Hγ, the alteration of electron density at this position influences the chemical shifts of the protons.[12,14] When compared with **2**, the chemical shift of ribose proton H5′ for **1**, **4**, and **6** shifts downfield from $\delta = 0.94$ to 0.98 ppm, thus suggesting that the net charge densities of these analogues are highly positive.[15] The extent of the difference in the chemical shift of the Hγ proton for the derivatives is also similar to that of H5′ (from $\delta = 0.91$ to 1.00 ppm).

The SAM-II motif exclusively binds SAM in contrast to SAM-I and rejects even those compounds that are most tightly bound by SAM-I, such as **4** and **6**.[7] This behavior suggests that the positive charge and the methyl group of SAM might both be critical for molecular recognition by SAM-II RNAs. Moreover, the dramatic difference in the binding affinity of **6** between the two aptamer classes implies that the extra methyl group sterically interferes with binding such that other contacts that exist between SAM-II and its ligand are offset.

Subsequent to the discovery of the potent activity of **4**, we further synthesized[8] a complete set of analogues of **4**, in which one of the heteroatoms is systematically eliminated or altered to a carbon atom while the remaining functional groups are kept intact. The SAM analogues were prepared from 5′-chloro-5′-deoxyadenosine derivatives,[16] which were converted into *S*-adenosyl-L-homocysteine analogues by the reaction with the L-homocysteine disodium salt.[17] Oxidation of *S*-adenosyl-L-homocysteine analogues with a molybdate

 © 2006 Wiley-VCH Verlag GmbH & Co. KGaA, Weinheim

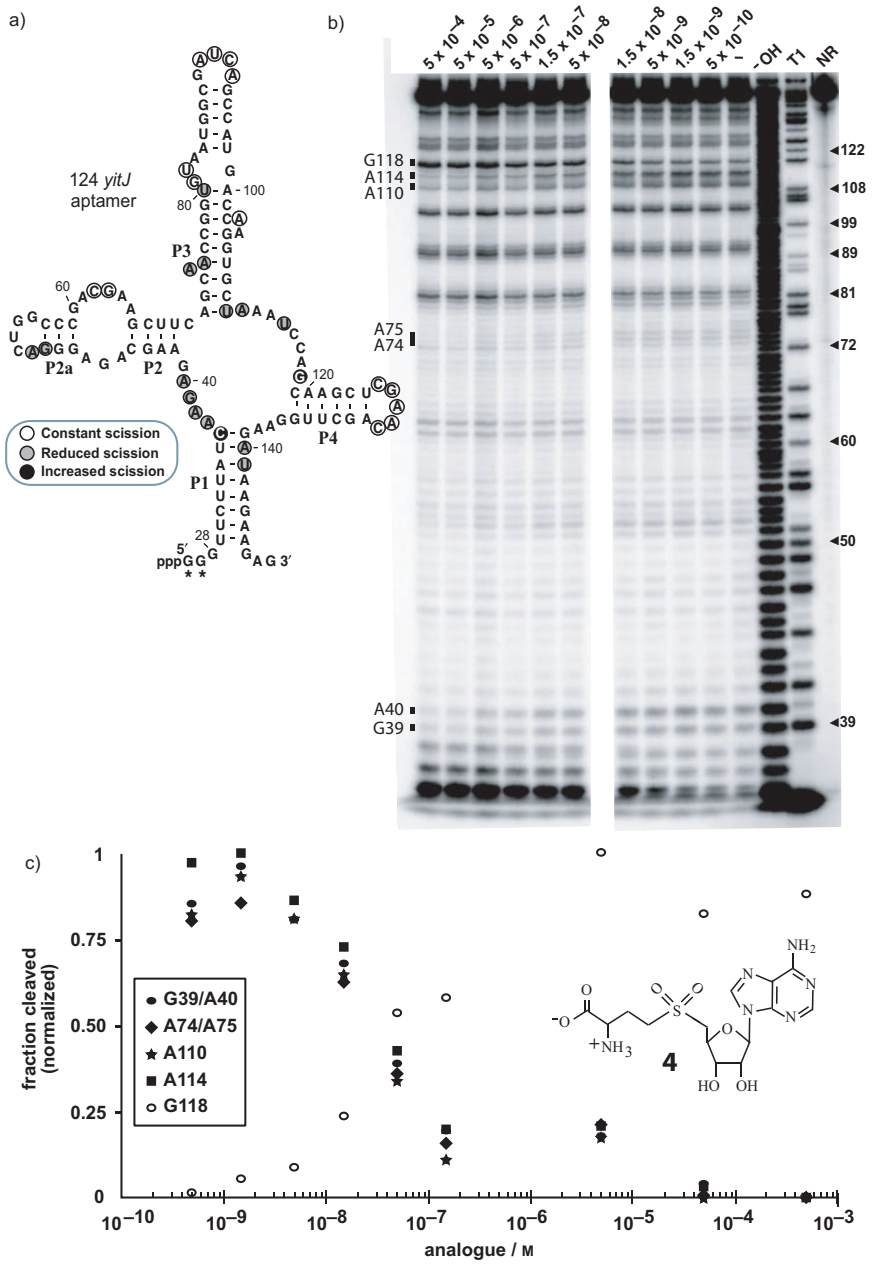


Figure 2. SAM-I riboswitches and a representative in-line probing assay using 124 *yitJ* RNA from *B. subtilis* and various concentrations of SAM. a) Sequence and secondary-structure model of the *yitJ* SAM-I aptamer. P1–P4 identify conserved base-pairing elements. Unshaded, encircled nucleotides indicate a putative pseudo knot interaction. Nucleotide 1 corresponds to the putative transcriptional start site. Asterisks identify nucleotides that were added to the construct to permit efficient transcription in vitro. The first nucleotide of the AUG start codon is 235 (not shown). Sites of structural modulation upon introduction of SAM are depicted as described. b) Spontaneous cleavage patterns of 124 *yitJ* in the absence (−) or presence of SAM at the molar concentrations indicated were examined after separation by polyacrylamide gel electrophoresis. NR = no reaction, T1 = partial digest with RNase T1, $^{-}$OH = partial digest with alkali, respectively. Certain fragment bands corresponding to digestion by T1 (which cleaves after guanine residues) are depicted. Bars identify positions of substantial modulation of spontaneous cleavage that were used for quantification (see the Experimental Section). c) Plot of the normalized fraction of 124 *yitJ* RNA cleaved at each site designated versus the concentration of the sulfone analogue **4** of SAM. Half-maximum change in spontaneous cleavage occurs at a concentration of **4** of approximately 50 nM, which reflects the apparent K_d value of this ligand with the *yitJ* aptamer.

solution containing hydrogen peroxide yielded **8**–**18** (Table 1).[11]

As SAM-II rejects **4**, all the synthesized sulfone analogues were not expected to bind significantly to the SAM-II motif, and thus they were tested only with SAM-I. The amino acid modified analogues, devoid of amine or carboxylic acid groups (**9** and **10**, respectively), had no detectable binding to SAM-I, thus implying that the amino acid might form strong electrostatic or hydrogen-bonding interactions with the RNA. By examining sugar-modified analogues, the 3′-hydroxy group appears to be less important than the 2′-hydroxy group (**13** and **12**, respectively). The 6-amino group of adenine is so important that replacement by either a hydroxy group or a hydrogen atom (**15** and **14**, respectively) is not tolerated. The 7-aza group is likely to be critical for hydrogen bonding, whereas the 3-aza group is less important than any other amine in the adenine ring (**16** and **17**, respectively). An extra amino group at the 2-position of adenine (**18**) decreases binding by a factor of 67, thus suggesting a tight pocket is formed in this case.

In summary, we have examined and compared the molecular-recognition characteristics of both the SAM-I and -II aptamers (Scheme 1) by using in-line probing assays with a series of SAM analogues. The 6-amino, 7-aza, and 2′-hydroxy groups of the nucleobase, and the functional groups on the amino acid moiety of SAM appear to participate in molecular recognition with SAM-I. However, SAM-II is far more selective for the thioether linkage of SAM, and therefore a different analogue set was used to further establish other molecular determinants for this RNA.[7] The fact that each riboswitch has different substrate-recognition determinants confirms that their sequence and structural differences form distinct binding pockets for SAM. Furthermore, there appears to be considerable opportunity to design novel SAM analogues that selectively trigger SAM-I riboswitches, perhaps without risk of interacting with other SAM-binding biopolymers. Given that SAM-I riboswitches in Gram-positive organisms control numerous genes whose products participate in fundamental metabolic pathways, such SAM analogues might find application as antibiotic compounds that selectively inhibit bacterial growth.

Experimental Section

The aptamer domain from the SAM-I riboswitch of the *yitJ* gene from *B. subtilis* (Figure 2a) was generated as described previously.[6c] 5′-^{32}P-Labeled

 © 2006 Wiley-VCH Verlag GmbH & Co. KGaA, Weinheim

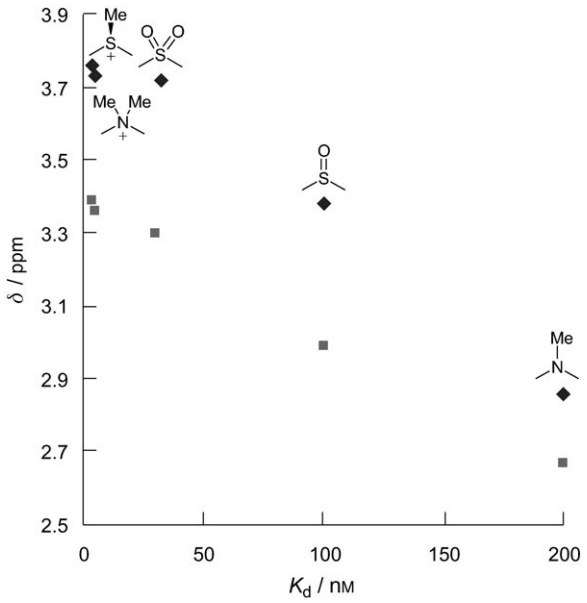
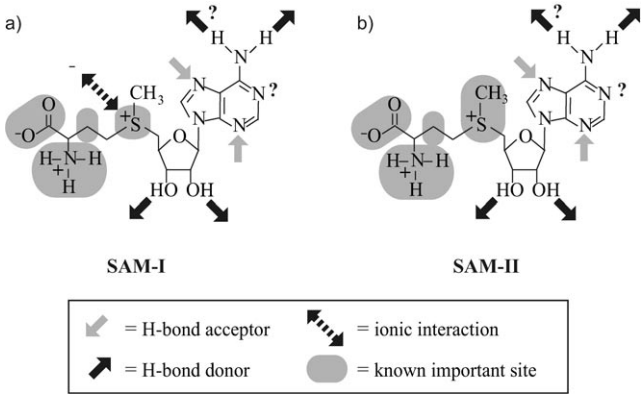


Figure 3. Charge-density correlation plot. Binding affinities (K_d) of analogues are inversely proportional to the chemical shifts of the protons H5′ (diamonds) and Hγ (squares) of the corresponding derivatives.

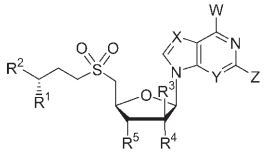


Scheme 1. Predicted molecular-recognition determinants of SAM riboswitches. The schematic representation reflects a possible pattern of molecular interactions between SAM and a) the aptamer domain of SAM-I riboswitches and b) the aptamer domain of SAM-II riboswitches. Note that, in some cases, the precise type of molecular contact or the number of contacts for a given functional group cannot be determined from the limited data currently available. Shading on the hydrocarbon side chain of the methionyl moiety reflects the importance of length. Also the molecular-recognition patterns are likely incomplete for both aptamer classes. A more comprehensive assessment of the contacts between SAM-II RNA and its ligand will require the use of analogues that retain the natural methylated thioether linkage, and the design of tight-binding analogues would be greatly aided by an atomic-resolution structure of the RNA bound to SAM.

RNA was prepared using calf intestinal phosphatase (Roche Diagnostics), T4 polynucleotide kinase (New England Biolabs), and [γ-^{32}P]ATP (Amersham Biosciences) according to the manufacturer's directions and purified by polyacrylamide gel electrophoresis. Similarly, radiolabeled RNAs that represent the SAM-II riboswitch aptamer for the *metA* gene from *A. tumefaciens* were prepared. Genomic DNA used to prepare the template for transcription of the SAM-II construct[7] was obtained from *Agrobacterium tumefaciens* strain GV2260 (a gift from the S. Dinesh-Kumar Lab, Yale University). For each probing reaction, approximately 1 nM 5′-^{32}P-labeled RNA was incubated for about 40 h at 25 °C in 50 mM Tris–HCl (pH 8.3 at 25 °C), 20 mM $MgCl_2$, 100 mM KCl, with added compounds as indicated for each experiment. Additional experimental details are similar to those described elsewhere.[2a–b] Polyacrylamide gels that separate the RNA cleavage products from in-line probing assays were scanned and quantitated using a molecular dynamics STORM 820 PhosphorImager system. The K_d value of 124 *yitJ* for SAM and for each SAM analogue was determined by plotting the normalized fraction of RNA cleaved at six regions (e.g., Figure 2c) versus the logarithm of the concentration of SAM in molar units. The concentration of SAM needed to induce half-maximum change in RNA-cleavage extent was interpreted as the apparent K_d value. Similar data for the SAM-II 164 *metA* RNA is reported elsewhere.[7]

Received: September 8, 2005
Published online: December 28, 2005

Table 1: Dissociation constant (K_d) values for SAM analogues with the *yitJ* SAM-I riboswitch aptamer from *B. subtilis*.



	R^1	R^2	R^3	R^4	R^5	W	X	Y	Z	K_d [μM]
4	NH_2	CO_2H	H	OH	OH	NH_2	N	N	H	3×10^{-2}
8	H	CH_2OH	H	OH	OH	NH_2	N	N	H	>1000
9	H	CO_2H	H	OH	OH	NH_2	N	N	H	>1000
10	NH_2	H	H	OH	OH	NH_2	N	N	H	>1000
11	NH_2	CO_2H	OH	H	OH	NH_2	N	N	H	40
12	NH_2	CO_2H	H	H	OH	NH_2	N	N	H	30
13	NH_2	CO_2H	H	OH	H	NH_2	N	N	H	5
14	NH_2	CO_2H	H	OH	OH	H	N	N	H	>1000
15	NH_2	CO_2H	H	OH	OH	OH	N	N	H	>1000
16	NH_2	CO_2H	H	OH	OH	NH_2	CH	N	H	>1000
17	NH_2	CO_2H	H	OH	OH	NH_2	N	CH	H	3
18	NH_2	CO_2H	H	OH	OH	NH_2	N	N	NH_2	2

 © 2006 Wiley-VCH Verlag GmbH & Co. KGaA, Weinheim

Keywords: aptamers · molecular recognition · riboswitches · RNA · structure–activity relationships

[1] a) E. C. Lai, *Curr. Biol.* **2003**, *13*, R285-R291; b) M. Mandal, R. R. Breaker, *Nat. Rev. Mol. Cell Biol.* **2004**, *5*, 451 – 463.

[2] a) A. Nahvi, N. Sudarsan, M. S. Ebert, X. Zou, K. L. Brown, R. R. Breaker, *Chem. Biol.* **2002**, *9*, 1043 – 1049; b) W. Winkler, A. Nahvi, R. R. Breaker, *Nature* **2002**, *419*, 952 – 956; c) A. S. Mironov, I. Gusarov, R. Rafikov, L. E. Lopez, K. Shatalin, R. A. Kreneva, D. A. Perumov, E. Nudler, *Cell* **2002**, *111*, 747 – 756; d) M. Mandal, B. Boese, J. E. Barrick, W. C. Winker, R. R. Breaker, *Cell* **2003**, *113*, 577 – 586.

[3] a) J. Gallego, G. Varani, *Acc. Chem. Res.* **2001**, *34*, 836 – 843; b) T. Hermann, *Biopolymers* **2003**, *70*, 4 – 18; c) G. J. R. Zaman, P. J. A. Michiels, C. A. A. van Boeckel, *Drug Discovery Today* **2003**, *8*, 297 – 306.

[4] a) H. L. Schubert, R. M. Blumenthal, X. Cheng, *Trends Biochem. Sci.* **2003**, *28*, 329 – 335; b) M. Fontecave, M. Atta, E. Mulliez, *Trends Biochem. Sci.* **2004**, *29*, 243 – 249; c) J. T. Jarrett, *Curr. Opin. Chem. Biol.* **2003**, *7*, 174 – 182; d) P. A. Frey, O. T. Magnusson, *Chem. Rev.* **2003**, *103*, 2129 – 2148; e) J. L. Martin, F. M. McMillan, *Curr. Opin. Struct. Biol.* **2002**, *12*, 783 – 793.

[5] F. J. Grundy, T. M. Henkin, *Mol. Microbiol.* **1998**, *30*, 737 – 749.

[6] a) B. A. M. McDaniel, F. J. Grundy, I. Artsimovitch, T. M. Henkin, *Proc. Natl. Acad. Sci. USA* **2003**, *100*, 3083 – 3088; b) V. Epshtein, A. S. Mironov, E. Nudler, *Proc. Natl. Acad. Sci. USA* **2003**, *100*, 5052 – 5056; c) W. C. Winkler, A. Nahvi, N. Sudarsan, J. E. Barrick, R. R. Breaker, *Nat. Struct. Biol.* **2003**, *10*, 701 – 707.

[7] K. A. Corbino, J. E. Barrick, J. Lim, R. Welz, B. J. Tucker, I. Puskarz, M. Mandal, N. D. Rudnick, R. R. Breaker, *Genome Biol.* **2005**, *6*, R70.

[8] Additional experimental and synthetic details are presented in the Supporting Information.

[9] G. A. Soukup, R. R. Breaker, *RNA* **1999**, *5*, 1308 – 1325.

[10] The rate of spontaneous cleavage of RNA by transesterification is affected by the position of the attacking nucleophile (2′-O) relative to the leaving group (5′-O); see F. H. Westheimer, *Acc. Chem. Res.* **1968**, *1*, 70 – 78. Changes in RNA shape, brought about by ligand binding thus change the pattern of RNA-cleavage products; see G. A. Soukup, E. C. DeRose, M. Koizumi, R. R. Breaker, *RNA* **2001**, *7*, 524 – 536.

[11] R. T. Borchardt, Y. S. Wu, *J. Med. Chem.* **1974**, *17*, 862 – 868.

[12] The profile of the pK_a values of **5** and ^{1}H NMR spectroscopic data of **5** and **6** are shown in M. J. Thompson, A. Mekhalfia, D. P. Hornby, G. M. Blackburn, *J. Org. Chem.* **1999**, *64*, 7467 – 7473.

[13] In-line probing used 50 mM Tris–HCl (pH 8.3 at 25 °C), 20 mM $MgCl_2$, 100 mM KCl, and typically 10 nM to 10 mM ligand.

[14] The ^{1}H NMR spectroscopic data of **3** and **4** is available in the Supporting Information and that of **1** and **2** are shown in M. L. Stolowitz, M. J. Minch, *J. Am. Chem. Soc.* **1981**, *103*, 6015 – 6019.

[15] The net ionic charge of sulfur derivatives were estimated as follows: $(CH_3)_3S^+I^-$, +0.749 *D*; $(CH_3)_2S$, −1.608 *D*; $(CH_3)_2SO$, −0.514 *D*; $(CH_3)_2SO_2$, +0.311 *D*; J. Jullien, H. Stahl-Larivière, A. Trautmann, *Bull. Soc. Chim. Fr.* **1966**, 2398 – 2399.

[16] M. J. Robins, F. Hansske, S. F. Wnuk, T. Kanai, *Can. J. Chem.* 1**991**, 69, 1468 – 1474.

[17] R. W. Miles, L. P. C. Nielson, G. J. Ewing, D. Yin, R. T. Borchardt, M. J. Robins, *J. Org. Chem.* **2002**, *67*, 8258 – 8260.

 © 2006 Wiley-VCH Verlag GmbH & Co. KGaA, Weinheim

Cyclophanes

DOI: 10.1002/anie.200503112

Exploitation of Perfluorophenyl–Phenyl Interactions for Achieving Difficult Macrocyclizations by Using Ring-Closing Metathesis**

*Yassir El-azizi, Andreea Schmitzer, and Shawn K. Collins**

Macrocycles continue to attract interest in light of their unique properties and abundance in natural products. Over the past decade, ring-closing olefin metathesis (RCM) has not only emerged as a powerful method for macrocyclization[1] but has inspired the development of ring-closing alkyne metathesis (RCAM)[2] and macrocyclic ene-yne metathesis.[3] Despite the convenience of olefin metathesis, numerous examples have been documented in which ring strain and entropic factors have spawned new and imaginative routes to coercing ring closure. Among these, templates,[4] dilution, and gearing elements[5] have been employed in directing macrocyclization processes.

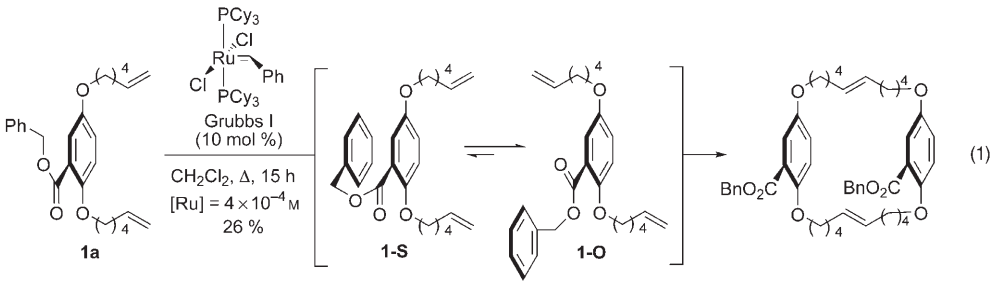
Our interest in the synthesis of the quinone natural product longithorone C[6] led us to investigate the preparation of 12-membered macrocyclic paracyclophanes by olefin metathesis. Numerous attempts to cyclize various substituted [12]paracyclophanes using the Grubbs first generation catalyst, such as benzyl ester **1a**, met with failure. Treatment with the Grubbs second generation catalyst also led to similarly low yields of dimeric products [Eq. (1)].[7] Furthermore, variation in the concentration and the nature of the aromatic substituents consistently led to preferential dimer and/or oligomer formation. Although **1a** likely exists in a variety of conformations in solution, we sought reaction conditions that would favor the conformation **1-S** (S = stacked) with π–π-stacking interactions versus the conformation **1-O** (O = open) [Eq. (1)]. The resulting shielding of one face in **1-S** would decrease the degrees of freedom for rotation in the olefin-bearing side chains and thus increase the probability of forming the desired macrocycle.

Consequently, we envisioned exploiting a perfluorophenyl–phenyl interaction as a novel gearing element to

[*] Y. El-azizi, Prof. Dr. A. Schmitzer, Prof. Dr. S. K. Collins
Department of Chemistry
Université de Montréal
C.P. 6128 Succursale Centre-ville,
Montréal, Québec, H3C3J7 (Canada)
Fax: (+1) 514–343–7586
E-mail: shawn.collins@umontreal.ca

[**] We are grateful to the National Sciences and Engineering Research Council of Canada (NSERC), Fonds de Québec pour la Recherche en Nature et Technologie (FQRNT), the Canadian Foundation for Innovation, and the Université de Montréal for generous financial support of this research. We thank the laboratories of A. Charette and H. Lebel (University of Montréal) for sharing equipment, chemicals, and fruitful discussions.

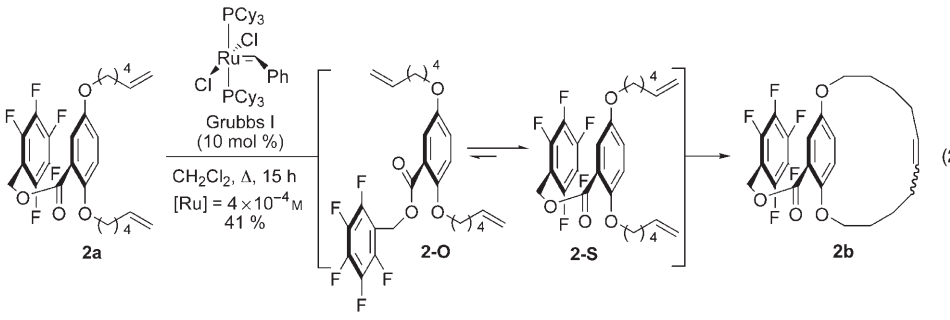
WILEY InterScience DISCOVER SOMETHING GREAT
© 2006 Wiley-VCH Verlag GmbH & Co. KGaA, Weinheim



(1)

favor the desired intramolecular macrocyclization. These nonbonding interactions are the result of the orthogonal electron densities of aromatic and perfluoro aromatic compounds.[8,9] As a consequence of their predictable preference for face-to-face stacking with other aromatic compounds in the solid state,[10] these interactions have attracted considerable interest in medicinal chemistry[11] and materials science.[12] Surprisingly, relatively little use of these interactions in catalysis has been demonstrated, despite the tremendous utility of intramolecular π–π interactions in synthetically useful face-selective transformations.[13] A sole example of such quadrupolar interactions in the solution state was previously observed by Marsella et al.,[14] which is in contrast to π-cation–arene interactions, whose applicability in the solution state was recently demonstrated by Yamada and Morita for the face-selective addition of nucleophiles to pyridines.[15] Herein, we report the development of a strategy that exploits quadrupolar perfluorophenyl–phenyl interactions, analogous to π-cation–arene interactions, for the construction of macrocycles.

Based on precedent,[10,11] fluorinated ester **2a** was expected to prefer the solution-state conformation **2-S** to a much greater degree than **1a** would prefer conformation **1-S** [Eq. (2)]. Consequently, fluorinated ester **2a** was treated with



(2)

the Grubbs first generation catalyst, and a dramatic change in product selectivity resulted, thus solely affording the cyclized cyclophane **2b** in 41% yield.[16]

Higher yields of paracyclophane **2b** were observed using the Grubbs I versus Grubbs II catalyst; the second generation catalyst was shown to affect ring opening of **2b**, and the formation of oligomers was observed. Solvent studies revealed that the quadrupolar-interaction gearing element was effective in selectively forming the desired cyclophane in a variety of solvents. However, the rate of metathesis is significantly decreased relative to reaction in CH_2Cl_2.[17] Ring-closing metathesis in THF afforded negligible product after 48 h at 40 °C despite the addition of two additional aliquots of catalyst (5 mol%). Similar reaction times and catalyst loading were necessary for macrocyclization with hexanes as the solvent at 40 °C (20% yield of **2b**, 58% conversion). Interestingly, reaction in benzene at 40 °C gave **2b** in 29% yield (57% conversion), and no dimer products were observed, thus suggesting that the excess benzene does not interfere with the intramolecular perfluorophenyl–phenyl interaction.

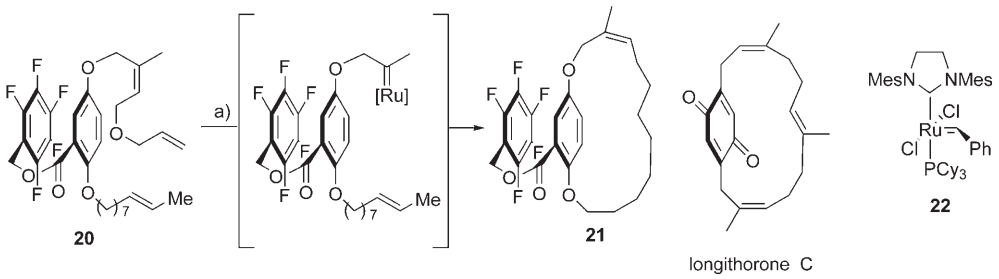
A variety of structures were cyclized by using this protocol (Table 1).[18] The site of metathesis had little effect on the yields of macrocyclization for [12]paracyclophanes. Diene **4** gave a slightly higher yield of the corresponding monomeric cyclophane (**5**: 48%) than diene **1a** (**2**: 41%; Table 1, entries 1 and 2, respectively). Further substitution of the aromatic nucleus had little impact on the yields of the cyclizations. The cyclization was found to be tolerant of a free hydroxy group (entry 3) and the addition of an additional electron-withdrawing ester substituent (entry 4). The addition of a second pentafluorobenzyl ester group had no effect on the yield of the macrocyclization, whereas the corresponding dibenzyl ester provided the dimer in only 39% yield. Larger ring sizes that produced solely dimeric products upon treatment with the olefin-metathesis catalyst gave good yields for the macrocyclic products following attachment of the pendant pentafluorobenzyl moiety. The [13]paracyclophane **11** was produced in 57% yield, whereas substitution of the pentafluorobenzyl ester for a methyl ester produced only dimeric products under identical conditions (entry 5). Although the corresponding benzyl ester of diene **12** yields the monomeric [14]paracyclophane in 51% yield, substitution for a pentafluorobenzyl ester provided an increased yield of 63% (entry 6). When the site of metathesis was moved closer to the aromatic core, the yield of macrocyclization decreased to provide **15** in 36% yield (entry 7). Interestingly, diene **16**, which possesses an additional arene moiety fused to the aromatic group, also gave the corresponding naphthylenophane **17** in 42% yield (entry 8). Examination of the ^{1}H NMR spectrum of **17** revealed diastereotopic signals for the protons of the methylene groups adjacent to the naphthenolic oxygen atoms and the ester oxygen atom, thus indicating an element of planar chirality. The trisubstituted olefins found in the cyclophane natural product longithorone C (Scheme 1) prompted us to explore their formation by using the penta-

 © 2006 Wiley-VCH Verlag GmbH & Co. KGaA, Weinheim

Table 1: Macrocyclizations by olefin metathesis exploiting perfluorophenyl–phenyl interactions.[a]

Entry	Metathesis precursor	Cyclophane	Yield [%]
1	**1a** ($n=4$, $m=4$, $R^1=H$)	**2**	41
2	**4** ($n=3$, $m=5$, $R^1=H$)	**5**	48
3	**6** ($n=4$, $m=4$, $R^1=CH_2OH$)	**7**	41
4	**8** ($n=4$, $m=4$, $R^1=CO_2CH_2C_6F_5$)	**9**	39
5	**10**	**11**	57
6	**12** ($n=5$, $m=5$)	**13**	63
7	**14** ($n=8$, $m=2$)	**15**	36
8	**16**	**17**	42
9	**18** ($n=8$, $R^1=H$)	**19**	10

[a] Substrate was added dropwise over 2 h to a solution of Grubbs I catalyst (10 mol%) in CH_2Cl_2 at reflux for 15 h ($[Ru]=4\times10^{-4}$ M).

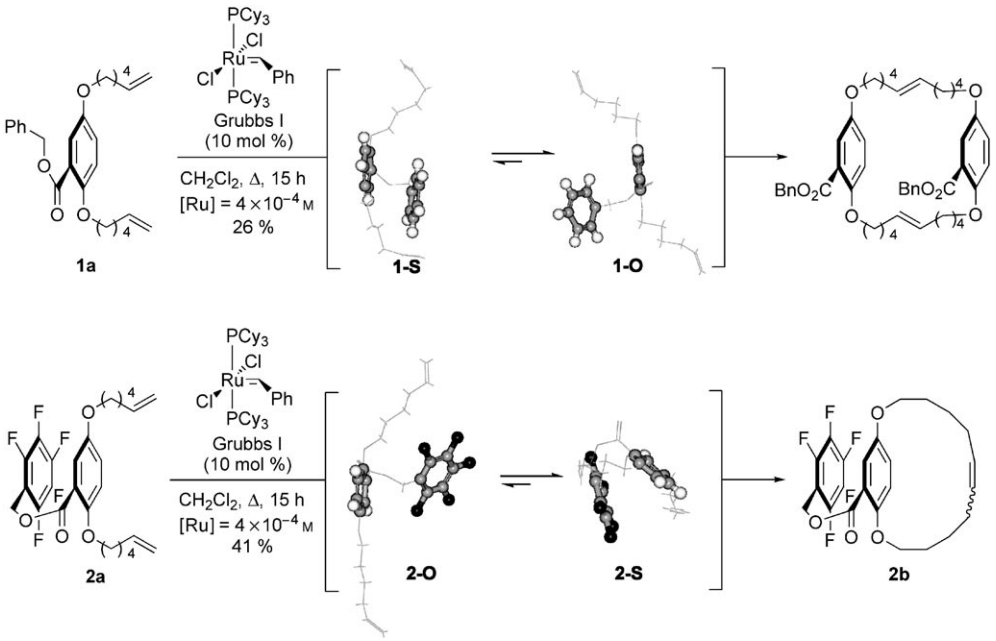


Scheme 1. Macrocyclic olefin metathesis exploiting perfluorophenyl–phenyl interactions and relay ring-closing metathesis to form tertiary olefins. Reagents and conditions: a) **22** (10 mol%), CH_2Cl_2, Δ, 15 h, (68% yield based on recovered starting material). Mes = mesityl, Cy = cyclohexyl.

fluorophenyl–phenyl interactions to influence macrocyclization. Standard conditions all favored the formation of dimeric or oligomeric products.[19] As we were enticed by the possibility of a relay ring-closing metathesis protocol[20] in tandem with the gearing effect of the pentafluorophenyl–phenyl interaction, diene **18** was prepared and subjected to ring closure. Unfortunately, a very low yield of cyclized product **19** was observed and a linear dimer was isolated as the major product (entry 9).[21] Subsequently, diene **20** was synthesized to preferentially favor initial metathesis of the relay segment versus intermolecular dimerization (Scheme 1). Although the addition of a Me group to the terminal olefin may result in a slower rate of macrocyclization, the nonproductive intermolecular processes are slowed to a much greater extent and cyclophane **21** was isolated in 68% yield. Cyclophane **21** was isolated as a single isomer with the tertiary olefin in the *Z* configuration. Furthermore, the methylene groups adjacent to the phenolic oxygen atoms and the ester oxygen atom all displayed diastereotopic signals in the ^{1}H NMR spectrum, thus revealing a possible element of planar chirality. Preliminary experiments (heating in C_6D_6) have revealed that cyclophane **21** is configurationally stable at 50 °C in [D_6]benzene.

The exact nature of the observed gearing effect in solution is still debatable,[22] despite the well-documented preference of perfluoroarenes and phenyl groups for face-to-face stacking. To probe the mechanism of the gearing effect further, molecular modeling studies were performed to explore whether a face–face or "slipped"[8] arrangement of both arenes were possible in the solution-state conformations. Accurate ab initio studies of aromatic clusters must include electron correlation to obtain good representations of dispersion and electrostatic forces that are responsible for conformation stability. High-level treatment of electron correlation or the use of large basis sets was precluded because of the large size of the molecules in question. The initial geometric optimizations for benzyl ester **1a** was performed by using semiempirical methods (AM1)[23] and afforded conformers **1-S** and **1-O** (Scheme 2). Conformer **1-O** displayed the "open" conformation, in which the benzyl ester is elongated away from the aromatic

 © 2006 Wiley-VCH Verlag GmbH & Co. KGaA, Weinheim

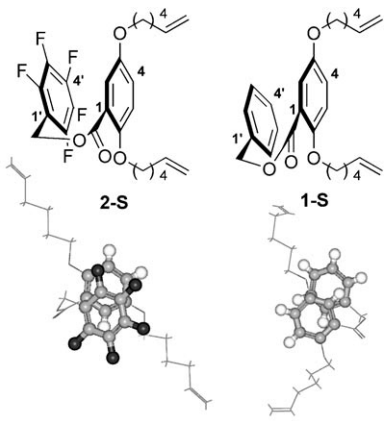


Scheme 2. Modeling studies of possible conformations that lead to productive metathesis.

core of **1a**. A conformation was observed that resembles **1-S**, in which the arene unit of the benzyl ester moiety is orientated underneath the aromatic core in a slipped-type arrangement.

The Moller–Plesset (MP2)[24] perturbation theory with a 6-31G* basis set was then used to provide more accurate energies for each conformer. Conformer **1-S** is estimated to be more stable than **1-O** by approximately -3.9 kcal mol^{-1} based on the difference of their relative heats of formation. Conformational analysis of the perfluorinated ester **2a** by using semiempirical methods (AM1) also revealed an open-type conformer **2-O**, in which the pentafluoroarene is elongated and oriented away from the aromatic core (Scheme 2). The minimum energy conformer was identified as **2-S**, in which the π–π overlap is predicted to a much greater extent than that observed for benzyl-substituted **1-S** (Scheme 3). Conformers **2-O** and **2-S** were further refined (MP2), and conformer **2-S** is estimated to be more stable than **2-O** by approximately -24.0 kcal mol^{-1}.

These calculations highlight the fact that both stacked conformers **2-S** and **1-S** are preferred relative to their respective open conformers **2-O** and **1-O**. Conformer **2-S** is preferred to **2-O** to a much greater extent than the benzyl analogues (**1-S**–**1-O** ≈ -4 kcal mol^{-1} vs. **2-S**–**2-O** ≈ -24 kcal mol^{-1}). Importantly, the nature of the π stacking in **2-S** differs considerably from **1-S** (Scheme 3). The arene units are offset in **1-S**, and minimal overlap is observed. In contrast, conformer **2-S** exhibits a face-to-face-type interaction with considerable overlap of the aromatic core and pentafluoroarene. For example, the distance between C1 and C1′ in conformers **1-S** and **2-S** are almost identical (3.27 and 3.22 Å, respectively). However, C4′ is much closer to C4 in **2-S** than **1-S** (4.08 and 5.61 Å, respectively). It is possible that the energetic preference for conformer **2-S** in conjunction with its superior π overlap is what leads to the inclination towards macrocyclization.



Scheme 3. π–π Overlap in benzyl and pentafluorobenzyl conformers **1-S** and **2-S**, respectively.

It is important not to infer that the difference in energy between conformers is due solely to the aromatic interactions. There is no quantitative comparison of the molecular-strain energy with the relative energy gained through the perfluorophenyl–phenyl interactions. Although the strain energy can be estimated by using empirical potential functions,[25] the evaluation of strain energy by semiempirical or ab initio calculations is tenuous. In comparing the relative differences in the MP2-optimized energies of the various conformers, the strain energy is dominant in all cases, thus the energy difference includes not only the aromatic–aromatic interactions but also a preferred conformation for the alkyl chains.

In summary, we have developed a novel gearing element to affect difficult macrocyclizations by using ring-closing olefin metathesis. Data obtained from molecular-modeling studies suggest a possible quadrupolar interaction between the pentafluorobenzyl appendage and the cyclophane core which orients the substrate in a conformation that favors macrocyclization. We have also developed a protocol for the preparation of stereodefined tertiary olefins in conjunction with a relay ring-closing-metathesis strategy. The presence of the tertiary olefin produces a configurationally stable cyclophane in select cases, thus inhibiting rotation of the macrocycle at temperatures that exceed 50 °C. Currently, we are optimizing conditions for ring-closing ene-yne and alkyne

 © 2006 Wiley-VCH Verlag GmbH & Co. KGaA, Weinheim

metathesis and pursuing a total synthesis of longithorone C by using the methods described herein. Although π-cation–arene interactions continue to be exploited in organic synthesis, pentafluorophenyl–phenyl interactions represent a novel and complimentary π-shielding element. Considering that intramolecular π–π interactions can be powerful conformation-controlling elements in various face-selective addition/cycloaddition reactions,[13] the development of chiral auxiliaries based upon solution-phase quadrupolar interactions have significant potential for a variety of chemical reactions.

Experimental Section

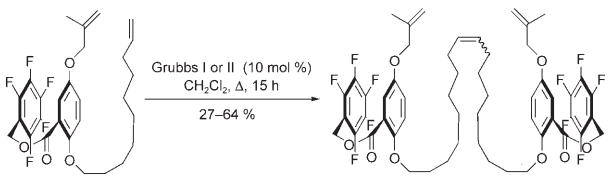
General procedure: A solution of **20** (25 mg, 0.04 mmol) in anhydrous CH_2Cl_2 (40 mL) was added dropwise over approximately 2 h to an anhydrous solution of Grubbs II catalyst (3.5 mg, 0.004 mmol) in CH_2Cl_2 (60 mL) at reflux. The solution was cooled to room temperature after 13 h at reflux. Silica gel was added, and the reaction mixture was concentrated and purified by chromatography on silica gel (hexanes/EtOAc = 7:1) to afford 16 mg of **21** (68 %) as a clear oil. ^{1}H NMR (300 MHz, $CDCl_3$): δ = 7.35 (d, J = 2.7 Hz, 1H), 7.06 (dd, J = 9.0, 3.2 Hz, 1H), 6.92 (d, J = 9.0 Hz, 1H), 5.43 (dd, J = 22.9, 8.6 Hz, 2H), 5.07 (m, 1H), 4.56 (d, J = 11.4 Hz, 1H), 4.47 (d, J = 11.4 Hz, 2H), 4.02 (m, 1H), 3.95 (m, 1H), 1.97 (m, 2H), 1.64 (m, 2H), 1.57 (s, 3H), 1.40–1.13 ppm (m, 10H); ^{13}C NMR (75 MHz, C_6D_6): δ = 165.3, 152.6, 151.4, 133.5, 130.2, 124.0, 122.9, 122.5, 120.0, 78.8, 67.6, 53.4, 30.0, 29.4, 27.6, 27.4, 27.3, 25.9, 24.0, 14.0 ppm; HRMS (ESI): m/z calcd for $C_{25}H_{25}O_4F_5$ ($[M+H]^+$): 485.1746; found: 485.1734 .

20 (clear oil): ^{1}H NMR (300 MHz, $CDCl_3$): δ = 7.33 (d, J = 3.6 Hz, 1H), 7.04 (dd, J = 9.1, 3.6 Hz, 1H), 6.89 (d, J = 9.1 Hz, 1H), 5.94 (m, 1H), 5.75 (m, 1H), 5.44 (m, 2H), 5.42 (s, 2H), 5.31 (ddd, J = 18.0, 3.2, 0.2 Hz, 1H), 5.21 (m, 1H), 4.40 (s, 2H), 4.09 (d, J = 6.6 Hz, 2H), 4.00–3.93 (m, 4H), 2.78–2.60 (m, 2H), 2.11 (m, 2H), 1.77 (s, 3H), 1.74 (m, 2H), 1.63 (d, J = 6.45 Hz, 3H) 1.34 ppm (m, 7H); ^{13}C NMR (75 MHz, $CDCl_3$): δ = 165.9, 153.8, 152.4, 135.2, 135.1, 131.2, 125.0, 124.1, 121.4, 120.0, 117.8, 117.6, 115.4, 74.1, 71.7, 70.1, 66.6, 54.0, 29.9, 29.7, 29.62, 29.61, 27.2, 26.3, 14.5, 13.2 ppm; HRMS (ESI): m/z calcd for $C_{32}H_{38}O_5F_5$ ($[M+H]^+$): 597.2643; found: 597.2634.

Received: September 1, 2005
Published online: December 28, 2005

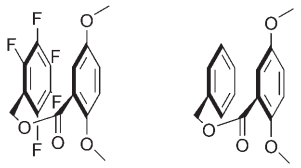
Keywords: alkene metathesis · cyclophanes · macrocyclization · perfluoroarenes · quadrupolar interactions

[1] a) R. H. Grubbs, *Tetrahedron* **2004**, *60*, 7117 – 7140; b) C. W. Lee, R. H. Grubbs, *J. Org. Chem.* **2001**, *66*, 7155 – 7158.
[2] U. H. F. Bunz, L. Kloppenburg, *Angew. Chem.* **1999**, *111*, 503 – 505; *Angew. Chem. Int. Ed.* **1999**, *38*, 478 – 481.
[3] a) E. C. Hansen, D. Lee, *J. Am. Chem. Soc.* **2004**, *126*, 15074 – 15080; b) E. C Hansen, D. Lee, *J. Am. Chem. Soc.* **2004**, *126*, 15074 – 15080.
[4] a) A. V. Chuchuryukin, H. P. Dijkstra, B. M. J. Suijkerbuijk, R. J. M. Klein Gebbink, G. P. M. van Klink, A. M. Mills, A. L. Spek, G. van Koten, *Angew. Chem.* **2003**, *115*, 238 – 240; *Angew. Chem. Int. Ed.* **2003**, *42*, 228 – 230; b) A. F. M. Kilbinger, S. J. Cantrill, A. W. Waltman, M. W. Day, R. H. Grubbs, *Angew. Chem.* **2003**, *115*, 3403 – 3407; *Angew. Chem. Int. Ed.* **2003**, *42*, 3281 – 3285.
[5] a) M. E. Layton, C. A. Morales, M. D. Shair, *J. Am. Chem. Soc.* **2002**, *124*, 773 – 775; b) A. G. J. Commeureuc, J. A. Murphy, M. L. Dewis, *Org. Lett.* **2003**, *5*, 2785 – 2788.
[6] a) X. Fu, M. B. Hossain, F. J. Schmitz, D. van der Helm, *J. Org. Chem.* **1997**, *62*, 3810 – 3819; b) For a synthesis of the closely related longithorone B, see: T. Kato, K. Nagae, M. Hoshikawa, *Tetrahedron Lett.* **1999**, *40*, 1941 – 1944.
[7] Interestingly, cyclophanes bearing unsubstituted aromatic compounds can be cyclized: J. Tae, Y.-K. Yang, *Org. Lett.* **2003**, *5*, 741 – 744.
[8] M. R. Battaglia, A. D. Buckingham, J. H. Williams, *Chem. Phys. Lett.* **1981**, *78*, 421 – 423.
[9] Although the exact nature of the perfluoroarene–arene interaction in the C_6H_6–C_6F_6 complex remains a controversial subject, this face-to-face stacking arrangement likely acts to minimize quadrupole–quadrupole interaction energies. The hypothesis of a charge-transfer (CT) interaction was discarded based on the absence of a characteristic CT band in the UV/Vis absorption spectrum; see T. G. Beaumont, K. M. C. Davis, *J. Chem. Soc. B* **1967**, 1131 – 1134.
[10] a) J. S. W. Overell, G. S. Pawley, *Acta Crystallograph. B* **1982**, *38*, 1966 – 1972; b) J. H. Williams, J. K. Cockcroft, A. N. Fitch, *Angew. Chem.* **1992**, *104*, 1666 – 1667; *Angew. Chem. Int. Ed. Engl.* **1992**, *31*, 1655 – 1657.
[11] E. A. Meyer, R. K. Castellano, F. Diederich, *Angew. Chem.* **2003**, *115*, 1244 – 1287; *Angew. Chem. Int. Ed.* **2003**, *42*, 1210 – 1250.
[12] a) K. Reichenbaecher, H. I. Suess, J. Hulliger, *Chem. Soc. Rev.* **2005**, *34*, 22 – 30; b) Grubbs and co-workers have formed polymers by using olefin metathesis that incorporates pentafluorophenyl moieties: M. Weck, A. R. Dunn, K. Matsumoto, G. W. Coates, E. B. Lobkovsky, R. H. Grubbs, *Angew. Chem.* **1999**, *111*, 2909 – 2912; *Angew. Chem. Int. Ed.* **1999**, *38*, 2741 – 2745; c) F. Ponzini, R. Zagha, K. Hardcastle, J. S. Siegel, *Angew. Chem.* **2000**, *112*, 2413 – 2415; *Angew. Chem. Int. Ed.* **2000**, *39*, 2323 – 2325.
[13] a) G. B. Jones, *Tetrahedron* **2001**, *57*, 7999 – 8016; b) G. B. Jones, B. J. Chapman, *Synthesis* **1995**, 475 – 497.
[14] M. J. Marsella, Z.-Q. Wang, R. J. Reid, K. Yoon, *Org. Lett.* **2001**, *3*, 885 – 887.
[15] Y. S. Yamada, C. Morita, *J. Am. Chem. Soc.* **2002**, *124*, 8184 – 8185.
[16] In general, the corresponding acids are pentafluorobenzylated by the Mistunobu reaction with pentafluorobenzyl alcohol or alkylated selectively using CsF on celite: a) S. Hayat, R. Atta, M. Iqbal-Choudhary, K. M. Khan, W. Schumann, E. Bayer, *Tetrahedron* **2001**, *57*, 9951 – 9957; b) J. C. Lee, Y. Choi, *Synth. Commun.* **1998**, *28*, 2021 – 2026; the alkyl chains were subsequently installed by sequential Mitsunobu alkylations.
[17] M. S. Sanford, J. A. Love, R. H. Grubbs, *J. Am. Chem. Soc.* **2001**, *123*, 6543 – 6554.
[18] The ^{1}H NMR signals for the alkene protons overlap and appear in the form of a complex multiplet for all compounds in Table 1; hence, the calculation of *E*/*Z* ratios was not possible.
[19] For a solution that exploits catalyst reactivity, see: A. Furstner, O. R. Thiel, L. Ackermann, *Org. Lett.* **2001**, *3*, 449 – 451.
[20] T. R. Hoye, C. S. Jeffrey, M. A. Tennakoon, J. Wang, H. Zhao, *J. Am. Chem. Soc.* **2004**, *126*, 10210 – 10211.
[21] The linear dimer below was commonly isolated in yields of up to 64 %.



 © 2006 Wiley-VCH Verlag GmbH & Co. KGaA, Weinheim

[22] Attempted X-ray analysis of simple models shown below have failed as both are isolated as oils at room temperature; low-temperature crystallization techniques were not successful.



[23] Calculations performed using Hyperchem v.7.5; M. J. S. Dewar, E. G. Zoebisch, E. F. Healy, J. J. P. Stewart, *J. Am. Chem. Soc.* **1985**, *107*, 3902 – 3909.
[24] C. Moeller, M. S. Plesset, *Phys. Rev.* **1934**, *46*, 618 – 622.
[25] N. L. Allinger, *J. Am. Chem. Soc.* **1977**, *99*, 8127 – 8134.

 © 2006 Wiley-VCH Verlag GmbH & Co. KGaA, Weinheim

Biosynthesis

DOI: 10.1002/anie.200503882

Biosynthesis of the Cyclotide Kalata B1 by Using Protein Splicing**

*Richard H. Kimura, Ahn-Tuyet Tran, and Julio A. Camarero**

Cyclotides are a newly emerging family of large-backbone cyclized polypeptides (≈30-residues long) characterized by a disulfide-stabilized core (3 disulfide bonds) with an unusual knotted structure.[1]

The core structural motif in cyclotides has been termed a cyclic cystine knot (CCK) and is characterized by a cystine knot that is embedded into a circular backbone topology.[1d] The cystine knot involves two disulfide bonds that form a ring that is penetrated by a third disulfide bond. The unique cyclic-backbone topology and knotted arrangement of the three disulfide bonds endow the cyclotides with exceptional stability and resistance to chemical, enzymatic, and thermal degradation.[2] Furthermore, their well-defined structures have been associated with a range of biological functions such as uterotonic activity, inhibition of trypsin and neurotension binding, cytotoxicity, anti-HIV, antimicrobial, and insecticidal activity.[1b–c] Together, these characteristics suggest that cyclotides are ideal molecular scaffolds for the development of stable peptide drugs.[1b]

Despite the fact that the chemical synthesis of circular peptides has been well explored and a number of different approaches involving the solid or liquid phases exist,[3] recent developments in the fields of molecular biology and protein engineering have now made possible the biosynthesis of cyclic peptides. This progress has been made mainly in two areas, nonribosomal peptide synthesis[4] and expressed protein ligation (EPL)/protein trans-splicing.[5] Access to biosynthetic cyclotides by using techniques of recombinant-DNA expression offers the exciting possibility of producing large combinatorial libraries of highly stable cyclic polypeptides. This would allow the generation of cell-based combinatorial libraries that could be screened either in vitro or in vivo for their ability to regulate cellular processes.

Herein, we describe the biosynthesis of the cyclotide Kalata B1 (KB1) by using an engineered intein. Our approach (Figure 1) is based on an intramolecular version of native chemical ligation (NCL).[6] NCL involves the chemoselective reaction between an N-terminal Cys residue of one peptide and an α-thioester group of a second peptide. Importantly, incorporation of these two groups into the same synthetic polypeptide leads to efficient circularization.[3]

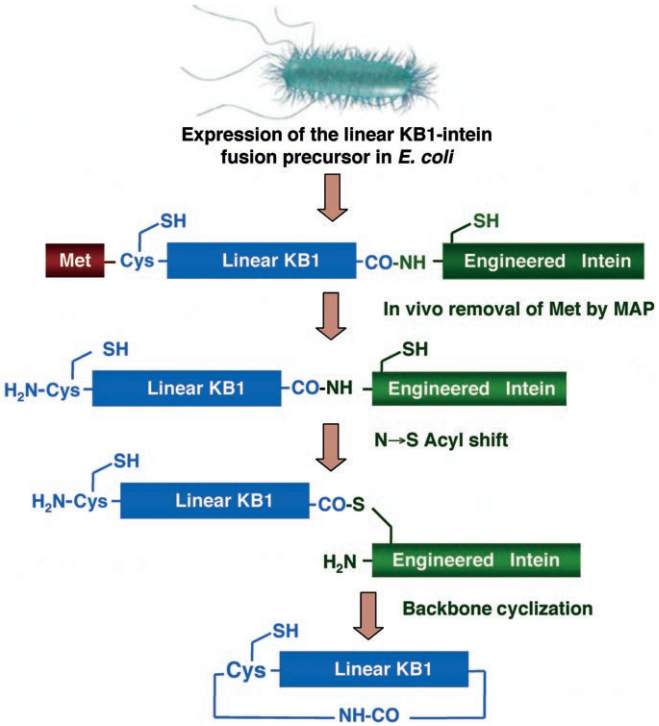


Figure 1. Backbone cyclization of a KB1 linear precursor by using an engineered intein.

To test this approach, we constructed several plasmids that encode different KB1 linear precursors (Figure 2) and

[*] Dr. R. H. Kimura, Dr. A.-T. Tran, Dr. J. A. Camarero
Chemical Biology and Nuclear Sciences Division
Lawrence Livermore National Laboratory
University of California
7000 East Avenue, Livermore, CA 94550 (USA)
Fax: (+1) 925-422-3160
E-mail: camarero1@llnl.gov

[**] This work was performed under the auspices of the U.S. Department of Energy by the University of California, Lawrence Livermore National Laboratory under Contract W-7405-Eng-48. We thank Dr. David Craik, University of Queensland, Australia, for kindly providing a sample of natural Kalata B1.

Supporting information for this article is available on the WWW under http://www.angewandte.org or from the author.

© 2006 Wiley-VCH Verlag GmbH & Co. KGaA, Weinheim

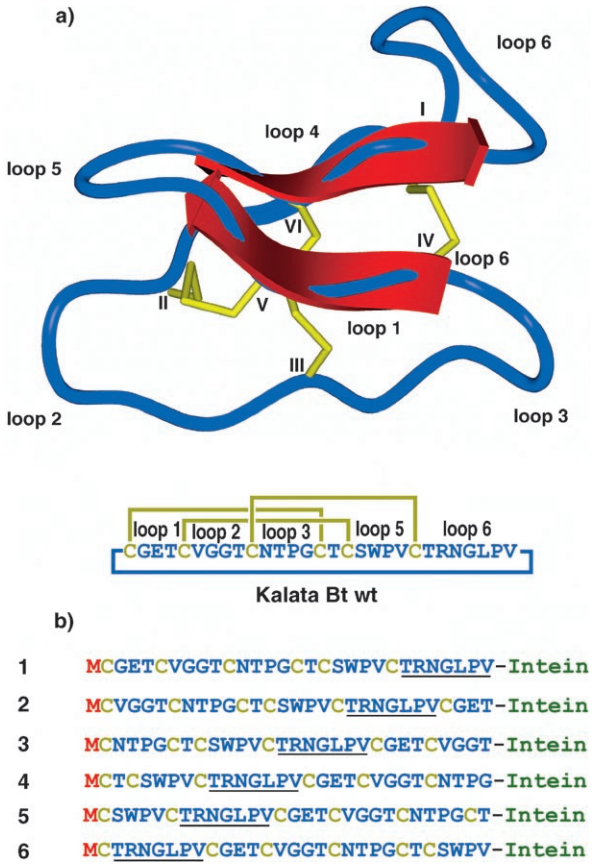


Figure 2. a) Structure (primary and tertiary) and disulfide connectivity of the cyclotide KB1. b) Sequences of the different linear precursors used for the backbone cyclization of KB1. The sequence corresponding to loop 6 has been underlined in all the linear precursors as a reference.

are fused in-frame at their C termini to a modified vacuolar membrane ATPase (VMA) intein.[5e] This allows the generation of the required C-terminal α-thioester function. Also, a Met residue was genetically introduced at the N terminus of the corresponding KB1 fusion protein. The Met residue is efficiently removed immediately after translation by the endogeneous Met aminopeptidase (MAP). This in vivo proteolytic event unmasks the N-terminal Cys residue required for NCL.[5a]

The KB1–intein fusion proteins (**1** through **6**, Figure 2b) were expressed in *E. coli* and purified by affinity chromatography. Analysis of the purified fusion proteins by SDS-PAGE revealed that the different linear precursors have different propensities for cleavage in vivo. Linear precursors **4** and **5** showed around 30% cleavage in vivo, **6** was almost completely cleaved (90%), and **1**, **2**, and **3** were cleaved to about 70% in vivo. Analysis of the soluble cell fractions that correspond to the constructs with high in vivo cleavage did not reveal the presence of any reduced or oxidized circular KB1. Analysis of the insoluble cellular fractions under reductive conditions, after being treated briefly at pH 12 to hydrolyze any residual thioester functionality, showed, on the other hand, the presence of the corresponding reduced linear carboxylated peptide. It is interesting to note that the linear precursors **1** and **6** also produced small amounts of reduced circular KB1 ($\leq 5\ \mu g\,L^{-1}$ of culture).

These results indicate that cleavage in vivo of KB1–intein fusion proteins is mostly triggered by internal Cys residues (rather than by the N-terminal Cys residues), which leads directly to backbone cyclization. These thiolactone intermediates have been shown to react by a "thia zip" mechanism that involves successive ring expansions through reversible thiol–thiolactone exchanges in the direction of the N terminus. The exchange continues until the thiolactone involving the N-terminal Cys residue is formed finally resulting in backbone cyclization.[7] It is very likely that some of these intermediates may aggregate before backbone cyclization can take place, thus explaining the low yield observed for the cyclization process in the bacterial cytoplasm.

We next tested the ability of the different linear precursors to cyclize in vitro. Cyclization was triggered by treatment of the purified KB1–intein fusion proteins with EtSH (3%) in column buffer solution (0.1 mM ethylenediaminetetraacetic acid, 50 mM sodium phosphate, 250 mM NaCl) at pH 7.2. In all the cases except **5**, the major product of the reaction was the reduced cyclic KB1. Among the different linear precursors, **1**, **3**, and **4** gave the best cyclization yields (Figure 3a). Precursor **6** also had a moderately good yield for the cyclization process. However, the fact that almost all of the precursor fusion protein was prematurely cleaved in vivo resulted in a small amount of circular KB1 being produced. Linear precursor **2** gave only a modest yield and although the reduced circular KB1 was still the major product, other minor products including the corresponding linear ethyl thioester precursor as well as thiolactone intermediates were also found in the cyclization crude mixture, even after 4 days of reaction. By far the worst result was obtained for the linear precursor **5**. In this case, cyclic reduced KB1 was found only as a minor product ($\leq 5\%$). Purified reduced KB1 was oxidatively folded in the presence of reduced glutathione (10 mM; GSH) in NH_4HCO_3 buffer solution (50 mM; pH 8.5) that contained *i*PrOH (50%) as described previously by Craik and co-workers[3c] Under these conditions, the folding of reduced KB1 is almost quantitative in less than 15 h (Figure 3b). The folding of reduced KB1 in the absence of organic cosolvents is relatively inefficient, being around 40% of that obtained by using *i*PrOH (50%). The use of Triton X-100 (0.5%) also improved the yield of folding (70% of that observed using *i*PrOH). The folded recombinant KB1 was shown by 2D NMR spectroscopy, HPLC, and ES-MS analysis to be identical to the natural product.

Encouraged by these results, we decided to explore the possibility of carrying out the cyclization and folding steps in a single-pot reaction. This was accomplished by treating **4** with different amounts and ratios of reduced and oxidized glutathione (GSH and GSSG, respectively). The best cleavage/cyclization conditions were accomplished by using GSH (100 mM; pH 7.2). Through the use of these conditions, cleavage of the linear intein precursor was almost quantitative in less than 18 h. Optimal conditions for oxidative folding of reduced KB1 were obtained by using a buffer solution that contained a GSH/GSSG ratio of 4:1 at pH 7.2 in *i*PrOH (50%). Hence, the purified linear precursor **4** was treated first

 © 2006 Wiley-VCH Verlag GmbH & Co. KGaA, Weinheim

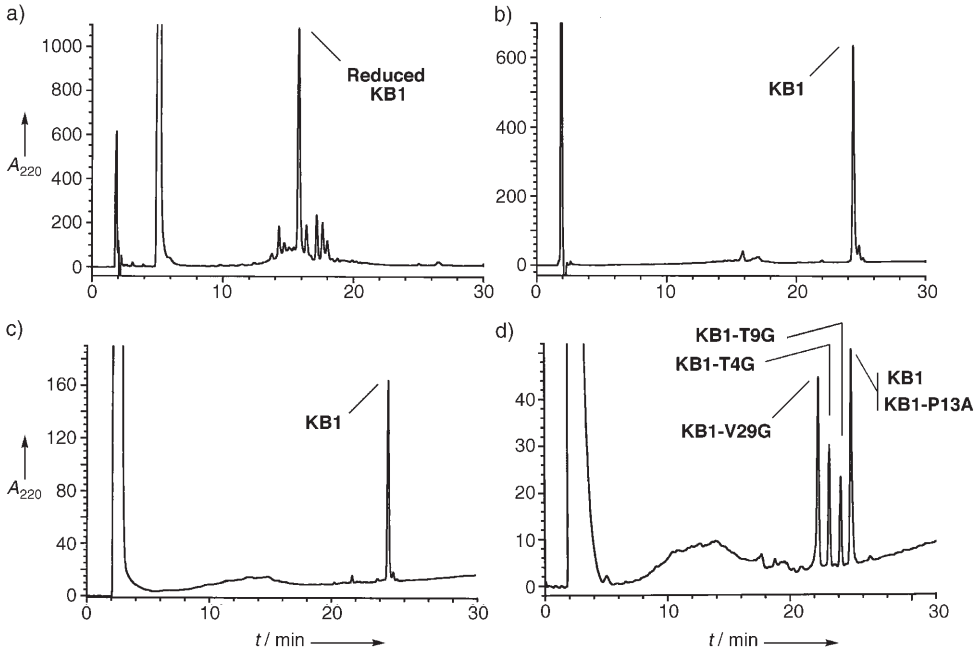


Figure 3. Cyclization and folding of native KB1. Analytical HPLC traces of: a) EtSH cleavage of purified linear precursor **4** after 2 days, b) oxidative refolding of reduced KB1 in GSH (10 mM), NH_4HCO_3 buffer (50 mM; pH 8.5) that contains *i*PrOH (50%) after 18 h, c) "one-pot" cyclization and folding of linear precursor **4** by using GSH/GSSG in *i*PrOH (50%; see text for details) and d) "one-pot" cyclization and folding of small libraries of KB1-based cyclotides by using the same procedure as described previously.

with GSH (100 mM; pH 7.2) for 18 h, and the crude reaction was then complemented with *i*PrOH (50% v/v) and GSSG (12 mM). Under these conditions, the folding reaction was extremely clean and efficient after 20 h (Figure 3c). When the oxidative cleavage was done in aqueous buffer at pH 7.2 in the presence of GSH (10 mM) and GSSG (2 mM) with no *i*PrOH, folded KB1 was also obtained with a yield of about 4% (based on the amount of linear precursor). Similar results were also obtained with **1**, **2**, **3**, and **6**.

We also explored the possibility of using this method to generate different KB1 mutants (KB1-V29G, KB1-T4G, KB1-T9G, KB1-P13A, KB1-W19A, KB1-W19R, and KB1-W19S).[8] Some of the mutants were designed to test the effect of replacement of different β-branched residues adjacent to Cys residues in loops 1, 2, and 6 by the highly flexible Gly residue (KB1-V29G, KB1-T4G, and KB1-T9G). Also, the replacement of the hydrophobic residue Trp in loop 5 by the more hydrophilic Arg and Ser residues (KB1-W19R and KB1-W19S) and the less hydrophobic Ala residue (KB1-W19A) was explored. Finally, the Pro residue in loop 3, which has been found to be important for defining the β turn in this loop,[9] was mutated to Ala (KB1-P13A).

The "one-pot" cyclization/folding reaction was very efficient for all the mutants tested with yields ranging from 10→60%, this therefore highlights the robustness of this structural fold for the construction of molecular libraries. The possibility of using this methodology to biosynthesize libraries based on the cyclotide KB1 was also explored. A small library that contained KB1 and the mutants KB1-V1G, KB1-T5G, KB1-T10G, and KB1-P14A were expressed in *E. coli* and then cyclized and folded as described above. The HPLC and ES-MS analysis of the single-pot cyclization/folding reaction revealed the presence of all of the five members of the library (Figure 3d). Quantification of the individual members by ES-MS and HPLC showed that all the cyclotides were produced with similar yields. Standard deviation for the yields of all the five members was within 30%.

In summary, we have described for the first time the biosynthesis of the cyclotide KB1 in *E. coli*. We have also shown that our biosynthetic approach very efficiently generates, in one single-pot reaction, natural KB1 as well as several mutants. This approach can also be used to generate cyclotide-based libraries that could be screened in vitro for biological activity. Furthermore, one can easily envision that by using cellular environments that are less reductive than *E. coli*'s cytoplasm, this biosynthetic method could be adapted for in vivo biosynthesis of cyclotides.

Received: November 3, 2005
Published online: December 28, 2005

Keywords: bioorganic chemistry · biosynthesis · circular peptides · protein engineering · protein ligation

[1] a) M. Trabi, D. J. Craik, *Trends Biochem. Sci.* **2002**, *27*, 132–138; b) D. J. Craik, N. L. Daly, J. Mulvenna, M. R. Plan, M. Trabi, *Curr. Protein Pept. Sci.* **2004**, *5*, 297–315; c) U. Goransson, E. Svangard, P. Claeson, L. Bohlin, *Curr. Protein Pept. Sci.* **2004**, *5*, 317–329; d) H. J. Vogel, D. I. Chan, *Structure* **2005**, *13*, 688–690.
[2] M. L. Colgrave, D. J. Craik, *Biochemistry* **2004**, *43*, 5965–5975.
[3] a) J. A. Camarero, J. Pavel, T. W. Muir, *Angew. Chem.* **1998**, *110*, 361–364; *Angew. Chem. Int. Ed.* **1998**, *37*, 347–349; b) J. P. Tam, Y. A. Lu, J. L. Yang, K. W. Chiu, *Proc. Natl. Acad. Sci. USA* **1999**,

 © 2006 Wiley-VCH Verlag GmbH & Co. KGaA, Weinheim

96, 8913 – 8918; c) N. L. Daly, S. Love, P. F. Alewood, D. J. Craik, *Biochemistry* **1999**, *38*, 10606 – 10614.
[4] C. T. Walsh, *Science* **2004**, *303*, 1805 – 1810.
[5] a) J. A. Camarero, T. W. Muir, *J. Am. Chem. Soc.* **1999**, *121*, 5597 – 5598; b) T. C. Evans, J. Benner, M.-Q. Xu, *J. Biol. Chem.* **1999**, *274*, 18359 – 18381; c) J. A. Camarero, D. Fushman, D. Cowburn, T. W. Muir, *Bioorg. Med. Chem.* **2001**, *9*, 2479 – 2484; d) C. P. Scott, E. Abel-Santos, M. Wall, D. Wahnon, D. , S. J. Benkovic, *Proc. Natl. Acad. Sci. USA* **1999**, *96*, 13638 – 13643; e) C. J. Noren, J. Wang, F. B. Perler, *Angew. Chem.* **2000**, *112*, 458 – 476; *Angew. Chem. Int. Ed.* **2000**, *39*, 450 – 456; f) F. B. Perler, E. Adam, *Curr. Opin. Biotechnol.* **2000**, *11*, 377 – 383; g) T. W. Muir, *Annu. Rev. Biochem.* **2003**, *72*, 431 – 434.
[6] a) P. E. Dawson, T. W. Muir, I. Clark-Lewis, S. B. H. Kent, *Science* **1994**, *266*, 776 – 779; b) J. P. Tam, Y. A. Lu, C. F. Liu, J. Shao, *Proc. Natl. Acad. Sci. USA* **1995**, *92*, 12485 – 12489; c) P. E. Dawson, S. B. H. Kent, *Annu. Rev. Biochem.* **2000**, *69*, 923 – 960.
[7] J. P. Tam, Y. A. Lu, *Protein Sci.* **1998**, *7*, 1583 – 1592.
[8] Numbering of the mutations is always with reference to construct **1**.
[9] K. J. Rosengren, N. L. Daly, M. R. Plan, C. Waine, D. J. Craik, *J. Biol. Chem.* **2003**, *278*, 8606 – 8616.

 © 2006 Wiley-VCH Verlag GmbH & Co. KGaA, Weinheim

Reaction Mechanisms

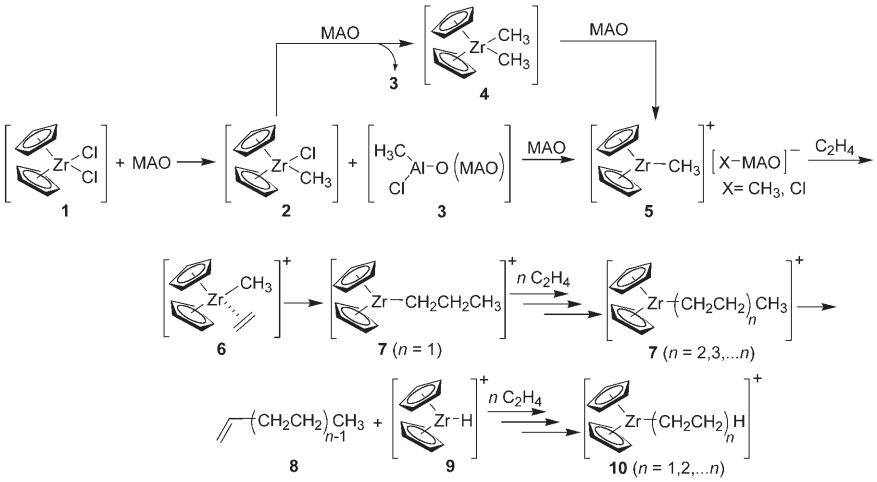
DOI: 10.1002/anie.200503307

Study of Homogeneously Catalyzed Ziegler–Natta Polymerization of Ethene by ESI-MS**

*Leonardo Silva Santos and Jürgen O. Metzger**

Homogeneous zirconocene catalysts for olefin polymerization are very important. The current standard procedure for the polymerization of ethene using this catalysts is the protocol developed by Kaminsky et al,[1] who observed a surprisingly high catalytic activity upon addition of water. This observation led to the discovery of a highly efficient activator, an oligomeric methyl aluminoxane (MAO).[2] This discovery rejuvenated Ziegler–Natta catalysis and opened the era of single-site polymerization catalysis.

Several mechanistic and kinetic studies led to the generally accepted reaction mechanism, which is depicted in Scheme 1. Treatment of a toluene solution of $[Cp_2ZrCl_2]$ (**1**) with MAO leads to a rapid initial ligand-exchange reaction that initially generates the monomethyl complex $[Cp_2ZrCH_3Cl]$ (**2**),[3] and an excess of MAO leads to $[Cp_2ZrMe_2]$ (**4**).[3a] Abstraction of chloride from **2** or methyl from **4** by MAO gives the catalytically active ion-paired species $[Cp_2ZrCH_3]^+$ (**5**) with the counterion X-$[Al(Me)O-]_n^-$ ($X = Cl, Me$),[3b] as proved by solid-state X-ray photoelectron spectroscopy (XPS)[4a] and ^{13}C NMR[4b] studies, as well as by ^{91}Zr and ^{13}C NMR investigations of $[Cp_2Zr(CH_3)_2]$/MAO solutions.[5] In the presence of ethene, cation **5** forms the π complex **6** and subsequently the insertion product **7** ($n = 1$), which is the first intermediate of the polymerization process. Step-by-step insertion of ethene then yields the cationic alkyl zirconocenes **7** ($n = 2, 3 \ldots n$). β Elimination gives the odd-numbered-chain polymer **8**, which contains a terminal C–C double bond, and the cationic zirconocene hydride **9**, which is able to initiate polymerization to give, via zirconocene cation **10**, the even-numbered-chain polymer.[6] However, some experimental evidence suggests that the general classification of zirconocene/MAO catalyst systems as single-site catalysts may be an oversimplification.[7]



Scheme 1. Proposed mechanism of the Ziegler–Natta polymerization of C_2H_4 with the homogeneous catalyst $[Cp_2ZrCl_2]$/MAO.

Electrospray ionization mass spectrometry (ESI-MS) is rapidly becoming an important technique for mechanistic studies of chemical reactions in solution[8,9] including homogeneously catalyzed reactions[10] and high-throughput screening of homogeneous catalysts.[11] Feichtinger et al.[12] reported on ESI tandem mass-spectrometric investigations (ESI-MS/MS) of Ziegler–Natta-like olefin oligomerization by alkylzirconocene cations generated by the reaction of $[Cp_2Zr(CH_3)_2]$ with boron-based activators.[13] Chen studied the polymerization of ethene with $[Cp_2ZrCl_2]$/MAO as the catalyst. The reaction mixture was quenched with *N*,*N*-dicyclohexylcarbodiimide (DCC), and the products were investigated by ESI-MS.[11b]

Since ESI normally releases ions preformed in solution,[14] we expected that transient ionic species such as **5**, **9**, **7**, and **10** (Scheme 1) should be detectable by ESI-MS in the reacting solution under steady-state conditions, despite the presence of a large excess of nonionic species. ESI is also known for the mild conditions used to form the gaseous ions; ever very labile molecules can be transferred to the gas phase.[15]

We report here on a preliminary study of the Ziegler–Natta polymerization of ethene with the homogeneous catalyst $[Cp_2ZrCl_2]$/MAO. We used a microreactor coupled directly to the ESI source of a Q-TOF mass spectrometer and focused on the direct detection and mass-spectrometric characterization of the transient cationic and catalytically active species involved and on the direct demonstration of their catalytic activity.

First, we set out to investigate the formation of the catalytically active species in a solution that was prepared from **1** and MAO in toluene according to a literature procedure.[16] Direct analysis of the toluene solution containing the catalyst afforded a low-quality spectrum with poor ion intensity, because toluene is not an ideal solvent for the ESI process. Dilution of the solution with acetonitrile on-line using a microreactor (Figure 1)[17,18] resulted in a very clean

[*] Dr. L. S. Santos, Prof. Dr. J. O. Metzger
Institut für Reine und Angewandte Chemie
Carl von Ossietzky Universität Oldenburg
Postfach 2503, 26111 Oldenburg (Germany)
Fax: (+49) 441-798-3618
E-mail: juergen.metzger@uni-oldenburg.de

[**] Financial support from the German Research Association (DFG) is gratefully acknowledged (Me 722/18). ESI-MS: Electrospray ionization mass spectrometry.

 © 2006 Wiley-VCH Verlag GmbH & Co. KGaA, Weinheim

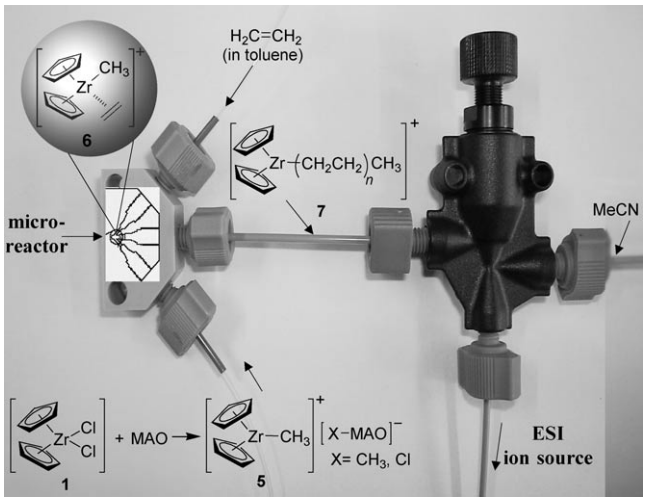


Figure 1. Microreactor coupled on-line to ESI source. In the first micromixer (left) toluene solutions of the preformed catalyst [Cp_2ZrCl_2]/MAO (1:1.2 equiv) and of C_2H_4 were mixed continuously to initiate the polymerization. The reaction occurred in the capillary transferring the reacting solution to the second micromixer (right), where it is quenched by MeCN and from which it is fed directly to the ESI source.

spectrum displaying five Zr-containing cationic species that were easily identified by their isotopic pattern: **5** (*m*/*z* 235), $[Cp_2ZrCl]^+$ (*m*/*z* 255), **5**·MeCN (*m*/*z* 276), and $[Cp_2ZrCl{\cdot}MeCN]^+$ (*m*/*z* 296) as well as the ion $[Cp_2Zr]^+$ (*m*/*z* 220) (Figure 2).[19]

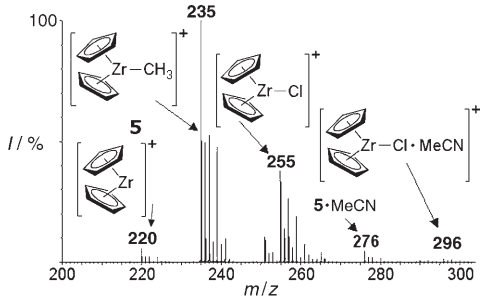


Figure 2. Positive-mode ESI mass spectrum of a solution of [Cp_2ZrCl_2]/MAO (1:1.2 equiv) in toluene after on-line dilution with MeCN.

Ion **5** was characterized by collision-induced dissociation (CID), which resulted in scission of the Zr−CH_3 bond, giving an intense fragment ion of *m*/*z* 220[12,20] (Figure 3a). The complexed ions **5**·MeCN and [Cp_2ZrCl^+·MeCN] readily lose MeCN by CID to give the respective cations **5** and $[Cp_2ZrCl]^+$ (Figure 3b).[21,22] These CID results give evidence that ions **5** and $[Cp_2ZrCl]^+$ found in the ESI mass spectrum (Figure 2) may arise by in-source decay of the respective MeCN adduct. $[Cp_2Zr]^+$ may be formed analogously by fragmentation of ion **5**.

The formation of ion **5** in solution is a fast reaction. Thus, when solutions of **1** and of MAO, both in toluene, were mixed in a microreactor and the reaction was quenched after 1.7 s with acetonitrile in a second microreactor (Figure 1), a mass spectrum similar to that in Figure 2 was obtained.

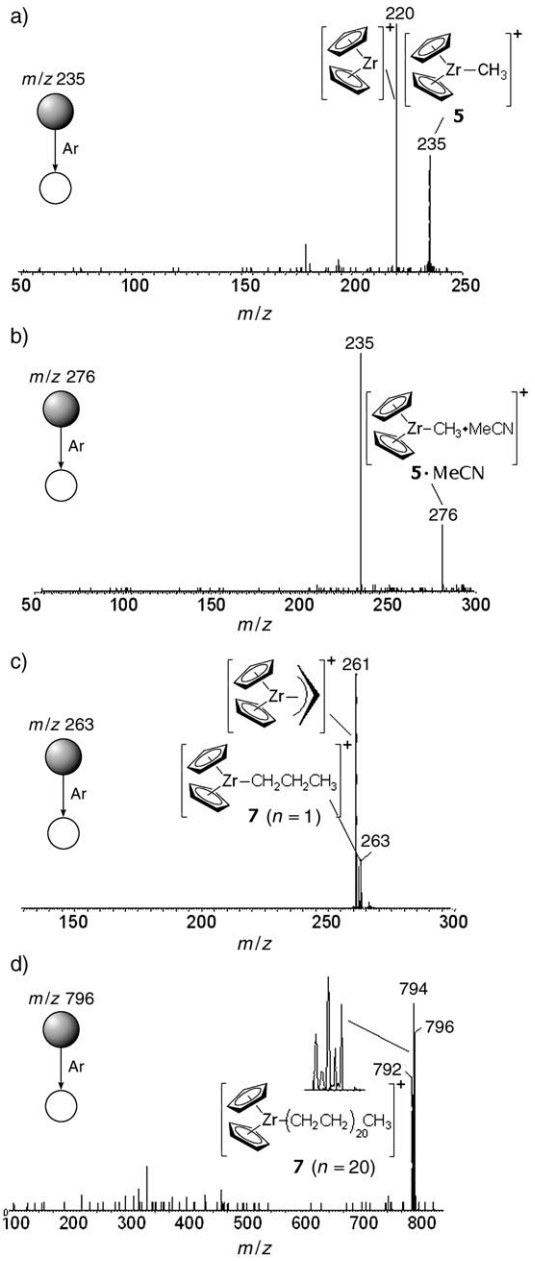


Figure 3. Positive-mode ESI tandem mass spectra of zirconocene intermediate cations: a) **5** of *m*/*z* 235, b) **5**·MeCN of *m*/*z* 276, c) **7** (*n* = 1) of *m*/*z* 263, and d) **7** (*n* = 20) of *m*/*z* 796 (exact mass 795.6324).

However, to probe directly that ion **5** is indeed the catalytically active species we studied the gas-phase reaction of the monoisotopic ion **5** of *m*/*z* 235 (selected in the quadrupole) in the collision cell of the Q-TOF with ethene and carried out mass analysis of the product ions using the TOF analyzer.[23–25] Under low-energy collisions (1.1–2.0 V) in the collision cell, the mass-selected and relatively cold cation **5** (which was quenched by low-energy collisions with the neutral species) reacted with C_2H_4 yielding the cationic addition product ions **7** (*n* = 1–4) in good yields (Figure 4a).[12,26,27]

In the second set of experiments, we examined the polymerization of ethene by mixing a toluene solution of

 © 2006 Wiley-VCH Verlag GmbH & Co. KGaA, Weinheim

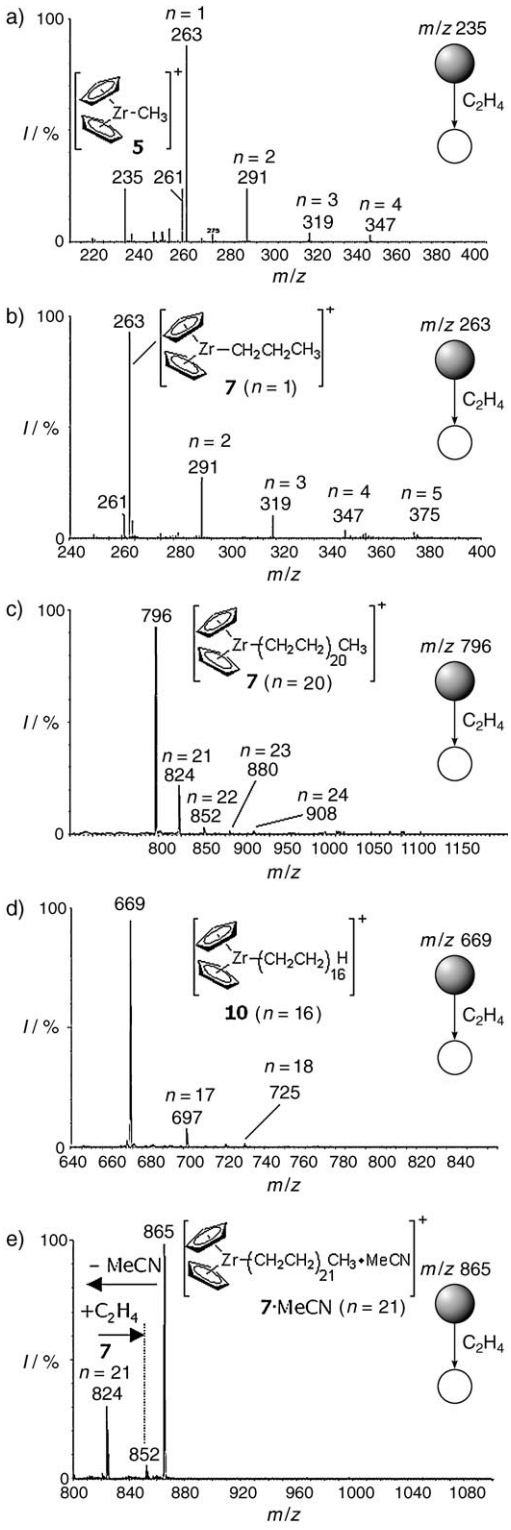


Figure 4. Proof of catalytic activity in the gas phase: MS/MS product-ion mass spectra for reactions of ethene with a) **5**, b) **7** ($n=1$), c) **7** ($n=20$), d) **10** ($n=16$), and e) **7**·MeCN ($n=21$).

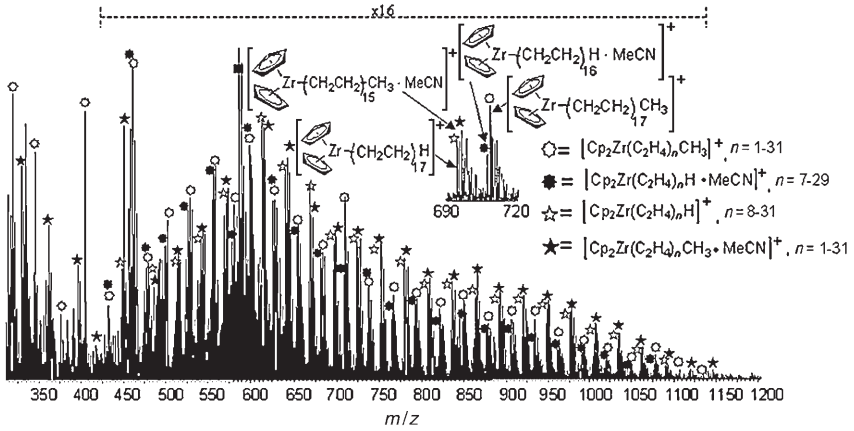


Figure 5. Ziegler–Natta polymerization of ethene: Positive-mode ESI mass spectrum of the MeCN-quenched reaction solution of [Cp_2ZrCl_2]/MAO (1:1.2 equiv) and C_2H_4 (see Figure 1). The spectrum shows the odd- and even-numbered-chain {Cp_2Zr}–alkyl species, as well as the MeCN adducts. The overall reaction time was approximately 1.7 s. The ion marked with (■) is a Zr dimer impurity.

[Cp_2ZrCl_2] and MAO with a saturated solution of ethene in toluene. The reacting solution was quenched with MeCN (Figure 1).[28] In the resulting spectrum (Figure 5) four series of ions can be observed: the odd-numbered-chain species **7** ($n=1$–31) as well as **7**·MeCN ($n=1$–31) and the even-numbered-chain ions **10** ($n=8$–31) as well as **10**·MeCN ($n=7$–29). It is known that in the solvent MeCN no polymerization activity is observed.[29] We rationalize that the dilution step, which was approximately 1.7 s after the initiation of the reaction of **5** and C_2H_4 in toluene, quenched all catalytically active intermediates[30] by blocking the empty d^0 Zr orbital with solvent,[29] as depicted in Figure 6.

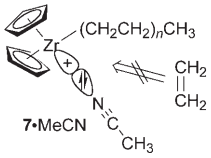


Figure 6. MeCN deactivates the cationic Zr species by blocking the free coordination site.

Several ions found in this experiment were characterized further in collision-induced dissociation (CID) experiments. For example, ion **7** ($n=1$) of m/z 263 shows a loss of H_2 to give the ion of m/z 261 ([$Cp_2Zr(allyl)$]$^+$) as the main fragmentation pathway (Figure 3c).[31] Similar behavior in the CID experiment was observed for most ions **7** and **10**.[20] Ions with higher alkyl groups, i.e. **7** ($n=20$) of m/z 796, undergo two consecutive losses of H_2 affording, in this case, the fragment ions of m/z 794 and 792, respectively (Figure 3d). The MeCN-adduct ions follow similar dissociative behavior after loss of the solvent molecule. As an example, the ion **7**·MeCN ($n=21$) of m/z 865 undergoes loss of MeCN to give the naked fragment ion **7** ($n=21$) of m/z 824, which further dissociates by two consecutive losses of H_2 (spectrum not shown).

All the ions **7** and **10** should be catalytically active, whereas the acetonitrile-adduct ions should not. This was proved directly by investigating their reaction with ethene in the gas phase. Ion **7** ($n=1$) of m/z 263 (the most critical compound for H_2 loss)[12] showed the addition of four units of ethene to give the product ions of m/z 291, 319, 347, and 375 (Figure 4b). The ions **7** ($n=3$, 10, 20) obtained in solution showed that these species are also reactive toward C_2H_4, as exemplified for ion **7** ($n=20$) in Figure 4c. The even-

 © 2006 Wiley-VCH Verlag GmbH & Co. KGaA, Weinheim

numbered chain species **10** ($n = 16$) of m/z 669 was also reactive toward C_2H_4 showing two insertion products of m/z 697 and 725 (Figure 4d). Finally, reaction of **7**·MeCN ($n = 21$) of m/z 865 is interesting since a loss of MeCN is initially accomplished to give the naked cation **7** ($n = 21$) of m/z 824, which is catalytically active, and ethene insertion can occur to give the product ion of m/z 852 (Figure 4e).[29]

In conclusion, cation $[Cp_2ZrCH_3]^+$ (**5**) was easily detected in the reaction solution of $[Cp_2ZrCl_2]$ and MAO by ESI-MS, it was characterized by MS/MS, and the catalytic activity was directly demonstrated by the ion/molecule reaction of **5** and ethene in the gas phase. Furthermore, for the first time, using a microreactor coupled on-line to the ESI source we have been able to intercept the intermediate alkyl zirconium cations **7** of the growing polymer chain in the homogeneous Ziegler–Natta polymerization of ethene directly from the solution, characterize them mass spectrometrically, and prove directly their catalytic activity by gas-phase reactions with ethene.

Received: September 16, 2005
Published online: December 30, 2005

Keywords: homogeneous catalysis · mass spectrometry · microreactors · polymerization · reaction mechanisms

[1] A. Andresen, H. G. Cordes, H. Herwig, W. Kaminsky, A. Merk, R. Mottweiler, J. Pein, H. Sinn, H. J. Vollmer, *Angew. Chem.* **1976**, *88*, 689–690; *Angew. Chem. Int. Ed. Engl.* **1976**, *15*, 630–632.

[2] a) H. Sinn, W. Kaminsky, *Adv. Organomet. Chem.* **1980**, *18*, 99–149; b) H. Sinn, W. Kaminsky, H.-J. Vollmer, R. Woldt, *Angew. Chem.* **1980**, *92*, 396–402; *Angew. Chem. Int. Ed. Engl.* **1980**, *19*, 390–392.

[3] a) W. Kaminsky, R. Steiger, *Polyhedron* **1988**, *7*, 2375–2381; b) D. Cam, U. Giannini, *Makromol. Chem.* **1992**, *193*, 1049–1055.

[4] a) XPS: P. G. Gassman, M. R. Callstrom, *J. Am. Chem. Soc.* **1987**, *109*, 7875–7876; b) ^{13}C NMR: C. Sishta, R. M. Hathorn, T. J. Marks, *J. Am. Chem. Soc.* **1992**, *114*, 1112–1114.

[5] a) A. R. Siedle, W. M. Lamanna, R. A. Newmark, J. N. Schroepfer, *J. Mol. Catal. A* **1998**, *128*, 257–271; b) I. Tritto, S. X. Li, M. C. Sacchi, P. Locatelli, G. Zannoni, *Macromolecules* **1995**, *28*, 5358–5362; c) I. Tritto, S. Li, M. C. Sacchi, G. Zannoni, *Macromolecules* **1993**, *26*, 7111–7115.

[6] a) W. Kaminsky, *Macromol. Chem. Phys.* **1996**, *197*, 3907–3945; b) W. Kaminsky, C. Strubel, *J. Mol. Catal. A* **1998**, *128*, 191–200.

[7] a) D. Coevoet, H. Cramail, A. Deffieux, *Macromol. Chem. Phys.* **1999**, *200*, 1208–1214; b) J.-N. Pédeutour, D. Coevoet, H. Cramail, A. Deffieux, *Macromol. Chem. Phys.* **1999**, *200*, 1215–1221; c) D. E. Babushkin, N. V. Semikolenova, V. A. Zakharov, E. P. Talsi, *Macromol. Chem. Phys.* **2000**, *201*, 558–567.

[8] L. S. Santos, L. Knaack, J. O. Metzger, *Int. J. Mass Spectrom.* **2005**, *246*, 84–104.

[9] a) J. Griep-Raming, S. Meyer, T. Bruhn, J. O. Metzger, *Angew. Chem.* **2002**, *114*, 2863–2866; *Angew. Chem. Int. Ed.* **2002**, *41*, 2738–2742; b) S. Meyer, R. Koch, J. O. Metzger, *Angew. Chem.* **2003**, *115*, 4848–4851; *Angew. Chem. Int. Ed.* **2003**, *42*, 4700–4703.

[10] a) L. S. Santos, C. H. Pavam, W. P. Almeida, F. Coelho, M. N. Eberlin, *Angew. Chem.* **2004**, *116*, 4430–4433; *Angew. Chem. Int. Ed.* **2004**, *43*, 4330–4333; b) J. B. Domingos, E. Longhinotti, T. A. S. Brandao, C. A. Bunton, L. S. Santos, M. N. Eberlin, F. Nome, *J. Org. Chem.* **2004**, *69*, 6024–6033; c) E. C. Meurer, L. S. Santos, R. A. Pilli, M. N. Eberlin, *Org. Lett.* **2003**, *5*, 1391–1394; d) A. A. Sabino, A. H. L. Machado, C. R. D. Correia, M. N. Eberlin, *Angew. Chem.* **2004**, *116*, 2568–2572; *Angew. Chem. Int. Ed.* **2004**, *43*, 2514–2518.

[11] a) C. Hilderling, C. Adlhart, P. Chen, *Angew. Chem.* **1998**, *110*, 2831–2835; *Angew. Chem. Int. Ed.* **1998**, *37*, 2685–2689; b) P. Chen, *Angew. Chem.* **2003**, *115*, 2938–2954; *Angew. Chem. Int. Ed.* **2003**, *42*, 2832–2847; c) C. Raminelli, M. H. G. Prechtl, L. S. Santos, M. N. Eberlin, J. V. Comasseto, *Organometallics* **2004**, *23*, 3990–3996.

[12] D. Feichtinger, D. A. Plattner, P. Chen, *J. Am. Chem. Soc.* **1998**, *120*, 7125–7126.

[13] a) X. M. Yang, C. L. Stern, T. J. Marks, *J. Am. Chem. Soc.* **1994**, *116*, 10015–10031; b) M. Bochmann, S. J. Lancaster, *Angew. Chem.* **1994**, *106*, 1715–1718; *Angew. Chem. Int. Ed. Engl.* **1994**, *33*, 1634–1637; c) L. Jia, X. M. Yang, A. Ishihara, T. J. Marks, *Organometallics* **1995**, *14*, 3135–3137.]

[14] a) C. M. Whitehouse, R. N. Dreyer, M. Yamashita, J. B. Fenn, *Anal. Chem.* **1985**, *57*, 675–679; b) J. B. Fenn, M. Mann, C. K. Meng, S. F. Wong, C. M. Whitehouse, *Science* **1989**, *246*, 64–71; c) R. B. Cole, *Electrospray Ionization Mass Spectroscopy*, Wiley, New York, **1997**.

[15] F. C. Gozzo, L. S. Santos, R. Augusti, C. S. Consorti, J. Dupont, M. N. Eberlin, *Chem. Eur. J.* **2004**, *10*, 6187–6193.

[16] W. Kaminsky, K. Kulper, H. H. Brintzinger, F. R. W. P. Wild, *Angew. Chem.* **1985**, *97*, 507–508; *Angew. Chem. Int. Ed. Engl.* **1985**, *24*, 507–508.

[17] A mixture of $[Cp_2ZrCl_2]$ (17.2 μmol, 5.0 mg) and MAO (20.6 μmol, 34.0 μL, 10% solution in toluene) in anhydrous and degassed toluene (5.0 mL) was mixed with anhydrous and degassed MeCN under Ar atmosphere using a dual-syringe pump operating at a flow rate of 5 $\mu L\,min^{-1}$ in an effective micromixer that was coupled directly to the ion source of the mass spectrometer (Figure 2), and the solution was fed continuously into the MS. The flow rate could be varied from 2.5 to 100 $\mu L\,min^{-1}$. By connecting the microreactor directly to the spray capillary, reaction times from 0.3 to 28 s could be covered.

[18] ESI-MS and ESI-MS/MS analyses were conducted in a high-resolution hybrid quadrupole (Q) and orthogonal time-of-flight (TOF) mass spectrometer (Q-TOF Premier, Micromass, UK) with a constant nebulizer temperature of 150 °C. The ESI source and the mass spectrometer were operated in the positive-ion mode, and the cone and extractor potentials were set to 10 and 4.5 V, respectively, with a scan range of m/z 200–3000. Samples were directly infused into the ESI source at flow rates of 5–100 $\mu L\,min^{-1}$ by means of a microsyringe pump. MS/MS experiments were carried out by mass selection of a specific ion in Q1 which was then submitted to collision-induced dissociation (CID) with argon in the collision chamber. The product-ion MS analysis was accomplished with the high-resolution orthogonal TOF analyzer.

[19] Because zirconium displays five isotopes—^{90}Zr (51.45%), ^{91}Zr (11.22%), ^{92}Zr (17.15%), ^{94}Zr (17.38%), and ^{96}Zr (2.80%)— the Zr-containing species were be mass detected as clusters of isotopologous ions.

[20] Similar CID behavior was described in Ref. [12] and by C. S. Christ, Jr., J. R. Eyler, D. E. Richardson, *J. Am. Chem. Soc.* **1990**, *112*, 596–607.

[21] Although P. Chen and co-workers[12] reported that high voltages were necessary to fragment similar clusters obtained through borates, we observed ready release of MeCN.

[22] It was reported that **5** reacts with MeCN to afford a stable product of m/z 276 $[Cp_2Zr{-}N{=}C(CH_3)_2]^+$ (Y. W. Alelyunas, R. F. Jordan, S. F. Echols, S. L. Borkowsky, P. K. Bradley, *Organometallics* **1991**, *10*, 1406–1416). We performed the same reaction

 © 2006 Wiley-VCH Verlag GmbH & Co. KGaA, Weinheim

as described by Jordan but employed MAO as co-catalyst, and even after 48 h no product arising from reaction of **5** and MeCN was observed by CID experiments.

[23] The T-wave collision cell in the Q-TOF Premier used, enabled us to observe several product ions: K. Giles, S. D. Pringle, K. R. Worthington, D. Little, J. L. Wildgoose, R. H. Bateman, *Rapid Commun. Mass Spectrom.* **2004**, *18*, 2401 – 2414.

[24] The argon in the collision cell was changed for highly pure C_2H_4. The ethene pressure used was between 3×10^{-3} and 2×10^{-2} mbar. For uses of QqTOFs, see: I. V. Chernushevich, A. V. Loboda, B. A. Thomson, *J. Mass Spectrom.* **2001**, *36*, 849 – 865.

[25] The product-ion mass spectrum was acquired under multiple-collision conditions that caused typical beam attenuations of 50–70 % in the collision cell so as to increase the reaction yields and to promote the collisional quenching of both the reactant and product ions. Reactant ions should therefore display no or negligible amounts of excess internal energy. For similar studies in ion/molecule reactions, see: A. E. P. M. Sorrilha, L. S. Santos, F. C. Gozzo, R. Sparrapan, R. Augusti, M. N. Eberlin, *J. Phys. Chem. A* **2004**, *108*, 7009 – 7020, and references therein.

[26] The gas-phase reaction with ion **5** demanded careful adjustment of the voltages of the quadrupole, collision cell, and TOF analyzer to prevent H_2 loss giving allyl derivatives, which are not catalytically active.[12,27] Although it was not possible to prevent the H_2 loss in this specific experiment completely, as depicted in Figure 6 a, we observed the product ions of up to four C_2H_4 molecule insertions ($n = 1$–4) in good yields.

[27] P. Watson, D. C. Roe, *J. Am. Chem. Soc.* **1982**, *104*, 6471 – 6473; J. E. Bercaw, D. L. Davia, P. T. Wolczanski, *Organometallics* **1986**, *5*, 443 – 450.

[28] A solution of **1** and MAO (Ref. [17]) in toluene was mixed in an effective micromixer with toluene saturated with ethene by using a dual-syringe pump set at one flow rate. The reacting solution was delivered to the second micromixer to accomplish the dilution with anhydrous and degassed MeCN, under Ar atmosphere. The second micromixer was coupled directly to the ion source of the mass spectrometer (Figure 1), and the solution was fed continuously into the MS. The reaction time with this device is estimated to be around 0.3 s (50 μL min^{-1}) to 1.7 s (5 μL min^{-1}) depending on the velocity of the syringe pump used to deliver the compounds to the second micromixer for MeCN dilution. Micromixer (MR_1): capillary 75 μm (ID), $l_1 = 3$ cm, $V = 2.2 \times 10^{-10}$ m^3; Micromixer (MR_2): capillary 75 μm (ID), $l_2 = 5$ cm.

[29] a) R. F. Jordan, W. E. Dasher, S. F. Echols, *J. Am. Chem. Soc.* **1986**, *108*, 1718 – 1719; b) R. F. Jordan, C. S. Bajgur, R. Willett, B. Scott, *J. Am. Chem. Soc.* **1986**, *108*, 7410 – 7411.

[30] Varying the length of the PEEK from the second micromixer (l_2), which brings the reaction solution after MeCN dilution to ESI ion source, did not affect the relative intensities of the observed ions (Figure 1, bottom right).

[31] D. B. Jacobson, B. S. Freiser, *J. Am. Chem. Soc.* **1983**, *105*, 736 – 742.

 © 2006 Wiley-VCH Verlag GmbH & Co. KGaA, Weinheim

Electrocatalysis

DOI: 10.1002/anie.200502172

Kinetics and Mechanism of the Electrooxidation of Formic Acid—Spectroelectrochemical Studies in a Flow Cell**

Yan Xia Chen, Martin Heinen, Zenonas Jusys, and Rolf Jürgen Behm**

The application of in situ infrared spectroscopy in electrochemistry is well established. It has been particularly useful in electrocatalytic studies, in which the knowledge of the adsorbed species can contribute significantly to a fundamental understanding of the reaction mechanism (see, for example, reviews [1–3] and references therein). Most of these studies were conducted by using IR reflection absorption spectroscopy (IRRAS) techniques in a thin-layer configuration, where the thickness of the electrolyte layer between the electrode and the IR window is limited to about 10 μm to keep spectral contributions from the electrolyte at a tolerable level. Under these conditions mass transport in the thin-layer gap is practically inhibited, which may result in strongly misleading conclusions on the reaction process owing to the depletion of reactants as well as accumulation and possibly readsorption of by-products.[2]

These limitations can be reduced by performing infrared absorption reflection spectroscopy measurements in an attenuated total reflection configuration (ATR-FTIRS),[4,5] in which a thin metal film deposited on an optical prism serves as a working electrode and the IR beam is transmitted internally from the back side of the prism to the film and totally reflected at the prism/film interface. In this technique the working electrode is freely accessible to the electrolyte. Nevertheless, despite the obvious improvements over the thin-layer configuration, diffusion of reactants to and products from the electrode is still ill-defined.

Herein we describe an extension of the present in situ ATR-FTIRS technique by coupling it to a thin-layer electrochemical flow cell. We demonstrate the potential of this technique for mechanistic and kinetic studies of electro-

[*] Dr. Y. X. Chen, M. Heinen, Dr. Z. Jusys, Prof. Dr. R. J. Behm
Dept. Surface Chemistry and Catalysis
University of Ulm
89069 Ulm (Germany)
Fax: (+49) 731-502-5452
E-mail: yan-xia.chen@uni-ulm.de
juergen.behm@uni-ulm.de

[**] We gratefully acknowledge the help of M. Osawa and S. Ye (University of Hokkaido, Japan) in introducing the ATR-FTIRS technique as well as financial support by the Forschungsallianz Brennstoffzellen (FABZ) Baden-Württemberg and by the Deutsche Forschungsgemeinschaft (BE 1201/8-4, BE 1201/11-1). Y.X.C. is grateful for a fellowship from the Alexander von Humboldt Foundation.

Supporting information for this article is available on the WWW under http://www.angewandte.org or from the author.

 © 2006 Wiley-VCH Verlag GmbH & Co. KGaA, Weinheim InterScience

catalytic reactions, with the electrooxidation of formic acid on a Pt film electrode as an example. This reaction can be considered as a model reaction for the electrooxidation of small organic molecules. In addition, it is also of technical interest, as formic acid is a reaction intermediate in direct methanol fuel cells[6] and was also proposed as a fuel for low-temperature fuel cells.[7] It is generally accepted that the reaction proceeds through two different reaction pathways ("dual-path mechanism"): an "indirect" pathway involving formic acid dehydrogenation and subsequent electrooxidation of the resulting adsorbed CO to CO_2, and a "direct" pathway, which proceeds directly, without CO_{ad} formation, to CO_2.[3,8,9] Recently, adsorbed formate was suggested as a stable intermediate.[10] Our data demonstrate that this picture is incomplete and that the reaction involves at least three different parallel reaction pathways. The relative contributions of the three pathways under current reaction conditions are estimated from the electrochemical and IR spectroscopic data.

This study demonstrates the general potential of in situ ATR-FTIRS studies under continuous flow conditions with well-defined mass transport to/from the electrode, which is particularly important for reaction studies involving dissolved gases or other dilute reactants. Among others, this technique allows:

1. transient, time-resolved spectroelectrochemical measurements upon sudden exchange of the electrolyte under potential control;
2. spectroelectrochemical adsorption/stripping measurements of nonvolatile species;
3. modification of electrode surfaces by chemical or electrochemical adsorption/deposition in the flow cell prior to the actual measurements, which opens the way for a direct comparison of different surfaces.

Thus, this technique is of general relevance for kinetic and mechanistic spectroelectrochemical studies, by far exceeding applications in electrocatalysis.

The thin-layer spectroelectrochemical flow cell used in this study is analogous to that of a dual thin-layer flow cell design introduced recently,[11,12] which was modified for the present measurements. It consists of a circular Kel-F plate with openings for inlet and outlet capillaries, counter- and reference electrodes, and a hemicylindrical silicon prism, which is pressed against the Kel-F plate through a circular gasket and a Cu foil current collector (Kel-F = poly(chlorotrifluoroethylene)). A thin Pt film deposited on the flat reflecting side of the Si prism serves as the working electrode.[5] The electrolyte flow through the cell can be switched between different electrolytes.

The interaction of formic acid with Pt electrodes at potentials below oxide formation leads to the build-up of an adsorbate layer, whose chemical nature/composition depends critically on the electrode potential.[9] The accumulation of the adsorbed species was monitored in potentiostatic, transient experiments under continuous electrolyte flow, changing from pure base electrolyte (0.5 M H_2SO_4) to formic acid containing electrolyte (0.5 M H_2SO_4 + 0.1 M HCOOH, $t = 0$–4.5 min); after reaching steady-state conditions ($t = 4.5$ min), the current electrolyte was changed back to pure base electrolyte (adsorption/oxidation potential 0.4, 0.5, and 0.6). The nature of the adsorbed species is evident from the sequence of IR spectra in Figure 1, which were taken during

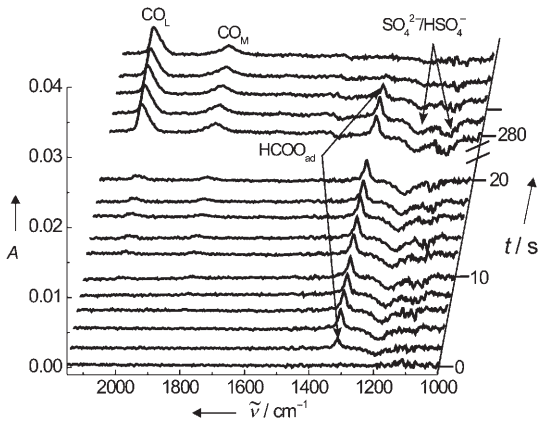


Figure 1. Selected IR spectra recorded during adsorption/oxidation of formic acid on a Pt thin film electrode at 0.5 V. Electrolyte exchange at $t = 0$ s from 0.5 M H_2SO_4 to 0.1 M HCOOH + 0.5 M H_2SO_4 and back after ≈4.5 min (270 s). Electrolyte flow rate: 50 μL s^{-1}, cell volume: 10–20 μL.

these transient experiments at a constant potential of 0.5 V. Characteristic features of these spectra are three positive bands, one with a signal at $\tilde{\nu} \approx 1322$ cm^{-1}, which was attributed to bridge-bonded adsorbed formate ($HCOO_{ad}$),[10,13] and two peaks centered at $\tilde{\nu} \approx 2010$ and 1790 cm^{-1}, which are related to linearly bonded (CO_L) and multiply bonded (CO_M) adsorbed CO (CO_{ad}). In addition, the spectra exhibit a two negative bands in the region $\tilde{\nu} = 1000$–1250 cm^{-1}, which correspond to displaced bisulfate and sulfate.[2] The presence of significant amounts of other adsorbates can be excluded based on the IR data. Spectra taken at 0.4 and 0.6 V exhibit similar characteristics as those above.

More quantitative information on the build-up of the adsorbate layer and on the relationship between adsorbate coverage and the Faraday reaction current is derived from the current densities in the chronoamperometric transients (Figure 2a) and from the integrated intensities of the IR signals as a function of time at the different adsorption potentials (Figures 2b–d). The current densities increase steeply when switching from the supporting electrolyte to HCOOH-containing solution ($t = 0$), reaching a maximum after approximately 3 s, and then decrease slowly with time under a continuous flow of HCOOH-containing electrolyte. When changing back to pure supporting electrolyte after about 4.5 min, they instantaneously drop to 0.

In contrast to the steep increase of the current densities, the intensities of the signals for adsorbed CO_L (Figure 2b) and CO_M (Figure 2c) develop slowly upon changing to 0.1 M HCOOH containing solution over the entire adsorption time (4.5 min). Both the final CO_{ad} coverage and the initial rate for CO_{ad} formation are highest for adsorption at 0.4 V, lower at 0.5 V, and very low at 0.6 V. When the electrolyte is switched

 © 2006 Wiley-VCH Verlag GmbH & Co. KGaA, Weinheim

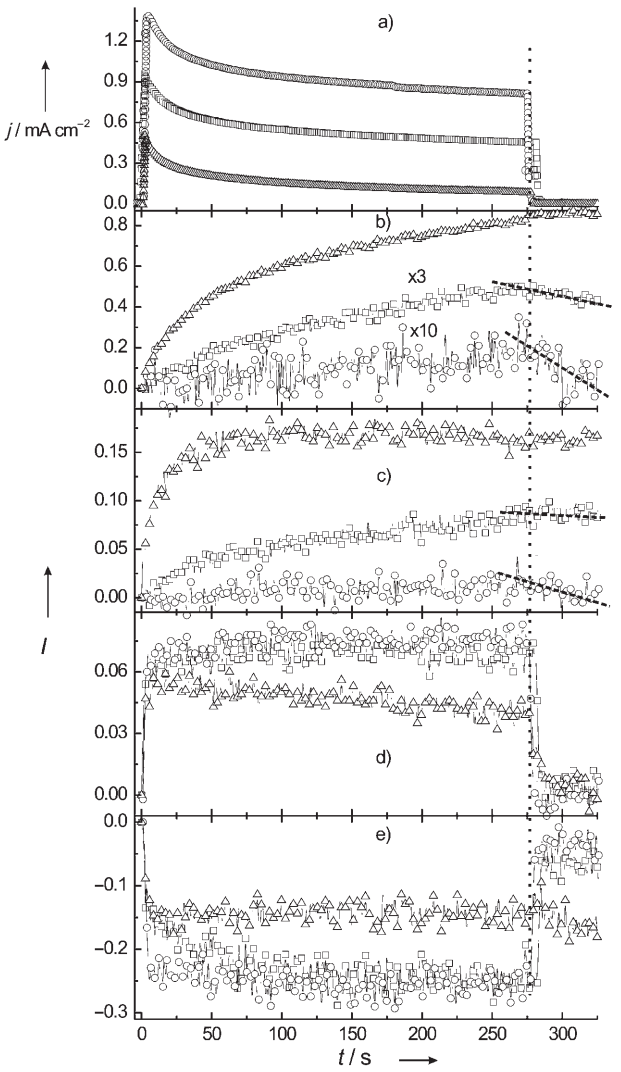


Figure 2. Chronoamperometric transients (a) and evolution of the IR peak intensities related to adsorbed CO_L (b) and CO_M species (c) as well as to adsorbed formate (d) and bisulfate and sulphate (e) during the interaction of formic acid with the Pt thin film electrode at 0.4 (△), 0.5 (□) and 0.6 V (○) (experimental conditions see Figure 1).

back to HCOOH-free solution, the intensities of the CO_{ad} signals (Figure 2b) decrease only slowly, as expected from the slow kinetics of CO_{ad} electrooxidation at potentials of 0.6 V and below. The $HCOO_{ad}$-related intensities (Figure 2d) show an abrupt increase when switching to HCOOH-containing solution and reach an approximately constant value approximately 3 s after the electrolyte exchange. For adsorption at 0.4 V we find a slight subsequent decay of the formate band intensity with time, probably owing to formate replacement by CO_{ad}. Formate formation is accompanied by a decrease in the bisulfate and sulfate band intensity (Figure 2e), which approximately mirrors the temporal evolution of the formate intensity (Figure 2d), implying that sulfate/hydrogen sulfate is displaced by more strongly adsorbed formate species.

Similar to the current density, the formate intensity drops instantaneously to 0 when changing back to pure supporting electrolyte, accompanied by a similarly fast increase in the bisulfate and sulfate intensity. Only at 0.4 V does the bisulfate and sulfate intensity remain virtually constant, despite the abrupt decay in formate intensity. This is tentatively explained by a combination of two effects: We expect that formate is randomly distributed in the CO adlayer and that at the high CO_{ad} coverage a relaxation of the CO adlayer is energetically more feasible than adsorption of the large and weakly adsorbed sulfate anions.

The above results clearly show that oxidation of formic acid is accompanied by the formation of adsorbed formate, in agreement with findings in a previous study,[10] and that under the present reaction conditions the build-up of these formate species is much faster than the formation of CO_{ad}. Hence, the rate of formic acid dehydrogenation/$HCOO_{ad}$ formation (in this term we also include contributions from adsorption of formate anions from the electrolyte) is much higher than that for formic acid dehydration (CO_{ad} formation) under the present reaction conditions.

The reaction rates for the dehydration of formic acid to CO_{ad} and subsequent oxidation of CO_{ad} can be determined quantitatively from the IR data by using the relationship between the CO_{ad} coverage and the IR intensities for the CO_M species at low CO_{ad} coverages and the CO_L-related intensity in the medium CO_{ad}-coverage regime, which were determined in calibration measurements (see Supporting Information). The CO_{ad} oxidation rate under steady-state conditions is determined from the initial slope of the CO_{ad} intensity–time curve, right after changing back from a HCOOH-containing solution (1M) to HCOOH-free electrolyte (Figure 2b), assuming that the CO_L/CO_M population ratios do not vary significantly between 0.4 and 0.6 V.[14] For clarity, we magnified the intensities of the CO_L species at 0.5 V (squares) by a factor of 3 and at 0.6 V (circles) by a factor of 10. We used a saturation coverage of 0.7 monolayers (ML) toe calculate turnover frequencies (TOFs) of 6.4×10^{-5} and 3.3×10^{-4} molecules per Pt site per second for CO_{ad} oxidation to CO_2 at 0.5 and 0.6 V, respectively, under the present steady-state reaction conditions. At 0.4 V the rate for CO_{ad} oxidation is below our detection limit (Table 1). The increase in CO_{ad} oxidation rate with potential agrees with the common explanation of enhanced OH_{ad} formation at higher potentials ("electrochemical activation").

In the same way we can determine the initial rates for CO_{ad} formation (HCOOH dehydration) on the initial, CO_{ad}- and $HCOO_{ad}$-free Pt surface from the initial slopes of the CO_{ad} intensity profiles, after switching from base electrolyte

Table 1: Turnover frequencies (TOF).[a]

Reaction	TOF [molecules s^{-1} $site^{-1}$]		
	0.4 V	0.5 V	0.6 V
HCOOH dehydration[b]	2.0×10^{-2}	1.8×10^{-3}	3.2×10^{-4}
CO_{ad} oxidation[c]	≈0	6.4×10^{-5}	3.3×10^{-4}
total HCOOH oxidation[d]	0.3	1.4	2.5

[a] TOF for [b] formic acid dehydration to CO_{ad} on a clean Pt surface (in the limit of very small CO_{ad} and OH_{ad} coverages), [c] CO_{ad} oxidation to CO_2 (steady state), [d] total oxidation of formic acid to CO_2 under steady state conditions, determined after 4.5 min under continuous flow of 0.1 M HCOOH + 0.5 M H_2SO_4 at different reaction potentials.

 © 2006 Wiley-VCH Verlag GmbH & Co. KGaA, Weinheim

to HCOOH-containing solution. This yields values of 2.0×10^{-2}, 1.8×10^{-3}, and 3.2×10^{-4} molecules per Pt site per second for turnover frequencies of 0.4, 0.5, and 0.6 V, respectively (Table 1).

In the later stages of the adsorption process the increase in CO_{ad} coverage represents the difference between CO_{ad} formation (formic acid dehydration) and CO_{ad} oxidation; under steady-state conditions the two rates are equal. At 0.6 V the rates for CO_{ad} oxidation (on a partly CO_{ad}-covered Pt surface) and formic acid dehydration (on a bare Pt surface) are of comparable magnitude, which explains the rather low steady-state CO_{ad} coverage detected at this potential. At 0.4 V the CO_{ad} oxidation rate is negligible, resulting in the observed pronounced accumulation of CO_{ad} with time up to saturation. The absolute values of the initial dehydration rates as well as the fact that at 0.4 V the initial rate for formic acid dehydration is about (more than) one order of magnitude higher than at 0.5 V (0.6 V) agree well with results derived by Sun from electrochemical transients.[3]

The relative contribution of the indirect reaction pathway to the total rate of oxidation of formic acid to CO_2 under the present steady-state conditions can be calculated from the ratio of the rate for oxidation of CO_{ad} determined above and the Faraday current under these conditions by using the values obtained from the chronoamperometric transients (Figure 2a) after oxidation of formic acid for 4.5 min (Table 1). Comparing the TOFs of 0.28, 1.4, and 2.5 molecules per Pt site per second for the oxidation of formic acid to CO_2 at potentials of 0.4, 0.5, and 0.6 V, respectively, and the above turnover frequencies for CO_{ad} oxidation at these potentials, we conclude that the indirect pathway, through dehydration of a $HCOOH_{ad}$ precursor to CO_{ad} and its further oxidation to CO_2, contributes less than 0.1% to the total rate of the oxidation of formic acid at 0.5 V and less than 0.01% at 0.6 V.

Interestingly, the ratio of the formate band intensities at the end of the HCOOH oxidation period at different potentials (Figure 2d) differs significantly from that of the Faraday currents (Figure 2a): 90% (0.5 V) and 50% (0.4 V) of the formate intensity at 0.6 V result in Faradaic currents of 55% (0.5 V) and ≈10% (0.4 V) of the value at 0.6 V, respectively. Since the dehydration pathway does not contribute significantly under these conditions, this observation requires either a potential-dependent variation (electrochemical activation) of both adsorbed formate formation and its oxidation to CO_2, or the existence of another, third reaction pathway. For more information on this point we performed similar transient oxidation measurements as in Figure 2 at the same potential (0.6 V), using two different formic acid concentrations.

Representative results are shown in Figure 3. Comparing the Faraday currents for the oxidation of 0.7 mM and 70 mM HCOOH solution at 0.6 V, we find current densities of 0.045 mA cm^{-2} and 0.85 mA cm^{-2}, respectively, after 100 s, that is, roughly a factor of 20 between the two electrolytes. The IR spectra acquired at $t=100$ s, in contrast, show that the respective formate intensities differ only by about a factor of 5. Hence, even at similar reaction potential the total steady-state rates for HCOOH oxidation are not at all proportional to the respective formate coverages. Based on the negligible

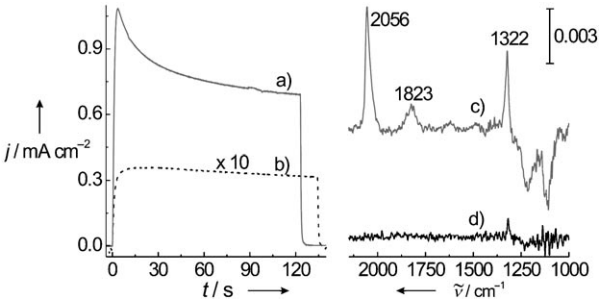


Figure 3. Chronoamperometric transients (a, b) and IR spectra of adsorbed formate (c, d) on a Pt thin film electrode at 0.6 V in a solution containing 70 mM (a, c) and 0.7 mM HCOOH (b, d). The spectra were acquired 100 s after changing to HCOOH-containing solution.

contribution of the indirect pathway under these conditions and assuming that the rate of formate decomposition is related linearly to formate coverage, these data clearly indicate that there must be a third reaction pathway.

Its contribution to the total reaction rate cannot be calculated precisely from these data, but we can estimate a higher limit for its contribution. Assuming that for 0.7 mM HCOOH solution the Faraday current results completely from the formate pathway, the fivefold-higher formate-band intensity in 70 mM HCOOH solution should at most result in a fivefold-higher current density. The experimentally observed increase by a factor of 20 is only possible if the reaction pathway via the adsorbed formate species detected by IR and dominating the formate IR signal ("formate pathway") contributes less than 25% to the total anodic current.

Although our IR spectra do not give any indication of another adsorbed species, this third pathway is dominant for room-temperature oxidation of a 0.1M formic acid solution. This can either be explained by an additional, thus far not detected adsorbed reaction intermediate, whose concentration is very low (low lifetime under reaction conditions), or by a direct reaction of weakly adsorbed $HCOOH_{ad}$ species. (The theoretical possibility of a flat-lying formate species with a very low IR cross-section is ruled out as considerable substrate–adsorbate bonding would be necessary for a stable reaction intermediate.)

We favor the latter explanation and propose a triple path mechanism; which starts with a weakly adsorbed $HCOOH_{ad}$ precursor that can subsequently either be directly oxidized to CO_2 (direct pathway), undergo dehydration to CO_{ad} ("indirect pathway"), or is dehydrogenated to stable bridge-bonded adsorbed formates (formate pathway), as it is schematically depicted in Figure 4. The stable, adsorbed intermediates resulting in the last two pathways can then, in a third step, be oxidized to CO_2. In this scheme adsorbed formates are indeed reaction intermediates, but, in contrast to recent concepts,[13] are not in the dominant reaction pathway.

In summary, we have 1) significantly improved the capability of in situ ATR-FTIRS measurements by combining this technique with a thin-layer flow cell, which allows mechanistic and quantitative spectroelectrochemical kinetic studies of electrocatalytic reactions under well-defined mass-

 © 2006 Wiley-VCH Verlag GmbH & Co. KGaA, Weinheim

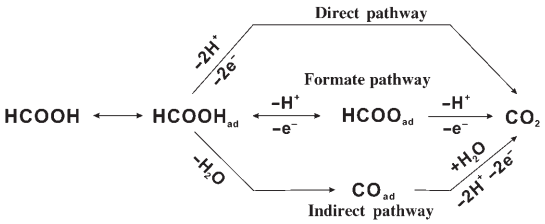


Figure 4. Tentative reaction scheme for the oxidation of formic acid on Pt which includes three different reaction pathways: the "indirect" pathway, the "formate pathway", and the "direct" pathway. The formate pathway relates to the formate species detected by IR (see text).

transport conditions, and 2) demonstrated the potential of this setup for studies of electrocatalytic reactions by measurements of the electrooxidation of formic acid on a Pt film electrode in acidic solution at constant potentials between 0.4 and 0.6 V. These measurements allowed us to quantify the contributions of the different pathways proposed previously and to provide clear proof that under the present reaction conditions both pathways are minor. Direct oxidation of weakly adsorbed $HCOOH_{ad}$ species to CO_2 is proposed to be the dominant reaction pathway.

Experimental Section

The electrolyte solutions were prepared by using p.a. grade formic acid, suprapure H_2SO_4 (Merck), and Millipore water (18.2 MΩ). They were de-aerated with highly pure Ar gas (6.0) for 20 min before each experiment. The Pt working electrode (exposed area ≈ 1 cm^2, surface roughness factor ≈ 10) was prepared by electroless Pt deposition on the Si prism, by following a procedure described in reference [10]; a Pt foil and a reversible hydrogen electrode (RHE) served as counter- and reference electrodes. All experiments were performed at room temperature. IR spectra were measured on a BioRad FTIR-6000 spectrometer equipped with a MCT detector (4-cm^{-1} resolution, coaddition of five interferograms for each spectrum (≈ 1 s per spectrum). The intensities are given by the absorbance, defined by $\log(R_0/R)$, where R_0 and R are the reflectance at the reference and sample potential, respectively. For background subtraction we used a spectrum recorded at the same potential in pure base electrolyte. This data processing results in spectra in which peaks pointing up reflect an increased absorption and peaks pointing down a loss of absorption.

Received: June 21, 2005
Revised: September 27, 2005
Published online: December 22, 2005

Keywords: electrochemistry · flow cell · IR spectroscopy · spectroelectrochemistry · time-resolved spectroscopy

[1] B. Beden, J. M. Leger, C. Lamy, *Modern Aspects of Electrochemistry* (Eds.: B. Beden, J. M. Leger, C. Lamy, J. O. Bockris, B. E. Conway, R. E. White), Plenum, New York, **1992**, p. 97.
[2] T. Iwasita, F. C. Nart, *Prog. Surf. Sci.* **1997**, *55*, 271–340, and references therein.
[3] S.-G. Sun in *Electrocatalysis* (Eds.: J. Lipkowski, P. N. Ross), Wiley-VCH, New York, **1998**, pp. 243–290.
[4] N. J. Harrick, *Internal Reflection Spectroscopy*, Harrick Scientific Products, Ossining, **1967**.
[5] M. Osawa, *Handbook of Vibrational Spectroscopy*, Wiley, Chichester, **2002**, pp. 785–799.
[6] W.-F. Lin, J.-T. Wang, R. F. Savinell, *J. Electrochem. Soc.* **1997**, *144*, 1917–1922.
[7] C. Rice, S. Ha, R. I. Masel, A. Wieckowski, *J. Power Sources* **2003**, *115*, 229–235.
[8] A. Capon, R. Parsons, *J. Electroanal. Chem.* **1973**, *45*, 205–231.
[9] O. Wolter, J. Willsau, J. Heitbaum, *J. Electrochem. Soc.* **1985**, *132*, 1635–1638.
[10] A. Miki, S. Ye, M. Osawa, *Chem. Commun.* **2002**, 1500–1502.
[11] Z. Jusys, H. Massong, H. Baltruschat, *J. Electrochem. Soc.* **1999**, *146*, 1093–1098.
[12] Z. Jusys, J. Kaiser, R. J. Behm, *Phys. Chem. Chem. Phys.* **2001**, *3*, 4650–4660.
[13] M. R. Columbia, A. M. Crabtree, P. A. Thiel, *J. Am. Chem. Soc.* **1992**, *114*, 1231–1237.
[14] S. C. Chang, M. J. Weaver, *J. Chem. Phys.* **1990**, *92*, 4582–4594.

 © 2006 Wiley-VCH Verlag GmbH & Co. KGaA, Weinheim

Protein Binding

DOI: 10.1002/anie.200502302

A Simple Protocol To Estimate Differences in Protein Binding Affinity for Enantiomers without Prior Resolution of Racemates

*Jasmine Fokkens and Gerhard Klebe**

In the early steps of preclinical drug discovery, putative drug candidates are synthesized and screened for activity against a particular target. Usually, diastereomerically pure compounds are tested, but as the resolution of racemic mixtures into pure enantiomers involves substantial analytical efforts, racemic mixtures are often used in the primary screening. Once biological activity has been detected for a racemate, the question arises as to whether only one or both enantiomeric forms contribute to the activity. Either one enantiomer shows no binding, and can be regarded as isomeric ballast, or both isomers bind significantly, though not necessarily equally.[1–5] Which situation prevails depends strongly on the mode of action and the adopted binding geometry of the enantiomers. Drug optimization by rational concepts depends on the correct correlation of stereochemistry with biological activity. Accordingly, as a prerequisite to any further optimization, the frequently tedious and elaborate process of chiral resolution has to be performed. Thus, simple protocols are needed to determine the differential binding affinity of enantiomers, ideally without requiring resolution of a racemic mixture for the initial tests. Herein, we report such a method.

Isothermal titration calorimetry (ITC)[6,7] is a versatile technique to determine the dissociation constants for the

[*] Dr. J. Fokkens, Prof. G. Klebe
Institut für Pharmazeutische Chemie
Philipps-Universität Marburg
Marbacher Weg 6, 35032 Marburg (Germany)
Fax: (+49) 6421-282-8994
E-mail: klebe@mailer.uni-marburg.de

© 2006 Wiley-VCH Verlag GmbH & Co. KGaA, Weinheim

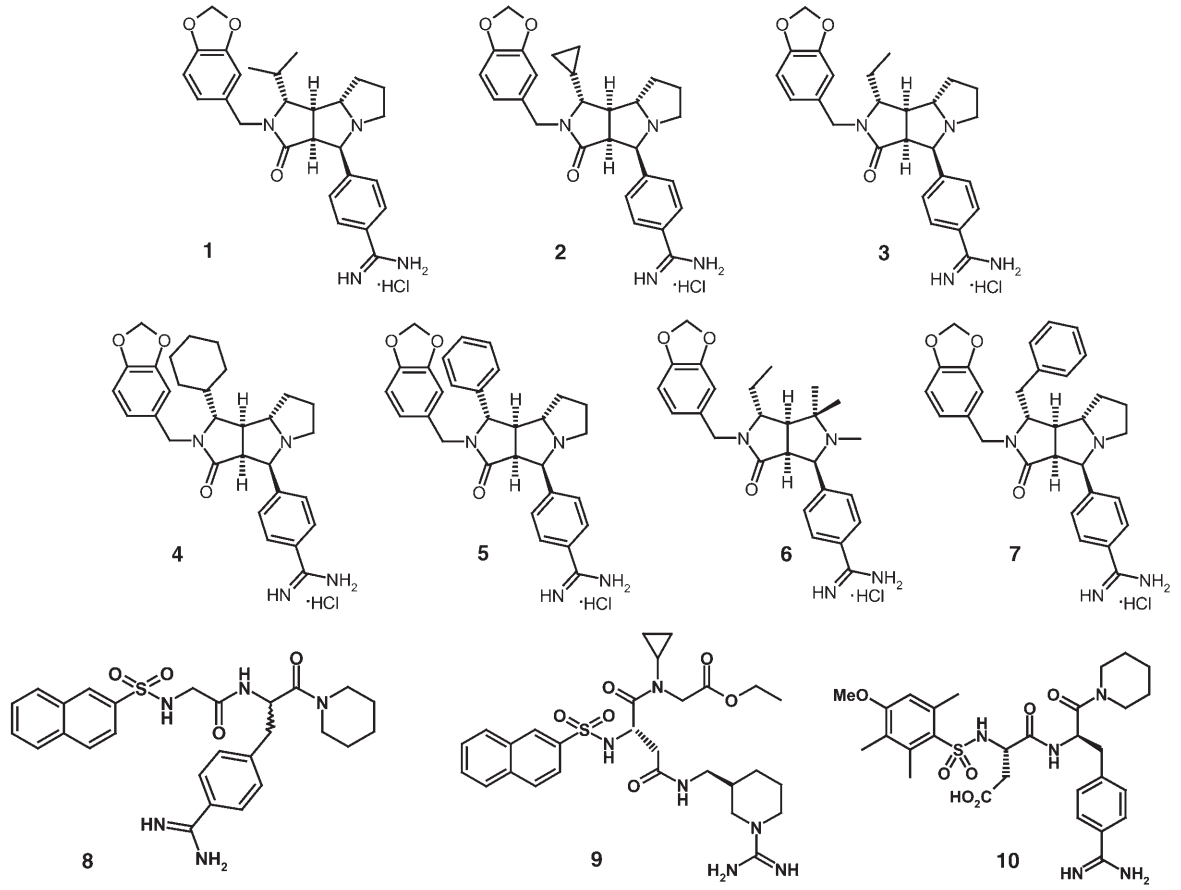
binding of small-molecule ligands to proteins. In this method, a buffered solution of a ligand is titrated into that of a target protein. The binding of the ligand to the protein results in the absorption or production of heat, which can be quantitatively recorded. The protein is gradually saturated by the bound ligand as the concentration of the ligand in the protein solution increases. This saturation can be measured as a standard titration curve and its slope relates to the binding constant (or to its inverse the dissociation constant) of the ligand.

We have studied racemic mixtures of a series of serine protease inhibitors **1**–**7** with respect to their binding to trypsin and thrombin (Scheme 1).The crystal structures of several derivatives of these enzymes were determined. Even though solutions of the racemates were used for crystallization, the difference electron density map gave clear evidence that, in all structures, only one enantiomer had bound, which is most likely the one with the higher potency. In a previous study, Obst et al.[8–10] succeeded in resolving the enantiomers of **1** and determined their protein-binding constants by a photometric assay (Table 1). Interestingly, (+)-**1** is more potent by a factor of 800 than (−)-**1** towards thrombin, whereas (+)-**1** is only 22 times stronger in binding to trypsin relative to its optical antipode (Table 1). Binding data for all the other derivatives in the series are available only for the racemic mixtures. The chiral resolution of *rac*-**1** was performed at the stage of an intermediate during the synthesis and the procedure required substantial effort.[8,9] In view of the affinities of (+)-/(−)-**1**, it is interesting to note that for both enzymes only the more potent (+) enantiomer is accommodated in the crystal structure. For the purpose of optimization, it is highly desirable to know also the enantioselectivity of the

Table 1: Binding constants of **1**–**10** to trypsin and thrombin determined by a photometric assay.[a]

Ligand	Binding constant		Selectivity
	Trypsin K_i [nM]	Thrombin K_i [nM]	K_i (trypsin)/ K_i (thrombin)
rac-**1**	9900	13	760
(+)-**1**	5500	7	785
(−)-**1**	120000	5600	21
rac-**2**	2300	10	230
rac-**3**	1680	8	210
rac-**4**	4420	1700	2.6
rac-**5**	5040	1400	3.6
rac-**6**	7315	95	77
rac-**7**	7700	1100	7
rac-**8**	690		
D-**8**	230		
L-**8**	35000		
9	30000		
10	400		

[a] K_i = [enzyme][ligand]/[enzyme·ligand].



Scheme 1. Chemical formulas of the derivatives **1**–**7** studied by isothermal titration calorimetry and crystallography. The ligands D-, L-, and *rac*-Napap (**8**), napsagatran ethyl ester (**9**), and CRC220 (**10**) were also studied for validation purposes. Note: Only the more-strongly binding isomer is shown for **1**–**7**, **9**, and **10**. This is know to be the (+) isomer for **1**, and similar behavior can be assumed for **2**–**7**.

 © 2006 Wiley-VCH Verlag GmbH & Co. KGaA, Weinheim

other members of the compound series. We performed isothermal titration calorimetry on racemic mixtures of these compounds. In some cases there was clear evidence for two-step titration curves (Figure 1). Closer inspection of the other plots, which at first glance suggested single binding events, revealed a small shoulder at either the onset or the end of the titration curve, which also suggests a two-step binding process. We interpret these deviations from a single-sigmoidal curve as indicating subsequent or competitive binding of both enantiomers to the protein. The actual form of the titration curve depends on the difference in affinity of the enantiomers towards the macromolecular receptor.

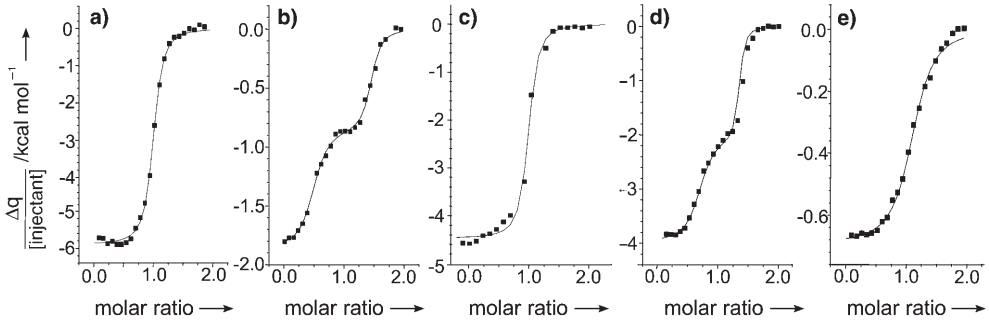


Figure 1. Titrations of trypsin and thrombin with the enantiopure and racematic ligands: a) titration of trypsin with D-Napap (**8**); a simple one-step sigmoidal curve is observed. The curve for the titration with the L enantiomer has a very similar shape, but with reduced slope (data not shown); b) titration of trypsin with *rac*-Napap (**8**); a two-step titration curve composed of two sigmoidal portions is observed; c) titration of thrombin with *rac*-**1**; the enantiomers differ in affinity by a factor 800; accordingly, a two-step titration curve is only indicated at the onset of the experiment; d) titration of thrombin with *rac*-**2**; a distinct two-step curve is observed, which suggests a difference in the affinity of both enantiomers towards thrombin on the order of about 100-fold; e) titration of trypsin with *rac*-**1**; both enantiomers bind to trypsin with a 22-fold difference in affinity; accordingly, the splitting into two steps is only indicated at the end of the curve.

The following binding model is assumed: The racemic mixture is titrated into the protein. As long as a 1:1 stochiometry of the racemate with respect to the protein is not yet obtained, each added ligand molecule finds an uncomplexed binding site. Two mutually competitive equilibria will evolve and the actual association/dissociation rates depend on the affinities of both enantiomers towards the protein. Thus, the stronger binding enantiomer remains on average bound for longer time, while the weaker binding enantiomer undergoes faster exchange. Accordingly, at the beginning of the experiment, the shape of the titration curve is determined by the average of the association/dissociation constants for the racemate. Its value determines the steepness of the titration curve. Once a 1:1 stoichiometry in the protein solution has been reached, the more-strongly binding enantiomer will replace the more-weakly binding enantiomer in a stepwise fashion until the protein is virtually saturated with the more-strongly binding enantiomer, and the titration curve adopts sigmoidal saturation character. If the affinity difference between both isomers is not too great, the more-strongly binding enantiomer has to accumulate in solution to some degree to detectably replace the weaker-binding enantiomer. As a consequence, the titration curve levels off to some degree in the central part. The shape of the second step of the titration curve is determined mainly by the binding constant of the more-strongly binding enantiomer replacing the more-weakly binding one. In this way, the titration resembles the technique that is frequently used to measure strong binding ligands by preincubating the target protein with a weaker binding ligand.[11] However, it must be remembered that in the titration with the racemate, the concentration of the weaker-binding ligand is also continuously increased in the course of the titration. This complicates the intertwined association/dissociation equilibria.

To test this model, we titrated trypsin with the racemate and the separated enantiomers of Napap (**8**). According to previously reported kinetic data, the binding constants of the two enantiomers differ by a factor of 152 (D-Napap: $K_i = 0.23\ \mu M$, L-Napap: $K_i = 35\ \mu M$, *rac*-Napap: $K_i = 0.69\ \mu M$).[12,13] Titration of the individual enantiomers revealed K_d values ($1/K_i$) for D-Napap, L-Napap, and *rac*-Napap of $43.9 \pm 4.4 \times 10^{+5}\ M^{-1}$, $0.2 \pm 0.1 \times 10^{+5}\ M^{-1}$, and $14.5 \times 10^5\ M^{-1}$, respectively. ITC studies on the racemate gave K_d values of $12.4 \pm 2.1 \times 10^{+5}\ M^{-1}$ for the first step and $40.57 \pm 13.8 \times 10^5\ M^{-1}$ for the second step.[14] These results are in good agreement with the assumption that the first step of the titration curve approximates the average binding constant of the racemate, whereas the second step reflects that of the stronger-binding isomer. As a second case study, we titrated a 1:1 mixture of enantiopure napsagatran ethyl ester (**9**)[15] and CRC220 (**10**)[16] into trypsin. They possess a 73-fold difference in affinity.[17] Titrations were also performed on the individual components. The mixture again displayed a two-step titration curve and separate evaluation of the individual binding events[14] gave binding constants in good agreement with the average value for either the mixture or the stronger-binding CRC220.

Of the series **1**–**7**, we observed two-step curves for the titrations of rac-**2**, **3**, and **6** with thrombin. A shape composed of two well-separated sigmoidal portions indicates a difference in binding constant in the range of approximately 50 to 200.[18] The titration of thrombin with rac-**1** indicates a slight distortion at the beginning of the titration curve (Figure 1), which is in good agreement with the difference in the photometrically determined binding constant of 800.[10] The titrations of thrombin with *rac*-**4, 5**, and **7** as well as of trypsin with all of the racemic ligands show minor distortions from clean one-step sigmoidal behavior at the end of the titration (Figure 1). These results suggest that both enantiomers bind with similar affinity to the protein.

Can these findings be rationalized with respect to the crystallographically observed binding geometries of the (+) enantiomers with trypsin and thrombin?[19] Firstly, we

 © 2006 Wiley-VCH Verlag GmbH & Co. KGaA, Weinheim

consider the binding of these enantiomers. All the ligands differ in the size of their C1 substituents (Scheme 1 and Figure 2). This hydrophobic group has been introduced to accommodate the S2 pocket in thrombin, which is spatially restricted by the covering 60 loop (Figure 2b). In trypsin, this region of the binding pocket opens towards the solvent. Accordingly, the optimal filling of the S2 pocket by a ligand affords selectivity towards thrombin. This selectivity is observed for (+) enantiomers of **1**, **2**, **3**, and **6**, which bind tightly to thrombin and weakly to trypsin. Bulkier substituents at this position, as are present, for example, in **4**, **5**, and **7**, are detrimental to thrombin binding. These ligands evidently fit less favorably into the S2 pocket. The affinity of ligands for trypsin correlates only slightly with the shape of the substitutent at C1 (Table 1). This fact is easily explained by the very open, poorly structured binding pocket of trypsin in this region (Figure 2a).

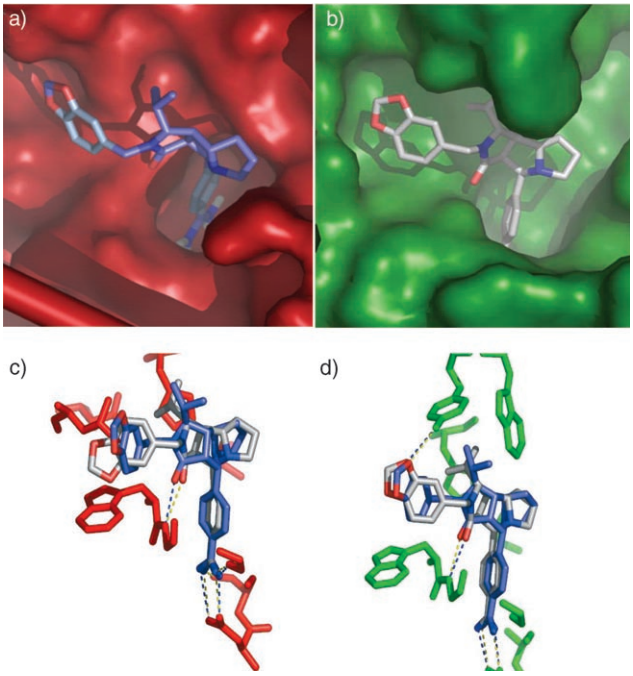


Figure 2. Binding modes in trypsin or thrombin determined by crystallography or molecular modeling studies: The crystal structure of (+)-**1** in trypsin (a) shows the S2 pocket next to the isopropyl substituent opening towards the solvent. Crystal structure of (+)-**1** in thrombin (b);[10] the isopropyl substituent is accommodated with ideal shape complementarity in the highly restricted thrombin S2 pocket, which is surrounded by the Trp60A and Trp60D groups of the 60 loop. Crystallographically determined binding modes of (+)-**1** (white) and modeled binding modes of (−)-**1** (blue) in the binding sites of trypsin (c) and thrombin (d). The (−) ligand adopts a very similar shape in both enzymes and identical binding modes can be assumed for both enantiomers. The isopropyl group is oriented towards the solvent in the rather-open S2 pocket of trypsin (c). In thrombin (d), the isopropyl group has optimal shape complementarity with the protein for (+)-**1** (white), whereas the accommodation appears less optimal for (−)-**1** (blue). Although one methyl group will fit next to the S2 groove, the other methyl group comes into close contact with the neighboring indole moiety of Trp60D. This steric crowding is most likely detrimental to ligand binding and results in an affinity loss by a factor of 800 compared with (+)-**1**.

Interestingly, all the (−) enantiomers in the present series bind with similar affinity to trypsin as their antipodes. The more-weakly binding (−)-**4**, (−)-**5**, and (−)-**7**, which have bulkier C1 substituents, also have similar binding affinity to thrombin as their (+) enantiomers. Thus, the only pronounced difference in affinity is observed for the binding of the individual enantiomers of **1**, **2**, **3**, and **6** to thrombin. Modeling studies show that inversion of the stereochemistry of **1**–**7** produces a geometry of the basic skeleton that can be easily accommodated in the binding pocket of both trypsin and thrombin (Figure 2c). With the exception of their C1 substituents, both enantiomers experience comparable contacts with the proteins. Trypsin exhibits an open binding pocket next to the C1 substituent, thus its binding is not affected by the orientation of this substituent. For similar reasons, the less optimally fitting, rather bulky C1 substituents in **4**, **5**, and **7** do not allow discrimination between both enantiomers in the binding to thrombin. However, significant discrimination between the enantiomers of **1**, **2**, **3**, and **6** with the smaller C1 substituents is observed (by a factor of 50 to 200 for **2**, **3**, and **6**; 800 for **1**). This discrimination is likely attributed to a pronounced shape complementarity with the thrombin S2 pocket, which is optimal for the isopropyl group in (+)-**1.** In case of (−)-**1**, the differently oriented isopropyl group fits less satisfactorily and is recognized by the protein comparably to the bulky groups in the (−) enantiomers of **4**, **5**, and **7**. The difference in affinity between the enantiomers of **2**, **3**, and **6** is less pronounced, presumably because the smaller cyclopropyl group in **2** and the conformationally flexible ethyl groups in **3** and **6** in the (−) enantiomers adapt better to the restricted volume of the S2 pocket in thrombin (Figure 2d).

This study presents a simple protocol in which isothermal titration calorimetry is used to estimate the difference in binding affinity of enantiomers to proteins without requiring prior resolution of the racemate. Any ligand binding that is detectable by ITC can be studied with this method. The sensitivity of ITC depends strongly on the heat signal produced,[18] which is related to the enthalpic portion of binding, the solubility of the binding partners, and the temperature chosen for the experiment. A difference of approximately 50–200 in the affinity of the enantiomers is required to observe a well-resolved two-step titration curve. If the enantiomers differ greatly (ca. 1000-fold) in affinity, a small shoulder is observed at the onset of a regular sigmoidal curve. If there is only a minor difference in binding affinity (< 50-fold), a shoulder is observed at the end of the titration curve. A series of derivatives has been used in this study to demonstrate that the differential binding of enantiomers to two related serine proteases can be attributed to differences in their structural fit. This fact explains how selectivity is determined and may guide further enhancements towards increased selectivity. Such stereochemical information is of utmost importance for ligand optimization in a drug-development program.

Received: July 1, 2005
Revised: September 2, 2005
Published online: December 22, 2005

 © 2006 Wiley-VCH Verlag GmbH & Co. KGaA, Weinheim

Keywords: calorimetry · drug design · enantioselectivity · ligand effects · protein structures

[1] A. H. Becket in *Progress in Drug Research, Vol. 1* (Ed.: E. Juaker), Birkhäuser, Basel, **1959**, pp. 455 – 530.
[2] P. S. Portoghese, *Annu. Rev. Pharmacol.* **1970**, *10*, 51 – 76.
[3] M. Simonyi, *Med. Res. Rev.* **1984**, *4*, 359 – 413.
[4] M. Eichelbaum, B. Testa, A. Somogyi, *Stereochemical Aspects of Drug Action and Disposition*, Springer, Berlin, **2003**.
[5] G. W. Mellin, M. Katzenstein, *New Engl. J. Med.* **1962**, *267*, 1184 – 1244.
[6] G. A. Holdgate, *Biotechniques* **2001**, *31*, 164 – 166.
[7] L. Indyk, H. F. Fisher, *Methods Enzymol.* **1998**, *295*, 350 – 364.
[8] U. Obst, P. Betschmann, C. Lerner, P. Seiler, F. Diederich, V. Gramlich, L. Weber, D. Banner, W. P. Schönholzer, *Helv. Chim. Acta* **2000**, *83*, 855 – 909.
[9] U. Obst, Dissertation (No. 12037), ETH Zurich (Switzerland), **1997**.
[10] U. Obst, D. Banner, L. Weber, F. Diederich, *Chem. Biol.* **1997**, *4*, 287 – 295.
[11] B. W. Sigurskjold, *Anal. Biochem.* **2000**, *277*, 260 – 266.
[12] A. Bergner, M. Bauer, H. Brandstetter, J. Stürzebecher, W. Bode, *J. Enzyme Inhib.* **1995**, *9*, 101 – 111.
[13] T. Steinmetzer, A. Schweinitz, S. Künzel, P. Wikström, J. Hauptmann, J. Stürzebecher, *J. Enzyme Inhib.* **2001**, *16*, 241 – 249.
[14] To analyze the two-step titration curve in terms of two separate single-step sigmoidal events, an artificial base line was added in the central part, and then routine evaluation of the titration curves was carried out.
[15] K. Hilpert, J. Ackermann, D. W. Banner, A. Gast, K. Gubernator, P. Hadvary, L. Labler, K. Müller, G. Schmid, T. B. Thschopp, H. van de Waterbeemd, *J. Med. Chem.* **1994**, *37*, 3889 – 3901.
[16] M. Reers, R. Koschinsky, G. Dickneite, D. Hoffmann, J. Czech, W. Stüber, *J. Enzyme Inhib.* **1995**, *9*, 61 – 72.
[17] F. Dullweber, M. T. Stubbs, J. Stürzebecher, D. Musil, G. Klebe, *J. Mol. Biol.* **2001**, *313*, 593 – 614.
[18] To our knowledge, a difference in K_d values of ca. 50–200 reveals well-resolved two-step titration curves. However, the intensity of a recorded ITC signal is determined by the absorbed or released heat, which correlates with the enthalpic contribution to the binding process. Only if the free energy of binding of both enantiomers factorizes similarly into enthalpic and entropic contributions such a straightforward correlation with the binding-constant difference will be possible. However, such similar behavior of both enantiomers is not necessarily the case.
[19] The crystal structures discussed herein are available from the Protein Data Bank (PDB) under the codes 1Y3U, 1Y3V, 1Y3W, 1Y3X, and 1Y3Y.

 © 2006 Wiley-VCH Verlag GmbH & Co. KGaA, Weinheim

Molecular Switch

DOI: 10.1002/anie.200502638

Vitamin B_{12}: A Methyl Group without a Job?**

*Philip Butler, Marc-Olivier Ebert, Andrzej Lyskowski, Karl Gruber, Christoph Kratky, and Bernhard Kräutler**

Dedicated to Professor Albert Eschenmoser on the occasion of his 80th birthday

The fascination with B_{12}-coenzymes, nature's "most beautiful" cofactors,[1] is a reflection of the uniqueness and complexity of their structure and chemistry.[2,3] B_{12} has also become a prominent testing ground for thoughts on the evolution of the catalytic moieties of essential cofactors.[4] According to Eschenmoser,[5] the corresponding corrin ligand may represent a further evolved form of the hypothetical B_{12} progenitor, "protocobyrinic acid". The attachment of methyl groups and the characteristic appendage of a nucleotide loop may have arisen from (nonenzymatic) adaptation and self-constitution, respectively.[4] Herein we report on norvitamin B_{12} (**1**, Co_β-cyano-5″,6″-dimethylbenzimidazolyl-176-norcobamide),[7] its organometallic analogue, methylnorcobalamin (**2**, Co_β-methyl-5″,6″-dimethylbenzimidazolyl-176-norcobamide), and on two B_{12} derivatives that lack the methyl group of the cobamide ligand at C176. Our studies were induced by the discovery of norpseudovitamin B_{12} (**3**, Scheme 1), the cyano-Co^{III} form of the cofactor of perchloroethylene reductase from *Sulfurospirillum multivorans*,[8] a natural "complete" B_{12} cofactor that lacks the methyl group at C176.

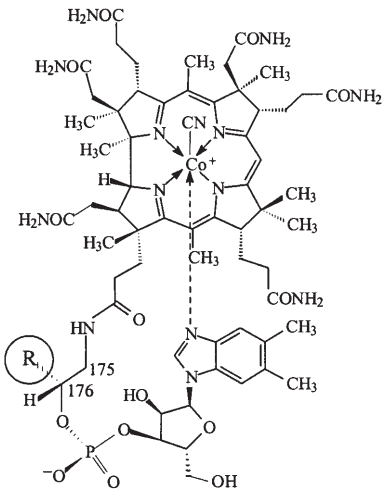
Norvitamin B_{12} (**1**) was prepared according to methods developed previously for the partial synthesis of vitamin B_{12} (**4**)[7,9,10] and was obtained in 73% yield through the condensation of cobyric acid (**7**) (from hydrolysis of **4**[7,11]) with (2-aminoethyl)-3′-(α-ribazolyl)diphosphate (**8**) and crystal-

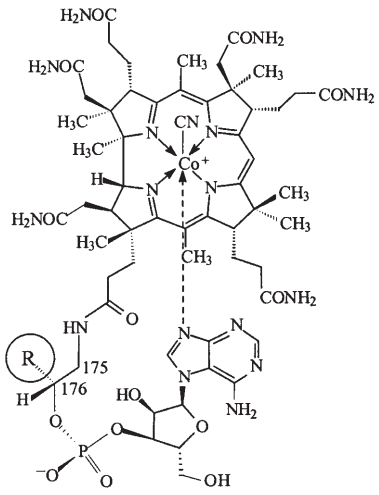
[*] Dr. P. Butler, Dr. M.-O. Ebert, Prof. Dr. B. Kräutler
Institute of Organic Chemistry
Innrain 52a
and
Center for Molecular Biosciences
Leopold-Franzens-Universität Innsbruck
6020 Innsbruck (Austria)
Fax: (+43) 512-507-2892
E-mail: bernhard.kraeutler@uibk.ac.at
A. Lyskowski, Prof. Dr. K. Gruber, Prof. Dr. C. Kratky
Institute of Chemistry
Karl-Franzens-Universität Graz
Heinrichstraße 28, 8010 Graz (Austria)

[**] We thank K.-H. Ongania for measuring FAB mass spectra. We are grateful to Hoffmann-LaRoche for a gift of vitamin B_{12}. The project was supported by grants from the European Commission (Proj. No. HPRN-CT-2002-00195), the Austrian National Science Foundation (FWF, projects P-13595 and P-17132). X-ray diffraction data were collected at the EMBL beamline BW7b at DESY in Hamburg (Germany).

Supporting information for this article is available on the WWW under http://www.angewandte.org or from the author.

 © 2006 Wiley-VCH Verlag GmbH & Co. KGaA, Weinheim





Scheme 1. Structural formulas of complete base-on corrinoids. Top: norvitamin B_{12} (**1**, R = H), vitamin B_{12} (**4**, R = CH_3). Bottom: norpseudovitamin B_{12} (**3**, R = H), pseudovitamin B_{12} (**6**, R = CH_3).

lized from aqueous acetone (see Scheme 2). The chromatographic behavior of **1** is similar to that of its homologue **4** and the UV/Vis spectroscopic data is practically indistinguishable. Fast-atom-bombardment (FAB) mass spectra exhibited a pseudomolecular ion at *m*/*z* 1341, that is, at 14 mass units less than that of **4**. Similarly, the ^{1}H and ^{13}C NMR spectroscopic chemical-shift values[12] indicate the absence of the methyl group at C176. Comparison of the NMR spectroscopic data of **4**[13,14] with the spectra of **1** shows only the expected local-substituent effects of a methyl group on the chemical-shift values (see the Experimental Section[15] and the Supporting Information).

Crystals of **1** were grown from aqueous acetone and the structure of **1** was determined at 0.85-Å resolution by using synchrotron radiation (Figure 1).[15] The resultant structure is very similar to that of **4**.[16] A slightly longer Co–N bond from the cobalt ion to the lower axial base in **1** (2.047(5) Å compared with 2.011(10) Å in **4**), a small increase in the base tilt angle (the difference of the angles Co–N3N–C9N and Co–N3N–C2N) of 11.6(0.6)° in **1** (compared with 9.7(1.1)° in **4**), and a small decrease in the corrin fold angle from 18.0(0.3)° in **4** to 15.8(0.1)° in **1** are all consistent with rather similar mechanochemical and steric effects of the nucleotide function in **1** and **4**.[17] Minor differences between the two structures are seen only in the region around the ethanolamine linker and the phosphate and ribose moieties of the nucleotide loop. With the exception of the orientation of the amide group of side chain a, even the conformations of the amide side chains are virtually identical between **1** and **4**.

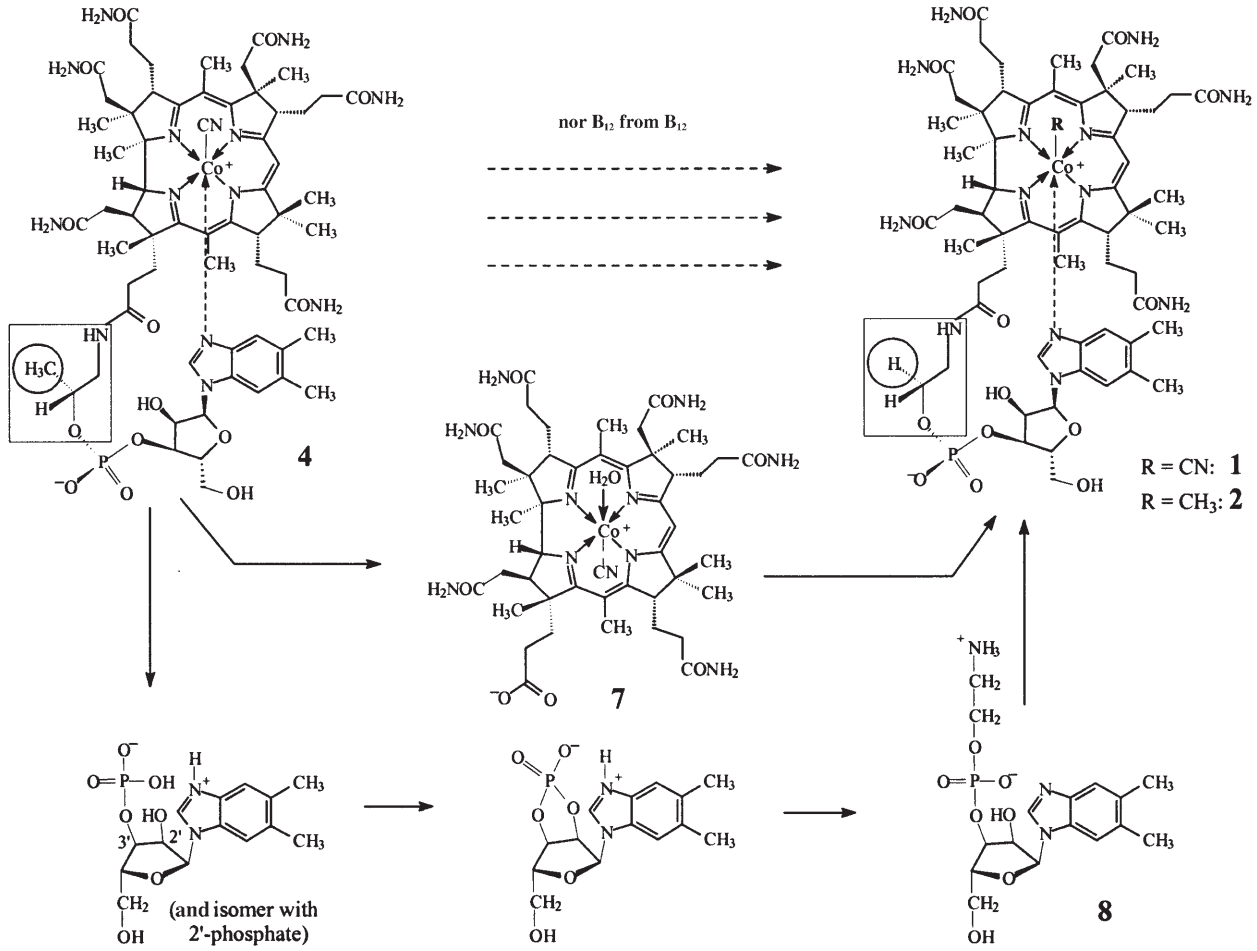
Crystalline **2** was prepared from **4** in situ by methylation of electrochemically produced norcob(ı)alamin (**9**)[18] with methyltoluenesulfonate in 80% yield. The UV/Vis spectrum of **2** is practically indistinguishable from that of the homologue, methylcobalamin (**5**). The FAB mass spectra of **2** exhibits a pseudomolecular ion at *m*/*z* 1330, that is, at 14 mass units less than that of **5**. Likewise, the absence of the methyl group at C176 is clearly indicated from comparison of the values of the ^{1}H and ^{13}C NMR spectroscopic chemical shifts[12] of **2** with those of **5**[13,19] (see the Experimental Section and the Supporting Information). Again, aside from the expected local-substituent effects of the methyl group on the chemical shift-values in the NMR spectra, there are no other significant differences.

The effect of the methyl group on the conformational properties of **4** and **5** could not be derived from the spectral data or from the crystal structure of **1**. Indeed, in the structure of **4** and in that of pseudovitamin B_{12} (**6**),[8] the methyl group at C176 occupies an uncrowded place, antiperiplanar to N174 and anticlinal to the P atom of the phosphate linker (it also occupies the place of H_{proR}(176) of **1**) (Figure 2). The methyl group at C176 thus does not specifically influence the nucleotide loop conformation of the known B_{12} coenzymes in their "base-on" forms, but is expected to destabilize the alternative staggered "base-off" conformations (see below and Figures 2 and 3).

The methyl group at C176 is derived from threonine phosphate,[20] whereas for the ethanolamine linker of norcobamides, serine has been considered as the biosynthetic precursor.[8] The presence of the methyl group in **4** appears to be a consequence neither of a restricted biosynthetic supply (threonine versus serine), nor of an inherent specific adaptation of the base-on form of the complete cobamides. However, as discussed by Eschenmoser,[4,6] the methyl group and an *R* configuration at C176 is expected to allow for (relatively) less instable "precyclic" (base-off) conformations of the nucleotide appendage in favor of the formation of the cobalt-coordinated base-on form. On one hand, this could assist the complete B_{12} structure to self-constitute,[6] however, it could also influence the base-on/base-off equilibria of complete cobamides. These cobamides are considered to be molecular switches[21] that are in control of their organometallic redox chemistry. Such a property could also be critical for the binding and recognition of complete B_{12} derivatives (either in their base-on or their base-off forms) by biological macromolecules, such as proteins[2,3,22,23] and oligonucleotides.[21,24]

To assess the effect of the C176 methyl group on a representative B_{12} base-on/base-off equilibrium, the tendency

 © 2006 Wiley-VCH Verlag GmbH & Co. KGaA, Weinheim



Scheme 2. Outline of the preparation of norvitamin B_{12} (**1**) and methylnorcobalamin (**2**) from vitamin B_{12} (**4**) via cobyric acid (**7**) (see the Supporting Information).[15]

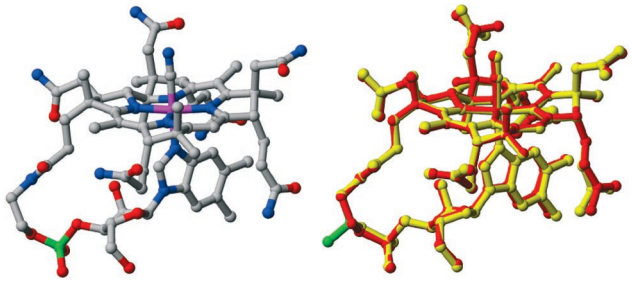


Figure 1. Left: Crystal structure of norvitamin B_{12} (**1**), ball-and-stick model with C, N, O, P, Co atoms colored gray, blue, red, green, and pink, respectively. Right: Superposition of models of the 3D structures of **1** (red) and of vitamin B_{12} (**4**)[16] (yellow, C176 methyl labeled green).

of **2** to undergo acid-induced decoordination of its nucleotide base was determined and compared with the corresponding process in **5**.[25] In the base-on form of **5**, the rather strong intramolecular coordination of the dimethylbenzimidazole base is reflected by a low $pK_a(\text{H-}\mathbf{5}^+) = 2.90$[25] (**5** protonated at N3N). The acidity of the corresponding protonated base-off form of **2**, that is, of H-$\mathbf{2}^+$, could be determined by UV/Vis spectroscopy (see Figure 3), which provides a $pK_a(\text{H-}\mathbf{2}^+) = 3.24$. As $pK_a(\text{H-}\mathbf{2}^+) - pK_a(\text{H-}\mathbf{5}^+) = 0.34$, **2** is therefore approximately twice as basic as **5** (with protonation at the dimethylbenzimidazole nitrogen N3N). From the two pK_a values, the nucleotide coordinated base-on state is deduced to be disfavored at room temperature by a factor of about 2.1 in **2**, when compared with **5**.

As was expected[4,5] in "complete" cobamides, such as **4** or **5**, the methyl group at C176 is influential. It helps constitute the base-on form, as explained by qualitative conformational analysis (see Figure 2). Indeed, a remarkable long-distance constitutional effect of the methyl group at C176 is observed at the corrin-bound cobalt center. The methyl group assists the nucleotide base to find its coordination partner at a distance of 11 bonds away. Norcobamides, which are devoid of the methyl-group pivot, are predicted to have a higher tendency to be base-off and to be, in general, reduced at more positive potentials.[18,26] This may be relevant in dehalogenating anaerobes, one of which was shown to use the norcobamide norpseudo B_{12} as a cofactor.[8]

The presence of the methyl group at C176 in cobamides is a feature of complete "B_{12} dinucleotides": they provide a more stable base-on constitution and assist the (reversible) back binding, in a loop, of one nucleotide appendage to the other (cobalt–corrin). The propensity for the formation of

 © 2006 Wiley-VCH Verlag GmbH & Co. KGaA, Weinheim

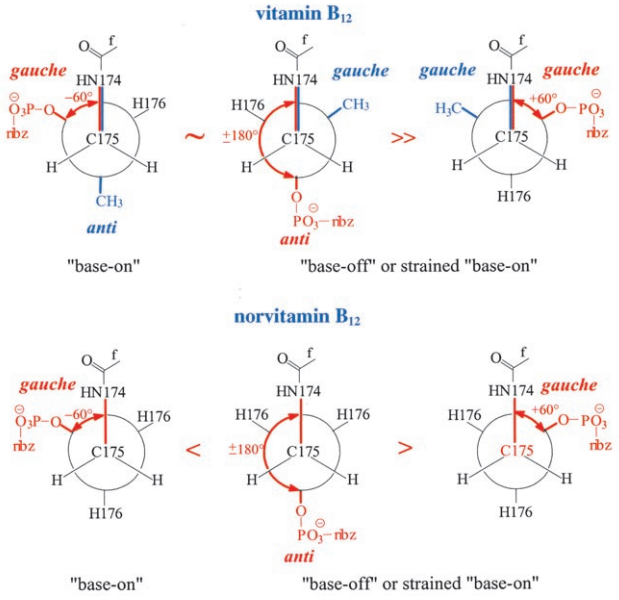


Figure 2. Qualitative analysis of the effect of the C176 methyl group by using idealized conformations around the (C175–C176) bond. Top: cobalamins (e.g. vitamin B_{12}); bottom: norcobalamins (e.g. norvitamin B_{12}). A torsion angle of approximately −60° is observed in the base-on cobalamins and is required in the "precyclic" forms (base-off form in which the base is preoriented towards coordination at the cobalt center);[6] other staggered conformations (+60°, 180°) are base-off and do not allow strain-free base-on forms. The methyl group at C176 of vitamin B_{12} is *gauche* and found to destabilize the 60° and 180° (base-off) conformations, but not the −60° (base-on) conformation (ribz = α-ribazole = 5′,6′-dimethylbenzimidazolyl-α-nucleoside).

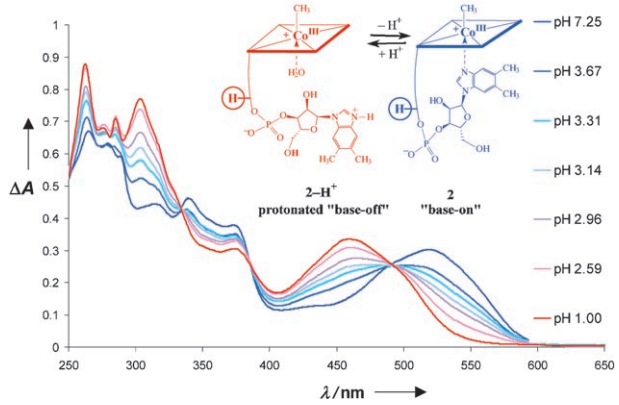


Figure 3. The B_{12} "molecular switch", as represented by **2** and 2-H^+: pH dependence of UV/Vis spectra of buffered aqueous solutions of methylnorcobalamin (**2**) ([**2**] = 0.45 mM; at the indicated pH values, 1.0 M KCl, room temperature; see the Supporting Information).

such a loop is inherent to the B_{12} structure and is conjectured to be critical for the presumed role of B_{12} in primordial life.[4] This nucleotide loop (as in B_{12}) is unique in cofactors and is preserved only in part in B_{12}-dependent enzymes. Both constitutional types of B_{12} cofactors are found as either base-on or base-off forms. In some organisms, the presence of the methyl group at C176 of the "complete" cobamides seems to offer no functional advantage, but may merely be a consequence of the genetically programmed B_{12} biosynthesis. The methyl group at C176 thus appears to reflect the "fossil origin" of the B_{12} structure[5] and invites further investigations, as are currently carried out in our labs.

Received: July 27, 2005
Published online: December 22, 2005

Keywords: bioorganometallic chemistry · conformation analysis · molecular switch · structure elucidation · vitamin B_{12}

[1] J. Stubbe, *Science* **1994**, *266*, 1663–1664.
[2] *Vitamin B_{12} and B_{12}-Proteins* (Eds.: B. Kräutler, B. T. Golding, D. Arigoni), Wiley-VCH, Weinheim, **1998**.
[3] *Chemistry and Biochemistry of B_{12}* (Ed.: R. Banerjee), Wiley, New York, **1999**.
[4] A. Eschenmoser, *Angew. Chem.* **1988**, *100*, 5–40; *Angew. Chem. Int. Ed. Engl.* **1988**, *27*, 5–40.
[5] A. Eschenmoser, *Nova Acta Leopold.* **1982**, *55*, No. 247.
[6] A. Eschenmoser, F. Kreppelt, unpublished work; see F. Kreppelt, PhD thesis no. 9458, ETH-Zürich **1991**.
[7] For a review of earlier work, see: W. Friedrich in *Fermente, Hormone und Vitamine, Vol. III/2* (Eds.: R. Ammon, W. Dirscherl), Georg Thieme, Stuttgart, **1975**, pp. 25.
[8] B. Kräutler, W. Fieber, S. Ostermann, M. Fasching, K.-H. Ongania, K. Gruber, C. Kratky, C. Mikl, A. Siebert, G. Diekert, *Helv. Chim. Acta* **2003**, *86*, 3698–3716.
[9] R. B. Woodward in *Vitamin B_{12}, Proceedings of the 3rd European Symposium on Vitamin B_{12} and Intrinsic Factor* (Eds.: B. Zagalak, W. Friedrich), Walter de Gruyter, Berlin, **1979**, pp. 37–87.
[10] a) W. Friedrich in *Vitamin B_{12} and Intrinsic Factor* (Ed.: H. C. Heinrich), Enke, Stuttgart, **1962**, pp. 62–72; b) K. Bernhauer, O. Müller, F. Wagner, *Angew. Chem.* **1963**, *75*, 1145–1188; *Angew. Chem. Int. Ed. Engl.* **1964**, *3*, 200–211.
[11] R. Bonnet in *B_{12}* (Ed.: D. Dolphin), Wiley, New York, **1982**, pp. 201–243.
[12] R. Konrat, M. Tollinger, B. Kräutler in *Vitamin B_{12} and B_{12}-Proteins* (Eds.: B. Kräutler, B. T. Golding, D. Arigoni), Wiley-VCH, Weinheim, **1998**, pp. 349–368.
[13] K. Brown in *Chemistry and Biochemistry of B_{12}* (Ed.: R. Banerjee), Wiley, New York, **1999**, pp. 197–237.
[14] A. M. Calafat, L. G. Marzilli, *J. Am. Chem. Soc.* **1993**, *115*, 9182–9190.
[15] Selected spectroscopic data: **1**: UV/Vis ($c = 5.59 \times 10^{-4}$ M, H_2O): 548(3.85), 518.5(3.80), 407(3.47), 360(4.36), 321.5(3.81), 304.5-(3.88), 277.5(4.10); FAB-MS: 1343.5 (13), 1342.5 (22), 1341.5 (24, $[M+H]^+$), 1317.6 (57), 1316.4 (100), 1315.5 (94, $[M+H-CN]^+$); **2**: UV/Vis ($c = 4.51 \times 10^{-4}$ M, 0.1 M phosphate buffer, pH 7.25): 518.5 (3.83), 373.5 (3.93), 339 (4.01), 314.5 (4.00), 279 (4.15), 265 (4.18); FAB-MS: 1332.6 (24), 1331.6 (43), 1330.6 (52, $[M+H]^+$), 1317.6 (68), 1316.5 (100), 1315.6 (76, $[M+H-CH_3]^+$); **8**: ^{1}H NMR (300 MHz, D_2O): $\delta = 2.37$ (3H, s; CH_3), 2.39 (3H, s; CH_3), 3.19 (2H, t; $H_2NCH_2CH_2O$), 3.83 (1H, dd; $J = 4.2$ Hz, $J = 12.6$ Hz; H_aC5R), 3.95 (1H, dd, $J = 2.7$ Hz, $J = 12.6$ Hz, H_bC5R), 4.08 (2H, m; $H_2NCH_2CH_2O$), 4.62 (1H, m; HC4R), 4.7–4.9 (water signal overlaps with signals of HC2R, HC3R), 6.41 (1H, d, $J = 4.5$ Hz; HC1R), 7.45 (1H, s; aromatic CH), 7.53 (1H, s; aromatic CH), 8.34 ppm (1H, s; HC2N). UV/Vis ($c = 9.97 \times 10^{-4}$ M, 0.1 M phosphate buffer, pH 7.25): 286.5(4.05), 278.5(4.07), 248(4.21). ESI-MS: 439.97 (20, $[M+K]^+$), 423.97 (5, $[M+Na]^+$), 404.03 (5), 403.02 (20), 402.01 (100, $[M+H]^+$), 146.97(10). Further details are given in the supporting information. Structure determination of **1**: Crystals were grown from water/

 © 2006 Wiley-VCH Verlag GmbH & Co. KGaA, Weinheim

acetone. Diffraction data (space group $P2_12_12_1$, $a = 15.573$ Å, $b = 22.846$ Å, $c = 24.583$ Å, $R_{sym} = 0.039$) to a maximum resolution of 0.85 Å were collected at 103 K by using synchrotron radiation ($\lambda = 0.8426$ Å) on beam line BW7b at EMBL/DESY in Hamburg. Refinement on F^2 (7744 unique reflections, 1131 parameters and 1693 restraints) converged at crystallographic residuals of $R1 = 0.0796$ and $wR2 = 0.2137$ for all reflections. Details are given in the supporting information. CCDC-278 482 (**1**) contains the supplementary crystallographic data for this paper. These data can be obtained free of charge from The Cambridge Crystallographic Data Centre via www.ccdc.cam.ac.uk/data_request/cif.

[16] B. Kräutler, R. Konrat, E. Stupperich, G. Färber, K. Gruber, C. Kratky, *Inorg. Chem.* **1994**, *33*, 4128 – 4139.

[17] C. Kratky, B. Kräutler in *Chemistry and Biochemistry of B_{12}* (Ed.: R. Banerjee), Wiley, New York, **1999**, pp. 9 – 41. The fold angle of the corrin ligand is defined (here) as the angle between the best planes through atoms N1-C4-C5-C6-N2-C9-C10 (plane 1) and C10-C11-N3-C14-C15-C16-N4 (plane 2); see the Supporting Information for atom numbering.

[18] B. Kräutler in *Chemistry and Biochemistry of B_{12}* (Ed.: R. Banerjee), Wiley, New York, **1999**, pp. 315 – 339.

[19] M. Tollinger, T. Dérer, R. Konrat, B. Kräutler, *J. Mol. Catal. A* **1997**, *116*, 147 – 155.

[20] D. Thibaut, F. Blanche, B. Cameron, J. Crouzet, L. Debussche, E. Rémy, M. Vuilhorgne in *Vitamin B_{12} and B_{12}-Proteins* (Eds.: B. Kräutler, B. T. Golding, D. Arigoni), Wiley-VCH, Weinheim, **1998**, pp. 63 – 80.

[21] S. Gschösser, K. Gruber, C. Kratky, C. Eichmüller, B. Kräutler, *Angew. Chem.* **2005**, *117*, 2324 – 2328; *Angew. Chem. Int. Ed.* **2005**, *44*, 2284 – 2288.

[22] S. Fedosov, L. Berglund, N. U. Fedosova, E. Nexø, T. E. Petersen, *J. Chem. Biol.* **2002**, *277*, 9989 – 9996.

[23] C. L. Drennan, S. Huang, J. T. Drummond, R. G. Matthews, M. L. Ludwig, *Science* **1994**, *266*, 1669 – 1674.

[24] A. Nahvi, N. Sudarsan, M. S. Ebert, X. Zou, K. L. Brown, R. R. Breaker, Chem. Biol. **2002**, *9*, 1043 – 1049.

[25] K. L. Brown, S. Peck-Siler, *Inorg. Chem.* **1988**, *27*, 3548 – 3555.

[26] D. Lexa, J. M. Savéant, *Acc. Chem. Res.* **1983**, *16*, 235 – 243.

 © 2006 Wiley-VCH Verlag GmbH & Co. KGaA, Weinheim

Drug Design

DOI: 10.1002/anie.200502770

NMR Characterization of Kinase p38 Dynamics in Free and Ligand-Bound Forms**

*Martin Vogtherr, Krishna Saxena, Swen Hoelder, Susanne Grimme, Marco Betz, Ulrich Schieborr, Barbara Pescatore, Michel Robin, Laure Delarbre, Thomas Langer, K. Ulrich Wendt, and Harald Schwalbe**

Rational drug design depends on the definition of targets, and today lead discovery often addresses target classes rather than single proteins. This approach increases efficiency because results can often be transferred to many other members of the same target class. Particularly attractive in this respect is protein kinases. These are involved in a multitude of cellular processes and thus involved in numerous diseases. All 518 known protein kinases[1] share the same tertiary structure and catalyze analogous reactions: the phosphorylation of proteins. Nevertheless, each kinase has unique structural details, for example, protein–protein interaction segments, or specific dynamic properties. This uniqueness of a protein kinase can be exploited pharmaceutically to create specificity.[2]

Many protein kinase inhibitors such as staurosporine bind to the highly conserved ATP binding site. They consequently target a multitude of protein kinases which limits their pharmaceutical use. However, some drugs are highly specific because they target a unique property of one protein kinase. For example, gleevec, a specific inhibitor of the Abelson kinase,[3,4] binds to the highly conserved Asp-Phe-Gly loop (DFG loop). When complexed with gleevec, the DFG loop adopts the "DFG-out" conformation that differs substantially from the "DFG-in" conformation seen in complex structures with ATP analogues and most ATP-competitive inhibitors. This movement accompaning the conformational change from DFG-in to DFG-out opens up a hydrophobic pocket

[*] Dr. M. Vogtherr, Dr. K. Saxena, Dr. S. Grimme, Dr. M. Betz, Dr. U. Schieborr, Dr. B. Pescatore, Dr. T. Langer, Prof. Dr. H. Schwalbe
Johann Wolfgang Goethe-University Frankfurt
Institute for Organic Chemistry and Chemical Biology
Center for Biomolecular Magnetic Resonance
Marie Curie Strasse 11, 60439 Frankfurt am Main (Germany)
Fax: (+49) 69-798-29515
E-mail: schwalbe@nmr.uni-frankfurt.de

Dr. S. Hoelder, Dr. K. U. Wendt
Sanofi-Adventis Deutschland GmbH
65926 Frankfurt am Main (Germany)

Dr. M. Robin, Dr. L. Delarbre
Sanofi-Aventis
Centre de recherche Vitry-sur-Seine
13, quai Jules BP 14
94403 Vitry-sur-Seine Cedex (France)

[**] These results were generated from a cooperation between Sanofi-Aventis and the Center for Biomolecular Magnetic Resonance. We thank Matthias Dreyer for critical comments on the manuscript.

© 2006 Wiley-VCH Verlag GmbH & Co. KGaA, Weinheim

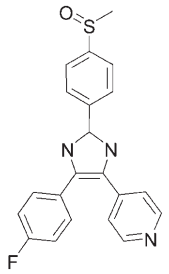
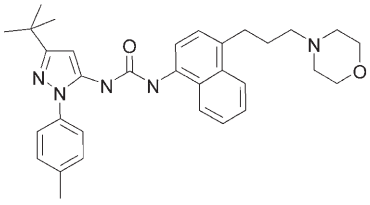
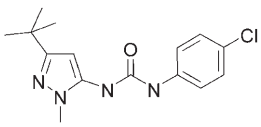
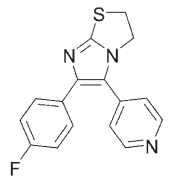
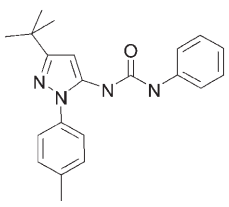
between the N- and C-terminal regions. Only kinases which can adopt the DFG-out conformation can form interactions with this pocket. Thus, selectivity is brought about by unique selection of the conformational space of the kinase.

This recognition principle has since been used with other kinases such as Raf,[5] p38,[6–8] and KDR[9] in a successful application of the target class philosophy. Classification of an inhibitor as DFG-in or DFG-out remains a difficult task that requires detailed structural or kinetic analysis. Moreover, knowledge on the DFG-in/DFG-out equilibrium is mainly based on static X-ray structures of free and ligand-bound proteins. NMR studies can complement these studies to gain a more thorough understanding of this equilibrium in solution.

We recently characterized MAP kinase p38 by NMR spectroscopy[10] and use this as a model to study the DFG-in/DFG-out equilibrium. p38 is involved in the regulation of pro-inflammatory cytokines[11,12] and its inhibition is utilized by anti-inflammatory drugs. Several p38 inhibitors are structurally and biophysically well-characterized (Table 1).[13–15] p38 inhibitors **1** and **4** bind to the DFG-in conformation[16] that is also observed for apo p38.[17] In contrast, p38 inhibitors **2** and **3** of the diarylurea class were found to bind to the DFG-out conformation.[6] In the p38·**2** complex, Phe169 (p38 numbering) is displaced by 10 Å from the position seen in apo p38.

The NMR assignment of p38[10] is incomplete. Spectra of uniformly ^{15}N-labeled p38 gives amide signals of only 254 (75%) out of 337 expected signals, 216 (85%) of which could be assigned. This is neither due to signal overlap nor to incomplete amide protonation,[18] since a similar number of signals is also missing in selectively ^{15}N-labeled samples. The absence of 25% of the expected signals must have more fundamental reasons. The assignment is nearly complete (79%) for the N-terminal domain of the kinase excluding the C helix. In the C-terminal region, the DFG motif (Asp168-Phe169-Gly170), the adjacent activation loop (Leu171-Glu178), and significant parts of subdomains VIII and X are unassigned. Notably, the related sequence stretches are also missing in our chemical-shift assignment of protein kinase A (PKA).[19] The C helix and activation loop have been shown to be involved in motions during kinase activation and cataly-

Table 1: Chemical structures, interaction modes, and published biophysical data for selected p38 inhibitors.[a]

	Structure	K_D [nM]	k_{on} [$M^{-1}s^{-1}$]	k_{off} [s^{-1}]	ΔH [kJ mol^{-1}]	$-\Delta S$ [J mol^{-1} K^{-1}]	PDB[b]	Mode
1		11.5	1.5×10^{7}	1.8×10^{-1}	−47.3	9.2	1a9u	DFG-in
2		0.1	8.4×10^{4}	8.3×10^{-6}	−52.7	−35	1kv2	DFG-out
3		1160	1.2×10^{5}	1.4×10^{-1}	−23.4	−14.5	1kv2	DFG-out
4		86.5	4.3×10^{7}	7.7×10^{-1}	−55.6	53.5		DFG-in
5		21	7.3×10^{4}	1.6×10^{-3}	−48.5	15.9		DFG-out

[a] Data for compounds **2**, **3**, and **5** at 296 K were taken from Refs. [7,13] (K_D, k_{on}, k_{off}) and Ref. [15] (ΔH), ΔS values were calculated from standard thermodynamic relationships. All data for compounds **1** and **4** were taken from Refs. [7,14]. [b] Reference number for Protein Data Bank.

 © 2006 Wiley-VCH Verlag GmbH & Co. KGaA, Weinheim

sis.[20] Such motions can explain the disappearance of signals since they lead to line broadening in the NMR spectra through exchange. Exchange processes can readily be detected by NMR spectroscopy and are classified as being fast (one average signal), slow (one signal for each conformational state), or intermediate (the signal is strongly broadened or not visible). If other experimental reasons are excluded, the disappearance of an NMR signal beyond the detection limit is due to conformational exchange processes in the intermediate timescale that lead to severe line broadening.

The NMR signals of the DFG loop (Asp168-Phe169-Gly170) were not assigned. Selectively ^{15}N-Phe-labeled p38 was investigated to study the DFG loop. p38 contains 13 phenylalanine residues, 12 of which can be detected in the

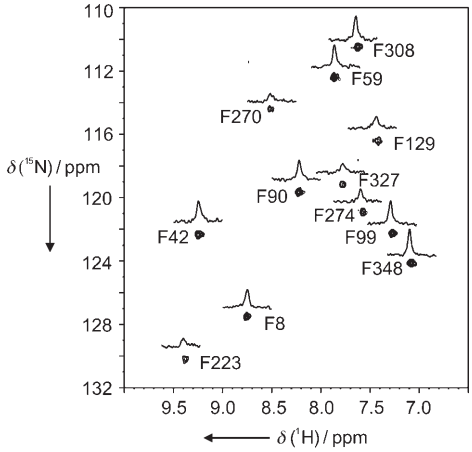


Figure 1. TROSY spectrum of selectively ^{15}N-Phe-labeled p38. The assignment of the signals is indicated. One-dimensional cross-sections are shown for each signal. The signal corresponding to Phe169 is missing.

^{1}H,^{15}N TROSY spectrum (Figure 1). The 12 visible signals have been unambiguously assigned; the unobserved signal belongs to Phe169 in the DFG loop. This finding was confirmed by the spectrum of selectively ^{15}N-Phe-labeled mutant Phe169Tyr which exhibited an identical TROSY spectrum with 12 signals. Altered field strengths (400–900 MHz proton resonance frequencies), temperatures (5–35 °C), and more sensitive acquisition conditions (0.5 mM sample, 12 h measurement time on a 900 MHz spectrometer with cryoprobe technology) did not affect the result. The absence of the amide signal for Phe169 in the DFG motif under all the conditions tested is consistent with a conformational equilibrium of intermediate timescale for this region of the kinase.

Diarylurea compounds such as **2** were shown to bind to the DFG-out conformation of p38. Binding of these compounds to p38 must interfere with conformational exchange processes of the DFG loop since it is not compatible with the DFG-in conformation.[6] If this interference is strong enough to suppress the DFG-in/DFG-out interconversion, then no exchange line broadening is expected and the Phe169 signal should be observed. The resulting NMR spectrum of p38 in the presence of **2** shows that this is indeed the case (Figure 2a). All 13 signals predicted from the primary sequence are visible. Since Asp168-Phe169 is the only Asp-Phe pair in the p38 primary sequence, the identity of the

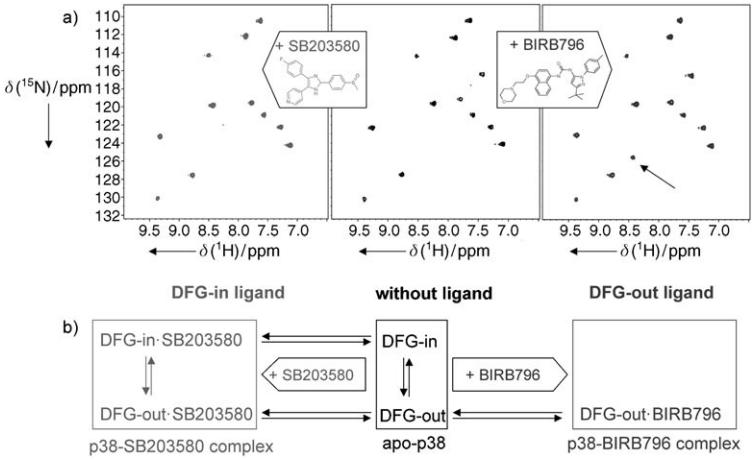


Figure 2. a) Effect of p38 inhibitors on the TROSY spectrum of selectively ^{15}N-Phe-labeled p38. The DFG-out inhibitor BIRB796 (**2**) leads to one additional signal (indicated by an arrow) belonging to Phe169 of the DFG motif. "DFG-in" binder SB203580 (**1**) produces chemical-shift perturbations but no additional signal. b) Kinetic scheme for the conformational exchange of the DFG motif in p38. In the apo protein the DFG-in and DFG-out forms are in slow (kHz) conformational exchange. Ligand **2** binds to the DFG-out conformation and freezes the conformational equilibrium in a defined state. Ligands such as **1** leave the DFG equilibrium unaffected.

additional signal (Phe169) is confirmed by a HNCO-type experiment on a selectively ^{13}C′-labeled Asp/^{15}N-labeled Phe sample. The appearance of the Phe169 signal confirms that no exchange and concomitant line broadenings takes place through exchange in the DFG-out inhibited state of the protein.

Similar results are obtained with other compounds of the diarylurea type, such as **3** (Table 1). These data provide evidence for a slow DFG-in/DFG-out equilibrium that results in disappearance of the Phe169 signal in the spectra of apo p38, while DFG-out inhibitors such as **2** and **3** appear to suppress the conformational exchange between conformers, thus resulting in the appearance of the Phe169 signal in the 2D NMR spectra. The experiments are consistent with the kinetic scheme shown in Figure 2b.

In contrast to the diarylurea compounds, most other p38 binders have been described as DFG-in binders. In the published crystal structure of such a compound bound to p38,[16] the protein has been found in the DFG-in conformation that is also seen in the crystal structures of apo p38.[17] SB203580 (**1**) is a DFG-in ligand of p38 and invokes no additional signals in the TROSY spectrum of ^{15}N-Phe-p38 (Figure 2a); this situation is also true for other DFG-in binders such as SKF86002 (**4**). Consequently, the equilibrium between different DFG states leading to the disappearance of the Phe169 signal is unperturbed by these ligands. We therefore suggest that the known "DFG-in" binders are perhaps better described as inhibitors for which the con-

 © 2006 Wiley-VCH Verlag GmbH & Co. KGaA, Weinheim

formation of the DFG loop does not affect binding (Figure 2b). This suggestion is in agreement with the finding that DFG-in ligands do not interfere with the activation of p38,[21] whereas DFG-out inhibitors block both the activity and activation of p38.[22]

The dynamic picture derived by NMR spectroscopy is supported by our crystal structure of **1** complexed with p38 (Figure 3). We observe both conformations of the DFG motif

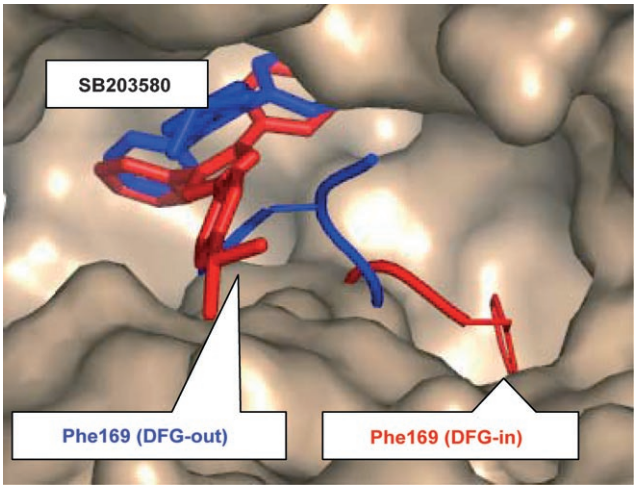


Figure 3. Crystal structure of p38 complexed with inhibitor **2** (2.1 Å resolution; $R_{factor} = 0.241$; $R_{free} = 0.279$). Shown is a molecular-surface representation of p38 with the main chain of the DFG motif highlighted in red (DFG-in conformation) and blue (DFG-out conformation). Phe169 and **2** are shown as stick representations and are color coded in red (DFG-in) and blue (DFG-out). In the DFG-in form, the side chain of Phe169 resides in a hydrophobic pocket, whereas it points outwards in the DFG-out form. We observe approximate occupancies of 50% for the DFG-in and DFG-out conformations in the ensemble average of our crystal.

(DFG-in and DFG-out) in the protein at relative occupancies of around 50%. In addition, we observe distinct binding positions of inhibitor **1** (50% occupancy) for each of the DFG conformations. Polar interactions between the inhibitor and the hinge region are maintained in both positions. The observation of two defined DFG states is in agreement with the lack of a Phe169 signal in the NMR spectra. It also confirms that interaction with DFG-in binders is compatible with the DFG-out conformation of the DFG loop, which has already been put to use in combining DFG-in and DFG-out ligands.[23]

To date, indirect evidence for a slow DFG-in⇄DFG-out equilibrium has come from analyses of rates for the binding of different DFG-out inhibitors. While the rates of DFG-in inhibitors binding to the protein can be regarded as diffusion controlled (Table 1), the rates of DFG-out inhibitors of similar molecular size are two orders of magnitude lower.[6,13] This observation has been interpreted as evidence for a slow equilibrium between DFG-in and DFG-out conformations in apo p38, where the DFG-out conformation is sampled only infrequently.[6,7] Our studies strongly suggest that the DFG motif in apo p38 is in conformational exchange between substantially different conformations in the intermediate NMR time regime. Diarylurea inhibitors suppress the conformational exchange and freeze the motion in the DFG-out conformation. These motions are influenced to a lesser extend by binders traditionally known as DFG-in binders. Possible restrictions on mobility must be neglible as they do not alter the dynamic NMR properties of p38 relative to the apo protein.

Since a DFG-out ligand suppresses the conformational exchange equilibrium between conformers, some degrees of freedom are lost and a negative entropy could be expected to be a hallmark of DFG-out binders. Available thermodynamic data[14,15] (Table 1) show, however, that there is no general trend for DFG-in versus DFG-out inhibitors. Thus, thermodynamic data cannot be used as an analytical tool to identify a DFG-out binding mode. In contrast, NMR studies of labeled p38 provide a tool to unambiguously and quickly classify a ligand as a DFG-in or as a DFG-out binder, which would otherwise require cocrystallization and/or a detailed kinetic analysis of the binding process. This approach can rapidly characterize new structures from screening for their principal binding mode (DFG-in versus DFG-out) with p38.

Experimental Section

Protein production: Murine p38α (2–349) was cloned into a modified pET16b vector with an N-terminal His tag followed by a TEV protease cleavage site. The resulting plasmid pETp38 was used as a template for site-directed mutagenesis of p38 F169Y. Recombinant p38 was overexpressed in *E. coli* strain BL21 (DE3) harboring the expression plasmid pETp38 and purified as in Ref. [19]. Bacterial cultures were grown to $OD_{600} = 0.6$, supplemented with isopropyl-β-D-thiogalactopyranoside (IPTG), and incubated at 30 °C for 4 h. Selective ^{15}N-labeling of amino acids was done according to a published method.[19].

NMR spectroscopy: NMR spectra were measured at 800 MHz proton frequency on a Bruker DRX800 spectrometer. Conditions: 0.2–0.7 mM protein, 150 mM NaCl, 50 mM 2-[4-(2-hydroxyethyl)-1-piperazinyl]ethanesulfonic acid (hepes) pH 6.8, 5 mM dithiothreitol (DTT) in H_2O/D_2O (9:10), measuring temperature 298 K. Ligands **1** and **4** (Sigma) and **2**, **3**, and **5** (synthesized according to Ref. [7]) were added as 50–100 mM stock solutions in DMSO to yield a final ligand concentration of 0.2–1 mM.

Table 2: X-ray diffraction data and structure refinement of the p38·**1** complex.[a]

	p38·**1**
space group	$P2_12_12_1$
resolution [Å]	2.1
completeness [%]	99.5 (99.3)
redundancy	4.8 (4.9)
$I/\sigma I$	8.2 (2.0)
R_{merge} [%]	5.3 (34.8)
Wilson *B* values [Å^2]	41.3
Refinement	
resolution range [Å]	50–2.1
no. reflections	23 123
R_{free}/R [%]	27.9/24.1
RMSD bonds/angles [Å/°]	0.0060/1.11
average *B* values [Å^2]	46.4

[a] Numbers in parentheses refer to the highest resolution shell.

 © 2006 Wiley-VCH Verlag GmbH & Co. KGaA, Weinheim

Crystallography: Crystals of the p38·**1** complex were obtained by vapor diffusion at 4 °C. The protein solution (5 mg mL^{-1}, 1 mM **1**, 1 mM tris(2-carboxyethyl)phosphine hydrochloride (TCEP), 50 mM NaCl, 5 mM tris(hydroxymethyl)aminomethane (Tris, pH 7.0)) was mixed with the same volume of precipitant solution (7% v/v 2-methyl-2,4-pentanediol (MPD) and 50 mM 2-(*N*-morpholino)ethanesulfonic acid (Mes) pH 6.0). Crystals were soaked in a cryo-protection solution (1 mM **1**, 30% v/v MPD, 50 mM Mes pH 6.0) and were then flash frozen in liquid nitrogen. Data were collected at 100 K on an ADSC Q4 CCD detector at the European Synchrotron Radiation Facility (Grenoble, France). The structure was obtained using standard software (Table 2).[24] The coordinates have been deposited in the Protein Data Bank with accession code 2EWA.

Received: August 5, 2005
Revised: October 15, 2005
Published online: December 22, 2005

Keywords: drug design · enzyme inhibitors · NMR spectroscopy · protein kinases

[1] G. Manning, D. B. Whyte, R. Martinez, T. Hunter, S. Sudarsanam, *Science* **2002**, *298*, 1912.
[2] M. E. M. Noble, J. Endicott, L. K. Johnson, *Science* **2004**, *303*, 1800.
[3] T. Schindler, W. Bornmann, P. Pellicena, W. T. Miller, B. Clarkson, J. Kuriyan, *Science* **2000**, *289*, 1938.
[4] B. Nagar, W. G. Bornmann, P. Pellicena, T. Schindler, D. R. Veach, W. T. Miller, B. Clarkson, J. Kuriyan, *Cancer Res.* **2002**, *62*, 4236.
[5] P. T. Wan, M. J. Garnett, S. M. Roe, S. Lee, D. Niculescu-Duvaz, V. M. Good, C. M. Jones, C. J. Marshall, C. J. Springer, D. Barford, *Cell* **2004**, *116*, 855.
[6] C. Pargellis, L. Tong, L. Churchill, P. F. Cirillo, T. Gilmore, A. G. Graham, P. M. Grob, E. R. Hickey, N. Moss, S. Pav, J. Regan, *Nat. Struct. Biol.* **2002**, *9*, 268.
[7] J. Regan, S. Breitfelder, P. Cirillo, T. Gilmore, A. G. Graham, E. Hickey, B. Klaus, J. Madwed, M. Moriak, N. Moss, C. Pargellis, S. Pav, A. Proto, A. Swinamer, L. Tong, C. Torcellini, *J. Med. Chem.* **2002**, *45*, 2994.
[8] J. Branger, B. van den Blink, S. Weijer, J. Madwed, C. L. Bos, A. Gupta, C. L. Yong, S. H. Polmar, D. P. Olszyna, C. E. Hack, S. J. H. van Deventer, M. P. Peppelenbosch, T. van der Poll, *J. Immunol.* **2002**, *168*, 4070.
[9] P. W. Manley, G. Bold, J. Bruggen, G. Fendrich, P. Furet, J. Mestan, C. Schnell, B. Stolz, T. Meyer, B. Meyhack, W. Stark, A. Strauss, J. Wood, *Biochim. Biophys. Acta* **2004**, *1697*, 17.
[10] M. Vogtherr, K. Saxena, S. Grimme, M. Betz, U. Schieborr, B. Pescatore, T. Langer, H. Schwalbe, *J. Biomol. NMR* **2005**, *32*, 175.
[11] K. A. Gallo, G. L. Johnson, *Nat. Rev. Mol. Cell Biol.* **2002**, *3*, 663.
[12] S. Kumar, J. Boehm, J. C. Lee, *Nat. Rev. Drug Discovery* **2003**, *2*, 717.
[13] J. Regan, C. A. Pargellis, P. F. Cirillo, T. Gilmore, E. R. Hickey, G. W. Peet, A. Proto, A. Swinamer, N. Moss, *Bioorg. Med. Chem. Lett.* **2003**, *13*, 3101.
[14] D. Casper, M. Bukhtiyarova, E. B. Springman, *Anal. Biochem.* **2004**, *325*, 126.
[15] R. R. Kroe, J. Regan, A. Proto, G. W. Peet, T. Roy, L. D. Landro, N. G. Fuschetto, C. A. Pargellis, R. H. Ingraham, *J. Med. Chem.* **2003**, *46*, 4669.
[16] Z. Wang, B. J. Canagarajah, J. C. Boehm, S. Kassisa, M. H. Cobb, P. R. Young, S. Abdel-Meguid, J. L. Adams, E. J. Goldsmith, *Structure* **1998**, *6*, 1117.
[17] a) K. P. Wilson, M. J. Fitzgibbon, P. R. Caron, J. P. Griffith, W. Chen, P. G. McCaffrey, S. P. Chambers, M. S. Su, *J. Biol. Chem.* **1996**, *271*, 27696; b) Z. Wang, P. C. Harkins, R. J. Ulevitch, J. Han, M. H. Cobb, E. J. Goldsmith, *Proc. Natl. Acad. Sci. USA* **1997**, *94*, 2327.
[18] F. Löhr, V. Katsemi, J. Hartleib, U. Günther, H. Rüterjans, *J. Biomol. NMR* **2003**, *25*, 291.
[19] T. Langer, M. Vogtherr, B. Elshorst, M. Betz, U. Schieborr, K. Saxena, H. Schwalbe, *ChemBioChem* **2004**, *5*, 1508.
[20] D. A. Johnson, P. Akamine, E. Radzio-Andzelm, Madhusudan, S. S. Taylor, *Chem. Rev.* **2001**, *101*, 2243.
[21] S. Kumar, M. S. Jiang, J. L. Adams, J. C. Lee, *Biochem. Biophys. Res. Commun.* **1999**, *263*, 825.
[22] Y. Kuma, G. Sabio, J. Bain, N. Shpiro, R. Márquez, A. Cuenda, *J. Biol. Chem.* **2005**, *280*, 19472–19479.
[23] A. L. Gill, M. Frederickson, A. Cleasby, S. J. Woodhead, M. G. Carr, A. J. Woodhead, M. T. Walker, M. S. Congreve, L. A. Devine, D. Tisi, M. O'Reilly, L. C. A. Seavers, D. J. Davis, J. Curry, R. Anthony, A. Padova, C. W. Murray, R. A. E. Carr, H. Jhoti, *J. Med. Chem.* **2005**, *48*, 414.
[24] a) Collaborative Computing Project Number 4, *Acta Crystallogr. Sect. D* **1994**, *50*, 760; b) A. T. Brünger, P. D. Adams, G. M. Clore, W. L. DeLano, P. Gros, R. W. Grosse-Kunstleve, J. S. Jiang, J. Kuszewski, M. Nilges, N. S. Pannu, R. J. Read, L. M. Rice, T. Simonson, G. L. Warren, *Acta Crystallogr. Sect. D* **1998**, *54*, 905; c) A. Jones, M. Kjeldgaard, *Methods Enzymol.* **1997**, *277*, 173.

 © 2006 Wiley-VCH Verlag GmbH & Co. KGaA, Weinheim